

Oceanic Fronts and Related Phenomena (Konstantin Fedorov Memorial Symposium), Pushkin, 1998

Intergovernmental Oceanographic Commission

Workshop Report No. 159

OCEANIC FRONTS AND RELATED PHENOMENA

Konstantin Fedorov International Memorial Symposium

Pushkin, Saint Petersburg
Russian Federation
18-22 May 1998

Proceedings

UNESCO

Workshop Report No. 159
Pushkin, Saint Petersburg, 18-22 May 1998
English only

ISBN 5-89118-155-X

© UNESCO 2000
Printed in Moscow
Russian Federation
GEOS

KONSTANTIN FEDOROV INTERNATIONAL MEMORIAL SYMPOSIUM

A Symposium organized by the

P.P. Shirshov Institute of Oceanology
Russian Academy of Sciences, Moscow
and the
Russian State Hydrometeorological University, St. Petersburg

With the assistance and sponsorship of

Intergovernmental Oceanographic Commission (IOC) of
UNESCO
Ministry of Science and Technologies of Russia
Russian Foundation for Basic Research
Scientific Committee on Oceanic Research (SCOR) of
International Council of Scientific Unions
European Commission,
Directorate-General XII Science, Research and
Development (EC DG-XII Group)
City of Saint-Petersburg
Russian Academy of Sciences
Russian Oceanographic Society

THE SYMPOSIUM SCIENTIFIC BOARD

G.I. Barenblatt (Russia)	Yu.G. Mikhailichenko (Russia)
B.M. Boubnov (Russia)	C. Mooers (USA)
Yu.D. Chashechkin (Russia)	V.G. Neimann (Russia)
A.I. Danilov (Russia)	J. Nihoul (Belgium)
M.V.Emelianov (Russia, Spain)	A.G. Ostrovskii (Japan, Russia) – Scientific Secretary
B.M. Filyushkin (Russia)	R.V. Ozmidov (Russia)
M.V. Flint (Russia)	V.T. Paka (Russia)
C. Garrett (Canada)	V.N. Pelevin (Russia)
A.I. Ginzburg (Russia)	E.A. Plakhin (Russia)
G.S. Golitsyn (Russia)	D. Renouard (France)
M. Gregg (USA)	K.D. Saninin (Russia)
E. Gross (SCOR)	V. Shannon (SA)
G.J. van Heijst (Netherlands)	G.I. Shapiro (Russia) – the Coastal Zone Workshop convener
A. Hill (UK)	S.M. Shapovalov (Russia)
B.I. Imerekov (Russia)	G. Siedler (Germany)
L.N. Karlin (Russia)	A.V. Souvorinov (Russia)
Ye.Yu. Kluikov (Russia)	M.E. Vinogradov (Russia)
G.K. Korotaev (Ukraine)	V.N. Vorobiev (Russia)
A.G. Kostianoy (Russia)	T. Yamagata (Japan)
M.N. Koshlyakov (Russia)	A.G. Zatsepin (Russia) – Chairman of International Scientific Committee
G. Kullenberg (IOC)	V.V. Zhmur (Russia)
S.S. Lappo (Russia)	V.M. Zhurbas (Russia)
P.F. Linden (UK)	
V.V. Lukin (Russia)	
T. McClimans (Norway)	

LOCAL ORGANIZING COMMITTEE (LOC)

E.Yu. Kluikov – Chairman, St. Petersburg	O.V. Khaimina - St. Petersburg
G.M. Veretennikova – St. Petersburg	N.A. Maximenko – Moscow
G.G. Gogoberidze - St. Petersburg	N.A. Sheremet – Moscow
A.E. Kluikov - St. Petersburg	S.G. Poyarkov - Moscow

PARTICIPANTS

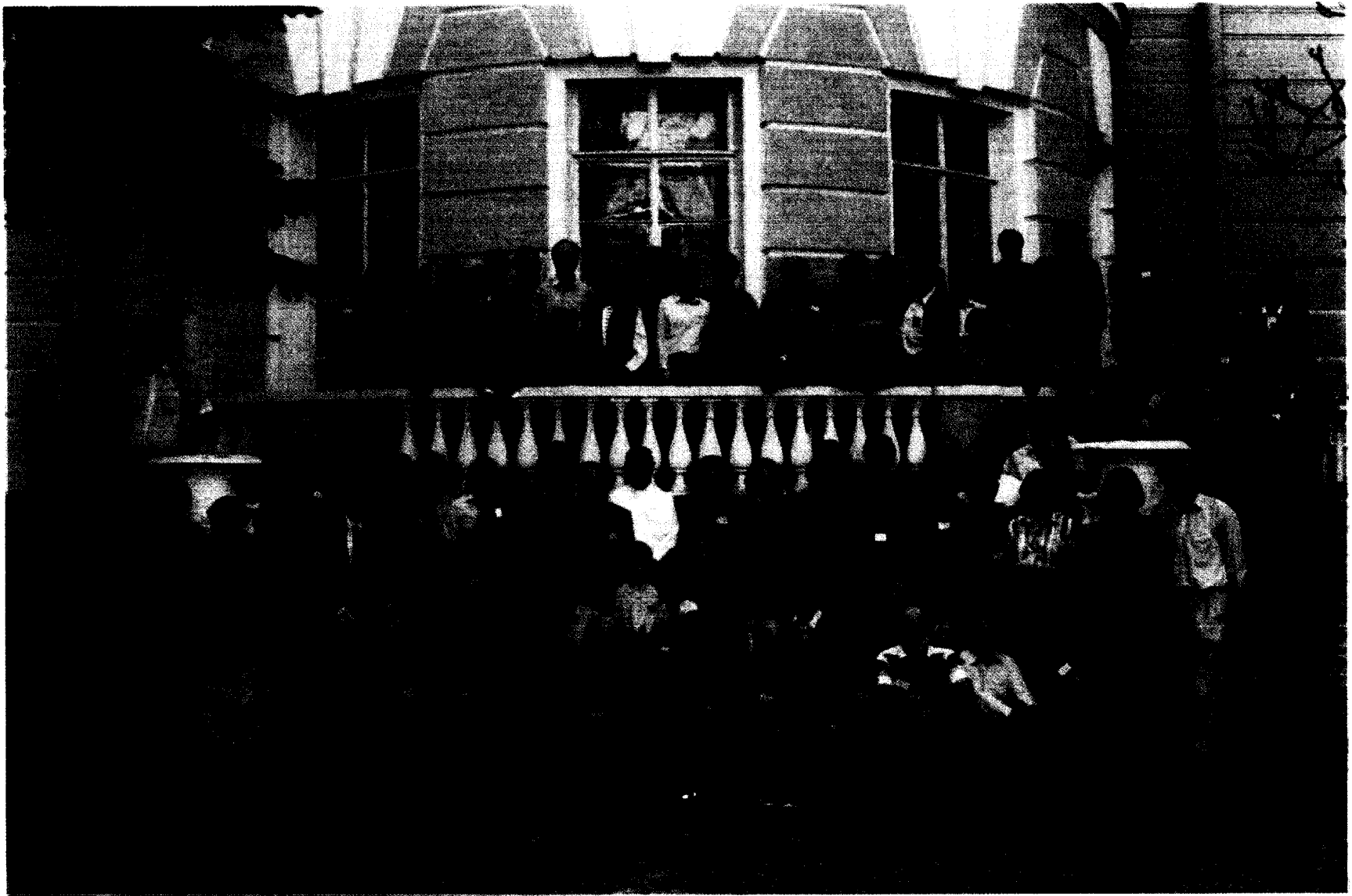
To the very large extent, the success of the Symposium was due to enthusiastic response of many scientists from all over the world to whom the Symposium Organizing Committee extends many tanks.

More than 170 scientists from 23 countries submitted the abstracts of their reports to the International Scientific Committee (ISC) of the Symposium. The ISC selected 223 scientific reports for the presentations. The abstracts of these reports and the Scientific Programme of the Symposium were published as a special volume and a brochure, respectively, and were distributed among the participants just before the beginning of the meeting.

About 126 participants from 21 countries presented their reports at the Symposium.

The distribution of these participants among the countries was as follows:

1.	Russian Federation	72
2.	Ukraine	12
3.	United States of America	7
4.	France	5
5.	United Kingdom of Great Britain & Northern Ireland	5
6.	Germany	3
7.	Belgium	3
8.	Japan	3
9.	Bulgaria	2
10.	Norway	2
11.	Spain	2
12.	Brazil	1
13.	Canada	1
14.	Italy	1
15.	Israel	1
16.	Republic of Korea	1
17.	Netherlands	1
18.	Poland	1
19.	South Africa	1
20.	Turkey	1
21.	Uruguay	1



Collective photo of the participants.
(Former palace of prince V.P.Kochubey, Pushkin, St.Petersburg vicinity, May 20, 1998)

PREFACE

This volume contains a selection of papers presented at the International Symposium "Oceanic Fronts and Related Phenomena" (ISOFRP) held in Pushkin, Saint Petersburg (18-22 May 1998). The Symposium commemorated Professor Konstantin N. Fedorov, a towering figure of the oceanic fronts research. The Symposium was dedicated to the program for the 1998 International Year of the Ocean. It was organized by the P.P. Shirshov Institute of Oceanology and the Russian State Hydrometeorological University with the help of the Russian Oceanographic Society. The smooth running of the Symposium was due to the support of the Ministry of Science and Technologies of Russia, Russian Foundation for Basic Research, Intergovernmental Oceanographic Commission (IOC) of UNESCO, Scientific Committee on Oceanic Research (SCOR) of the International Council of Scientific Unions and of the DG-XII of the European Commission.

More than 130 scientists from 21 country participated in the meeting with keynote lectures, oral and poster presentations. It was a good opportunity to discuss the oceanic fronts problems by many scientific leaders, young scientists, and students. The Symposium's sessions covered topics of:

- *the dynamics and structure of the oceanic fronts;*
- *the upper ocean as a boundary layer in the ocean-atmosphere system;*
- *the oceanic coherent structures (eddies, vortical dipoles, lenses, jets) and their role in mixing and transport;*
- *the biochemistry of oceanic fronts;*
- *the flow dynamics and the fronts in straits and channels;*
- *the oceanic thermohaline fine structure (intrusions, double diffusion, small-scale turbulence), the internal waves, and the mixing processes;*
- *exchange processes and fronts in coastal zone and marginal seas.*

The Volume of the Collected Papers contains more than 90 selected papers. The selection of the papers illustrates the progress in the research of the oceanic fronts and related phenomena. The volume covers various issues of laboratory experiments, field observations, remote sensing, and numerical modeling. It is hoped that this publication will encourage those scientists with particular interests in any of these topics to explore the oceanic fronts in more detail. It is also hoped that this publication will stimulate regular discussion on the oceanic fronts.

The Organizing Committee is very thankful to all of the authors who found time to prepare and submit the manuscripts and to all of the volunteers who kindly helped to edit and to publish this volume. The thanks are extended to the Intergovernmental Oceanographic Commission (IOC) of UNESCO, and particularly, to Dr. Iouri Oliouline and Mr. Patrice Boned for the opportunity to publish this volume in a series of the UNESCO Workshop Reports and comprehensive support.

*Andrei G. Zatsepin
Chairman, ISOFRP*

*Alexander G. Ostrovskii
Scientific Secretary, ISOFRP*

Konstantin N. Fedorov
(1927 - 1988)

Konstantin Fedorov was born in Leningrad (Saint-Petersburg) in the family with strong intellectual traditions. His maternal relatives belonged to the cultural establishment of Russian society of 18-19 centuries. Ancestors of some of them moved to St.-Petersburg, the former capital of Russia, from western Europe during the Peter the Great reign or soon after that. His great-grandfather Ya. K. Grot was an Academician and grandfather K. Ya. Grot a Corresponding Member of Russian Academy of Sciences, both the experts in Russian literature. His father was an electrical engineer and his mother - editorial supervisor of Publishing house of Academy of Sciences of the USSR.

During World War II Konstantin was evacuated to the countryside. After return to Leningrad he graduated from S.O. Makarov Arctic Marine Institute and entered research studentship of P.P. Shirshov Institute of Oceanology in Moscow where in 1955 he earned a Ph.D. in physical oceanography under the guidance of Prof. V.B. Shtockman. In 1958 and 1959 he received a UNESCO grant for postdoctoral studies at the University of Liverpool and the Imperial College in London. From 1961 to 1969 he served at the Intergovernmental Oceanographic Commission (IOC) of UNESCO in Paris, being Secretary of the Commission from 1963 to 1969.

Upon returning to Moscow, he continued the work in P.P. Shirshov Institute. In 1973 he maintained his professorship thesis and from 1974 to 1988 headed Laboratory and Department of experimental and satellite oceanology. In 1987 he was elected as a Corresponding member of the Academy of Sciences of the USSR and became also a Deputy director of P.P. Shirshov Institute on Physical Oceanography Division. He was on the peak of scientific and administrative career when suddenly ceased to be.

His scientific work started with studies of the wind-driven circulation, but closest to his heart were problems concerning finestructure and mixing in the ocean. From his early paper of 1967, written jointly with Henry Stommel on small-scale structure near Timor and Mindanao, to his 1978 book "The Thermohaline Finestructure of the Ocean" (Russian edition appeared in 1976) and to the 1986 book "The Physical Nature and Structure of Oceanic Fronts" (Russian edition of 1983) and 1992 book "The Near-surface Layer of the Ocean" (Russian edition of 1988), co-authored with his wife Anna Ginzburg, he produced a long line of scientific accomplishments and publications on the topics of the thermohaline finestructure, convection, temperature inversions, intrusion processes, transformation of water masses and coherent motions in the ocean. While he also dealt with laboratory experiments and satellite-borne data, most of his research was related to ship observations, with much of the data obtained during his numerous cruises on research vessels.

His productive work as a leader of numerous research projects was successfully combined with substantial service to the international oceanographic community. From 1976 to 1980 he was president of the Scientific Committee on Oceanic Research (SCOR) and then served as Past-president of SCOR until 1988. He was also Chairman of SCOR Working Group 69, "Small-Scale Turbulence and Mixing in the Ocean", which successfully finished its job in 1988.

Konstantin Fedorov was a widely talented man. Besides his professional work, he was fascinated by poetry (the book of his verses and translations of foreign poetry was recently published in Russia), painting, carving and even cooking. It's regretful that usually he was so busy with numerous duties that had no time to fulfill his various interests. Only on the research vessels, during long sea passages, he was able to do that more or less freely. He was a committed Scientist whose contribution to physical oceanography considerably expanded our understanding of mixing processes in the ocean.

He was one of key persons in international marine science during almost three decades, drawing together intergovernmental and non-governmental organizations and promoting the scientific communication between east and west.

KONSTANTIN N. FEDOROV



Konstantin N. Fedorov

TABLE OF CONTENTS

	Page
Preface	vii
Konstantin N. Fedorov	ix
OPENING SPEECH	1
SCIENTIFIC PAPERS	
Aleynik D.L., B.N. Filyushkin, E.A. Plakhin: Generation of the Mediterranean Lenses on the Continental Slope of the Gulf of Cadiz	5
Anisimova E.P., I.V. Petrenko, A.A. Speranskaya, S.N. Dikarev, O.A. Speranskaya: Self-organization of the Water-Air Boundary Layer in the Conditions of Free Convective Movement	11
Arnoux-Chiavassa S., P. Broche, J.L. Devenon, N. Durand, A. Fiandrino, P. Forget, P. Fraunie, S. Ouillon, V. Rey: Dispersion of Suspended Matter in a Supercritical River Plume Discharging in a Microtidal Sea: An Integrated Approach	15
Blokhina N.S., A.E. Ordanovich, O.V. Kravchenko: Langmuir Circulations as Coherent Structures	22
Bogorodsky P.V.: Onset of Thermohaline Convection in Sea Ice	28
Boubnov B.M., P. B. Rhines: Laboratory Experiments on Convection in Coastal Seas and Large Lakes... ..	34
Bouruet-Aubertot P., C. Koudella, C. Staquet, K. B. Winters: Vertical Eddy Diffusivity Induced by Breaking Internal Gravity Waves: A Comparison Between Particle Dispersion and Diapycnal Diffusive Flux.	42
Bowman M.J., D.E. Dietrich, B.G. Sanderson: Nonlinear Interactions of East Australian Current Eddies	48
Buongiorno Nardelli B., E. Salusti: On Criteria for Forming Dense Water and its Application to the Mediterranean Sea	54
Chashechkin Yu. D.: Internal Waves and Fronts in a Stratified Fluid	60
Chubarenko B.V., I.P. Chubarenko: The Field Study of the Frontal Area Between Coastal Zone and the Vistula Lagoon (South-Eastern Baltic)	71
Debolskaya E.I.: Mathematical Model of Pollutant Propagation in North Tidal River Mouth	77
Debolskaya E.I., V.N. Zyryanov: Turbulent Structure of Open and Ice-covered Shallow Flow in a Channel	83
Didkovskii V., A. Semenov, A. Zatsepin: Mesoscale Currents Upon the Smooth Sloping Bottom and in the Presence of Ridges and Canyons	89
Dikarev S.N., S.G. Poyarkov, K. Korolkov: A Balance Model of the Upper Quasi-homogeneous Layer: The Black Sea Cited as an Example	95
Djenidi S., A.G. Kostianoy, N.A. Sheremet, A. El moussaoui: Seasonal and Interannual SST Variability of the North-East Atlantic Ocean	99
Dmitrenko, I.; P. Golovin, V. Gribanov, H. Kassens: River Run-off Fronts in the Siberian Shelf Seas: Structure, Formation Mechanisms and Environmental Effects	106
Eldevik T., K.B. Dysthe: Short Frontal Waves: Can Frontal Instabilities Generate Small Scale Spiral Eddies?	112
El moussaoui A., S. Djenidi, A.G. Kostianoy, J.M. Beckers, J.C.J. Nihoul: Circulation and Boundary Processes off Northwest Africa	118
Emelianov M.V., E. Gacia-Ladona, J. Font: Small-scale Processes Activity and Levantine Intermediate Water Characteristics in the Western Mediterranean Sea	126
Emelianov M.V., C. Millot, J. Font, I. Taupier-Letage: New Data on Levantine Intermediate Water Circulation in the Western Mediterranean Sea	132
Evdoshenko M.A.: On Some Sub-mesoscale Coherent Structures at the Steep Slope of Northwest Africa	138

	Page
Fernando H.J.S.: Convection in Rotating Fluids and its Geophysical Relevance	144
Garrett C., M. Ott, R. Dewey, K. Stansfield: Juan de Fuca Strait as a Fluid Dynamics Laboratory	150
Ginzburg A.I., A.G. Kostianoy, D.M. Soloviev, S.V. Stanichny: Mesoscale Dynamics in the Southeastern Black Sea	155
Ginzburg A.I., A.G. Kostianoy, A.G. Ostrovskii: Surface Circulation of the Japan Sea (Satellite Imagery and Drifters Data)	162
Gogoberidze, G.G.; Karlin, L.N.; Kluikov, Ye. Yu.: Mathematical Modeling of the Near-Surface Layer	168
Golovin P., I. Dmitrenko, H. Kassens, J. Holemann: Frazil Ice Formation Along the Upper Boundary of Seasonal Pycnocline and its Role in Glacial Marine Sedimentation in the Laptev Sea during Wintertime	174
Gregg M.C.: Turbulent Mixing in the Ocean	181
Gregoire M., J.-M. Beckers, J.C.J. Nihoul, E. Stanev: Coupled 3D Eddy-resolving General Circulation Model and Ecosystem Model Applied to the Black Sea. First Results	186
Gritsenko V.A., A. A. Yurova: On the Evolution of a Pressure Field under a Separation of a Bottom Gravity Current from Bottom Slope	192
Gritsenko V.A., A.G. Kostianoy: On Numerical Modeling of Upwelling Filaments	198
Hacker J.N., P.F. Linden, S.B. Dalziel: The Evolution of Forced Quasi-two-dimensional Vortices in a Stratified Fluid: Symmetries, Pattern Formation and Symmetry Breaking	206
Ibraev R.A., E. Ozsoy, A.S. Sarkisyan, H.I. Sur: Seasonal Variability of the Caspian Sea Dynamics: Barotropic Motions Driven by Climatic Wind Stress and River Discharge	212
Ivanov, A. Yu.; Grodsky, S.A.; Kudryavtsev, V.N.: Observations of the Gulf Stream Frontal Zone Using the ALMAZ-1 Synthetic Aperture Radar	218
Ivanov L.I., S. Besiktepe: Black Sea Cold Intermediate Water Mass Volumetric Structure and its Variability	226
Kartashov A.S.: Turbulent Flow as an Oscillatory System	232
Kizner Z., D. Berson: Evolution of Barotropic and Baroclinic Mesoscale Eddies on the β -plane: Numerical Testing and Diagnostics of Exact Solutions	238
Kluikov Ye.Yu., P.P. Provotorov, K.B. Utkin: Analysis of Condition of Increasing and Decreasing Density Due to Mixing of Sea Water Masses	244
Konyaev K.V., G.I. Kozoubskaia, A.J. Plueddemann, K.D. Sabinin: Internal Waves at the Barents Sea Polar Front	248
Korotaev G.K.: Significance and Physics of Frontal Eddies	256
Korotenko K.A.: Matter Transport in Meso-scale Oceanic Fronts of River Discharge Type	268
Kosarev A.N., A.V. Kouraev: Main Features of Fresh and Saline Waters Mixing Processes in the Northern Caspian Sea	274
Kostianoy A.G., M. Astraldi, G.P. Gasparini, S. Vignudelli: Variability of the Sicilian Upwelling....	279
Koterayama W., J.-H. Yoon, A. Ostrovskii: Development of an Intelligent Towed Vehicle "Flying Fish" for Comprehensive Measurements of Physical and Chemical Properties and Examples of Data Obtained in the Japan Sea	284
Koziy L., V. Maderich, N. Margvelashvili, M. Zheleznyak: Numerical Modelling of Seasonal Dynamics and Radionuclide Transport in the Kara Sea	296
Kuzmina N.P., V.M. Zhurbas: Influence of Double Diffusion on Symmetrical Baroclinic Instability of Oceanic Fronts	302
Liapidevskii V.Yu.: A Mathematical Model of Density Current on an Incline	308
Lozovatsky I.D., H.J.S. Fernando: Turbulence in Stratified Patches on a Shallow Shelf	314
Lutjeharms J.R.E.: Frontal Structures and Eddy Formation in the Greater Agulhas Current System	320
Maderich V.S.: Two-layer Exchange Flows Through Long Straits With Sill	326
Maximenko N.A., G.G. Panteleev, P.P. Niiler, T. Yamagata: Mean Surface Circulation in the North Western Pacific	332

	Page
McClimans T.A., B.O. Johannessen, J.H. Nilsen: Laboratory Simulation of Fronts Between the Various Water Masses in the Kara Sea	338
McCreary J.P. Jr., Peng Lu: Influence of the Indonesian Through Flow on the Circulation of Intermediate Water in the Pacific Ocean	349
Mooers, C.N.K.; HeeSook Kang: Simulation of the Variability of the Subpolar Front and Jet in the Japan (East) Sea	359
Navrotsky V.V., V.V. Novotryasov: Inertial Motions and Internal Waves in the Ocean Frontal Zones	367
Nelezin A.D.: Forecast Possibility of the Kuroshio Front Mean Position	371
Ostrovskii A.G., T. Setoh: Antarctic Circumpolar Wave and Oceanic Fronts	375
Ovchinnikov I.M.: Formation and Dynamics of the Cold Intermediate Layer Determining the State of the Black Sea Ecosystem	381
Ozsoy E., M.C. Gregg, H. Fohrmann, J.O. Backhaus: The Bosphorus Strait and its Shelf Outflow into the Black Sea: Experiments and Modeling	386
Paka V.T., N.M. Stashchuk, V.I. Vlasenko, N.N. Golenko: Peculiarities of the Formation of the Thermohaline Water Structure in the Stolpe Channel of the Baltic Sea	392
Paka V.T., V.I. Vlasenko, N.M. Stashchuk, N.N. Golenko: Some Aspects of the Hydrophysical Fields Formation in the Gotland Deep of the Baltic Sea in Summer	398
Pelevin V.N., V.V. Rostovtseva: Chlorophyll and Other Natural Admixtures Concentrations Estimation in Sea Water of Different Types from Contact and Remote Sensing Data	404
Peneva E.L., E.V. Stanev: Gravity Currents Over Smooth and Rough Topography – Modeling Study on the Mediterranean Outflow in the Black Sea	410
Plueddemann A.J., G.G. Gawarkiewicz, C.L. Harris: The Barents Sea Polar Front: Topographic Control and Seasonal Variability	416
Polonsky A., E. Voskresenskaya: Low-frequency Climate Variability Over the Eastern Europe as a Result of the North Atlantic and Pacific Changes	422
Polonsky A., E. Ostrovsky: On a Decadal Variability in the Coupled Ocean-atmosphere System over the North Atlantic Ocean	427
Ponomarev V.I, O.O. Trusenkov: Regular Dynamic Structures in the Japan/East Sea	433
Poyarkov S.G., M.V. Emelianov: Peculiarities of the Thermohaline Structure and Variability of the St. Paul Island Coastal Front (the Bering Sea)	439
Poyarkov S.G.: Mesoscale Frontal Structure in the Pribilof Region of the Eastern Bering Sea Shelf	446
Renouard D., J.-M. Baey: Experimental Study of the Stability Conditions for an Underwater Current	454
Resnyansky Yu. D., A.A. Zelenko: The Response of the Upper Ocean to Synoptic Variations of Atmospheric Forcing: Immediate and Indirect Manifestations	460
Ro Y.J., J.C. Lee: Thermohaline and Current Structures of the Polar Front Along 134°E in the East (Japan) Sea	467
Samolyubov B.I., V.V. Kremenetskiy, A.A. Moya: Near-bottom and Intermediate Stratified Currents	473
Samolyubov B.I., A.V. Silaev, L.V. Silaeva: Heat and Suspended Particles Turbulent Transfer in Density Currents	479
Samolyubov B.I., M.V. Sluev: Secondary Ignitive Flows and Internal Waves in Density Current	485
Scott J.C., T. Sawyer, K. Kelly: Spatial and Temporal Variability Measurements in the Iceland-Faeroes Frontal Zone Using Towed Distributed Sensors and Remote Sensing	491
Sein D.V., J.O. Backhaus, P. Brandt, A. Izquierdo, B.A. Kagan, A. Rubino, L. Tejedor: Flow Exchange and Tidally Induced Dynamics in the Strait of Gibraltar Derived from a Two-layer, Boundary-fitted Coordinate Model	497
Severov D.N., V.A. Severova, M. Blanco: Some Aspects of SST Fronts Dynamics in the Southwestern Atlantic	503
Shapiro G.I., T.M. Akivis, N.N. Pykhov, S.M. Antsyferov: Transport of Fine Suspended Matter in the Coastal Zone by Mesoscale Currents	509

	Page
Shcherbina A.Yu., N.A. Maximenko: New Possible Mechanisms of the North Pacific Intermediate Water Formation	517
Sherstyankin P.P., V.V. Khokhlov, L.N. Kuimova, N.G. Melnik: Classification, Physical Nature and Structure of Fronts on Lake Baikal	523
Sklyarov V.E., A.V. Berezutskii: The Combined Hydrophysical and Acoustic Study of Thermohaline Fine Structure in the Atlantic Ocean	531
Takematsu M., A.G. Ostrovskii, Z. Nagano: Wind Forcing and Deep Circulation in the Japan Sea	536
Tsarev V.: Three-dimensional Modeling of Bottom Dense Lens Evolution	542
Tychensky A., X. Carton: Hydrological and Dynamical Characterization of Meddies in the Azores Region: Interaction with the Azores Current	547
Ullman D.S., P.C. Cornillon, T.P. Mavor,: SST Fronts in Winter off the East Coast of North America	557
Vasilieva V.V., O.D. Shishkina: Numerical and Experimental Modeling of a Pattern of Internal Waves Induced by a Drifting Iceberg	563
Vinayachandran P.N., T. Yamagata: Cyclonic and Anti-cyclonic Vortices in the Eastern Indian Ocean During the Summer Monsoon	568
Voropayev S.I., G.B. McEachern, D.L. Boyer, H.J.S. Fernando: Drifting Sand Ripples and Burial of Cobbles in Near-shore Zones	574
Voropayev S.I., G.B. McEachern: Stern-Radko Self-propagating Eddy	580
Walczowski W.: The Arctic Front: Structure and Cross-Frontal Transport Processes	586
Yakushev E.V., E.I. Debolskaya: Particulate Manganese as a Basic Factor of Oxidation of Hydrogen Sulfide in Redox Zone of the Black Sea	592
Yakushev E.V.: Modeling of Fine Hydrochemical Structure of the Zone of Contact of Oxidic and Anoxic Waters in the Black Sea	598
Yurova A.A., V. A. Gritsenko: Novel Exact Solutions Describing the Evolution of Lenses Frontal Vorticity	606
Zavialov P.O., O.O. Moller Jr.: Modeling and Observations of Currents off Southern Brazil and Uruguay - The Rio Grande Current	612
Zavialov P.O., J.M. Absy: Low Frequency SST Variability in Southwestern Atlantic	618
Zhurbas V.M., V.T. Paka, M.V. Anisimov, N.N. Golenko, M.M. Subbotina, G.A. Koshkosh: Stolpe Channel Overflow in the Baltic Sea – Observations and Modeling	624
Zuenko Yu.I.: Year-to-year Changes of Dense Bottom Water Spreading in Peter the Great Bay Shelf (the Japan Sea) and Possibility of Cascading	631

OPENING SPEECH

Y. Oliouline
IOC-UNESCO
1 Rue Miollis
75743 Paris-Cedex, France
(33 1) 45683983, fax (33 1) 40569316

It is a pleasure and honour for me to introduce the welcome address on behalf of IOC-UNESCO to the participants of the International Symposium on Oceanic Fronts and Related Phenomena organized in honour of Prof. K. Fedorov.

I would like to start by sharing briefly with you my personal reflections and esteem for a man who was a bright personality in every sense of the word and whose career, to a certain degree, almost mystically influenced my own. The first time I met him at the Second Oceanographic Congress in Moscow in 1966, when I was among many young scientists in the conference room and he was on the podium as the IOC Secretary. As fate would have it, I saw him again that same year in Le Havre, France, when he came to this harbour from Paris to meet the research vessels *Oceanographer* and *Iceberg* and to welcome his former Professor Dr. Davidan. On leaving the post, Dr. Davidan said the prophetic words speaking about the post of the Secretary of IOC: "*This is the place you might work in one day*". Is this not a fact?! After 1966, I met Prof. Fedorov a number of times in Moscow and Paris, and was always impressed by his foresight of the importance of the ocean to humanity as a whole, and the need to study the ocean from many points of view. It was during his tenure in the post of Secretary IOC, that IOC started gaining a worldwide reputation as a respected, useful and operational mechanism for the implementation of ambitious, large-scale expeditions, such as joint investigations of Kuroshio, Overflow Studies in the Farero/Scotland and Greenland/Island Straits, Integrated Investigations of the Indian Ocean and many others. This was during his days in 1969 that IOC Member States, jointly with other UN agencies, formulated a long-term framework programme of oceanographic research and monitoring. This was the first binding, comprehensive document which laid the basis for many IOC activities in the 1970's-1980's and many ideas of which are still valid and underlie this document:

1. Interaction of ocean and atmosphere, ocean circulation and variability;
2. Living resources and marine environment;
3. Marine pollution;
4. Marine geology, geophysics and mineral resources;
5. Integrated Global System of Ocean Stationary, etc.;
6. Data and Information Management;
7. Training and Capacity Building.

All these activities are the pillars of the IOC programme today.

His intellectual curiosity was high and it was always stimulating and rewarding to discuss with Konstantin matters related to ocean research and protection, and to the IOC. He was at the cradle of the Commission and jointly with Prof. Kort, Mr. Simsakian and Dr. Sabo, participated in the formulation of the first constitutional and formal texts. That is why he always considered IOC his baby to which he devoted his best years. Thanks to the vision of Prof. Fedorov and other IOC founders, the Commission was designed for the future and consequently geared to meet the new and growing uses that humankind will expect the marine element to serve. He was a man of dialogue and those who had the privilege of sharing ideas with him found the frontiers of their own minds considerably expanded.

He was a visionary, a champion of international co-operation, a great scientist and an extraordinary warm and friendly person. When exceptional individuals, such as Prof. Fedorov disappear from the world community, they leave behind a mission for all of us, as individuals and in our official capacities, to further the goals to which he was committed.

Your Symposium is the natural and appropriate forum for the indispensable dialogue and co-operation between scientific communities of different countries. I expect that your Conference will help to establish a truly global partnership in which the countries of the North and South, East and West, join fully in a global effort. The ocean is *par excellence* a natural area for international co-operation.

The efforts of Prof. Fedorov during his stay in Paris as the Head of IOC have been amongst the most daunting and intensive in the history of the Commission. He succeeded in pulling together scientists from developing and developed countries, united in a single cause - to sharpen our understanding of the World Ocean, its environment and resources and chart effective, equitable global responses.

The scientific and technical programmes of IOC are based upon the reality that the ocean is not restrained by national boundaries and that each nation needs the same wide-ranging set of information in order to provide marine services.

The safety and welfare of all people, the wise and efficient use of the worlds national and intellectual resources and the protection of the natural environment for future generations, all depend upon gaining greater knowledge and understanding of all earth sciences and applying this knowledge and understanding for sustainable development. Meteorology, Hydrology, Oceanography and other related sciences now face their greatest challenge ever in increasing the knowledge and understanding of the atmosphere, oceans and land surface and in co-operating to use this new knowledge for the benefit and welfare of humankind. We believe that the work of your Symposium will provide valuable knowledge base-scientific, economic, social and public policy-feeding into and responding to the objectives of the 1998 International Year of the Ocean (IYO).

It is now also very clear that all three major components of our terrestrial environment, the atmosphere, oceans and the land are highly mutually interactive, in particular with reference to global climate and climate change. It is essential therefore, that long-term global environmental monitoring should encompass all three components of our terrestrial environment in a coherent, consistent and systematic way. To do so will require an even higher level of co-operation and co-ordination, internationally, regionally and nationally than the one that prevails today.

I note with satisfaction that the organizers of the Symposium share this view and the agenda contains a number of interesting presentations covering problems of interaction. I was told that you are very creative people with lots of ideas. You will have a hard task to choose the best way forward from among the many alternatives that are possible, but it is important that you succeed.

At this Symposium you will learn from each other's experiences, you will discuss possible initiatives and will work out new approaches. The Symposium should demonstrate to all, the progress achieved and identify new targets to aim at.

The fact that so many of you are prepared to give your time to be here this week shows that you feel that the topic before you is very important. As the poet said, "*Here is the sea that guards the secrets of all things*". Today we might agree that it guards the secret of almost everything. Your Symposium is a step towards resolving some of the secrets. You have the responsibility for helping to obtain the key that will unlock that secret for humanity.

The ocean represents a priority domain for the expansion of scientific interest, especially in the search for new and imaginative solutions to the pressing socio-economic problems of mankind. It is a domain that rapid scientific and technological development has made somewhat more accessible - but not less complex.

It is important that the recommendations you make at the Conference provide a basis for evolving a sound and workable strategy, both to guide IOC in ocean studies and to make IOC to fulfill its role in the ocean scientific activities as a joint specialized mechanism for co-ordinating ocean research within the United Nations system. I hope that your recommendations will be noted widely and they will be of use to many other scientists and organizations concerned.

On the part of IOC, the Commission will always be attentive to your efforts, will remain receptive to your aspirations and it places great hopes in your work.

Finally, I would like to join in expressing the deep appreciation to the Government of Russia and the Russian Academy of Sciences for hosting this memorial Symposium.

I would like to express my profound gratitude to all those who have been associated with the organization of the Symposium and wish you every success and a very good stay in Russia, warmed by Russian hospitality.

GENERATIONS OF THE MEDITERRANEAN LENSES ON THE CONTINENTAL SLOPE OF THE GULF OF CADIZ

D.L. Aleynik, B.N. Filyushkin, E.A. Plakhin

(P.P. Shirshov Institute of Oceanology, RAS. ✉ Nakhimovski pr. 36, 117851, Moscow, Russia;
☒ E-mail: aleynik@rav.sio.rssi.ru)

Data of two CTD surveys during the period of August 12-22, 1988, carried out by the R/V "Vityaz" and XBT survey during September 1988, by R/V "Oceanus" in the Gulf of Cadiz Region ($35^{\circ}50'-36^{\circ}45'N$, $7^{\circ}30'-9^{\circ}30'W$) make it possible to investigate the formation mechanism of Mediterranean lenses (Meddy) in the continental slope canyons.

It is shown that the Mediterranean Water (MW) flow moving westward above the canyons partly loses its stability. In this case some water volume separates from the flow through the canyon. Data of all the surveys show water tongue with salinity (S) above 36.2 psu and temperature (T) above $11.8^{\circ}C$ to appear directly opposite of the canyon axis. The vertical sections of T and S along the canyon axis show that the water moves near the bottom and at the estuary edge (about 800 m depth) the tongue of the MW separates from the continental slope to propagate further as the lenses into the surrounding water.

These lenses (diameter about 15-20 km) develop, their main core being located within the 800-1300 m layer. During this inflow of the MW from the continental slope edge to depth, the intramass front zone is organized isotherms, isohalines pass almost vertically at 800-1200 m depths, and horizontal salinity gradient is 0.5 psu per 5 km. At a distance of 30 miles south of the western canyon estuary, an anticyclonic lens arises. The lens is well pronounced on the August maps of T and S distributions for 800-1200 m depths. On the September temperature maps this lens is well seen to changes its position westward. Comparison of the T and S vertical profiles in the lens center shows their full coincidence. Current meters on moored buoy stations set in this area register velocities of up to $0.5 \text{ m}\cdot\text{s}^{-1}$ at 1000-1500 m depths and confirms the existence of currents from the canyon continental slope and anticyclonic rotation of the newly generated lens.

INTRODUCTION

The outflow of the Mediterranean waters (with character parameters $T=13.5^{\circ}C$, $S=37-38$ psu) in the ocean with the lower current in Gibraltar strait is subject to an essential temporal variability. The evaluations of its total volume vary from 0.36 to 2.26 Sv, and mean value is 1.21 Sv [12]. At small distance from the strait (50 km) these waters are intermixed with surrounding Atlantic waters, their temperature is reduced down to $12.5^{\circ}C$, and salinity down to 36.5 psu, and they sank on a level of their densities at depths 500-800 m, and continuing already less intensive to be cooled and became more fresh. These waters move westward in the gulf of Cadiz over bottom along the continental slope before withdrawal from it. The spreading of MW into this area were investigated in the papers [3,4,12,14], and meddies generation here in [8,13,15].

In this paper the materials of sequential hydrophysical stations and five autonomous buoy stations (ABS), permitting be analyzed and show, that the inflow of MW from the main near-bottom current in the Gulf of Cadiz at the intermediate depths occurs mainly along canyons, to investigate the character of this process and to describe the mechanism of intratermocline lens (meddy) formation.

DATA AND METHODS

In the summer and in the autumn of 1988 two expeditions inspected region of the continental slope of the Gulf of Cadiz along the coast of Spain and Portugal. On a polygon with coordinates $35^{\circ}50'-36^{\circ}45'N$ and $7^{\circ}30'-9^{\circ}30'W$, RV "Vityaz" (IO RAS) in a phase from August 12 to August 22 has executed sequentially two CTD surveys with a selection of samples and observations for the hydrochemical, microstructural and hydrooptical analysis. In this region in a mouth of Canyons two clusters with six and three ABS with the currents meters at horizons 500, 1000, 1200, 1350, 1500 and 2200 m were moored, these observations were carried out

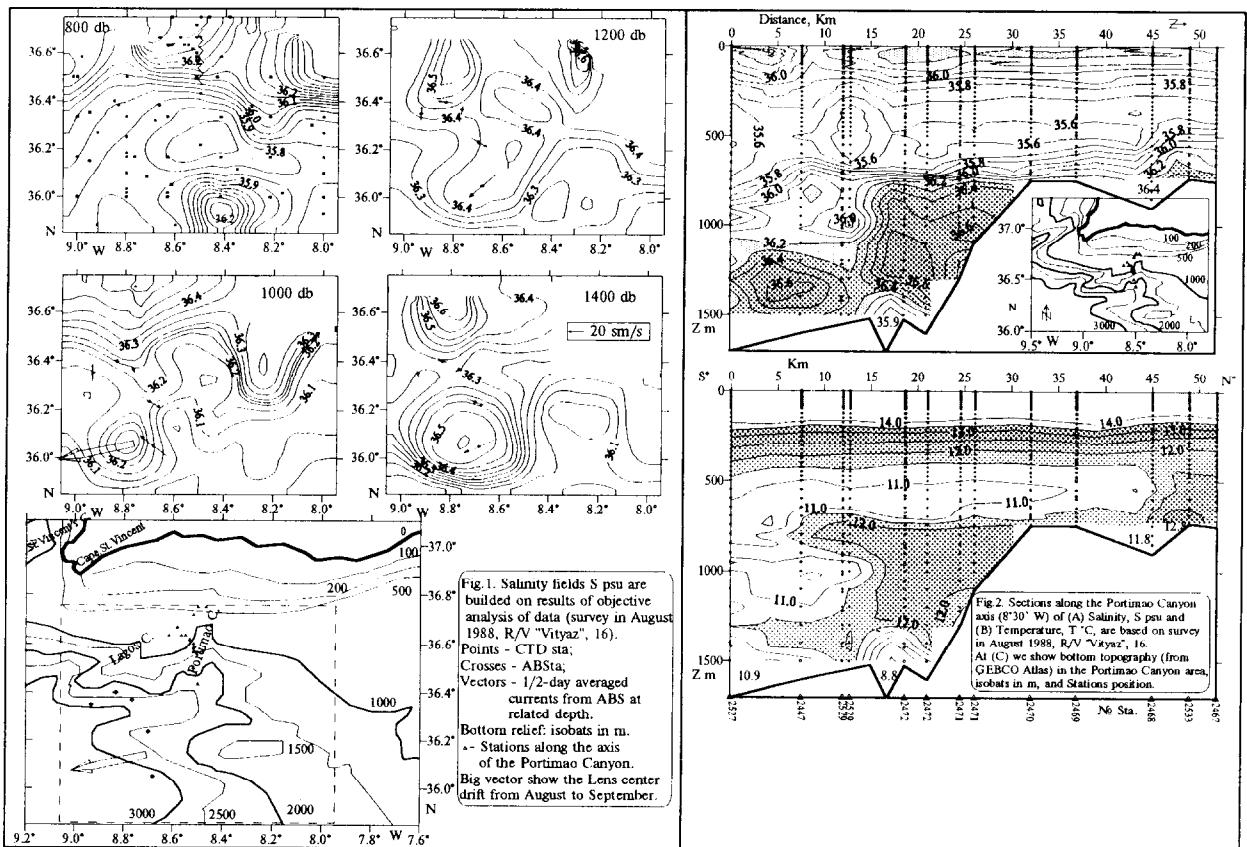
from August 18 to August 22. The currents-meters on ABS wrote average for 15 minutes data of velocity. These files during handling averaged in hour and half-diurnal intervals.

American research vessel "Oceanus" in September 1988 has executed CTD and XBT surveys in the same region [13]. For the analysis maps of a space variability of the temperature are attracted, as the stations outside of lens mainly was carried out with the help of XBT. The distances between CTD stations on the whole polygon were too large for a construction of salinity and densities distribution maps.

In a connection with the irregular distribution of the stations with the measurements of the temperature and salinity in a polygon the objective analysis of data for their representation in the knots of the selected regular grid (2x2 km) on 100 horizons (through 20 dbar) were spent. For this purpose, a method of restoring information in the knots of an interpolation grid with the use of multi-weighted functions [2] was applied.

RESULTS

In fig. 1, we show the maps of the salinity distribution in August (1a). We built also the maps of the temperature in August and September at the horizons 800, 1000, 1200 and 1400 dbar. A character of a distribution of temperature and salinity in August 1988 shows clearly that the areas of their maximum value on the intermediate depths are located on the north, and the outlines isohaline and isotherms follow almost by parallel isobats. Distribution of temperature in September also shows steady connection between a basic stream of the Mediterranean waters and the bottom topography in the area of the continental slope of the Gulf of Cadiz. In August as well as in September the basic MW jet is adjoined to a continental slope in the field of a condensation of isobates 1000-1500 m and occupied a layer with a thickness of 200-400 m. The analysis of T, S maps and topography shows (fig. 1), that the tongue of MW in the increased temperature ($> 12^{\circ}\text{C}$) and salinity (> 36.4) at the depths 1000-1300 m were localized near the nose of Portimao canyon.



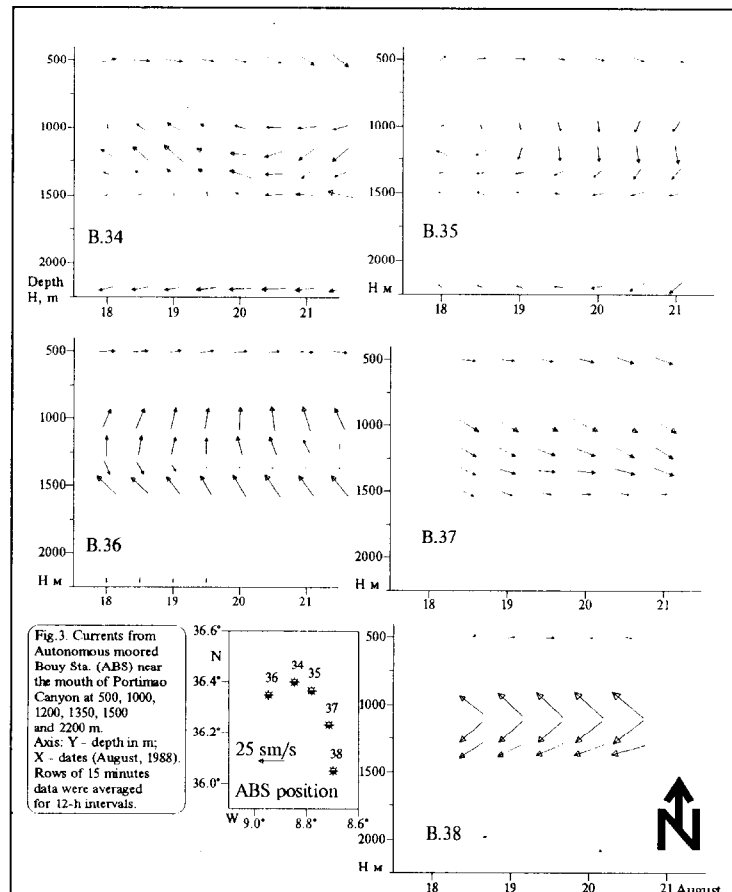
In 1965 along the axes of the largest canyons some sections were carried out [11], one of them was repeated in 1988. On a section along an axis of the Portimao canyon on a distribution of salinity and temperature (fig. 2a, b) the mechanism of MW inflow from a top of the continental slope into abyssal in the south of a polygon is well traced. On these sections it is visible, that the waters with increased T and S are spread on canyon bottom in a layer about 100 m and in its mouth, at depth about 800 m, the separation of the MW tongue from a bottom and its intrusion in the surrounding waters was occurred. When the inflow of these waters from an edge of a continental slope to the greater depths the intramass front zone was formed: the isotherms and isohalines place are almost vertically at the depths 800-1200 m, and the horizontal gradients in the zone of narrow front (width about 5 km) reach $0.1 \text{ psu} \cdot \text{km}^{-1}$.

We should note the fact that MW flow down along canyon as the separate portions, which formed on the large depths the series of the lenses with a diameter of 15-20 km and a thickness of 200-600 m. The complicated character of waters inflow from the continental slope can be seen and on the maps of the space variability of temperature and salinity. So, on the south-east part of a polygon we can see the warm ($12.6 \text{ }^\circ\text{C}$) and salty (36.3 psu) eddy with a diameter of 15 km and thickness not more than 300 m in layers 600-900 m, with center coordinates 35.9°N and 8.1°W at the depth 800 dbar, already completely isolated from the Mediterranean waters.

In the western part of a polygon in a mouth of Portimao Canyon the practically generated lens is registered: coordinates of its center was 36.1°N and 8.8°W , horizontal sizes is about 25 - 35 km and thickness more than 600 m with two maximums of temperature and salinity, on a vertical: the upper core with a maximum $T=11.8 \text{ }^\circ\text{C}$, $S=36.3 \text{ psu}$ at the depth 1050 m, and lower at the depth 1380 m with $T=12 \text{ }^\circ\text{C}$, $S=36.6 \text{ psu}$. Thus, their northern edge was still in a connection with the "mother" water mass, extending from a mouth of the canyon by the tongue of the warm and salty waters in the layers 900-1400 m. Almost full coincidence of the vertical profiles of a temperature and salinity for the "Vityaz" and "Oceanus" stations in a center of this eddy shows, that in September the American expedition investigated the same two-core eddy, which was displaced in south-western direction on 50 km during one month and already was completely isolated from the initial flow of the Mediterranean waters [13].

For this lens, detected on withdrawal from a mouth of Portimao Canyon in a stage of a completion of a formation, volume (500 km^3 in limits of isopycnal anomaly $S^2=0.1$) was calculated. At a width of a MW stream of 30 km, thickness of 0.4 km and velocity of $0.2 \text{ m} \cdot \text{s}^{-1}$ for a formation of such lens was required 2-2.5 days.

Vectors of the average half-diurnal currents on the various depths from 500 up to 2200 m on five autonomous buoy stations (ABS) by south from a mouth of Portimao Canyon from August 18 to 22 are shown on fig. 3. The analysis of these data testifies to the complicated structure of the currents on a vertical and their fast variability on value as well as on the direction. For four days at the level 1000 m (ABS 35) directions has varied on the opposite, at a depth 1200 m its average value in one day has increased by an order (from 2 up to 20 cm s^{-1} , ABS 34 and 35). It is necessary to note that on all buoy stations at the horizon 500 m the current was eastward, at a depth 2200 m it was westward, that coincides with the common scheme of the circulation in this region of the ocean.

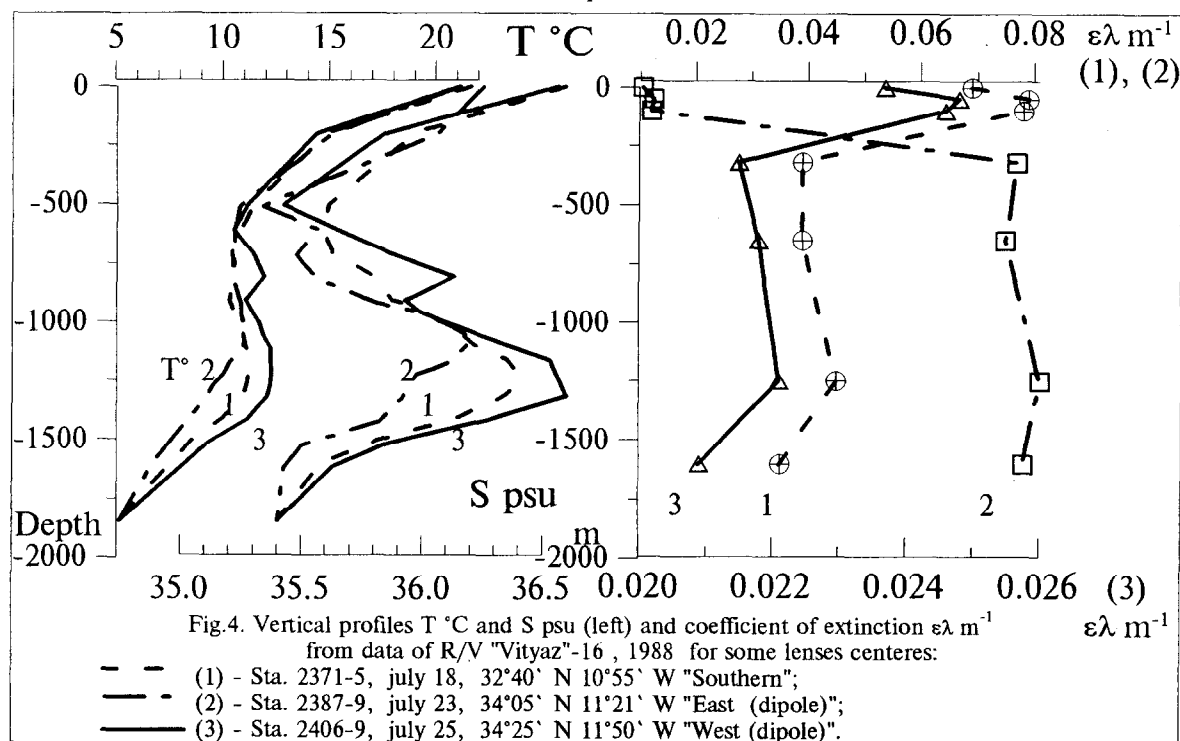


The variability of the currents on the intermediate depths from 800 up to 1500 m is certainly connected to the dynamics of MW distribution. On the maps of salinity fields at the horizons 1000, 1200 and 1400 dbar (fig. 1), we put the vectors of the average currents at the appropriate depths. The analysis of these characteristics allows to note a series of the interesting features. The system of three ABS, moored near a mouth of a canyon rather well describes the dynamics of MW flow: the direction of vectors of currents coincides a position of isohalines, that is on the most northern station all time were observed steady westward current with the average velocity $10 \text{ sm} \cdot \text{s}^{-1}$. On the eastern ABS, the southward currents, and on the western one northward predominate. Such vectors coincide with the newly formed lens, with the anticyclonic rotation.

The currents observations on two ABS (37 and 38), moored in a region of the regenerated two-core lens, have shown well expressed anticyclonic rotation at the lens core depth. At a level 1400 dbar the flow rate in the lens core exceed $20 \text{ sm} \cdot \text{s}^{-1}$ and its direction coincides with a position of isotherms and isohaline. At the same time, at horizon 1000 dbar such good fitness with direction of the current vectors with a course of T and S isolines are not marked. It is probably connected to an amplification of the westward current on the southern station, that has reduced in a displacement of the upper core of a lens to west concerning their common center, and on northern ABS the amplification of a current was connected to continued flow of MW jet. At level 1200 dbar, in a region of a disposition of the lens center, is not present characteristic for the lenses closed isohaline, reflecting to rotation. Such erosion of T and S fields is probably connected with the continued inflow of MW at these horizons and further increase of newly formed lens volume. The currents vectors confirm this water inflow, and besides, its is the confirmation of the new lens generation in a mouth of Portimao Canyon, mentioned in [9].

An inflow of the fluid jet with the different characteristics can produce the mushrooms-like structures, reducing in a formation of the dipole system with the well-expressed anticyclonic and cyclonic lens [7].

As a confirmation of a reality of the mechanism of the canyon inflow of waters, forming lens on the large depths, along northern continental slope in the Gulf of Cadiz, outcomes in the laboratory experiments [17] in the distribution of more dense waters above sloping bottom in the rotated fluid was investigated. It was established two basic conditions: geostrophic and beta-induced (wave-rotational), stipulated by topographical beta-effect. It was shown, that these currents intersect edges and trough with slanting slopes (triangular cut) along isobate trajectories without any essential modifications of both structure and dynamics, whereas the edges and trough with the sharp slopes (rectangular form) render force influence to a structure, direction and velocity of these currents. The obstacles as the along-sloping canyons with the plumb walls transform quasi-isobatic current in a shift, directed along an axis of a canyon. These (secondary) currents can have the important role for the water exchanges between the shelf zone and deep ocean.



For a confirmation of this conclusion could be maps of MW distribution at the intermediate depth (fig. 1), which clearly show, that the tongue of highly saline (and warm) waters was connected to the mouths of canyons. Also it was shown theoretically [10], that in the process of the geostrophical accommodation of the coastal stratified current above underwater canyon could be develop the force of along-canyon current.

Inflow of the waters from the continental shelf and its consequent transition on the continental slope along the canyons with large velocities, more than $20 \text{ cm}\cdot\text{s}^{-1}$ [11], should reduce in a capture of the base deposits and suspended matter and increasing the turbidity of the waters, forming lenses. Obviously, it is meaningful to use the data of the hydrooptical observations and evaluations of an amount of the suspended matter, transferable by a formed lens. In [1] was shown, that the average content of the weighed material in north-eastern Atlantic evaluates $0.4\text{-}0.7 \text{ mg}\cdot\text{l}^{-1}$, the average content of suspended matter in the lens exceeds $1.6\text{-}11.0 \text{ mg}\cdot\text{l}^{-1}$, that is higher in some times than it a characteristicall for the region.

Confirmation of this fact are the hydrooptical measurements, executed in July 1988 on RV "Vityaz" by V.N.Nicolayev [16] in a region to the south of 35°N in the limits $10^{\circ}\text{-}12^{\circ}\text{W}$, that is in zone of the consequent lenses transport from the continental slopes of the Gulf of Cadiz. On fig. 4.b the vertical profiles of the average (on sections through centers of three lenses, circumscribed in [7,9]), hydrooptical measurements of the extinction coefficient $\varepsilon\lambda$, giving the summarized information about an amount of the dispersing particles of the different origin. On these profiles in the limits of depths 1200-1300 m a significant maximums of turbidity, i.e. decrease of a transparency, were marked.

The additional verifying of a reality of transposition of dispersing particles by Mediterranean waters in the lens structures are the observations of a position of sound-dispersive layers on HF-echosound data, obtained in the 2-nd cruise of RV "Ak. Ioffe" [5] in the Canary basin for a lens with center coordinates at $31^{\circ}40' \text{ N}$, $26^{\circ}40' \text{ W}$.

This implies, that if the lens, is detected on rather large distance from a source, more than 1000 km, transfers in their core the increased amount of the suspended matter, it can be the indirect confirmation of its "canyon" origin.

CONCLUSIONS

1. Separation of the water volumes from the main MW current, flowing to west, in primary happens in the regions of the canyons, which cut the continental slope in the Gulf of Cadiz from the north to the south. Just in the deep part of the continental shelf in upper part of the canyons with the steep slopes, there are the dynamic conditions, reducing in a creation of the along-canyon currents, ensuring inflow of the warm and salty waters into the intermediate depths.
2. Separation of MW portions from the main current has a casual character, as on frequency of an event, and on volume of water flowing through the canyons. It is turn to a generation of the complicated mechanism of the waters distribution into deeper abyssal after the separation of MW stream from a bottom in the canyon mouth. The small volumes of the waters, moving with the significant velocity and possessing large impulse, create a jet, which have a possibility to move down to a depth of a threshold of the canyon mouth, that could reduce to a formation of the shallow lenses with the core at a level 800 m and a thickness of 200-300 m. In case of the inflow of the large MW volumes the intramass front to the surroundings waters with horizontal gradients in its forward part up to 0.1 psu km^{-1} could be formed.
3. Separated lens, adjoining to the continental slope in a mouth of canyon, save a possibility of reception of the additional portions of "mother" waters in the results of consequent "injection" through a canyon. Just this multiplicity of an inflow of the waters could reduce in a generation of the large, multi-core lenses.
4. Inflow of the waters from the continental shelf and slope with the intensive stream through the canyon's bottom should reduce increasing the contents of the suspended matter. Formed thus lens should differ by the increased turbidity of their core in a comparison with the surrounding waters. Confirmations of this point of view were found in 1988 observations for a turbidity in Canary Basin, where in the lens structures formed in the Gulf of Cadiz go. At the systematic hydrooptical and hydrobiological measurements in the canyons there would be the possibility for a separation of the lenses by an amount of the suspended matter in their core for an identification of the probable region of its generation and classification on the lenses of "open ocean" and "canyon".

The authors thank doctor M.Prater for his data of hydrophysical XBT and CTD sta. 202-th cruise of R/V "Oceanus". The work was carried out with financial support of Russian fund of basic researches (RFBR 96-05-65287).

LITERATURE

1. Abrantes E., Moreno J., Pinto J., Ambar I., Zenk W., Hinrichsen H., Zahn R. 1994. Suspended Matter of the Mediterranean Water Outflow off Portugal // Ocean Sciences Meeting. P. 227.
2. Benjamin S.G., Seaman N.L. 1985. A Simple Scheme for Objective Analysis in Curved Flow // Monthly Weather Review. V. 113. P. 1184-1198.
3. Bower A.S., Armi L., Ambar I., 1995. Direct evidence of the Meddy formation off the south-western coast of Portugal // Deep-Sea Res. Vol. 42. N 9. P. 1621-1630.
4. Bubnov V.A. 1971. A structure and dynamics of Mediterranean waters in Atlantic ocean // Oc. research., M.: Science, N 22. P. 220-227.
5. Dychno L.A., Filyushkin B.N. 1991. A detection of IT lenses with the help of echosound // Oceanology, V. 31. N 6. P. 1065-1069.
6. Filyushkin B.N., 1989. A research of IT lenses of a Mediterranean origin (16-th exp. RV "Vityaz", June 3 - Sept. 16, 1988) // Oceanology. V. 29. N 4. P. 696-698.
7. Filyushkin B.N., Plakhin Eu.A. 1995. An experimental research of an initial stage of shaping of a lens of Mediterranean water // Oceanology. V. 35. N 6. P. 875-882.
8. Hebert D.L., 1988. Mediterranean salt lens / Ph.D. Thesis, Dalhousie University, Halifax, NS. P. 187.
9. Ivanov Yu.A., Mikhailichenko Yu.G., Nikitin S.V., Plakhin Eu.A., Podymov S.I., Filyushkin B.N. 1990. Formation and evolution IT Lenses of Mediterranean origin // Dokl. RAS. 310. N 4. P. 980-984.
10. Klinck J.M., 1989. Geostrophic Adjustment over submarine canyons // J. Geoph. Res. V. 94. P. 6133-6144.
11. Madelain F., 1970. Influence de la topographie du fond sur l'écoulement Méditerranéen entre le Détroit de Gibraltar et le Cap Saint-Vincent // Cah. Oc. V. 22. P. 43-61.
12. Ovchinnikov I.M. 1976. A water balance of the Mediterranean sea. Water exchange through straits // In A hydrology of the Mediterranean sea. / Ed. Burkov V.A. L.: GMI. P. 70-84.
13. Prater M.D., 1992. Observations and hypothesized generation of a Meddy in the Gulf of Cadiz. / Ph. D. Thesis School of Oceanography, University of Washington, Seattle. P. 131.
14. Shapiro G.I., Meschanov S.L. 1996. Spreading pattern and mesoscale structure of Mediterranean outflow in the Iberian Basin estimated from historical data // J. of Marine Systems. V. 7. P. 337-348.
15. Swallow J. C., 1969. A deep eddy off Cape St. Vincent // Deep-Sea Res. V. 16. P. 285-295.
16. Report of 16-th expedition of RV "Vytaz" 1988, V.1. The Final Report of the group chiefs... M.: IO RAS. 200 P.
17. Zatsepin A.G. 1997. Laboratory models of structure-generated processes and frontal of appearances in ocean. An abstract of thesis... PhD., M.: IO RAS. p. 48.

SELF-ORGANIZATION OF THE WATER-AIR BOUNDARY LAYER IN THE CONDITIONS OF FREE CONVECTIVE MOVEMENT

E.P. Anisimova¹, I.V. Petrenko¹, A.A. Speranskaya¹, S.N. Dikarev², O.A. Speranskaya²

¹ Moscow State University, Vorobievi gori, Moscow, 119899, Russia,

² P.P Shirshov Institute of Oceanology, 36, Nakhimovsky Pr., Moscow, 1179851, Russia.

E-mail: zatsepin@glasnet.ru

Abstract. The appearance and evolution of the convective instability in the coupled water-air boundary layers is discussed on the basis of laboratory experiments. In these experiments the water-air system evolved from the thermodynamically equilibrium conditions (covered adiabatic basin) to the quasistationary free convection state (the upper cover open). By means of the flow visualization and temperature measurements it is observed, that the velocity and temperature fluctuation simultaneously occurred in the air and water thin (<1mm) nearsurface layers. This was during the first few seconds after the heat-mass transfer process began. These processes are evaporation, contact heat exchange with air, drops emission. It was recognized, that in the water a dense package of a small scale convective cells have been formed first of all. The form of cells, their vertical and horizontal scales, the period of micro temperature pulsations are determined. An order of magnitude larger convective motions scales appeared later over the already existed small scale pattern. Finally the small scale convection let the large alone. As a result, it is concluded, that the achievement of the quasistationary free convection state has been proceeded through the cascade of instabilities. Such behavior is known to be general for various selforganised thermodynamically open nonlinear systems. Possible physical mechanisms of the effects observed are proposed.

Introduction

Convective movements is one of the main exchange mechanisms in the hydrosphere-atmosphere system. Forced convection can be regarded as one of the most well investigated regime. At the same time the peculiarities of free convective movement is less known. Free convection attracts the attention of researches not only because it is broadly spread. It also can serve as a model to investigate two important mechanisms:

- the appearance, development and interaction of the cascade of hydrodynamic instabilities;
- the competing influence of molecular and turbulent forces governing the self organization processes of the boundary layers in general and particularly of the water-air boundary layer.

Professor Konstantin Fedorov realized the necessity to investigate the peculiarities of free convective movement in the contact ocean-atmosphere zone. For many years he was the head of a well known scientific school aimed to investigate physical modeling of the processes in the ocean. Among the publications it is important to note the investigations of small-scale convective process regularities in the near surface layer of water, carried out by Dr. Anna Ginzburg [1].

For a long time it was considered that convective movement in the water cooling from the surface emerged when the thickness of cooling layer and the temperature in it became critical as a result of molecular heat exchange. And the conditions for the thermogravitational Rayleigh convection are formed. Moreover the investigations conducted at the Physical Faculty of Moscow State University proves that the mechanism of free convection in the boundary water-air layer is much more complicated [2,3]. The group of researches, headed by

Fedorov, found out high frequency temperature fluctuations while it was investigating free convection in the thin near surface water layer. Their origin was not clear till the recent time.

Experimental setup

The goal of this publication is to further investigate the mechanism of the origin and development of free convection in the boundary water-air layer. The work has been carried out by laboratory modeling as in nature it is very complicated to conduct such delicate physical researches because of technical difficulties and multifactor character of processes in nature. The trustworthiness of this publication is provided by simultaneous using of three independent methods of research:

- IR thermal pictures using Swedish device AGEMA;
- contact temperature measurements using the micro resistors MT-67;
- visual methods using PH indicators which allow to measure the parameters of the convective velocity field in the water.

The heat isolated vessel with a cover that can be taken off was filled with warm water so that there was the layer of air between the water surface and the cover. When the vessel was closed the water and the layer of air had the same temperature. At that time there were no measurable temperature fluctuations in the water and in the layer of air and also no possibility to pollute the water surface.

To find out the source of first temperature fluctuations appeared on the water surface in the condition of free convection a number of experiments was carried out. In all of them the temperature was measured simultaneously on three levels:

1. in the air 0,5 mm from the water surface;
2. on the water surface;
3. 0,5mm under water surface.

Results and discussion

The received thermograms show that after the cover is taken off the vessel temperature fluctuations emerge in several seconds in the nearwater layer of air and on the water surface. Temperature fluctuations in the air appear a little bit earlier than on the water surface. The period when first temperature fluctuations appear depends on the temperature difference between the air in the room and in the water. High frequency temperature fluctuations in the thin boundary water-air layer appear as a result of competing interaction between molecular and turbulent heat conductivity. When the cover is taken off the vessel warm water touches the cooler and turbulent air from outside where temperature fluctuations exist initially. On the boundary layer of these two substances step-like turbulent filed emerges, temperature gradient is greatly increased, As a result heat flow determined by molecular mechanism increases sharply. The near water layer of air is becoming warmer, temperature gradient is decreasing and turbulent heat exchange prevails again. Such process is repeated with some quasiperiodocal frequency that stimulates the appearance of temperature fluctuations on the water surface and above it. The evaluations have shown that in the point where air temperature on the temperature fluctuations curve above the heated water surface reaches its minimum, Rayleigh number is lower than its critical value. In the point when the air temperature reaches its maximum, Rayleigh number is higher than its critical value. Critical Rayleigh number is realized in the air only in the moments when the boundary layer is destroyed and air temperature reaches its maximum on the temperature fluctuations curve [2].

On the photographs of the water surface temperature field, taken with the help of AGEMA in consecutive periods from the beginning of the water cooling, the process of micro scale cell structure of the temperature field on the water surface is starting to form during water cooling [3]. Against previously uniform temperature background separate micro cells emerge, their number considerably grows and form a dense package with the wrong shaped polygons as an elements. Having emerged the dense package of convective cells existed during the whole experiment (the time periods of some experiments were as long as several hours).

Mutual analysis of thermograms, thermo pictures of water surface and data of velocity field vision in the thin near surface water layer permitted to determine the period of the instability emergency, temperature

change in a single cell, horizontal and vertical scale of cells. All these measurements have been done using concrete values of temperature changes between water surface and its depth [3].

The cell structure in the near surface layer of water cooling from the surface is forming in the following way. Contact heat exchange with the near water layer of air leads to the formation of places with different temperature on the water surface. Between them surface tension makes water to move from the warmer to the cooler parts. While warm spot is spreading about, in its central part the compensate water lifting is forming from the undersurface level. This leads to the increase in temperature difference between the center of the spot and its periphery. As a result the parts with lower temperature are becoming smaller, turning into the convergence lines of cell structure, which outline the places with higher temperature.

Cold water accumulates in the zones of the convergence lines intersection. And in the same places one can observe the maximum crookedness of the water surface. It is in these places there is a maximum vertical water temperature gradient. At the moment when this vertical temperature difference reaches the critical value a descending cold water stream or a so cold vortex flowing is forming. This is how the conception about a critical hydrodynamic instability providing water circulation in a cell of microthermoconvection emerges.

Vertical and horizontal shapes of microthermoconvection which appears during water surface cooling in the thin (1mm) near surface layer of water were determined using instruments and calculated analytically. The measured and calculated values was in good agreement within the limits of the measurements accuracy.

Experimental data allowed to determine Rayleigh number which was about 1 before the first temperature fluctuations were registered. So the circulation of the microthermoconvective cells is not a Rayleigh convection.

Marangoni number, calculated using experimental values and minimum temperature difference equal to $0,1\text{ C}^\circ$ ($\Delta T_{ws} = 0,1\text{ C}^\circ$) was 48 ± 2 which coincides with the critical Marangoni number calculated according to the linear theory of instability and experimental conditions [3]. With the higher temperature difference (ΔT_{ws}) the Marangoni number increases its critical value and grows together with the growth of ΔT_{sw} .

So it became possible to show that microthermoconvection forming in the millimeter near surface layer of water cooling from the surface is the microthermocapillary Marangoni convection.

As was already noted respectively cold water accumulates in the places of the convergence lines intersections and the high density water are quasiperiodically descending and slowing down below the low border of Marangoni cells. It is there where cooled water accumulates in drops which grow, connect with crosspieces and form a system of mosaic structure. Directly below the low border of Marangoni cells water layer with lower temperature appear. It can be clearly seen on the temperature profiles. When density instability of cooled water layer reaches its critical value, some drops tear off and fall down forming thermals. Soon the process of drop alienation is becoming avalanche like, a sort of rain of thermals appear. With the increase of ΔT_{ws} the time period between the beginning of water surface cooling and first thermals formation is decreased as well as the depth of their penetrating.

The analysis of thermograms and the field of velocity in the near surface layer of water allow to fix the moment when cooled near surface layer of water loses its density stability. This moment is the beginning of thermogravitational convection development and is characterized by separate thermals formation. Calculated Rayleigh number for this moment was 385 which coincides with the critical Rayleigh number for the layer of liquid with two free boundaries. When there is a 'rain' of thermals large scale thermogravitational convection is being developed which covers the whole depth of water in the vessel. This convective movement should be regarded as the convection in the layer which has one free and one solid boundary (water surface and vessel bottom respectively). For these conditions the critical Rayleigh number is 1100. The average Rayleigh number determined experimentally for the moments when the thickness of cooled layer under Marangoni cells reached its maximum was about 1105.

Summary

Conducted experiments revealed that the process of the formation of free convective movement in the water cooling from the surface has several stages. When water is cooled from the surface thermocapillary Marangoni convection is being developed. It prepares and accelerates the appearance of Rayleigh thermogravitational convection for the layer with two free boundaries ($Ra = 385$). Larger scale thermogravitational convection is developed later on with the average Rayleigh number about 1105. This

number is very close to the critical Rayleigh number for the convection in the water layer with one free and one rigid boundary.

This work is partially supported by Russian Fond of Fundamental Research (Grant № 97-05-65528) and Russian Ministry of Science and Technology Project "Laboratory modeling".

References

- [1]. Ginzburg A.I., Fedorov K.N. The Near-surface Layer of the Ocean, Gidromet, 1988, 303p. (in Russian) / Transl. to English in 1992.
- [2]. Anisimova E.P., Petrenko I.V., Speranskaya A.A. On the determination of the Rayleigh number critical value in the free convection conditions. Vestnik MSU, 1991, V.32, N2 (in Russian).
- [3]. Anisimova E.P., Petrenko I.V., Speranskaya A.A. . Origin of free convection in water cooled from the surface. FAO, 1994, V.30, N1 (in Russian).

DISPERSION OF SUSPENDED MATTER IN A SUPERCRITICAL RIVER PLUME DISCHARGING IN A MICROTIDAL SEA : AN INTEGRATED APPROACH

S. Arnoux-Chiavassa, P. Broche, J.L. Devenon, N. Durand, A. Fiandrino, P. Forget, P. Fraunié, S. Ouillon, V. Rey

Laboratoire de Sondages Electromagnétiques de l'Environnement Terrestre, UPRESA 6017 CNRS, Université de Toulon et du Var, BP 132, 83957 La Garde cedex, France
arnoux, broche, devenon, durand, fiandrino, forget, fraunie, ouillon, rey@lsect.univ-tln.fr

Abstract. River plume discharges represent the main source of freshwater and suspended matter in coastal areas. Complex spatio-temporal mechanisms of exchanges are investigated for successively highly stratified and mixed situations, using *in-situ* measurements, remotely sensed observations, and numerical modeling involving higher order discretization schemes.

In this way, 3D salinity, temperature and suspended matter fields were investigated in the Rhône and Ebro river plumes. Depending on the wind conditions, these exhibit weak to large vertical diffusion patterns, leading to a challenging case for modeling.

As a result, the occurrence of fronts along the plume boundaries is shown to inhibit exchanges in the region near the plume, but to enlarge the region of freshwater influence.

I. Introduction

The Region of freshwater influence (ROFI zone) as introduced by Simpson [1] has been investigated for several sites [1] [2] [3] or academic situations [4]. At smaller scale, the plume dynamics has been extensively investigated [5] [6] [7] [8] [9] [10] [11]. In particular, the hyperbolic behavior of supercritical plumes has been pointed out, up to the far plume mixing region, inducing either a coastal jet, or an offshore diffusion area.

In microtidal seas, the frontal structure of supercritical plumes is clearly visible on satellite images and complete investigations of characteristic situations in Mediterranean sites (Rhône and Ebro rivers) are reported here, in order to describe the mixing processes between the plume and the sea.

In particular, the wind effect is expected to involve complex interactions between the river plume (time scales on the order of hours) and 3D upwelling effects in complex geometries (time scales on the order of days [12]). Moreover, the horizontal and vertical diffusion coefficients in the plume layer are strongly dependent on the wind friction.

Basically, we are here interested in the description of the dispersion of dissolved and suspended matters in a frontal zone. Numerical modeling approach and turbulent closure problem will be addressed from this point of view.

II. Methodology

Several tools have been used to investigate the dynamics and suspended matter budget of a river plume [13] [14]: satellite images inversion [15] [16] provided a complete instantaneous Eulerian map of surface - or small

depth integrated - concentrations, where fronts of actual as well as former plumes are clearly observable. In addition, VHF radar surface velocity measurements provided high frequency temporal evolution of the plume dynamics during short periods (several weeks).

These high resolution techniques (50 meters pixel for SPOT images, 500 meters integration cell for the radar resolution, 10 cm for vertical CTD profiles) are similar to the 100 to 500 meter horizontal grid size and 25 to 50 cm vertical grid size used in numerical simulations. Moreover, CTD Lagrangian measurements have been performed following a drifter in the plume in order to describe the mixing process for a "fixed" water mass, at least at the surface [17].

Unfortunately, simultaneous measurements using all these techniques are sparse, but typical situations have been recovered in such a way that quantitative conclusions can be proposed.

III. The river plume dynamics

The river plume extension can be easily quantified from series of satellite images. The sampling time scale (less than once a day) does not allow to follow the plume dynamics, but small scale features, such as former plumes in unsteady wind conditions or local Kelvin-Helmholtz instabilities in the horizontal front are clearly observable.

For all the cases presented here, only weak interactions with the mesoscale circulation were observed, due to the reduced size of the plume extension on the continental shelf. In this way, such river plumes (10-50 km) can be considered as real size "laboratory experiments".

Then, two main classes of situations can be pointed out: quasi-steady reproducible situations, when flow inputs and wind climate are under control even for impulsively started plumes (e.g. due to an upstream dam opening in the river) and, on the other hand, varying wind situations when the river plume reacts very quickly, as compared to the surrounding upwelling flow, in such a way that several former plumes can superimpose.

Wind variations, especially in direction, introduce complex plume dynamics and drastically change mixing processes, when several former situations can superimpose. Such unsteady situations are very important for telluric matter dispersion in the extended ROFI zone but remain difficult to reproduce by modeling: complex scenarii have to be computed in order to provide any budget.

Another complex situation can occur when the mesoscale variability of the wind in the atmospheric boundary layer affects the sea surface layer as it currently happens in the Ebro site (Fig. 1).

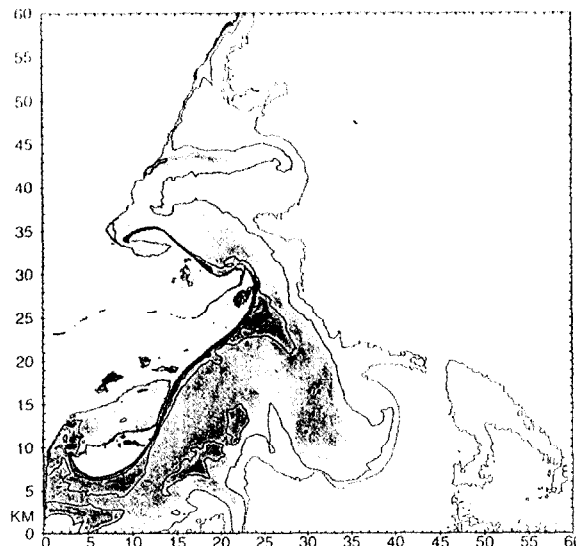


Fig. 1: TSM concentration map derived from XS2 data. TSM isolines: 1.5-1-0.5-0.4 mg/l.

IV. The quasi-steady situation

Supercritical plumes with quasi-steady discharge and wind conditions are currently observed. Such situations have been investigated for both sites based on SPOT images and surface current modeling for the Ebro river site (Fig. 2), for the Rhône river site (Fig.3).



Fig. 2: TSM concentration map derived from XS2 data. TSM isolines: 15-10-5-1 mg/l.



Fig. 3: extra atmospheric radiance from SPOT XS2.

The frontal plume is deflected by Coriolis effects and the reproducible shape is dependent on the wind: extended offshore by the effect of a "mistral" wind blowing from the land, or attached to the coast with a coastal jet, by the effect of an onshore wind.

Then, the mixing process mainly occurs downstream the front destabilization, sometimes with characteristic Kelvin-Helmholtz type oscillations. However, Lagrangian vertical CTD profiles for the Rhône river (Fig. 4 and Fig. 5) (measurements points are shown on Figure 7) exhibit a mixing process involving increasing salinity in the plume.

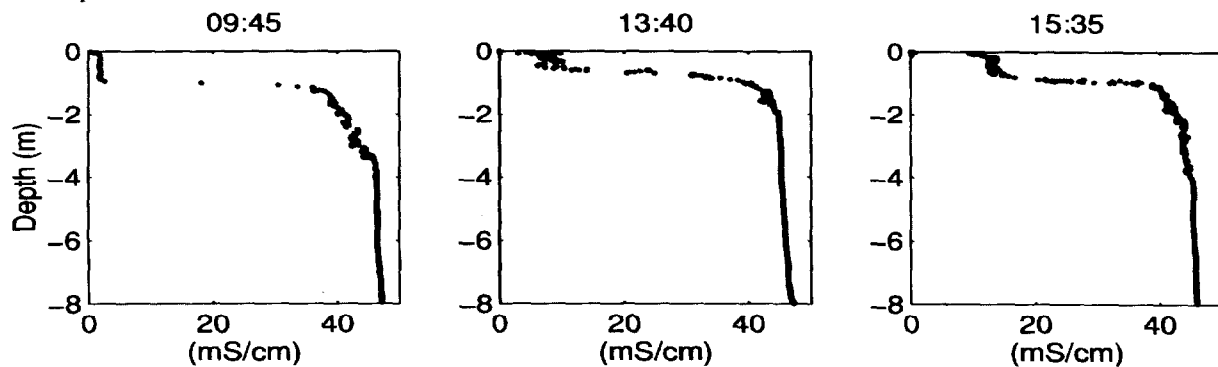


Fig. 4: Rhône site, CTD profiles, weak wind stress situation.

The vertical profile in the plume layer strongly depends on the wind strength: the plume depth keeps an almost constant thickness with weak wind friction (Fig. 4) and thickens with higher wind stress (Fig. 5).

In such a case, the vertical profile of temperature or salinity exhibits a quasi-homogeneous layer of freshwater and a sharp gradient at the interface with the sea. However, salinity is increased, due to an efficient entrainment mechanism.

Usual 3D numerical models are able to reproduce the global dynamics of such plumes except the frontal zone, where a reduced numerical diffusion is required.

Moreover, quasi-isotropic two-equation models of turbulence do not work in such situations, and algebraic models based on a Richardson's number parametrization have been shown to be more appropriate, when associated to non-diffusive numerical schemes [18]. A river plume, as a buoyant jet, appears to be a very

complex flow combining highly stratified situations [19] with a Richardson's number value more than one and non-equilibrium shear flows [20]. Especially, the surprisingly efficient mixing observed in the near plume without wind (Fig. 4) can be related to basic studies, from laboratory and *in-situ* experiments, concerning high Richardson number situations [21] [22] [23].

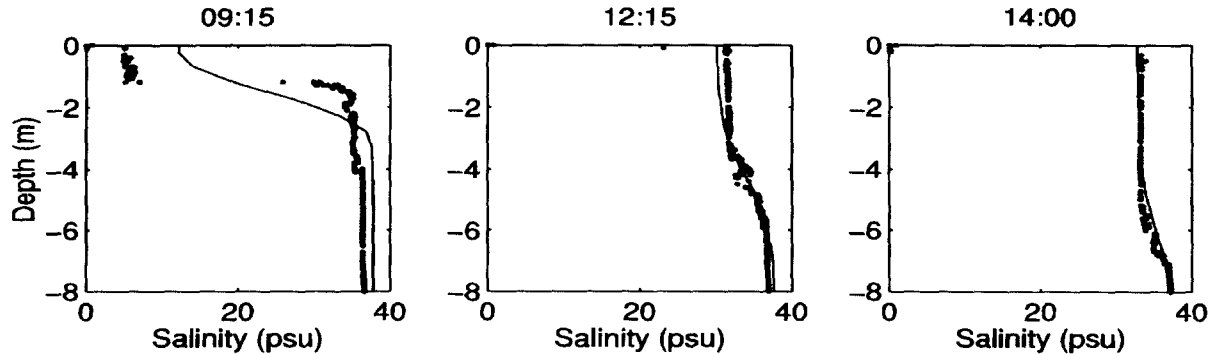


Fig. 5: Rhône site, CTD profiles, high wind stress situation. Solid line: model results.

The downstream mixing parametrization is extremely important for the ROFI zone description of river inputs as well as for the plume equilibrium in numerical modeling. In fact, quasi-steady or impulsively started plumes have been found to be optimal situations for comparison with *in-situ* data (Fig. 2). This situation, when suspended matter is confined in the freshwater layer of the frontal plume has been observed to improve the biological blooms after the downstream mixing.

V. Numerical modeling

Only quasi-steady situations have been numerically investigated in order to quantify the exchange rates between the plume layer and the sea.

The 3D numerical model developed in LSEET [24] has been applied to the two previously presented sites [14] [25]. The 3D Cartesian grid is variable from 100 to 500 meters in the horizontal direction and .25 to 10 meters in the vertical direction. The turbulence closure is algebraic [26] and the inflow profile is prescribed at the river mouth in order to represent the salt wedge.

Qualitative agreement with observations can be observed by comparing Figure 2 and Figure 8. The specific feature of the detached coastal jet is well reproduced, although mesoscale structures are not taken into account in the model. This demonstrates, the "blue waters" recirculation along the coast is resulting from complex 3D interactions between the plume jet and the coastal upwelling.

The front description has been recently improved by use of a SMART type numerical discretization [27] for momentum and transport equations [18].

Comparison between different computations capturing (SMART scheme) or not the frontal structure, shows significant differences in the mixing efficiency on the supercritical plume boundaries. The use of such a higher order scheme enables good evaluation of the dynamic fronts for an offshore wind steady-situation, as shown by the comparison between surface velocity fields obtained by radar measurements (Fig. 6) and modeling (Fig. 7). In this situation, a good qualitative and quantitative agreement is also found between the vertical density plume structure, as deduced from the CTD data, and the one obtained from modeling (Fig. 5). This result confirms the importance of the flow confinement for the plume extension. However, refined measurements through the frontal zone would be necessary to better quantify these exchanges.

Anyway, isolines of total suspended matter (TSM) concentration (Fig. 9) qualitatively agree with image inversions (Fig. 2).

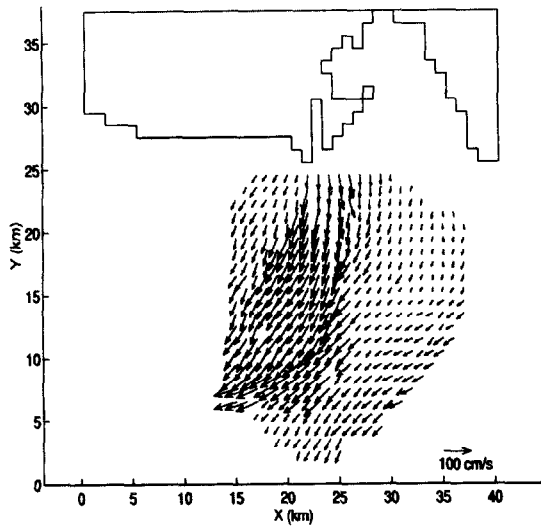


Fig. 6: Rhône case, VHF Radar map.

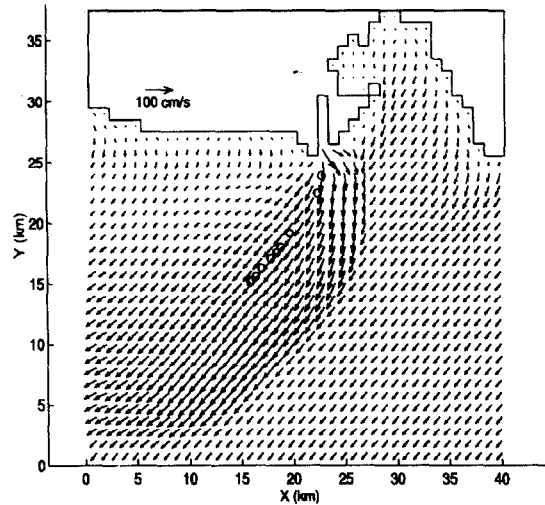


Fig. 7: Rhône case, horizontal view of computed velocity field at sea surface.

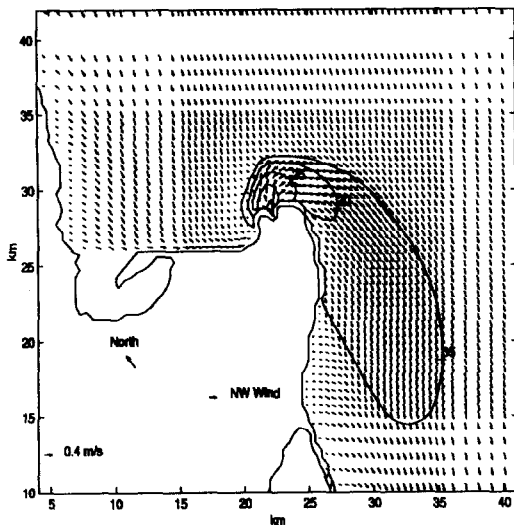


Fig. 8: Ebro case, horizontal view of computed velocities and isosalinity contours at sea surface.

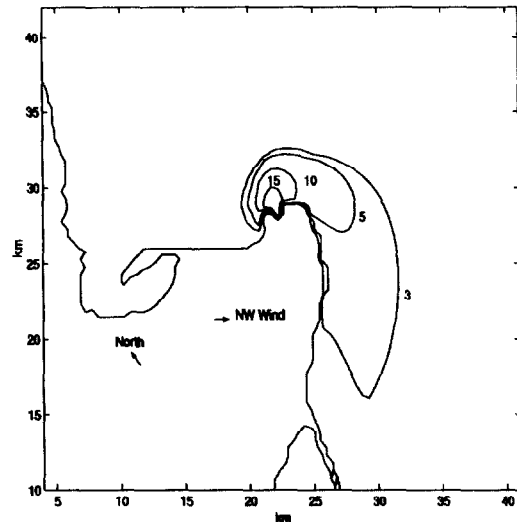


Fig. 9: Ebro case, horizontal view of TSM iso-concentrations (mg/l) at sea-surface.

Conclusions

Different situations were investigated for river plumes in a microtidal sea when considered as "real site laboratories". Complete sets of measurements and modeling techniques were put together to provide the calibration of satellite images and numerical models that can be useful tools for TSM budget, when associated to temporal series for climatic boundary conditions.

Accurate parametrization for dynamics and suspended matter modeling were proposed for quasi-steady situations, for which promising validation was obtained. However, the wind shear was shown to be the major influent effect and the most difficult to be taken into account.

In such a case, only ocean-atmosphere coupled mesoscale models could provide the description of the complex plume dynamics which is observed (Fig. 1).

Acknowledgements

This research was supported by the french Programme National d'Océanographie Côtière and EC Mast III Program FANS (Contract MAS3-CT95-0037). *In-situ* measurements were performed with Arago laboratory and due to the CIRMED allocation of ship cruises.

References

- [1] J.H. Simpson, 1997, Physical processes in the ROFI regime, *J. Mar. Syst.*, 12, 3-15.
- [2] V.H. Kourafalou, L.Y. Oey, J.D. Wang and T.N. Lee, 1996, The fate of river discharge on the continental shelf: 1: modelling the river plume and the inner shelf coastal current, *J. Geophys. Res.*, 101, 3415-3434.
- [3] R.E. Turner and N.N. Rabalais, 1994, Coastal eutrophication near the Mississippi river delta, *Nature*, 368, 619-621.
- [4] L.Y. Oey and G.L. Mellor, 1993, Subtidal variability of estuarine outflow, plume and coastal current: A model study, *J. Phys. Oceanogr.*, 23, 164-171.
- [5] R.W. Garvine, 1974, Dynamics of small scale fronts, *J. Phys. Oceanography*, 4, 557-569.
- [6] R.W. Garvine, 1977, Observations of the motion field of Connecticut river plume, *J. Geophys. Res.*, 82, 441-452.
- [7] R.W. Garvine, 1995, A dynamical system for classifying buoyant coastal discharges, *Cont. Shelf Res.*, 15, 1585-1596.
- [8] S.Y. Chao, 1988, River forced estuarine plumes, *J. Phys. Oceanography*, 18, 72-88.
- [9] S.Y. Chao, 1988, Wind driven motion of estuarine plumes, *J. Phys. Oceanography*, 18, 1144-1166.
- [10] R.G. Ruddick, E. Deleernijder, P.J. Luyten and J. Ozer, 1995, Haline stratification in the Rhine-Meuse freshwater plume: a three dimensional model sensitivity analysis, *Cont. Shelf Res.*, vol 15, 13, 1597-1630.
- [11] P. Marsaleix, C. Estournel, V. Kondratychoff and R. Vehil, 1998, A numerical study of the formation of the Rhône river plume, *J. Marine Systems*, 14, 99-115.
- [12] C. Verdier-Bonnet, P. Angot, P. Fraunié and M. Coantic, 1998, Three dimensional modelling of coastal circulations with different k-ε closures, *J. Marine Systems*, in press.
- [13] P. Broche, J.L. Devenon, P. Forget, J.C. de Maistre, J.J. Naudin and G. Cauwet, 1998, Experimental study of the Rhône river plume Part I: physics and dynamics, *Oceanologica Acta*, in press.
- [14] S. Arnoux-Chiavassa, V. Rey and P. Fraunié, 1998, Modelling of suspended sediment fluxes off the Rhône river mouth, *J. Coastal Res.* in press.
- [15] P. Forget, S. Ouillon, F. Lahet and P. Broche, 1998, Inversion of reflectance spectra of non-chlorophyllous turbid coastal waters, *Remote Sensing of Environment*, in press.
- [16] S. Ouillon, N. Durand, P. Forget, A. Fiandrino and P. Fraunié, 1998, Remote sensing as a tool for suspended sediment transport modelling in coastal areas, *proc. Third Int. Conf. on Multiphase Flow, ICMF'98*, Lyon, june 8-12.
- [17] J.J. Naudin, G. Cauwet, M.J. Chretiennot-Dinet, B. Deniaux, J.L. Devenon, H. Pauc, 1997, River discharge and wind influence upon particulate transfer at the land-sea interaction. Case study of the Rhone river plume, *Estuarine, Coastal and Shelf Science*, 45, 303-316.
- [18] S. Arnoux-Chiavassa, P. Angot and P. Fraunié, 1998, Numerical simulation of supercritical river plumes in microtidal sea by TVD schemes, *JONSMOD 98*, Delft, july 20-23.
- [19] J.R. Ledwell, A.J. Watson and C.S. Law, 1993, Evidence for slow mixing across the pycnocline from an open ocean tracer-release experiment, *Nature*, 364, 701-703.
- [20] I. Danaila, J. Dusek and F. Anselmet, 1997, Coherent structures in a round, spacially evolving unforced, homogeneous jet at low Reynolds numbers, *Phys. of Fluids*, vol.9.
- [21] L.F. Linden, 1980, Mixing across a density interface produced by grid turbulence, *J. Fluid Mech.*, 100, 691-703.
- [22] G.N. Ivey and J. Imberger, 1991, On the nature of turbulence in a stratified fluid. Part I: the energetics of mixing, *J. Phys. Ocean.*, 21, 650-658.
- [23] T. Gerz and H. Yamazaki, 1993, Direct numerical simulation of buoyancy-driven turbulence in stably stratified fluid, *J. Fluid Mech.*, 249, 415-440.

- [24] C. Verdier-Bonnet, P. Angot and P. Fraunié, 1997, Paramétrisation de la turbulence pour le phénomène d'upwelling côtier en milieu stratifié, C.R. Acad. Sci, t 324, Série II b, 229-238.
- [25] N. Durand, A. Fiandrino, S. Ouillon, P. Fraunié and P. Forget, 1997, 3D numerical study of the Ebro delta zone hydrodynamics, MEDCOAST 97, Malta, november 11-14.
- [26] W.H. Munk and E.A. Anderson, 1948, Notes on a theory of the thermocline, J. Mar. Res., 7, 276-295
- [27] P.H. Gaskell and A.K.C. Lan, 1988, Curvature-compensated convective transport: SMART, a new boundedness-preserving transport algorithm, Int. J. for Num. Meth. in Fluids, 8, 617-641.

LANGMUIR CIRCULATIONS AS COHERENT STRUCTURES

N.S. Blokhina 1, A.E. Ordanovich 2, O.V. Kravchenko 1

1. Moscow State University, Department of Physics, 119899 Moscow, Vorobyevy Gory,
E-mail: ecoc47@phys.msu.su, Tel. (7) -095-9393698, Russia
2. Moscow State University, Department Mechanics and Mathematics, 119899 Moscow, Vorobyevy Gory,
E-mail: orda7@inmech.msu.su, (7)-0950-9393383, Russia

Abstract. At present regular large-scale vortex formations in a turbulence currents have been named of coherent structures. In this paper the theory of coherent structures developed by authors is considered on an example of Langmuir circulations (LC). The mathematical LC model contains the equation systems, like Reynolds equations, for the description of averaged and ordered movements. The small-scale turbulence is taken into account integrally by the calculation of turbulent exchange coefficient. The results of calculations are discussed and compared with the data of nature observations.

Natural observations show that regular large-scale vortex formations arise in many strong turbulence geophysical currents in the atmosphere and hydrosphere. These vortex formations had received the name of coherent structures (CS). Langmuir circulations (LC) may be considered as an example of CS. These circulations represent a system of parallel vortex wisps stretching out along the direction of wind and covering the upper quasihomogeneous layer of the oceans or reservoirs. The vortex wisps have an opposite direction of rotation. They could be visible on water surface as the agglomerations of a foam and pollutions in convergence zones.

LC play a significant and often decisive role in formation of active layer of a reservoir. They cause intermixing this layer, transportation of oxygen, organic substances and different ecologically important elements in reservoirs.

Calculations and analysis of observations in reservoirs show that the main reasons of LC excitation are the fluxes of explicit heat and fluxes of latent (due to evaporation) heat. These fluxes lead to the cooling of water surface the excitation of convection. The drift current orient convective vortices along the wind direction.

Determination of excitation conditions and characteristics of LC are of significant interest from the ecological point of view. This allows us to estimate the influence of the hydrometeorological conditions and pollution of reservoir surface on a state of the upper active water layer.

In this paper, our approach uses the earlier developed theory of coherent structures [1,2]. This theory was based on a similarity between coherent structures in turbulent flows secondary currents, which arise in laminar flow after the loss of stability. This similarity allows us to formulate and a model of the turbulent flow and to

consider this flow as viscous medium with special properties where the secondary currents develop. In future what these secondary currents in turbulent flows will be called coherent structures.

Several problems were solved using this theory: modeling of coherent structures in the open turbulent flows [2]; modeling of coherent structures in the stratified turbulent currents in channels [3]; modeling of «cloudy streets» in the boundary layer of the atmosphere [4,5]; modeling of Langmuir circulations in the active layer of a reservoir [6-12].

Let us consider the potentials of the proposed approach on an example of the LC modeling.

This model includes a liquid motion in a basin which has a constant depth H and is boundless in the horizontal direction. It was supposed that convection penetrates down up to the bottom.

The liquid motion is described by a system of thermohydrodynamic Navier-Stokes equations in the Boussinesq approximation. The state of the water at each point of the basin is described by the temperature T and three velocity components: U_1 is the component along the wind direction, U_2 and U_3 are the horizontal and vertical components perpendicular to the wind direction. It is assumed that the water surface is free and the wind velocity V over the water is constant in its value and direction. Wave movements on the water surface is ignored, i.e., $U_3(H)=0$. The thermal and dynamic interaction of the reservoir and atmosphere are taken into account only in the boundary conditions on the upper free surface of the reservoir. In particular, the tangent stress is taken as $\tau=\rho_a C_u V^2$, explicit heat flux - $Q_T=\rho_a c_p C_T (T-T_a)V$, latent heat flux - $Q_L=LC_L(q-q_a)V$ and radiation balance heat flux - Q_R . It is assumed that on the bottom of the basin the constant temperature $T=T_b$ and conditions of adhesion and nonflow for the velocity are given.

Here τ is the friction stress; C_u is the resistance coefficient; C_T and C_q are the Stanton and Dalton numbers, respectively; ρ_a and c_p are the density and the specific heat of the air at constant pressure; L is the latent heat of evaporation; T_a and q_a are the temperature and humidity of the air; T and $q=q(T)$ are the water temperature and specific humidity of the air near the water surface.

Let us briefly describe method for separation of coherent structures in turbulent medium [1]. According to this method, all variables are represented as the sum of three components:

$$\alpha(x_1, x_2, x_3, t) = \bar{\alpha}(x_3, t) + \tilde{\alpha}(x_2, x_3, t) + \alpha'(x_1, x_2, x_3, t), \quad (1)$$

where $\bar{\alpha}$ is a mean value; $\tilde{\alpha}$ describes the ordered large-scale coherent structures, and characterizes the mathematical expectation of α under condition of a preliminary choice of a coordinate system; α' describes a deviation from averaged and ordered movements. This value is interpreted as small-scale turbulence. It is assumed that the turbulence is not correlated with the averaged and ordered movements.

Substituting all the variables of form (1) into the thermohydrodynamic equations and the boundary conditions and using the rules described in [1], we obtain three systems of the Reynolds type equations for: the averaged movement (drift current), coherent structures (LC) and small-scale turbulence. The first two systems of equations contain the analogs of Reynolds stresses r_{ij} and turbulent heat fluxes q_i , which take into account the influence of small-scale turbulence on the averaged and ordered motions. Hereinafter the equations for description of small-scale turbulence are ignored. Following to Bussinesq hypothesis, the coefficients of

turbulent exchange (ν_T) and temperature conductivity (λ_T) are introduced for the closing of first two systems of equations. It is assumed that:

$$\begin{aligned}\bar{r}_{ij} &= -(\overline{U'_i U'_j}) = \nu_T \left(\frac{\partial \bar{U}_i}{\partial x_j} + \frac{\partial \bar{U}_j}{\partial x_i} \right) + \frac{1}{3} \bar{r}_{kk} \delta_{ij}, & \tilde{r}_{ij} &= -\left[\overline{U'_i U'_j} \right] - (\tilde{U}_i \tilde{U}_j) = \nu_T \left(\frac{\partial \tilde{U}_i}{\partial x_j} + \frac{\partial \tilde{U}_j}{\partial x_i} \right) + \frac{1}{3} \tilde{r}_{kk} \delta_{ij}, \\ \bar{q}_i &= -(\overline{T' U'_i}) = \lambda_T \frac{\partial \bar{T}}{\partial x_i}; & \tilde{q}_i &= -\left[\overline{T' U'_i} \right] - (\tilde{T} \tilde{U}_i) = \lambda_T \frac{\partial \tilde{T}}{\partial x_i}.\end{aligned}$$

It is assumed that the coefficient of turbulent exchange is constant in the entire medium and much larger than the corresponding molecular value. The turbulent Prandtl number is equal to 1 ($\lambda_T = \nu_T$). To determine the value of the coefficient of turbulent exchange, we will use the widely known relation

$$\nu_T = C \varepsilon^{1/3} H^{4/3}.$$

Here ε is the mean dissipation rate of the small-scale turbulent kinetic energy, H is the typical scale of turbulent structures and C is an empirical constant. The value ε can be found from the energy balance equations for the small-scale turbulence.

The system of equations with boundary and initial conditions is written down in the streamline function and vortex variables and in the dimensionless form.

The equations for averaged values and boundary conditions are:

$$\begin{aligned}\frac{\partial \bar{U}_1}{\partial t} &= \mu \frac{\partial^2 \bar{U}_1}{\partial x_3^2} + \frac{\partial (\tilde{U}_1 \tilde{U}_3)}{\partial x_3} & x_3=1: & \mu \frac{\partial \bar{U}_1}{\partial x_3} = \text{ru}^2; \\ \frac{\partial \bar{\Theta}}{\partial t} &= \mu \frac{\partial^2 \bar{\Theta}}{\partial x_3^2} + \frac{\partial (\tilde{\Theta}_1 \tilde{U}_3)}{\partial x_3} & & -\mu \frac{\partial \bar{\Theta}}{\partial x_3} = R + A_1 u + A_2 (\bar{\Theta} - \Theta_a) \\ & & x_3=0: & \bar{U}_1 = \bar{\Theta} = 0.\end{aligned}$$

The equations and boundary conditions for the ordered structures are:

$$\begin{aligned}\frac{\partial \tilde{U}_1}{\partial t} - \mu \Delta \tilde{U}_1 + \tilde{U}_3 \frac{\partial \tilde{U}_1}{\partial x_3} &= L(\tilde{U}_1) & x_3=1: & \frac{\partial \tilde{U}_1}{\partial x_3} = \frac{\partial \tilde{\Psi}}{\partial x_2} = \frac{\partial^2 \tilde{\Psi}}{\partial x_3^2} = 0; \\ \frac{\partial \tilde{\Phi}}{\partial t} - \mu \Delta \tilde{\Phi} + \frac{\partial \tilde{\Theta}}{\partial x_3} &= L(\tilde{\Phi}) & & -\mu \frac{\partial \tilde{\Theta}}{\partial x_3} = A_2 \tilde{\Theta} u \\ \frac{\partial \tilde{\Theta}}{\partial t} - \mu \Delta \tilde{\Theta} + \tilde{U}_3 \frac{\partial \tilde{\Theta}}{\partial x_3} &= L(\tilde{\Theta}) & x_3=0: & \tilde{U}_1 = \frac{\partial \tilde{\Psi}}{\partial x_2} = \frac{\partial \tilde{\Psi}}{\partial x_3} = \tilde{\Theta} = 0. \\ \tilde{\Phi} &= \Delta \tilde{\Psi}\end{aligned}$$

The closure equation for calculation of the dimensionless coefficient of turbulent exchange is

$$\mu^2 = \frac{C^3}{\lambda} \int_0^1 dx_3 \int_{x_{20}}^{x_{20}+\lambda} \left\{ \left[\left(\frac{\partial \bar{U}_1}{\partial x_3} \right)^2 - \frac{\partial \bar{\Theta}}{\partial x_3} \right] + \left[\left(\frac{\partial \tilde{U}_1}{\partial x_3} \right)^2 + \left(\frac{\partial \tilde{U}_1}{\partial x_2} \right)^2 + 4 \left(\frac{\partial^2 \tilde{\Psi}}{\partial x_2 \partial x_3} \right)^2 + \left(\frac{\partial^2 \tilde{\Psi}}{\partial x_3^2} - \frac{\partial^2 \tilde{\Psi}}{\partial x_2^2} \right)^2 \right] \right\} dx_2.$$

Where

$$L(f) = \left(\tilde{U}_2 \frac{\partial f}{\partial x_2} + \tilde{U}_3 \frac{\partial f}{\partial x_3} \right) - \left(\tilde{U}_2 \frac{\partial f}{\partial x_2} + \tilde{U}_3 \frac{\partial f}{\partial x_3} \right),$$

$$\tilde{U}_2 = \frac{\partial \tilde{\Psi}}{\partial x_3}; \quad \tilde{U}_3 = -\frac{\partial \tilde{\Psi}}{\partial x_2}; \quad \Delta f = \frac{\partial^2 f}{\partial x_2^2} + \frac{\partial^2 f}{\partial x_3^2}; \quad \Theta = T - T_b.$$

In this system the following variables are used for scaling: unit of length - $L_m=H$; unit of speed - $U_m=V/\sqrt{gH}$; unit of time - $t_m=\sqrt{H/g}$; unit of temperature - $\Theta_m=1/\beta_0$. Here β_0 is the temperature coefficient of thermal expansion of the water; $\lambda=d/H$ is the dimensionless period of repetition of ordered structures along the x_2 -axis ; $\mu = v_T/H\sqrt{gH}$ is the coefficient of turbulent exchange; $R=Q_R/Q_m$ is the dimensionless radiation heat flux , here $Q_m=c_0\rho_0\sqrt{gH}/\beta_0$; $r=\rho_a C_u/\rho_0$; $\Theta_m=\beta_0(T_b-T_a)$,

$$A_1(T_a, f) = \frac{C_q L(1-f)\beta_0 \phi(T_a)}{\rho_a c_0} \quad A_2(T_a) = \frac{\rho_a C_T c_p + F(X_2)L(\partial \phi(T_a)/\partial T)}{\rho_a c_0}, \quad \text{where}$$

$$F(X_2) = C_{qcon} + \frac{C_{qdiv} - C_{qcon}}{2} \left(1 + \frac{\cos(\pi X_2)}{16} \right) - \text{in the case of pollution modeling and } F(X_2) = 1 \text{ in the other cases.}$$

C_{qdiv} and C_{qcon} are the values of Dalton numbers in zones of LC divergence and convergence; $q=f\phi(T_a)$ and $q=\phi(T)$ are the specific humidity of the air and specific humidity of the air near the water surface; f is the relative humidity of the air.

Verification of the LC mathematical model using data of natural measurements on Mojaisk reservoir in May 1989 was accomplished for checking this model [11]. Analysis of these data shown that the upper quasihomogeneous layer of the water was cooled losing about 80 w/m^2 through the water surface. Herewith the water temperature decreased uniformly in the whole layer. This fact indicated that in the reservoir the intensive convective mixing of the water takes place. The empirical data (wind velocity , relative air humidity , air and water temperature, radiating heat flux) were used for LC modeling. Velocity and temperature profiles for the average current (drift) and characteristics of the coherent structures (distribution in temperature, velocity,

stream function, coefficient of turbulent exchange, etc.) were obtained. Some of these results could be compared with the data of natural measurements.

Figure 1 shows the calculated temperature profiles for $Q_R = 80 \text{ w/m}^2$. Profile 1 corresponds to the convergence zone, 2 - to the divergence one, 3 - to the center part of the eddy. The dots correspond to the natural measurements of the water temperature. The horizontal lines correspond to an accuracy of temperature measurements. We can see a good coincidence between the calculated and observed temperatures. The results of this comparison demonstrate that this LC model describes the natural processes correctly on the whole.

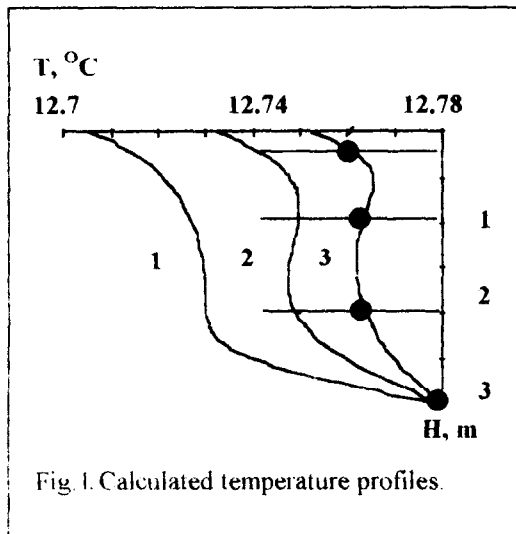
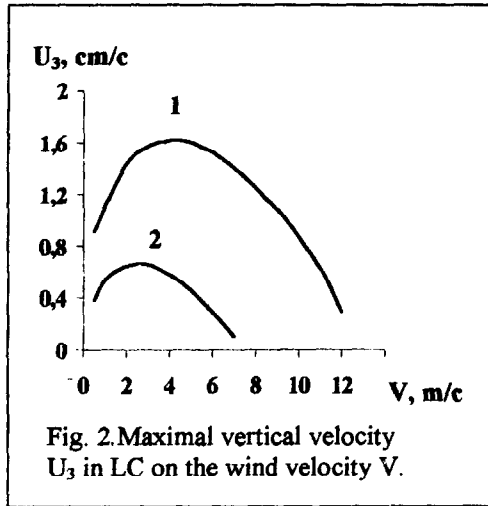


Fig. 1. Calculated temperature profiles.

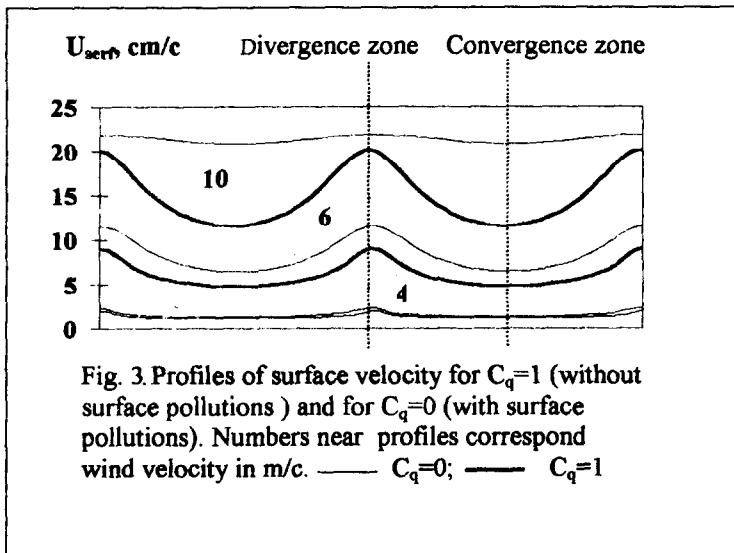
Let us consider the results of calculations in details. The conditions of LC origin and their parameters were investigated for various hydrometeorological situations. The following parameters: $H=10$ m, $f=60, 80, 95$ %, $T_b=25^\circ\text{C}$ and $12,7^\circ\text{C}$; $T_a=23, 27$ and $6,5^\circ\text{C}$ were used for LC modeling. Radiation heat flux changed from 70 w/m^2 in night time to 420 w/m^2 in the afternoon. The wind velocity varied from 1 m/c up to 24 m/c .



The calculations show that our LC model describes many peculiarities in natural LC.

Modeled LC took place for wind velocities up to $7-14$ m/c depending on hydrometeorological conditions. Asymmetry of these structures was observed. The region of liquid rise was wider than the region of lowering. The centers of eddy were displaced to the top border and to convergence zones. Vertical velocity of the liquid movement had the greater values in the convergence zones than in the divergence zones. The liquid was colder in all horizons of convergence zones. Our calculations shown that the vertical velocities (U_3) in LC and intensity of eddies reached there maximum at wind velocities $3-6$ m/c (fig.2)

depending on the hydrometeorological conditions. Regimes when LC took place at the air temperature higher than the water temperature were modeled. Curve 2 in the figure 2 corresponds to this case (the difference between water and air temperature was $\Delta T = -2^\circ\text{C}$). Curve 1 corresponds to the difference between these temperatures $\Delta T = +2^\circ\text{C}$. LC disappeared for smaller values of the wind velocity in the first case ($\Delta T = -2^\circ\text{C}$) than values of wind velocity in the second case. The intensity of eddies was less in the first case. In the first case the maximum vertical velocity of the water rise approximately 2,5 times less than in the second one.



On the basis of constructed mathematical model the situations when pollution films covered the water surface were investigated. Characteristics of water surface pollution were taken into account in the model as parameters in boundary conditions. The water surface pollution changed the latent heat flux most essentially due to evaporation from the water surface. These effect were taken into account in the model using the different Dalton numbers.

Series of calculations were performed for uniform and non-uniform surface pollution distributions and various wind velocities. Some of these results are represented in figures 3. In the first case the decrease of the Dalton number (C_q) and increase of the wind velocity (V) led to increasing the drift current velocity, water temperature, and water mass stability. At the same

time, the difference in the velocities and temperatures in the convergence and divergence zones decreased. A non-uniform pollution of the water surface can reduce dynamic characteristics of LC system by 20 % depending of pollution thickness.

Thus, all the peculiarities of LC known from the literature were described by the our mathematical model both qualitatively and quantitatively. This model also may be successfully used for various types of turbulence currents.

The work was supported by RFBR grants (projects 96-01-01118, 96-05-64547, 96-05-65856).

References

1. V.A.Kovalev, A.E Ordanovich., 1981, Physical-mathematical model of turbulent horizontal stratified flow with account for coherent structures, Pt.1, The model formulation, VINITI, 27-081.
2. V.A Kovalev., A.E Ordanovich., 1991, Theoretical study of turbulent structures in a turbulent channel flow, *Izv. Acad. Sci. USSR Mekhanika Zhidkosti i Gaza*, 3, 32-38 A.V.
3. Latyshev, A.E Ordanovich., 1981, Modeling of ordered structures in open turbulent flows, *Izv, Acad. USSR, Mekhanika Zhidkosti i Gaza*, 4, 45-52.
4. A.E Ordanovich., 1988, Mathematical modeling of «cloud streets» in the boundary layer of the atmosphere, *Izv. Acad. Sci. USSR, Atmos. Oceanic Phys.*, v.24, 9, 922-931.
5. L.A Mikhailova., A.E Ordanovich., 1988, Mathematical modeling of ordered structures in the atmosphere boundary layer, *Izv. Acad. Sci. USSR, Atmos. Oceanic Phys.*, v.24, 10,1023-1032.
6. T.B. Glukhovskaya., A.E Ordanovich., 1987, Theoretical study of ordered structures developing in the upper layer of water body due to the action of wind on its surface, *Meteorologiya i Hydrologiya*, 12, 62-70.
7. N.S. Blokhina, A.E. Ordanovich, 1992, Mathematical modeling of convective eddy patterns developing in a water body under wind forcing, *Soviet Meteorology and Hydrology*, 3, 23-30.
8. N.S Blokhina., A.E Ordanovich.,1992, The effect of hydrometeorological conditions on convective eddy structures, *Soviet Meteorology and Hydrology*, 10, 43-49.
9. N.S. Blokhina, A.E. Ordanovich, 1993, The influence of air humidity on the development of convective eddy in the upper layer of a water body, *Russia Meteorology and Hydrology*, 1, 9-12.
10. N.S Blokhina., A.E Ordanovich.,1995, Mathematical modeling of vortex structures in the upper layer of a water basin, *Izvestiya, Atmospheric and Oceanic Physics, English Translation*,30, N 5, 1995, 655-664.
11. N.S. Blokhina, A.G. Kochurov, A.E. Ordanovich, 1995, The study of Langmuir circulations in water reservoirs using mathematical modelling, *Vestnik Mockovskogo Yniversiteta, series 5, geografiya*, 5,39-44.
12. N.S Blokhina., A.E Ordanovich, 1998, The influence of surface pollution's on processes of convective mixing in the upper layer of the water body, *Vestnik Mockovskogo Yniversiteta, series 3. , Physika. Astronomia*, 4, 27-29.

ONSET OF THERMOHALINE CONVECTION IN SEA ICE

P.V.Bogorodsky

Arctic and Antarctic Research Institute, 38 Bering Str., 199397 St.Petersburg Russia, e-mail: bekryaev@aari.nw.ru, fax:7 (812) 352 2688

Abstract. A linear stability analysis is applied to a horizontal layer of porous medium saturated with compressible binary mixture the parameters of which correspond to sea ice. Soret and Dufour effects are allowed for. The limits of monotonic and oscillatory instability domains with respect to small perturbations are defined; a domain of parameters corresponding to double-diffusive instability in brine within sea ice is described.

1.Introduction

Sea ice represents a natural multiphase medium consisting of fresh water ice skeleton saturated with liquid salt solution (brine) gaseous inclusions, and solid salt [1]. This ice totally transforms into a single-phase solid system at temperatures virtually not occurring in the ice cover (-55°C [1]). At higher temperatures the sea ice is always saturated by liquid phase, the brine, amounting up to 50% of the total ice mass [1]. Such a structure of the ice cover is formed under its cooling conditions, depending on the ice crystal formation and growth. A significant temperature gradient in the cooled layer forms a skeleton structure of fresh-water ice, including separate solution cells with a low crystallization rate. Further cooling changes the skeleton growth of crystals by their continuous growth and the fresh water freezing in the cells, accompanied by a significant increase in pressure and solution concentration.

Within a cold season, when the temperature in ice elevates with its thickness, an unstable density distribution exists in the brine channels. This evidently results in convective motion (filtration) of brine, thus it flows out of ice and is substituted with less saline seawater [1]. Dissipative processes (heat conduction and diffusion) retard this motion, tending to return the brine into its equilibrium state. If it is the case, the convective filtration, apart from its impact upon the ice biological productivity, should intensify the heat and salt fluxes through the sea ice cover [2]. Therefore, to describe correctly the energy and mass exchange processes through sea ice, it is necessary to find the criteria of brine convective instability.

To solve the problem, we assume that (i) sea ice represents an isotropic porous medium saturated by brine, while the gaseous component and vapor are absent, (ii) the brine is a binary (two-component) liquid with the flow obeying the Darcy law, (iii) the porous medium skeleton is weakly compressible and its motion can be neglected, and (iv) ice and brine coexist under the local thermodynamic equilibrium. These assumptions are sufficiently valid for young sea ice, via which the most part of energy and mass exchange between sea and atmosphere proceeds [1,2].

2. Linear analysis

We study the mechanical equilibrium stability of brine saturating the ice layer of vertical and horizontal sizes h and L , respectively, in which transverse gradients of temperature A and salinity B are produced. Hydrodynamic processes depend on various dimensional parameters of ice: the solution dynamic viscosity η , compressibility α , thermal expansion β_T , and salinity compression β_S , the ice porosity m and permeability K , ice and brine isobaric heat capacities C_m and C_p , the ice heat conductivity κ and heat diffusivity χ , the brine diffusivity D , and brine thermodynamic parameters N and ε .

We choose the axes z and x respectively across and along the layer and put the coordinate origin at its lower boundary. We use the conventional theory of small perturbations [3] which are assumed to be proportional to the product of an amplitude function depending on the coordinate x and the harmonic oscillation $\exp(-\lambda t)$, where λ is the characteristic decrement. The problem of small normal perturbations is reduced to an analysis of the spectrum of longitudinal perturbations from an equilibrium; the stability criterion has the form $Re\lambda \geq 0$. The spectrum contains as real as complex λ relevant to monotonic and oscillatory perturbations. According to [4], the boundary problem in dimensionless variables has the form

$$\lambda Pr T(x) = (1 + G)(Ra T(x) - Rs S(x) - CP(x)) - (1 + D) - DS^{-1} d^2 S(x), \quad (2.1a)$$

$$\lambda Sc S(x) = -(Ra T(x) - Rs S(x) - CP(x) + d^2 S(x) + S d^2 T(x)), \quad (2.1b)$$

$$\lambda Q (Ra T(x) - Rs S(x) - CP(x)) = d^2 P(x), \quad (2.1c)$$

$$x = 0, 1: P(x) = T(x) = S(x) = 0, \quad (2.1d)$$

where $P(x)$, $T(x)$, and $S(x)$ are the perturbation amplitudes of pressure, temperature, and salinity horizontal components in the ice layer; $d = d/dx$. The problem includes nine dimensionless parameters, the Rayleigh filtration and filtration-diffusion numbers $Ra = \rho_0 g \alpha A h^2 K / \eta \chi$ and $Rs = \rho_0 g \beta_S B h^2 K / \eta D$, the Prandtl filtration and filtration-diffusion numbers $Pr = C_m h^2 \eta / K \kappa \rho_0$ and $Sc = m h^2 \eta / K D \rho_0$, the number $Q = m L^2 \eta^2 / g h K^2 \rho_0^2$ defining the ratio of characteristic times for perturbation propagation in the brine and ice units, the number $C = \rho_0 g \alpha h$ characterizing the brine compressibility due to pressure, the numbers $D = \varepsilon N D \rho_0 / \kappa$ and $S = A \varepsilon D / B \chi$ responsible for Dufour (diffusive heat conductivity) and Soret (thermal diffusion) effects and number $G = g / A C_p$, which characterize gravity force work.

The solution of problem (2.1), relevant to the basic instability level, has form $(P(x), T(x), S(x)) \sim \sin \pi x$. The decrements are coupled by the cubic equation

$$p \lambda^3 + q \lambda^2 + r \lambda + s = 0, \quad (2.2)$$

$$p = Pr Sc C Q, \quad q = -\pi^2 (Pr Sc + C Q (Pr + Sc(1 + D))),$$

$$r = \pi^2 (\pi^2 (C Q + Pr + Sc(1 + D)) - Rs Pr - Ra Sc(1 + G)),$$

$$s = \pi^4 (Ra(1 + G - DS^{-1}) + Rs(1 + D - S(1 + G)) - \pi^2).$$

The monotonic and wave instability boundaries are found from the conditions [3]

$$s = 0, \quad (2.3a)$$

$$qr - ps = 0. \quad (2.3b)$$

In the following the Dufour and Soret effects are neglectible [3]. If introduce the Darcy number $Da = K/h^2$ characterizing dimensionless permeability of medium, the conditions (2.3) will be written as

$$Da_1 (Ra_* - Rs_*) = \pi^2, \quad (2.4a)$$

$$Da_2^2 (CQ((Ra_* Sc_*^2 - Rd_* Sc_*^2) - \pi^2 CQ(Pr_* + Sc_*))) + \quad (2.4b)$$

$$+ Da_2 (-\pi^2 CQ(Pr_* + Sc_*)^2 + Pr_* Sc_* (Ra_* Sc_* - Rs_* Pr_*)) - \pi^2 Pr_* Sc_* (Pr_* + Sc_*) = 0,$$

where $Da_{1,2}$ are the critical Darcy numbers for monotonic and wave instabilities, $(Ra_*, Rs_*) = (Ra, Rs) / Da_{1,2}$, $(Pr_*, Sc_*) = (Pr, Sc) Da_{1,2}$ (at the absence of skeleton the parameters Ra_* and Rs_* are equal to the Rayleigh numbers for liquid). The relevant critical Darcy numbers are calculated by the formulas

$$Da_1 = \pi^2 / (Ra_* - Rs_*), \quad (2.5a)$$

$$Da_2 = (1/2 CQ((Ra_* Sc_*^2 - Rs_* Pr_*^2) - \pi^2 CQ(Pr_* + Sc_*))) \times \quad (2.5b)$$

$$\times (\pi^2 CQ(Pr_* + Sc_*)^2 - Pr_* Sc_* (Ra_* Sc_* - Rs_* Pr_*) - (\pi^2 CQ(Pr_* + Sc_*)^2 + Pr_* Sc_* (Ra_* Sc_* - Rs_* Pr_*))^2 + 4\pi^2 Pr_* Sc_* CQ(Pr_* + Sc_*) (Sc_* (Ra_* Sc_* - 1) + Pr_* Sc_* (Ra_* Sc_* - Rs_* Pr_*))^2 + 4\pi^2 Pr_* Sc_* CQ(Pr_* + Sc_*) (Sc_* (Ra_* Sc_* - 1) - Pr_* (Rs_* Pr_* + 1)))^{1/2}.$$

The relationship between the parameters entering the critical Darcy numbers allows them to be either positive or negative. The latter condition corresponds to the brine stability relative to longitudinal perturbations at any permeability [4]. Violated conditions (2.4a) and (2.4b) yield monotonic and wave instability, respectively.

3. Compressible brine

The critical Darcy numbers calculated by (2.5) with typical of cold time characteristics of young sea ice parameters [1] show that (i) the brine to be unstable and (ii) $|Rs| \gg Ra$, $Sc > Pr$. Furthermore the convection-diffusion effects suppress the temperature ones and the solution instability is defined only by inhomogeneous salinity. In this case «crossing» kinetic effects are absent ($D = S = 0$) and the degree of dispersion equation (2.2) lowers by unity to yield the roots

$$\lambda_{1,2} = (\pi^2 (CQ + Sc) \pm \pi (\pi^2 (CQ - Sc)^2 + 4RsScCQ)^{1/2} / 2ScCQ). \quad (3.1)$$

It follows from (3.1) that values λ are real at salinization from above ($B < 0, \beta_s < 0, Rs > 0$). One of two roots is always positive and grows as Rs increases, while another diminishes and becomes negative at sufficiently high Rs , thus leading to instability. At salinization from below, perturbations are monotonic only at small Rs ($B > 0, \beta_s < 0, Rs < 0$). A complex-conjugate decrements arises when $Rs^* = -(\pi^2 CQ / 4Sc)(Sc / CQ - 1)^{-2}$ and at

$|Rs| > |Rs^*|$ perturbations oscillate at the frequency $\lambda^* = \pm 2(ScCQ(Rs^* - Rs))^{1/2} / \pi$. As follows from (6), the real parts of decrements are positive at $Rs < 0$, that is both oscillatory and monotonic perturbations are damped at salinization from below.

The density inhomogeneity due to pressure and the compressibility in (2.2) are characterized by the product of parameters CQ. Therefore, at $CQ = 0$, we arrive at the Boussinesq model. Condition (2.5a) as distinct from (2.5b) does not contain that, hence (2.5a) is the same for compressible and incompressible brine and the compressibility affects only the wave perturbations. At these conditions the critical Darcy numbers calculated at $CQ = 0$ are underestimated more than by an order of magnitude, compared to the case of $CQ \neq 0$. Hence, the account of compressibility characterized by the product CQ expands the domain of stability.

4. Incompressible brine

The conditions of incompressible brine stability are defined by coefficients q, r and s are analyzed in the plane of coordinate (Rs, Ra) [3]. The relevant regions are divided by straight lines of monotonic (2.3a) and wave (2.3b) instabilities, as well as by the discriminant curve $r^2 - 4qs = 0$ as well as by the points of their intersections (Fig.1). The latter are easily determined from simultaneous solution of these equations. The domain of oscillatory stability for incompressible brine lays totally in that of monotonic stability. Therefore we have $|Da_1| < |Da_2|$ and the stability criterion is $Da_2 < 0$ ($RaSc < RsPr$), that is the difference between the rates of dissipative processes. At cooling from above ($A > 0, \beta_T > 0, Ra_s > 0$) this difference changes its sign at the arbitrary small negative salinity gradient. Hence, the equilibrium is unstable in the case of salinization from above. At salinization from below, the brine is unstable if $Ra > RsPr/Sc$. In the vicinity of this threshold the evident constraint onto the Darcy number is violated and a discontinuity arises in the curve corresponding to (2.3b) at exact equality.

Now we enlarge on the feasible differential-diffusion convection of incompressible brine in sea ice. A necessary condition of the solution equilibrium is the constant vertical gradient of density. The zero density gradient corresponds to the equation [3]

$$RaL + Rs = 0, \tag{4.1}$$

where parameter $L = \chi / D$ characterizes the ratio of temperature and salinity leveling rates. Depending on the diffusion Rayleigh number sign, the straight line (4.1) can be either in quadrants I and III (the case of salinization from below) or in quadrants II and IV (salinization from above; relevant dividing (dashed) lines are plotted in Fig.1) of the coordinate (Rs, Ra) . However, in any case the differential-diffusion convection proceeds at negative ordinary Rayleigh numbers relevant to heating from above ($A < 0, \beta_T > 0, Ra < 0$). This symmetrizes the dividing lines' arrangement about the axis Ra . For definiteness, we analyze the example of salinization from above (solid dividing lines).

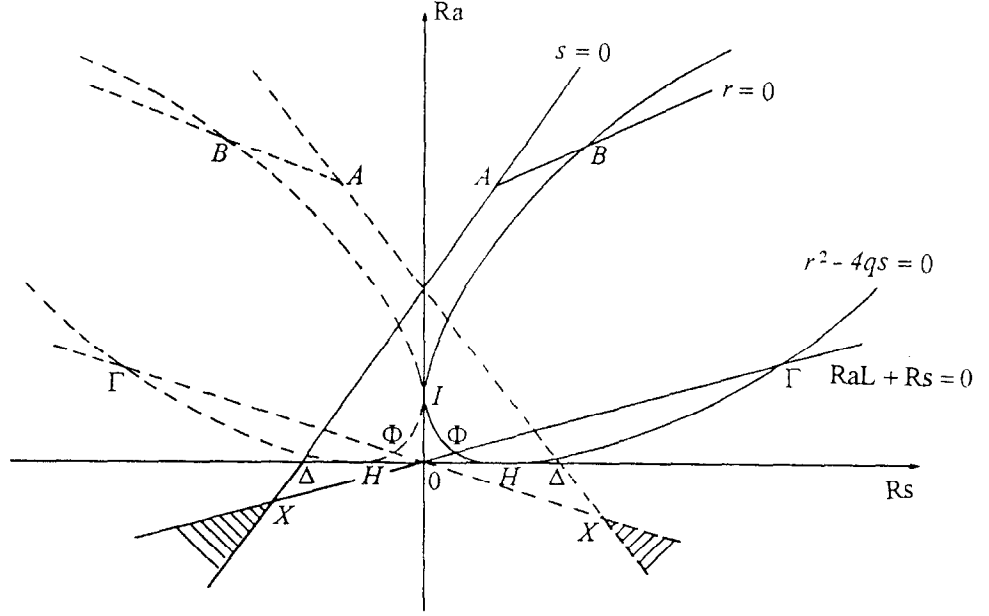


Fig.1. Domains of the incompressible brine instability.

Table 1. Coordinates of crossing the boundaries lines in (Rs,Ra) plane.

Point	Expression
A	$R_s = -\pi^2 Pr / (Sc - Pr)$ $R_a = \pi^2 Sc / (Sc - Pr)$
B	$R_s = Pr / (Pr - Sc)$ $R_a = (\pi^2 (Pr^2 - Sc^2) - Pr^2) / Sc(Pr - Sc)$
X	$R_s = -\pi^2 L / (1 - L)$ $R_a = \pi^2 Sc / (Sc - Pr)$
Δ	$R_s = 0$ $R_a = \pi^2$
Φ	$R_s = \pi^2 L (Pr - Sc) (2(\Pr Sc L)^{1/2} + (\Pr L + Sc)) / (Sc - \Pr L)^2$ $R_a = -\pi^2 (Pr - Sc) (2(\Pr Sc L)^{1/2} + (\Pr L + Sc)) / (Sc - \Pr L)^2$
Γ	$R_s = -\pi^2 L (Pr - Sc) (2(\Pr Sc L)^{1/2} - (\Pr L + Sc)) / (Sc - \Pr L)^2$ $R_a = \pi^2 (Pr - Sc) (2(\Pr Sc L)^{1/2} + (\Pr L + Sc)) / (Sc - \Pr L)^2$
H	$R_s = 0$ $R_a = -\pi^2 (Sc - Pr) / Sc$
I	$R_s = \pi^2 (Pr - Sc) / Pr$ $R_a = 0$

In the plane (Rs,Ra), below the straight line (4.1) a domain is arranged where the solution becomes heavier with depth. Coordinates of crossing the lines defining the stability domains are listed in Table 1. The straight line (4a) at all L (except for L = 1) crosses the neutral line of monotonic perturbations, thus forming a domain of «stability paradox» (hatched in Fig.1). As was shown above, this domain corresponds to the negative diffusive and ordinary Rayleigh numbers relevant to heating from above and salinization from below. For the chosen thermophysical characteristics of sea ice, the zero gradient line slope (1/L) is much smaller than the monotonic perturbations' line slope, $L \gg 1$. The value χ characterizes the brine volume heating due to total heat conductivity of both phases (at the absence of salinity it would be equal to the liquid thermal conductivity). Thus, the condition $\chi \gg D$ means that the temperature inhomogeneities are leveled much faster than the salinity ones. Then a brine particle, accidentally displaced upward, is fast heated but slowly salinized. At a new site the particle temperature is lower than an ambient temperature, but the particle should be more desalted. At the relevant gradients A and B (their minima are defined by coordinates of point X: $Rs_x = -\pi^2 L / (1-L)$, $Ra_x = \pi^2 / (1-L)$), the displaced particle density is lower than the ambient density and the particle emerges infinitely (monotonic instability), although the salt solution is heavier at the layer bottom. Calculations shows that minimum temperature and salinity differences, at which the differential-diffusion convection is observed in sea ice, are quite real values of a few hundredth fractions of degree and a few thousandth fractions of PSU, respectively. Obviously, the ice thermophysical parameters variations can change ratios of Prandtl numbers, as well as the slope of straight line (4a). These effects can be estimated by equations (4). In the boundary case $Pr = Sc$, the discriminant curve degenerates into the straight line $Ra = Rs$ parallel to the straight lines of monotonic and wave instabilities, whose crossing points tend to infinity. In this case, only the monotonic instability of brine is possible and its equilibrium is stable relative to wave perturbations.

At isothermal convection, dispersion equation (2) becomes linear and determination of the brine stability criterion appears to be trivial. The root takes on the form $\lambda = (\pi^2 - Rs) / Sc$, hence all the normal perturbation decrements are real that furnishes their monotonic evolution in time. The critical diffusion Rayleigh number relevant to instability initiation is $Rs = \pi^2$.

The work was supported by the Russian Foundation for Basic Research (Project Code 97-05-65926).

References

- [1] G.Z.Gershuni and E.M.Zhukhovitskii, 1972, Convective instability of incompressible fluids, Moscow, Nauka, 392p.(in Russian).
- [2] V.L.Lytle and S.F.Ackley, 1996, Heat flux through sea ice in the western Weddell Sea: Convective and conductive transfer processes, J.Geophys.Res., Vol.101, pp.8853-8868.
- [3] W.F.Weeks and S.F.Ackley, 1986, The growth, structure and properties of sea ice. In: The geophysics of sea ice, N.Untersteiner (Ed.), Plenum Press, N.Y., pp.9-164.
- [4] D.G.Polonsky, 1995, Effects of compressibility under conditions of miscible fluids convective stability in a porous medium, Bull.Rus.Acad.Sci., Suppl. Fluid and Gas Mech., No.1, pp.16-23 (in Russian).

LABORATORY EXPERIMENTS ON CONVECTION IN COASTAL SEAS AND LARGE LAKES

By B.M. Boubnov^{1,2} and P.B. Rhines²

¹A.M.Obouhov Institute of Atmospheric Physics RAS, 109017, Moscow, Russia,
boubnov@boubnov.msk.ru, boris@ocean.washington.edu

²School of Oceanography, University of Washington, Seattle, WA 98195-7940, USA,
rhines@ocean.washington.edu

Abstract

We are interested in the parameter space of rotation rate, Ω , temperature difference, ΔT , (or related surface buoyancy flux B_0), boundary shape and symmetry of boundary forcing, for a rotating basin driven by surface buoyancy flux. The geophysical problem is that of lakes and marginal seas cooled by the atmosphere, or saline oceans freezing at the top. The topographic shape of the basin and spatial variation and symmetry of the forcing both exert strong control over the resulting convection and circulation.

The fluid in, (i), a 1-m diameter constant-depth, circular basin is driven by a 0.29 m diameter circular-disk cooling plate at its center, at high Rayleigh number ($Ra_H = g\alpha\Delta TH^3/\kappa\nu > 10^7$). At low rotation, the 'meridional overturning (i.e., radial/vertical) circulation is intense and symmetric. As Ω increases the problem passes through the stages of symmetric, steady zonal circulation, unsteady baroclinic wave/vortex regime, and turbulent, convective vortices of increasing small scale. Meridional and zonal circulation diminishes at high rotation. When the same forcing is applied to, (ii), a spherical-cap basin of the same diameter, the symmetric circulation is similar, but with increasing Ω is topographically confined to the center. The long waves and smaller-scale convective vortices are confined near the basin center. If we move the cooling disk to the side of the basin, the constant depth cylinder (iii) shows a reversal of direction (to anticyclonic) of the principle gyre of circulation. A small cyclonic gyre remains about the cooling region. With a bowl-shaped basin, (iv), a similar pair of gyres occurs at small Ω , steady at first, and then with mesoscale eddies at higher rotation. Boundary currents become concentrated and intense, and at as Ω exceeds 1. we see a dense pattern of jets aligned along the topography.

Exchange processes and fronts in coastal zone and marginal seas

1. Introduction

The history of a systematic experimental studies of convection in rotating fluids started with "dishpan" experiments Fultz [1], where the local heating or cooling from a disk was studied. After Hide's experiments [2] the experiments on convection between vertical differentially heated coaxial cylinders became a basic model for a study of baroclinic instability, where a horizontal temperature gradient and stable vertical temperature gradient are important. In parallel, convective motions in rotating plane fluid layer heated from below were studied in the laboratory by Nakagawa & Frenzen [3]. For a plane layer an unstable vertical temperature gradient develops. Boubnov & Golitsyn [4] reviewed studies on both of these forms of convection in a rotating fluids.

When convection from a local heating or cooling source is considered, vertical and horizontal temperature gradients appear. In different places of a vessel both stable and unstable vertical temperature gradients can exist.

Convective motions from a local source of buoyancy are discussed, usually with most attention paid the flows near the buoyant plume. In some cases a source of buoyancy can be considered as isolated (see [5]) in others, it is necessary to take into account an interactions of a flows with boundaries.

A new interest in convective motions in rotating fluids from a local heating was stimulated by a study of a deep convection in the ocean. It was shown (see, [6-9], that a small regions of deep convection (in the Labrador and Mediterranean Seas) significantly change a heat balance in the World Ocean.

Typical horizontal scale of a sea L is about 100-1000 km, horizontal scale for deep convection region D is about 10-100 km, while a depth of a sea H is 1-3 km. A main aspect ratios $\delta_1 = D/H = 3-100$ and $\delta_2 = L/D = 1-1000$. For these aspect ratios an interactions of the flow with boundaries are important, and some modifications of a "dishpan" experiments [1] can be suitable for simulated a deep convection in the ocean.

This paper describes experiments designed to investigate convection and circulation from a cooling disk in shallow rotating vessels with a different bottom shapes. Two forms of bottom were used: plane and bowl shape, the latter being approximately a section of a sphere. The different positions of the disk with compare to the center and sides of the vessel are considered. In small and shallow vessel the flow from a source of buoyancy very soon after a start of convection begins to interact with a bottom and a side walls, and a quasi-stationary regimes after interactions are studied.

2. Experimental apparatus and procedure. The experiments were conducted with two shallow vessels, one cylindrical, with diameter $L=96.5$ cm and one an approximately spherical-cap 'bowl' of blown plexiglas. The bowl diameter was 97cm, at which point the greatest depth is 19.2cm. Bottom and sides of the vessels were thermally insulated with at least 5cm of closed-cell foam, the net side/bottom heat conduction was negligible for the earlier parts of the life-cycle of the experiments; this will be discussed below. The upper free surface was open to the air, but protected by a cone of transparent plastic, extending 1.5m above the surface. Convective motions in this same bowl-shaped basin were described in [10,11].

Buoyancy driving was provided by a thermoelectrically driven circular cooling plate of aluminum, with diameter $D=29$ cm. and height 1.2 cm. The disk was mounted horizontally, flush with the free surface. Waste heat from the apparatus was removed with a continuous water cooling system. Thermistors embedded in the disk provided temperature of the disk T_D , and air temperature T_A was monitored together with the water temperature, T_w , and the temperature difference $\Delta T=T_w-T_D$ are the most important thermal parameters. A linear array of thermistors in the fluid provide time histories of the experiment, including the development of stratification. Spacing of the thermistors was 2 cm., the final one being 1 cm. from the bottom. The cooling disk was located either in the center or near the side of the water surface.

The 1m-diameter rotating table, constructed in our laboratory has a direct-drive, brushless synchronous d.c. motor, with feedback control, and is patterned after a design from Australian National University. Rotation rate is accurately maintained, with accuracy better than 10^{-4} . Levelling is carried out regularly to remove tides. Rotation rate Ω ranged from 0.005 to 2. sec^{-1} . These slow rotation rates involve lead to new regimes of rotating convection [12]. We are particularly interested in the sense of the basin-scale circulation, cyclonic (that is, in the same sense as the rotation of the platform), or anticyclonic.

The experiments were carried out by spinning up the basin at room temperature. The fluid is initially unstratified. Cooling is then turned on abruptly, and both transient and quasi-steady behavior examined. Processes involving the build-up of thermal stratification required long runs (more than 24 hours). This distinguishes the experiments from those that concentrate on initial development (e.g., [5,13]).

Surface circulation was visualized with fine aluminum powder, photography and time-lapse video. Time-series of subsurface velocities were made using an infra-red diode laser velocimeter, which measures two velocity components. This device can accurately sense flows as slow as 0.1 mm sec^{-1} .

3. Regimes and Parameters

The basic convective regimes for a centered, axisymmetric cooling pattern with fixed ΔT and Ω are familiar: zonal circulation develops axisymmetrically when Ω is small. Our interest is only in high-Rayleigh number flows, and so the convection beneath the forcing disk is always turbulent (whereas in the classic annulus, the flow at small Ω is laminar providing the sidewall boundary layers are stable). At higher rotation rates baroclinic waves and vortices develop, which decrease in lateral scale and become turbulent at still higher rotation rates.

This is summarized in Fig. 1, showing the results of 24 experiments at variety of values of Ω and ΔT , for water depth $H=10$ cm. Symmetric zonal circulation (ZC), baroclinic waves and orderly vortices (BV) and turbulent convective vortices (CV) occur at progressively higher rotation. The regime boundaries are nearly vertical, perhaps with a slight lean to the right; this independence from ΔT occurs for strong cooling.

These symmetrically forced flows in the cylinder are strongly related to earlier work, but the goal of this paper is to consider the effects of both non-symmetric forcing and bowl-like topography. As a result of the weak dependence of regimes on mean temperature difference, we will do most experiments in the new configurations at a single imposed value of buoyancy forcing.

Main dimension parameters of a system are: length scales (diameter of cooling disk D , depth of fluid H , horizontal size of vessel L), temperature difference ΔT , rotation rate Ω , gravity acceleration g and parameters of fluid (density ρ , specific heat contents c_p , coefficients of viscosity ν , thermodiffusivity k and thermal expansion α). Reduced gravity accelerations can be introduced as $g^*=(\Delta\rho/\rho)g$. For thermal convection $g^*=\alpha g\Delta T$, and a heat flux f for turbulent convection defines a kinetic energy dissipation $\epsilon=\alpha g f/\rho c_p$ (see, for example [14]). For density convection an analog of a kinetic energy dissipation ϵ is a buoyancy flux per unit area $B=g^* V$, where V is a velocity of a more dense fluid which come from source of buoyancy [13].

As non-dimensional parameters we will use Rayleigh number $Ra_D=g\alpha\Delta TD^3/\kappa\nu$, as a measure of cooling

and thermal Rossby number $Ta=4\Omega^2 D^4/\nu^2$ as a measure of rotation.

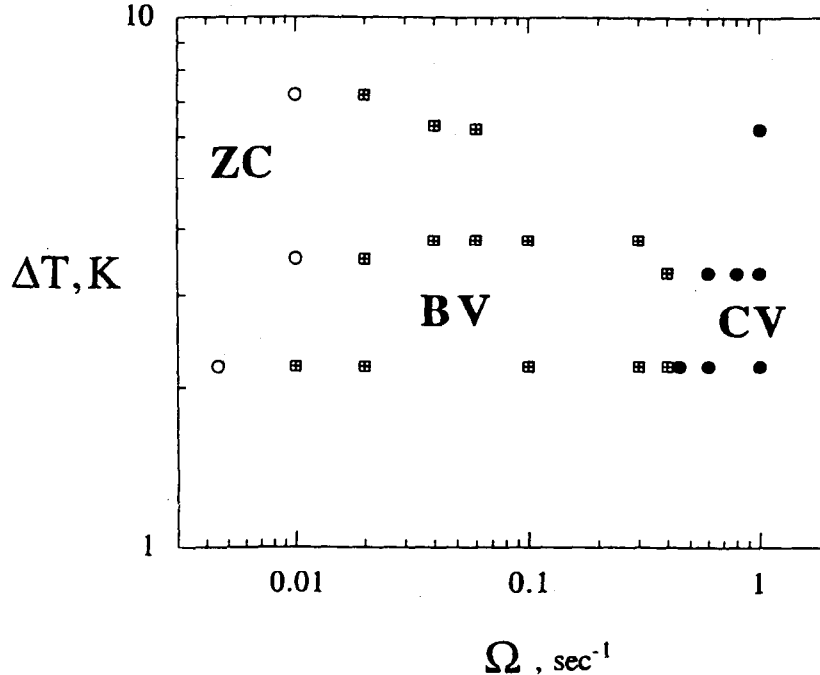


Fig.1. Regime diagram in $(\Delta T, \Omega)$ space for convective motions in a cylinder with symmetric cooling ($H=10$ cm). Regimes: **ZC** - zonal circulation (circles), **BV** - baroclinic vortices (crossed squares), **CV** - convective vortices (black circles).

4. Results

Cylinder, symmetric forcing (CC). Stable stratification is characteristic of the annulus experiment; unstable stratification is characteristic of uniformly forced convection, and here we have elements of both. The zonal cyclonic circulation at low rotation is basin-filling, in balance with a strong Hadley cell of overturning. Coriolis effects dominate the basin-scale circulation when they are negligible at the scale of the convection (correspondingly, lakes of rather small size exhibit Coriolis effects). At high rotation the zonal flow initially takes the form of a rim current close to the edge of the cold disk, as has been explored in numerical experiments [15] and in the laboratory [13].

The experiments begin with the development of plumes characteristic of uniformly rotating convection. A large-scale buoyancy gradient soon develops, and this drives the larger scale overturning, and symmetric zonal circulation. Despite the turbulent convection the outer flow remains laminar and symmetric at low rotation. In the higher-rotation regimes become non-symmetric as large-scale baroclinic vortices develop. Comparing with the classic annulus, we do not see a simple wave regime and snaking 'jet-stream'. The lack of an organized jet is a reflection of the lack of a rigid inner sidewall, which helps to organize the annulus flow, both through its heat flux and by defining the channel width. At large radius, far from the forcing the zonal flow is typically weaker than in the corresponding annulus experiment, which is forced at both walls.

The lateral scale of the convective vortices decreases strongly with increasing rotation. At high, fixed rotation rate, in the convective vortex regime, if we wait for typically one hour, the distribution of vortices becomes well-developed. Their diameter increases with distance from the forcing, by a factor of about 2.5 at the outer rim (Fig. 2). This would be the nature of two-dimensional turbulence generated locally, and self-advecting to large radius [16].

Cylinder, asymmetric forcing (CS). Natural flows lack the symmetry imposed in the case above. Motivation for non-symmetric forcing comes both from the planetary scale ocean circulation (with buoyancy forcing varying with latitude), basin-scale ocean circulation (where cooling often occurs at the edge of the

ocean, where cold air flows off the land), and from lake circulations, where uneven buoyancy forcing occurs. Simply by moving the cooling plate to the edge of the cylinder we find the main body of the fluid rotates in the opposite direction, anticyclonically. This tendency is seen most clearly at low rotation ($\Omega = 0.01 \text{ sec}^{-1}$). A residual cyclone exists beneath the cold plate. The baroclinic vortex regime (a.k.a. wave regime in the annulus) involves large eddies, predominantly cyclonic, which tend to self-advect round the outer boundary of the cylinder.

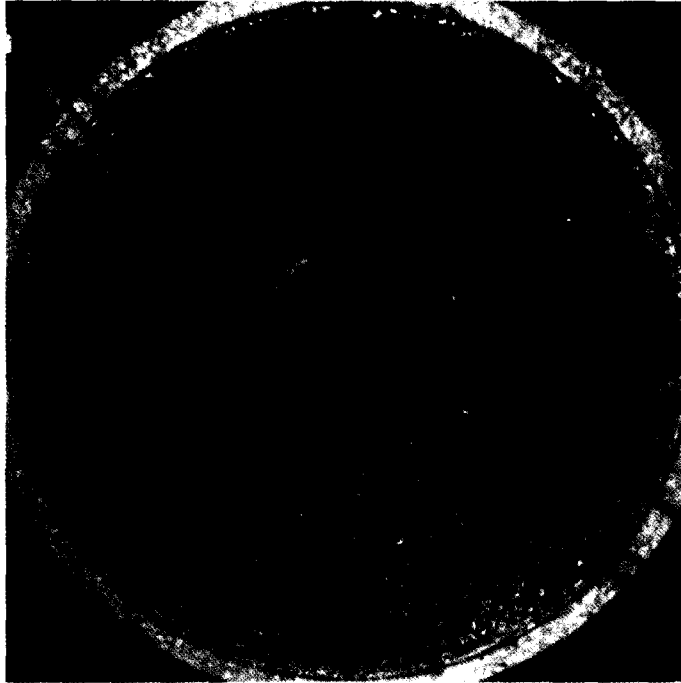


Fig.2. Vortex structure at the free surface for a cylinder with symmetric cooling. $\Delta T = 5.1 \text{ K}$, $\Omega = 1.5 \text{ sec}^{-1}$ ($Ra_D = 1.33 \times 10^8$, $Ta_D = 6.4 \times 10^{10}$).

Bowl, symmetric forcing (BSS). The axisymmetric bowl should, one might think, act rather like the axisymmetrically forced cylinder. The parade of regimes, however deviates greatly. As Ω increases above the symmetric (cyclonic) regime, a well-defined wave-regime occurs where, in the cylinder, there were disorganized baroclinic vortices. The topographic restoring effect is clearly at work, providing a strong, symmetric field of Rossby-wave 'elasticity'. The resemblance to the classic annulus' wave regime is thus in the organization provided by the symmetric topography. Trapped, long-lived vortices are a dominant feature of the annulus wave regime, and these are less prominent here.

At large rotation (Fig. 3a) the convective vortices are arrested near the forcing region, and very strong cyclonic circulation is confined also to the inner one-half of the domain. Zonal circulation and eddies are nearly absent at large radius. The boundary between flowing and stagnant fluid is sharp, and yet it moves outward with time.

With relatively weak stratification, the dynamics of this regime resemble that of β -plane two-dimensional turbulence. Rather than the outward advecting vortices of the cylindrical case, we see confinement by the mean potential vorticity field, and an indication that the lateral scale of the vortices is limited (in the β -plane case, this size is $\sim (U/\beta)^{1/2}$).

The side view of the weak rotation case shows a particularly well-defined Hadley cell; the turbulence level in the convection beneath the cold disk is strong.

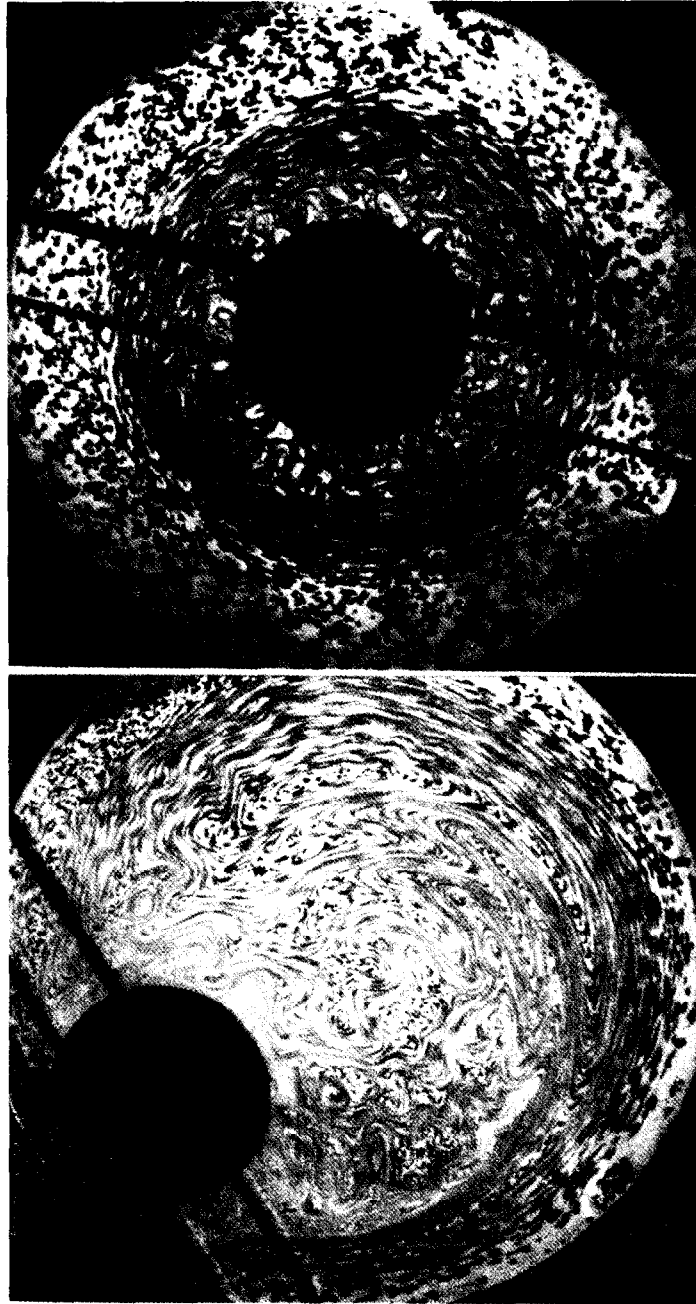


Fig.3. Vortex structure at the free surface for a bowl with symmetric (a) and asymmetric (b) cooling. $\Delta T=5.1$ K, $\Omega = 1.5 \text{ sec}^{-1}$ ($Ra_D = 1.33 \times 10^8$, $Ta_D = 6.4 \times 10^{10}$).

The lateral scale of the vortices produced in this configuration decreases monotonically with rotation, Ω .

Bowl, asymmetric forcing (BA). This configuration was in [17, 18] as a simple model for Labrador Sea convection, where there is significant bottom slope and asymmetry in the cooling to the atmosphere. Here we extend this work by considering a large range of Ω and making comparisons with the other three configurations.

At low rotation, $\Omega=0.01 \text{ sec}^{-1}$ the circulation is nearly steady, though still turbulent beneath the cooling.

The side view shows that the overturning circulation still resembles that of the non-rotating case, with little restraint due to Coriolis forces. Nevertheless the lateral, Coriolis driven circulation is fully developed. It resembles the case of the asymmetrically forced cylinder.

At large rotation, $\Omega=1.5 \text{ sec}^{-1}$ (Fig.3b) the strength of the circulation is reduced, and its form is now strongly controlled by topography. The intense convection transmits circulation in the sense of topographic waves, along the 'pseudo-westward' direction (to the left, facing large values of mean potential vorticity). Near the outer rim there is an anticyclonic flow drawn *toward* the cooling region, which extends round the entire basin, connecting to form a narrow, interior anticyclone.

The energy level of the circulation is such that this nearly-barotropic flow cannot readily move across contours of mean depth. The convection persists with that constraint, yielding jets that increase in number as Ω increases.

The zonal circulation shows important differences between bowl and cylindrical vessels. Indeed, this quantity is a key variable which is not often emphasized in classical annulus studies. For the centered bowl geometry (BC), the maximum zonal velocity increases rapidly with Ω , at low values, and reaches a maximum at $\Omega = 0.02$ to 0.04 sec^{-1} (Fig.4). It then rapidly decreases to a plateau between 0.04 and 0.4 sec^{-1} , finally diminishing by a further factor of 2 at all larger values of Ω that we have explored.

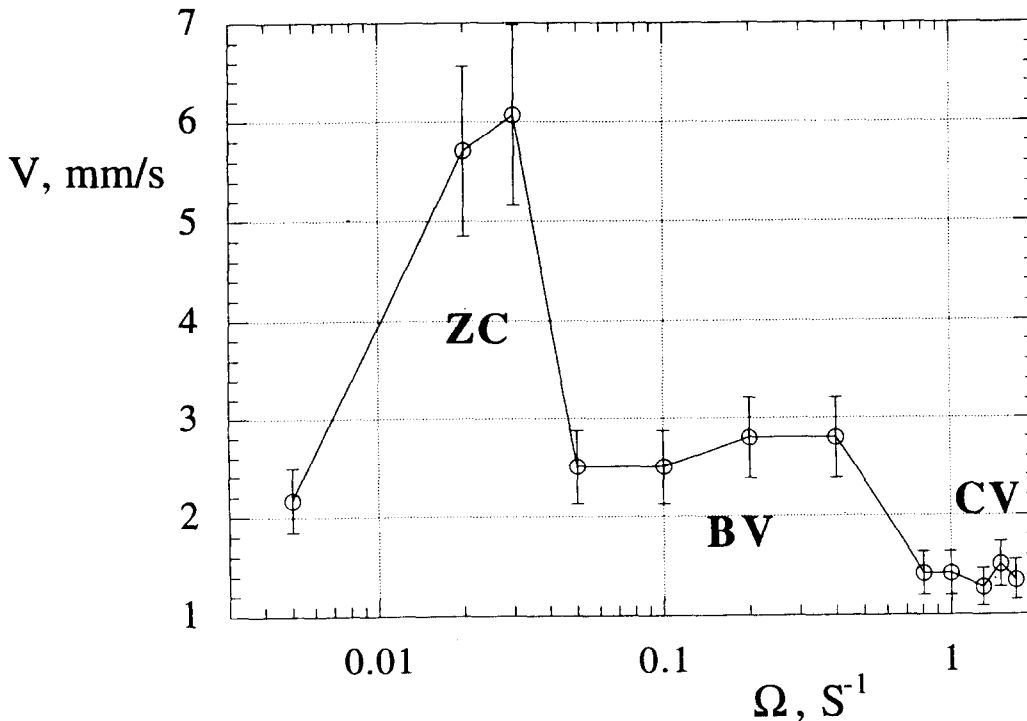


Fig. 4. Dependence of a maximal zonal velocity V_z at a surface on Ω for different regimes in symmetric cooled bowls.

There is an exceedingly long life cycle in this problem, and we have attempted to follow it beyond the stage of initial convective development. The stages involve (i) thermal instability and plume development, (ii) chimney and rim current development, (iii) mesoscale vortex generation, (iv) basin-scale circulation develops, with meridional overturning, and (v), stable stratification is built.

Thus, the presence of a directly convected region leads to stronger eddy activity in the near-field, contrasting both the annulus experiments (where thermal forcing occurs through side-wall boundary layers) and typical baroclinic instability experiments, where a jet is thermally maintained, yet its mean and eddy velocity components are comparable. Some of the longer-timescale aspects of the life-cycle of the experiment are seen in Fig.5. The establishment of stratification far from the convective source for centered cooling in the bowl occurs from a well-mixed initial state. The initial temperature, 12.75°C , was colder than room temperature (21°C), so that as convection proceeds, so too does restratification due to surface heat

gain. This experiment was carried on for several days, changing only the rotation rate through 3 values. At first, with $\Omega=1.3 \text{ s}^{-1}$, the initially homogeneous fluid develops stable stratification over about 10 hours, with top-to-bottom contrast of about 3°C . The heat gain for the case without cooling is seen at the end of the run, where the temperature rises with an e-folding time scale of 1500 min.

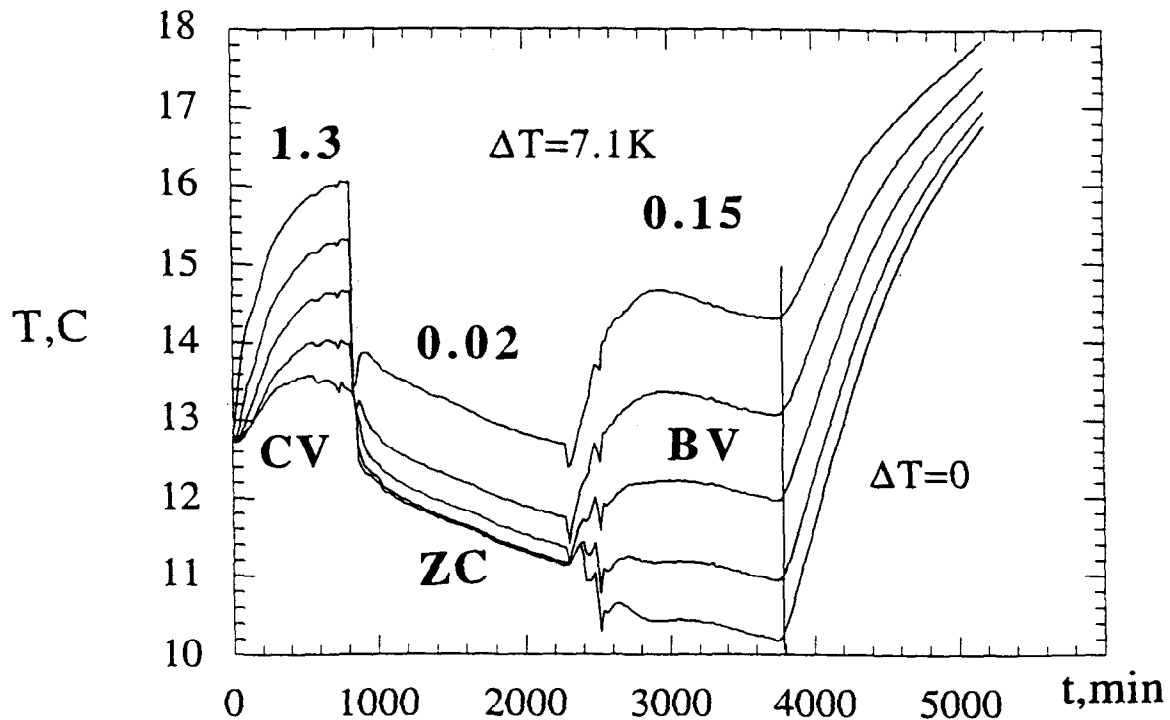


Fig.5. Temperature records at 5 different levels at distance 30 cm from the center of a symmetric cooled bowl ($\Delta T=7.1 \text{ K}$, $Ra_D = 1.85 \times 10^8$) for different rotation rate (numbers) and regimes (letters). At $t=3800 \text{ min}$ (63,3 hours) a cooling was off on constant rotation.

The rapid rotation case at the beginning warms more gradually, as a consequence of the cooling. When the rotation rate is reduced to 0.02 s^{-1} , the overturning circulation is much more efficient, and the temperature gradient is much reduced at depth; the lowest 4 cm is nearly homogeneous. The side-view illustrate the strength of overturning at lower rotation values. The temperatures overall are colder because the meridional circulation and attendant heat flux is so much more efficient at low rotation. Then, when the rotation rate is again increased to 0.15 s^{-1} , we see a much greater stratification extending the temperature to warmer values. The timescale for establishing the stratification (~ 8 hours in the more rapidly rotating cases, much shorter (~ 1 hour) at the lower rotation) is well-defined, followed by a longer period of drift of the temperature as it seeks equilibrium with the net surface heating and cooling.

The dependence of stable vertical temperature gradient, T_z , shows that between $\Omega=0.05$ to 1.0 s^{-1} T_z changes greatly. For centered cooling experiment T_z is nearly a factor of 3 greater than for asymmetric cooling (despite the fact that the vertical thermistor stick is closer to the cooling in the symmetric case; in both instances the thermistors are 30cm from the basin center). For very low rotation, and very fast rotation, the stratification has weak dependence on the position of the cooling region. The efficiency of the lateral gyre circulation is so great in the asymmetric forcing that, rather like the strong overturning at very low rotation, it more effectively homogenizes the temperatures. At very high rotation the intricate jet structure is weak in amplitude, and small in scale, so that it does not thoroughly stir the fluid.

5. Conclusion

There is a great change in convective structure with configuration: basin geometry and the disposition of buoyancy forcing. For example, at rapid or intermediate rotation, centered cooling in a cylinder fills the fluid with convective vortices, while for the same parameters in a bowl, the convection is arrested close to the center and fails to penetrate far outward. By contrast, the mean zonal circulation in the bowl is much stronger than in the cylinder.

In the bowl, where mean circulation is particularly strong, the position of the buoyancy forcing greatly affects the sense of the basin-wide circulation, shifting for example from a large cyclonic gyre with centered forcing to a large anticyclone (and much smaller cyclone about the forcing region), with asymmetric cooling. At the largest rotation, multiple jets of alternating sign occur, and the basin-wide gyres are lost.

The conversion from potential energy supplied by buoyancy forcing to kinetic energy of circulation is most efficient at rather low rotation, where the mean circulation has scale comparable with the basin diameter.

The authors acknowledge principal support of National Science Foundation, Ocean Sciences Division. B.B. is also supported by Inco-Copernicus Grant from the European Community.

References

- [1] Fultz, D., 1951 Experimental analogies to atmospheric motions. In: Compendium of Meteorology (Ed. Malone T.F.), Boston, 1235-1248.
- [2] Hide, R., 1953 Some experiments on thermal convection in rotating fluids. *Quart. J. Roy. Meteor. Soc.* 78, No. 339, 161.
- [3] Nakagawa and Frenzen, 1955 A theoretical and experimental study of cellular convection in rotating fluids. *Tellus*, V.7 1-21.
- [4] Boubnov, B.M. & Golitsyn, G.S. 1995 *Convection in Rotating Fluids*. Kluwer Academic Publishers, 224p.
- [5] Boubnov, B.M. and Fernando, H.J.S. 1998 Regimes of convection from isolated source of buoyancy in rotating fluids. *Izv. RAS, Atmos. Ocean Physics.*, (in press).
- [6] MEDOC Group 1970 observation of formation of geepwater in the Mediteranean Sea, 1969. *Nature* 227, 1037-1040.
- [7] Schott, F., Leaman, K. 1991 Observations with moored acustic Doppler current profiles in convective regimes in Golfe du Lion. *J. Phys. Oceanogr.* 21, 558-574.
- [8] Gascard, J.S. 1978 Mediterranean deep water formation, baroclinic instabilities and ocean eddies. *Oceanol. Acta.*, 1, 315-330.
- [9] Gascard, J.S., Clarke, A.R. 1983 The formation of Labrador Sea water. Part II: Mesoscale and smaller processes. *J. Phys. Oceanogr.* 13, 1779-1797.
- [10] Condie, S.A., Rhines, P.B. 1994 Topographic Hadley cells. *J. Fluid Mech.*, 280, 349-368.
- [11] Condie, S.A., Rhines, P.B. 1994 a A convective model for the zonal jets in the atmospheres of Jupiter and Saturn. *Letters to Nature*, 367, 711-713.
- [12] Boubnov, B.M. 1997 Convection from local source of heating in slow rotating fluid. *Izv. RAS, Atmos. Ocean Physics.*, 33, No.6, 795-803.
- [13] Maxworthy, T., Narimosa, S. 1994 Unsteady, turbulent convection into a homogeneous, rotating fluid, with oceanographic applications. *J. Phys. Oceanogr.* 24, 865-887.
- [14] Boubnov, B.M. & Golitsyn, G.S. 1995 *Convection in Rotating Fluids*. Kluwer Academic Publishers, 224 p.
- [15] Jones, H. and J.M. Marshall, 1993: Convection in a neutral ocean: a study of open-ocean deep convection, *J. Phys. Oceanogr.* 23, 1009-1039.
- [16] Rhines, P.B., 1977: The dynamics of unsteady currents, in *The Sea*, Vol. VI, E.D. Goldberg Ed., Wiley Interscience, 189-318.
- [17] Rhines, P.B., 1998: Circulation, convection and mixing in rotating, stratified basins with sloping topography, in *Physical Processes in Lakes and Oceans*, Amer. Geophys. Union, 434-451.
- [18] Rhines, P.B., R.W. Hallberg and E.G. Lindahl, 1998: Convection and circulation in a rapidly rotating basin, preprint.

VERTICAL EDDY DIFFUSIVITY INDUCED BY BREAKING INTERNAL GRAVITY WAVES : A COMPARISON BETWEEN PARTICLE DISPERSION AND DIAPYCINAL DIFFUSIVE FLUX

P. BOURUET-AUBERTOT¹, C.KOUDELLA², C. STAQUET³ & K.B. WINTERS⁴

1. D.A.M.T.P., U. of Cambridge, Silver street, Cambridge CB93EW, UK, e-mail : pb244@damtp.cam.ac.uk

2. Lab. de Physique, E.N.S. de Lyon, 46 allée d'Italie, F69364 Lyon cedex 07

3. L.E.G.I., BP 53, F38041 Grenoble cedex 9

4. Appl. Physics Lab. & Dept of Appl. Math., U. of Washington, Seattle, WA 98105-6698, USA

ABSTRACT

We estimate mixing induced by the breaking of a large scale primary internal gravity wave, either propagating or standing. The data are the results of two-dimensional direct numerical simulations. We first investigate the vertical dispersion of particles released in the flow after the onset of wavebreaking. The eddy diffusivity is also inferred from the diapycnal diffusive flux. We show that the two methods are in good agreement, which is of interest regarding the interpretation of *in situ* measurements. We eventually provide a parameterization of mixing versus a Froude number of the flow which is similar to that found for a stratified shear layer [1]. The latter result is consistent with the scenario of wavebreaking for a low amplitude (statically stable) high frequency wave and suggests that the breaking of such a wave may be modeled by a spatial distribution of shear layers.

I. INTRODUCTION

In the stratified Ocean, vertical mixing is one of the basic processes which sets the intensity of the general circulation [2]. An appropriate parameterization of vertical turbulent mixing must therefore take into account the different processes through which turbulent mixing occurs. Whereas recent *in situ* measurements [3] have shown that important mixing occurs at the boundaries in regions of enhanced topography for instance, a better understanding of mixing within the interior of the ocean is still required [2]. There it is well-known that shear instability is an important process which promotes mixing (*e.g.* [4]). Furthermore, it is more than likely that internal gravity waves play an important part in this process, therefore "understanding mixing in the ocean interior is thus intimately linked to understanding the finescale shear field associated with the internal gravity waves" [2].

Our approach is a process-oriented one and we focus on mixing induced by the breaking of a large scale internal gravity wave freely evolving in a background linear stratification, a situation likely to occur in the oceanic thermocline. In this idealized situation we provide comparisons between the estimate of vertical eddy diffusivity inferred either from particle dispersion or from the diapycnal diffusive flux. We also determine whether mixing can be related to the dynamics of the large scale wave, namely the instabilities leading to wavebreaking.

We first briefly describe the mechanisms leading to wavebreaking, which permits one to understand how mixing occurs. We present in a second section the results of particle dispersion experiments. The eddy diffusivity is inferred from the diapycnal diffusive flux in a third section. The results are discussed in the last section.

II. EVOLUTION OF THE PRIMARY WAVE TOWARD BREAKING

Our case of interest is a large scale low amplitude, statically stable, internal gravity wave, referred to as the primary wave, which is either propagating or standing and evolves within a linearly stratified fluid. The reader is referred to Bouruet-Aubertot *et al.* [5],[6] for standing waves and Koudella & Staquet [7] for propagating waves for further details.

We solve the two-dimensional Navier-Stokes equations in the Boussinesq approximation and the initial condition is a linear mode of the Boussinesq equations. The resolution is of 513^2 for standing waves and of 512^2 for propagating waves. The Froude number of the wave, $Fr=k^2a/N$ (where k is the modulus of the wavevector, a the amplitude of the stream function and N the buoyancy frequency) is within $[0,36 ; 1,06]$ and the Reynolds number within $[1,5 \cdot 10^{-4} ; 10^{-3}]$. The Prandtl number is equal to 1.

The weakly nonlinear regime which first sets in is characterized by the growth of small scale perturbations extracting their energy from the primary wave through a mechanism of resonant interactions. These interactions result from the parametric instability of the primary wave. This behaviour is predicted by the resonant interaction theory ([8],[9]) and is recovered from a linear stability analysis of an internal gravity wave ([10],[11]). Basically

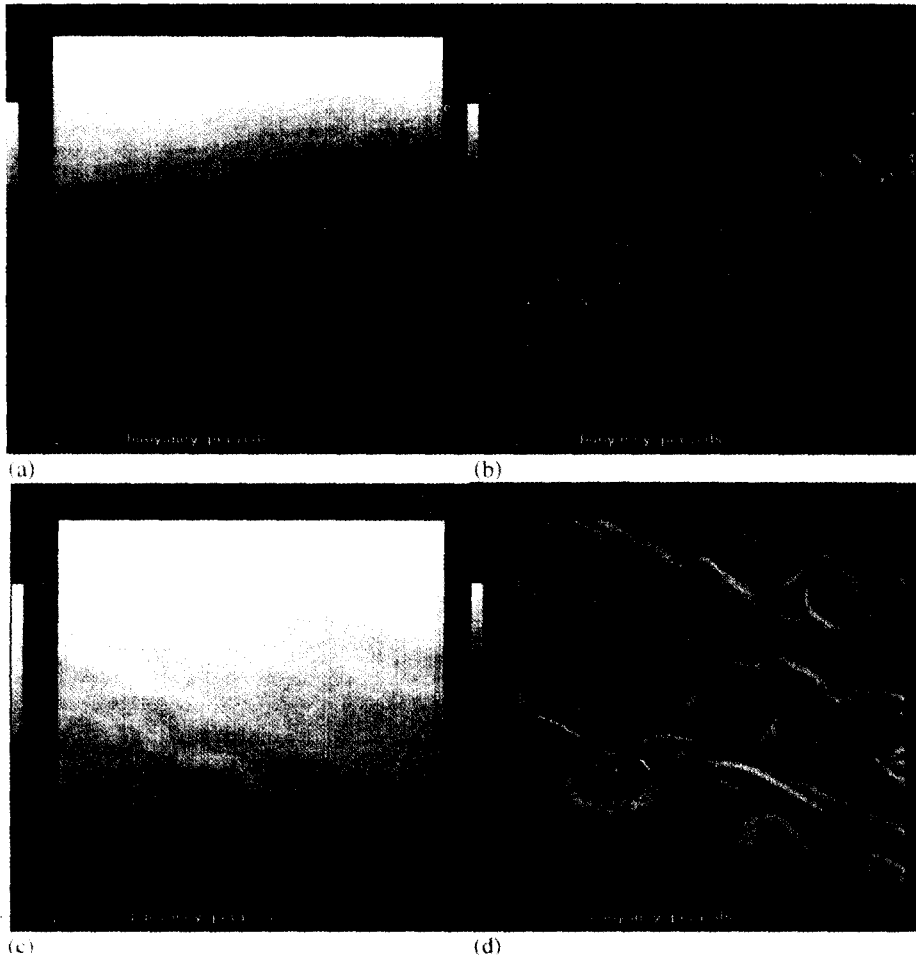


fig.1 : Density and vorticity fields at the onset of wavebreaking (a,b standing waves, c,d propagating waves)
 a. : density field at $t=72T$, b. : vorticity field at $t=72T$ (values within $[-12.6,16.2]$, to be compared with the initial range $[-0.512,0.512]$);
 c. : density field at $t=36.6T$, d. : vorticity field at $t=36.6T$ (values within $[-10.8,7.5]$, to be compared with the initial range $[-0.512,0.512]$).

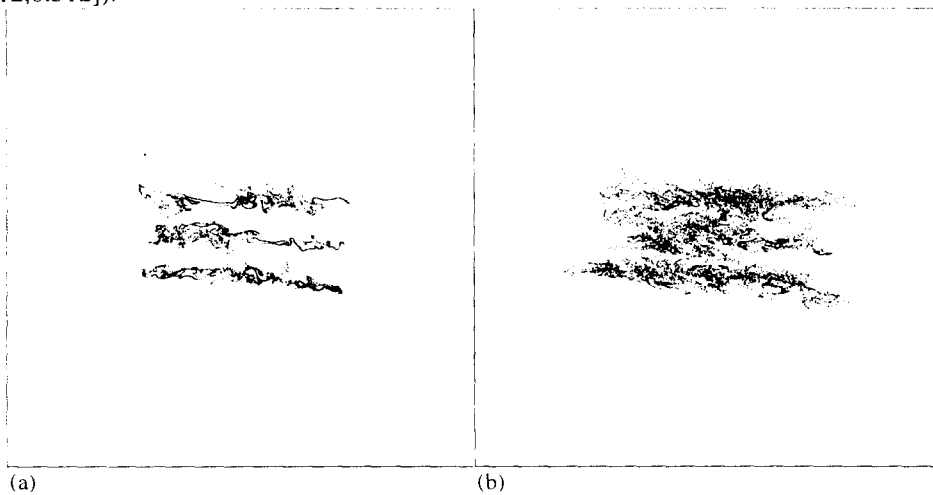


fig. 2 : Time evolution of three lines of particles released in the flow (propagating waves) at $t_0=36.6 T$. An extended domain of size $[-2\pi,4\pi]^2$ instead of $[0,2\pi]^2$ is taken to give a realistic view of the dispersion : a. particles at $t/T = t_0+ 1.6$, b. particles at $t/T = t_0+ 8$.

the physical mechanism of parametric instability can be described by a parametric oscillator when the scale of the primary wave is large compared with that of the perturbation ([12],[5],[13]). The oscillation of the primary wave leads to a periodic variation of the frequency of the small scale perturbations. This modulation induced by the primary wave can arise either from the variation of the direction of the wavevector of the perturbation or from the variation of the local buoyancy frequency. The former mechanism is efficient for standing waves while the latter dominates for propagating waves. This explains why, whereas the instability leads to the development of shear layers in both cases, the spatial organization differs depending on the nature of the wave. While localized shear layers develop in the case of standing waves (fig. 1.b), shear layers regularly spaced arise in the case of propagating waves (fig. 1.d). Wavebreaking eventually occurs when these shear layers become unstable. By contrast the three-dimensional dynamics of the same wave eventually involves a convective instability which arises as a result of the shear instability [7]. Therefore the evolution of the low amplitude wave toward breaking is well described by two-dimensional simulations. This behavior is in agreement with the linear stability analysis of a propagating wave subjected to three-dimensional perturbations performed by Klostermeyer [14] and Lombard & Riley [15] : for a low amplitude (statically stable) primary wave, the fastest growing perturbations are two-dimensional.

III. VERTICAL EDDY DIFFUSIVITY

III.1 PARTICLE DISPERSION

Particle trajectories $\mathbf{x}(\mathbf{a},t)$ for weightless particles are calculated by solving the equation $d\mathbf{x}/dt=\mathbf{u}$, $\mathbf{x}(0)=\mathbf{a}$ where \mathbf{u} is the fluid velocity at time t and location \mathbf{x} (see [16], [17] for further details).

Particle dispersion experiments are performed in the case of propagating waves. Three lines of particles, each made of 3072 particles, are introduced in the flow after the onset of wavebreaking at time $t=36.6T$ (fig. 1.c, d) and the motions are followed for ten buoyancy periods, until breaking ends. The particles are represented at two successive times to illustrate a change in behavior. The evolution of the particle sets is first highly variable (fig. 2.a) : lines are either elongated under the action of a strain field induced by long vortices of small vertical scales or vertically spread by small intense eddies in regions of overturning. For increasing times however, the vertical dispersion is fairly homogeneous (fig.2.b).

Following Hunt [18], we infer the vertical dispersion of the particles of a given line from the time evolution of the variance of their vertical displacement from the instantaneous center of mass of the line ($Z_0(t)$) (fig.3). After about 6 buoyancy periods a smoother evolution is obtained and the curve then slightly oscillates about a linear temporal law. These residual oscillations result from low frequency wave motions which are not statistically averaged. The eddy diffusivity K is usually computed from the slope of $Z_0(t)$ ([19], [18]) but here, because of the residual oscillations, we rather compute this parameter from the slope of the least square line. When normalized by the molecular diffusivity, values within [12 ; 16,3] are obtained, that is a variation of 30%. We find this result satisfactory owing to the rather short duration of wavebreaking. This variation could very likely be reduced by considering a forced primary wave, a case for which particle experiments could be conducted over a longer time interval.

III.2 DIAPYCNAL DIFFUSIVE FLUX

Background : we apply the analysis of mixing in stably stratified fluids proposed by Winters *et al.* ([20], [21]). By definition, the eddy diffusivity is equal to the diapycnal flux, which always results from diffusive effects, divided by a mean (temporally or horizontally averaged) density gradient. The determination of the diapycnal flux is difficult from a practical point of view because it amounts to extract a diffusive contribution from a turbulent field. Models are therefore usually employed to compute it (see *e.g* [4] or [2], for a review). A new method has been recently proposed by Winters & D'Asaro [21] to compute that flux exactly. The key ingredient is a stable density profile obtained by sorting the fluid particles so that the heaviest particle lies on the lowest altitude. Thus, the expression for the diapycnal flux is : $\Phi_d(z,t)=-\kappa\langle(\nabla\rho)^2\rangle_I / (d\rho^*/dz)$, where κ is the molecular diffusivity, the index I refers to an average along an isopycnal and $\rho^*(z)$ is the sorted profile. Note that the diapycnal flux thus defined is always positive. Also, its expression is formally similar to that proposed by Osborn & Cox [22], but using an average along the isopycnals and a sorted density profile in place of an horizontal average and a mean density gradient. Following these lines, the eddy diffusivity should be defined as $K_d=-\Phi_d(z,t)/(d\rho^*/dz)$ [21]. Note that K_d is always positive, whatever the flow dynamics.

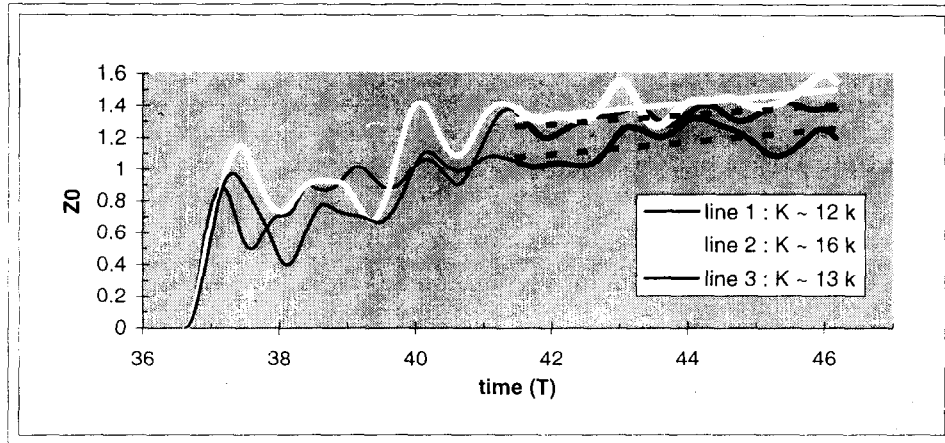


fig.3 : Variance of the vertical displacement relative to the instantaneous centre of mass for each line, versus time.

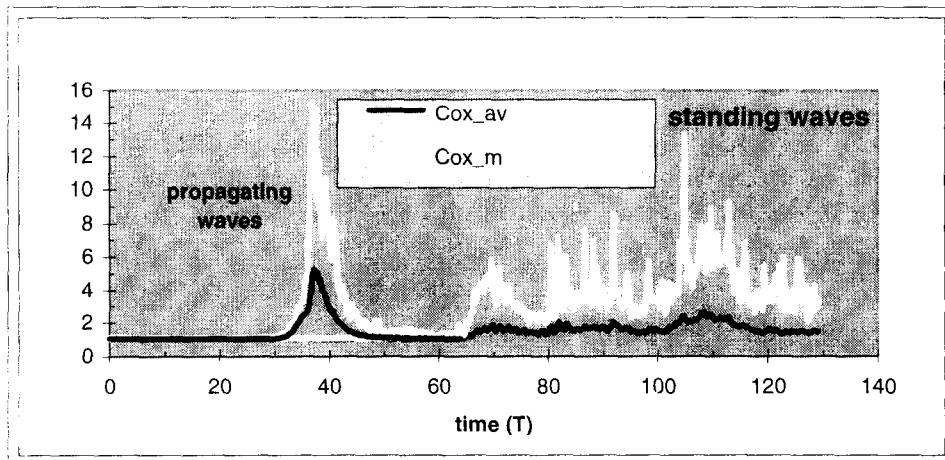


fig. 4 : Time evolution of the maximum Cox number, Cox_m and the spatially averaged Cox number, Cox_{av} : a : standing waves, b : propagating waves.

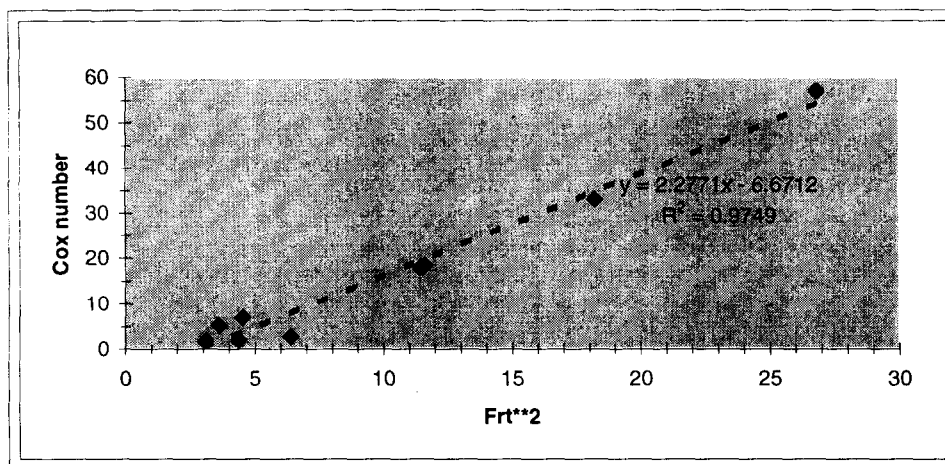


fig. 5 : Maximum over time of Cox_{av} versus the square of the maximum turbulent Froude number, Fr_t^2 for both propagating and standing waves.

The eddy diffusivity from the diapycnal flux : The time evolution of K_d/κ , referred to as the Cox number, is displayed in figure 4 for propagating and standing waves of equal amplitude (equal to 0.256). Both the maximum and the spatially averaged Cox number, Cox_m and Cox_{av} respectively, are represented. The former quantity provides an estimate of eddy diffusivity in overturning regions while the latter characterizes the averaged diffusion over a wavelength of the primary wave. During the quasi-periodic stage, the averaged Cox number is closed to 1 because $Cox_{av} \sim 1 + o(A^2)$ for a periodic wave of amplitude A . As the wave becomes unstable, the maximum Cox number increases, reaching maximum values of about 15 (fig.4). This value is in agreement with those inferred from particle dispersion, which range between 12 and 16.3. This is one of the main results of this paper.

The eddy diffusivity is fairly independent on the nature of the wave, either propagating or standing. The only difference we noted comes from the duration of wavebreaking which is much shorter for propagating waves than for standing waves. This results from the spatial structure of the instability which occurs within broadly distributed shear layers for a propagating wave whereas it is limited to few localized shear layers for a standing wave. Therefore the energy of the primary wave is more rapidly dissipated in the former case than in the latter.

Toward a parameterization of the eddy diffusivity : Our purpose is to find whether the eddy diffusivity can be linked with the large scale dynamics. We are therefore looking for a relationship between the eddy diffusivity and a non dimensional parameter characterizing the dynamics at larger scales. It is natural to introduce the Froude number, Fr_t , defined as : $Fr_t = \max_{time} [2 Z(t)/N]^{1/2}$ where $Z(t)$ is the enstrophy. Fr_t is a relevant quantity regarding large scale dynamics since kinetic energy spectra behave like k^{-3} [23] : the maximum of the enstrophy will be at larger scales than those at which mixing occurs.

The maximum over time of Cox_{av} is displayed in figure 5 versus the square of the turbulent Froude number, for different calculations of propagating and standing breaking waves of various amplitudes. The whole range of values is [5,60] for Cox_{av} . Figure 5 shows that the data can be fitted by a linear law versus Fr_t^2 . This result is consistent with the fact (not shown) that the averaged mixing efficiency $\gamma = \Phi_d/\epsilon$ is fairly constant during wavebreaking ; Φ_d is the volume average of $\Phi_d(z)$ and ϵ the dissipation rate of kinetic energy. Indeed, one has : $Cox_{av} = K_d/\kappa \sim \Phi_d/\kappa N^2 = \gamma \epsilon / (\kappa N^2) = (2Z/N)(Pr \gamma/N)$ so that $\max_{time} Cox_{av} \approx (Pr \gamma/N) Fr_t^2$ if γ remains constant for the different calculations (since Pr and N are kept constant). We find that this is indeed the case. More generally a relationship between the Cox number and the Froude number can be established, which is valid at any time of the wave evolution and for the wave amplitude within the range considered here [23].

IV. DISCUSSION

We estimate the mixing produced by the breaking of a large scale, low amplitude internal gravity wave. The breaking of the wave is initiated by a parametric instability, a mechanism through which energy is transferred to lower frequencies and smaller vertical scales, but breaking eventually occurs through shear instability. The former process is analogous to the Parametric Subharmonic Instability ("PSI") type resonant triad identified by McComas & Muller [24] in the Garrett & Munk spectrum.

We discuss two methods to evaluate mixing, which either relies upon particle dispersion or upon potential energy budgets.

We perform particle dispersion experiments and find that a diffusion law is eventually reached provided that the effect of the waves is statistically averaged both spatially and temporally. Thus particle dispersion experiments must be conducted over a fairly long duration compared with the wave periods and for sufficient large number of particles. We find that in numerical simulations where these two constraints are difficult to ensure, the diffusion law crucially depends upon the spatial distribution of the particles [23].

We also calculate the eddy diffusivity from the diapycnal diffusive flux, using a general, exact method which does not require the assumption of a statistically steady state. A good agreement is obtained with the values of eddy diffusivity inferred from particle dispersion simulations. This is of great interest regarding *in situ* experiments. It is also consistent with previous *in situ* experiments (e.g. [25]) for which an agreement within a factor of two between dye dispersion and microstructure measurements was obtained.

The eddy diffusivity is found to vary like the square of the turbulent Froude number, which scales like an inverse Richardson number. This relationship is similar to that obtained for a two-dimensional stratified shear

layer [1]. This similarity is consistent with the process of wavebreaking which eventually occurs through shear instability. Moreover it suggests that the breaking of a large scale, weak amplitude internal gravity wave can be modeled by the instability of shear layers. Interestingly the relationship between vertical eddy diffusivity and the squared Froude number is analogous to mixing models based upon a linear dependency between the dissipation rate of turbulent kinetic energy and the finescale shear level of the internal wave field in the ocean (e.g. [26]).

REFERENCES

- [1] C. Staquet & K.B. Winters 1998. Mixing in a two-dimensional stably stratified shear layer. Submitted to Physics of Fluids.
- [2] J.M. Toole 1998. Turbulent mixing in the ocean : intensity, causes, and consequences. Proceedings of Les Houches Winter School, "Ocean modeling and parameterization" E.P. Chassignet and J. Verron ed., Kluwer Academic Publishers, 171-190.
- [3] K.L. Polzin, J.M. Toole, J.R. Ledwell & R.W. Schmitt 1997. Spatial variability of turbulent mixing in the abyssal ocean. Science, 276, 93-96.
- [4] M.C. Gregg 1987. Diapycnal mixing in the thermocline : a review. J. Geophys. Res., 92-C5, 5249-5286.
- [5] P. Bouruet-Aubertot, J. Sommeria & C. Staquet 1995. Breaking of internal gravity waves trough two-dimensional instabilities. J. Fluid Mech., 285, 265-301.
- [6] P. Bouruet-Aubertot, J. Sommeria & C. Staquet 1996. Stratified turbulence produced by internal wave breaking : two-dimensional numerical experiments. Dyn. of Atmos. and Oceans, 23, 357-369.
- [7] C. Koudella & C. Staquet. Two-dimensional breaking internal gravity waves : from instabilities to turbulence, in preparation.
- [8] K. Hasselmann 1967. A criterion for nonlinear wave stability. J. Fluid Mech., 30, 737-739.
- [9] O.M. Philips 1966. The dynamics of the upper ocean. Cambridge university press.
- [10] R.P. Mied 1976. The occurrence of parametric instabilities in finite amplitude internal gravity waves. J. Fluid Mech., 78, 763-784.
- [11] P.G. Drazin 1977. On the instability of an internal gravity wave. Proc. R. Soc. Lond., A356, 411-432.
- [12] A.D. McEwan, R.M. Robinson 1975. Parametric instability of internal gravity waves. J. Fluid Mech., 67, 667-687.
- [13] D. Bénélli & J. Sommeria 1996. Excitation of internal waves and stratified turbulence by parametric instability. Dyn. Of Atmos. And Oceans, 23, no1-4, 335-343.
- [14] J. Klostermeyer 1991. Two and three-dimensional parametric instabilities in finite amplitude internal gravity waves, Geophys. Astrophys. Fluid Dyn., 61, 1-25.
- [15] P.N. Lombard & J.J. Riley 1996. Instability and breakdown of internal gravity wave : 1. Linear stability analysis. Phys. of Fluids, 8, no.12, 3271-3287.
- [16] A. Babiano, C. Basdevant, P. Le Roy & R. Sadourny 1987. Single particle dispersion, lagrangian structure function and lagrangian energy spectrum in two-dimensional incompressible turbulence. J. Marine Research, 45, 107-131.
- [17] N. Zouari & A. Babiano 1990. Expériences numériques lagrangiennes à partir de modèles eulériens. Atmosphères-Océans, 3, 345-364.
- [18] J. Hunt 1985. Diffusion in the stably stratified atmospheric boundary layer. J. of Climate and Applied Meteorology, 24, 1187-1995.
- [19] H.J. Pearson, J.S. Puttock, J.C.R. Hunt 1983. A statistical model of fluid elements motions and vertical diffusion in a homogeneous stratified turbulent flow. J. Fluid Mech., 129, 219-249.
- [20] K.B. Winters, P.N. Lombard, J.J. Riley & E.A. D'Asaro 1995. Available potential energy and mixing in density-stratified fluids. J. Fluid Mech., 289, 115-128.
- [21] K.B. Winters & E.A. D'Asaro 1996. Diascalar flux and the rate of fluid mixing. J. Fluid Mech., 317, 179-193.
- [22] T.R. Osborn, C.S. Cox 1972. Oceanic finestructure. Geophys. Fluid Dyn., 3, 321-345.
- [23] P. Bouruet-Aubertot, C. Koudella, C. Staquet & K.B. Winters. Particle dispersion and mixing produced by breaking internal gravity waves, in preparation.
- [24] P.G. McComas & P. Muller 1981. The dynamic balance of internal waves. J. Phys. Oceanogr., 11, 970-986.
- [25] A. Wuest, D.C. Van Senden, J. Imberger, G. Piepke & M. Gloors 1996. Comparison of diapycnal diffusivity measured by tracer and microstructure techniques. Dyn. of Atm. and Oceans, 23, no.1-4, 27-39.
- [26] K. Polzin 1996. Statistics of the Richardson number : mixing models and finestructure. J. Phys. Oceanogr., 26, No8, 1409-1425.

NON LINEAR INTERACTIONS OF EAST AUSTRALIAN CURRENT EDDIES

M.J. Bowman¹, D.E. Dietrich² and B.G. Sanderson³

¹School of Environmental & Marine Sciences, University of Auckland, PO Box 92019, Auckland, NZ
m.bowman@auckland.ac.nz

²Center for Air Sea Technology, Mississippi State University, Stennis Space Center, MS 39529, USA
dietrich@cast.msstate.edu

³School of Mathematics, University of New South Wales, Sydney, NSW 2052, Australia
bxs@alpha.maths.unsw.edu.au

Abstract

The DieCAST ocean model is applied to the southwestern Pacific Ocean using 1/4 deg resolution. New Zealand is near the center of the modeled region, which spans from Tasmania on the west and northward from 65 deg S. Surface forcing and open lateral boundary conditions are based on annual cycle climatology, with no data assimilation. The results are consistent with many detailed observations, including the dynamics of the East Australian Current (EAC). Although EAC large-scale cyclonic eddies are seen only in the deep water, intense, small-scale cyclonic parasitic eddies often originate along the shelfbreak and near headlands, and get advected offshore in spurts, around the south side of major warm core anticyclonic EAC eddy features. These parasitic eddies interact strongly with the EAC separated large scale warm core eddies. They affect separation and reconnection with the main coastal current as well as the collision, merging and subsequent splitting apart of EAC eddies.

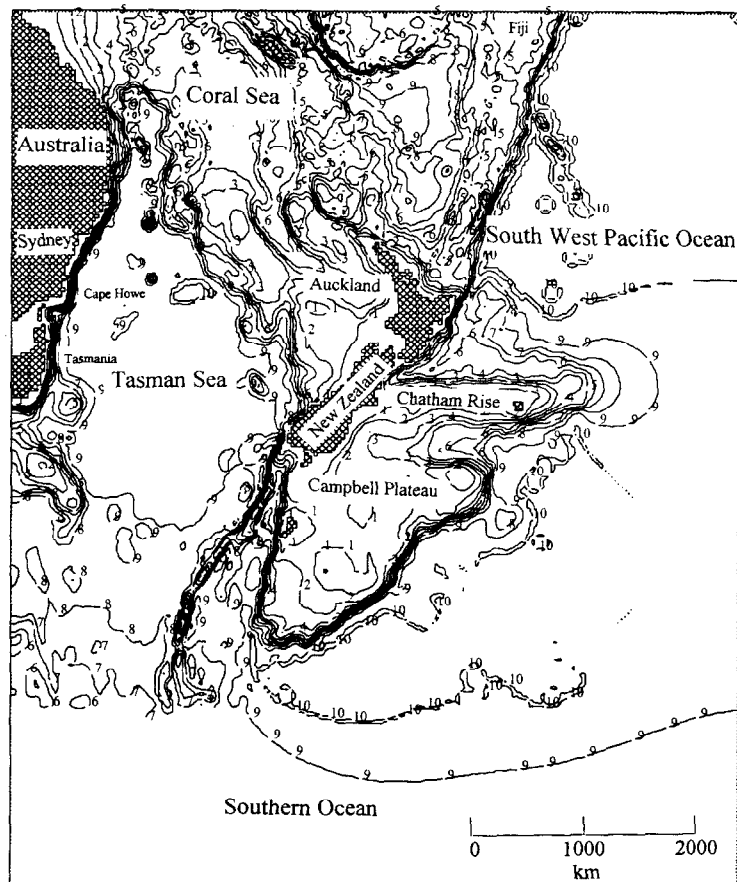


Figure 1: locator map and bathymetry of the modeled region (filtered south of the Campbell Plateau and east of the Chatham Rise).

1. Introduction

The East Australian Current (EAC) sheds some of the most plentiful and energetic eddies in the world ocean. It has been of considerable interest, particularly the observations and merging dynamics of its pinched off warm-core eddies [1, 2]. The EAC is a southern hemisphere version of the Gulf Stream, but has a much weakened analog of the Labrador Current in spite of the large Antarctic Circumpolar Current (ACC) to its south. This may be related to blocking by the Campbell Plateau south of New Zealand and the associated more southward course of the ACC. This may reduce the tendency for baroclinic instability in the EAC compared to the Gulf Stream.

Here, we focus on the effect of parasitic cool core cyclonic eddies on the dynamics of the EAC itself and its shed anticyclonic eddies, as it retroflects near Sydney and flows across the Tasman Sea towards the northern tip of New Zealand. Simulations by the DieCAST ocean model show that these cool core parasitic eddies, which often originate along the shelfbreak, may interact strongly with

the much larger, offshore warm core eddies after being swept offshore by the strong warm core frontal currents.

We describe the model and EAC setup in Section 2. In Section 3, we compare model results with observations, then focus on the dynamics of the EAC, its shed warm core eddies and their interactions with the cool core parasitic frontal eddies.

2. The Model

The model is the DieCAST Ocean Model. DieCAST is a z-level model using a semi-located horizontal grid and fourth-order-accurate horizontal advection and baroclinic pressure gradient formulation. It uses unfiltered real bathymetry and is robust with very low dissipation. Sheng, et al. [3] discuss a closely related CANDIE version in great detail. A modified incompressibility treatment [4], along with its fourth-order accuracy and small diffusion parameters, results in low numerical dissipation and dispersion [4, 5]. Further details are available at:

<http://cast.msstate.edu/DieCAST> and <http://www.maths.unsw.edu.au/~bxs/DieCAST/MANUAL/>

The boundaries (Fig. 1) are 146 deg E (Tasmania), 18 deg S (Fiji Islands), 160 deg W and 65 deg S. Bathymetry is unfiltered etopo5 with nearshore New Zealand waters corrected out to 500 m deep from published navigation charts. All four boundaries are open. Seasonally varying inflows are specified, based on climatological data, on the western and northern boundaries (ACC and cross equatorial drift feeding the EAC, respectively). Monthly COADS wind forcing and seasonal 90-day time scale restoring to Levitus surface climatology are used.

The northern Tasman Sea inflows are patterned after observations analyzed by Ridgeway and Godfrey [6]. A top level Ekman layer inflow of ~ 4.1 Sv is uniformly distributed along the northern boundary. This is added to a seasonal thermal wind of ~ 3 Sv based on layer 10 (500 m) reference level for Levitus climatology. A uniform northward barotropic drift of 0.002 cm/sec is added, giving about 0.3 Sv outflow. The net northern boundary inflow is ~ 7 Sv.

The western boundary is inflow only, based on seasonally varying climatological thermal wind with level of no motion at ocean bottom. This gives ~ 100 Sv specified ACC inflow. Tangential velocity is damped on the western and eastern boundaries. Longitudinal upwind conditions then determine normal boundary velocity along the eastern boundary. However, north of 28 deg S, the flow is nudged toward a specified vertical profile of ~ 4 Sv inflow [6], and south of 28 deg S the conditions are outflow-only.

The southern boundary is treated in a similar manner to the outflow region of the eastern boundary.

Ongoing development of an automated two-way nested modeling approach within a global version of DieCAST will avoid the guesswork and the need for tangential velocity damping along open boundaries.

3. Results

The model results show many of the observed features of the EAC region, including a time-mean southward EAC transport of ~ 31 Sv at 28 deg S. This is ~ 4 Sv more than carefully analyzed observations [6], but is within the range of uncertainty of the actual inflows and transport estimates, especially the eastern inflow. The time mean flow reverses ~ 100 km offshore. Most of the EAC (~ 18 Sv) returns northward, across the 28 deg S latitude, east of the main coastal jet. Model maximum EAC currents are typically ~ 150 cm/sec, eddy diameters ~ 250 km, time scales of variability ~ 150 days for the main warm core eddies. These and other features are in close agreement with EAC observations [1, 2].

The model is in good agreement with many other observed flow features, including the major eddy field in the ACC south of New Zealand, the Tasman Front, and many detailed features near New Zealand, including the East Cape Current, the Hikurangi Eddy, the Southland Current, and fine-scale Mernoo Gap jet [7].

Figs. 2-4 display the region off the southeast coast of Australia and illustrate the strong interaction between the EAC, its shed eddies and associated cyclonic parasitic eddies.

Fig. 2 shows three cool core parasitic eddies (A, B, C) around the main warm core anticyclonic eddy at day 510. Eddy C on the north side disappears by day 530 after it moves toward the coast, as may occur due to divergence as the cyclonic vortex moves toward shallow water and compresses vertically. This behavior is common in model results. Between days 530 and 550 a new cool core eddy D develops as cyclonic coastal water E advects around the south side of the merging warm cores, thus strengthening the cyclonic circulation on the

east side of the merging warm cores F. By day 570, the cyclonic eddy D has quickly moved westward to G and caused a separation H of the northern lobe of the merging warm cores, northeast of the main warm core.

Fig. 3 shows a similar event, at days 660, 680, 700 and 720, except the northern warm core I is stronger when the cool core cyclonic eddy J cuts between the two warm cores I, K after day 720 (not shown).

Fig. 4 shows the top layer temperature evolution during the Figure 3 sequence. The warmer 21 deg. water from the northern warm core I and EAC advects around and over the original warm core K to its south, whose core temperature is 19 deg., because of seasonal cooling effects and its greater age.

These model results show that, once offshore, the cyclonic parasitic eddies may grow in amplitude and scale. The scale increase reflects geostrophic adjustment as the eddies grow to a scale corresponding to the deep-water Rossby radius-of-deformation. As they grow in scale, they tend to slow down, as Rossby wave effects start to oppose the offshore advection. This allows them to gather strength from smaller-scale cyclonic vorticity features that are advected offshore by the warm core eddy as it attempts to drift westward (Rossby wave effect) allowing it to entrain coastal water along its shelfbreak front. As the entrained water is advected toward deeper water, it naturally develops cyclonic vorticity because of vortex stretching, and a cool core develops as part of deeper water slow mode geostrophic adjustment in accordance to the q-g omega equation. The small-scale cyclonic parasitic eddy features tend to move faster and merge into the offshore developing larger-scale cyclonic cool core eddies. Thus, the cyclonic features may grow in amplitude and scale as they mature offshore. The opposite effect occurs when they sometimes move toward the shore on the north side of warm core eddies, so that near shore the significant cyclonic eddy features are usually ephemeral. This behavior is closely related to the observed dynamics of western Gulf of Mexico warm core eddies relating to nonlinear critical areas [4].

4. Discussion and Acknowledgements

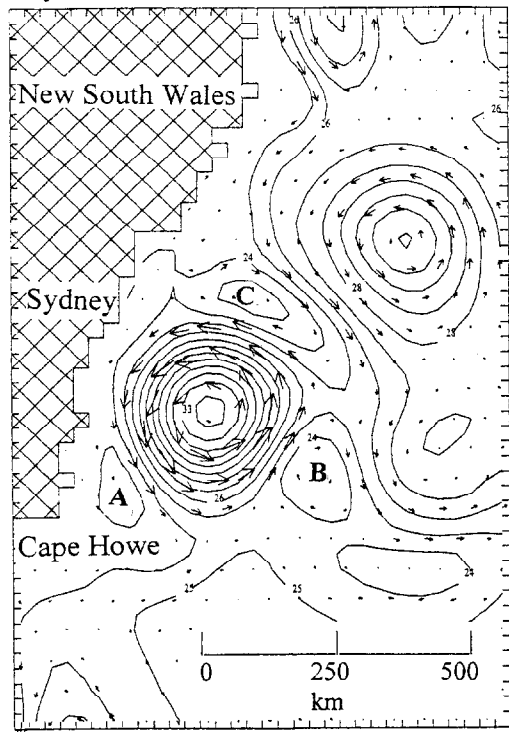
The small-scale parasitic frontal eddies, while having space and time scales that may be too small to be easily observed for data assimilation into a model, may be important for the purpose of defining the main EAC features. This may limit forecasting capability, but there is some recent encouraging research by Kreiss, et al. (pers. comm.) that suggests that one may be able to predict the small scale features by assimilating only the available large-scale data into a model having fourth-order-accurate numerics (e.g. the present DieCAST ocean model). This is possible if the observed large-scale features determine the small-scale features, as in nonlinear cascade dynamics which occurs over a range of energetic scales smaller than the unstable Rossby radius range. Thus, successful sub-observation-scale forecasting is most plausible for features smaller than the Rossby radius of deformation, assuming enough good data is available in the unstable Rossby radius range of scales. The most energetic sub-Rossby-radius scales may then be determined by the observed scales combined with a good fourth order accurate model capable of accurate simulation of nonlinear cascade dynamics ("local interactions in scale space"). Satellite data, suitably assimilated, including projection to thermocline depths, may be adequate for such purposes.

We thank Oliver Ross and Eric Soyez for preparing the near-shore New Zealand bathymetry, and John Wilkin for useful comments and suggestions.

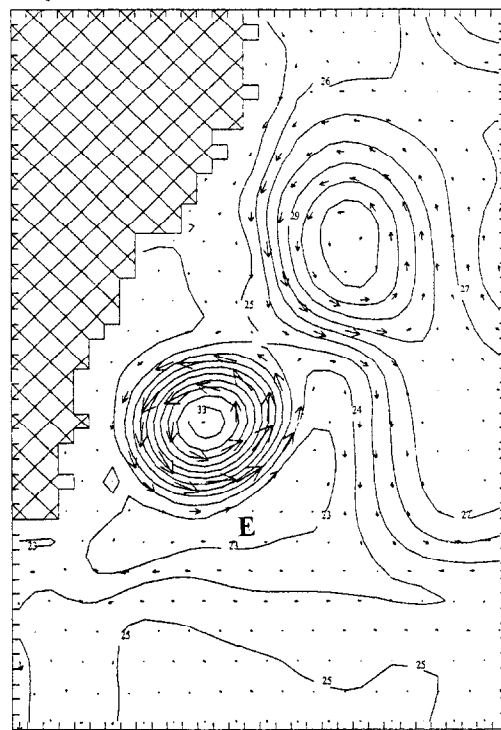
References

- [1] G. Cresswell, 1982. The Coalescence of Two East Australian Current Warm Core Eddies, *Science*, 215, 161-164.
- [2] A.F. Bennett, 1983. The South Pacific Including the East Australian Current, *Eddies in Marine Science*, ed. A.R. Robinson, Springer-Verlag, Berlin Heidelberg.
- [3] J. Sheng, D.G. Wright, R.J. Greatbach and D.E. Dietrich, 1998. CANDIE: A New Version of the DieCAST Ocean Circulation Model. *JAOT* (in press).
- [4] D.E. Dietrich, 1997. Application of a modified 'a' grid ocean model having reduced numerical dispersion to the Gulf of Mexico circulation. *Dynamics of Atmospheres and Oceans*, special issue honoring Richard L. Pfeffer, 27, 201-317.
- [5] B.G. Sanderson, 1997. Order and Resolution for Computational Ocean Dynamics, *J. Phys. Oceanogr.*, 28, 1271-1286.
- [6] K.R. Ridgeway and J.S. Godfrey, 1994. Mass and Heat Budgets in the East Australian Current: A Direct Approach, *J. Geophys. Res.*, 99, 3231-3248.
- [7] R.A. Heath, 1975. Oceanic circulation off the east coast of New Zealand, *New Zealand Oceanogr. Inst. Memoir* 55, Wellington, 80pp.

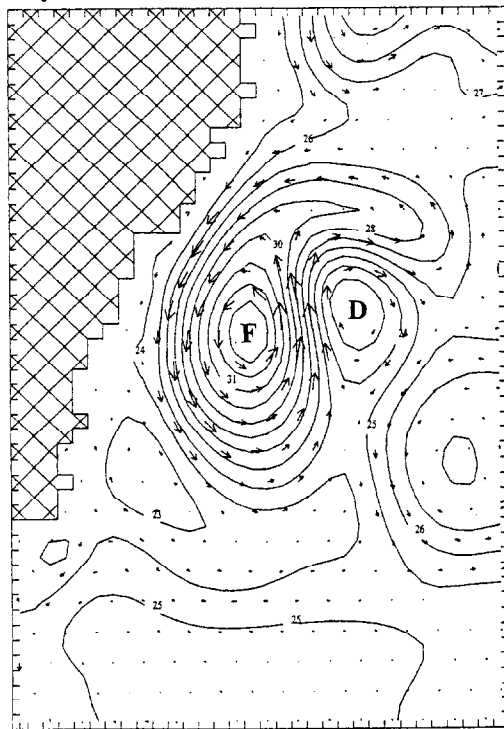
Day 510



Day 530



Day 550



Day 570

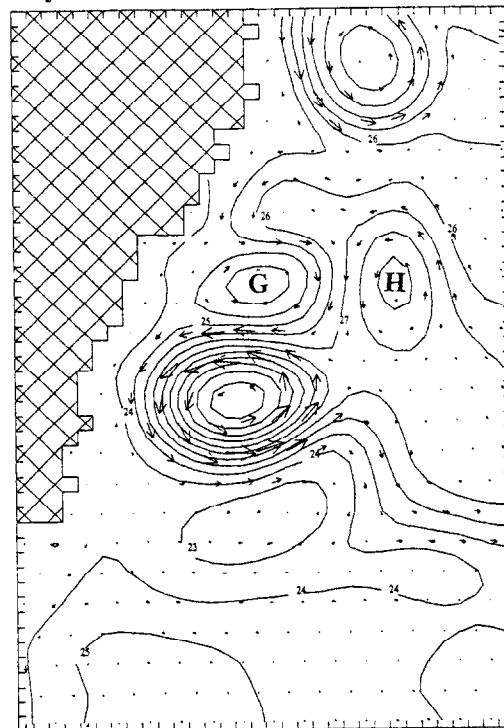
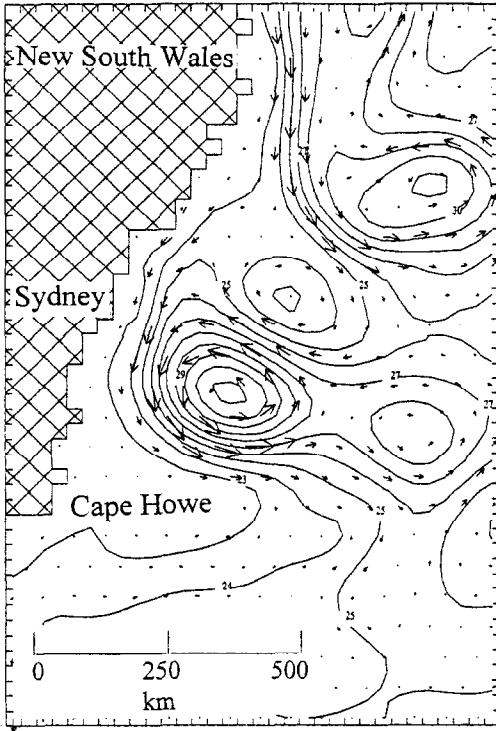
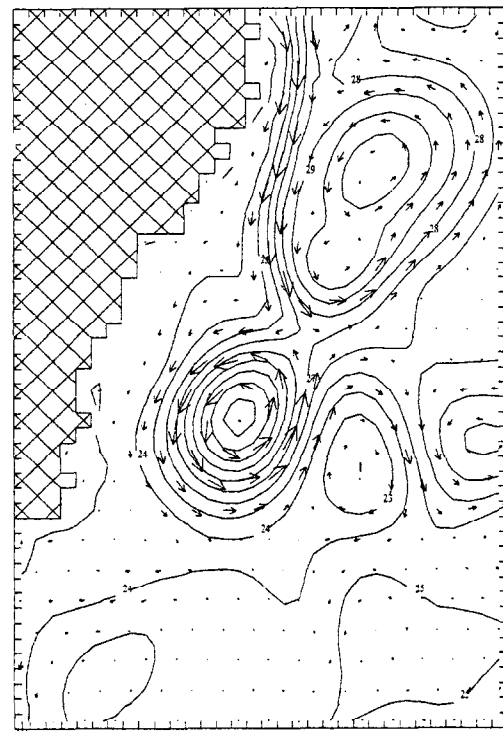


Figure 2: top layer model pressure and velocity vectors at days 510, 530, 550 and 570 for the region off New South Wales.

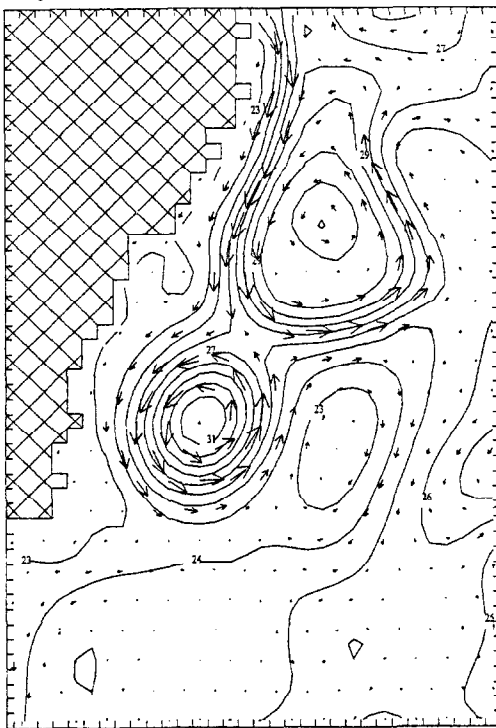
Day 660



Day 680



Day 700



Day 720

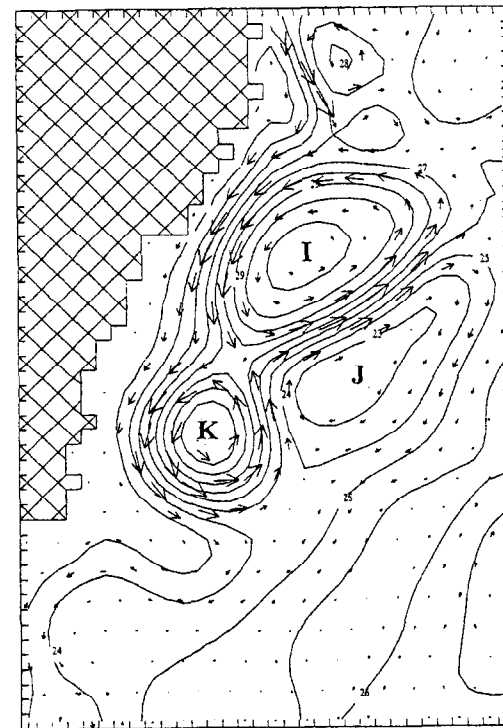
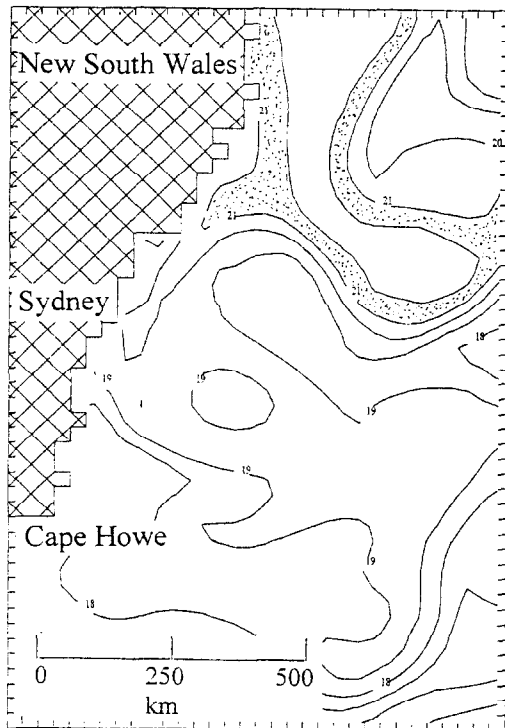
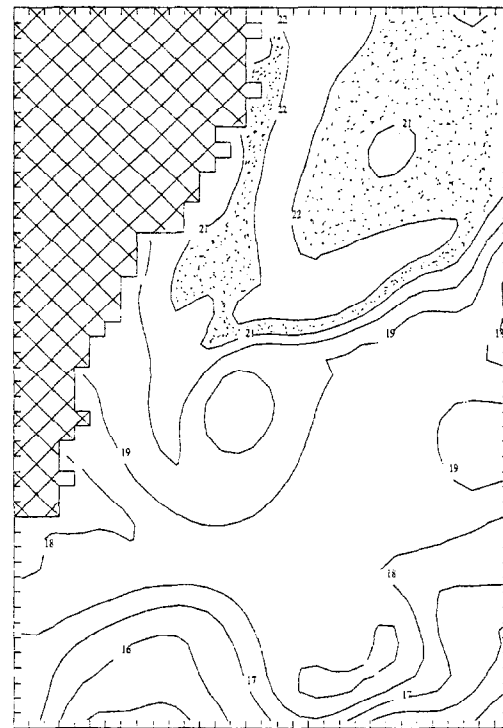


Figure 3: top layer model pressure and velocity vectors at days 660, 680, 700 and 720 for the region off New South Wales.

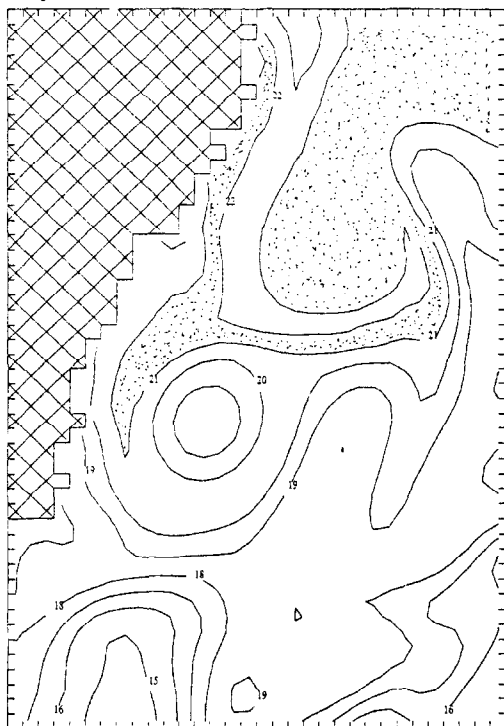
Day 660



Day 680



Day 700



Day 720

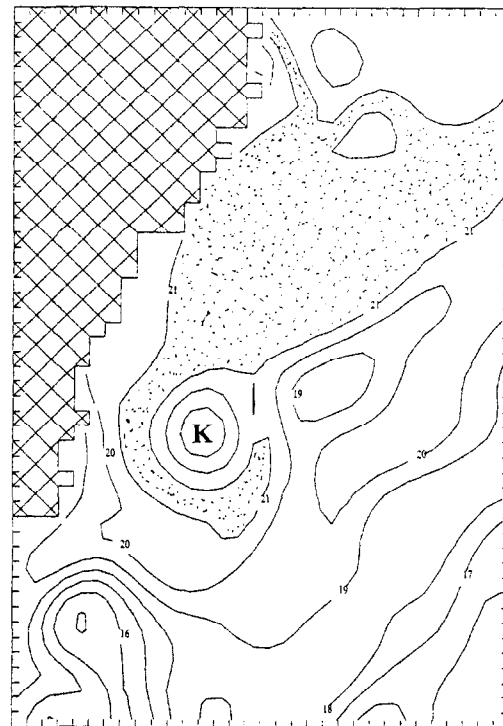


Figure 4: top layer model temperature (deg. C) at days 660, 680, 700 and 720 for the region off New South Wales. The band between 21 deg. and 22 deg. is stippled.

ON CRITERIA FOR FORMING DENSE WATER AND ITS APPLICATION TO THE MEDITERRANEAN SEA

B. Buongiorno Nardelli
ENEA C.R. "CASACCIA" Roma, ITALY
E-mail: bruno@gorgona.casaccia.enea.it

E. Salusti
I.N.F.N. - Dip.to di Fisica, Università "La Sapienza"
Piazzale A. Moro 2, 00185 Roma (Italy)

Abstract

Criteria to identify sites, and characteristics of dense water formation in the Mediterranean basin are developed from results first obtained through tank experiments [Narimousa and Maxworthy, 1994; Narimousa, 1996] and numerical and theoretical studies [Visbeck, Marshall, Jones, 1996; Tzipperman, 1986]. Using these criteria, general characteristics of dense water can be inferred from the wintertime pre-conditioned stratification, g' , from the increase in buoyancy, B , and from the size, R , of the region. R is usually defined by a $0.5 - 1^\circ\text{C}$ decrease in the SST.

The criteria have been applied to the Mediterranean Sea using several well-defined sets of observations in addition to climatological values of the stratification, numerical estimates of the buoyancy flux, and SST from satellite imagery. This produces a stimulating picture of these dramatic phenomena and gives some insight about the possibility of forecasting in real time the sites and times of dense water formation. This approach also can produce estimates of the final depth reached by the dense water.

Introduction

The Mediterranean Sea represents a sort of test basin for many oceanographic studies, allowing more continue and less expensive monitoring of the phenomena observed. Its thermohaline circulation has often been compared to the global conveyor belt, because in the semi-enclosed Mediterranean basin many processes driven by water masses modification and mixing are known to occur. In particular, Dense Water Formation (DWF in the following) processes are often observed as the result of violent air-sea interactions. In the past years, a great effort has been done to understand how deep water is formed, both from a theoretical and from an experimental point of view. As a consequence, different criteria to estimate the depth reached during the convection have been produced (Narimousa and Maxworthy, 1994; Narimousa, 1996; Visbeck et al., 1996; Tzippermann, 1986). Since the first observation of deep wintertime convection in the Gulf of Lions (Medoc Group, 1970; Gascard, 1973, 1978; Shott and Leaman, 1991) we know the basic mechanism for DWF. During winter, some relatively small zones present a particularly vertically homogeneous density field, as various dynamical structures, usually characterized by a weak stratification are eroded through the winter cooling of the sea surface. This phase, called 'pre-conditioning', is of fundamental

importance for later DWF processes and represents the real core of these phenomena. During severe storms a vertical density inversion can be produced by both cooling and evaporation and consequently turbulent convection takes place. The sea response is only due to small space scale convection cells, called plumes, mainly because of the constraint related to the finite depth of the basin and to the earth rotation. The space scale of the region involved in the convection is that of the pre-conditioned area, reaching several tens of kilometers. On the other hand Shott and Leaman (1991) stressed how the dimensions of the plumes can be surprisingly small (of the order of 1 Km), using ADCP (Acoustic Doppler Current Profiler) data collected during a DWF event in the Gulf of Lions. Similar conclusions were obtained through numerical simulations with hydrostatic and not-hydrostatic models (Crepon et al. 1989; Jones and Marshall, 1993;). Tank experiments and numerical simulations show that after a time $1/f$ (f being the Coriolis parameter) the denser fluid column is constrained by the earth rotation and a vorticular motion develops (Coates et al, 1995). The plumes start to carry dense water until a naturally buoyant level is reached. This denser water forms an homogeneous column, originating from the plumes in their initial overturing phase, which is called chimney. After a few days, baroclinic instability processes affect the chimney. Perturbations develop and the structure is broken in fragments, known as cones, that finally bring dense water away from the core (Killworth, 1976; Marshall and Jones, 1993). In this work we focus on the estimates of the convective penetration depth, which is a fundamental quantity on climatological grounds. After a brief introduction on the criteria, DWF penetration depth is estimated from both in situ, remotely-sensed, climatologica data and numerical computation of sea stratification and air-sea fluxes. For the Mediterranean, these criteria are here applied to the known sources of deep and intermediate waters and to areas where this processes are only supposed to occur.

The criteria for estimating the chimney floating depth h

Maxworthy and Narimousa (1994) pointed out that a natural, and useful, manner to interpret the main results of tank experiments was given by dimensional scale analyses. In particular, paralleling a classical study on the buoyancy balance in the Red sea, they found that g' has to be proportional to $(BR)^{2/3}/H$, this H being the bottom depth. All this can be seen as a balance of the input of buoyancy at the air-sea surface, which is $B\pi R^2$, and the radial outflow of buoyancy from the lower layer, namely $g'2\pi RH$ times a characteristic velocity scaled as $\sqrt{g'H}$. Note that similar considerations hold if the chimney doesn't arrive to the sea bottom, but with $H \rightarrow h$; *Maxworthy* (1997) fully discusse such problem on dimensional and theoretical grounds.

In addition *Narimousa* and *Maxworthy* (1996) and *Narimousa* (1997) found from tank experiments that, for a two-fluid rotating system, the penetrative depth is essentially ruled only by

$$\mathcal{N} = g'h_o(BR)^{2/3} \quad (1)$$

where now h_o is the upper layer thickness. In their experiment a dense water source is placed at the top of a tow-layer rotating non turbulent fluid. A dense water plume then develops, moving downward till h_o is reached. If $\mathcal{N} > 12 \pm 1$, the dense water starts

floating in an horizontal direction as a density current, or an intrusion, or sinks into the bottom layer if $\mathcal{N} < 12$. Note that one can also have a different view point, namely to assume "a priori" $N = 12 \pm 1$ and then find h_o , that now is the critical value separating floating and sinking plumes, namely in this case h_o somehow plays the role of H .

It is noteworthy how this generalization resembles an other interesting criterion due to *Visbeck, Marshall and Jones (1996)* that assumes, as in the atmospheric case but on a much smaller space scale (*Green, 1970; Stone, 1972*), that the lateral dispersion of buoyancy due to baroclinic instabilities balances the sea surface buoyancy influx. The corresponding estimate

$$h = 3.9 \pm 0.9 \sqrt{BR}/N; N^2 = -\frac{\partial \rho}{\partial z} / \rho \simeq const \quad (3)$$

gives realistic values for h also in the oceanographic case. If in addition one equates $g \frac{\rho(h_c) - \rho_{surface}}{h \rho_{surface}} = N^2$, then the NM criterion gives $h = (3.5 \pm 0.2) \sqrt{BR}/N$ which is again an estimate similar to the others used for stratified fluids. Using these criteria, general characteristics of newly formed dense water can be inferred from the knowledge of only the density stratification, the radius of the region involved in the convection and of the buoyancy flux.

Results

Both VMJ and NM criteria have been applied to the few measured DWF events in the Mediterranean. The regions considered are:

- Gulf of Lion. Here strong wind outburst of continental aim (Mistral) combine with the pre-conditioning due to a permanent cyclonic circulation, giving raise to the main source of deep water in the western Mediterranean. The data analysed are those collected by Shott and Leaman (1991) during winter time 1987, and by Shott et al. (1996) during February 1992.
- Ligurian Sea. A cyclonic circulation affects also this basin. Convective events have been measured during February 1969 and 1991 (Sparnocchia et al. 1995).
- Rhodes gyre. This area is characterized by intense phenomena of intermediate water formation. Sometimes particularly strong polar air storms force convection to the deeper layers. Here we present computation based on the data collected in march 1987, February 1990, March 1992 by Gertman et al. (1990; 1994;) Sur et al (1992).
- South Adriatic. even if the major contribute to DWF in the Adriatic comes from the northern shallow continental shelf area, also the south Adriatic has been indicated as a source of deep water. Bregant and Manca (1998) observed deep convection during winter 1996.
- North Aegean. This sea presents very interesting aspects from a thermodynamical point of view. During winter, very cold, dry and strong winds blow over the region. This sea is still relatively unexplored. Evidence of DWF is found in Theocharis and Georgopoulos (1993) during winter 1987. The results are presented in Table 1.

Both criteria give convincing estimates of the depth h_c reached by the turbulent convection. The measured and computed values in the case of VMJ criterion coincide within the error ($\sim 20\%$) proposed by the authors. On the other hand, the error

estimated in tank experiments seems too optimistic for real ocean cases: NM values of $\sim 6\%$ should reasonably be increased to 20%. It has however to be stressed that our data cannot represent the "best" data set imaginable. So better results could probably be obtained if, for example, measured values were used instead of time averaged numerical data in the estimate of B . Note how a 20% difference between extrapolated and observed values of B leads to a $\sim 13\%$ error. An additional error (not easily quantifiable) has obviously to be added if we consider that the density profile adopted in our calculations does not always represent the real preconditioned value (immediately before severe storms). These differences finally result in a mild underestimation of the strength of mixing phenomena that accompany DWF, namely of the value h_c discussed in the text. On the other hand if we compare our phenomenological results with those obtained by *Lascarat* (1993), assuming in our estimate only one DWF event for year, we finally find the same order of magnitude even though a ratio of ~ 2 can also be obtained.

Our subsequent attempt, namely the climatological analysis of the sites where DWF processes are known to occur and of their penetration depths, certainly give rather small values of h_c . They consequently have to be considered as a kind of time averaged value, in practice as a lower boundary of the real situation. Also in this case the picture we obtain is of interest; the known sources of Deep and Intermediate waters correspond to our knowledge. Deep waters are indeed formed in the Gulf of Lions for the western Mediterranean basin and in the northern Adriatic sea. The Rhodes gyre, usually depicted as the main source of Intermediate water masses in the Levantine sea, effectively produces water down to a depth of between 400 - 600 m. In the Ligurian sea a particularly dense Intermediate water sinks to $\sim 700\text{m}$ depth. All the other sites (North-Aegean sea, Cretan sea, South Adriatic sea), where there is not observational evidence of DWF, seem to be characterized by mixing processes that reach only the layers between 200-600 m depth. In conclusion, even if we cannot exclude isolated deep events, it can be observed that on a climatological basis the main contribution of these sources in the production of dense marine waters involves only intermediate layers.

REFERENCES

1. Coates M.J., Ivey G.N., Taylor J.R., 1995, *Unsteady, turbulent convection into a rotating linearly, stratified fluid: modeling deep ocean convection*. J.Phys.Oceanogr., 25, 3022-3050.
2. Crepon M., Boukthir M., Barnier B. and Aikman F., 1989, *Horizontal Ocean circulation forced by deep water formation. Part I. An analytical study*. J. Physical Ocean. 19, 1781-1793.
3. Gascard J.C., 1973, *Vertical motions in a region of deep water formation*. Deep-Sea Res., 20, 1011-1027.
4. Gascard J. C. , 1978, *Mediterranean deep water formation, baroclinic instability and oceanic eddies*. Oceanol. Acta, 1(3), 315-330.

5. Green J.S.A., 1970, *Transfer properties of the large-scale eddies and the general circulation of the atmosphere*. Quart. J.Roy. Meteor. Soc., 96, 157-185.
6. Jones H. and Marshall J., 1993, *Convection with rotation in a neutral Ocean: A study of open ocean deep convection*. J. Phys. Ocean 23, 1009-1039.
7. Killworth P.D., 1976, "The mixing and spreading phases of MEDOC I." Progress in Oceanography vol.7, 59 - 90.
8. Maxworthy T., 1997, *Convection into domains with open boundaries*. Annual Review Fluid Mech., 29.
9. Maxworthy T., Narimousa T., 1994, *Unsteady, turbulent convection in a homogeneous rotating fluid with oceanographic application*. J. Phys. Ocean., 24, 865-887.
10. MEDOC group, 1970, *Observations of formation of deep water in the Mediterranean sea, 1969*. Nature, 227, 1037-1040.
11. Narimousa S., 1997, *Dynamics of mesoscale vortices generated by turbulent convection at large aspect ratios*. J.Geophys. Res., 102 (C3), 5615-5624.
12. Narimousa S., Maxworthy T., 1996, *The interaction of unsteady, rotating convection with a density interface*. Ocean Modelling, 103 (unpublished manuscript).
13. Schott F., Leaman K.D., 1991, *Observation with moored acoustic Doppler current profiles in the convection regime in the Golfe du Lion*. J. Phys. Ocean., 21, 558-574.
14. Stone P., 1972, *A simplified radiative-dynamical model for the static stability of rotating atmospheres*. J.Atmos. Sci., 29, 405-418.
15. Visbeck M., Marshall J., Jones H., 1996, *Dynamics of isolated convective regions in the ocean*. J.Phys. Ocean, 26, 1721-1734.
16. Gertman I.F., Ovchinnikov I.M., Popov Yu. I., 1990, *Deep convection in the Levantine sea* Rapp. Comm. Mer Medit. (C.I.E.S.M.), 32, 1, 172.
17. Gertman I.F., Ovchinnikov I.M., Popov Yu. I., 1994, *Deep convection in the eastern basin of the Mediterranean Sea*. Oceanology, 34, 1, 19-25.
18. Lascaratos A., 1993, "Estimation of deep and intermediate water mass formation rates in Mediterranean sea". Deep-Sea Research, Vol., 40, 1327-1332.
19. Schott F., Visbek M., Send U., Fisher J., Stramma L., Desaubies Y., 1996, *Observations of deep convection in the Gulf of Lions, Northern Mediterranean, during the winter 1991/92*. Jour. Phys. Ocean., 26, 505-524.
20. Sparnocchia S., Picco P., Manzella G., Ribotti A., Copello B., Brasey C., 1995, *Intermediate water formation in the Ligurian sea*. Oceanologica Acta, 18, 151-162.
21. Sur H.I., Orzsoy E., Unluata U., 1992, *Simultaneous deep and intermediate depth convection in the Northern Levantine sea, winter 1992*. Oceanologica Acta 16, 33-43.
22. Theocharis A. and Georgopoulos D., 1993, *Dense water formation over the Samoraki and Linnos Plateaux in the North Aegean Sea (Eastern Mediterranean Sea)*. Continental Shelf Research, 13, 8-9, 919-939.
23. Tzipermann E., 1986, *On the role of interior mixing and air-sea fluxes in determining the stratification and circulation of the oceans*. J.Phys. Ocean, 16, 680-693.

Tab. I
Synthesis of DWF data from field observations

Region	Period	$R(Km)$	$B(m^2s^{-3})$	$g \frac{\Delta \rho}{\rho} (ms^{-2})$	$h_{ez}(m)$	$h_{NM}(m)$	$h_{VMJ}(m)$	$\pi R^2 h_{ez} / 3 \times 10^7 s$
MEDOC	March 1987	70	4.3×10^{-7}	6×10^{-5}	2000	2100	2300	0.97
MEDOC	Feb. 1992	60	2.5×10^{-7}	6×10^{-5}	1500	1300	1500	0.54
Ligurian	Feb. 1969	30	4×10^{-7}	6×10^{-5}	1200	1100	1300	0.11
Ligurian	Feb. 1991	40	5×10^{-7}	7×10^{-5}	800	900	1000	0.13
Rhodes	March 1987	60	3×10^{-7}	10^{-4}	1000	800	900	0.36
Rhodes	Feb. 1990	80	2×10^{-7}	10^{-4}	1000	900	1000	0.64
Rhodes	March 1992	90	3.5×10^{-7}	10^{-4}	1200	1000	1100	0.97
South Adriatic	Feb. 1996	15	2.6×10^{-7}	8×10^{-5}	600	600	700	0.02
North Aegean	Feb. 1987	40	3.5×10^{-7}	10^{-4}	600	700	800	0.10

The first columns show quantities as described in the text. The last column gives volumes of marine water involved in one event of DWF, expressed as one year long flow in Sv.

Tab. II
climatological values

Region	$R (Km)$	$B(m^2s^{-3})$	$g \frac{\Delta \rho}{\rho} (ms^{-2})$	$h_{VMJ}(m)$	$h_{NM}(m)$	$\pi R^2 h_{VMJ} / 3 \times 10^7 s$
MEDOC area	40	$2 - 4 \times 10^{-7}$	$7 - 11 \times 10^{-5}$	1000 - 1200	900 - 1100	0.19
Ligurian	30	$2 - 3 \times 10^{-7}$	10^{-4}	500 - 700	450 - 600	0.06
Rhodes	50	$1.5 - 3.5 \times 10^{-7}$	1.2×10^{-4}	500 - 600	400 - 500	0.15
North Aegean	40	$2 - 4 \times 10^{-7}$	2×10^{-4}	500 - 600	400 - 500	0.10
Southern Aegean	30	$2 - 4 \times 10^{-7}$	1.2×10^{-4}	500 - 600	400 - 500	0.05
North Adriatic	50	2×10^{-7}	2×10^{-4}	> bottom	> bottom	
South Adriatic pit	20	$1.5 - 2.5 \times 10^{-7}$	10^{-4}	450 - 550	350 - 450	0.02
Drin	20 - 200	2×10^{-7}	$1 - 4 \times 10^{-4}$	170 - 700	150 - 700	

Volume of marine water involved in DWF, measured as one year long flow in Sv.

INTERNAL WAVES AND FRONTS IN A STRATIFIED FLUID

Yuli D. Chashechkin

(Laboratory of Fluid Mechanics of the Institute for Problems in Mechanics
of the RAS, 101 prospect Vernadskogo, Moscow, 117526, Russia,
ph: +7-095-434-0192, fax: +7-095-938-2048, E-mail: chakin@ipmnet.ru)

Abstract. The nature of 'fine structure' of the ocean and the atmosphere is subject of detailed theoretical and experimental studies. Data of theory and laboratory investigations of formation of thin elongated interfaces in a flow of a continuously stratified fluid are presented below. Results of Lie groups analysis of general set of equations as well as asymptotic solutions, describing diffusion induced boundary currents of topography, are discussed briefly. Presented data of laboratory investigations of stability and evolution of a 3D and 2D flows in a continuously stratified salt brine, received by conventional, narrow laser beam and 'natural rainbow' Schlieren methods combining with dyeing, density markers, electrolytic precipitation, probes and echo-sounding, show different kind of the fine structure. We study the flows in a wide range of flow parameters, corresponding to laminar, vortex and turbulent regimes. Effects of arising self consistent high gradient interfaces on a double diffusive convection flow, on internal waves and wakes on geometry as well as on the backscattering of the ultrasound are discussed.

Introduction. The paper of H. Stommel and K.N. Fedorov, 1967 [1] and following book of K.N. Fedorov [2] have initiated tremendous flux of papers and books concerning measurements of the fine structure in the real ocean and atmosphere; analytical and numerical studies of the main forming processes and their laboratory modelling. The high gradient interfaces are observed in wide variety of the geophysical situation. They can be intrinsic elements of natural processes (decaying turbulence, double diffusion, vortices and their arrays, wakes, jets and so on) or reveal specific universal process that accompany all mentioned phenomena.

From analysis of transient thermo- and hydrodynamic equations as well as from highly resolved laboratory experiments follow that high gradient interfaces are formed in a continuously stratified fluid due to the separation of a boundary current from a solid surface or even directly in a fluid interior in result of non-linear interaction of more large scale phenomena. In the last case they manifest themselves as a new form of stratified fluid motions, namely as Internal Boundary Currents. The main features of the internal boundary current, namely their universality, anisotropy of sizes, difference of spatial variability scales for different variables one can receive from general analysis of the set of governing equations.

Resume of theory. The most general method of analysis of non-linear systems of differential equations namely Lie groups method was used to investigate 1D, 2D, 3D stratified fluid dynamic equations in [3] and multi-components double diffusive convection equations in [4]. Under the Boussinesq approximation the general system of fluid dynamics equations with arbitrary state equation $\rho = \rho_0 + \rho'(S_i, T)$ has form [5]

$$\begin{aligned} \frac{\partial \mathbf{u}}{\partial t} + (\mathbf{u} \nabla) \mathbf{u} &= -\nabla P + \nu \Delta \mathbf{u} + \rho'(S, T) \mathbf{g}, \\ \frac{\partial S_i}{\partial t} + (\mathbf{u} \nabla) S_i &= k_i \Delta S_i, \quad i = 1 \dots n, \\ \frac{\partial T}{\partial t} + (\mathbf{u} \nabla) T &= k_T \Delta T, \end{aligned} \tag{1}$$

$$\operatorname{div} \mathbf{u} = 0, \quad \rho = \rho_0 + \rho'(S_i, T).$$

Here \mathbf{u} is velocity, P is pressure, \mathbf{g} is gravity acceleration, T is temperature, S_i is i -th component of impurity, ν is kinematic viscosity coefficient, k_i is diffusivity coefficient for given component of impurity, k_T is temperature conductivity coefficient. Stable stratification is characterised by intrinsic length-scale $\Lambda = |\ln \rho / dz|^{-1}$ or buoyancy frequency $N^2 = g/\Lambda$ and buoyancy period $T_b = 2\pi/N$.

Properties of the system (1) depends on state equation and ratios of dissipative coefficients. The most often used linearized state of equation is marked, but not unique in symmetry sense.

It is important to note that properties of the system change with increasing of physical space dimension. In 1D and 2D cases one component problem is characterised by split boundary currents and waves. 3D

problem besides boundary currents and waves are characterised additionally by vortex motion with vertical direction of vorticity.

Moreover, invariant characteristics of stationary and non-stationary problems are different in 1D case [3]. From this it follows that stationary phenomena in 1D approximation are classified as singular phenomena that are not a limiting state of equivalent transient problem. Moreover some transient problems in 1D space, on contrary with 2D and 3D problems, has no stationary limit [6].

This result explains difference of equations solutions for 1D diffusion induced currents on a sloping plane received in stationary approximation [7,8], small-time asymptotic [9,10] and exact solution of transient problem [6].

The main difference between these solutions manifest itself in spatial structure of the flow. Stationary solution describes self-similar motion with the same scale of spatial variability of different parameters

$\delta = \sqrt[4]{\nu k_s / N^2 \sin^2 \alpha}$ (here α is the slope of plane to horizontal). All transient solutions contain

set of scales, that are intrinsic for every variable, namely for velocity $\delta_v = \sqrt{\nu / N}$, temperature

$\delta_T = \sqrt{k_T / N}$, salinity $\delta_s = \sqrt{k_s / N}$, etc.

From these analysis follows that the group properties of the set of equation (1) are defined in general by diffusion that is by the process describing by the smallest transfer coefficient value.

For dissipative media there are three distinguished types of stratification, namely: linear, exponential and quadratic. They are characterised by the most wide groups of symmetry. Ideal fluids are characterised by another Lie groups properties than dissipative one. Due to this solutions of correspondent or equivalent problems can not be transformed from one model of media to another by a simple limiting transfer.

Thus, the diffusion manifests itself both: in existence of an intrinsic boundary current with its own scale of spatial variability and in symmetry properties of governing equations, which reveal themselves in structure of macro scales elements of motion. Omitting the terms with diffusion change dramatically the symmetry properties of system (1).

Main geometric features of a stratified flow one can see on example of the simplest kind of a stratified motion, namely diffusion induced boundary currents on an obstacle at rest.

Diffusion induced currents on topography (cylinder and sphere).

Small-time asymptotic solutions stratified fluid dynamics equations describing formation of diffusion induced boundary current on a submerged sphere or cylinder in a stratified fluid at rest (initial value problems)

$$\begin{aligned} \frac{\partial \mathbf{U}}{\partial t} + (\mathbf{U} \nabla) \mathbf{U} &= -\frac{1}{\rho_0} \nabla P + \nu \Delta \mathbf{U} - g S \mathbf{e}_z, \\ \frac{\partial S}{\partial t} + (\mathbf{U} \nabla) S &= k_s \Delta S + U_z / \Lambda, \end{aligned} \quad (2)$$

$$\text{div} \mathbf{U} = 0, \quad \rho = \rho_0 (1 - z / \Lambda + S),$$

where ρ_0 is reference density, salt contraction coefficient is included into salinity,

with boundary conditions

$$\left. \frac{\partial S}{\partial r} \right|_{r=R} = \gamma f(\varphi), \quad \mathbf{U}|_{r=R} = 0 \quad \text{when } t > 0, \quad (3)$$

can be written in form [3,11] for variation of salinity

$$S = -\frac{2}{\Lambda} \sqrt{k_s t} \left(\frac{R}{r} \right)^n i \operatorname{erfc} \left(\frac{r-R}{2\sqrt{k_s t}} \right) \sin \varphi, \quad (4)$$

tangential component of induced velocity

$$\mathbf{U} = \frac{N^2 (4k_s t)^{3/2}}{2 \nu - k_s} \left(\frac{R}{r} \right)^n \left[i^3 \operatorname{erfc} \left(\frac{r-R}{2\sqrt{\nu t}} \right) - i^3 \operatorname{erfc} \left(\frac{r-R}{2\sqrt{k_s t}} \right) \right] \sin 2\varphi \quad (5)$$

and radial components of velocity of the fluid

$$V = N^2 \frac{(4k_s t)^2}{v - k_s} \left\{ \frac{1}{r} \left(\frac{R}{r} \right)^n \left[\sqrt{\frac{v}{k_s}} i^4 \operatorname{erfc} \left(\frac{r-R}{2\sqrt{vt}} \right) - i^4 \operatorname{erfc} \left(\frac{r-R}{2\sqrt{k_s t}} \right) \right] - \alpha \left(\frac{R}{r} \right)^{2(n+1)} \right\} F(\varphi).$$

Here φ is angle to horizontal and $n = 1/2$, $F(\varphi) = \cos 2\varphi$ for cylinder and $n = 1$, $F(\varphi) = 1 - 3\cos 2\varphi$ for sphere.

The flow consists of four vortices (one in each quadrant). Since the motion is symmetrical with respect horizontal and vertical centre plane, only the first quadrant is shown. Fluid flows to the body around horizontal central plane and away from the body near poles. The radial and tangential velocity components differ almost by an order of magnitude. The thickness of the current is prescribed by kinematic viscosity coefficient. The more pronounced tangential velocity survives when cylinder radius is going to infinity. Radial component which shows a power decrease instead of exponential one with distance and become relatively more pronounced far from the body.

Like a plane case, the thickness' of the velocity and density boundary currents are growing monotonously with time. The ratio of square of length scales remains constant with time and defined by the

$$\text{Prandtl or Schmidt number } \left(l_v / l_s \right)^2 = \text{Pr} = v / k_\tau \text{ or } \text{Sc} = v / k_s.$$

The typical patterns of disturbances in salinity and velocity fields are shown in Fig 1a, b.

In this figures one can see two sets of interfaces contacted with cylinder near its poles. Salinity perturbations are concentrated in a thin layer adjoining to the body. A maximum of salinity perturbations falls in the polar areas over and beneath the cylinder where isohalines are maximally displaced toward the body in consequence of interruption of the molecular flux existing in a free stratified medium. Outer disturbances in the every quadrant consist of three adjoining bands. The central band is formed by disturbances with positive sign, upper and lower bands contain the negative ones. The internal structure of thin layer near the body can not be resolved in this scale.

The calculated and observed patterns of flow are similar to each other. In the both cases the pattern of flow consists of four vortices (one in each quadrant). Since the motion is symmetrical with respect horizontal and vertical centre plane, only the first quadrant is shown. Fluid flows to the body around horizontal central plane. The current separates on the equator and moves along a body surface to the convergence points, namely to the upper and lower poles. Past the poles diverging flow separates from the body. The radial and tangential velocity components differ almost on the order of magnitude.

The similar features has diffusion induced flow near a sphere, but the velocity is more weak due to the geometry of the problem. Thus the asymptotic solutions of all transient problems: 1D (sloping plane [9, 10]), 2D (cylinder [3, 11]) and 3D (sphere [3]) describe the similar flows that are characterised by different scales of spatial variability for velocity, density, vorticity, pressure and so on. In the limiting cases the asymptotic solutions uniformly transform from 3D to 2D and to 1D, consequently. This result is in good agreement with well known exact solutions of the 1D transient problem [6] and do not compatible with 1D stationary solutions [7, 8].

When a body begin to move, the diffusion induced boundary current separates from a surface and forms a high gradient envelop of a density wake in all flow regimes, namely laminar, transient and turbulent.

Length-scales of a flow past an obstacle.

The governing equations (2) and boundary conditions (3), describing stratified flow around a moving body contain different dimensional parameters (density and its gradient, velocity U and size of an obstacle, gravity acceleration, viscosity and salt diffusivity coefficients). They are characterised by different dimensions. Conditions of geometric, kinematic and dynamic similarity become equivalent if all basic variables are reduced to the same dimension. The length scales being the most universal parameters is taken usually as the basic variable.

This problem is characterised by two external (geometric) and several intrinsic (dynamic and dissipative) length scales. The geometric parameters are the buoyancy scale Λ and the body size D . The intrinsic scales are the length of attached (lee) internal waves $\lambda = UT_b$, the thickness of velocity boundary current $\delta_u = v / U$ and density boundary current $\delta_\rho = k_s / U$. These five length scales along with co-ordinate scales constitute the complete set of basic parameters.

Another set of length scales can be formed on basis of dissipative scales for velocity $\delta_v = \sqrt{v / N}$ and density $\delta_k = \sqrt{k_s / N}$. These scales arise when the expressions like (4, 5) are reduced to a non-dimension form and characterise the diffusion induced currents, too.

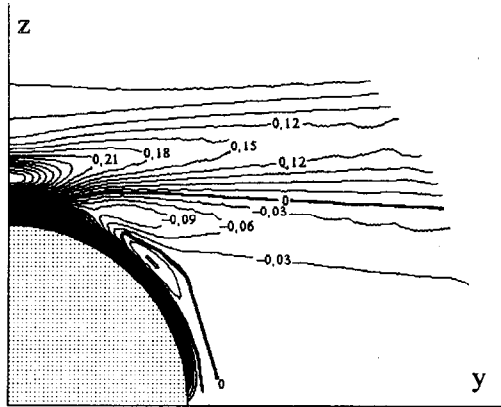


Fig. 1.a. Isohalines of salinity disturbances for horizontal cylinder at rest $R = 201$, $l = \sqrt[4]{k_s \nu / N^2}$ (numerical solution of (1)).

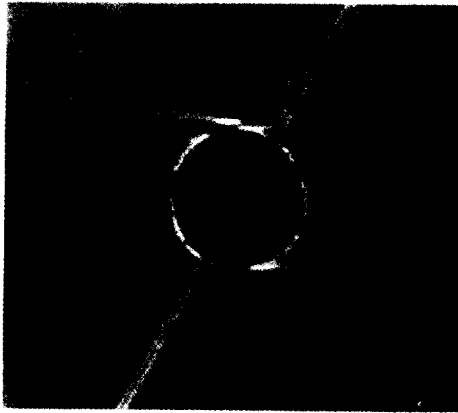


Fig. 1.b. Schlieren pattern of the diffusion induced current around submerged horizontal cylinder at rest. Exposition time of the body at rest in the stratified solution is 2 days.

From these basic scales the countable number of derivative scales can be formed. Part of them describes the sizes and thickness' of transfer zones of secondary elements of flow (shear layer, vortices, sharp interfaces and so on). The distinguished ones among these scales are the viscous wave scale $L_v = \sqrt[3]{\Lambda \lambda \delta_u} = \sqrt[3]{g \nu} / N$ which characterises the modal structure of periodic internal wave beam [12], the limiting vortex scale $L_v = \sqrt[3]{\lambda^2 \delta_u^2 / \Lambda} = \sqrt[3]{\nu^2 / g}$, combined Prandtl scale $L_\delta = \sqrt{\delta_v \delta_k} = \sqrt[4]{\nu k_s / N^2}$ and so on.

From this point of view the conventional dimensionless parameters mean not only the ratio of appropriate forces but the ratio of the basic scales too: Reynolds number is $Re = UD / \nu = D / \delta_u$, Froude number $Fr = U / ND = \lambda / D$, Péclet number $Pe = UD / k_s = D / \delta_p$. Additional dimensionless number $C = \Lambda / D$ is the ratio of external geometrical scales. The number define the transformation of density gradient for a given coefficient of length scale reduction in the laboratory modelling of environmental flows. For weak stratified and slightly viscous fluid the values of a basic scales are different ($\Lambda \gg \lambda \gg \delta_u \gg \delta_p$; ratio D / λ can be of any value) and form a set of imbedded gauges. The equality of combination scale of different nature means spatial synchronism and possible strong interaction of different forms of motion (for example internal waves and free vortices). The basic scales manifest themselves in all kind of a stratified flow. The most impressive phenomena one can observe in a flow around uniformly towing horizontal cylinder.

Experimental study of stratified wake past circular cylinder

Experimental studies of a stratified flow past a towing cylinder show that besides upstream and downstream wakes, internal waves, imbedded and soaring vortices [13] the split internal boundary currents exist. They are presented as high gradient interfaces on the outer boundary of the density wake and contact with internal boundary current on the body surface at the points of separations. They are clear visible in the Schlieren picture of a laminar flow past a cylinder presented in Fig. 2

Distortion of a density marker past a body visualises the profile of velocity. The thickness of shear layer on the wake boundary in several times large than the thickness of interfaces. Transient internal waves

ahead of the body are more pronounced than lee (adjoin) waves past it. Parameters of high gradient interfaces in a wake past a cylinder are studied in [14].

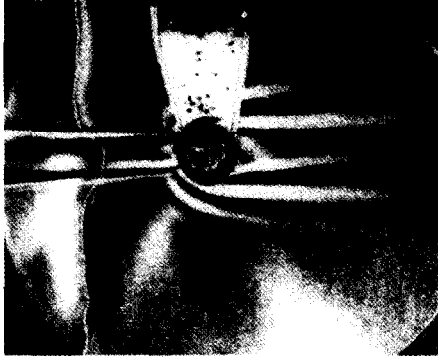


Fig. 2. Laminar stratified flow around a cylinder, moving uniformly from left to right. $D = 2,5$ cm; $U = 0,067$ cm/s; $T_b = 6,9$ s; $Fr = 0,03$; $Re = 16,5$.

With increasing the Reynolds number the density boundary current lost its stability and small scale irregularities are observed in the wake past the cylinder presented in Fig. 3. Profile of velocity here is so smooth as in Fig. 2, flow is laminar. The complicated relief is created in vicinity of points of separation of the density boundary currents and transports by the mean flow. The contrast of interfaces slowly falls due to the diffusion smoothing.



Fig. 3. Pattern of laminar flow around horizontal cylinder with intensive fine structure. ($D = 5$ cm, $T_b = 7,6$ c; $U = 0,133$ cm/s; $C = 287$; $Re = 67$; $Fr = 0,033$).

In addition to the high gradient interfaces inside the density wake, isolated interfaces are formed past a cylinder in the region of adjoin internal waves. They formed directly in the fluid interior outside the density wake and do not contain any features (vortices or other singularities) on their leading and trail edges. The interfaces are separated from the wake by water strips without any small scale irregularities.

Schlieren pictures of this kind of flow past the cylinder produced by “slit-knife” and “slit-thread” methods are presented in Fig. 4 a, b. The “slit-thread” method shows only loci of crests and troughs of internal waves and is more suitable for observations of a fine structure. In this pictures both sets of interfaces inside and outside the density wake are presented.

With increasing of internal Froude number the length of these interfaces and jump of density are increased (see Fig. 5). Their thickness is less than 0.5 mm and length depending on Froude and Reynolds numbers is changed from a several units to several tens centimetres. They are located inside more thick shear velocity layers containing both pure shear and wave components. In general, the geometrical properties of isolated interfaces look like the diffusion induced boundary current near a body at rest.

These soaring and embedded interfaces are observed in a wide range of parameters corresponding to laminar and transient density wakes. These interfaces are located inside or on external envelope of a density wake, they form a shell of arbitrary oriented vortices and soaring surfaces inside adjoined internal waves field. Soaring interfaces are treated as internal boundary currents in a fluid interior. They are formed by separating of density boundary current and due to non-linear interaction of more large scale elements of motion. The thickness of these interfaces depends weakly on the parameters of flow on their leading edges. Typical kind of flow with soaring vortices of the leading edge of isolated interfaces is shown in Fig. 7.

Decay of vertical motion is followed by sharpening of fine structure which is mostly expressed on the upper and lower boundaries and forms the external envelopes of the wake past the cylinder. This effect may be caused by internal waves penetrating inside the wake and sharpening the existing interfaces through formation of the internal boundary currents.



Fig. 4 a, b Pattern of flow past a horizontal cylinder moving from right to left with soaring interfaces. $U = 0,04$ cm/s; $D = 7,6$ cm; $T_b = 20,5$ s; $Fr = 0,017$; $Re = 30$; $C = 1370$.



Fig. 5. Pattern of flow around horizontal cylinder moving from left to right with long soaring interfaces. Density wake is split on separated interfaces ($D = 2.5$ cm, $T_b = 7.6$ s $U = 0.29$ cm/s; $Re = 74$ $Fr = 0,28$).



Fig. 6. Soaring vortices on the leading edges of isolated interfaces inside adjoin internal waves past a horizontal cylinder. Rear vortices are distorted by internal waves. $T_b = 20.5$ s, $D = 5$ cm, $U = 0.17$ cm/s, $Fr = 0.11$; $Re = 84$.

The sharpening of local gradients manifests in fields of all physical variables: gradient of refractive index, coefficient of backscattering and electric conductivity. The interfaces also affect on stability of flows, heat and substances transport. These interfaces act as sharp boundaries preventing the transport of contaminants into some areas of flow. The example is shown in Fig. 7, 8.

The central part of the density wake bounded by interfaces shown in Fig. 7 is clear from dye (see Fig. 8). In spite of difference in Reynolds numbers value the patterns of flow in Fig. 7, 8 have similar structure. These photos prove that the large scale structure of the flow is determined by the internal waves (and depend on internal Froude number value mainly) and thickness of the boundaries is prescribed by the scale formed with the smallest transfer coefficient.

On account of direct interaction between the thin internal boundary currents and more large scale internal waves a contrast of interfaces can intensify while turbulence decay and vertical motion becomes more and more weak, as it was measured by optic and acoustic methods [15].



Fig. 7. Schlieren image of stratified flow around the cylinder moving from left to right. $D = 7.6$ cm; $T_b = 12,5$ s; $U = 0.31$ cm/s; $Fr = 0,08$; $Re = 234$.

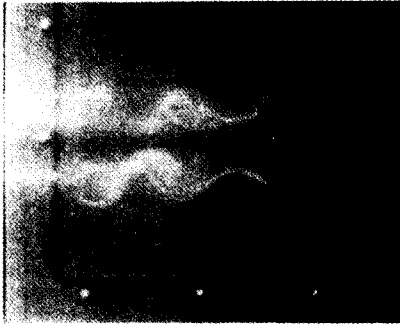


Fig. 8. Dyeing of the flow past the cylinder. The dye are introduced ahead of the cylinder. The central part of the downstream wake is clear. $D = 7,6$ cm; $T_b = 7,15$ s; $U = 0,69$ cm/s; $Fr = 0,1$; $Re = 524$.



Fig. 9. Turbulent wake past the cylinder. $D = 2,5$ cm; $U = 4,34$ cm/s; $T_b = 7,4$ s; $Fr = 2,02$; $Re = 1085$.

Pattern of the turbulent flow past the cylinder, bounded by interfaces and contain inside a lot of thin high gradient structures, is shown in Fig. 9. Curved lines are crests and troughs of the adjoin internal waves and more short waves produced by embedded vortices.

Length-scales of internal waves. By taking into account the internal boundary current one can solve a wide range of internal wave problems (generation [16], propagation and reflection off a solid surface [17]) as a self consistent well posed boundary value problem. We study generation of internal waves by a strip oscillating with constant amplitude and frequency along its plane inclined under the angle φ to horizontal. In 2D case we retain only the x - and z - components of all entities in (1) and receive the next equation for the stream function Ψ

$$\left(\omega^2 \Delta - i \nu \omega \Delta^2 - N^2 \partial_x^2\right) \Psi = 0, \quad \Delta = \partial_x^2 + \partial_z^2. \quad (6)$$

It is convenient to introduce the co-ordinate system (ξ, ζ) where the ξ -axis lies in the plane, and ζ -axis is normal to ξ . The boundary conditions are

$$\left. \frac{\partial \Psi}{\partial \zeta} \right|_{\zeta=\pm 0} = U(\xi), \quad \left. \frac{\partial \Psi}{\partial \xi} \right|_{\zeta=\pm 0} = 0, \quad \left. \frac{\partial \Psi}{\partial \xi}, \frac{\partial \Psi}{\partial \zeta} \right|_{\zeta=\pm \infty} = 0. \quad (7)$$

The general solution (6) consists of two groups of terms corresponding to the two internal wave beams on every side of the plane (in the upper/lower or in left/right half-spaces depending on the relation between angles of plane inclination φ and direction of wave propagation θ)

$$\Psi_w^\pm = \mp(1 + i\mu) \sqrt{\frac{\nu \sin \theta}{2N} \left| \frac{\sin(\theta \mp \varphi)}{\sin(\theta \pm \varphi)} \right|} \int_0^\infty V_0(\pm k \sin(\theta \mp \varphi)) \exp \left[ikp_\pm - \frac{\nu k^3 q_\pm}{2N \cos \theta} \right] dk,$$

where $V_0(k)$ is Fourier transformation of the $U(\xi)$, and the internal boundary currents on the emitting plane with the characteristic scale of their spatial variability $\sqrt{2\nu \sin \theta / N |\sin^2 \theta - \sin^2 \varphi|}$

$$\Psi_b = -(1 + i\mu) \sqrt{\frac{\nu \sin \theta}{2N |\sin^2 \theta - \sin^2 \varphi|}} U(\xi) \exp \left(-i \frac{\mu \zeta}{\lambda_b} \right) \exp \left(-\frac{\zeta}{\lambda_b} \right). \quad (8)$$

Here p_\pm, q_\pm are transversals and longitudinal intrinsic co-ordinate system of these beams. A fluid motion in the spatially oscillating boundary current decays exponentially along the transverse co-ordinate ζ , and reproduces the boundary velocity profile $U(\xi)$ in the longitudinal direction, $\lambda = \text{sign}(k)$, $\mu = \text{sign}(\sin^2 \theta - \sin^2 \varphi)$, and $\theta = \arcsin(\omega/N)$ is the inclination of the internal waves beam to the horizontal.

In the linear approximation the internal waves and the boundary currents do not interact with each other and the principle of superposition is fulfilled. In the asymptotic limit it is assumed that the wave beams are quite well separated.

The spectral velocity function of the plate oscillating with small-amplitude b is $V_0(k) = (U/\pi k) \sin(ka/2)$, where $U = -i\omega b$, gives

$$\eta = -(1 + i\mu) \frac{\alpha b \sin \theta}{6\pi} \sqrt{\frac{\nu \sin \theta}{2N} \left| \frac{\sin(\theta - \varphi)}{\sin(\theta + \varphi)} \right|} \left\{ F \left(p + \frac{a^*}{2}, q \right) - F \left(p - \frac{a^*}{2}, q \right) \right\} \quad (9)$$

Here $\alpha = \sqrt[3]{2N \cos \theta / \nu q}$, $a^* = a \cdot \sin(\theta - \varphi)$ is the projection of plate's width on the beam propagation direction; and

$$F(p, q) = \int_0^\infty y^{-2/3} e^{-y} \exp(i\alpha p y^{1/3}) dy = \sum_{m=0}^\infty \frac{(i\alpha p)^m}{m!} \Gamma \left(\frac{m+1}{3} \right).$$

The envelope of fluid particle displacements in the beam is described by the function $\Phi(p, q) = |F(p + a^*/2, q) - F(p - a^*/2, q)|$. The function Φ exhibits two modal forms: bi-modal with maxima at the edges of the beam and uni-modal with central maximum. Solution (9) is a regular function of all physical parameters of the problem.

In the limiting case $\nu \rightarrow 0$ the solutions for the waves and boundary currents uniformly go to zero. Expression (9) has a regular limit to zero as $\omega \rightarrow 0$, or $\omega \rightarrow N$ (in absence of any wavelike disturbance). In the far-field region the bi-modal beam transformed to the uni-modal one. The transition from the bi-modal to the uni-modal structure takes place at a distance L . From detailed analysis [16] follows that there are two critical lengths

$$L_1 \approx \frac{a^3 N \cos \theta \sin^3(\theta - \varphi)}{100\nu}, \quad L_2 \approx \frac{a^3 N \cos \theta \sin^3(\theta - \varphi)}{2000\nu},$$

meaning that the beam, which is bi-modal for $L < L_2$ becomes uni-modal when $L > L_1$.

The solution (9) tends uniformly to the well known classical solution of Stokes for the homogeneous fluid [5] as $N \rightarrow 0$

$$V_\xi = U \exp \left(-\sqrt{\frac{\omega}{2\nu}} \zeta \right) \cdot \exp \left[i \left(\sqrt{\frac{\omega}{2\nu}} \zeta - \omega t \right) \right], \quad V_\zeta = 0.$$

The theory is based on the assumption $\Lambda \gg a \gg \sqrt{\nu/N}$. For typical values of buoyancy frequency $N = O(1 \text{ s}^{-1})$ and viscous wave scale $L_\nu = O(1 \text{ cm})$ the modality change is observed in the area of $20 \times 20 \text{ cm}^2$ for plates of 1–2 cm width. For the observation of internal boundary currents the spatial resolution must be higher than 1 mm.

Schlieren images of periodic internal waves, generated plates of different width shown in Fig. 10 a, b are in good agreement with theory. Wave motions are concentrated in the narrow beams emitted from source edges.

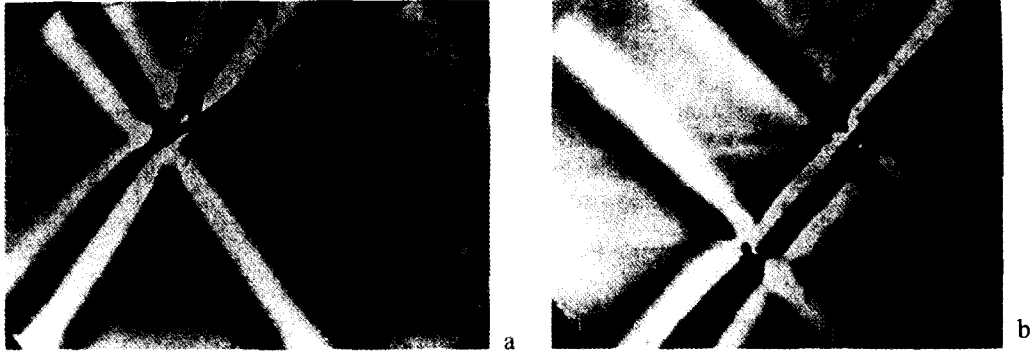


FIG.10 . Schlieren image of periodic internal waves generated by oscillating strip, $A_0 = 0.15\text{cm}$,
 a: $N = 1.14 \text{ rad/s}$, $a = 1 \text{ cm}$, $\varphi = 33^\circ$, $\omega = 1.01 \text{ rad/s}$, $\theta = 63^\circ$; b: $N = 0.84 \text{ rad/s}$,
 $a = 6 \text{ cm}$, $\varphi = 50^\circ$, $\omega = 0.64 \text{ rad/s}$, $\theta = 50^\circ$.).

Boundaries between black and white bands inside the beam show the shape of the wave crests and troughs. In the wave field produced by the generator with sharp edges there are no visible mixing effects at small-amplitude oscillations ($A_0 / a \leq 0.15$). The boundary currents on the surface of the plates can not be visualised by Schlieren techniques. But there is indirect evidence of their existence due to the thin horizontal interfaces clearly visible on the photographs. They are caused by the separation of the internal boundary currents from the plate.

The interfaces originate on the plate's edges and extend far beyond the observation field. These currents are characterised by their different scales in the velocity and density spatial variability [6, 10].

Fine structure of side-wall double diffusive convection.

Formation of regular step-like structure under side heating of a continuously stratified liquid was studied in close details for large values of density gradient [18]. The flow consists of thin arising current near a wall, a sequence of cells bounded by high gradient interface, moving heat front and zero frequency internal waves, propagating in an ambient fluid. The cells look like a system of deformed vortex [19] with permanent direction of vorticity. The vertical size of cells depend on the adiabatic height $h = k\alpha\Delta T\Lambda$ (here α – thermal expansion coefficient, ΔT – wall overheating, empirical coefficient $k = 0.4 \div 1$), the scale of interfaces thickness is an order of $\delta_v = \sqrt{\nu / N}$.

In side wall convection interfaces can originate from the boundary current near heated wall and can be formed in a fluid interior on the upper edge of cold entertainment fluid. In the last case the number of interfaces is twice as great as the number of the cells. Typical Schlieren image of the flow is shown in Fig. 11b. The thickness of boundaries between the cells and thickness of additional interfaces that does not contact any solid surfaces equals the thickness of the diffusion induced boundary current on a motionless body or to the thickness of soaring and embedded into the wake interfaces past a horizontally towing cylinder.

Typical pattern of flow above the point heat source (Fig 12) demonstrates the main features of the double diffusive convective motion namely arising plume, convective cells with high gradient interfaces and zero frequency internal waves emitting by the outer boundary of cells. Small scale structures (threads or fingers) slowly move along the upper boundary of convective cells.

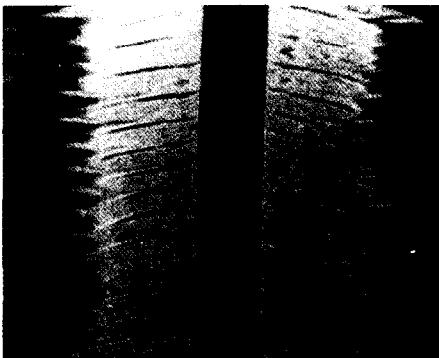


Fig. 11 a. Schlieren image pattern of flow near a vertical heater in a continuously stratified salt solution (weak gradient).

$T_b = 20.2 \text{ s}$; $\Delta T = 1.25^\circ\text{C}$; $t = 15 \text{ min}$;
 Width of the heater $d = 1.5 \text{ cm}$; average height of cells $h = 1,3 \text{ cm}$; adiabatic coefficient $k = h/\alpha\Delta T\Lambda = 0.3$.

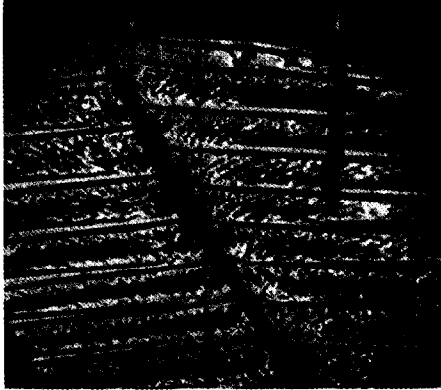


Fig. 11 b. Doubling of interfaces in the side double diffusion convection ($T_b = 9,1$ c, $\Delta T = 6,5^\circ$, $\alpha = 30^\circ$, $t = 30$ min).

All features of the flow are conserved with decreasing of density gradient. Pattern of this flow is shown in Fig. 11 a. Interfaces do not touch the heater and break near the heat front where they are broken by incoming cold water.

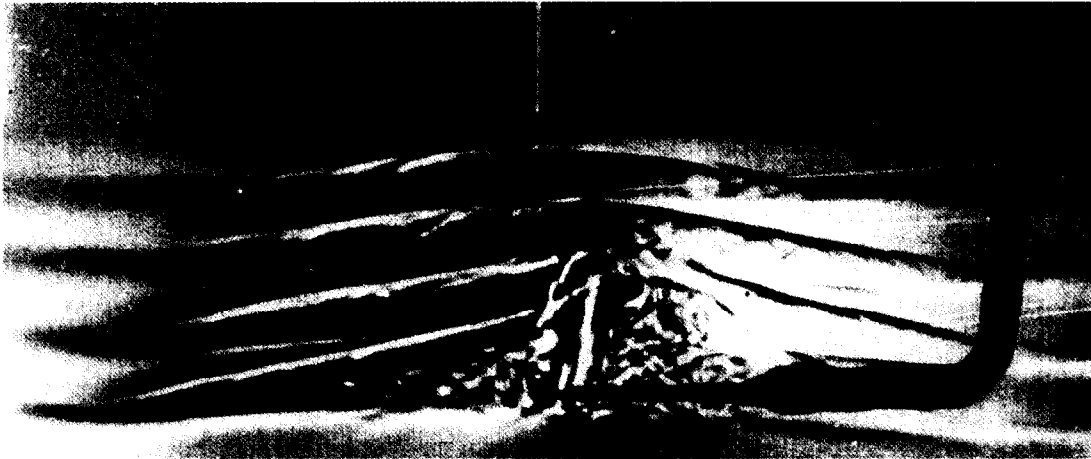


Fig. 12. Pattern of convective motion above the point heat source (tip of conductivity probe) in a continuously stratified common salt brine ($\Lambda = 4.4$ m, $T_b = 4.2$ s, $P = 3,2$ W, $t = 40$ min).

Observations of the flow structure transformation show that thin high gradient interfaces and threads can be formed directly in a fluid interior in consequence of the sharpening of initially smooth disturbances (as shown in Fig 1 b), in result of split of interfaces (as it is happens inside a cell) or in account of separation of the boundary current from a solid surface (arising plume). Longitudinal thin irregularities (interfaces) propagating from a source without a mixing or overturning represent specific kind of a fluid motions and will be named by internal boundary current.

Conclusions.

The theoretical and laboratory investigations show that the thin sharp interfaces are one of the main features of a flow continuously stratified fluids. These thin layers with different scales of spatial variability for velocity, density and concentration of components which are formed near a solid boundary and directly in a fluid interior with and without any mixing and turbulence. These interfaces really represent active form of motions, namely the *internal boundary currents*. Their transverse length scales are the same as those in the diffusion induced boundary currents on a body at rest in a continuously stratified fluid. Their lengths depend on geometry and duration of a process.

Taking into account the internal boundary currents, one can solve the periodic internal wave generation problem as self-consistent closed boundary value problem. Geometry and energetics of the wave beam, which is in agreement with experimental data, are obtained without employing additional hypotheses.

The fine structure of convective cells flow near a heated sloping plane in a stably stratified brine shows the possibility of doubling of interfaces number in consequence of formation sharp boundary (the internal boundary current) on upper edge of cold entertainment fluid wedge.

Visualisation of a 2D stratified flow near a perfect body demonstrates that besides the upstream and downstream wakes with embedded or soaring vortices, internal waves, split internal boundary currents on the cylinder surface, *internal boundary currents* (soaring discontinuities) are formed inside lee (attached) internal waves in a wide range of flow parameters. To this end improved models of flow instability and turbulence, including effects of viscosity, temperature and mass transfer are needed. Some of the presented results can be directly extrapolated on natural conditions, including theory of internal waves and geometry of a downstream wakes. Fore quantitative comparisons data of most fine resolve measurements must be used.

Acknowledgements

This study was supported by Russian Foundation for Basic Research (96-05-64004) and Ministry of Science and Technology of the Russian Federation (National Programme for studies of the Ocean, Arctic and Antarctic).

List of References

1. Stommel H., Fedorov K.N., Small-scale structure in temperature and salinity near Timor and Mindanao, *Tellus*, 1967, 19(2), 306-325.
2. Федоров К.Н., Тонкая термохалинная структура вод океана, Гидрометеиздат, Л-д, 1976, 184 (English edition: Federov K.N., *The Thermohaline Fine Structure of the Ocean*, Pergamon, Oxford, 1978, 170).
3. Baydulov V.G., Chashechkin Yu.D., General properties of free and boundary currents in a continuously stratified liquid, Preprint IPM RAS., 1997, No. 596, 71. (In Russian),
4. Kistovich A.V., Chashechkin Yu.D., Group analysis of the partially symmetrized form of the system of equation of free thermoconcentrational convection, *J. of Applied Mechanics and Technical Physics*, 1996, 37(2), 159-169.
5. Batchelor G.K., *An introduction to fluid dynamics*, CUP, 1970, 700.
6. Kistovich A.V., Chashechkin Yu.D., The structure of transient boundary flow along an inclined plane in a continuously stratified medium, *J. Appl. Maths. Mechs.*, 1993, 57(4), 633-639.
7. Phillips O.M., On flows induced by diffusion in a stably stratified fluid, *Deep-Sea Res.*, 1970, 17, 435-443.
8. Wunsch C., On oceanic boundary mixing, *Deep-Sea Res.* 1970,17, 293-301.
9. Linden P.F., Weber J.E., The formation of layers in a double diffusive system with sloping boundary, *J. Fluid Mech.*, 1977, 81(4), 757-773.
10. Baydulov V.G., Chashechkin Yu.D., The diffusion effect on the boundary flow in a continuously stratified fluid, *Izvestiya, Atmospheric and Oceanic Physics*, 1994, 29(5), 642-647.
11. Baydulov V.G., Chashechkin Yu.D., A boundary current induced by diffusion near a motionless horizontal cylinder in a continuously stratified fluid, *Izvestiya. Atmospheric and Oceanic Physics*, 1996, 32(6), 751-756.
12. Makarov S.A., Neklyudov V.I., Chashechkin Yu.D., Spatial structure of two-dimensional Monochromatic Internal-Wave Beams in an Exponentially Stratified Liquid, *Izvestiya AS, Atmospheric and Oceanic Physics*, 1990, 26(7), 548-554.
13. Chashechkin Yu.D., Voeykov I.V., 1994 Vortex systems past a cylinder in a continuously stratified fluid, *Izvestia RAS. Atm. and Oceanic. Phys.*, 29(6), 787-795.
14. Voeykov I.V., Chashechkin Yu.D, Formation of discontinuities in the wake of a cylinder in a stratified flow, *Fluid Dynamics*, 1994, 28(1), 14-18.
15. Prokhorov V.E., Chashechkin Yu.D., Backscattering of ultrasonics from flow past a cylinder in a continuously stratified fluid, *Izvestiya AS. Atmospheric and Oceanic Physics*, 1995, 30(6), 734-741.
16. Chashechkin Yu.D., Kistovich Yu.V., Generation of monochromatic internal wave problem: exact solution and model of force sources, *Doklady Akad. Sci. Russ.*, 1997, 355(1), 54-57.
17. Kistovich Yu.V., Chashechkin Yu.D., The reflection of beams of internal gravity waves at a flat rigid surface, *J. of Applied Mathematics and Mechanics*, 1996, 59(4), 579-585.
18. Levitskii V.V., Chashechkin Yu.D., Thermoconcentration convection under uniform lateral heating, *Fluid Dynamics*, 1995, 30(5), 734-744.
19. Belyaev V.S., Savinkov A.M., Chashechkin Yu. D., Dynamics of laminar vortex rings in a stratified liquid, *J. of Applied Mechanics and Technical Physics*, 1987, 28(1),. 34-43.

THE FIELD STUDY OF THE FRONTAL AREA BETWEEN THE COASTAL ZONE AND THE VISTULA LAGOON (SOUTH-EASTERN BALTIC)

B.V. Chubarenko, I. P. Chubarenko

Atlantic Branch of P.P.Shirshov Institute of Oceanology of Russian Academy of Sciences,
Prospect Mira, 1, Kaliningrad, 236000, Russia, E-mail: CHUBORIS@IORAN.KERN.RU

Abstract. The field studies of frontal zone between the lagoon and sea waters, that permanently exists at the area of the Vistula lagoon entrance, were fulfilled. The variations of the main hydrological parameters at crossing the frontal zone are presented. The dynamic of frontal zone location versus forcing factors variations is described. The quantitative estimations of mesoscale variability of water exchange parameters are given.

Introduction

Nowadays Atlantic Branch of P.P.Shirshov Institute of Oceanology of Russian Academy of Sciences has a Marine Research Station on the Vistula Spit, which is in the closest vicinity of Baltiysk Strait connected the Vistula lagoon with the Gdansk Bay of the Baltic Sea. Being based on this Research Station two expeditions (each about 10-12 days) were held during summer time in 1996 and 1997 and were devoted to experimental investigations of water exchange between both of coastal zone and the Vistula lagoon.

There are a lot of problems concerning the waste water treatment both on the Russian and the Polish sides of the lagoon. For example, about 50% of the domestic and industrial waste waters from Kaliningrad (regional centre) come to the Vistula lagoon without any treatment. Under such circumstances the water exchange processes play the leading role in the ventilation of the lagoon area which is under the great pollution load from the coastal point sources. On other hand, this process promotes to the intensive pollution load to the Baltic coastal area that has the great recreation significance for the Kaliningrad region.

The water exchange process is exposed to the resulting influence of the various driving forces that are characterized by the wide spectra in the time variability. The main of these forcing factors is the water level variation that has the maximum variability with the periods of 5, 6, 7.5, 9, 12 and 24 hours [1]. For this reason, the hydrological structure in the Vistula lagoon entrance and the surrounding area is very changeable [2,3]. But, there is the only permanent peculiarity consisting in the presence of the frontal zone between the lagoon and coastal sea waters. This zone has a very dynamical behaviour and is characterized by the sharp gradients of all the hydrological parameters.

The purpose of this paper is to represent the field study results of the frontal zone between the lagoon and coastal sea waters and to give the quantitative estimation of the mesoscale variability of the water exchange parameters.

Methods

Field studies included the measurements of vertical profiles of temperature, salinity and dissolved oxygen, pH and Eh as well as determinations of the water transparency and variations of the water level and meteorological parameters. All the measurements were carried out during both inflows of salt Baltic waters into the lagoon aquatory and the outflows of fresh lagoon waters towards the Baltic coastal area. The research motor boat with a draught about 70 cm was used. The vertical structure of the mentioned above parameters were measured by the IDRONAUT profiler that had a real time data processing or the SEA CAT CTD-profiler, that stored the data in the internal memory. The water transparency was measured by Secchi disk.

Results and discussion

Hydrological front

The area of the lagoon entrance (the Baltiysk Strait and the surrounding radius area of the order 2-4 km) is the transitional region, where the front between the Baltic coastal water and the lagoon water permanently exists. The Baltic water is characterized by Seccki depth (SD) of 1.5-3.0 m and the salinity range of 6.5-7.5 psu. The Vistula lagoon water has the transparency and salinity in the limits of 0.4-0.7 m and 3.5 - 5.5 psu respectively. It was found out that there were no significant differences in the dissolved oxygen, temperature, pH and Eh values at crossing the frontal zone. That is why these parameters were not indicative of both the lagoon or coastal zone water mass.

The frontal zone is clearly marked by drastical water transparency changes and by significant sharpening of the horizontal and vertical salinity gradients at the frontal zone. The gradients values are in the range of 0.5-1.0 psu per km and 2-4 psu per meter respectively.

The frontal zone is strongly pronounced and constantly migrates hither towards the lagoon area thither towards to the coastal zone. The velocity of its movement is about 3-10 km per day.

The frontal zone steadily divides the lagoon and sea water mass and migrates in the range of 4-10 km in the case of 12-16 hours level variations. During the prolonged level changes (with the time scales of more than one day) the frontal zone is partly destroyed because of the active interpenetrating of water mass, for example, during deep sea water inflow. In this case the sea water penetrates into the lagoon, occupying the total water column in the 1-4 km area surrounding the lagoon entrance. The frontal zone restoration occurs rather rapidly because the situation when the more heavy salt water occupies the total water column is dynamically unsteady. When the inflow intensity decreases the sea water falls down to the deep layer (under the lagoon water) just a matter of hours.

The Baltic water inflow

The one example of the salinity vertical structure during the Baltic water inflow event (12 cm/day of level rising, the maximum velocity in the range of 15-20 cm/sec, the event duration is near 15 hours) is represented in Fig. 1 [3]. The rate of the marine water flowing into the lagoon is so great, that the mixture of sea and lagoon waters practically do not occur. The total volume of marine water which has flown into the lagoon during the period of 24 hours can be estimated as 23 million cubic metres, which makes about 1% of the total water body of the lagoon. It is possible to estimate, that the salt income (in this situation) is about of 42 thousand tons and makes 0.1% of the total. The lost of heat from the lagoon is about $1.5 \cdot 10^{11}$ kkal ($6.2 \cdot 10^{14}$ Dj).

The measurements revealed that the mass of inflow salted waters does not penetrate mainly into the narrow and deep (12 m) Kaliningrad Marine Channel, but spreads firstly along the more shallow lagoon area (3-5 m) in case of intensive sea water inflow. Although the ratio between cross sections of the channel and lagoon mouth is approximately 1:3, the volume of water reaching the lagoon is estimated as 90% from the incoming one, whereas the volume penetrating the channel is about 10%.

The Vistula lagoon water outflow

The lagoon water flows from the lagoon entrance periodically portion by portion. The fresh lagoon waters spread as a plume in the upper layer of sea waters mostly in the direction of wind and wave.

The example of the hydrological structure at the moment of the lagoon water outflow (on July 13, 1997) is shown in Fig. 2. The crossection axis is directed along the lagoon entrance. The frontal zone was not so sharp as it usually was during the inflow event, because the salinity distribution on July 13 is the result of the superposition of two consecutive outflows. The water of the recent outflow ($SD=0.6-0.8 \text{ M}^{-1}$) spread over the water of previous ones ($SD=1.2 - 1.5 \text{ M}^{-1}$) that are partly mixed with the sea water ($SD = 3.0 - 3.9 \text{ M}^{-1}$).

The spatial and vertical gradients for the upper end of front were about 0.25 psu per km and 0.25 psu per m, respectively. The deep end of the front was characterized by the gradients of about 0.8 psu per km and 2 psu per m in the horizontal and vertical directions respectively.

As for the temperature, the vertical and horizontal differences of 2°C per m and 2°C per km were observed at the deep end of the front. In the upper layer, the maximum values of the vertical and horizontal gradients were about 0.7°C per m and 0.5°C per km.

During outflow, the lagoon water occupied the upper 5-6 m in the narrow Baltiysk strait (stations 318, 319) and spread in the wide thin upper layer (2 - 3 m) after reaching the open coastal zone. Judging from the vertical salinity and temperature structure, the upwelling movement occurred along the bottom slope as the result of the dynamic influence of the lagoon water outflow.

The volume of lagoon water outflow (13.07.97) can be estimated just over 23 million of cubic meters. The volume of previous outflows is about 135 million of cubic meter. The outflow duration was about 6 hours. Therefore, counting that the outflow depth in the Baltiysk strait is about 6 m, the discharge was of about 3.8 million of cubic meter per hour and the average velocity was over 0.5 m per sec. This results fitted in magnitude order with the field measurements, during which the average velocity of about 30-40 cm per sec and the maximum outflow velocity (1.2 - 1.4 m per sec) were obtained.

The extended sense of the obtained results

In this paper we present the general opinions on the hydrological behaviour at the Vistula lagoon entrance area based on the results of 12 - 15 days summer expeditions. But it doesn't limitate the applicability of paper conclusions to the year as a whole. According to the results of the four years Vistula lagoon monitoring [4], the seasonal variations do not significantly change the salinity of the front made water mass. As for the level variation, which defines the front position and its reciprocating movements, it is possible to say, that in spite of the seasonal level variations have the big amplitude [5], the synoptical and mesoscale level variability are similar in any period. So, we can generalize the paper conclusions to any season.

Conclusions

The field mesoscale investigation results of the Vistula lagoon entrance area, connected the Vistula lagoon and the Baltic coastal waters, are given here for the first time. This zone is the transition one both for the lagoon water entering the coastal area as for the Baltic waters flowing into the lagoon.

The hydrological front permanently exists at this transition area and divides two water mass which are different by their characteristics and genesis. The frontal zone is clearly marked by drastical water transparency changes and by significant sharpening of the horizontal and vertical salinity gradients that are in the range of 0.5-1.0 psu per km and 2-4 psu per meter respectively. This zone constantly migrates hither towards the lagoon area thither towards the coastal zone with the velocity 3-10 km per day in the range of 4-10 km.

The transfrontal flow of substances undoubtedly occurs in this area along with the periodical portion advective water exchange. The substances carried by this flow throughout the geochemical frontal barrier have to alter, and, therefore, the characteristics of coastal zone onloading vary as well.

The Vistula lagoon waters accumulate all the pollution and suspended matter from its catchment. Therefore, the investigation of the spatial-temporal dynamic of the frontal zone behaviour is of great significance not only for understanding of the coastal front genesis processes, but for the quantitative estimations of the pollution loading on the Baltic coastal zone too.

Acknowledgements

The authors are thankful to the following colleagues for their participation in the 1996-1997 field studies and in the initial data treatment: D. Markovtsov (motor boat driver), A. Sidorenko, A. Mezin, A. Gaidukov, G. Kershukov, D. Galinsh (all are the students of Moscow Institute for Physics and Technology). We are indebted to the interpreter L.S. Emelyanova for her help on preparing of this paper. The 1996-1997 field programmes were held in the frame of internal scientific programme "The Vistula lagoon" of the Atlantic Branch of P.P. Shirshov Institute of Oceanology (Russia) and the National Russian Project "The Baltic sea"(N 01970007321).

References

1. V.F. Dubravin, V.D.Egorikhin, B.V.Chubarenko, F.Y.Babakov, S.N.Ivanov, 1997, Near bottom currents at the Gulf of Kaliningrad (Northern part of the Vistula lagoon), Ecological Problems of Kaliningrad Region, 90-96, (in Russian).
2. B.V. Chubarenko, I.P. Chubarenko, 1997, Regionalisation of river Pregel estuary and Russian part of the Vistula lagoon on hydrophysical parameters: Extended Abstracts of Int. Conf. on Regionalization in Hydrology, Braunschweig, Federal Republic of Germany, 10-14 March, 1997, 41-44, (in English).
3. I.P. Chubarenko, In press, Water-exchange in the Baltiysk Strait Region, Proc. of Symposium of freshwater fish and the herring population in the Baltic coastal lagoons. May 5-6, 1998, Gdynia, Polan, (in English).
4. B. V. Chubarenko, I.P. Chubarenko, A.F. Kuleshov, In press, The results of 1994-1997 field investigations of hydrological structure and transparency of water in the Russian part of the Vistula lagoon, Proc. of Symposium of freshwater fish and the herring population in the Baltic coastal lagoons. May 5-6, 1998, Gdynia, Poland, (in English).
5. N.Lazarenko and A.Maevskiy (Editors), 1971, Hydrometeorological regime of the Vistula lagoon, (in Russian).

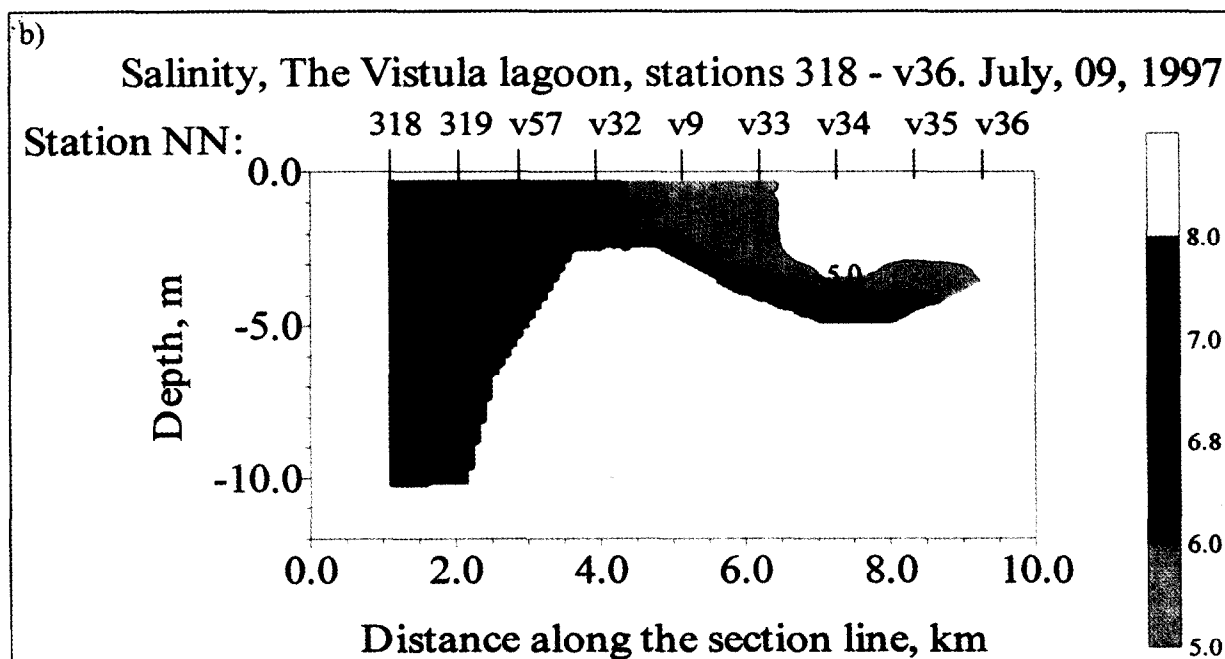
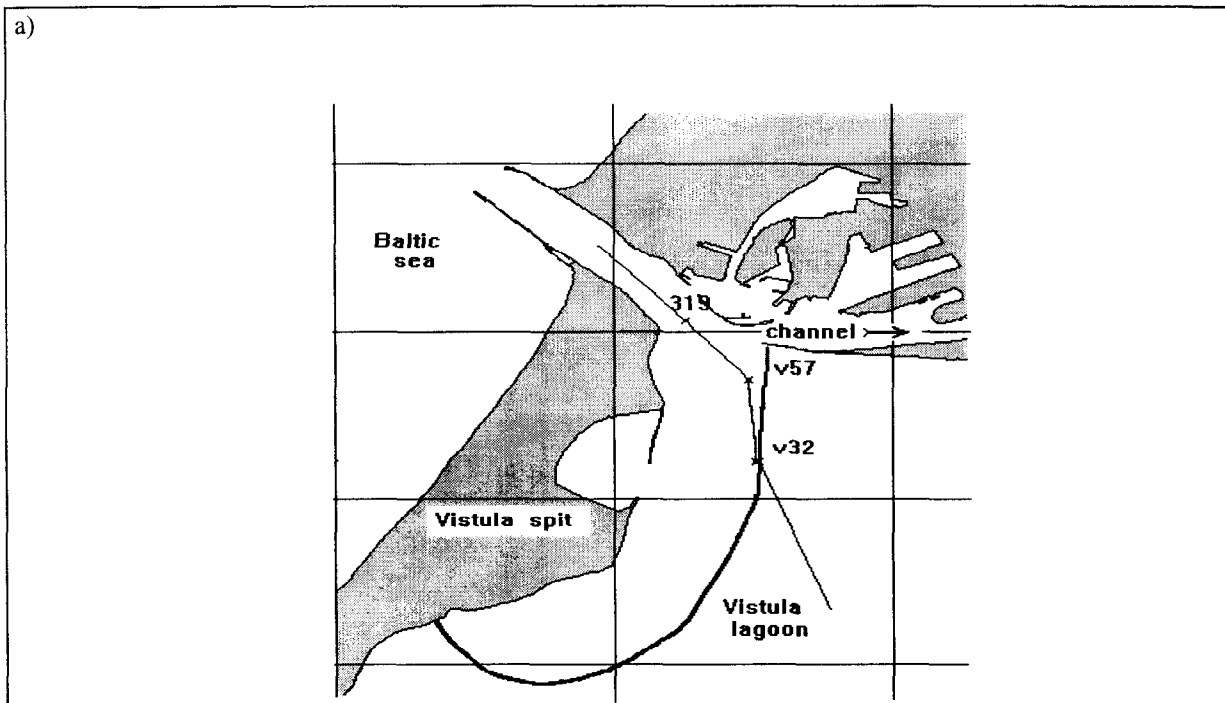


Fig.1. Baltic water inflow into the Vistula lagoon on 09.07.97. The solid thick line (a) indicates the upper layer boundary of the inflow sea water. The solid thin line (a) indicates the line of cross-section (b).

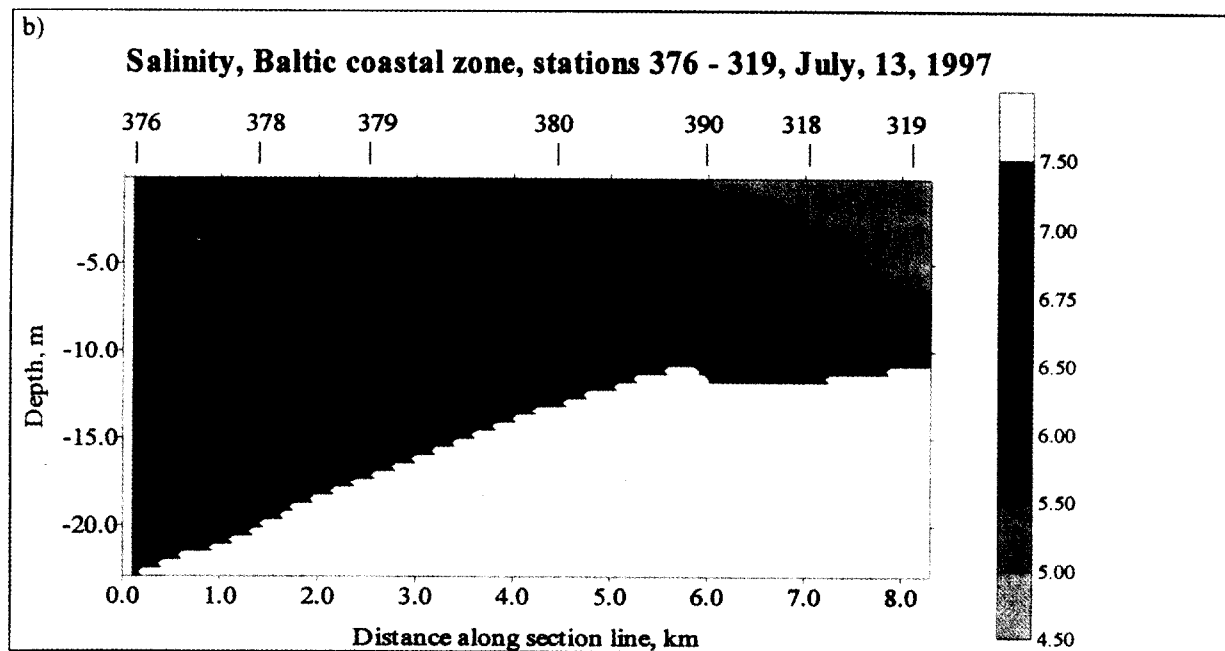
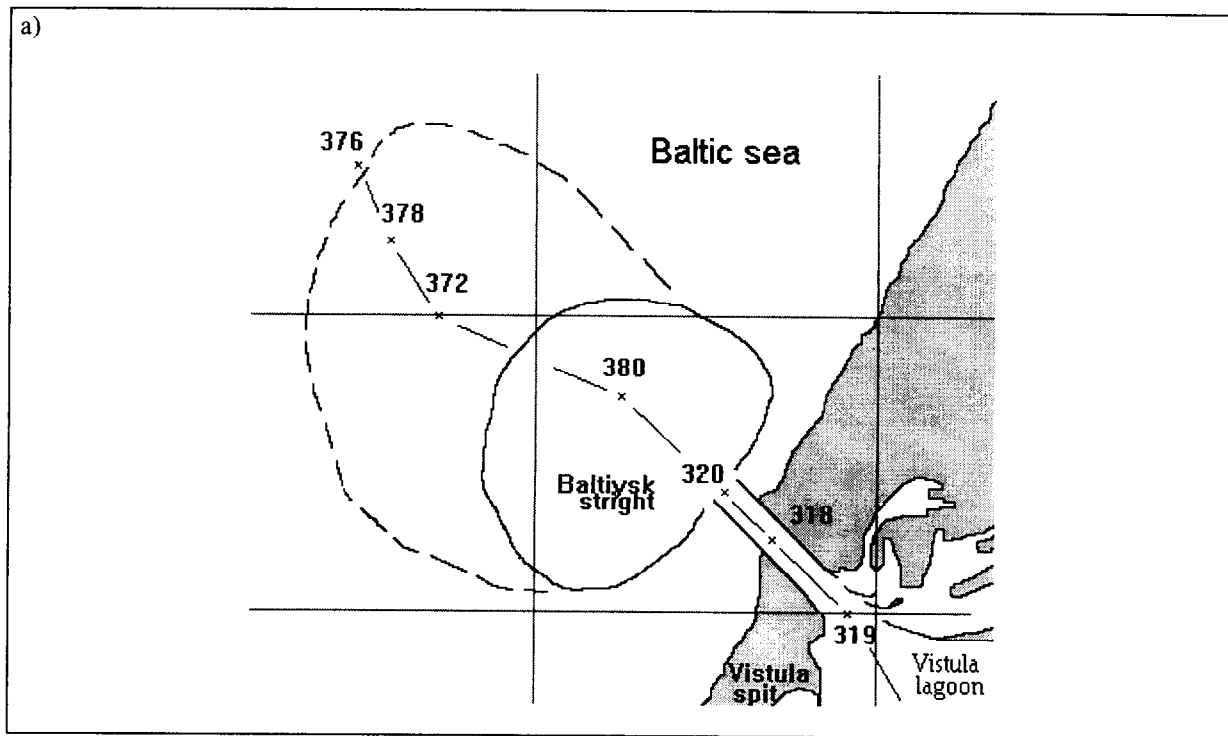


Fig.2. Vistula lagoon water outflow into the Baltic sea on 13.07.97. The thick solid and dotted lines (a) indicates the upper layer boundaries of two consecutive outflows of the lagoon water. The thin dotted line (a) indicates the line of crosssection (b).

MATHEMATICAL MODEL OF POLLUTANT PROPAGATION IN NORTH TIDAL RIVER MOUTH

E.I.Debol'skaya

Institute of Water Problems of RAS, 3, Gubkina St., Moscow, Russia, e-mail: elena iwapr.msk.su

Abstract: The mathematical model of pollutant propagation under ice cover in the tidal estuary are presented. Two plan directions of pollutant propagation are taken into account along and across of the flow with assumption of full mixing of the pollutant over the depth. The empirical relations for longitudinal and cross-sectional momentum transfer coefficients are used. For hydrodynamic block of the model the momentum equation for vertical axis must be attracted. The tidal wave influence is calculated in the model too. The comparison of the calculation result with data of observations show that the model is in satisfactory accordance with natural process.

Introduction

The investigation of pollutant propagation in rivers of north regions acquires particular meaning in connection with accident discharge of sewage and accident in pipelines. The estimate of ecological consequences from these accidents is a serious problem. It is difficult to solve this problem without working out the corresponding mathematical models of pollutant spot propagation in the flow. The particularities of river flow in north regions make suppose that such models must take into account not only really morphology of river bed but two-dimensional character of pollutant propagation and existence of tidal wave and ice cover during long time of the year. However at present such models are absent in practice, that make difficulty to receive forecast estimates.

The model of longitudinal-transverse transfer

In connection with these facts the model of pollutant propagation in tidal ice covered estuary was worked out in order to forecast the consequences of the accident discharge of sewage. The model based on enough strong hydrodynamics thesis permits us to obtain pollutant distribution at any studied reach of the river. The base equation of the model is the transfer equation with assumption of full mixing of the pollutant over the depth:

$$\frac{\partial c}{\partial t} + u \frac{\partial c}{\partial x} + v \frac{\partial c}{\partial y} = \gamma_1 \frac{\partial}{\partial x} (|u|h \frac{\partial c}{\partial x}) + \gamma_2 \frac{\partial}{\partial y} (|u|h \frac{\partial c}{\partial y}), \quad (1)$$

$$\frac{\partial c}{\partial t} + u \frac{\partial c}{\partial x} + v \frac{\partial c}{\partial y} = \gamma_1 \frac{\partial}{\partial x} \left(|u|h \frac{\partial c}{\partial x} \right) + \gamma_2 \frac{\partial}{\partial y} \left(|u|h \frac{\partial c}{\partial y} \right), \quad (1)$$

where c is pollutant concentration; t is time; u, v are averaged longitudinal and cross-sectional components of flow velocity; $|u|$ is module of averaged longitudinal velocity; h is flow depth; $\gamma_1 = 0.06$, $\gamma_2 = 0.024$ are empirical constants from relations for the longitudinal and cross-sectional momentum transfer coefficients: $D_x = \gamma_1 |u|h$ and $D_y = \gamma_2 |u|h$ respectively obtained by Dolgoplova & Orlov (1987). After differentiation the equation (1) may be written in the following form:

$$\begin{aligned} \frac{\partial c}{\partial t} + (u - \gamma_1 \frac{\partial |u|}{\partial x} h - \gamma_1 \frac{\partial h}{\partial x} |u|) \frac{\partial c}{\partial x} + (v - \gamma_2 \frac{\partial |u|}{\partial x} h - \gamma_2 \frac{\partial h}{\partial x} |u|) \frac{\partial c}{\partial y} \\ = \gamma_1 |u|h \frac{\partial^2 c}{\partial x^2} + \gamma_2 |u|h \frac{\partial^2 c}{\partial y^2} \end{aligned} \quad (2)$$

The values of the depth averaged longitudinal and cross-sectional components of flow velocity were calculated from the momentum equation for vertical axis z . (The coordinate system is choosing so that the axis x is directed along river flow, the axis y - from right bank to left one, axis z - vertically upwards).

$$\frac{\partial}{\partial z} \left(D_z \frac{\partial \bar{u}}{\partial z} \right) = -g(i - \zeta_x), \quad (3)$$

where $u = u(z)$, $D_z = \gamma_3 |u|h$ is the vertical momentum transfer coefficient, $\gamma_3 = 0.008$, i is a slope of river bottom, ζ_x is the water of ice surface elevation depending on tidal wave. The other members of the equation are omitted because as the preliminary investigations by Debolsky (1984) have shown gradiently-viscous regime of the flow is characteristic for this region, when gradient of pressure and turbulent viscosity are balanced. In chosen coordinate system:

$$\frac{\partial p}{\partial z} = \rho g(i - \zeta_x). \quad (4)$$

After integrating of the equation (4) along the depth taking into account the boundary conditions for flow velocity on the bottom and ice surface:

$$u|_{z=0} = 0, \quad u|_{z=H} = 0 \quad (5)$$

and some assumption about division of the flow into two parts by the surface of zero shear stress (i.e. resistance of bottom and ice surfaces are equal) we obtain:

$$u = \sqrt{\frac{g|i - \zeta_x|h}{12\gamma_3}} \text{sign}(i - \zeta_x), \quad (6)$$

$$\frac{\partial |u|}{\partial x} = \frac{1}{2} |u| \frac{\zeta_x}{h}, \quad \frac{\partial |u|}{\partial y} = \frac{1}{2} |u| \frac{\partial h}{\partial y} \frac{1}{h}. \quad (7)$$

The estimation of members' values of the equation (2) with consideration of really significance of flow parameters and exhibition (7) permits us to write the equation (2) with enough accuracy in following form:

$$\frac{\partial c}{\partial t} + u \frac{\partial c}{\partial x} + (v - \frac{3}{2} \gamma_2 \frac{\partial h}{\partial x} |u|) \frac{\partial c}{\partial y} = \gamma_1 |u| h \frac{\partial^2 c}{\partial x^2} + \gamma_2 |u| h \frac{\partial^2 c}{\partial y^2}. \quad (8)$$

It may be shown that consideration of the different of the resistance on bottom and ice surfaces (i.e. non equality of flow parts sizes divided by the surface of zero shear stresses) for concrete task, when time of vertical turbulent mixing is considerably lesser than time of longitudinal mixing, not strongly defines more precisely but strongly makes difficulty the calculations. The equation (8) was solved numerically by splitting method on x and y . The boundary conditions of the second kind at left and right boundaries and at banks were assigned exempt point of output of pollutant where boundary condition of the first kind was assigned.

At first the cross-sectional averaged longitudinal velocity was calculated for conditions of the natural situation (river flow and tidal wave). Then we obtained the values of velocity depending on suite of calculated point in each cross-section and the time taking into consideration the depth changes over flow width. The following relationships were used:

$$dh = \zeta = \zeta_0 e^{-kx} \sin(\omega t - kx) , \quad (9)$$

$$\zeta_x = \frac{\partial \zeta}{\partial x} = -\sqrt{2} k \zeta_0 e^{-kx} \sin(\omega t - kx + \pi / 4), \quad (10)$$

$$h = h_0 + dh,$$

where ζ_0 is amplitude of tidal wave in suite of river flowing in the sea, $k=2\pi/L$ is wave number, L is length, $\omega=2\pi/T$ is frequency and T is period of tidal wave, obtained from the measurements of flow velocity and directions. The correction of velocity values depending on point location in the cross-section was carried out by formula (6). The values of the slope i and wave length L were obtained from the calculations with employment of formula (9) and famous significance of tidal wave characteristics in point of river flowing into the sea and in control station. The results of hydrodynamics calculations are demonstrated on Figure 1, where change of surface level deviation and flow velocity module are shown in observe station.

These curves demonstrate the satisfactory agreement of values calculated by model and obtained by measurement. This allows us to conclude the possibility of using the above mentioned hydrodynamics relations for pollution transfer calculations. The time averaged value of pollutant concentration obtained by model calculation in observe point coincides with measurement value. The results of the calculations show that the model sufficiently sensitive to the changes of parameter of the discharge of sewage, the duration and original pollutant concentration in output point (Fig.2a) and in point situated at 15 km down stream at opposite bank (Fig.2b), when the sewage was produced in 'steep' regime, i.e. during 8 hours with intervals during 16 hours for two values of pollutant concentration in sewage water $0.005 \text{ kg} / \text{m}^3$ and $0.02 \text{ kg} / \text{m}^3$.

The comparison of calculated values of velocity, surface elevation and pollutant concentration with measurement result demonstrates satisfactory agreement. Thus we can suggest forecast estimation of water quality and ecological damage from accident discharge of sewage water knowing the hydrodynamics characteristics and regime of water discharge and pollutant concentration.

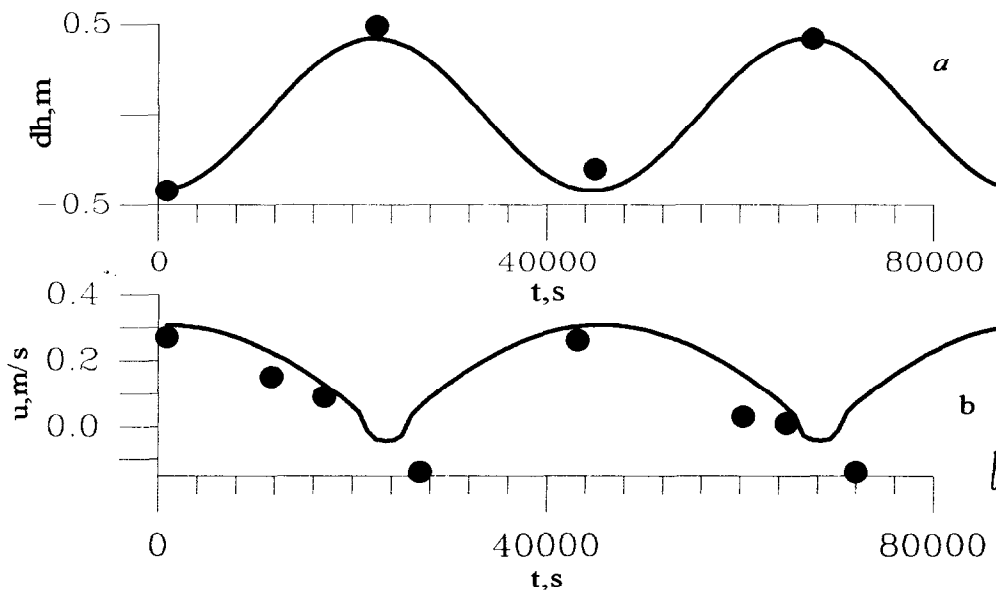


Fig 1 The dependence of surface level deviation (a) and flow velocity module (b) from the time; solid line - result of the calculation, dots - data of measurement.

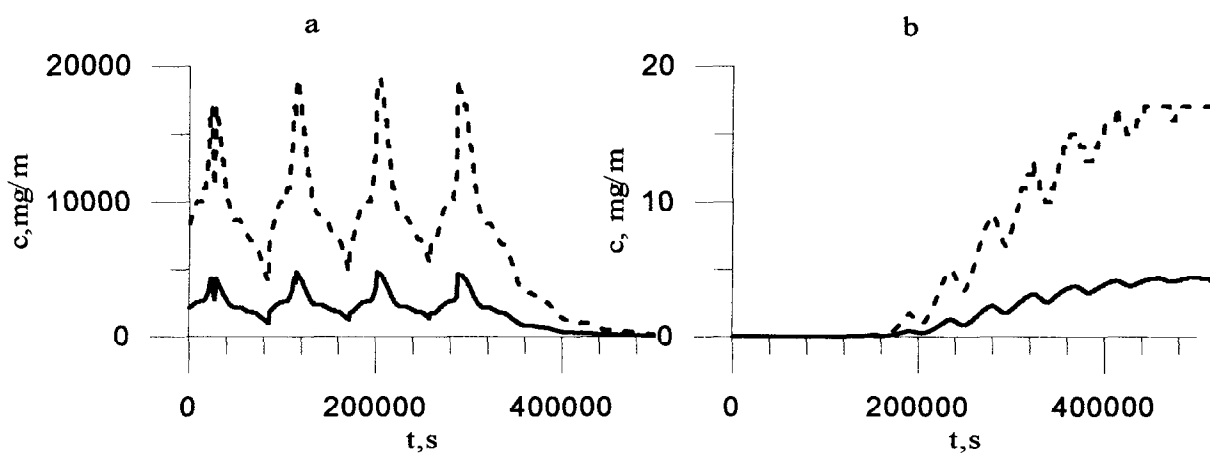


Fig2 The dependence of the pollutant concentration from the time in output point (a) and in point at 15 km downstream at an opposite bank (b); solid line - pollutant concentration in sewage water 5 g/m, dush line - pollutant concentration in sewage water 20 g/m.

The model of longitudinal - vertical transfer

The second model was working out to calculate the longitudinal-vertical diffusion of passive pollution in ice-covered tidal flow. In this case we must know the change of vertical turbulent exchange coefficient over the depth. That is why the kinetic energy of turbulence and Prandtl and Kolmogorov hypothesis were used in hydrodynamic block of this model. The velocity and the turbulent exchange factor $A(z)$ distribution over the depth are necessary for further calculations. To calculate this values we need to use original depth, bottom slope, deviation of water and ice surface level and dimensions of roughness juts of the bottom and ice surfaces as initial and boundary conditions. The hydrodynamic block permits us to solve the problem of uniform bed flow and flow without ice cover as particular case of total task with the tidal wave. The tide was calculated as the (x-y) model. The concentration of passive pollution was calculated from turbulent diffusion equation in the following form:

$$\frac{\partial c}{\partial t} + u \frac{\partial c}{\partial x} + w \frac{\partial c}{\partial z} = \gamma_1 |u| h \frac{\partial^2 c}{\partial x^2} + \frac{\partial}{\partial z} \left(A \frac{\partial c}{\partial z} \right). \quad (11)$$

Here u changes over the depth, w is vertical component of the velocity which can be calculated from continuity equation. The equation (11) was solved numerically by splitting method on x and z . The boundary conditions of the second kind at left and right boundaries and at bottom and ice surfaces were assigned except point of output of pollutant. The boundary condition of the first kind was assigned here. There are two temporal processes of different scales in the system. The time of a change of the depth and slope of water and ice surface due to tidal wave is more considerably than the time during which the turbulent characteristics become constant. It allows us to divide the task into two temporal cycle. At first, the new values of slopes and depth in dependence on tidal phase are calculated for even moment of "slow" time, and then the task on statement of the turbulent characteristics during "fast" time are decided for the same moment of "slow" time for even cross-section of the river. These characteristics are used to calculate the field of the concentrations during any moment of "slow" time. The model permits us to carry out the calculations for point and spreading output of the pollution with a different duration and a moment of the action beginning at the bottom and at flow surface.

Conclusions

1. The results of the calculations show that: the model sufficiently sensitive to the changes of parameters of the discharge of sewage, the duration and original pollutant concentration in output point.
2. The observation and numerical experiments demonstrate that the existence of ice cover during small discharges of water is the reason for more intensive mixing and rise of the pollutant stream in the transverse direction.
3. The pollutant stream width depend considerably on transverse gradients of the bed and flow lines curvatures due to the streamlines of banks and islands.

4. The thesis about vertical mixing may be assumed for distant fields from the source only. The concentration changes in few times on close fields.
5. The ice cover makes difficult the pollutant propagation into the depth of the flow.
6. Pollutant propagation from the surface sources is more intensive than from the bottom.

Acknowledgment

Investigation was supported by the Russian Fundamental Science Foundation (grant No 96-05-65151).

Reference

1. Debol'sky V.K., Zyryanov V.N., Mordasov M.A., 1984, Turbulent exchange in tidal mouth under ice cover. Dynamics and thermic regime of rivers and reservoirs, Moscow, Nauka, 279-290.
2. Dolgoplova E.N., Orlov A.S., 1987, River streams. Structure, propagation of impurities, transport of contact load. Problem of research and employment of water resources, Moscow, Nauka, 250-266.

TURBULENT STRUCTURE OF OPEN AND ICE-COVERED SHALLOW FLOW IN A CHANNEL

E.I. Debolskaya 1, V.N. Zyryanov 2

1 Water Problems Institute of Russian Academy of Science, 3 Gubkina St., Moscow, Russia, e-mail:
elena@iwapr.msk.su

2 Water Problems Institute of Russian Academy of Science, 3 Gubkina St., Moscow, Russia, e-mail:
zyryanov@iwapr.msk.su

Abstract. One of the main problem connected with calculation of a current structure in any flows is the parametrization of turbulent characteristics. There are many dependencies for the velocity vertical profile for open and ice-covered flows but there are not many for turbulent momentum transfer coefficient (eddy viscosity) $A(z)$ though it is the most important characteristic for example during calculations of the transport process of impurities. The objective of this paper is to obtain a parametric dependence of $A(z)$ on the base of a numerical simulation.

Model

Model equations describe the steady flows when the gradient of pressure and turbulent viscosity are balanced:

$$\frac{\partial}{\partial z} \left(A(z) \frac{\partial u}{\partial z} \right) = -gi, \quad (1)$$

$$\alpha \frac{\partial}{\partial z} \left(A(z) \frac{\partial b}{\partial z} \right) - \frac{b^{\gamma}}{A(z)} + A(z) \left(\frac{\partial u}{\partial z} \right)^2 = 0, \quad (2)$$

$$A(z) = l\sqrt{b}, \quad (3)$$

$$l = c^{1-\gamma} \kappa \left| \frac{\partial u}{\partial z} \right|, \quad (4)$$

where $A(z)$ is the momentum transfer coefficient (eddy viscosity), $u(z)$ is a velocity of the flow, i is a slope, $l = l(z)$ is a scale of turbulence, $b = b(z)$ is a turbulent kinetic energy, $\alpha = 0.32$, $\gamma = 0.09$, $c = 0.4$, $\kappa = 0.4$ is

the von Karman constant. The axis x lies in the bottom surface, the axis z is directed vertically upwards. The origin of coordinates is placed at the bottom.

Boundary conditions for $A(z)$ at the bottom and at the ice surface can be received from the expressions:

$$A|_{z=z_b} = A_b = -\frac{\tau_b}{\rho_w} \frac{\partial u}{\partial z} \Big|_{z=z_b} = \frac{u_{*b}^2}{\frac{\partial u}{\partial z} \Big|_{z=z_b}}, \quad A|_{z=z_i} = A_i = -\frac{\tau_i}{\rho_w} \frac{\partial u}{\partial z} \Big|_{z=H-z_i} = \frac{u_{*i}^2}{\frac{\partial u}{\partial z} \Big|_{z=H-z_i}},$$

where τ_b, τ_i are boundary shear stresses, u_{*b}, u_{*i} are dynamic velocities, z_b, z_i are dimensions of roughness juts of the bottom and ice surfaces respectively. From the logarithmic speed distribution law in layers adjacent to z_b, z_i it follows:

$$\frac{\partial u}{\partial z} \Big|_{z=z_b} = \frac{u_{*b}}{\kappa z_b}, \quad \frac{\partial u}{\partial z} \Big|_{z=H-z_i} = \frac{u_{*i}}{\kappa z_i}.$$

Taking into account that $z_b \ll z_0$, $z_i \ll H - z_0$ and (1) is valid, one can write:

$$A_b = u_{*b} \kappa z_b = \kappa z_b \sqrt{g i z_0}, \quad A_i = u_{*i} \kappa z_i = \kappa z_i \sqrt{g i (H - z_0)},$$

where z_0 is a vertical coordinate of the surface of zero shear stress or maximum of velocity, H is a depth. To obtain the boundary value of the turbulent energy let the scale of turbulence at the bottom and ice surfaces be equal to dimensions of the roughness juts. Then the Kolmogorov's hypothesis (3) gives:

$$b|_{z=z_b} = b_b = (A_b / l_b)^2 = \kappa^2 g i z_0, \quad b|_{z=z_i} = b_i = (A_i / l_i)^2 = \kappa^2 g i (H - z_0).$$

At the bottom and ice surfaces the velocity of the flow is assumed to be zero:

$$u|_{z=z_b} = 0, u|_{z=z_i} = 0.$$

Boundary conditions at the upper surface of the open flow are [1]:

$$A \frac{\partial u}{\partial z} \Big|_{z=H} = \frac{\tau_w}{\rho_w}, \quad A|_{z=H} = 4.3 \cdot 10^{-4} W^2, \quad b|_{z=H} = 2 \cdot 10^{-4} \beta W^2,$$

where $\tau_w = 10^{-3} \beta \rho_a W |W|$ is the shear stress at upper surface of water due to the wind influence, ρ_a is the air density, ρ_w is the water density; the coefficient β can take two different values depending on the degree of wave development which is determined from the wind velocity W and the flow depth H : for $H > \mu W$ $\beta = 0.23$, for $H < \mu W$ $\beta = 0.75$, where $\mu = 7.58$ s is a dimensional and the wind velocity W is expressed in m/s everywhere.

To determine the coordinate z_0 in an ice-covered flow it is enough to know the bottom-ice roughness relation. Really, as it follows from empirical data the average velocity of the near bottom flow section is equal to that of the top section (near the ice surface). The interface between these sections coincides with plane of zero shear stress, i.e. with z_0 -plane. Taking into account the Chezy formula for the average velocity and Shtrichler formula

$$n_{b,i} = 0.15 \cdot z_{b,i}^{1/6} / \sqrt{g}, \quad (5)$$

one can receive:

$$z_0 = H / (\tilde{k} + 1), \quad (6)$$

where $\tilde{k} = \left(\frac{n_i}{n_b} \right)^{3/2} = \left(\frac{z_i}{z_b} \right)^{1/4}$, n_b, n_i are Manning's roughness coefficients of bottom and ice surfaces respectively.

The position of the point z_0 for the open flow is determined from the ratio of the shear stress at the top boundary τ_w to the bottom friction stress without wind $\tau_b^0 = \rho_w g i H$, i.e. from the parameter:

$$k = \frac{\tau_w}{\rho_w g i H}, \quad (7)$$

where ρ_w is the water density. To obtain the dependence of z_0 on k it is necessary to notice that for the gradiently-viscous regime of the flow described by the equation (1), the following relation is valid:

$$\tau_b = \tau_w + \rho_w g i H. \quad (8)$$

Taking into consideration (7) and (8) it can be obtained:

$$\tau_b / \tau_w = 1 + 1/k.$$

From linearity of distribution of the turbulent friction stress with depth at the gradiently-viscous regime it follows that the point z_0 position at any wind (fair and contrary) will be determined by expression $z_0 = H(k + 1)$.

At the fair wind $k > 0$ and $z_0 > H$.

From equations (1) - (4) the differential equation of the first order about $A(z)$ with the point of singularity $z = z_0$ was obtained. The solution of this equation may be written in the following form:

$$A = \left[\kappa c^{1/4} \int_{z_b}^z \frac{\sqrt{b} dz}{z - z_0} + \frac{A(z_b)}{z_b - z_0} \right] (z - z_0) \quad \text{at } z < z_0,$$

$$A = \left[\kappa c^{1/4} \int_z^H \frac{\sqrt{b} dz}{z - z_0} + \frac{A(H)}{H - z_0} \right] (z - z_0) \quad \text{at } z > z_0.$$

To calculate these integrals, it is necessary to know the value of the turbulent energy b , which was obtained from equation (2) numerically by the run method.

Parametrization

In case when the current is influenced by a favourable wind the following dependence for $A(z)$ was proposed based on numerical experiments results:

$$A(z) = az\sqrt{gi(H-z)} + \frac{\eta W^2}{H} \left(\frac{z^3}{gi} \right)^{1/2}, \quad (9)$$

where $a=0.45$, $\eta=2 \cdot 10^{-6}$ are non dimensional constants, W - wind velocity.

In case when the current is influenced by a head wind, the point z_0 lies within the flow and it is necessary to divide the cross section of the flow into two parts. For the bottom part, when $z < z_0$, the dependence of $A(z)$ can be expressed in the form:

$$A(z) = az\sqrt{gi(z_0-z)}. \quad (10)$$

For the top part ($z > z_0$) it is possible to write:

$$A(z) = GW^2(z-z_0) \left[\frac{4(H-z)}{(H-z_0)^2} + \frac{1}{H-z_0} \right], \quad (11)$$

where $G = 4.3 \cdot 10^{-4}$ s is the dimensional constant taken from empirical dependence of turbulent exchange factor on wind velocity of the surface "water-air".

In Fig. 1, vertical distributions of $A(z)$ are given in case of the effect of various wind velocity on the flow. These distributions were received due to numerical calculations of equations (1)-(4) and from formulas (9),(10),(11).

In case of ice-covered flow the following dependence for $A(z)$ was proposed :

$$A(z) = az\sqrt{gi(z_0-z)}, \text{ if } z < z_0, \quad (12)$$

$$A(z) = a(H-z)\sqrt{gi(z-z_0)}, \text{ if } z > z_0 \quad (13)$$

Fig 2 shows the curve $A(z)$ plotted by results of the numerical calculations and by formulas (12), (13) for two different ice-covered flows. It is necessary to remark that the zero value of $A(z)$ at $z = z_0$ is reached both from formulas (12),(13), but this effect is absent on our curves because we used the averaging of $A(z)$ over three nearest points

The substitution of expressions (12) and (13) in expression for velocity obtained by integrating the equation (1) and by integrating separately in each layer, allows to receive a parametric dependence for ice-covered current velocity $u(z, i, H, z_b, z_i)$:

$$u(z) = u_0 + \frac{2\sqrt{gi}z_0}{a} \left(\sqrt{1-y} - \ln \frac{\sqrt{1-y}+1}{\sqrt{y}} \right) \quad \text{at } z < z_0, \quad (14)$$

$$u(z) = u_0 + \frac{2\sqrt{gi}z_0}{a} \left(\sqrt{y-1} + \frac{1}{2} \ln \left| \frac{\sqrt{y-1}-r}{\sqrt{y-1}+r} \right| \right) \quad \text{at } z > z_0, \quad (15)$$

$$\text{where } y = z/z_0, y_b = z_b/z_0, r = (d_i/d_b)^{1/8}, u_0 = \frac{2\sqrt{gi}z_0}{a} \left(\ln \frac{\sqrt{1-y_b}+1}{\sqrt{y_b}} - \sqrt{1-y_b} \right).$$

Fig.3 shows a distribution of velocity , constructed according to field measurements, numerical experiments and formulas (14) and (15): fig.3(a) - the comparison with Larsen's experiments [2], fig.3(b-d) - with our measurements in the river Moskva..

In the case of a free flow which is influenced by a head wind the integration gives for the bottom layer ($z < z_0$) expression (14) and for the top layer ($z > z_0$):

$$u_t(z) = u_0 + \frac{gi}{\varphi} \ln\left(\frac{\tilde{y}-1}{\tilde{y}-y}\right), \text{ where } \varphi = 4G \frac{W^2}{(H-|z_0|)^2}, \tilde{y} = \left(H + \frac{(H-|z_0|)^2}{4(H-z_0)}\right) / z_0.$$

The model of open and ice-covered current permits to receive the distribution of turbulent characteristics of the flow along the vertical.

Acknowledgement

This research was supported by the grant 97-05-65151 from the Russian Foundation for Basic Research.

References

1. Pierson, W.J., 1955, Wind waves, J. Adv. Geophys., 2, 93.
2. Larsen P.A., 1969, Head Losses Caused by an Ice Cover on Open Channels, Journal of the Hydraulics Division, ASCE, 96 (HY3), 703-724.

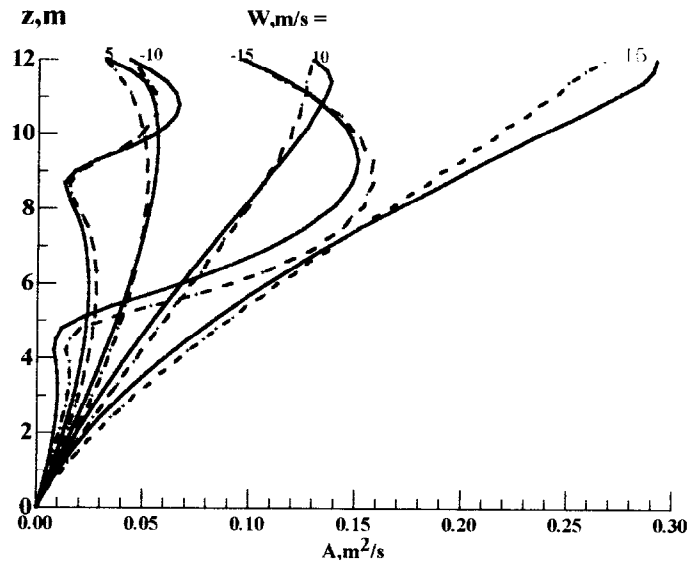


Fig.1 Vertical distributions of turbulent exchange factor $A(z)$ calculated numerically by equations (1)-(4) (dashed) and by formulas (9),(10),(11) (solid). W is wind velocity.

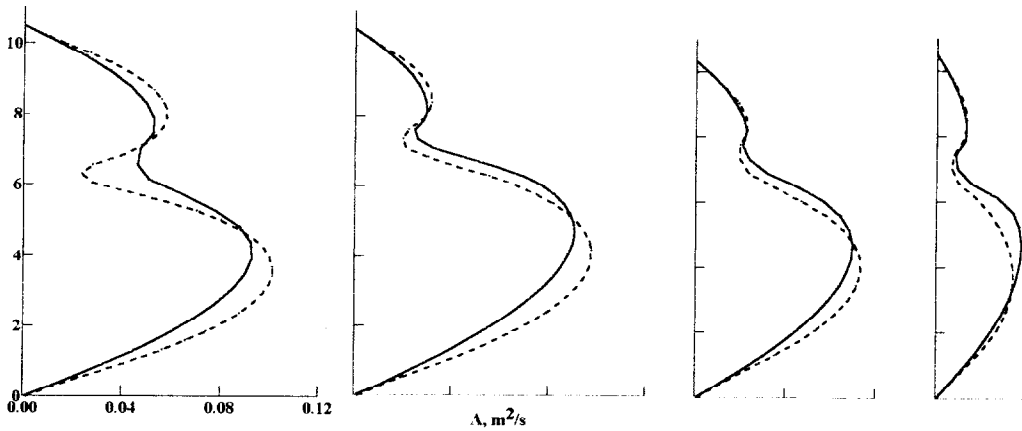


Fig2. Vertical distributions of $A(z)$ calculated numerically (dashed), by formulas (12),(13) (solid) and by Larsen's experimental data.

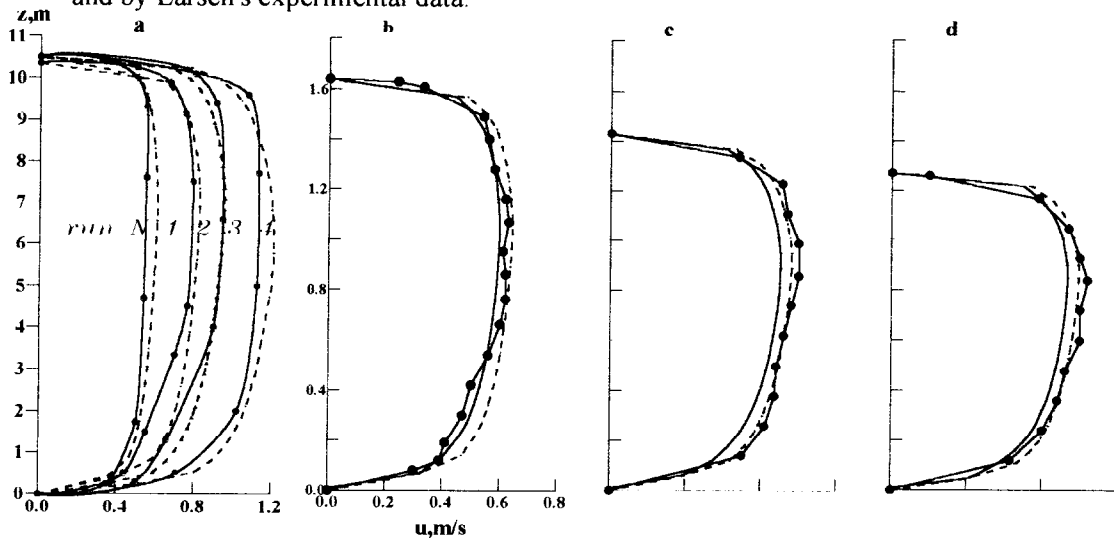


Fig.3 The distribution of ice-covered flow velocity by field measurements (solid lines with symbols), by numerical experiments (dashed lines) and formulas (28),(29) (solid lines): (a) is comparison with Larsen's experiments for four runs, (b,c,d) with measurements on the river Moskva.

MESOSCALE CURRENTS UPON THE SMOOTH SLOPING BOTTOM AND IN THE PRESENCE OF RIDGES AND CANYONS

V. Didkovskii, A. Semenov and A. Zatsepin

P.P. Shirshov Inst. of Oceanology, Nakhimovsky pr., 36, 117851, Moscow, Russia;
e-mail: zatsepin@glasnet.ru

Abstract. The self-oscillatory mechanism of periodic eddy formation produced by a stationary local mass source upon the sloping bottom in the rotating fluid is investigated by means of the laboratory experiment. It is shown, that under this mechanism the quasi-isobatic mesoscale current is disintegrated into a series of drifting eddies. Two main regimes of dense water mesoscale current are established experimentally: geostrophic and topographic beta-induced. The influence of moderate (compared to the fluid depth) downslope ridges and canyons on the dynamics and structure of mesoscale currents is considered, too. It is pointed out that the steep local topography on the continental slope enhances the water exchange between the shelf zone and the deep ocean.

Introduction. The continental slope is an enough narrow zone (about 100 km wide) which separates the shallow shelf region (0-200 m) from the deep ocean (4000 m or even more). This zone is characterized by a very specific dynamics of the water flows and may be considered as a frontal zone for the potential vorticity. Due to the high up-slope gradient of the potential vorticity, the large- and mesoscale quasigeostrophic currents are usually directed along the isobatic lines and so they are unable to provide directly any significant shelf - deep water exchange. The instability of the flow, bottom friction, and relief inhomogeneities change the dynamics and trajectory of the oceanic currents upon the continental slope and thus influence the mentioned above exchange. The main aim of this short report is to present some results of the recent laboratory studies of the dynamics and structure of mesoscale homogeneous and density currents in the rotating fluid. Such currents are generated by a local mass source upon the smooth sloping bottom and in the presence of downslope ridges and canyons.

The experiments described here were started with the aim to study the dynamics of dense water lens-like eddy on the sloping bottom in the rotating (in the same one direction as the Earth) fluid. We produced the dense water lens-like eddy by the local constant flux source of more saline and colored water. We tried to "pump" during the limited time the isolated blob of dense water, then to switch off the source and to observe the evolution of the fixed volume lens. To our surprise, the periodic formation of isolated dense water lenses was observed even during the continuous work of the source at least in the case of weak density contrast between the injected and ambient fluids. In this case the enough high (compared to the depth of the ambient fluid) dense water lens-like eddy was formed (under the conservation of angular momentum of injected fluid) just upon the source. After reaching the certain diameter, it moved away from the source and then drifted rightwards about the downslope direction. While that, a formation of a new lens upon the source was started and the whole cycle repeated many times (fig.1b). Such a cyclic process of a lens-like eddy formation might be classified as a self-oscillatory one. Nearly the same phenomenon was observed previously in the laboratory experiments of [1] and [2], but its physical nature was not enough clarified. Similar periodic regime of eddy structure formation from the stationary local source on beta-plain was obtained in numerical experiments of [3] and [4].

We supposed that the topographic beta-effect, produced by the bottom slope in the rotating fluid [5], might be the main physical reason for the self-oscillatory regime of lens-like eddy formation and for its «westward» drift from the source. So far as the topographic beta-effect is mostly pronounced in homogeneous fluid, the best periodic eddy structure should be formed in purely barotropic case: when the injected fluid has the same density, as the ambient fluid in the tank. The results of the experiment with barotropic source flow are analyzed just below the description of the experimental setup and after that they are used for the interpretation the phenomenon of disintegration of dense water flow into a series of lens-like eddies. Finally, the influence of ridges and canyons on the mentioned above barotropic and dense water flows upon the slope is described.

Experimental setup. The experiments were provided in the rectangular organic glass tank $50 \times 50 \times 46$ cm³ filled by distilled or salted water and positioned in the center of the one-meter rotating table. The rotating (in the same direction as the Earth) table had four fixed rates of rotation: $f = 1.0; 1.6; 2.7; 4.1$ rad/s. Here $f = 2\Omega$ - the Coriolis parameter. In some of the experiments the sloping bottom (slope angle $\alpha = 39^\circ$) was simulated by the cone that peaked up just in the center of the tank. The round tube source of diameter about 2.0 cm was smoothly mounted ortho to the sloping surface of the cone at the middle between the peak and the base. In other of experimental runs the sloping bottom was simulated by the inclined plane surface displaced jointly to one of the tank walls. The inclination angle of this plane surface was changed from 5° up to 50° . The flow rate Q was changed from one experimental run to the other in the following range: $Q = 0.3 - 10.0$ cm³/s and kept constant during each experimental run using a Mariott bottle. In order to minimize turbulent mixing between the injected and ambient fluid in most of experimental runs the inflow produced by the source was quasi-laminar. In some of experimental runs the density of the source fluid was the same as of the ambient fluid in the tank. In such cases the barotropic quasi-isobatic current, driven by topographic beta-effect was generated. In other cases the density (salinity) of the source fluid was higher than of the ambient one and the baroclinic quasi-isobatic current was generated. The reduced gravity acceleration $g' = g\Delta\rho/\rho$, where g is the acceleration due to gravity, $\Delta\rho$ is the density difference between the injected and the ambient fluid and ρ - the density of the ambient fluid, was changed in following range: $g' = 0.2 - 10$ cm/s². The height H_0 of the ambient fluid upon the source was changed from 7 cm up to 32 cm. The injected fluid was colored with thymol blue indicator. Small paper pellets were putted at the surface of the fluid to make visible the fluid motion. The top and side views of the injected fluid were observed on the TV monitor and recorded by the video camera positioned on the rotating table above the tank.

In some experiments the downslope ridges and canyons were mounted on the pathway of the flow produced by the source. We used two kinds of ridges and canyons: 1) with triangular symmetric cross-section; 2) with rectangular cross-section. The height of these obstacles usually was several times less than the fluid depth.

Dynamics and structure of the mesoscale currents upon the smooth sloping bottom. In order to study the role of topographic beta effect on the barotropic flow produced by the local mass source, a special experiment was provided in the homogeneous rotating fluid upon the cone [6]. During the experimental runs the fluid of the same density as the ambient fluid in the tank was injected with constant flux from the source mounted at the middle of the sloping side of the cone. From one run to another we changed the values of basic parameters Q , f and H_0 . Almost in every run the flow was self-oscillatory and a chain of anticyclonic barotropic eddies drifting along isobats was produced (fig. 1a). The diameter D of the eddies and their drift velocity V_b were measured.

To describe the self-oscillatory mechanism of barotropic eddy formation the simple model was suggested. In this model an assumption is made, that the anticyclonic eddy column initially is spreading radial just upon the source with the velocity $U = 0.5dD/dt = Q/(\pi DH_0)$ as in the case of the horizontal bottom. But under the topographic beta-effect induced by the bottom slope the barotropic eddy has to drift. According to the theory, the beta drift velocity V^* is "westward" - clockwise in our case («north pole» is in the center of the tank). It increases non-linearly with diameter of the eddy: $V^* = \beta D^2/4$, where $\beta = f \times \text{tg} \alpha / H_0$ (α - the slope angle) and when D overcomes the critical lengthscale D^* , then V^* overcomes U . After that the eddy gets off from the source and formation of the new one begins, etc.

From the critical condition, $V^* = U$, we obtain the expression for the critical lengthscale D^* :

$$D^* = (4Q / (\pi f \times \text{tg} \alpha))^{1/3}. \quad (1)$$

Using (1), we get the expression for the critical drift velocity scale V^* :

$$V^* = \beta D^{*2} / 4 = (2\pi)^{-2/3} \times (Q^2 f \times \text{tg} \alpha)^{1/3} / H_0. \quad (2)$$

It has been obtained that the measured values of D and V_b depended approximately linearly on the corresponding scales D^* and V^* : $D = 4.5 \times D^*$; $V_b = 5.0 \times V^*$. Thus, the experiment enough well confirms the model.

The periodic lens-like eddy formation (fig. 1b) in the dense water bottom flow follow the pattern seen in the barotropic case. It was mentioned above that this phenomenon occurred only when the height H of the dense water layer upon the source was not small compared to the total depth H_0 of the fluid: if $H/H_0 > 0.2$. In this case due to the shortening of vortex lines, the anticyclonic vorticity was created in the upper layer upon the dense water anticyclonic lens. Thus, the vertically quasicohherent anticyclonic structure was formed and it might drift to the "west" under the topographic beta effect. Indeed, the coherent eddy structure was formed, but before to drift to the "west" direction it moved down the slope to the "south" under some unclear reasons. At that moment due to the stretching of vortex lines it changed the relative vorticity from anticyclonic to cyclonic one at least in the upper layer. The cyclonic eddy column with a trapped dense water lens at the bottom was formed and drifted to the "west" with the velocity scale V_b . When $H/H_0 < 0.2$, the upper layer fluid was not strongly affected by the dense

water source flow. The quasibarotropic anticyclonic column was not formed upon the source. In this case the spreading of dense water on the surface of the cone took form of the gravity current that was quasi-monolith and geostrophic. The direction of spreading was the same as for the topographic beta-induced drift, but the velocity scale was different: $V_g = g' \times \text{tg} \alpha / f$. The boundary between these two regimes of the flow was well marked by the ratio V_g / V_b - the Burger number. For $V_g / V_b > 1$ the flow was driven by gravity force (geostrophic regime), for $V_g / V_b < 1$ - by topographic beta-effect (fig.2). When $H / H_e \sim 1$ (H_e - the Ekman scale) the gravity current might disintegrate into a multi-frontal structure due to roll-waves formation. So, at least three definite regimes of the dense water flow occurred on the sloping bottom in the rotating fluid: beta-induced, geostrophic and roll-wave [7].

It should be mentioned, that baroclinic instability considerably affected the structure of the dense water flow in the parameter space close to the boundary between wave-vortex and geostrophic regimes. The analysis of these effects (as well as the effects of friction) is beyond the scope of this report.

Influence of ridges and canyons on mesoscale currents upon the sloping bottom. With the same experimental set up described above, we studied the influence of the downslope ridges and canyons on the beta-induced eddy currents and gravity currents, produced by local mass source upon the sloping bottom in the rotating fluid. Some experiments were provided with ridges on the cone and the others - with ridges and canyons on the plain sloping bottom. We used two kinds of obstacle: 1) with triangular cross-section and wide symmetric sloping sides; 2) with rectangular cross-section.

In the first case the quasibarotropic (beta-induced) and strongly baroclinic (gravity) currents were crossing the obstacles along the isobats without significant difficulties. The structure and velocity of these currents did not change considerably after crossing the obstacles. The currents were deflected down to the basic slope upon the upstream sides of ridges and up to the basic slope - upon the upstream sides of the canyons. Upon the downstream sides - vice versa (fig.3 and 4). So, after crossing such obstacles, the barotropic and baroclinic currents usually returned to the same isobatic level. The trajectory of the flow was quite equal for both types of currents. Only very thin gravity currents ($H / H_e < 10$) were displaced down to the basic slope under the friction effects (fig.6a).

In the second case (rectangular obstacles) there was a considerable reduction of the quasibarotropic flow velocity just before the obstacles. Also, the structure of the flow was changed by such obstacles. The large eddy column was formed just in front of the obstacle (canyon) and the recirculating zones appeared up and down to the basic slope. The quasi-isobatic eddy flow was transformed into the sheared and divergent flow directed along the axis of the rectangular canyon and no well pronounced eddies were observed from behind it (fig.5a,b). In the same case a gravity current was partly trapped in the rectangular canyon and a considerable part of denser water moved down to the flat bottom of the tank (fig.6b).

Finally, we should point out that only the obstacles with abrupt walls (the width of the wall was much less than the diameter of the eddy for quasibarotropic beta-induced currents, or it was much less of the local radius of deformation for gravity current) were able to slow down and to deflect irreversibly the mesoscale currents upon the rigid slope. It should be concluded that the steep local topography on the continental slope might enhance the mesoscale exchange processes between the shelf zone and deep ocean.

Acknowledgements. This work was partly supported by Russian Ministry of Science and Technology, RFBR grant N 96-05-65584, EC INTAS grant N 93-405 EXT, EC INCO-Copernicus grant N ERBIC15CT960111.

References.

- [1] R. Griffiths, 1983. *Inertial wave drag and the production of intense vortices by turbulent gravity currents with implications for sinking of bottom waters*. Ocean Modeling, **50**, 9-12.
- [2] J. Whitehead, M. Stern, G. Flierl and B.Klinger, 1990. *Experimental observations of baroclinic eddies on a sloping bottom*. J.Geophys. Res., **95** (C6), 9585-9610.
- [3] M. Davey and P. Killworth, 1989. *Flows produced by discrete sources of buoyancy*. J.Phys. Oceanogr., **19**, 1279-1290.
- [4] Yamagata, T., Sakamoto, K. and Arai M. 1990 *Locally induced nonlinear modes and multiple equilibria in planetary fluids*. PAGEOPH., **133** (4), 733-748.
- [5] H.Greenspan, 1968. *The theory of rotating fluid*. Cambridge Univ. Press, London and New York.
- [6] A. Zatsepin, and V. Didkovskii, 1996. *About one mechanism of mesoscale vortex structure formation in the ocean sloping bottom zone*. Doklady Akademii Nauk, **347** (1), 109-112 (in Russian).
- [7] A. Zatsepin, V. Didkovskii, A. Semenov, 1998. *Self-oscillatory mechanism of periodic vortical structure formation from stationary local source on the sloping bottom in rotating fluid*. Okeanologiya, **34** (1), 47-55 (in Russian).

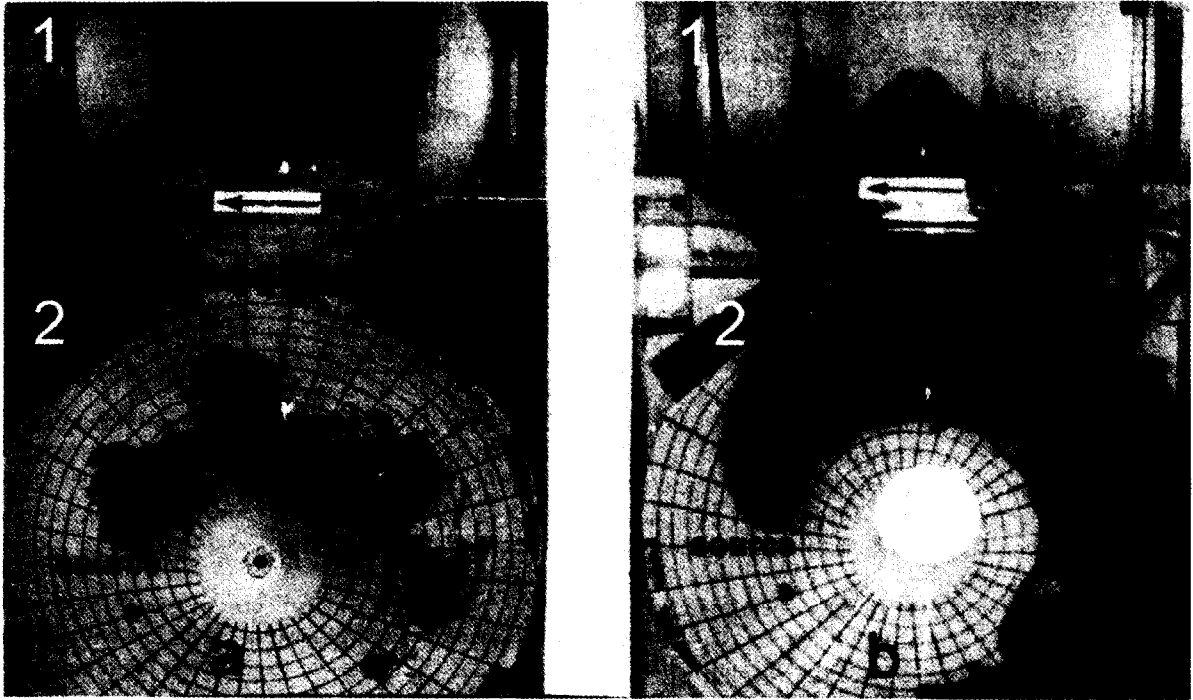


Figure 1. a) barotropic ($V_g/V_b \sim 0$) and b) baroclinic ($V_g/V_b = 0.4$) mesoscale currents produced by the local mass source upon the sloping bottom in rotating fluid; 1 - side view, 2 - top view. The depth of the fluid $H_0 = 18$ cm, the distance between the circles at the cone - 2 cm. The arrow indicates the direction of basic rotation.

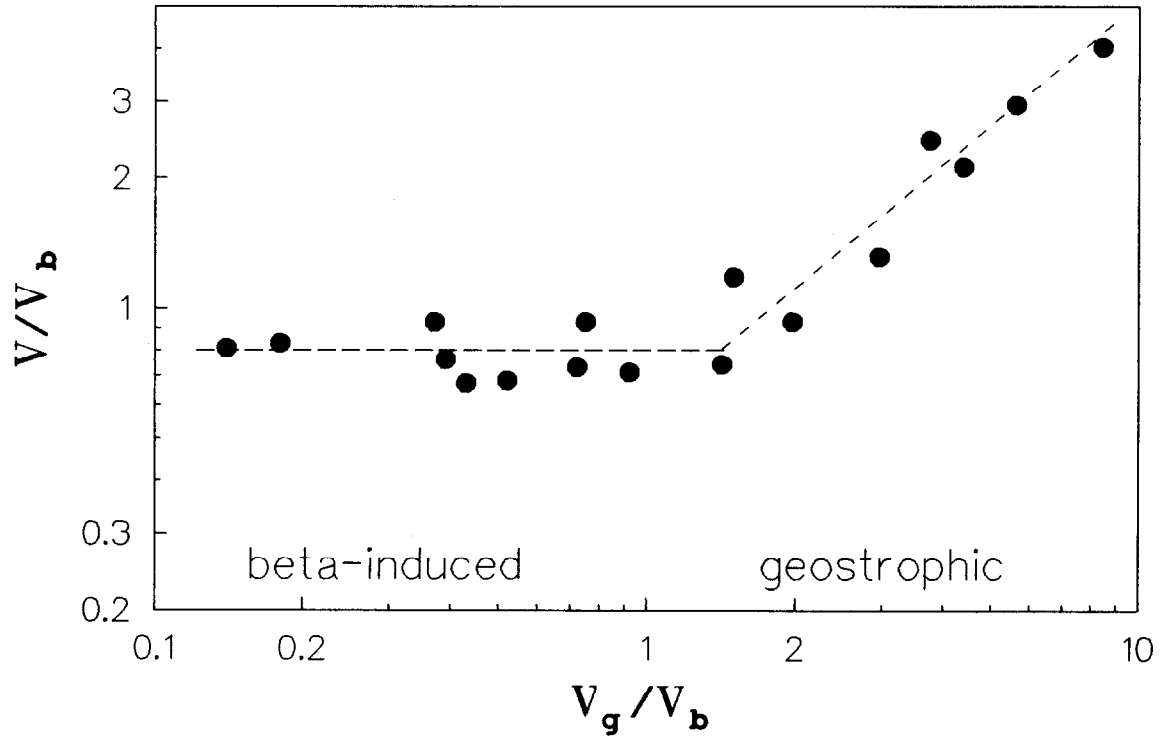


Figure 2. The ratio of isobatic velocity component of dense water flow to the beta-drift velocity (V/V_b) versus the ratio of geostrophic velocity scale to the beta-drift velocity scale (V_g/V_b).

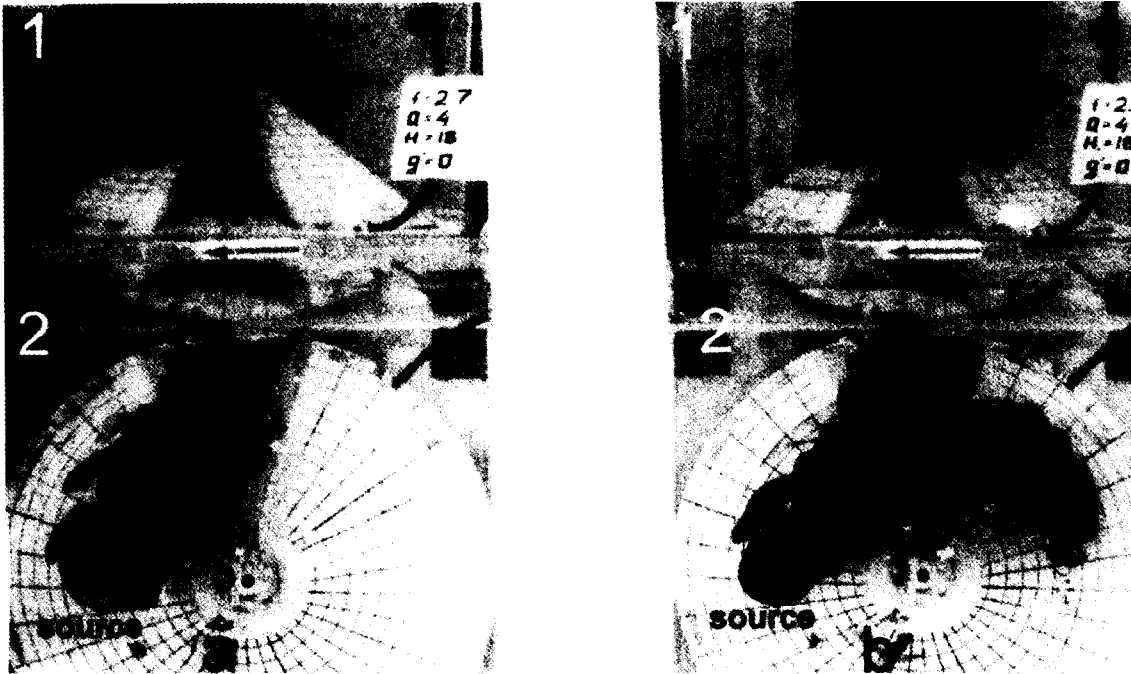


Figure 3. The side (1) and top (2) views of the beta-induced, quasibarotropic ($V_g/V_b \sim 0$) current upon the cone with downslope triangular ridge: a) before the ridge; b) after crossing it.

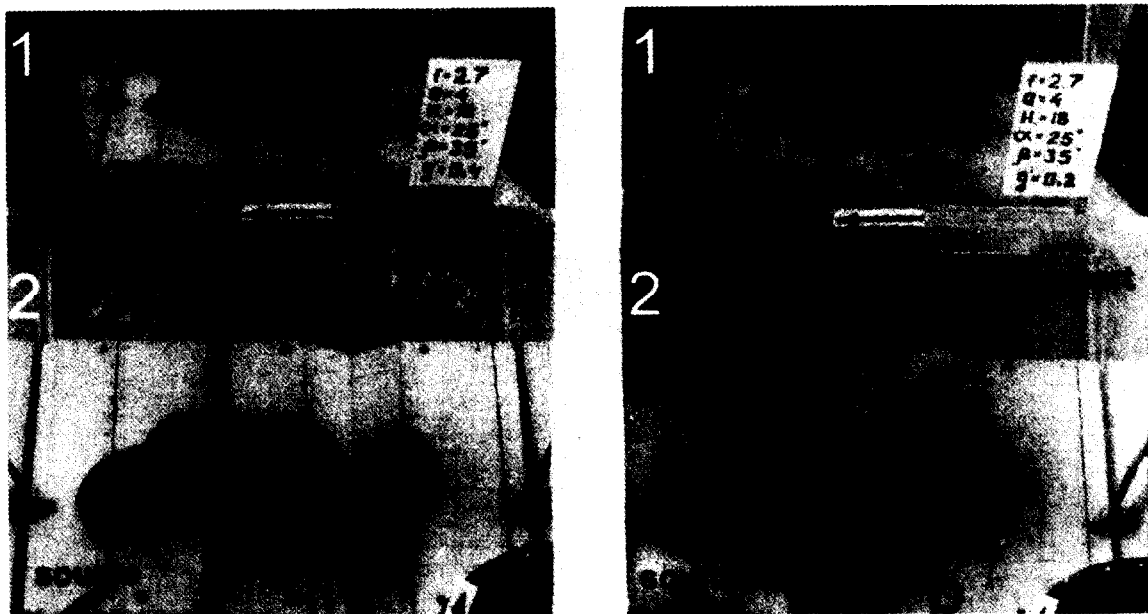


Figure 4. The side (1) and top (2) views of the beta-induced current upon the flat sloping bottom with downslope triangular : a) canyon ($V_g/V_b = 0.3$); b) ridge) ($V_g/V_b = 0.15$). The width of the canyon (ridge) - 10 cm, its depth (height) at the central line - 3.5 cm, $H_0 = 18$ cm, the slope - 25° .

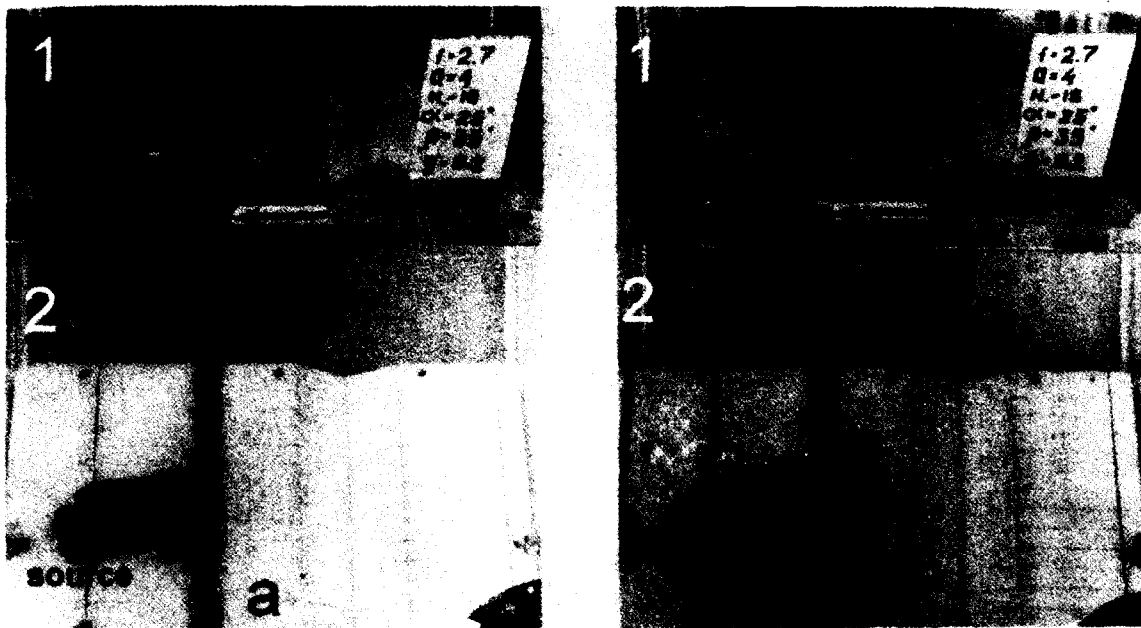


Figure 5. The influence of the downslope rectangular canyon on the structure of the beta-induced current ($V_g/V_b = 0.15$) upon the flat sloping bottom at two consequent moments of time: a) $t = 35$ c; b) $t = 115$ c. The width and depth of the canyon - 2 cm, $H_0 = 18$ cm, the slope - 25° .

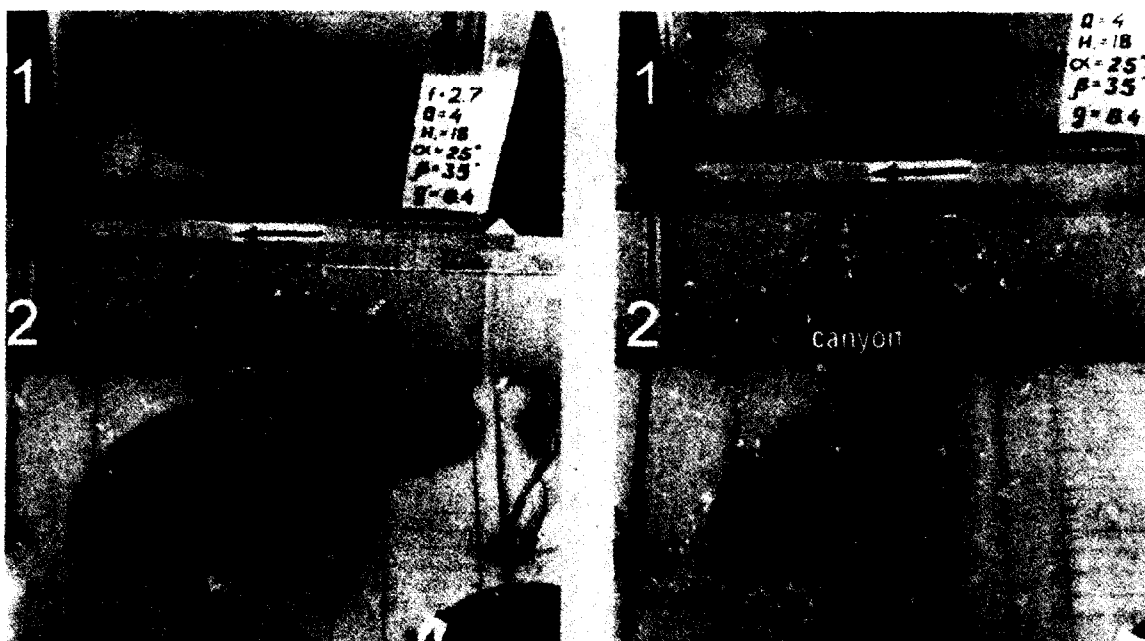


Figure 6. The influence of canyons on the structure of the gravity current ($V_g/V_b = 4.8$) on the flat sloping bottom. a) the triangular canyon; b) the rectangular canyon. (1) - the side view; (2) - the top view. $H_0 = 18$ cm, the slope - 25° .

A BALANCE MODEL OF THE UPPER QUASIHOMOGENEOUS LAYER: THE BLACK SEA CITED AS AN EXAMPLE.

Dikarev S.N.¹, Poyarkov S.G.¹, Korolkov K.²

¹ P.P.Shirshov Institute of Oceanology, 36, Nakhimovsky Pr., Moscow 117851, Russia.

² Moscow Institute of Physics and Technology, 9, Institutskii per., Dolgoprudnii city, Russia.

Abstract. The turbulent mixed layer formation mechanism is demonstrated in the series of laboratory experiments. When the sufficiently intensive tap water jet fell down into the vessel the quasihomogeneous foam layer appeared. It is shown, that the depth of the foam layer is not only proportional to the Monin-Obukhov length scale, as usually one suggests for the ocean conditions. It is also proportional to the square root from the Reynolds number. A simple box balance model of the upper quasihomogeneous layer (UHL) is considered. It is used for the obtaining of the UHL depth and salinity relationships from the external parameters. On the basis of the Black Sea data review the numerical estimations of the UHL physical state are obtained.

Introduction.

In a hydrological box models the internal structure is usually treated as a not essential feature of the system and simply assumed to be isotropic. Commonly these models are applied to mass, passive trassers transfer via a water basin (like a semi-enclosed sea) and are aimed to find regularities in the steady state regimes [2]. One may formulates the main problem as follows: what is the integral output of the system for the externally defined input? This approach is suited well for water, salinity and passive scalar budgets of the basin, but problems arise when a chain of interacting boxes is considered for the sake of better discription. In this case it seemes to be important to get an additional characteristic parameter of the system. If now remember that the externally driven mechanical energy flux always exists in natural conditions, then we come up to a class of layer models (two-layers is the simplest one) with the depth of an upper homogeneous layer (UHL) as a characteristic parameter. In this situation the standart way is to split the initial one box for the whole basin into two at least. To our mind it is worth considering just the same box with the internal two-layers vertical structure. This prevents us from multiplying problems by the number of boxes and allowes to use an additional parameter (UHL depth) in the budget relationships. So in this paper we analyse in some details two-layers box model keeping in mind it perspective role as an element in a few boxes chain buildings for their applications to the semi-enclosed seas.

Laboratory-scale UHL image or "a beer pouring" effect.

The UHL formation mechanism is illustrated in the series of simple preliminary laboratory experiments. The sufficiently intensive tap water thin jet fell down into the narrow tube-like vessel and the quasihomogeneous air-water foam layer appeared and kept steady. (In case of beer it is wellknown to everybody that the foam is used to present in a glass according to almost all intensities of pouring.) We did not interested in the specific and fearly complex mechanism of the foam formation itself, but the point is that in terms of buoyancy and turbulent energy fluxes the foam layer may be realised quite similar to the upper homogeneous layer (UHL) of the sea.

Physically treated the steady depth of the foam layer (h_f) is the consequence of the equality of the water entrainment rate into the foam and the overall income rate of tap water. In the set of experiments we mostly varied only one external driving parameter: Q - the volumetric income jet water flux. Of course, Q was constant throughout each experiment. Assuming that h_f is equal to the Monin-Obukhov length scale (h_{MO}), i.e. $h_f = h_{MO} = E^{3/2}/B$, where $E = E_0 \eta (r_0/r)^2 = 0.5 W_0^2 \eta (r_0/r)^2$ - part of the falling water jet kinetic energy (E_0), $B = Wg' = Wg(\rho - \rho_f)/\rho = Wgh_a/h_f = Q(\pi r^2)^{-1} gh_a/h_f$ - buoyancy water flux, $\eta = \eta_0 f(Re)$ - the efficiency coefficient of the process, depending on the jet Reynolds number $Re = W_0 r_0 / \nu$. Here r_0, r, W_0, W - radii and mean vertical velocities of water jet and the lab vessel, ρ, ρ_f - water and foam densities, h_a - experimentally measured depth of air occurring in the vessel after switching the jet off at the end of each observation. h_a has been chosen because it can be measured much more accurately than h_f . For experimental parameters: $2r_0 = 0.43$ (cm), $2r = 5.5$ (cm), $40 < Q < 150$ (cm^3/s) and water kinematic viscosity $\nu = 10^{-2}$ (cm^2/s), the measured depth varied in the range $1 < h_a < 30$ (cm) for $Re = O(10^4)$.

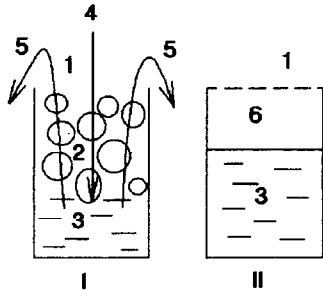


Fig. 1. Laboratory scheme:
1- air, 2- foam, 3- water, 4- falling water jet, 5- water outflow, 6- air entraining into the foam.
I- quasistationary stage,
II- final stage.

$h_a = \text{const } Q^{5/2}$ (coefficient of regression 0.98) in terms of the process efficiency coefficient: $\eta = \eta_0 Re^{1/3}$, where $\eta_0 = (1.7 \pm 0.2) 10^{-2}$. We would like to stress out that beyond doubt these numerical values depend on many factors such as the dissolved gas content, for example.

So, nevertheless the experimental setup was very simple, we have got a fearly "condensed" result which can be reasonably treated. It also gave us a sort of physical lab image of the natural UHL, showing on the real object how the Monin-Obukhov length scale could be simply incorporated into a hydrological box model of a semi-enclosed sea.

Elementary two-layers box model.

In a two-layers box structure only upper one is active in the sense of turbulent mixing of incoming buoyancy fluxes. Basically we will deal with this active layer.

Problem formulation. Let's consider a vertically homogeneous water layer in the steady state under the gravity force. There are two sources of buoyancy in the layer which bring salt water (S_1, S_2) with rates (W_1, W_2) respectively. The externally driven turbulent energy flux (Q_K) is spent in the layer on mixing process to the constant salinity (S) through its depth (h). It is needed to find the relationships between the external and internal problem parameters.

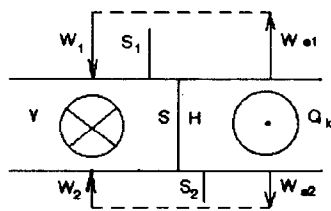


Fig. 2. Model scheme.

Budget equations must be balanced for water, salt and turbulent energy.

One can easily obtains the relationships:

$$S_1 W_1 + S_2 W_2 = S(W_1 + W_2), \quad (1)$$

$$2h W_1 W_2 g (S_2 - S_1) = Q_K (W_1 + W_2), \quad (2)$$

where - coefficient of salinity shrinking for the salt water equation of state, also $S_2 > S_1$.

Physically the steady state of our thermodynamically open layer climbs its lower (and upper) boundaries to stay still.

The usually used 'energy' approximation of the turbulent entrainment rate [3], $W_e/W' \propto Ri^{-1}$ for (1),(2) is equivalent to $W_{1e}/W_{e2} = W_1/W_2$. This demonstrates the internal dynamic boundary balance of the layer.

In order to represent the dependences of two internal (S, h) on five external (W_1, W_2, S_1, S_2, Q_K) dimensional parameters it is worth to use the nondimensional form. Let $W_{1,2} = V w_{1,2}$, $S_{1,2} = \Delta S s_{1,2}$, $h = h_{MO}' H$, with the scaling $V = W_1 + W_2$, $\Delta S = S_2 - S_1$, $h_{MO}' = Q_K / (Vg \beta \Delta S)$. Then (1),(2) take the form:

$$s-s_1-w_2=0, \quad (1')$$

$$2hw_1w_2=1, \quad (2')$$

with the condition $w_1+w_2=s_1-s_2=1$. This leads to a universal function

$$y=(2x(1-x))^{-1}, \quad x < 1, \quad y > 2, \quad (3),$$

where x may represent nondimensional velocities or salinity differences across the layer boundaries and y - nondimensional layer thickness or a time period. The latter could be introduced as $T=T'$, $T'=h/V$ - the time scale of the process which we need to consider if dealing with quasistationary way of environmental changes. Function (3) is convenient for an analytical analysis: $y(x)$ - is symmetric with respect to the line $x=0.5$ and $H > 2$, for example. The geometric appearance of (1'),(2') may be shown on the s - w diagram.

All the above description is obviously corresponds to the condition when the overall depth of the basin (H_0) is more then mixed layer depth, i.e. $2h_{MO}' < h < H_0$, that is why this regime of 'deep basin' takes place if $h_{MO}'/H_0 = Q_K/(H_0 V g \beta \Delta S) < 0.5$. This elementary model can be generalised for a number of buoyancy sources and a chain of boxes which seams to be important for accurate field applications.

The Black Sea example.

It may be of some interest to realise what sort of real semi-enclosed sea description we come up to with the proposed two-layers model applied to the whole basin. As a first approximation we ignore the Black-Azov seas exchange processes (the Azov sea salinity $S_A = 10 \text{ ‰}$, volumetric water exchange fluxes via Kerch strait $U_{BA} = 33.4 \pm 5 \text{ (km}^3/\text{y)}$, $U_{AB} = 49.8 \pm 8 \text{ (km}^3/\text{y)}$, [4]). One can get estimations of mean external parameters values ($_{[4,5]}$), although they turn out to be quite different even in the summary reviews [4, 5]:

a) for salinities:

$S_1 = 0$ - rivers (Danube) and precipitation salinity input,

$S_2 = 37 \text{ ‰}$ - salinity input through the strait of Bosforous;

b) for water velocities (W) estimations the volumetric values (U) should be divided by the Black sea area ($A_B = 4.2 \times 10^5 \text{ km}^2$), so $120 \text{ (km}^3/\text{y)} \leftrightarrow 10^{-6} \text{ (cm/s)}$:

$U_1 = U_r + U_p - U_e$, where the right-hand part contains in order rivers discharge, precipitation and evaporation ,

$U_{[14]} = 338 \pm 52 + 237.7 \pm 38 - 395.6 \pm 42 = 180 \pm 132 \text{ (km}^3/\text{y)}$,

$U_{[15]} = 350 + 300 - 350 = 300 \text{ (km}^3/\text{y)}$;

$U_2 = U_{in}$ - Marmara sea salt water input through the strait of Bosforous,

$U_{2[4]} = 176 \pm 36 \text{ (km}^3/\text{y)}$, $U_{2[5]} = 300 \text{ (km}^3/\text{y)}$;

c) for turbulent energy flux $Q_K = 0.5 - 5 \text{ (cm/s)}^3$, we assume the parametrisation $Q_K = ((C_D \rho_a / \rho)^{1/2} u_{10})^3$, where u_{10} - the wind velocity at 10 meters high, $C_D = (3-5) \cdot 10^{-3}$ - a drag coefficient for the range $5 < u_{10} < 10 \text{ (m/s)}$, ρ_a , ρ - air and water dencities [6].

The internal basin parameters could be estimated :

$S = 17.1 \text{ ‰}$ - the upper layer salinity,

$V = U_{out}$ - Black sea water output through the strait of Bosforous, $V_{[4]} = 371 \pm 58 \text{ (km}^3/\text{y)}$, $V_{[5]} = 600 \text{ (km}^3/\text{y)}$.

In spite of considerable discrepancy in V the salinities of the upper layer are close together: $S_{[4]} = 17.3 \text{ ‰}$, $S_{[4]} = 18.5 \text{ ‰}$. Actually it is no surprise, because not all components of the water budget (such as evaporation) have been measured independently. The depth thickness estimates from (2) gave $h = 2h_{MO}'$, $h_{[5]} = 60 - 600 \text{ (m)}$, which is comparable with upper quasihomogeneous layer mean depth $O(100 \text{ m})$ in the winter time ($h_{[4]}/h_{[5]} = V_{[5]}/V_{[4]} = 1.6$). The time scale $h/V = O(100y)$ is unreasonably big, but if remember that the lower layer of the Black sea has the salinity $S_2' = 22 \text{ ‰}$ because of incoming plume salt water mixing in the vicinity of the Bosforous strait, then easily find $V' > W_1 + W_2 (S_2 - S) / (S_2' - S) = 2.5V$ and so the time scale $l(y) < T' < 40(y)$. It is clear that the sesonal cycle of the heat flux could be filtered out asuming the net heat balance allthough the amplitude of buoyancy variability due to the heat flux is an order of magnitude bigger then from the salt input.

It is evident now that the two-layers box model may be useful for some estimations of the hydrologic changes (tendencies) in the semi-enclosed sea on a climatic time scale. The model sensitivity to the wind velocity makes it preferable to use relative values of the upper homogeneous layer depths if the few boxes chain is considered. This is the matter for the future work.

References.

1. Evolution of Physical Oceanography. Scientific surveys in honor of Henry Stommel, 1981, B.A.Warren, C.Wunsh (editors), MIT Press, 623pp.
2. W.S.Broecker, Geochemical tracers and ocean circulation, in [1], p.434.
3. J.S.Turner, Small-scale mixing processes, in [1], p.236.
4. Applied ecology of sea regions. The Black sea, 1990, pp. 11-34, (in Russian).
5. E.Ozoy, U.Unluata, 1997, Oceanography of the Black sea: a review of some recent results, in: E.Ozoy, A.Mikaelyan (editors), Sensitivity to Change: Black Sea, Baltic Sea and North Sea, NATO ASI Series, Kluwer Academic Publishers (in print).
6. H.Charnock, Air-sea interaction, in [1], p.482.

SEASONAL AND INTERANNUAL SST VARIABILITY OF THE NORTH-EAST ATLANTIC OCEAN

S. Djenidi¹, A. G. Kostianoy², N. A. Sheremet² and A. Elmoussaoui¹

¹ GeoHydrodynamics and Environment Research (GHER), University of Liege, B-5 Sart Tilman, B-4000, Liege, Belgium, E-mail: sdjenidi@ulg.ac.be

² P.P. Shirshov Institute of Oceanology, 36 Nakhimovsky Pr., 117851 Moscow, Russia
E-mail: kostianoy@glasnet.ru

Abstract. "ACURATE" (African Coastal Upwelling Research, Analysis and Thematic Experiments) is a new European International long-term programme launched during summer 1997. Part of this Programme is devoted to the investigation of thermal variability of large area of the Atlantic Ocean located between 5-45°N and 25°W - coast of Africa and Europe. 1982-1992 weekly satellite SST data set has been analysed to study seasonal variability of SST field, its variance, SST gradients (position and intensity of thermal fronts), seasonal cycles of mean SST and SST difference between coastal and oceanic waters (upwelling index for 100-500 km distance), as like as seasonal variability of SST field for the Cape Blanc and the Cape Ghir regions (North-West Africa). The study has been coupled with analysis of seasonal variability of the wind stress and of total heat fluxes over the region.

Introduction

North-West and South-West African upwellings are the largest and most important upwelling zones in the Atlantic Ocean. Their persistency and seasonal variability are conditioned by the Azores and South Atlantic Anticyclones forcing. Since sixties numerous oceanographic investigations have been made in the East Atlantic Ocean which revealed general circulation and water mass distribution, basic upwellings characteristics and regional peculiarities, structure and variability of upwelling fronts, Cape Verde and Angola-Benguela Frontal Zones (ABFZ), and etc.

During the 1980s, syntheses and overview of research relating the physical oceanography of the upwelling zones and adjacent areas appeared [1,2]. Satellite data (thermal and colour imagery) have changed our view on the mesoscale structure and variability, physical and biological processes in the surface layers of the West African upwellings. For example, discovery of cold and chlorophyll-rich offshore flowing filaments [3], short-period pulsing of the upwelling fronts, ABFZ and local upwelling cells was made possible by the advent of satellite remote sensing technology.

Essential progress have been achieved in the understanding of physical and biological functioning of these upwelling zones as large-scale systems. Now it is well known that these zones are the regions of high physical energy and biological activity (fishery). They are characterized by different hydrodynamic regimes related with atmospheric forcing, air-sea interactions, solar radiation, surface and bottom stresses, currents, buoyancy and material fluxes at the boundaries, bottom topography etc. These regions are coupled with the surrounding deep ocean by exchanges across the shelf break and upwelling fronts involving transport of heat, mass, momentum, vorticity, suspended matter, chemical and biological constituents, and pollution.

Nevertheless we have to enrich our fundamental knowledge on the large- and mesoscale hydrophysical and hydrobiological processes, on seasonal and interannual trends of thermal regime, on atmospheric forcing, on El Nino type phenomena in the East Atlantic Ocean and their relationships with global parameters. All this is also important for fishery and ecology of the coastal zones of West Africa.

ACURATE

"ACURATE" (African Coastal Upwelling Research, Analysis and Thematic Experiments) is a new European International Long-Term Programme launched during summer 1997 by GeoHydrodynamics and Environment Research (GHER) of the Liege University and P.P.Shirshov Institute of Oceanology (Moscow, Russia). Programme is devoted to the investigation of thermal variability (general characteristics, large-scale fronts, upwelling fronts, filaments and cells, etc.) of the NE Atlantic Ocean located between 5-45°N and 25°W - coast of Africa and Europe (Portugal) and the SE Atlantic Ocean located between 10-35°S and 5°E - coast of Africa. Among others we distinguish the following pressing problems that we intend to investigate:

1. El Nino type phenomena in the Atlantic Ocean.

ENSO in the Pacific Ocean is well known, but there are a lot of questions concerning the existence of the analog in the South Atlantic Ocean and for the most degree in the North Atlantic Ocean. Still there are no clear definition, methodics of detection, indicators of El Nino activity in the Atlantic Ocean, understanding of its impact on the upwelling zones, ecosystems and fishery, and relationships with the Pacific ENSO (e.g. [4,5]). Since Kudersky and Berenbeim [6] new promising results on that problem, including the correlation of El Nino events with variations of solar activity and Earth rotation velocity have been obtained.

2. Systems of upwelling filaments.

The most important and energetic mesoscale structures of the upwelling regions are nonstationary filaments. Ginzburg and Fedorov [3] first reported the observations of filaments in the World Ocean. Kostianoy [7,8] reviewed Canary and Benguela upwelling filaments. They represent the most effective mechanism of seaward transport (1 m/s, 1-2 Sv) of water, nutrients and plankton biomass from the coastal zone, and that this transport contributes significantly to production offshore (e.g. [9]). Complete systems of filaments along coasts of Portugal, NW and SW Africa, their characteristics, three-dimensional structure, seasonal and spatial variability are hardly investigated [7-13]. Moreover, we still don't know the physical nature (generation mechanism) of upwelling filaments.

3. Cross-frontal water exchange.

Filaments represent a very effective mechanism of transport of coastal water to the open ocean (sea), that is very important for the biology, fishery and ecology of the upwelling regions. Zatsepin and Kostianoy [14] proposed an original method of cross-frontal water exchange estimations that permit to calculate the permeability of upwelling fronts conditioned by filaments. Kostianoy and Zatsepin [15] showed that up to a half of water mass upwelled by Ekman pumping process in the coastal zone is transported by filaments to the open ocean. The united scheme of seasonal variability of upwelling frontal zones permeability from Portugal to Cape Town is of vital importance.

4. Three-dimensional numerical model.

There is no 3D numerical model that was implemented directly to the most intense upwelling regions of West Africa. Such model is in the list of primary needs. Elaboration of the model that will be fully three dimensional (multi level) primitive equation model, free surface, time dependent, non linear, baroclinic, that will include real topography, wind stress and heat fluxes is a very difficult task. The GHER base model of the Liege University which has been already implemented to several sites of the World Ocean in different conditions, is meant to be an appropriate candidate to tackle the relevant problems addressed by the proposed Project [16,17].

First results

First part of this Programme is devoted to the investigation of thermal variability of the NE Atlantic Ocean located between 5-45°N and 25°W - coast of Africa and Europe (Portugal). 1982-1992 weekly satellite sea surface temperature (SST) data set of about 16 km resolution has been analysed to study seasonal and interannual variability of the upper ocean thermal regime. First step study concerned:

1. Analysis of seasonal variability of SST (Fig.1), SST variance (Fig.2) and SST gradients (position and intensity of thermal fronts) (Fig.3) distribution.
2. Analysis of seasonal cycles of the mean SST for the whole region of investigation to determine climatological trends in 1982-1992 (Fig.4,5).
3. Analysis of seasonal cycles of SST difference between coastal and oceanic waters (upwelling index for a 100-500 km offshore distance) in 1982-1992 (progress of the research done in [18]).
4. Combined analysis and correlation of seasonal variability of SST characteristics with a wind stress variability and total heat fluxes over the regions off North-West Africa.
5. Special analysis of seasonal variability of SST distribution for the Cape Blanc and the Cape Ghir regions of North-West Africa for use in the numerical 3D GHER Model.
6. Search for the signatures of the Cape Ghir upwelling filaments in the SST Data Bank (1982-1992).

Mean SST fields for all seasons of 1982-1992 time period revealed characteristic tongue of relatively cold water to the south associated with the Canary Current (Fig.1). The Capes Blanc (21°N) and Ghir (31°N) regions, as like as south-western area off the Gibraltar Strait were found to be distinct by SST regime from adjacent areas (Fig.1). It is well known that the Cape Blanc region is the most intense and persistent upwelling area of NW Africa throughout the year [18,19]. 3D GHER numerical model is being implemented now to this region to study seasonal and short-period variability of thermohaline characteristics, currents and of upwelling frontal zone structure and intensity [20,21]. Another cold region (<21°C) located in front of the Cape Ghir (31°N) is distinguished by a persistent generation of the upwelling filaments in summer [7,10,12] that results into a clear "cold" climatologically significant signal (Fig.1b). South-western area off the Gibraltar Strait is characterized by a "warm" climatological signal (>22°C) conditioned by high heat fluxes, low wind stress, absence of upwelling, and weak circulation leading to the stagnation zone (Fig.1b).

SST variance for all seasons of 1982-1992 time period revealed a dominant maximum between 10 and 20°N (Fig.2) related with a variability of a coastal upwelling and the Cape Verde Frontal Zone position and intensity [22]. SST variance in winter has values <1.6°C which are basically located southward of 30°N (Fig.2a) and are associated with interannual and intraseasonal SST variability. Northward of 30°N SST variance is less than 1°C. In summer SST variance maximum of 2.2°C shifted northward to the region between 15 and 20°N which is probably related to the seasonal variability of an upwelling and the Cape Verde Frontal Zone position (Fig.2b). Besides that northward of 25°N SST variance now is quite notable (1.2-1.6°C).

Fig.3 shows mean distribution of SST gradients in winter and summer. In winter (Fig.3a) there are two distinct zones with gradients higher than 0.01°C/km: the first one is located northward of 35°N and is related to the Azores Frontal Zone, the second one is located southward of 25°N and is related to the Cape Verde Frontal Zone and the upwelling front along the coast of Africa. It is well known that maximum of the Canary upwelling intensity is located southward of 25°N in winter and then moves northward and reaches the coast of Portugal in summer, being strong throughout the year between 20 and 25°N [1,2,23]. This scheme of seasonal movements of the upwelling intensity is in a good correlation with SST gradient distribution in summer (Fig.3b). Some patches of high gradients are still seen in the north-western corner of the area, but they are not so coherent like in winter.

We analysed seasonal cycles of the mean SST for the whole region of investigation to determine climatological trends in 1982-1992 (Fig.4,5). Seasonal and interannual variability of a mean SST calculated for a whole region of investigation is demonstrated in Fig.4. The diagram shows very warm winters in 1987 and 1988 and unusually long and warm summer in 1989. Fig.5a demonstrates year to year variability of a mean SST seasonal cycles. It clearly revealed a warming of a whole area by about 1°C since 1982 till 1987 with subsequent slow cooling till 1993 (Fig.5a). Superposition of all eleven seasonal cycles gives a supplementary information on the ranges of SST variability in every season as well as on the beginning, duration and finishing of every season (Fig.5b).

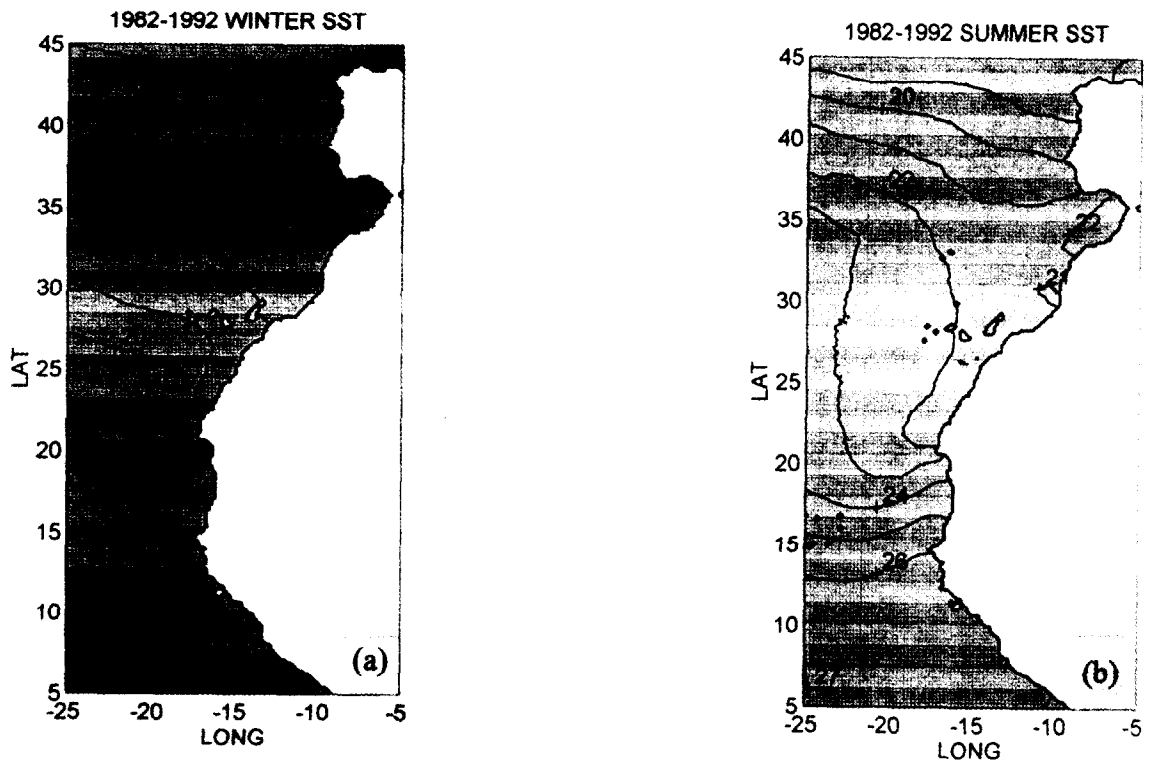


Fig.1. Mean SST ($^{\circ}\text{C}$) field for (a) 1982-1992 winters (January-March) and (b) 1982-1992 summers (July-September).

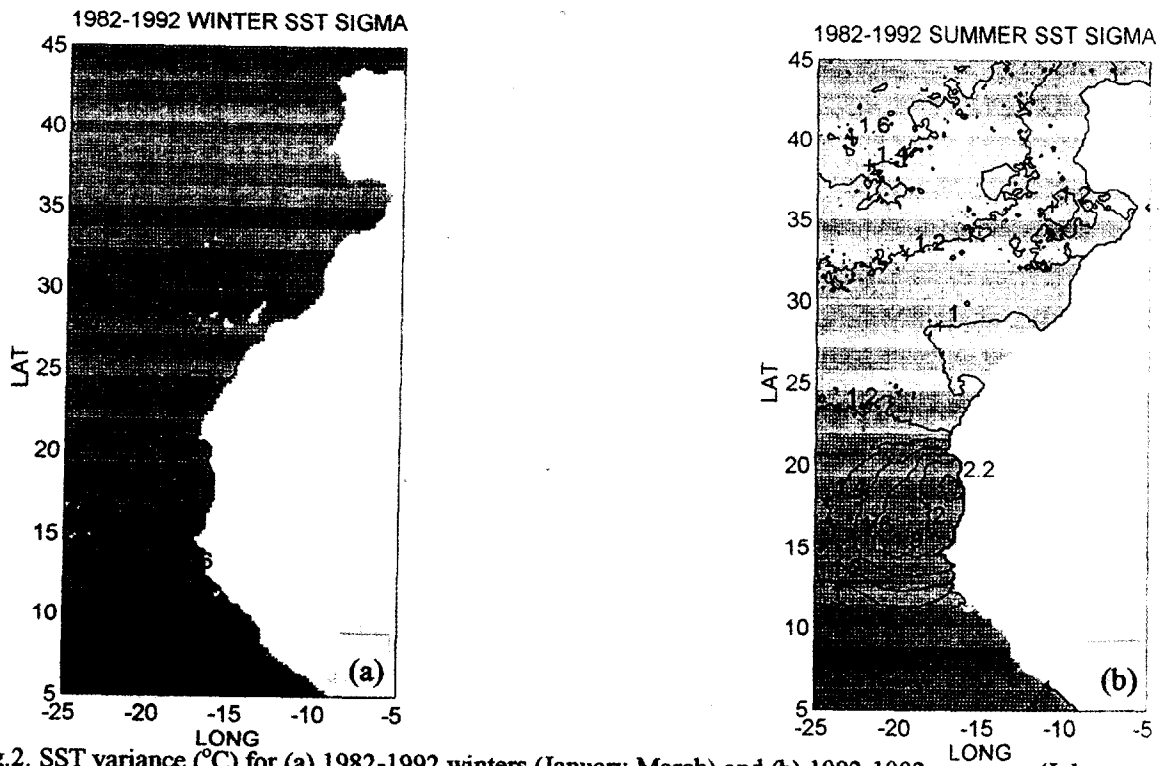
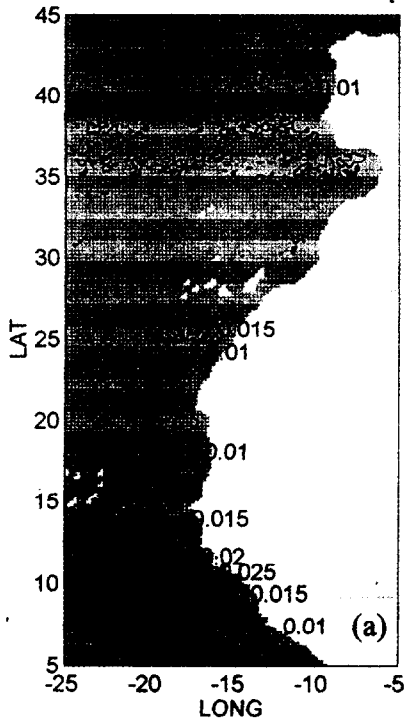


Fig.2. SST variance ($^{\circ}\text{C}$) for (a) 1982-1992 winters (January-March) and (b) 1982-1992 summers (July-September).

1982-1992 WINTER SST GRADIENT [C/KM]



1982-1992 SUMMER SST GRADIENT [C/KM]

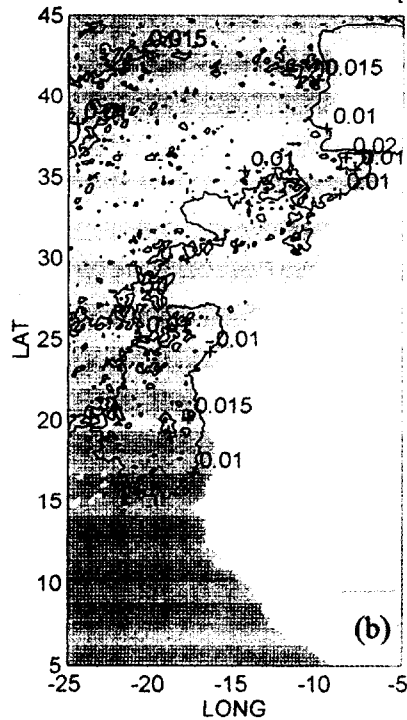


Fig.3. Mean SST gradient ($^{\circ}\text{C}/\text{km}$) for (a) 1982-1992 winters (January-March) and (b) 1982-1992 summers (July-September).

SEASONAL VARIABILITY OF MEAN SST (5-45N, 5-25W)

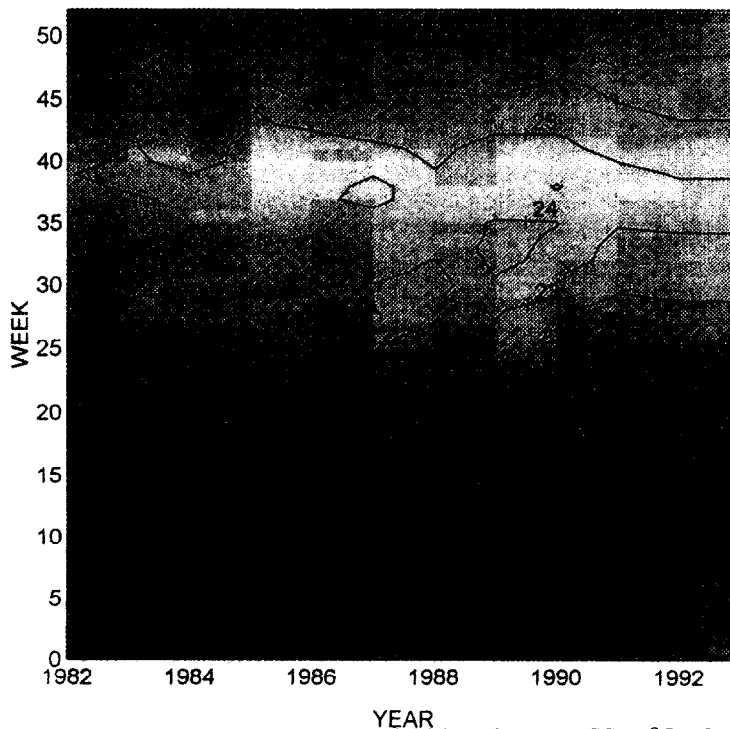
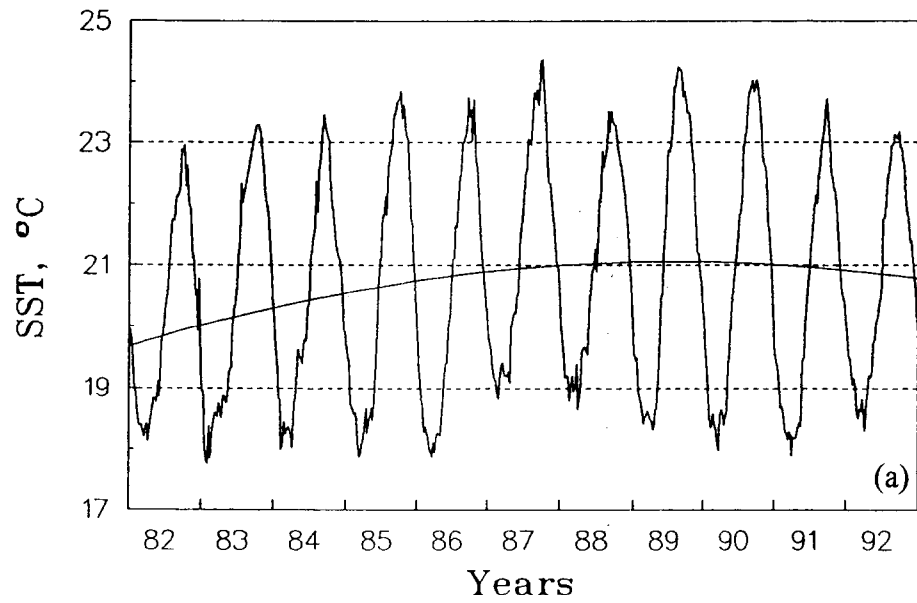


Fig.4. Diagram of seasonal and interannual (1982-1992) variability of mean SST ($^{\circ}\text{C}$) for a whole region 5-45 $^{\circ}\text{N}$, 5-25 $^{\circ}\text{W}$.

Mean SST for region 5-45N, 5-25W



$$19.67 + (x * 1E-03) - (x * x * 1.8E-07)$$

Seasonal variability (1982-1992) of the mean SST for region 5-45N, 5-25W

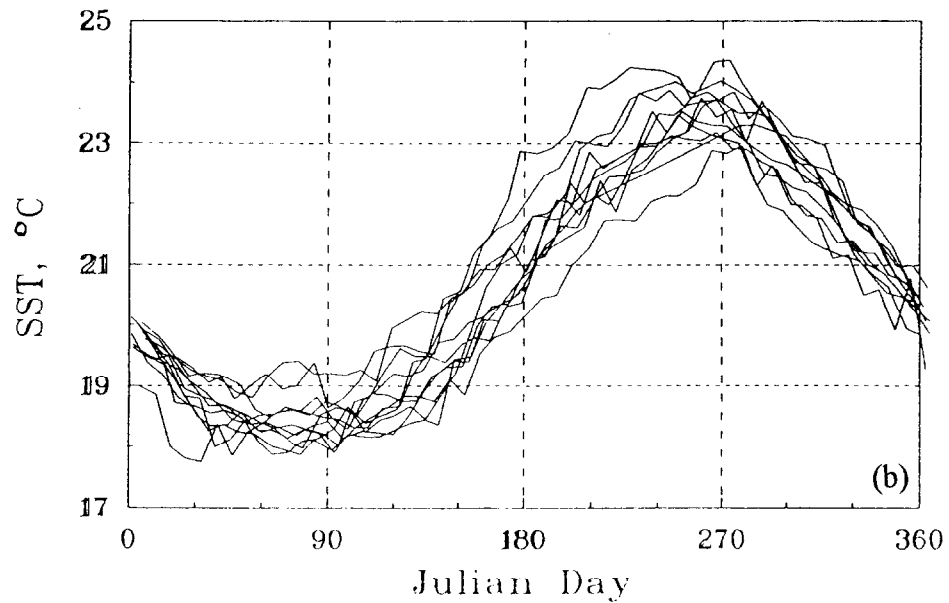


Fig.5. Seasonal cycles of mean SST (°C) for a whole region 5-45°N, 5-25°W in 1982-1992: (a) interannual variability, (b) seasonal variability.

Acknowledgements:

The research was partly supported by the International Project "Upwelling" of the Russian Ministry of Science and Technologies and by the "Commissariat Général aux Relations Internationales" (CGRI) of the "Communauté Française de Belgique".

References:

1. Mittelstaedt E., 1983, The upwelling area off Northwest Africa - a description of phenomena related to coastal upwelling, *Prog. Oceanog.*, 12, 307-331.
2. Mittelstaedt E., 1991, The ocean boundary along the northwest African coast: Circulation and oceanographic properties at the sea surface, *Prog. Oceanog.*, 26, 307-355.
3. Ginzburg A.I. and K.N. Fedorov, 1985, Systems of transverse jets in coastal upwellings, *Issled. Zemli iz kosmosa (Russian Journ. Remote Sensing)*, 5, 3-10 (in Russian).
4. Carton J.A., X. Cao, B.S. Giese and A.M. da Silva, 1996, Decadal and interannual SST variability in the Tropical Atlantic Ocean, *J.Phys. Oceanogr.*, 26, 1165-1175.
5. Enfield D.B. and D.A. Mayer, 1997, Tropical Atlantic sea surface temperature variability and its relation to El Nino - Southern Oscillation, *J.Geoph. Res.*, 102 (C1), 929-945.
6. Kudersky S.K. and D.Ya. Berenbeim, 1987, Global phenomenon El Nino, fishery and Earth rotation velocity, *Trudy AtlantNIRO*, 46-54 (in Russian).
7. Kostianoy A.G., 1991, The system of the Canary upwelling filaments, *Issled. Zemli iz kosmosa (Russian Journ. Remote Sensing)*, 5, 78-86 (in Russian).
8. Kostianoy A.G. and G.G. Boubnov, 1995, Investigation of the Benguela upwelling filaments basing on satellite data, *Issled. Zemli iz kosmosa*, 4, 67-75 (in Russian).
9. Gabric A.J., L. Garcia, L. Van Camp, L. Nykjaer, W. Eifler and W. Schrimpf, 1993, Offshore export of shelf production in the Cape Blanc (Mauritania) giant filament as derived from Coastal Zone Color Scanner imagery, *J.Geophys. Res.*, 98 (C3), 4697-4712.
10. Nykjaer L., L. Van Camp and P. Schlittenhardt, 1988, The structure and variability of a filament in the Northwest African upwelling area as observed from AVHRR and CZCS images, *Proc. IGARSS'88 Symp.*, Edinburgh, 1097-1100.
11. Fiuza A.F.G. and F.M. Sousa, 1992, Mesoscale variability in the Portuguese coastal ocean studied with satellite imagery, *Annales Geophys.*, 10(2), 208.
12. Hagen E., C. Zulficke and R. Feistel, 1996, Near-surface structures in the Cape Ghir filament off Morocco, *Oceanologica Acta*, 19 (6), 577-598.
13. Haynes R., E.D. Barton and I. Pilling, 1993, Development, persistence and variability of upwelling filaments off the Atlantic coast of the Iberian Peninsula, *J.Geophys. Res.*, 98.
14. Zatsepin A.G. and A.G. Kostianoy, 1992, On the intensity of cross-frontal water exchange in the ocean, *Doklady USSR Acad.Sci.*, 323(5), 949-952 (in Russian).
15. Kostianoy A.G. and A.G. Zatsepin, 1996, The West African coastal upwelling filaments and cross-frontal water exchange conditioned by them, *J.Mar.Systems*, 7, 2-4. 349-359.
16. Nihoul J.C.J., E. Deleersnijder and S. Djenidi, 1989, Modelling the general circulation of shelf seas by 3D k-e models, *Earth-Sci. Rev.*, 26, 163-189.
17. Beckers J.M., P. Brasseur, S. Djenidi and J.C.J. Nihoul, 1994, Investigation of the Western Mediterranean's hydrodynamics with the GHER three-dimensional primitive equation model, In: *The seasonal and interannual variability of the Western Mediterranean Sea*, P La Violette ed., *Coastal & Estuarine Studies*, 46, 287-324.
18. Nykjaer L. and L. Van Camp, 1994, Seasonal and interannual variability of coastal upwelling along northwest Africa and Portugal from 1981 to 1991, *J.Geoph. Res.*, 99 (C7), 14197-14207.
19. Hernandez-Guerra A. and L. Nykjaer, 1997, Sea surface temperature variability off north-west Africa: 1981-1989, *International Journal of Remote Sensing*, 18, 2539-2558.
20. Elmoussaoui A., S. Djenidi, A. Kostianoy and J.-M. Beckers, 1996, A numerical investigation in the transition zone of the NW African upwelling, *Bull. Soc. Roy. Sc. Liege*, 65, 1, 75-78.
21. Elmoussaoui A., S. Djenidi, A. Kostianoy, J.M. Beckers and J.C.J. Nihoul, 1999, Circulation and boundary processes off Northwest Africa, *This issue*.
22. Zenk W., B. Klein and M. Schroder, 1989, Cape Verde Frontal Zone, *Deep-Sea Res.*
23. Shaffer G., 1976, A mesoscale study of coastal upwelling variability off NW-Africa. "Meteor" *Forschungsergebnisse*, 17A, 21-72.

RIVER RUNOFF FRONTS IN THE SIBERIAN SHELF SEAS: STRUCTURE, FORMATION MECHANISMS AND ENVIRONMENTAL EFFECTS

I.Dmitrenko¹, P.Golovin¹, V.Gribanov¹, H.Kassens²

¹ State Research Center the Arctic and Antarctic Research Institute, 38 Bering Str., 199397, St.Petersburg, Russia, e-mail: dia@aari.nw.ru, fax: +(7) 812-352-26-88

² GEOMAR Research Center for Marine Geosciences, Wischhofstrasse 1-3, Bild. 4, D-24148, Kiel, Germany, e-mail: hkassens@geomar.de, fax: +(49) 431-600-28-50

Abstract. The formation mechanisms of the runoff fronts are investigated under the conditions of a predominant contribution of sea water salinity to the density field formation. Based on CTD-measurements, it is demonstrated that under the conditions of the Arctic Seas the fronts have a two-layer structure. The upper part to the depth of freshened water spreading (7-10 m) is baroclinic whereas the lower part up to the 30 m depth is sharply thermoclinic resulting from frontal convergence of surface warm water under the seasonal pycnocline. During the autumn-winter period the vertical heat exchange with the water layer below the seasonal pycnocline in the zones of summer location of the runoff fronts influences the formation of ice conditions.

1. Introduction

The freshwater discharge and its spreading in the Arctic shelf seas have a decisive effect on the formation of the ice and hydrological regime. The Ob' and Yenisey Rivers (Kara Sea) are second in the world by their mean annual runoff volume - 1428 km³/year, and the Lena river (Laptev Sea) with the 650 - 700 km³/year volume is at the fifth place. 70-80% of the total runoff falls on two summer months. Such a powerful factor results in the formation of the runoff hydrological fronts in the spring-summer restricting the freshened water lens. The paper is devoted to investigating the hydrophysical structure of the runoff fronts, their formation mechanisms and the influence on ice formation during the autumn-winter period.

2. Materials and Methods

The analysis and calculations were based on CTD-soundings during the Russian-German expeditions to the Laptev Sea (TRANSDRIFT expeditions) in 1993, 1994 (summer investigation), 1995 (autumn), 1996 (winter-spring) and the Russian-Norwegian expeditions to the Kara Sea in 1993, 1994 and 1995 (summer). CTD-soundings were conducted using a sounding set OTS-PROBE Serie 3 (Meerestechnik Electronic GmbH, Germany).

For estimating the rate of ice formation in the winter season daily averaged data of standard meteorological air temperature observations at the hydrometeorological polar stations were used. The land fast ice edge position was taken from the AARI composite 10-day ice charts that mainly based on NOAA and METEOR satellite imagery. The water layer heat content was calculated using actual CTD-data.

3. Observation Results

An analysis of 419 oceanographic stations occupied in the Kara Sea and 362 stations in the Laptev Sea has allowed the following general summary.

- In the zone of river water spreading, multilayer density (salinity) stratification is as a rule observed. The upper freshened water layer that was formed under the influence of the spreading river runoff and melting ice is separated by the seasonal pycnocline from the water layer emerging from river/sea water interaction. The lower boundary of this layer is the main pycnocline, which separates water influenced by the seasonal processes from sea water proper (Figure 1A). The seasonal pycnocline deepens with increasing distance from the river water source (between 5 to 10-11 m);

- Under the surface runoff lens of freshened water an intermediate water layer is formed that is distinguished from water at the corresponding depths in the adjoining regions by its quasi-isothermal characteristics at relatively high water temperatures. In the summer, they differ practically little from the surface temperature in the freshened water lens so that the upper sea layer up to the main pycnocline is actually quasi-isothermal by vertical (Figure 1A) [2]. In the autumn, the water temperature of the river water lens rapidly decreases with developing thermal convection phase and wave-wind mixing tending to the freezing temperature. Under the seasonal pycnocline restricting the river water lens from below there is a thick well heated water layer (Figure 1B)

extending to the main pycnocline with temperatures reaching 4°C [4], which is significantly higher than in the regions beyond the outflow zone at the same depths;

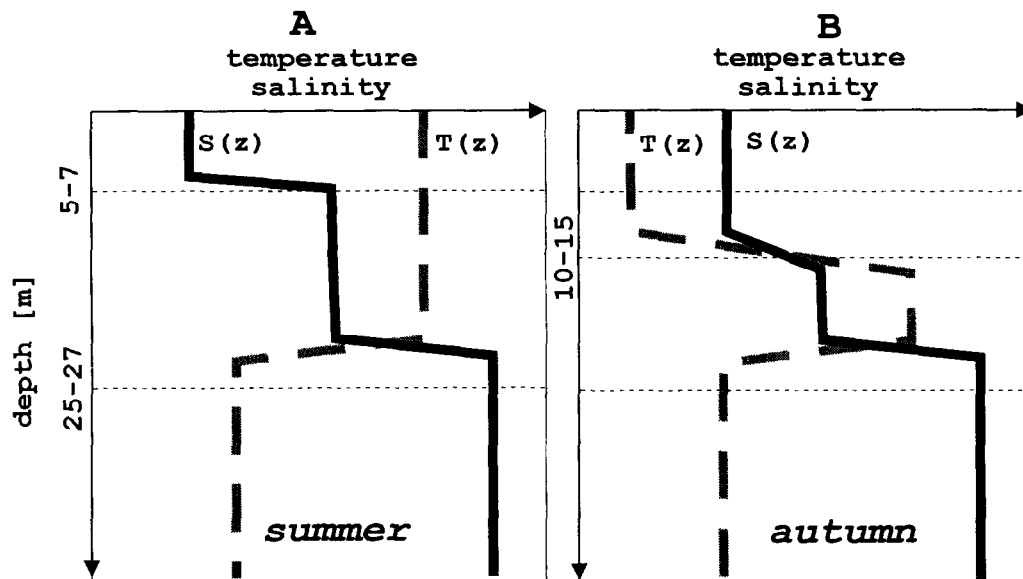


Figure 1. Typical evolution of thermohaline characteristics in the Arctic shelf seas in the zones of river runoff spreading from summer (A) to autumn (B).

- The intermediate water layer is characterized by the increased concentrations of dissolved oxygen, chlorophyll "a" fluorescence, the maximum light transmission coefficient values as compared with the upper and lower water layers and the dissolved silicon minimums [2, 6];

- The depth of the runoff front penetration corresponds to that of river water penetration. Up to the runoff lens spreading depth at the runoff front the isopycnals, isotherms and isohalines are parallel to each other, vertical and intersected by equal pressure surfaces [2] (a baroclinic front). In the lower quasi-isothermal water layer, especially at the periphery of the outflow zone directly under the baroclinic front at the depths between the seasonal and the main pycnocline a front is formed where the isopycnals and isohalines are practically parallel to equal pressure surfaces. They intersect at an angle of up to 90° with the isotherms [2] (thermoclinic front). The terms "baroclinicity" and "thermoclinicity" are used here in the sense of intersection of isopycnic surfaces with equal pressure and temperature surfaces [7, 8]. Thus, the runoff fronts are two-layer: from the surface to the depth of river water penetration they are baroclinic and in the lower layer extending up to the main pycnocline they are thermoclinic (Figure 4).

Two interconnected problems follow from these statements, which require special study:

1. How could a intermediate warm water layer with anomalous hydrophysical characteristics form at such strong density stratification of the surface layer in the zone of river water spreading?
2. How do the runoff fronts spread to the depths 4-5 times exceeding the depth of freshwater penetration and what are the mechanisms forming the two-layer runoff fronts?

4. Discussion

The upper part of the front is formed due to the outflow of freshwater of river origin and spreads up to the depth of river water penetration (seasonal pycnocline) being sharply baroclinic at it [1]. The formation mechanisms of baroclinic fronts at the periphery of the runoff lens are sufficiently well described. However, the mechanisms of transformation of the runoff baroclinic fronts to sharply thermoclinic at the runoff lens periphery in the intermediate layer deeper than 7 m were not investigated up to now and require special explanation. The important role of thermoclinicity and thermoclinic fronts in the formation of isopycnic heat transfers by intrusions and intrusion stratification of fronts in the oceans was repeatedly pointed out [14, 15]. This becomes especially important under the Arctic Ocean conditions where the density field is entirely governed by the salinity distribution. However, up to 1994 any information about the existence of the thermoclinic fronts in the Arctic Seas was absent.

Theoretical publications on numerical modeling of the front genesis processes for the cases where the temperature acts as a scalar admixture [9, 10] indicate a possible deepening of the thermocline under the influence of intense surface front genesis and frontal convergence. This process can be most efficient when there

is an initial inclination of isotherms to isopycnals. In this case a semi-geostrophic front genesis will result in further deformation of the temperature field towards the increase of the inclination angle of isotherms to isopycnals [9]. The existence of convergence at the stationary runoff fronts was repeatedly pointed, including [1, 11]. Frontal convergence was also considered as one of the mechanisms leading to deepening of the main thermocline and pycnocline in the region of water outflow from the Ob and Yenisey Rivers in the Kara Sea [12].

Now let us analyze the real oceanographic situation under the conditions of the Arctic Seas where the density field is practically entirely governed by the salinity distribution and the temperature with the development of geostrophic motions can be considered as a scalar admixture. In the wintertime, the river runoff is significantly weaker. However even under the influence of the weakened river runoff the salinity field in the subsurface water layers in the near-mouth regions will be deformed. At the same time, the temperature field will remain constant and close to the freezing temperature in the subsurface water layer (Figure 2A). Thus during the period preceding the spring-summer intense river water inflow the isotherms at the peripheries of the near-mouth regions will be inclined relative to the isohalines. The angle between them is $+\alpha$. Under the conditions of the dominating salinity contribution to the density field formation the geostrophic current will contribute to the redistribution of the temperature field as a scalar admixture. Hence $+\alpha \rightarrow 0^\circ$, which in the presence of temperature stratification will contribute to a deeper location of the thermocline. Obviously, under the winter conditions this process if it takes place, hardly has any significant influence on the redistribution of thermohaline characteristics.

During the spring development of the river runoff and correspondingly the frontal convergence processes, the geostrophic circulation deforming the temperature field as a scalar admixture field will lead to its redistribution. As a result, the seasonal thermocline will be deeper relative to the seasonal pycnocline. The radiation heating will further develop this process. However in all cases the depth of the seasonal thermocline will not be able to exceed the depth of the main pycnocline (Figure 2B). Then the ice melting processes forming the seasonal pycnocline beyond the river runoff spreading zone will lead to the angle between the isotherms and isohalines $+\alpha \rightarrow -\alpha$. The near-frontal isopycnic convergence in this event will result in the occurrence of a thermoclinic front beneath the baroclinic front of river origin where the horizontal isohalines and isopycnals will intersect with the vertical isotherms (Figure 2C).

The aforementioned phenomenological model of the formation of a two-layer by vertical runoff front can be realized in the event the spring flood and river water outflow to the sea will precede the intense development of ice melting. Another formation mechanism is connected with the isopycnic convergence of surface water heated by solar radiation, beneath the river water lens with lighter fresh river water flowing into saline sea water. Probably, the former of the suggested mechanisms will be realized at a small distance from the

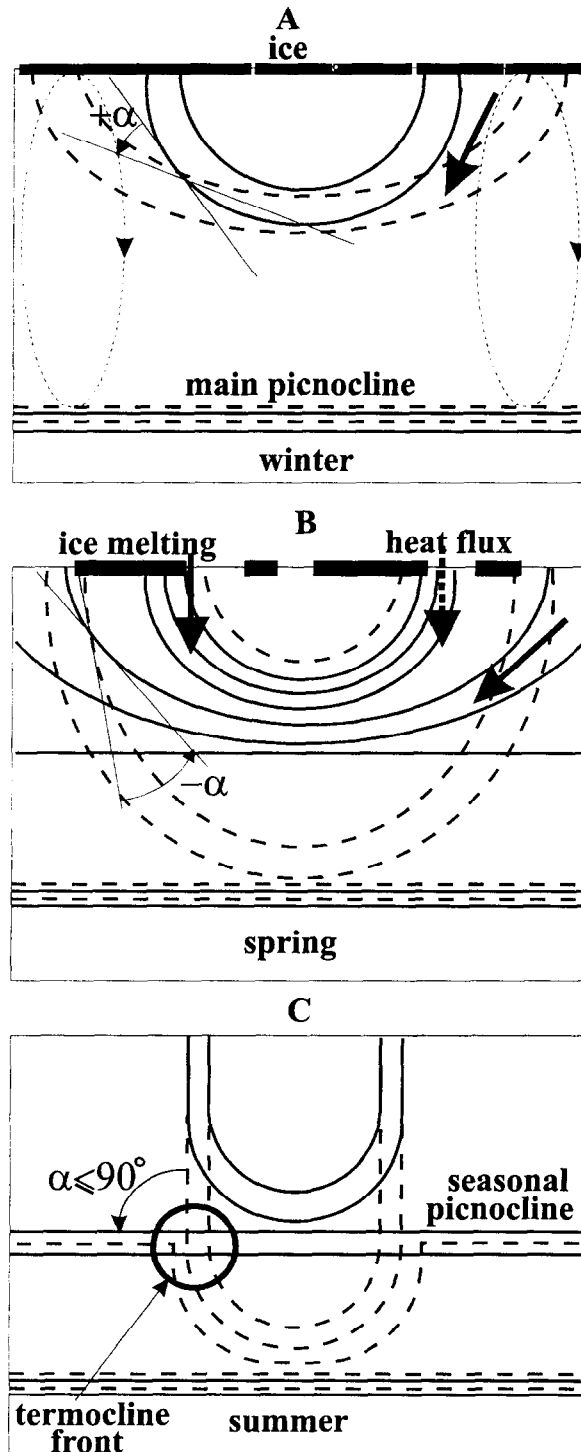


Figure 2. A scheme of formation of the runoff front under conditions of the Arctic Seas;
 ———— - isopycnals and isohalines,
 - - - - - isotherms.

mouth areas. It will be most efficient in the years when the onshore type of river water spreading is more manifested whereas the main processes of front genesis occur at a relatively small distance from the mouth regions (for example, the 1994 summer in the Laptev Sea). The latter of the suggested mechanisms will be predominant at significant spreading of river water northward of the river mouths provided ice clearance in these regions occurred sufficiently early and water had enough time to warm under the effect of solar radiation (for example, the 1995 summer in the Laptev Sea). Obviously, the polynya located here in the spring-winter will contribute to heat accumulation and warmer water will be “entrained” under the river water lens.

Thus, one of the main causes of the formation of two-layer runoff fronts in the Arctic Seas is the physical properties of sea water, and namely that at low temperature the density field is entirely determined by the salinity distribution. Now with understanding that the frontal convergence is one of the leading processes governing the hydrophysical structure of the sub-surface layer we can consider differently the distribution of hydrophysical characteristics in the outflow zone. The effect of convergent processes in the region of the runoff fronts and under the river water lens lead to a significant redistribution of oceanographic characteristics. In the intermediate layer, the dissolved silicon minimums are observed (less than 300 mg/l at the surface and near-bottom concentrations of 700 and 1000 mg/l, respectively). Their spatial location coincides with the oxygen maximums, elevated chlorophyll “a” fluorescence, which reach here the values typical of sea surface, as well as the maximums of light transmission coefficients. Obviously, water with such characteristics has surface origin. It is formed beyond the river water outflow zone. Then as a result of frontal convergence in the spring-summer, it sinks to the lower water layers forming a sufficiently thick intermediate water layer with anomalous hydrochemical and hydrooptical characteristics.

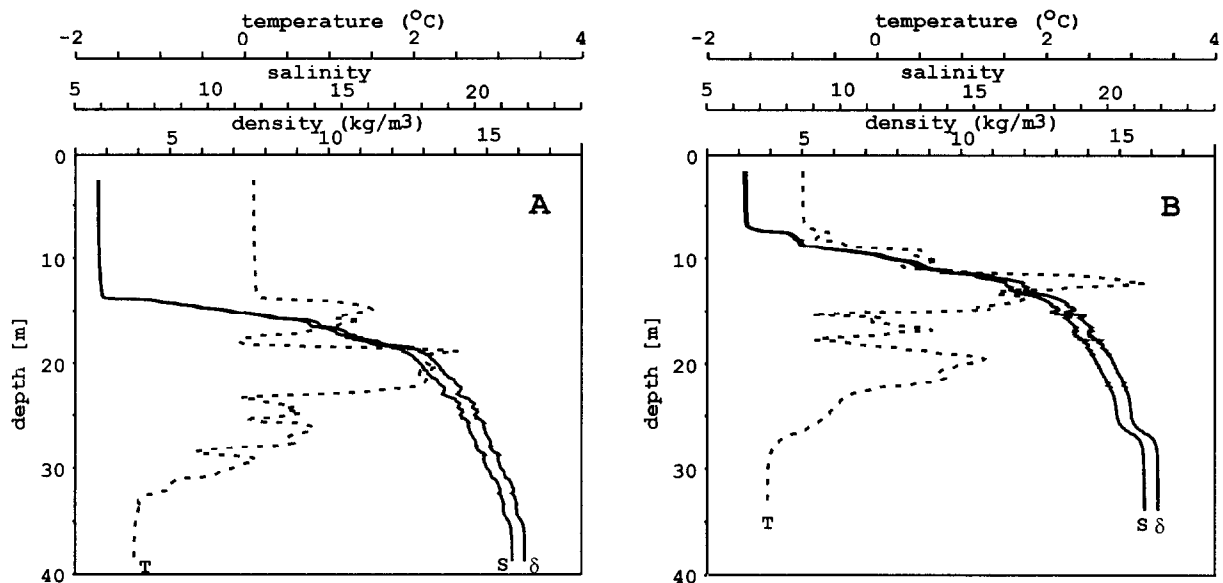


Figure 3. The intrusion stratification of the intermediate water layer beneath the zone of freshening before (A) and after (B) the onset of ice formation in autumn 1995 in the Laptev Sea.

The consequence of the existence of two-layer baroclinic-thermoclinic runoff fronts in the Arctic Seas and one more proof of their existence in the Arctic Seas appear to be numerous isopycnic intrusions of warm and cold water. They were repeatedly observed in the course of expedition studies in 1993-1995 in the Laptev and Kara Seas in the intermediate layer near the runoff fronts (Figure 3) [2, 3, 4, 13]. Observations revealed that their thickness in the Arctic Seas could reach 10 m and the temperature gradients at the boundaries of the interlayers – 2-2.5°C/m [13]. The intrusion stratification and the formation of numerous temperature inversions is possible and most efficient under the conditions of thermoclinicity [8]. In the absence of horizontal density and salinity stratification but in the presence of strong horizontal temperature stratification, any horizontal impulse will lead to the formation of isopycnic intrusion (Figure 4). Hence, due to the absence of horizontal density stratification the secondary thermoclinic front will be unstable in terms of hydrodynamics practically to any perturbations in the horizontal plane. Its instability will result in the formation of both warm intrusions, which are observed outside the river water outflow zone (Figure 3A) and cold intrusions, which are located directly under the water of river origin (Figure 3B).

The mechanism of intrusion stratification of the secondary runoff thermoclinic front is obviously quite efficient due to the isopycnic character of the process. As a result of the isopycnic advection processes the intrusions are transferred by an average flow over considerable distance without any significant change in the

characteristics thus transforming the vertical distribution of oceanographic characteristics even being rather far from the front. However, as noted by Woods [8], at a certain distance from the front beyond the frontal zone boundaries the development of double diffusion convection at the upper periphery of intrusions will prevent the efficient advective heat transfer, contained in intrusions, but will instead contribute to the convective heat exchange.

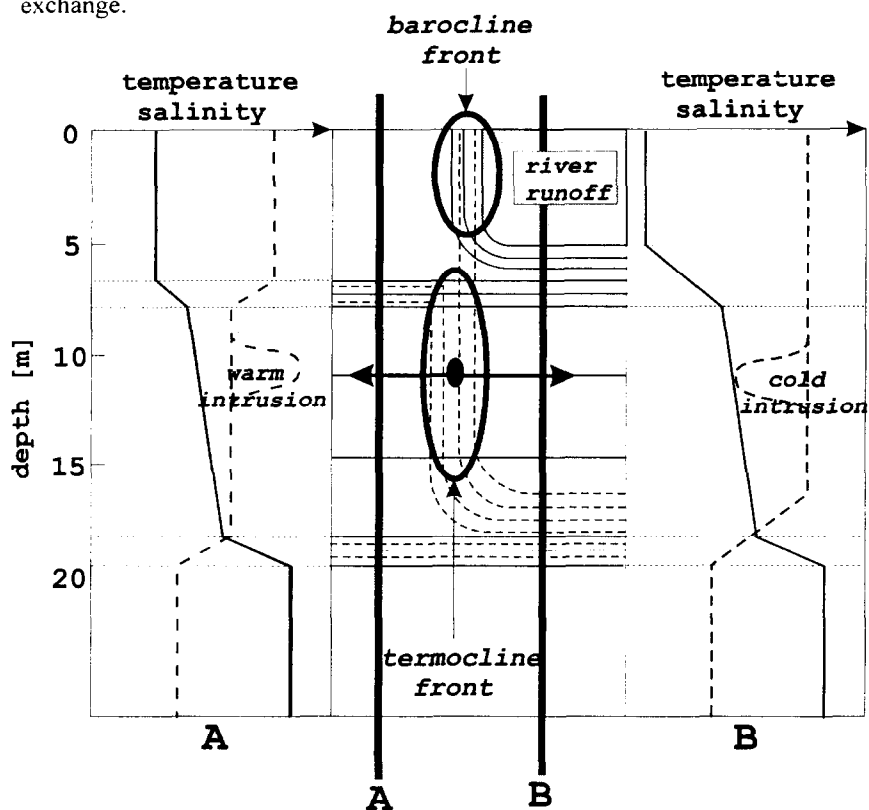


Figure 4. A scheme of formation of temperature isopycnic intrusions at the runoff front; ———— - isopycnals and isohalines, - - - - - isotherms.

An analysis of 1995 autumn experimental observations confirmed that the intrusion stratification of the secondary thermocline front also continues at the onset of ice formation processes (Figure 3B). The latter is extremely important for estimating the convective heat flux from the warm interlayer to the surface in the course of ice formation processes.

Another consequence of the development of convergent circulation is an anomalous deepening of the upper well-heated quasi-isothermal layer. With developing autumn processes, including radiation cooling, wave-wind mixing, etc., the upper water layer rapidly cools. However, a significant in thickness well-heated water layer remains "buried" at depths between 10-12 to 25-27 m (Figure 3). As a result, in the zones of river water runoff lens quite a thick anomalous warm water interlayer is formed in the summer-autumn whose formation is

connected with the convergence development at the runoff fronts. The stability of its existence is governed by the coincidence of the upper boundary of the warm layer with the seasonal pycnocline location (Figure 1B).

Calculations revealed that the intermediate water layer heat content in the zone of transformed river water spreading exceeds $20 \cdot 10^4$ KJ/m² reaching $60 \cdot 10^4$ KJ/m² at the front location. The heat content of the intermediate layer beyond the zone of freshening is not as a rule greater than $5 \cdot 10 \cdot 10^4$ KJ/m², which is consistent with the seasonal heating estimates connected with shortwave solar radiation penetration to the seasonal pycnocline layer [18]. The existence of the warm intermediate layer influences the autumn ice formation process, which occurs 2-3 days later in the near-frontal zones [16]. Remote-sensing ice data analysis has shown that land fast ice formation and distribution occurs in accordance with the intermediate water layer heat storage. Calculations for all the possible heat exchange mechanisms indicated that heat advection in the conditions of intrusion stratification of the secondary thermocline front in combination with the double-diffusion processes at the peripheries of the freshened zone are responsible for the heat transfer to the bottom ice surface during winter time. The amount of heat transferred to the surface by these processes is great enough to reduce more than twice the initial ice thickness on the periphery of the river water lens. It will cause land fast ice edge formation in accordance with the configuration of the zone of river water distribution [17]. Thus a complex of processes "frontal convergence at the periphery of the freshened water lens in the summer" → "warm intermediate layer formation" → "heat transfer from the intermediate layer to the surface during winter" can influence the land fast ice edge and flaw polynya position as well as ice production in this region.

5. Conclusions

1. In the Kara and Laptev Seas the runoff thermocline fronts were revealed resulting from the development of frontal convergence. They form in the intermediate subsurface layer directly under the surface baroclinic runoff

front. One of the main causes leading to their formation is that at low temperatures of sea water the density field is entirely governed by the salinity distribution.

2. The baroclinic-thermoclinic two-layer runoff fronts play an important role in the summer-autumn period in the formation of the mesoscale spatial thermohaline structure of the subsurface layer. In the summer, as a result of convergent processes the subsurface water layer under the river water outflow zone has anomalous hydrophysical characteristics and primarily the increased heat content. This determines its influence on the evolution of ice-hydrological conditions in this region during the autumn-winter period of the year.

3. Instability of the thermoclinic runoff front leads to numerous subsurface high-gradient interlayers (intrusions) forming in the adjoining water column. The intrusion stratification of the thermoclinic runoff front leads to effective heat and passive admixture advection from beneath the river water outflow zone. This process is decisive in heat transfer to the surface from the intermediate warm layer in the autumn-winter period.

6. References

- [1] K.N.Fedorov, 1983, *Physical Nature and Structure of Oceanic Fronts*, Leningrad, Gidrometeoizdat, 296 p. (in Russian).
- [2] P.N.Golovin, V.A.Gribanov and I.A.Dmitrenko, 1995, Macro- and Mesoscale Hydrophysical Structure of the Outflow Zone of the Lena River Water to the Laptev Sea, In: H.Kassens, D.Pipenburg, J.Thiede, L.Timokhov, H.-W. Huberten and S.Priamikov (eds.), *Russian-German Cooperation: Laptev Sea System*. Ber. Polarforsch., 176, pp.99-106.
- [3] H.Kassens and I.Dmitrenko (eds.), 1995, *The Transdrift II Expedition to the Laptev Sea*, Ber. Polarforsch., 177, pp. 1-180.
- [4] H.Kassens, I.Dmitrenko, L.Timokhov and J.Thiede (eds.), 1997, *The Transdrift III Expedition: Freeze-up Studies in the Laptev Sea*, Ber. Polarforsch., 248, pp. 1-192.
- [5] I.Dmitrenko, 1995, *The Distribution of the River Run-Off in the Laptev Sea: The Environmental Effect*, In: H.Kassens, D.Pipenburg, J.Thiede, L.Timokhov, H.-W. Huberten and S.Priamikov (eds.), *Russian-German Cooperation: Laptev Sea System*. Ber. Polarforsch., 176, pp.114-120.
- [6] A.Anoshkin, I.Popov and I.Ushakov, 1995, *Hydrooptical Measurements in the Laptev Sea: Spatial Distribution of Light Attenuation and Chlorophyll Fluorescence*, In: H.Kassens, D.Pipenburg, J.Thiede, L.Timokhov, H.-W. Huberten and S.Priamikov (eds.), *Russian-German Cooperation: Laptev Sea System*. Ber. Polarforsch., 176, pp.178-186
- [7] K.N.Fedorov, 1991, *On the thermal characteristics of fronts in the ocean*, In: K.N.Fedorov, *Selected Proceedings on physical oceanography*, Leningrad, Gidrometeoizdat, pp. 106-111 (in Russian).
- [8] J.D.Woods, 1980, *The Generation of Thermohaline Finestructure at Fronts in the Ocean*, *Ocean Modeling*, 32, pp. 1-4.
- [9] M.K.Mac Vean and J.D.Woods, 1980, *Redistribution of Scalars During Upper Ocean Frontogenesis*, *Quart. J. Roy. Met. Soc.*, Vol. 106, N 448, pp.193-311.
- [10] N.P.Kuzmina, 1980, *On the oceanic front genesis*, *Izvestiya AN SSSR, Fizika Atmosferi i Okeana*, Vol. 16, N 10, pp. 1082-1090 (in Russian).
- [11] R.W.Garvin and J.D.Monk, 1974, *Frontal Structure of a River Plume*, *J.Geophys. Res.*, 79(15), pp.2251-2259.
- [12] V.I.Burenkov and A.P.Vasilkov, 1994, *On the influence of the continental runoff on the distribution of hydrological characteristics in Kara Sea water*. - *MIAK NAUKA, Okeanologiya*, Vol. 34, N5, pp. 652-661 (in Russian).
- [13] V.A.Gribanov and I.A.Dmitrenko, 1994, *Types and peculiar features of distribution of thermohaline characteristics in the Laptev Sea in the summer of 1993.*, In: L.A.Timokhov (ed.), *Scientific results of the LAPEX-93 expedition*, S.Petersburg, Gidrometeoizdat, pp. 76-82 (in Russian).
- [14] J.D.Woods and P.J.Minnett, 1979, *Analysys of Mesoscale Thermoclinicity with an example from the tropical thermocline during GATE*, *Deep-sea Res.*, Vol. 26A, pp. 85-98.
- [15] J.D.Woods, R.L.Wiley and M.Briscoe M., 1977, *Vertical Circulation at Fronts in the Upper ocean*, In: M.Angel (ed.), *A Voyage of Discovery*, *Deep-Sea Res.*, supplement, pp. 253-276.
- [16] I.Dmitrenko, P.Golovin, V.Gribanov, H.Kassens and J.Holeman, 1998, *Influence of the Summer River Runoff on Ice Formation in the Kara and Laptev Seas*. *Proc. 14th Internat. IAHR Ice Sympos.*, Potsdam, N.Y.
- [17] I.Dmitrenko, P.Golovin, V.Gribanov and H.Kassens, in press, *Oceanographic Causes for Transarctic Ice Transport of River Discharge*, In: H.Kassens, H.Bauch, I.Dmitrenko, H.Eicken, H.-W.Hubberten, M.Melles, J.Thiede and L.Timokhov (eds.), *Land-Ocean System in the Siberian Arctic: Dynamics and Hystory*. Springer-Verlag, Lecture Notes in Earth Sciences, Berlin.
- [18] V.M.Petrov and I.Ye.Frolov, 1984, *The Mechanism of Formation of Warm Water Interlayer in the Pycnocline Layer of the Arctic Seas*, *Meteorologiya i Gidrologiya*, N 11, pp. 110-112 (in Russian).

SHORT FRONTAL WAVES: CAN FRONTAL INSTABILITIES GENERATE SMALL SCALE SPIRAL EDDIES?

T. Eldevik¹ and K. B. Dysthe²

Department of Mathematics, University of Bergen, J. Bruns gt. 12, 5008 Bergen, Norway

¹ Tor.Eldevik@mi.uib.no

² Kristian.Dysthe@mi.uib.no

Abstract. Small cyclonic spiral eddies with a scale of 10 km, are very frequently observed at the ocean surface, both from satellites and space shuttles. We are investigating whether their generation may be due to frontal instabilities, *i.e.* short scale cyclogenesis. The comparison of our numerical experiment to observations and linear stability analysis of two-layer frontal models, are promising. Spiraling short wave instabilities are clearly seen. The spiral eddies observed at the Almeria-Oran density front, among others, may possibly be explained by this model.

1. Introduction

At low wind speeds, a rich variety of surface structures are observed by remote sensing, particularly the so-called spiral eddies, with small scale, $O(10\text{ km})$, spiraling structure. Up to the eighties, they were considered to be rare dynamic features in the ocean. Photographs of the world's oceans from space shuttles [1], and images of Norwegian coastal waters from radar satellites [2], have shown that such eddies are indeed common. In the former survey they are found to be always cyclonic, with a diameter of 12 to 15 km, while in the latter, 85% of the eddies were cyclones and 15% anti-cyclones. The average diameter of the anti-cyclonic eddies was more than three times that of the cyclones, which was estimated to be approximately 7 km. We therefore define spiral eddies to be of order 10 km, and from the observational material they are assumed to be cyclones. They are observed in many oceans in both hemispheres, but not in the vicinity of the Equator. This has lead us to the conclusion that the phenomenon is influenced by the rotation of the earth. It seems from the two surveys mentioned above that the dimensions of the cyclones decrease with increasing latitude. Although speculative, this is consistent with the Coriolis effect. The measures of length scales from the observations are approximate. The variation in diameter of the eddies may just as well be caused by different density stratifications at the different locations. It is also possible that their size changes during their evolution. Although not discussed herein, there are indications of the latter in our simulations [3].

The horizontal dimension of the spiral eddies is in the very low range of the internal radius of deformation in the ocean. If the background rotation is to play a part, stratification must be present and the dynamics restricted to an upper shallow layer of the ocean. Both moderate and large Rossby numbers, Ro , are estimated from the observations [4]. It has been proposed that the spiral eddies are the consequence of large (greater than unity) Ro dynamics [5]. As far as we understand, this work does not account for the generation of the eddies, but explains why there would be a preference for cyclonic eddies from an initial field of vortices of both orientations. In this regime, anti-cyclones are unstable from a mechanism akin to the so-called "centrifugal instability" [6]. The structures displayed in our simulations are of moderate Rossby number.

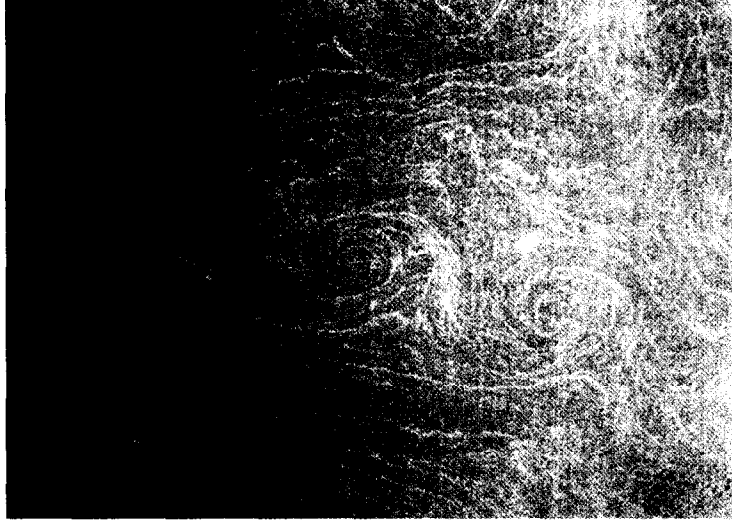


Figure 1: Photograph of spiral eddy street in the Mediterranean Sea off the coast of the Egyptian/Libyan border, from [4].

A beautiful eddy street is shown in Figure 1. The pattern is made visible by the sun's reflection from the surface of the sea, the sun glitter. The specular point is close to the center of the image. The relatively bright lines are thought to represent areas where the local roughness of the sea surface is smoother than the surrounding water [1]. The presence of surfactants are known to cause such slicks. It should be noted that the observed eddy patterns in general are more random than the one shown here.

Apart from understanding the phenomena as such, there are several other important reasons to study such submesoscale dynamics. They are often essential to the understanding of the larger system, but the dynamics of this scale are missing due to the coarse resolution of most numerical ocean models. The parameterization of sub-grid scale physical effects in numerical models is essential for their performance. The observations are, however, all snapshots. To our knowledge, there is no temporal data available for these features. Knowledge of how spiral eddies are generated, may improve the interpretation of satellite data. It has also been suggested [7], that cyclonic eddies are important in the development of frontal phytoplankton blooms.

2. Frontal instability as a generation mechanism

In geostrophic balance, the shear over a front separating water masses of different densities and velocities is cyclonic because of the thermal wind relation. Thus, there is a reservoir of cyclonic relative vorticity associated with the front that is essential for the deformation of the front when exposed to an unstable perturbation. This is one of the basic insights that led to the formulation of the celebrated cyclone model of the Bergen School [8] in meteorology. Also associated with frontal areas, is the presence of relatively strong horizontal convergence. At the ocean surface, this can lead to the accumulation of slicks.

The generation of spiral eddies through cyclogenesis at ocean fronts, could be the common denominator of the observations of [1] and [2]. The former author argue that the streaks trace out velocity shear and the latter authors claim that the eddies seem to be "situated exactly at the border between, in all probability, two different masses" in several of the images. A special case is found in the the Alboran Sea, between Spain and Algeria. At the same location where spiral eddies were observed from the space shuttle, *in situ* measurements later confirmed there to be an intense density front, the Almeria-Oran front [9]. This has led us to our working hypothesis that spiral eddies are surface signatures of small scale ocean frontal instabilities in regions of strong horizontal convergence.

A stationary geostrophic surface front in a two-layered fluid has been found to be linearly unstable to

short wavelength perturbations in the direction of the front when the pycnocline separating the two fluids of constant densities initially is assumed to be of constant slope [10, 11], parabolic [12], or exponential [13]. In these models, the fluid motion in each layer is governed by the non-viscous shallow water equations in an f -plane, and no external forcing is present. Under the amplification of a disturbance, energy is extracted from the available potential energy of the density distribution and the kinetic energy of the mean flow.

The initial assumption of a *parabolic* or an *exponential* profile can be related to simple physical arguments concerning the conservation of potential vorticity (PV). The former will be the result when the lighter fluid has been compressed to the surface from a large (infinite) thickness. Geostrophic adjustment of an originally motionless upper layer of uniform depth will produce the latter. In both these cases, the PV of the upper layer is uniform and there is relative vorticity present within the layer.

There does not seem to be any such basic argument available for choosing the initial pycnocline to have a *constant slope*, where the flow in each layer is uniform, but not the PV. Still, this will be the case of the numerical experiments described and discussed in the following. We have chosen to focus on the shear *across* the front. The streaks tracing out the spiral eddies are thought to be associated with a cyclonic shear of $O(10^{-3}\text{s}^{-1})$ [1]. This is an order of magnitude larger than any relative vorticity that may be present *within* the layers, regardless of the initial profile. We suggest that this model is a near front approximation to the two conditions mentioned above.

3. The numerical experiment

The numerical experiment was performed with a three dimensional, primitive equation, σ -coordinate ocean model [14], the computational domain being a periodic channel in the x -direction, with a free surface and a flat bottom. In order to simulate the upper ocean layer, the boundary at the bottom was set to be stress-free. The initial geostrophic state (Figure 2) consists of two fluids of different uniform densities, separated by a pycnocline of constant slope (in the y -direction), intersecting both the bottom and the surface. The surface elevation and the steepness of the pycnocline is such that the upper (lighter) layer is flowing with a constant velocity in the positive x -direction and the lower layer is at rest. The

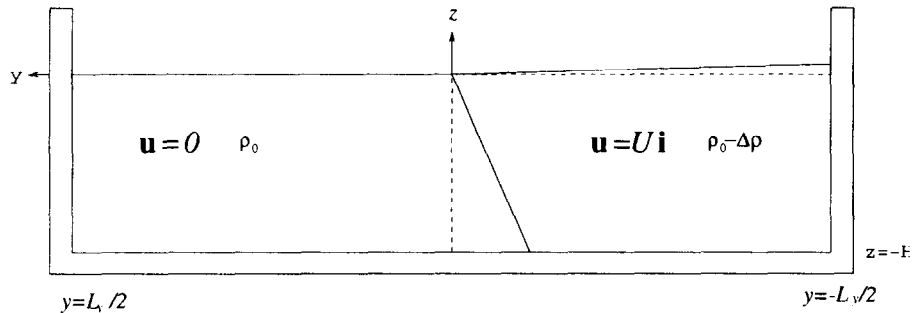


Figure 2: The initial geostrophic frontal configuration, the x -axis pointing inwards.

characteristics of the unperturbed geostrophic flow (at $t = 0$, see below) are given in Table , where R is the internal radius of deformation, U is the equilibrium geostrophic velocity of the upper layer, ρ_0 is the density of the heavier fluid, $\Delta\rho$ is the density difference between the two layers, f is the Coriolis parameter and H is the depth of the channel. The chosen values are not intended to represent any specific location,

R	U	ρ_0	$\Delta\rho$	f	H	L_x	L_y	Δx	N_σ	Δt
[km]	[m/s]	[kg/m ³]	[kg/m ³]	[1/s]	[m]	[km]	[km]	[km]		[s]
6.92	0.4	1025.0	1.0	10^{-4}	50.0	32.0	128.0	0.50	11	75.0

Table 1: The physical and numerical parameters governing the flow at $t = 0$.

but should be representative for a mid-latitude density front. L_x and L_y are the length and width of the channel, respectively. Decreasing the width by 25% yields no significant difference in the simulations for the times displayed herein, thus it is reasonable to state that the validity of the experiment is not restricted to coastal currents. The horizontal spatial step Δx , the number of σ -layers N_σ , and the time step Δt , give the resolution of the numerical scheme.

A strictly two-layered model is not possible to sustain in a three dimensional numerical model (nor in nature). The discontinuity that represents the front in the former model, will become continuous in the latter. The flows were therefore allowed to adjust to a state where further smoothing of the density and velocity profiles over the front was negligible, at which time ($t = 0$, say) they were perturbed. The effective horizontal diffusivities at the front in the simulations were estimated to be between 10 and 20 m²/s. Such values affect only length scales much smaller than the scale of the spiral eddies. This keeps the front quite narrow and lets the instability set in, unaffected by dissipation. Thus the strong shear associated with the eddies are present, and a comparison with two-layer linear stability theory [11] is relevant.

It has been shown [10, 11] that for a given (two-layer) Richardson number,

$$Ri \equiv \frac{\Delta\rho gH}{\rho_0 U^2},$$

the linear stability of the geostrophic two-layer flow is determined by the perturbation Rossby number

$$Ro_k \equiv \frac{kU}{2f},$$

the prescribed (infinitesimal) perturbation with wavenumber k being in the direction of the flow. For the values of Table , $Ri = 3.0$. The most unstable perturbation is then predicted to be $Ro_k = 0.4$, amplifying with an e -folding time $T_e = 20$ h, through a mixed baroclinic/barotropic instability, dominated by the former [11]. This Rossby number corresponds to a wavelength equal to the chosen length of the channel, L_x .

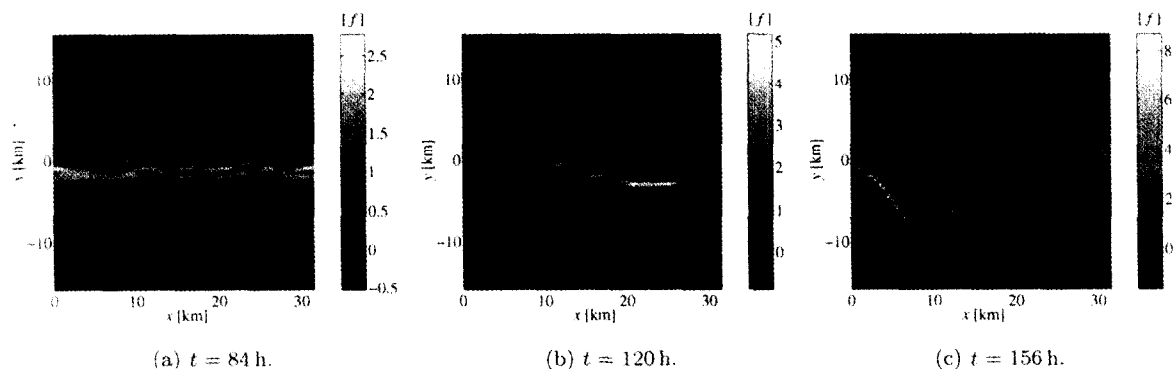


Figure 3: The onset of instability and the generation of a spiral eddy as seen in the surface relative vorticity. The gray scale is related to the planetary vorticity f , and $y = 0$ is the initial position of the surface front.

The onset of instability in the experiment, initially perturbed with wavelengths L_x , $L_x/2$, and $L_x/4$ at $t = 0$, is shown for the surface relative vorticity in Figure 3. It is clearly seen that the dominant mode corresponds to the wavelength predicted above: in the early stages, Fig. 3(a), all wavelengths are clearly present, at the intermediate stage, Fig. 3(b), the wavelength L_x dominates and will soon be breaking. A control run with a channel of double length was made, and the most unstable perturbation was confirmed to be $Ro_k = 0.4$. In the last snapshot, Fig. 3(c), where nonlinear effects are clearly present, the front curls into a cyclonic spiral with a central patch of vorticity several times f .

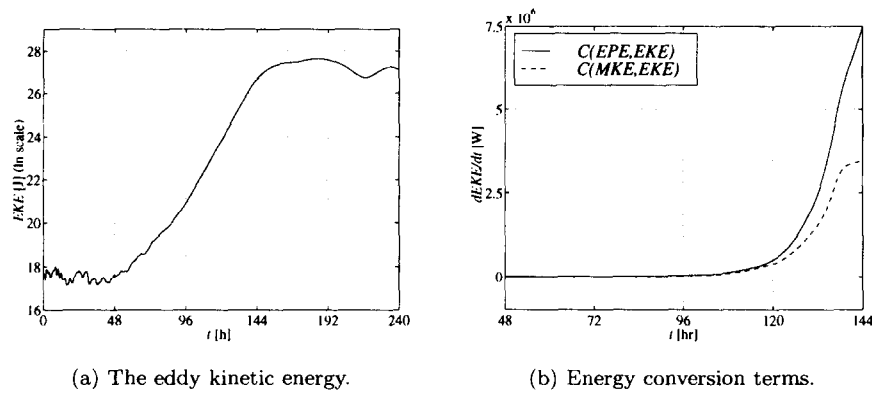


Figure 4: Energetics of the instability: (a) the EKE (ln scale) and (b) the conversion rate of energy into EKE from EPE , $C(EPE, EKE)$, and from MKE , $C(MKE, EKE)$, (linear scale).

The energetics of the instability, given by the eddy kinetic energy (EKE) and the rates of conversion of mean kinetic energy (MKE) and eddy potential energy (EPE) into EKE [15], are shown in Figure 4. From about $t = 48$ h to 144 h, the EKE shows an exponential growth (Fig. 4(a)), with an e-folding time of about 10 hours (corresponding to $T_e \approx 20$ h for the amplifying wave). In the same period, we see that EKE is extracted mainly from EPE , but there is also a contribution from MKE , Fig. 4(b). The former conversion constitutes a baroclinic instability, and the latter a barotropic instability. Thus the wavelength, growth rate, and energetics of the fastest growing wave are in good agreement with the linear theory [11].

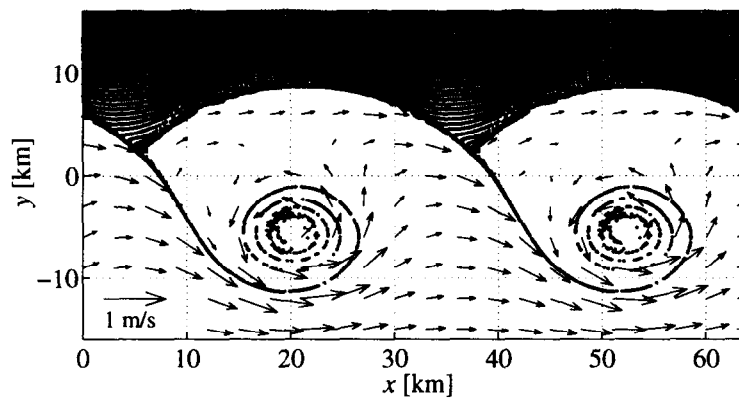


Figure 5: The spiral eddies displayed in the passive surface floats and the surface velocity field at $t = 168$ h. The periodic domain is shown twice.

In Figure 3, the onset of the instability and the birth of the spiral eddies are displayed in terms of the relative vorticity at the surface. Relative vorticity is not a conserved quantity, but the same evolution was observed in the surface density distribution. In order to look at the details of the surface patterns generated from the instability, surface floats were distributed uniformly in the motionless part of the

surface ($y > 0$, $\rho = \rho_0$) at $t = 0$. A snapshot of the pattern generated by these passive tracers is shown in Figure 5. There is a strong horizontal convergence at the front $O(10^{-4}\text{s}^{-1})$, accumulating floats that trace out the front, including spiral eddies at the scale of 10 km. At the time displayed, the concentration is about 75 times the initial at the main front and up to 50 at the spiral eddies. This convergence implies significant vertical downdrafts that are essential for the transformation from the (quasi-)linear regime displayed in Figure 3(b), to the fully developed cyclone in Figure 3(c) [3].

At later stages, $t \sim 18$ days, secondary instabilities set in and generate a more random eddy pattern [3]. This could account for the observations of less organized structures than displayed in Figure 1.

4. Conclusions

Spiral eddies are clearly observed in the experiment. From the given initial frontal configuration, their generation may be explained by a short scale, predominantly baroclinic, frontal instability. In the presence of surface floats, the front and the spiral eddies are associated with streaks that would make them detectable by remote sensing.

Acknowledgments. The authors thank Professor J. Berntsen for helping to set up the numerical experiment and Professor T. A. McClimans for valuable comments and suggestions in the preparation of this manuscript. The first author would also like to express his thanks to Dr K. Iga and Dr D. Renouard for fruitful discussions. This work has received support from The Research Council of Norway (Programme for Supercomputing) through a grant of computing time.

References

- [1] P. Scully-Power. Navy Oceanographer Shuttle Observations, STS 41-G, Mission Report. Technical Report NUSC TD 7611, Naval Underwater Systems Center, New London, Connecticut, 1986.
- [2] S. T. Dokken and T. Wahl. Observations of spiral eddies along the Norwegian coast in ERS SAR images. Technical Report 96/01463, Norwegian Defence Research Establishment (NDRE), 1996.
- [3] T. Eldevik and K. B. Dysthe. On spiral eddies in the ocean. In preparation, 1998.
- [4] D. C. Honhart, editor. *Oceanography from the Space Shuttle*. University Corporation for Atmospheric Research and the Office of Naval Research, United States Navy, Boulder, Colorado, 1989. URL: http://daac.gsfc.nasa.gov/CAMPAIGN_DOCS/OCDST/shuttle_oceanography_web/oss_cover.html.
- [5] C. Y. Shen and T. Evans. Submesoscale dynamics and sea surface spiral eddies. Abstract for the IAPSO in Hawaii, Symposium PS-08, 1995.
- [6] P. K. Kundu. *Fluid Mechanics*. Academic Press, San Diego, California, 1990.
- [7] R. D. Pingree. Cyclonic eddies and cross-frontal mixing. *J. Mar. Biol. Ass. U.K.*, 58:955–963, 1978.
- [8] J. Bjerknes. On the structure of moving cyclones. *Geof. publ.*, 1(2), 1919.
- [9] J. Tintore, P. La Violette, I. Blade, and A. Cruzado. A study of an intense density front in the Eastern Alboran Sea: The Almeria-Oran front. *J. Phys. Oceanogr.*, 18:1384–1397, 1988.
- [10] I. Orlanski. Instability of frontal waves. *J. Atmos. Sci.*, 25:178–200, 1968.
- [11] K. Iga. Reconsideration of Orlanski’s instability theory of frontal waves. *J. Fluid Mech.*, 255:213–236, 1993.
- [12] N. Paldor and M. Ghil. Shortwave instabilities of coastal currents. *Geophys. Astrophys. Fluid Dyn.*, 58:225–241, 1991.
- [13] P. D. Killworth, N. Paldor, and M. E. Stern. Wave propagation and growth on a surface front in a two-layer geostrophic current. *J. Mar. Res.*, 42:761–785, 1984.
- [14] J. Berntsen, M. D. Skogen, and T. O. Espelid. Description of a σ -coordinate ocean model. Technical Report ISSN 0071-5638, Institute of Marine Research, Bergen, Norway, 1996.
- [15] I. Orlanski and M. D. Cox. Baroclinic instability in ocean currents. *Geophys. Fluid Dyn.*, 4:297–332, 1973.

CIRCULATION AND BOUNDARY PROCESSES OFF NORTHWEST AFRICA

**A. El moussaoui¹, S. Djenidi¹, A. Kostianoy², J.M. Beckers¹
and J.C.J. Nihoul¹**

- (1) GeoHydrodynamics and Environment Research (GHER), University of Liège, B-5 Sart Tilman, B-4000, Liège, Belgium. A.El moussaoui@ulg.ac.be
- (2) Russian Academy of Sciences, P.P. Shirshov Institute of Oceanology, Laboratory of Experimental Physics of the Ocean, 36, Nakhimovsky Pr., Moscow, 117851 Russia

Abstract: In the frame of the ACURATE project, this study is devoted to the investigation of the hydrophysical structure, circulation and dynamics of the Northwest African coastal upwelling region between 19°N to 26°N using the GHER 3D model. In this study, the model is applied to a typical summer situation forced by climatological winds. The GHER Variational Inverse Model has been implemented in order to have better initial conditions for temperature and salinity fields. Preliminary runs show that major dynamical features of this area are reproduced by the model with the right order of magnitude, and are thus encouraging for long range simulations with appropriate atmospheric forcing.

Introduction:

The major important classic coastal upwelling zones are located along eastern oceanic boundaries where during the warmer seasons of the year, the large-scale weather patterns produce strong northerly and northwesterly longshore wind inducing Ekman transport of surface ocean layers offshore. The cooler, nutrient-enriched oceanic waters which are upwelled onto the surface layers of the slope and the continental shelf balances the resulting loss of surface water and bring essential nutrients to the surface that promote high local primary production. Rich phytoplankton growth supports an abundant trophic web, including valuable fishery resources. Upwelling in all these regions tends to be highly seasonal in temperate latitudes, where it peaks in spring and summer, but tends to be toward year round in the more tropical zones (Bakun, 1989). Compared to other oceanic ecosystems, where the productivity may be limited to a single major event per year, the primary production in the coastal upwelling zones are significantly greater on period and rate.

The northwest African coast is one of these upwelling regions. In this region the most important upwelling phenomena occur in the area between 19°N and 26°N (Cape Blanc in the south and Cape Bojador in the north). This region is characterized by complex upwelling structures, because in the north of 24°N (Dakhla) and south of 21°N (Cape Blanc) the upwelling is characterized by a seasonal variability, and the area between Dakhla and Cape Blanc represents a region conflict between these two upwelling regimes and the upwelling occurs throughout the year. The dynamical features of upwelling in the Northwest African area have been notably described by Mittelstaedt (1991). Under favorable wind conditions the main characteristics are an equatorward coastal jet at the surface, quasi-barotropic fluctuations in the longshore flow, and compensatory surface and subsurface poleward countercurrents.

The source waters for the upwelling are either North Atlantic Central Water (NACW) or the less saline, warmer South Atlantic Central Water (SACW) (Tomczak and Godfrey, 1994). In the vicinity of Cape Blanc a complex mesoscale regime persists since the area is a frontal zone between NACW and the more nutrient-rich, lower-density SACW, causing the circulation to be influenced by thermohaline mixing process (Barton, 1987).

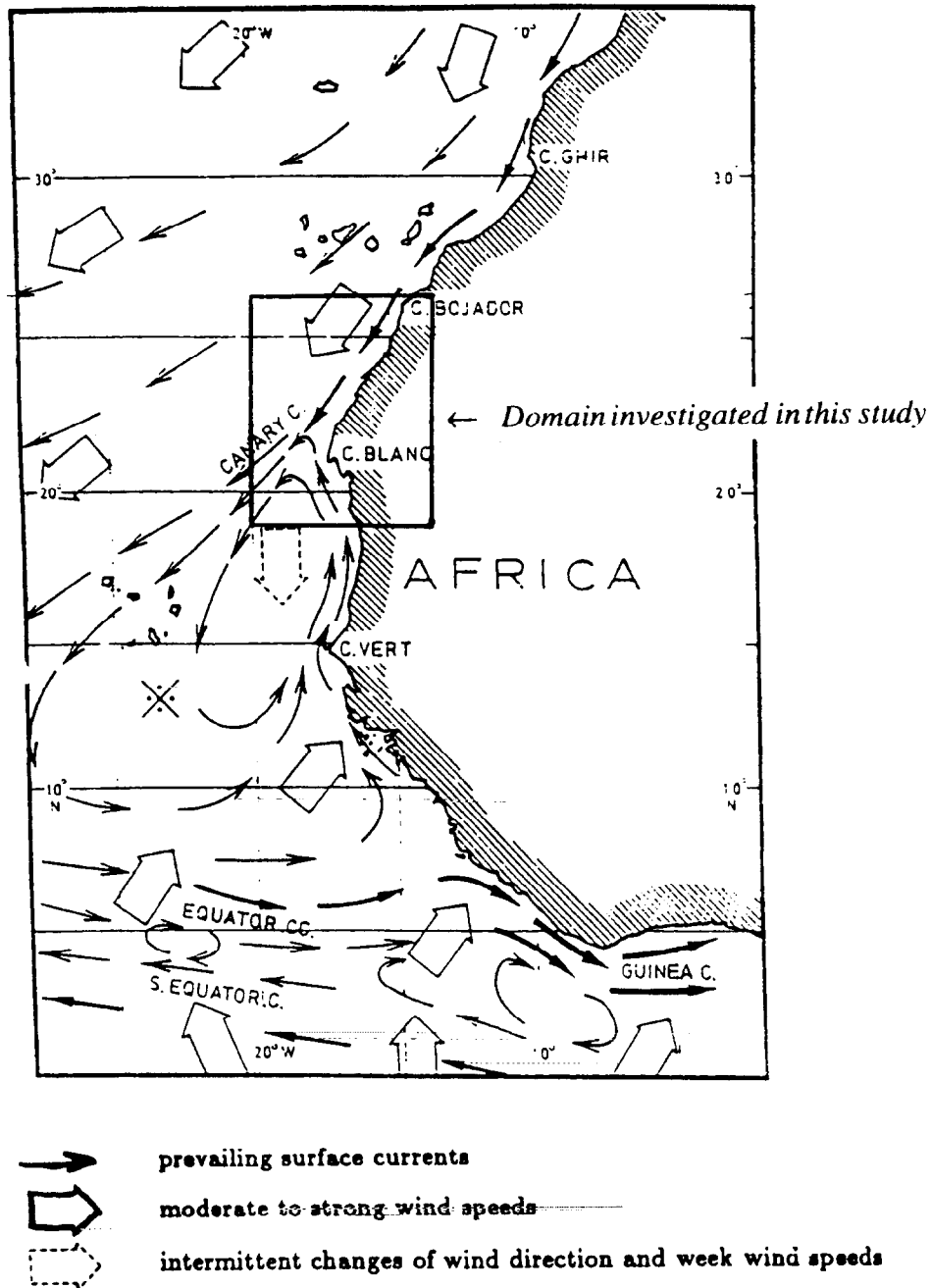


Figure I: Idealized surface circulation during summer along the NW African coast according to Mittelsteadt (1991).

The upwelled waters near Cape Blanc will thus vary in nutrient concentration depending on their origin, although the poleward transport of SACW by the undercurrent on the slope will tend to detach from the meridional nutrient gradient. Figure I shows the large-scale near-surface circulation of northwest Africa as described by Mittelsteadt (1991). Between 25°N and 21°N the Canary Current detaches from the continental slope and flows southwest, entraining shelf water from the north and south offshore. South of Cape Blanc there is a persistent mesoscale cyclonic gyre between 15°N and 21°N whose position varies with the season, being furthest north in winter and autumn. The location of the gyre can be an important factor in enhancing zonal

offshore advection. As a result of the offshore advection of shelf water, which is usually rich in phytoplankton, an extensive pigment plume is formed which was first described from analysis of CZCS data by Van Camp et al. (1991).

The long-term objectives of ACURATE (African Coastal Upwelling Research, Analysis and Thematic Experiments) are the investigation and the description of physical processes responsible for the mesoscale variability of hydrophysical structure in the coastal upwelling zone, using the mathematical/numerical modelling tools based on the VIM and 3D GHER Models. Previous studies (Elmoussaoui et al., 1996; Elmoussaoui and Djenidi, 1998) have highlighted some physical processes and bottom topography effects on the permanent upwelling mechanism in the transition zone located between Cape Blanc (21°N) and Dakhla (24°N). In the present paper, we look at the summer general circulation and spatial variability of the upwelling and the Canary Current in the area located between Cape Bojador and Ras Timirist (Fig. 1). Geographically this area has been chosen in order to study two major different seasonal upwellings of Northwest Africa (north of 24°N and south of 21°N) and their impact on the permanent upwelling on the transition zone.

Application of the GHER Model:

The GHER model is a fully three dimensional (multi-level) primitive equation model, free surface, time dependent, non linear, baroclinic, and with elaborated one or two equation turbulence closure schemes (Nihoul and Djenidi, 1987). The state variables are the three components of the velocity vector, the buoyancy (or the temperature and the salinity), the pressure (or the surface elevation), the turbulent kinetic energy, and the energy dissipation rate (or mixing length). Other features of the model: (i) a double σ coordinate transformation in the vertical, (ii) a mode splitting technique based on a separate treatment of barotropic and baroclinic components of the flow (Beckers, 1991). The free surface and the turbulence closure scheme allow to impose in a simple way the air-sea boundary conditions, namely the continuity of the momentum and heat fluxes at interface. The vertical turbulent viscosity and turbulent diffusion are computed by using the turbulent kinetic energy k and taking into account the stratification effect through the flux Richardson number.

In the preliminary runs, the model is applied to a typical summer circulation. The model is then operated under the following conditions: (i) horizontal grid of 10x10 km within a 690x850 km domain ; (ii) 18 non-uniform meshes on the vertical with higher resolution near the surface ; (iii) maximum depth of the upper layer 200m (sigma coordinates); (iv) real bathymetry and coastline of the region under interest ; (v) barotropic time step of 30s for the vertically integrated equations, baroclinic time step of 450s for 3D model. (vi) a total duration of the numerical experiment up to 12 days corresponding to the month of June.

For the atmospheric forcing, we impose zero heat and salt fluxes and a typically climatological wind interpolated in space and at regular time intervals (Djenidi et al., 1998). At the open sea western boundary we impose zero gradient for velocity and initial values for temperature and salinity. Along the northern and southern boundary we impose: zero normal gradient for outflow and initial value for inflow for temperature and salinity; zero normal gradient for tangent velocity (3D); zero gradient on baroclinic transport and zero normal gradient for topography for normal velocity (3D); geostrophic equilibrium for tangent mean velocity (2D) and constant mean velocity with a given flux for normal mean velocity (2D).

For the initialization of the model, about 1050 CTD profiles (covering the period 1960-1992, corresponding to May, June and July ; 80% of the data concern years 1973-1983) are used in this work. These profiles originated from the NOCD database, the archive of oceanographic and biological data of the Atlantic Research Institute for Fisheries and Oceanography (AtlantNIRO, Kaliningrad, Russia) and the P.P. Shirshov Institute of Oceanology (Moscow and Kaliningrad, Russia). Due to the inhomogeneous distribution of historical profiles, it is very often needed to process the data in order to filter the noise associated to small scale processes and measurements errors. And in order to produce gridded data fields of temperature and salinity which are used as initial conditions in the numerical model, the GHER Variational Inverse Model is used (Brasseur et al., 1996). This model has been developed to analyse hydrographic measurements taking into account the specificities of the ocean system. The finite element numerical technique makes this method much more efficient. For the initialization of the velocity field, we used the reconstructed temperature and salinity data to determine the geostrophic currents. Then, and for obtaining better initial conditions, we performed a barotropic and then a baroclinic adjustment.

Results and discussion:

The geographical limits of our regional interest in the Northwest African upwelling are focused in a zone which extends from Ras Timirist (19°N) to Cape Bojador (26°N). The studied area east-west extension is 14.3°W-20°W. From the model results, the circulation is well correlated with the wind forcing, with a time lag of 2 to 3 day. It consists of an offshore transport from the surface to about 50m and an onshore flow in the lower part of water column over the shelf and extending to a depth of about 200 to 300m depending on the local bottom topography variation (Elmoussaoui and Djenidi, 1998). Isotherms that slope upward toward on the continental slope and on the shelf (Fig. II, III) indicate the upwelling, the vertical motions up the slope occurring only within a strip of about 20 to 30 Km from the shelf break. The upwelled water is originated from depths which do not exceed 200-300 m (Fig. II, III), and the cross-shelf circulation associated with coastal upwelling does not extend beyond the continental slope due to the upwelling front along the slope. This front is characterized by a latitudinal variability related to the upwelling intensity over the slope which is more influenced by the persistence of the under-current and its interaction with the slope bottom topography

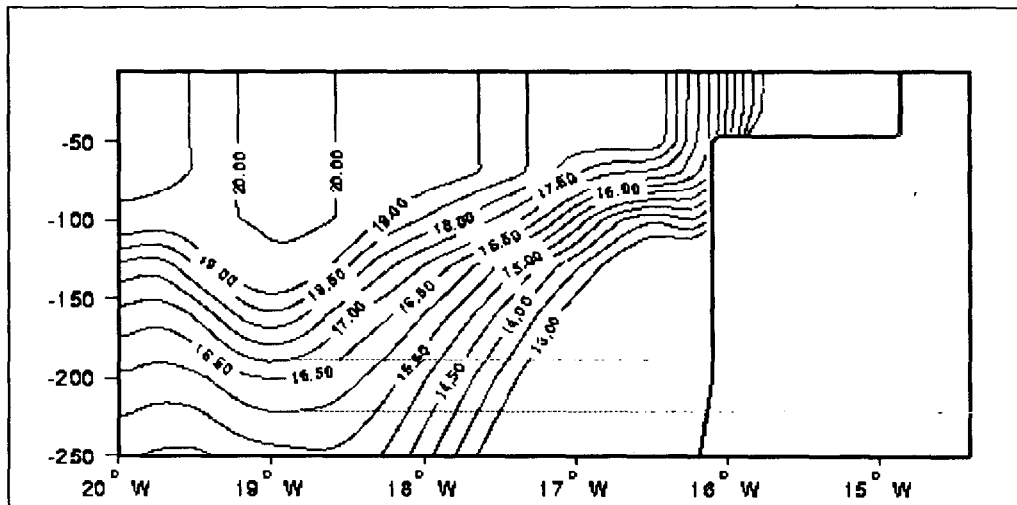


Figure II: Temperature cross section in the northern zone (25°N).

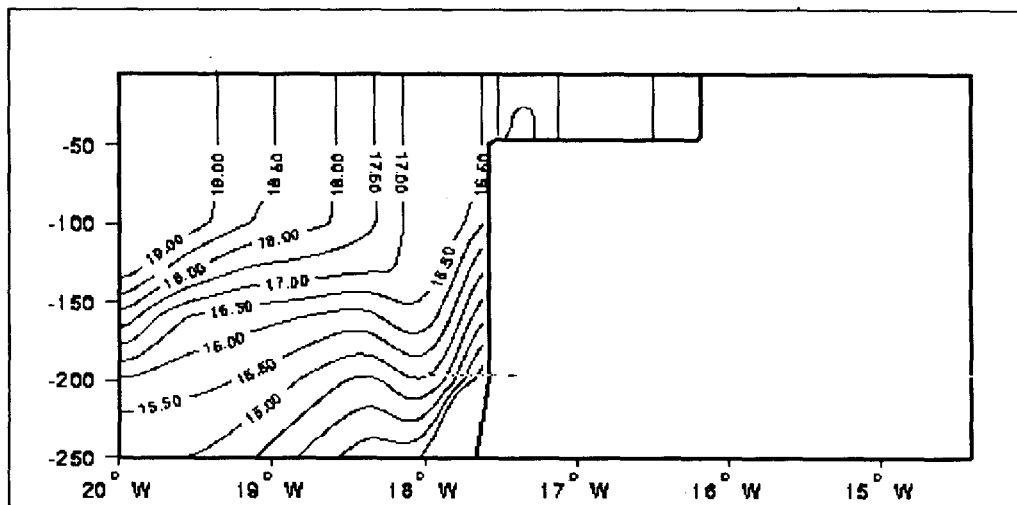


Figure III: Temperature cross section in the southern zone (21°N).

(Elmoussaoui and Djenidi, 1998). Figures II and III show also that the stratification over the shelf is weak, according to Barton (1987), this feature corresponds to strong vertical mixing, with the mixed layer frequently reaching the bottom on the inner shelf.

The surface coastal current flows equatorwards (Figure IV) with an intense current over the slope. The surface horizontal current velocities range from 0.15 to 0.35 m/s over the shelf and from about 0.4 to 0.65 m/s

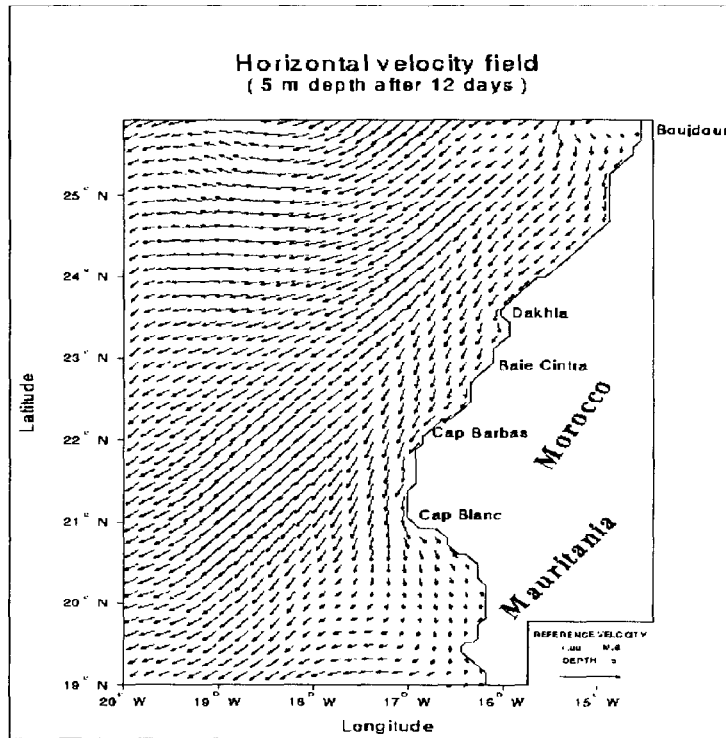


Figure IV: Surface horizontal velocity.

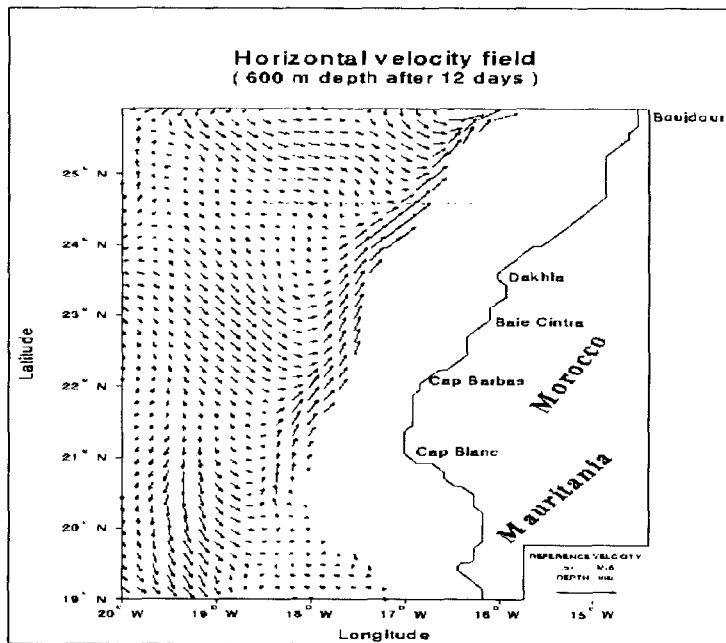


Figure V: Velocity field at 600m depth.

over the slope. The vertical velocities are up to 0.08 cm/s on the shelf and up to 0.17 cm/s along the slope. It is well known that a poleward flowing countercurrent is present over the slope and the whole shelf south of Cape Blanc (Fig. 1).

The countercurrent carries along warm and more saline surface water from the southern regions to Cape Blanc area. Because of the vigorous wind used as a forcing (characterizing summer climatological wind north of Cape Blanc), the warm surface water cannot move any further to the north, its northern limit being located along the southern part of the domain (Fig. IV). Otherwise, Figure V shows the horizontal velocities at 600m depth and we can observe the existence and persistence of a poleward flowing undercurrent. Sinking along the continental slope, the poleward undercurrent width becomes narrow from the southern part to the northern one. The undercurrent width varies from approximately 80 km around 21°N (Cape Blanc) to 50 km around 23°N (Cintra Bay) and 30 km near 26°N (Cape Bojador) (Fig. IV). This narrowing of the width increases the undercurrent velocities. As shown in Fig. IV, from 22°N (Cape Barbas) the undercurrent width starts to decrease however the velocities are increasing. This increase of velocities forces the undercurrent to continue so far to northern regions of the Northwest African coast and reach the Iberian coast (Barton, 1987).

In order to investigate the 3D variability of the Canary Current, three cross-sections of the latitudinal component of velocity are performed (negative values indicate equatorward direction). The first (Fig. VI) corresponds to the northern part of the domain (25°N), the second (Fig. VII) to the center one (23°N) and the third (Fig. VIII) to southern one (21°N). These three situations show that the lower part of the CCC (Canary Current Core) is located approximately about depth of 250m. But one of the most interesting information which is revealed is the offshore moving of the CCC, clearly following the continental slope width. By comparing Figures VI and VIII, we can observe that the water mass characterized by a north-south component value of the velocity larger than 0.8m/s is located in the northern part around 17°N, and vertically extends between 100 to

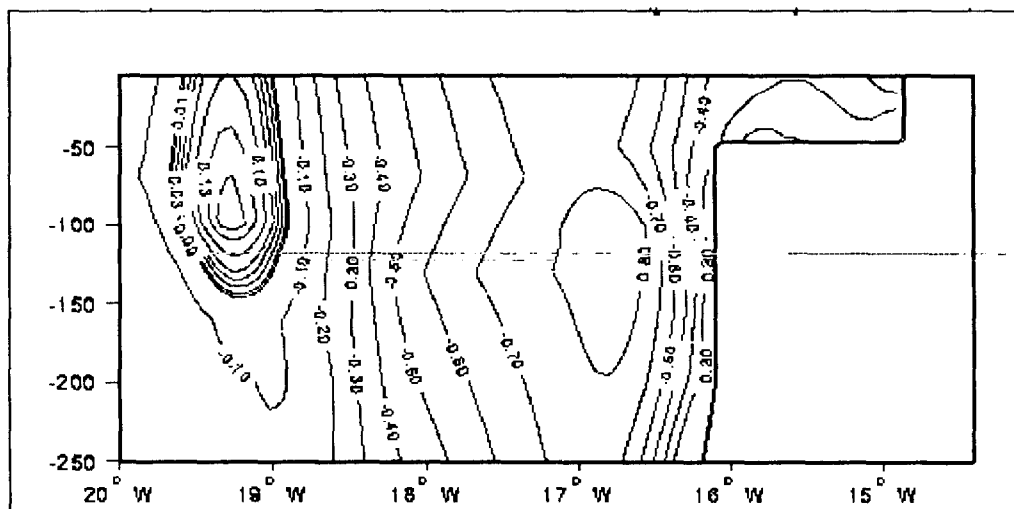


Figure VI: Latitudinal velocity component; cross section in the northern zone (25°N).

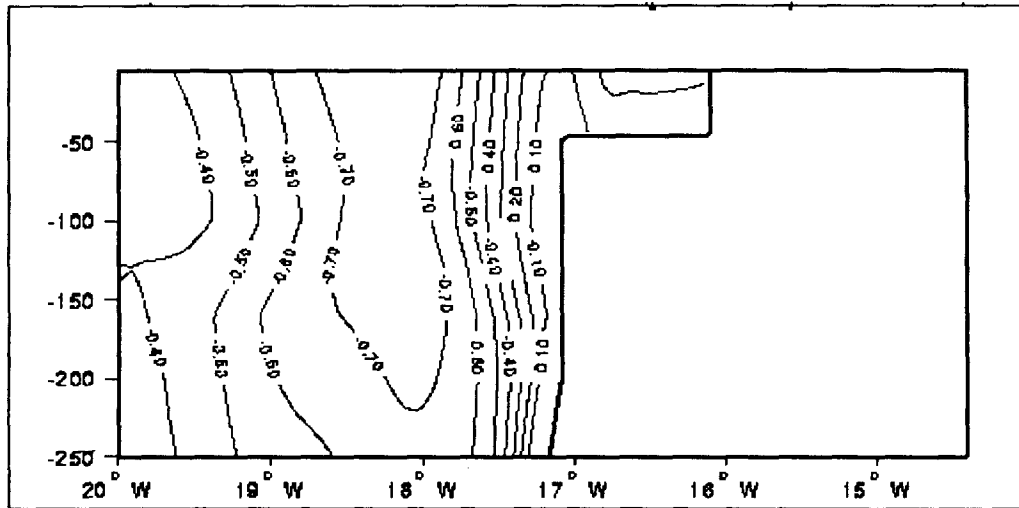


Figure VII: Latitudinal velocity component in the center area (23°N).

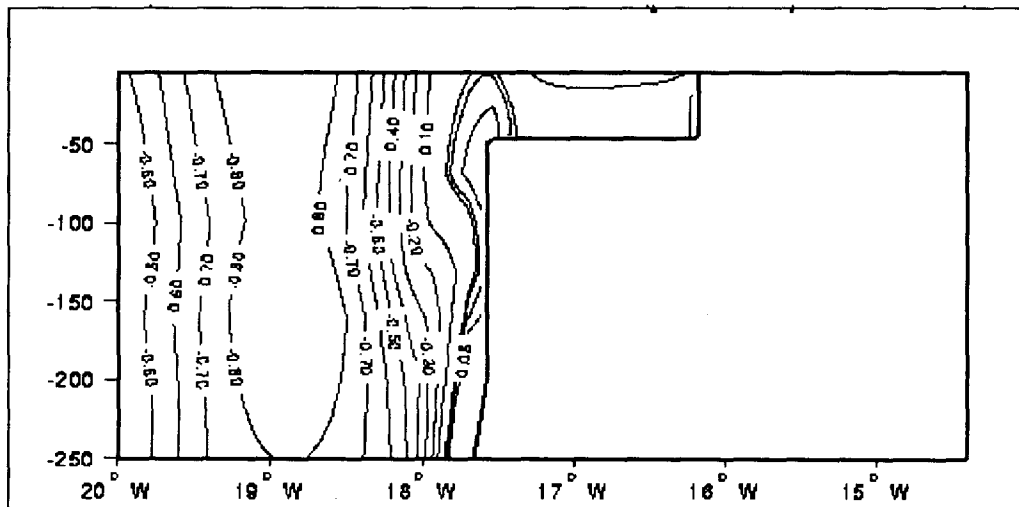


Figure VIII: Latitudinal velocity component in the southern zone (21°N).

150m depth. In the southern part the same water mass is located around 19°N and extends from 250m depth to reach the surface inducing an intensification of the surface current (Fig. IV). This intensification is related to the bottom topography effect on the upwelling system along the continental slope (Elmoussaoui and Djenidi, 1998). Figures VI, VII and VIII suggest also that, according to the continental slope morphology, the CCC is forced to detach from its alongshore position in the northern zone (Fig. VI) to the offshore position (Fig. VIII) with a southwest direction around 21°N (Fig. IV). This change in direction does not depend only on the convergence between the Canary Current and the surface countercurrent at mid-latitude (Mittelsteadt, 1991), but may result also from the impact of the continental slope on the Canary Current. This characteristic may be explained by the fact that in our case (summer situation), the northern boundary of the countercurrent is located at the southern limit of the domain (Fig. IV), far of more than 100km from the area (21°N) where the Canary Current changes completely its direction to southwest. The offshore displacement of the CCC plays an important role for seaward transport of nutrients and plankton biomass from the coastal zone, and this transport may contribute significantly to the offshore production. Kostianoy and Zatsepin (1996) suggest that

approximately half of the water mass upwelled by Ekman pumping process in the coastal zone is transported to the open ocean around of 21°N (Cape Blanc).

These results show that major dynamical features of this area are reproduced by the model with the right order of magnitude, and are thus encouraging for long range simulations with appropriate atmospheric forcing.

Acknowledgements:

The authors are indebted to the "Commissariat Général aux Relations Internationales" (CGRI) of the "Communauté Française de Belgique" and to IBM for supporting this study and providing computing facilities. The research was partly supported by the International Project "Upwelling" of the Russian Ministry of Science and Technologies.

References:

- [1] Bakun A., 1989, Global climate change and intensification of coastal ocean upwelling. *Science*, 247, 198-201.
- [2] Barton E. D., 1987, Meanders, eddies and intrusions in the thermohaline front off northwest Africa. *Oceanol. Acta*, 10, 267-283.
- [3] Beckers J.M., 1991, Application of a 3D model to the Western Mediterranean. *Journal of Marine Systems* 1, 315-332.
- [4] Brasseur P., J.-M. Beckers, J.-M. Brankart, and R. Schoenauen, 1996, Seasonal temperature and salinity fields in the Mediterranean Sea: Climatological analyses of an historical data set., *Deep-Sea Res.*, 43(2), 159-192.
- [5] Djenidi S., A. Kostianoy, N. Sheremet and A. El moussaoui, 1998, Seasonal and Interannual SST Variability of the North-East Atlantic Ocean. (this issue).
- [6] El moussaoui A., S. Djenidi, A. Kostianoy and J.M. Beckers, 1996, A numerical investigation in the transition zone of northwest african upwelling. *Bulletin de la Société Royale des Sciences de Liège*, 65, 1, 75-78.
- [7] El moussaoui A. and S. Djenidi, 1998, Effets topographiques sur un upwelling côtier. *Annales de l'Institut Océanographique de Paris*. (under revision).
- [8] Kostianoy A. and A. G. Zatsepin, 1996, The west african coastal upwelling filaments and cross-frontal water exchange conditioned by them. *J. Mar. Sys.*, 7, 349-359.
- [9] Mittelsteadt E., 1991, The ocean boundary along the northwest African coast: Circulation and oceanographic properties at the sea surface. *Progress in Oceanography*, 26, 307-355.
- [10] Nihoul J.C.J and S. Djenidi, 1987, Perspective in three-dimensional modelling of the marine system. *Three-Dimensional Models of Marine and Estuarine Dynamics*, J.C.J. Nihoul & B.M. Jamart eds, Elsevier Science Publ., 1-34.
- [11] Tomczak M. and J. S. Godfrey, 1994, *Regional oceanography: An introduction*. Pergamon, 422 p.
- [12] Van Camp L., L. Nykjaer, E. Mittelsteadt and P. Schlittenhardt, 1991, Upwelling and boundary circulation off Northwest Africa as depicted by infrared and visible satellite observations. *Progress in Oceanography*, 26, 357-402.

SMALL-SCALE PROCESSES ACTIVITY AND LEVANTINE INTERMEDIATE WATER CHARACTERISTICS IN THE WESTERN MEDITERRANEAN SEA

M.V. Emelianov^{1,2}, E. García-Ladona¹, J. Font¹

¹Institut de Ciències del Mar, CSIC, P. Joan de Borbo, s/n, 08039 Barcelona, SPAIN

e-mail: mikhail@icm.csic.es, emilio@icm.csic.es, jfont@icm.csic.es

²P.P.Shirshov Institute of Oceanology, RAS, Nakhimovski pr., 36, 117851 Moscow, RUSSIA

Abstract

The interaction of warm and salty Levantine Intermediate Water (LIW) with colder and fresher environmental water masses in the western Mediterranean creates favourable conditions for small-scale mixing processes. The present analysis is based on the CTD data obtained during two cruises on board the R/V "Garcia del Cid" (158 CTD profiles during "FE-91" in spring 1991 in the Catalan Sea, and 134 CTD profiles in the Alboran Sea during "FE-92" in autumn 1992). The analysis of the spatial distribution of small-scale processes activity, calculated using several statistical properties of the thermohaline profiles, allows to distinguish the areas of predominance of dia- or isopycnal regimes in the small-scale mixing processes. According to our results in the Catalan and the Alboran seas, the diapycnal processes are more intense on the upper limit of LIW than on its lower limit, and the dia- and isopycnal processes intensity spatial distribution coincide with mesoscale circulation features of LIW.

Introduction

The Levantine Intermediate Water (LIW), the saltiest Mediterranean water mass [4], which originates in the eastern Mediterranean, flows in the western basin at intermediate depths (~300-600 m). The mean circulation of LIW is anticlockwise along the continental slope in the whole western basin [1,5]. The LIW vein enters in the Catalan Sea by the north (Fig.1), flows along the Spanish continental slope and in the southern area it splits into two branches. One branch continues its spreading to the south-west, enters into the Alboran Sea and flows to the strait of Gibraltar. The second one returns to the north-east along the continental slope of the Balearic islands [2]. It seems that part of the former vein returns to the east along the Almeira-Oran front and incorporates into the Algerian current circulation system [5]. As LIW is more saline and warmer than western resident waters, it has a strong influence on the redistribution of the thermohaline characteristics of these waters and, on the other hand, the thermohaline characteristics of LIW itself change due to these interactions.

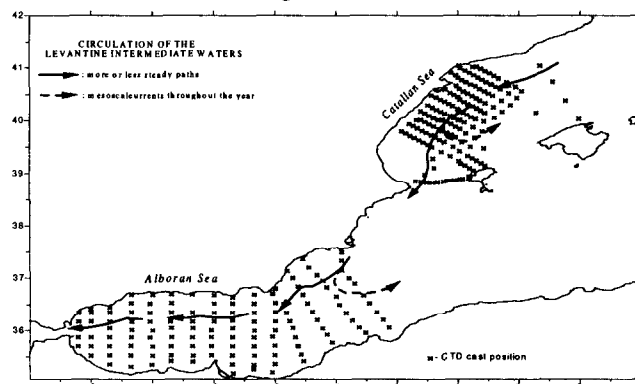


Fig. 1. LIW circulation scheme in the Catalan and Alboran Basin according C. Millot [5].

The mixing processes that modify the LIW characteristics occur at different scales in space and time. The finestructure inhomogeneities observed in the vertical thermohaline profiles, account for the occurrence of complex mixing processes [11] which can act across or along the isopycnals.

The different shapes of finestructure inhomogeneities in a vertical profile have a relationship with the type of processes that formed them. These processes are usually divided into two main classes: diapycnal and isopycnal. Diapycnal processes lead, as a rule, to the creation of step-like structures, whereas isopycnal advection leads to the formation of inversions on the thermohaline profiles [3,6,10,12].

In [12] it was proposed a method to classify the main types of oceanic finestructure and characterize their nature. This method allows to describe a variety of fine thermohaline structures within the framework of step-like and inversion-like shapes. A modification of this method [7], varying the vertical scale within a chosen range, allows to analyse the whole ensemble of finestructure inhomogeneities in a CTD profile, and to determine the range of scales for the two main structure forming processes, if both shapes of finestructure inhomogeneities coexist in the same profile. The statistical characteristics of the finestructure peculiarities, in the selected range of vertical scales, make possible to evaluate the intensity of dia- or isopycnal processes and to obtain their spatial distribution in the investigated area. This method was used to analyse the nature of the finestructure inhomogeneities found in the LIW layer during two CTD cruises.

Materials and methods

To analyse the intensity of the small-scale processes, and how they affect the LIW thermohaline characteristics, several CTD profiles recorded on board the Spanish RV "García del Cid" were used: 158 from "FE-91" cruise in the Catalan Sea (May-June 1991) and 134 from the "FE-92" cruise in the Alboran Sea (Sept.-Oct. 1992) (Fig. 1). All the profiles had been interpolated to 1 meter vertical resolution.

The mean vertical gradients of temperature and salinity were used to split the small-scale mixing processes analysis into three characteristic layers:

- A - the layer above the LIW core, with positive mean temperature and salinity gradients;
- B - the LIW core with quasi homogeneous distributions of temperature and salinity;
- C - the layer below the LIW core, with negative mean gradients of temperature and salinity.

To highlight the finestructure inhomogeneities, the original CTD profiles were separated into mean and pulsating components by cosine filtering. The different vertical scales of finestructure inhomogeneities were obtained by smoothing the original profiles with a variable width of cosine filter window.

To quantify the structure-forming processes intensity, the root mean square deviations of temperature (T_{rms}) and salinity (S_{rms}) fluctuations, obtained with different scales from the chosen range, were calculated. The range of scales to analyse the thermohaline inhomogeneities was selected from 2m (the minimal scale to smooth CTD data with 1 meter vertical resolution) to 50 m (the maximal vertical size of inhomogeneities according to phenomenological analysis). Thus, the CTD profiles were analysed using a filter window width (λ) increasing from 2 to 50 m at one meter step. Then the intensity of diapycnal (Id_T , Id_S) and isopycnal (Ii_T , Ii_S) processes in the temperature and salinity fields, respectively, was determined using the techniques proposed in [7].

Results and discussion

In Fig. 2 are presented the spatial distributions of diapycnal (D-T) and isopycnal (I-T) processes intensity in the temperature field calculated for the layers A, B and C in the Catalan Sea. The intensity of diapycnal processes was comparatively higher in layer A. In this layer the areas of high intensity (D-T A) have a spotty character and are concentrated from north-east to south-west along the continental shelf border of the Iberian peninsula. In the southern part they tend to occupy all the basin. The comparison of these spots location with the mesoscale features of geostrophic circulation in the LIW spreading depth, shows that the areas of high diapycnal activity are situated along the main geostrophic flow of LIW and coincide with mesoscale anticyclone features in the southern part of the basin. The higher diapycnal intensity in layer A may be explained by the marked thermohaline contrast between the upper LIW layer and the layer above it. This contrast intensifies the processes of heat and salt exchange between two adjacent water masses. Thus we can assume that, in the diapycnal range scale, LIW can loose heat due to diffusive processes of mixing. The existence of anticyclonic mesoscale activity in the southern part of the basin can also induce vertical motions, what is reflected in the presence of step-like inhomogeneities. The LIW core (layer B) has a minimum thermohaline contrast with the

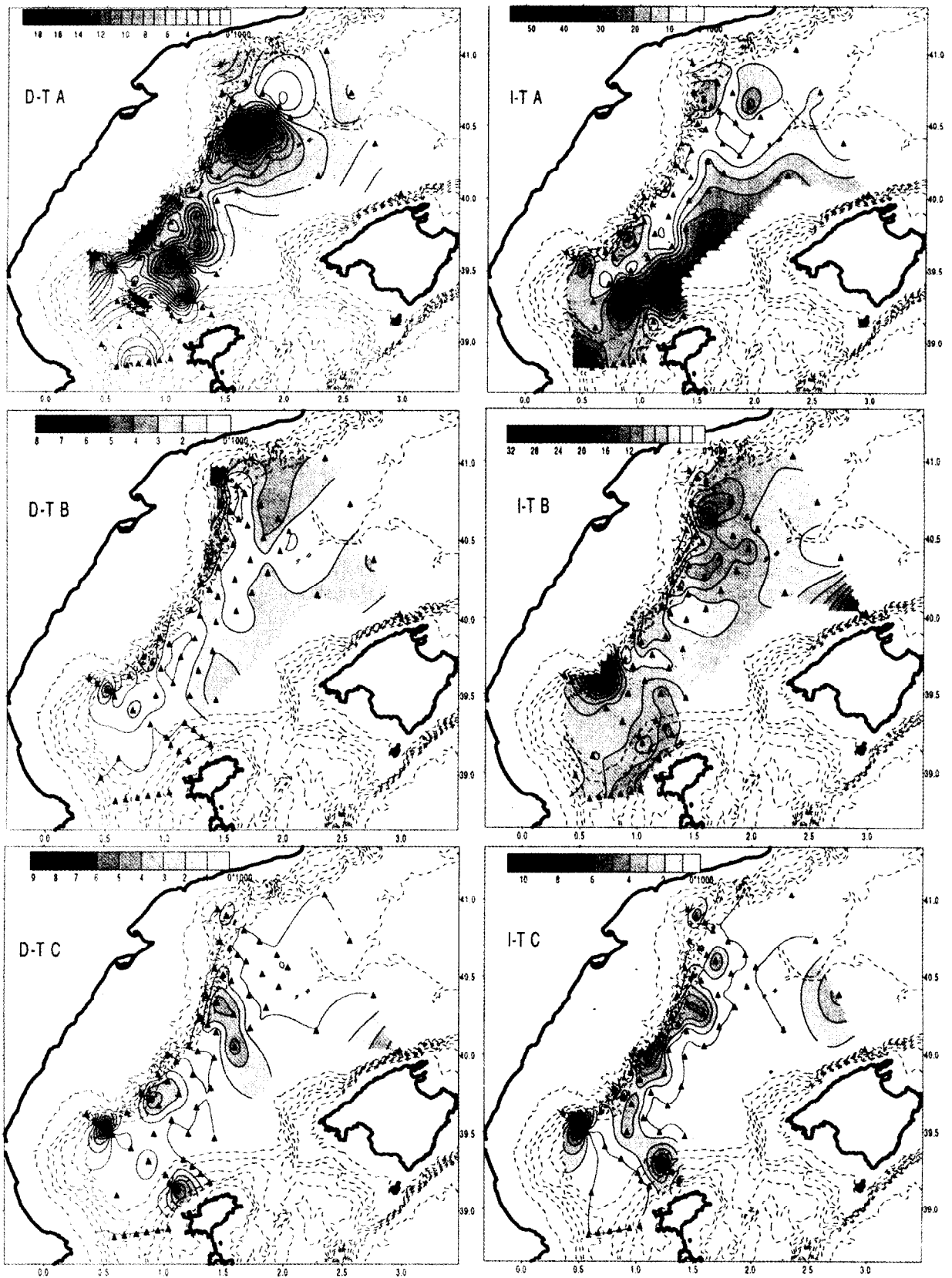


Fig. 2. Spatial distribution of diapycnal (D-T) and isopycnal (I-T) processes intensity in the Catalan Sea in the temperature field calculated for the layers A, B and C.

layers above and below it, as is reflected in the values of diapycnal processes intensity (D-T B). In this layer the highest diapycnal activity area is situated in the North of the sampled area. The contrast there between the LIW core and the resident waters of the Catalan sea is stronger than downstream. In the lower LIW layer (C) the intensity of diapycnal processes (D-T C) is characterised by intermediate values between layers A and B. This can be explained by lesser differences between the lower LIW layer thermohaline characteristics and deeper water masses. In general the positions of high diapycnal activity spots coincide with those detected in layer A and with the position of geostrophic circulation features in the layer of LIW spreading.

The spatial distributions of isopycnal processes intensity have also a spotty character, and layer A is also characterized by higher isopycnal activity (I-T A) in comparison with layers B and C. But, unlike the diapycnal intensity spatial distribution, the spots of high isopycnal intensity in layer A are closer to the Balearic Islands shelf. The area of highest isopycnal activity is situated in the southern part of the basin where the anticyclonic mesoscale features were detected in the dynamical relief of LIW layer spreading. In layer B the spots of high isopycnal activity (I-T B) are situated along the Iberian continental slope and form an area of high isopycnal activity stretched from north-east to south-west. In the spatial distribution of isopycnal activity in layer C (I-T C) one can see a distinct distribution of the spots positions. If in the northern and central parts of the basin the high isopycnal intensity spots are situated near the peninsular shelf, in the southern part of the basin these spots are situated near the Ibiza island shelf. This isopycnal intensity spatial distribution coincides with the LIW circulation scheme in the Catalan Sea [2] and shows the deflection of the branch of LIW to the north-east.

In Fig. 3 are presented the spatial distributions of diapycnal (D-T) and isopycnal (I-T) processes intensities in the temperature field calculated for layers A, B and C in the Alboran Sea. In this case the areas of high diapycnal intensity have also a spotty character, and the intensity of diapycnal processes in layer A (D-T A) is higher than in layers B (D-T B) and C (D-T C). The blanked areas in the dia- and isopycnal intensity spatial distribution maps (Fig. 3) indicate the absence of pronounced LIW in the analysed CTD profiles according to θ, S analysis. The blanked areas coincide with the big Alboran anticyclonic gyre positions, which displace the LIW outflow toward the Spanish continental slope. There are two areas of high diapycnal intensity in layer A (D-T A). One of them is situated in the eastern part of the basin. Inside this area the spots of high diapycnal intensity are situated near the Spanish continental slope and coincide with the strongest signal of LIW on the CTD profiles. Another is situated in western Alboran Sea. The comparison of the diapycnal intensity spatial distribution in layer A with the LIW circulation scheme shows that the mesoscale circulation features are reflected in the small-scale processes intensity fields. In the western Alboran the position of the areas of high diapycnal processes intensity in layer A is close to the position of the anticyclonic circulation features. The areas of high diapycnal intensity in this layer coincide with the areas of vertical velocity maxima [8] situated on the periphery of the big western anticyclonic gyre. In layer B the diapycnal intensity spatial distribution (D-T B) also has a spotty character. One of the high diapycnal intensity areas is situated in the eastern part of the basin close to the Spanish continental slope. Another one is situated close to the position of the anticyclonic circulation feature, mentioned above. In layer C the eastern part of the basin is also characterized by high diapycnal intensity (D-T C). There are high diapycnal intensity spots close to the Spanish continental slope and one spot in the area of the big eastern anticyclonic gyre. One spot of the high diapycnal activity was also detected close to the northern limit of the big western anticyclonic gyre.

The spatial distributions of isopycnal processes intensity in layers A (I-T A), B (I-T B) and C (I-T C) also are characterized by different spots of high isopycnal activity distributed throughout the basin. The isopycnal processes are more active in layer A than in the other characteristic layers. In layer A the area of high isopycnal activity is situated in the north-eastern part of the basin, just near the LIW entrance in the Alboran sea. In layer C the same area is characterised by high isopycnal activity. The comparison of high isopycnal intensity spot position in layer B with the geostrophic circulation scheme shows that this spot is situated close to the northern limit of the big eastern anticyclonic gyre. In the same place a spot of high isopycnal activity was detected in layer C.

Conclusions

The analysis of the spatial distribution of diapycnal and isopycnal processes intensity in the Catalan Sea shows that the areas of high intensity are situated, in general, along the peninsular continental shelf. In this part of the sea there exists an intensive thermohaline exchange between LIW and adjacent waters. At the smallest scales the diapycnal processes transformed the LIW thermohaline structure, while the nature of the structure forming

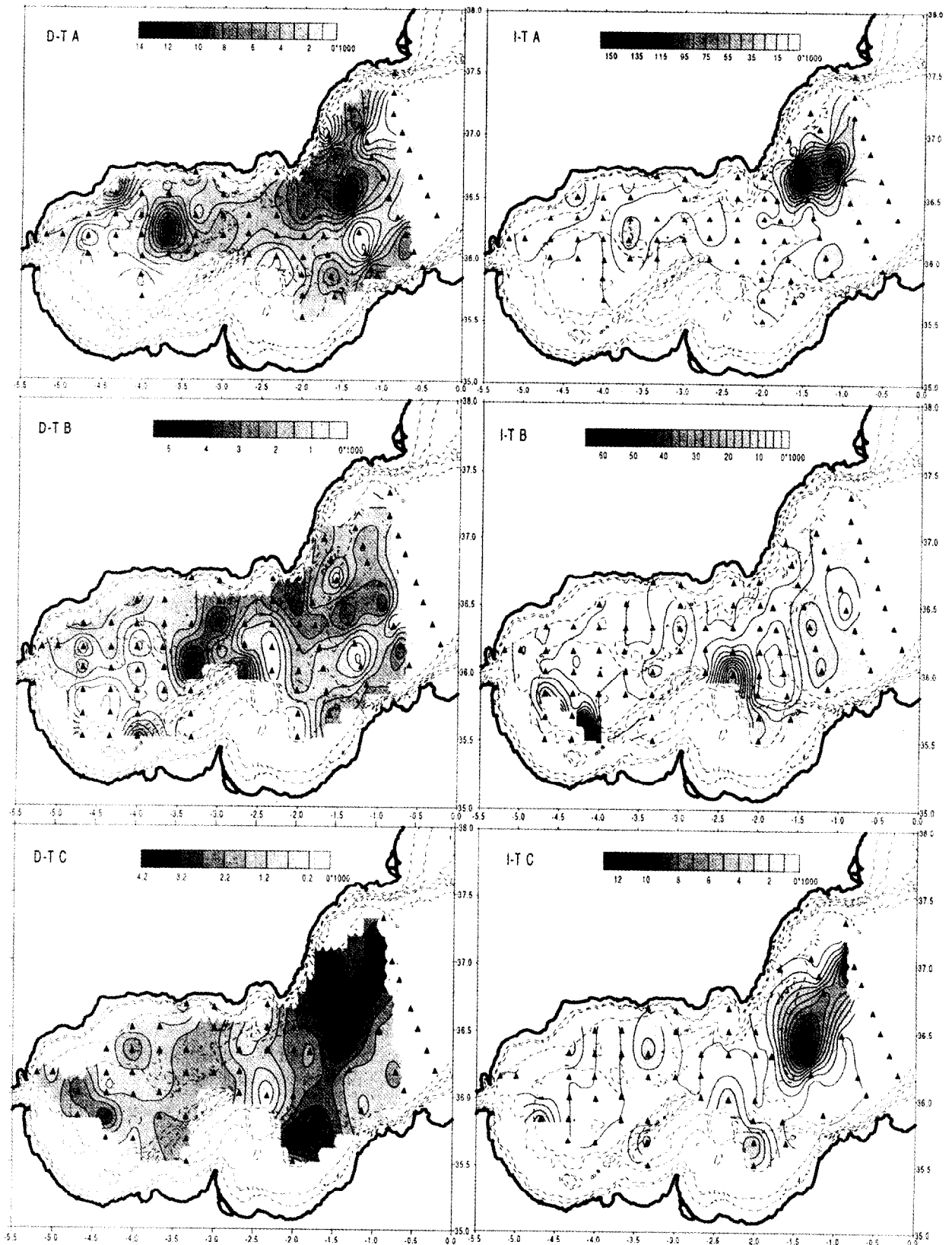


Fig. 3. Spatial distribution of diapycnal (D-T) and isopycnal (I-T) processes intensity in the Alboran Sea in the temperature field calculated for the layers A, B and C.

processes changes when we increase the analysed scale range. Our analysis shows that the diapycnal processes intensity is weak near the Balearic Islands shelf, but the isopycnal processes are still active in this area. It is possible that the deflected part of LIW does not have a sufficient stock of heat and salt to produce an intensive diapycnal exchange through its upper and lower limits.

The high diapycnal activity in the eastern part of the Alboran sea can be explained from the point of view of the thermohaline contrast between recently entered LIW and the resident waters. Thus, it is possible to assume that due to the thermohaline contrast between LIW and resident waters the diapycnal processes are still active in the area of LIW entrance in the Alboran Sea. The high diapycnal activity close to the limits of the big anticyclonic gyres can be produced by the vertical ageostrophic motions which exist near these borders [9]. The comparison of isopycnal processes intensity spatial distribution with the LIW circulation scheme shows that the high isopycnal activity spots trace the LIW entrance in the basin and the existence of isopycnal advection close to the northern border of the big eastern anticyclonic gyre.

The spots of high diapycnal intensity are generally situated in the areas of higher thermohaline contrast between LIW and resident waters of the Catalan and Alboran basins, or close to mesoscale features of geostrophic circulation. The spots of high isopycnal intensity generally trace the entrance of LIW into the basin. The isopycnal processes are more intense in the Alboran sea than in the Catalan sea. This can be explained by a higher dynamical activity in the Alboran basin.

Acknowledgements: This is a contribution to the OMEGA Project, funded by the European Union Marine Science and Technology Program (contract MAS3-CT95-0001) and INTERMESO Project funded by the Spanish R+D National Plan (AMB95-0901).

M.Emelianov acknowledges a Ministerio de Educación y Ciencia Fellowship for temporary stay of foreign scientists in Spain (SB95-A02550835).

References

- [1] Benzohra, A., Millot C., 1995. Characteristics and circulation of the surface and intermediate water masses off Algeria. *Deep-Sea Res.*, 42, 1803-1829.
- [2] Font, J., 1987. The path of the Levantine Intermediate Water to the Alboran Sea. *Deep-Sea Res.*, 34, 10, 1745-1755.
- [3] Fedorov, K.N., 1978. Thermohaline finestructure of the ocean. *Pergamon Press Sciences*, London, 170.
- [4] Hopkins, T.S., 1978. Physical processes in the Mediterranean basin. In: *Estuarine transport processes*, de B.Kjerfe, *Univ. South California Press.*, 269-310.
- [5] Millot, C., 1998. Circulation in the western Mediterranean. *Journal of Marine System* (in press).
- [6] Ruddick, B., Turner, J.S., 1979. The vertical length scale of double-diffusion intrusions. *Deep-Sea Res.*, 26, 8A, p.903-914.
- [7] Shapiro G.I., Emel'yanov M.V., 1994. Relationship between characteristics of the mesoscale and finestructure in the antarctic polar front zone. *Oceanology Engl. translation*, 34, 2, 180-185.
- [8] Viudez, A., Tintoré J., Haney, R.L. 1996. Circulation in the Alboran Sea as determined by quasi-synoptic hydrographic observations. Part I: Three-dimensional structure of the two anticyclonic gyres. *J. Phys. Oceanogr.*, 26, 5, 684-705.
- [9] Viudez, A., Haney, R.L., Tintoré J., 1996. Circulation in the Alboran Sea as determined by quasi-synoptic hydrographic observations. Part II: Mesoscale ageostrophic motion diagnosed through density dynamical assimilation. *J. Phys. Oceanogr.*, 26, 5, 706-724.
- [10] Woods, J.D., 1980. The generation of thermohaline finestructure at fronts in the Ocean. *Ocean Modelling*, 32, 1-4.
- [11] Yemel'yanov, M.V., Fedorov, K.N., 1985. Structure and transformation of intermediate waters of Mediterranean sea and Atlantic ocean. *Oceanologia, Engl. transl.*, 25, 2, 155-161.
- [12] Zhurbas, V.M., Ozmidov, R.V., 1987. Forms of ocean thermohaline finestructure catalogue. *Geophys. Committee, USSR Academy of Sciences, Moscow*, 134, (in Russian).
- [13] Zhurbas, V.M., Lips, U.K., 1987. Discrimination of the main types of thermohaline fine structure in the ocean. *Oceanology, Engl. transl.*, 27, 4, 416-420.

NEW DATA ON LEVANTINE INTERMEDIATE WATER CIRCULATION IN THE WESTERN MEDITERRANEAN SEA.

M. V. Emelianov^{1,3}, C. Millot², J. Font¹, I. Taupier-Letage²

- 1 - Institut de Ciències del Mar, P.Joan de Borbo, s/n, 08039 Barcelona, SPAIN,
e-mail: mikhail@icm.csic.es ; jfont@icm.csic.es
- 2 - Laboratoire d'Océanographie et de Biogéochimie, Centre d'Océanologie de Marseille, Antenne LOB-COM-CNRS, BP 330, F-83507 La Seyne, FRANCE
e-mail: cmillot@ifremer.fr ; itaupier@ifremer.fr
- 3 - P.P.Shirshov Institute of Oceanology, Nakhimovskii pr., 36, 117851 Moscow, RUSSIA

Abstract

The Levantine Intermediate Water (LIW) flows in the western Mediterranean at intermediate depths. The mixing processes of LIW occur at different scales in space and time. One of the possible processes at mesoscale is the interaction between Algerian eddies and the LIW vein. These anticyclonic eddies propagate eastward along the Algerian slope and then, at the entrance of the Sardinia channel, initiate an anticlockwise circuit in the Algerian basin. LIW initially enters in the Algerian basin as a quasistationary vein flowing alongslope around Sardinia. The result of the interaction between the LIW vein and the Algerian eddies is the transport of filaments of LIW from the south-eastern part of Sardinia toward the interior of the basin and their eventual trapping by the eddies. At a much smaller scale, inhomogeneities in the thermohaline profiles account for the occurrence of complex turbulent processes. The data recently gathered during the ELISA experiment (1997/1998) allow to analyse in detail the thermohaline structure of the mesoscale Algerian eddies and to observe how the interaction between the eddies and the filaments reflects in field of the small-scale mixing processes intensities.

Introduction

The Levantine Intermediate Water (LIW) originates in the eastern Mediterranean. In the whole western basin it flows at intermediate depths. The mean circulation of LIW is mainly anticlockwise along the continental slope [1,7]. As LIW is more saline and warmer than the western resident waters its interaction changes its thermohaline characteristics.

The mixing processes of LIW occur at different scales in space and time. At mesoscale, as it was confirmed recently [5], one of the possible processes which participate in LIW mixing with the resident waters in the Algerian basin, are the interactions between mesoscale eddies and the LIW vein. These anticyclonic eddies, generated from the Algerian current, propagate eastward along the slope and at the entrance of the Sardinia channel flow back thus completing an anticlockwise circuit. LIW initially enters in Algerian basin as a quasistationary vein flowing alongslope around Sardinia. The result of the interaction between the LIW vein and Algerian eddies is the transport and eventual trapping of filaments of LIW from the south-western part of Sardinia toward the interior of the basin.

At the finestructure scale [4], inhomogeneities in the thermohaline profiles account for the occurrence of complex turbulent processes [15]. Finestructure inhomogeneities on the vertical temperature and salinity profiles are known to be observed frequently in the frontal zones where interactions between waters with different thermohaline characteristics exist. In these zones an active transformation of mesoscale horizontal irregularities into fine thermohaline stratification takes place. This spreading of kinetic energy of mean currents from the mesoscale to smaller scales reflects in the different shapes of inhomogeneities in the thermohaline profiles [4].

The shape of fine structure inhomogeneity has a relationship with the process of its creation [17]. In general these processes are divided into two main classes: diapycnal and isopycnal. Diapycnal processes lead, as a rule, to the creation of step-like structures [4, 16], whereas isopycnal advection processes lead to the formation of inversions on the thermohaline profiles [10, 14]. The relationship between mesoscale and finestructure

characteristics has been investigated in different frontal zones of the Ocean, such as those associated with Kuroshio [6], the Gulf Stream [18], the subarctic Pacific [12], the Barents Sea [9] and the Antarctic [13].

Analysing the finestructure inhomogeneities in the vertical profiles of temperature and salinity it is possible to determine its dia- or isopycnal nature and evaluate the intensity of small-scale finestructure forming processes. The spatial distribution of dia- and isopycnal processes intensities allows to determine the areas of predominance of one of these processes.

Data obtained during the ELISA-1 cruise (July 1997) allow to analyse in detail the thermohaline structure of a mesoscale Algerian eddy and to observe how the interaction between the mesoscale eddy and a filament reflects in the field of small-scale dia- and isopycnal processes intensities.

Materials and Methods

A mesoscale structure, formed by a filament entrained around an Algerian anticyclonic eddy away from the south-western corner of Sardinia, was detected on SST images (Fig.1 a). The eddy centred at 38°20'N and 5°30'E had a diameter of ~180 km. The cold filament had the same spatial scale, and displaced from the south-western corner of Sardinia toward the southern part of the eddy. To obtain the thermohaline structure of the eddy-filament system 7 CTD sections were made. One diametrical section from south-east to north-west (st. 18-35 in Fig.1b), two radial sections from south-west to north-east (st. 36-39 in Fig.1b) and from north to south (st. 40-47 in Fig.1b), and three sections across the south-western slope of Sardinia (st. 48-57; st.58-62 and st.63-67 in Fig.1b). During a further leg, the radial north-south section (st.68-82 in Fig. 1b) was repeated and a new radial section from the centre of the eddy to the east (st.100-121 in Fig. 1b) was made.

All CTD casts were performed with a CTD SBE 911+ down to 1000 m, except two casts (st.45a and 47a) performed down to 2000 m. The raw data were processed using the standard SeaBird Inc. Software. The processed CTD data files had 1-m resolution. The finestructure inhomogeneities on the CTD profiles were analysed using the method proposed by Zhurbas and Lips [17] and modified by Shapiro and Emelianov [13]. This method, based on previous results, permits to classify the main types of finestructure inhomogeneities and characterize their nature. It allows to describe a variety of fine thermohaline structures within the framework of step-like and inversion-like shapes, by extracting the finestructure component from a CTD profile using cosine filtering [13]. The filtering uses a varying vertical scale within a chosen range of finestructure scale. The range of scales to analyse the thermohaline inhomogeneities was selected from 2 m (the minimal scale to smooth CTD data with one-meter vertical resolution) to 50 m (the maximal vertical size of inhomogeneities according to phenomenological analysis). This allows to analyse the whole ensemble of finestructure inhomogeneities in a CTD profile, and to determine the range of scales for the two main (diapycnal and isopycnal) finestructure forming processes, if both shapes of finestructure inhomogeneities coexist in the same profile. The statistical characteristics of the finestructure inhomogeneities, in the range chosen of vertical scales, make possible to evaluate the intensity of dia- and isopycnal processes and to obtain their spatial distribution in the area investigated.

We analysed obtained CTD profiles, calculating the parameter γ to characterize the isopycnal or diapycnal nature of finestructure inhomogeneities. γ is defined by $(tg\phi_p - tg\phi_i)/(tg\phi_d - tg\phi_i)$, where $tg\phi_p$, $tg\phi_i$ and $tg\phi_d$ are the characteristic angles of normalised finestructure inhomogeneities of temperature and salinity in the $1/\beta S', \alpha T'$ - plane [13]. The inhomogeneities are normalised by α (thermal expansibility coefficient) and β (salinity contraction coefficient) and the resulting inhomogeneities cloud in the $1/\beta S', \alpha T'$ - plane is fitted to a line. Then γ , that ranges from 0 to 1, indicate the proximity of the fit line ($tg\phi_p$) to the lines which characterise the pure diapycnal ($tg\phi_d = R_\rho$, where R_ρ is the mean density relationship in the analysed layer [11]) or pure isopycnal ($tg\phi_i = 1$) conditions. When $0 < \gamma < 0.5$, the finestructure temperature and salinity inhomogeneities are mainly formed by isopycnal processes, and when $0.5 < \gamma < 1.0$ by diapycnal ones [17, 2].

To quantify the finestructure forming processes intensity, the root mean square deviations of temperature (T_{rms}) and salinity (S_{rms}) inhomogeneities obtained with different vertical scales from the chosen range were calculated. Thus, the CTD profiles were analysed using a filter window width (λ) increasing from 2 to 50 m at one meter step [13]. Then the intensity of diapycnal (I_{dT} , I_{dS}) and isopycnal (I_{iT} , I_{iS}) processes in the temperature and salinity fields, respectively, was determined by a combined analysis of the dependency of γ vs λ and of T_{rms} and S_{rms} vs λ . See [3] for details on the analysis.

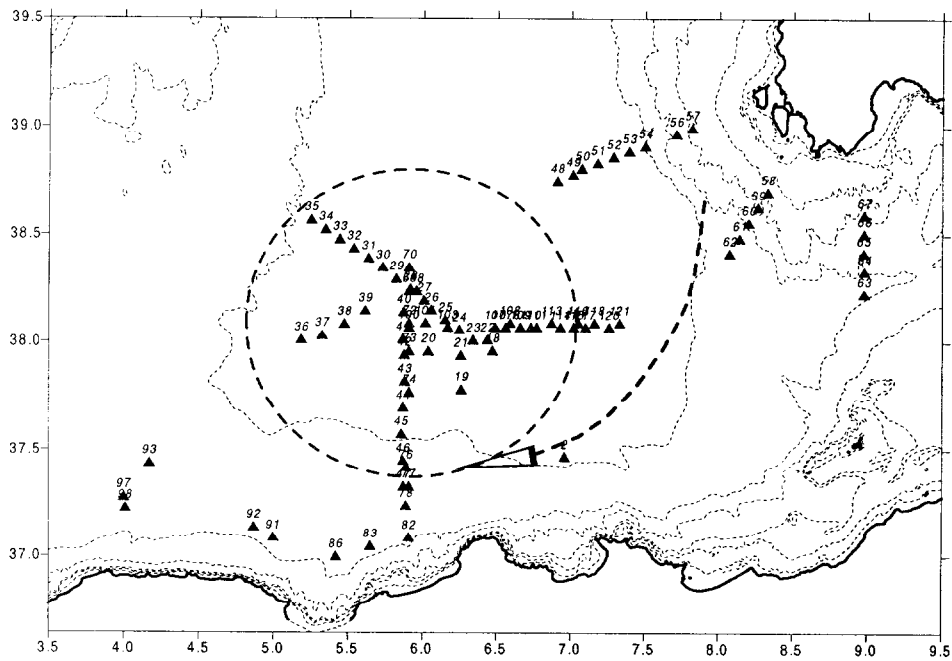
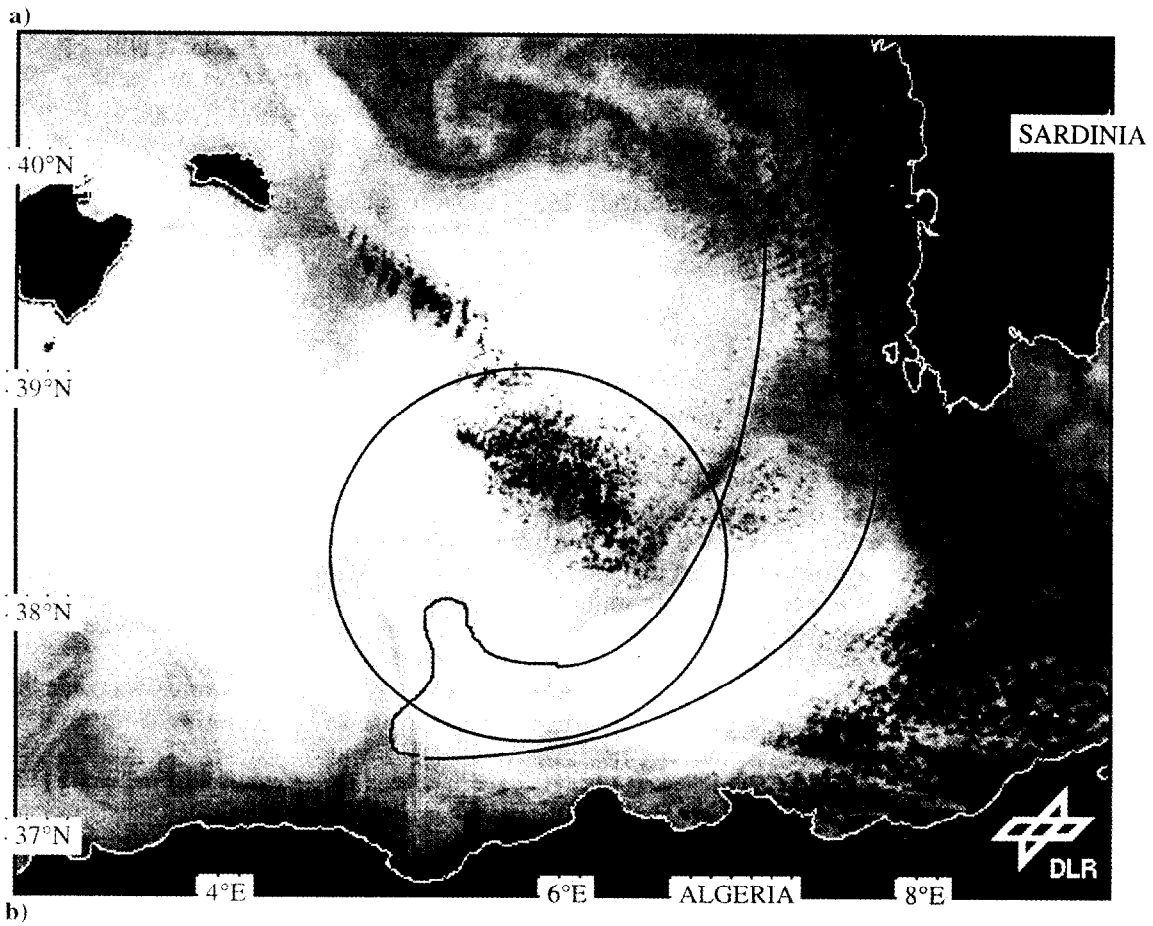


Fig. 1. a) mesoscale system formed by a filament entrained around an anticyclonic eddy detected in the NOAA/AVHRR SST image from 27.07.97;
b) CTD cast positions during ELISA-1 cruise.

Results and Discussion

The inclinations of the T and S isolines in all sections performed in the area of the eddy account for an intense anticyclonic rotation in the top 200 meters. Below 200 metres the warmer and saltier waters formed by "old" LIW, resident in the basin and transformed by mixing with adjacent waters were located (Fig. 2). In the southern part of the eddy, inside the higher temperature and salinity layer, the portion of warmest and saltiest waters was detected.

According to θ, S analysis of the intermediate layer (200-600 m) there were two different types of LIW signature were determined in the investigated area:

- "new" LIW, inflowing from the Thyrrenian Sea with $13.75 < \theta < 13.85$ and $38.60 < S < 38.70$;
- "old" LIW resident in the Algerian Basin, strongly mixed and characterised by $13.25 < \theta < 13.38$ and $38.50 < S < 38.54$ (Fig.2).

The spatial distribution of the different types of LIW shows that the "new" LIW was encountered in the southern part of the area of the eddy and near the Sardinia slope. The "old" LIW was situated in the western and north-western parts of the eddy area as well as offshore Sardinia (Fig. 2). The θ, S curves have a lot of irregularities especially in the upper layer of the LIW core. This reveals the presence of finestructure forming processes. The upper layer of LIW was defined as the layer above the LIW core (maxima of θ and S), with positive mean potential temperature and salinity vertical gradients. The depth range occupied by the upper layer of LIW in the investigated area was between ~200 m and ~350 m.

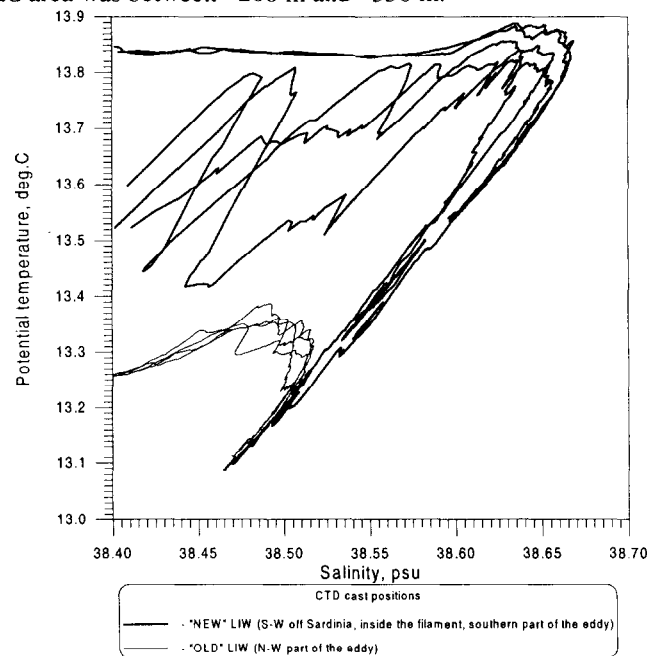


Fig.2 θ, S curves obtained in different parts of investigated area .

In Fig. 3 the spatial distribution of the intensities of diapycnal and isopycnal processes in the upper layer of LIW are presented in the temperature field. According to the presented distributions it is possible to distinguish the following areas:

- 1 - The area of the eddy, with two different parts. In the northern and north-western parts the diapycnic processes predominate, and in the southern part the isopycnic processes predominate;
- 2 - The area of the continental slope of Sardinia. In this area the isopycnic processes predominate near the coast and the diapycnic processes predominate offshore;
- 3 - The area of the filament, characterised by the prevalence of the isopycnic processes. It is important to note that the isoline 0.25 in Fig. 2b forms a belt that unites the southern part of the eddy with the south-western corner of Sardinia.

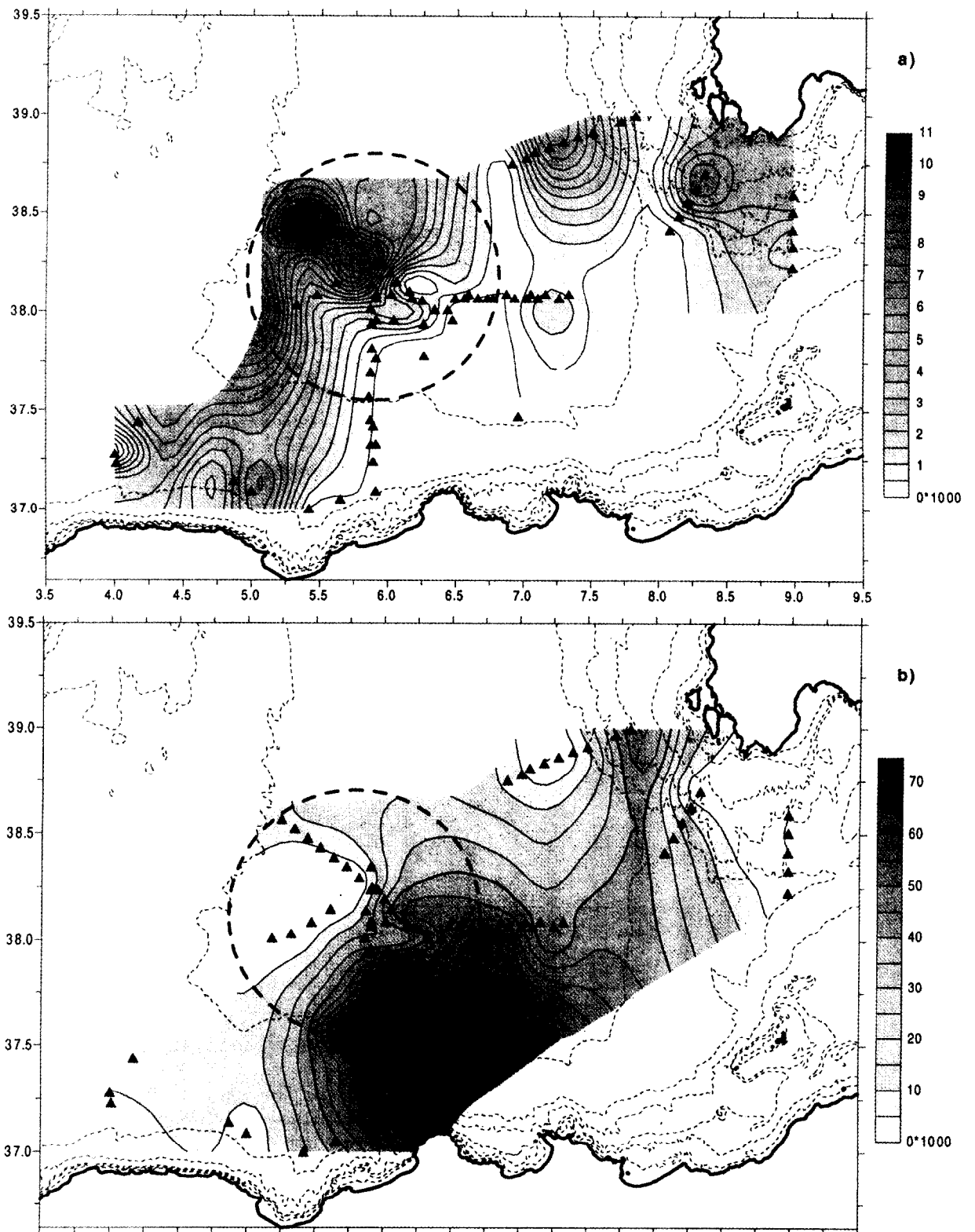


Fig. 3. Spatial distribution of diapycnal (a) and isopycnal (b) processes intensity in the upper layer of LIW in the temperature field.

Conclusions

The analysis of data obtained during the ELISA-1 field experiment demonstrates that the anticyclonic eddies shed by the Algerian current can deflect filaments of LIW from the vein that passes along the Sardinia slope. The spatial distribution of small scale processes intensities in the upper layer of LIW shows that the area of the filament connected with the southern part of the eddy is characterised by higher isopycnal processes activity. The spatial distribution of isopycnal processes intensities mark well the “new” inflowing LIW captured by the eddy. The spatial distribution of diapycnal processes intensities mark the area occupied by “old” LIW, concentrated in the north-western and northern parts of the eddy and in the south-western part of the investigated area. The comparison of these distributions allows to conclude that the mesoscale eddies shed by the Algerian current participate in the redistribution of LIW throughout the Algerian basin capturing the recently inflown LIW, and mixing it with more transformed LIW, situated earlier in the layer of LIW displacement.

Acknowledgements: This is a contribution to the Mediterranean Targeted Project phase II-MATER (number MTP II-MATER/024) We acknowledge the support from the European Commission’s Marine Science and Technology Programme (MAST-III) under contract MAS3-CT96-0051, as well as the collaboration of the crew and colleagues on board the NO “Le Suroit” during ELISA-1 cruise.

M. Emelianov acknowledges a Ministerio de Educación y Ciencia Fellowship for temporary stay of foreign scientists in Spain (SB95-A02550835).

References

- [1] Benzohra, M., Millot, C., 1995. Characteristics and circulation of the surface and intermediate water masses off Algeria. *Deep-Sea Res.*, 42, 10, 1803-1829.
- [2] Emelianov, M.V., 1993. Mesoscale and fine structure of the frontal zones in the Atlantic sector of the Southern ocean. Ph.D.Thesis, P.P.Shirshov Institute of Oceanology, Moscow: 194. (in Russian).
- [3] Emelianov M.V., Garcia-Ladona, E., Font, J., 1998. Double-diffusion processes and LIW characteristics in the Alboran sea. *Rapp. Comm. Int. Mer Médit.*, 35, 138-139.
- [4] Fedorov, K.N., 1978. Thermohaline finestructure of the ocean. *Pergamon Press Sciences*, London, 170.
- [5] Fuda, J.L., Millot, C., Taupier-Letage, I., Send, U., Bocognano, J.M., 1998. XBT sections across the Western Mediterranean Sea., *Deep-Sea Res.*, in press.
- [6] Meshchanov, S.L., Fedorov, K.N., 1990. On thermoclinicity and baroclinicity of the Kuroshio frontal zone. *Oceanology*, Engl. Transl., 29, 7, 34-38.
- [7] Millot, C., 1987. Circulation in the Western Mediterranean. *Oceanol.Acta*, 10, 2, 143-149.
- [8] Pingree, R.D., 1972. Mixing in deep stratified ocean. *Deep-Sea Res.*, 19, 8, 549-562.
- [9] Rodionov, V.B., 1991. Frontal zone structure and frontogenetic processes in northern seas. Ph.D.Thesis, P.P.Shirshov Institute of oceanology, Moscow, 210. (in Russian).
- [10] Ruddick, B., Turner, J.S., 1979. The vertical length scale of double-diffusion intrusions. *Deep-Sea Res.*, 26, 8A, 903-914.
- [11] Ruddick, B., 1983. A practical indicator of the stability of the water column to double-diffusive acting. *Deep-Sea Res.*, 30, 10A, 1105-1107.
- [12] Sagdiev, A.M., 1992. Thermohaline finestructure peculiarities in frontal zones and mesoscale ocean eddies. Ph.D.Thesis, P.P.Shirshov Institute of oceanology, Moscow, 180 (in Russian).
- [13] Shapiro, G.I., Emel’yanov, M.V., 1994. Relationship between characteristics of the mesoscale and fine structure in the antarctic polar front zone. *Oceanology*, Engl. Transl., 34, 2, 180-185.
- [14] Woods, J.D., 1980. The generation of thermohaline finestructure at fronts in the Ocean. *Ocean Modelling*, 32, 1-4.
- [15] Yemel’yanov, M.V., Fedorov, K.N., 1985. Structure and transformation of intermediate waters of Mediterranean sea and Atlantic ocean. *Oceanologia*, Engl. transl., 25, 2, 155-161.
- [16] Zhurbas, V.M., Ozmidov, R.V., 1987. Forms of ocean thermohaline finestructure catalogue. *Geophys. Committee, USSR Academy of Sciences*, Moscow, 134. (in Russian).
- [17] Zhurbas, V.M., Lips, U.K., 1987 Discrimination of the main types of thermohaline fine structure in the ocean. *Oceanology*, Engl. transl., 27, 4, 416-420.
- [18] Zhurbas, V.M., Kuzmina, N.P., Lozovatskii, I.D., 1988. On baroclinicity’s role in intrusive ocean stratification. *Oceanologia*, Engl. transl., 28, 1, 50-53.

ON SOME SUBMESOSCALE COHERENT STRUCTURES AT THE STEEP SLOPE OF NORTHWEST AFRICA

M.A. Evdoshenko

P.P. Shirshov Institute of Oceanology, Russian Academy of Sciences, 117851 Moscow, Russia.
e-mail: mar@manta.sio.rssi.ru

Abstract - Processes occurring in near bottom boundary layer of littoral ocean regions with intensive upwelling circulation are important for investigation of suspended matter transport and current of biogen elements carried out from bottom to surface. Vertical profiles of turbidity with Sea Tech Mark nephelometer and also profiles of temperature, salinity and potential density with Neil Brown probe were obtained from the ocean surface to bottom during the research vessel "Academic Mstislav Keldysh" cruise in winter 1991 - 1992. Measurements were performed at shelf and continental slope near western Africa. More than hundred profilings in the continuous mode at the steep ocean slope during the vessel drift were made. A small scale vortex structure occupying practically all water column was found. The vortex had a horizontal dimension ~ 3 km, a ratio of its vertical to horizontal size was about 0.3, its life time was more than 2.5 days. Displacement of isotherms at the center of the vortex was maximum in near bottom layer and consisted of 68 m, isopycnic bend was about 10 m. The vortex had an asymmetrical horizontal structure which changed with depth varying. A benthic turbid event evidently caused by the vortex was characterized by a strong mixing in near bottom layer of 125 m thickness at ocean depth of about 1 km. Turbidity profiles revealed the existence of 'detached' near bottom nepheloid layers spread by equal density lines from higher region slopes. High turbidity near bottom nepheloid layer was also found at the depth of ~ 560 m; the benthic event was evidently caused by upwelling influence on near bottom layer and followed approach of the characteristic inclination value for the semi-diurnal internal tide M2 to the value of bottom slope.

I. Method and instrumentation

Measurements were performed in the Atlantic Ocean near northwest Africa during the cruise of research vessel "Academic Mstislav Keldysh" in winter 1991 - 1992. The water area included the region of Canary upwelling where ocean properties are changeable and not uniform. Measurements were carried out with use of Rosette sample complex containing Sea Tech Mark nephelometer and CTD Neil Brown probe. The nephelometer is a high-sensitive optical device for measuring of light scatter at the angle of $\sim 90^\circ$. Vertical profiles of salinity S and specific density σ_t were calculated by temperature T , conductivity C and pressure P measurements. Profilings were performed practically from ocean surface to bottom. The space vertical interval provided by casts was about 1 m (this corresponded to data averaging by 20 - 25 readings). Measurements with such interval gave possibility to distinguish fine vertical structure of water characteristics. Distance to bottom was controlled with the acoustic pinger installed in Rosette. Profilings were stopped at 1 - 6 m from ocean bottom at steep slope region. Mean time interval between profilings was about 20 minutes.

A testing area included ocean rectangular region disposed between $22^\circ 0' N - 21^\circ 25' N$ and $17^\circ 14' W - 17^\circ 59' W$, divided by about hundred stations separated by 5 minutes by latitude and longitude. Besides of these stations two drift stations (d.s.) were carried out at steep continental slope with Rosette complex profilings in continuous mode. Preliminary results of measurements at 5' stations are discussed in [1].

II. Results

A. Measurements at the first drift station

Bottom relief and positions of two drift stations are shown in Fig. 1. During the first d.s. 73 profilings were performed. A space and time intervals between the first and the last profilings were correspondingly 24.5 km and 31.46 hour. The direction of drift was uneven, the depth ranged from 930 m to 1150 m, the bottom slope changed from 0.7° to 1.2° .

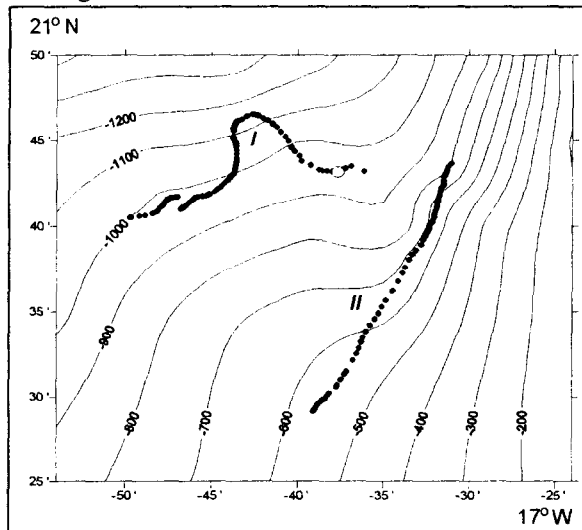


Fig. 1. Isobathes and location of drift stations.

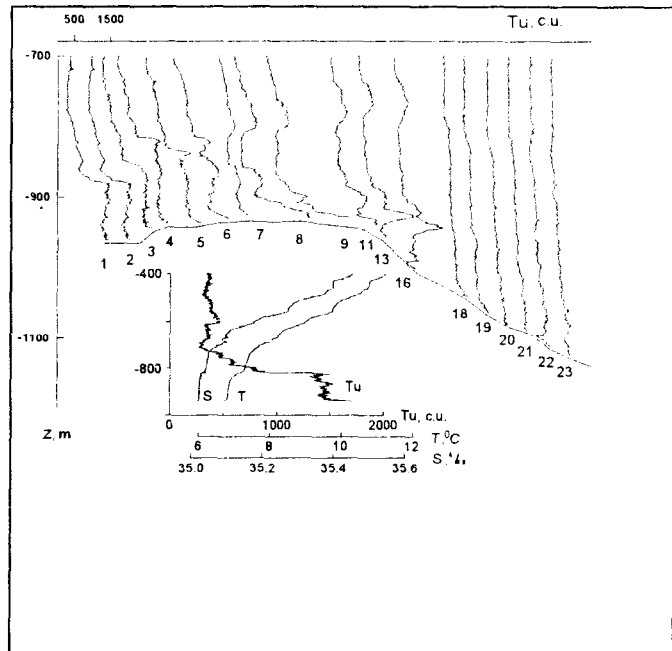


Fig. 2. Vertical profiles of Tu for the first 15 km of 1-st d.s.; at the bottom of picture are profiles of measured characteristics for the 4-th profiling.

Vertical profiles of turbidity for the first 15 km during the first 12.40 hours (the first 24 profilings of the d.s.) are shown in the upper plot of Fig. 2 (the direction of horizontal axis is opposite to drift direction). The character element of near bottom ocean layer is high turbidity layer or bottom nepheloid layer (BNL) formed by high concentration of matter suspended in sea water. In connection with [2] BNL is defined as a layer of thickness ΔH between depths of maximum transparency D (minimum of turbidity) and ocean bottom H . BNL is practically observed at all Tu profiles, however its time-space structure currently changes. At steep slope BNL structure was mainly multilayer, frequently it was the two layer structure. The lower relatively narrow near bottom layer was characterized by larger Tu values while the upper thicker layer - by less Tu values. Evolution of BNL during the d.s. showed gradually increasing of Tu to 1430 conventional units (c.u.) and significant increasing of lower mixed part. For the fourth profiling (lower plot in Fig. 2) BNL thickness reached its maximum value of 125 m while all measured characteristics were smoothed and maximum value of Tu exceeded more than four times the Tu value at $z = D$. Such abnormal distribution of Tu in BNL was typical for "high energy near bottom layer" (HEBL) [3]. For the first 6 profiles BNL upper part was characterized by the absence of any Tu maximum. Profiles obtained during casts 5 - 9 showed the gradual washing out of BNL - decreasing of its thickness in lower part with increasing of turbidity gradient and thermohaline characteristics. Steady upper Tu maximum at the depth of ~ 800 m observed distinctly by profiles 7 - 19 is supposed to be caused by turbid intrusion from other slope region. Vertical structure of temperature in BNL for all profilings besides the third and the fourth, where it was smoothed, is characterized by negative gradient in BNL caused by T decreasing with approaching to the bottom.

For most profiles maximum turbidity value Tu_{max} was reached at the lowest measuring level (1 - 5 m above bottom), so it can be concluded that it was mainly caused by local process - resuspension from the bottom. For some cases values of Tu_{max} were achieved at several meters from the bottom, for four profiles - at tens meters (up to 70 m) from the bottom, the latter was possibly caused by "detached" BNL spread from other slope

region. Maximum value of Tu_{max} was observed for the fourth profiling and thickness of mixed near bottom layer was also maximum. BNL thickness ΔH was 21% - 38% relatively to H at the first d.s.

For a classification of BNL power it is convenient to use a dimensionless parameter R being a ratio of Tu_{max} in BNL and Tu_{min} at the $z = D$, calculated for each profile of Tu . The parameter R was also used in [4] by analogy with classification defined by suspension concentration given in [2]. So if R values do not exceed 1.5 BNL is called weak, if $1,5 < R < 2,5$ BNL is called middle, if $R > 2,5$ BNL is called powerful. Calculations showed that at the first d.s. R values were in the range of 3 - 3,9 so BNL were powerful. Most likely powerful BNL formation was connected with features of bottom relief at the region.

Isolines of turbidity Tu and temperature T over all water column are shown in Fig. 3 a,b,c. By isolines it is possible to reveal a connection between processes occurred in BNL and layers above them. Fig. 3a shows that turbidity isolines in BNL generally leave traces of bottom relief. At HEBL region (at 1 ~ 12 km) BNL thickness is increased. Distinctly observed is the "detached" layer with Tu values of 600 c.u. at the depth of about 780 m, spreading downslope by equal density levels. The space expansion of "detached" layer was about 4 km. Near bottom turbid water, characterized by Tu values > 400 c.u., sank downslope.

Temperature and also salinity isolines in BNL are roughly stretched by equal depth levels (Fig. 3b). Over the HEBL region the dome bend of temperature, salinity and density from near bottom layer up to the surface is observed. In this region strong mixing in BNL accompanied by increasing of ΔH and Tu is fixed. However strong correspondence between ascend of Tu isolines from one hand and isolines of T , S and σ_t from the other hand is not marked. At Fig. 3c isolines of T were plotted with use of potential density σ_t as a vertical component instead of z . (The upper bounds of the shaded regions at these plots correspond to maximum values of σ_t achieved at last points of profilings but not at the bottom depth). $T(\sigma_t)$ and also $S(\sigma_t)$ isolines dome bend in HEBL was retained, so it may be concluded that the main contribution to the isolines ascent was not connected with internal waves.

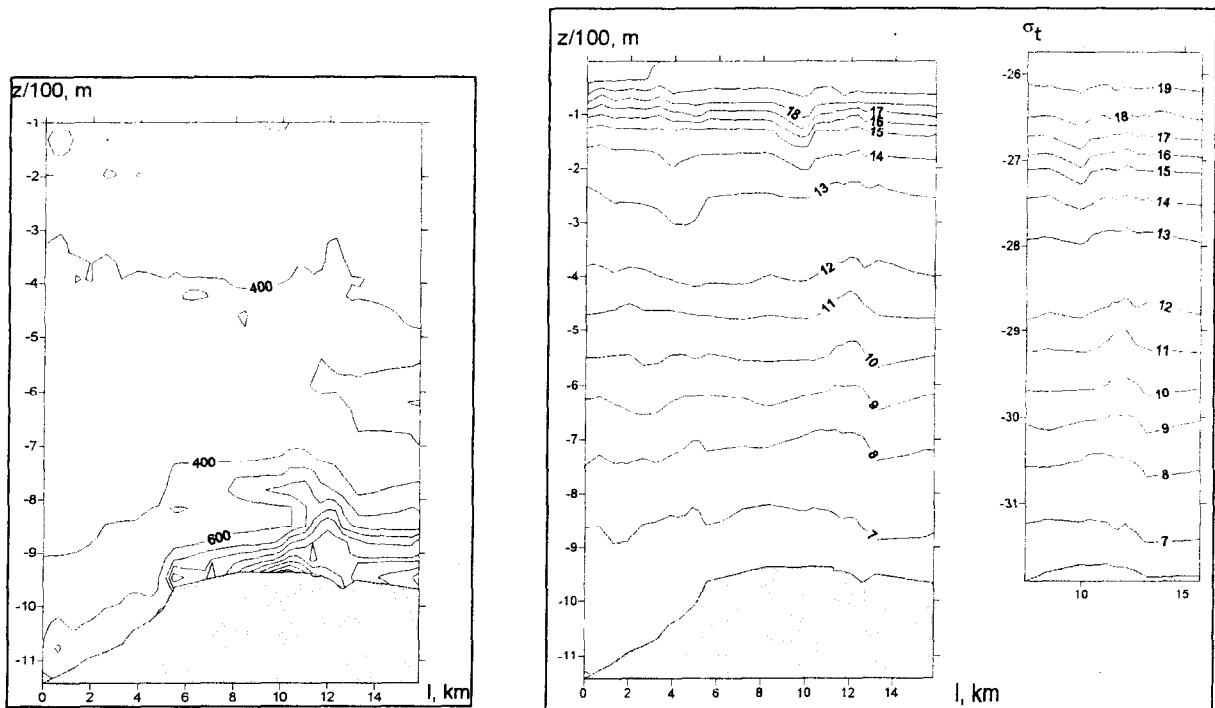


Fig. 3. Vertical structure of a) $Tu(z)$; b) $T(z)$, c) $T(\sigma_t)$ - for the first drift station.

The dome bends of all measured characteristics and strong mixing in near bottom layer possibly indicated a vortex occupying a layer from pycnocline to near bottom, thickness of the layer was ~600 m. The center of the vortex at the given depth is conventionally determined by maximum of T or σ_t dome isoline, its boundaries - by two isoline minima corresponded to the nearest water parts with rather uniform properties or with the least σ_t gradients. It is seen that the vortex had an asymmetrical horizontal structure which changed with depth.

Displacement of isotherm ΔT in the vortex was slightly varied with depth and consisted of $\sim 0,5^{\circ}\text{C}$. However with account of vertical gradient of temperature the isotherm ascend increased with depth increasing: at thermocline ($z = 80 - 100 \text{ m}$) it was several meters, at the depth of 760 m it reached maximum value of 68 m. On the contrary the ascend of σ_t isolines in thermocline was 17 m, at the rest depths - about 10 m.

A map of surface temperature measured with space interval 0.5 km at the study area made during the survey is shown in Fig. 4. It is seen that the main upwelling front separating cold coastal waters from warmer ocean waters passed approximately along the shelf boundary at the upper part of the area and was separated onto two fronts at the low part of the area. Several cold and warm temperature anomalies with horizontal sizes of the order of mile and with elliptical structure were discovered along the front. Anomalies were arranged so that cold structures were at "cold" front side while warm structures were at "warm" front side. A single cold vortex at "cold" side of SW front at eastern side of Canary Current with the center nearly at $21^{\circ} 44.4' \text{ N}$, $17^{\circ} 40' \text{ W}$ fixed 21/12/1991 at 16:15 approximately coincided by location with the center of vortex having coordinates $21^{\circ} 45' \text{ N}$, $17^{\circ} 41' \text{ W}$ observed 24/12/1991 at 4:54 hour (it is designated by empty circle in Fig. 1 and by asterisk in Fig. 4). Assuming that the two fixed structure represented one and the same vortex we could find that the vortex moved approximately NW and its lifetime was not less than 2.5 days. Vortex space size was estimated as its horizontal time extent (defined as distance between its left and right boundaries) multiplied by the velocity of vessel drift being 1.16 km/h at the time when the vortex was fixed. (Vortex translation velocity was small in comparison with vessel drift velocity so the Doppler shift has been considered as negligible). So vortex size was $\sim 2.5 \text{ km}$ in average and the ratio of its vertical to horizontal size was about 0.33. It should be noted that intensity and horizontal size of the vortex were probably understated because transect crossed it by accidental trajectory (we suppose that vortex had an elliptical form).

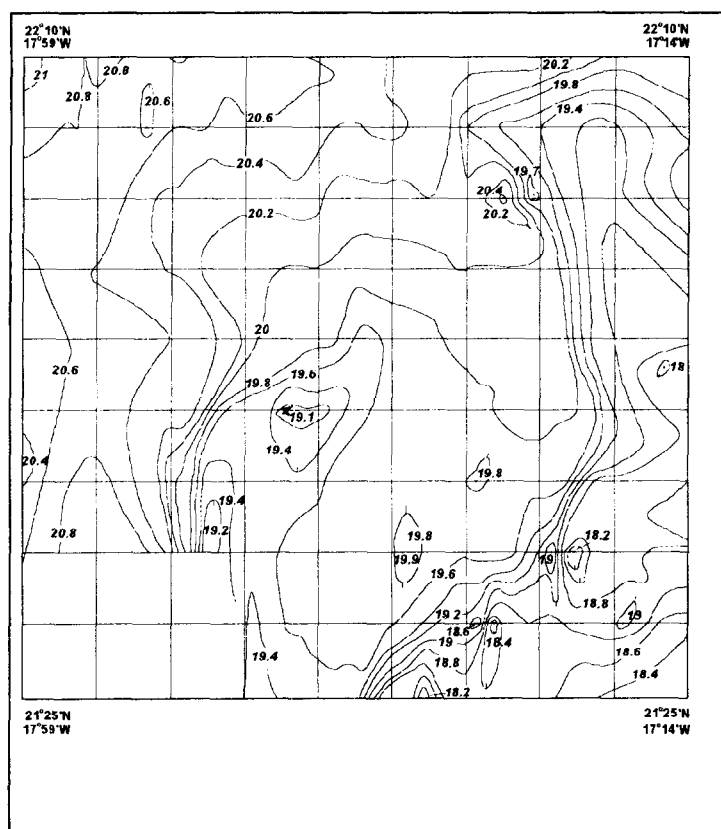


Fig. 4. A map of surface temperature.

As it is seen from Fig. 1 a little further to the east from the region where the vortex was observed the current had a shape of meander with sizes of $3 * 5 \text{ km}$, the meander being characterized by cyclonic vorticity. It is confirmed by literature data - according to [5] meanders with wave length of $2\pi\rho$ can be formed around the vortices, where r - a vortex radius.

The origin of the vortex is not yet clear. Isolines of σ_t have shown that the vortex had not a convective nature and it was not caused by baroclinic instability as $r \ll R_d$. Estimations of semi-diurnal tide amplitudes for given time and site calculated with using of formulas and tables from [6] have shown that the vortex was not connected with tide cycle. But the tide influence on vortex formation could be indirect. It is known that at regions where bottom inclination β is close to a characteristic angle α amplitudes of internal tides can significantly increase. Intensification of internal motions is connected with reflection of tides from steep continental slope and with enhance of turbulent mixing. Magnitude of characteristic inclination α is determined as

$$\alpha^2 = (\sigma^2 - f^2) / (N^2 - \sigma^2)$$

where σ is frequency of tidal wave, N is buoyancy frequency, f is Coriolis parameter, Moored current and temperature measurements in 20-m near bottom layer conducted at the same time as vertical profilings were performed have revealed the prevailed influence of semi-diurnal lunar tide M2. Values of characteristic

inclination α were calculated for semi-diurnal lunar tide M2, buoyancy frequency N was calculated by using of vertical profiles of potential density σ_t .

Bottom slope β was determined by isobath map with the step of 50 m calculated by measurements in the study area. β was defined as dH/dL , where dH is depth overfall between two isobaths and dL is the shortest distance between two isobaths in normal to bathymetric contour at the profiling point. Computations showed that at the first d.s. β changed from 0.011 to 0.018, α was in range 0.01 - 0.06 in BNL. For most profiles near bottom layer was mixed, N -values were small and values of α were close to maximum value of 0.06. For a few profiles characteristic inclination in BNL was close to bottom slope ($\alpha = \beta = 0.02$), but maximum of any BNL structural parameters in these cases has not been observed.

Formation of small eddies in the region can be connected with interaction of Canary Current having a deep stream between $17^{\circ} 50'$ and $17^{\circ} 40'$ W with the upwelling constantly existing at the study area. The latter result in formation of frontal stream in neighbourhood of which submesoscale vortices form.

It is still a little known from accessible literature about submesoscale cyclonic eddies occupying almost all water column and characterized by high ratio of vertical and horizontal scales - about 0.3. Here it can be mentioned the cyclonic eddy with a diameter of ~ 14 km spreading from surface to the depth of ~ 4 km observed in Weddelle Gyre at the Antarctic Region [7]. Another example - the eddy of size 10 km discovered in the Gulf of Lyons in the Mediterranean Sea at depths from 300 - 2000 m [5]. It should be mentioned that these eddies had significantly larger sizes than the vortex considered and slightly smaller ratio of vertical and horizontal scales. The lack of information on submesoscale eddies occupying practically all water column is probably connected with limited amounts of corresponded measurements that could revealed them. Really to discover such eddy it is necessary to conduct special measurement for example prolonged multiple profilings at fixed ocean point or at vessel drift in dynamically active region where appropriate conditions for their generation exist.

B. Measurements at the second drift station

During the second drift station 57 profilings were made. The length of the second d.s. was 29.6 km, its time duration was 14.78 hours. Vessel drift was rather uniform, depth ranged from 520 m to 800 m, bottom slope changed from 4° to 0.7° . Bottom relief was uneven and characterized by terraces and ledges formed by underwater hill and canyon (Fig. 1).

Vertical profiles of Tu obtained at the II d.s. are shown in Fig. 5. Variability of Tu in BNL was mainly determined by heterogeneities of bottom relief. With depth decreasing the values of Tu and ΔH were intensified as the whole. At the end of the upper ledge and above upper terrace mixed "cold" near bottom layer characterized by enhanced values of Tu which could define as HEBL was observed. Thickness of this mixed layer was about several meters near the ledge and increased to 41 m at minimal depth (43-d profiling). Temperature overfall over the mixed layer was about 0.8° in relation to the upper layer. Further to the end of d.s. mixing in BNL became weaker - thickness of mixed layer reduced and vertical gradients of Tu , T and S increased.

Maximum turbidity values for most profiles were reached close to the very bottom while for the last six turbidity profiles Tu_{max} were achieved in average at ten meters from the bottom. The latter can be explained by drifting of turbid water downslope from shallower water.

Values of R parameter varied from 1.6 to 4.2 being depended from ocean depth H . At $H > 600$ m BNL was mainly of mean power. At $H \sim 600$ and at smaller depths BNL becomes powerful, the latter was possibly caused by increasing of dynamical processes with approaching to the shore, mean value of R was about 3.5.

Isolines of Tu in near bottom layer are shown in Fig. 6. Tu isolines were stretched approximately parallel to bathymetric contour (for Tu more than 500 c.u.). At depths < 600 m BNL was characterized by increased values of Tu_{max} (> 1440 c.u. near the very bottom) and by increased thickness ΔH . At HEBL area a dome bend of Tu isolines up to ~ 500 m and their thickening and also dome bend of T isolines up to the surface were observed.

As for the first drift stations estimations of semi-diurnal tide amplitudes for the second d.s. showed that HEBL was not directly connected with tide cycle. Values of characteristic inclination $\alpha(z)$ in BNL at the second d.s. were in the range of 0.01 - 0.06 as at the whole study area. Bottom slope changed approximately at the same limits as α - from 0.062 to 0.11 gradually decreased from the first to the last probing. For the first

part of d.s. (profilings 1 - 25) β was in the range 0.062 - 0.053 and exceeded changes of α (fits in Fig 5). For the profilings 30 - 43 a curve $\alpha(z)$ was repeatedly intersected by bottom slope β which decreased from 0.035 to 0.014. For the last 15 profilings β was 0.18 - 0.11 and significantly less than α . At the HEBL region where values of α were close to $\beta \sim 1^0$ the enhanced values of Tu_{max} , ΔH and also maximum of near bottom mixed layer thickness were observed. Evidently intensive dynamical processes occurring at the region were caused by reflection features of semi-diurnal internal tide M2 from the steep slope.

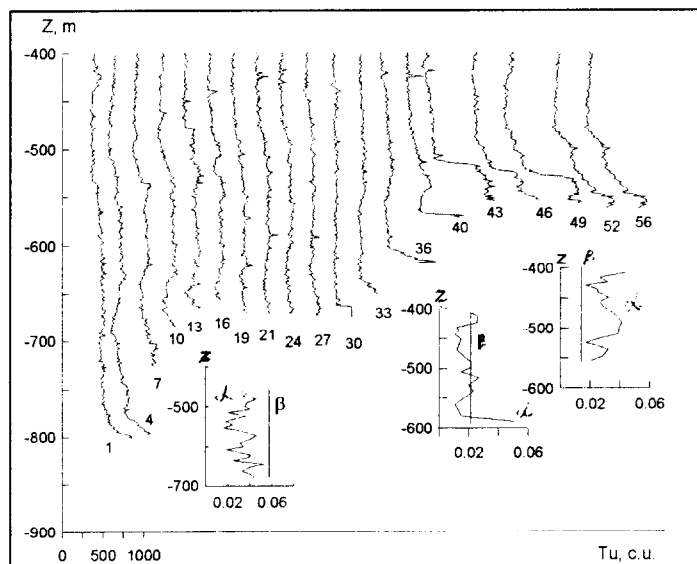


Fig.5. Vertical profiles of Tu at the second drift station.

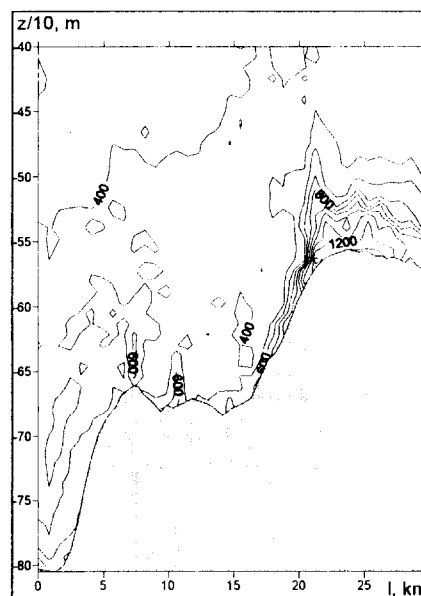


Fig.6. Isolines of Tu for the II d.s.

Acknowledgments

The author greatly appreciates Dr. T.A. Demidova for her help and supporting of the paper and Dr. A.G. Kostianoy for his useful remarks. This work was funded by ISF grant NDW 300.

References

- [1] Evdoshenko M.A., Lozovatsky I.D., Time-space variability of the near bottom nepheloid layer at the West Sahara continental slope and shelf, *Proceedings of the Conference "Ocean' 94"*, vol. 1, pp. 502 - 505, 1994.
- [2] K.Hunkins., E.Thorndike., G.Mathieu, 1969, Nepheloid layers and bottom currents in the Arctic Ocean, *Journal of Geophysical Research*, 74, 6995 - 7008.
- [3] G.I.Barenblatt, N.Galerkina, I.Lebedev, 1992, Mathematical model of downer quasiuniform layer. - General statement and model of locking, *Izvestiya Academy of Sciences, Physics of atmosphere and ocean.*, 28, 91 - 100 (in Russian).
- [4] M.A.Evdoshenko, 1998, Variability of near bottom nepheloid layer near the coast of North- West Africa, *Okeanologiya*, 38, N6 (in Russian).
- [5] J.-C.Gascard, 1978, Mediterranean deep water formation baroclinic instabilities and ocean eddies, *Oceanology Acta*, 1, 315 - 330.
- [6] E.W.Schwiderski, 1981, Global ocean tides. Part II: The semi-diurnal principal lunar tide M2. Atlas of tidal charts and maps. Naval Surface Weapons Center, KO5, Dahlgren, Virginia 22448, Tr. 79-414.
- [7] A.L.Gordon, 1978, Deep Antarctic convention West of Maud Rise, *Journal of Physical Oceanography*, 8, 601 - 612.

CONVECTION IN ROTATING FLUIDS AND ITS GEOPHYSICAL RELEVANCE

H.J.S.Fernando

Arizona State University
Environmental Fluid Dynamics Program
Mechanical and Aerospace Engineering
PO Box 879809
Tempe, AZ 85287-9809
E-mail: J.Fernando@asu.edu

Abstract

Laboratory experiments on turbulent convection in rotating fluids are reviewed, mainly in the context of oceanic deep convection occurring in regions known as "chimneys." It is shown that, although chimney turbulence may not be directly affected by Earth's rotation, the overall dense water formation in chimneys is subjected to rotational control through lateral baroclinic processes. The vertical extent of convection appears to be governed by the depth of penetration of turbulent eddies against underlying stratification. The lateral buoyancy transport out of chimneys and other oceanic convecting regions can be manifested *via* hetons resulting from the interlacing between eddies emanating from the rim currents and baroclinic instabilities of the dense water column.

Introduction:

Turbulent convection is a common phenomenon in oceans and atmosphere. The effects of convection, in particular, are pervasive in high latitude oceans where convective plumes penetrate to greater depths (known as deep convection) as a result of favorable air-sea interaction processes. Deep convection occurs in preselected areas known as "Chimneys," wherein the stratification in the upper oceanic layers is weak as a result of convection in yesteryears or due to the preconditioning of the area to produce upward doming isopycnals. Collusion of weak stratification and the unstable buoyancy flux and turbulence generated by cold winds generates turbulent convection that penetrates to depths of one to three kilometers, spanning a horizontal region of 10 to 100 kilometers (Marshall & Schott 1998). Chimneys remain active for several days to months, depending on the nature of surface forcing. The dense water masses so generated is a potential source of intermediate water and possibly a carrier of climatic signals (McCartney et al. 1996).

Upon initiation of a chimney, plumes originating at the surface descend deep into the ocean, entraining the underlying stratified layer. Thus, descending plumes are dynamically constrained by the ability of eddies to erode the stratification. Since the local Rossby radii of deformation in oceans are smaller than typical chimney diameters, the lateral boundaries of chimneys are prone to baroclinic instabilities. Once a chimney is established, the surface buoyancy flux is balanced by the lateral transport of buoyancy by eddy-like structures, thus establishing a quasi steady state. After the demise of surface forcing, convection ceases rapidly and the defunct chimney is restratified as a result of the lateral collapse of chimney fluid.

Another case of isolated convection is hydrothermal plumes that form near the ocean flow due to the solidification of magma upwelling from Earth's interior (Lupton et al. 1985). The resulting buoyant hot springs rise to their equilibrium level and spread horizontally, thus distributing hot warmer fluid both horizontally and vertically. Here the source diameters are on the order of tens of centimeters, smaller than characteristic Rossby radii, and hence the lateral processes are expected to be different from those of deep convection. There are a rich variety of fluid dynamical processes pertinent to oceanic convection from isolated buoyancy sources which should be understood before a coherent picture of relevant phenomena can be constructed and satisfactory models can be developed. In this communication, some laboratory-based results pertinent to convection in geophysical flows will be described, paying particular attention to the flow under buoyancy sources, depth of convection and the nature of the base of convective layer.

Convection in Homogeneous Fluids:

Consider the release of a (dense) plume of source diameter D at the surface of a homogeneous, non-rotating fluid. Observations show that the development of the plume takes place in several phases. First, the fluid layer below the source becomes unstable, forming a turbulent layer which expands by entraining fluid from the surroundings. With time, this turbulent layer grows while drifting downward, thus initiating a lateral entrainment flow. The flow in the vicinity of the source assumes a quasi-steady state at a time $t > 1.8(D^2/B_0)^{1/3}$ after the initiation; here B_0 is the buoyancy flux supplied by the source. Once the quasi-steady state is established, the flow under the source can be subdivided into two regimes; the "near source" region (regime I) where the plume shrinks until a minimum diameter is achieved at a vertical distance of $z \approx 0.2D$ and the "far field" region (regime II) where the plume expands as in the case of point plumes. In regime I, the maximum horizontal velocity within the plume was found to be given as $V_x \approx 0.66(B_0 D)^{1/3}$ whereas the vertical mean velocity in this regime could be estimated by $w \approx 0.27(B_0 D)^{1/3}(z/D)$. In regime II, the vertical velocity was found to scale as $w \approx 1.2(B_0 z)^{1/3}$, which is similar to that observed in the point-plume case. Apparently, at large z/D , the plume loses its memory on the lengthscale D imposed by the finite diameter effect. In oceans the typical vertical heights of plumes are on the order 2-5 km with $D \approx 10$ -100 km, according to which the regime II is never achieved.

The evolution of plumes in the presence of rotation is of interest in geophysical studies. The plumes should be affected by background rotation at a time scale of the order f^{-1} , where f is the planetary vorticity, in that a cyclonic rim current develops surrounding the plume. This rim current stems from the cyclonic deflection of entrainment flow into the plume by the action of background rotation. The width of the rim current increases with time and finally, *via* barotropic instability, the current breaks up into a number of outward propagating cyclonic eddies. Figure 1 shows the development of such an unstable flow, as marked by slightly positively buoyant particles suspended in the fluid surface. Figure 2 shows the evolution of a point plume, as visualized by adding fluorescent dye to the source fluid. At the time of the photograph, the source fluid has descended to the tank bottom, deflected and have started its horizontal spreading along the tank bottom. For the case shown, the descending phase of the plume has not been affected by the rotation and hence, upon impingement, the plume spreads as a gravity current with a speed $c \sim (g'h_g)^{1/2}$; here g' and h_g are the characteristic buoyancy and height of the plume-induced gravity current. As the gravity current spreads, however, the lengthscale of the flow increases and the rotation arrests the spreading of the current at the Rossby deformation radius $\sim c/f$. There will be an accumulation of fluid behind the retarded front, thus developing a conical-shaped fluid column spanning the entire depth as evident from Figure 2. Baroclinic instability of this column causes the development of eddies surrounding the plume, which detach and propagate away from the primary plume. Note that the above scenario is valid only when the diameter of the plume is less than the pertinent Rossby radius of deformation. Otherwise, the dense water column can be broken into eddies prior to the initiation of the horizontal gravity current. The former case is typical during the spread of oceanic hydrothermal plumes (Helfrich & Battisti 1991) whereas in deep ocean convection the latter is the norm. Atmospheric deep convection typically occurs in tropics, characterized by plumes ascending to tens of kilometers with horizontal scales on the order of several hundred kilometers. These horizontal scales are smaller than characteristic Rossby radii, and hence plume columns are not immediately subjected to baroclinic instabilities.

Figure 3 shows a plan view of an experiment in which a dense point plume colored with fluorescein dye is located at the center of the tank. The background fluid is suspended with neutrally buoyant particles. Note that the instabilities of the plume fluid and background rim currents have already produced vortices. A noteworthy observation is the approximate vertical alignment of cyclonic vortices of the upper lighter fluid formed due to barotropic instability with the anticyclonic vortices formed due to the baroclinic instability of the spreading dense fluid. This configuration represents a system of "hetons," as first described theoretically by Hogg & Stommel (1985). The pressure perturbations associated with the top and bottom vortices cause the interface to deflect upward, as clearly evident from the shed vortex visible in Figure 2. As hetons move, due to their upward deflected interfaces, a net transport of bottom layer fluid occurs, which can be construed as a mechanism of horizontal transport of dense fluid. Some previous theoretical studies (Legg & Marshall 1993) have modeled the lateral spreading of dense fluid originating from deep convective regions using hetons, and the observations described herein provide support for reality of such models.



Figure 1: The formation of cyclonic vortices by the breakdown of rim currents around a point plume in a homogeneous rotating fluid. The plume is marked by an arrow.



Figure 2: The breakdown of a point plume into anticyclonic vortices after it reaches the bottom surface. Also note the formation of a conical fluid column surrounding the plume due to the retardation of front.

Convection in Stratified Fluids:

In deep convection, as in the atmospheric convective boundary layer, the convective turbulent layer deepens into the contiguous stratified layer. This phenomenon is typically (and rather simplistically) modeled as a plume source delivering an unstable buoyancy flux into a linearly stratified fluid of buoyancy frequency N . As pointed out by Deardorff et al. (1969), the depth of convective layer at a time t can be evaluated by assuming that the buoyancy jump across the entrainment interface is negligible (i.e. penetrative convection), the mixed layer possess no buoyancy gradients and that the growth of convective layer is one dimensional. In non-rotating fluids or in rotating fluids where the turbulence in the convective layer is not affected by rotation, this growth law can be written as $h = (2)^{1/2} (B_0/N^2)^{1/2} t^{1/2}$. Figure 4 shows a photograph of the convective layer in a non-rotating linearly stratified fluid; numerous observations indicate that the growth follows the above law, and hence the assumptions made in its derivation are justifiable. Note the penetration of rising fluid parcels into the

layer aloft, which encroach lighter fluid elements into the bottom layer. The measured buoyancy gradients in the convective layer are close to zero.

The scenario of convection in the presence of rotation is much different. Laboratory experiments show that the entrainment interface in this case consists of an ensemble of slender vortices penetrating into the upper non-turbulent layer, and this occurs when the non-dimensional number $(h^2\Omega^3/B_0)^{2/3} > 100$ or so, where $\Omega = f/2$ is the rate of rotation (see Figure 5). At larger values of rotation, $(h^2\Omega^3/B_0)^{2/3} > 200$, the turbulent layer tends to sustain substantial buoyancy gradients, thus altering the mixed-layer growth law. Under these circumstances, the mixed-layer deepening velocity u_e can be written as $u_e/w_* = \text{Ri}^{-1} (1 + 0.02N^2/\Omega^2)^{-1}$, where $\text{Ri} = N^2h^2/w_*^2$ is the Richardson number based on the convective velocity $w_* = (B_0h^3)^{1/3}$ and the turbulent layer depth h .

Assuming that the turbulent velocity in highly rotating thermal convection flows can be given by $(B_0/\Omega)^{1/2}$ (Fernando et al. 1991), the depth of penetration δ of vortices into the non-turbulent layer aloft can be evaluated by a simple kinetic/potential energy balance between convective eddies and buoyancy forces associated with them, viz., $(B_0/\Omega) \sim N^2\delta^2$ or $\delta/h \sim \text{Ri}^{-1/2} \text{Ro}^{1/2}$, where $\text{Ro} = w_*/\Omega h$ is the Rossby number. The measurements taken during the experiments, such as those shown in Figure 5, are depicted in Figure 6. Here the lengthscale of undulations at a given h was measured by locating isopycnals and by evaluating their r.m.s. variation about the mean value. A fair agreement can be seen between the data and the prediction, with a proportionality constant of approximately 70. Based on Lagrangian float trajectories, D'Asaro et al. (1996) have noted the presence of deep undulations in the base of Labrador sea deep convective layer, an observation which is in agreement with the laboratory results presented above.

Concluding Remarks:

Convection in rotating fluids can be affected by background rotation in three ways. First, the turbulence in the convective layer can be affected by rotation when the lateral turbulent lengthscale grows beyond the scale $4.5(B_0/\Omega^3)^{1/2}$. This condition is untenable in most geophysical situations. Second, the nature of flow near the buoyancy source can be modified due to the presence of rotation. It has been observed both experimentally (Chen et al. 1989) and numerically (Jones & Marshall 1993) that small-scale vortices develop under the buoyancy source and these vortices may increase the averaged buoyancy gradient in the convective layer by trapping buoyant fluid within these vortices. Such vortices have been observed in field experiments (Schott et al. 1996). Third, the horizontal transport of mixed fluid out of the chimney can be governed by baroclinic processes, wherein hetons can transport the dense fluid horizontally. In all, Earth's rotational effects can play a crucial role in developing oceanic chimneys and hence in the formation of dense water in world's oceans.



Figure 3: The location of cyclonic (particle streaks) and anticyclonic (dye patches) vortices in the rotating plume system.



Figure 4: The growth of a convective layer in a linearly stratified, non-rotating fluid induced by heating the fluid layer from below with a constant heat flux.

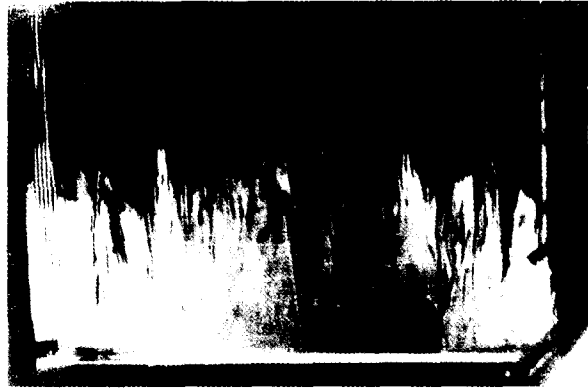


Figure 5: Convection in linearly stratified fluid in the presence of strong rotation.

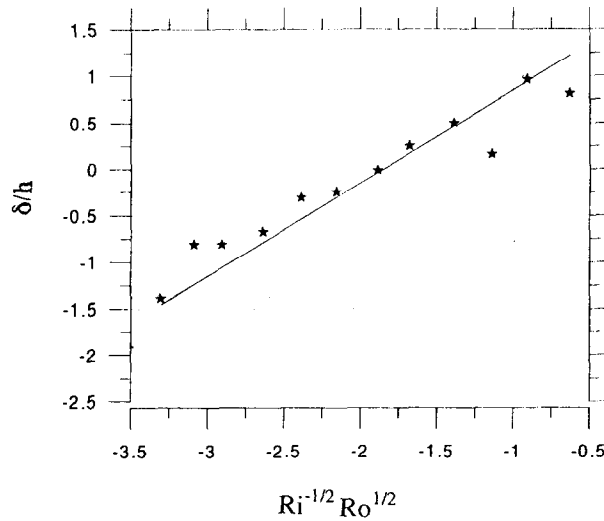


Figure 6: A plot of δ/h versus $Ri^{-1/2} Ro^{1/2}$ based on the experimental data taken during the convective-layer growth in linear stratified, rotating fluids.

Acknowledgments: The author wishes to thank the High Latitude Processes Program of the Office of Naval Research for Financial Support. During the period of this research, the author was also supported by the National Science Foundation (Fluid Mechanics Program) and the Army Research Office.

References:

- Chen R., H.J.S. Fernando and D.L. Boyer, 1989. Formation of isolated vortices in a rotating convecting fluid. *J. Geophys. Res.* **94**(D15), 18,445-18,453.
- D'Asaro, E.A., D.M. Farmer, J.T. Osse and G.T. Dairiki, 1996. A lagrangian float. *J. Phys. Oceanogr.* **13**, 1230-1254.
- Deardorff J. W., G.E. Willis and D.K. Lilly, 1969. Laboratory investigation of non-steady penetrative convection. *J. Fluid Mech.* **35**(1), 7-31.
- Fernando H.J.S., R.R. Chen and D.L. Boyer, 1991. Effects of rotation on convective turbulence. *J. Fluid Mech.* **228**, 513-547.
- Helfrich, K. and D. Battisti, 1991. Experiments on baroclinic vortex shedding from hydrothermal plumes. *J. Geophys. Res.* **96**, 12511-12518.
- Hogg, N. G. and H.M. Stommel, 1985. The heton, an elementary interaction between discrete baroclinic geostrophic vortices, and its implications concerning eddy heat-flow. *Proc. R. Soc. London. Ser A.* **397**, 1-20.
- Jones, H. and J. Marshall, 1993. Convection with rotation in a neutral ocean; a study of open-ocean deep convection. *J. Phys. Oceanogr.* **23**, 1009-1039.
- Legg S. and J. Marshall, 1993. A heton model of the spreading phase of open-ocean deep convection. *J. Phys. Oceanogr.* **23**, 1041-1056.
- McCartney, M.S., R.G. Curry and H.F. Bezdek, 1996. North Atlantic's transformation pipeline chills and redistributes subtropical water. *Oceanus* **39**(2), 19-23.
- Lupton, J. E., J.R. Delaney, H.P. Johnson, and M.K. Tivey, 1985. Entrainment and vertical transport of deep-ocean water by buoyant hydrothermal plumes. *Nature* **316**, 621-623.
- Schott, F., M. Visbeck, U. Send, J. Fischer, L. Stramma and Y. Desaubies, 1996. Observations of deep convection in the Gulf of Lions, Northern Mediterranean, during the winter of 1991/92. *J. Phys. Oceanogr.* **26**, 505-524.
- Marshall, J. and F. Schott, 1998. Open-ocean convection: Observations, theory and models. Report # 52, Center for Global Change, Massachusetts Institute of Technology.

Epilogue: I met Professor Federov for the first and last time at the Joint Oceanographic Assembly, Acapulco, Mexico, in 1988, where I presented a poster on double-diffusive step-like structure formation -- a subject to which Professor Federov contributed immensely. Assuming, perhaps erroneously, that a laboratory experimental poster may not be of much interest to the oceanographic community, I swayed to the beach fronts of Acapulco rather than being at the poster. Upon my return, I found a note from Professor Federov expressing his interest on my results and requesting me to contact him if possible. My meeting with him on the same day was most enjoyable and enlightening, notably his tolerance of my naiveté of the subject as a novice researcher. The conversation ended with an invitation for me to visit Russia. I took up the invitation seriously, firmed up the dates and wrote to Professor Federov about my plans. To my dismay, I received a reply from Professor Zatsepin informing the sad news of Professor Federov's untimely death. Though my initial plan of visiting Russia was unsuccessful, it was an honor to be able to attend the Konstantin Federov Memorial Symposium ten years later.

JUAN DE FUCA STRAIT AS A FLUID DYNAMICS LABORATORY

Chris Garrett, Michael Ott, Richard Dewey and Kate Stansfield

School of Earth and Ocean Sciences
University of Victoria
Victoria, B.C., V8W 3P6, Canada
email: garrett@phys.uvic.ca

Abstract

Juan de Fuca Strait provides an excellent outdoor laboratory for the investigation of rotating stratified shear flow in the presence of sloping lateral boundaries. The along-strait pressure gradient seems to be balanced by internal friction, and should thus have associated cross-strait secondary flows. Bottom-moored ADCP data do show such flows, but with a pattern that is not easily related to the action of a simple internal “eddy viscosity”. Turbulent microstructure measurements, in fact, hint at the possibility that some of the internal mixing is associated with internal wave critical layer absorption which would require a different parameterisation. It is hoped that refined ADCP data will be of sufficient accuracy to permit the direct determination of the vertical Reynolds stresses and resolve these issues.

Introduction

Estuaries everywhere are of local concern because of their role in transportation, fisheries and recreation. Juan de Fuca Strait (Figure 1) is no exception; it is a major shipping lane, a pathway for migrating salmon, and a mecca for sports fishermen, whale watchers and yachtsmen. With a mean centreline depth of about 200 metres, however, it is deeper than most estuaries, and hence provides an accessible “laboratory”, about 20 km across and 100 km long, for many fluid dynamical processes that are relevant in the open ocean as well as in other, shallower, estuaries. Its attractiveness as a laboratory is increased by its fairly simple geometry, by the strength of the tidal currents which can exceed 1 m s^{-1} , by a summertime estuarine shear flow with a mean current in each layer of about 0.2 m s^{-1} , and also by the fact that it is wide enough for the circulation to be influenced by the earth’s rotation.

An interesting parameter which can help to characterise an estuary is the “estuarine Richardson number” given by

$$Ri_E = \frac{g\Delta\rho}{\rho_0} \frac{Q_f}{Wu_t^3}, \quad (1)$$

where g = gravity = $9.81 \text{ m}^2 \text{ s}^{-1}$, $\Delta\rho/\rho_0$ is the fractional density difference, between fresh water and ocean water, $\simeq 0.025$, Q_f is the freshwater discharge rate $\simeq 10^4 \text{ m}^3 \text{ s}^{-1}$, W is the width of the estuary $\simeq 20 \text{ km}$ and u_t is the r.m.s. tidal current $\simeq 0.5 \text{ m s}^{-1}$. These give $Ri_E \simeq 1$, just above the transition range of 0.1 to 0.8 between well mixed and strongly stratified conditions [1]. Thus Juan de Fuca Strait is probably restratifying after vigorous tidal mixing to the east between the freshwater discharge (mainly of the Fraser River) and intruding salt water from the Pacific Ocean. Sea level and atmospheric data may be used to determine the along-strait sea level gradient which seems to be balanced by internal rather than bottom friction on the sloping sidewalls [2], and implies a vertical eddy viscosity as high as

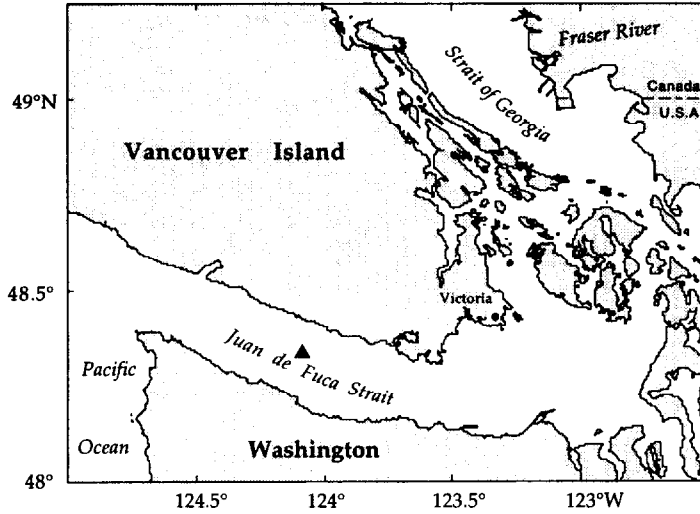


Figure 1: Juan de Fuca Strait showing the location (solid triangle) of the bottom-moored ADCP in 1996.

$0.02 \text{ m}^2 \text{ s}^{-1}$ at the level of the interface between inflow and outflow. In a rotating system this friction should produce internal ageostrophic flows across the strait, as described by Konstantin Fedorov in his brilliant monograph on oceanic fronts [3] and shown in the schematic diagram (Figure 2) from [4]. The internal and bottom Ekman layers produce a thinning of the interface by convergence at the side of the strait with a deep upper layer, and a thickening at the other side. This is found in Juan de Fuca Strait [2], as in other locations.

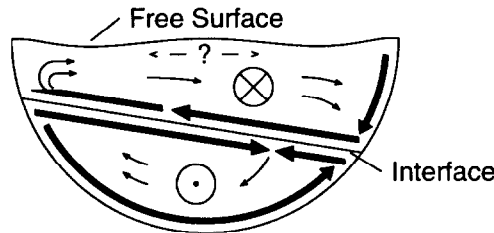


Figure 2: Cross-strait secondary flows in a two-layer rotating exchange flow, based on observations from a laboratory experiment. (Redrawn from [4]).

Cross-Strait Flows

Our main objective has been to seek direct evidence of these internal cross-strait secondary flows and also, if possible, to measure the Reynolds stresses and other associated dynamical processes. Figure 3 shows the location, in a cross-section of the strait, of a bottom-moored 300-kHz broadband ADCP deployed for three weeks in the summer of 1996. The density structure, also shown, is not strictly two-layer but has a transition from a strongly stratified outflow to a weakly stratified inflow.

The mean along-strait flow (Figure 4a) shows a reversal from outflow to inflow at a depth of about 85 m. The expected mean cross-strait flow is not as simple as the internal Ekman layers depicted in Figure 2 for a two-layer situation, but should be approximated by

$$\bar{v} = \bar{v}_g - f^{-1} \frac{\partial}{\partial z} \left(A_v \frac{\partial \bar{u}}{\partial z} \right), \quad (2)$$

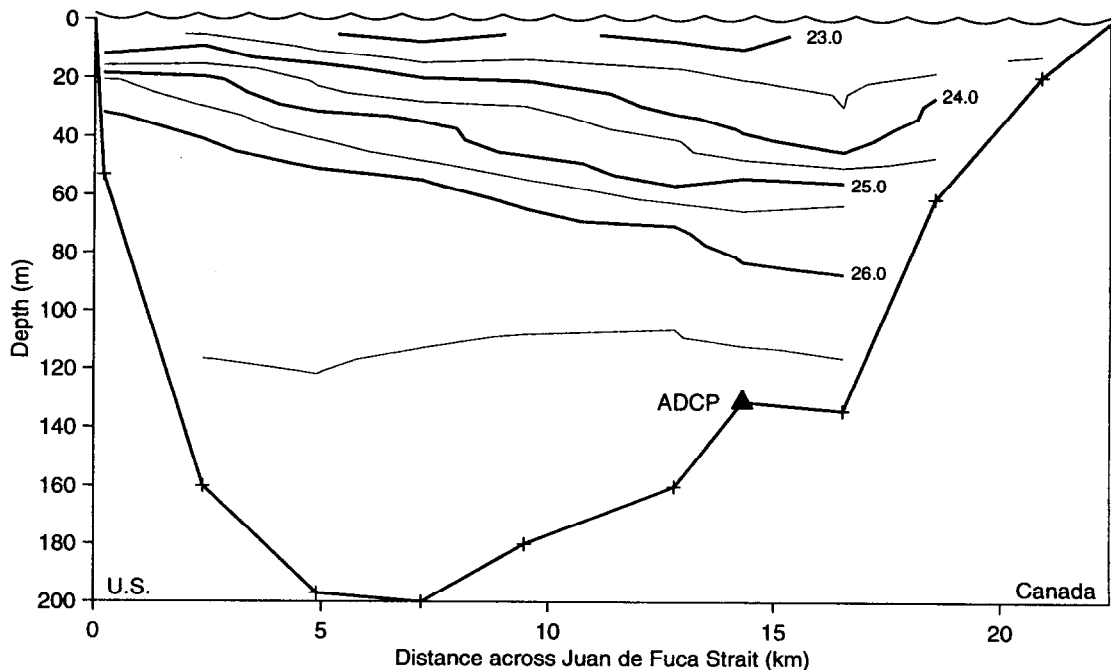


Figure 3: Density cross-section of Juan de Fuca Strait, showing the location of the ADCP at 135 m.

where \bar{v}_g is the cross-strait geostrophic flow corresponding to the along-strait depth-dependent pressure gradient, and A_v is the eddy viscosity, which may be a function of depth and time. If A_v is constant, the ageostrophic part of \bar{v} should be proportional to the curvature of \bar{u} . In the present situation, it should thus be positive above about 65 m, and negative from 65 m to the interface between inflow and outflow at about 85 m. Below that the cross-strait flow should be successively positive, then weak and finally positive again in a bottom Ekman layer.

The actual cross-strait flow is shown in Figure 4b. The calculated geostrophic part of this changes sign above 50 m instead of the expected 85 m corresponding to the transition from outflow to inflow, possibly because of an underestimate of the along-strait surface pressure gradient or unrepresentativeness of our limited along-strait sections. The ageostrophic flow is small at the shallowest depths recorded, then negative as expected, but with a reversal at about 75 m, though this would be closer to 85 m if we adjust the geostrophic part. The magnitude of up to 0.02 m s^{-1} in this region of negative $\bar{v} - \bar{v}_g$ corresponds to a value of about $0.01 \text{ m}^2 \text{ s}^{-1}$ for A_v . Below this there is a thin layer of positive flow, and also a clearly defined positive flow near the bottom which we can identify with the expected bottom Ekman layer (and its flux is roughly what is anticipated for the estimated bottom drag). The most puzzling feature of Figure 4b, however, is the strong and unexpected negative ageostrophic flow between about 90 m and 100 m. This does not seem to have any simple interpretation in terms of a positive eddy viscosity.

Other Measurements

It is hoped that direct measurements of the Reynolds stress $\overline{u'w'}$ will elucidate the actual stress (modelled as an eddy viscosity) and clarify its origin. Such measurements depend on obtaining precise estimates of the vertical velocity, and hence on knowing the orientation of the instrument very precisely and also allowing for the effects of small bottom slopes. This is facilitated by various analysis techniques including the comparison of the integrated vertical velocity with the displacement, by internal waves, of scattering structures revealed in the backscatter intensity data. We will report this elsewhere.

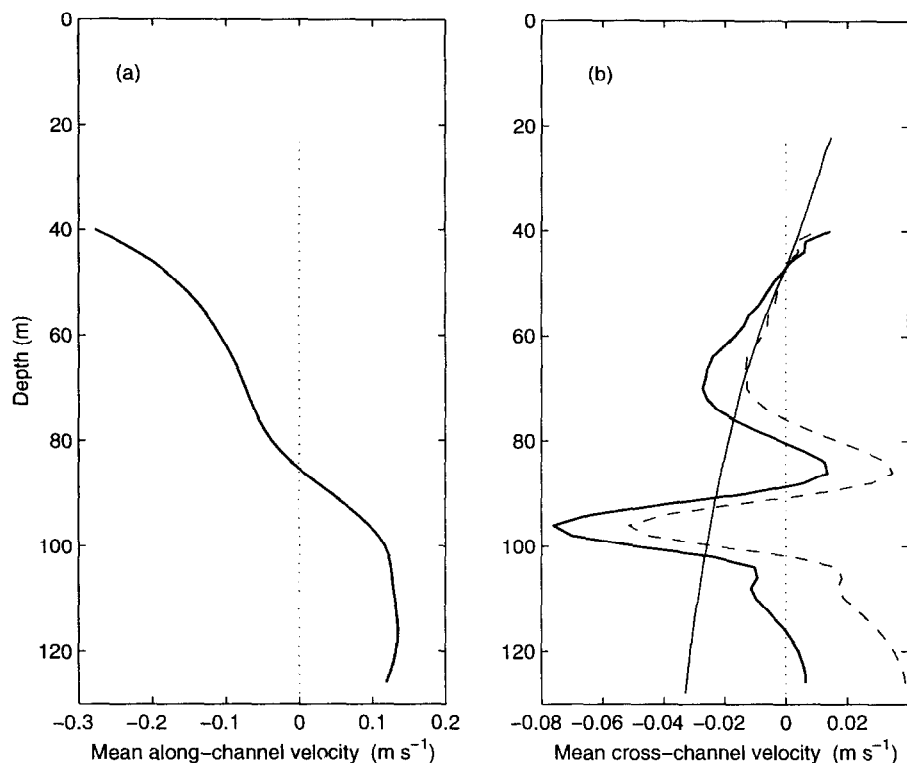


Figure 4: The mean flow profile, with no data available above about 40 m due to the limited range of the ADCP during daylight hours. (a) Along-strait (negative westward). (b) Cross-strait (positive towards the northern, Canadian, side of the strait); the thick solid line shows the measured mean flow, the thin solid line is the geostrophic component based on the along-strait surface pressure gradient and an along-strait density section. The ageostrophic flow is the difference between these two and is shown as a dashed line.

Energy dissipation within the water column may also provide clues. If there is an eddy viscosity A_v , then one might expect the dissipation rate to be at least as big as $A_v(\partial\bar{u}/\partial z)^2$, with more dissipation probably associated with processes other than those involved in extracting energy from the mean flow. If A_v is as big as $0.02 \text{ m}^2 \text{ s}^{-1}$, then the expected dissipation rate is about $10^{-6} \text{ W kg}^{-1}$ or more. We have measured average values comparable with this, but not with great statistical confidence yet. Our microstructure data do, interestingly, hint at a level of high dissipation that tracks the level of no along-strait motion in the water column as it moves vertically during the change of the tidal current from flood to ebb, suggesting the possibility of critical layer breaking of internal waves generated at the sea floor (Figure 5). If this is substantiated by further measurements, it may account for secondary flows that do not fit in with the simple concept of constant vertical eddy viscosity.

A dissipation rate of about $10^{-6} \text{ W kg}^{-1}$ in stratified water with $N \simeq 10^{-2} \text{ s}^{-1}$ implies a vertical mixing rate $K_v \simeq 10^{-3} \text{ m}^2 \text{ s}^{-1}$ and a Thorpe scale $L_T \simeq 1.2(\epsilon/N^3)^{1/2} \simeq 0.7 \text{ m}$. We have, in fact, found typical Thorpe scales about a factor of three less than this based on a water column average, with the main point being that Thorpe scale measurement with a good CTD is a valuable alternative to microstructure measurement in coastal and estuarine waters with reasonably vigorous mixing; even if the smaller overturns cannot be resolved, it is the large, resolvable, ones which dominate the Thorpe scale.

We are also evaluating the lateral Reynolds stress $\overline{u'v'}$, as this plays a role in determining the lateral profile of the along-strait current, though there does not appear to be a clear spectral gap between the mean flow and the eddies. Finally, Juan de Fuca Strait offers the opportunity to investigate internal wave and mixing processes at the sloping sides, in an environment where the signals are strong because of the strong mean flow and tidal currents.

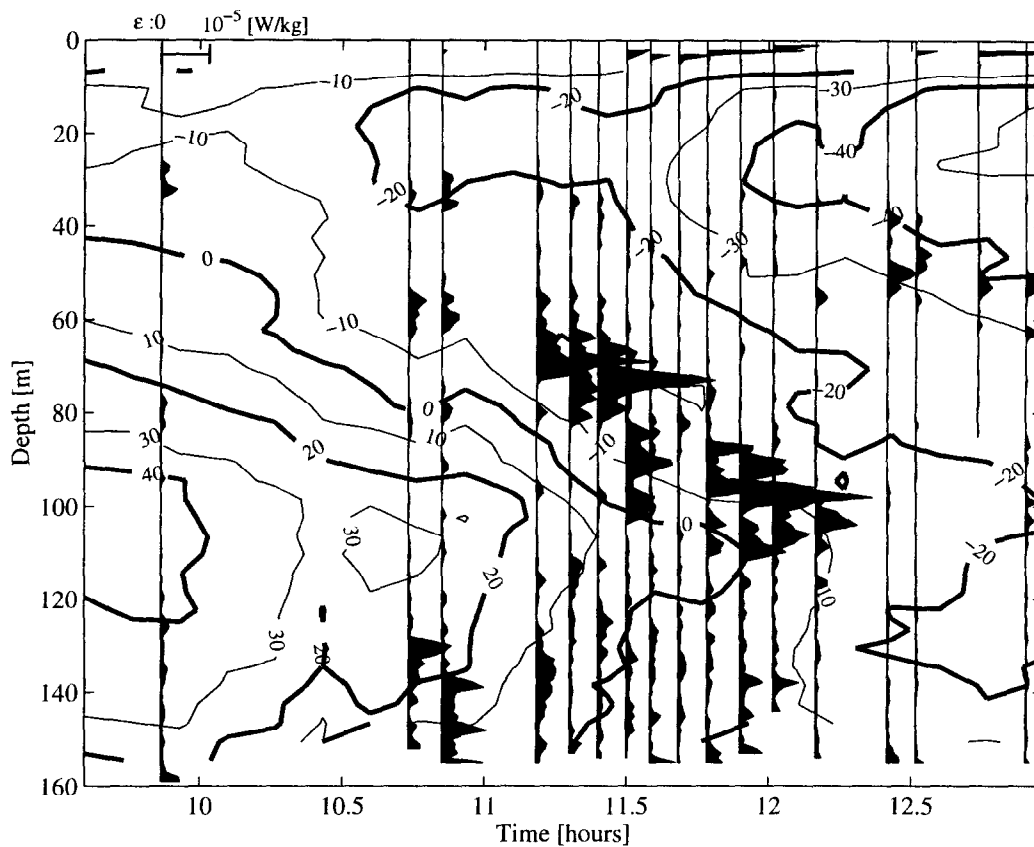


Figure 5: Turbulent energy dissipation rate profiles (linear scale) at various times on 5 August 1996, superposed on contours of the low-passed along-strait velocity component, negative westward (cm s^{-1}). The scale for the dissipation rate is shown in the upper left part of the diagram.

Acknowledgments

We thank the U.S. Office of Naval Research and Canada's Natural Sciences and Engineering Research Council for support. C.G. also remembers with gratitude the friendship, scientific inspiration and international leadership of Konstantin Fedorov, and thanks the organisers for an exciting symposium that Konstantin himself would have greatly enjoyed.

References

- [1] J.S. Turner, 1973, *Buoyancy Effects in Fluids*, Cambridge University Press.
- [2] M. Ott and C. Garrett, 1998, Frictional estuarine flow in Juan de Fuca Strait, with implications for secondary circulation. *J. Geophys. Res.* 103, 15,657–15,666.
- [3] K.N. Fedorov, 1986, *The Physical Nature and Structure of Oceanic Fronts*, Springer-Verlag, New York. Translated from K.N. Fedorov, 1983, *Fizicheskaya Priroda i Struktura Okeanicheskikh Frontov*, Gidrometeoizdat, Leningrad
- [4] G.C. Johnson and D.R. Ohlsen, 1994, Frictionally modified rotating hydraulic channel exchange and ocean outflows. *J. Phys. Oceanogr.* 24, 66–78.

MESOSCALE DYNAMICS IN THE SOUTHEASTERN BLACK SEA

A.I. Ginzburg¹, A.G. Kostianoy¹, D.M. Soloviev² and S.V. Stanichny²

¹ P.P. Shirshov Institute of Oceanology, 36 Nakhimovsky Pr., Moscow, Russia
E-mail: kostianoy@glasnet.ru, akfedorov@glasnet.ru

² Marine Hydrophysical Institute, 2 Kapitanskaya, Sevastopol, Ukraine
E-mail: odmi@alpha.mhi.iuf.net

Abstract. Analysis of sequence of six daily NOAA HRPT infrared images for November 13-18, 1996 and available satellite/hydrographic data has shown that anticyclones, cyclones and their combinations (dipoles, multipoles) can be generated both over the continental slope and in the open basin in the southeastern Black Sea, where anticyclonic gyre is usually considered as quasi-permanent feature of circulation, in all seasons. Conclusive evidences of predominantly cyclonic circulation during cold season, which could confirm known hypothesis and results of numerical modelling, are not found. Local circulation can be considerably changed over the course of several days because of eddies movements (translation velocity ranges up to about 25 cm/s), their interactions, formation and disruption of dipoles. Variability of coastal current direction is determined by the proximity to the coast of an anticyclonic eddy or its associated cyclone.

1. Introduction

It is generally taken that a large anticyclonic eddy (the so-called "Batumi eddy" [1,2]) is quasi-permanent feature of circulation in the southeastern Black Sea, which is separated from the rest of the basin by main flow of the cyclonically propagated Rim Current [3] and where excess of precipitation over evaporation is observed throughout the year [4,5]. The position of centre of the eddy, its form, diameter and vertical scale vary with time [6,7], however spatial and temporal scales of the variability are unknown. Moreover, there is reason to believe, basing on hydrographic and satellite data [7-11], that real circulation can be considerably more complicated due to concurrently existing eddies, including cyclones. There is also no agreement among investigators of the region regarding the seasonal variability of the circulation character. Known hypothesis for change of the circulation from anticyclonic in summer to predominantly cyclonic in cold season [3,12] is in good agreement with results of numerical modelling of seasonal variability of climatic circulation [4,5] but in contradiction with a few winter observations [13,14].

This paper is devoted to space-time variability of typical elements of the southeastern corner mesoscale dynamics, role of the elements in the coastal-open sea water exchange and in the coastal current regime, seasonal variability of the observed eddy picture and its correspondence with known hypothesis and results of numerical modelling. The study was based on analysis of satellite imagery and generalization of available hydrographic data.

2. Data

Series of six daily satellite infrared (IR) images from NOAA-14 (AVHRR) received in high resolution picture transmission (HRPT) regime in Marine Hydrophysical Institute (Sevastopol) from 13 to 18 November, 1996 was used in the present study. Procedures of atmospheric correction and transmission to Mercator projection were applied to the images. Because of technical difficulties absolute values of the sea surface temperature (SST) were not calculated; only SST differences between selected points of the images were deduced. Meteoroinformation from seaports of the Ukraine and Novorossiysk and a ship of opportunity (in a point 43°09'N, 39°00'E on 18 November, 1996) was used as well as available hydrographic/satellite observations of different years.

3. Eddy picture in November 1996

In Figs.1 and 2 one can see 4 concurrently existing anticyclonic eddies with diameters of about 40-50 km: A1 in the open sea, which forms a quasi-symmetrical dipole with a cyclone C1 at its southeastern periphery, A2 also in the deep basin and two coastal anticyclones A3 and A4. Both the latter eddies together with associated cyclones form tripoles and tetrapoles (such multipole structures were observed for the first time in laboratory experiment [15]).

Sequence of IR images in Fig.1 gives a possibility to trace evolution of the surface circulation over the period 13-18 November, 1996. A4 practically held its location and A2 and A3 moved southward and northwestward, respectively, with mean velocity u no more than 8.5 cm/s during the observational period. A1 after displacement southwestward between 13 and 15 November ($u \approx 18$ cm/s) began to move along periphery of A2 with $u \approx 28$ cm/s, that resulted in disruption of dipole A1-C1. Wind at the period was rather light (1-2 m/s) and only by 18 November wind velocity increased up to 10 m/s (wind from the east). So movement of A1 was likely conditioned by influence of more intensive A2. However, it is quite possible that formation of two new dipoles on 17-18 November on the basis of A1 and A2 due to generation of associated cyclones at their southern peripheries (Figs.1e and 1f) was determined by westward wind strengthening. Thus, local circulation can be considerably changed over the course of several days.

Deep-basin dipoles are the main mechanisms of horizontal mixing in the area. Configuration of dipole A1-C1 in Fig.1 conditions water transport from the coastal zone to the deep basin. In other configuration (cyclone north of anticyclone, as in [7], or packing of two mushroom-like structures, as in [10,11]), water transport from the deep basin to the coast or two opposite flows are observed. Zonal location of dipole's components provides water transport in meridional direction. Coastal anticyclones and their associated cyclones determine the coastal current regime: flow in the Rim Current general direction when a cyclone is close to the coast (e.g., eastward of A4 in Figs.1 and 2b) or in the opposite direction when maternal anticyclone is near the coast (westward of A4 in Figs.1 and 2b).

Interestingly, anticyclonic eddies in November 1996 had different manifestation in the SST field (Fig.1). The most high temperature, about 2°C higher than in the deep basin, was at the centre of A1, the most low, up to 1°C lower than in the deep basin, at the centre of A2. SST difference between centres of these two anticyclones achieved 2.6°C. In the absence of synchronous hydrographic measurements, only common considerations can be applied to the difference. Doming of isotherms in the upper about 50 m, typical for the Black Sea anticyclones [6,7], should result in SST minimum in eddies centres, especially under high position of cold intermediate layer and in more intensive eddies. Positive SST anomaly under the same anticyclone structure implies hydrostatically stable temperature inversion in the near-surface freshened layer (due to precipitation, river discharge), which prevents propagation of convection to the deeper layer [11]. We do not know if A1 and A2 differed in the near-surface thermohaline structure, but it is evident that in autumn SST anomalies at anticyclones centres can be both warm and cold. Change of the SST anomaly from positive to negative at the centre of A3 on 18 November could be determined by more intensive mixing of the surface layer after wind strengthening.

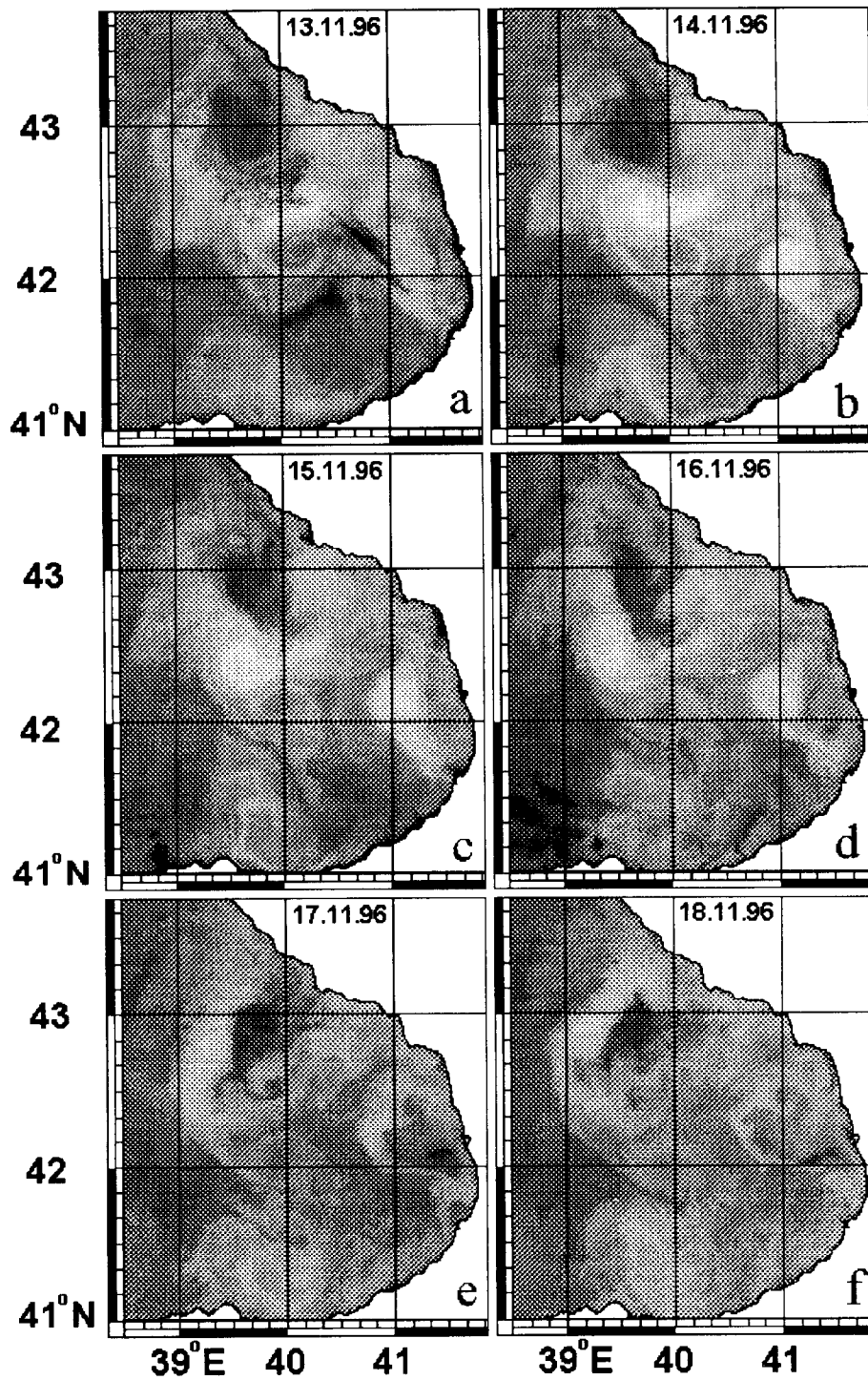


Fig. 1. NOAA-14 IR images of the southeastern Black Sea on (a) 13, (b) 14, (c) 15, (d) 16, (e) 17 and (f) 18 November, 1996. Light (dark) tone corresponds to warm (cold) water.

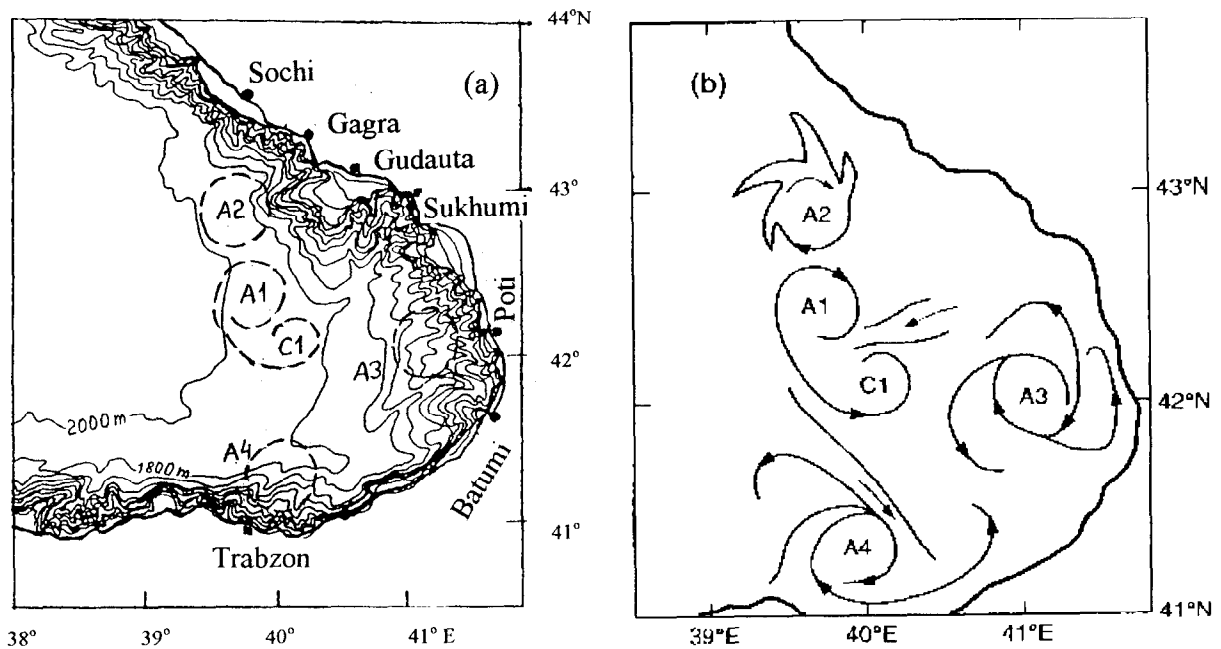


Fig.2. Eddy field in the study region on 14 November, 1996: (a) position of anticyclones A1-A4 relative to the bottom topography, (b) scheme of surface circulation determined by A1-A4 and associated cyclones.

4. On seasonal variability of eddy field

Eddy picture in the southeastern corner in November 1996 is evidently not consistent with observations here of two cyclones in November-December 1977 [12,16], which with regard to measurements [3] gave rise to supposition that predominant cyclonic circulation occurred during cold season associated with seasonal intensification of the Rim Current, its meandering over the slope and pinching off cyclones in much the same way as the Gulf Stream rings [12].

To answer the question whether circulation in the area changes from anticyclonic in summer-autumn to cyclonic in winter we have analysed available observational data of different years, mainly of field measurements with low spatial and temporal resolution. The data are summarized in Table 1. They are separated into seasons. Data on eddies observed during several seasons are given in every season, although in reality they could relate to different structures because of low temporal resolution of measurements. It should be taken into account also that most of data are based on hydrographic observations, which could cover only a part of the area or have inadequate spatial resolution to detect eddies with diameters of about 30 km. Because of this, availability of any eddy in the Table in a certain month (season) does not eliminate existence of another eddies at the same time, including those of opposite direction of rotation. Besides, horizontal scales and forms of eddies found by nonsynchronous low resolution hydrographic measurements can considerably differ from real ones in the cases of closely-spaced eddies and their movements.

Analysis of the data has shown that coastal eddies, both anticyclonic and cyclonic, are generated in all seasons. In particular, eddies of opposing directions of rotation are observed in Batumi region in warm and cold seasons. The only quasi-stationary structure with unchanged direction of rotation is anticyclone north of Trabzon. In the open sea anticyclones or dipoles were observed in warm season. Diameters of eddies were of about 100 km, vertical scale exceeded 200 m and their positions were changed within one degree both in latitude and longitude. In cold season (from December to March) both anticyclones and cyclones were observed. It is important to note that in the absence of extended survey of all the area the fact of a cyclone detection is not indicative of predominant cyclonic circulation at all. For example, cyclones in winters 1933 and 1956 (see Table 1) were detected in the same region as cyclone C1 in November in Fig.1 and the deep sea cyclone in June 1981 in [10,11]. In both the latter cases cyclones were parts of vortical dipoles. And it is not

unlikely that observed in winter cyclones in the deep sea were in reality, at least in some cases, counterparts of anticyclones. Only high resolution satellite images give real picture of surface circulation. Amount of the available cold season observations is considerably less than that of warm season (see Table 1), so further accumulation of information is needed for the net inference about possibility, in certain situations, of exceptionally cyclonic circulation in the deep sea of the area in cold season.

It may be seen that the deep sea eddies have as a rule greater diameters than coastal ones. Diameters of all observed eddies in the southeastern Black Sea were changed within $(1.5-5) \cdot R_d$ where R_d is baroclinic Rossby radius of deformation equal to 20-30 km in the deep sea and 5-15 km in the coastal zone [16]. Factors that condition variety of eddy motions in the area can be anticyclonic velocity shear at the shoreward periphery of the Rim Current, its meandering or instability, availability of freshened water throughout the year due to precipitation and rivers discharges, local atmospheric forcings and irregularities of bottom or shore line relief. Besides, presence of a seaward large eddy can be the determining factor of generation of a coastal eddy of the opposite rotation, as it likely occurred in [7].

Table 1. A summary table of eddies observations in the southeastern Black Sea

Season	Month, year	Types of eddies and their positions	D, km	H, m	Reference
Winter	Nov.-Dec., 1977	C, centre at 42°30'N, 40°20'E	56	200	[12,16]
		C, northwest of Batumi	60	200	
	December, 1985	A, northwest of Batumi	30	-	[17]
	January, 1989	A, north of Trabzon	80	-	[18]
	Feb.-Aug., 1957	A, east of the line C.Yeros-Gudauta, most developed in February	150	>200	[13]
	winters 1933, 1956	C, within 41°50'-42°40'N, 39°50'-41°00'E	-	-	[6]
	winter	A, north of Trabzon	75	-	[19]
		A, west of Poti	40	-	
		A, southwest of Sukhumi	40	-	
Spring	Febr.-Aug., 1957	A, between shore and the line C.Yeros-C.Anakria in May	130	>200	[13]
	Mar.-Nov., 1992	A, centre at 42°10'N, 41°00'E in March, with displacement southward and increasing diameter in the following months	100	200	[14]
	April, 1989	A, north of Trabzon	80	-	[18]
	May-Nov., 1985	A, at 70 km from the Georgian coast in May	110	>200	[17]
Summer	August, 1951	A, with large axis from Trabzon to Sukhumi	>160	-	[13]
	Feb.-Aug., 1957	A, in the central part of the SE area, less developed in August than in February and May	<100	-	[13]
	Mar.-Nov., 1992	A, with greater diameter in May and July than in March	150	-	[14]
	May-Nov., 1985	A, centre at >70 km from the Georgian coast	110	>200	[17]
	June, 1985	C, northwest of Batumi	30	-	[17]
	June 8, 1981	A, centre at 42°25'N, 40°00'E	100	-	[10,11]
		C, centre at 41°40'N, 40°00'E	100	-	
		C, in the region of the Gudauta shoal	100	-	
	June-Sep., 1984	A, centre at 41°40'N, 40°45'E	130	1000	[20]
	July 1-13, 1990	A, centre at 42°35'N, 40°17'E	35	100-150	[9]
		A, northwest of Batumi	30	100-150	
	A, in the region of C.Kodor	40	100-150		
August, 1938	A, centre at 42°10'N, 40°25'E	110	500	[6]	
August, 1962	A, centre at 41°56'N, 39°39'E	165	500	[7]	
	C, centre at 42°45'N, 39°44'E	155	500		

		A, west of C. Anakria	40	-	
		C, in the region of Batumi	40	-	
August, 1983		A, centre at 42°05'N, 39°40'E	90	-	[21]
summer		A, centre at 41°56'N, 40°25'E	135	-	[8]
		C, centre at 41°21'N, 40°30'E	135	-	
Autumn	Mar.-Nov., 1992	A, centre at 42°00'N, 41°00'E most developed in September	150	>200	[14]
	May-Nov., 1985	A, centre at 130 km from the Georgian coast in September	110	>200	[17]
	June-Sep., 1984	A, centre at 41°40'N, 40°45'E	130	1000	[20]
	September, 1988	A, north of Trabzon	80	-	[18]
	September, 1991	A, centre at 41°53'N, 40°15'E	150	>500	[2]
	Sep.-Oct., 1990	A, centre at 41°30'N, 40°30'E	100	1000	[1]
	Nov.-Dec., 1977	C, centre at 42°30'N, 40°20'E	56	200	[12,16]
		C, northwest of Batumi	60	200	
	November, 1996	A1, centre at 42°24'N, 39°50'E	50	-	Figs. 1
		A2, centre at 42°55'N, 39°40'E	45	-	and 2 in
		A3, west of Poti	40	-	this
		A4, north of Trabzon	50	-	paper
		C1, centre at 42°10'N, 40°05'E	40	-	
		associated cyclones at peripheries of A3 and A4	<40	-	

Note: A (C) indicates anticyclone (cyclone); D - maximum eddy diameter; H - its vertical scale.

5. Conclusions

Our analysis of available satellite imagery and hydrographic data has shown that:

1. Anticyclones, cyclones and their combinations (dipoles, multipoles) can exist in the southeastern Black Sea both over the continental slope and in the open sea. So name the "Batumi eddy" for the characterization of the area circulation is uncertain.

2. Anticyclonic eddies can be generated in all seasons. Conclusive evidences of predominantly cyclonic circulation during cold season that could confirm known hypothesis and results of numerical modelling were not found. It is quite possible that at least in some cases cyclones detected by hydrographic measurements were not isolated eddies, but parts of vortical dipoles.

3. Diameters of all the observed eddies in the southeastern Black Sea were changed from about 30 km to more than 100 km, i.e. within $(1.5-5) \cdot R_d$ (baroclinic Rossby radius of deformation); positions of centres of the deep sea anticyclones were changed within one degree both in latitude and longitude.

4. Dipoles (multipoles) are effective mechanisms of local horizontal mixing and of the coastal-deep basin water exchange. Coastal anticyclones and associated cyclones at their peripheries influence the coastal current regime (flow either in the Rim Current direction when associated cyclone is close to the coast or in the opposite direction when maternal anticyclone is near the coast).

5. Local circulation can be considerably changed over the course of several days because of eddies movements, their interactions, disruption of dipoles and formation of new ones.

6. Surface temperature difference between anticyclone centre and surrounding water depends on local near-surface thermohaline structure, eddy intensity and the sea-atmosphere exchange conditions and can be both negative and positive in autumn.

Acknowledgements

This study was supported by the INCO-COPERNICUS Project N IC15-CT96-0111 and by a Grant N 98-05-64715 of the Russian Foundation for Basic Research.

References

1. T. Oguz, V.S. Latun, M.A. Latif, V.V. Vladimirov, H.I. Sur, A.A. Markov, E. Ozsoy, V.V. Kotovshchikov, V.V. Eremeev and U. Unluata, 1993, Circulation in the surface and intermediate layers of the Black Sea, *Deep-Sea Res.*, 40 (8), 1597-1612.
2. T. Oguz, D.G. Aubrey, V.S. Latun, E. Demirov, L. Koveshnikov, H.I. Sur, V. Diaconu, S. Besiktepe, M. Duman, R. Limeburner and V. Eremeev, 1994, Mesoscale circulation and thermohaline structure of the Black Sea observed during HydroBlack'91, *Deep-Sea Res.*, 41 (4), 603-628.
3. O.N. Bogatko, S.G. Boguslavsky, Yu.M. Beljakov and R.E. Ivanov, 1979, Surface Currents in the Black Sea, In: *Kompleksnye Issledovaniya Chernogo morya*, Marine Hydrophysic Institute, Sevastopol, Ukraine, 25-33 (in Russian).
4. R.A. Ibraev and D.I. Trukhchev, 1996, Seasonal variability of climatic circulation in the Black Sea, *Doklady Akad. Nauk*, 350 (4), 541-543 (in Russian).
5. T. Oguz and P. Malanotte-Rizzoli, 1996, Seasonal variability of wind and thermohaline-driven circulation in the Black Sea: Modeling studies, *J. Geophys. Res.*, 101 (C7), 16551-16569.
6. P.V. Morozov, 1960, Distribution of hydrological elements and water dynamics in the southeastern Black Sea, *Trudy of AzCherNIRO*, 18, 21-28 (in Russian).
7. V.A. Bibik, 1964, Peculiarities of water dynamics in the southeastern Black Sea and distribution of oceanographic elements, *Trudy of AzCherNIRO*, 23, 23-31 (in Russian).
8. G. Neumann, 1942, Die absolute topografie des physikalischen Meeresniveaus und die Oberflächenströmungen des Schwarzen Meeres, *Ann. Hydrogr. Maritimen Meteorol.*, Berlin, 70, 265-282.
9. A.A. Dubnov, V.L. Lebedev, A.F. Maslov, A.A. Smirnov and N.K. Strachuk, 1991, The Black Sea Current near the Caucasian coast and its influence on the pollutions transport, *Vestnik Moskovskogo Universiteta*, Ser.5 (Geografija), 3, 53-57 (in Russian).
10. A.S. Kazmin and V.E. Sklyarov, 1982, Some peculiarities of the Black Sea circulation inferred from the Meteor satellite, *Issledovaniye Zemli iz kosmosa*, 6, 42-49 (in Russian).
11. K.N. Fedorov and A.I. Ginzburg, 1992, *The Near-surface Layer of the Ocean*, VSP, Utrecht, The Netherlands, 259 p.
12. A.S. Blatov and A.N. Kosarev, 1983, On water dynamics in the southeastern Black Sea, In: *Priroda Okeana*, Moscow, 82-85 (in Russian).
13. D.M. Filippov, 1968, *Circulation and water structure in the Black Sea*, Moscow, Nauka, 135 p. (in Russian).
14. V.T. Georgiev, S.A. Gerasimov and Yu.I. Popov, 1994, Hydrodynamic state of open water in the northern half of the Black Sea in 1992-1993, *Issledovaniye ekosistemy Chernogo morja*, UNCM, Odessa, 1, 18-24 (in Russian).
15. K.N. Fedorov, A.I. Ginzburg, and A.G. Kostianoy, 1989, Modelling of "mushroom-like" currents (vortex dipoles) in laboratory tank with rotating homogeneous and stratified fluids, In: *Mesoscale/Synoptic Coherent Structures in Geophysical Turbulence*, Elsevier Oceanogr. Series, 50, Amsterdam, Oxford, New York, Tokyo, P.15-24.
16. A.S. Blatov, N.P. Bulgakov, V.A. Ivanov, A.N. Kosarev and V.S. Tuzhilkin, 1984, Variability of Hydrophysical Fields of the Black Sea, Leningrad, Hydrometeoizdat, 240 p. (in Russian).
17. B.N. Panov and A.K. Chashchin, 1990, Peculiarities of dynamic water structure in the southeastern Black Sea as a prerequisite for formation of winter accumulation of khamisa near the Caucasian coast, *Okeanologija*, 30 (2), 328-334 (in Russian).
18. T. Oguz, P.E. La Violette and U. Unluata, 1992, The upper layer circulation of the Black Sea: its variability as inferred from hydrographic and satellite observations, *J. Geophys. Res.*, 97 (C8), 12569-12584.
19. I.M. Ovchinnikov, V.B. Titov, V.G. Krivosheja and Yu.I. Popov, 1993, The main hydrophysical processes and their role in the ecology of the Black Sea waters, 33 (6), 801-807 (in Russian).
20. V.S. Latun, 1989, Anticyclonic eddies in the Black Sea in summer 1984, *Morskoy Gidrofisichesky Zhurnal*, 3, 27-35 (in Russian).
21. D.Ya. Fashchuk and T.A. Ayzatullin, 1986, On possible transformation of the anaerobic zone of the Black Sea, *Okeanologija*, 26 (2), 233-242 (in Russian).

SURFACE CIRCULATION OF THE JAPAN SEA (SATELLITE IMAGERY AND DRIFTERS DATA)

A.I. Ginzburg, A.G. Kostianoy and A.G. Ostrovskii

P.P. Shirshov Institute of Oceanology, 36 Nakhimovsky Prospect, Moscow, Russia
E-mail: kostianoy@glasnet.ru, akfedorov@glasnet.ru

Abstract. Joint analysis is carried out of NOAA infrared images (1993-1994) and of trajectories of ten surface drifters (1992-1995) to investigate space-time variability of main elements of the Japan sea dynamics and estimate their kinematic parameters. The most typical diameters, mean orbital velocities and periods of rotation of the observed eddies in the southern area were 90-140 km, 26-34 cm/s and 12-15 days, respectively. Their translation velocity did not exceed 2 cm/s. A role of eddies in the formation of some elements of the sea dynamics is shown and associated dissimilarity of the observed picture from the known schemes of circulation is noted. In a late autumn between 40 and 42°N the Liman Cold Current changed to the northward flow, may be associated with local anticyclonic eddy.

1. Introduction

Schemes of general circulation of the Japan Sea based on hydrographic measurements usually include two main branches of the Tsushima Warm Current (TWC), one of which flows along the Japanese coast and the another one, the East Korean Warm Current (EKWC), along the Korean coast, the Liman Cold Current (LCC), the Subpolar Front and cyclonic gyres north of the front (e.g., [1,2]). Some elements of the circulation (separation of the EKWC from the Korean coast at about 37-38°N and its propagation along the Subpolar Front, cyclonic gyre in the East Korean Bay) are reproduced in numerical modelling [2].

However satellite imagery of the sea [3-6] showed that eddies play an important role in the current variability, which can determine dissimilarity of real circulation from the schemes. Spatial and kinematic (angular and orbital velocities, translation velocity) characteristics of these eddies and seasonal variability of the observed eddy patterns are poorly known as well as velocities and seasonal variability of the climatic currents. In this paper we consider role of mesoscale eddies in the Japan Sea surface circulation and association of some of them with the bottom topography, space-time variability and kinematic parameters of main elements of the circulation (eddies, climatic currents) and also correspondence of the observed circulation with known schemes and results of numerical modelling. The study is based on joint analysis of NOAA infrared (IR) images and trajectories of satellite-tracked surface drifters.

2. Data

Data set included 41 relatively cloud-free IR images, 24 of which were received during autumn 1993 (from 15 September to 8 November), 16 during spring 1994 (from 28 March to 19 May), and one on 25 October 1994. Used IR images were received from the Advanced Very High Resolution Radiometer (AVHRR) on the polar orbiting NOAA-10,11,12 satellites in high resolution picture transmission (HRPT) regime. Procedure of

atmospheric correction and transformation to Mercator projection were applied to the images [6]. Trajectories of ten satellite-tracked drifters propagated in the study area in the period from November 1992 to August 1995 were also used in the analysis as well as published results of hydrographic surveys in the southeastern area in August [7] and October [8] 1993 and in March 1994 [9].

3. Eddies in the Japan Sea

Scheme of surface circulation of the Japan Sea based on IR images for 18-19 September 1993 is shown in Fig.1. The scheme includes mesoscale anticyclonic eddies aligned in two chains (one along the Korean coast, A1, A5 and A6, and the another meridionally oriented, A1-A4) with a common A1, the TWC with its branches (in particular, zonal flow D), anticyclonic shear vortices of the A7 type between the LCC and the Siberian/Korean coast, and anticyclonic loops of the A8 type at the Subpolar Front. The same eddy features are seen on drifter trajectories (Fig.2; trajectories of the rest four drifters are presented in [10]). Values of diameters D , mean orbital u and angular ω velocities and revolution periods T for the eddies estimated from the trajectories are given in Table 1. It may be seen from the Table that the most typical D , u and T of eddies in the southern area were about 100-140 km, 26-34 cm/s and 12-15 days, respectively.

Sequence of satellite images allowed to trace variation of diameters and spatial positions of eddies A1-A6 in time. Diameter of the quasi-stationary eddy A1, which provides the northward transfer of the TWC warm waters via the systems of adjacent eddies A2-A4 and A5-A6, changed with time, but its location was relatively stable. From 18 September to 8 November, 1993 eddies A2 and A3 shifted basically to the west by 60 km and 20 km, respectively. Trajectory of drifter N03156 (Fig.2a) shows that eddy A3 moved by 50 km to the west from June to December 1993. Eddy A4 was not manifested in satellite images in November, but according to drifter N1993b trajectory (Fig.2c, Table 1) it existed even in December, although its diameter decreased significantly. From September to December 1993 the eddy drifted to the northwest approximately by 110 km. "Coastal" anticyclone A5 was not traced on satellite images in October-November; more likely it combined with A2 displaced to the west. Another eddy of the "coastal" chain, A6 in the East Korean Bay, displaced unlike to A1-A4 about 55 km east by November. Translation velocity of eddies A1-A6 did not exceed 2 cm/s.

In August-September 1993 a cyclonic eddy centered at about 37.8°N, 129.5°E was observed near the Korean coast (structure C in Figs.1 and 2a, velocity achieved 52 cm/s near the Korean coast; ADCP and CTD-measurements on 6-14 September 1993, [11]). Probably, the intense southward flow was associated with the LCC. It is not excluded also that entrainment of the LCC cold waters by cyclonic vortices of the C type associated with coastal anticyclonic eddies (A5 and A6 in Fig.1) could lead to propagation of these waters practically up to the northern periphery of quasi-stationary eddy A1. From the other side, the propagation of these cold waters along the eastern sides of eddies A5 and A6 can reach 37.5 °N.

Eddy picture in spring 1994 was the same in general terms in the southwestern area and more complicated in the southeastern one (see Fig.4 in [10]) that could be determined by two factors. Firstly, it is in spring, with increasing the TWC transport, that intensive eddy formation occurs [12], which is confirmed by the larger number of eddies at the 200 m - monthly mean temperature map in March 1994 [9], with respect to October 1993 [8]. Secondly, because of the eroded sea surface temperature gradients in autumn eddies in the area could not be traced.

It follows from comparison of autumn 1993-1994 and spring 1994 satellite images that coastal eddies and anticyclones of the "meridional" chain are typical for both seasons. The same likely relates to the largest anticyclone (or anticyclones) with diameter of more than 120 km in the region of the Yamato Rise. In spring the anticyclone was centered at about 38°N, 134°E (it was manifested also in monthly mean temperature at a depth of 100 and 200 m in March 1994 [9]). In autumn 1993 similar eddy was centered about 1° north [8]. This anticyclone for sure determined intensive zonal flow around the Yamato Rise (structure D in Fig.1) due to entrainment of the northward TWC branch over the Oki Bank. In October-November 1993 this flow was absent, but large area of warm water was still present in the region. Form of the area, shear cyclonic vortices at its northern and eastern peripheries, its location in the region of frequent observation of warm eddies [5] and monthly mean temperature distribution maps for October 1993 [8] pointed on its relationship with an anticyclonic eddy. The presence of the intensive flow at the periphery of the quasi-stationary anticyclone in September 1993 and its absence in October-November 1993 can be explained by seasonal variation of the TWC volume transport, which is minimum from February to May and maximum in August-September [5]. It

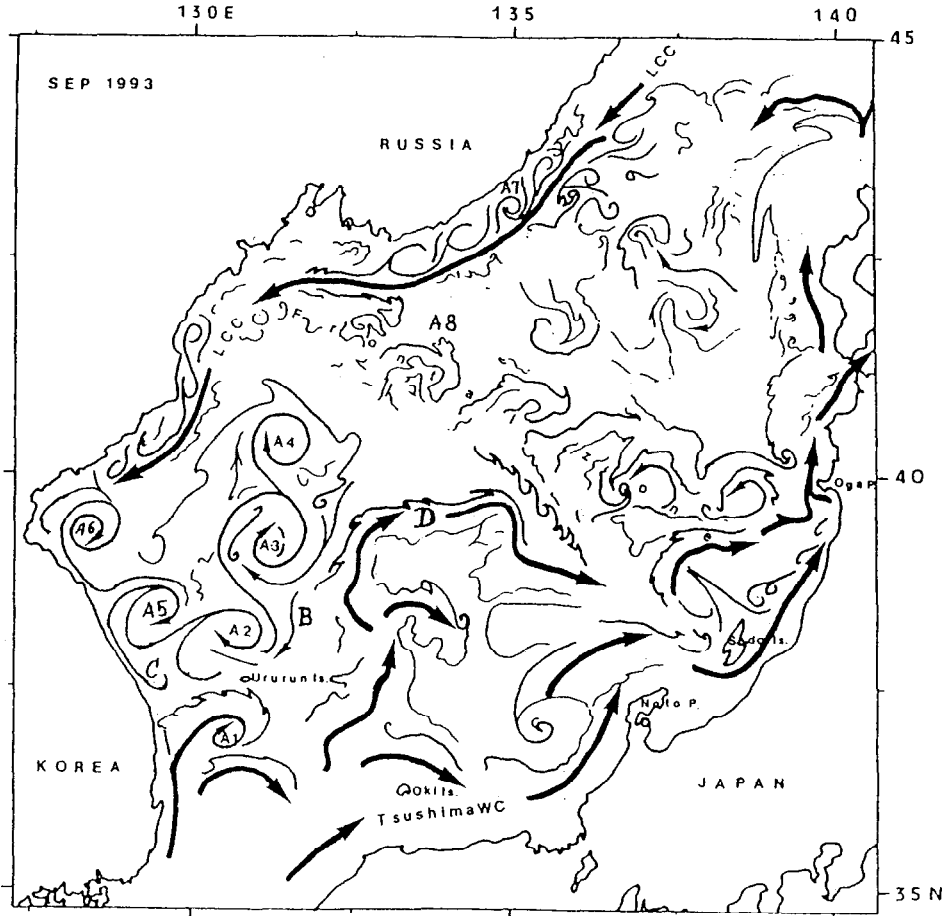


Fig. 1. Scheme of surface circulation of the Japan Sea in September 1993 based on the NOAA AVHRR IR images (similar scheme in [6] is assumed as a basis).

Table 1. Spatial and mean kinematic parameters of anticyclonic eddies in Fig. 1 determined from surface drifters trajectories

Eddy	D, km	T, days	ω , rad/s	u, cm/s	Drifter	Month	Year
A1	100	14.4	$5.0 \cdot 10^{-6}$	26	03156	July	1993
A2	103	14.1	$5.2 \cdot 10^{-6}$	26	03156	Aug.-Sep.	1993
A2	103	12.4	$5.9 \cdot 10^{-6}$	30	03156	Nov.	1993
A3	140	15.2	$4.8 \cdot 10^{-6}$	34	03156	June	1993
A3	140	15.2	$4.8 \cdot 10^{-6}$	34	03157	June	1993
A3	130	9.5	$7.7 \cdot 10^{-6}$	50	03156	Dec.	1993
A4	56	7.0	$10.4 \cdot 10^{-6}$	29	1993b	Dec.	1993
A6	70	18.7'	$4.0 \cdot 10^{-6}$	14	1993b	Sep.-Oct.	1993
A6	85	18.0	$4.0 \cdot 10^{-6}$	17	1994b	Oct.	1994
A7	40	6.0	$12.0 \cdot 10^{-6}$	23	21577	Aug.	1994
A7	25	5.0	$14.5 \cdot 10^{-6}$	18	1994a	July-Aug.	1995
A8	65	10.7'	$6.8 \cdot 10^{-6}$	22	1993a	Oct.	1993
A8	60	12.8	$5.6 \cdot 10^{-6}$	17	1994b	June-July	1995

Note: values with ' are determined from the drifters trajectories and IR image-borne diameters.

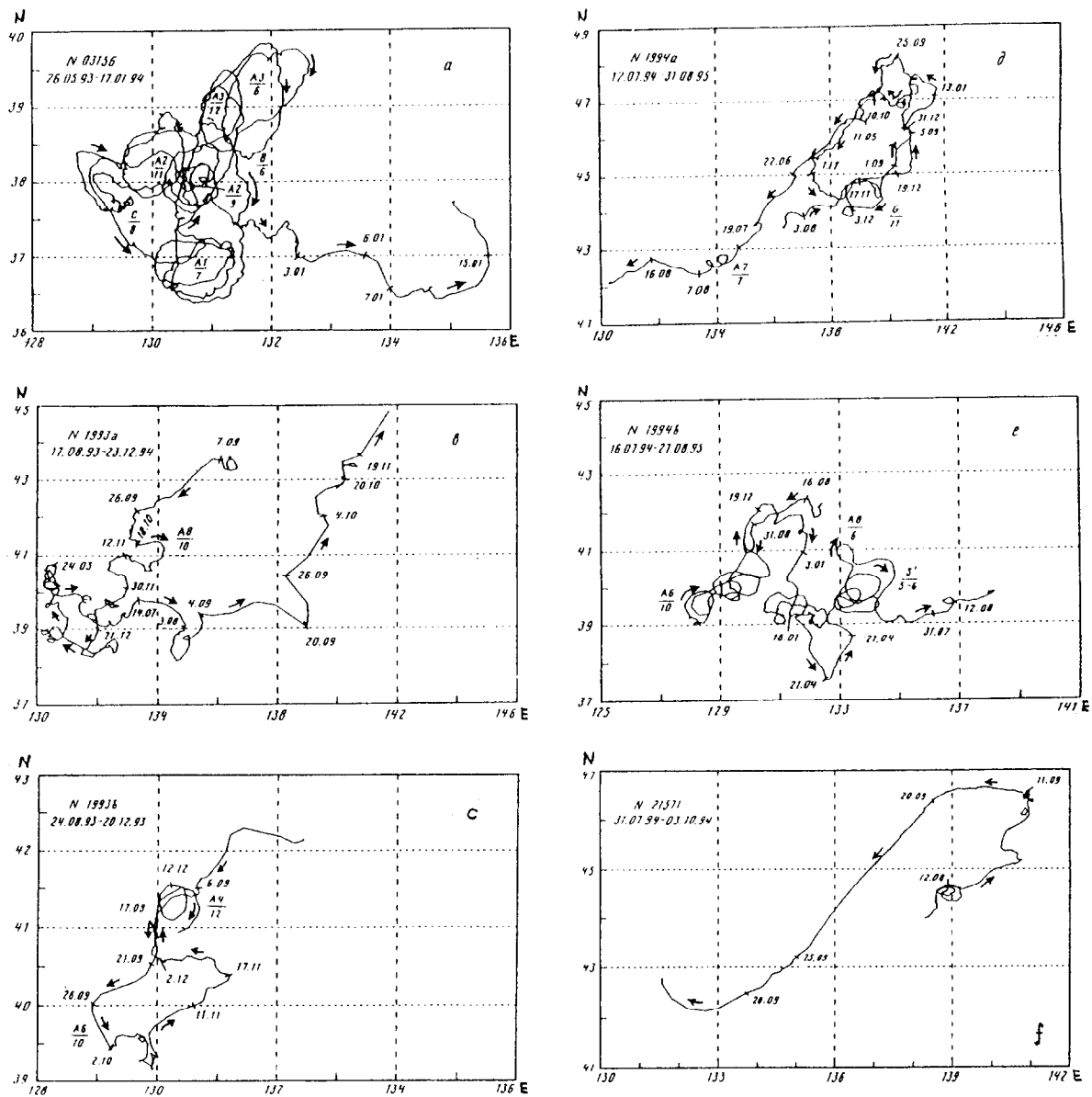


Fig.2. Trajectories of drifters: (a) N03156, (b) N1993a, (c) N1993b, (d) N1994a, (e) N1994b, (f) N21571. Letters denote discussed elements of circulation (months of the structures observations are indicated under lines). Periods of drifters propagation in the sea are given in the left corners of figures. Some points of reference are marked by dates.

is of interest whether the observed in autumn and spring large anticyclones in the region of the Yamato Rise were the same quasi-stationary bottom controlled eddy, which changed its position in time (for example; due to self-propelling mechanism of a dipole on its basis) or seasonally. In particular, displacement of centre of this eddy to the south by 30 km from 2 April to 6 May, 1994 (Figs.3 and 4 in [10]) might be related with dynamics of a dipole formed from the eddy and associated cyclone at its periphery (Fig.4 in [10]).

Analysed satellite images suggest that the stable EKWC as the branch of the TWC does not exist that is in accordance with result of investigation [5] and is confirmed by comparison of Fig.1 with practically synchronous velocity field obtained with ADCP measurements [11]: unidirectional northward flow near the Korean coast in September 1993 was absent and velocity distribution corresponded to eddy picture in Fig.1. In fact warm water band along the Korean coast is conditioned by successive transmission of the TWC-origin warm water by chain of coastal anticyclones. It is evident also that zonal flow around the Yamato Rise is not extension of the EKWC but the TWC-origin water flowing northward from the Oki Spur.

From four anticyclonic loops observed at the Subpolar Front (Fig.1) the only eddy A8 northwest of the Yamato Rise (Fig.1 and Table 1) kept its identity in September-October 1993. Probably, it still existed in November 1993, judging from the spot of the warm waters in its location area. Its orbital velocity derived from drifter N1993a trajectory in October 1993 (Fig.2b) was equal to 22 cm/s and its revolution period estimated with regards to IR image-borne diameter was about 11 days (Table 1). It is surprising that anticyclonic eddies at the same place were observed in October 1994 (IR image) and in June-July 1995 (trajectory of drifter N1994b in Fig.2e). It would be of interest to clarify the reason of rather stable position of the eddies.

Shear anticyclones of the A7 type of about 35 km in diameter observed in September 1993 disappeared in October that was supposedly determined by seasonal variability of the LCC. Trajectory of drifter N1994a within such eddies in July 1995 is seen in Fig.2d.

4. Boundary currents

The Tsushima Warm Current (TWC). Propagation of the TWC along the Japan coast was accompanied by its meandering, branching near the Oki Spur and the Noto Peninsula and entrainment by local eddies. Velocity in the Nearshore Branch changed, according to drifters data (Figs.2a, 2b and 2e), from 16 to 32 cm/s and increased to 40-50 cm/s near the Oki Spur, in cyclonic meander west of the Noto Peninsula and in the northward flow up to the Tsugaru Strait. Lesser velocities were observed near the Subpolar Front: 11-15 cm/s between 133 and 137°E with increasing to 22-33 cm/s, as the Japan coast and the Tsugaru Strait were approached. Velocity of the flow north of the Tsugaru Strait (Figs.2b, 2d and 2f) changed from about 14 to 30 cm/s with tendency to decrease in cold season and northward. For example, velocity of drifter N1994a (Fig.2d) changed from 30 cm/s in September to 14 cm/s in December 1994 between 45 and 46°N and from 30 to 16 cm/s in September, as the drifter moved from 45 to 48°N. Registration of anticyclonic eddies or dipole structures by two different drifters in different seasons (drifter N1994a in November-December, structure G, and drifter N21571 in August 1994 in Figs.2d and 2f, respectively) in the same region west of the Musasi Bank implies their relationship with bottom topography. Westward branches of the TWC were observed in the regions 43-44, 46.7 and 47.5-48°N (Figs.2d and 2f).

The Liman Cold Current (LCC). Velocity of the LCC between 48 and 42°N changed in the range from 14 to 38 cm/s (Fig.2d) and increased up to about 90 cm/s between 46.6 and 43°N in September 1994 (Fig.2f). It is unknown whether the increase was associated with increasing velocity of the current in September (as compared with October or May) or with intensive drift current due to strengthening of northerly wind. It is important to note that by a late autumn (between September and December) there is a change of the local current direction between 40 and 42°N from the southward LCC to the northward flow, as indicated by trajectories of two drifters N1993b and N1994b (Figs.2c and 2e, respectively). For example, the southward LCC with 15-19 cm/s at 40.5-41.5°N in September 1993 was changed by the northward flow with 12 cm/s in December 1993, determined by seasonal absence of the LCC and presence here of anticyclonic eddy, may be A4 (Fig.2c). This change of the local current direction after September well conforms with circulation peculiarities seen in satellite imagery, namely the warm water northward transport conditioned by its entrainment from the south by neighbouring anticyclonic eddies and disappearance of shear anticyclonic vortices near the coast (see above). Trajectory of drifter N1994a in November 1994 (Fig.2d) showed the LCC branching to the east with velocity of 14 cm/s near 44.3-45.0°N.

5. Conclusions

Analysis of satellite and drifters data detected marked mesoscale activity in the Japan Sea and associated variability of the climatic currents. Kinematic parameters of various mesoscale eddies and the currents were estimated. The analysis allowed to conclude that:

1. General features of the eddy field in the western area of the Sea were the same in autumn and in spring, however in the southeastern area more intensive eddy generation was observed in spring, probably conditioned by the seasonal increase of the TWC transport.

2. It is anticyclonic eddies along the Korean coast, within 130-132°E ("meridional" group) and over the Yamato Rise that provide northward transport of the TWC-origin warm water to the Subpolar Front and even farther in the western area as well as cold water southward intrusions along the eddies eastern peripheries.

3. Some of the observed eddies are likely associated with the bottom topography peculiarities (e.g., anticyclones in the Ullung Basin, over the Yamato Rise and west of the Musasi Bank). It is unknown if anticyclones with centres at 39°N, 134°E and at 38°N, 134°E observed in August-November 1993 and in March-May 1994, respectively, were manifestation of one the same quasi-stationary bottom controlled eddy, which could be shifted in time or seasonally. Reason of rather stable position of anticyclones in the Japan Basin northwest of the Yamato Rise is also unclear.

4. Anticyclonic rotation of the eddy in the East Korean Bay is typical at least for spring and autumn. Considering, that the opposite (cyclonic) rotation was shown in [1,2] further investigation is needed of the circulation in this region basing on the oceanographic data and numerical modelling.

5. Because of the eddy nature of the EKWC there is no sense to consider its deviation from the Korean coast near 37-38°N and further propagation to the east along the Subpolar Front, as it is tried to be shown in numerical modelling (see [2]).

6. Between September and December (probably in October) in the region 40-42°N the change of the current direction from the southward LCC to the northward flow is possible. With consideration of [13], we can assume that the LCC at this region is absent at least from a late autumn to March. The fact as well as possibility of appearance in this season of the opposite (northward) flow associated with local anticyclone should be taken into account in numerical modelling of the region circulation.

The authors were supported by grant N98-05-64715 from the Russian Foundation for Basic Research.

References

1. V.G. Yarichin, 1980, Study state of the Japan Sea circulation. In: Problems of Oceanography, Ed. V.Pokudov, Hydrometeoizdat, Leningrad, 46-61 (in Russian).
2. C.-H. Kim and J.-H. Yoon, 1996, Modelling of the wind-driven circulation in the Japan Sea using a reduced gravity model. *J.Oceanography*, 52, 359-373.
3. Y. Toba, H. Kawamura, F. Yamashita and K. Hanawa, 1984, Structure of horizontal turbulence in the Japan Sea. In: *Ocean Hydrodynamics of the Japan and East China Seas*, Ed. T.Ichie, Elsevier, 39, 317-332.
4. K. Kim and R. Legeckis, 1986, Branching of the Tsushima Current in 1981-83. *Prog.Oceanog.*, 17, 265-278.
5. Y. Isoda and S. Saitoh, 1993, The northward intruding eddy along the east coast of Korea. *J.Oceanography*, 49, 443-458.
6. A. Ostrovskii and Y. Hiroc, 1994, The Japan Sea circulation as seen in satellite infrared imagery in autumn 1993. *Proc. CREAMS'94 Int.Symp.*, 24-26 Jan. 1994, Fukuoka, Japan, 75-88.
7. Oceanographic Prompt Rep. N383, Maizuru Marine Observatory, Nov. 1993, 38 pp.
8. Oceanographic Prompt Rep. N384, Maizuru Marine Observatory, Feb. 1994, 32 pp.
9. Oceanographic Prompt Rep. N385, Maizuru Marine Observatory, May 1994, 23 pp.
10. A.I. Ginzburg, A.G. Kostianoy and A.G. Ostrovskii, 1998, Surface circulation of the Japan Sea (satellite information and drifters data). *Issledovaniye Zemli iz kosmosa*, 1, 66-83.
11. S.-K. Byun, C. Kim and H.-R. Shin, 1994, Result of September'93 survey conducted in the southwestern part of East Sea (Japan Sea). *Proc. CREAMS'94 Int.Symp.*, 24-26 Jan. 1994, Fukuoka, Japan, 108-110.
12. Y. Isoda, 1994, Warm eddy movements in the Eastern Japan Sea. *J.Oceanography*, 50, 1-15.
13. V. Yarichin and O. Ryabov, 1994, Current field structure of the Japan Sea in February-March 1990. *Proc. CREAMS'94 Int.Symp.*, 24-26 Jan.1994, Fukuoka, Japan, 99-101.

MATHEMATICAL MODELLING OF THE NEAR-SURFACE LAYER

Gogoberidze G. G., Karlin L. N., Kluikov Ye. Yu.

Russian State Hydrometeorological University,
St.-Petersburg, 195196, Malookhtinsky Av. 98, Russia

Abstract

In the early 80s K. N. Fedorov isolated five regimes of the near-surface ocean layer: those of wind-wave mixing, convective mixing, volume absorption of radian energy, freshening through precipitation, Langmuir circulation. Later, researchers found features of the near-surface layer evolution which could also be qualified as a regime of the near-surface layer: the regime with a fine thermohaline structure of the near-surface layer and the regime of openings and polynyas, often observed in the Arctic basin. The present report presents analysis of the mathematical models of near-surface layer for various regimes. The commonness of theoretical basis for these models is shown. As a result, a unified mathematical model is proposed, in which the models of individual regimes are the constituents.

The notion of the ocean near-surface layer was first introduced by K. N. Fedorov at the beginning of the 80s and has attracted close attention of researchers ever since. The identification of the ocean near-surface layer as the subject of investigation made it possible to highlight many changeability aspects of the hydrophysical fields in the layer in a more detailed and logical way, to demonstrate the important relationship between the phenomena on the surface and atmospheric processes as well as the processes going on in the ocean's deep layer. Thus, we can say that the near-surface layer plays the part of the principal transmitting climatic link between the atmosphere and the ocean.

Based on the current level of knowledge of the near-surface layer, the following constituent parts in its structure are identified:

- thermal boundary layer;
- upper mixed layer;
- diurnal thermocline.

In its turn, the upper mixed layer includes a daytime mixed layer and all those separations that emerge due to the instability of atmospheric effects on the ocean surface.

Below the diurnal or near-surface thermocline, there goes on the decrease in temperature down to the seasonal (main) thermocline, i. e. in the general case in the vertical structure of the ocean there exist the main, the seasonal and the diurnal (during the day-time) thermoclines.

It should be noted that besides the thermal changeability of the near – surface layer, the salinity changeability in the layer is also observed caused mainly by precipitation as well as horizontal advection of the more freshened waters.

Hence it is easy to notice that the thermohaline structure of the ocean near-surface layer is significantly different with various interactions of the ocean and atmosphere and energy exchange between them. On this basis at the beginning of the 80s the five significantly different regimes of the near-surface layer were identified [17]:

- the regime of intense wind-wave mixing (the wind velocity exceeding 8-10 m/s);

- the regime of intense convection (the night-time, autumn-winter one);
- the regime of the Langmuir circulation (the wind velocity being 3-10 m/s);
- the regime of intense solar heating in calm and low-wind weather (the wind velocity being not more than 3–5 m/s);
- the regime of the near-surface sweetening through precipitation.

Development of the near-surface layer investigation methods [9, 20] allowed to identify a sixth regime, related to the fine structure of the near-surface layer due to horizontal advection.

The seventh specific regime of the ocean near-surface layer is, in its turn, related to the peculiarities of the thermohaline structure of leads in the polar and near-polar seas [1, 16]. In summer these ice lanes act like thermal accumulators, where in addition to this, the melt water flowing from the surface of ice fields is stored. As a result, there emerges a freshened layer which has its lower boundary in the form of a thick pycnocline and, because of sustained heating and sweetening, is characterised by high density stability. In winter the leads are the fields of development of free gravitational thermohalinal convection, resulting in a continuous active inflow of salt water into the near-surface layer.

Because of its location, the near-surface layer of the ocean is under a constant varying atmospheric influence. It has been proven that it is the atmospheric anomalies resulting in about 60 % changeability that are the major causes for space anomalies of the sea-surface thermohalinal characteristics, while the drift-advection contribution only amounts to about 10–15 % [12].

Most of the available mathematical models can describe seasonal variability of the near-surface layer parameters [10, 13, 18, 21] as well as the diurnal changeability of the layer [6, 7, 9, 11, 15, 17]. In recent years due to the development of computer engineering allowing to perform large volumes of calculations, there has emerged a new line in modelling the ocean near-surface layer related to numerical methods of solving the problem. In these models, as a rule, simulated are the turbulent processes in the interacting boundary layers of the ocean and atmosphere as a unified system, in particular, in the non-stationary form, too [4, 5]. There the meteorological and hydrophysical processes, turbulence characteristics and the parameters of interaction of the two media, including the sea-surface temperature, are jointly determined by set conditions at the outer boundaries of the interacting media [14]. The advent of such mathematical models has made it possible to simulate to sufficient accuracy the processes of the diurnal cycle occurring in the near-surface layer.

However it should be noted that the mathematical models obtained are rather bulky and include a very large number of outer set parameters. Besides, one should also allow for the fact of errors in the numerical schemes in solving the problem. This leads to attempts to create models on the basis of analytical solutions of a system of hydrothermodynamic equations and a balance equation of turbulent kinetic energy with a possibly minimal employment of parametrizations and with application of numerical methods [8, 22]. This fact allows us to conclude that the most effective line in modelling the changeability of the ocean near-surface layer parameters is symbiosis of the analytical and numerical solutions with parametrizations for problems with parameters without significant sacrifice of precision.

The mechanisms of formation and evolution of the near-surface layer considered under the condition of a steady-state turbulent regime, horizontal homogeneity, absence of advection and vertical homogeneity within the limits of the upper mixed layer, are based on a system of the three equations: the equation of water temperature evolution in the daytime mixed layer, the equation of balance of turbulence energy and the equation of dissipation:

$$\frac{\partial T}{\partial t} = - \frac{\partial Q^T}{\partial z}, \quad (1)$$

$$k \left[\left(\frac{\partial u}{\partial z} \right)^2 + \left(\frac{\partial v}{\partial z} \right)^2 \right] + \alpha_b \frac{\partial}{\partial z} k \frac{\partial b}{\partial z} - \varepsilon - g \alpha Q^T = 0, \quad (2)$$

$$\alpha_1 \frac{\varepsilon}{b} k \left[\left(\frac{\partial u}{\partial z} \right)^2 + \left(\frac{\partial v}{\partial z} \right)^2 \right] + \alpha_2 \frac{\partial}{\partial z} k \frac{\partial \varepsilon}{\partial z} - \alpha_3 \frac{\varepsilon}{b} - \alpha_4 \frac{\varepsilon}{b} g \alpha Q^T = 0, \quad (3)$$

where b is turbulence energy, m^2/s^2 , (ϵ is dissipation of turbulence energy, m^2/s^3 ; k is turbulence coefficient, m^2/s ; u, v are horizontal constituents of the current, m/s ; Q^T is reduced heat flux, $^\circ C \cdot m/s$; α is coefficient of thermal expansion, $^\circ C^{-1}$; $\alpha_b, \alpha_1, \alpha_2, \alpha_3, \alpha_4$ are dimensionless coefficients.

For completion of the system, the Kolmogorov relations are employed, as well as an assumption on the constancy of turbulent energy values along the vertical and of the gradient of dissipation within the daytime mixed layer, is introduced. The boundary conditions at the water-air boundary are written in the form of a turbulent energy flux and dissipation gradient along the vertical. In doing so, we consider the dissipation gradient to depend on the turbulent energy flux across the water-air interface and roughness parameter. The solution of the system is the transcendental equation for thickness of the daytime mixed layer and the equation for temperature evolution of the mixed layer:

$$H = 1.04 \frac{A}{C} \frac{1}{q_0^T + q_H^T} + 3.8 \frac{D}{C} \frac{1}{q_0^T + q_H^T} - 2 \frac{P_1}{C} \frac{k^{1/2}}{q_0^T + q_H^T} \left[(A + D) \frac{1}{H} - C(q_0^T + q_H^T) \right]^{-1/2}, \quad (4)$$

$$\frac{\partial T}{\partial t} = \frac{q_0^T - q_H^T}{H}, \quad (5)$$

where A, C, D, P_1 are dimensional complexes; q_0^T and q_H^T are heat fluxes at the water-air boundary and at the lower boundary of the mixed layer, $^\circ C \cdot m/s$. In order to determine the magnitude of q_0^T , the notion of the two so-called sub-regimes is introduced here:

- sub-regime of detrainment ($q_H^T = 0$);
- sub-regime of entrainment ($q_H^T \neq 0$).

Here for the entrainment sub-regime we assume self-similarity of the temperature profile below the mixed layer:

$$q_H^T = - \frac{\partial T}{\partial T} (H - H_s) (1 - \alpha_T) + \frac{\partial H}{\partial T} (T - T_H) \alpha_T, \quad (6)$$

where H_s is the depth of the thermocline position, m ; T_H is water temperature at the lower boundary of the thermocline, $^\circ C$; α_T is dimensionless heat content in the layer $[H - H_s]$, a self-similarity coefficient.

As a solution of the system (4–6), we have evolution equations to calculate thickness of the mixed layer and water temperature in the layer. In order to solve the given system, it is necessary to pay attention to the new calculation of the self-similarity coefficient α_T from the ratio of the real heat content of the layer from the lower boundary of the daytime mixed layer with a minimal thickness down to the lower boundary of the diurnal thermocline, to the possible heat content of this layer if the thickness of the daytime mixed layer reached the lower boundary of the diurnal thermocline, i.e.:

$$\alpha_T = 1 - \frac{q_\Sigma - H(T - T_H)}{(T - T_H)(H_d - H)}, \quad (7)$$

where q_Σ is the quantity of the heat obtained by the layer across the ocean-atmosphere interface during the detrainment regime, $m \cdot ^\circ C$; H_d is the depth of the upper thermocline, m .

For the regime of the volume absorption of radiant energy, a term is introduced into Eq.1 which is related to the account for the radiant energy flux through the water-air boundary.

For the regime of sweetening through precipitation, as well as allowing for salinity effects due to the influence of evaporation, the model is transformed, and the system is complemented by the equation of salinity evolution:

$$\frac{\partial S}{\partial t} = - \frac{\partial Q^S}{\partial z}, \quad (8)$$

where Q^S is reduced salt flow, ‰·m/s.

In doing so, for the regime of sweetening through precipitation the dynamic impact on the daytime mixed layer is considered as a sum of addends, standing for dynamic wind forcing, kinetic energy of falling raindrops and friction velocity at the lower boundary of the freshened layer, respectively: H

$$\tau' = c_d U^2 + c_\tau^2 \frac{I^2 (U^2 + W^2)}{4g^2 H^2} + c'_d c_d^2 \frac{U^4}{f^2 H^2}, \quad (9)$$

where I is rainfall intensity, m/s; W is vertical velocity of falling raindrops, m/s; c_d is coefficient of resistance; $c'_d = 10^{-3}$, dynamic friction coefficient at the lower boundary of the layer [11]; $c_\tau = 790$ [3].

The solutions allowing for changes in salinity are more complete. However, in the absence of precipitation during the day and night periods, and providing that the contribution of the thermal factor into buoyancy flow is greater than that of the salt one, the salt flow can be neglected, and one can use the solution without regard for salinity.

In order to check upon adequacy and accuracy of the results of modelling, the model was tested by the data of two long-term stations in the Gulf of Finland. The correlation coefficients K_r and conformity criteria K obtained through statistical analysis show close relationship between the results of the modelling and the in situ data, which proves goodness of fit of the simulated calculations and the data of the in situ observations. The ratio S/σ as a characteristic of reliability and efficiency shows that it is possible to use the model.

To verify the model in the regime of the upper layer sweetening through precipitation, the observational data obtained by J. Price [19] in the Western Atlantic as well as by Fedorov and Ginzburg [2] were used.

Also performed was modelling with various combinations of meteoroparameters in order to isolate the principal mechanisms of formation and evolution of the near-surface layer features. For the calculations, varied combinations of the values of wind velocity and cloudiness were taken which were set to be constant during the entire calculation period, and the air temperature changeability T_a was assumed to be sine-shaped, due to which the changeability of the heat flux q_0^T through the water-air boundary was also found to be close to a sine curve. The calculation period was three days, and as shown by the results, this time lapse is sufficient for achieving a stable pattern of changeability of the above parameters.

According to the conducted calculation experiments, among the common trends in changeability of the near-surface layer features the following ones should be pointed out:

- an increase in the diurnal amplitude of temperature changeability with decreasing wind velocity and a lower amount of clouds, which is explained, in its turn, by a higher amplitude of the heat flux changeability across the water-air interface;
- a decrease in the mean diurnal temperature of the near-surface water layer is observed with strong winds even with a positive net heat flux, which is explained by reaching the lower boundary of the mixed layer of the depth of the diurnal thermocline position and large mass flows at the lower boundary of the mixed layer;
- a stable natural temperature trend with low wind velocities resulting in the heating of the daytime mixed layer, depending on the amount of clouds (in the evolution of the diurnal mixed layer thickness, the interdiurnal changeability trend is expressed only slightly);
- a well-pronounced trend towards increasing of the mixed layer thickness at high wind velocities because with the deepening regime of the mixed layer its thickness reaches the thermocline very quickly and increases the depth of position of the latter till the operation period of the night convection regime is over;
- in the absence of precipitation during the day and night periods and provided that the contribution of the thermal factor into buoyancy flux is larger than that of the salt one, the salt flux can be neglected, and one can use the solution without regard for salinity.

To calculate formation and evolution of the near-surface layer structure, a computerised equipment system was developed for assimilation of satellite information. The scheme of the operation of the system can

be arbitrarily divided into three stages. First, the calculation points are selected covering the target body of water, and the initial profiles of thermohalinal characteristics in each point are specified. Then, a calculation based on the above near-surface layer model is made for each point of the area till the new satellite information is received. In doing so, used are the necessary meteorological data of coastal stations, on-route ship observations etc., interpolated for each of the calculation points in the assigned area.

On receiving information from a satellite at a certain moment of time, the calculated temperature field of the daytime mixed layer is compared with that obtained by the results of the satellite surveys, and then the temperature profiles calculated as a result of modelling are adjusted for the satellite data. If need be, the profiles obtained and the maps of distribution of the thermohalinal characteristics can be employed for further work, and the operation of the computerised equipment system goes on, based on the corrected information till the next packet of space information is received. The adjustment of the temperature and salinity profiles is performed by the data of the expedition and on-route ship observations, as the materials become available for the system's database.

The water body of the Gulf of Finland was chosen as an example of employment of the computerised equipment system for calculation of changeability of the near-surface layer characteristics. In our work utilised were images obtained from the NOAA-14 satellite as well as meteorological data in the form of ring weather maps with 3hr resolution.

Comparison of data of the modelling and those of satellite surveys on the mixed layer temperature show that on the whole the picture of the modelled temperature distribution fits adequately the temperature distribution of the layer obtained by the satellite data and demonstrates the major peculiarities of its distribution well.

References

1. Vertical structure and dynamics of the ocean under-ice layer / Ed. by L. A. Timokhov. – Leningrad: Gidrometeoizdat Publishers 1989. 141 p.
2. Ginzburg A. I. et al. Precipitation effects in the ocean near-surface layer / A. I. Ginzburg, A. G. Zatsepin, V. E. Sklarov, K. N. Fedorov // *Okeanologiya*. 1980. V.20. ¹ 5. pp. 828-836.
3. Gogoberidze G. G., Karlin L. N. Modelling of formation and evolution processes of freshened layer near the ocean surface // *Okeanologiya*. 1977. V.37, ¹ 2. pp. 195-201.
4. Dmitriyev N. V. Mathematical modelling of vertical turbulent exchange in the upper ocean. – Novosibirsk: Published by the Computer Centre of SB of RAS, 1993. 154 p.
5. Dmitriyev N. V., Dvurechenskaya E. A. Numerical analysis of impurity transport for the upper turbulent layers of seas and oceans // *Meteorologiya i gidrologiya*. 1994. ¹ 12. pp. 53-62.
6. Zatsepin A. G., Ostrovsky A. G. Development of the upper mixed layer with increasing stability and in the presence of wind // *USSR AS Proceed. Ser. FAO*. 1984. V.20, ¹ 2. pp. 213-217.
7. Zilitinkevich S. S. A theoretical model of penetrating turbulent convection // *USSR AS Proceed. Ser. FAO*. 1987. V.23, ¹ 6. pp. 593-610.
8. Kalatsky V. I. Modelling of the vertical thermal active layer of the ocean. – Leningrad: Gidrometeoizdat Publishers, 1978. 342 p.
9. Karlin L. N., Kluikov Ye. Yu., Kut'ko V. P. Small-scale structure of hydrophysical fields of the upper ocean. – Moscow: Gidrometeoizdat Publishers, 1988. 164 p.
10. Kitaigorodsky S. A., Miropolsky Yu. Z. On a theory of the active layer of the open ocean // *USSR AS Proceed. Ser. FAO*. 1970. V.6, ¹ 2. pp. 177-188.
11. Monin A. S., Ozmidov R. V. Oceanic turbulence. – Leningrad: Gidrometeoizdat Publishers. 1981. 320 p.
12. Moshonkin S. N., Diansky N. A. Physical mechanisms of temperature anomaly evolutions in the upper ocean mixed layer in middle latitudes // *Okeanologiya*. 1994. V. 34, ¹ 4. pp. 513-526.
13. Resnyaansky Yu. D. On parametrization of integral dissipation of turbulent energy in the upper quasi-homogeneous layer of the ocean // *Okeanologiya*. 1975. V.11. ¹ 7. pp. 726-733.
14. Tarnopolsky A. G., Shnaidman V. A. A non-stationary model of interaction of boundary layers of the ocean and the atmosphere // *USSR AS Proceed. Ser. FAO*. 1991. V.27, ¹ 12. pp. 1349-1357.
15. Solovyev A. V. On the vertical structure of the fine mixed layer of the ocean with weak winds // *USSR AS Proceed. Ser. FAO*. 1982. V.18, ¹ 7. pp. 751-760.
16. Timokhov L. A., Golovin P. N., Kochetov S. V. Features of the thermohalinal structure of ice lanes in summer in the Arctic ice // *Okeanologiya*. 1993. V. 33, ¹ 6. pp. 833-838.

17. Fedorov K. N., Ginzburg A. I. The near-surface layer of the ocean. – Leningrad: Gidrometeoizdat Publishers, 1988. 304 p.
18. Niiler P. P., Kraus E. B. One-dimensional models of the upper ocean. Modelling and prediction of upper layers of the ocean. – Oxford, 1977. pp. 143-172.
19. Price J. Observation of a rain-mixed layer // J. Phys. Oceanogr. 1979. V. 9, ¹ 3. pp. 643-647.
20. Rodhe J. Wind mixing in a turbulent surface layer in the presence of a horizontal density gradient // J. Phys. Oceanogr. 1991. V.21, ¹ 7. pp. 1080-1083.
21. Woods J. D. Diurnal and seasonal variations of convection in the wind-mixed layer of the ocean // Quart. J. Roy. Met. Soc. 1980. V. 106, ¹ 449. pp. 379-394.
22. Yan X.-H. et al. An analytical model for remote sensing determination of the mixed layer depth / X.-H. Yan, A. Okubo, J. R. Schubel, D. W. Pritchard // Deep-Sea Res. A. 1991. V. 38, ¹ 3. pp. 267-287.

FRAZIL ICE FORMATION ALONG THE UPPER BOUNDARY OF SEASONAL PYCNOCLINE AND ITS ROLE IN GLACIAL MARINE SEDIMENTATION IN THE LAPTEV SEA DURING WINTERTIME

P. Golovin 1, I. Dmitrenko 2, H. Kassens 3, J. Holemann 4

1 and 2 State Research Center of the Russian Federation the Arctic and Antarctic Research Institute, 38, Bering St., St. Petersburg, 199397, Russia, e-mail: dia@aari.nw.ru, 007(812) 352 3149.

3 GEOMAR Forschungszentrum für Marine Geowissenschaften, Gebäude 4, Wischhofstrasse 1-3, D-24148, Kiel, Germany, e-mail: hkassens@geomar.de, 49 0431 600 2850.

4 GEOMAR Forschungszentrum für Marine Geowissenschaften, Gebäude 4, Wischhofstrasse 1-3, D-24148, Kiel, Germany, e-mail: jholema@geomar.de, 49 0431 600 2852.

Abstract. The article deals with typification of the winter vertical thermohaline profiles performed on the basis of all available data obtained during hydrological surveys in the central and eastern parts of the Laptev Sea during 1960-1984. Five characteristic types have been established. The possibility of overcooling and subsequent frazil ice formation along the boundary between the upper quasihomogeneous layer (UQL) and seasonal pycnocline has been analyzed. This was the basis for geographical zonation of the central and eastern parts of the sea according to existing hydrological situations of different types. The following regions have been established: possible flaw polynya, peripheries with freshened water, areas of possible overcooling and frazil ice formation, and the regions with warm seasonal pycnocline and lower layer. The areas of possible or impossible frazil ice formation have been shown to have "spotted" spatial distribution patterns.

Using the results of laboratory modelling we have estimated the intensity of frazil ice formation (V_i) along the boundary between seasonal winter pycnocline and UQL depending upon the UQL dynamic state (or the range of average flow rate - U). Spatial distribution of V_i in the central and eastern parts of the Laptev Sea during wintertime has been reconstructed. The highest rate of frazil ice formation appeared to be restricted to the near delta regions of the Laptev Sea (especially near the main branches of the Lena River). It ranges from 0.2-1.4 cm/day, if the average rate in UQL (U) equals 2 cm/day, to 3.0-34.0 cm/day at $U=10$ cm/day. In the regions where during wintertime drift ice dominates over fast ice the rate of frazil ice formation is 10-20 times less. The intensity of the possible sediment flow (U_{sd}) towards the lower drift or fast ice surface depending upon frazil ice formation (V_i) has been evaluated. This is the lowermost estimation of U_{sd} since calculations took into consideration only the mechanism of sediment incorporation from water during formation of frazil ice crystals.

The process of sediment "scavenging" during uprise of frazil ice crystals in UQL has been ignored. In the average, U_{sd} value varies from 1.2 mg/m² day at average $U=2$ cm/day in UQL to 30.0 mg/m² day at $U=10$ cm/day.

1. Introduction

Many large rivers fall to the Siberian shelf seas (in particular, the Laptev Sea). They carry a vast amount of fresh water and sediments. In the winter the freshwater runoff is small, being actually absent in some rivers and branches of the Lena River. However, the upper quasi-uniform layer (UQL) in the eastern Laptev Sea in winter remains considerably freshened. Freshening of the winter UQL leads to a higher temperature in this region of the Laptev Sea, than the temperature in the pycnocline and the lower salinity layer. Thus at the UQL/pycnocline boundary the conditions typical of the double-diffusion heat and salt exchange are created and exist during the entire winter period. These conditions contribute to supercooling and subsequent frazil ice formation [5,17]. This effect was described by Nansen [10] who found that part of water desalinated by the river runoff at the contact with underlying saline and cold water would supercool and form frazil ice, especially in the near-mouth sea regions.

The main cause for supercooling of the desalinated by the river runoff water and subsequent frazil ice formation is a more rapid heat sink to the lower cold and saline sea water, as compared with the counter salt flux. The different efficiency of heat and salt exchange is due to the fact that the molecular temperature diffusion coefficient (K_{tm}) exceeds the molecular salt diffusion coefficient (K_{sm}) by two orders ($K_{tm}/K_{sm}=10^2$). This

permits us to call the mechanism for supercooling and frazil ice formation under consideration the double-diffusion [8]. Frazil ice formation in the zone of contact of fresh and salty waters results in the growth of practically freshwater ice crystals. As a result, ice with a chaotic orientation of crystals is formed. Thus interlayers of this ice 2 cm to several meters thick can be identified by structure and texture in the total strata of multiyear drifting and fast ice in the Arctic [7,11,18].

When frazil ice forms, the suspended sedimentary material [14], brought with river water, are trapped. Hence the mechanism of frazil ice formation will play quite a significant role in transport of sediments to the surface of fast and drifting ice but also, probably, in wintertime.

2. Results

Regioning and geographical analysis of the conditions for possible supercooling and subsequent frazil ice formation were based on data of the winter oceanographic expeditions "Sever" and the Tiksi Administration for Hydrometeorology and Environmental Control (TAHEC) from 1960 to 1984. These expeditions were carried out in the Laptev Sea in the winter from December to May.

A combined analysis of the vertical temperature and salinity distribution at all available oceanographic stations for twenty five years has shown the winter vertical thermohaline structure in the central and eastern Laptev Sea to be quite diverse and strongly dependent on the preceding summer hydrological situation. On the basis of this analysis a composite chart was constructed which provides understanding on the diverse winter hydrological situations and their geographical distribution in the sea (Fig. 1). The analysis was performed in terms of probable frazil ice formation.

Of all diverse winter vertical thermohaline profiles, five most typical profiles can be identified on the whole. They are presented in Fig. 1. As is seen, the supercooling at the UQL/seasonal pycnocline boundary and subsequent frazil ice formation are possible in principle, only in two cases (a) and (e) (see Fig. 1). In the other three cases it is impossible, but the reasons are different. In one case - (b) (see Fig. 1), stratification is actually absent. This temperature and salinity distribution is most often observed in the winter at the stations located in the central and western Laptev Sea (Fig. 1). The influence of the freshwater runoff there is either absent or insignificant. Such distribution is also observed in the region of the flaw polynya. The region delineated on the basis of this analysis is situated between the extreme (the northernmost and the southernmost) positions of the fast ice edge (Fig. 1).

Figure 1 (cases -c and -d) present the situations where supercooling and frazil ice formation at the UQL/pycnocline boundary are impossible under winter conditions, as the pycnocline and the lower layer are much warmer than the UQL, although they are more saline. At some stations the warm near-bottom layer is preserved up to the end of the winter season. The presence of a strong seasonal pycnocline which is not destroyed during the entire winter period and in a way "locks" the warm layer contributes to its preservation.

Special attention should be paid to the situation presented in Figure 1 (case -e). It is very common and is observed exceptionally in the most shallow near-delta sea regions (Fig. 1). In these regions the temperature and salinity distribution is such that there are simultaneously the conditions for supercooling and frazil ice formation with the warm layer located near the bottom (see Fig. 1, case -e). The pycnocline occupies the entire water column under fast ice. The heating of the uppermost sub-ice layer and the increase in the pycnocline thickness after the autumn storm and convective (seasonal) UQL increase are probably governed by the subsequent winter river runoff. It leads to the secondary sub-ice desalination after stable fast ice formation creating the secondary pycnocline which merges with the seasonal pycnocline. In addition, one may suggest that the temperature minimum that is frequently observed in the near-delta region (see Fig. 1, case -e) can also be of advective origin. Due to isopycnic motion, water of approximately similar salinity (density) but much more cold from the nearby more shallow region with uniform temperature and salinity conditions from the surface down to the bottom, can penetrate to this level (see Fig. 1, case -b). They are governed by the autumn storm mixing that reaches here the bottom.

The presence of a cold intermediate layer (see Fig. 1, case -e) creates an additional "blocking" effect for heat penetration from the lower warm layer to the ice cover along with the "blocking" effect of salinity (density) stratification. The heat fluxes from the upper and lower layer are directed to the cold layer and are lost due to its heating.

The main conclusions that are based on the analysis of a composite chart of different winter hydrological situations given in Fig. 1 are completely confirmed by the analysis of the spatial distribution of such a

characteristic as $\Delta T_f = T - \tau_s$. It was determined for the seasonal pycnocline and where the pycnocline was weakened or absent - for the lower layer. Here T- the measured water temperature and τ_s - the temperature of water freezing at a given salinity were calculated by standard algorithms.

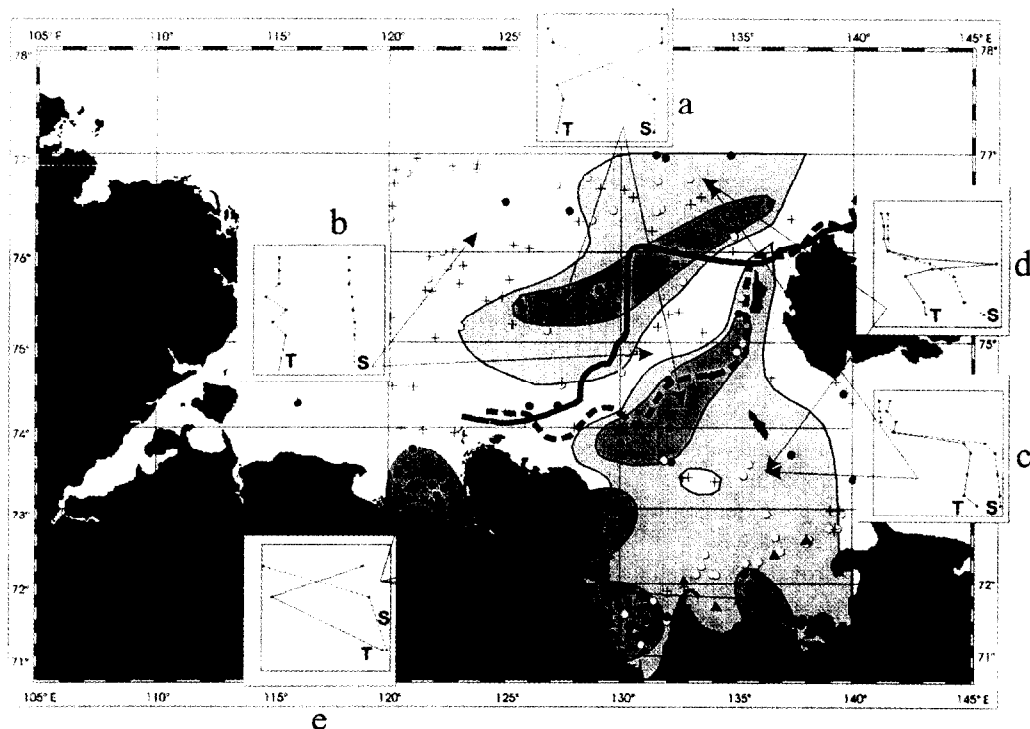


Figure 1. A composite chart of winter hydrological situations in the central and eastern Laptev Sea in terms of analyzing the principal possibility for supercooling and subsequent frazil ice formation at the UQL/seasonal pycnocline boundary. From data of oceanographic stations of the "Sever" expeditions and the Tiksi Administration for Hydrometeorology and Environmental Control for the 1960 to 1984 period. Typical vertical temperature and salinity profiles in the winter in central and eastern Laptev Sea (5 cases - a, b, c, d, e).

- - stations and regions where frazil ice formation is possible;
- ⊕ - stations and regions where frazil ice formation is impossible due to the weak pycnocline and the absence of thermocline;
- - stations and regions where frazil ice formation is impossible due to the presence of the warm seasonal pycnocline and the lower layer;
- ▲ - stations and regions where frazil ice formation is possible due to the presence of the intermediate cold layer insulating the heat transfer from the lower warm layer.

It is of importance that although at the stations with the conditions for supercooling and frazil ice formation the temperature of the pycnocline and the near-bottom layer is below the UQL temperature. It is significantly above the freezing temperature. Thus in the zones with a principal possibility for frazil ice formation, the situation where the pycnocline and the lower layer are close to supercooling or are supercooled has not been observed.

However based on the analysis of ΔT_f distribution there are clear regions where stratification is actually absent - small (close to 0 °C) and negative ΔT_f values. Hence the area of the possible winter existence of the flaw polynya (see Fig. 1, case -b) is well contoured. Due to a rapid surface ice formation there, governing the intensive salt flux to water, even the sufficiently strong salinity (density) stratification is destroyed (see Fig. 1, case -b).

3. Discussion

Dynamic aspect of frazil ice formation

It was found during the studies of contact (double-diffusion) frazil ice formation under the laboratory conditions, that if in the both layers of a two-layer system the external turbulizing impact is absent and the heat and salt exchange through the density interface between fresh and saline waters occurs at the molecular level, the extent of supercooling is not large and not more than several millimeters of frazil ice can form during a day [5,8,9,15]. Obviously, such small rates of ice formation cannot provide the formation of meter layers of frazil ice that were observed in the near-mouth regions of the Arctic Seas [1].

It was found in the laboratory experiments [5,17] that with artificial turbulization of a two-layer system and the increased heat-salt exchange level through the pycnocline the rate of frazil ice formation strongly increases. The study of the rate of frazil ice formation was made by means of "grid" turbulence, since it is best of all parametrized. In these experiments parametrization of dimensionless rate of entrainment U_e/U_* through the pycnocline at turbulent mixing in the layers and interpretation of the experimental results (including the rate of frazil ice formation) was performed by means of the local Richardson number $Ri_* = g(\Delta\rho/\rho)L/U_*^2$. The local Richardson number is an analogue of the global number but with replacement of the external integral scale of mean horizontal velocity by root-mean-square velocity of turbulent fluctuations of U_* near the interface. Also, the thickness of the mixed layer is changed to the integral scale of turbulence L . The latter characterizes the mean scale of the most "energy-containing" eddies near the density interface that result in the pycnocline deformation and govern the process of turbulent entrainment [12,13,16,].

In the winter sea covered by fast or drifting ice the tidal force governs to a great extent the mean motion. The tide in a strongly stratified by density sea (which is the Laptev Sea both in the summer and winter seasons - especially its eastern part) will be probably baroclinic, rather than barotropic. There is partial "slowing" of the pycnocline in the barotropic tidal motion of the entire sea column, as compared to the UQL. Thus although the initial action of the tidal-forming force on the water column is of a barotropic character, the time response in a strongly stratified sea attains a baroclinic character.

Turner [16] considering the geophysical applications of the entrainment process, suggested that entrainment in the upper part of the density interface due to the turbulent motion of the upper layer can be considered as entrainment at the margin of a flat turbulent jet when the balance of momentum and buoyancy between the mixed layers of different density is reached and the entrainment velocity is quasi-stationary. Modern laboratory studies of the exchange process across the density interface when the turbulence at the boundary is created due to the motion of the entire layer on the whole, i.e. with a velocity shear at the interface, confirm this interpretation [4]. This allows us to use the tested in the laboratory experiments theory of turbulent entrainment at the expansion of the flat turbulent jet margin [13] for relating the external mean velocity of the freshened layer U (the scale of the mean flow velocity) and the root-mean-square velocity of turbulent fluctuations of U_* near the pycnocline, if the moving freshened winter UQL is assumed to be the turbulent jet.

When the turbulent flat jet is mixed with the ambient immobile fluid, then the length of the mixing distance corresponding to the integral scale of turbulence L in each cross-section is proportional to the width of jet b in this section:

$$L = \alpha_v \cdot b \quad (1),$$

where α_v - is the entrainment constant whose value varied in different experiments from 0.08 to 0.125 [13,16]. In our case when entrainment at the freshened/sea water boundary is quasi-stationary, the jet width b will present the thickness of the freshened layer (winter UQL thickness) at a specific place Z . Thus:

$$L = \alpha_v \cdot Z \quad (2).$$

The eddy structure of mean motion near the density interface results in turbulent deformations in the upper part of the pycnocline that lead to internal waves. After some time they are destroyed due to Kelvin-Heimholz instability, generating vorticity in the pycnocline itself [4,12,16]. As a result, part of freshened water is entrained to more saline and hence colder water of the pycnocline whereas part of more saline water is entrained to a mean motion of the turbulent winter UQL. In the vorticity area of the pycnocline that governs the thickness of the layer covered by turbulent entrainment [12] there is an active contact of saline and freshened water leading to supercooling of the latter. The thickness of this layer and intensity of supercooling will depend on the characteristic scale of the "energy-containing" eddies moving in the mean flow. In turn, the scale of these eddies will depend on the scale of mean motion velocity (horizontal velocity) in the freshened layer. It follows from the above that the supercooled layer thickness is in fact the integral scale of turbulence L penetrating the pycnocline.

According to Prandtl's [13] theory, for free turbulence at the boundary of entrainment of the parallel turbulent jet either with a stationary fluid or with a fluid whose horizontal motion velocity is smaller, an additional tangential stress is created:

$$\tau = \rho \alpha_v^2 U_{\max}^2 \quad (3),$$

where U_{\max} - is the maximum velocity in a flat turbulent jet. In the case under consideration it is the typical scale of the horizontal velocity ($U_{\max}=U$) in the upper freshened layer (mean motion velocity scale). Based on the semi-empirical turbulence theory [13], the friction or dynamic velocity is equal to :

$$U_* = (\tau/\rho)^{1/2} \quad (4).$$

Thus from (4) and (3) the expression for determining U_* will have the following form:

$$U_* = U_{\max} \alpha_v, \text{ or } U_* = U \alpha_v \quad (5).$$

The expression for the local Richardson number for the pycnocline in the winter under the conditions when the density field is governed by the salinity field ($\Delta\rho/\rho \cong \beta\Delta S$) will have the following form:

$$Ri_* = g \cdot \Delta\rho/\rho \cdot L / U_*^2 = g \cdot \beta \cdot \Delta S \cdot Z / \alpha_v \cdot U^2 \quad (6).$$

Based on this interpretation of entrainment at the upper boundary of the seasonal pycnocline and applying (6), we can use for estimating the frazil ice formation rate at the winter UQL/ pycnocline boundary the expression derived in the laboratory experiments [5]:

$$V_i = B \cdot U_* \cdot \Delta S \cdot Ri_*^{-1/2} \cdot \{(\Delta T/\Delta S - (7 \cdot a/Ri_*))\} \quad (7).$$

Here the coefficient $B=3.3 \cdot 10^{-3} (\text{°C})^{-1}$ [5] at the frazil ice density $\rho_i = 0.1-0.3 \text{ g/cm}^3$ [18]; $\Delta T = T_1 - T_2 > 0$ and $\Delta S = S_2 - S_1 > 0$ are the temperature and salinity differences in the seasonal pycnocline; $a \approx 0.055 [^\circ\text{C} \cdot \text{‰}^{-1}]$ is the linear relation coefficient between the freezing temperature and salinity.

An analysis of the composite chart of distribution of frazil ice formation (see Fig. 2) indicates that with the different dynamic state of the UQL the largest frazil ice formation rate V_i is observed in the near-delta regions. The V_i values here vary from 0.2-1.4 cm/day at $U=2$ cm/s to 3.0-34.0 cm/day at $U=10$ cm/s (see Fig. 2). This is governed by the features of vertical temperature and salinity distribution in these regions (see Fig. 1, case -e) that are primarily connected with the secondary freshening of the winter river runoff (especially directly near the main branches of the Lena) as well as with the advective origin of the cold insulating layer. Its presence governs the principal possibility for frazil ice formation in these regions. With distance from the Lena delta the rate of frazil ice formation sharply decreases.

Estimates of the rate of possible enrichment by suspended in sea water sedimentary material of the lower ice cover surface during frazil ice formation at the winter seasonal pycnocline/the UQL boundary.

Based on the above estimates of the frazil ice formation rate V_i and its spatial distribution (see Fig. 2), as well as on the concentrations of suspended sedimentary material (sediments) C_{sd} in water which forms ice, one can approximately estimate what its amount is transported by frazil ice to the lower fast or drifting ice surface (the suspended matter (sediments) flux value - U_{sd}) in the near-delta and more seaward regions. Such estimates of U_{sd} are quite difficult, since winter observations of the concentrations of suspended sedimentary material in sea water C_{sd} in the Laptev Sea are absent except for the observations in the TRANSDRIFT-IV expedition at the very end of winter (May 1996) during the period of preceding flood [3].

For estimating U_{sd} , let us take into account that the density of frazil ice $\rho_i \approx 0.2 \text{ g/cm}^3$ [18]. However there is another approach for determination of ρ_i . Thus in [17] the density of the frazil ice crystal itself was assumed $\rho_i = 0.92 \text{ g/cm}^3$, i.e. similar to the density of surface ice. But there was introduced a notion of the concentration of frazil ice crystals C_i in the sub-ice layer (under the natural conditions this is the layer under the fast or drifting ice surface) where they gather after surfacing. It was found in these laboratory experiments [17] that in the sub-ice layer in the water-crystalline mixture $C_i \approx 0.2-0.25$.

The physical mechanism of entrapment (incorporation) of suspended matter from water by growing frazil ice crystals has not been well studied especially under the natural conditions. In connection with this, let us consider that during the formation of frazil ice crystals the entire suspended sedimentary material is entrapped. Thus the formula for calculating the sediment flux to the lower ice surface U_{sd} at the rate of frazil ice formation V_i will have the following form:

$$U_{sd} = \rho_i \cdot V_i \cdot C_{sd} \quad (8).$$

If we take into account like in [17] that $\rho_i \approx 0.92 \text{ g/cm}^3$ and $C_i \approx 0.2-0.25$, then (8) will have the following form:

$$U_{sd} = 1.9 \cdot V_i \cdot C_{sd} \quad (9).$$

Here the rate of frazil ice formation V_i is substituted in [cm/day] and the content of sediments in water C_{sd} in [mg/dm³] or which is equal to [mg/l], i.e. in same units in which C_{sd} is usually measured. The dimension of U_{sd} in (9) will be [mg/m²·day].

According to measurements in the TRANSDRIFT-IV expedition, the C_{sd} value in the UQL varied from 1.6 mg/l to 3.4 mg/l [3] and did not have a clear spatial-zonal variability with distance from the Lena delta to the sea, like V_i (see Fig. 2). The mean C_{sd} value in the UQL was about 2.0 mg/l.

Calculations indicate that at the mean flow velocity in the UQL $U = 2$ cm/s, in the near-delta regions due to significantly larger V_i values, the U_{sd} value changes from 0.6 to 3.0 mg/m²·day and in the more seaward region from 0.46 to 1.5 mg/m²·day at mean values of 1.0 mg/m²·day and 1.2 mg/m²·day, respectively in each of the regions. With increasing mean motion velocity in the UQL up to $U = 10$ cm/s, and hence a sharp increase in V_i , in the near-delta region U_{sd} changes from 6.0 to 60.0 mg/m²·day and 23 mg/m²·day, respectively in each of the regions. Thus with increasing mean motion velocity U and increased V_i in the UQL, a pronounced spatial-zonal variability (decrease) of U_{sd} occurs with distance from the delta whereas at small U and V_i it is practically absent (see Fig. 2).

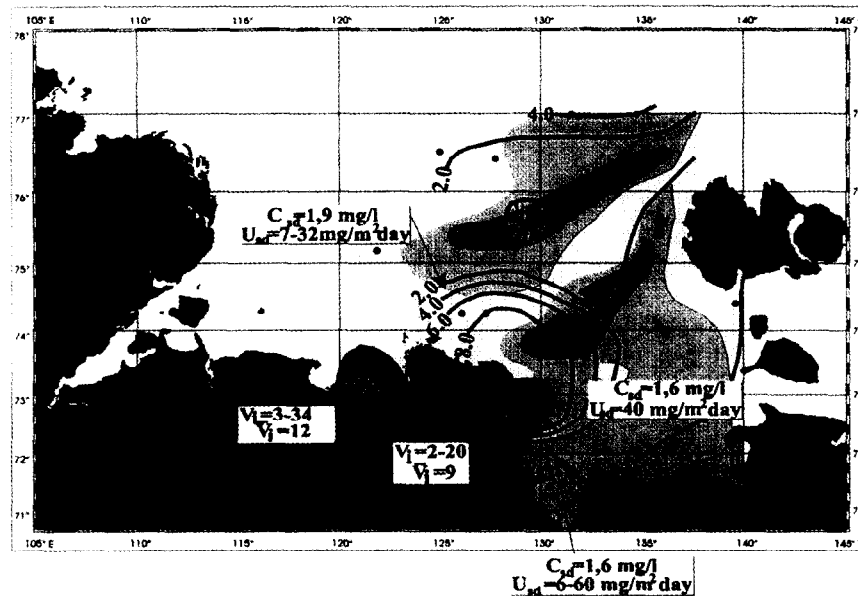


Figure 2. Spatial distribution of possible frazil ice formation intensity V_i [cm/day] at the interface UQL/ seasonal pycnocline in the eastern Laptev Sea in winter. Mean velocity in the UQL is 10cm/sec. Suspension concentrations in the UQL are presented in digital form: C_{sd} [mg/l] in the period before flood (winter hydrological conditions, expedition TRANSDRIFT-IV, 1996) and corresponding suspension fluxes U_{sd} [mg/m²·day] caused by the frazil ice formation V_i [cm/day].

At first glance, the obtained estimates of the U_{sd} value are small. However one should not forget that their determination took into account only the process of incorporation of suspended sedimentary material from sea water to frazil ice crystals directly at the moment of its formation. The process of filtration - "scavenging" of sediments at surfacing of crystals in the UQL to the lower surface of fast ice or drifting ice was not taken into account at all. It was noted in the laboratory experiments for investigating incorporation of sediments to frazil ice and their transfer to the surface [14] that the process of "scavenging" of sediments by frazil ice can be quite efficient at enrichment of surface ice by suspended sedimentary material.

The U_{sd} value can be however even much larger. Thus fine observations of sea water transparency which is in good correlation with the content of suspended matter C_{sd} in it, carried out in September 1989 in the near-delta regions of the Laptev Sea [6] have shown that the C_{sd} value in the pycnocline can 5-15 times exceed C_{sd} in the UQL. Whereas this pattern of vertical C_{sd} distribution in sea water is also observed in the winter, the U_{sd} value obtained above only taking into account their entrapment at frazil ice crystal formation, will be much larger, since these crystals are formed at the UQL/pycnocline boundary.

Acknowledgments. This article was initiated and written during the joint work of Russian and German authors in 1997 in GEOMAR, Kiel University. We are grateful to German Ministry for Science and Technology, who provided this possibility. From the Russian side this work was supported by the Ministry for Science and Technology under the Russian-German project "Laptev Sea System".

References

- [1] R.N. Bulatov, 1963, Some results of studies of ice in the Yenisey Gulf, *Voprosy geografii*, 62, pp.192-197, (in Russian).
- [2] N.V. Cherepanov, 1972, Systematization of crystalline structures of ice in the Arctic, *Problemy Arctiki i Antarktiki*, 40, pp. 78-83, (in Russian).
- [3] P. Golovin, I. Dmitrenko, H. Kassens, and J. Holemann, 1997, The effect of turbulence on the rate of frazil ice formation during the spring flood and its role in upward sediment transport in the Siberian Arctic. *Annales Geophysicae, Part II, Hydrology, Oceans, Atmosphere & Nonlinear Geophysics, Supplement II to Vol. 15*, p.377.
- [4] K. By Kan and N. Tamai, 1994, Direct measurements of the mutual-entrainment velocity at a density interface, in *International symposium on the stratified flows, pre-print 4, Vol. 2, Grenoble, France*.
- [5] A.D. Krylov and A.G. Zatsepin, 1992, Frazil ice formation due to difference in heat and salt exchange across a density interface, *J. Marine Systems*, 3, pp. 497-506.
- [6] R. Letolle, J.M. Martin, A.J. Thomas, V.V. Gordeev, S. Gusarova, and I.S. Sidorov, 1993, ^{18}O abundance and dissolved silicate in the Lena delta and Laptev Sea (Russia), *Marine chemistry*, 43, pp.47-64.
- [7] S. Martin, 1981, Frazil ice in rivers and oceans, *Ann. Rev. Fluid Mech.*, 13, pp. 379-397.
- [8] S. Martin, and P. Kauffman, 1974, The evolution of under ice melt ponds, or double-diffusion at the freezing point, *J. Fluid Mech.*, 64, pp. 507-527.
- [9] T.A. McClimans, C.E. Steen, and G. Kjeldgaard, 1978, Ice formation in fresh water cooled by a more saline underflow, *Proc. IAMR Symp. ice problems, Pt.2*, pp. 331-336.
- [10] F. Nansen, 1956, *The "Fram" in the polar sea*, Gos. izd. geogr. lit-ry, 384 pp., Moscow (in Russian).
- [11] I.G. Petrov, 1971, Experience of regioning the ice cover of the Arctic Seas by structure, *Proc./AARI*, 300, pp. 39-55, Leningrad (in Russian).
- [12] O.M. Phillips, 1980, *The dynamics of the Upper Ocean*, Gidrometeoizdat, 319 pp, Leningrad (in Russian).
- [13] L. Prandtl, 1949, *Hydroaeromechanics*, Izd. Inostrannoy lit-ry, 520 pp, Moscow (in Russian).
- [14] E. Reimnitz, J.R. Clayton, E.W. Kempema, J.R. Payne, and W.S. Weber, 1993, Interaction of rising frazil with suspended particles: tank experiments with applications to nature, *Cold Regions Science and Technology*, 21, pp. 117-135, Amsterdam.
- [15] A. Stigebrandt, 1981, On the rate of ice formation in water cooled by a more saline sublayer, *Tellus*, Vol. 33, N 6, pp. 604-609.
- [16] J.S. Turner, 1977, *Buoyancy effects in fluids*, Izd. Mir, 432 pp, Moscow (in Russian).
- [17] S.I. Voropayev, H.J.S. Fernando, and L.A. Mitchell, 1995, On the rate of frazil ice formation in polar regions in the presence of turbulence, *J. of Physical Oceanography*, Vol. 25, N 6, Part II, pp. 1441-1450.
- [18] W.F. Weeks and S. Ackley, 1982, *The growth, structure and properties of sea ice*, - N.H.: U.S. Cold Region Research and Engineering Lab.; Springfield, Va. available from N.T. I. S., 130 pp, Hanover.

TURBULENT MIXING IN THE OCEAN

M.C. Gregg

Applied Physics Laboratory, University of Washington
1013 N.E. 40th St., Seattle, WA 98015 USA
email: gregg@apl.washington.edu

Abstract

Studies of turbulent mixing are producing realistic estimates of diapycnal diffusivity in many ocean regimes. The major surprise is the low diffusivity found over large areas of the open ocean where internal waves are at their background state. Mixing hot spots, however, have diffusivities many decades larger than in the background areas. The most intense hot spots are found where swift currents flow over rough topography.

Observing and Quantifying Mixing

After using one of the first salinity-temperature-depth (STD) recorders, Stommel and Fedorov [1] concluded that

... The resolution of the current meter is not so fine-scaled as that of the STD and hence we cannot identify micro-variations of the velocity structure that may coincide with similar small scales in the thermal and salinity structure. It would, of course, be extremely interesting to be able to make such comparisons. ...

Their recognition of the need for improved vertical resolution and of the importance of relating scalar and velocity fluctuations foreshadowed much of work done on small-scales during the ensuing 30 years. Charles Cox at the Scripps Institution made the major improvement in instrumentation by developing free-fall profilers. Their uniform and slow descent permits resolution of the vertical gradients of temperature and velocity in much of the open ocean. Length scales containing the variances of these gradients are termed microstructure to distinguish them from the finestructure observed by Stommel and Fedorov. For both fine and microstructure, much of the progress has come from comparing temperature and velocity, as envisioned by Stommel and Fedorov. Now observations have been reported from many places around the globe (Fig. 1) and it is possible to discern patterns in the results. (See [10] for citations of the data.)

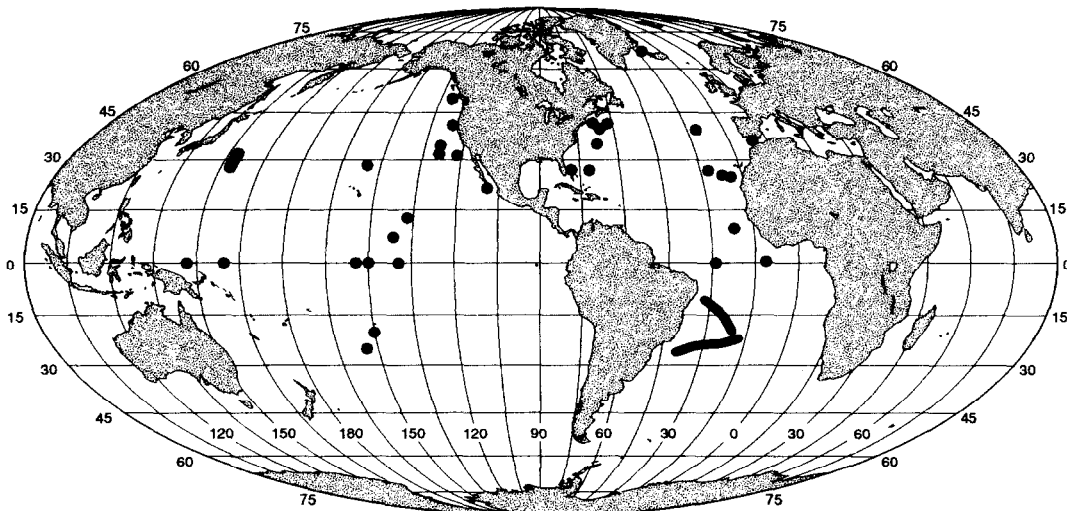


Figure 1: Sites where microstructure has been observed.

The primary measures of microstructure are $\chi_T \equiv 6\kappa_T(\partial T'/\partial x_3)^2$ [$\text{K}^2 \text{s}^{-1}$] and $\epsilon \equiv 7.5\nu(\partial v'/\partial x_3)^2$ [W kg^{-1}], where ν and κ_T are the molecular viscosity and thermal diffusivity. The numerical multipliers account for gradient components not measured and are based on assuming that the microstructure is isotropic. Microstructure produced by moderate-to-strong turbulence in stratified profiles is isotropic [2]. Assuming isotropy appears valid in many cases, but it will produce overestimates when the microstructure is weak.

Although ϵ and χ_T are the primary turbulence parameters, oceanographers are generally more interested in the diapycnal (orthogonal to density surfaces) diffusivities that can be estimated from them. Simplifying the turbulent balance equations for temperature variance and kinetic energy leads to

$$K_T = \frac{\chi_T}{2(\overline{\partial T/\partial x_3})^2} [\text{m}^2 \text{s}^{-1}] \quad , \quad K_\rho = \frac{0.2\epsilon}{N^2} [\text{m}^2 \text{s}^{-1}] \quad (1)$$

[3, 4]. Thus, turbulent diffusivities exceed molecular ones in direct proportion to the ratio of gradient variances to the squares of the mean gradients.

An evaluation of the assumptions leading to K_T concluded applying it to the general circulation remains an ad hoc procedure in view of the present ignorance about $(T')^2$ [5, 6]. Comparison with tracer observations, however, indicates that K_T is an accurate measure of diapycnal diffusivity over intervals of at least a year or more and within its sampling error [7, 8, 9]. Presumably the same is true for K_ρ .

Although K_T and K_ρ observations have sampled a miniscule portion of the ocean, they have been reported from sufficient diverse oceanic regimes to detect patterns. The most basic separation is between mixing in the open ocean, far from topography and strong mesoscale features, and that in mixing hot spots.

The Open Ocean

Figure 2 summarizes diffusivity profiles from the open ocean. Obtained from ships, the averages represent conditions over a few days to a few weeks. They span a 1000-fold variation and are least in the tropical thermocline and greatest in the mid-latitude abyss. To understand the variability it is necessary

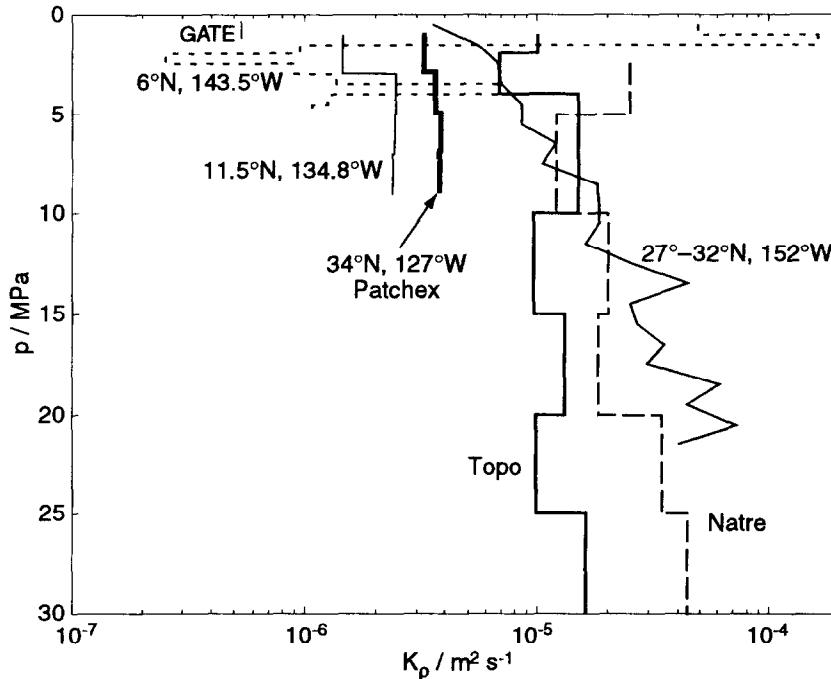


Figure 2: Diapycnal diffusivity determined from microstructure measurements in the open ocean.

to consider the source of the turbulence.

Mixing in the open ocean seems to result mainly from breaking internal waves. Consequently, since the mid-1980s, microstructure has been measured simultaneously with high-resolution velocity profiles in attempts to characterize the internal wave field. The heavy line, labeled Patchex, in Figure 2 shows the level of mixing when internal waves are at their background level, as parameterized by Garrett and Munk [11]. Variations about this level, i.e. about $K_p = 3 \times 10^{-6} \text{ m}^2 \text{ s}^{-1}$, occur when internal waves have different finescale shear variances or shear-to-strain ratios than those in the Garrett and Munk spectrum. Detailed comparisons demonstrate that the variability in ϵ and K_p can be predicted within a factor of 2 from the internal wave measurements [12, 8] in a manner that is consistent with theoretical predictions [13] based on the Garrett and Munk model. The problem of mixing in the open ocean, is therefore primarily one of understanding the patterns and variability of the internal wave field.

Figure 3 summarizes the present first-order understanding of mixing in the open ocean. Three types of observations - observations of microstructure, internal wave shear, and tracer thickening - agree with numerical calculations of the rate at which energy moves through the internal wave spectrum as a result of interactions among the waves. Lacking major surprises, obtaining a more comprehensive description of mixing in the open ocean requires determining where and how internal waves differ from their background state.

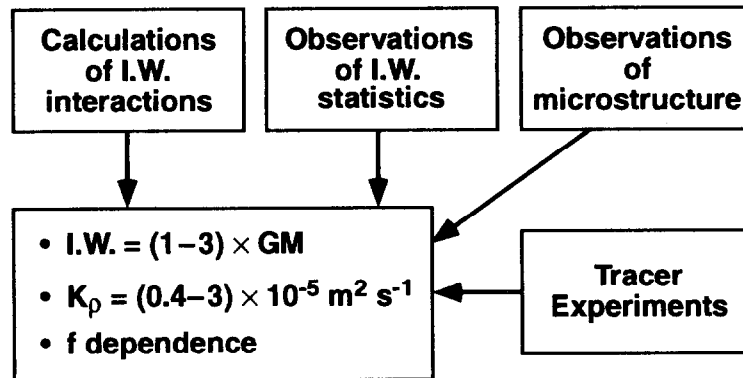


Figure 3: Summary of mixing and internal waves at the open ocean sites away from topography, fronts, and strong mesoscale features.

Mixing Hot Spots

Sites close to topography and fronts should potentially be mixing more vigorously than those in the open ocean, owing to the effect of mean shear adding to that of internal waves which should be at least as intense as those in the background. This is partially borne out in Figure 4 which displays an even wider range of diffusivities, 10,000-fold, than found in the open ocean. Many presumed hotspots, however, have K_p no larger than found in the more energetic open sites. Some warm-core rings and the Florida Strait are in this category because the finescale shears producing mixing are only moderately above the background internal wave levels. Moderate hot spots have levels of $(1-3) \times 10^{-4} \text{ m}^2 \text{ s}^{-1}$.

The places with intense mixing, Monterey Canyon and the Denmark and Gibraltar Straits, have fast currents flowing over rough topography and consequently cannot be put in the framework of open ocean internal waves. These are the true mixing hot spots, and more recent work is finding others, particularly where tidal currents flow across sharp bottom relief. A search for parameterizations of hot spots is underway, but is likely to be considerably more difficult than it is for the open ocean. Nor is there any understanding of the global significance of intense mixing in relatively small hot spots.

Discussion

The turbulent diffusivity produced by background internal waves, $K_p = 3 \times 10^{-6} \text{ m}^2 \text{ s}^{-1}$, is much

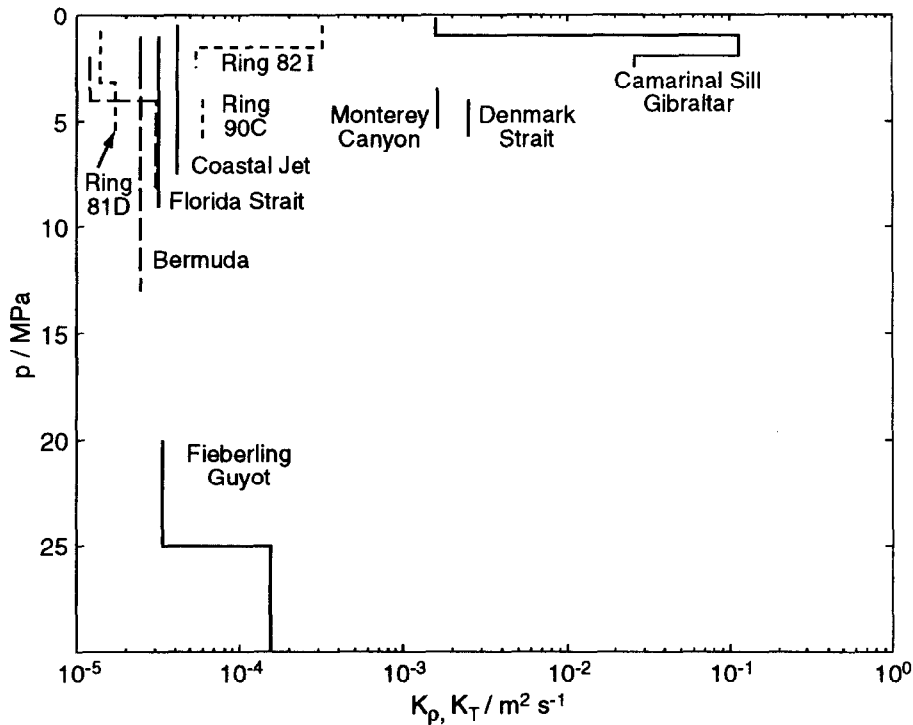


Figure 4: Diapycnal diffusivities near topography and in fronts and mesoscale features, not including the equatorial undercurrent.

lower than the $10^{-4} \text{ m}^2 \text{ s}^{-1}$ used for numerical stability in many models of the large-scale circulation. Because internal waves appear to be at background over large portions of the open ocean, numerical models having $K_\rho = 10^{-4} \text{ m}^2 \text{ s}^{-1}$ cannot be considered realistic. At present, however, observations are much too limited for forming realistic estimates across ocean basins.

To define mixing over the scales needed for large-scale models, turbulence studies are entering a new phase. Because K_ρ and K_T in the open ocean can be related to internal wave levels, the problem of developing basin-wide diapycnal diffusivities is one of describing and probably also understanding the basin-wide internal wave field. The most optimistic situation is that internal waves have a relatively weak seasonal variability and can be described as functions of location and depth. This would avoid the need to model the global internal wave field as a component of large-scale models. If this is not the case, the dynamics of the internal wave field must be understood well enough to support accurate predictions of diapycnal diffusivity in models of long-term climate fluctuations. Also, we do not yet understand the role of mixing hot spots, which occur primarily at oceanic boundaries, on the general circulation. If globally important mixing does occur on the boundaries and the mixed water is advected into the interior, hot spots must be included in the mixing developed for large-scale models.

References

- [1] H. Stommel and K. N. Fedorov. Small scale structure in temperature and salinity near Timor and Mindanao. *Tellus*, 19:306–325, 1967.
- [2] A. E. Gargett, T. R. Osborn, and P. W. Nasmyth. Local isotropy and the decay of turbulence in a stratified fluid. *J. Fluid Mech.*, 144:231–280, 1984.
- [3] T. R. Osborn and C. S. Cox. Oceanic fine structure. *Geophys. Fluid Dyn.*, 3:321–345, 1972.

- [4] T. R. Osborn. Estimates of the local rate of vertical diffusion from dissipation measurements. *J. Phys. Oceanogr.*, 10:83–89, 1980.
- [5] R.E. Davis. Diapycnal mixing in the ocean: Equations for large-scale budgets. *J. Phys. Oceanogr.*, 24:777–800, 1994.
- [6] R.E. Davis. Diapycnal mixing in the ocean: The Osborn-Cox model. *J. Phys. Oceanogr.*, 24:2560–2576, 1994.
- [7] J. R. Ledwell, A. J. Watson, and C. S. Law. Evidence for slow mixing across the pycnocline from an open-ocean tracer-release experiment. *Nature*, 364:701–703, 1993.
- [8] K. Polzin, J. M. Toole, and R. W. Schmitt. Finescale parameterization of turbulent dissipation. *J. Phys. Oceanogr.*, 25:306–328, 1995.
- [9] J. T. Sherman and R. E. Davis. Observations of temperature microstructure in NATRE. *J. Phys. Oceanogr.*, 25:1913–1929, 1995.
- [10] M. C. Gregg. Estimation and geography of diapycnal mixing in the stratified ocean. In J. Imberger, editor, *Proceedings of the IUTAM Conference on Physical Limnology, Broome, Australia, 10–14 Sept., 1995*, page in press. American Geophysical Union, 1999.
- [11] C. J. R. Garrett and W. H. Munk. Space-time scales of internal waves: A progress report. *J. Geophys. Res.*, 80:291–297, 1975.
- [12] M.C. Gregg. Scaling turbulent dissipation in the thermocline. *J. Geophys. Res.*, 94:9686–9698, 1989.
- [13] F. S. Henyey, J. Wright, and S. M. Flatté. Energy and action flow through the internal wave field. *J. Geophys. Res.*, 91:8487–8495, 1986.

COUPLED 3D EDDY-RESOLVING GENERAL CIRCULATION MODEL AND ECOSYSTEM MODEL APPLIED TO THE BLACK SEA. FIRST RESULTS.

M. Gregoire^{1,2}, J.M. Beckers¹, J.C.J. Nihoul¹ and E. Stanev³

1. GeoHydrodynamics and Environment Research Laboratory (GHER), University of Liège, B5 Sart-Tilman, 4000 Liège, Belgium. Tél : 32 4 3663354, fax : 32 4 3662355. e-mail : mgregoire@ulg.ac.be.

2. Research Assistant National Fund for Scientific Research, Belgium.

3. Dept. of Meteorology and Geophysics, 5 J. Bourchier Str., 1126 Sofia, Bulgaria. Fax : 359 2 9625276, e-mail : stanev@phys.uni-sofia.bg.

Abstract. A basin scale study of the general circulation and the associated synoptic and mesoscale structures, their variability and their effect on the primary and secondary productions space-time patterns is made with the GHER 3D ecohydrodynamic model. An eddy resolving model with a 5 km horizontal resolution and with 25 vertical levels is used to compute the typical seasonal cycle by forcing the model with climatological monthly mean fields of temperature, salinity and wind stress at the air sea interface. Furthermore, the corresponding river discharges of the Danube, Dnestr and Dnepr are taken into account. A simple ecosystem model at basin scale is defined by a nitrogen cycle which is described by 5 state variables i.e. NO_3^- , NH_4^+ , Phytoplankton, Zooplankton and Detritus. The ecosystem model is imbedded on-line into a 3D hydrodynamical model with a superimposed cycle for the light intensity. The results of the model are compared with CZCS data of surface chlorophyll fields. In this paper, the ecosystem model is briefly described and the results are analysed emphasising the effects of the physical processes on the ecodynamics.

Introduction

The Black Sea is almost an enclosed sea with restricted exchanges with the Mediterranean Sea through the Bosphorus strait. The intrusion of the saline Mediterranean waters into the Black Sea creates a strong permanent pycnocline (halocline) which prevents deep ventilation in the basin interior. Thus, the vertical circulation is extremely weak that leads to anoxia in more than 87 % of its volume. Observations show that toxic hydrogen sulphide is generated below depths of 100-150m inhibiting the penetration of all higher animals and leading to the loss of valuable living marine resources.

Besides, eutrophication and other types of ecosystem degradation have led to reduced biodiversity and imbalanced ecosystems in the Black Sea. These problems are particularly dramatic on the northwestern shelf receiving runoffs

profiles (nitrate and ammonium) are computed as a function of the density rather than depth so as to exclude variability resulting from dynamical effects, the influence of the Danube's plume is also taken into account. For the other ecosystem state variables, initial constant values are used considering for detritus the river influence.

Discussion

The physical model is integrated until a steady state solution is reached and then the ecosystem model is initialised. The integration of the later is carried out for one year to reproduce a complete seasonal cycle.

Due to the river discharges on the northwestern shelf, shelf waters are less saline than open sea waters and a sharp haline front forms close to the coast reducing strongly the exchanges between shelf waters rich in nutrients and open sea waters. In spring, this fresh water front amplifies due to increased river runoffs and anticyclonic current on the shelf tend to retain large amount of fresh water close to the coast. Figure 2 shows the sea surface salinity distribution in May simulated by the model emphasizing the performance of the model in resolving meanders and mesoscale eddies caused by frontal instabilities. The materials originating from northwestern shelf rivers are transported towards the Anatolian coast by the boundary current flowing along the continental slope topography. In summer, unstable motions are initiated along the Anatolian coast by interactions of the boundary current with the coastline geometry and with the sharp topographic variations in the along-shore direction. These unstable motions serve as the main mixing agent between coastal and interior regions and have an important influence on the spreading of the productivity.

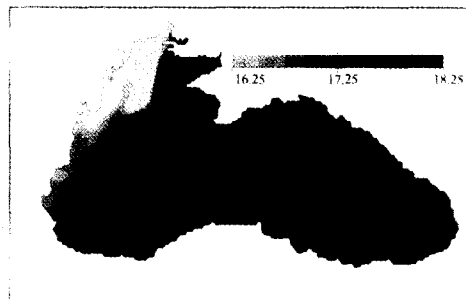


Figure 2 : Salinity distribution at 10 m at the end of May. A strong haline front forms close to the coast preventing the exchanges between coastal waters and open sea waters.

In winter, the simulated mixed layer depth distribution shows important horizontal variations. For instance, on the northwestern shelf, the intrusion of the river fresh water towards the open sea results in a strong vertical stratification of the water column in the Danube's plume area. The upper margin of the main pycnocline (halocline) moves to the sea surface, thus strongly limiting the depth of penetration of surface signal caused by strong winter convective mixing. This shallow mixed layer is easily enriched with nutrients, creating in the same time optimal conditions for the phytoplankton growth. On the rest of the shelf, to the south and to the east of the river plume however the cooling and the extreme convective mixing penetrate to the bottom and thus the water column is not strongly stratified.

So, on the shelf, the results show a winter bloom occurring in the region of the river plume. This bloom must be made

of arctic species which are able to grow under the very low temperatures occurring on the shelf in winter. This bloom is then advected along the western coast and the Anatolian coast by the boundary current. It has been reported that a massive explosion of plankton mainly chaetoceros sp., occurred during February 1990 along the west southern coast. However, following Sur et al. [9], it is not clear whether this high abundance of phytoplankton species was linked with the transport of plankton from the northwestern shelf, local production resulting from nutrients either supplied via the ribbon of cold northwestern shelf waters, or entrained from the deep waters. At the end of spring, the results show that the bloom extends on the whole shelf reaching the eastern coast of the northwestern shelf with cross-shelf exchanges along the shelf break (figure 3). This strong bloom can also be observed on the satellite picture showing the chlorophyll concentration on the 17 th of July 1980 (figure 4). Some patches of high phytoplankton concentrations can also be observed along the Anatolian coast on these two figures.

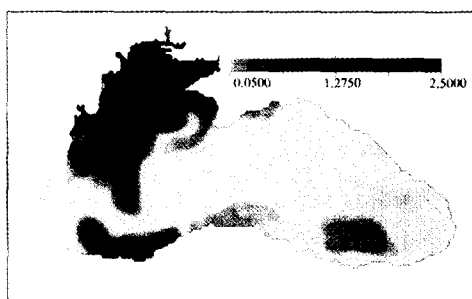


Figure 3 : Sea surface phytoplankton distribution at the end of July (in $\mu\text{atgN/l}$). The bloom extends on the whole shelf with cross shelf exchanges along the shelf break.

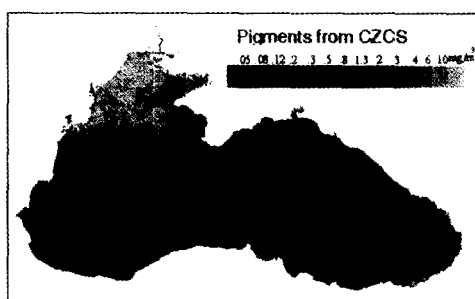


Figure 4 : CZCS estimate of the sea surface chlorophyll field for the 17 th of July (in mgm^{-3})

In the central part of the sea where the strong permanent upwelling brings to the sea surface cold nutrients rich waters, the results show an end-fall winter bloom which begins in November, continues in February and then is combined with the spring bloom to develop a single relatively long bloom season for the entire winter. In April, this bloom decreases progressively as nutrients are exhausted and the grazing pressure increases. In summer, the bloom occurs in the layer between the thermocline and the base of the euphotic zone. The chlorophyll-a and primary productivity data obtained by Vedernikov and Demidov [10] show during some years the same winter bloom structure, but these data reveal the presence of a year to year variability in the productivity pattern which seems strongly dependent on the regional oceanographic conditions occurring during December and February [8]. A winter bloom, occurring in the central Black Sea, has also been observed by A. Mikaelyan [11] and has been identified as made of the diatoms *Nitzschia Delicatula*.

CONCLUSIONS

In this paper, one showed how a hydrodynamical eddy resolving model was implemented and extended to include an ecosystem model. The results show the spatial structuring of the phytoplankton field by the hydrodynamics constraints (horizontal and vertical advection, upwellings, mesoscale instabilities, ...). The results of this coupled model show a rather good agreement with the satellite data.

Obviously, a lot of problems still remain open and give motivation for further improving the model version used here. Some of them are :

1. The initialisation and calibration of the ecosystem model have to be further improved
2. The model is too simple and for instance, it does not take into account the possibility of development of some species, for instance the gelatinous ones due to eutrophication.
3. In the open sea, all the oxidation-reduction processes occurring in the transitional layer between oxic and anoxic waters are not taken into account. However, they can affect strongly the nutrient content of the pelagic waters in the region of cyclonic gyres where the transitional layer moves to the sea surface.
4. The benthic processes are oversimplified in the present model.

One of our future aim is the implementation of a nested model in the Black Sea. The Black Sea domain would be divided in subdomains according to the complexity of the local ecohydrodynamics. For instance, on the northwestern shelf, the eutrophication process has led to dramatic alterations in the ecosystem structure by, for instance, favouring the entry of gelatinous species. Hopefully, these dramatic changes are less severe in the central Black Sea because of its isolation from coastal and shelf waters by the boundary current frontal zone. So, this frontal interface separates different plankton populations adapted to different salinity and nutrients conditions. For instance, it has been reported [9] that in summer, populations rich in chlorophyll-a are present near the fresh water sources while on the other side of the front coccolithophore species are found. Thus, in the future, it seems to be necessary to implement further two different ecosystem model structures : one for shelf waters which are influenced by the river discharges and another one for open sea waters, which are more or less isolated from the coastal eutrophication. These two models will have to be connected at the common boundaries (defined approximately by the frontal interface) setting the problem of coupling a complex ecosystem model with a simplified model by aggregation of the state variables.

References

- [1] Nihoul, J.C.J. and Djenidi, S. (1987) Perspective in three-dimensional modelling of the marine system. In : Three-dimensional Models of Marine and Estuarine Dynamics. J.C.J. Nihoul and B.M. Jamart (ed.), Elsevier Oceanogr. Ser., 45, pp 1-34.
- [2] Nihoul, J.C.J. and Beckers, J.M. (1989) Preliminary results of a three-dimensional model of the Western Mediterranean's general circulation. In : Research in the North Western Mediterranean. H. Barth (ed.), Commission of the European Communities, Brussels, pp 7-26.
- [3] Beckers, J.M. (1991) Application of a 3D model to the Western Mediterranean. *Journal of Marine Systems* 1 : 315-332.
- [4] Grégoire, M., Beckers, J.M., Nihoul, J.C.J. and Stanev, E. (1997) Coupled Hydrodynamic Ecosystem model of the Black Sea at basin scale. First results. In : Sensitivity to change : Black Sea, Baltic Sea and North Sea. E. Ozsoy and A. Mikaelyan (eds.), NATO ASI Series, Kluwer Academic Publishers, vol. 27, pp 487-499.
- [5] Globec (1995) Report of Working Group 1, "Critical variables and dominant scales", Globec Numerical

Modelling Group Meeting, Nantes, July 17-20, 1995.

- [6] Billen, G. and Lancelot, C. (1988) Modelling Benthic Nitrogen Cycling in Temperate Coastal Ecosystems. In : Nitrogen Cycling in Coastal Marine Environments. T.H. Blackburn and J. Sorensen (eds.) Published by J. Wiley & Sons Ltd, pp 341: -378.
- [7] Andersen, V. and Rassoulzadegan, F. (1991) Modèle vertical de l'écosystème pélagique marin. Réseau microbien et sédimentation de particules biogéniques. J. Rech. Oceanogr. vol. 16, 1, pp 16-22
- [8] Oguz, T., Malanotte-Rizzoli, P. and Ducklow, H. (1997) Towards coupling three dimensional eddy resolving general circulation and biochemical models in the Black Sea. In : Sensitivity to change : Black Sea, Baltic Sea and North Sea. E. Ozsoy and A. Mikaelyan (eds.), NATO ASI Series, Kluwer Academic Publishers, vol. 27, pp 469-485.
- [9] Sur, H., Ozsoy, E. and Unluata, U., 1994 Boundary current instabilities, shelf mixing and eutrophication processes in the Black Sea. Progress in Oceanography 33 : 249-302.
- [10] Vedernikov, V.I. and Demidov, A.B. (1993) Primary production and chlorophyll in the deep regions of the Black Sea. Oceanology, 33 : 193-199.
- [11] Mikaelyan, A.S. (1995) Winter bloom of the diatom *Nitzschia delicatula* in the open waters of the Black Sea. Marine Ecology Progress Series, 129 : 241-251.

ON THE EVOLUTION OF A PRESSURE FIELD UNDER A SEPARATION OF A BOTTOM GRAVITY CURRENT FROM BOTTOM SLOPE

V.A. Gritsenko ¹, A.A. Yurova ²

¹ Atlantic Branch of P.P. Shirshov Institute of Oceanology, RAS, pr. Mira, 1, Kaliningrad, 236000, Russia

² The State Technical University of Kaliningrad, Sovetskiy pr., 1, Kaliningrad, 236000, Russia

Model calculations were able to reproduce the effect that upon reaching the halocline a separation occurs (three main phases were distinguished) between the bottom gravity current and the inclined, along with its transformation into an intrusive flow. Pressure field, which was calculated by the author, shows clearly the structure of pressure field in the surroundings of a separation point. The given example illustrates that the numerical model is able to study behavior of stratified currents in areas with complex bottom topography.

1. Problem.

Intrusive currents are noted for wide spread occurrence in the ocean as it follows from a number of papers [1,6,16,17]. K. Fedorov and H. Stommel has registered a current, which is considered to be a classical one for the case, in the Timor Sea [16]. On the other hand, there is the confusing fact that the main phases of origination of such currents still remain to be non-clarified. Indeed, experimental, analytical and model research of the process for the case of unstable, intermittent non-homogeneous in density water masses, moving over steep slope, present a problem. All these parameters take place in currents born by the inrush of the North Sea waters into the Baltic Sea [9]. The aim of the given work is application of numerical modeling to determine main phases of separation from surface of bottom gravity current and its successive transformation into intrusive flow [2,3], as well as study of current structure in the separation point.

2. Model.

Bottom gravity current is noted for stable distribution over flat bottom [15,17], as well as for nearly isotropic fluctuations inside the water masses. Strong stratification and intermittent motions within the near-bottom current prevent from application of model of turbulence which use transfer equations for tangential strains [4,8]. That's why effective viscosity [2,3] was used in numerical model to consider the turbulence. This made us possible to tune the model in a way to consider difference of fluctuation intensity between interior and exterior areas of near-bottom currents, including the final stage of those in the form of intrusive currents. Let us take additional assumption that the flow is homogeneous horizontally normally to direction of movement as it usually takes place in areas of occurrence of stable near-bottom currents [9,15-17]. Then, the model the set of equations will be as follows:

$$\frac{\partial \omega}{\partial t} + \mathbf{u} \frac{\partial \omega}{\partial \mathbf{x}} + \mathbf{w} \frac{\partial \omega}{\partial \mathbf{z}} = \frac{\mathbf{g}}{\rho_0} \frac{\partial \sigma}{\partial \mathbf{x}} + \nu_T \Delta \omega, \quad (1)$$

$$\frac{\partial \sigma}{\partial t} + \mathbf{u} \frac{\partial \sigma}{\partial \mathbf{x}} + \mathbf{w} \frac{\partial \sigma}{\partial \mathbf{z}} = \mathbf{D}_T \Delta \sigma, \quad (2)$$

$$\Delta\psi = \omega, \quad (3)$$

where u and w - components of velocity along the x and z axis, respectively; g = gravity acceleration; ρ_0 - characteristic density of fluid; $\sigma = \rho - \rho_0$ density variation; ρ density of fluid; t - time; $\omega = \partial\mathbf{u}/\partial z - \partial\mathbf{w}/\partial x$ vorticity; ψ stream function; $\mathbf{u} = \psi'_z$, $\mathbf{w} = -\psi'_x$; $\nu_T = \nu_0 + \nu_{ef}$, $\mathbf{D}_T = \mathbf{Sc} \cdot \nu_T$ - coefficients of turbulent viscosity and diffusion; \mathbf{Sc} - Schmidt number; ν_{ef} coefficient of efficient turbulent viscosity; ν_0 coefficient of molecular viscosity; $\Delta \equiv \partial^2/\partial x^2 + \partial^2/\partial z^2$; the x -axis is horizontal; the z -axis is directed vertically upward, originating from the level of maximum depth of the model space.

Because of small vertical scales of bottom gravity currents in the Baltic Sea [9] and ocean [15-17] the assumption of viscous attachment to the bottom seems to be quite natural. Nevertheless, the problem is not so evident in the case of transition from continuous equations to a discrete model [2].

Indeed, structure of viscous boundary layer might be resolved only when its thickness is larger than the model's spatial quantization - ΔY . Starting from the available estimates of thickness of a displacement layer [14] and coming then to dimensionless parameters by means of characteristic scales of current velocity (U_∞) and length (L_0) we obtain that: $\Delta y < 1/\sqrt{Re}$, where $\Delta y = \Delta Y/L_0$, $Re = U_\infty L_0/\nu_0$. It is easily to show that in non-stationary problems the physical requirement formulated above transforms into more strong inequality:

$$\Delta y < 3 / Re. \quad (4)$$

In any case, assumption of viscous attachment in discrete model requires $\Delta x = \Delta y \sim 1/Re$. Otherwise, this condition couldn't be assumed for the solid wall. In this case tangential viscous interactions convert to the category of sub-grid motions and require parameterization [2,3]. In practice, this inequality gives finite viscous scale for finite-difference models, which is similar to the Nyquist frequency for viscous processes..

Considering the above mentioned limit (4) we changed the viscous attachment on the tilted bottom for condition of slippage and non-passage of fluid [2,3]. This made us possible to escape from analysis of viscous boundary layer and focus on the process of penetration of one water mass into another.

Velocity and current density at the inlet into the model space were assumed to be as follows: $\mathbf{u} = \mathbf{u}(0, \mathbf{z}, t)$, $\sigma = \rho(0, \mathbf{z}, t) - \rho_0$, $\forall \mathbf{z} \in [\mathbf{z}_0, \mathbf{z}_1], \forall t \geq 0$. Boundary conditions at the outlet from the model space were given following [13]. In particular, normal derivatives of velocity and density, i.e. commonly used boundary conditions, was assumed to be equal to zero. In the course of modeling the "soft" requirements for horizontal velocity and fluid density were also used [13]. To build up discrete model equations [2,3], an algorithm of discrete directed differences has been used [13]. Solution of the Poisson equation in order to find the stream function ψ was carried out by iterative methods. All computations have been done for the grid with dimensionality of 201x111.

In order to derive the necessary boundary conditions on the bottom slope we rotate the coordinate system until it is coincident with the bottom line, causing (U), which is the component of flow velocity, to become tangential to the bottom. The new coordinate system also provides for easy built up of one-dimensional transport equation. The numerical realization of this approach has the simplest solution if the system is rotated by an angle $\pm \pi/4$. In this case, equations of the model variables, including vorticity and stream functions, remained the same. while discrete grid for a new problem coincides completely with old knots of the regular grid ($\Delta x = \Delta z = \text{const}$). For computation of velocity (U) along slope component we used triplet formula providing for difference approximation with an accuracy of the second order. In particular, for the taken angle of bottom inclination of 45° it was as follows:

$$U_{i,j} = \frac{4\Psi_{i+1,j+1} - 3\Psi_{i,j} - \Psi_{i+2,j+2}}{2\sqrt{2}\Delta z}, \quad (5)$$

where i, j - number of boundary knot, and $(i+1, j+1)$, $(i+2, j+2)$ - two knots nearest to boundary by normal.

3. Computation.

The model built up has been used for a series of numerical experiments. Fig. 1 show a separation of head part of the bottom gravity current from the tilted bottom. Characteristic scales of the bottom gravity current were chosen according to the available data about such currents in the Baltic sea: $H = 10$ m, $U = 10$ cm/s, $\Delta\rho_0 = 0,0001$ g/cm³ [9]. Density of water mass was taken to be equal to $(\rho_0 + \Delta\rho_0)$, near-bottom layer – $(\rho_0 + 2 \cdot \Delta\rho_0)$, Froud number - $Fr = \rho_0 u_0^2 / \Delta\rho_0 g h_0 = 0.81$. Model calculations were able to reproduce the effect that a separation occurs between the bottom gravity current and the inclined bottom, along with its transformation into an intrusive flow. Buoyancy forces prevented penetration of the bottom current into the heavier part of the near-bottom layer. Disturbance of isopycnals is large enough and results seemingly from the large angle of bottom inclination. Let us note that the picture of collapse of original uprush, arisen due to a collision between the nose of the current and heavier near-bottom water, has been obtained. It should be stated that compared to the collapse of wave on the free surface [6,12], resolution of fluid motion inside the uprush is much easier case, because all estimated points belong to the interior area of the flow. Following H. Lacombe [6], the picture observed might be classified as a plunging break.

Fig. 2 (left column) shows a sequence of phases of bottom current under the laboratory scales ($Fr=3,1$). Firstly, it should be stated that the distribution of the head part of the bottom gravity current compares qualitatively quite well with the laboratory and field observations [5-7,10,17]. Shape of the nose of the near-bottom current is also modeled satisfactory, for exception of the top of the front, which is normally found just above bottom. Evidently, that this effect results from assumption of the fluid slippage on the bottom line. Note that compared to the first current (Fig. 1) the second one is more smoothed.

For analysis of structure of the current in the vicinities of a separation point we calculated the pressure field by means of the following relationships [13]:

$$\frac{1}{\rho_0} \Delta P = -2 \left(\frac{\partial u}{\partial z} \frac{\partial w}{\partial x} - \frac{\partial u}{\partial x} \frac{\partial w}{\partial z} \right) - \frac{g}{\rho_0} \frac{\partial \rho}{\partial z}. \quad (6)$$

Computation of initial pressure P for iteration algorithm has been carried out proceeding from the principles of hydrostatics.

Fig. 2 (right column) represent computed distribution of pressure in the model space. When analyzing the plots obtained it should be noted that the pycnocline actively responds to spreading of the near-bottom current well before direct contact between water masses and the near-bottom layer. Having being characterized by a high velocity of the distribution of a disturbances the pressure serves as a link chain for the above mentioned interaction (however weak, because there is no contact between water masses).

Even at the first phase (Fig. 2-a) the non-coincidence of isobaric and isopycnal lines is clearly seen. The inflowing water mass doesn't get in contact with the near-bottom layer yet, but an interaction between those, represented in the form of adjustment of the density field to the available pressure field, has already started. This effect isn't traditionally used for analysis of the corresponding field observations in the areas of run-off/breaking away of the near-bottom current, but this is the effect which may be responsible for generation of internal waves, e.g. in the central Baltic's'.

During the second phase the bottom gravity current touches the near-bottom (more dense) layer. At the time the appearance of the second local maxim of pressure takes place, as it clearly seen in Fig. 2-b. Final establishment of the maxim is associated with the separation of the bottom gravity current from the bottom.

Distribution of the pressure during the third phase, as it shown in Fig. 2-c, illustrates the separation of bottom gravity current from the bottom due to occurrence of counter gradient of pressure resulted from the second maxim of pressure, situated lower and to the right of the first maxim. It is noteworthy that the behavior of the more light water (compared to the water of bottom layer) is characterized by well distinguished phase sequence. Shape of the nosal part of an intrusion depends on the density drop in water masses above and below the transition layer (halocline). The available distributions show give clear indications that the structure of a flow, or more precisely its topology, depends completely on the character of distribution of the pressure field.

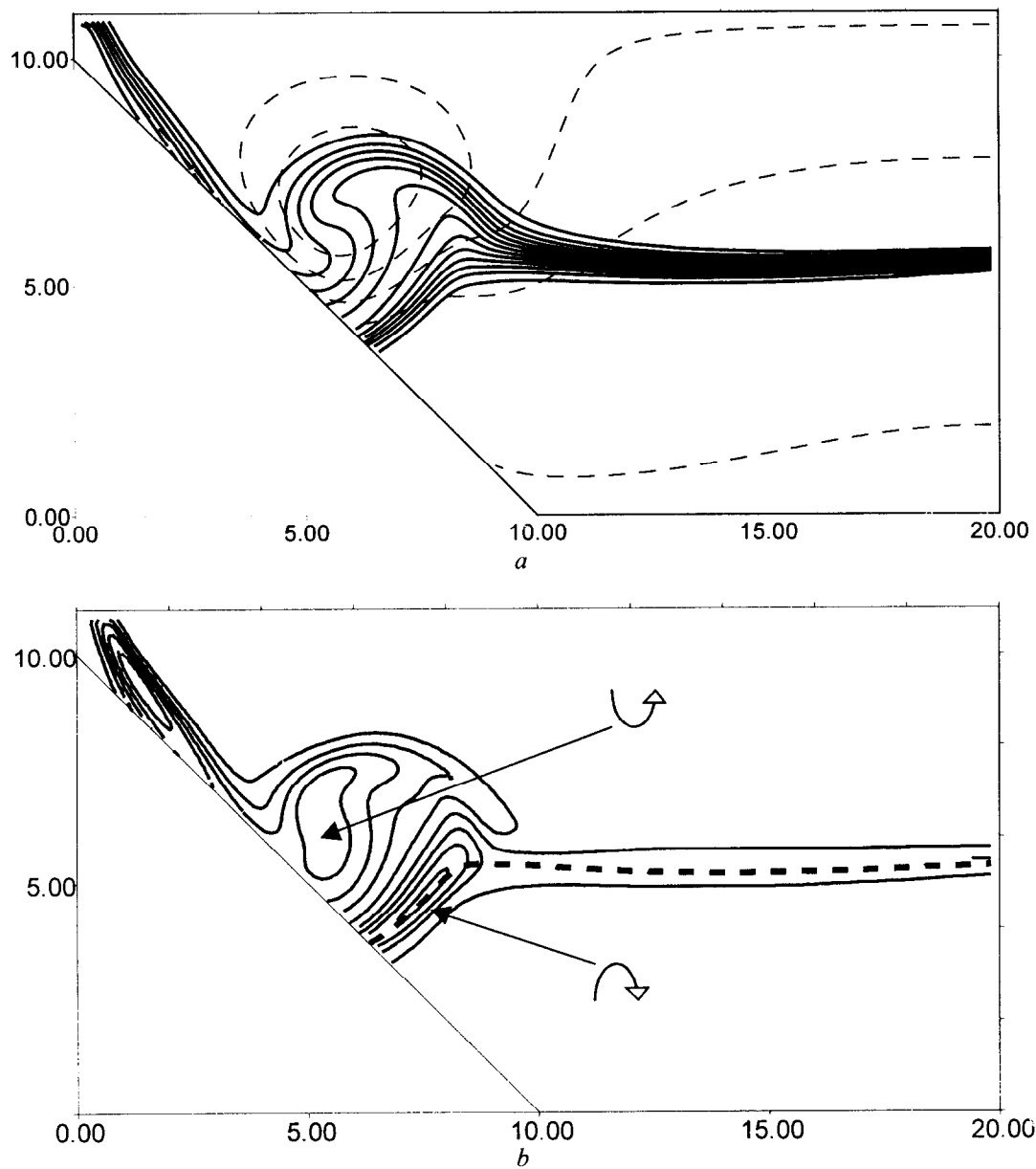


Fig. 1. Computational data on the separation of the bottom gravity current from the bottom slope:

- distribution of density isolines $\sigma = (\rho - \rho_0) / \Delta\rho_0$ (represented as solid lines, range of meanings from 0.1 to 1.9 with spacing of 0.15) and stream function ψ (dashed line, meanings 0.1, 1.0, 1.9, 2.7, 3.6). Characteristic scales were as follows: $h_0 = 10$ m, $u_0 = 10$ cm/s, $\rho_0 = 0.0005$ g/cm³ [9], density of water mass $\rho_0 + \Delta\rho_0$, density of near-bottom layer $\rho_0 + 2.0 \cdot \Delta\rho_0$, $\nu_{Ef} = 3$ cm²/s, α - angle of bottom inclination = 45° ;

- field of vorticity ω (solid lines, meanings from -3.5 to 2.0 with spacing of 0.6); dashed line corresponds to isopycnal line $\sigma = 1.6$. Arrows indicate the direction of rotation. Size of the model space equals to 210x110 m.

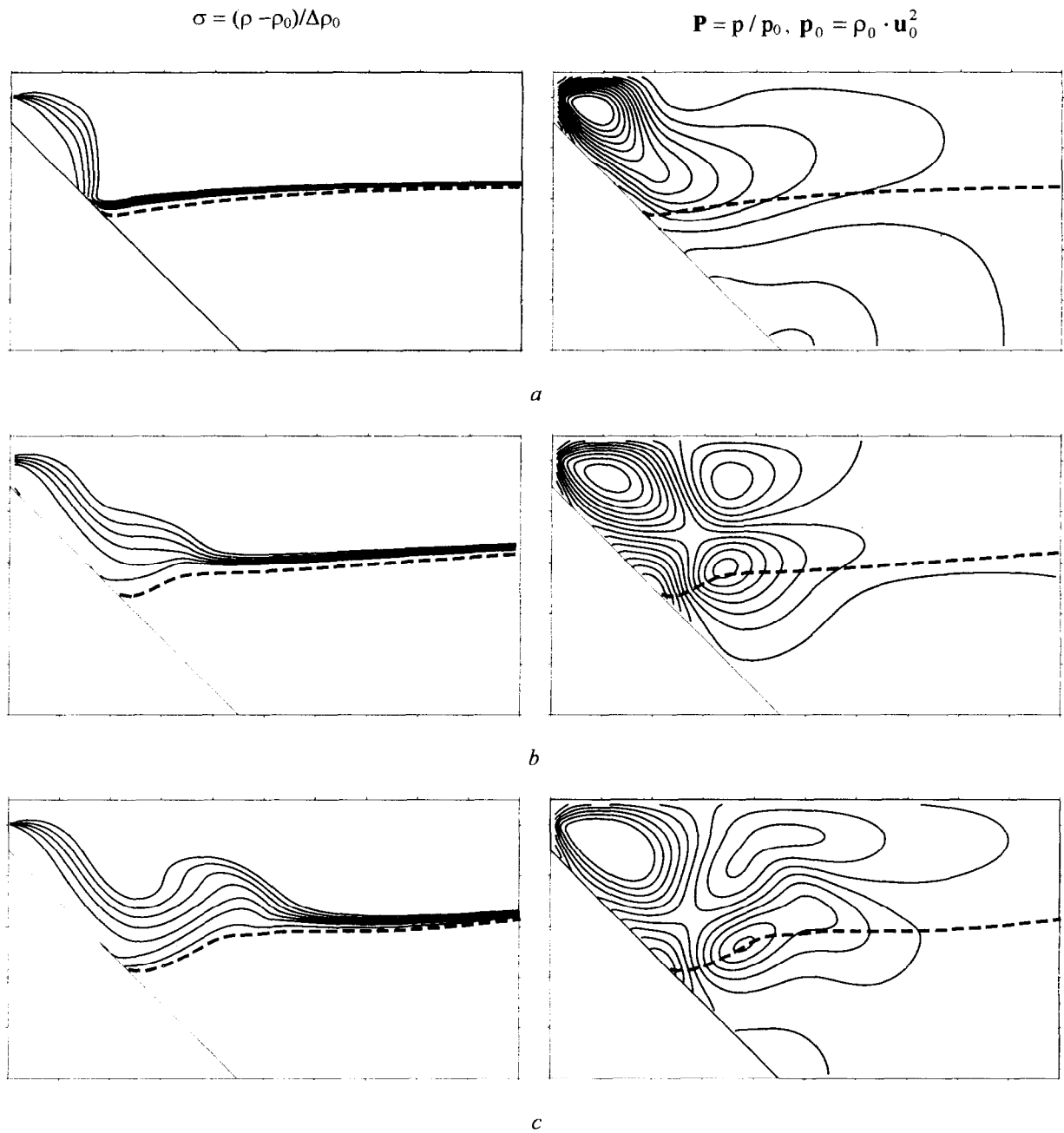


Fig. 2. Distribution of density $\sigma = (\rho - \rho_0) / \Delta\rho_0$ (left column) and pressure \mathbf{P} (right column) for the successive phases of separation of the bottom gravity current from the bottom slope. Downward successive distribution of isolines $\sigma = \{0.25, 1.0, 0.15\}$ and pressure \mathbf{P} (ranges from -55 to 5 , with spacing of 3). Layer of maximal density gradient ($\sigma = 1.6$) is represented by the thick dashed line. Characteristic scales for counting: $h_0 = 3$ cm, $u_0 = 3$ cm/s, $\Delta\rho_0 = 0,001$ g/cm³.

4. Conclusions.

The suggested model was able to reveal the continuous phase sequence of the process of a separation of the bottom gravity current from the bottom slope and to distinguish the key stages of the process. The implication of an additional parameter – pressure field – allows for better understanding of structure of the current in the surroundings of a separation point and what is the reason of the separation. Further development of this model should make it possible to analyze results of the field observations in the ocean.

The work was supported partly by RFFR, project 96-15-98336.

Literature

1. K.N. Fedorov, 1983. Physical Nature and Structure of Oceanic Fronts. Leningrad.
2. V.A. Gritsenko, A.A. Yurova, 1997. On the Propagation of Bottom Gravity Current Front over a steep Slope. *Oceanology*, 37, 1, 44-49.
3. V.A. Gritsenko, V.V. Sivkov, 1997. Some results of numerical modelling of suspension-carrying deep currents in the Baltic Sea: sedimentological aspect. In: Proc. of the Fourth Marine Geological Conference - the Baltic, Uppsala. 1995. *Sveriges Geologiska Undersökning*, ser. Ca 86, 57-60.
4. A.N. Gulyaev, V.E. Kozlov and A.N. Sekundov, 1993. On the creation of the universal single-parametric model of the turbulent viscosity. *Gas and Fluid Mechanics*. 4. 69-81.
5. J.Y. Holyer J.Y., H. Huppert. 1980: Gravity currents entering a two-layer fluid. *J. Fluid Mech.*, 100, 4, 739-767.
6. H. Lacombe, 1965. *Cours D'oceanographie Physique*. Gauthier-Villars. Paris.
7. J.J. Monaghan, 1996. Gravity currents and solitary waves. *Physica D* 98, 523-533.
8. A.S. Monin, A.M. Yaglom, 1971. *Statistical Fluid Mechanics*. Vol. 1. London, England: MIT Press.
9. D. Nehring, W. Matthaus, 1991/92. Die hydrographisch-chemischen Bedingungen in der westlichen und zentralen Ostsee im Jahre 1991. *Deut. hydr. Zeit.* 44, 5/6, 217-238.
10. Y. Noh Y, H.J.S. Fernando, 1991. Gravity current propagation along an incline in the presence of boundary mixing. *J. Geoph. Res.* 96, C7, 12.586-12.592.
11. R.V. Ozmidov, 1986. Diffusion of contaminants in the ocean. Leningrad.
12. D.H. Peregrine, 1981. The fascination of fluid mechanics. In. *J. of Fluid Mech. A Spec. Iss.*, 106, 91-119.
13. Roache P.J. 1976: *Computational fluid dynamics*. Hermosa Publishers, Albuquerque.
14. H. Schlichting, 1968. *Boundary layer theory*. New York: McGraw-Hill Book Co.
15. J.E. Simpson, 1986. Mixing at the Front of a Gravity Current. *Acta Mechanica*, 63, 245-253.
16. H. Stommel, K.N. Fedorov, 1967. Small-scale structure in temperature and salinity near Timor and Mindanao. *Tellus*, 19, 2, 306-325.
17. J.S. Turner, 1973. *Buoyancy Effects in Fluids*. Cambridge University Press, Cambridge.

ON NUMERICAL MODELLING OF UPWELLING FILAMENTS

V.A. Gritsenko¹, A.G. Kostianoy²

¹ Kaliningrad State University, 14 Al. Nevskogo str., Kaliningrad, 236039, Russia,
E-mail: geocn@email.kern.ru

² P.P.Shirshov Institute of Oceanology, Russian Academy of Sciences, 36 Nakhimovsky Pr., Moscow, Russia,
E-mail: kostianoy@glasnet.ru

Abstract. Two-dimensional numerical model was developed to simulate the evolution and structure of the upwelling filaments after their generation. A number of preliminary qualitative numerical experiments was done for a case of wide source of dense water (jet) which is flowing into the rectangular (105x105 grid) area in a wide band of governing parameters: flow velocity (5-100 cm/s), width of the flow (30-200 km), density difference between the flow in the source and surrounding water (0.000025-0.005 g/cm³) and Rossby number (0.003-0.42). Resulting currents revealed different behaviour in accordance with given parameters. Symmetrical and slightly asymmetrical currents with a dipole vortical head demonstrated well the structure and evolution of filaments and mushroom-like currents very often observed in the upwelling regions of the World Ocean. Also, these results may be applied to the flows between islands (for example, formation of dipole structure behind the chain of the Canary Islands). Divergence of the current after the source to the coast and flow along it describes many flows behind the Straits. Other applications may be done for river run-off in the ocean.

Introduction

Upwelling filaments extending hundreds of kilometers offshore from west coasts of North America, North and South Africa are the most interesting features of coastal upwellings (Fig.1). Discovery of filaments in the beginning of eighties was made possible by the advent of satellite remote sensing technology. Ginzburg and Fedorov [1] first described this feature as cold ($\Delta T = -1.5 \dots -2^\circ\text{C}$), chlorophyll-rich, narrow (10-60 km wide) jets moving offshore for distances of 300-500 km. They are well displayed on the satellite images derived from infra-red (IR) and optical scanners like AVHRR (NOAA), CZCS (NIMBUS-7) and SeaWiFS.

A number of papers have been devoted to the study of main spatial, temporal, thermal and dynamical characteristics of filaments in the California and Oregon upwelling regions [1-11], the Benguela upwelling [1,12-17], the Canary and Portugal upwellings [1,18-24] and in the Sicily upwelling [25]. Basing on the estimates of filaments velocity that may reach 1-2 m/s [12, 17, 19] and direct drifters measurements (up to 1.3 m/s) [11], it has been pointed out that these features represent an effective mechanism of seaward transport (1-2 Sv) of suspended matter, nutrients and plankton biomass from the coastal zone, and that this transport contributes significantly to production offshore [13, 15, 22]. Zatsepin and Kostianoy [26] proposed an original method of cross-frontal water exchange estimations that permit to calculate the permeability of upwelling fronts conditioned by filaments. Kostianoy and Zatsepin [27] showed that up to a half of water mass upwelled by the Ekman pumping process in the coastal zone may be transported by filaments to the open ocean, that is very important for the biology, fishery and ecology of the upwelling regions.

A huge number of filaments investigations in different upwelling regions of the World Ocean and diverse hypotheses on their generation mechanisms did not allow to understand physical nature of upwelling filaments.

It's very difficult to investigate filaments in situ in the sea because they arise sporadically in different parts of the upwelling region, display on the sea surface during few days (a week) and have very high velocities. This is why remote sensing remains the most effective method of filaments investigation giving the unique possibility to follow their formation and get their spatial, temporal, thermal and dynamical characteristics daily on a wide aquatory. The most important demerit of the remote sensing studies concerns the fact that we can follow just surface manifestation of filaments and cannot have information on their real dimensions, form, structure and dynamics. ADCP measurements [28] showed that there is a significant downward vertical component of the velocity in the filament's core, that means submergence of a filament with a distance from the upwelling front. Thus, on the sea surface we, probably, see just a part of a filament and its initial stage of development before disappearance from the sea surface. Unfortunately, ship-borne measurements (CTD, ADCP) are also planned basing on the satellite images and on the visible parts of a filament. Naturally no one will do measurements before the filament's head. In consequence, it's very likely that real shape and dimensions of upwelling filaments are still unknown.

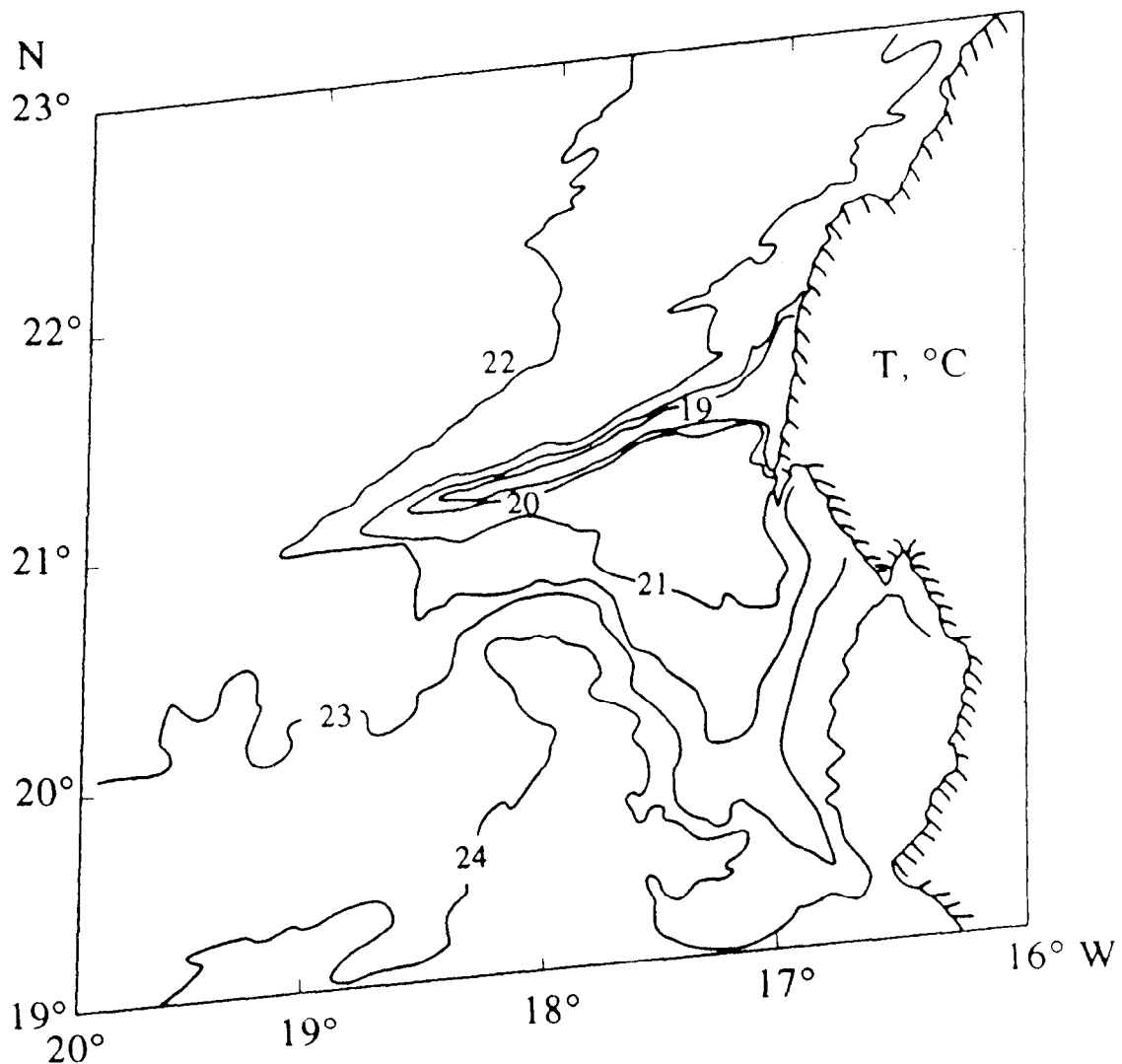


Fig.1. IR image of a cold filament of upwelled water near 21-22°N, the Cape Blanc region of the NW Africa (NOAA-11, 29 September 1990).

Model

A simple two-dimensional numerical model was developed to simulate the evolution and structure of the upwelling filaments after their generation. General scheme of the numerical experiments is shown in Fig.2. Arrows show the input of denser ($\rho_0 + \Delta\rho$) water with a velocity U_0 in the rectangular (105x105 grid) model area through a gap L (initial flow width) which equals to a 1/13 part of the right side. Left side is open and allows water to flow out. Initially water in the model area has density ρ_0 and is motionless.

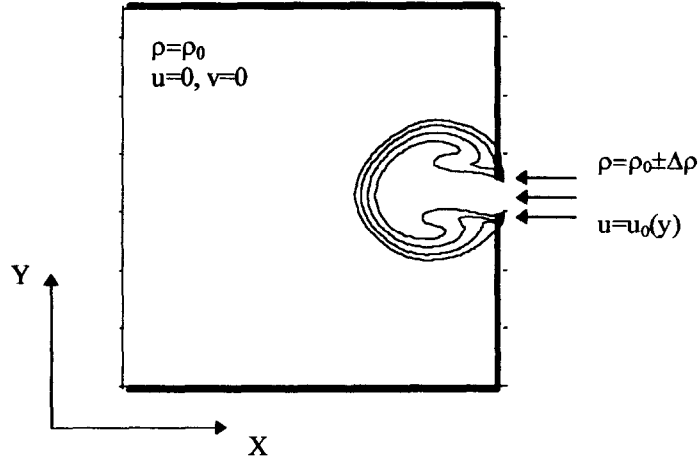


Fig.2. General scheme of numerical experiments.

For correct study of this phenomenon it's necessary to take into account a number of important physical factors like the Earth rotation, horizontal non-uniform density field, mixing processes, non-stationarity, and high (up to 1 m/s) horizontal velocities. Of course a filament is a three-dimensional feature, but as a first attempt we will focus on the horizontal movements and will use the following equations in the traditional approximation for a f -plane [29]:

$$\rho \frac{du}{dt} - \rho f v = -\frac{\partial P}{\partial x} + \mu_{\text{eff}} \Delta u,$$

$$\rho \frac{dv}{dt} + \rho f u = -\frac{\partial P}{\partial y} + \mu_{\text{eff}} \Delta v,$$

$$d\rho/dt = D\Delta\rho,$$

where ρ is a fluid density, u and v are components of horizontal velocity, t is time, f is the Coriolis parameter, P is pressure, μ_{eff} is effective viscosity, D is effective diffusion, Δ is laplacian. Comparison of the term determined by the Coriolis force and the convective one in the dimensionless equations of motion gave the following dimensionless parameter:

$$Ro' = \rho_0 / \Delta\rho_0 \cdot U_0 / (fL),$$

that we propose to call the reduced Rossby number by analogy with the reduced gravity $g' = g \cdot \Delta\rho / \rho$. In comparison with ordinary Rossby number $Ro = U_0 / (fL)$ there is a supplementary multiplier $\rho_0 / \Delta\rho_0$ responsible for a character of interaction of water masses with different density. Numerical model was based on the model of bottom gravity current described in details in [30]. Laboratory and numerical experiments with jets generated by the point source of momentum are described in [31].

Results

A number of preliminary qualitative numerical experiments (21 runs) was done for a wide band of governing parameters: width of the flow ($L = 30-200$ km), flow velocity ($U_0 = 5-100$ cm/s), density difference between the flow in the source and surrounding water ($\Delta\rho_0 = 0.000025-0.005$ g/cm³) and Rossby number

($Ro=0.003-0.42$). Parameters for numerical calculations, Burger (Bu) , Rossby (Ro) and reduced Rossby (Ro') numbers as well as resulting flow types are collected in the Table. Burger number $Bu=(g'H)^{1/2}/(fL)$ was estimated basing on the filament's thickness $H = 100$ m [28] and Coriolis parameter typical for the Canary and other upwelling zones $f = 0.79 \cdot 10^{-4} \text{ c}^{-1}$.

Table. Parameters for numerical calculations and resulting flow type.

Run	L, km	U_o , cm/s	$\Delta\rho_o$, g/cm ³	Bu	Ro	Ro'	Flow type
1	30	5	0.001	0.42	0.021	21	contour current
2	30	10	0.00025	0.21	0.042	169	slightly asymmetrical
3	30	15	0.001	0.42	0.063	63	deviation of jet
4	30	25	0.00025	0.21	0.105	422	symmetrical
5	30	25	0.001	0.42	0.105	105	deviation of jet
6	30	50	0.000025	0.066	0.21	8439	symmetrical
7	30	50	0.00025	0.21	0.21	844	symmetrical
8	30	50	0.0005	0.30	0.21	422	symmetrical
9	30	100	0.0005	0.30	0.42	844	symmetrical
10	50	5	0.001	0.25	0.013	13	contour current
11	50	5	0.005	0.56	0.013	2.5	contour current
12	100	5	0.001	0.13	0.006	6	contour current
13	100	10	0.001	0.13	0.013	13	contour current
14	100	20	0.001	0.13	0.025	25	deviation of jet
15	100	25	0.001	0.13	0.032	32	deviation of jet
16	100	30	0.001	0.13	0.038	38	deviation of jet
17	100	50	0.0005	0.09	0.063	127	slightly asymmetrical
18	100	50	0.001	0.13	0.063	63	deviation of jet
19	200	5	0.001	0.063	0.003	3	contour current
20	200	10	0.001	0.063	0.006	6	contour current
21	200	30	0.001	0.063	0.019	19	contour current

Resulting currents revealed different behaviour in accordance with initial parameters. "Symmetrical" (Fig.3) and "slightly asymmetrical" currents with a dipole vortical head demonstrated the structure and evolution of filaments and mushroom-like currents very often observed in the upwelling regions of the World Ocean. Also, these results may be applied to the flows between islands (for example, formation of dipole structures behind the chain of the Canary Islands). Divergence of the current ("deviation of jet" (Fig.4) and "contour current") after the source to the coast and flow along it describes many flows behind the straits, for example the outflow of the Mediterranean water through the Gibraltar Strait in the Gulf of Cadiz. Other applications may be done for river run-off in the ocean [32].

Analysis showed that there is no possibility to classify resulting flow types basing on the Burger and/or Rossby numbers (see Table). The single dimensionless parameter that clearly determine the behaviour of the flow independently of combination of initial parameters (L, U_o , $\Delta\rho_o$) is a new parameter - the reduced Rossby number Ro' . According to the Table "symmetrical" flow arise approximately when $300 < Ro' < 10000$, "slightly asymmetrical" - $100 < Ro' < 300$, "deviation of jet" - $25 < Ro' < 100$ and "contour current" - $0 < Ro' < 25$.

It's interesting to compare these ranges with real oceanographic features like the Mediterranean outflow, river run-off and firstly with the upwelling filaments. Basing on the statistical data on the Canary upwelling filaments Kostianoy [19] showed that their characteristic width is of 30 km (10-75 km), estimated velocity is 90 cm/s (35-218 cm/s) and density difference with surrounding oceanic water is about 10^{-4} g/cm^3 . Thus, the characteristic reduced Rossby number for filaments equals to 3000 with total range 500-20000, that corresponds to the range of the "symmetrical" flow type of the model. Analogous estimates for the Mediterranean outflow in the Gulf of Cadiz through the Gibraltar Strait ($L=30$ km, $U_o=30-60$ cm/s, $\Delta\rho_o = 10^{-3} \text{ g/cm}^3$) give values $Ro'=100-200$ that are at the limit between "deviation of jet" and "slightly asymmetrical" flow

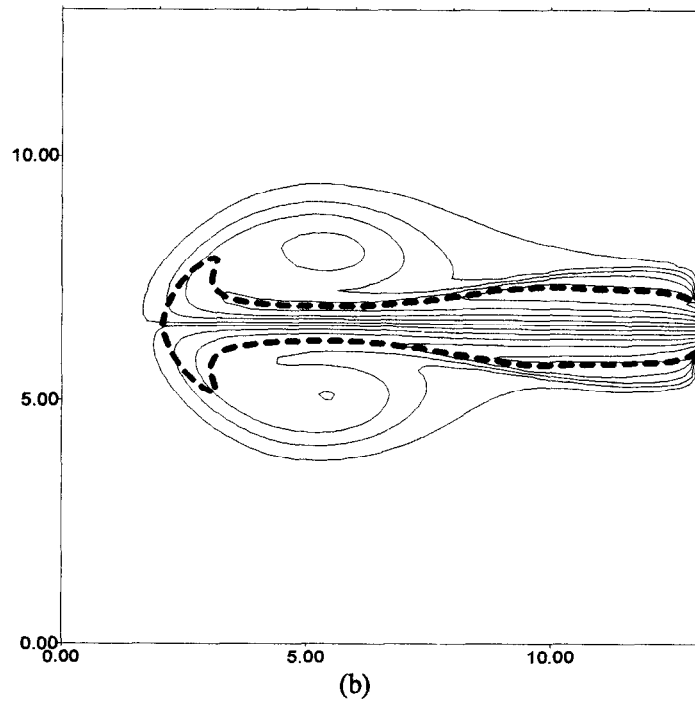
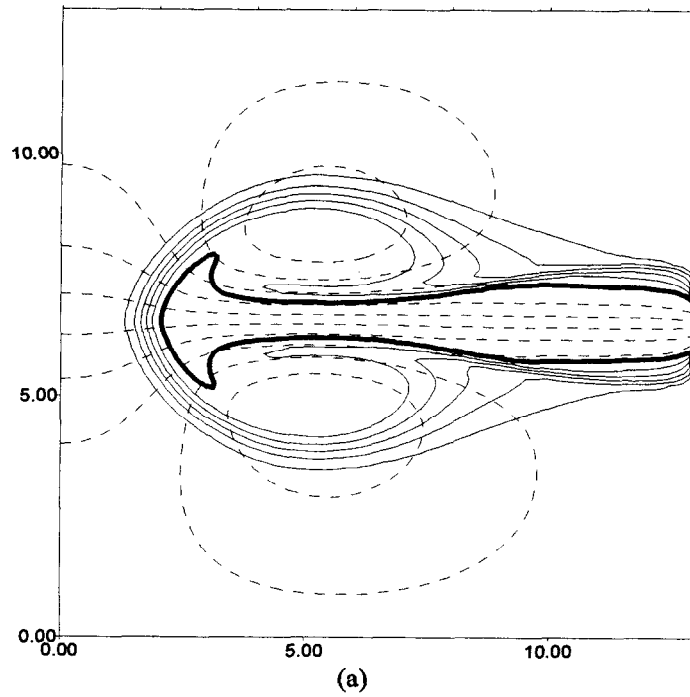


Fig.3. View of a symmetrical flow (see run N9 in the Table). $L=30$ km, $U=100$ cm/s, $\Delta\rho=0.0005$ g/cm³, $t=13.6$ days. (a) - tracer (solid lines drawn between 0.1 and 0.85 relative values with 0.15 interval) and stream function (dashed lines drawn between -1.3 and 0.2 with 0.15 interval); (b) - vorticity (solid line drawn between -1.1 and 1.0 with 0.15 interval) and tracer isoline 0.85 drawn by a bold dashed line.

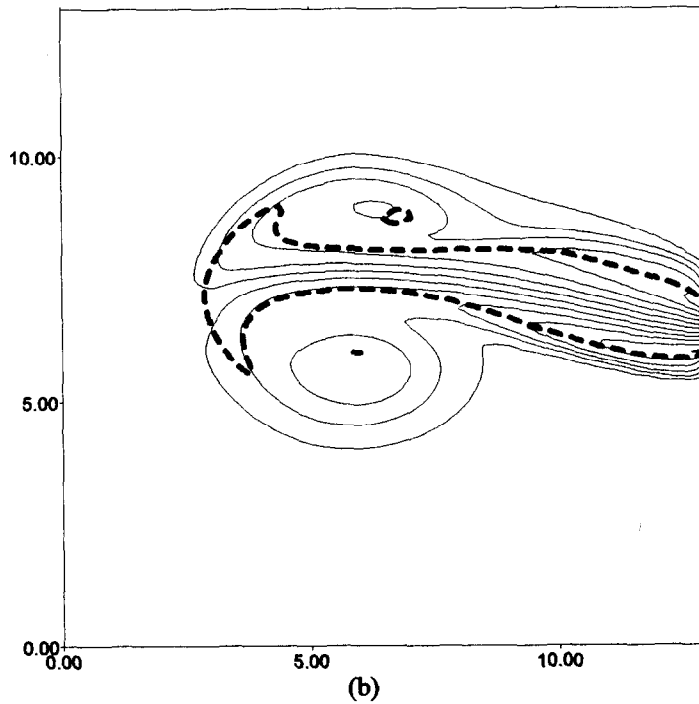
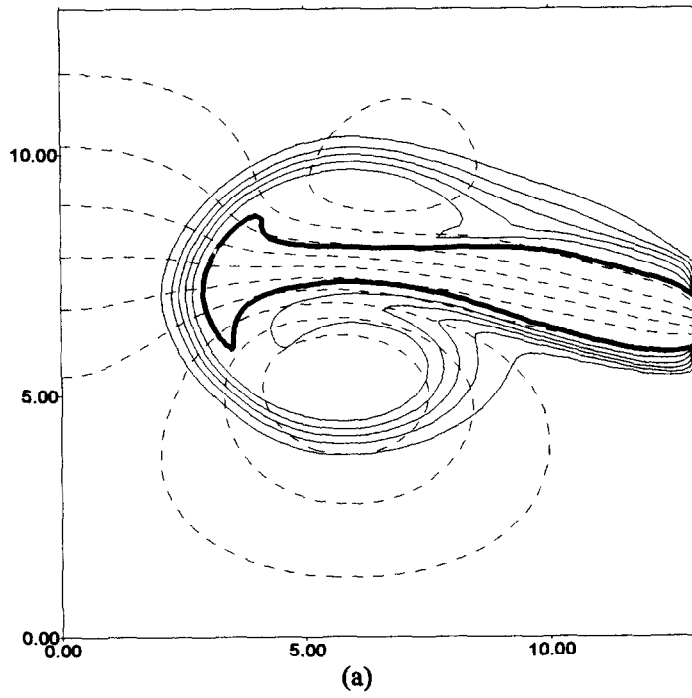


Fig.4. View of a deviation of jet (see run N14 in the Table). $L=100$ km, $U=20$ cm/s, $\Delta\rho_s=0.001$ g/cm³, $t=226$ days. (a) - tracer (solid lines drawn between 0.1 and 0.85 relative values with 0.15 interval) and stream function (dashed lines drawn between -1.1 and 0.4 with 0.15 interval); (b) - vorticity (solid line drawn between -1.1 and 1.0 with 0.15 interval) and tracer isoline 0.85 drawn by a bold dashed line.

types. Numerous observations of the Mediterranean outflow demonstrate various similar deflections of general flow toward the slope off Spain. River run-off in the ocean leads to the formation of a fresh water plume in the upper layer pressed to the right coast (in the northern hemisphere). Estimates of Ro' for typical river run-off conditions ($L=10-20$ km, $U_0=20-50$ cm/s, $\Delta\rho_0 = (1-2)\cdot 10^{-2}$ g/cm³) give values 5-50 that are in accordance with corresponding flow types - "contour current" and "deviation of jet" and their Ro' ranges.

Conclusions

A simple numerical model reproduces different flow types that may be applied to the simulation of the upwelling filaments and other density currents of different scales. Cases of "symmetrical" flow, typical for filaments, display a jet with a characteristic dipole vortical head that is very rarely observed on the satellite IR or visible images. Usually filaments (Fig.1) look like central part of the numerically generated flow (bold solid and dashed lines in Fig.3). It seems that the dipole structure remains hidden below the sea surface as well as lateral parts of a filament. Moreover, submergence of a filament with a distance from the upwelling front leads to a significant reduction of its length displayed on the sea surface. Diversity of the observed forms of filaments (i.e. a long or short jet, a jet with a dipole structure, a jet with one of the eddy pair) in different upwelling regions of the World Ocean [1, 19] might be explained by different vertical stratification, typical for every upwelling region, and its seasonal variability. To verify these new suggestions on the real structure of the upwelling filaments it is necessary to organize special ship-borne measurements including ADCP and CTD casts.

Acknowledgements

This research was partly supported by the International Project "Upwelling" of the Russian Ministry of Science and Technologies, and by the grant of the Russian Ministry of Education.

References

1. Ginzburg A.I. and K.N. Fedorov, 1985, Systems of transverse jets in coastal upwellings, *Issled. Zemli iz kosmosa* (Russian Journ. Remote Sensing), 5, 3-10 (in Russian).
2. Traganza E.D., D.A. Nestor and A.K. McDonald, 1980, Satellite observation of a nutrient upwelling off the coast of California, *J.Geophys. Res.*, 85(C7), 4101-4106.
3. Ikeda M. and W.J. Emery, 1984, Satellite observations and modeling of meanders in the California current system off Oregon and Northern California, *J.Phys. Oceanogr.*, 14(9), 1434-1450.
4. Davis R.E., 1985, Drifter observations of coastal surface currents during CODE: The method and descriptive view, *J.Geophys.Res.*, 90, 4741-4755.
5. Flament P.L., L. Armi and L. Washburn, 1985, The evolving structure of an upwelling filament, *J.Geophys. Res.*, 90, 11765-11778.
6. Kosro P.M. and A. Huyer, 1986, CTD and velocity surveys of seaward jets off northern California. July 1981 and 1982, *J.Geophys. Res.*, 91, 7680-7690.
7. Kosro P.M., 1987, Structure of the coastal current field off northern California during the Coastal Ocean Dynamics Experiment, *J.Geophys. Res.*, 92(C2), 1637-1654.
8. Rienecker M.M. and N.K. Mooers, 1989, Mesoscale eddies, jets and fronts off Point Arena, California, July 1986, *J.Geophys. Res.*, 94, 12,555-12,569.
9. Hood R.R., M.R. Abbot, A. Huyer and P.M. Kosro, 1990, Surface patterns in temperature, flow, phytoplankton biomass, and species composition in the coastal transition zone off Northern California, *J.Geophys. Res.*, 95 (C10), 18,081-18,094.
10. Paduan J.D. and P.P. Niiler, 1990, A lagrangian description of motion in Northern California Coastal transition filaments, 95(C10), 18,095-18,109.
11. Swenson M.S., P.P. Niiler, K.H. Brink K.H. and M.R. Abbott, 1992, Drifter observations of a cold filament off Point Arena, California, in July 1988, *J.Geophys. Res.*, 97(C3), 3593-3610.

12. Van Forest D., F.A. Shillington and R. Legeckis, 1984, Large scale, stationary, frontal features in the Benguela current system, *Continental Shelf Res.*, 3(4), 465-474.
13. Lutjeharms J.R.E. and P.L. Stockton, 1987, Kinematics of the upwelling front off southern Africa, *S.Afr.J. mar. Sci.*, 5, 35-49.
14. Shillington F.A., W.T. Peterson, L. Hutchings, T.A. Probyn., H.N. Waldron and J.J. Agenbag, 1990, A cool upwelling filament of Namibia, South-West Africa: preliminary measurements of physical and biological features, *Deep-Sea Res.*, 37(11A), 1753-1772.
15. Lutjeharms J.R.E., F.A. Shillington and C.M. Duncombe Rae, 1991, Observations of extreme filaments in the Southeast Atlantic Ocean, *Science*, 253(5021), 774-776.
16. Shillington F.A., L. Hutchings., T.A. Probyn., H.N. Waldron and W.T. Peterson, 1992, Filaments and the Benguela frontal zone: offshore advection or recirculation loops?, *S.Afr.J.mar.Sci.*, 12, 207-218.
17. Kostianoy A.G. and G.G. Boubnov, 1995, Investigation of the Benguela upwelling filaments basing on satellite data, *Issled. Zemli iz kosmosa*, 4, 67-75 (in Russian).
18. Nykjaer L., L. Van Camp and P. Schlittenhardt, 1988, The structure and variability of a filament in the Northwest African upwelling area as observed from AVHRR and CZCS images, *Proc. IGARSS'88 Symp.*, Edinburgh, 1097-1100.
19. Kostianoy A.G., 1991, The system of the Canary upwelling filaments, *Issled. Zemli iz kosmosa* (Russian Journ. Remote Sensing), 5, 78-86 (in Russian).
20. Van Camp L., L. Nykjaer, E. Mittelstaedt and P. Schlittenhardt, 1991, Upwelling and boundary circulation off Northwest Africa as depicted by infrared and visible satellite observations, *Prog. Oceanog.*, 26, 357-402.
21. Fiuza A.F.G. and F.M. Sousa, 1992, Mesoscale variability in the Portuguese coastal ocean studied with satellite imagery, *Annales Geophys.*, 10(2), 208.
22. Gabric A.J., L. Garcia, L. Van Camp, L. Nykjaer, W. Eifler and W. Schrimpf, 1993, Offshore export of shelf production in the Cape Blanc (Mauritania) giant filament as derived from Coastal Zone Color Scanner imagery, *J.Geophys. Res.*, 98(C3), 4697-4712.
23. Haynes R., E.D. Barton and I. Pilling, 1993, Development, persistence and variability of upwelling filaments off the Atlantic coast of the Iberian Peninsula, *J.Geophys. Res.*, 98.
24. Hagen E., C. Zulicke and R. Feistel, 1996, Near-surface structures in the Cape Ghir filament off Morocco, *Oceanologica Acta*, 19 (6), 577-598.
25. Kostianoy A.G., 1996, Investigation of the Sicilian upwelling on the base of satellite data, Technical Report, Stazione Oceanografica CNR, La Spezia, November 1996, 99 pp.
26. Zatsepin A.G. and A.G. Kostianoy, 1992, On the intensity of cross-frontal water exchange in the ocean, *Doklady USSR Acad.Sci.*, 323(5), 949-952 (in Russian).
27. Kostianoy A.G. and A.G. Zatsepin, 1996, The West African coastal upwelling filaments and cross-frontal water exchange conditioned by them, *J.Mar.Systems*, 7(2-4), 349-359.
28. Berezutsky A.V., A.G. Kostianoy, S.E. Maksimov and V.E. Sklyarov, 1991, Three-dimensional structure of the velocity field in the upwelling filaments, *Doklady Russia Acad. Sci.*, 321(5), 1095-1098 (in Russian).
29. Monin A.S., 1988, Theoretical bases of geophysical fluid dynamics, Leningrad, Gidrometeoizdat, 424 p.
30. Gritsenko V.A. and A.A. Yurova, 1997, On the propagation of bottom gravity current on a steep slope, *Okeanologiya*, 37(1), 44-49 (in Russian).
31. Voropayev S.I. and Y.D. Afanasyev, 1994, Vortex structures in a stratified fluid: order from chaos. Chapman & Hall, 240 p.
32. Gritsenko V.A. and A.G. Kostianoy, 1999, On numerical modelling of river plumes in the ocean, *Annales Geophysicae*, 17(2).

The Evolution of Forced Quasi-Two-Dimensional Vortices in a Stratified Fluid: Symmetries, Pattern Formation and Symmetry Breaking

J. N. Hacker¹, P. F. Linden² & S. B. Dalziel¹

1. Department of Applied Mathematics and Theoretical Physics, University of Cambridge, Silver Street, Cambridge CB3 9EW, UK.
2. Department of Applied Mechanics and Engineering Science, University of California at San Diego, 9500 Gilman Drive, La Jolla CA 92093-0411, USA.

Abstract. The dynamics of forced quasi-two-dimensional coherent vortices are considered in a laboratory experiment in which motions were created in a stratified fluid by injecting and withdrawing neutrally-buoyant fluid through an arrangement of horizontally-directed sources and sinks positioned at mid-depth. Vorticity, and three-dimensional turbulent motions were introduced at the sources, and these organised to form coherent horizontal vortices. Previous work using this technique [5]–[8] has shown that there is a upscale energy transfer in the flow, which occurs through the merger of vortices of like sign, and is closely analogous to the *inverse-energy-cascade* of two dimensional turbulence. In these earlier experiments, it was shown that while certain configurations of sources and sinks led to the formation of a single shielded vortex on the scale of the domain [5], in other situations multipolar vortex topologies were established and maintained in a quasi-steady state [6]–[8]. In this paper, we consider further the processes controlling pattern formation in this experiment by using two new configurations of forcing. In particular we focus on the role of the symmetries in the forcing configuration, and the conditions under which the evolution of the vortex field may break these symmetries and thereby allow the inverse-cascade to progress to the largest available scale. The experiments illustrate generic aspects of quasi-two-dimensional vortex dynamics, and, in particular, illustrate how boundary forcing may exert topological control on the evolution of a vortex field. This effect may be an important one in the environment, influencing, for example, the formation of gyre-like circulations in stratified lakes and semi-enclosed seas.

1. Introduction

The dynamics of quasi-two-dimensional vortices in stratified fluids are of fundamental importance because of the relevance of these dynamics to the large-scale flow in the oceans and atmosphere. While the dynamics of geophysical vortices are strongly influenced by the rotation of the Earth, the study of nonrotating systems provides important information regarding the dynamics of smaller-scale situations and the effects of density stratification, and elucidates generic aspects of the vortex dynamics. Of particular interest, is the capacity of density stratification to suppress vertical motions and thereby facilitate the self-organisation of vortex structures through the mechanism of the inverse-energy-cascade of two-dimensional turbulence. On the simplest conceptual level, this process is a consequence of the fact that both energy and enstrophy are conserved in a purely two-dimensional, non-dissipative flow, since vortex lines cannot be twisted or stretched. These conservation properties indicate that the energy spectrum of such a flow will evolve towards smaller wave

numbers, and hence large-scale vortices will tend to emerge from a field of initially random two-dimensional turbulence [1].

While these simple arguments are not directly applicable to stratified fluids, in which diffusive and wave transfer processes are operable, and in which vortex lines may be twisted away from the horizontal by the relative movement of horizontal layers, analogous upscale energy transfer processes occurring in stratified fluids have been observed in the laboratory by several workers (see for example [2]–[8]). However, rather than progressing to the largest available scale (e.g. the horizontal scale of a laboratory tank), the inverse-cascade in these cases has often been observed to produce multipolar vortex topologies. For example, in the case of decaying turbulence, van Heijst & Flór [2] showed that a turbulent jet, impulsively injected at some horizontal level, will collapse in the vertical and organise to form a quasi-two-dimensional vortex dipole (a positive–negative vortex pair). In related work Flór & van Heijst [3] showed that a shielded monopolar vortex (a vortex with a core of vorticity of one sign and a periphery of opposite sign) will evolve from the decay of turbulence produced by azimuthal stirring, or by the tangential injection of fluid into a cylinder that is subsequently removed, and that these monopoles may become unstable to form tripoles. More recently Maassen *et al.* [4] have observed the formation of vortex dipoles and quadrupoles during the decay of turbulence produced by dragging a rake of vertical bars through a stratified fluid contained in a cylindrical tank.

In the case of continuously forced turbulence, the simple arguments based on conservation of energy and enstrophy in spectral space may be less relevant than in the freely decaying case, since the configuration of the forcing may impose external lengthscales on the flow. However, Boubnov *et al.* [5] have observed similar upscale energy transfer processes occurring in forced turbulence in a laboratory experiment in which small-scale motions were created around the boundary of a laboratory tank containing stratified fluid, by continually injecting and withdrawing neutrally buoyant fluid through an arrangement of sources and sinks. The characteristics of this system were dependent on the Froude number $F_s = V_0 / Nd$, where V_0 is the mean velocity in the sources and sinks, N is the buoyancy frequency, and d is the source/sink orifice diameter. For weakly stable systems ($F_s > 10$), a mixed layer containing fully-three dimensional turbulence was produced. In contrast, for more strongly stratified systems ($F_s < 10$), there was little vertical mixing, and coherent quasi-two-dimensional vortices formed. In this second case, the vortices grew in scale through merger with vortices of like sign, and, after some time, a single dominant vortex grew to fill the whole domain. This behaviour is an illustration of the inverse-cascade operating in a stratified fluid to produce a single vortex structure on the largest available scale. However, subsequent work [6]–[8] in which the sources and sinks were spaced equidistantly around the inner perimeter of a large circular ring suspended in the fluid, rather than being positioned around the perimeter of a square domain, as was the case in [5], showed that such behaviour does not always occur. While there was again an upscale transfer of energy in the central part of the domain, robust coherent vortices formed between each pair of sources (with scale equal to the source separation scale) and a quasi-steady state was established in which there was a central vortex surrounded by a number of smaller vortices of opposite sign. In these experiments, therefore, the inverse-cascade did not lead to the emergence of a single structure on the scale of the domain, but established a multipolar topology. However, it has been argued [6]–[7] that this behaviour can be conceptualised in terms of the inverse-energy-cascade process, since, given that there is a propensity for coherent vortices to form between each source, there is an ‘effective largest available scale’ in this system.

The formation of the peripheral vortices in the ring-forced experiments [6]–[8] appears to be a consequence of the strong symmetry present in this forcing configuration, which was not present in the earlier work [5]. In this paper, we investigate this issue by considering two new types of forcing configuration. In particular, it is shown how the symmetries present in the forcing configuration influence the initial pattern formation, and how in certain circumstances this symmetry may be broken, thereby allowing the inverse-cascade to proceed to the largest available scale. In §2 the experiments are described and in §3 the conclusions are given.

2. The Experiments

The experiments were carried out in a Perspex tank of square horizontal cross-section measuring $61\text{cm} \times 61\text{cm}$, which was filled to a working depth of 20cm with linearly stratified saline water of buoyancy frequency N . The experimental arrangement is shown in Fig. 1. At mid-depth in the stratification, a circular perspex ring of inner diameter 56cm , width 2cm and depth 1.5cm was positioned in a horizontal plane. Around this ring there were 80 equidistantly spaced horizontal, radially-directed circular channels, of diameter $d=0.4\text{cm}$. Any even number of these channels could be connected to a peristaltic pump, to provide a particular configuration of source-sink pairs. Measurements of horizontal velocities were made by tracking approximately 3000 neutrally-buoyant particles (of diameter $0.6\text{--}1.0\text{mm}$), situated in a horizontal layer approximately 1.5cm thick and 1.5cm

above the level of the forcing, using the image processing system DigImage [9]. The laboratory apparatus and measurement system are the same as those used in [6]–[8] and further details may be found therein. The experiment is described by three nondimensional groups: the source Froude number $Fr_s = V_0/Nd$, introduced in §1, which provides a measure of the extent of vertical mixing at the sources; an overall Froude number $Fr_L = nV_0/NA^{1/2}$, where n is the number of source-sink pairs and A is the horizontal area of the domain, which provides a measure of the total energy input into the system; and the Reynolds number $Re_s = V_0d/\nu$, where $\nu = 0.01\text{cm}^2\text{s}^{-1}$ is the kinematic viscosity of the working fluid.

Two types of source-sink configuration were used. These are shown in Fig. 2. In each case, 16 equidistantly spaced channels were used. In the first configuration (Fig. 2(a)), there was an arc of sources, formed by 8 adjacent channels, situated diametrically opposite a similar arrangement of sinks. In the second configuration (Fig. 2(b)), there were two diametrically opposed arcs of sources, formed by two groups of 4 adjacent channels, which were separated by similar groups of sinks. In the first of these configurations there was one axis of reflectional symmetry, while in the second arrangement there were two axes of reflectional symmetry.

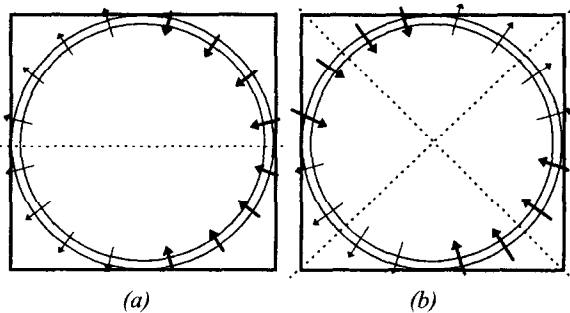


FIGURE 2 The forcing configurations used in the experiments. The arrows indicate the approximate locations of sources and sinks around the forcing ring. The dashed lines indicate the axes of reflectional symmetry.

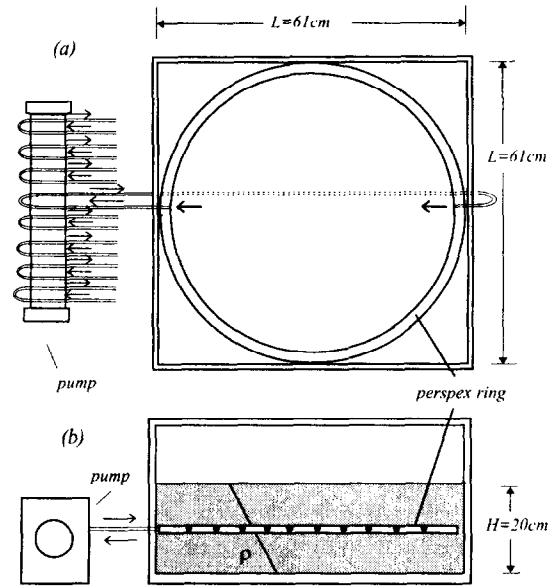


FIGURE 1. The laboratory apparatus (a) plan; (b) elevation. In the configuration shown a single source-sink pair is connected.

The evolution of an experiment with $Fr_s=2.5$, $Fr_L=0.13$, $Re_s=60$ and the first type of forcing configuration (Fig. 2(a)) is shown in Fig. 3. Shortly after the initiation of the forcing eight dipoles formed on the right-hand side of the domain (Fig. 3(a)). Each dipole was centred on a source, and clearly this initial pattern results from the configuration of the sources. Note that relatively small velocities were produced by the sinks on the opposite side of the domain. As further vorticity was supplied to the flow through the sources, the vortices continued to grow. However, the growth of the

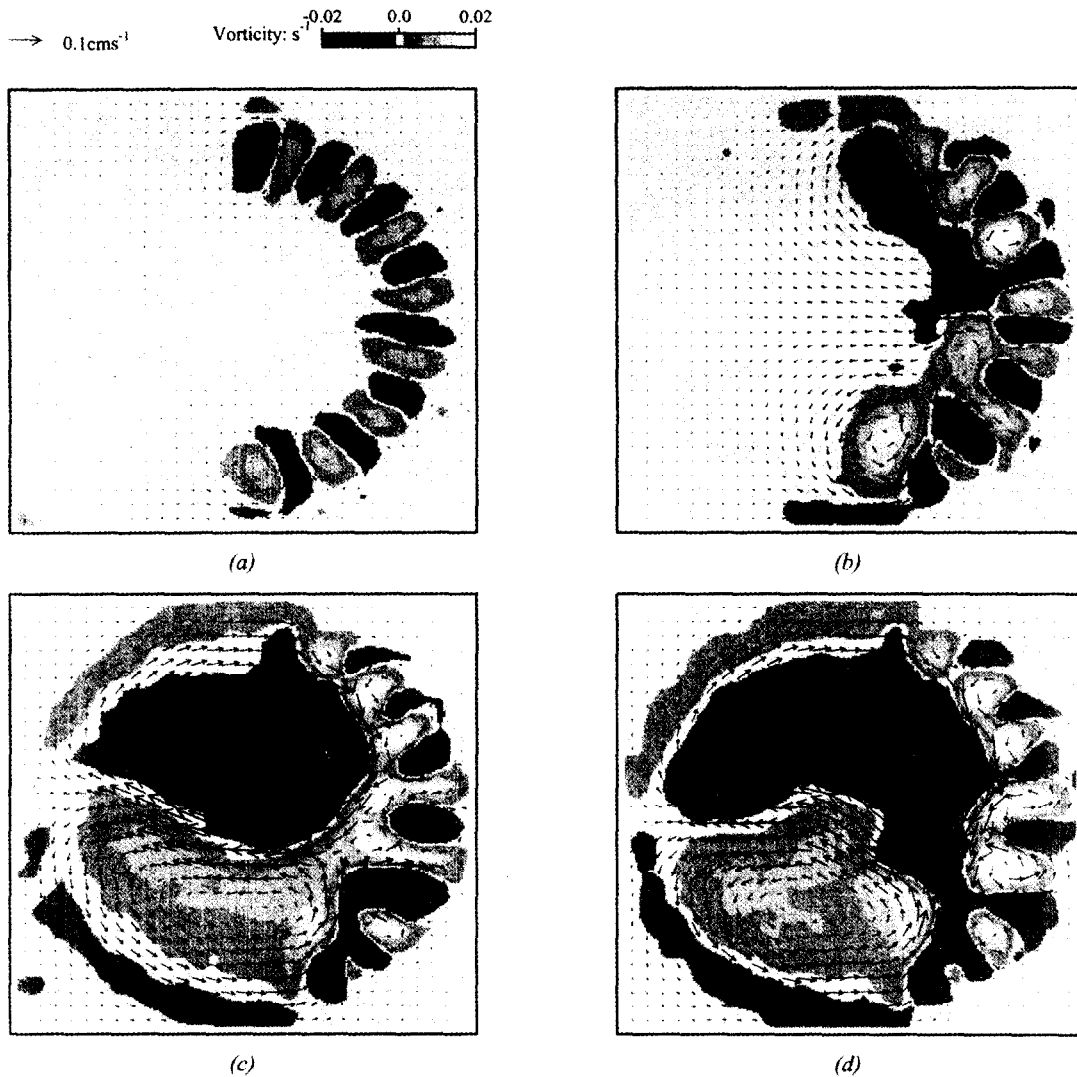


FIGURE 3. Evolution of an experiment with $Fr_s=2.5$, $Fr_L=0.13$ and $Re_s=60$ and the forcing configuration shown in Fig. 2(a) at times (mins:secs) (a) 1:35, (b) 3:30, (c) 17:20 and (d) 38:00 after the initiation of the forcing. The arrows indicate the horizontal fluid velocities and the greyscale shows the associated vorticity field.

vortices within the arc of sources (the 'line-source') was limited by the presence of neighbouring vortices, and only the two vortices at the ends of the line source were able to continue to grow in scale. As a result, an essentially dipolar topology emerged (Figs. 3(b)–(d)). This topology then persisted in a quasi-steady state for as long as the flow was forced. The major vortices of the dipole were sustained, against the effects of dissipation, by vorticity supplied from the parent source, and also from the entrainment of vorticity of like sign from the smaller vortices in the forcing region. Such entrainment events involved the connection of one of the major vortices with regions of like signed vorticity in the forcing region. For example, in Fig. 3(c), there is a connection between the positive major vortex and the positive minor vortices on the opposite side of the axis of symmetry, whereas in Fig. 3(d) the situation is reversed. The system oscillated between these two states with a relatively regular period of approximately 600s. This timescale corresponds closely to the eddy turnover time of the vortices in the forcing region.

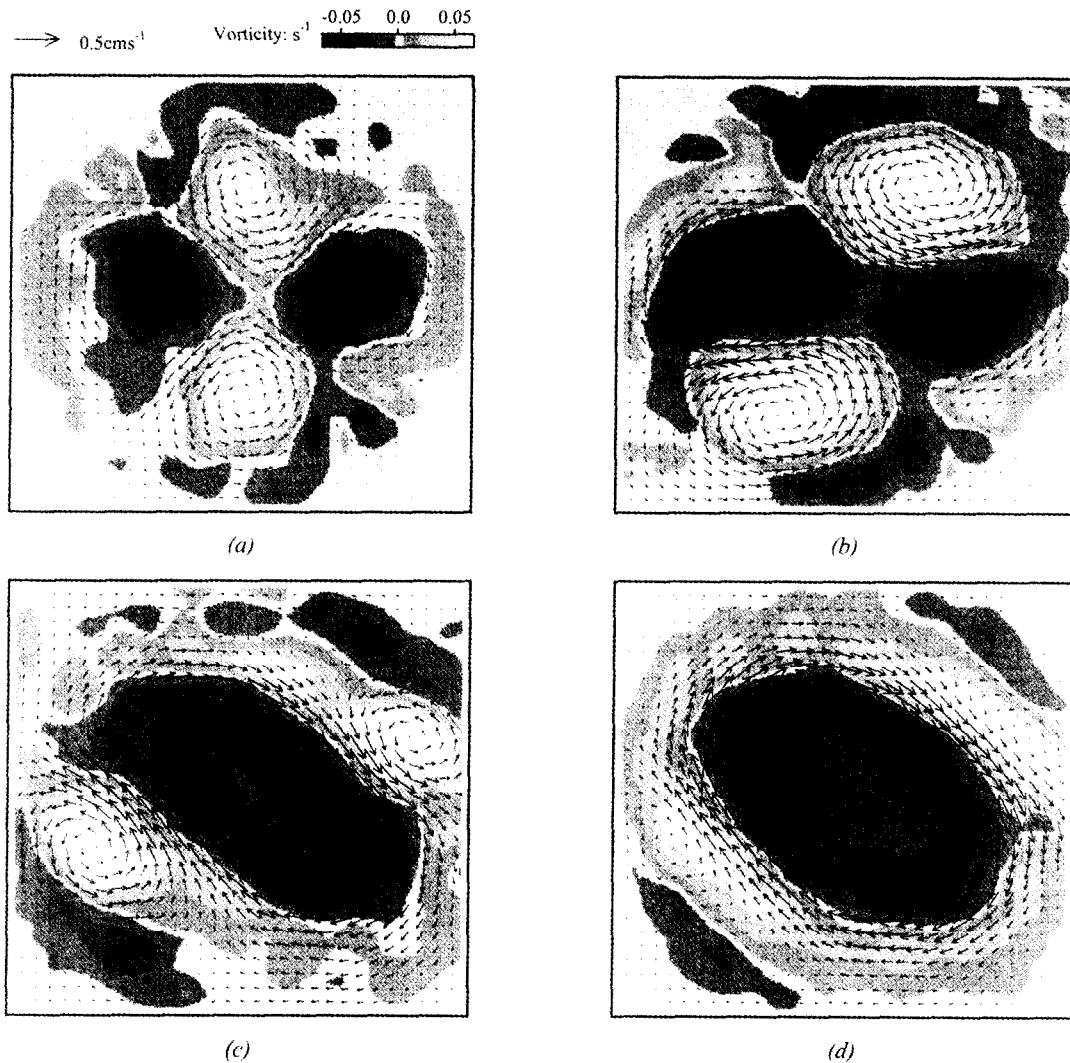


FIGURE 4. Evolution of an experiment with $Fr_s=6.0$, $Fr_L=0.31$ and $Re_s=144$ and the forcing configuration shown in Fig. 2(b) at times (mins:secs) (a) 1:40, (b) 5:00, (c) 23:20 and (d) 35:40 after the initiation of the forcing. The arrows show the horizontal fluid velocities and the greyscale shows the associated vorticity field.

The evolution of an experiment with $Fr_s=6.0$, $Fr_L=0.31$, $Re_s=144$ and the second type of the forcing configuration (Fig. 2(b)) is shown in Fig. 4. In this case, there were two 'line-sources' of vorticity (the sources), and initially coherent vortices grew from the ends of these line-sources to form two opposing dipoles (note that there was less coherence in the forcing region than in the previous experiment due to the large value of F_s). Shortly after the initiation of the forcing, the two dipoles met at the centre of the domain to form a quadrupolar structure (Fig. 4(a)). After a short period of oscillatory behaviour in which both pairs of vortices attempted to merge, a robust connection formed between the two negative vortices, and by the stage shown in Fig. 4(b) these vortices had begun to merge. As a result of this merger, the symmetry imposed by the forcing, which led to the formation of the two initial dipoles, was broken, and there was a transition to a tripolar topology. Initially, the tripolar structure rotated, and then became locked with the central vortex adopting an elliptical form along the line of symmetry connecting the sources (Fig. 4(c)) and with the two satellites remaining in the corners occupied by the sinks. Thereafter, the structure initially imposed on the flow by the symmetry of the forcing configuration was lost. In particular, there was a greater propensity for positive vorticity supplied from the sources to be

wrapped around the central vortex, rather than to penetrate into and maintain the satellites, and hence the satellite vortices decayed over time, and eventually a shielded monopolar topology emerged (Fig. 4(d)).

3. Summary and Conclusions

The two experiments discussed above illustrate several aspects of the process of the inverse-energy-cascade occurring in forced turbulence in a stratified fluid contained in a bounded domain. In particular, the experiments show how different symmetries present in the forcing configuration can produce different types of vortex topology. In the first experiment, in which there was a single axis of symmetry present, an essentially dipolar topology formed, and this configuration was stable in the sense that it was not possible for either of the major vortices of the dipole to grow to the extent that it dominated the other. In this experiment, therefore, the symmetry of the forcing constrained the vortex field in such a manner that a transition to a monopolar topology was not possible, and hence the progress of the inverse energy cascade was halted at a scale less than the scale of the domain. In the second experiment, in which there were two axes of symmetry, an essentially quadrupolar topology formed, but in contrast to the previous experiment, this configuration was unstable, in the sense that a pair of vortices of like sign could merge to form a single vortex that dominated the flow field, and subsequently led to the formation of a tripole, and ultimately a shielded monopole. In this second case, therefore, there was a capacity for the vortex evolution to break the symmetry imposed initially by the forcing, and thereby facilitate the progress of the inverse-energy-cascade to the largest available scale.

We note that in the first experiment, there was a net input of linear momentum into the system from the sources and sinks, whereas in the second experiment there was zero net input of momentum (to within experimental error). Hence, it might be expected that in the first case a vortex structure with linear momentum (a dipole) would be produced, whereas in the second experiment, a structure with zero net linear momentum (a quadrupole consisting of two opposing dipoles, a tripole or a monopole) would be produced. However, we have observed qualitatively the same evolution in experiments where the sinks were interspersed between the sources in such a way that the symmetry of the forcing was maintained but the nature of the net linear momentum input was greatly altered. In addition, while the configuration of the sources was of fundamental importance, the sinks played only a passive role through their ability to affect the flow through a nearby source, and hence influence the symmetry of the system. It would appear, therefore, that it is the symmetry of the forcing configuration, in particular the symmetry of the vorticity input from the sources, that governs the pattern formation in this system. We conclude, therefore, that it is the nature of the local momentum inputs, rather than the nature of the net momentum input, that governs the properties of this system.

References

- [1] Rhines, P.B. 1979 Geostrophic turbulence *Ann. Rev. Fluid Mech.* **11**, 401–41.
- [2] van Heijst, G.J.F. & Flór, J.B. 1989 Dipole formations and collisions in a stratified fluid. *Nature* **340**, 212–214.
- [3] Flór, J.B. & van Heijst G.J.F. 1996 Stable and unstable monopolar vortices in a stratified fluid. *J. Fluid Mech.* **311**, 257–287.
- [4] Maassen, S.R., Clerx, H.J.H. & van Heijst G.J.F 1998 Decaying quasi-2D turbulence in a stratified fluid with circular boundaries. *submitted to Europhys. Letters*
- [5] Boubnov, B.M. Dalziel, S.B. & Linden, P.F. 1994 Source-sink turbulence in a stratified fluid. *J. Fluid Mech.* **261**, 273–303.
- [6] Linden, P.F., Boubnov, B.M. & Dalziel, S.B. 1995 Source-sink turbulence in a rotating, stratified fluid. *J. Fluid Mech.* **298**, 81–11
- [7] Dalziel, S.B., Linden, P.F. & Boubnov, B.M. 1996 Experiments on turbulence in stratified fluids. *in Waves and Non-linear Processes in Hydrodynamics, pp.317–330. J.Grue et. al. (eds). Kluwer Academic Publishers (Netherlands)*
- [8] De Rooij, F., Linden, P.F. & Dalziel, S.B. 1998 Interactions and decay of vortices in stratified turbulence. *to appear in J. Fluid Mech.*
- [9] Dalziel, S.B. 1993 Rayleigh-Taylor instability: experiments with image analysis. *Dyn. Atmos. Oceans* **20**, 127–153

SEASONAL VARIABILITY OF THE CASPIAN SEA DYNAMICS: BAROTROPIC MOTIONS DRIVEN BY CLIMATIC WIND STRESS AND RIVER DISCHARGE

R. A. Ibrayev¹, E. Ozsoy², A. S. Sarkisyan¹, H. I. Sur²

¹ Institute of Numerical Mathematics, Russian Academy of Sciences, Gubkin str.8, Moscow, 117951, GSP-1, Russia (e-mail: ibrayev@inm.ras.ru)

² Institute of Marine Sciences, Middle East Technical University, P.K.28 Erdemli, Icel, 33731, Turkey (e-mail: ozsoy@ims.metu.edu.tr)

Abstract. A 3-D PE OGCM is used for the study of seasonal cycle of the Caspian sea barotropic circulation driven by wind stress and water input/output through lateral boundaries. Barotropic model represents a valid first approximation, especially in view of the mainly wind forced, extensive shallow areas of the Caspian Sea and the weak, mainly thermal, stratification in deep parts. We show that the circulation has Ekman drift and gradient current components, which is strengthened in the extensive shallow shelf areas of the Caspian Sea, taking the form of coastal jets. Summer upwelling and southerly jet along the eastern coast with compensation currents steered by topography are novel features found in the seasonal circulation persist in a wide range of parameter variations and settings. Satellite remote sensing and hydrological data support these features of solution.

1. Introduction.

The Caspian Sea is the largest totally enclosed water body on Earth. Topographically the sea divided into three sub basins: North Caspian Basin (NCB), Middle Caspian Basin (MCB) and the South Caspian Basin (SCB), see **Fig. 1a**. Shelf areas, mainly along the northern and eastern coasts, account for 62 % of the total area. The general circulation has been described to be cyclonic, based on the investigations carried out from the end of the 19th century till the 1950's, using indirect methods of current measurement (floats, bottles or the dynamic method), and mostly relying on hydrodynamical arguments. A synthesis of these results led to the current schemes of Zenin (1942), Lednev (1943) and others, see [1]. Since the 1950's, regular oceanographic observations and current measurements in coastal areas (depth < 100 m), have confirmed some of the features of classical schemes, but observations showing southerly currents along the eastern coast of MCB in summer

[2, 3] contradict with the above description of the general circulation. The main deep water ventilation processes are winter mixing and upwelling along eastern coast of the sea. Upwelling occurs predominantly in summer, as it is shown by hydrographic data (Fig. 2) and satellite images.

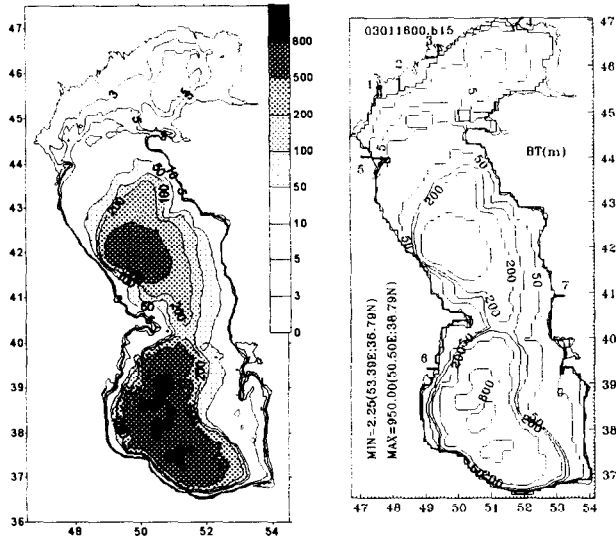


Figure 1. Bottom topography of the Caspian sea, m (a) and model bottom topography (b). Arrows indicate open lateral boundaries, which include branches of Volga river mouth: 1 - Bakhtemir; 2 - Kamyzyak; 3 - Buzan; 4 - r. Ural; 5 - r. Terek; 6 - r. Kura; 7 - outflow to Kara-Bogaz-Gol bay.

In this study we investigate the spin-up of the Caspian sea general circulation and its seasonal variability, and concentrate on the barotropic motions driven by wind stress and rivers' run-off, as a first step to understand the underlying dynamics.

The three-dimensional, barotropic model represents a valid first approximation, especially in view of the mainly wind forced currents in extensive shallow areas of the Caspian Sea and the weak, mainly thermal, stratification in deeper parts. As the next step, in our continuing studies, we will consider a baroclinic model with a sea-ice component, driven by surface and riverine buoyancy and momentum fluxes, and investigate baroclinic circulation and deep water ventilation processes.

2. Formulation of the problem.

We use a 3-D PE OGCM developed in the Institute of Numerical Mathematics of the Russian Academy of Sciences [4, 5], employing the rigid lid, Boussinesq and hydrostatic approximations. Model is driven by climatological monthly wind stress and water input/output through open lateral boundaries. Horizontal grid step in the model is less than 10 km in longitude and latitude, that allow us to approximate realistically main features of bottom topography of the sea and explicitly resolve two islands, Fig. 1b. Vertical grid includes 22 levels defined at depths of 0.5, 1.5, 3, 6, 11, 17, 25, 35, 50, 75, 100, 125, 150, 200, 250, 300, 400, 500, 600, 700, 800, 900 meters. In the model we use seven open lateral boundaries.

Yearly mean wind stress from [6] is presented on Fig. 3a. Seasonal cycle of winds is characterised by N-W, N and N-E winds prevailing over MCB and SCB in warm period of the year, with stronger northern components along

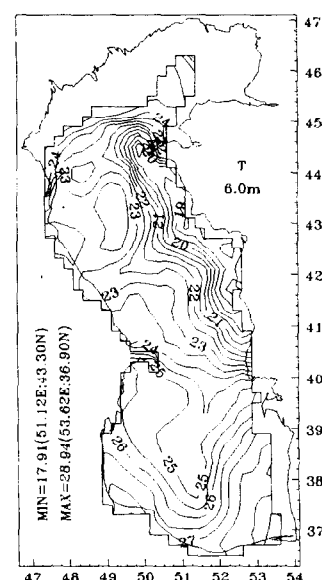


Figure 2. Climatological temperature, deg. C, at 6m depth in August.

Table 1. Parameters of experiments.

Exp	Wind	River	Bottom topography
A	yearly	no	no
B	yearly	no	yes
B1	N-W	no	yes
B2	N	no	yes
B3	N-E	no	yes
C	monthly	no	yes
D	no	yes	yes
E	monthly	yes	yes

eastern coast of the sea. Eastern monsoon winds dominate over eastern part of the sea and NCB from October till March. Total water input into the sea by rivers is about 289.1 km³/yr [7]. The Volga river run-off, which accounts for about 80% of the total river run-off, shows strong seasonal variability with maximum values of about 40-50 km³/month in May and of about 15 km³/month from August till March. Other rivers give about 5-15 km³/yr of freshwater input each. An output to Kara-Bogaz-Gol bay is estimated to be of 10 km³/yr [7].

A number of numerical experiments are carried out for systematic study of the response of the Caspian Sea dynamics to the two driving forces considered: wind stress and lateral water input/output. According to the results of experiments the following questions are addressed: What is the relative roles do wind and rivers' inflow in generating the general circulation of the Caspian Sea? What role does sea bottom topography play in development of existing sea current system? What is the general circulation of the sea forced by the annual inflow? Table 1 summarises the parameters of each experiment.

3. Discussion

Circulation of the sea in the case of flat bottom, as it is seen from sea level topography, closely follows

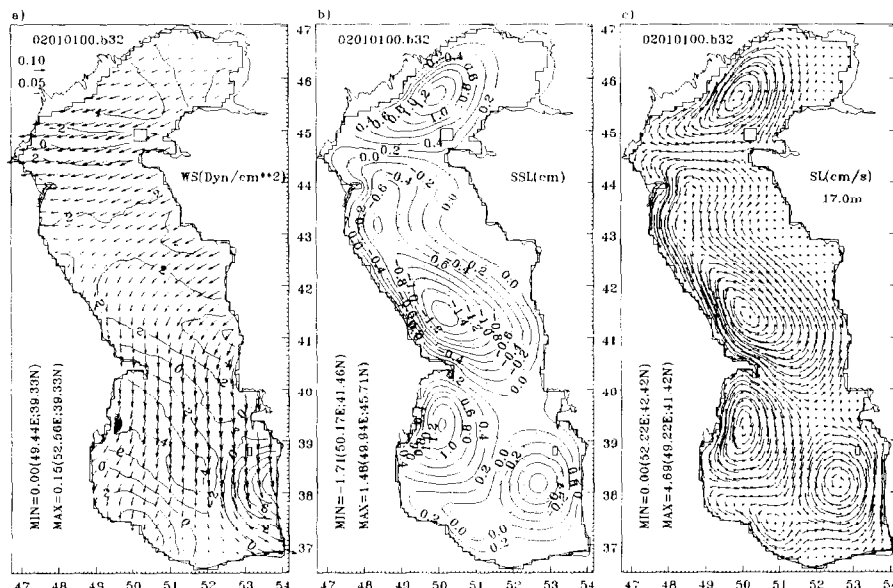


Figure 3. Yearly mean climatological wind stress (vectors, dyn/cm²) and its vorticity (isolines, 10⁻⁹ dyn/cm³) (a). Sea surface topography, cm, (b) and horizontal currents, cm/s, at depth 17 m (c) in case of flat bottom topography.

the pattern of the curl of wind stress, see Fig. 3ab. Under upper friction layer, the gradient currents totally follow sea surface topography pattern, Fig. 3c. In the case of realistic bottom topography (Exp. B), the circulation is totally different from the flat bottom case, see sea level pattern at Fig. 4a.

The most valuable sea level gradients in response to the wind are created in the shallow continental shelf areas along the northern and eastern coasts. Strong sea level gradient drives jet-like coastal currents in NCB and near eastern coast of MCB and of SCB. An influence of wind vorticity on circulation preserved only in central deep part of the sea out of the belt of strong sea level gradients over the shelf. Sea level rise and draw corresponding to anticyclonic and cyclonic gyres are less pronounced at the sea surface topography map (see Fig 4a). Stream function chart clearly shows the cyclonic eddy positioned over the deep part of MCB, Fig. 4b.

Southward current along the eastern coast of MCB, forced by sea level draw, and eastern and northern parts of cyclonic deep water eddy of MCB build up an anticyclonic eddy stretched along 52°E (Fig. 4b). The southern part of this meridional anticyclonic eddy is merged with anticyclonic eddy of SCB. This meridionally stretched anticyclonic eddy is a robust feature of circulation pattern and we will meet it in following experiments. Similar structure, when anticyclonic eddy generated by wind vorticity, stretches out an eddy of opposite sign along its periphery is seen near S-W coast of SCB. Below the Ekman layer the pressure gradient is the main driving agent of the currents (Fig. 4c). Narrow southward jets along the north-west and east coasts of the MCB are connected by wide current flowing anticyclonically along the north shelf slope of the MCB. In the deeper waters of the MCB and especially in the SCB, the deep currents can be related to the curl of wind stress as in the flat bottom case.

Few additional experiments without curvature of the wind stress were carried out to clarify the driving force of along shelf anticyclonic gyre. Results of experiments forced with uniform N-W, N, N-E winds show remarkable correlation with the results of previous experiment. Almost the same pattern of the anticyclone gyre along northern and eastern shelf indicates that the main driving mechanism of the gyre is the dynamics of

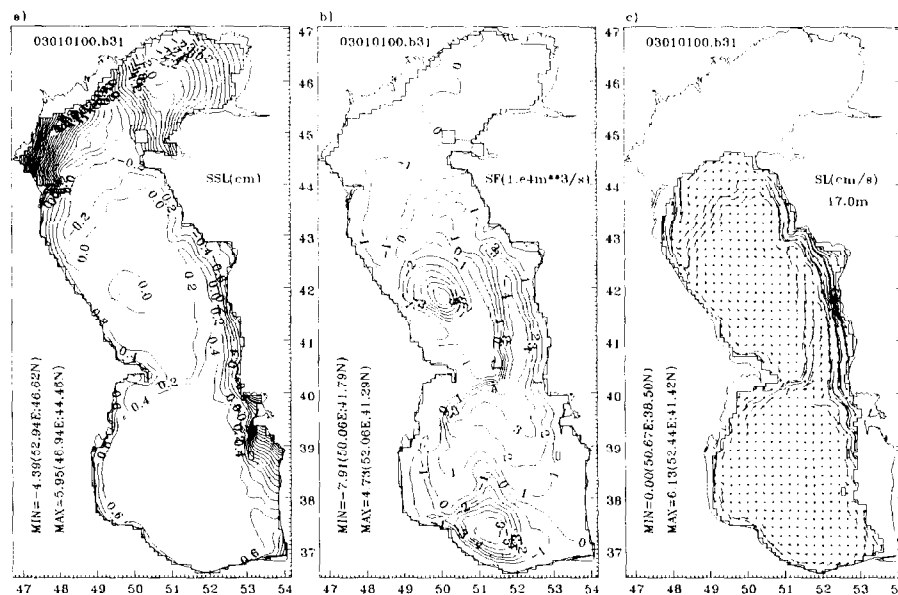


Figure 4. Sea surface topography, cm (a); stream function, $10^4 \text{ m}^3/\text{s}$, (b) and horizontal currents, cm/s, at depth 17 m (c) for yearly mean wind driven circulation with realistic bottom topography.

shelf currents. This gyre constitutes a recirculation current to the eastward current over the northern shelf and southward current over eastern shelf. Noticeable that the cyclonic eddy in southern part of SCB, which was likely generated by wind vorticity like in flat bottom experiment, in also present is last experiments. The

experiments B1-B3 show that, the circulation pattern driven by yearly mean wind is defined by dynamics of shelf currents, moreover this eastern anticyclonic recirculation gyre is present with little modifications when N-W, N, N-E winds force the circulation.

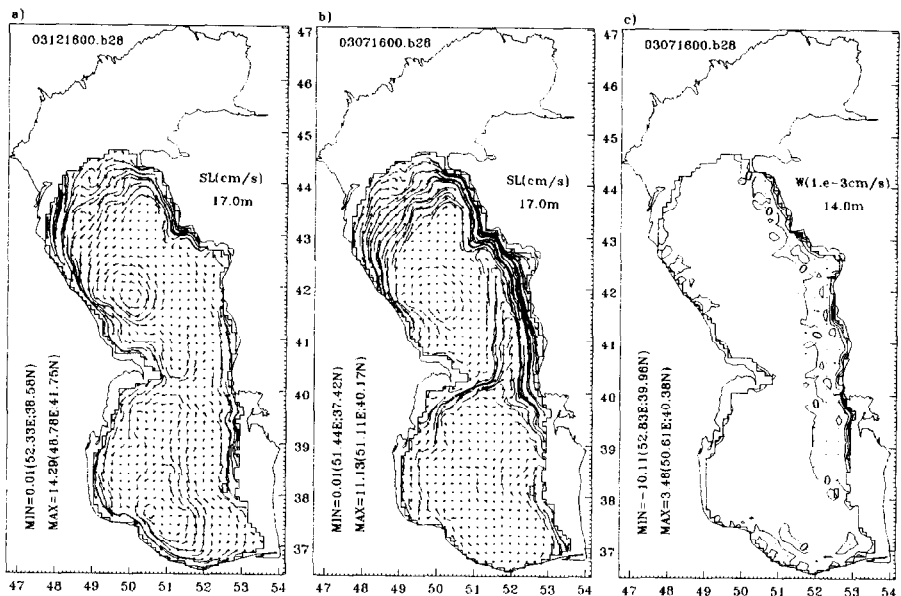


Figure 5. Horizontal currents at depth 17 m in December (a) and July (b), and vertical currents in July (c) at depth 14 m for the circulation driven by monthly wind stress.

The characteristic feature of seasonal variability (Exp. C) of circulation in the MCB and SCB is changing of cyclonic type of circulation in winter to the anticyclonic type in summer. In September the circulation pattern is very close to the mean year situation. The onset of monsoon westward wind over eastern part of the sea results in N, N-W Ekman drift and in this way drives cyclonic gyre in deep MCB and SCB, see subsurface currents in Fig. 5a. With little changes such a circulation lasts up to March, when easterlies in SCB are changed by northerlies. Southward wind gives an onset to meridionally stretch anticyclonic type of circulation discussed before. Maximum development of this anticyclonic gyre occurs in July, see Fig. 5b.

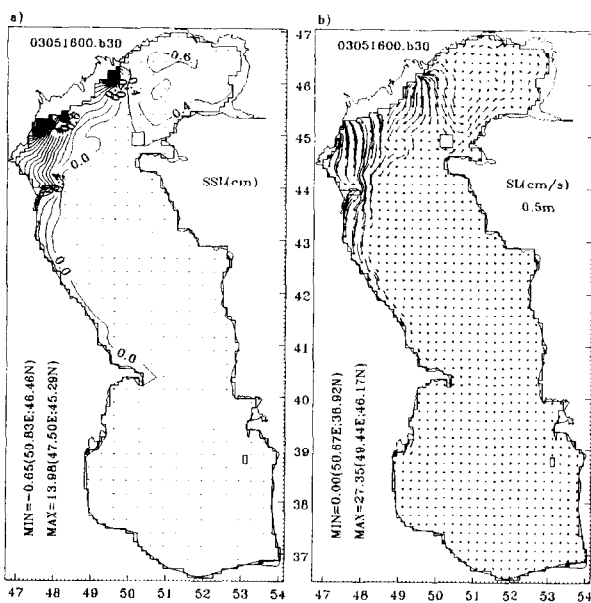


Figure 6. Sea surface topography, cm, and surface currents, cm/s, driven by water input from rivers

Upwelling along the eastern coast is generated by off coast Ekman drift in all seasons with maximum upward velocity in summer, Fig. 5c.

Sea surface topography and surface currents shown in Fig. 6ab illustrate circulation driven only by river run-off. Volga river induced currents are about 5-10 cm/s at the distance 100-150km from the river mouth, the value that is close to currents driven by moderate wind in NCB. Hydraulic pumping gives rise of sea level of about 15-20cm close to mouths of the Volga. Coriolis force turns river inflow to the right, giving sea level build-up along north-western coast of NCB.

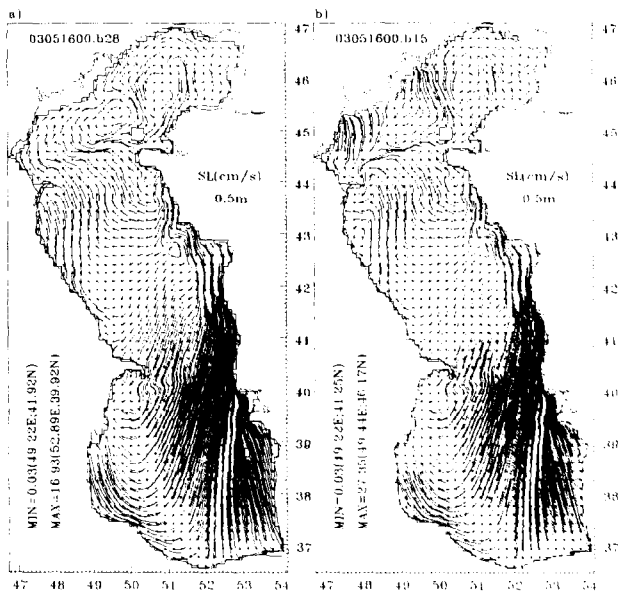


Figure 7. Surface currents in May in wind and river run-off driven experiment (a) and in only wind driven experiment (b).

this coastline. As a consequence, southward gradient current is generated on shelf in sub-surface layer, independent of the direction of surface current, which obeying to Ekman drift may be north, north-westward like in winter or south, south-westward like in summer. Southward surface current over the eastern shelf is consistent with observation, as well as an elongated anticyclonic gyre over north and east shelf edge of the sea in summer is consistent with cyclonic circulation of deep MCB, SCB of the classical schemes.

Acknowledgments. This research was sponsored by Russian Basic Research Foundation grants 96-15-98472, 96-05-65599 and by NATO Linkage Grant SA.12-2-02.

References

- [1] Terziev, F. S., A.N. Kosarev and A.A. Kerimov (Eds.), 1992: Hydrometeorology and Hydrochemistry of Seas. Vol. VI: Caspian Sea. Issue 1: Hydrometeorological Conditions, S.- Petersburg, Hydrometeoizdat, 359 p. (in Russian).
- [2] Klevtsova, N.D., 1967: Sea currents' regime near East coast of the Middle and South Caspian Basins, In: Proceedings of Baku Hydrometeoobservatory, Baku, Issue 3, 44-49. (in Russian).
- [3] Bondarenko, A.L., 1993: Currents of the Caspian Sea and formation of salinity field of the waters of the North Caspian Sea. Moscow, Nauka, 122 p. (in Russian).
- [4] Demin, Y.L. and Ibraev, R.A., 1986: A numerical method of calculation of currents and sea surface topography in multiply-connected domains of the oceans. Soviet Journal for Numerical Analysis and Mathematical Modelling, 4, 211-225.
- [5] Ibraev, R.A., 1993: Reconstruction of climatic characteristics of the Gulf Stream, Izvestiya, Atmos. Oceanic Phys 29(5), 803-814. (in Russian).
- [6] Samojlenko, V. S., and A.I. Sachkova (Eds.), 1963: Complex meteorological atlases of the Caspian and Aral seas. Leningrad, Hydrometeoizdat, 179 p. (in Russian).
- [7] Bajdin, S.S., and Kosarev, A.N. (Eds.), 1986: The Caspian Sea. Hydrology and Hydrochemistry, Moscow, Nauka, 262 p. (in Russian).

Circulation driven by combined effects of wind and exchanges through open lateral boundaries do not differ much from purely wind driven circulation (Exp. C) except for the region close to Volga river mouth. In case of climatological winds the river induced currents are always stronger than wind currents, an example is presented on Fig 7ab.

4. Conclusions.

The barotropic currents represent some realistic features of the Caspian sea circulation. Prevailing in all months North and East winds over eastern shelf of the sea force sea level drop along

Observations of the Gulf Stream Frontal Zone Using the ALMAZ-1 Synthetic Aperture Radar

A.Yu. Ivanov¹, S.A. Grodsky² & V.N. Kudryavtsev²

1. P.P. Shirshov Institute of Oceanology, Russian Academy of Sciences, Nakhimovsky pr., 36, Moscow, 117851, RUSSIA

2. Marine Hydrophysical Institute, Ukrainian Academy of Sciences, Kapitanskaya 2, Sevastopol, 335000, UKRAINE

Abstract. Observations of the Gulf Stream frontal zone with use the SAR aboard Russian satellite ALMAZ-1 are analyzed. Sea surface temperature fields extracted from NOAA-10 AVHRR IR images are additionally used. Imaging from space was accompanied by measurements of upper ocean and lower atmosphere parameters on board the R/V Akademik Vernadsky, as well as registration of surface currents along the ship tracks crossing the frontal zone. The experiments were conducted at moderate westerly winds when the wind waves and swell propagated in directions close to current direction. At these conditions the effects of wave reflection produced the zones of wave concentration and wave shadow. It is shown that using spectral analysis of SAR images and model calculations the effects of waves refraction can be studied. Contact measurements documented the existence of zones of convergence with strong current shear. Linear-like structures seen in the SAR images were located near these current shears and convergence zones and accompanied by organic film accumulation and/or wave concentration. The strips were oriented along the Gulf Stream thermal front and reflected the structure of cross current non-homogeneity. Possible explanations of an appearance frontal features in the SAR imagery are given.

1. Introduction

Ocean fronts as areas of an intensive energy and substance exchange between ocean and atmosphere influence essentially on a number of oceanic processes and manifest itself on the sea surface. Potential capability of their observation by spaceborne synthetic aperture radars (SAR) was for the first time shown in the experiments with SEASAT SAR [1]. These observations and later ones carried out with ERS-1 SAR [2,3] have shown a possibility to investigate structure of the frontal zones and detect intensive current boundaries.

Current variations across the frontal zones may significantly influence surface wave field. Theory predicts [4] the most interesting effects: wave reflection by a fair current and waveguide-like propagation of the trapped waves towards to current. Concentration of trapped waves in a jet can cause a danger to navigation [5].

Spaceborne SAR resolves long surface waves that allows to study surface wave refraction on the currents [6,7]. Wave evolution on the Gulf Stream (GS) and wave refraction on a warm core ring were observed by SEASAT SAR [8,9]. The SIR-B were used to study the trapped waves on the Agulhas current [10], and wave behavior in the Circumpolar area [6]. However, these data were not supported by contact measurements.

The most complete observations of wave evolution in the GS area were performed on board of the R/V Akademik Vernadsky using ship-based radar and contact measurements [11]. Field data analysis and model calculations run with real wind and currents fields allowed to reveal the most prominent peculiarities of wave-current interaction [12]. Shipboard measurements were supported by quasisynchronous ALMAZ-1 SAR imaging of the experimental area.

In this paper an analysis of ALMAZ-1 SAR image signatures of the GS and wave behavior on the shear current based on the fast Fourier transform (FFT) of the SAR images and model calculations is conducted. Preliminary results are also presented in [13,14].

Date	28.08.91	29.08.91	7.09.91
Orbit	2396 as.	2418 des.	2560 as.
Time, UTC	12:16	21:45	19:32
Slant range, km	340	330	370
incidence angle	29°	29°	33°
image size, km	58x215	63x98	55x217
wind speed, m/s	10	8	12
wind direction	260°	280°	290°
wavelength, m	150/150	150/90	150
wave direction	20÷50°/ 80÷90°	135°/ 80÷110°	130÷140°

Table 1

2. The Experiment

The SAR images of the Gulf Stream were acquired on Aug. 28, 29 and Sept. 7, 1991. These days contact measurements by R/V Akademik Vernadsky were also collected. The experiments were performed under westerly winds with speed from 5 to 15 m/s.

The position of the GS temperature front was determined from sea surface temperature (SST) map extracted from NOAA-10 AVHRR IR imagery acquired by ship receiving station in APT regime. The contact measurements were carried out from the R/V crossing the current in direction perpendicular to the front with measurements of the parameters of upper ocean and

atmosphere boundary layer. They had been conducted within the SAR images.

The ALMAZ-1 SAR surveys were planned such way that the SAR images covered both the northern and southern sides of the GS. It allowed to image front signatures and study spatial inhomogeneity of surface waves due to interaction with strong current. Tab.1 summarizes the parameters of collected SAR images and weather/sea state conditions.

The ALMAZ-1 SAR allowed to observe long surface waves [15]. To investigate them, SAR image spectra have been calculated. Each spectrum represents squared modulus of FFT transform of radiance distribution within an elementary 128x128 subscenes (pixel 10x10 m). Final spectrum estimates were smoothed over scene containing $7 \times 7 = 49$ subscenes (9x9 km) with the subsequent smoothing on squares 3x3 in k-space, that provided ~900 degrees of freedom and corrected by SAR impulse response function [15].

3. SAR Observations of Evolution of Wave Field

Experiment Aug. 28, 1991. Fig.1 shows the scheme of the experiment as a composition of NOAA AVHRR IR image and smoothed ALMAZ-1 SAR image. The GS thermal front separates cold shelf waters (24°C, dark) and warm waters (28-29°C, bright). The location of a zone with maximum temperature gradients coincides rather precisely with a zone of maximum of current speed.

According to the ship observations, on the southern side of the GS there was the mixed wave field consisting of wave systems traveling in the NE sector. On the northern side only one system of NNE direction was observed [13]. The SAR image spectra presented in Fig.1 illustrate the basic peculiarities of wave field. A close inspection of spectra in Fig.1 shows that wave field south off the jet consists of two wave systems, A and B, and on northern side of the GS only one wave system A prevails. Both systems had wavelength ~150 m. On the northern side of the current the SAR image spectra have of one-peak (system A) while on the southern side spectrum angular width increases due to presence of two wave systems. At the same time the spectra have higher energy level on the northern side of the GS, that indicates wave concentration in this part of current.

The local maximum A is observed on all spectra and corresponds to waves crossing the current. The maximum B registered only on the southern side, can be referred to waves reflected by the GS. This effect is confirmed by wave ray model calculation performed for an uniform wave field south off the GS with a wave vector corresponding to system A (Fig.1a). It shows that due to refraction the background surface wave field separated on two wave systems (A and B) depending on a local wave incidence angle. In southern part of the SAR image the trajectories are crossed, that corresponds to a superposition of waves. Only system A penetrates on northern side of current, where SAR has imaged unimodal wave field. The reflection of waves occurs to the west of the area imaged by the SAR where a local incidence angle is greater due to curving of a jet. Wave rays calculations presented in Fig.1b explains the absence of wind wave system on the SAR image. Really, the waves directed along wind were deviated by the current that forms shadow area. At the same time locally generated developing wind waves probably are not resolved by the SAR.

Experiment Aug. 29, 1991 was carried out at conditions similar to previous day at moderate westerly wind of 5-11 m/s. In Fig.2 the smoothed SAR image overlaps the NOAA AVHRR IR image. The observable thermal structure is less pronounced that was caused by influence of cloudiness. The GS temperature front divides core warm waters ($T_w=28^\circ\text{C}$) and more cold shelf water ($T_w=25^\circ\text{C}$). The right up corner fragment illustrates general structure of SST field with thermal front marked by a solid line.

The sample of SAR image spectra reflects the basic characteristics of waves field variability. On the northern periphery of the GS two wave systems are observed, to which the spectral maximum A and B correspond. The waves

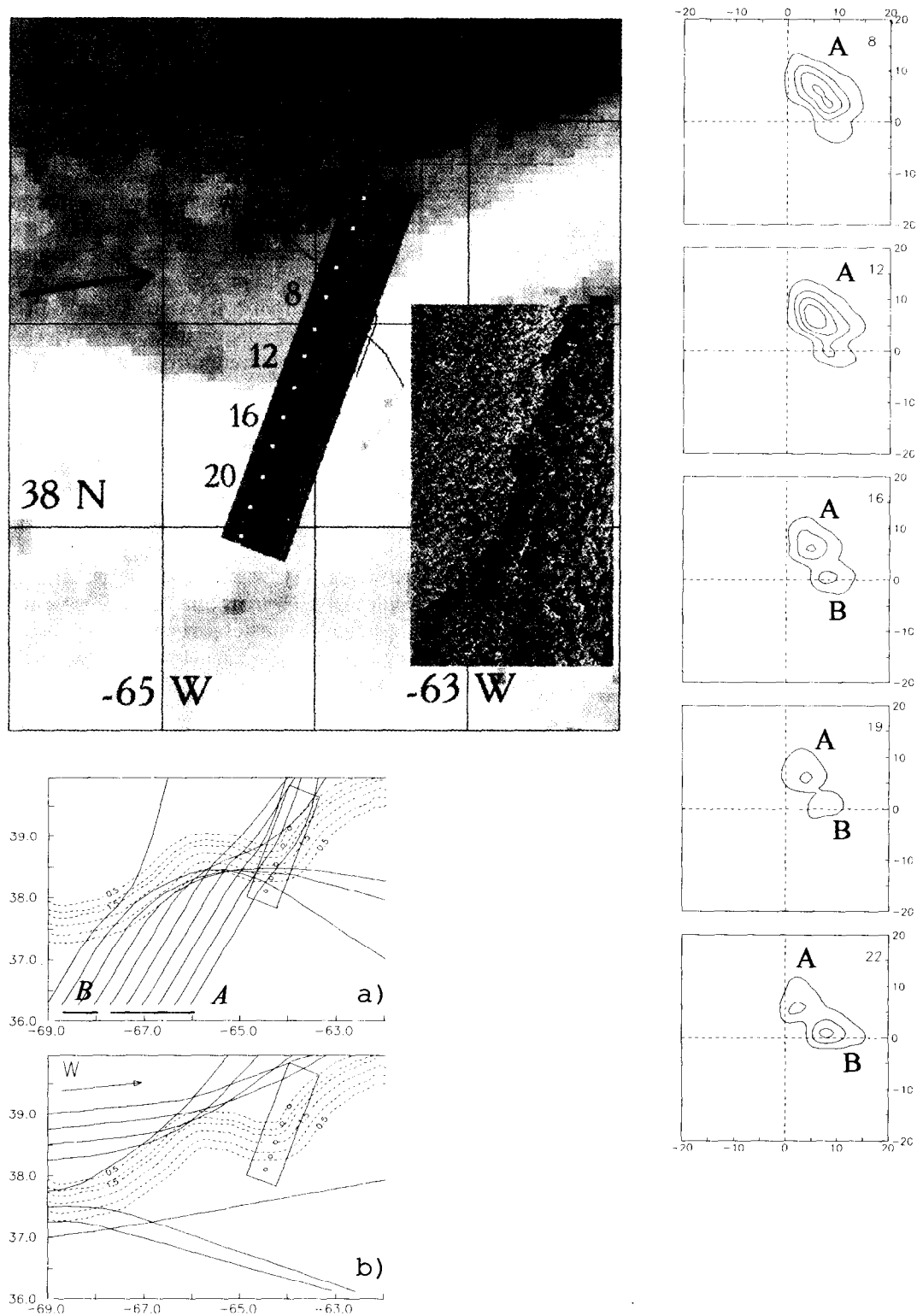


Fig. 1. Scheme of experiment of Aug. 28, 1991 as a composition of the ALMAZ-1 SAR image (12:16 UTC) of the Gulf Stream and NOAA AVHRR IR image (08:00). Also shown are the numbers and positions of subscenes where SAR image spectra were calculated, the wind direction and ship tracks. The southern part of the SAR image is presented in detail. At the right, sample of SAR image spectra. Hereafter, discreteness in wavenumber is 0.005 rad/m, isolines are drawn in $0.2S_{max}$, where S_{max} is the maximum level in this series of spectra and 180° -ambiguity in wave direction is eliminated using ship observations. The bottom plate represents model surface current field (hereafter current velocity isolines are drawn in 0.5 m/s), wave rays of systems *A* and *B* (a) and trajectories of wind waves (b). Also shown are the SAR image frame and SAR image spectra points, arrow marks wind direction. Model current is constructed by using the cross current profile measured along the track #16.

A (1–150 m) propagating in the SE direction are visible in all spectra and cross the current without reflection. Spatial non-uniformity of wave field is formed basically by wave system B. Characteristic wavelength of these waves (90 m) is smaller than that of system A. They were observed only on the northern side of the GS and were not observed in the area of current strengthening.

The peculiarities of wave field are qualitatively explained by wave packet kinematics on a non-uniform current. Fig.2a,b shows model surface current field and wave rays for wave system B (a) and A (b). Trajectories of system B were calculated for a spatially uniform background wave field directed along wind direction. Due to refraction on the meander located at 38.5° latitude, wind system divides on two subsystems deviating accordingly to the north and to the south of jet. However, unlike the previous day, only the southern part of the SAR image is in a zone of shadow where the energy of wind waves is much lower background. As a result wind wave system is not stand out against system A in the SAR image spectra in Fig.2. Wave rays of system A (Fig.2b) finds out weaker influence of current on the trajectories of packets. It is caused by smaller incident angle and greater wavelength as compared to system B.

The concentration of waves on the northern periphery of the GS is proved by increase in ship heave variance and agrees with spatial changes of wave energy inferred from the SAR image spectra [14]. This also suggests that growth of energy is caused by spatial concentration of waves of system B.

Experiment Sept. 7, 1991 was carried out at moderate westerly winds (11–15 m/s). In difference from the previous days, the SST field had complex character, caused by current instability. As follows from Fig.3 the SAR image covers a zone of evolving GS disturbance, thus its northern part appears is on a forward front of the warm waters tongue.

Experimental scheme is shown in Fig.3 as a composition of the SAR image of Sept. 7 and NOAA AVHRR image of Sept. 4. To estimate possible displacement of the front during 3 days separating the moments of ALMAZ-1 and NOAA surveys, the coordinates of points are drawn in which the R/V crossed thermal front on Sept.6 and 7. Referring to Fig.3, we find only small changes in spatial location of the GS front, that allows to use its position for analysis data collected on Sept.7. At the same time, one can expect that used earlier hypothesis of constant cross current speed profile will be not valid in conditions of a complex configuration of the front, connected with current instability. Nevertheless, we have performed wave calculations with model current field built using the above assumption.

Fig.3 also presents SAR image spectra. All of them has local maximum corresponding to waves propagating in the SE direction. They crossed current keeping practically constant wavelength (150 m) and direction (135 $^{\circ}$), that agrees with a picture of wave rays which look like quasi-parallel lines. It results from mutual orientation of waves and current when the rays penetrate into a jet along a normal to the front, and so refraction effects are minimum.

At the same time, decrease in energy of SAR image spectra on the southern side of current pays attention. This effect is not explained with simplified surface current scheme as a flat parallel jet following configuration of the thermal front.

4. Front Signatures on the SAR Images

The analysis of the SAR images has allowed to reveal a number of features associated with current structure in the GS frontal zone.

Experiment Aug.28, 1991. Fig.1 shows an enlarged fragment of the southern part of the SAR image which reveals contrast boundary oriented parallel to the temperature front and separating the areas with different backscatter level. This day ship measurements were performed along the track located outside of the fragment, that doesn't allow to interpret the SAR image reliably. Apparently its origin may be attributed to the difference of atmospheric boundary layer stability over waters with different temperature. Attention also pays bright linear-like structure located to the south of considered boundary on a distance of ~5 km and parallel it. Similar features were frequently observed by remote sensing technique in the GS in close vicinity of current convergences [1]. Under certain conditions, the waves experience intensification here and cause sea surface roughness increase and give increased backscatter.

Experiment Aug.29, 1991. Let us consider in detail the observations of linear structures based on data of Aug.29, when the ship measurements were carried out in the area covered by the SAR image (see Fig.2). The SAR image presents two strips having negative (A) and varying (B) contrast. They are oriented in parallel to thermal front, and strip B perfectly coincides with its location. Within line A the level of radar backscatter is lower than background one. At the same time, line B posses varying radar contrast. the western part of this strip looks as bright feature, the eastern one has negative contrast.

For interpretation of these structures we use the data of ship measurements, collected during several hours before satellite survey. When R/V was crossing the strips A and B oil slicks and sargassum accumulations were visually observed that indirectly indicated on the presence of current convergence [14]. Mentioned above attributes allow to

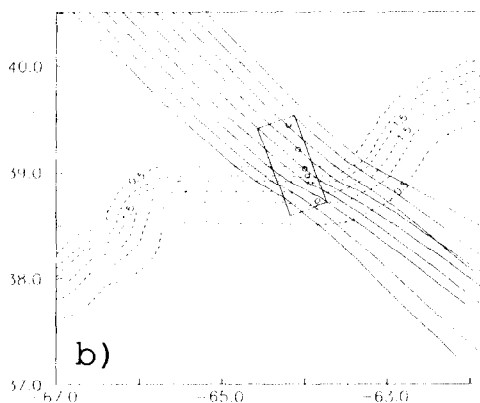
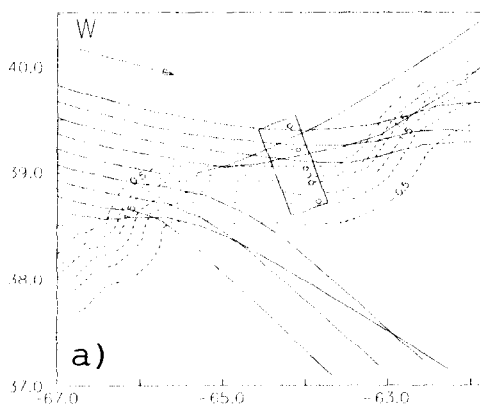
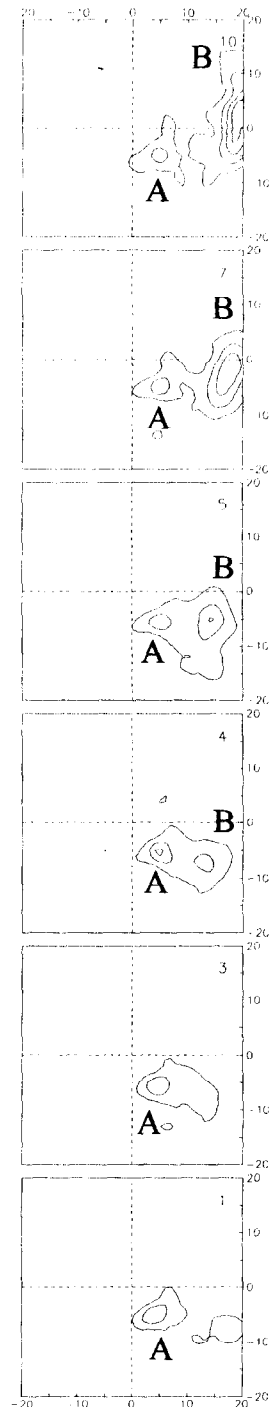
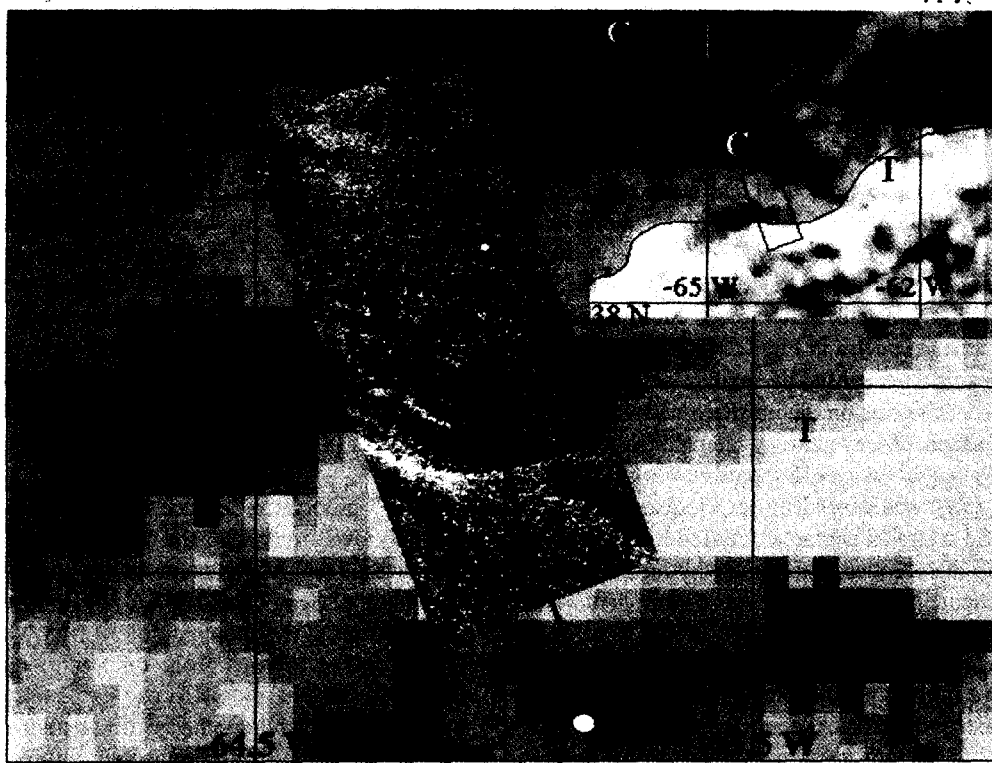


Fig. 2. Scheme of experiment on Aug. 29, 1991 as a composition of the ALMAZ-1 SAR image (21:45 UTC) and NOAA AVHRR IR image (06:36). Also shown are the ship track and the numbering of SAR image subscenes used for spectra calculations. The upper-right plate displays general viewing of the thermal front. The symbols A and B mark linear features, thermal front (T), clouds (C) and the test site (E) where in-situ wave measurements were collected. At right, sample of SAR image spectra. The symbols A and B mark local maximum of wave systems. The bottom plate presents reconstruction of surface current field, wave rays of system B (a) and wave trajectories of system A (b).

interpret dark strips on the SAR image as expressions of current convergence, the negative contrast of which can be explained by ripple damping due to organic films.

Distinction in radar signatures of structures A and B pays attention. Distance between strips was a few kilometers, and they were observed at the same wind conditions. The measurements show that in a vicinity of the line B strong cross current shear occurred which was absent in vicinity of line A [14]. Thus we concluded that the negative contrast of the strip A is of slick origin, and the contrast of the line-like feature B is determined as by accumulation of floating substances including sargassum (which usually aligned along current boundaries in the GS frontal zone) in convergence zone, as well as by wave interaction with both convergence and current shear. This is the possible reason of brightness change along the strip B.

The contrast strips, being radar manifestations of convergence structures, were frequently observed at weak and moderate winds [3]. The signatures of the convergence structures are determined by wind speed. At a weak wind the effect of pollution accumulation prevails, that results in slicks with negative radar contrast. With wind growth the surface films are destroyed, and the determining factor becomes concentration of wave energy in convergence zones that forms bright lines due to roughness increase. If convergence acts along with cross current velocity shear the resulting radar signatures can be more complicated. Under strong winds all surface signatures disappear. In general case, the radar contrasts will depend on wind velocity, radar viewing geometry, components of current shear tensor and surface films or substances concentration.

Experiment Sept. 7, 1991. Increase of wind and waves strengthening destroys linear-like structures which are not visible on the SAR image acquired on Sept. 7 (Fig. 3). Its basic peculiarity are linear structures in the image northern part located in zone of the forward front of warm water tongue of the GS disturbance. Its development is accompanied by the formation of convergence zone due to warm water advection toward slowly moving shelf waters. The local amplification of waves owing to convergence action forms bright SAR feature oriented along the convergence front (1) in the NW-SE direction (enlargement to Fig. 3). To the north from it wave-like disturbances (2) oriented perpendicularly to the front are seen. Characteristic distance between strips is a few km. Probably, they result from intensive interaction between warm and cold waters displaying an unstable current field in evolving GS disturbance accompanied by generation of signatures look like internal wave manifestations. We shall note, that to the south of front where, probably, the currents are small these disturbances are absent. The similar structures in a warm ring of the GS (so-called "mottled texture") were imaged earlier by the SEASAT SAR [1].

5. Summary and Conclusions

The observations of the GS frontal zone were performed with ALMAZ-1 SAR and from board of the R/V Akademik Vernadsky. Low orbiting ALMAZ-1 satellite provided rather small values of R/V ratio, therefore the contribution of SAR nonlinear effects was minimum [15]. This allows to determine wavelengths and wave directions by FFT processing of SAR images.

The theory of interaction with jet current [4] predicts an opportunity of wave reflection and trapping by a flow. Using spaceborne SAR, we observed wave reflection by fair shear current, that proves to be true by SAR image spectra analysis and wave trajectories calculations. The reflection of waves appeared as a combined result of the current shear and upstream curving of the GS. Wave refraction forms local areas of their intensification and weakening. The concentration of waves at the current boundaries due to superposition of several wave systems may produce a danger to ships, among them due to significant broadening of the angular spectrum. The operative control of such situations has practical interest and possible only with the help of a spaceborne SAR.

The convergence strips at the current boundaries are characteristic of the ocean fronts. There is a number of processes forming different sign radar signatures. Surface films and pollution accumulations damps the Bragg waves backscattering radar signal. Moreover energy of waves concentrates in convergence zones with possible occurrence of stochastic wave strips. The sea surface roughness growth induced by waves steeping and chaotic breaking increases radar backscatter, and after occurrence of a bright strip an appearance of a dark one is possible. The relative contribution of these two effects depends on wind speed, surface films characteristics, and current non-uniformity. At weak winds (<5-8 m/s) the film effect prevails, and convergence strip had negative radar contrast. With wind increase the sea surface films will be destroyed, and the convergence zones get positive contrast. At a strong wind the efficiency of both mechanisms falls and the waves forming the sea surface roughness are in balance with a local wind.

Comparison of the SAR images and contact data has shown that linear-like structures were oriented along thermal front and delineated the zones with maximum current gradients [14]. The convergence strips delineated by organic films had negative contrast (were black on the SAR image) at wind speed up to 8 m/s (Fig. 2). Another type of strips on a distance of several km from those became visible in the SAR image due to significant local cross current shear. It was displayed as line with varying radar contrast. Its value and sign depended on mutual orientation of

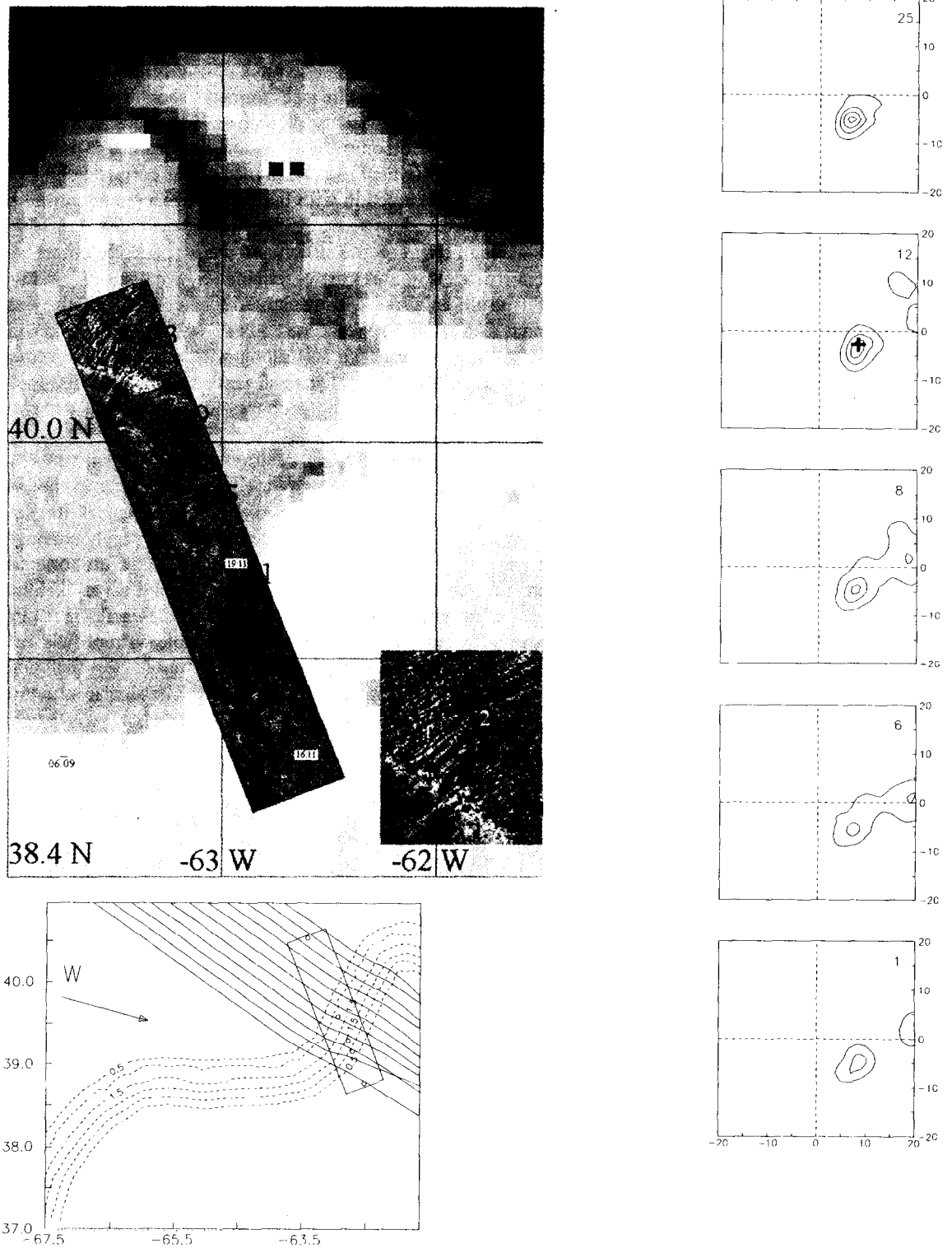


Fig. 3. Scheme of experiment of Sept. 7, 1991 as a composition of the ALMAZ-1 SAR image (19:32 UTC) and NOAA AVHRR IR image of Sept. 4, 91. Also shown are the ship track, numbering of SAR image subscenes used for spectra calculations and the GS front location on Sept. 6 and 7 according to ship data. The lower plate presents the northern part of the SAR image with convergent front (1) and mottled texture (2). At right, sample of SAR image spectra, symbol + marks the position of spectrum maximum according to ship-based radar data. The bottom plate represents model wave packet trajectories overlaid on the surface current field.

waves, current gradients and SAR look direction. On the SAR image acquired at 12 m/s the liner-like structures near the thermal front were not observed (Fig.3). But there were features coinciding with convergence front caused by warm waters advection into shelf waters, and the wave-like structures orthogonal to the front. The nature of “wavy” signatures crossed this front is not clear and requires additional investigations.

References

- [1] Spaceborne SAR for oceanography: 1981, Eds: Beal, R.C., I. Katz & P. De Leonibus, The Johns Hopkins University Press.
- [2] Johannessen, J.A., R.A. Shuchman, G. Digranes, D.R. Lyzenga, C. Wackerman, O.M. Johannessen & P.W. Vachon: 1996, Coastal ocean fronts and eddies imaged with ERS-1 synthetic aperture radar, *J.Geophys.Res.*, **101**, C3, 6,651-6,667.
- [3] Beal, R.C., V.N. Kudryavtsev, D.R. Thompson, S.A. Grodsky, D.G. Tilley, V.A. Dulov & H.C. Graber: 1997, The influence of the marine atmospheric boundary layer on ERS-1 synthetic aperture radar imagery of the Gulf Stream, *J.Geophys.Res.*, **102**, C3, 5,799-5,814.
- [4] Kenyon, K.E.: 1971, Wave refraction in ocean currents, *Deep Sea Research*, **18**, 1023-1034
- [5] Gutshabash, E.Sh. & I.V. Lavrenov: 1986, Swell transformation on Agulhas current, *Izvestiya Russian Acad. Sci, Atm. and Oceanic Phys.*, **22**, N 6, 643-648, (in Russian).
- [6] Barnett, T.P., F. Kelley & B. Holt: 1989, Estimation of the two-dimensional ocean current shear field with a Synthetic aperture radar, *J.Geophys.Res.*, **94**, C11, 16,087-16,095.
- [7] Sheres, D., K.E. Kenyon, R.L. Bernstein & R.C. Beardsley: 1985, Large horizontal surface velocity shears in the ocean obtained from images of refracting swell and in situ moored current data, *J.Geophys.Res.*, **90**, C3, 4943-4950.
- [8] Beal, R.C., T.W. Gerling, D.E. Irvine et al: 1986, Spatial variations of ocean wave directional spectra from SEASAT SAR, *J.Geophys.Res.*, **91**, C2, 2433-2449.
- [9] Mapp, G.R., C.S. Welsh & J.C. Munday: 1985, Wave refraction by warm core rings, *J.Geophys.Res.*, **90**, C4, 7,153-7,162.
- [10] Irvine, D.E. & D.G. Tilley: 1988, Ocean wave directional spectra and wave-current interaction from Shuttle Imaging Radar-B synthetic aperture radar, *J.Geophys.Res.*, **93**, C12, 15,389-15,401.
- [11] Kudryavtsev, V.N., S.A. Grodsky, V.A. Dulov & A.N. Bol'shakov: 1995, Observation of wind wave field in the Gulf Stream frontal zone, *J.Geophys.Res.*, **100**, C10, 20,715-20,727.
- [12] Grodsky, S.A. & V.N. Kudryavtsev.: 1993, Observations of wind waves refraction in the Gulf Stream frontal zone, *Izvestiya Russian Ac. Sci, Atm. and Oceanic Phys.*, **29**, N 1, 113-122 (in Russian).
- [13] Grodsky, S.A., V.N. Kudryavtsev, A.Yu. Ivanov, V.V. Zaitsev & D.M. Solov'ev: 1997, Interaction of surface wave with the Gulf Stream according to ALMAZ-1 SAR data, *Earth Obs. & Rem. Sens.*, **14**, 393-405.
- [14] Grodsky, S.A., V.N. Kudryavtsev & A.Yu. Ivanov: 1996, Investigation of the Gulf Stream frontal zone with use of ALMAZ-1 SAR and contact ship data, *Issledovanie Zemli iz Kosmosa (Earth Research from Space)*, N 6, 59-70 (in Russian).
- [15] Wilde, A., C. Brüning, W. Alpers, V. Etkin, K. Litovchenko, A. Ivanov & V. Zajtsev, 1993: Comparison of ocean wave imaging by ERS-1 and Almaz-1 synthetic aperture radar, *Proc.2nd ERS-1 Symposium*, Hamburg, Germany, 11-14 Oct. 1993, (ESA SP-361), 239-245.

BLACK SEA COLD INTERMEDIATE WATER MASS VOLUMETRIC STRUCTURE AND ITS VARIABILITY

L.I. Ivanov¹, S. Besiktepe²

¹ Marine Hydrophysical Institute / National Academy of Sciences of Ukraine, 2, Kapitanskaia, Sevastopol, Crimea, UKRAINE, leonid@alpha.mhi.iuf.net

² Institute of Marine Sciences / Middle East technical University, Erdemli, Icel, TURKEY, sukr@solli.ims.metu.edu.tr

Abstract.

The focus is on the temperature/salinity analysis of the CIW, based on recent data sets, depicting normal, severe and mild winter conditions in the Black Sea since 1984 (more than 50 hydrographic surveys). The period was characterized by gradual cooling of the pycnocline waters in response to three major cooling events: 1985, 1987 and 1993. These cooling events resulted in 6 - 8 years period temperature fluctuation superimposed over linear trend. On the average, the CIL lower boundary was located at 87 m, and the overall range of its vertical excursions was about 25 m with the shallowest position in 1984-85 and the deepest position in 1995. Such variations in position of the boundary of the layer yield 8750-km³ variation of its volume. Studies of spatial variability of the CIL volumetric structure revealed that these variations are pre-determined by stratification of the upper layer.

1. Introduction.

The Cold Intermediate Water (CIW) mass in the Black Sea constitutes the Cold Intermediate Layer (CIL), commonly characterized by waters with temperature $T < 8^{\circ}\text{C}$. The CIL core, or the layer of minimum temperature, is observed within a depth range of about 30-80 m overlying the main pycnocline, where vertical stratification is maintained basically by the salinity gradient.

A profound understanding of the sources, formation and spreading mechanisms of the CIW mass is essential for better understanding of the impact of surface mixing on transport of pollutants and of organic matter. Also, the CIL exerts some controls on the biogeochemical cycling of the region. Intensity of the CIW formation is directly connected with the level of biological productivity through new production resulting from the entrainment of nutrients from the pycnocline into the euphotic zone.

First explanations of the CIL origin were suggested in 1930's by Knipovich [1] and Zoobov [2] who described the layer as a remnant of an upper mixed layer formed due to cooling and convection during previous winter. Later Kolesnikov [3] introduced an idea of advective nature of the CIW. Filippov [4] and other scientists [5, for example] supported the hypothesis. According to their notion, cold waters that replenish the CIL are formed mostly in the northwest part of the basin, where winter conditions are the most severe. However, with the CTD probes becoming available, CIW renewal was registered also within the cyclonic gyres in the central part of the sea [6], where the CIL is relatively thin, and the main pycnocline shoals to 30 - 40 meter depths.

The basic debatable in the past issue related to CIW formation may be defined as 'What is the main CIW source region?' To answer this question, formation and distribution of the CIL were analyzed in [7] on the basis of the basin wide CTD data collected in September 1991 and July 1992. A comparison of physical characteristics of the CIL showed the formation of considerable amount of CIL during the winter of 1991-1992. The results revealed that the CIL of the Black Sea forms over the northwestern shelf area, at the center of the cyclones as well as in the convergence zone. A basic conclusion derived from the comparative analysis of the

Black Sea volumetric T,S diagrams for different years and for different regions is that water formed due to winter convection within the vast area of cyclonic circulation in the central part of the basin, in terms of water masses, does not replenish CIL of the convergence zone. In general, CIW is of 'local' formation if the term 'local' is used to discriminate areas of cyclonic and anticyclonic circulation but not in terms of their *in situ* formation (figure 1). Though some indications of the penetration of a part of shelf waters into anticyclonic regions were discovered, the role of this mechanism is relatively small.

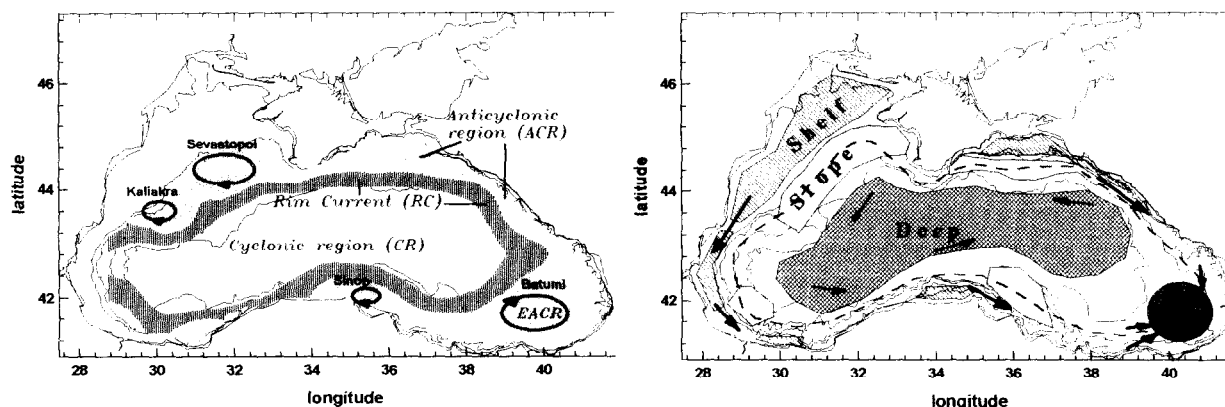


Figure 1. Schemes of Black Sea circulation (left) and of CIW formation (right) [7].

For a cold winter, formation of the CIW within anticyclonic eddies yield for more than half of the entire CIL volume. At the same time, cooling is more 'effective' over the shelf and in the central part of the sea, where heat losses per unit volume, apparently, exceed such values for the anticyclonic areas.

A certain gap in the studies of the CIL origin has been a negligence of quantitative descriptions of its structure. Few attempts have been made in the past to give quantitative estimates of CIW mass volume. The only reference that had been found in the literature was an estimate of the average summer CIL volume reported by Glazkov [8]. It is 16035 km^3 . However, CIL volume calculated for September 1991 and July 1992 was 18361 km^3 and 19888 km^3 respectively [7]. A comparison of these estimates implies an appreciable interannual variability in CIL volumetric structure, therefore the objectives of this paper is to reveal such temporal changes, their magnitude, dominating time scales as well as basic mechanisms responsible for spatial variability in CIL thickness / volume.

2. Data and methods.

In the present study the focus is on the volumetric temperature / salinity analysis of the CIW based on recent data sets depicting normal, severe and mild winter conditions in the Black Sea since 1984. These are more than 50 hydrographic surveys of the Marine Hydrophysical Institute and of the Institute of Marine and Atmospheric Science / Middle East technical University. General description of the data can be found in [9]. Temporal and spatial variability in CIW properties is analyzed versus salinity and density coordinates. Traces of winter mixing events appear well preserved in temperature-salinity structure, particularly due to the peculiarities of the Black Sea pycnocline where temperature acts as a passive tracer with a smaller contribution to density as compared to salinity.

For the period starting from 1984 and until now, we have been able to delineate temperature fluctuations within the pycnocline. The series is shown in figure 2. The temperatures were calculated as mean temperatures for a survey area for fixed salinity ranges (0.1). Such non-traditional approach was used to filter, to an extent possible, random bias in temperature. Though not all of the cruises provided basin wide coverage there is no much scattering in temperature variability revealing that mean values do not depend much upon survey area.

Actually, this is not a surprising result because main differences in temperatures for isopycnal surfaces are between cyclonic gyre and anticyclonic eddies [7]. The horizontal scale of the transition zone associated with the Rim Current is about 20 to 40 kilometers. A spatial scale of the anticyclonic eddies range from 30 to 70 km [10], and most of the surveys were designed to reveal spatial inhomogeneity of oceanographic fields within the

Rim Current and to resolve basic mesoscale features. Therefore estimates of averaged temperatures even for surveys of relatively small regions or for a cross current transects are close to basin wide averages.

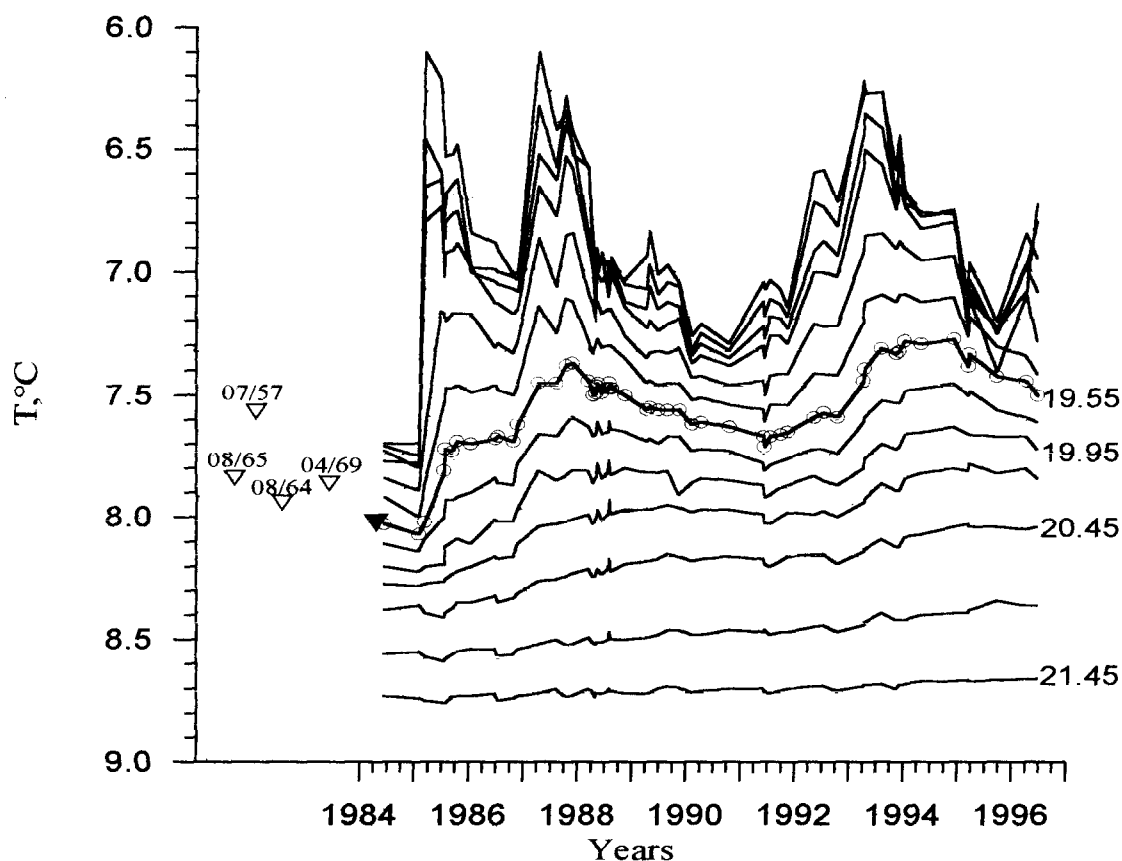


Figure 2. Temperature variations at a fixed salinity ranges, 18.6-18.7, ..., 21.4-21.5. Circles at 19.55 reveal timing of the surveys, open triangles reveal temperature at 19.55 salinity in some previous years (dates shown).

3. Results.

Vertical distribution of the magnitudes of temperature oscillations within the pycnocline (figure 2) indicates that convection events have limited effects in modifying the structure of the main pycnocline on a seasonal time scale. However, long-term (5 to 10 years period) fluctuations of the thermal structure of the pycnocline are well recognized within the whole pycnocline layer.

The period starting from 1984 and until now was characterized by gradual cooling of the pycnocline waters in response to three major cooling events: 1985, 1987 and 1993 and, on the average, temperatures were lower than in 60's. Also, partial renewal of water that form the core of the cold intermediate layer (the level of 14.2-14.8 isopycnal surfaces) took place in 1989, 1991 and 1992. Hence, residence time of the CIL core was about two years. Seasonal and short-term (about two years) fluctuations are confined to the upper pycnocline (salinity lower than 19.0-19.5) and are negligible in terms of modifying temperature structure of deeper layers.

The major cooling events resulted in 6 - 8 years period temperature oscillations superimposed over linear trend. They are well noticeable practically in the whole pycnocline layer. The magnitude of the oscillations decreases with increasing depth (figure 3). The dependence of the magnitude upon depth was then used to estimate mean value of the mixing coefficient. Theoretical decrease of the magnitude was modeled in accordance with the law of thermal wave propagation from a harmonic source. The result of the best fit is shown in figure 3. It was achieved with $k_r \div 0.9 - 1.2 \cdot 10^{-5} m^2 \cdot s^{-1}$ (depends upon the period chosen for the evaluation). The observed temperature fluctuations in the middle and lower pycnocline are a result of a combined effect of vertical mixing (diffusion) and lateral advection [11]. Indeed, deviations between the two

curves in figure 3 imply more effective (compared to theoretical) penetration of the cooling signal into the lower pycnocline (salinity > 20).

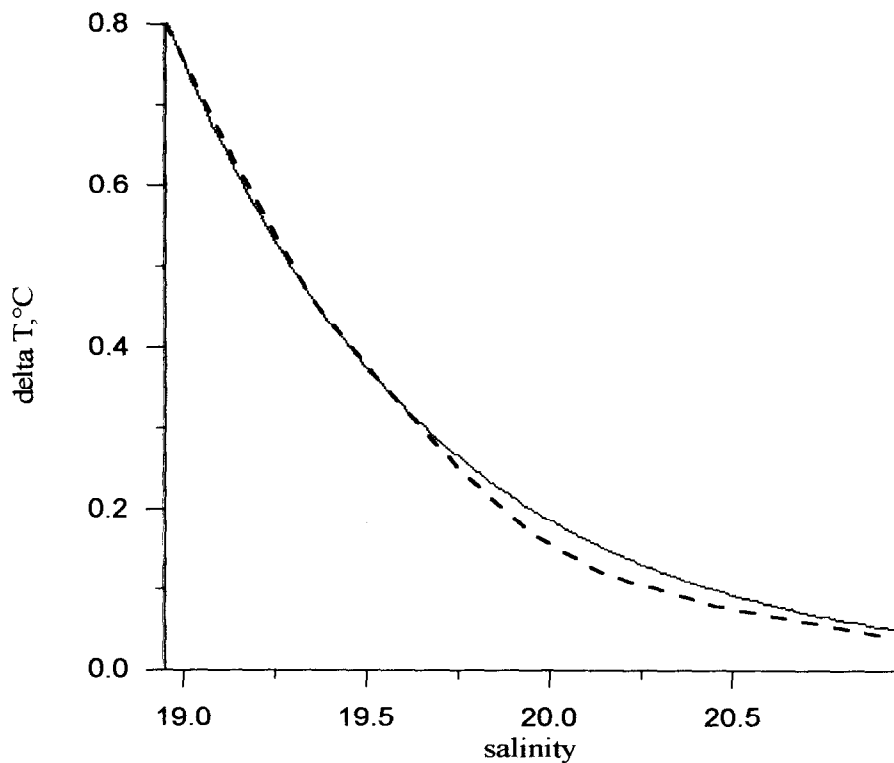


Figure 3. Decrease of the magnitude of 8 years period temperature fluctuations in the pycnocline according to data shown in figure 3 (dashed line) and 'theoretical' (solid line).

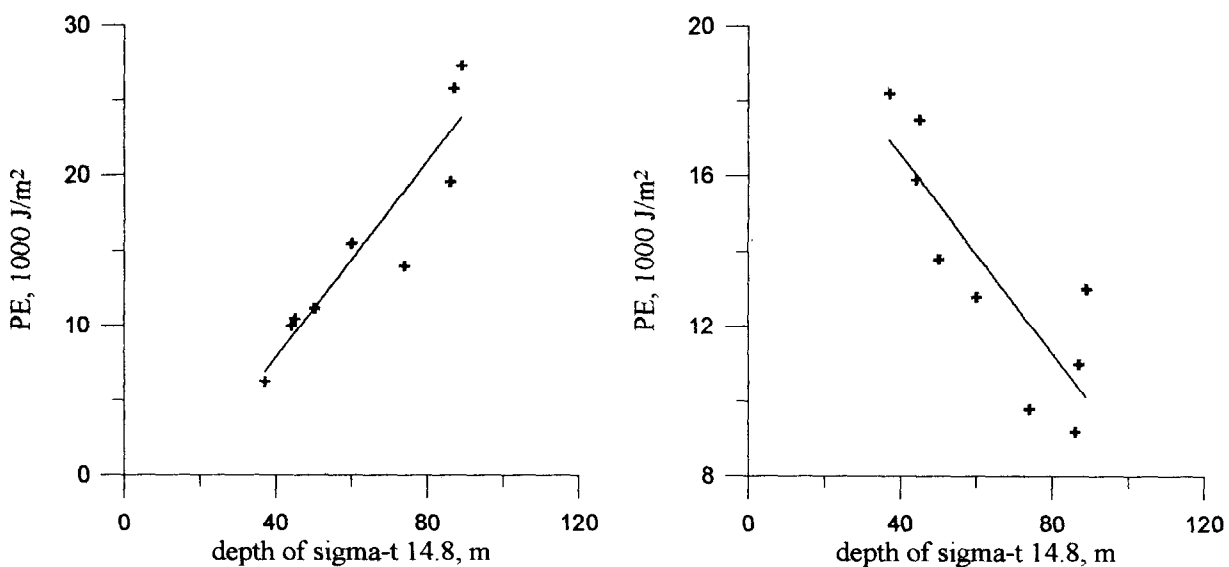


Figure 4. Potential Energy hypothetically spent to mix the water column with real stratification of October 1992 down to 14.8 sigma-t surface (left) and down to 70 m (right) at different stations, which positions in the system cyclon-anticyclon are characterized by position of the 14.8 sigma-t.

On the average, the CIL lower boundary was located at 87 m, and the overall range of its vertical excursions was about 25 m with the shallowest position in 1984-85 and the deepest position in 1995. Such variations in position of the boundary of the layer yield 8750 km³ variation of its volume. To check this estimate we calculated the total CIL volume for the summer of 1984. It was about 11600 km³ or about 8400 km³ less than in 1992. No seasonal variations at the level of the CIL lower boundary can be seen from the data.

There is no linear relationship between winter meteorological conditions and the total CIL volume because of a one to two years delay in response of the mid pycnocline to cooling at the surface [7,10]. However, cooling conditions determine the amount of the new portion of the water mass that forms the CIL core. In 1992, the volume of the newly formed waters made up about 4000 km³ for the anticyclonic area. This constituted 57 per cent of the CIL total volume for this area. For the cyclonic region, same value was 2700 km³ (approximately, 50 per cent of the total CIL volume). The largest portion of newly formed waters characterized the T,S diagram for the Batumi anticyclonic region.

Using CTD data of one of the surveys conducted in the northwest part of the basin in October 1992 we calculated values of a Potential Energy hypothetically spent to mix the water column with existing stratification down to a certain level. The results were then compared with the real data, which describe situation after the winter of 1992-93. Calculations have been done to disclose basic mechanism responsible for spatial variations in thickness of the newly formed portion of the Cold Intermediate Layer or in the depth of the CIL core. The results are shown below in the figures 4 & 5. It can be easily verified from figure 4 that about the same amount of energy (~ 10000 J/m²) should be spent to mix the water column down to 40 m in a cyclonic gyre (depth of the 14.8 sigma-t surface is about 40 m) and down to 70 m in an anticyclonic eddy (depth of the 14.8 sigma-t surface is about 80 m).

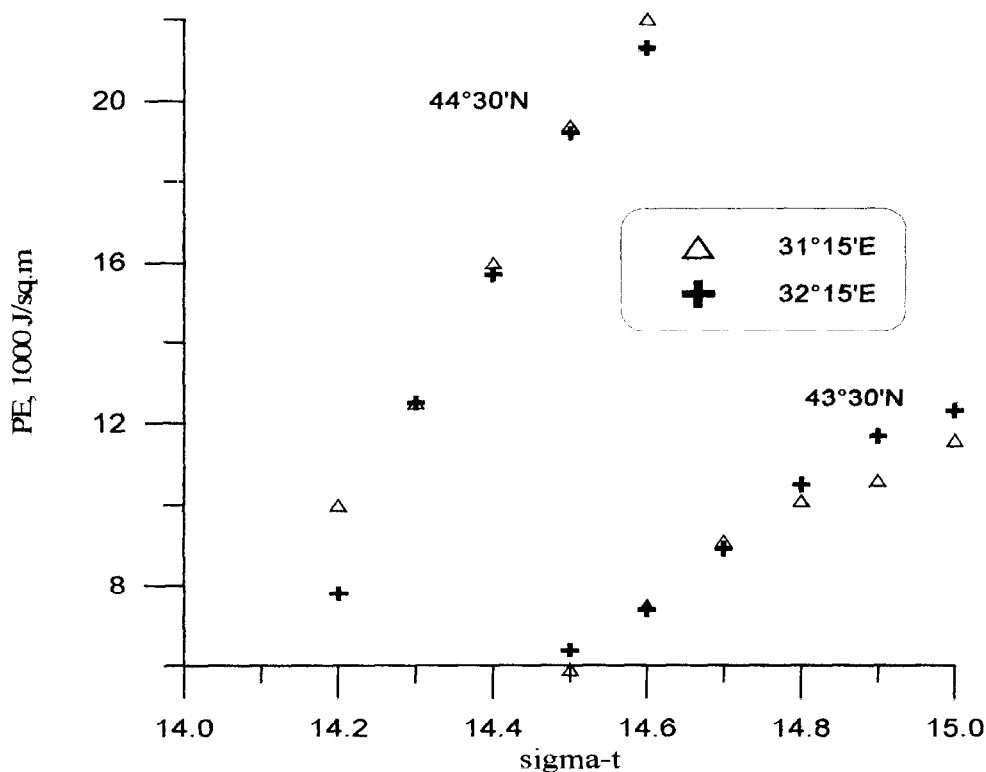


Figure 5. Potential Energy hypothetically spent to mix the water column with real stratification of October 1992 down to selected sigma-t surfaces in the center of the western cyclonic gyre (43°30'N) and over the slope west off Crimea (44°30'N).

According to CTD data collected in April of 1993, convective mixing during the winter of 1992-93 penetrated, approximately, down to 14.8 sigma-t surface (or down to 40 m) in the central part of the basin and down to 14.3 sigma-t (corresponds to 70-80 m depths) in the areas of anticyclonic eddies [11]. Same result could be predicted from the fall data with known estimate of energy spent for mixing. Indeed, figure 5 shows that if about 10-12·10³ J/m² were spent convective mixing would penetrate down to 14.8-15.0 sigma-t in the

center of the western cyclonic gyre and down to 14.3 sigma-t over the slope (area of anticyclonic circulation). Actually, this reveals that even with a spatially uniform energy flux characteristic inhomogeneity in CIL thickness is formed due to spatial differences in stratification of the upper layer.

4. Acknowledgments. The study has become possible through the support coming from the EC INCO COPERNICUS Project (IC15CT96-113). Preparation of the pooled data sets was done with support coming from NATO (TU Black Sea Project and Linkage Grant, ENVIR.LG 591190).

5. References.

- [1] Knipovich, N.M. (1932) The hydrological investigations in the Black sea, *tr. AzovoChernomorsk. Nauchnopromysl. Eksped.*, **10**, 1-274. (in Russian).
- [2] Zoobov, N.N. (1938) *Marine waters and ice*, M.:Hydro-meteoizdat. P.451.(in Russian).
- [3] Kolesnikov, A.D. (1953) Seasonal course of temperature, stability and vertical turbulent heat exchange in the open part of the Black sea, *Tr. Mor. Gydrophys.Inst. USSR AS*, **3**, 3- 13. (in Russian).
- [4] Filippov, D.M. (1965) To the question about the cold intermediate layer in the Black sea, *Okeanologia*, **5**, 635-641. (in Russian).
- [5] Tolmazin, D. (1985) Changing coastal oceanography of the Black Sea. Part I: Northwestern shelf, *Prog. Oceanogr.*, **15**, 217-276.
- [6] Ovchinnikov, I.M., Popov, Yu.I. (1987) Cold intermediate layer formation in the Black Sea, *Okeanologia*, **27**, 739-746.
- [7] Ivanov, L.I., S.Besiktepe, E., Ozsoy (1997). Black Sea Cold Intermediate Layer, in A.Mikaelyan and E.Ozsoy (eds.), *Sensitivity to change: Black Sea, Baltic Sea and North Sea*, Kluwer Academic Publishes, Dordrecht, NATO ASI Series, 253-264.
- [8] Glazkov, V.V. (1970) Volumetric statistical T,S analysis of the Black sea water masses, *Okeanologia*, **10**, 958-962.
- [9] Ivanov L.I., Konovalov S., Melnikov V., Mikaelyan A., et al. (1998) Physical, Chemical and Biological Data Sets of the TU Black Sea Data Base: Description and Evaluation. In: L.Ivanov, T.Oguz (eds.) *NATO TU-Black Sea Project: Ecosystem Modeling as a Management Tool for the Black Sea, Symposium on Scientific Results*. Kluwer Academic Publishes, Dordrecht, NATO ASI Series. V.1, P.11-38.
- [10] Blatov, A.S. (1981) Hydrological structure and energy storage of the Main Black Sea Current eddies, *Meteorologia i Gydrologia* **7**, 86-93.
- [11] Ivanov L.I., Konovalov S., Belokopytov V., E., Ozsoy (1998) Regional Peculiarities of Physical and Chemical Responses to Changes in External Conditions Within the Black Sea Pycnocline: Cooling Phase. In: L.Ivanov, T.Oguz (eds.) *NATO TU-Black Sea project: Ecosystem Modeling as a Management Tool for the Black Sea, Symposium on Scientific Results*. Kluwer Academic Publishes, Dordrecht, NATO ASI Series. Vol.2, P.53-68.

TURBULENT FLOW AS AN OSCILLATORY SYSTEM

A. S. Kartashov

Russian State Hydrometeorological University
S.-Petersburg, Russia, tot@mail.wplus.net

Abstract

Undisturbed state of a fluid flow represents a laminar shift current. Turbulence arises instantly in the whole volume of the current if the Reynold's number exceeds a critical significance. Turbulent perturbations create a new stable state appropriate to specific environmental conditions. It is similar to a direct elastic rod losing stability by the longitudinal load action and acquires a new stable state at the expense of form modification. Elastic deformation of the rod is characterized by a transversal deviation of the rod from initial state and is described by the equation of oscillations. State of the turbulent flow is changed in a similar way if the analogy is correct and it can be described in terms of the oscillatory system model. The specific parameters appropriate to the model should be constructed with use of average physical parameters of the turbulent flow.

Introduction

Turbulence is represented to an observer as a very complicated physical phenomenon of random movement of liquid with irregular chaotic modification of velocity [1, 3]. Statistical parameters of turbulent flow are constructed by average of physical parameters and reveal some natural properties permitting to realize quantitative analysis of the phenomenon [1, 2]. Designing of statistical parameters has the important heuristic significance as a base of adequate language for the turbulence quantitative theory. Search of analogies with the physical systems described by the well investigated mathematical models is one of the possible approaches in this direction. The nature is economical in means and the same principle is realized often in various physical systems. For example the classical oscillatory system model is applied in the most various parts of physics: mechanics, the elasticity theory, the nuclear physics etc.

Given work is an attempt to apply the classical model of the oscillatory system to the stratified turbulent shift flow. This is initiated by the problem to create rather simple and informative model of turbulent regime for the ocean boundary layer which allows to imitate appearance and evolution of the vertical fine structure of hydrophysical parameters as a response on external effects.

1. Deviation of the turbulent flow from undisturbed state.

Let's consider turbulence kinetic energy, b , as initial statistical parameter. The equation of a turbulence energy balance for the quasistationary one-dimensional flow has a kind [1]

$$C_b \frac{\partial}{\partial z} K \frac{\partial b}{\partial z} + G - \varepsilon = \frac{\overline{g\rho'w'}}{\rho}.$$

The equation contains the members circumscribing turbulent diffusion, turbulence generation at the expense of shift instability - $G = u_*^2 \partial u / \partial z$, turbulence dissipation - ε , and source of turbulence connected to buoyancy forces. Here: C_b - numerical constant connecting coefficient of turbulent exchange to impulses K with coefficient of turbulent diffusion of turbulence energy, z - vertical coordinate, ρ - density of water, ρ' and w' - turbulent pulsing of density and transversal current velocity, g - gravity constant.

Coefficient of turbulent exchange by impulse and dissipation rate are determined both by energy of turbulence, b , and local scale of turbulent perturbations of the current l : $K = l\sqrt{b}$; $\varepsilon = C_\varepsilon b^{3/2}/l$. [1, 2]. Scale of turbulence is noted in a linearized kind $l = a(z)z$, where $a(z)$ - numerical factor. Boundary conditions is set for the top of an area of developed turbulence, \bar{z} , and are included kinetic energy of turbulence, b_0 , and its derivative - $(\partial b / \partial z)_0 = 0$. For determination of numerical significances of parameters on the bound the logarithmic asymptotics it is supposed: $K = \kappa u_* \bar{z}$, $b_0 = u_*^2 / C_1$, -where κ - Karman's constant, $C_1 = \sqrt{C_\varepsilon}$ - numerical factor [1, 5]

Normalization of the energy equation in relation to dissipation rate:

$$\frac{2C_b a}{\varepsilon} \left[(1 + \alpha) \frac{\partial (b^{3/2})}{\partial z} + z \frac{\partial^2 (b^{3/2})}{\partial z^2} \right] + (\gamma - 1) = R_f \gamma$$

allows to enter following parameters of similarity: 1) number $\gamma = G/\varepsilon$ describing attitude of generation and dissipation rates; 2) dynamic Richardson's number - $R_f = \overline{g\rho'w'}/\rho$; 3) nonlinearity coefficient of turbulence local scale - $\alpha = (z/a)(\partial a / \partial z)$.

By change of variables: $y = (b/b_0)^{3/2}$, $x = \ln(z/\bar{z})$ - the normalized equation of energy is linearized:

$$\ddot{y} + \alpha \dot{y} + C(\gamma - 1)\varphi^2(x)y = C\bar{R}_f \varphi(x) \exp(x) -$$

where: $C = 1.5C_\varepsilon / C_b a_0^2$ - numerical coefficient, $\varphi(x) = a_0/a$ - function defined by scale factor $a(z)$, $\bar{R}_f = \kappa \overline{g\rho'w'}/\rho u_*^2$ - boundary dynamic Richardson's number, $\kappa = a_0 C_1^{3/2} / a_\varepsilon$ - Karman's constant, $a_0 = a(0)$ - boundary significance of scale factor. Points above the equation designate derivation on a variable x . Function $y(x)$ satisfying to the obtained linear differential equation characterizes deviation of turbulent flow from undisturbed state.

2. Local scale of turbulent perturbations.

The evaluation of nonlinearity coefficient of local turbulence scale can be made with use of outcomes from experimental research of non-stationary phenomena in a viscous stratum of the shift turbulent current [4]. By laboratory experiences it was revealed that in a thin boundary layer enveloping hundred characteristic linear sizes of a viscous stratum, ν/u_* , there are local separations of a stream. Process has statistically certain periodicity [5]:

$$\Delta t = 4.0 \frac{\nu}{u_*^2} \left(\frac{u_* h}{\nu} \right)^{0.83},$$

where h - external scale of the current.

If circumscribed process is settled then energy of turbulence generated on the top of boundary layer should have time to dissipate completely in the whole current during between the explosions: $b_0 = \varepsilon \Delta t$. It is possible to receive a ratio defining scale factor $a(h)$ on the base of the Kolmogorov's law for dissipation:

$$\varepsilon = C_\varepsilon b_0^{3/2} / a h,$$

$$a(h) = 4.0 C_\varepsilon \text{Re}_*^{-0.17} \frac{\sqrt{b_0}}{u_*} = 4.0 \frac{C_\varepsilon}{\sqrt{C_1}} \text{Re}_*^{-0.17}, \quad \text{Re}_* = \frac{u_* h}{\nu}.$$

where h is a lower bound of the boundary layer.

Then it is possible to receive equivalent expression by replacement in the ratio the lower bound h of the developed turbulence area by the upper one, \bar{z} , to definite boundary Reynolds number:

$$a(h) = a_0 \left(\frac{h}{\bar{z}} \right)^{-0.17}, \quad a_0 = 4.0 \frac{C_\varepsilon}{\sqrt{C_1}} \overline{\text{Re}_*}^{-0.17}, \quad \overline{\text{Re}_*} = \frac{u_* \bar{z}}{\nu}.$$

The obtained outcome results in two suppositions important for a case in point.

1. It is possible to assume the parity for scale factor $a(h)$ is executed not only on a lower bound, $z = h$, but also in the whole area of developed turbulence:

$$a(z) = a_0 \left(\frac{z}{\bar{z}} \right)^{-0.17}$$

Then differentiating the last equation we'll discover significance of nonlinearity coefficient of local turbulence scale:

$$\alpha = \frac{z}{h} \frac{\partial a}{\partial z} = -0.17.$$

2) Boundary scale factor can be changed in the limits: $\kappa \sqrt{C_1} \leq a_0 \leq 1$ inside transitional area, $z < \bar{z}$. Local scale of turbulence cannot exceed thicknesses of considered stratum and it gives value for the

upper limit. The lower limit is determined by a logarithmic asymptotics. These restrictions install the boundaries of transitional area of turbulent flow: thickness of viscous stratum - z_0 and upper bound of the developed turbulence area - \bar{z} .

$$\mathbf{Re}_{*0} = (4C_\varepsilon / \sqrt{C_1})^{-1/\alpha}; \quad \overline{\mathbf{Re}}_* = (4C_\varepsilon / C_1 \kappa)^{-1/\alpha}.$$

Thus nonlinearity coefficient of turbulence scale is connected to Reynold's number. It is possible to find Reynold's numbers for boundaries of the transitional area setting numerical evaluations of coefficients as $\alpha = -0.17$, $C_\varepsilon = 0.09$ and $C_1 = \sqrt{C_\varepsilon}$ [1]:

$$\mathbf{Re}_{*0} = 0.09; \quad z_0 = 0.09 \frac{V}{u_*}; \quad \overline{\mathbf{Re}}_* = 640; \quad \bar{z} = 640 \frac{V}{u_*}.$$

Significance of numerical coefficient defining parameter z_0 is confirmed by experimental evaluations [2, 6]. It is possible to consider significance of boundary Reynold's number $\overline{\mathbf{Re}}_* = 640$ as critical significance of a dynamic Reynold's number. Using as law of a resistance as $u_* = 0.05u$ [5] we can receive for critical Reynold's number significance $\mathbf{Re}_{*p} = 12800$ conterminous with significance obtained in classical experience of Reynolds [7].

Indicated analysis of experimental researches gives a basis to consider nonlinearity coefficient of turbulence local scale as independent on a vertical coordinate parameter and installs for it rather reliable evaluation $\alpha = -0.17$. In that case function $\varphi(x)$ has a kind $\varphi = \exp(-\alpha x)$ and the equation of energy takes the form equivalent to the equation of forced elastic oscillations [8]:

$$\ddot{y} + \alpha \dot{y} + \beta y = f(x).$$

where $f(x) = C R_f \exp[(1 + \alpha)x]$ and $\beta = C(\gamma - 1) \exp(-2\alpha x)$.

"Elasticity" of turbulent flow is determined by attitude of generation and dissipation rates. "Friction" is connected to nonlinearity of the turbulence local scale. Driving force formed by buoyancy.

3. Turbulent flow as the oscillatory system.

The obtained equation can be presented as

$$\frac{\partial}{\partial x}(T + V) = -2\alpha(T - qV) + f \dot{y},$$

where T - kinetic energy of the deviation; V - potential energy; $q = 0.5 \dot{\beta} / \alpha \beta$ - parameter describing inner properties of the system.

The special interest represents the mode $q = 0$. In this case turbulent flow is the oscillatory system described by an ordinary differential equation with constant coefficients and has analogs among the physical systems. Parameter determining a solution kind of the equation of forced elastic oscillations is a number

$p = \alpha^2 / 4\beta$. Definition of parameters p and q for turbulent flow is a problem of special experimental research.

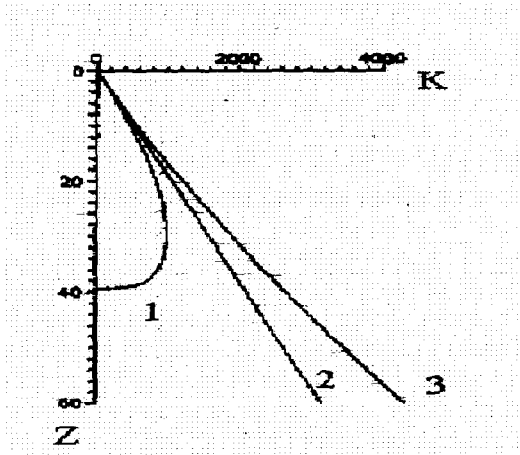


Fig. 1.

Vertical structures of turbulence coefficient $K(m^2 c^{-1})$.

On the figure the vertical structure of turbulence coefficient for various conditions of stratification is represented. Calculations have been made in supposition the high layer of the sea represents an oscillatory system $q = 0$ and $p = 1$. Significances of surface thermal balance were accepted equal 100, 0 and -100 $\text{Дж}/\text{м}^2 \text{с}$. The positive thermal balance limits area of turbulence distribution by the level 40 m. and the sharp boundary of turbulent area is formed. For neutral stratification the structure is linear. For negative thermal balance turbulence coefficient grows faster with depth owing to convective instability.

Velocity of the shift current can be determined from the parity for generation rate: $G = \gamma \varepsilon$ - as

$$\frac{u}{u_*} = \frac{1}{\kappa} \int \gamma y \left(\frac{z}{z_*}\right)^{-(1+\alpha)} d\left(\frac{z}{z_*}\right).$$

and following structures of the current velocity take place for $\gamma = 1$ and $f = 0$:

1. Degree, $\alpha \neq 0$:

$$\frac{u}{u_*} = \frac{1}{\kappa \alpha} \left(\frac{z}{z_*}\right)^{-\alpha} + const;$$

2. Logarithmic, $\alpha = 0$:

$$\frac{u}{u_*} = \frac{1}{\kappa} \ln\left(\frac{C_0 z}{z_*}\right), \quad C_0 = \frac{z_*}{z_0} = 7111.$$

Thus nonlinearity coefficient of turbulence local scale is equal to an exponent of the degree law for current velocity. Experimental researches show the exponent is not a constant and depends on a Reynold's number [5]. For nonlinearity coefficient $\alpha = -0.17$ Reynold's number is determined by significance

$Re = 5 \cdot 10^4$. It corresponds to a range of Reynold's numbers in which the experimental researches were conducted [4]. The function $\alpha(Re)$ can be obtained by approximation of experimental data.

When the system is far from a local equilibrium state and influence of buoyancy forces is insignificant, i.e. the number p is close zero, the equation for deviation of turbulent flow from undisturbed state has a kind

similar to the equation of elastic rod oscillations: $\ddot{y} + C(\gamma - 1)y = 0$. By delivering boundary conditions: $x = 0, y = 0, x = \ln(h/\bar{z}), y = 0$, - it is possible to define critical "load" γ which results in emerging a nontrivial solution of the equation. This classical problem of elastic theory has a discrete spectrum of eigenvalues:

$$\gamma - 1 = \frac{1}{C} \left(\frac{n\pi}{\ln(h/\bar{z})} \right)^2, \text{ where } n = 1, 2, 3, \dots$$

Turbulence does not occur and the current is laminar if the relation of generation and dissipation rates does not exceed the significance:

$$\gamma_{\text{кр}} = 1 + \frac{1}{C} \left(\frac{\pi}{\ln(h/\bar{z})} \right)^2, -$$

When the number $\gamma = \gamma_{\text{кр}}$ a sinusoidal deviation of turbulent flow from undisturbed state is appear instantly. Evaluating for ocean conditions initial magnitudes of upper layer as:

$h = 100M, \mu_* = 0.01M/c, C = 1.5\sqrt{C_\varepsilon}/C_b\kappa^2 \approx 3$, - it is possible to receive following significances of turbulent flow parameters: $\bar{z} = 0.076m, \gamma_{\text{кр}} = 1.064, \beta = 0.19$.

The stated method of study allows to consider various hydrophysical phenomena connected to density stratification from the point of view of the small oscillations theory and opens possibilities for revealing new regularities in ocean turbulent current

References:

1. Turbulence. 1980, Principles and application.- Moscow (in Russian).
2. À.S. Monin, À.N. Iaglom. 1965, Statistical hydrodynamics, Mechanics of turbulence, v. 1, Moscow. (in Russian).
3. À.S. Monin, R.V. Ozmidov. 1981, Ocean turbulence. Leningrad (in Russian).
4. H.T. Kim, S.J. Kline, W.C. Reynolds. 1971, The production of turbulence near a smooth wall in turbulent boundary layer, J. Fluid Mech., No 50, p. 133 - 160.
5. G.I. Barenblatt. 1982, Similarity and intermediate asymptotics, Leningrad (in Russian).
6. O.M. Fillips. 1980, Dynamics of a high layer of the sea, Leningrad (in Russian).
7. G. Lamb. 1947, Hydrodynamics, Moscow - Leningrad (in Russian).
8. P.À. Kuzmin, 1973, Small oscillations and stability of movement, Moscow (in Russian).

EVOLUTION OF BAROTROPIC MESOSCALE EDDIES ON THE β -PLANE: NUMERICAL TESTING AND DIAGNOSTICS OF EXACT SOLUTIONS

Z. Kizner and D. Berson

Department of Physics, Bar-Ilan University, Ramat-Gan, 52900, Israel

E-mail: zinovyk@mail.biu.ac.il, bersond@mail.biu.ac.il

The evolution of some modon-like vortex configurations is studied numerically. They are shown to radiate vortex pairs that propagate toward the east and west and evolve very slowly. These dipoles are identified as Larichev and Reznik modons and cores of quasi-stationary non-linear Rossby waves, respectively.

Introduction

One of the theoretical interpretations of the mesoscale eddies is the so-called Rossby soliton, a stationary solitary wave that exists due to the balance between nonlinearity and the dispersion caused by the β -effect (see, e.g. [14]). Stern [17] suggested the first model of such a kind representing an exact solution to the equation of potential vorticity conservation in a barotropic ocean with flat bottom on the β -plane and looking like a standing pair of vortices; he also introduced the term "modon" to designate such dipole current systems. Following Lamb [7] he constructed his solution by dividing the (x, y) -plane into two parts, a circular area and its exterior, and by matching the internal solution (the streamfunction and the velocity fields) with the motionless exterior (where the streamfunction is zero). At the matching contour the acceleration and the vorticity of fluid particles are discontinuous in Stern's modon. Larichev and Reznik [8] subsequently constructed a modon that under the "rigid lid" condition propagates toward the east and possesses greater smoothness: its acceleration and vorticity are also continuous. Henceforth, the current systems characterized by continuous streamfunction, velocity and vorticity will be called high-smoothness ones. Despite that to date no flawless proof of the stability of Larichev and Reznik's modon has been put forward (see, e.g., [15]), a considerable robustness of these propagating modons was demonstrated numerically [9-13] and in laboratory experiments [3, 19, 20]. The geophysical significance of modons is attested by numerous observations by means of high-resolution remote sensing imagery [1, 4-6, 18], in which mesoscale vortical pairs were detected in different regions of the World Ocean. However the question remains as to whether any vortical pair, under

idealized conditions, will necessarily either transform into a classical eastward-propagating modon or disintegrate; or, maybe, some other evolutionary scenario may arise?

In the present paper, the evolution of a non-stationary barotropic modon-like vortex structure that initially propagates toward the east is tested numerically. This structure collapses within a quarter of a synoptic period, but two long-lived vortical pairs are radiated traveling east and west with nearly constant translation speeds and exhibiting high smoothness. We formulate a number of criteria for identification of these dipoles in terms of exact stationary solutions. According to our diagnostics, the eastward-propagating eddy pair is a modon of Larichev and Reznik, while the westward-propagating dipole, is the core of a quasi-stationary nonlinear Rossby wave whose vorticity is strong within a circular area and is much weaker in the exterior.

Governing equations and initial conditions.

Under the "rigid lid" condition, the equation of conservation of the potential vorticity in a barotropic ocean with flat bottom on the β -plane in terms of the streamfunction ψ for the velocity components u and v can be written as:

$$\frac{\partial}{\partial t} \Delta\psi + \beta \frac{\partial\psi}{\partial x} + \frac{\partial(\psi, \Delta\psi)}{\partial(x, y)} = 0 \quad (1)$$

(see, e.g., [16]), where t is time, x and y are the zonal and meridional coordinates respectively, Δ and $\frac{\partial}{\partial(x, y)}$ are the Laplacian and Jacobian in the (x, y) -plane, $\beta = \text{constant}$ is the meridional gradient of the Coriolis frequency.

When the solutions of equation (1) that represent form-preserving structures traveling in the x -direction with constant translation speed U are looked for, equation (1) can be replaced with

$$\frac{\partial}{\partial(\xi, y)} [\psi + Uy, \Delta\psi + \beta y] = 0, \quad (2)$$

where $\xi = x - Ut$ and y are the coordinates in the reference frame moving with the solution, and the differentiation is carried out with respect to ξ and y [8]. Thus, according to equation (2), in the moving reference frame, the potential vorticity, $q = \Delta\psi + \beta y$, functionally depends on the full streamfunction, $\Psi = \psi + Uy$.

The only truly localized high-smoothness exact solution to (2) found to date is the Larichev and Reznik modon [8]. We, however, are about to study the evolution of a vortical pair different from this exact solution. That is why, the initial condition for the numerical experiment described below is specified as

$$\psi = \begin{cases} a[J_1(br) + cr^3 + dr] \sin a, & r < r_0, \\ 0, & r > r_0, \end{cases} \quad (3)$$

where r and α are defined by the equations $x = r \cos\alpha$, $y = r \sin\alpha$ [note, that $t = 0$ in (3)], $r_0 = \text{const}$, J_1 is a cylindrical first order Bessel function, a , b , c and d are constants. By a proper choice of parameters b , c and d , the high smoothness of the initial structure (3) can be achieved. Below, the case $a < 0$ will be considered.

Evolutionary experiments

The evolution of the above current structures was studied by means of a non-dimensional numerical model, the space and time scales being $L = 70$ km and $T = 1/\beta L \approx 8.3$ days respectively (synoptic scales). A square $10L \times 10L$ box containing 150×150 grid intervals was considered, and the time step δt was controlled in the course of computations by the gradients of ψ and q and did not exceed $2.5 \cdot 10^{-4} T$. The boundary conditions assumed were periodicity in the x -direction and $\psi = 0$ at the northern and southern boundaries. Henceforth, the scales of the variables are omitted.

The evolution of the vortex current system given at $t = 0$ by equation (3) at $a < 0$ is shown in Fig. 1. Such a structure initially propagates eastward, and collapses within a quarter of the synoptic period (Fig. 1 a-c, e-g) but two high-smoothness vortical pairs traveling both east and west are radiated, becoming well formed by $t = 2.3$ (Fig. 1 d, h). These dipoles have relatively long life spans, propagate with nearly constant translation speeds and are strong enough to survive in interactions that occur due to the periodicity in the boundary conditions.

Diagnostics of exact solutions

Based on (2), a number of criteria for testing the stationarity of the generated vortical pairs can be supplied. First, away from the dipole core, the proportionality between the relative vorticity and the streamfunction, $\Delta\psi \approx \pm l^2 \psi$, must be good. Second, the translation speed, $\tilde{U} = \beta/\pm l^2$, estimated using the above factor of proportionality $\pm l^2$, must conform the estimate U obtained by analysis of the displacements of the vortices. The third and the most important criterion is that the scatter diagram of q vs. $\Psi = \psi + Uy$ must display clear-cut functional dependence between q and Ψ . All these criteria are obeyed in the analyzed experiment (Fig. 2). The coefficients of correlation between $\Delta\psi$ and ψ are about 0.98 and -0.99 for the eastward and westward dipoles respectively. The two estimates of the translation speed are $U \approx 2.2$ and $\tilde{U} \approx 2.1$ for the eastward dipole and $U \approx -1.4$ and $\tilde{U} \approx -1.3$ for the westward one. The scatter-diagrams (Fig. 2 a, d) indicate quite a good direct proportion between potential vorticity and the full streamfunction in both the external and the internal regions (Fig. 2 e, f), the coefficients of correlation for the interior being about -0.99 for the both dipoles. Thus, the following relationship is valid to a high level of approximation for the two quasi-stationary dipoles generated in the course of collapse of the initial structure:

$$\Delta\psi + \beta y = \begin{cases} -k^2(\psi + Uy), & r < r_1, \\ \pm l^2(\psi + Uy), & r > r_1. \end{cases} \quad (4)$$

Here and below r and α are polar coordinates in the coordinate frame attached to the vortex, k^2 and r_1 are constants. When $U > 0$, i.e. for $+l^2$, equation (4) yields Larichev and Reznik's modon [8], while for $U < 0$ we have:

$$\psi = \begin{cases} [AJ_1(kr) - (\frac{\beta}{k^2} + U)r] \sin \alpha, & r < r_1, \\ [BJ_1(lr) + CN_1(lr)] \sin \alpha, & r > r_1, \end{cases} \quad (5)$$

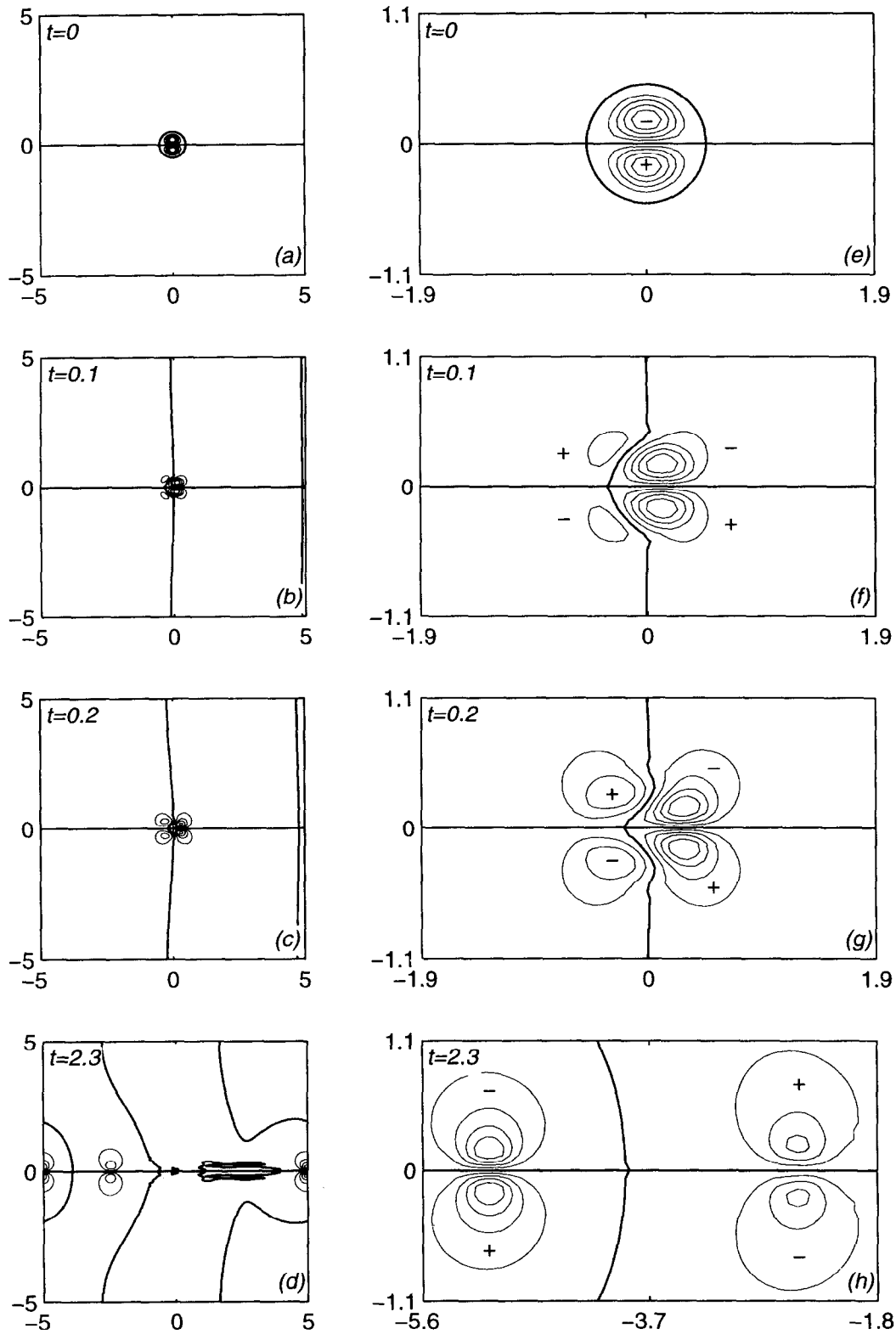


Figure 1. Collapse of the initial current structure and birth of two high-smoothness paired vortices traveling east and west (contours of ψ): Full-size fields (a - d) and enlarged cuttings (e - h).

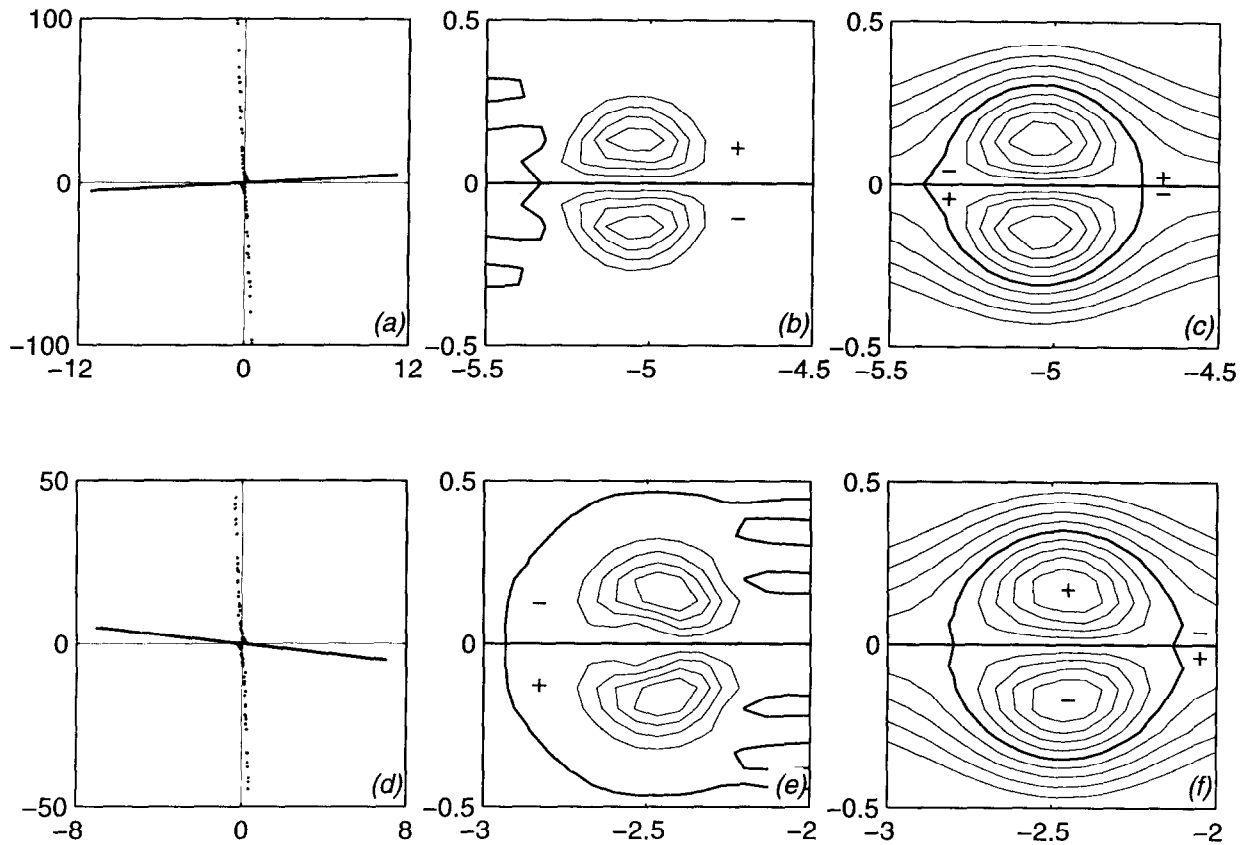


Figure 2. Functional dependence between q and Ψ in the eastward (a - c) and westward (d - f) dipoles generated in the course of collapse of the initial current structure by $t = 2.3$: Scatter diagram of q vs. Ψ (a, d), contours of constant potential vorticity (b, e) and full streamfunction in the reference frame related to the dipoles (c, f).

where N_1 is the first-order Neumann function and the coefficients A , B and C are determined by matching ψ , u , v and q at the contour $r = r_1$. The solution given by (5) (Boyd [2]) drops off slowly and oscillates at $r \rightarrow \infty$. This means that, essentially, our westward vortex pair is imbedded into a nonlinear Rossby wave field.

Conclusions

The selected results discussed in the present paper are typical for our numerical experiments. Very often collapse of unstable current structures leads to the birth of robust eastward- and westward-propagating dipoles that can be identified, respectively, as the Larichev and Reznik modons and slowly evolving cores of high-smoothness nonlinear Rossby waves that, in a limited area (say, $r < 3r_1$), can be approximated by equation (5). Therefore it seems reasonable to suggest that both types of paired vortices are of considerable importance in forming the pattern of synoptic currents in the ocean.

References

- [1] K. Ahlnas, T. C. Royer and T. H. George, 1987, Multiple dipole eddies in Alaska Coastal Current detected with Landsat Thematic Mapper data, *J. Geophys. Res.*, 92, 13041-13047.
- [2] J. P. Boyd, 1994, Nonlocal modons on the beta-plane. *Geophys. Astrophys. Fluid Dyn.* 75, 163-182.
- [3] G. R. Flierl, M. E. Stern and J. A. Whitehead Jr., 1983, The physical significance of modons: Laboratory experiments and general integral constraints, *Dyn. Atmos. Oceans*, 7, 233-264.
- [4] S. B. Hooker, J. W. Brown and A. D. Kirwan Jr., 1995, Detecting "dipole ring" separatrices with zebra palettes, *IEEE Trans. Geosci. Remote Sens*, 33, 1306-1312.
- [5] S. B. Hooker, J. W. Brown, A. D. Kirwan Jr., Lindemann, G. J. and R. P. Mied, 1995, Kinematics of a warm-core dipole ring, *J. Geophys. Res.* 100 (C12), 24797-24809.
- [6] M. Ikeda and W. J. Emery, 1984, Satellite observations and modelling of meanders in the California Current system off Oregon and Northern California, *J. Phys. Oceanogr.*, 14, 1434-1450.
- [7] H. Lamb, 1932. *Hydrodynamics*, 6th ed. Dover, New-York, NY, 738 pp.
- [8] V. D. Larichev and G. M. Reznik, 1976, Two-dimensional solitary Rossby waves, *Rep. USSR. Acad. Sci.*, 231, 1077-1080.
- [9] V. D. Larichev and G. M. Reznik, 1982, Numerical experiments on the study of collision of two-dimensional solitary Rossby waves, *Rep. USSR. Acad. Sci.*, 264, 229-233.
- [10] V. D. Larichev and G.M. Reznik, 1983, Colliding solitary Rossby waves, *Oceanologia*, 23, 725-734.
- [11] M. Makino, T. Kamimura and T. Taniuti, 1981, Dynamics of two-dimensional solitary vortices in a low- β plasma with convective motion, *J. Phys. Soc. Japan*, 50, 980-989.
- [12] J. C. McWilliams, G. R. Flierl, V. D. Larichev and G. M. Reznik, 1981, Numerical studies of barotropic modons, *Dyn. Atmos. Oceans*, 5, 219-238.
- [13] J. C. McWilliams and N. J. Zabusky, 1982, Interactions of isolated vortices. I: Modons colliding with modons, *Geophys. Astrophys. Fluid Dynamics*, 19, 207-227.
- [14] A. S. Monin, 1990, *Theoretical Geophysical Fluid Dynamics*, Kluwer Academic Pub., Dordrecht, Ser. Environmental fluid mechanics, 6, 399 pp.
- [15] J. Nycander, 1992, Refutation of stability proofs for dipole vortices. *Phys. Fluids*, 4A, 467-476.
- [16] J. Pedlosky, 1979, *Geophysical Fluid Dynamics*, Springer-Verlag, 624 pp.
- [17] M. E. Stern, 1975, Minimal properties of planetary eddies, *J. Mar. Res.*, 33, 1-13.
- [18] R. E. Thomson, 1984, A cyclonic eddy over the continental margin of Vancouver Island: Evidence for baroclinic instability, *J. Phys. Oceanogr.*, 14, 1326-1348.
- [19] S. I. Voropaev, Ya. D. Afanasyev and I. A. Filippov, 1991, Horizontal jets and vortex dipoles in a stratified fluid, *J. Fluid Mechanics*, 227, 543-566.
- [20] O. U. Velasco Fuentes and G. J. F. van Hejst, 1994, Experimental study of dipolar vortices on a topographic β -plane. *J. Fluid Mech.* 259, 79-106.

ANALYSIS OF CONDITION OF INCREASING AND DECREASING DENSITY DUE TO MIXING OF A SEA WATER MASSES.

Kluikov Ye. Yu., Provotorov P.P., Utkin K.B.

Russian State Hydrometeorological University,
St.-Petersburg, 195196, Malookhtinsky Av. 98, Russia

Abstract

On the basis of an equation for changing the mixture density $\delta\rho$, written in the form of a series accurate up to the squared terms, the authors analysis the realization conditions and manifestation boundaries of the density increasing and decreasing effects with mixing sea waters of different T, S -indices. Constructed are the diagrams of the three possible patterns for the function of density variation which allow to determine its sign and magnitude by mean temperature and salinity values of the water masses and ΔT and ΔS jumps between them.

Among the numerous processes due to mixing of a sea water masses with different temperature and salinity, the most important in forming thermohaline fields is the effect of changing of mixture density, as compared to the density of initial components [3,5]. In this work, based on the expression for density variation $\delta\rho$, written in the form of a series, accurate to squared forms

$$\delta\rho = -\frac{1}{8}(\rho_{TT}\Delta T^2 + 2\rho_{TS}\Delta T\Delta S + \rho_{SS}\Delta S^2) \quad (1)$$

analyzes the condition of the decreasing density effect (DDE) and increasing density effect (IDE) at adiabatic mixing of water masses. In expression (1) ρ_{TT} , ρ_{SS} – are the second, ρ_{TS} – second mixed derivatives of density function with respect to temperature and salinity, $\Delta T = (T_2 - T_1)$, $\Delta S = (S_2 - S_1)$ – are the differences in indices of the mixing water masses.

Using US-80, the diagrams of functions ρ_{TT} , ρ_{SS} and ρ_{TS} was constructed in relation to average temperature \bar{T} and salinity \bar{S} of two water masses. The first and second of them are negative with all combinations of average temperature and salinity: $\bar{T} \in [0.38]^\circ\text{C}$, $\bar{S} \in [0.40]\text{‰}$; the ρ_{SS} function is with alternating signs on the (\bar{T}, \bar{S}) plane, but at $S \leq 9\text{‰}$ it is negative within the entire temperature range.

The analytic study of the function $\delta\rho$, in the form (1) (the square-law form), it is possible in terms of linear algebra (criterion Sylvester), or, what is equivalent, in terms of geometry. Here will be used the geometric terminology.

Let's note (1), in the form

$$A\Delta\bar{T}^2 + 2B\Delta\bar{T}\Delta\bar{S} + C\Delta\bar{S}^2 + 8\Delta\rho = 0. \quad (2)$$

In this expression, for simplification, the labels are entered $A = \rho_{TT}$, $B = \rho_{TS}$, $C = \rho_{SS}$. In three-dimensional space, equation (2) describes a certain surface of second order, the type of which is determined by the sign of its discriminant. This discriminant it is function of average temperature and salinity. The quick estimation of the sign and magnitude of discriminant may be produced using diagram fig. 1.

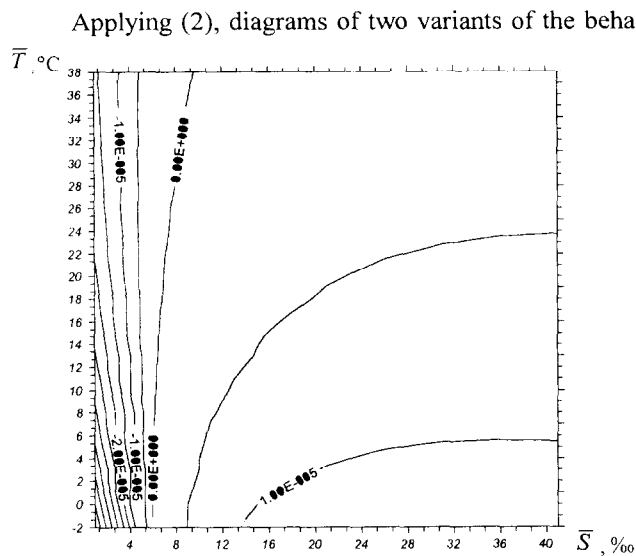


Fig. 1. The diagram of the meaning of function $(\rho_{TS}^2 - \rho_{TT} \cdot \rho_{SS})$ in dependence on temperature and salinity.

3. if discriminant there is less zero then, always positive, magnitude of $\delta\rho$ is determined till a fig.3b

Diagrams fig.2b and fig.3b was constructed at $\bar{T} = 17^\circ\text{C}$ and $\bar{S} = 35\text{‰}$, however the coefficients A, B, C are not changed hardly on the (\bar{T}, \bar{S}) plane and thus these diagrams are applicable for neighboring meanings of temperature and salinity.

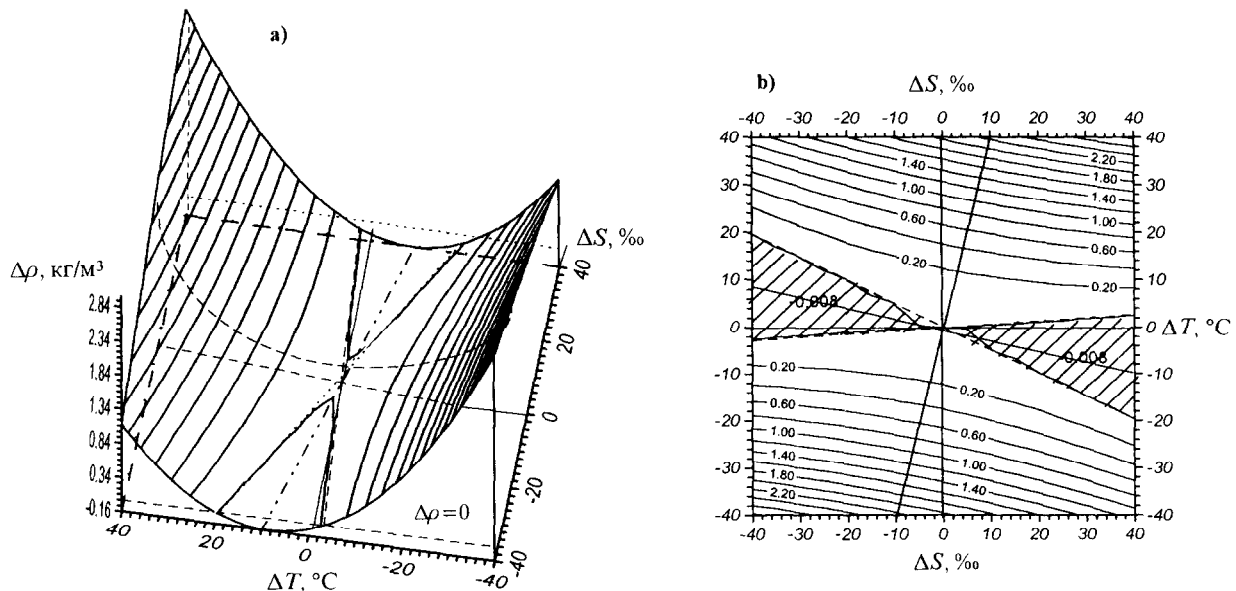


Fig. 2. Kind of a surface circumscribed function (2) at $(\rho_{TS}^2 - \rho_{TT} \cdot \rho_{SS}) > 0$ (a) and projection of the surface $\delta\rho = -(1/8)(\rho_{TT}\Delta T^2 + 2\rho_{TS}\Delta T\Delta S + \rho_{SS}\Delta S^2)$ on the plane $\delta\rho = 0$ at $(\rho_{TS}^2 - \rho_{TT} \cdot \rho_{SS}) > 0$ (b).

Applying (2), diagrams of two variants of the behavior of the function $\delta\rho$ are constructed, for the cases $(B^2 - AC) \ll 0$. The third possible variant of mixing – parabolic cylinder $(B^2 - AC) = 0$ is very seldom meeting, on the practice will not be realized.

With the help of these diagrams it is possible fast to receive an evaluation of effect of density change, i.e. sign and magnitude $\delta\rho$. In agreement with fig. 1, 2, 3, the sign $\delta\rho$ is determined, in main, by the magnitude of average salinity, but the magnitude of the effect by differences of temperature and salinity.

The method of estimation of the function $\delta\rho$ – two simple operations with using one auxiliary and two main diagrams:

1. having \bar{T} and \bar{S} , with the help of diagram of a fig.1, sign of discriminant $(B^2 - AC)$ is determined;
2. if discriminant there is more zero then magnitude of $\delta\rho$ is determined till a fig.2b;

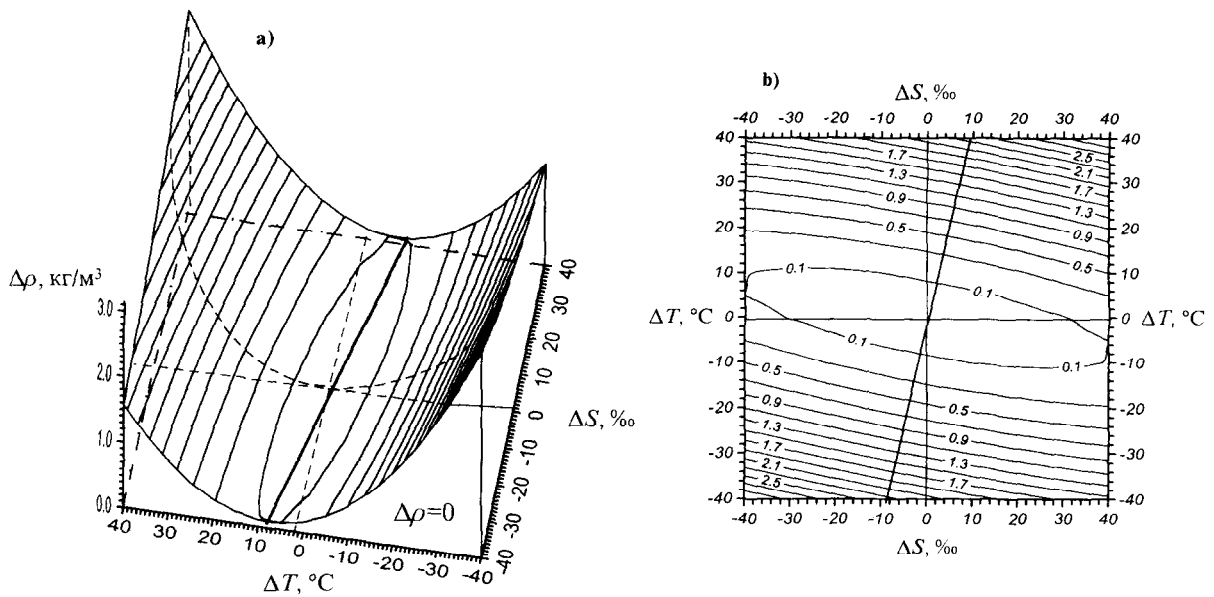


Fig.3. Kind of a surface circumscribed function (2) at $(\rho_{TS}^2 - \rho_{TT} \cdot \rho_{SS}) < 0$ (a) and projection of the surface $\delta\rho = -(1/8)(\rho_{TT}\Delta T^2 + 2\rho_{TS}\Delta T\Delta S + \rho_{SS}\Delta S^2)$ on the plane $\delta\rho = 0$ at $(\rho_{TS}^2 - \rho_{TT} \cdot \rho_{SS}) < 0$ (b).

The results of the estimation of $\delta\rho$ magnitude, with the help of the method mentioned above, for the two variants of mixing are represented in the table

№	Water masses 1-2	T_1 °C	S_1 ‰	T_2 °C	S_2 ‰	$\delta\rho$ кг/м ³
1	Gulfstream - Labrador's current [4]	14.5	35.9	-0.8	33.3	0.361
2	Northmarine - Baltic (autumn season) [2]	10.0	34.5	8.0	8.0	-0.015

Based on these and other variants of mixing, in different regions of world ocean, is shown, that for average conditions, the ratio between the magnitudes of DDE and IDE effects, in variations of the mixture density is found to be 100:1, and the maximum and minimum limiting values (at $\Delta T=20$ °C and $\Delta S=20$ ‰) of density changes may amount 1.2 and -0.05 kg·m⁻³, respectively. At $\bar{S} \leq 9$ ‰, within the entire temperature range DDE effect is not possible. The DDE effect can be noticed when warm freshened water and cold salt water are in contact, or during the mixing process of water masses with pronounced differences in salinity. In the latter case, vertical mixing attenuates, and thermohaline fronts would dissipate. The vertical mixing and frontogenes become most noticeable at the mixing of the water with equal salinity, when $\delta\rho$ is greatest due to IDE, this process is favorable for the transfrontale transfer [5,6].

References

1. Aleksandrov P.S. The course of analytical geometry and linear algebra. M.:Nauka, 1979. 511 pp.
2. Vorobiev V.N., Korovin V.P., Provotorov P.P. The thermohaline structure of Baltic sea waters in autumn region. // Collection of works of Leningrad's hydrometeorological institute. vol. 2 (15). 1985. L. Gidrometeoizdat. p. 139-150.

3. Zubov N.N., Sabinin K.D. The evaluation of increasing density effect at mixing of sea water. M.: Hydrometeorological publishing house (department), 1958. 38 pp.
4. Mamaev O.I. Thermohaline analysis of World Ocean water. L.: Gidrometeoizdat, 1987. 296 pp.
5. Fedorov K.N. The physical nature and structure of oceanic fronts. L.: Godrometeoizdat, 1983. 269 pp.
6. Sherstyankin P.P., Kuimova L.N. Thermohaline analysis of the mixing processes and frontogenes of Baikal waters // Dokl. RAN. 1995. vol. 344. № 2. p 247–251.

INTERNAL WAVES AT THE BARENTS SEA POLAR FRONT

K. V. Konyaev¹, G.I. Kozoubskaia², A. J. Plueddemann³ and K. D. Sabinin⁴

1. Andreyev Acoustics Institute, 4 Shvern timer St., Moscow 117036, Russia. E-mail: bvp@asu.acoins.msk.su
2. Shirshov Institute of Oceanology, 36 Nakhimovskiy Pr., Moscow 17851, Russia. E-mail: gala@sabinin.msk.ru
3. Woods Hole Oceanographic Institution, Woods Hole MA 02543-1541 USA. E-mail: aplueddemann@whoi.edu
4. Andreyev Acoustics Institute, 4 Shvern timer St., Moscow 117036, Russia. E-mail: kosta@sabinin.msk.ru Russia.

Abstract: Semidiurnal oscillations of baroclinic currents were detected in acoustic Doppler current profiler (ADCP) and moored current meter data obtained at over the southeast slope of Spitsbergen Bank in the Barents Sea. Multi-dimensional spectral analysis of the data shows that the semidiurnal internal tide radiated from the upper part of the slope, in a direction that varied between southwest and south, and with a wavelength that decreased in accordance with the decreasing vorticity of the background current field. The very existence of the freely-propagating semidiurnal internal tide observed here, at the critical latitude, seems to be connected with the measured negative background vorticity that lowers the effective inertial frequency below the M_2 semidiurnal tidal frequency. Moored temperature and current records also show intense internal soliton-like wave trains similar to those typical for the temperate ocean shelves.

Introduction

Internal waves in the Barents Sea are poorly known, although they seem to be rather strong and very unique. Their unique nature is connected with an important role of the Earth's rotation at this latitude that may suppress generation of the internal tide and solitons. As far as we know, there are only two significant publications discussing internal waves in the Barents Sea. Zubow [1] described observations of the semidiurnal internal tide in the central part of the Barents Sea and Lynch et al. [2] analyzed internal waves using moored temperature data from the Barents Sea Polar Front Experiment (BSPFX). Here we present the results of further analysis of ADCP and moored current meter data obtained during BSPFX.

The BSPFX experiment took place over the south flank of Spitsbergen Bank, about 60 km east of Bear Island, from 6 to 26 August, 1992 [3]. Repeated shipboard surveys were conducted within a 70×80 km box entered at 22.5°E, 74.3°N (Fig. 1). Velocity observations were made during the surveys from a shipboard acoustic Doppler current profiler (ADCP) [4]. Several full and partial surveys were made during the experiment, but only the first (full) survey is analyzed here. Each full survey took about 3 days to complete. Moorings with temperature sensors

and current meters at depths of 20, 50, and 80 m were placed at three corners of the survey area. The moorings were deployed between 11 and 23 August.

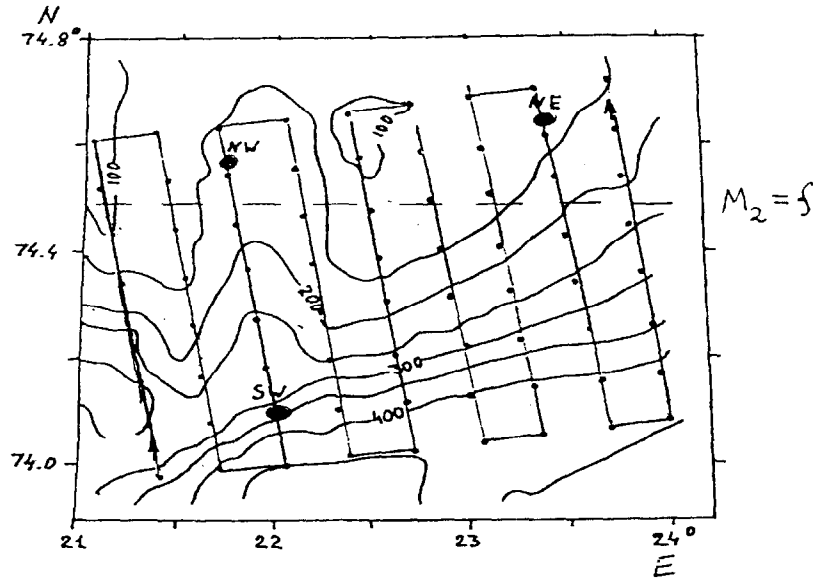


Fig. 1. Plan view of the ADCP survey (straight lines) conducted during 6-9 August 1992 about 60 km east of Bear Island in the western Barents Sea. A CTD survey (small dots) with 10 km resolution was conducted at the same time. Moorings were deployed from 11-23 August at the southwest (SW) northwest (NW) and northeast (NE) corners of the survey region (large dots). Isobaths are shown by solid lines (numbers correspond to depth in m). Broken line marks the critical latitude for M_2 internal tide.

Semidiurnal Internal waves

Semidiurnal oscillations dominated the current field observed during BSPFX. This can be seen in Fig. 2 which shows frequency spectra from current meter measurements at the three BSPFX moorings. While the 50 m spectra (not shown) represent rather well the barotropic oscillations, the spectra of the difference between currents at 20 m and 50 m represent the baroclinic oscillations. This is due to the structure of the first baroclinic mode at the BSPFX mooring sites. At each site the horizontal displacements for this mode have a zero crossing near 50 m and a maximum near 20 m. The three-minute average ADCP data had along-track resolution of 1 km, cross-track resolution of 10 km, and vertical resolution of 8 m. The two components $u(t, x, y), v(t, x, y)$ of the velocity field were sampled at discrete vertical levels $n = 1, 2, \dots, N$ along the ship's track. The ship track can be described by the parametric representation

$$\vec{X}(n) = [t(n), x(n), y(n)]. \quad (1)$$

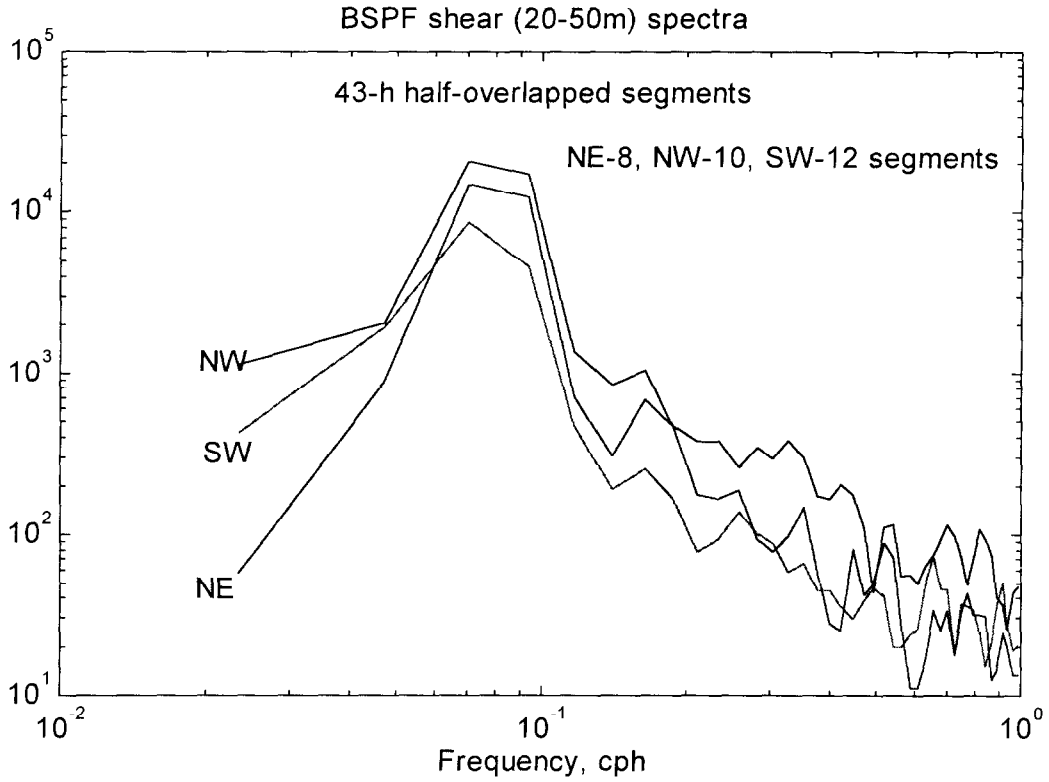


Fig. 2. Spectra of velocity difference between 20 m and 50 m depth from NW, SW and NE moorings.

The three-dimensional amplitude spectrum of current components at a given level is then computed from

$$A_u(\vec{k}) = q \left| \sum_{n=1}^N u(n) \exp[-i2\pi(\vec{k} \cdot \vec{X})] \right|, \quad (2)$$

where $\vec{k} = \vec{k}(\omega, k_x, k_y)$ and q is a normalization coefficient related to the size of the survey area and the number of samples N . An analogous expression applies to the v component.

The space-time sampling of velocity from the shipboard surveys is rather sparse, and not optimal for four-dimensional spectral analysis. Still, the data may be successfully used for the investigation of narrow-band oscillations with known frequency. This is the case for the semidiurnal internal tide at the BSPFX site, as shown above (Fig. 2). The capability of the spectral analysis to distinguish such signals is characterized by the spectral window

$$A_0 = \left| \sum_{n=1}^N \cos[2\pi(\vec{k}_0 \cdot \vec{X})] \exp[-i2\pi(\vec{k} \cdot \vec{X})] \right|. \quad (3)$$

This is the spectral response to a sinusoidal wave with known wavenumber vector $\vec{k}_0(\omega_0, k_{x0}, k_{y0})$.

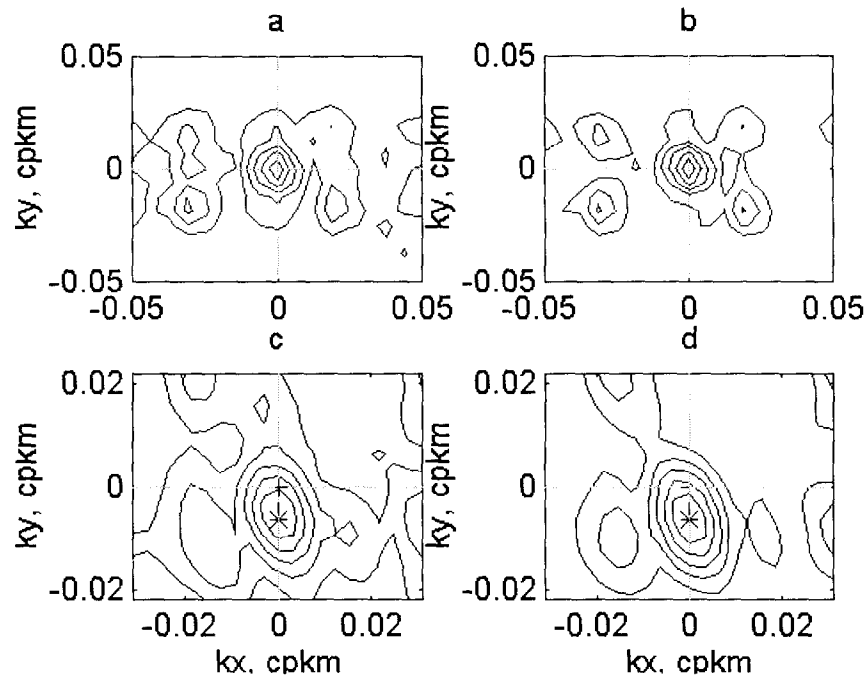


Fig. 3. Horizontal wavenumber spectra at the semidiurnal frequency computed from the ADCP survey data. (a) Spectrum for baroclinic currents, (b) spectrum for barotropic current, (c) spectral window for baroclinic current, and (d) spectral window for barotropic current.

Estimates of the wavenumber spectra of semidiurnal currents from the first ADCP survey of BSPFX are shown in Fig. 3. Discrimination between barotropic and baroclinic oscillations in the ADCP records was made using the vertical average of the currents. The vertical mean represents the barotropic current and the deviation from the mean represents the baroclinic current. The main peak of the barotropic current spectrum is situated at the origin of the wavenumber coordinates, a result of the very long wavelength of the barotropic tide. The main peak of the baroclinic current spectrum is displaced by -6.25×10^{-3} cpkm on the k_y axis. This corresponds to a 160 km wavelength wave propagating southward. There are four additional peaks surrounding the main peak in each spectrum. These peaks are situated in the same manner as the side lobes in the spectral window.

Horizontal wavenumber spectra of the semidiurnal internal tide were also calculated from the current meter records at the three moorings. The velocity difference between 20 and 50 m depths was used to isolate the baroclinic component. Running spectra were calculated between 14 and 22 August using 18 half-overlapped segments of 21.3 h each. Note that the moored measurements started about 3 days after the finish of the first ADCP survey. Since distances between moorings are large we must take into account a possibility of the spatial aliasing. Bearing in mind results of the ADCP data analysis described above and supposing that a gradual change of the wavenumber vs. time is more likely than sharp changes we have chosen some spectral peaks (peaks for segments 7-18) situated outside the spatial Nyquist frequency along the meridional axis $N_y=0.0094$ cpkm. Under

such assumption the running wavenumber spectra (Fig. 4) show a gradual decrease of the horizontal wavelength from 140 km to 40 km, and a gradual turning from the southwest towards the south.

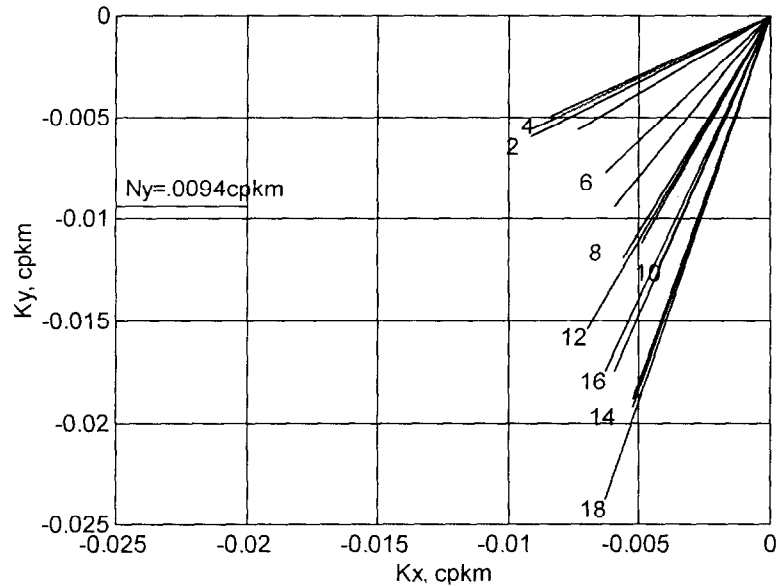


Fig. 4. Wavenumber vectors corresponding to peaks of the running wavenumber spectra of semidiurnal oscillations of the current shear between 20 m and 50 m depth estimated from the mooring data. Vectors are marked by numbers corresponding to the numbers of segments of the records used for the spectral analysis.

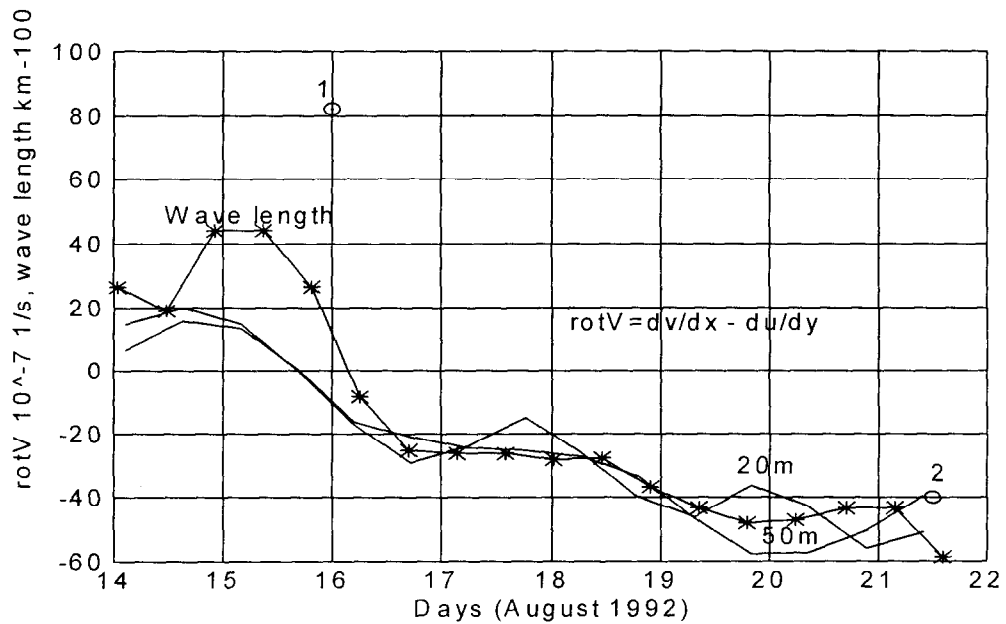


Fig. 5. Semidiurnal internal tide wave length vs. time (presented as deviations from the mean length of 100 km by asterisks) together with the low-frequency vorticity at 20 m (dotted line) and 50 m (solid line). By open circles designated by numbers 1 and 2 theoretical estimates of the wave lengths are shown.

Thus, both ADPC and moored data revealed a propagating semidiurnal internal tide, although the measurements were made at the critical latitude for the main semidiurnal component ($M_2 = 0.0805$ cph; the inertial frequency $f = M_2$ at 74.5° N). In this case the vorticity of the low-frequency flow may play an important role, since it governs the effective inertial frequency $f_{eff} = f + \zeta / 2$, where $\zeta = \partial v / \partial x - \partial u / \partial y$ is the relative vorticity [5]. Positive background vorticity in the vicinity of the critical latitude may close the wave guide for M_2 , whereas negative vorticity promotes emanation of the M_2 internal tide from the shelf break. In the situation of negative vorticity, the closer f_{eff} is to local f , the shorter must be the wave length. The time variation of the low-frequency vorticity is presented together with the observed wave length and two theoretical estimates of wave length in Fig. 5. The low-frequency vorticity was estimated from the current meter array, the observed wave length comes from the same spectral analysis used for Fig. 4, and the theoretical estimates come from observed buoyancy frequency profiles and the background vorticity.

Internal Solitons

The velocity and temperature records from the moorings show evidence of soliton-like internal waves.

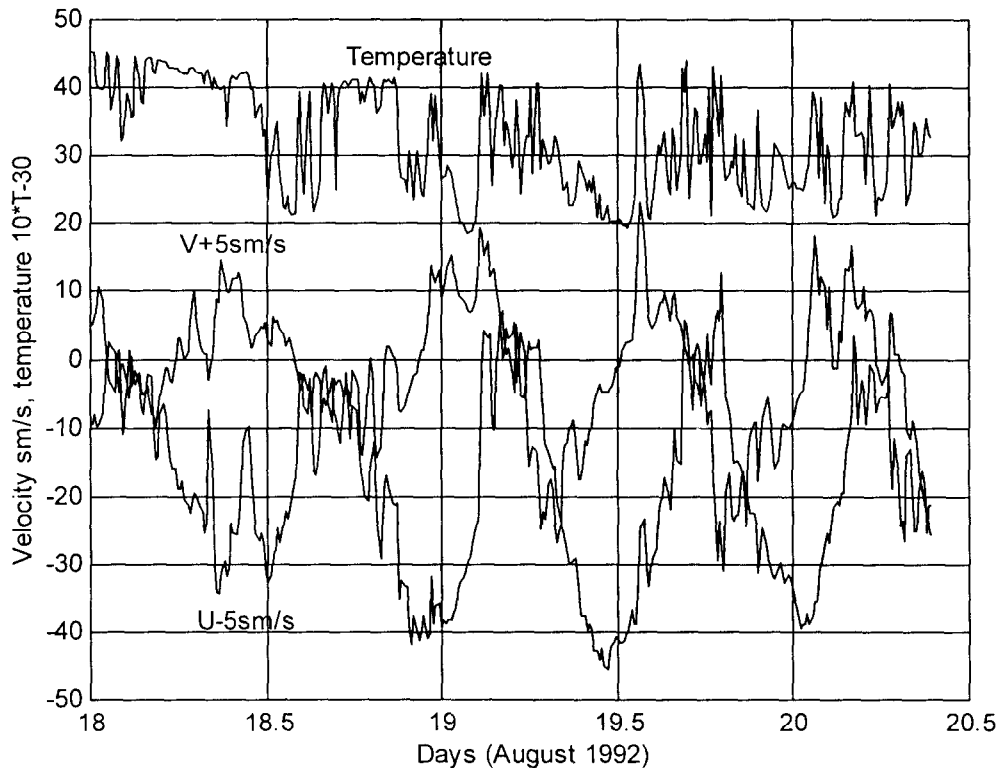


Fig. 6. A segment of the temperature and velocity records from 20 m depth on the southwest mooring. The scale is correct for the two components of velocity shifted by 5 cm/s. Temperature has been normalized according to $T' = 10 T - 30$ in order to be presented on the same scale.

Figs. 6 and 7 present two components of velocity from 20 m depth on the southwest mooring along with temperature scaled to fit on the same plot. The semidiurnal signal analyzed above is evident, most clearly in the u velocity component. However, at higher frequency, strong oscillations are seen in both temperature and velocity which appear to be the manifestation of internal solitons. For example, just after mid-day on 19 August a 2°C temperature spike is seen, indicating a depression of the thermocline. At the same time a large spike is seen in the v component of velocity and a smaller spike in the u component. This is consistent with a solitary wave propagating approximately across the shelf. Similar events is seen at other times in the record.

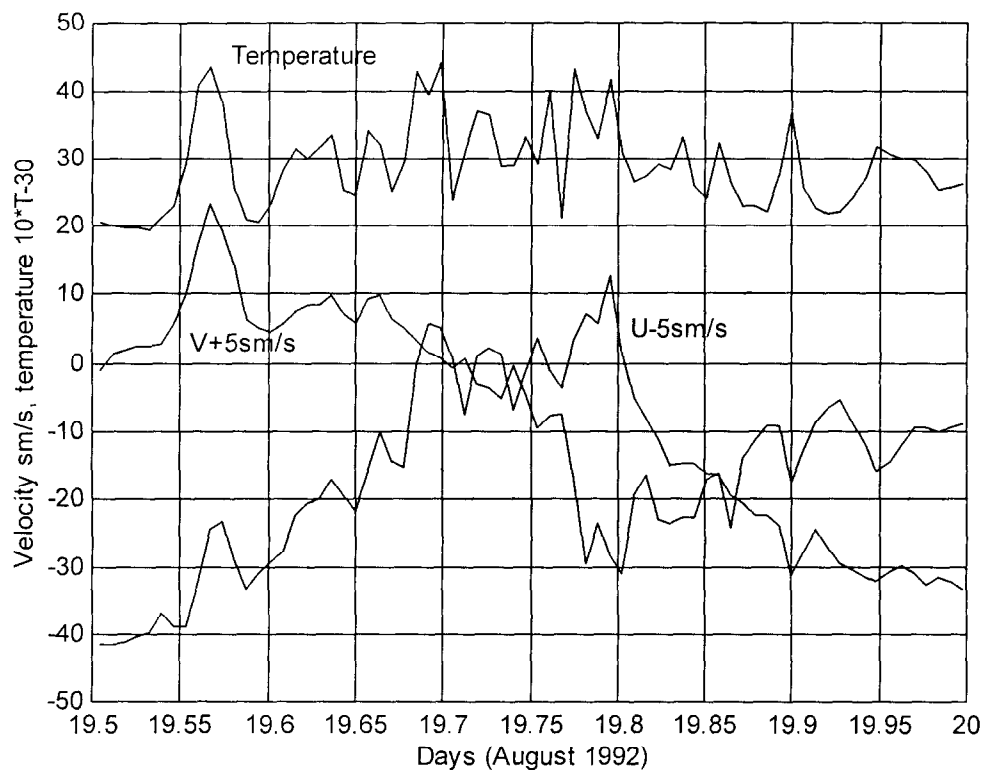


Fig. 7. An expanded portion of the record , shown in Fig.6.

Conclusions

There are three principal conclusions from the analysis of current records from BSPFX:

1. A prominent semidiurnal internal tide exists over the southeast slope of Spitsbergen Bank, even though this region is in the vicinity of the critical latitude for the main tidal component --- lunar semidiurnal (M_2).
2. The background vorticity strongly influences the internal tide, presumably allowing its generation at the critical latitude and governing its evolution. Specifically, the horizontal wavelength of the semidiurnal tide was found to decrease in conjunction with a decrease in the magnitude of the background vorticity.

3. Soliton-like internal waves exist in the Barents Sea, and have properties similar to those seen at lower-latitude sites.

Acknowledgments. The Barents Sea Polar Front Experiment was conducted by R. Bourke, C.-S. Chiu, J. Lynch, J. Miller, R. Muench, A.R. Parsons, and R. Pawlowicz. This work was supported in part by the Office of Naval Research through contract N00014-90-J-1357, and by RFFR grants 97-05-64225 and 98-05-64712.

References

1. Zubow N.N., 1932. Hydrological investigations in the south-western part of the Barents Sea during the summer 1928. (In Russian). Transactions of the Oceanographical Institute, Moscow, Vol. 2, No. 4.
2. Lynch, J. F., G. Jin, R. Pawlowicz, D. Ray, A. J. Plueddemann, C.-S. Chiu, J. H. Miller, R. H. Bourke, A. R. Parsons and R. Muench, 1996. Acoustic travel-time perturbations due to shallow water internal waves and internal tides in the Barents Sea Polar Front: Theory and experiment. *J. Acoust. Soc. Am.*, 99 (2), 803--821.
3. Parsons, A.R., R.H. Bourke, R.D. Muench, C.-S. Chiu, J.F. Lynch, J.H. Miller, A.J. Plueddemann and R.Pawlowicz, 1996. The Barents Sea polar front in summer, *J. Geophys. Res.*, 101(C6), 14,201--14,221.
4. Harris, C.L., A.J. Plueddemann, R.H. Bourke, M.D. Stone and R.A. Pawlowicz, 1995. Collection and processing of shipboard ADCP velocities from the Barents Sea Polar Front Experiment, Woods Hole Oceanog. Inst. Tech. Rept, *WHOI-95-03*, 71 pp.
5. Kunze, E., 1985. Near-inertial wave propagation in geostrophic shear, *Phys. Oceanogr.* 15, 544--565.

SIGNIFICANCE AND PHYSICS OF FRONTAL EDDIES

G.K. Korotaev

Marine Hydrophysical Institute
Kapitanskaya 2 335000 Sevastopol
Crimea Ukraine
e-mail: ipdop@fossil.ukrcm.sebastopol.ua

Abstract. The process of formation of frontal eddies is well documented by oceanographic observations beginning from [1] work. Detachments of Gulf Stream rings and other frontal eddies from the flow are presented obviously in thermal imagery. The same process probably is responsible for the formation of deep lenses of the Meddy type. The conservation of the angular momentum plays a crucial role in the formation of the structure of frontal eddies. The theory of nonlinear geostrophic adjustment is developed and is applied to the analyses of a warm core Gulf Stream ring. A structure of a warm core ring is calculated using archive hydrology as the input to the theoretical model. The density and velocity distributions from the paper of [2] are used for the evaluation of simulations. Good correspondence of simulated and observed fields shows the consistency of the theory. Hypothetically the same physic describes the structure of other eddies of the frontal origin.

1. INTRODUCTION

Field researches carried out intensively during 70-80s discovered that mesoscale eddies are observed in all regions of the World Ocean [3]. Simultaneously numerical studies of two-dimensional turbulence have revealed that eddies play an essential role in turbulent field [4]. It was shown that the famous cascade of energy from small scales to larger one is realized by merging of eddies of the same sign. Numerical simulations showed however that eddies do not formed in a two-dimensional turbulent field. Without external forcing there is only propagation and collision of eddies and two-dimensional turbulence is a decaying one. This theoretical result looks as a contradiction with direct observations of mesoscale variability in an open ocean where formation of eddies was documented [3]. Explanation can be found in the confusion with a term "eddy" in oceanography. Really, mesoscales are often observed through distribution of either temperature, salinity and density or dynamic height fields. Usually eddies are identified as a closed contours of mentioned above fields. However closed contours may be resulted from interference of Rossby waves. Hence not each closed loop corresponds to an eddy. Thus, it is necessary to define better a term "eddy" trying to interpret numerical simulations of two-dimensional turbulence.

Direct oceanographic observations have revealed another distinction in mesoscale eddies. There were distinguished frontal eddies and eddies of an open ocean. An essential role of frontal eddies have been discussed broadly by Konstantin Fedorov in his book [5]. Frontal eddies are marked by high intensity and by relatively independent dynamics. A typical example of frontal eddies are Gulf Stream rings. Mesoscale eddies of an open ocean have associated usually with "closely packed" patterns which were considered originally as interference of Rossby waves. However intense, long-lived eddy-like features were also discovered definitely in different regions of an open ocean during large-scale mid-ocean experiments POLYGON, MODE, POLYMODE.

In this paper I would like to propose a new physical explanation a formation of frontal eddies and to point out an essential role of frontal cyclogenesis which was paid attention in Fedorov's book and which is presumably main source of open ocean eddies.

2.STRUCTURE AND TRAJECTORY OF MESOSCALE EDDIES

Spatial structure of mesoscale variability of an open ocean can be found in observations of temperature or pressure field on different levels. I have mentioned earlier that temperature or pressure field is often presented as a set of cells with closed contour which usually are considered as eddies. Observations of temperature distribution from hydrographic surveys provide impression of closed packed eddies in an open ocean. However this consideration ignores fundamental difference between mesoscale phenomenon of high and low intensity. The difference of high and low amplitudes is manifested in a simple example of an interference of two Rossby waves which caused appearance of closed contours of stream function (or that is the same, temperature and pressure). Closed contours of a stream function are observed for all range of amplitudes. However only an interference of intense waves with amplitude exceeding some critical threshold calls transport of a fluid (Fig.1). Mass transport happens when closed lines are formed in a moving frame where both waves are stationary. Let us mention that the trapped fluid is bounded from the other part by separatrix of the stream function. Since a potential vorticity does not vary along the stream function contours we can conclude that mass transport should be associated with closed lines in a vorticity field.

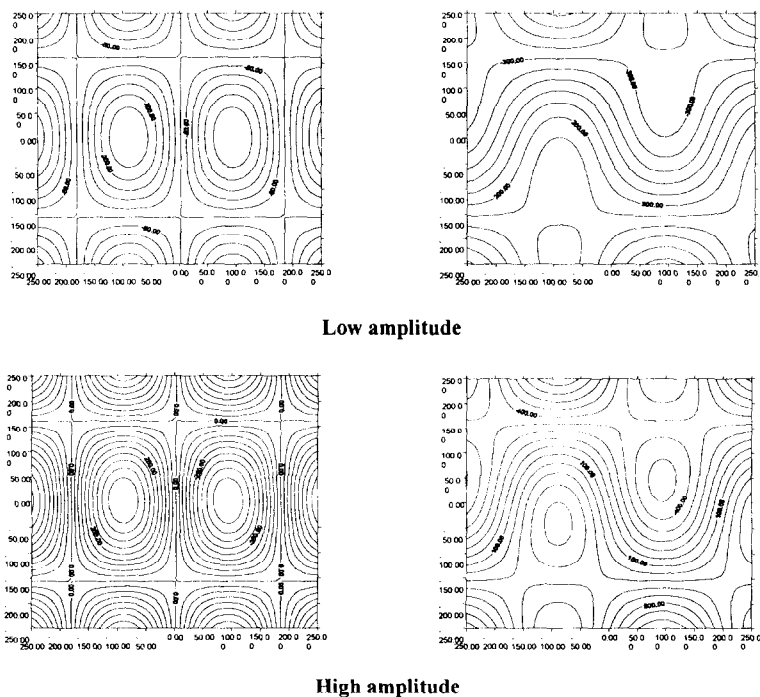


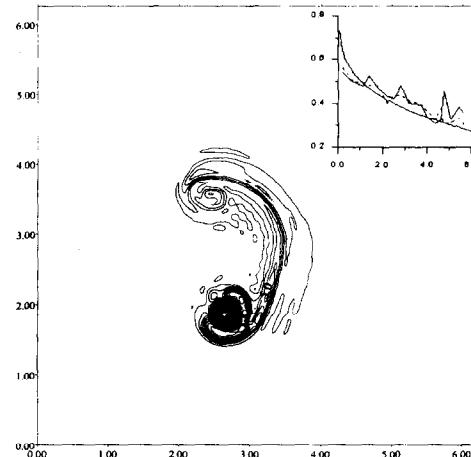
Fig.1 Contours of a stream function in fixed frame (left) and in moving frame (right). Closed cells formed in a moving frame indicate transport of mass. Mass transport happens only in the case of high amplitude.

Lagrangian trajectories of fluid particles which were measured by means of surface or subsurface free floating buoys provide direct indication of mass transport by mesoscales. Long-term observations of free floating buoys in different parts of Atlantic Ocean show loops on trajectories if a buoy is situated near the center of intense eddy [6] or small-scale oscillations if the float is far from strong eddies. It means that an intense eddy involves in a movement a certain volume of fluid which we name a trap zone, and moves with respect to an ambient fluid. A trap zone is well seen in numerical simulations of a single vortex through the distribution of relative vorticity and in laboratory experiments by observation of a dye injected at the vortex [7,8]. Numerical simulations and laboratory experiments show also existence of a filament of vorticity or dye behind a moving vortex. Explanation of observed facts follows from the theory of a vortex on a beta-plane. It is shown in [7] that as in a simple example of interference of two waves, a boundary of a trap zone is a separatrix of a stream function in a frame moving together with the vortex. The vortex moves with respect to an ambient fluid and radiates Rossby waves like a ship generating surface

waves. It loses energy, radiating Rossby waves and decreases its size. As a result fluid particles leave the trap zone along the branch of separatrix of the stream function, forming filament either vorticity (Fig.2) or dye [8].

However majority of trajectories of a free floating buoy manifest simple translation with superimposed small oscillations. Thus the background field is occupied by Rossby waves of low energy which do not transport masses of fluid. These waves being observed in distribution of temperature or pressure show a set of cyclones and anticyclones which are not real eddies.

Fig.2. Distribution of a vorticity in numerical calculations. Formation of a vortex sheet due to decrease of size of an eddy is seen of a figure. Dependence of radius of an eddy (vertical axe) as function of a meridional displacement (horizontal axe) is presented in the upper right corner from numerical simulation (two broken lines) and from analytic theory (smooth line).



There are a few different sources of Rossby waves in the ocean. Seasonal variability of a large-scale circulation is accompanied by radiation of Rossby waves from an eastern coast as was shown by [9] and is confirmed now by satellite observations [10], direct atmospheric forcing may excite Rossby waves due to resonance, Rossby waves are radiated due to oscillation of fronts. However numerical simulations of eddy-wave turbulence on a beta-plane [11] show that a rather small amount of intense mesoscale eddies may be responsible for a closed packed structures of stream function cells. Fig.3 shows plots of vorticity and stream function for the case when the statistics of eddy field is in crude agreement with hydrographic surveys of POLYMODE program. We can see that eddies being only source of energy are not predominated in a field of stream function (or temperature, salinity and pressure)!. Thus careful consideration of mesoscale variability of open ocean provides a concept of coexistence of intense eddies and Rossby waves. Eddies are intense mesoscale features which are transporting large volumes of fluid and radiating Rossby waves. They may be rather rare objects in an open ocean but may provide significant portion of energy of Rossby waves. Results of the work [11] show that there is energy exchange between eddies and waves, and eddies not only radiate Rossby waves but also absorb energy from the field of Rossby waves. However numerical simulations showed also that the two-dimensional turbulence on a beta-plane does not generate eddies. Life of eddies increases due to eddy-wave interaction but nevertheless the number of eddies only decreases and energy passes slowly to waves as in [12]. Thus, there is the question where from eddies come to an open ocean.

I mentioned earlier that mesoscale eddies on a beta-plane (or on a rotate sphere) move with respect to an ambient fluid. An intense isolated vortex moves in a unperturbed fluid according to a simple rule: cyclonic vortices move toward the north-west and anticyclonic ones move toward the south-west in the northern hemisphere. A few well-known oceanographic examples confirm this simple rule. Among them warm core Gulf stream rings, salt Mediterranean lenses, eddies of Agulhas current. However some intense eddies like cold core Gulf Stream rings demonstrate exclusion from the rule. Numerical simulations show [7] that abnormal propagation of eddies happens if a background vorticity differs from a simple planetary one. In this case there is a more common rule of propagation of eddies. The generalization of previous law is that an eddy moves toward a nearest local extreme of a background vorticity field. A background vorticity field may differs from a planetary one due to a bottom slope, horizontal gradient of a vorticity of mean flow or vertical gradient of a mean flow. In particular, abnormal propagation of cold Gulf Stream Rings may be induced partially by a local slope of thermocline [7]. Numerical examples of a single vortex propagation over a bottom topography and due to influence of a mean flow vorticity gradient are presented on Fig. 4. Physics of a vortex propagation is essentially the same as for a beta-plane case. A vortex moves with respect to ambient fluid and radiates waves or wave-like perturbations. It crosses contours of background vorticity and may transport momentum, energy and other substances against their gradients.

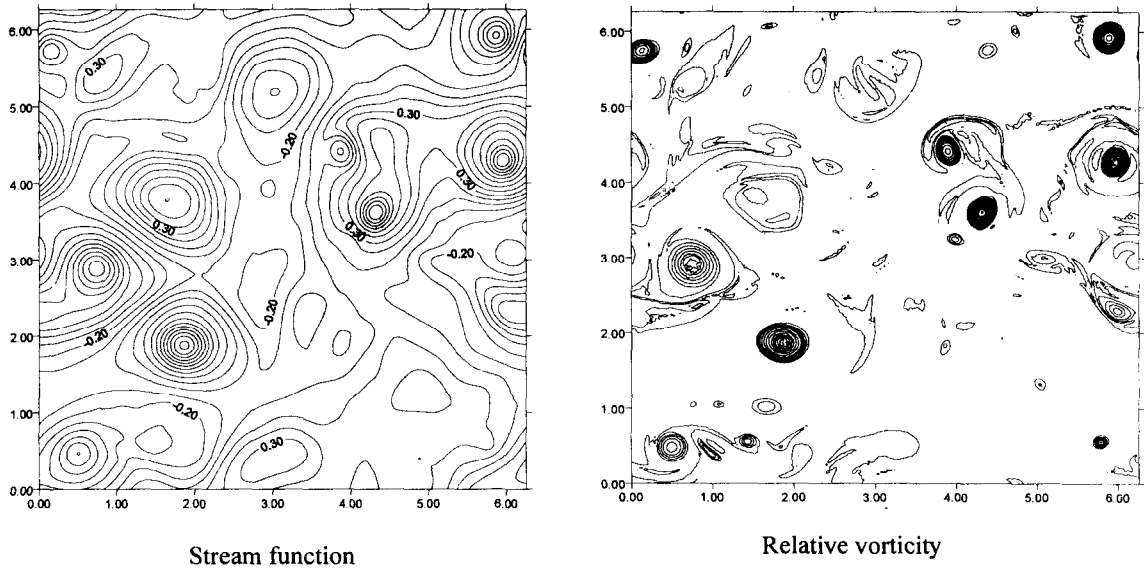


Fig.3. Distribution of the stream function and relative vorticity All extremes in the stream function are induced by eight intense vortices presented on the right panel.

Long-distance excursions are typical for very intense frontal eddies like meddies, rings, eddies of Agulhas current. Eddies of an open ocean have more complicated trajectories which demonstrate chaotic properties (Fig. 5).

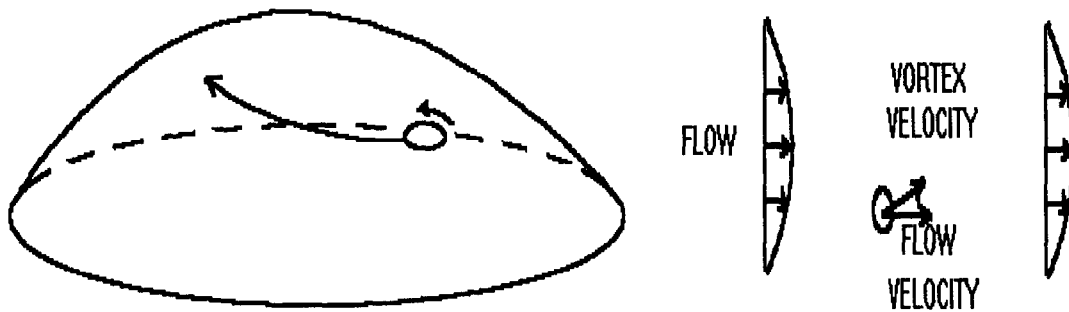


Fig. 4 Left-propagation of a barotropic eddy over a hill. An eddy climbs to the top of a hill. Right-propagation of a barotropic eddy in a flow with vorticity gradient. An eddy moves across the flow.

Simulations of turbulent field on a beta-plane fulfilled in [11], explain the cause of chaotization of trajectories. It is connected with eddy-wave interaction under a special synchronism condition. [7]. The synchronism condition has the same physical meaning as for particles in plasma field and trajectory of eddies in turbulent field on a beta-plane are in full analogy with stochastic trajectories of particles in plasma physics [13].

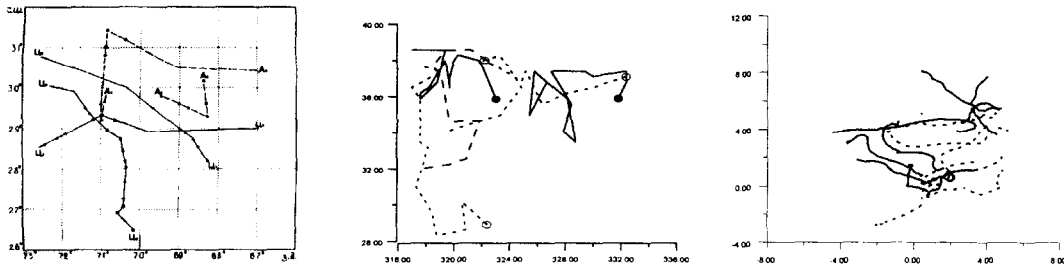


Fig. 5. Trajectories of mesoscale eddies observed in POLYMODE area (upper panel). Trajectories of eddies in Central Atlantic derived from ERS-1 altimetry (mid panel). Trajectories of eddies in numerical simulation of turbulence on a beta-plane (lower panel). Trajectories of cyclones are shown by solid line.

3. ENERGY OF MESOSCALES IN THE OCEAN.

Energy of mesoscales in the open ocean demonstrate strong intermittence. High energy levels near the Gulf Stream, Kuroshio, Circumpolar current coexist with low levels in the middle of large scale oceanic gyres. Thus, highest energies are concentrated near large-scale fronts. It is not surprising, since fronts usually are unstable. Their instability is expressed in large amplitude meanders. Meanders displace the front where concentrated high gradients of any field from its mean position inducing variability with large dispersion. However meandering of fronts cannot explain the existence of open ocean eddies.

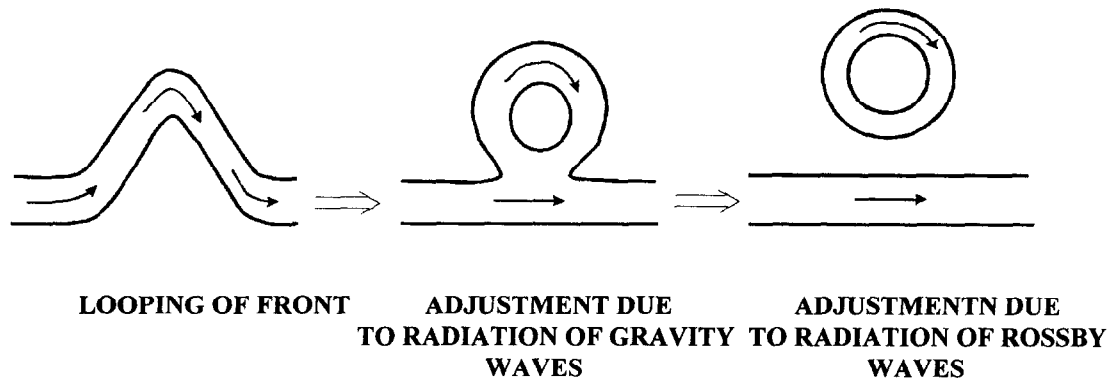


Fig. 6. Main stages of evolution of a frontal eddy.

Another reason of increase of energy of mesoscales towards fronts is explained by the frontal cyclogenesis. A formation of a frontal eddy from meander was observed first by Fuglister [1]. Main stages of an eddy formation consist from formation of meander, its closing and detachment from the front (Fig. 6). Fedorov in his book [5] assumed that formation of eddies after meandering of front happens not only on large-scale climatic fronts but also on small-scale fronts. However we can assume that the most intense long-lived eddies are formed by the climatic fronts and propagate after that to an open sea. If there are no causes for formation of eddies in open ocean then we can assume that intense eddies which were found during mid-ocean experiments are formed near fronts. Their amplitudes decrease due to radiation of Rossby waves and they are not so prominent as eddies in the vicinity of a front. Radiation of Rossby waves by small amount of intense eddies, as it seen from numerical simulations of turbulence on a beta-plane (Fig. 3) can be responsible for "close packed" structures in a stream function field. This concept which assumes that fronts are source of open ocean eddies corresponds to numerical simulations of eddy-wave turbulence on a beta-plane and explains geographic distribution of energy of mesoscales in ocean.

4. CONSERVATION OF AN ANGULAR MOMENTUM AND STRUCTURE OF FRONTAL EDDIES.

We showed in previous section that mesoscale eddies are self-propagating. This means that frontal eddies may be found far from the place of their origin. They also can provide a significant part of energy of an open ocean mesoscale due to radiation of Rossby waves. In this section I would like to discuss how a frontal eddy forms and to show that the law of conservation of angular momentum determine an eddy structure.

Formation of a frontal eddy was documented in details by Fuglister [1] for a Gulf Stream ring. However the same process is typical for formation of eddies near another fronts like Kuroshio, Azores, North-Atlantic, Circumpolar fronts and probably for formation of salt lenses like meddy. Slightly another examples of eddy formation are presented by the retroflexion of North Brazilian and Agulhas currents. Let us mention also formation of chimneys after surface cooling which tend to evolve as mesoscale eddies. There is clear similarity in all these cases. The process of mesoscale eddy formation begins from intrusion of a volume of water which has a vertical density stratification distinct from an ambient water due to a sharp difference of water properties across a front or a fast convective mixing. A following evolution of an intruded volume presents a typical example of geostrophic adjustment.

The problem of adjustment of heavy rotated fluid to an equilibrium in details was considered and investigated in [14,15] in linear statement, where was shown, that the final equilibrium can be found from a condition of conservation of a potential vorticity. The linear theory is inapplicable, if the initial perturbation has finite amplitude. However, in case of a symmetry of initial perturbations of any amplitude the equilibrium condition also can be found without solutions of a developmental problem as was shown for chimneys [16]. Chimneys were considered as a patch of homogeneous fluid embedded into another fluid of uniform density. The same model was applied to meddies by [17]. However if the approximation of an eddy as a patch of homogeneous fluid fits well to chimneys it obviously fails in the case of meddies where density stratification should be important. Recently Korotaev [18,19] have shown how to find solution of the problem of geostrophic adjustment of axisymmetric perturbation in continuously stratified fluid and that application of the law of conservation of angular momentum permits to describe not only formation but also evolution of a frontal mesoscale eddy. Presumably the formation of a frontal eddy on a beta-plane (or on rotating sphere) consists from a few steps (Fig. 6). The first step is the formation of a meander. The second step is detachment of the meander and geostrophic adjustment due to radiation of gravity waves which is fast process in comparison with characteristic time of a vortex evolution. The next step is evolution of an eddy followed by radiation of Rossby waves and adjustment of a trap zone to a quasi-equilibrium.

To apply the conservation of angular momentum to the formation of a frontal eddy, let's remark that after the detachment of the meander in a center of eddy there is the water, situated before on the other side from a stream. At once after formation of eddy the overfall of depths of density surfaces in his center and on a rim is equal to overfall of depths of density surfaces through front of current. Further there should be an adjusting of eddy to a quasi-equilibrium by means of a radiation of inertial-gravity waves at conservation of an angular momentum in a particle of fluid. By virtue of a small size of an eddy in a comparison with a planetary scale, the process of a radiation of inertial-gravity waves happens also, as well as on a plane rotated with an angular velocity $\frac{f}{2}$, where f is local value of a Coriolis parameter. However now eddy is adjusted to a quasi-equilibrium, as rotation of the Earth causes his further evolution. Above we have shown that the latitude heterogeneity of a Coriolis parameter induces propagation of an eddy as whole. The moving eddy is in a permanent quasi-equilibrium, radiating Rossby waves [20,21,22]. The conservation of an angular momentum is still fulfilled, however not on all infinite plane, but only in a finite volume of fluid consisting from particles moving together with an eddy, i.e. inside the trap zone [19]. A conservation of an angular momentum permits to write the system of equations which describes the structure of frontal eddy if parameters of the front are known (see Appendix).

5. APPLICATION TO A STRUCTURE OF A WARM GULF STREAM RING.

Gulf Stream rings give a unique possibility to apply a law of an angular momentum conservation for explanation of their structure as they usually have almost circular form. At the first half of 80-th one warm-core ring was tracked in details within several months since a moment of detachment from the stream. Two depth-sea hydrographic surveys of the ring have allowed in work [2] to construct radially-symmetric approximation of distributions of an azimuth velocity of currents and depths of density surfaces. Further we use these outcomes for

checking of described above physics of formation of a ring by means of comparison of its calculated structure with observations.

Calculation of a structure of a ring under the equations (13)-(15) and boundary conditions (11), (16) required to know a Coriolis parameter, profile of Brunt-Vaisala frequency, an amplitude of displacements of density surfaces, a scale of a ring in a place of its formation and current value of a Coriolis parameter. At reviewing of evolution warm core ring we suppose that the initial displacement of density surfaces along a radius is a Gaussian. The undisturbed distribution of a density of sea water with depth is natural to identify with characteristic stratification of waters located to the north of Gulf Stream front. In our calculation we use profiles of temperature and salinity measured by r/v "Atlantis" on the station N 5189 with coordinates $38^{\circ}54'N$, $65^{\circ}00'W$, taken from atlas of Fuglister. The point is located near a place of detachment of a warm core ring, described in work [2]. The Brunt-Vaisala frequency is calculated using the distribution of a density at this point.

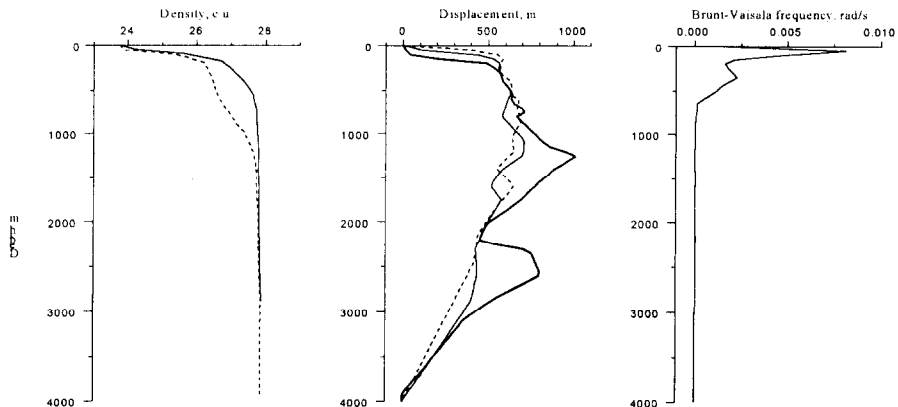


Fig.7. Density profiles south (dash line) and north (solid line) of the Gulf Stream front (left panel), displacement of density interfaces across the Gulf Stream from different pairs of stations (mid panel) and background Brunt-Vaisala frequency.

At an evaluation of initial amplitude of a displacement of density surfaces we use the circumstance that in a center of ring is seized the water located before to the south from the front. Therefore, the distribution of temperature

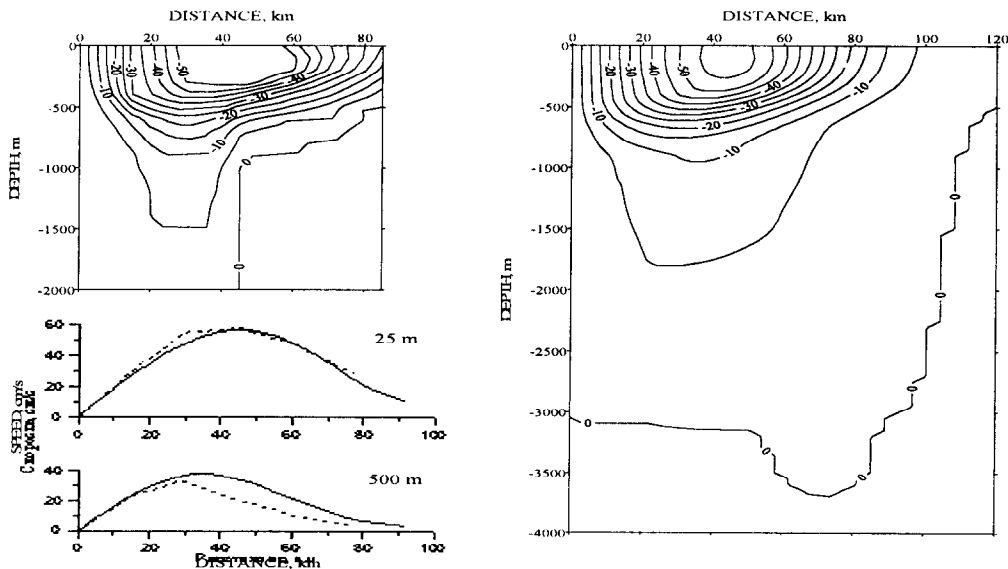


Fig. 8. Radial section of an azimuthal velocity from observation (upper left panel) and from the theory (right panel). Lower left panel-dependence of surface azimuthal velocity from the distance from the center of the ring. Dash line-observations, solid line-from the theory.

and salinity from depth in a center of ring initially should be the same as on a southern rim of the Gulf Stream. For realization of calculations the characteristic distributions of temperature and salinity with depth were taken from the atlas Fuglister on measurements r/v "Atlantis", station N 5195 in a point with coordinates $36^{\circ}33'N$, $65^{\circ}00'W$. The amplitude of a displacement of a density surface was determined as a difference of its depths on the right and to the left of the front of the Gulf Stream. The distributions of $\sigma_t(z_0)$, $N(z_0)$ and $a(z_0)$, used in calculations are presented on

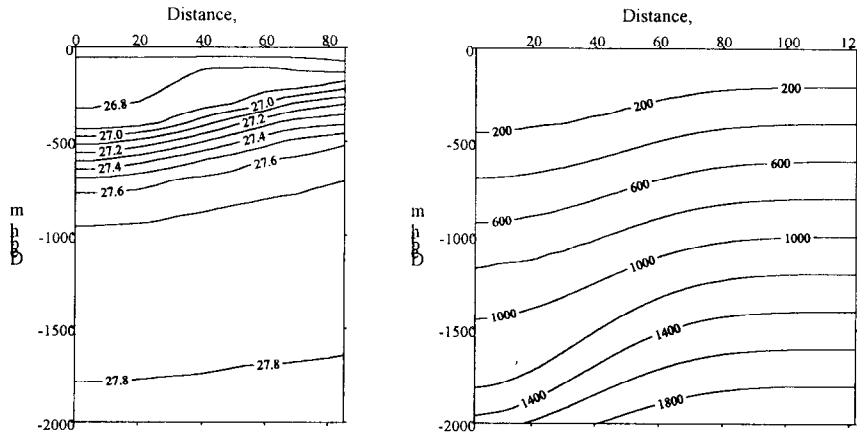


Fig. 9. Radial section of density field. Left panel-observations, right panel-theory.

Fig. 7. The initial value of the Coriolis parameter f_0 got out equal $2\omega \sin \varphi_0$, where ω - angular velocity of rotation of the Earth, and φ_0 - latitude of the most northern disposition of ring. Finally, $f_0 = 9.2 \cdot 10^{-5} s^{-1}$. A scale of the eddy is taken proportional to radius of Rossby $l = R_d / \sqrt{2}$ and $R_d = 40$ km.

At realization of the first survey the center of the ring was on a latitude $\varphi_1 = 38^{\circ}55'$. Accordingly the Coriolis parameter is equal $f_1 = 9.14 \cdot 10^{-5} s^{-1}$. The calculations have shown, that during the first survey the ring was rather intense and almost have reached the bottom, which was located on depth of 4 km. The azimuth velocity have maximum 57.2 cm/s on the surface and practically coincides with observations (Fig. 8). The maximum velocity both in calculations and in observations was on a distance approximately 50 km from a center of the ring. On depth 500m a divergence between the theory and experiment become more essential. The distribution of a velocity along a radius

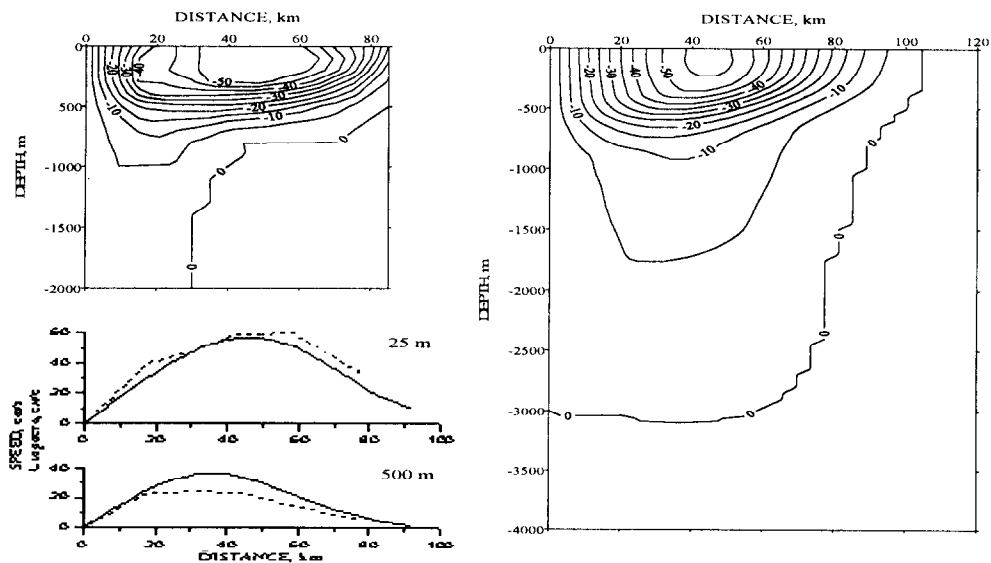


Fig. 10. The same as in Fig. 8 but for the second survey.

(Fig.8), shows the qualitative correspondence of the theory and observations. The maximum velocity both under the theory and on observations is on a distance about 30 km from a center of the ring however simulated velocity above observed. Probably it is connected with distinction of initial displacements of density surfaces estimated from the atlas from what was observed at shaping of the ring. The observed and calculated distribution of density in a vertical-radial section of the ring also correspond each other qualitatively in all range of depths and quantitatively in the upper layer of the sea (Fig.9).

At realization of the second survey the center of the ring was on a latitude $\varphi_2 = 37^{\circ}11'$ and $f_2 = 8.79 \cdot 10^{-5} s^{-1}$. The calculation of a structure of the ring, carried out for the second survey, in whole has given outcomes similar to the cited above. The simulated velocity at a surface approximately corresponds to observations and on depth 500i the calculations give large intensity of motion. At the same time, according to calculations the ring penetrates already to smaller depths and is observed only in the upper 3000-meter layer. The observed and the simulated distributions of a velocity on a radial section of the ring rather well correspond each other (Fig. 10). The good correspondence of theoretical outcomes and observations allows to state that the conservation of an angular momentum is defining the structure of ring.

6.SUMMARY.

We have discussed in this paper how theoretical achievements of the last two decades in study of two-dimensional turbulence and eddy dynamics on a beta-plane can be projected on the knowledge of the mesoscale variability of the open ocean from observations with emphasizing of a special role of frontal eddies. Presumably oceanic fronts are only source of long-lived mesoscale eddies. The latter self-propagate off fronts, forming an open ocean, eddy-wave turbulence. Well-known geography of energy of mesoscales can be interpreted then in terms of statistics of eddies. The number of eddies on unit of square decreases with distance from front and energy of mesoscales decreases proportionally. Moderate number of mesoscale eddies, radiating Rossby waves provide "close packed" cells in fields of temperature, salinity or pressure. However, only eddies itself transport water volumes and other properties and are responsible for horizontal mixing in an open ocean.

Bearing in mind an exclusive role of frontal eddies, we have considered the problem of formation of their structure. We showed how a density difference across the front influences the structure of a frontal eddy. The geostrophic adjustment determines final shape of a frontal eddy.

A conservation of an angular momentum in a particle of fluid on a rotated plane appears to be the fundamental law defining equilibrium condition of any eddy-like axisymmetric perturbation. The fundamental meaning of conservation of an angular momentum is preserved if to include a differential rotation of a plane. The initial axisymmetric perturbation due to a radiation of gravity waves now tends to quasi-equilibrium. The further slower evolution of perturbation is connected to its motion and spending of an energy on a radiation of Rossby waves. A conservation law of an angular momentum is fulfilled only in a finite volume of fluid. The successful reproduction of a three-dimensional structure of a warm core ring allows to assume, that other eddies of a frontal origin submit to a conservation of an angular momentum.

New generation of satellite altimeters make possible to measure spatial statistics of eddies in the World Ocean and the theory gives the key for the account of horizontal mixing induced by mesoscales.

APPENDIX

Let's consider circular motion of a perfect continuously-stratified fluids on a rotated plane. The approximation of a hydrostatics allows to write the equations of motion of fluid by a convenient way, by replacing a vertical coordinate on isopycnal one. The density of fluid thus becomes known function of an isopycnal coordinate. In Boussinesque approximation the equations of motion of fluid in a cylindrical frame have a shape:

$$\frac{\partial u}{\partial t} + u \frac{\partial u}{\partial r} - \frac{v^2}{r} - fv = -\frac{\partial \Phi}{\partial r}, \quad (1)$$

$$\frac{\partial v}{\partial t} + u \frac{\partial v}{\partial r} + \frac{uv}{r} + fv = 0, \quad (2)$$

$$N^2(z_0)z = -\frac{\partial \Phi}{\partial z_0}, \quad (3)$$

$$\frac{\partial z_{z_0}}{\partial t} + \frac{1}{r} \frac{\partial ruz_{z_0}}{\partial r} = 0. \quad (4)$$

Where r is radial coordinate, z_0 is isopycnal coordinate having a sense of depth of density surface in a undisturbed condition, t is time, u -and v -are radial and tangential components of a fluid velocity, Z is a current depth of a density surface, $\Phi = \frac{1}{\rho_0}(p - g\rho z)$ and $z_{z_0} = \frac{\partial z}{\partial z_0}$, f is parameter of the Coriolis, $N(z_0) = \frac{g}{\rho_0} \cdot \frac{d\rho}{dz_0}$ is

frequency of Brunt-Vaisala, $\rho(z_0)$ is density of sea water depending only from an isopycnal coordinate, ρ_0 is average density of sea water, g is acceleration of gravity. From the equations (2) and (4) follows the conservation of an angular momentum in a particle $\mu = rv + \frac{1}{2}fr^2$

$$\left(\frac{\partial}{\partial t} + u \frac{\partial}{\partial r}\right)(rv + \frac{1}{2}fr^2) = 0 \quad (2')$$

and volume of fluid between two close located density surfaces $= \int_0^r r \cdot z_{z_0} dr$

$$\left(\frac{\partial}{\partial t} + u \frac{\partial}{\partial r}\right)\left(\int_0^r r \cdot z_{z_0} dr\right) = 0. \quad (4')$$

The initial conditions allow to establish functional connection between Q and μ on everyone density surface and this relationship is an integral of motion valid for all times. Let's assume now that the motion of fluid is absent initially, and density surfaces are rejected from an equilibrium (horizontal) position under the law

$$z = z_0 + a(z_0) \cdot \exp(-r^2/2 \cdot l^2). \quad (5)$$

Then

$$z_{z_0} = 1 + a_{z_0} \cdot \exp(-r^2/2 \cdot l^2) \quad (6)$$

and

$$= \int_0^r r z_{z_0} dr = \frac{1}{2}r^2 + a_{z_0}l^2(1 - \exp(-r^2/2 \cdot l^2)). \quad (7)$$

The initial angular momentum does not depend on depth and is equal

$$\mu = \frac{1}{2}fr^2. \quad (8)$$

Therefore

$$= \frac{\mu}{f} + a_{z_0}l^2(1 - \exp(-r^2/2 \cdot l^2)) \quad (9)$$

not only initially, but also during all consequent evolution of perturbation. The equation (9) together with the equation of a hydrostatics (3) and balance of a momentum

$$\frac{v^2}{r} + fv = \frac{\partial \Phi}{\partial r} \quad (10)$$

form the closed set of equations describing distribution of a velocity and a topography of density surfaces in a steady-state equilibrium condition. The set of equations (3), (9), (10) is solved with the following boundary conditions:

$$z = 0 \text{ at } z_0 = 0, \quad (11)$$

$$z = H \text{ at } z_0 = H \quad (12)$$

in the assumption that a free surface and bottom of pool are density surfaces. This mathematical problem describes geostrophic adjustment due to radiation of inertia-gravity waves, i.e. the structure of the eddy just after the detachment of a meander. The following evolution of the eddy will happen due to radiation of Rossby waves and represents the shift of the eddy along the meridian. According to conservation of an angular momentum, equation () still is satisfied. However momentum equation should include the Coriolis force with current value of Coriolis parameter. Thus, if f_0 is value of a parameter of the Coriolis on a latitude of formation of an eddy, and f is current value of a parameter of the Coriolis, the structure of an eddy is described by the equations

$$\frac{v^2}{r} + fv = \frac{\partial \Phi}{\partial r}, \quad (13)$$

$$-N^2(z_0) \cdot z = \frac{\partial \Phi}{\partial z_0} \quad (14)$$

$$= \frac{\mu}{f_0} + a_{z_0} \cdot l^2 \cdot (1 - \exp(-\frac{\mu}{f_0} \cdot l^2)) \quad (15)$$

if to assume as well as earlier, that there are no currents and the shape of density surfaces is set by the formula (5). In the

equation (15) as well as earlier $Q = \int_0^r r \cdot z_{z_0} dr$ and $\mu = rv + \frac{1}{2} fr^2$. The set of equations (13)-(15) it is necessary to

solve with a boundary condition (11) on a free surface and with an additional boundary conditions

$$\text{at } r = R(z_0) \quad v = 0, \quad z = z_0. \quad (16)$$

Two boundary conditions (16) allow to find the unknown boundary of an eddy.

REFERENCES

1. Fuglister F. C. 1970 Cyclonic rings formed by the Gulf Stream 1965-1966. In: Studies in Physical Oceanography, 1, Gordon and Breach, pp. 137-168.
2. Joyce T. M., McDougall T. J. 1992 Physical structure and temporal evolution of Gulf Stream warm core ring 82B. Deep-Sea Research, 39, Suppl. 1, pp 519-544.
3. Eddies in Marine Science 1983 A.R. Robinson, editor, Springer-Verlag, Berlin.
4. McWilliams 1984 The emergence of isolated coherence vortices in turbulent flow. J. Fluid Mech. 146 pp. 21-43.
5. Fedorov K. N. 1983 Physical nature and structure of oceanic fronts. Leningrad, Gidrometeoizdat, 296 p. (in Russian).
6. Richardson P. L. 1993 A census of eddies observed in North Atlantic SOFAR float data. Progr. Oceanog. 31 pp. 1-50.
7. Korotaev G.K. 1997 Radiating vortices in geophysical fluid dynamics. Surveys in Geophysics, 18, pp. 567-619.
8. Carnevale G.F., Kloosterziel R.C., van Heigst G.J.F. 1991 Propagation of barotropic vortices over topography in a rotating tank. J. Fluid Mech. 223 pp. 119-139.
9. Bernstein R.L., White W.B. 1974 Time and length scale of baroclinic eddies in the Central North Pacific Ocean. J. Phys. Oceanogr. 4 pp. 613-624.
10. Hughes C. W. 1995 Rossby waves in the Southern Ocean: comparison of TOPEX/POSEIDON altimetry with model prediction. Journ. Geoph. Res. 100 C8 pp. 15.933-15.950.
11. Korotaev, Dorofeev, 1998 Evolution of ensemble of geostrophic eddies on a beta-plane. (submitted to Fizika atmos. i okeana, in Russian).
12. Rhines P. 1975 Waves and turbulence on a beta-plane. J. Fluid Mech. 69 pp. 417-443.
13. Zaslavsky G.M., Sagdeev R.Z. 1988 Introduction to nonlinear physics: from pendulum to turbulence and chaos. Moscow, Nauka 369 p. (in Russian).
14. Rossby C. G. 1937 On the mutual adjustment of pressure and velocity distributions in certain simple current systems. I. J. Mar. Res. 1 pp. 15-28.
15. Rossby C.G. 1938 On the mutual adjustment of pressure and velocity distributions in certain simple current systems. II. J. Mar. Res. 2 pp. 239-263.

16. Dewar W.K., Killworth P.D. 1990 On the cylinder collapse problem, mixing and the merger of isolated eddies. *J. Phys. Oceanogr.* 20, pp. 1563-1575
17. McWilliams J. C. 1988 Vortex generation through balanced adjustment. *J. Phys. Oceanogr.* 18, pp. 1178-1192.
18. Korotaev G.K. 1998 Nonlinear adjustment of a heavy rotating fluid to equilibrium. *Marine Hydrophysical Journal, Sevastopol*, N 5, pp. 13-19 (in Russian)
19. Korotaev G.K. 1998 A role of conservation of an angular momentum in formation of frontal eddies. (submitted to *Fizika Atmos. i Okeana*, in Russian)
20. Korotaev G.K. 1980 Asymptotical regime of dynamics of intense barotropic eddy. *Marine Hydrophysical Researches* N1 (88), Sevastopol, MHI, pp. 5-18 (in Russian).
21. Flierl G. R. 1984 Rossby wave radiation from a strongly nonlinear warm eddy. *J. Phys. Oceanography* 14, N 3, pp 365-379.
22. Korotaev G.K., Fedotov A.B. 1994 Dynamics of an isolated barotropic eddy on a beta-plane. *J.Fluid Mech.* 264, pp. 277-301.

MATTER TRANSPORT IN MESO-SCALE OCEANIC FRONTS OF RIVER DISCHARGE TYPE

K.A.Korotenko

P.P.Shirshov Institute of Oceanology, Russian Academy of Sciences
Moscow, Russian Federation

ABSTRACT

A hybrid model based on the Random Walk approach and third-order turbulence modelling is developed to forecast transport processes of matter in coastal oceanic fronts of river discharge type. Diurnal variations in processes of cooling and heating as well as wind changes are considered as main reasons to govern conditions of the matter transport in the ocean surface layer. Numerical simulations are performed for the Rhine river discharge zone in the North Sea show a tremendous influence of convection on the vertical matter transport.

1.0 Introduction

A meso-scale oceanic front of the river discharge type is defined to be an interface between salty sea and fresh river water across which the fluid density changes abruptly. It can be observed in coastal waters and can affect the pollutant transport from rivers into the ocean and accumulation of nutrients and thus of fish and other biological populations [1,2].

Such fronts are exposed to weather conditions and often coupled with other coastal processes (i.e. tides, up- and downwelling, re-stratification, etc.) therefore it is difficult to isolated and investigated in the field. The main problem in a realistic prediction of matter transport processes is to estimate turbulent fluxes of buoyancy and momentum with much accuracy. In flow and transport models employed by a number of authors to simulate current velocity, temperature, and salinity distributions, vertical turbulent mixing based on a gradient hypothesis was input to depend on the bulk Richardson number Ri , the latter having been input in 'damping' functions $F(Ri)$ and $G(Ri)$. These functions have to account for effects of stratification when $Ri > 0$. In the case of $Ri < 0$ instantaneous vertical mixing is proposed to simulate. This artificial manner is usually used in simple approaches to describe transport processes in unstable-state stratified flows including convective regime in diurnaly varying surface boundary layer (SBL). However, a use of gradient expression for the vertical flux of eddy kinetic energy in the SBL in the case of convection, as is shown by experiments and theory [3,4], is not only unsuitable to describe the flux but it leads to underestimate the deepening of the mixed layer. *An accurate models of the discharge regions must then describe precisely convection phenomenon as well as processes of stabilisation of the SBL under solar heating.* Such models must account for buoyancy effects in the transport of energy and matter.

The purpose of this paper is to present a methodology of incorporation a third-order closure turbulence model in a random particle technique to predict processes of turbulent transport of matter under strong diurnal changes of the surface heat flux with a special reference to the ocean coastal waters in river discharge regions.

Main effect to be lighted is an influence of solar heating and water surface cooling on a matter concentration distribution in such region.

In shallow frontal zones such as river discharge regions, the heating-cooling effects can play important role in evolution of hydrophysical fields and then, in turn, in transport processes of various additives which enter in water. We consider these effects and their role in the transport processes in the sea surface layer.

Solar heating and wind forcing

General features of an influence of solar heating and wind stress on matter transport processes in the ocean surface layer were investigated analytically in [5,6,7] and numerically in [8]. As it was clearly traced, there are some phases in the development of these processes in surface waters:

1. Intensive heating and slight wind lead to the formation of a shallow quasi homogeneous surface layer, in which contaminant propagates. A vertical size of an admixture jet can be extremely shortened under intensive solar heating influence that leads to relatively high concentration level.

2. Strengthening of the wind with sufficiently intense heating leads to a thickening of the turbulent layer and to a deepening of a mixed layer. The region occupied by the contaminant is also determined by the thickness of the mixed layer.

3. With the beginning of cooling and for a sufficiently high wind velocity there is a rapid deepening of the surface layer. The contaminant propagation process into the sea depth at this stage proceeds rather intensively, and the depth of penetration for additives was restricted by the condition of the particle transport experiment.

Convection

The mixing in the sea surface layer is the mainly due the following mechanisms: wind shear generates turbulence very near the surface, which then diffuses downward; and the cooling of the surface occurring at night sets up an unstable stratification near the surface which again generates turbulence. The latter process is also called *penetrative convection*. Most of the energy provided by both wind and surface cooling to the turbulence is dissipated in the mixed layer, but some of it is used up to erode the lower part of the pycnocline by entraining colder water and thereby deepening the mixed layer.

A number of turbulence models have been applied to the situation of penetrative convection of the mixed layer due to heat loss from the surface. Various laboratory studies of a similar situation were performed, in which a stable layer in a tank with initially a linear vertical temperature gradient was eroded from below by an unstable mixed layer generated by heating the bottom. A close inspection of numerical and experimental results reveals some detailed differences. In the experiments, the temperature gradient is positive over a sizeable region in the upper part of the mixed layer; but the heat flux is still upward over most of this region so that the turbulent heat flux is therefore against the temperature gradient. As an eddy-diffusivity model such as the $k-\varepsilon$ model cannot cope with such a phenomenon, the temperature gradient is predicted to be negative until the heat flux changes sign, leading to the detailed differences near the inversion height. This "negative" turbulent viscosity phenomenon, reflects its non-local, *countergradient* character of turbulent transport in the convective layer. To describe this phenomenon there are a few numerical models of inhomogeneous turbulence based on high-order approximations to the statistical theory of turbulence where *double* correlation (turbulent fluxes) as well as *triple* (turbulent diffusion terms) are included [4,9,10]. Ideas of the triple correlations modelling are used in the hybrid model based on a random walk concept.

2.0 Description of the hybrid model

The Random Walk approach (or *Monte-Carlo* method) are flexible techniques for numerical investigation of complex problems associated with heat and mass transport in the ocean [11]. Being free from well-known numerical problems and artefacts in numerical solutions of the transport equation which associated with finite-differences methods, statistical methods, such as the Monte-Carlo methods, can be used for any

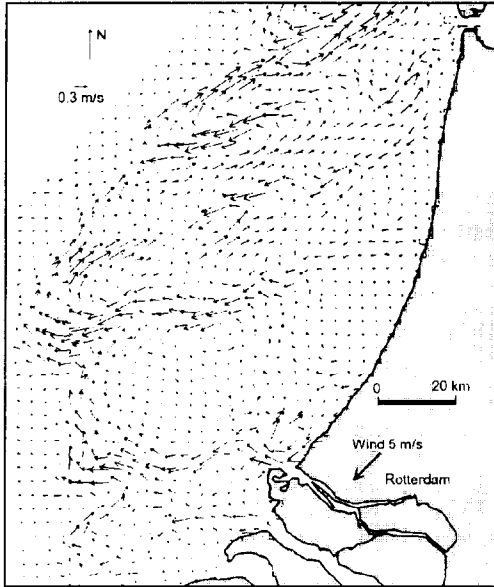


Fig. 1. Eddy velocity field structure in the S-E part of the North Sea [12].

complex geometry, and biochemical effects can be accounted without much difficulty. They has been successfully employed to solve some general problems of matter transport in the coastal waters including the complex atmosphere-ocean interaction influence on the transport processes. In this method, it is proposed that during the j -th time step Δt_j , displacements $(\Delta x_i)_{j,k}$ of the k -th particle are determined as deterministic part of the motion due to mean velocity field $V_{i,j}$ and random one due to fluctuations of velocity with a certain statistical law $(\eta_{i,j,k})$. The following equation for the displacements of each particle moving in space are assessed as it is given by following expressions:

$$(\Delta x_i)_{j,k} = V_{i,j} \Delta t_j + (\eta_i)_{j,k} \quad (1)$$

$$(i = 1-3; j = 1, 2, \dots, N_t; k = 1, 2, \dots, N)$$

where x_i is axis, N_t is a number of time step and N is a number of released particles.

Besides knowledge on mean velocity components,

calculations of each particle trajectory require to know about the law $(\eta_{i,j,k})$ as a function of time and space. Type of this law is determined by statistical structure of deviations (fluctuations)

of velocity from its mean value at time step Δt . Since these fluctuations prove to be independent, the law $(\eta_{i,j,k})$ are believed to be Gaussian. In this case, the $(\Delta x_i)_{j,k}$ could be derived directly from Reynolds stresses (double correlations) $\overline{u_i u_j}$, where brackets denote ensemble average values of the velocity fluctuation components.

The Reynolds stresses, in turn, should be defined as a function of the triple correlations as it is required for the correct description of the non-local mechanism of transport under the penetrative convection.

Note that in the proposed method, besides the particle distribution we can define a concentration of particles $C(x,y,z,t)$ in a given cell as a number of particles being in the cell related to the volume of the latter.

2.1 Equations for the double and triple correlations

Note, that particle distribution numerical simulations were performed for the S-E part of the North Sea at that the mean velocity field (Fig.1) was taken from numerical simulation made by De Kok [12]. A derivation and description of equations for the double and triple correlations turbulent quantities one can find in the work by Andre et al [4]. Here, we adduce of an instance oversimplified equations for these turbulence parameters and necessary initial and boundary conditions which were used in the model.

Governing equations:

$$\frac{\partial T}{\partial t} = - \frac{\partial \overline{wT'}}{\partial z}, \quad (2)$$

$$\frac{\partial \overline{wT'}}{\partial t} = - \frac{\partial \overline{w^2 T'}}{\partial z} - \overline{w'} \frac{\partial T}{\partial z} - \alpha g \overline{T'^2} - c_6 \frac{k^{-1/2}}{l} \overline{wT'} + c_7 \alpha g \overline{T'^2} + c_3 \frac{\partial}{\partial z} \left(k^{-1/2} l \frac{\partial \overline{w^2 T'}}{\partial z} \right), \quad (3)$$

$$\frac{\partial \overline{w^2}}{\partial t} = - \frac{\partial \overline{w^3}}{\partial z} - \overline{w'} \frac{\partial T}{\partial z} - \frac{2}{3} c_1 \frac{k^{-1/2}}{l} \left(2 - \frac{4}{3} c_3 \right) \alpha g \overline{wT'} - c_4 c_4 \frac{k^{-1/2}}{l} \left(\overline{w^2} - \frac{2}{3} k \right) + 2c_3 \frac{\partial}{\partial z} \left(k^{-1/2} l \frac{\partial \overline{w^2}}{\partial z} \right), \quad (4)$$

$$\frac{\partial k_h}{\partial t} = - \frac{\partial \overline{wk_h'}}{\partial z} - \frac{2}{3} c_1 \frac{k^{-1/2}}{l} - \frac{2}{3} c_5 \alpha g \overline{wT'} - c_4 c_4 \frac{k^{-1/2}}{l} \left(k_h - \frac{2}{3} k \right), \quad (5)$$

$$\frac{\partial \overline{T^2}}{\partial t} = -\frac{\partial \overline{w^2 T^2}}{\partial z} - 2\overline{wT} \frac{\partial T}{\partial z} - \alpha g \overline{T^2} - c_1 c_2 \frac{k^{-1/2}}{l} \overline{T^2}, \quad (6)$$

$$\frac{\partial \overline{w^3}}{\partial t} = -3\overline{w^2} \frac{\partial \overline{w}}{\partial z} - 3\alpha g \overline{w^2 T}; \quad |\overline{w^3}| \leq (2\overline{w^2})^{1/2}; \quad (7;7a)$$

$$\frac{\partial \overline{wk'_h}}{\partial t} = -\overline{w^2} \frac{\partial k'_h}{\partial z} - \alpha g k'_h \overline{T}; \quad |\overline{wk'_h}| \leq k'_h (\overline{w^2})^{1/2} \quad (8;8a)$$

$$\frac{\partial \overline{w^2 T}}{\partial t} = -2\overline{w^2} \frac{\partial \overline{T}}{\partial z} - \overline{wT} \frac{\partial \overline{w^2}}{\partial z} - \overline{w^3} \frac{\partial T}{\partial z} - 2\alpha g \overline{wT^2}; \quad |\overline{w^2 T}| \leq \left[\overline{w^2} (\overline{w^2 T^2} + \overline{wT^2}) \right]^{1/2} \quad (9;9a)$$

$$\frac{\partial \overline{wT^2}}{\partial t} = -\overline{w^2} \frac{\partial \overline{T^2}}{\partial z} - 2\overline{wT} \frac{\partial \overline{T}}{\partial z} - \overline{w^2 T} \frac{\partial T}{\partial z} - \alpha g \overline{wT^3}; \quad |\overline{wT^2}| \leq \left[T^2 (\overline{w^2 T^2} + \overline{wT^2}) \right]^{1/2} \quad (10;10a)$$

$$\frac{\partial \overline{k'_h T'}}{\partial t} = -\overline{wT'} \frac{\partial k'_h}{\partial z} - \overline{wk'_h} \frac{\partial T'}{\partial z}; \quad |\overline{k'_h T'}| \leq k'_h \overline{T'^2}^{1/2} \quad (11;11a)$$

$$\frac{\partial \overline{T'^3}}{\partial t} = -3\overline{wT'} \frac{\partial \overline{T'^2}}{\partial z} - 3\overline{wT'^2} \frac{\partial T'}{\partial z}; \quad |\overline{T'^3}| \leq 2(\overline{T'^2})^{1/2} \quad (12;12a)$$

where $k'_h = (u^2 + v^2) / 2$ is horizontal turbulent kinetic energy, l is turbulence scale to be equal to the convective layer depth $l=h(z)$. The empirical coefficients according to [4] are chosen to be as $c_1 = 1.6$; $c_2 = 2.5$;

$c_3 = -0.004$; $c_4 = 4.50$; $c_5 = 0$; $c_6 = 4.85$; $c_7 = 0.394$.

Initial and boundary conditions:

An intergration of (2)-(12) was performed under the following conditions: all double correlation are assumed to be zero except the surface boundary (Fig.2):

$\overline{v_s w} = \overline{u_s v_s} = 0$; $\overline{wT'} = q_0$; $\overline{u_s w} = u_*^2$; $\overline{w_s^2} = 1.8u_*^2$; $\overline{T_s^2} = 1.8q_0 / u_*$, where $u_* = -(\alpha g q_0 z)^{1/3}$, g is the gravity acceleration and α is the thermal expansion coefficient. All triple cor-relations are chosen initially to be zero. An initial distribution of particles was taken as it is shown in Fig. 3.

Following to [4], the third-order correlations appearing in eq. (7)-(12) are modelled with a use of the "clipping approximation" deduced from Schwartz's inequality. In the quasi-normal approximation which is usually used to close of turbulence equations, the equations for second- and third-order correlations are expressed exactly, but fourth-order correlations are expressed in terms of those of the second order, as if the velocity were a Gaussian random variable. For homogeneous and isotropic turbulence, the quasi-normal

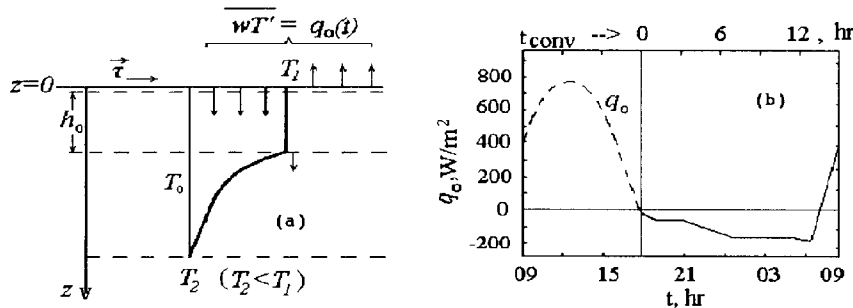


Fig.2. The initial and boundary conditions of the convective layer model (a) and the surface heat flux $q_0(t)$ diurnal variation (b).

approximation leads to the development of negative values of the energy density in the spectral range. This defiance can be traced to an excessive growth of third-order correlations, since one effect of exact fourth-order correlations is to limit the built-up of triple correlations. This effect is lost in the quasi-

normal approximation and must be thus be replaced by an damping mechanism in the equations for the rate of change of third-order correlations. The clipping approximation expressed by eq. (7a,8a,9a,10a,11a and 12a) is an example of such a dumping mechanism.

3.0 Numerical experiments

Numerical experiments with the Random Walk technique were performed to emphasise an influence of solar heating diurnal variations on spreading of an particle jet in the sea surface layer. A continuous source (1000 particles/min) was situated at the sea surface at the Rhine outflow area.

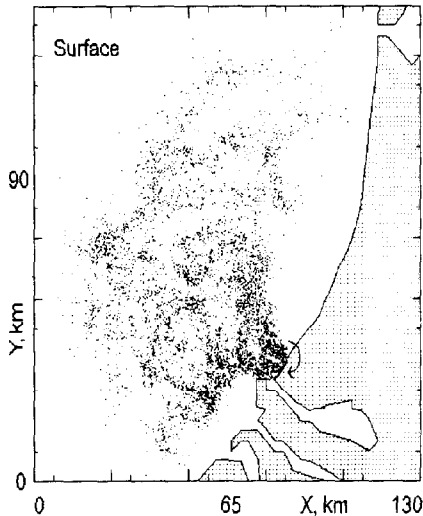


Fig.3. The particle distribution taken as an initial in numerical experiments.

Fig.4 depicts an evolution of the particle jet in the upper layer of the sea. One can notice a tremendous changes of particle concentration at different layers. Progressing of the convection to diminish of particles at the sea surface and their frontal-like transport to lower layers. Similar diurnal variations of the sea surface temperature and admixture concentrations have been observed by NOAA satellites [12].

4.0 Conclusion

Understanding the daily cycle influence on processes of turbulent transport of admixtures in the sea surface layer requires studies of daytime warming and nocturnal cooling and mixing. Both phases of the daily cycle are very important, as it is their net effects that controls average sea surface temperature. The density structure changed during daytime phase also affect the distribution of different additives. The proposed random particle method allows to investigate a complex problem associated with the matter transport in the coastal ocean. To effectively use this method one need to have information about both mean velocity and density fields and their turbulence characteristics. Despite a wide spectrum of flow and turbulence models being able to predict behaviour of the mean and fluctuation characteristics just a few of them can really be applied for such a phenomenon as the penetrative convection requires to calculate diffusion terms (triple correlations) in equations at turbulence modelling. Such a sort of approach was employed in the proposed hybrid model. Performance of the model is demonstrated by calculations of the particle transport in the coastal water river discharge type in period nocturnal convection.

Acknowledgements

The author would like to thank J. de Kok for fruitful consultations on the problem. The work was performed in part due to support from the Ministry of Science and Technologies of the Russian Federation (Projects "Structure" and "Methodology") and in part by the RFBR-Grant No 96-05-64323.

5.0 References

- [1] M.J. Bowman and W.E. Esaias (Eds.), 1978, Oceanic fronts in coastal processes, Springer-Verlag, New York, 239 p.
- [2] K.N. Fedorov, 1978, The physical nature of oceanic fronts, Springer-Verlag, New York, 189 p.
- [3] G.E. Willis and J.W. Deardorff, 1974, A laboratory model of the unstable planetary boundary layer, J. Atmosph. Sciences, 31, 1297-1307.

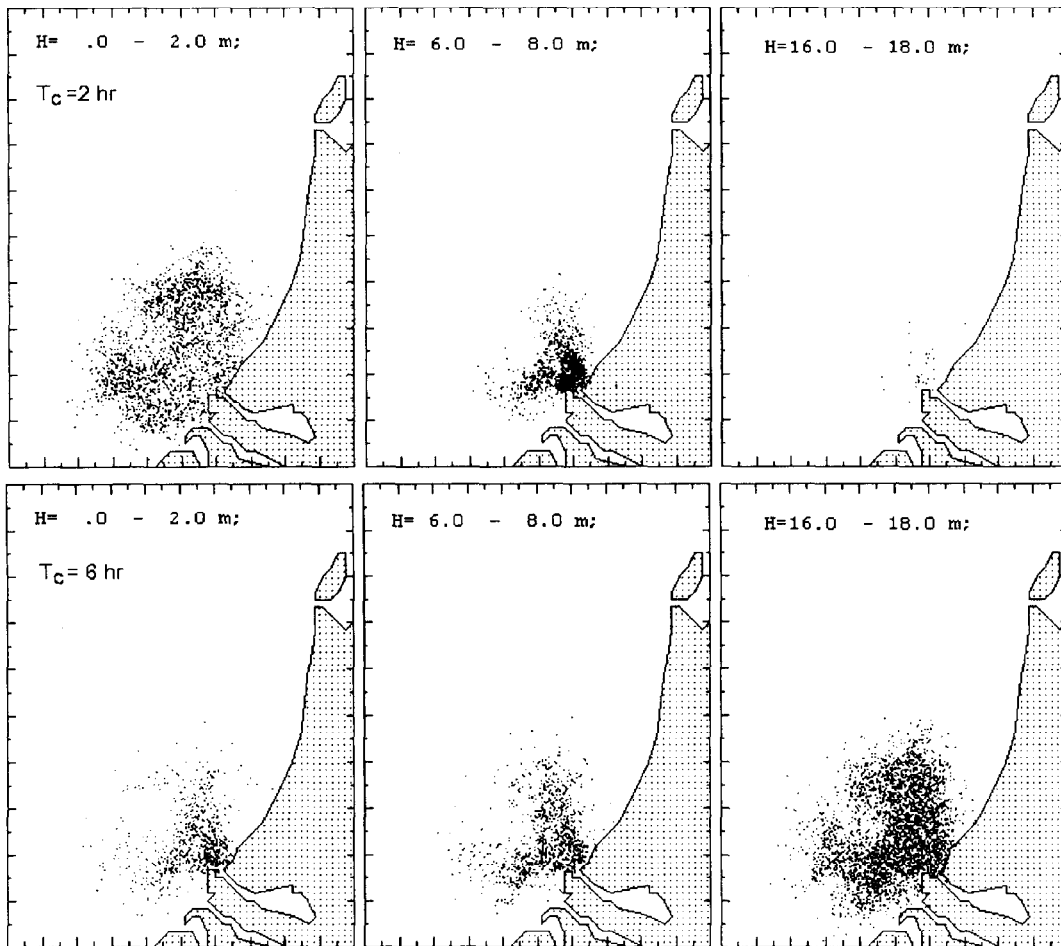


Fig.4. Spatial distribution of particles at the nocturnal convection period; $T_c = 2$ hours (above) and $T_c = 6$ hours (below) after the convection start.

- [4] J.C. Andre, G.De Moor, P. Lacarrere, G.Therry and R du Vachat, 1978, Modeling the 24-hour evolution of mean and turbulent structures of the planetary boundary layer, *J. Atmosph. Sciences*, 35, 1861-1883.
- [5] K. A. Korotenko, 1987, On the vertical turbulent matter transport in a thin ocean surface layer in a day warming period, *Oceanology*, 27(1), 47-51.
- [6] K. A. Korotenko, 1988, On turbulent transport of matter in a non-stationary shear current in the ocean, *Oceanology*, 28(4), 545-549.
- [7] K. A. Korotenko, 1990, On admixture jet spreading in the ocean surface layer, *Oceanology*, 30(4), 546-550.
- [8] K. A. Korotenko, 1992, Modelling turbulent transport of matter in the ocean surface layer, *Oceanology*, 32(1), 5-13.
- [9] O. Zeman and J.L. Lumley, 1976, Modeling buoyancy driven mixed layers, *J. Atmosph. Sciences*, 33, 1974-1987.
- [10] A.F. Kurbatsky, 1988, Modelling of a non-local turbulent transport of momentum and heat. "Nauka", Novosibirsk, 239 p.
- [11] K.A. Korotenko. 1994. The Random Walk concept in modelling matter transport and dispersion in the sea, *J. Moscow Phys.Soc., Allerton Press, New York*, 4, 335-358.
- [12] J.M. De Kok, 1994, Numerical modelling of transport processes in coastal waters, Ph.D Thesis, University of Utrecht, Utrecht, the Netherlands, 158 p.

MAIN FEATURES OF FRESH AND SALINE WATERS MIXING PROCESSES IN THE NORTHERN CASPIAN SEA

A.N. Kosarev¹, A.V. Kouraev^{1,2}

1 Moscow State University, Geographical faculty, department of oceanology, Vorobyevy gory, MGU, 119899, Moscow

2 Nansen International Environmental and Remote Sensing Center (NIERSC), Korpusnaya str. 18, 197110, St. Petersburg

E-mail: kosarev@ocean.geogr.msu.su, kouraev@ocean.geogr.msu.su

Abstract. Main features of mixing zone between fresh and saline waters in the Northern Caspian sea are studied.

It was found that mixing processes and spatial salinity distribution in this zone are influenced mainly by such factors as river runoff, water exchange and dynamics, as well as by sea level. These factors can significantly vary intensity of mixing processes, that are characterised by the well-pronounced seasonal variability. Interannual variations are also high; in spite of revealed stability of multi-year spatial location of the frontal zone, salinity values on its boundaries undergo sharp changes from year to year.

Northern Caspian (NC) is a shallow (with average depths about 5 m) shelf part of the Caspian sea, where combination of big river runoff, small depths and big surface area results in existence of vast zones of fresh water transit and large-scale processes of mixing of fresh and saline water. Main features of the mixing zone explain high biological productivity of this region of the Caspian sea. According to the K. N. Fedorov classification, frontal zone of the NC is of climatic type with local impact, i.e. zone of interaction between various basins and aquatories. Here fresh waters of the Volga, Ural and Terek rivers (with Volga discharge being more than 90% of the total fresh water input in the NC) interact with salt water of the open regions of the NC and MC (11-13 ppt).

Previous investigations show that three main water types can be discriminated in the NC: freshened water (1-6 ppt), proper sea water (10-12 ppt and higher) and water of the frontal zone (area of the most intensive mixing processes - 5-10 ppt). Absolute salinity values considered as boundary values for distinguishing between different water types differs in various publications [1-5], but typical zones revealed in the mixing zone are the same: a) fresh water transit, b) frontal zone and c) sea water influence zone.

Analysis of the seasonal and interannual variations of the mixing zone characteristics was based on the more than 30 years (1961-1993) of observations on five standard transects in the NC (fig. 1.), mainly on salinity data as the most changing parameter [6, 7]. It was found that in several regions of the aquatory two processes take place with similar possibility: (i) gradual mixing (diffusion) and (ii) 'pushing' (advection) of one type of water by the other. Both processes are strongly related with seasonal distribution of the river runoff, what necessitate separate analysis of salinity distribution for each season; otherwise averaged annual values may hide or misinterpret character of various natural processes taking place in the mixing zone. Besides, spatial and temporal salinity variations in the NC result in the need to use median (and not average) values as mean salinity values, because some extreme data may result in incorrect assessment of the mean salinity value. These facts should be taken into account when applying various models of river and salt water interaction and models of passive substance transport in the NC.

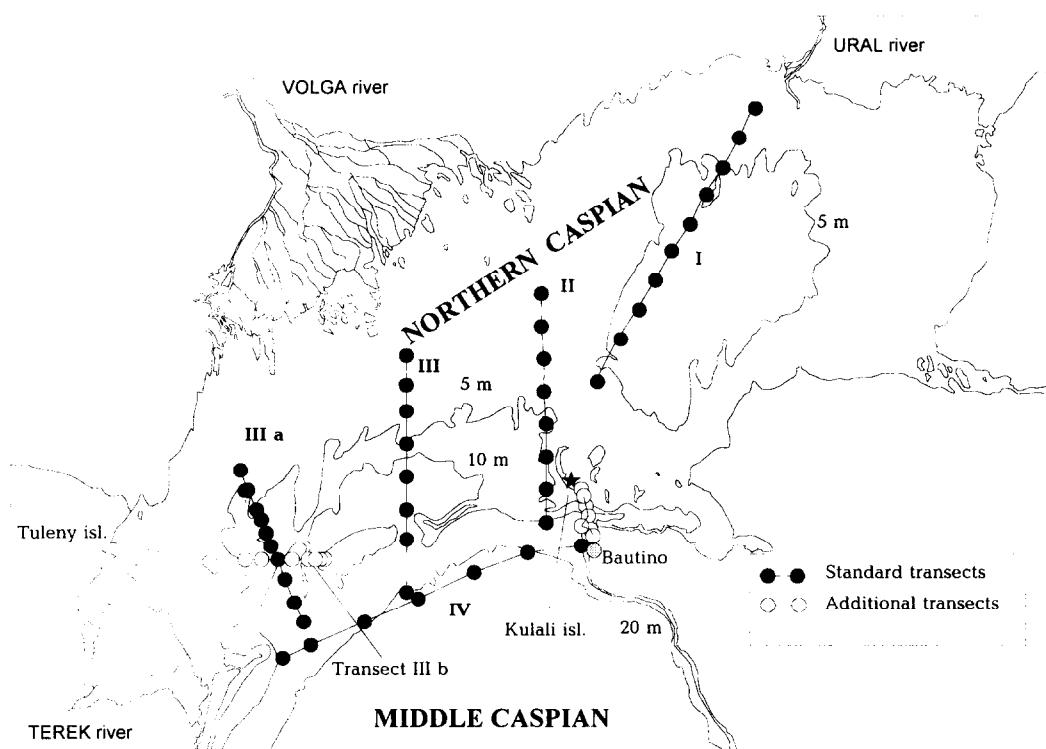


Fig. 1. Hydrological transects in the Northern Caspian.

Analysis of maps of for water with specific salinity range occurrence (in %) during spring, summer and autumn (1961-1993) revealed relation between spatial salinity distribution and processes of water mixing, circulation and exchange. In April main part of the aquatory is dominated by the MC water; salinity is mainly above 8 ppt. In June, when river discharge is maximal for the studied months, surface area and presence of freshened water increase. In August decrease of river runoff result in the intensification of water inflow from the MC, there is an increase of occurrence of water with salinity above 8 ppt (up to 80% on the boundary between NC and MC) and, especially, above 10-12.5 ppt (up to 85-90% in the southern part of the NC). In October an

intensification of water inflow from the MC is observed; water with salinity above 10 -12.5 ppt occupy all central part of the NC (with maximal occurrence 80-85%).

Analysis of seasonal distribution of spatial salinity gradients on the sea surface shows that the north-western part of the NC, where main branch of the Volga discharge flows, is characterised by the constant presence (from April to October) of high gradients (up to 1.2 ppt/km). For most of the NC maximal salinity gradients (0.6-0.8 ppt/km) are typical mainly for April-June, they decrease in August, in October salinity is distributed most evenly.

Spatial distribution of the mixing zone boundaries has seasonal and interannual variations, stipulated by changes of river discharge and intensity of the MC water inflow. The period of actual sea level rising is characterised by the increased influence of Volga runoff (what manifests in widening of the river waters transit area), and at the same time by decrease of the penetration of MC waters in the central part of the NC. Location of the frontal zone is stable (as compared with other mixing zone boundaries); it is mainly located at a 80-120 km distance from the Volga delta edge. In spite of the spatial stability of the frontal zone, there are significant salinity variations at the boundaries of this zone, related with the Volga water abundance. Therefore the seasonal salinity changes should be taken into account for the discrimination of the frontal zone in the NC. In the region of the main Volga stream (western part of the aquatory) the mixing of fresh and saline waters is the most intense, what is proven by (i) low probability of the observation of the boundary of the sea water influence and (ii) cases of simultaneous formation of several frontal zones at the same time (according to transects data).

Interaction between river and sea waters in the boundary region between NC and MC is influenced by joint action of river discharge and sea level, that both have interannual variations. After 1997, when sea level was minimal for the last 400 years, occurrence of water with high salinity (12-13 ppt) decreased from more than 50% to 40%, while salinity variability in the western part of the boundary (area 20-30 km wide where influence of the Volga discharge is maximal) increased from 3-5% to 10-15%. These changes can be explained mainly by the increase of Volga discharge started after 1977; sea level variations have minor effect on water dynamics in this relatively deep (maximal depths up to 25 m) region.

For the first time joint influence of the sea water level and amount of Volga discharge on the salinity distribution and water dynamics in the whole NC was studied (fig. 2). It was found that due to small depths of the aquatory, sea level changes on 1-2 m form a background determining range of MC water penetration and character of interaction between NC and MC waters. On this background amount of the Volga discharge leads to different types of spatial salinity distribution (fig. 2).

Under high sea level (above -28.4 m in absolute level scale) there is a possibility for the MC water to enter into the NC and there exist good relation between salinity and amount of Volga discharge - increase of fresh water input lead to salinity decrease, especially near the Volga delta. Decrease of Volga discharge result in the intensification of water inflow from the MC and domination of these waters in the central part of NC.

Under low sea level conditions interaction between fresh and saline waters is more complicated and vary according to the amount of fresh water input. Under low sea level conditions morphology of the NC hinders inflow of water from the middle part of the sea, and, at the same time, contributes to formation of big fresh water

transit zone and large-scale mixing processes. However, in the years with high Volga discharge ($Q > 7270 \text{ m}^3/\text{s}$), main part of freshened waters pass by along the western shallow part of the NC directly into the MC, causing high compensation inflow of the saline MC waters. It results in freshening of the north-western part of the NC (though not so pronounced as under high sea level conditions) and in the increase of the presence of saline waters in the central part of the NC aquatory.

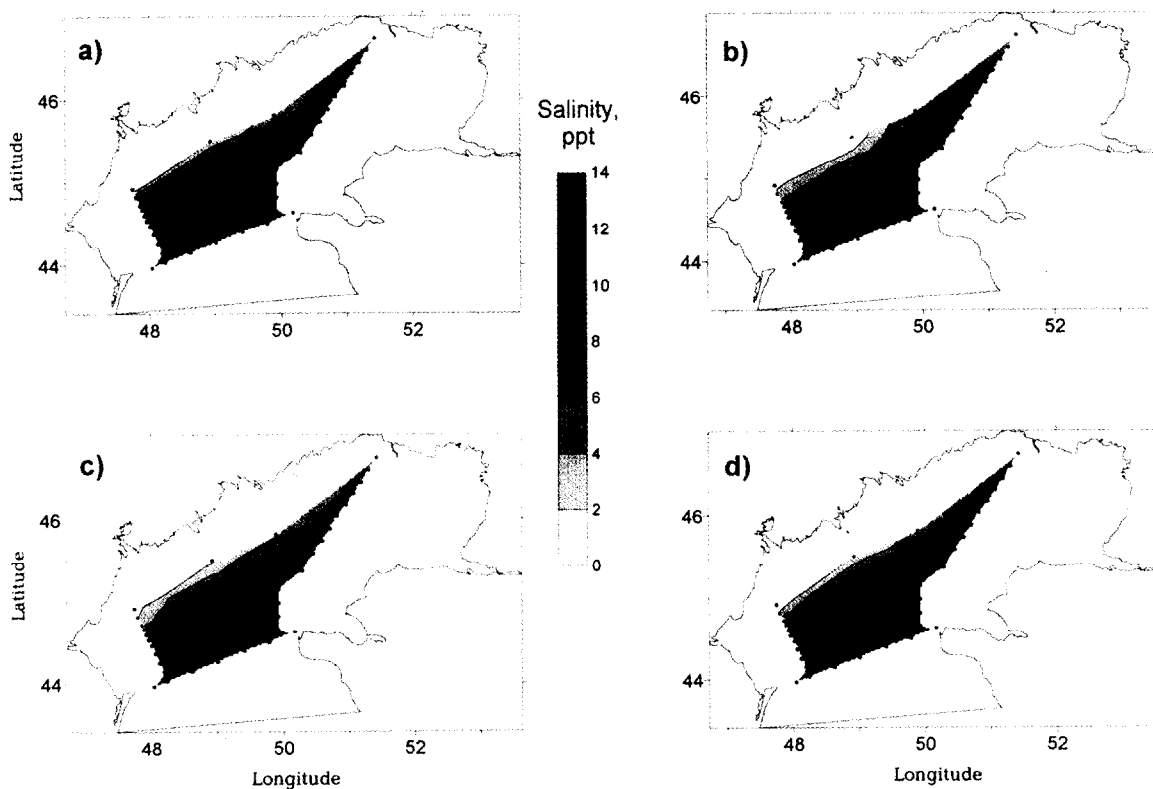


Fig. 2. Mean salinity (ppt) distribution in the Northern Caspian under various hydrological conditions during the beginning of the Volga spring flood.

- a) high sea level, low discharge*
- b) high sea level, high discharge*
- c) low sea level, low discharge*
- d) low sea level, high discharge*

[1] A. N. Kosarev, 1975, "Hydrology of the Caspian and Aral seas" Moscow, MSU publishing, 272 pp.
 [2] A. N. Kosarev and E. A. Yablonskaya, 1994, "The Caspian sea", The Hague, SPB Academic Publishing, 259 pp.
 [3] V. F. Polonskiy, Yu. V. Lupachev, N.A. Skriptunov, 1992, "Hydrological and morphological processes in the river mouths and methods for their calculations". St Petersburg, Hydrometeoizdat, 383 pp.
 [4] N. A. Skriptunov, 1958, "Hydrology of the Volga near-shore" Moscow, Hydrometeoizdat, 143 pp.
 [5] B. M. Zatchnaya, 1970, "Particularities of salt composition of the northern Caspian sea waters", GOIN proceedings, issue 101, p. 74-79.

- [6] A. N. Kosarev, A. V. Kouraev, 1997, "*About influence of the river Volga runoff on hydrological conditions of the Northern Caspy during modern sea level rise*". International Hydrological Programme, IHP-V, Technical Documents in Hydrology, N3, Environmental and socio-economic consequences of water resources development and management, Proceedings of the Moscow Symposium (15-20 May 1995), UNESCO, Paris, p.134-137.
- [7] A. V. Kouraev, 1998, "*Particularities of hydrological conditions of the Northern Caspian during the period of actual sea level rise*", Ph.D. thesis, Moscow State University, Moscow, 234 pp.

VARIABILITY OF THE SICILIAN UPWELLING

A.G. Kostianoy¹, M. Astraldi², G. P. Gasparini² and S. Vignudelli²

¹ P.P. Shirshov Institute of Oceanology, 36 Nakhimovsky Pr., Moscow, 117851, Russia
e-mail: kostianoy@glas.apc.org

² CNR-Istituto per lo studio dell'Oceanografia Fisica, 19100 Lerici, La Spezia, Italy
e-mail: fisggs@estof.santateresa.enea.it

Abstract. The analysis of a large set of IR satellite images has permitted to estimate the typical parameters of the upwelling in the Strait of Sicily, along with its interannual and seasonal variability. While the interannual variability shows during the period 1983-88 a progressive weakness of the upwelling, which might be related to a corresponding decreasing of the wind intensity, the seasonal cycle exhibits its maximum surface evidence during September with a lack of evidence during the colder season. However, the results inferred from hydrological measurements and wind intensity seem to suggest a much more intense upwelling during the colder season than the warmer one.

Introduction

During the last 30 years our knowledge on the dynamics of the Mediterranean Sea circulation, especially of its western part, has substantially increased, while few attention has been focused on its wind-driven upwelling systems. One of the most important upwelling systems in the Mediterranean Sea is the Sicilian upwelling, which is governed by the strong southeastward wind stress in the Western Mediterranean caused by the characteristic Mistral.

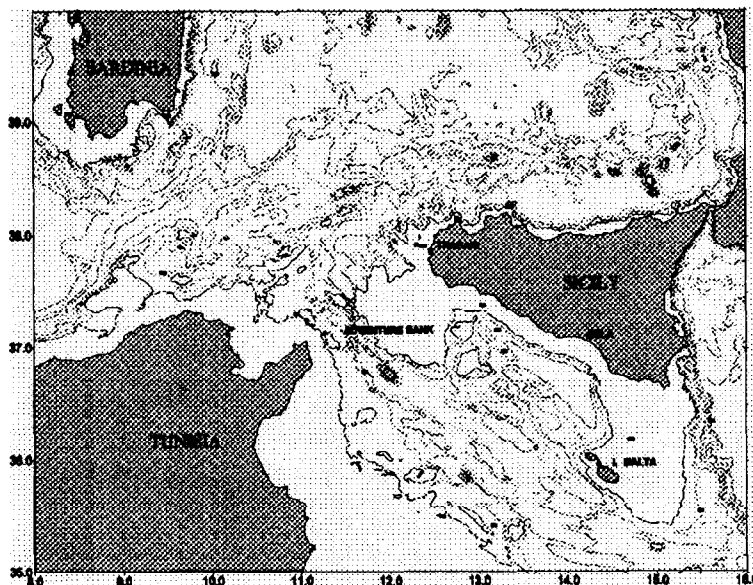


Fig. 1: The region of the Sicily Strait.

The Strait of Sicily (Fig. 1) has always been a region of special attention to oceanographers, because of its importance in controlling the water exchanges between the western and eastern basins of the Mediterranean Sea. Although much progress has been achieved in the understanding of the Modified Atlantic and Levantine Intermediate Water mass exchange [1-6], the three-dimensional thermohaline structure as well as the dynamics and seasonal variability of the Sicilian upwelling remains still somewhat poorly known.

Philippe and Harang [7] were the first to show IR satellite images of the Sicily upwelling. What emerged from their study was that the upwelled waters could reach 150 km offshore. The general dynamics of the Sicilian upwelling is governed by the wind stress with a delay of three days between the N-NW wind and the appearance of upwelling phenomena. Usually, upwelling events begin south of Trapani and thereafter evolve eastward along the coast of Sicily [8].

This report focuses on the main spatial and thermal characteristics of the Sicilian upwelling, as derived from satellite AVHRR data from 1983 to 1988 [9]. The interannual and seasonal variability of its characteristics is investigated and related to the wind observations obtained from the ECMWF weather-prediction model. The results are based on a large set of Sea Surface Temperature (SST) maps, which represent a statistically consistent data set for the analysis of the seasonal variability.

Upwelling characteristics

The main characteristics and seasonal variability of the Sicilian upwelling were determined from a set of 243 satellite IR weekly maps of sea surface temperature (SST) and of the thermal fronts located in the Mediterranean Sea, published by Le Centre de Meteorologie Spatiale (Lannion, France). The time period covered by these data spans from September 1983 to November 1988. The total distribution of data among seasons and years is quite uniform. These maps have been analysed in order to estimate the length of the upwelling zone along the southern coast of Sicily (L), the width (D), the minimal temperature of the upwelled water (T_m), the temperature contrast (dT) and the temperature gradient (grT) across the upwelling front. Fig. 2 is a sample image showing the upwelling phenomena along the Sicily coast.



Fig. 2: *Sea surface temperature distribution relative to the 27 August 1985. The lighter areas are colder radiated temperatures.*

The descriptive statistics for the main parameters indicates that usually upwelling involves more than 2/3 of the southern coast of Sicily with a uniform frequency distribution. In 2/3 of the cases, the width of the upwelling zone is about 20-40 km. The widths more than 100 km are rare, but do exist. Usually, the upwelling zone is irregular for what concerns the size because of a very complex bottom topography (see Fig. 1). The Adventure Bank and the Malta Platform are separated by the deep (500-1000m) Gela and Malta Basins. Accordingly, the width of the upwelling zone is greater over these banks (especially over the Adventure Bank) and smaller in the middle of the coast, where the shelf (depth < 200m) is only 20-30 km wide. It was also found that the upwelling first appears in the western part of the coastal zone and then propagates eastward. Sometimes, it was observed only over the Adventure Bank where the upwelling zone often looks like a very large meander. A mean value of the temperature contrast across the upwelling front is -1.4°C and the temperature gradient is of $\sim 0.23^{\circ}\text{C}/\text{km}$.

Interannual and seasonal variability

The interannual variability of the length of the Sicilian upwelling, inferred from the weekly SST maps, indicates that it seems to be uniform from one year to another one and its values are obviously limited to the length of the Sicilian coast. Its width is much more variable and a decreasing trend seems to exist from 1983/84 to 1988 (Fig. 3).

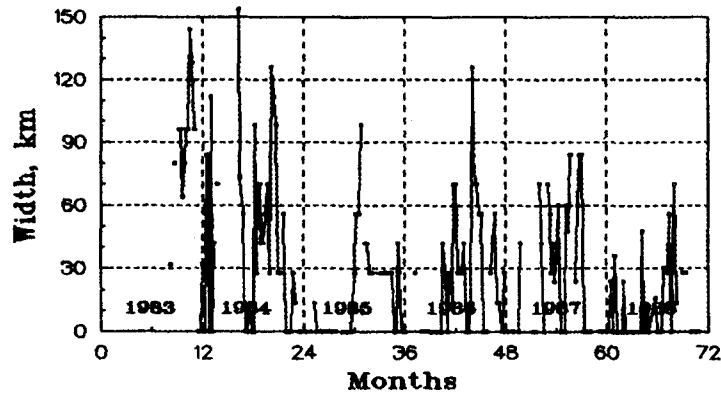


Fig. 3: Interannual (1983-1988) variability of the width (D) of the upwelling zone.

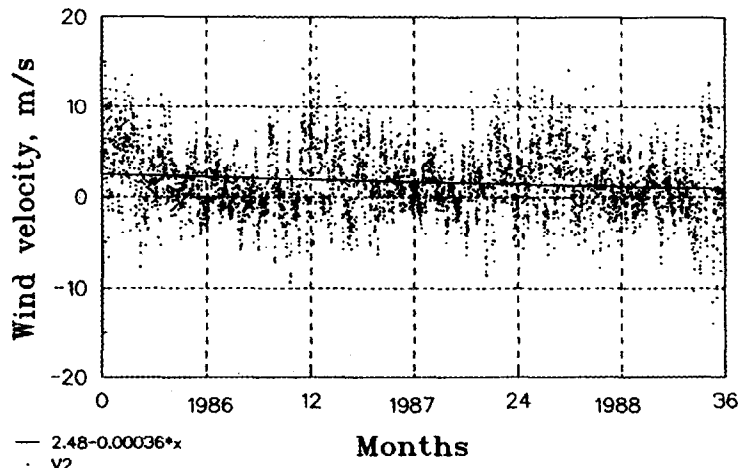


Fig. 4: Wind velocity along the southern coast of Sicily during 1986-1988.

During the same time period, a climatological decrease of the wind (favourable wind stress) over this region is observed (Fig. 4) and consequently a corresponding diminution of the upwelling intensity is expected. The interannual variability of the minimal temperatures indicates a seasonal variability, but with a notable increase of amplitude from year to year. This is due to the rise of late summer minimum from 21°C in 1983 to 26°C in 1987. The late winter minima vary very little, i.e., between 13 and 14°C that correspond to the typical characteristic temperatures of the upper layer in winter. The rise in summer of T_m is consistent with the consequent decrease in the width of the upwelling zone, because the narrower the upwelling zone (less intense upwelling) the higher the temperatures observed at the surface. Consequently, the trend in temperature may be related to the general decrease of the upwelling intensity and could be explained by the climatic warming in the Mediterranean Sea [10].

From the study of the seasonal variability of the Sicilian upwelling it appears a pronounced gap in the observation of the upwelling events during March-April, which is prevalently due to the thermal homogeneity of the upper layer during these months. This is absolutely consistent with the seasonal cycle of T_m . Conversely, there is a persistency (there are no interruptions) of the upwelling event during September over, at least, 6 years of observations.

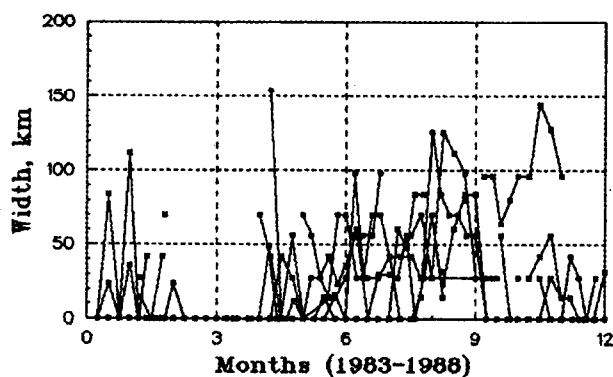


Fig. 5: Seasonal variability of the width (D) of the upwelling zone during 1983-1988.

With reference to the seasonal variability of the parameters, there are no pronounced cycles in the length (L) and width (D) of the upwelling zone (Fig. 5), but there is a well defined cycle in the minimal temperature T_m and a less defined one in the temperature contrast (dT) and gradient (grT) (Fig. 6).

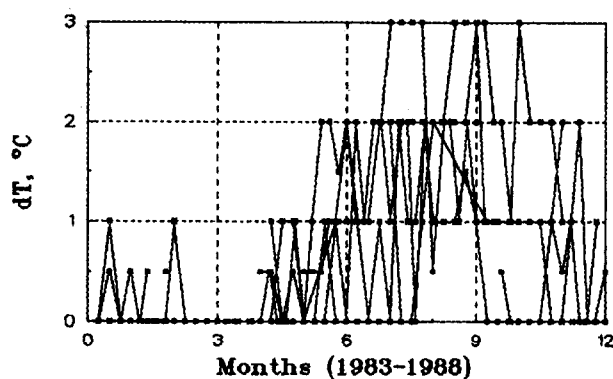


Fig. 6: Seasonal variability of the temperature contrast (dT_m) between coastal and offshore waters during 1983-1988.

Usually minimum temperatures (13-15°C) were observed during January-March and maximum temperatures (20-25°C) in August-October. As a rule, during August-October the temperature contrast and gradient across the upwelling front reach 3°C and 0.4°C/km, respectively. The absence of a seasonal cycle in the upwelling width is surprising, because the meteorological data indicate that the wind stress in winter in the Sicily Strait is three times greater than in summer. This should result in a significant increase of the upwelling intensity during winter leading to a noticeable enlargement offshore of the upwelling zone, which is not seen. This paradox may be explained by the principal difference in the vertical density field, which is strongly related to temperature in the upper layer of the sea, between winter and summer. During winter, there is a relatively homogeneous 100-150 m upper layer, and the pycnocline is located much deeper than in summer; in this case, much stronger favourable wind stress is required to lift the pycnocline, such that the signatures of upwelling are evident on the sea surface.

Conclusions

The previous results show that the upwelling is a persistent feature of the Sicily Strait during all the seasons. Due to a winter intensification of the wind over the region, a more intense upwelling should be expected in winter than in summer. However, the Sicilian upwelling is not a purely near-shore phenomenon: it often occupies a very large area (up to 50%) of the Strait of Sicily, thus influencing the large scale dynamics of the upper layer and has important consequences on the biological productivity and fishing activity. All the characteristics of the upwelling are obtained using only SST data. The investigation of the three-dimensional structure, by using in situ measurements, is certainly necessary for a better understanding of the seasonal cycle and also for evaluating the connection with the biological production.

Acknowledgements

This research was financed by NATO-CNR Guest Fellowship Programma (Ann. No. 217.28/1.02) and by the EU-MAST project MATER (MAS3-CT96-0051), and by the International Project "Upwelling" of the Russian Ministry of Science and Technologies.

References

- [1] I. M. Ovchinnikov, E. A. Plakhin, L. V. Moskalenko, K. V. Neglyad, A. S. Osadchiy, A. F. Fedoseev, V. G. Krivosheya and K. V. Voitova, 1976, *The Hydrology of the Mediterranean Sea*, Gidrometeoizdat, 375 pp.
- [2] S. Garzoli and C. Maillard, 1979, Winter circulation in the Sicily and Sardinia Straits region, *Deep Sea Research*, 26 A, 933-954.
- [3] G. F. Grancini and A. Michelato, 1987, Current structure and variability in the Strait of Sicily and adjacent area, *Annales Geophysicae*, 1, 75-88.
- [4] G. M. R. Manzella, G. P. Gasparini and M. Astraldi, 1988, Water exchange between the eastern and western Mediterranean through the Strait of Sicily, *Deep Sea Research*, 35, 6, 1021-1035.
- [5] G. M. R. Manzella, T. S. Hopkins, P. J. Minnett and E. Nacini, 1990, 95, C2, 1569-1575.
- [6] M. Astraldi, G. P. Gasparini, S. Sparnocchia, M. Moretti and E. Sansone, 1996, The characteristics of the water masses and the water transport in the Sicily Strait at long time scales, *Bulletin de l'Institut oceanographique*, 17, 95-115.
- [7] M. Philippe and L. Harang, 1982, Surface temperature fronts in the Mediterranean Sea from infrared satellite imagery, *Hydrodynamics of semi-enclosed seas*, J. C. J. Nihoul (ed.), Elsevier, 91-128.
- [8] A. Piccioni, M. Gabriele, E. Salusti, E. Zambianchi, 1988, Wind-induced upwellings off the southern coast of Sicily, *Oceanologica Acta*, 11, 4, 309-314.
- [9] A. G. Kostianoy, 1996, Investigation of the Sicilian upwelling on the base of satellite data, Technical Report, Stazione Oceanografica CNR, La Spezia, November 1996, 99 pp.
- [10] R. Santoleri, E. Bohm and M. E. Schiano, 1994, The sea surface temperature of the Western Mediterranean Sea: historical satellite thermal data, In *Seasonal and interannual variability of the Western Mediterranean Sea*, Coastal and Estuarine Studies, 46, 155-176.

**Development of an Intelligent Towed Vehicle "Flying Fish"
for Comprehensive Measurements of Physical and Chemical Properties
and Examples of Data Obtained in the Japan Sea**

Wataru Koterayama, Jong-Hwan Yoon and Alexander Ostrovskii

Research Institute for Applied Mechanics, Kyushu University
Kasuga-Koen 6-1, Kasuga 816-8580, JAPAN
E-mail: kotera@riam.kyushu-u.ac.jp

Abstract: A research project on development of observation systems for heat, momentum and substance circulation in the ocean and atmosphere was carried out in the Research Institute for Applied Mechanics, Kyushu University from 1992 to 1997. A pitch, roll and depth controllable towed vehicle called "Flying Fish" was developed, which houses an acoustic Doppler current profiler (ADCP), CO₂ analyzer and sensors for measuring temperature, salinity, dissolved oxygen, pH, turbidity and chlorophyll. Length of the vehicle is 3.84m, breadth 2.26m, height 1.4m, weight in air 1400kg and weight in water about 0kg.

Flying Fish enables us to obtain space continuous data of physical and chemical properties efficiently in the upper mixed layer of the ocean. From 1994 to 1997, the vehicle was used to carry out observations in the northern, southern and central part of the Japan Sea in a collaborative study among Japan, Korea and Russia. Examples of data obtained are shown in this paper and the results of the current velocities are compared with those of other observation systems.

INTRODUCTION

In the ocean upper mixed layer where air-sea interaction is very active, variations in the physical and chemical properties require detailed research because they play an essential role in the so called greenhouse effect. Physical phenomena such as currents, wave motions, fronts and vortices of various time-space scales, transport, diffuse and sometimes condense dissolved substances in seawater. Observations of physical and chemical properties are therefore essential, but are difficult to implement with existing methods because the lengthy processing required for each one on board of the ship means that simultaneity of the results is lost.

During the past thirty years the Research Institute for Applied Mechanics (RIAM) was engaged in a series of research projects [1] to develop ocean measurement systems: a cloverleaf buoy and a spar buoy for wave mechanism research, and submerged and surface buoy systems for research on ocean circulation and air sea interaction. Since 1992, the ocean engineering group in RIAM has been involved in developing an intelligent towed vehicle system, "Flying Fish", to research momentum, heat flux and substance transport in the Japan Sea. In this paper we present the engineering features of Flying Fish aimed on space continuous measurements that complement data of spatial the mooring buoy systems as it will be shown in the observation results.

BRIEF INTRODUCTION OF FLYING FISH

While detailed description of the structure of Flying Fish has been given in paper [2], it is worth to outline the basic features here. See Table 1. The vehicle has large main wing and two horizontal wings driving depth, pitch and roll. The main wing is actuated by a rack-pinion mechanism and the horizontal wings are controlled by timing-belts.

Table 1 Principal features of Flying Fish

Operating depth	0~200m
Dimensions (L×B×H)	3.84m×2.26m×1.40m
Weight in air	1300kg
Weight in water	-20kg
Instrumentation	ADCP, CO ₂ , CTD, DO Turbidity, PH, Chlorophyll
Towing velocity	0~12knot
Motion control	Heave, Pitch, Roll

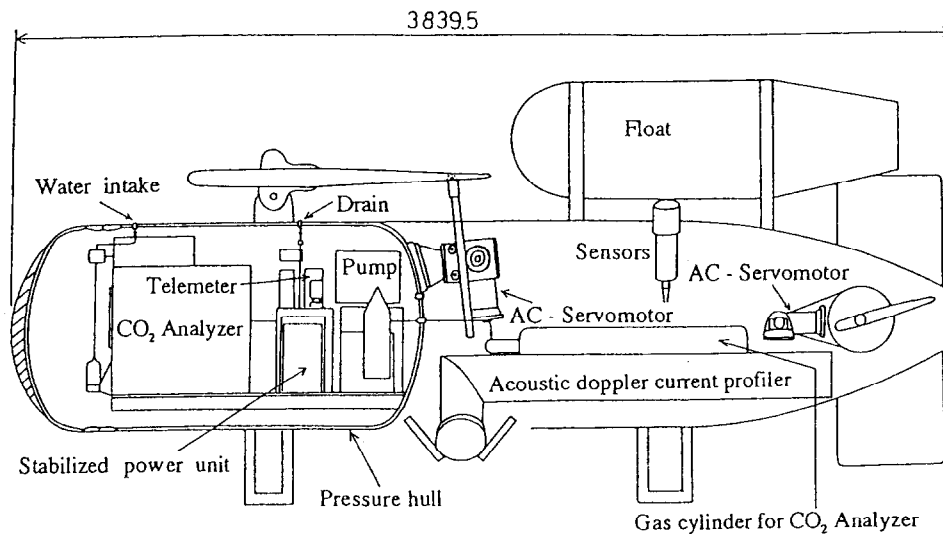


Fig.1. Vertical profile of Flying Fish.

Figure 1 is a vertical profile of Flying Fish, which houses an acoustic Doppler current profiler (ADCP), CTD sensor, CO₂ analyzer, the chlorophyll, turbidity, and pH sensors, all for ocean observations, and the roll, pitch, and depth sensors for a motion control. The large pressure hull contains the CO₂ analyzer, its support system and a telemeter system. The ADCP and other sensors such as those for CTD, dissolved oxygen, turbidity, chlorophyll and pH are accommodated in each pressure vessel.

The ADCP can measure its own velocity relative to the Earth by bottom tracking ability in shallow water of less than 500m. In deeper water, the speed of the mother ship is measured by a kinematic differential global positioning system (KGPS) and the average speed of the towing ship during 15 minutes is regarded to be the same as that of Flying Fish. Field experiments verified that the accuracy of the overall system in measuring the current velocity is almost the same in two cases.

MATHEMATICAL MODEL FOR DESIGN OF MOTION CONTROL SYSTEM

Motions of the towed vehicle are expressed by a 6-degree freedom motion equation and those of the towing cable are described by a three dimensional lumped mass model [3].

We carried out model tests using a 1/5 scale model in a water circulating tank to obtain hydrodynamic coefficients for the mathematical model. Two experiments were conducted, the first was a static experiment in a steady flow to obtain the drag and lift coefficients, the second was a forced oscillation test in a steady flow to

determine the damping and added mass coefficients for the surge, sway, heave, roll, pitch and yaw of the vehicle. To improve the performance of the controller designed using the hydrodynamic coefficients from the tank tests, a more accurate mathematical model is needed and field experiments are important.

In this paper the hydrodynamic coefficients were obtained using regression analysis on the measured tension of the towing cable and motions measured in field experiments. We use many hydrodynamic coefficients to describe the motions of the towed vehicle but a few of them are particularly important such as the drag and lift and damping coefficients for heave and pitching motions of the vehicle. The drag of the body and lift coefficients of the wings are estimated from the static balance under steady towing conditions. Induced moment coefficients by the wing action are calculated by using obtained lift coefficients. Damping coefficients of the heave and pitch are estimated from data during the change of depth in field experiments. Generally speaking, these effective parameters for motions are obtained accurately from the regression analysis.

FIELD EXPERIMENTS

During development of the hardware we used the PID control system because it is flexible and can easily cope with hardware troubles. The PID controller worked well throughout the field experiments. In steady towing, error in depth keeping was less than $\pm 0.05\text{m}$, and those of rolling and pitching angles were less than ± 1.0 degree even when the mother ship moved in rough sea. In the depth changing mode, however the maximum error in pitching increased to 3 degrees [4] because it is basically single input and single output system.

In 1997, to improve on this point we adopted, LQI (Linear Quadratic with Integral), controller in field experiments. In Fig.2 the sensor arrangement in field experiment is shown. The depth of Flying Fish was measured with a pressure sensor, and the roll and pitch angles by vibratory angular sensors. The ship motions were measured with a 6-component motion sensor fixed in an onboard laboratory and the cable tension was done with a strain gage type tension meter set at the towing point on the main deck of the mother ship.

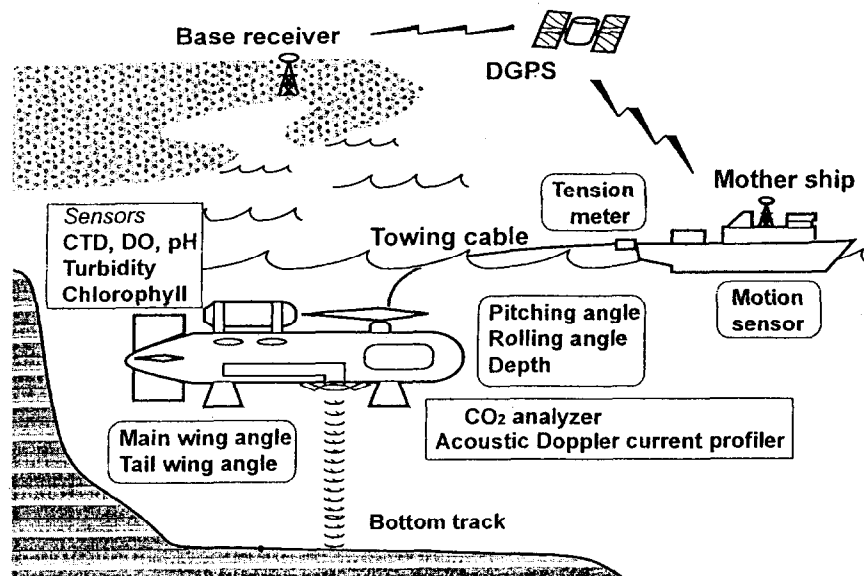


Fig.2. Sensor arrangement in field experiments.

Figure 3 shows comparisons of a time series of motions and wing angles obtained from a field experiment and numerical simulations for the LQI controller. The results of two numerical simulation are shown for comparison; one uses the hydrodynamic coefficients acquired by the model experiments and the other uses those from regression analysis of the field experiment data. The figure shows generally good agreement between two results, and the effect in difference of the hydrodynamic coefficients is observed only in the tail wing angle.

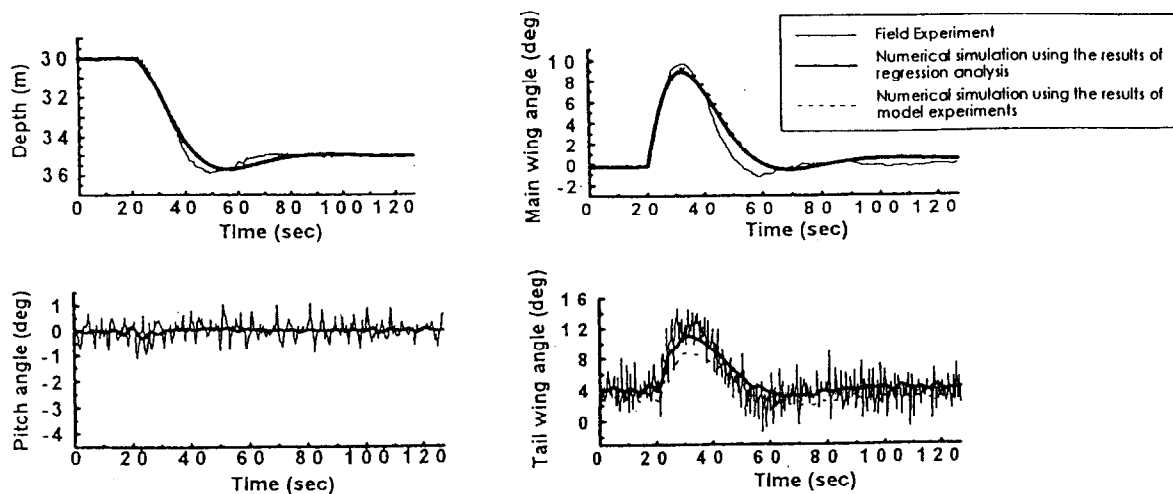


Fig. 3. Comparison of numerical simulations and field experiments on motions in the case of the PID controller.

This assures the accuracy of the mathematical model tuned by using the field experiment data. The amplitude of the pitching angle is maintained within one degree throughout the depth change. It is presumed that the short period oscillation of the tail wing angle is caused by insufficient resolution of the depth sensor. The small amplitude vibration of the depth sensor affects the instruction value of the tail wing angle through the operation in the controller. This phenomenon might cause serious damage to the mechanics of the horizontal wings if they operate during long term observation. We will improve it by using a filter or other control system such as H_{∞} controller in the next field experiment.

RESULTS OF OBSERVATION IN THE JAPAN SEA

A wealth of new information on the upper Japan Sea was obtained by using Flying Fish during the six years project period from 1992 to 1997 in which Japan, Korea and Russia collaborated. For example, demonstrates oceanographic data obtained along section B shown in Fig.4 is demonstrated briefly in Fig.5. In this case the submerged depth was 30m and towing speed was 9 knots. Letters A-E on the abscissa represent the location on the map in Fig.4. If necessary, the precise location and time can be defined for each data point because the GPS (Global Positioning System) data was recorded together with oceanographic data. Temperature, salinity, depth, dissolved oxygen, pH, turbidity, chlorophyll, dissolved inorganic carbon dioxide and molecular carbon dioxide are shown. The CO_2 analyzer of Flying Fish could not measure the molecular carbon dioxide directly; this was derived by applying an equilibrium state equation and processing collected data on dissolved inorganic carbon dioxide, water temperature, salinity and pH. The distance between points A and E was about 300km and Flying Fish was required to work without stopping, thus requiring high level of reliability.

A rapid $5^{\circ}C$ drop in temperature and decline of salinity, accompanied by an increase in dissolved oxy-

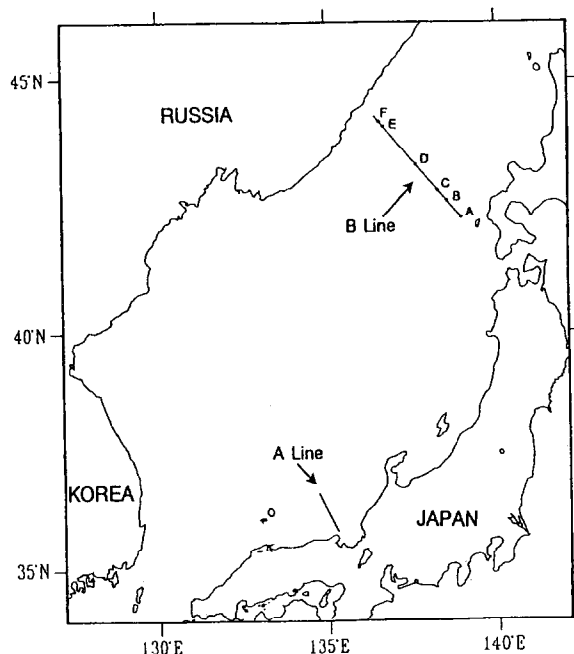


Fig. 4. Map showing the experimental field in the Japan Sea.

gen and turbidity can be seen between points D and E. This suggests that cold water mass originating from the north moved along the Russian coast. The data variability of chlorophyll was different from variations of other parameters in that it contained a period with high frequency signal due to photosynthesis activity, and day-by-day fluctuation. The dissolved inorganic carbon dioxide decreases near point D, and increases near point E, so that it might have some correlation with the chlorophyll. The time series in the bottom of Fig.5 is for molecular carbon dioxide calculated from data of dissolved inorganic carbon dioxide, water temperature, salinity, pH and equilibrium state equation. This parameter is very important because it indicates the exchange rate of the carbon dioxide between air and sea and therefore is believed to be a main factor in the greenhouse phenomenon. Designing the overall system, we worried about the accuracy of the measurement of molecular carbon dioxide because of limitation in accuracy of the pH-sensor. However as shown in Fig.5 the range of variation in pH is very narrow so that the total accuracy of the molecular carbon dioxide seems good. It is natural that the molecular carbon dioxide has correlation with the dissolved inorganic carbon dioxide, water temperature, salinity, and pH because of the form of the equilibrium state equation, but the figure suggests it has especially strong relation with water temperature. In these experiments we measured horizontal distributions, next we want to research vertical profiles, especially for, carbon dioxide.

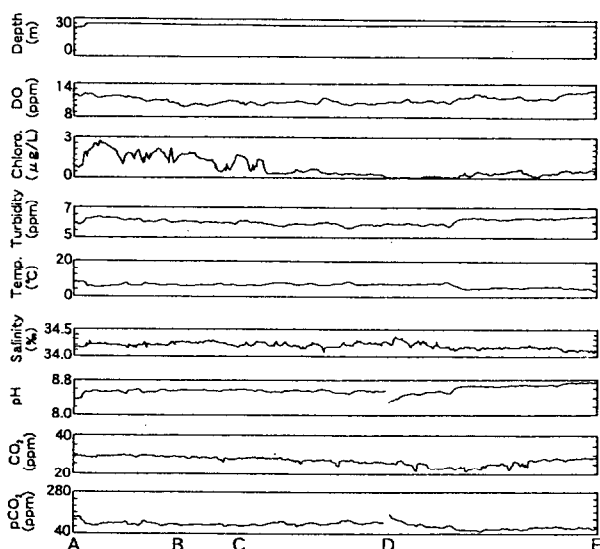


Fig.5. Observation results of temperature T, salinity S, depth D, dissolved oxygen DO, pH, turbidity, Chlorophyll, dissolved inorganic carbon dioxide CO₂ and molecular carbon dioxide PCO₂ obtained from equilibrium equation with measured T, S, pH and CO₂.

In Fig.6 the values of molecular carbon dioxide measured by Flying Fish by so-called indirect method are compared with those of direct measurement [5] by Prof. Kim Kyung-Ryul. Prof. Kim's group sampled the water 5m beneath the surface from the water intake of the observation ship throughout the cruise and carried out continuous chemical measurements of dissolved substances were carried out through gas-chromatography. The measurements by Flying Fish were restricted to times when the vehicle occasionally came up near the water surface, and therefore results of these two methods cannot be compared over many points; but such comparisons show very good agreement confirming the accuracy of the CO₂ measurements of Flying Fish because the direct method is recognized from the view point of accuracy.

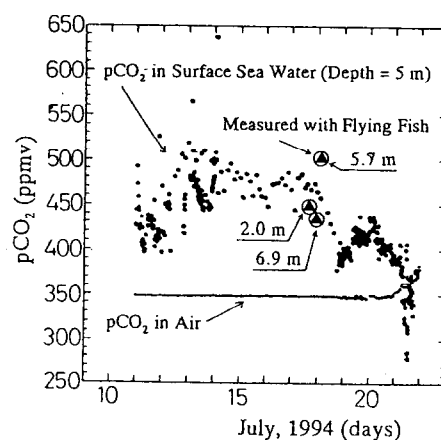


Fig.6. Molecular carbon dioxide pCO₂ observed by direct method and Flying Fish system.

The Flying Fish measurements give us a chance to study how the dissolved oxygen (DO) is related to chlorophyll, temperature, salinity and other parameters on a wide variety of spatial scales. This is an important problem because knowledge on redistribution of oxygen by processes of different scales is needed for understanding the sea ventilation. To decompose the signals into elementary modes well localized both in space and wave number we use a wavelet analysis. The wavelet transform characterizes local regularity of signals and is particularly suitable in detecting secular changes. Here we analyze the Flying Fish data by means of the Harmonic wavelet transform that is known to be compact in the Fourier space [6]. The emphasis is placed on the fluctuations from the averages along the cruise tracks in the Japan Sea.

An example of the wavelet decomposition of the DO signal measured along the section AD (Fig.4) is shown in Fig.7. The plots on the right panel of Fig.7 demonstrate wavelet modes of the original signal from the largest scale of about 24-48km (right top plot) to the smallest scale of about 50-100m (right bottom plot). The low level modes represent variability of the longer wavelengths while the high levels are associated with the shorter wevelengths. By using these modes, the original signal can be reconstructed as it is shown on the left panel of Fig.7. Notice that the final (left bottom) plot involves whole set of wavelet modes allowing exact reconstruction of the original signal and thereby proving robustness of the wavelet technique.

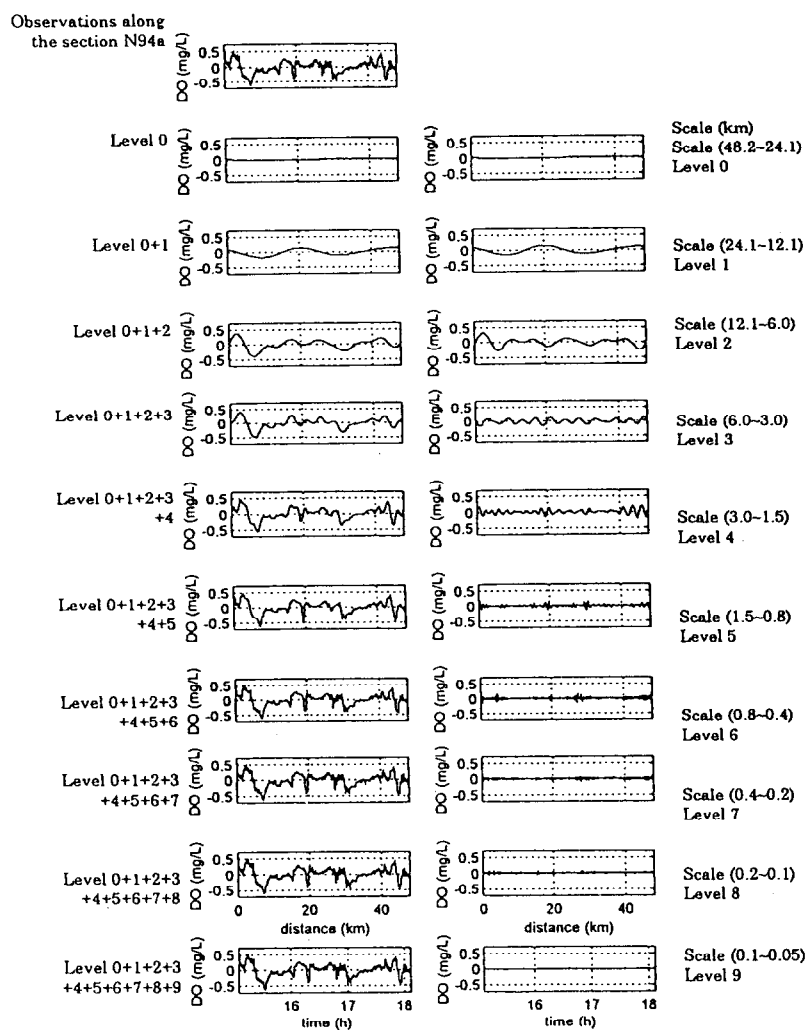


Fig.7. The wavelet decomposition and reconstruction of the DO variations.

To consider links between DO and other parameters on the individual scales we used conventional cross-correlation analysis. Perhaps, most interesting was link between DO and chlorophyll since the latter is regarded as proxy of phytoplankton. One could anticipate that DO and chlorophyll are negatively correlated at night time when oxygen is utilized by phytoplankton. DO and chlorophyll were found to be either negatively correlated or had no strong relationship at night time in the northern Japan Sea (Fig.8). New, however, is the fact that the correlation decreases with increasing scale so that the correlation coefficient can be as low as -0.75 at the scales of the order of 10km, implying that the utilization of the oxygen by phytoplankton during respiration was significant at the sea mesoscale rather than locally.

At day time, by contrast, oxygen is produced by phytoplankton during photosynthesis. DO can be accumulated in the sea when phytoplankton grows. The estimates of the cross-covariances between DO and chlorophyll at day time along the sections in the northern Japan Sea show that the covariances were often significant and positive indicating the phytoplankton growth. Thus oxygen was produced by phytoplankton in the northern Japan Sea in July 1994. The largest positive covariances were observed at the scales of 1-25km. It seems that phytoplankton was more intermittent at day time with patches of the various scales between 1 and 25km.

As to the southern Japan Sea, DO and chlorophyll there were always correlated negatively at the end of May 1995 (Fig.9). Thus there was no indication of the oxygen production at the depths of 20-30m.

The relationships between chlorophyll on the one hand and temperature and turbidity on the other were particularly clear at nights. The chlorophyll was negatively correlated with temperature and positively correlated with turbidity. The cold waters were richer with chlorophyll and more muddy. Once again, the correlation coefficients grow in absolute values towards the scales of several kilometers. This implies that the variations tend to be more coherent at the larger scales.

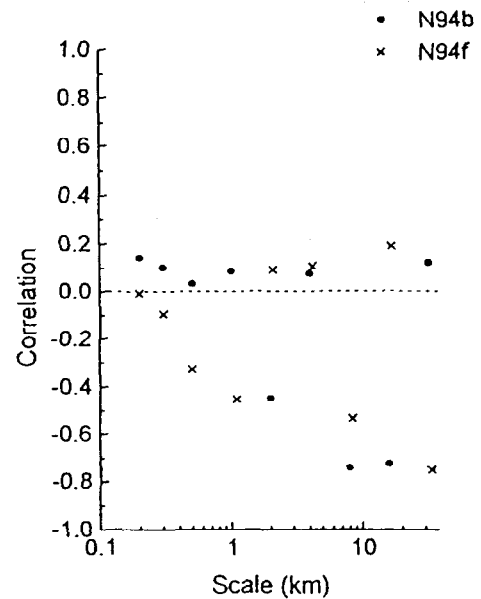


Fig.8. Correlation between dissolved oxygen and chlorophyll at night along the sections $42^{\circ}51'N, 138^{\circ}26'E-43^{\circ}12'N, 138^{\circ}12'E$ (●) and $40^{\circ}25'N, 134^{\circ}24'E-40^{\circ}01'N, 132^{\circ}24'E$ (×) in the northern Japan Sea.

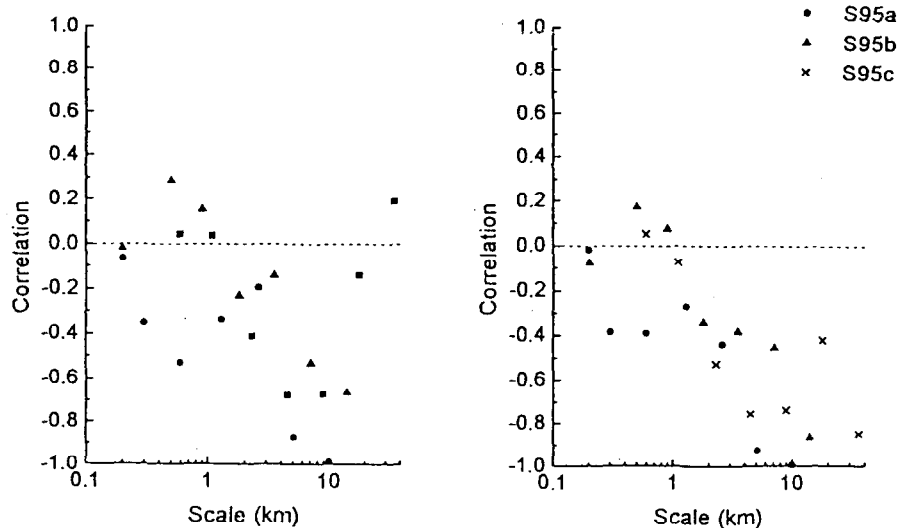


Fig.9. Correlation between dissolved oxygen and chlorophyll at day time in the southern Japan Sea.

Hydrochemical observations (Kim et. al., 1994) showed that the vertical profiles of DO had a subsurface maximum at the depth of 20-50m, DO was 25%-40% higher than near the surface in the northern Japan Sea in summer. Since the vertical profile of chlorophyll a had a subsurface maximum at the same depth (Kim et. al., 1994), the subsurface maximum of oxygen can be accounted to the production by phytoplankton.

Some earlier studies of the covariability between temperature and chlorophyll suggested that at least some of variability of chlorophyll observed on wavelengths between 1km and 100m can be explained by vertical displacements of vertical microstructures by common mechanism such as internal waves, while the biochemical mechanisms are more important on the larger scales. Our study of the Flying Fish data indicate that the variations of DO are associated with those of phytoplankton at the scales larger than few kilometers. Our findings imply that the oxygen production by phytoplankton is important resource of DO in the subsurface Japan Sea in summer. It should be also important in October-December, because phytoplankton blooms in the northern Japan Sea in this season too. Therefore, due to vertical diffusion from the sea subsurface into the sea interior the biologically produced oxygen can contribute substantially into the dissolved oxygen variation in the underlying layer of the Japan Sea Proper Water.

Figure 10 shows the current velocity distribution in the cross section between points B and F in Fig.4. This figure showing readings from 1995 cruise and the results of 1994 are almost the same. The quality of 1995 data, however, is much better than that of 1994 due to use of the DGPS (Differential Global Positioning System) for measuring ship speed. The cruising speed has been subtracted from the ADCP data to get the absolute velocity of the currents. Between B and D the northeast current is comparatively strong, and this suggests the effect of the Tsushima warm current and agrees with the results of temperature and salinity measurements. Near point D a strong current was found between the depths of 200m and 340m. Near the Russian coast the current is very weak and is homogeneous from the surface to a depth of 340m. These data on the flow field show good correspondence to the other data in Fig.5.

The Flying Fish measurements of currents are validated by comparing them with 1) the conventional estimates of geostrophic currents and 2) long-term direct measurements by moored current meters.

In 1996 and 1997, observation cruises were carried out to research the Tsushima warm current, which has a great effect on the environment of the Japan Sea by transporting the heat and momentum from the West Pacific. Figure 11 is a map showing the observational lines. Flying Fish was towed on the A-line and the dots indicate the stations of CTD measurements. The total length of this section was 90km and between Stations A8 and A13 bottom tracking with ADCP was possible. Between A1 and A8 the KDGPS system determined the accurate ship speed, which was removed from the ADCP data to get the absolute current velocity. The reference station for the DGPS system was set in RIAM and the distance between this station and the research vessel was more than 500km. This distance was greater than usual use of the DGPS system, for which the error of speed measurement is estimated as less than 1cm/sec.

In Fig. 12, the ship speed measured with the KDGPS system and the relative velocity of Flying Fish to the earth measured using the bottom tracking system of the ADCP are compared along the section A8-A13. The maximum discrepancy between these two systems was 4cm/sec. There are several reasons for this discrepancy: the vertical distributions of the water temperature and salinity might affect the speed of the ADCP acoustic beam and cause error, or the reference location of the KDGPS might be too far to keep the error within 1cm/sec. The measurement error of the current velocity with the ADCP was assumed to be around 2cm/sec in the case of 15minute average and the overall error of the Flying Fish current velocity measurement was sought to be less than 4cm/sec. In Fig. 12, the dotted line indicates the measured ship velocity with the single GPS system and the

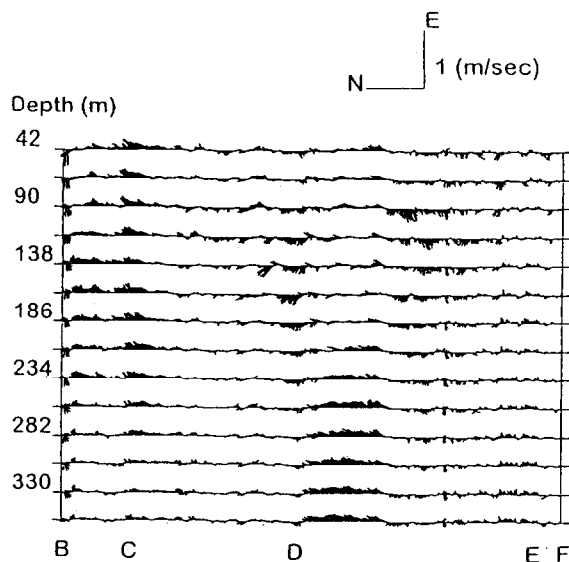


Fig. 10. Current distribution in the cross section along B line.

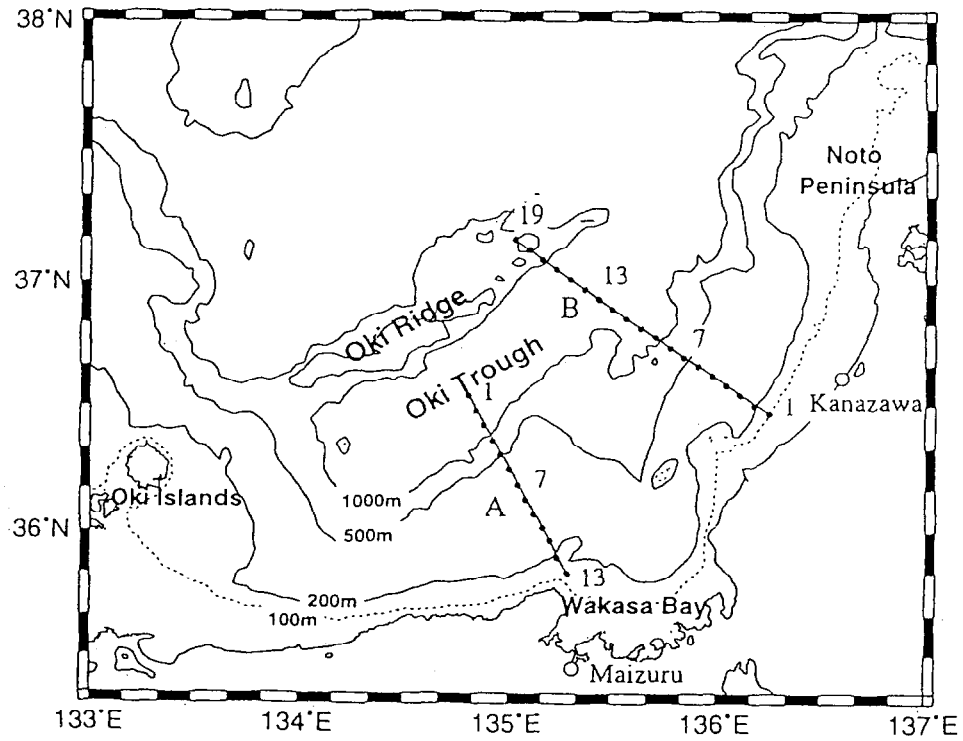


Fig.11. Map showing the experimental field for the observation cruise of Tsushima Warm Current.

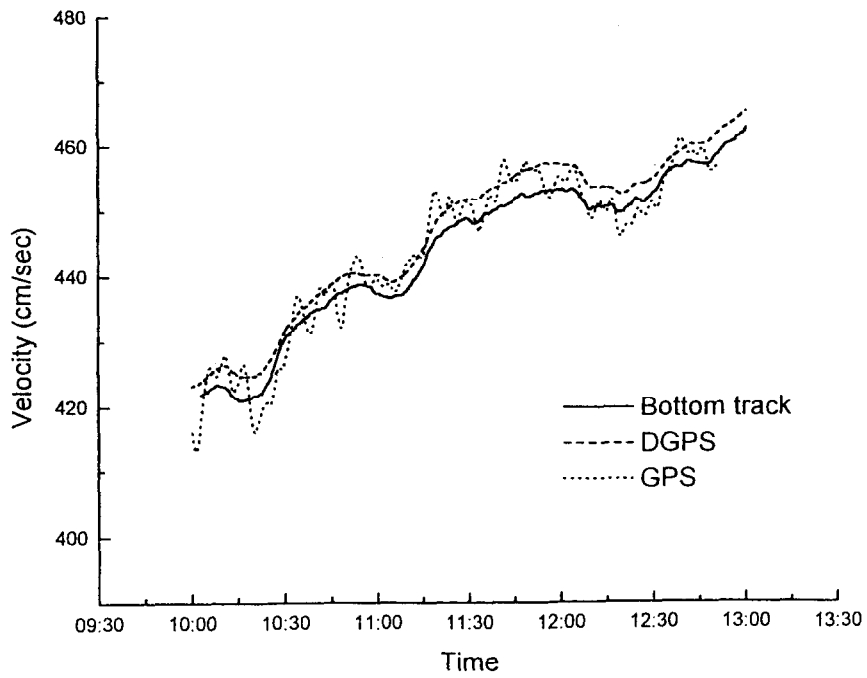


Fig.12. Comparison of ship velocity measured with DGPS and bottom tracking of ADCP.

maximum error in this case is 7cm/sec. The KDGPS system is thus better than the single GPS system.

To eliminate the tidal current, Flying Fish was towed eight times along the observation line at a towing speed of 9 knots. About 50 hours was required to carry out the observation on the A-line. A harmonic analysis was made to separate the mean current, the diurnal tidal current and the semi-diurnal tidal current. Three mooring systems were deployed on the A-line for two years to measure in situ current and temperature. Figure 13 shows the mooring locations and current meter arrangements. Circles indicate the rotor type current meter and triangles the ADCP.

Figure 14 compares the vertical structure of the velocity normal to the cross section of the A-line measured with the ADCP of Flying Fish with the geostrophic calculation. Flying Fish was towed at the depth of 30m and the current data between the water surface and 30m depth could not be obtained. In general the two results agree broadly. The figure shows that the Tsushima Warm Current along the Japanese coast has two streams, a near shore stream and an offshore stream, which have been predicted by multi-level numerical model [7]. The observation with Flying Fish verified the numerical simulation.

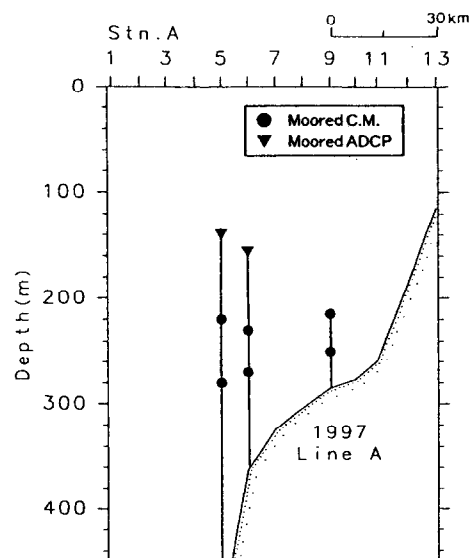


Fig. 13. Mooring locations and current meter arrangements.

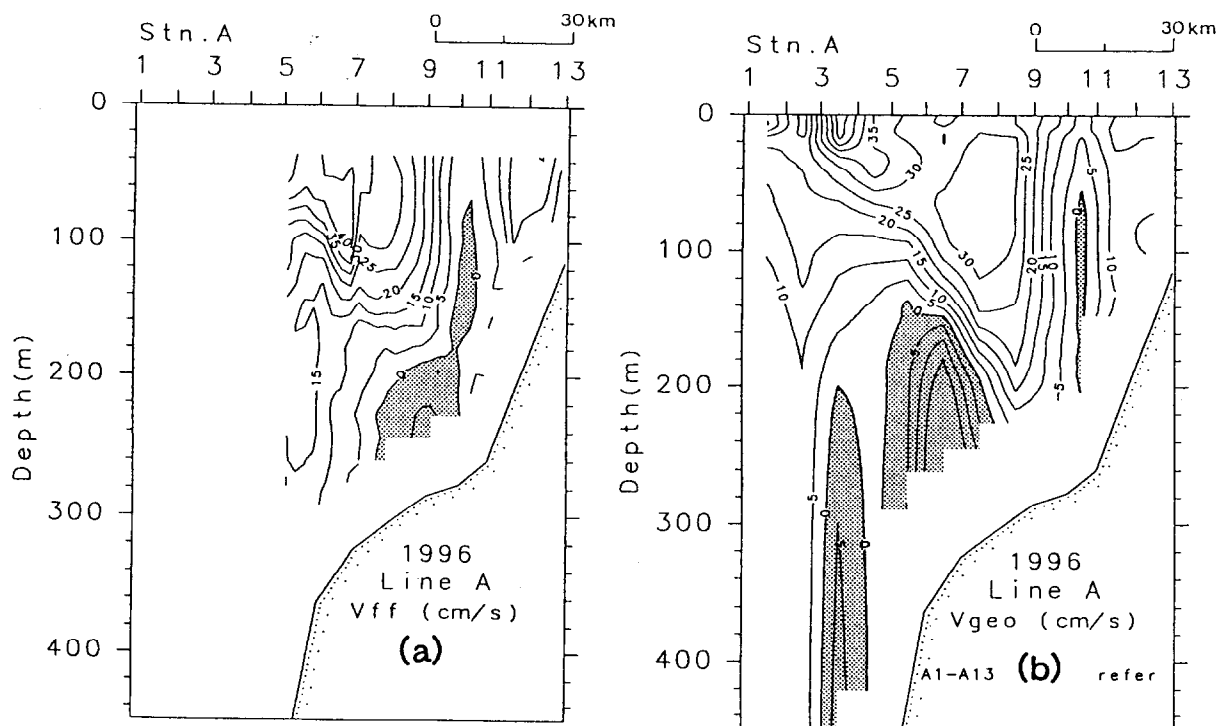


Fig. 14. Comparison of velocity Distributions of Tsushima Warm Current in A-section obtained from geostrophic calculation (b) and direct measurement (a) with the Flying Fish system.

In Fig.15 vertical profiles at Stns.5, 6, 9 measured by the Flying Fish are compared with those of mooring systems. In these cases the moored ADCP emits the acoustic beam downward which makes it possible to compare the results with those of moored current meters. At Stn. A5 the data of the moored current meters, the moored ADCP and the ADCP of Flying Fish coincide very well, but at Stn.A6 the moored ADCP data is slightly lower than those of Flying Fish and the moored current meter. The current velocity measured with the ADCP of Flying Fish also agrees with those of the moored current meter at Stn.9. These figures clearly confirm the accuracy of the current measurement of the Flying Fish system.

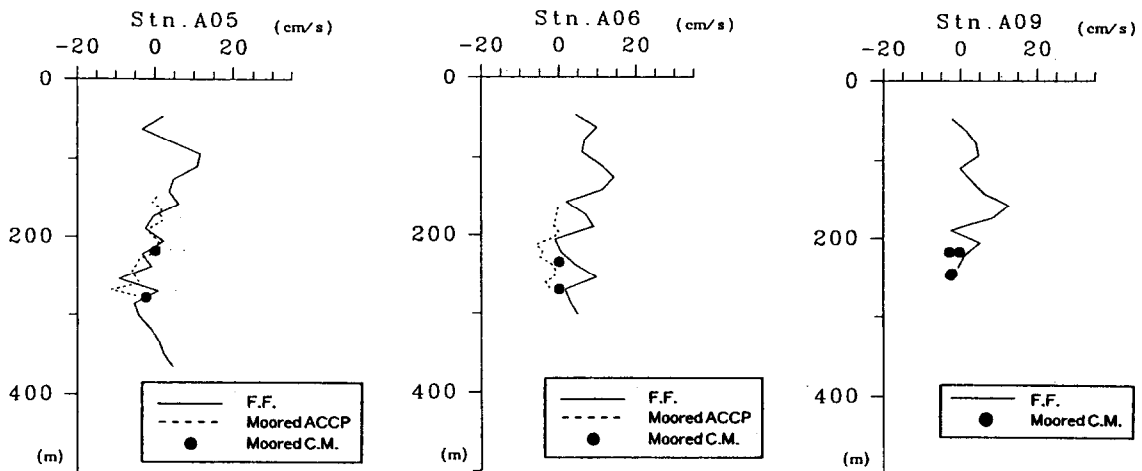


Fig. 15. Vertical profiles at Stns.05, 06, 09 measured with Flying Fish and with the mooring system.

CONCLUDING REMARKS

A series of field experiments verified superiority of Flying Fish which can measure the physical and chemical properties simultaneously. In order to understand the chemical parameters of the ocean we have to know its physical phenomena and the reverse is also true. The accuracy of the current measurement system using the towed vehicle Flying Fish with a Kinematic Differential Global Positioning System is confirmed in this paper by comparing with the traditional geostrophic estimates and the current meter mooring data. This is partly due to progress in the differential global positioning system but is mainly the result of the high accuracy motion control which prevented the oscillation of acoustic beams of the acoustic Doppler current profiler. The superiority of a towed vehicle is crucial for the spatially continuous measurements, because of its high reliability and real time data sampling, but ocean science still needs more accurate measurements for a mathematical modeling of sea environment. Ocean engineers are being counted on to play dominant role in this achievement.

ACKNOWLEDGEMENTS

The authors thank members of the ocean-atmosphere research project of RIAM for their collaboration in carrying out the field experiments and data analyses. They also express their appreciation to crews of the Kakuyo-maru of Nagasaki University and research vessel Prof. Khromov of FHRHRI for their sincere and superior ability in the operation techniques of the ship and the machines on board.

REFERENCES

- [1] W. Koterayama, "The Role of Ocean Engineers in Japanese Ocean Measurement Research," Proc. of the 1st International Offshore and Polar Engineering Conference, pp. 112-119, 1991.

- [2] W. Koterayama and T. Akamatsu, "Development of a Towed Vehicle for Physical and Chemical Measurement in the Ocean Upper Mixed Layer," Proc. of Oceans' 93, Vol.3, pp. 497-501, 1993.
- [3] W. Koterayama, S. Yamaguchi, M. Nakamura and A. Moriyama, "A Numerical Study for Design of Depth, Pitch and Roll Control System of a Towed Vehicle," Proc. of the 4th International Offshore and Polar Engineering Conference, pp. 337-343, 1994.
- [4] W. Koterayama and S. Yamaguchi and M. Nakamura, "Field Experiments on a Towed Vehicle Flying Fish for Physical and Chemical Measurement in the Upper Mixed Layer of the Ocean," Proc. of Oceans' 96, pp. 1008-1013, 1996.
- [5] K.-R. Kim et. al., A Summary of Chemistry Results from CREAMS'94, communication at the 3rd Workshop on Circulation Research of the East Asian Marginal Seas, Seoul, Korea, November 7-8, 1994
- [6] Newland, D. E., 1993: An Introduction to Random Vibrations, Spectral & Wavelet Analysis. Longman Scientific & Technical, UK, John Wiley & Sons, NY, USA, 478 p.
- [7] H. Hase, J. H. Yoon, M. Takematsu, W. Koterayama and S. Yamaguchi, "The Structure of the Tsushima Warm Current off the Wakasa Bay During 1995-1996," Engineering Science Reports, Kyushu University, Vol.19, No.1 pp.61-66, 1997.

NUMERICAL MODELLING OF SEASONAL DYNAMICS AND RADIONUCLIDE TRANSPORT IN THE KARA SEA

L. Koziy, V. Maderich, N. Margvelashvili, M. Zheleznyak

Institute of Mathematical Machine and System Problems of National Academy of Sciences of Ukraine
Glushkova pr., 42, Kiev, 252187, Ukraine, E-mail: nm@dem.ipmms.kiev.ua

Abstract. The numerical THREETOX code was used to simulate 3-D hydrodynamics fields, suspended sediment and the dispersion of the radionuclide released from the scuttled reactors and containers with the liquid radioactive wastes in the Novaya Zemlya bays and Kara Sea Trough. The code includes a set of submodels: hydrodynamics submodel, ice submodel, suspended sediment transport and radionuclide transport submodels. The seasonal dynamics of the Kara sea was considered. The simulation was done on the basis of the scenarios of the possible releases from the nuclear units. It was shown that the marine radionuclide concentration due to the releases will be increased on the values that are much less than the present day concentration.

Introduction

The consequences of the possible leakage from the nuclear reactors and containers with liquid wastes that have been scuttled in the Novaya Zemlya fjords and the Kara Sea Trough during the period 1960-1991 have been intensively studied last years by the international groups of the experts (e.g., [1]). The recent study [2] was focused on the radiological consequences of the phenomenon for man. The radiological collective dose calculations were carried out on the basis of the marine radionuclide concentration values simulated in the long-term projection by the box model [2]. The parameterisation of the water fluxes between the model compartments and radionuclide fluxes from the Novaya Zemlya bays as also parameterisation of the radionuclide dispersion in the box model required more detailed analyses of the hydrodynamic and radionuclide transport processes. Such analysis in a seasonal time scale could be done on the basis of the relevant 3-D model. The model should take into account that the Kara Sea circulation and consequently the radionuclide transport is governed by the strong seasonal freshwater inflow from the Ob and Enisey rivers and the water inflow from the Arctic ocean and Barents Sea. The wind and tides are important forcing of the sea circulation, especially in the shallow regions. The winter ice cover is the specific factor that influences on the radionuclide transport. All these processes were considered in the presented in this paper modelling study, that was provided as a part of the European Commission project [2]. Three-dimensional simulation of the Kara Sea circulation and radionuclide transport from the Novaya Zemlya bays and in the whole sea was carried out with THREE-dimensional model of TOXicants transport (THREETOX) that was recently developed [3].

Model

The THREETOX code includes a set of submodels.

Hydrodynamics submodel. The hydrodynamics is simulated on the basis of the three-dimensional, time-dependent, free surface, primitive equation model. The prognostic variables of the hydrodynamics code are the

three components of the velocity, temperature, salinity and surface elevation. The water body is assumed to be hydrostatic and incompressible. The concept of eddy viscosity/diffusivity and Prandtl's hypothesis, with the variable turbulence length scale, is used to define the turbulent stresses. At the free surface, all fluxes (momentum, heat, etc.) are prescribed. At the bottom and the land boundaries, the conditions of no diffusive fluxes of any property are used. The open lateral boundary conditions are modified radiation conditions. Sigma co-ordinates were used to reduce the difficulties in the numerical solution of problem for realistic bottom topography. To improve time characteristics of the submodel the barotropic and baroclinic modes split [4] was used in the code.

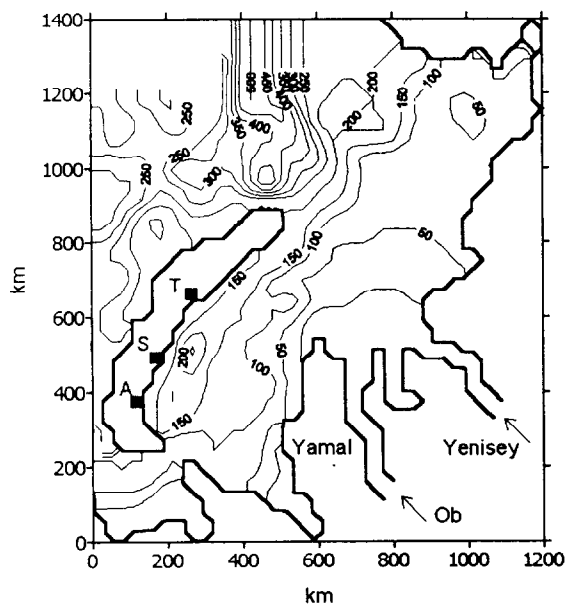


Fig. 1. Bathymetry of the Kara Sea "A" Abrosimov fjord, "S" Stepovogo fjord, "T" Tsvolki fjord.

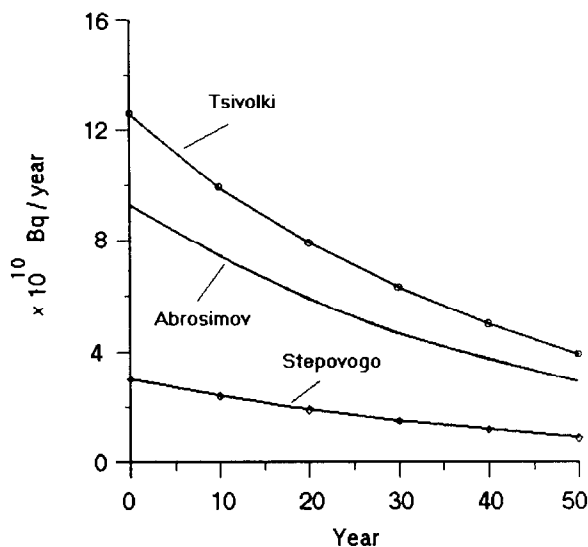


Fig. 2. Scenario of ¹³⁷Cs release from the dump sites in the Novaya Zemlya fjords [2].

Ice submodel. The submodel was developed to simulate a seasonal cycle of moving ice in the seas of temperate zone [5]. It is based on the dynamic-thermodynamic model of Hibler [6-7]. The submodel describes 1) the *momentum balance* that defines the ice drift induced by wind and currents; 2) the *ice rheology*, connecting stresses with deformations and strength; 3) the *mass balance* connecting ice thickness with its growth or loss due to freezing, melting and ice drift; and 4) the *ice strength* dependent on the size and thickness of floes. The ice thickness distribution is a two-level representation that considers the compactness and the mean ice thickness, averaged over an entire grid cell.

Suspended sediment transport submodel. The suspended sediment transport is described by the advection-diffusion equation, taking into account the fall velocity of the sediment grains. The bottom boundary condition describing sediment resuspension or deposition depends on the ratio between equilibrium and actual near bottom suspended sediment concentrations. The van Rijn [8] approach is used to calculate equilibrium concentration. The thickness of upper (movable) layer of sediments is governed by the equation of the bottom deformation.

Radionuclide transport submodel. The equations of radionuclide transport govern the radionuclide concentration in solute, in the suspended sediments and in the top layer of the bottom deposits [3]. The exchanges between these variables are described as adsorption-desorption and sedimentation-resuspension processes. Three - dimensional advection -diffusion equations are used to simulate the radionuclide transport in the water column and an ordinary differential equation is applied to simulate the concentration of a radionuclide averaged over the thickness of an upper, mobile layer of bottom deposits. The boundary condition at the water surface is no flux of dissolved and particulate radionuclides. At the bottom boundary the net flux is equal to the sum of fluxes of the particulate and dissolved radionuclides.

Model Geometry, Forcing and Release Scenario

A schematic bottom topography of the Kara Sea and locations of the sites of the potential radionuclide sources in Novaya Zemlya are shown in Fig. 1. The area under consideration includes the Kara Sea and the eastern part of the Barents Sea. It is about 1240 km long and 1440 km wide. The model resolution was approximately 27 km in the along-basin direction, resulting in 46 grid points, and 27 km in the across-basin direction, providing 53 lateral points. The vertical direction was resolved by 15 levels with the logarithmic stretching of the upper layers. The monthly wind and air temperature fields from [9] were used as a forcing in the simulations. The river run-off of Ob and Yenisey was obtained from [10]. At the open sea boundaries M_2 tide was prescribed. The boundary and initial values of the temperature and salinity fields were specified using the data [11]. The local scale modelling was performed by the THREETOX program, for dump sites in three fjords (Abrosimov, Stepovogo and Tsivolki). Two years of the radionuclide (^{137}Cs and ^{239}Pu) dispersion were simulated for the potential releases. Information on the fjords has been obtained from the cruise reports [12]. The scenarios of the release of ^{137}Cs [2] are given in Fig. 2. Strong seasonal effects on the circulation in the

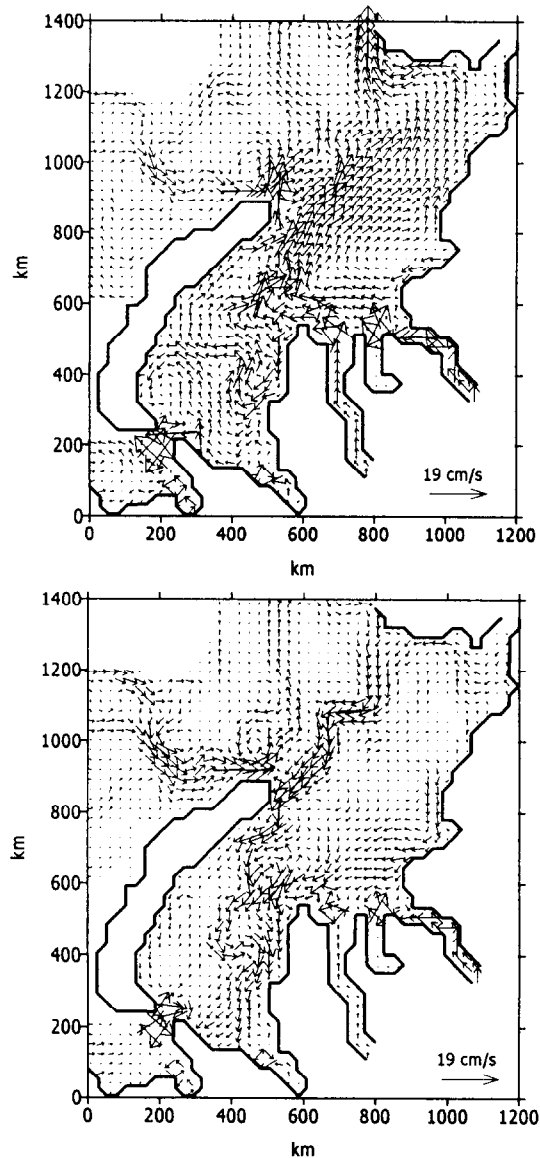


Fig.3. Simulated velocity at the surface (a) and bottom (b) of the Kara Sea averaged in August and September [13].

fjords caused by summer run-off from a snow melting, and winter ice sheets, in addition to wind and semidiurnal tides were shown. The calculated flushing times ranged from 0.3 months (summer) to 3.4 months simulated for the potential releases. Information on the fjords has been obtained from the cruise reports [12]. The scenarios of the release of ^{137}Cs [2] are given in Fig. 2. Strong seasonal effects on the circulation in the (winter) in the relatively small Stepovogo fjord, to 0.6 and 6.0 months for summer and winter, respectively, in the large Tsivolky fjord. Based on the THREETOX estimates of the flushing times, a simple box model for the fjords was developed to extrapolate the results of the 3-D simulation from a two years to the fifty years. The box model predicted that, after 50 years since the beginning of a release, the residual amount of the ^{137}Cs in the fjords is about 3 % from the total input and the average concentration of ^{137}Cs in the water of the fjords didn't exceed 80 Bq m^{-3} .

Results

The averaged over the August and September fields of the surface and bottom currents are given in Fig. 3. In August the Kara Sea is ice free (Fig.4). The influence of the river inflow on the circulation is clearly visible. The western and northern flows of the Ob and Enisey plume is transformed in the slope current that flows to

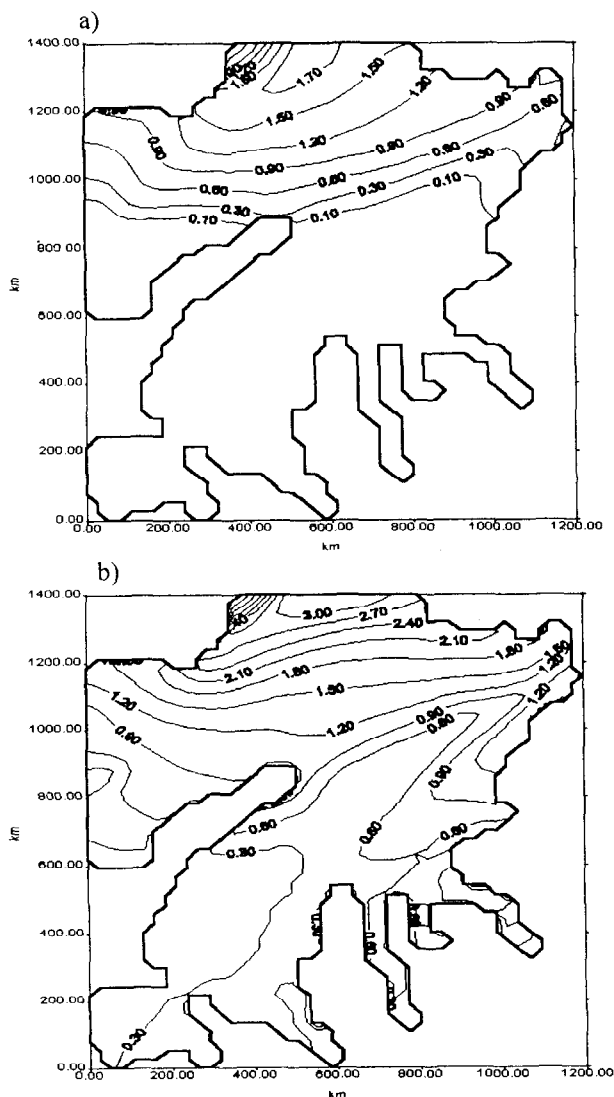


Fig.4. Simulated ice thickness distribution (m) for August and February (b).

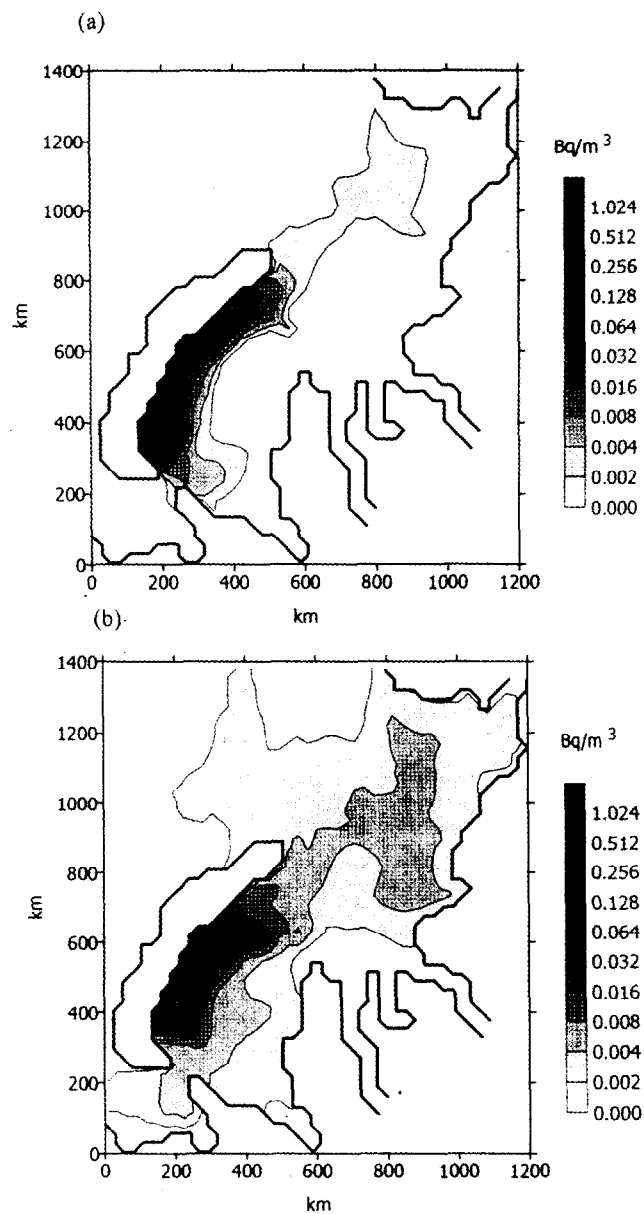


Fig. 5. Simulated ^{137}Cs distribution (Bq m^{-3}) at the surface of the Kara Sea after (a) one year and (b) 8 year since the beginning of a release.

the Severnaya Zemlya. Another current flows along the north coast of the Novaya Zemlya. It turns to north next to the Severnaya Zemlya and merges with main flow from Yamal. The current pattern in the south-west part of the Kara Sea is complicate. It consists system of weak gyres. The currents near the northern Novaya Zemlya

coast are directed to the north-east whereas currents near the southern coast are directed to the Karskie Vorota strait. The residual tidal current is important in narrows (e.g. Karskie Vorota Strait and Ob and Enisey estuary mouths). The water exchange through the Karskie vorota is bi-directional. The strong bottom undercurrent exists along the slope Novaya and Severnaya Zemlya. The undercurrents are also visible along the south-east coast of the Novaya Zemlya. The calculations do not contradict as the general current pattern based on the historical data [10] as the laboratory experiment [12]. At winter almost all area of the Kara Sea is covered by the ice sheet (Fig. 4). At winter the strong current flows from the Karskie Vorota and merges with the Ob-Enisey flow in the northern part of the sea. The current along the Novaya Zemlya coast flows to north. Other parts of the current system are qualitatively similar to the summer circulation.

These peculiarities of the Kara Sea circulation strongly affected on the radionuclide transport. Weak and seasonally varied currents near Novaya Zemlya coast result in the long residence time for radionuclide dumped in the Novaya Zemlya fjords and the Novaya Zemlya Trough. In fig.5 the simulated ^{137}Cs distribution at the surface of the Kara Sea after one year and 8 year since the beginning of a release are given. The radionuclide flow is directed both the Barents Sea and the Arctic ocean. It should be noted here that the natural level of the Kara Sea water contamination is about 3 Bq m^{-3} , while the simulated level of contamination due to the release of radionuclides from the dump sites is less than 0.2 Bq m^{-3} . The simulated by THREETOX water fluxes and dispersion parameters were used after the integration to parameterise the water and radionuclide exchange in the long-term box model of the Kara Sea contamination [2].

Acknowledgements

This study was supported by the EU (CEC Study Contract No B7-6340/95/000879/MAR/C3).

References

- [1] Joint Russian-Norwegian Expert Group for Investigation of Radioactive contamination in the Northern Areas, 1996, Dumping of radioactive waste and investigation of radioactive contamination in the Kara Sea. Results from 3 years of investigations (1992-1994) in the Kara Sea, NRPA, Osteras.
- [2] EC, 1997, Evolution of the radiological situation around the nuclear reactors with spent fuel which have been scuttled in the Kara Sea, Final Report, CEC, Luxembourg, EUR 17634, 559.
- [3] N. Margvelashvili, V. Maderich and M. Zheleznyak, 1997, THREETOX - computer code to simulate three-dimensional dispersion of radionuclides in stratified water bodies, Radiation Protection Dosimetry, 73, 177-180.
- [4] A. F. Blumberg and G. L. Mellor, 1987, A description of a three-dimensional coastal ocean circulation model. In: Three-Dimensional Coastal Ocean Models, ed N. Heaps, American Geophysical Union, 1-16.
- [5] L. Kozij and V. Maderich, 1997, A simulation of seasonal sea ice dynamics in coastal areas, In: Proc. 1-st International Conference "Port, Coast, Environment". Varna, v. 2, 220-228.
- [6] W. D. Hibler, 1979, A dynamic thermodynamic sea ice model. Journal of Physical Oceanography, 9, 815-846.
- [7] W. D. Hibler, 1980, Modeling of a variable thickness sea ice cover, Monthly Weather Review, 108, 1943-1973.
- [8] L. C. van Rijn, 1984, Sediment transport. Pt 2. Suspended load transport, Journal of Hydraulics Engineering, V. 110: 1613-1641.
- [9] Climate of USSR, 1980, V. 1, Hydrometeorological Publishers, Moscow.
- [10] V. Pavlov, 1994, Oceanographical description of the Kara and Barents Sea. Working Material of the International Arctic Seas Assessment Project, International Atomic Energy Agency, Vienna, 134.
- [11] World Ocean Atlas-94, 1994, National Oceanographic Data Center.
- [12] T. A. McClimans, B.O. Johannessen and J.H. Nilsen, 1998, Laboratory simulation of fronts between the various water masses in the Kara Sea (this volume).
- [13] L. Kozij, V. Maderich, N. Margvelashvili, M. Zheleznyak, 1998, Three-dimensional model of radionuclide dispersion in estuaries and shelf seas, Environmental Modelling and Software, (in press).

INFLUENCE OF DOUBLE DIFFUSION ON SYMMETRICAL BAROCLINIC INSTABILITY OF OCEANIC FRONTS

N.P.Kuzmina ¹, V.M.Zhurbas ²

1. P.P.Shirshov Institute of Oceanology, 36, Nakhimovsky Pr., Moscow, 117851, Russia, kuzmina@rssi.ru

2. P.P.Shirshov Institute of Oceanology, 36, Nakhimovsky Pr., Moscow, 117851, Russia, zhurbas@glasnet.ru

Abstract. We analyze analytically the problem of linear instability of 2D thermohaline baroclinic front taking into account vertical mass and momentum transfer caused by both double diffusion and turbulent mixing. Special attention is paid to a new type of baroclinic instability driven by coupled effect of double diffusion and baroclinicity. Being discovered by Kuzmina and Rodionov (1992) this instability in contrast to the McIntyre instability (1970) can exist with no limit on geostrophic Richardson number. A necessary condition for this new instability is nonzero Schmidt number, that is viscosity produced by double diffusion. We investigate the question of how the turbulence acts on this instability.

Introduction

It is known that in an ideal fluid the instability of a geostrophically balanced baroclinic 2D front with respect to a lateral intrusive-like motion cannot occur unless the geostrophic Richardson number is $Ri < 1$ [1]. The same criterion for instability, $Ri < 1$, is valid for the case of viscous fluid provided that $Pr = 1$, where Pr is the Prandtl number, i.e. the ratio of momentum to mass transfer coefficients. However, if $Pr \neq 1$ the viscous/diffusive destabilization of the flow is possible [1], and the instability criterion reduces to $Ri < Ri_M^*$, where $Ri_M^* = (1 + Pr)^2 / 4Pr$. Since $Ri_M^* > 1$ both for $Pr < 1$ and $Pr > 1$, the viscous/diffusive destabilization of geostrophic flow at $1 < Ri < Ri_M^*$ is referred to as the McIntyre instability.

Since the pioneering work by Stern [2], several models of double-diffusively driven interleaving have been developed for the purely thermohaline front of no baroclinicity, e.g. [3-6]. The first model treating the effects of baroclinicity and turbulent mixing on double-diffusive interleaving in the framework of a linear instability problem was suggested by Kuzmina and Rodionov [7] (hereafter referred to as KR92). The further development of the KR92 model has been recently undertaken by May and Kelley [8].

Analytical description and analysis

In the wake of the KR92 model, let us consider the case of an infinitely wide, baroclinic, thermohaline frontal zone with constant background gradients of temperature (\bar{T}_x and \bar{T}_z), salinity (\bar{S}_x and \bar{S}_z) and density ($\bar{\rho}_x = -\bar{T}_x + \bar{S}_x$ and $\bar{\rho}_z = -\bar{T}_z + \bar{S}_z$) both in a cross frontal (x axis) and a vertical (z axis) direction. For the convenience of notation, under T , S and ρ we imply the product of the thermal expansion coefficient, α , by the temperature, the product of the salinity contraction coefficient, β , by the salinity, and the ratio of density to reference density respectively. The z axis is directed upward. The x axis is directed across the front in such a manner that $\bar{S}_x \geq 0$ while \bar{T}_x and $\bar{\rho}_x$ are allowed to be both positive and negative in sign. The background stratification is assumed to be hydrostatically stable (i.e., $\bar{\rho}_z < 0$) and favourable for salt fingering ($0 < \bar{S}_z < \bar{T}_z$).

The base state is geostrophic, so

$$-f\bar{v} = -\frac{\partial\bar{p}}{\partial x}, \quad (1)$$

$$\frac{\partial\bar{p}}{\partial z} = -g\bar{\rho}, \quad (2)$$

where \bar{v} is the y -component of background velocity, \bar{p} is the pressure divided by the reference density, and g is the gravity acceleration. According to (1) and (2), the vertical shear, \bar{v}_z , is related to the horizontal density gradient by the thermal wind relationship

$$\bar{v}_z = -\frac{g}{f}\bar{\rho}_x.$$

According to the KR92 model, the linearized governing equations for the two dimensional perturbations are

$$\frac{\partial u}{\partial t} - fv = -\frac{\partial p}{\partial x} + Sc k \frac{\partial^2 u}{\partial z^2} + Pr k^* \frac{\partial^2 u}{\partial z^2}, \quad (3)$$

$$\frac{\partial v}{\partial t} + fu + w\bar{v}_z = Sc k \frac{\partial^2 v}{\partial z^2} + Pr k^* \frac{\partial^2 v}{\partial z^2}, \quad (4)$$

$$\frac{\partial p}{\partial z} = -g\rho, \quad (5)$$

$$\frac{\partial u}{\partial x} + \frac{\partial w}{\partial z} = 0, \quad (6)$$

$$\frac{\partial S}{\partial t} + u\bar{S}_x + w\bar{S}_z = k \frac{\partial^2 S}{\partial z^2} + k^* \frac{\partial^2 S}{\partial z^2}, \quad (7)$$

$$\frac{\partial \rho}{\partial t} + u\bar{\rho}_x + w\bar{\rho}_z = (1-n)k \frac{\partial^2 S}{\partial z^2} + k^* \frac{\partial^2 \rho}{\partial z^2}, \quad (8)$$

where u, v, w, p, S, ρ are perturbations of velocity components, pressure, salinity and density, k is the apparent diffusivity for salt due to salt fingering, k^* is the apparent diffusivity for salt, heat, and mass due to the small scale turbulence, Sc is the Schmidt number, $n = \alpha F_T / \beta F_S$ is the nondimensional flux ratio for salt fingering ($n < 1$). Following [2], the momentum balance in the vertical direction is reduced to the hydrostatic relationship (5) implying that the slope of intrusions is small and intrusive motions are quasihorizontal. The first terms in the right side of (7) and (8) are the parameterization of salinity and mass fluxes owing to salt fingers suggested by Stern [2], while the second terms describe the action of small scale turbulence. Similarly, the terms in the right side of (3) and (4) describe the friction caused by salt fingering and wave/turbulence mixing. Following the KR92 model, the effect of baroclinicity is presented by the terms of $w\bar{v}_z$ in (4) and $u\bar{\rho}_x$ in (8).

To perform a linear instability analysis we have to seek harmonic solutions for the equations (3)-(8), namely

$$\Psi = \text{Re}\{\Psi' \exp(\omega t + ilx + imz)\}, \quad (8')$$

where Ψ denotes any of variables to be found (u, v, w, p, S, ρ), Ψ' is the complex amplitude for Ψ , Re is the real part of {...}, ω is the growth rate (real or complex) and l and m are the real cross-front and vertical wavenumbers respectively.

The problem (1)-(8) is in the same way considered in the KR92 model except $Sc \neq Pr$.

When analyzing the instability problem (1)-(8), for simplicity we will only consider a case of

$S_c = Pr$. Substituting (8') into (3)-(8) gives a system of linear, uniform, algebraic equations. Therefore, a solution of the form (8') exists only if the determinant of this system vanishes. This yields the following equation for growth rate ω :

$$\omega^4 + C_3 \omega^3 + C_2 \omega^2 + C_1 \omega + C_0 = 0, \quad (9)$$

where C_0, C_1, C_2, C_3 depend upon parameters of the model and wavenumbers.

If $C_0 < 0$, we are assured of at least one real root for which ω is greater than zero (e.g., [2]), and a growing, non-oscillating intrusion exists. It is easy to obtain that $C_0 / k^2 m^4$ is

$$\frac{C_0}{k^2 m^4} = Pr(1 + \zeta) N^2 \left[\varepsilon_z \frac{l}{m} \left(\frac{l}{m} - \frac{\bar{S}_x}{\bar{S}_z} \right) + (1 + \zeta) \frac{l}{m} \left(\frac{l}{m} - \frac{\bar{\rho}_x}{\bar{\rho}_z} \right) \right] + \zeta(\zeta + 1) \left[Pr^2(1 + \zeta)^2 k^2 m^4 - N^2 \frac{l}{m} \frac{\bar{\rho}_x}{\bar{\rho}_z} + f^2 \right], \quad (10)$$

where $\zeta = k^* / k$ is the ratio of turbulent to salt fingering vertical diffusivities, $\varepsilon_z = (1 - n)/(R_\rho - 1)$ is a nondimensional measure of contribution of the mean salinity gradient to the vertical density gradient scaled by the efficiency of density diffusion by salt fingers introduced by *Tool and Georgi* [4], and R_ρ , the density ratio, is more than one when the stratification is favourable for salt fingers. The frontal zone is unstable if

$$Pr(1 + \zeta) N^2 \left[\varepsilon_z \frac{l}{m} \left(\frac{l}{m} - \frac{\bar{S}_x}{\bar{S}_z} \right) + (1 + \zeta) \frac{l}{m} \left(\frac{l}{m} - \frac{\bar{\rho}_x}{\bar{\rho}_z} \right) \right] + \zeta(\zeta + 1) \left[Pr^2(1 + \zeta)^2 k^2 m^4 - N^2 \frac{l}{m} \frac{\bar{\rho}_x}{\bar{\rho}_z} + f^2 \right] < 0. \quad (11)$$

Introducing the following nondimensional variables and parameters

$$l' = lL, \quad m' = mH, \quad \omega' = \omega \frac{H^2}{k}, \quad H = \left(\frac{Pr k}{f} \right)^{1/2}, \quad \frac{H}{L} = \varepsilon_z \frac{\bar{S}_x}{\bar{S}_z}, \quad \chi = \frac{fN}{g(1-n)S_x},$$

where L and H are typical horizontal and vertical scales of intrusion, and rewrite (11) in a nondimensional form

$$Pr(1 + \zeta) \left\{ \varepsilon_z \left(\frac{l'}{m'} \right)^2 - \frac{l'}{m'} + (1 + \zeta) \left[\left(\frac{l'}{m'} \right)^2 - \text{sign}(\gamma_S \gamma_\rho) \chi Ri^{-0.5} \frac{l'}{m'} \right] \right\} + \zeta(1 + \zeta) \left[(1 + \zeta)^2 \chi^2 m'^4 - \text{sign}(\gamma_S \gamma_\rho) \chi Ri^{-0.5} \frac{l'}{m'} + \chi^2 \right] < 0, \quad (11')$$

$\gamma_S = -\bar{S}_x / \bar{S}_z$ is the cross-front slope of isohalines, $\text{sign}(\gamma_S \gamma_\rho) = 1$, when the isopycnal and isohaline slopes have the same sign (i.e., in the temperature front [9]) and $\text{sign}(\gamma_S \gamma_\rho) = -1$, when the isopycnal and isohaline slopes are of opposite sign (i.e. in the haline front).

To start with, we will not consider the effect of wave/turbulent mixing. With $\zeta = 0$, (11') reduces to the simple form

$$\left[\varepsilon_z \left(\frac{l'}{m'} \right)^2 - \frac{l'}{m'} + \left(\frac{l'}{m'} \right)^2 - \text{sign}(\gamma_\rho \gamma_S) \chi Ri^{-0.5} \frac{l'}{m'} \right] < 0. \quad (11'')$$

The left side of (11'') consists of four terms. Two of them, the second and the fourth, are allowed to be negative, so two types (mechanisms) of instability exist. The second term is responsible for thermohaline, double-diffusive instability which was discovered by *Stern* [2]. The fourth term is responsible for another type

of instability which can exist only in baroclinic fronts. The last type of instability has already been described by *Kuzmina and Rodionov* [7] and may be referred to as a form of baroclinic instability. However, in contrast to the classic baroclinic instability that works only if $Ri < 1$, and the McIntyre instability that cannot occur unless $1 < Ri < Ri_M^*$, the double-diffusive destabilization of the baroclinic front can occur with no limitation on Ri (if wave/turbulent mixing is absent), as in accordance with (11''). The causes of this instability are the difference of $\bar{\rho}_x$ from zero, and viscosity owing to salt fingers.

According to (11''), at $\chi Ri^{-0.5} \ll 1$, $\chi Ri^{-0.5} \gg 1$, and $\chi Ri^{-0.5} \sim 1$, the instability is determined by thermohaline, baroclinic, and both effects or factors (this terminology was accepted in KR92) respectively. Therefore, being first introduced in KR92, the $\chi Ri^{-0.5}$ - criterion makes it possible to recognize which factor, thermohaline or baroclinic, dominates to generate double-diffusive interleaving in an oceanic front (see also the discussion of the double-diffusive and baroclinic wedges of instability in [8]).

We will now assume that ζ , the ratio of turbulent to double-diffusive salt diffusivities, decreases with the Richardson number, and following [7], take

$$\zeta = ARi^{-q}, \quad (12)$$

where $q \geq 0$ and A are constants. To understand the influence of wave/turbulent mixing on double diffusive interleaving let us consider the case only if $\chi Ri^{-0.5} \ll 1$, $\zeta \ll 1$.

In this limit, (11') reduces to

$$Pr(\varepsilon_z + 1) \left[\frac{l'}{m'} - \frac{1}{2(\varepsilon_z + 1)} \right]^2 - \frac{Pr}{4(\varepsilon_z + 1)} + A \frac{\chi^2}{Ri^q} (1 + m'^4) < 0. \quad (13)$$

The first and second items in the left part of (13) describe the double-diffusive instability controlled by the thermohaline factor, they do not depend on Ri , and their sum is negative in the event of instability. The last item in the left side of (13) describes the effect of turbulent mixing, is positive and depends upon Ri . Therefore, owing to the effect of turbulent mixing, the maximum growth rate of double-diffusive intrusions controlled by the thermohaline factor is expected to decrease and even vanish on some occasions.

Detailed analytical consideration of the instability problem (1)-(8) and new criteria for different types of instability may be found by the reader in [10].

Numerical examples

To illustrate the above theory we calculate numerically the maximum growth rate of intrusions, ω'_{max} , versus Ri for different sets of input parameters Pr , χ , ε_z , A , σ . Following [7], we will use a parameter $\delta \equiv Ri^{-0.5}$ instead of Ri . Being proportional to the isopycnal slope γ_ρ , this δ is referred as the parameter of baroclinicity [11]. Calculating δ -dependencies of ω'_{max} has been done only for $\delta \leq 1$ (or $Ri \geq 1$) to avoid treating the case of the classical instability dominating at $Ri < 1$. The problem has too many nondimensional parameters and instability criteria, and we are not able to demonstrate all the possibilities in the framework of a single paper. For this reason we restrict our consideration to the case $\varepsilon_z = 0.5$, $\chi \geq 1$, $Pr \geq 1$.

Figure 1 is ω'_{max} versus δ with the following input parameters: $Pr = 1$, $\chi = 10$, $A = 0$, $\varepsilon_z = 0.5$. The only difference in parameters is in the sign of isohaline and isopycnal slopes: $sign(\gamma_\rho \gamma_\sigma) = 1$ (the top curve) and $sign(\gamma_\rho \gamma_\sigma) = -1$ (the bottom curve). If isohalines and isopycnals are of the same sign and the turbulence is dropped, ω'_{max} approaches some positive constant when $\delta \rightarrow 0$ (double-diffusive interleaving controlled by thermohaline factor) and is growing monotonically with δ due to the baroclinicity. If isohaline slope opposes isopycnal slope, ω'_{max} approaches the same value at $\delta \rightarrow 0$, decreases with δ as long as it vanishes at $\chi\delta = 1$, and then increases with δ at $\chi\delta > 1$.

Figure 2 shows the effect of turbulence on double-diffusive interleaving for $q = 1$. In this case, owing to the effect of turbulent mixing, the maximum growth rate of double-diffusive interleaving controlled by the thermohaline factor is expected to decrease and even vanish on some occasions.

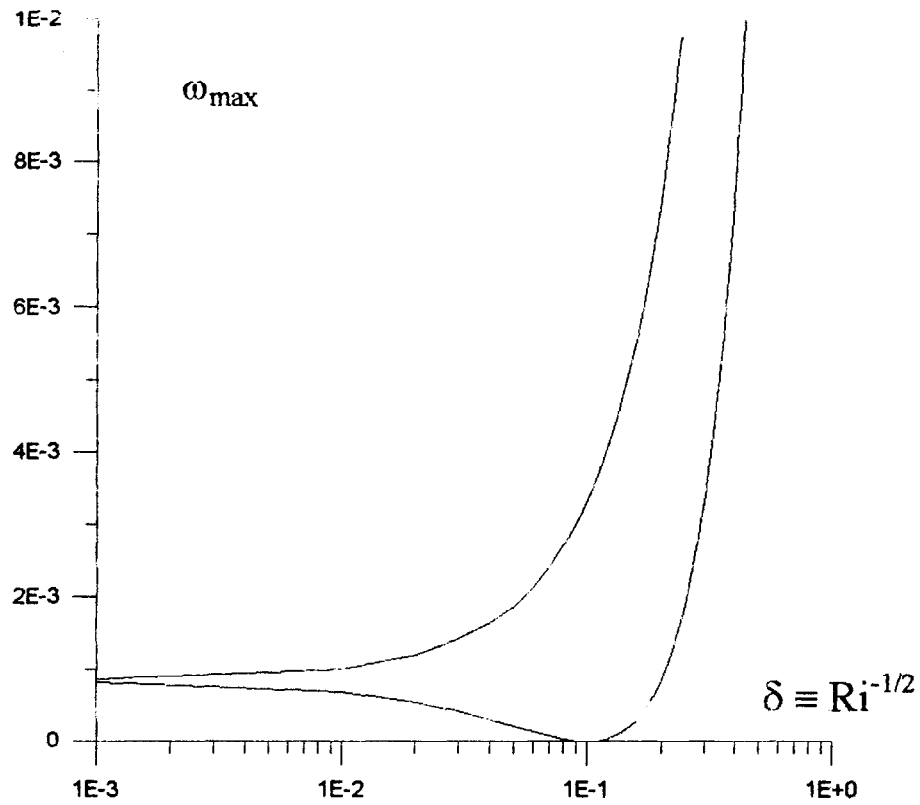


Figure 1. Maximum growth rate, ω'_{max} , versus $\delta = Ri^{-0.5}$ at $Pr = 1$, $\chi = 10$, $A = 0$, $\epsilon_z = 0.5$, and $sign(\gamma_\rho \gamma_S) = 1$ (top curve) and $sign(\gamma_\rho \gamma_S) = -1$ (bottom curve).

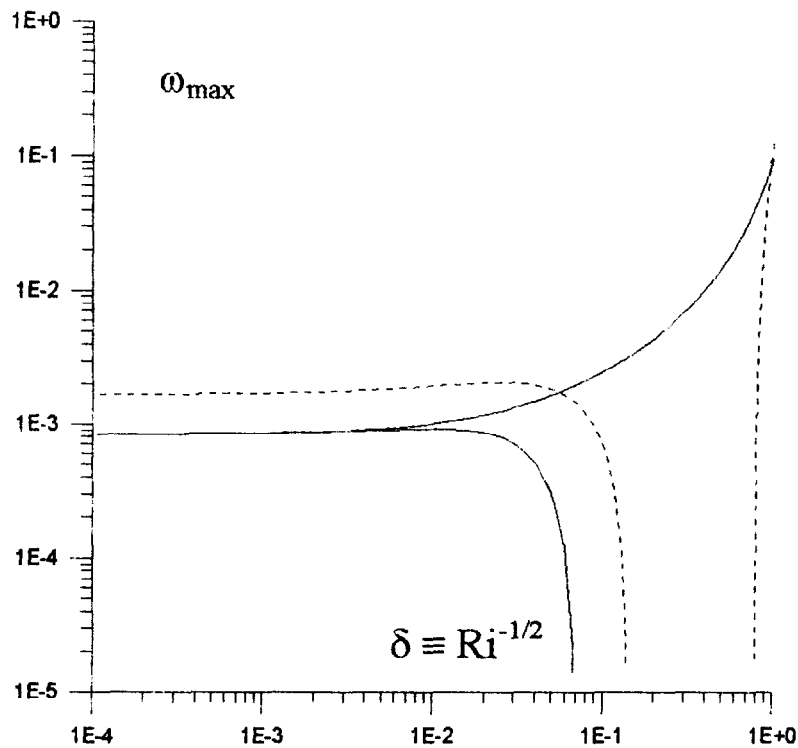


Figure 2. The same as in Figure 1 but for the following input parameters: $q = 1$, $\chi = 10$, $\epsilon_z = 0.5$, $sign(\gamma_\rho \gamma_S) = 1$ (all the curves), and $Pr = 1, A = 1$ (bold solid), $Pr = 1, A = 0.1$ (solid), $Pr = 2, A = 1$ (dashed).

Conclusions

In this paper, we have examined the effects of double diffusion and turbulent mixing on interleaving in baroclinic oceanic fronts in the framework of linear instability approach. An important result of this study is the conclusion that the viscous/diffusive destabilization of geostrophic flow is possible at any (large) value of Ri provided that the momentum/mass transfer is governed by double diffusion. This differs essentially from the case of non-double-diffusive interleaving in the baroclinic front which cannot occur unless $Ri < (1+Pr)^2 / 4 Pr$. (i.e., the McIntyre instability).

The situation is complicated largely if one takes into account turbulent mixing. In general, turbulent mixing works to suppress the double diffusive interleaving, whether it be controlled by the thermohaline or baroclinic factors. However the abrupt decrease of a maximum growth rate is more likely if $\chi Ri^{-0.5} < 1$ (double-diffusive interleaving controlled by the thermohaline factor).

Acknowledgement

This work was financially supported by the Russian Foundation for Basic Research, Grant # 97-05-65381.

References

- [1] McIntyre M.E., 1969: Diffusive destabilization of the barocline circular vortex. " Geophys. Fluid Dynamics", 1, No 1-2, 19-58.
- [2] Stern M.E., 1967: Lateral mixing of water masses. Deep-Sea Res. V.14. No.12A. P.747-753.
- [3] Ruddick B.R., Turner J.S., 1979: The vertical length scale of double-diffusive intrusions. Deep-Sea Res. V.26. No 8A. P.903-913.
- [4] Toole J.M., Georgi D.T., 1981: On the dynamics and effects of double-diffusively driven intrusions Progr. Oceanogr., V. 10, No. 1, P. 123-145.
- [5] McDougall T.G., 1985: Double-diffusive interleaving. Part 11: Finite amplitude, steady state interleaving. J. Phys. Oceanogr. V.15. No 11.P.1542-1556.
- [6] Niino H., 1986: A linear stability theory of double-diffusive horizontal intrusions in a temperature - salinity front. J. Fluid Mech. , V.171, Pt.1, 71-100.
- [7] Kuzmina N.P., Rodionov V.B., 1992: About the influence of baroclinicity upon generation of the thermohaline intrusions in the oceanic frontal zones. Izvestiya Akad. Nauk SSSR, Atmospheric and Oceanic Physics, V. 28, No 10-11,1077-1086.
- [8] May B.D., Kelley D.E., 1997: Effect of Baroclinicity on Double-diffusive Interleaving. J. Phys. Oceanogr., V.27, p.1997-2008.
- [9] Fedorov, K.N. 1983: Fizicheskaya priroda i structura okeanicheskikh frontov. (Physical Nature and Structure of Ocean Fronts).Gidrometeoizdat, Leningrad, .296 p.
- [10] Kuzmina N.P., Zhurbas V.M., 1998 Effects of double diffusion and turbulence on interleaving at baroclinic oceanic fronts. Submitted to J. Pays. Oceanogr.
- [11] Zhurbas, V.M., N.P. Kuzmina, and I.D.Lozovatskiy, 1988: The role of baroclinicity in intrusive layering in the ocean. Oceanology (English Ed.), V. 28, No 1, 34-36.

A MATHEMATICAL MODEL OF DENSITY CURRENT ON AN INCLINE

V. Yu. Liapidevskii

Lavrentyev Institute of Hydrodynamics, Novosibirsk 630090, Russia

E-mail: liapid@hydro.nsc.ru

Abstract. A mathematical model of density flow down a sloping floor which takes into account the entrainment of ambient fluid into a thin turbulent layer of the heavier fluid is developed. The structure of steady flows and travelling waves is investigated. It is shown that in a steady flow the entrainment rate may be found in the frame of the model as a function of the angle of inclination only. The travelling wave and the steady flow may be matched and it gives the simple solution which describes the nonstationary evolution of the head of a gravity current.

Introduction

Gravity or density currents are types of stratified flows, which have a very complicated structure. They are usually realized as either top or bottom currents, and entrainment and mixing processes play an important role in the dynamics of the flows.

At the front of a gravity current a specific "head"-structure with a zone of breaking waves and intense mixing behind it is formed. The behavior of the head is different for horizontal and sloping bottoms. In a gravity current flowing horizontally the structure of the head is quasi-stationary, but in a current down an incline the head is linearly growing in size with the distance from a source of constant intensity.

The structure of the head of a gravity current flowing along of horizontal surface have been investigated in [1 - 2]. The mathematical model of gravity flow in a horizontal channel of finite depth have been developed in [3]. It is based on the two-layer flow model taking into account mixing and short wave generation at the interface. An intermediate layer where mixing between homogeneous layers occurs is taken in the model as the third one. The conservation law of the total energy of the flow is added to the system to find the entrainment rate into the intermediate layer together with other unknown variables. This makes it possible to describe a fine structure of the head and, in particular, to explain the strong dependence of a gravity flow on the total depth of a channel.

The aim of this paper is to derive the simplest mathematical model of gravity current down an incline, which can be used for simulation of entrainment processes in unsteady flows.

The density flows on an incline have been studied experimentally in [4 – 7]. It was shown that a gravity current consists of a jet-like flow region where the density of the jet decreases rapidly due to the entrainment of the ambient fluid and the boundary layer of almost unmixed dense fluid (Fig. 1). The interaction between the layers have been investigated in [6]. The steady density currents have been studied in [4] and the structure of the head has been investigated in [5].

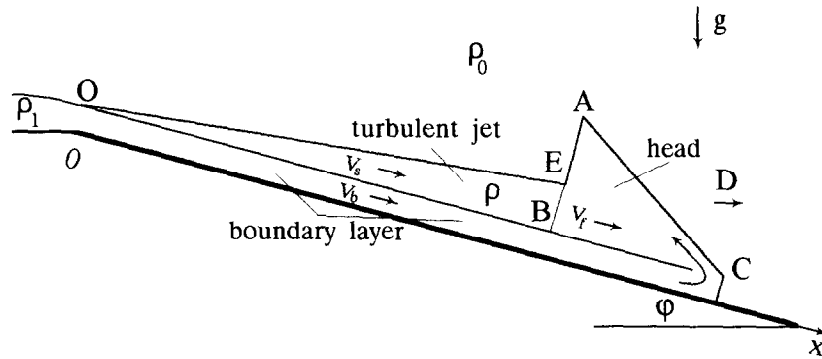


Figure 1: Sketch of the density flow on an incline

A distinguishing feature of the mathematical model of density current given below is the possibility to derive the entrainment rate into turbulent jet from the model itself instead of using an empirical function as suggested in previous investigations. In the study we consider only two-dimensional flows. The effect of the earth's rotation is neglected.

Governing equations

In Boussinesq approximation the evolution of the thin turbulent layer of mixible fluid flowing down an incline in the ambient lighter fluid may be described by the system [3, 8]:

$$\begin{aligned}
 (b\eta)_t + (b\eta v)_x &= 0 \\
 (\eta v)_t + (\eta v^2 + \frac{1}{2}b\eta)_x &= \alpha b\eta \\
 (\eta(v^2 + q^2 + b\eta))_t + (\eta v(v^2 + q^2) + 2b\eta^2 v)_x &= 2\alpha b\eta v - \beta q^3 \\
 \eta_t + (\eta v)_x &= \sigma q.
 \end{aligned}
 \tag{1}$$

Here h is the layer depth, v is the mean velocity, q is the mean-square velocity, ρ, ρ_0 are the densities in a turbulent layer and an ambient fluid, g is the gravity acceleration, $b = (\rho - \rho_0)g/\rho_0$ is the buoyancy of the turbulent layer, $\alpha = \text{tg}\varphi$, φ is the angle of bottom inclination.

The system (1) is a version of the shallow water equations taking into account the entrainment from the ambient fluid. It consists of the mass, momentum and energy conservation laws. The energy equation is necessary to find the entrainment rate of the ambient fluid into the turbulent layer. The empirical coefficient $\sigma = 0.15$ is responsible for scaling horizontal and vertical motions and may be eliminated from the system by replacing independent variables. Therefore, there is only one empirical coefficient $\delta = \beta/\sigma$ in the model, which presents the rate of dissipation of turbulent energy in the

layer. Note that the shallow water approximation is reasonable for moderate angles of inclination.

Boundary layer

Experiments [4, 6, 7] show that near the bottom there is a boundary layer characterized by the mean velocity u_b , the depth h_b and the density ρ_1 . The entrainment from the boundary layer into the turbulent layer is negligible as compared with the entrainment from the ambient fluid. For the sake of simplicity, let $\rho_1 \equiv \text{const}$ ($\rho_1 > \rho$) and there be no interaction between the layers. In this case, the Reynolds stress vanishes at the interface and the equations of motion for the turbulent and boundary layers are splitted. In (1) there is no bottom friction terms, but the bottom friction governs the flow in the bottom layer, i.e. the flow is steady and gravity and friction forces are in equilibrium:

$$\alpha b_1 h_b = c_b u_b^2. \quad (2)$$

Here $b_1 = (\rho_1 - \rho)g/\rho_0$ is the buoyancy of the unmixed dense fluid, c_b is the friction coefficient ($c_b = \text{const}$). The normal depth h_b and the velocity u_b may be found from (2), if the buoyancy flux in the boundary layer $A_b = b_1 \cdot h_b \cdot u_b$ is given. Although the boundary layer doesn't influence the motion of the turbulent layer, it is the source of mass input into the head of a gravity flow in the nonstationary problem.

Self-similar solutions

For the solutions of the form

$$v = v(\xi), \quad m = b\eta = m(\xi), \quad q = q(\xi), \quad \eta = x\lambda(\xi), \quad \xi = x/t. \quad (3)$$

Eqs. (1) transform into the system of ordinary differential equations

$$\begin{aligned} \xi(v - \xi)\lambda' + \xi\lambda v' &= \sigma q - \lambda v, \\ (v - \xi)m' + mv' &= 0, \\ \xi \left[(v - \xi)(\lambda v)' + \lambda v v' + \frac{1}{2}(m\lambda)' \right] &= \alpha m - \lambda v^2 - \frac{1}{2}\lambda m, \\ \xi(v - \xi)q' &= \frac{\sigma}{2\lambda}(v^2 - m - (1 + \delta)q^2). \end{aligned} \quad (4)$$

It is shown in [4, 5] that (3) describes a gravity flow down an incline generated by the dense fluid source of constant intensity which starts at the origin of the coordinate system at $t = 0$. Eqs. (4) are rather complicated, but we consider a class of solutions having a very simple structure to construct the nonstationary flow configuration.

Steady flow

Consider a steady flow. The flow with $v = v_s$, $m = m_s$, $q = q_s$, $\lambda = \lambda_0$ is the solution of (1) when the following relations are fulfilled:

$$\begin{aligned} \lambda_0 v_s &= \sigma q_s, \\ \lambda_0 \left(v_s^2 + \frac{1}{2} m_s \right) &= \alpha m_s, \\ v_s^2 - m_s - (1 + \delta) q_s^2 &= 0. \end{aligned} \quad (5)$$

The flow constants v_s , m_s , q_s , λ_0 may be found from (5), if the buoyancy flux A_s is given, i.e.

$$m_s v_s = A_s. \quad (6)$$

In dimensionless variables $v_0 = v_s/A_s^{1/3}$, $m_0 = m_s/A_s^{2/3}$, $q_0 = q_s/A_s^{1/3}$ we can reduce (5), (6) to the equation

$$\frac{2\alpha}{\sigma} v_0^{3/2} = \sqrt{\frac{v_0^3 - 1}{1 + \delta}} (1 + 2v_0^3). \quad (7)$$

For every $\alpha/\sigma > 0$ there is a unique solution of (7) ($v_0 > 1$), corresponding to the case of supercritical flow ($v_s^2 > m_s$). From (4), (5) the flow parameters λ_0 , m_0 , q_0 may be derived as functions of the variable v_0 and, as consequence, as functions of the angle of inclination φ . Notice that for steady flows the entrainment rate

$$E = \frac{1}{v} \frac{d\eta v}{dx} = \lambda_0$$

may be found by the model itself, without invoking any empirical functions. The dependence E on φ for $\delta = 0, 2, 4$ is shown in Fig. 2 (solid lines) together with experimental data from [4], Fig. 8.

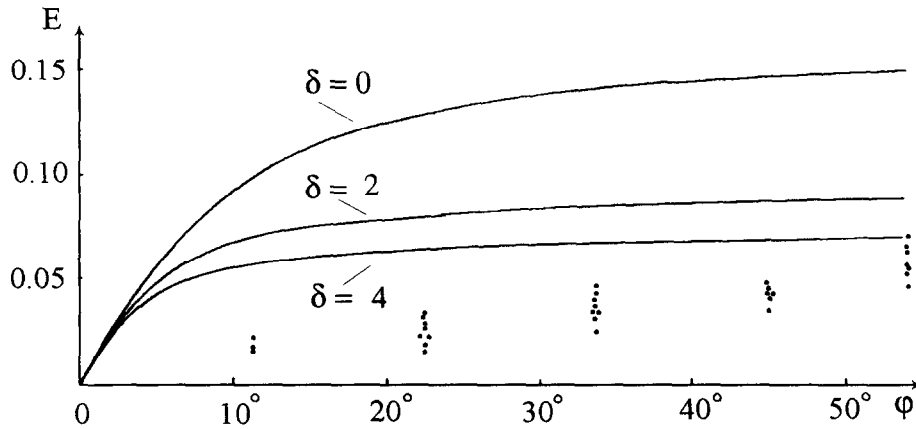


Figure 2: Entrainment as a function of slope: the mathematical model (1) with $\delta = 0, 2, 4$ (solid curves), data from [4], Fig. 8 (dots).

Travelling waves

The motion of the head of a density current has been investigated in [5]. It has been shown experimentally that nonstationary problem may be described by self-similar flows of the type (3). Therefore, Eqs. (4) may be used for simulation of a density flow evolution for large time.

Consider a special class of solutions of (4), and, consequently, of (1). Let a solution of (1) depend on the variable $\xi = x - Dt$ in the following way: $v \equiv v_f$, $m \equiv m_f$, $q \equiv q_f$, $\eta = \lambda_1(Dt - x)$, $\lambda_1 > 0$. Here $D > 0$ is the travelling wave velocity. In this case (1) reduces to the relations

$$\begin{aligned} \lambda_1(D - v_f) &= \sigma q_f, \\ \lambda_1 \left((D - v_f)v_f - \frac{1}{2}m_f \right) &= \alpha m_f, \\ \lambda_1 \left((D - v_f)(v_f^2 + q_f^2 + m_f) + v_f m_f \right) &= 2\alpha m_f v_f - \sigma \delta q_f^3. \end{aligned} \quad (8)$$

Now we can construct a solution of nonstationary problem by matching a steady flow with a travelling wave through a contact discontinuity. Let OEB in Fig. 1 be the region of steady flow, ABC be the region of travelling wave, AB be the contact discontinuity. The relations at AB may be derived from conservation laws (1):

$$\begin{aligned}\eta^+ m_f &= \eta^- m_s, \\ v_f &= v_s,\end{aligned}\tag{9}$$

Here $\eta^- = \lambda_0 v_s t$ and $\eta^+ = \lambda_1 (D - v_f) t$ are depths at the left and at the right of the discontinuity AB .

For given buoyancy flux A_s all parameters of the steady flow are known. Therefore, we can obtain flow parameters D , v_f , m_f , q_f from (8), (9). We look for a flow with $D > v_f$, wherein the head ABC grows linearly in size with time, as this has been shown in [5]. Eqs. (8), (9) may be reduced to one equation

$$q_f^2 + \frac{\lambda_0 v_s m_s}{\sigma q_f} = v_s^2.\tag{10}$$

Note that $q_f = q_s$ is the solution of (10), but it corresponds to the case $D = 0$, $\lambda_1 = -\lambda_0 < 0$, so it describes the steady flow (5). The only admissible solution ($q_f > 0$) may be found from (10) in the following way:

$$q_f = \frac{\sqrt{(1 + \delta)^2 q_s^2 + 4(1 + \delta) m_s} - (1 + \delta) q_s}{2(1 + \delta)}.\tag{11}$$

The solution (11) satisfies the condition $D > v_s$ for $\lambda_1 > 0$, i.e.

$$\sigma q_f v_f > \alpha m_f.$$

The dimensionless variables $m_1 = m_f / A_s^{2/3}$, $q_1 = q_f / A_s^{1/3}$, $v_1 = v_f / A_s^{1/3}$ and λ_1 may be found by (8), (9), (11) as functions of the angle φ . Therefore, for given buoyancy flux A_s we may find all flow parameters of the nonstationary problem, but the solution for the head ABC is meaningful only when there exists a mass input source at the "nose" of the head.

Remember now that in the boundary layer we have the steady flow with the density ρ_1 , the buoyancy flux A_b and the velocity u_b . If $u_b > D$ and there is no interaction between layers, from the continuity equation we have

$$b_1 h_b (u_b - D) = (D - v_f) m_f.\tag{12}$$

From (12) we can derive the buoyancy flux A_b in the boundary layer as a function of the buoyancy flux A_s . Therefore, for given total intensity of the source

$$A = A_s + A_b$$

we can find from (12) the buoyancy fluxes A_s and A_b , and then all flow parameters in the turbulent layer and the boundary layer.

Conclusions

The mathematical model (1) is shown to be appropriate for entrainment simulating in density flows down an incline. For steady flows it gives the entrainment rate of ambient fluid into turbulent layer as a function of the angle of inclination. For description of nonstationary head evolution the simple solution of (1) which consists of a steady flow and a travelling wave is constructed. Mass and momentum transfer between layers is not taken into account in (1), nevertheless, the model gives the limiting values of flow parameters in the nonstationary problem, which may be used in more complicated models.

The work was supported in part by the Russian Foundation of Basic Research under grant No. 98-01-00750 and by Russian Academy of Sciences, Siberian Division under grant No. 43.

References

- [1] R. E. Britter, J. E. Simpson, 1978, Experiments on the dynamics of a gravity current head, *J. Fluid Mech.*, 88, 223-240.
- [2] J. E. Simpson, R. E. Britter, 1979, The dynamics of the head of a gravity current advanced over a horizontal surface, *J. Fluid Mech.*, 94, 477-495.
- [3] V. Yu. Liapidevskii, 1998, The gravity flow structure in mixible fluid, *J. Appl. Mech. Tech. Phys.*, 39, (to appear).
- [4] T. H. Ellison, J. S. Turner, 1959, Turbulent entrainment in stratified flows, *J. Fluid Mech.*, 6, 423-448.
- [5] R. E. Britter, P. F. Linden, 1980, The motion of the front of a gravity current travelling down an incline, *J. Fluid Mech.*, 99, 531-543.
- [6] V. Alavian, 1986, Behaviour of density currents on an incline, *J. Hydraul. Engng.*, 112, 27-42.
- [7] M. H. Garcia, 1993, Hydraulic jumps in sediment-driven bottom currents, *J. Hydraul. Engng.*, 119, 1094-1117.
- [8] V. Yu. Liapidevskii, 1989, Dynamics of a uniform turbulent layer in a stratified fluid, *J. Appl. Mech. Tech. Phys.*, 30, 235-238.

TURBULENCE IN STRATIFIED PATCHES ON A SHALLOW SHELF

I.D. Lozovatsky* and H.J.S. Fernando

Environmental Fluid Dynamics Program, Department of Mechanical and Aerospace Engineering, Arizona State University, Tempe, AZ 85287-6106, USA; i.lozovatsky@asu.edu, j.fernando@asu.edu

* also at the P.P. Shirshov Institute of Oceanology Russian Academy of Sciences, Moscow, 117851, Russia.

Abstract. Successive measurements of temperature, conductivity and small-scale shear profiles at the Black Sea shelf revealed the existence of several microstructure patches (layers). The layers evolve in time, and some of them appear to be energized by the local shear associated with a low-saline intrusion in the measurement area. The measurements were used to calculate the turbulent kinetic energy dissipation rate, buoyancy diffusivity, activity parameter, mixing efficiency and buoyancy and mixing Reynolds numbers. Some findings of the field data analysis were compared with available laboratory data on stratified turbulent patches.

1. Introduction

The aim of this paper is to present certain observations made in the shallow shelf waters of Black Sea that appear to be useful in the studies of stratified turbulence. During the observations, several layers rich in microstructure exhibited interesting evolutionary patterns. The observational region was essentially free of tidal forcing and strongly-sheared currents, and hence it is anticipated that turbulent layers observed may have some resemblance to laboratory experiments that have been carried out under idealized conditions (with only a few energy input mechanisms), thus making comparisons between laboratory and field data feasible. In addition, the measurements could be compared with available theoretical predictions or used to test underlying assumptions of various theories.

2. Data

The measurements were carried out as a part of a special microstructure field experiment [1] on October 11, 1989, from an anchored ship, so that the problems associated with ship drift could be minimized. The distance from the shore line to the measurement location was about 3 miles and the corresponding water depth was $z = 25$ m. A free fall "BAKLAN" profiler [2] was used to measure the vertical profiles of temperature, conductivity, and small-scale shear from the sea surface down to the bottom. Technical characteristics of the "BAKLAN" sensors and details of data processing are given in [2].

A series of twelve consecutive casts was implemented from 17:26 until 17:51 (local time). The cycle time was 2 minutes. Meteorological conditions during the observational period and the background hydrology on the shallow part of the Black Sea shelf off the Bulgarian port of Varna are given in [3].

Density stratification at the site of measurements showed well-mixed upper and near-bottom boundary layers, each is about 5 m in thickness; a daytime pycnocline ($4 < z < 7$ m) and a sharp narrow thermocline, which was found in the depth range of 18-20 m. A weakly stratified layer with low turbulence ($15 < z < 18$ m) and a layer with substantial patchiness of microstructure activity ($7 < z < 15$ m) were identified between the upper and lower pycnoclines. The present study will be focused only on the last region where the buoyancy frequency varied from 0.04 to 0.016 s^{-1} and the mean shear was much less than those in surface and bottom boundary layers [3]. To analyze microstructure activity in different patches, we calculated the kinetic energy dissipation rate $\varepsilon(z) = 7.5 \nu (du/dz)^2$, the buoyancy diffusivity $K_N = 0.2\varepsilon / N^2$, and the activity parameter [4]

$A_G = (\varepsilon / 13DCoN^2)^{1/2}$ based on the conductivity Cox number $Co = \overline{(\nabla c')^2} / (\overline{\nabla c})^2$; ν is the molecular viscosity, D is the molecular diffusivity of the scalar. All variables were averaged over $\Delta z = 0.2$ m.

3. General Characteristics of Microstructure Patches

Several types of microstructure patches in the pycnocline were distinguished in the depth range $7 < z < 15$ m. These were: quasi homogeneous patch (QHP) -- region with $N^2 < 10^{-4}$ s⁻²; active turbulent patch (ATP) - region with $\varepsilon / \nu N^2 > 25$, active patch (AP) - region with $\varepsilon > 1.25 \times 10^{-9}$ W/kg; stratified dissipative patch (SDP) - region with $\varepsilon > 10^{-9}$ W/kg but $N^2 > 10^{-4}$ s⁻²; microstructure displacement patch (MDP) - regions with the r.m.s Thorpe scale $LT_h > 0$. The boundaries of these patches, identified by careful inspection of individual profiles showed very little overlap between these different types of patches, with the exception that the boundaries of ATP approximately encompass both QHP and AP.

The presence of three-dimensional turbulent motions in a non-sheared stratified layer can be identified by using the parameter $G = \varepsilon / \nu N^2$. When G is greater than some critical value, G_{cr} , the three-dimensional turbulent motions are expected. Various laboratory experiments show marked variability, $10 < G_{cr} < 33$, and the commonly used value is $G_{cr} = 25$ [4].

3.1. Quasi-homogeneous patch. QHP was observed between 8.2 and 10.1 m (Fig. 1), with a mean thickness of $h_{QHP} \approx 0.85$ m. During the first ten minutes of observations, h_{QHP} continuously decreased from 0.95 to 0.58 m and a best fit lines indicates that this decrease can be expressed as $h_{QHP} \approx 1.06 \times e^{-0.06 N_0 \Delta t}$, where $N_0 = 0.016$ s⁻¹ is the background buoyancy frequency of QHP, Δt is the time elapsed from 17:27, at which time the patch is assumed to have been generated (see corresponding discussion below). Five minutes later, however, the thickness of QHP rapidly increased to a maximum of $h_{QHP} = 1.6$ m, and then reduced by a factor of two during the next two minutes. The rapid increase of the thickness can be attributed to several reasons:

- A quasi-homogeneous turbulent patch generated elsewhere may have advected to the measurement location while a part of the patch was still active (note that the upper part of QHP has a local increase of A_G).
- The edge of QHP, i.e., the interface between the QHP and the adjoining stratified region, may have become locally unstable and broken down into a secondary patch, thus increasing the vertical size of QHP at the measurement location. The local increase of A_G at the upper edge of QHP, together with the appearance of Thorpe displacements in this area and increases in ε and G support this notion. Laboratory experiments of [5] provide clear evidence for the possibility of such sporadic local instabilities at the edges of turbulent patches (see Fig. 6 in [5]). The observations collectively show that the turbulence in QHP has been mostly affected by the buoyancy forces, albeit the patch is a quasi-homogeneous relatively ambient stratification. This situation has similarities to certain laboratory experiments dealing with continuously agitated or decaying isolated turbulent regions in stratified fluids [5].

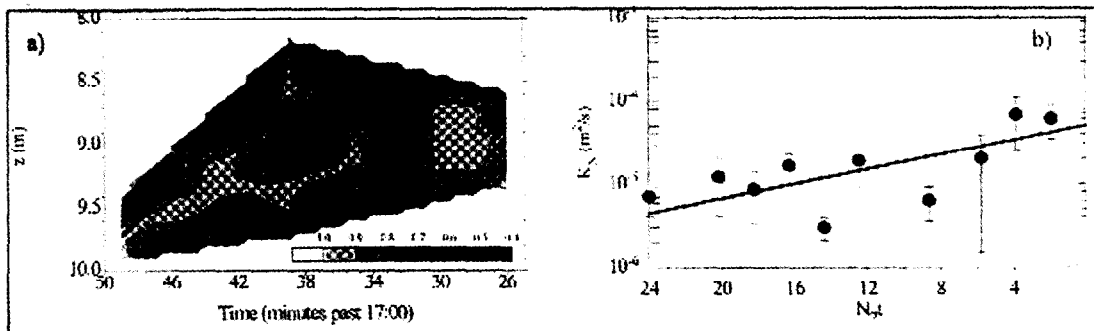


Fig. 1. A contour plot of the mixedness parameter m in the QHP (a). This shows that only the narrow core of the patch was well-mixed. High values of m , which were observed in the second and third profiles coincide with the highest estimates of the mean diffusivity K_N at the right panel. The solid line is the exponential approximation (1). The error bars show 90% bootstrap confident intervals of the mean for each cast. Time elapses from right to left.

The mixed nature of a stratified patch can be parameterized using the mixedness parameter defined in [5] as $m = 1 - (N^2/N_o^2)$, where N_o is a background buoyancy frequency. Fig. 1(a) shows the variation of m in QHP. Note that at least a narrow region at the center of the patch is well-mixed, except at around 17:32. The latter anomaly suggests that our measurements may have been carried out close to an irregular lateral boundary of the patch, so that the fourth cast has probably been obtained out of the patch, in a more stratified region. The patch was almost completely mixed ($m > 0.9$) at 17:28 and 17:30, while at 17:26 the mixedness was lower ($m \approx 0.4 - 0.8$). Based on these observations, it is reasonable to conjecture that there has been turbulent energy generation within the quasi-homogeneous patch just before the cast at 17:28. The time variation of the mass diffusivity K_N shown in Fig. 1(b) supports this assumption. A maximum value of K_N was observed during the time period of 17:28 to 17:30. Two minutes before and after, values of K_N were about 5 - 7 times lower.

The activity parameter A_G also significantly rose during this time, further corroborating the notion of a rapid, turbulence-generating event at $t_o \approx 17:27$. The evolution of turbulence following this event can be described by using the time elapsed after the onset of the event, by assigning 17:27 as $t = t_o$. If so, we can present the variations of the buoyancy diffusivity in the patch as a function of non-dimensional time $N_o(t-t_o)$, where $N_o = 0.016 \text{ s}^{-1}$ is a background buoyancy frequency. Fig. 1(b) exhibits an evident decay of K_N with time. This trend was approximated by an exponential function

$$K_N = K_N^o \times e^{-0.1N_o(t-t_o)}, \quad (1)$$

where $K_N^o = 5 \times 10^{-5} \text{ m}^2/\text{s}$ is the diffusivity at the onset of turbulent mixing in the patch. The result of the least-squared fit of (1) is shown in Fig. 1(b) by a straight line. Despite two samples in Fig. 1(b) considerably depart from (1), an exponential decay of the buoyancy diffusivity in QHP seems to be proven.

3.2. Strongly-stratified patches. It is expected that SDP and MDP may have similarities as both these patches were produced in a background of strong ambient stratification, perhaps by the same generation process. Note, that the difference between SDP and MDP is mainly relates to our definition of the primary variable to bound a microstructure or turbulent patch (enhanced turbulent dissipation for SDP versus the vertical microstructure displacements for MDP). Time variability of the vertically averaged (over the whole patch thickness) mixedness parameter $\langle m \rangle$ in SDP and MDP is similar indeed. During this initial period (17:26 - 17:39), the rate of turbulent dissipation $\varepsilon(z, t)$ and the buoyancy frequency $N(z, t)$ gradually decreased with time, enhancing $\langle m_{SDP} \rangle$ from 0.6 to 0.84. At 17:39, the SDP began to sink across the isopycnal surfaces, leading to a sharp reduction of $\langle m_{SDP} \rangle$ to 0.4 at the end of the observations. MDP was even less mixed than SDP, the highest $\langle m_{MDP} \rangle = 0.64$, the lowest was 0.12, but the mixedness parameter in MDP lowered in time more gradually compared to those in SDP. Strong ambient stratification may have quickly suppressed mixing in both patches. Some active turbulence ($Re_b > 1$, which is equivalent to $G > 25$) survived only in the narrow core of MDP. Based on the parameter G , SDP is completely non-turbulent region at the time of observation ($G < 15$ always). It might be transformed from active to a fossil state or represents a region of random dissipating small-scale internal waves. As such, no new overturning or strong mixing activity is expected in SDP. Relatively high dissipation in SDP appears to simply reflect that random internal wave activity is pronounced and small-scale internal waves are dissipating energy to heat. In this case, weakly-turbulent small-scale velocity fluctuations might be highly anisotropic and did not produce vertical mixing.

3.3. Patch generation. It is of interest that the enhancement of ε was found above and below QHP, but not inside the patch. The upper layer of high- ε , the active patch, was relatively thin but energetically active. The mean thickness of AP was equal to 0.67 m, with a standard deviation of 0.18 m, whereas the thickness of the lower layer, SDP, was twice as much, $\langle h_{SDP} \rangle = 1.68 \text{ m}$ with r.m.s. of 0.3 m. Insights into the genesis of AP and SDP can be obtained by scrutinizing the salinity section of the area under investigation, shown in Fig. 2. A local salinity minimum in the depth range $8 < z < 10 \text{ m}$ likely identifies a low-saline intrusion with possible local shears at its upper and lower boundaries, which cause enhance the kinetic energy dissipation rate. The fact that the lower boundary of the intrusion coincides with SDP and the upper boundary is in the proximity of AP suggest that indeed this scenario is plausible. A local minimum of ε is seen in the central part of the inversion between 8.6 m and 9.4 m. At the same time, the density profile shows the almost homogeneous, well-mixed layer at the depths of the salinity inversion. Inspection of Fig. 2 indicates that the fluid in the intrusion was stably stratified with respect to temperature and unstably stratified with respect to salinity, thus raising the

possibility of salt-finger convection. Double-diffusive processes are usually characterized by the density ratio $R_\rho = \alpha\Delta T/\beta\Delta S$, where α and β are the thermal expansion and salinity contraction coefficients, respectively, and ΔT and ΔS are the temperature and salinity differences across the layer. Salt-finger mixing occurs if $R_\rho < 1.6$. Calculation of $\Delta T = 0.041$ C and $\Delta S = 0.009$ psu between 8.4 and 9.2 m, leads to $R_\rho = 1.2$ for $\alpha/\beta = 0.23$, indicating the possibility of salt-finger convection. This produces effective mixing of intrusion waters, which may account for the weakly stratified core of the intrusion. Owing to the low shear in that region, the turbulent kinetic energy production and dissipation rates, however, are expected to be small in the core.

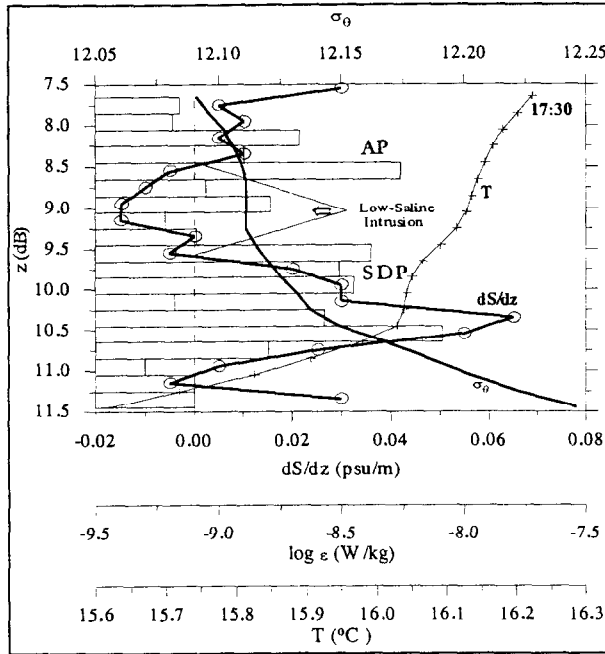


Fig. 2. The profiles of the logarithm of the kinetic energy dissipation rate (bars), temperature (line with crosses) specific potential density σ_θ and salinity gradient (line with circles) for the third cast, 17:30.

not be applicable to sustained turbulent patches.

As the activity parameter A_G can be used to describe the hydrodynamic state of turbulence in a stratified non-sheared patch, we plotted A_G data on a $A_G - R_b$ plane, which is called a hydrodynamics phase diagram. Such a diagram is shown in Fig. 3 and the following can be identified:

- (i) 3-D turbulence *unaffected* by buoyancy and viscosity at scales of the order of maximum Thorpe displacements, $A_G > 1$, $R_b > 1$ (active turbulence).
- (ii) Large-scale turbulent fluctuations (larger than L_{Th}) *affected* by buoyancy but the smaller scales are actively overturning $A_G < 1$, $R_b > 1$ (active-fossil turbulence).
- (iii) All scales of the motion field are affected by the stratification and viscosity $A_G < 1$, $R_b < 1$ (fossil turbulence).

Most of the data taken lie in the range $\log(A_G) < 0$, indicating at first glance fossil or active-fossil turbulence. There is a cloud of samples in the quadrant $0 > \log(R_b) > -2$ and $0 > \log(A_G) > -2$. The line 1 shown corresponds to (2) with $c_A \approx 1$, introduced by Gibson [4] to describe the locus of $A_G(R_b)$, when the patch decays from an active to a fossil state. This derivation assumes that ε decreases monotonically and ε_0 , based on the microstructure overturn scale, $\varepsilon_0 \sim L_{Th}^2 N^3$ or the Cox number, $\varepsilon_0 = 13DC_0 N^2$, is a constant. These assumptions imply a constant scalar eddy diffusivity of $K_{sc} = R_m \nu$, where $R_m \equiv K_{sc} / \nu = 25 / 13 c_A^2$ is the mixing Reynolds number. If $c_A = 1$, then $R_m \approx 2$ and $K_{sc} \approx 2\nu$. Note that only the data from SDP lie surrounding the line 1. Almost all other data are overpredicted by (2), indicating that the decaying patches may

4. Patch Energetics

4.1. Activity parameter. If turbulence exists (i.e., $\varepsilon / \nu N^2 > 25$), then $A_G > 1$ implies active turbulence, and $A_G < 1$ implies active-fossil turbulence. On the other hand, $\varepsilon / 25\nu N^2 < 1$ implies that the turbulence is in a full fossil state. The parameter $\varepsilon / 25\nu N^2$ can be called the buoyancy Reynolds number, R_b , albeit several physical meanings can be given to it. Although the numerical constants appearing in these identities are controversial and have not been rigorously established, we will use them as "canonical" values for comparison purposes. For an impulsive-generated turbulent patch, initially $A_G > 1$. The locus described by activity parameter in the $A_G - R_b$ plane for stratified decaying turbulence was derived by Gibson [4] by assuming that ε decays monotonically from the "dissipation at the onset of fossilization" ε_0 , viz.,

$$A_G = c_A R_b^{1/2}, \quad (2)$$

where c_A is a constant. It should be borne in mind that (2) have been derived for a patch that falls into the framework of fossil turbulence theory, and may

not follow the proposed relationship between R_b and A_G . Inspection of Fig. 3 also shows that the active quasi-homogeneous regions tend to follow a decay curve with a smaller c_A . For QHP, AP and for the central part of MDP the dependence $A_G(R_b)$ can be represented by line 2, having $c_A \approx 0.3$. This indicates that AP and the active turbulent segments from QHP and MDP are stamped by the mixing Reynolds numbers approximately equal to 20, which is ten times higher than for SDP.

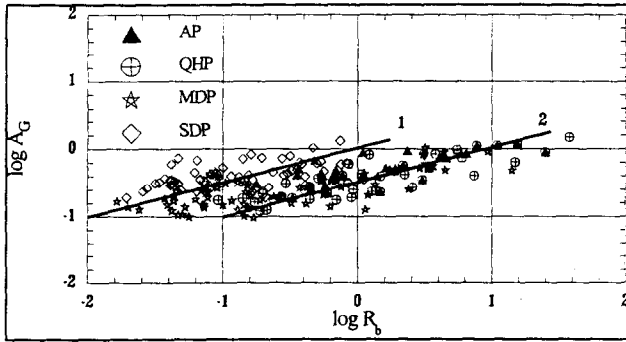


Fig. 3. Hydrodynamic phase diagram for different patches. Line 1 shows (2) for $c_A = 1$, line 2 - $c_A = 0.3$.

At this juncture, it should be noted that the disagreement between (2) and the present data may well be due to the absence of conditions necessary to satisfy the underlying assumptions for (2). The presence of even small shear in the regions under consideration makes the assumption of monotonic decay of ε and instantaneous generation of a turbulent patch specified by ε_0 invalid. Further, the patches do not grow instantly and hence some of the observations might have been taken during the growth phase of the patches; if $\varepsilon < \varepsilon_0$ for the growth phase, then $A_G < 1$ although the patches are not in a decaying state.

4.2. Mixing efficiency. Mixing efficiency γ is related to the activity parameter (2) as $\gamma = 1/13A_G^2$. It is another commonly used measure defining the ratio of buoyancy flux to the kinetic energy dissipation during a mixing event. It shows the capability increasing the potential energy of a stratified layer at the expense of kinetic energy owing to vertical mixing. Thus, it can be used to distinguish the phases of mixing inside a patch and characterize the evolution of mixing state for a whole patch.

The wide variability of individual γ samples in the patches under consideration, which spans one and a half decades of magnitude, suggests an analysis of the probability distribution functions to describe the stages of mixing within the different patches. The histograms $f(\gamma)$ and the cumulative functions $F(\gamma)$ in Fig. 4 show a substantial differences in the distribution of mixing efficiency for weakly (AP and QHP) and strongly (SDP and MDP) stratified patches. Note that, for AP and QHP, the discrepancy between respective distributions of γ were statistically insignificant. Thus we show united functions $f(\gamma)$ and $F(\gamma)$ for these two patches calculated using 32 AP samples and 47 QHP samples (Fig. 4a). It means, we examine ATP, where $G \equiv \varepsilon / \nu N^2 > 15$, which entirely incorporates AP and QHP. The γ -distributions for SDP and MDP contain 98 and 68 samples respectively. The histograms were obtained using non-equal bins ($\Delta\gamma = 1$, if $0 < \gamma < 10$; $\Delta\gamma = 5$, if $10 < \gamma < 20$; $\Delta\gamma = 10$, if $\gamma > 20$). Moreover, the detailed distributions of γ within the bin $0 < \gamma < 1$ are shown by dark narrow bars in all three panels ($\Delta\gamma = 0.2$ at this case) to highlight the low γ related to the turbulent mixing.

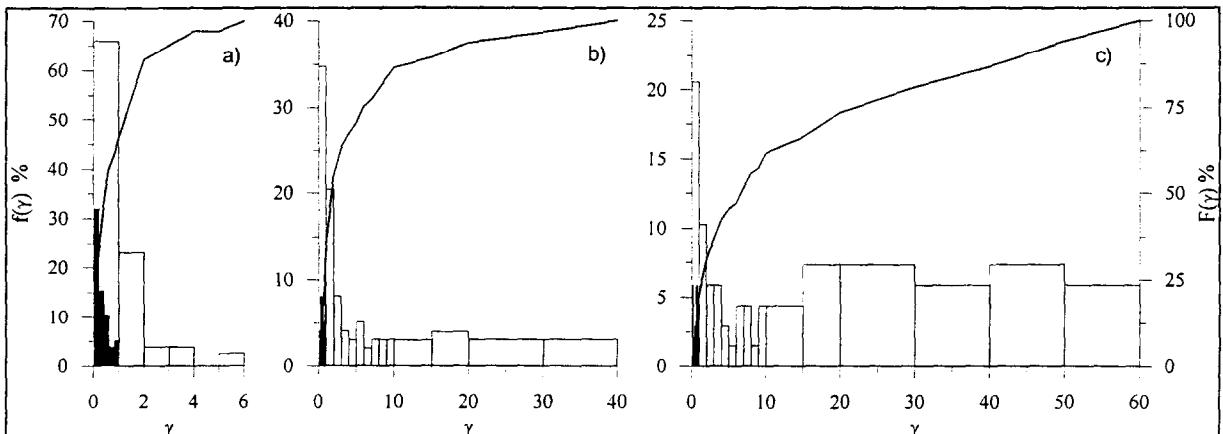


Fig. 4. Histograms $f(\gamma)$ and distribution functions $F(\gamma)$ of the mixing efficiency γ in ATP (a), SDP (b) and MDP (c).

As noted, turbulent mixing in highly stratified layers was low, in spite of relatively high values of the dissipation rate ε . The probability plots for these patches exhibit long tails of the pdfs' with approximately equal probabilities at the high γ (particularly for $\gamma > 10$). The observations can be attributed to the existence of two different mixing regimes in highly-stratified patches. In SDP, for example, about 40% of all γ samples corresponding to the initial period of our measurements gave $\langle \gamma \rangle = 2.5$. The samples taken after 17:35 showed very low turbulence activity in SDP and extremely high values of $\langle \gamma \rangle = 9.3$.

It can be seen that more than 30 % of all γ samples from ATP did not exceed 0.2, which is the typical value used for calculation the buoyancy diffusivity K_N . The lowest γ were confined to the central part of the patches, indicating high turbulence activity in these regions. As mentioned above, the mixedness parameter m was also relatively high in the same regions of AP and QHP. For ATP, the median of the distribution, $m_d(\gamma)$, was close to 0.4. The total percentage of $\gamma < 1$ in ATP was over 65% compared to $F_{SDP}(\gamma < 1) = 34\%$ and $F_{MDP}(\gamma < 1) = 21\%$. The SDP and MDP were so weakly mixed that less than 4% of γ samples were smaller than 0.2 in the first case and 6% in the second. The modes of distributions in stratified patches are shifted from the smallest γ (which is the feature for ATP) toward $\gamma \approx 1$. Lacking of a well-grounded theoretical model of probability distribution for the mixing efficiency, a bootstrap method was used to calculate means of γ and their 90% confidence limits. The data were resampled 1000 times for each particular patch. This gave the following bootstrap estimates of the mean: AP: $0.6 < \tilde{\gamma}_{AP} = 0.8 < 1.0$, QHP: $0.8 < \tilde{\gamma}_{QHP} = 1.2 < 1.6$, SDP: $4.5 < \tilde{\gamma}_{SDP} = 6.3 < 8.5$, MDP: $11.1 < \tilde{\gamma}_{MDP} = 14.3 < 17.8$.

5. Summary

Microstructure patches of 1-3 meters in thickness occupied the central part of the water column at the shallow, 25 meters depth, shelf of the Black Sea. It was shown that these patches could have been generated by the local shear at the edges of low saline intrusions. This shear can be caused by small-scale internal waves, and this notion agrees well with the laboratory findings reported in [5]. At the time of generation, the typical turbulent buoyancy diffusivity K_N was about 5×10^{-5} m²/s. Variations of the ambient buoyancy frequency N_0 influenced the evolution of turbulence inside the patches. The characteristic time scale for the exponential decay of K_N in a quasi-homogeneous patch was close to $1/10N_0$. Mixing activity A_G in the decaying patches may follow the Gibson's law (2), but with a lower c_A , which is correspondent to the mixing Reynolds number of $R_m \approx 20$. Mixing efficiency γ was less than 1 only in so-called active patches corresponding to the initial stage of turbulence evolution.

Acknowledgments. The field measurements were carried out as a part of an international coastal experiment Varna-89, which was funded by the Bulgarian and Russian Academies of Sciences. We are indebted to Valeri Nabatov and Anatoli Erofeev of the P. P. Shirshov Institute of Oceanology, Russian Academy of Sciences, who headed observational and data processing teams during the experiment. The analysis was performed under the grant N00014-97-1-0140 of the US Office of Naval Research.

References

- [1] I.D. Lozovatsky and R.V. Ozmidov (editors), 1992, The variability of the hydrophysical fields in the coastal zone during autumn cooling, Data of Oceanographic Study, 5, Geophys. Commit. Publisher, Moscow, 212p, (in Russian).
- [2] V.T. Paka, V.N. Nabatov, I.D. Lozovatsky, and T.M. Dillon, 1998, Oceanic microstructure measurements by "Baklan" and "Grif", J. Atmospheric and Oceanic Technology, (in press).
- [3] I.D. Lozovatsky, T.M. Dillon, A.Yu. Erofeev, and V.N. Nabatov, 1998, Variations of thermohaline structure and turbulent mixing on the Black Sea shelf at the beginning of autumn cooling, J. Marine Systems, (in press).
- [4] C.H. Gibson, 1986, Internal waves, fossil turbulence, and composite ocean microstructure spectra, J. Fluid Mech., 168, 89-117.
- [5] I.P. D. De Silva and H J S. Fernando, 1992, Some aspects of mixing in a stratified turbulent patch, J. Fluid Mech., 240, 601-625.

FRONTAL STRUCTURES AND EDDY FORMATION IN THE GREATER AGULHAS CURRENT SYSTEM

J. R. E. Lutjeharms

Department of Oceanography, University of Cape Town, 7700 Rondebosch, South Africa
johann@physci.uct.ac.za

Abstract

A brief summary is presented of what has been learnt about the greater Agulhas Current system and its dynamics during the last ten years or so. In conclusion I attempt to identify the key scientific problems that currently present themselves and that need to be addressed if we want to progress in our understanding of the way in which this unusual system works.

Introduction

During the past decade there has been remarkable international interest in the greater Agulhas Current system. The reasons for this intense interest are probably threefold. First, this was arguably the least studied western boundary current in the 1980s. Second, the horizontal thermal gradients as well as the sea height anomalies are so extreme in this system that it lends itself particularly well to investigations by thermal infrared and by altimetric observations, thus making it an attractive region for specialists using these observational techniques. Thirdly, it has become apparent that the Agulhas Current may be a key element in the global thermohaline circulation, thus lending additional importance to a better understanding of the dynamics of this current. This international, as well as local, interest has led to a period of concentrated research effort on the greater Agulhas Current system from which has come remarkable increases in our knowledge and understanding of the system. It has also led to the identification of a substantial number of new questions on the workings of the system that now need to be addressed.

The greater Agulhas system

The greater Agulhas system may be considered to consist, first, of an inflow to the Agulhas Current proper from the north and from the east; then the Agulhas Current itself, extending to its south-western termination in the South-east Atlantic Ocean; the return flow eastwards and, last, a recirculation in the South-west Indian Ocean by which the cycle is completed. An additional, and very important, component of the system consists of a uni-directional leakage from the Agulhas termination into the South Atlantic. The system is shown diagrammatically in figure 1. On a global scale the mesoscale turbulence in this system is intense [e.g. 2]. This is the result of the creation of a range of vortices and of extensive frontal meandering in the various components of the system. The first of these components is the inflow.

The dominant inflow to the Agulhas Current is from recirculation in a wind-driven subtropical gyre that is largely restricted to the western part of the South Indian Ocean [3]. Inflow is therefore mostly from the regions south and east of Madagascar (viz. figure 1), the latter not necessarily by way of the East Madagascar Current [4]. The contribution through the Mozambique Current is small. Both these tributaries seem to be highly turbulent [e.g. 5] exhibiting high mesoscale variability. The fully constituted Agulhas Current at about 32° S extends to a depth of at least 2 000 m [6] and has a volume flux of $65 \times 10^6 \text{ m}^3 \text{ s}^{-1}$ to a depth of 1 000 m, making it the largest western boundary current in the

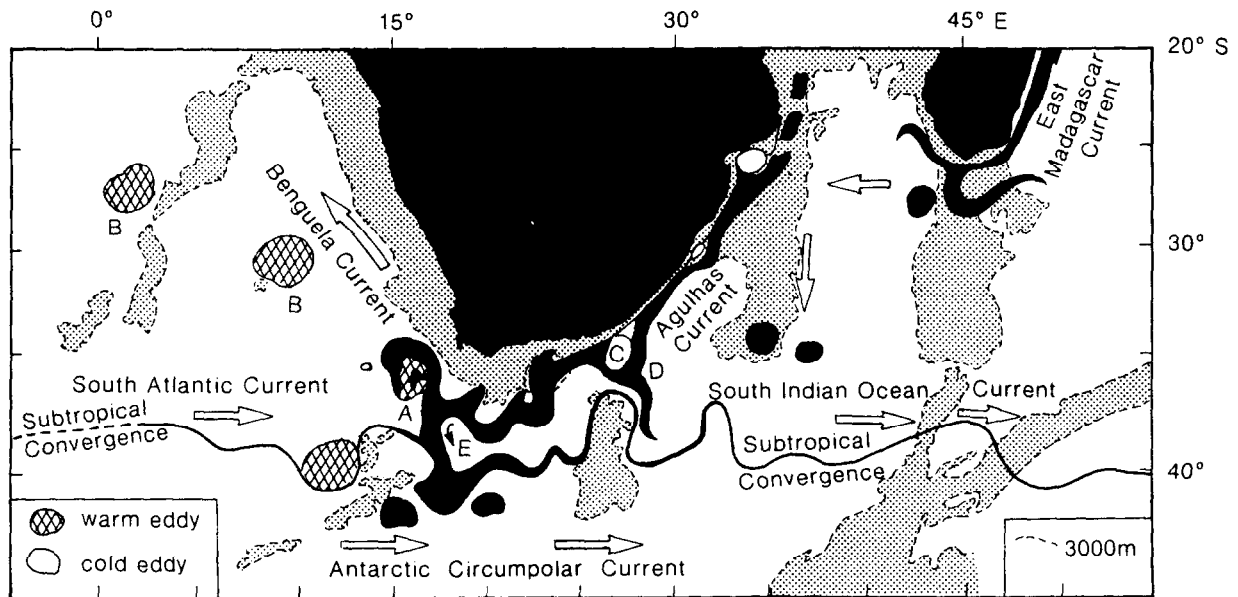


Figure 1. Elements of the circulation in the greater Agulhas Current system, including **A** a recently shed Agulhas ring, **Bs** Agulhas rings moving off into the South Atlantic, **C** a Natal Pulse, **D** an upstream retroflexion and **E** a normal retroflexion. Open arrows show the general motion of the subtropical gyres and the Antarctic Circumpolar Current south of the Subtropical Convergence [after 1].

southern hemisphere. By contrast to most western boundary currents, the trajectory of the northern Agulhas is remarkably stable.

Gründlingh [7] has shown that the meandering of this northern part of the Agulhas Current is in fact less than 15 km to either side. This unusual stability is interrupted 4 to 9 times a year by a soliton meander, the Natal Pulse, that has its origin in a region along the South African east coast just north of 30° S [8]. Natal Pulses travel downstream (viz. figure 1) at a steady rate of about 20 km/day. In their south-westward progression they grow in amplitude and may in extreme cases even lead to an early retroflexion at the Agulhas Plateau (viz. figure 1), a relatively shallow region south of the African continent [9], thus briefly depriving the interbasin leakage south-west of Africa of a supply of water. Under normal circumstances the current behaviour is more conventional.

Once the waters in the Agulhas Current reach the widening shelf and the weaker continental slope south of the continent, the current starts to exhibit the meanders, shear edge eddies and plumes normally associated with western boundary currents [10]. None of these eddies generated at the landward border have been observed to detach themselves from the current, although occasionally eddies at the seaward side have been observed to do this [11]. On moving past the southern tip of the African continental shelf, the Agulhas Current retroflects sharply [12,13, figure 1], with all its water flowing eastward as the Agulhas Return Current. This process of retroflexion consists of a continuous westward progradation of the retroflexion loop until a ring is occluded [14], causing the subsequent retroflexion to lie farther to the east, after which the whole sequence of events is repeated.

These rings are the largest to have been observed in the ocean to date [15] and drift off into the South Atlantic (viz. figure 1) carrying their extra burden of heat and salt with them. Their trajectories take them in a north-westerly direction [16], across the Walvis ridge and towards the Brazilian coast. They are estimated to have lifetimes of 3 to 4 years, but by that age they will have lost most of their

angular momentum, excess heat and characteristic salt content. Van Ballegooyen *et al.* [17] have estimated a net heat flux of 0.05 PW/year and a salt flux of 78×10^{12} kg/year by way of these Agulhas rings. This is probably an overestimate since it does not take into account the substantial changes that take place in the rings at the retroflection. It has been shown [e.g. 18,19] that in this region the warm surface waters of the Agulhas Current and its offshoots experience enormous losses of heat and moisture to the atmosphere. As a result there also is significant salinity enhancement in the surface layers of Agulhas rings here. Depending on how long the rings remain in this region and on the time of year, there may thus be substantial changes to the heat and salt content of the rings as well as their internal structure [20]. Interbasin leakage also occurs due to Agulhas filaments [21] but it is estimated that these features contribute only 6% of the total net salt flux from the Indian to the Atlantic Ocean. As in the Agulhas retroflection region, the eastward continuation of the Agulhas Current is also beset by high mesoscale variability.

The Agulhas Return Current flows along the Subtropical Convergence (viz. figure 1), creating a strong meridional shear. This leads to substantial meandering and eddy shedding to both sides of the front [e.g. 22]. The Agulhas Return Current leaks water equatorward into the South West Indian Ocean subgyre along its full path, up to 60° E [23]. The tongue of high mesoscale variability associated with this current and evident particularly in satellite altimetry, also ends about here. Based on what has been described above, it seems evident that mesoscale eddies play an important part in the dynamics of most parts of the Agulhas Current system.

Dynamics of the system

Many aspects of the dynamics of the Agulhas Current remain poorly understood. The remarkable westward intensification of the subtropical gyre, when related to comparable gyres, has not been adequately explained. Modelling studies with and without bottom topography have to date not indicated that the meridional ridges in the South Indian Ocean play a role in the gyre structure. Perhaps it is even more important to understand the unusual stability of the northern Agulhas Current.

De Ruijter *et al.* [24] have demonstrated that this stability is a function of the sharp gradient in the continental slope along the east coast of South Africa. This gradient severely limits any baroclinic or barotropic instability in the current path. However, the solitary meanders, the Natal Pulses, still need to be explained in terms of this concept. They seem to originate only from one region along the coast, an offset in the coastline called the Natal Bight. De Ruijter *et al.* [24] have shown that the slope gradient here is so much lower that it allows the current jet to reach values close to the baroclinic instability threshold where the path can become unstable. To reach such values the current needs some perturbation. Deep-sea eddies coming from the east [25, viz. figure 1] are known to get adsorbed onto the seaward front of the current and have therefore been proposed as the triggering factors, but only if they reach the current in the Natal Bight. The resulting Natal Pulses evidently have a marked influence on coastal circulation. The remaining question is what their impact on the highly unstable retroflection configuration might be.

Van Leeuwen *et al.* [26] have shown that, with very few exceptions, every single Natal Pulse leads to a ring shedding event at the Agulhas Current retroflection far downstream. This makes these meanders sufficient but not necessary conditions for ring spawning. In the absence of a Natal Pulse for a sufficiently long period, it would seem that the current loop would reach a degree of deformation that would induce a loop occlusion in the absence of a major perturbation such as a Natal Pulse. To date the record of the occurrence of Natal Pulses shows no evidence of any seasonality. However, there may be other seasonal variations in the system.

Ffield *et al.* [27] have, for instance, suggested a seasonal pattern in the flow of the system as a whole related to wind stress and observations of the volume flux [28] have hinted at similar variations, but these tantalising results have to date lacked statistical rigour due to the shortness of the records used. Other analyses [e.g. 29] have not shown any seasonal variations in the speed of the Agulhas Current. The influence of varying wind stress over the South Indian Ocean and its influence on the Agulhas Current is starting to receive increased attention [e.g. 30,31] but much more is required. Not only this, but a number of other key questions need to be studied further.

Key scientific problems

One of the major problems that remains to be solved is a solid quantification of the various tributaries to the Agulhas Current. This could conceivably be achieved by utilising the collection of high-quality hydrographic data collected over the past few years in the region, but there remain a number of glaring gaps in the geographic coverage of hydrographic stations such as in the Mozambique Channel and the region south of Madagascar. This can only be resolved by extensive and well-planned hydrographic cruises in these regions. This is particularly important because the information derived from satellite altimetry [e.g. 2] show high levels of mesoscale variability in the Mozambique Channel while some numerical models focused on this region [32] as well as some other Global Circulation Models [e.g. 33] exhibit no such enhanced levels of variability in the region. A much better understanding of the currents in the Mozambique Channel as well as south-east of Madagascar is furthermore required if the origin of the deep-sea eddies described by Gründlingh [25] are to be identified. This is particularly important since these eddies seem to play such a critical triggering role in the overall dynamics of the system.

Much has been learnt about the surface flow and behaviour of the greater Agulhas Current system, but in certain cases the vertical extent of some of this behaviour is not known. Previously this was true of ring shedding at the Agulhas retroflection also. This process had been evident in thermal infrared imagery [34] but was only verified as involving the greater vertical part of the current once a properly dedicated cruise was able to intercept a ring spawning event [14]. A remaining case in which similar studies need to be carried out is the early retroflection brought about by large Natal Pulses [9]. To date we have no information about the depth to which this process extends and how much Agulhas water is siphoned off in this way. Deeper water movement in the Agulhas Current system, particularly at intermediate depths, is currently the subject of a multi-national research endeavour using Rafos floats [35]. The results are being awaited with keen anticipation, but they may not solve all the problems of deeper movement that have been identified.

Of even greater importance is a better understanding of how the Agulhas rings mix out and distribute their excess heat and salt over the South Atlantic Ocean. This is required for a better understanding of the South Atlantic heat and salt budget and also for an estimation of how these rings affect South African climate and, in particular, rainfall [36; 37]. A recent modeling study [38] has demonstrated how a significant anomaly in the sea surface temperatures at the Agulhas retroflection may noticeably affect the atmospheric tropical-temperate trough that is the major system bringing precipitation to the summer rainfall regions of southern Africa.

Last, but not least, the effect that the many eddies, both warm and cold, that are spun off the Subtropical Convergence south of Africa [e.g. 39, viz. figure 1] have on the configuration of that front needs to be investigated. Evidence from biogeography suggests that these eddies return to the front and in effect continuously strengthen it. This has not yet been shown from the physics of the system and should be an important study topic.

Notwithstanding the many important parts of the dynamics of the greater Agulhas Current system about which our ignorance remains, the progress in our understanding over the past decade, and described above, has been gratifying and our increased understanding has made it possible for more relevant and pertinent research questions to be asked.

References

- [1] Lutjeharms, J. R. E., 1996, The exchange of water between the South Indian and the South Atlantic Oceans, in *The South Atlantic; present and past circulations*, edited by G. Wefer, W. H. Berger, G. Siedler and D. J. Webb, pp. 125-162, Springer-Verlag, Berlin.
- [2] Cheney, R. A., J. G. Marsh and B. D. Beckley, 1983, Global mesoscale variability from colinear tracks of SEASAT altimeter data, *J. geophys. Res.*, **88**, 4343-4354.
- [3] Stramma, L. and J. R. E. Lutjeharms, 1997, The flow field of the subtropical gyre in the South Indian Ocean, *J. geophys. Res.*, **102**, 5513-5530.
- [4] Lutjeharms, J. R. E., N. D. Bang and C. P. Duncan, 1981, Characteristics of the currents east and south of Madagascar, *Deep-Sea Res.*, **28**, 879-899.
- [5] Saetre, R., and A. Jorge da Silva, 1984, The circulation of the Mozambique Channel, *Deep-Sea Res.*, **31**, 485-508.

- [6] Beal, L. M., and H. L. Bryden, 1998, The velocity and vorticity structure of the Agulhas Current at 32° S., *J. geophys. Res.*, submitted.
- [7] Gründlingh, M. L., 1983, On the course of the Agulhas Current, *S. Afr. geogr. J.*, **65**, 49-57.
- [8] Lutjeharms, J. R. E. and H. R. Roberts, 1988, The Natal Pulse; an extreme transient on the Agulhas Current, *J. geophys. Res.*, **93**, 631-635.
- [9] Lutjeharms, J. R. E. and R. C. van Ballegooyen, 1988a, Anomalous upstream retroflexion in the Agulhas current, *Science*, **240**, 1770-1772.
- [10] Lutjeharms, J. R. E., R. Catzel, H. R. Valentine, 1989, Eddies and other border phenomena of the Agulhas Current, *Cont. Shelf Res.*, **9**, 597-616.
- [11] Lutjeharms, J. R. E., S. J. Weeks, R. C. van Ballegooyen and F. A. Shillington, 1992, Shedding of an eddy from the seaward front of the Agulhas Current, *S. Afr. J. Sci.*, **88**, 430-433.
- [12] Gordon, A. L., J. R. E. Lutjeharms and M. L. Gründlingh, 1987, Stratification and circulation at the Agulhas Retroflexion, *Deep-Sea Res.*, **34**, 565-599.
- [13] Lutjeharms, J. R. E. and R. C. van Ballegooyen, 1988b, The Agulhas Current retroflexion, *J. phys. Oceanogr.*, **18**, 1570-1583.
- [14] Lutjeharms, J. R. E., and A. L. Gordon, 1987, Shedding of an Agulhas Ring observed at sea, *Nature*, **325**, 138-140.
- [15] Olson, D. B. and R. H. Evans, 1986, Rings of the Agulhas, *Deep-Sea Res.*, **33**, 27-42.
- [16] Byrne, D. A., A. L. Gordon and W. F. Haxby, 1995, Agulhas eddies: a synoptic view using Geosat ERM data, *J. phys. Oceanogr.*, **25**, 902-907.
- [17] Van Ballegooyen, R. C., M. L. Gründlingh and J. R. E. Lutjeharms, 1994, Eddy fluxes of heat and salt from the southwest Indian Ocean into the southeast Atlantic Ocean: a case study, *J. geophys. Res.*, **99**, 14053-14070.
- [18] Walker, N. D. and R. D. Mey, 1988, Ocean/atmosphere heat fluxes within the Agulhas Retroflexion region, *J. geophys. Res.*, **93**, 15473-15483.
- [19] Lee-Thorp, A. M., M. Rouault and J. R. E. Lutjeharms, 1997, Moisture uptake in the boundary layer above the Agulhas Current: a case study, *J. geophys. Res.*, submitted.
- [20] Arhan, M., H. Mercier and J. R. E. Lutjeharms, 1998, The disparate evolution of three Agulhas rings in the South Atlantic Ocean, *J. geophys. Res.*, submitted.
- [21] Lutjeharms, J. R. E. and J. Cooper, 1996, Interbasin leakage through Agulhas Current filaments, *Deep-Sea Res.*, **43**, 213-238.
- [22] Lutjeharms, J. R. E. and H. R. Valentine, 1988, Eddies at the Sub-Tropical Convergence south of Africa, *J. phys. Oceanogr.*, **18**, 761-774.
- [23] Lutjeharms, J. R. E. and I. J. Anson, 1997, The Agulhas Return Current, *J. phys. Oceanogr.*, submitted.
- [24] De Ruijter, W. P. M., P. J. van Leeuwen and J. R. E. Lutjeharms, 1997, A triggering mechanism for solitary meanders in the Agulhas Current, *J. phys. Oceanogr.*, submitted.
- [25] Gründlingh, M. L., 1988, Review of cyclonic eddies in the Mozambique Ridge Current, *S. Afr. J. mar. Sci.*, **6**, 193-206.
- [26] Van Leeuwen, P. J., W. P. M. de Ruijter and J. R. E. Lutjeharms, 1997, Natal Pulses and the formation of Agulhas rings, *J. geophys. Res.*, submitted.
- [27] Field, A., J. M. Toole and W. D. Wilson, 1997, Seasonal circulation in the South Indian Ocean, *Geophys. Res. Lett.*, submitted.
- [28] Gründlingh, M. L., 1980, On the volume transport of the Agulhas Current, *Deep-Sea Res.*, **27**, 557-563.
- [29] Pearce, A. F. and M. L. Gründlingh, 1982, Is there a seasonal variation in the Agulhas Current?, *J. mar. Res.*, **40**, 177-184.
- [30] Reason, C. J. C., R. J. Allan and J. A. Lindesay, 1996, Dynamical response of the oceanic circulation and temperature to interdecadal variability in the surface winds over the Indian Ocean, *J. Climate*, **9**, 97-114.
- [31] Reason, C. J. C. and J. R. E. Lutjeharms, 1998, Variability of the South Indian Ocean and implications for southern African rainfall, *S. Afr. J. Sci.*, **94**, 115-123.
- [32] Luther, M. E. and J. J. O'Brien, 1985, A model of the seasonal circulation in the Arabian Sea forced by observed winds, *Progr. Oceanogr.*, **14**, 353-385.
- [33] Semtner, A. J. and R. M. Chervin, 1988, A simulation of the global ocean circulation with resolved eddies, *J. geophys. Res.*, **93**, 15502-15522.

- [34] Lutjeharms, J. R. E., 1981, Features of the southern Agulhas Current circulation from satellite remote sensing, *S. Afr. J. Sci.* **77**, 231-236.
- [35] Boebel, O., C. Duncombe Rae, S. Garzoli, J. Lutjeharms, P. Richardson, T. Rossby, C. Schmid and W. Zenk., 1998, Float experiment studies interocean exchanges at the tip of Africa, *Eos, Trans. Am. geophys. Un.*, **79**, 1, 7-8.
- [36] Walker, N. D., 1990, Links between South African summer rainfall and temperature variability of the Agulhas and Benguela Current systems, *J. geophys Res.*, **95**, 3297-3319.
- [37] Mason, S. J., 1995, Sea-surface temperature-South African rainfall associations, 1910-1989, *Intn J. Climatol.*, **15**, 119-135.
- [38] Crimp, S. J., J. R. E. Lutjeharms and S. J. Mason, 1998, Sensitivity of a tropical-temperate trough to sea-surface temperature anomalies in the Agulhas reflection region, *Water SA*, **24**, 93-100.
- [39] Lutjeharms, J. R. E., 1988, Meridional heat transport across the Subtropical Convergence by an eddy, *Nature*, **331**, 251-254.

TWO-LAYER EXCHANGE FLOWS THROUGH LONG STRAITS WITH SILL

V. S. Maderich ¹

Institute of Hydromechanics NASU, Zheliabov st.,8/4 Kiev 252057, The Ukraine

Abstract. Water exchange through the narrow strait with two-layer flow structure and net barotropic transport was investigated both experimentally and theoretically. The experimental facility consisted of the tank that was divided on two basins, connected by a shallow and narrow rectangular channel. One basin was heated at the bottom. Another basin was cooled at the top. The velocity and temperature measurements were made using the hydrogen-bubble technique and the temperature probes, respectively. The measured depths of interface and volumetric flow rate in the laboratory analogue agree reasonably well with a laminar hydraulic model based on the principle of maximal exchange. The influence of the sills, that were placed inside of the long strait, on the exchange was studied. The results showed strong influence of the position of sill on the exchange in the long straits.

Introduction

The internal hydraulics of a steady two-layer exchange flow through the channel was extensively studied in the last decades [1]. A complexity of the real straits geometry, uncontrollable time-dependent effects caused by tides and wind surges, the turbulent mixing between layers make verification of the theoretical predictions difficult [2]. Thus the laboratory modelling with close control of experimental conditions is important but these studies still few [3].

Two-layer exchange in the long frictional straits of constant depth and width was studied in the laboratory experiments [4-6]. The present paper concentrates on the effects of position and shape of the sills on the water-exchange through the long strait. The simple model of the laminar laboratory strait is considered in Sect.2. The experimental arrangement is described in Sect.3. The results of the laboratory experiments and computations are given in Sect.4.

Theory

Let us consider a simple model for the two-layer stationary water exchange through the laboratory analogue of the sea strait. Two deep basins are connected by the shallow and narrow channel. The coordinate x is taken along the strait, y is the transverse coordinate. The vertical axis, z , is directed upward from the equilibrium level of the free surface. The basins are maintained at the different density ρ_1 and ρ_2 respectively ($\rho_1 \leq \rho_2$). The net barotropic flow Q is directed from the basin with lighter water ($Q \geq 0$). The strait is rectangular with length L , depth $H(x)$ and constant width A . The ratio $A/H \ll 1$ and only laminar side friction can be important. The averaged along strait depths of upper layer and bottom layer are D_1 , D_2 , respectively, and

$$D = D_1 + D_2. \quad (1)$$

¹Present address: Institute of Mathematical Machine and System Problems NASU, Glushkova pr. 42, Kiev 252187, The Ukraine. E-mail vlad@maderich.pp.kiev.ua

The instantaneous thicknesses of the upper and bottom layers are

$$H_1 = D_1 - \eta + \zeta, \quad H_2 = D_2 + \eta - H_s \quad (2)$$

and $H = H_1 + H_2$. Here ζ is the free surface elevation, η is the interface deviation and H_s is the bottom level deviation from the averaged value D . Invoking the hydrostatic and Boussinesq approximations, the governing equations of the two-layer model of the strait can then be written as

$$\frac{\partial}{\partial x} u_1 H_1 + \frac{\partial}{\partial y} v_1 H_1 = 0, \quad (3)$$

$$\frac{\partial}{\partial x} u_2 H_2 + \frac{\partial}{\partial y} v_2 H_2 = 0, \quad (4)$$

$$\frac{\partial}{\partial x} u_1^2 H_1 + \frac{\partial}{\partial y} u_1 v_1 H_1 = -H_1 \frac{\partial}{\partial x} g\zeta + \nu H_1 \frac{\partial^2 u_1}{\partial y^2}, \quad (5)$$

$$\frac{\partial}{\partial x} u_2^2 H_2 + \frac{\partial}{\partial y} u_2 v_2 H_2 = -H_2 \frac{\partial}{\partial x} (g\zeta + g'\eta) + \nu H_2 \frac{\partial^2 u_2}{\partial y^2}. \quad (6)$$

Here u_1, u_2 and v_1, v_2 are the longitudinal and transversal velocity components in the upper and bottom layer, respectively, ν is the kinematic viscosity. The nonslip conditions are used on side walls.

These equations can be reduced to the system of the one-dimensional equations after replacement of left sides of eqns. (5)-(6) on averaged across channel values. Integrating eqns.(3) - (6) across the strait leads to the momentum equations

$$\frac{d}{dx} \frac{1}{AH_1} Q_1^2 + AH_1 \frac{dg\zeta}{dx} = -\frac{12\nu}{A^2} Q_1, \quad (7)$$

$$\frac{d}{dx} \frac{1}{AH_2} Q_2^2 + AH_2 \frac{d}{dx} (g\zeta + g'\eta) = -\frac{12\nu}{A^2} Q_2, \quad (8)$$

and balance mass equation

$$Q_1 + Q_2 = Q = Q_f. \quad (9)$$

The volumetric flow rates in the upper (Q_1) and bottom (Q_2) layers relate to the velocity u_1, u_2 by $Q_1 = AH_1 u_1$ and $Q_2 = AH_2 u_2$, Q_f is the volumetric inflow rate in the basin with lighter water.

It is a common practice in the internal hydraulics to use models based on a so called "hydraulic control" principle, which requires that the internal composite Froude number $G = 1$ at some critical sections of strait. Maximal exchange occurs when the two locations of control are linked by a region of subcritical flow [7-8]. In the general case the locations of control x_{c1} and x_{c2} depend on the geometry, barotropic flow and friction. At a small density difference ($(\rho_2 - \rho_1)/\rho_2 \ll 1$) the control condition is

$$G^2 = F_1^2 + F_2^2 = 1. \quad (10)$$

Here

$$F_1^2 = \frac{Q_1^2}{g'H_1^3 A^2}, \quad F_2^2 = \frac{Q_2^2}{g'H_2^3 A^2}.$$

The system of equations (7)-(8) can be reduced to a single equation for the height of bottom layer with assumption that $H_1 \gg \zeta$, i.e. $H_1 \approx D - H_s - H_2$. This equation in the nondimensional form is

$$(1 - G^2) \frac{d}{d\tilde{x}} (\tilde{H}_2 + \tilde{H}_s) = -Fr_2^2 \frac{d\tilde{H}_s}{d\tilde{x}} + \gamma \frac{\tilde{H}_2 q - \tilde{Q}_2}{(1 - \tilde{H}_s - \tilde{H}_2)\tilde{H}_2}, \quad (11)$$

Here $\tilde{x} = x/L$, $\tilde{H}_1 = H_1/D$, $\tilde{H}_2 = H_2/D$, $\tilde{H}_s = H_s/D$, $\tilde{Q}_1 = Q_1/Q_m$, $\tilde{Q}_2 = Q_2/Q_m$, $q = Q_f/Q_m$, $Q_m = AD\sqrt{g'D}$. The parameter $\gamma = 12\nu L/(A^2\sqrt{g'D})$ describes the influence of the side wall laminar friction. The laboratory straits are short when $\gamma \ll 1$, intermediate when $\gamma \sim 1$ and long when $\gamma \gg 1$. The ratio between barotropic and baroclinic flows $\beta = |(Q_1 + Q_2)/(Q_1 - Q_2)|$ is also important parameter.

The first order equation (11) contains the unknown variable $\tilde{H}_2(\tilde{x})$ and parameter \tilde{Q}_2 . When barotropic flow is moderate ($\beta < 1$) eqn. (11) is completed by the two control conditions (10) at the locations of control \tilde{x}_{c1} and \tilde{x}_{c2} . Below is considered strait with single sill. In the strait without sills and contractions two control sections exist at the ends of strait $\tilde{x}_{c1} = 0, \tilde{x}_{c2} = 1$. When friction is not significant, the controls at $q \geq 0$ are positioned with one at the crest of sill and one at the exit on the side of dense reservoir [8]. In the long strait position of controls depend on the location of sill and barotropic component. If flow over the sill is subcritical or the sill crest coincide with the end of strait then the controls located at both ends. Otherwise one control (\tilde{x}_{c2}) is located at the right end of the strait. The position of the other control (\tilde{x}_{c1}) is evaluated from (11) with $G = 1$. For considered configuration of the strait and $q \geq 0$ the control points shifted to the left end of strait relatively to the non-frictional case. The eqn.(11) together with control conditions was solved numerically combining the Pickard method and the bisection.

In the case of strong barotropic component ($\beta = 1$) the exchange is one-way. The bottom layer is transformed in the arrested salt wedge. With $q = \tilde{Q}_1 > 0, \tilde{Q}_2 = 0$ and $G^2 = F_1^2$ eqn. (11) can be rewritten as

$$(\tilde{H}_1^3 - q) \frac{d\tilde{H}_1}{dx} + \gamma q \tilde{H}_1^2 = 0. \quad (12)$$

Solution of (12) with control condition on the downstream side $F_1^2 = 1$ at $\tilde{x} = 1$ gives us shape of the arrested density wedge

$$(\tilde{H} - \tilde{H}_2)^3 + [2\gamma q(\tilde{x} - 1) - 3q^{4/3}](\tilde{H} - \tilde{H}_2) + 2q^2 = 0. \quad (13)$$

Experimental arrangement

The experiments were conducted in a rectangular Plexiglass tank, 200 cm long, 17 cm wide and 40 cm deep. The tank was divided on two basins. These basins were connected by a shallow and narrow rectangular strait placed along the front wall. A two-layer water exchange was maintained by the heating of the small basin (length 33 cm) using an electric heater placed near the bottom and by the cooling of the large basin using a tap water cooler. The cooling box was situated at the surface of the large basin. The strait and small basin were insulated.

A series of experiments was carried out to study the influence of the sill on the exchange in the long strait. The sill was shaped as

$$H_s = H_{s0} \sin^2\left(\frac{\pi(x - l_s + L_s/2)}{L_s}\right), \quad 0 \leq (x - l_s + L_s/2)/L_s \leq 1 \quad (14)$$

where H_{s0}, L_s, l_s are the height, length and position of the sill crest, respectively. Two sills with the same length ($L_s = 20$ cm) and different height ($H_s = 2$ and 4 cm) were used. The strait parameters are given in Table 1. The barotropic flow was directed from the heated basin to cooled one. The constant flow rate was provided by using of the Marriotte vessel. The outflow from the large basin was through the funnel at the surface. The rate of the outflow from the tank was determined by use of measuring vessel. The temperature distribution in the strait was measured by the vertical profiling in the ten sections with a thermistor probe attached to the traversing platform. The platform can be moved along the strait. The velocity measurements were made by hydrogen-bubble technique in the ten vertical sections along the strait halfway between the side walls. Details of the experimental arrangement are given in [4].

Results

The results of measurements for the short, intermediate and long straits of constant depth in dependence on the magnitude of the net barotropic transport are given in [4] (series 1-3). To analyse the role of position of the obstructions on the exchange in the long strait the four further series of the experiments were carried out with the sills located in the long strait.

In the series 4-6 the influence of the position of the sill was studied. In the Fig. 1-3 are shown the measured and computed thickness of bottom layer H_2 , composite Froude number G^2 and the interface

Table 1: Long laboratory strait with sill

Exp.	H_s cm	l_s cm	g' cm c ⁻²	Q_f cm ³ c ⁻¹	Q_1 cm ³ s ⁻¹	Q_2 cm ³ s ⁻¹	β	γ
401	2.0	52.0	1.50	0.0	1.37	-1.37	0	2.59
402	2.0	52.0	1.27	1.50	2.31	-0.82	0.48	2.81
403	2.0	52.0	1.29	2.91	3.11	-0.20	0.88	2.79
404	2.0	52.0	1.32	0.76	1.72	-0.96	0.28	2.76
501	2.0	30.0	1.17	1.47	1.84	-0.37	0.67	2.93
502	2.0	30.0	1.48	0.0	0.93	-0.93	0	2.60
503	2.0	30.0	1.78	2.18	2.18	0.	1.0	2.38
504	2.0	30.0	1.18	0.78	1.29	-0.51	0.43	2.92
601	2.0	8.7	1.61	0.0	0.95	-0.95	0	2.50
602	2.0	8.7	1.54	1.57	1.92	-0.35	0.69	2.55
603	2.0	8.7	1.13	2.90	2.90	0	1.0	2.98
604	2.0	8.7	1.46	0.70	1.35	-0.65	0.35	2.62
701	4.0	30.0	1.48	0.0	0.97	-0.97	0	2.60
702	4.0	30.0	1.38	1.26	1.41	-0.14	0.81	2.70

deviation η along the strait with the same sill. The sill with $H_s/D = 0.25$ was placed at the right end, centre and left end, respectively. As seen from figures, the sill at the right end has no effect on the interface position and exchange whereas the sill at the left end controls the exchange (exp. 602). Given enough large barotropic flow (exp. 603) the bottom undercurrent is arrested. When the sill is placed in the centre of the strait (Fig. 2) the influence of the sill on the interface is local with zero (exp.502) and moderate (exp.504) values of the net barotropic flow for as long as the local Froude number is subcritical. With enough strong barotropic flow (exp. 503) the bottom undercurrent is so much weak that it cannot be measured. An existence of the bottom flow was established from photo. It is notable that the interface deviation η along the strait is close to the self-similar even with the sill location at left end of the strait. The calculations are in a good agreement with the experiments, including case of the lower layer blocking (Fig. 3).

In Fig. 4-5 the measured and computed thickness of bottom layer, the composite Froude number and the temperature profiles along the long strait with the large sill ($H_s/D = 0.5$) at the centre of the strait are presented. This sill together with the right end of strait controls the exchange under any barotropic flow. The lower flow is supercritical on the left side of the sill. At the foot of the sill the large vortex structures are seen in photo. They are connected with the instability. These effects show up as the thermocline thickness growth at the left side and foot of the sill in Fig. 5. On further moving to the left the flow is back to the subcritical state through the hydraulic jump. The flow reach the critical state at the left end. However, dynamically this point is not essential. It fixes the position of interface between right end point of the flow transition to the supercritical state. Measurements show that temperature in the layers is not changed markedly because of local mixing is not strong enough. Therefore the hydraulic model can be applied to the strait between right end and sill. As seen from Fig. 4 the model predict the interface position quite well.

These results can be compared with flow pattern in the Bosphorus, where flows are controlled by the sill at the north end of the strait and the constriction inside of the strait. The southern sill is also dynamically insignificant [9]. One important distinction in the Bosphorus case from the simple laboratory model is that the sill primary affects on the lower layer, whereas constriction affects both

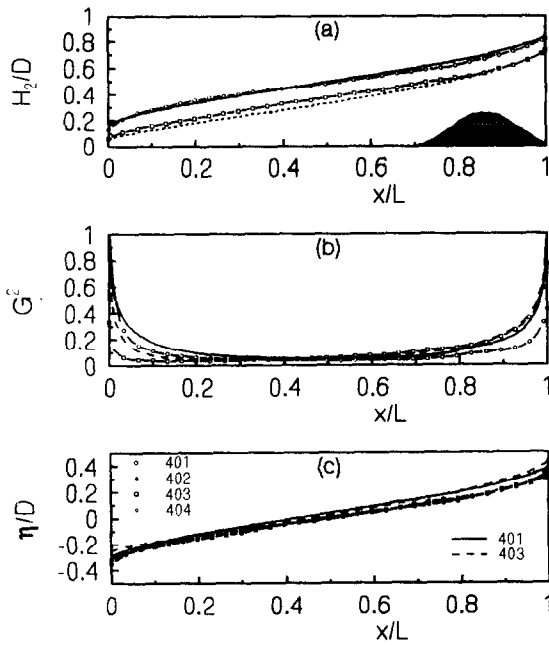


Fig.1. The measured and computed thickness of the bottom layer H_2 (a), composite Froude number G^2 (b) and the interface deviation η along the long strait with sill at the right end.

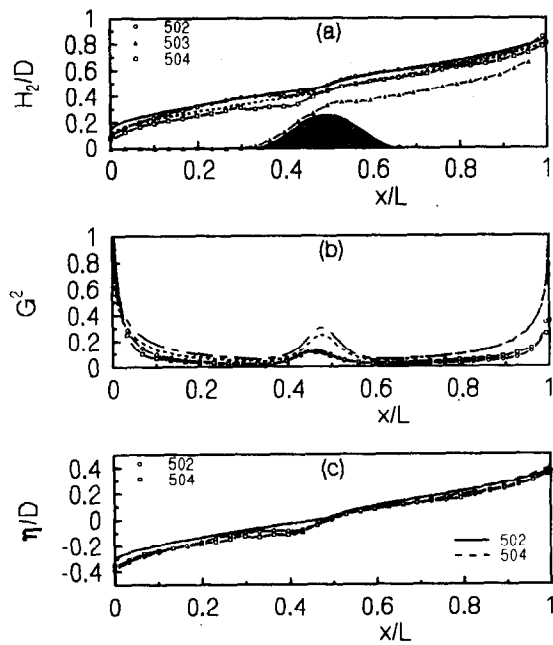


Fig.2. The measured and computed thickness of the bottom layer H_2 (a), composite Froude number G^2 (b) and the interface deviation η along the long strait with sill at the centre of strait.

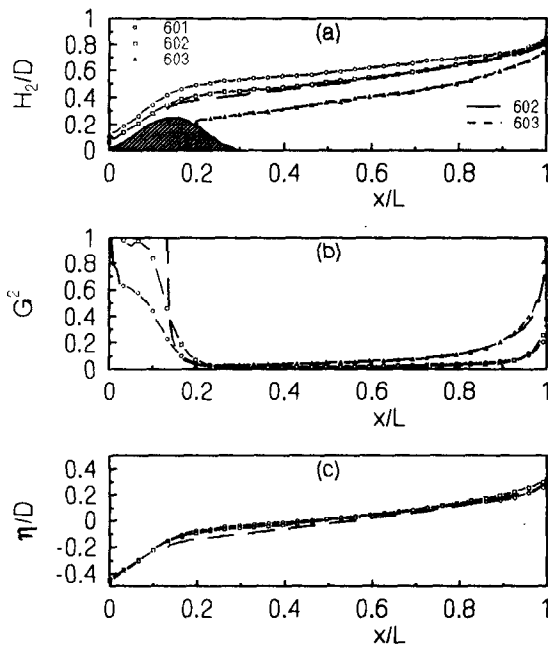


Fig.3. The measured and computed thickness of the bottom layer H_2 (a), composite Froude number G^2 (b) and the interface deviation η along the long strait with sill at the left end.

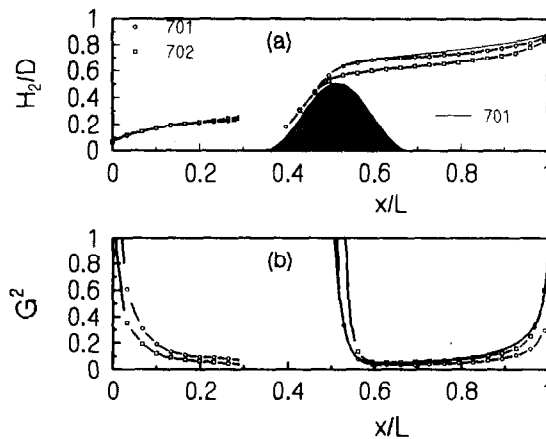


Fig.4. The measured and computed thickness of the bottom layer H_2 (a) and composite Froude number G^2 (b) along the long strait with large sill at the centre of the strait.

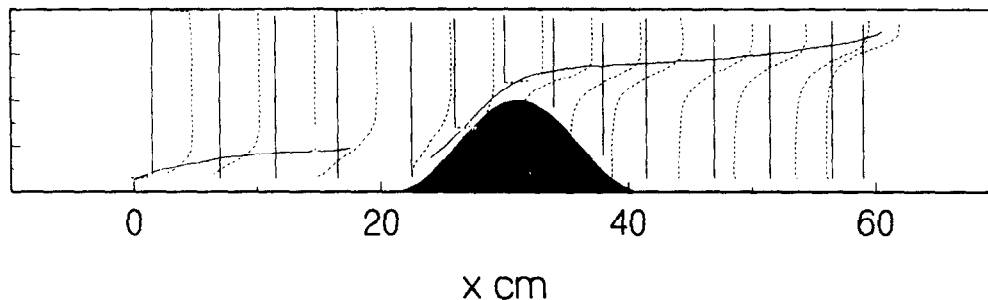


Fig.5.The temperature profiles along the long strait with large sill at the centre of the strait (exp.702).

layers [7-8]. Therefore in the Bosphorus the supercritical flow and mixing zone placed at south side of constriction whereas flow is subcritical between the north sill and the constriction. Other distinction is that the dynamics of the Bosphorus is essentially nonstationary, whereas this laboratory model describes steady response of strait on the forcing. The further experimental study of these effects is necessary to understand a complicated nature of exchange between the Black and Mediterranean seas.

Acknowledgments

The experimental part of work was carried out with assistance of S. Konstantinov, A. Kulik and V. Oleksiuk, their input is gratefully appreciated.

References

- [1] H. L. Bryden and T. H. Kinder, 1991, Recent progress in strait dynamics, *Rev. Geoph. Suppl.*, 617-131.
- [2] M. Bormans and C. Garrett, 1989, The effects of nonrectangular cross section, friction, and barotropic fluctuations on the exchange through the strait of Gibraltar, *J. Phys. Oceanogr.*, 19, 1543-1557.
- [3] T. McClimans, 1990, Role of laboratory experiments and models in the study of sea strait processes, In: L.J. Pratt (Editor) *The physical oceanography*, Kluwer Academic Publ, 373-390.
- [4] D. A. Anati, G. Assaf and R. O. R. Y Thompson, 1977, Laboratory models of sea straits. *J. Fluid Mech.*, 81, 341-352.
- [5] V.S. Maderich, A.I. Kulik and V.V. Oleksiuk, 1994, Laboratory experiments on two-layer exchange through long straits, In: E. Hopfinger, B. Voisin, G. Chavand (Editors) *Preprints of Fourth International Symposium on Stratified Flows*, Vol.3. L.E.G.I-I.M.G, Grenoble.
- [6] V.S. Maderich, S.I. Konstantinov, A.I. Kulik and V.V. Oleksiuk, 1998, Laboratory modelling of the water exchange through the sea straits. *Oceanology*, 38, (in press) .
- [7] L. Armi and D.M. Farmer, 1986, Maximal two-layer exchange through a contraction with barotropic net flow, *J. Fluid Mech.*, 164, 27-52.
- [8] D.M. Farmer and L. Armi, 1986, Maximal two-layer exchange over a sill and through the combination of a sill and contraction with barotropic flow, *J. Fluid Mech.*, 164, 53-76.
- [9] T. Oğuz, E. Özsoy, M.A. Latif, H.I. Sur and Ü. Ünlüata, 1990, Modeling of hydraulically controlled exchange flow in the Bosphorus strait, *J. Phys. Oceanogr.*, 20, 945-965.

MEAN SURFACE CIRCULATION IN THE NORTH WESTERN PACIFIC

N.A. Maximenko¹, G.G.Pantelev^{1,2}, P.P.Niiler³ and T.Yamagata⁴

¹P.P.Shirshov Institute of Oceanology, 36 Nahimovsky Prospect, Moscow 117851, Russia

²Department of Oceanography, Dalhousie University, Halifax, Nova Scotia B3H4J1, Canada

³Scripps Institution of Oceanography, 9500 Gilman Drive, La Jolla, California 92093-0230, USA

⁴Graduate School of Science, University of Tokyo, 7-3-1 Hongo, Bunkyo-ku, Tokyo 113, Japan

E-mails: maximen@sio.rssi.ru, pantel@karluk.physics.mun.ca, niiler@nepac.ucsd.edu,

yamagata@geoph.s.u-tokyo.ac.jp

Abstract. Mean circulation in the North Western Pacific is studied from WOCE/TOGA SVP drifter data both to derive mean velocity field and figure out peculiarities in kinematics of some groups of trajectories. Along with detection of main oceanic currents revealed are the lack of meridional water exchange across the Kuroshio Extension (KE) and signature of westward countercurrent between KE and Subarctic Front (SF) eastward jets. Velocity field is optimized with original variational scheme.

Data

To obtain mean velocities in the upper mixed layer of the North Western Pacific (20-60°N, 120-180°E) we analyzed data of 296 WOCE/TOGA Surface Velocity Programme [1] Lagrangian drifters (106.8 drifter years in total), deployed in 1987-96, with a drogue centered at 15 m depth. The data were quality-controlled and krigged for 6-hour intervals [2] by NOAA Atlantic Oceanographic and Meteorological Laboratory. Complete set of trajectories can be got by combining Figs. 1a and b.

Horizontal water exchange across KE

Behavior of two groups of drifters, separated artificially by their deployment north or south of 35°N (Figs.1 and b, respectively) revealed the lack of drifters having visited both Subtropical and Subarctic Gyres. Mixing zone, defined by the southern edge of area covered with “northern” drifters and the northern limit of the “southern” ones is located in the northern part of KE and remains as narrow as $2\text{-}3^{\circ}\text{N}$ at $140\text{-}180^{\circ}\text{E}$ that contradicts to traditional ideas of large-scale mixing. Indeed, drifters ensemble, composed of buoys, having penetrated into the mixing zone (Fig. 1c) does behave typically for turbulent jet. One may estimate diffusion and fluxes with statistical methods and miss their actual vanishing contribution into the inter-gyre exchange. At the same time, mixing seems to be significant north and south of KE. This effect can be due to isopycnals outcropping at the fronts replacing horizontal motions by isopycnal ones.

Mean velocities, their variability and optimization

Fig.2 displays mean velocities averaged within $1^{\circ}\text{N}\times 1^{\circ}\text{E}$ boxes, for which data are available. When their variability (not shown in figures) agrees well with eddy kinetic energy distribution, obtained in previous studies [3], mean velocity field reveals, along with Kuroshio Current, KE, Tsushima Warm Current, Kamchatka Current and Subtropical Countercurrent, the lack of distinct Oyashio Current and the existence of strong and narrow eastward jet associated with SF.

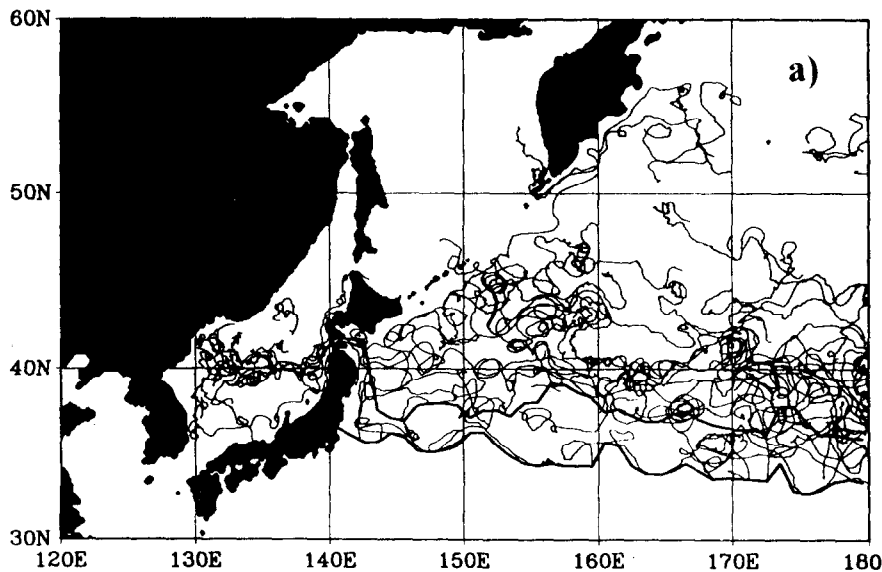


Fig.1. Trajectories of drifter, deployed north (a) and south (b) of 35°N and of ones, visited mixing zone (c).

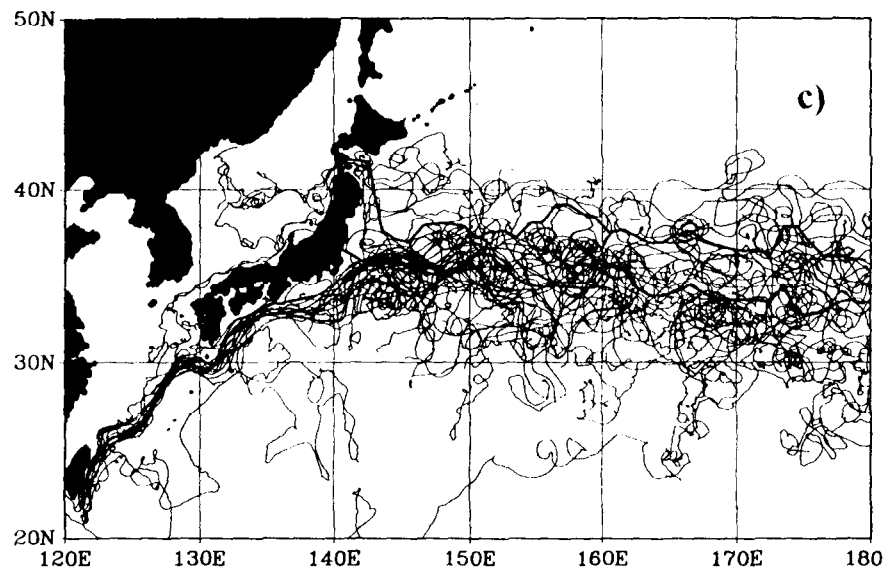
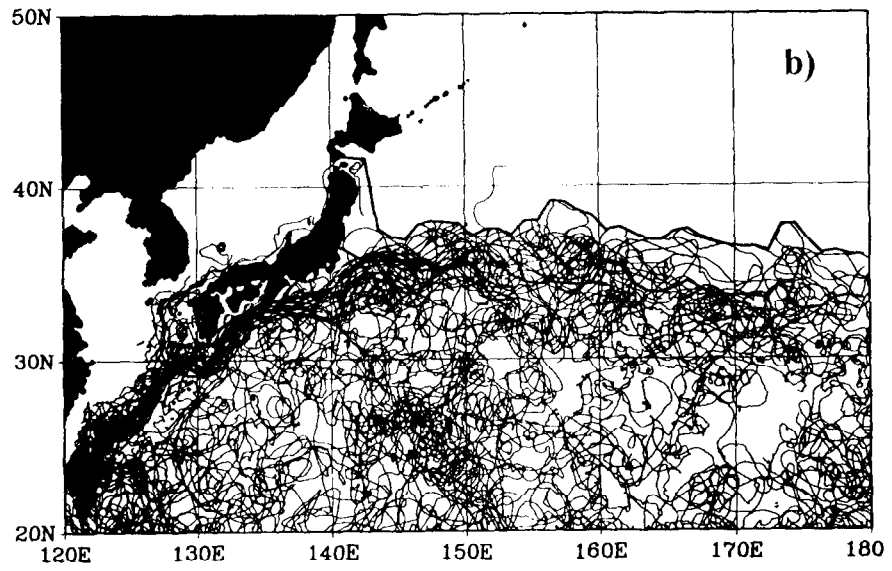


Fig.1 (continued).

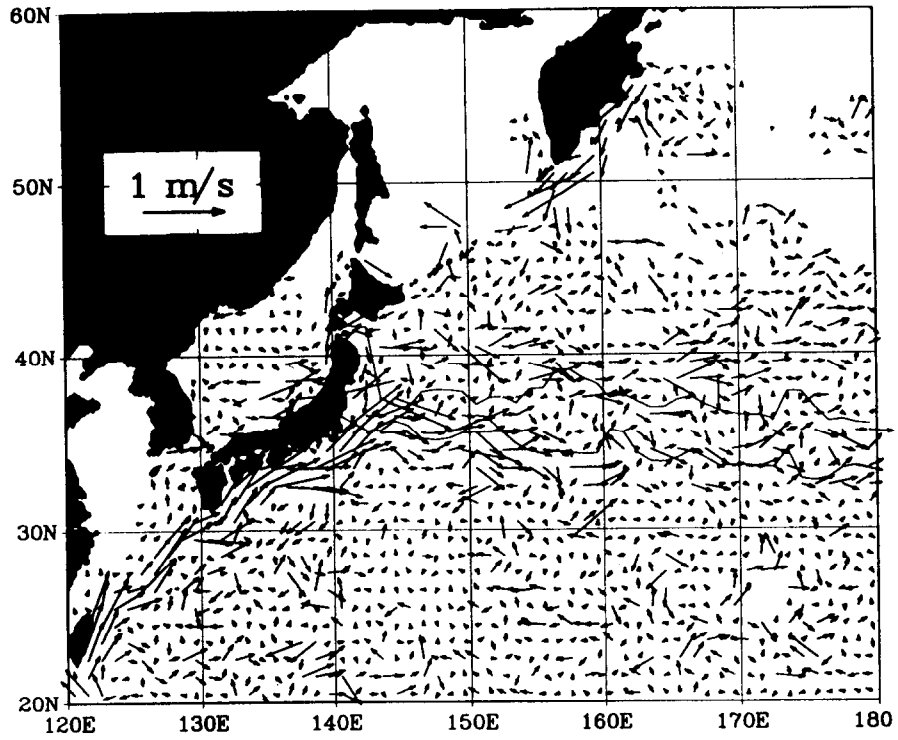


Fig.2. Mean surface velocities, calculated in $1^{\circ}\text{N} \times 1^{\circ}\text{E}$ boxes.

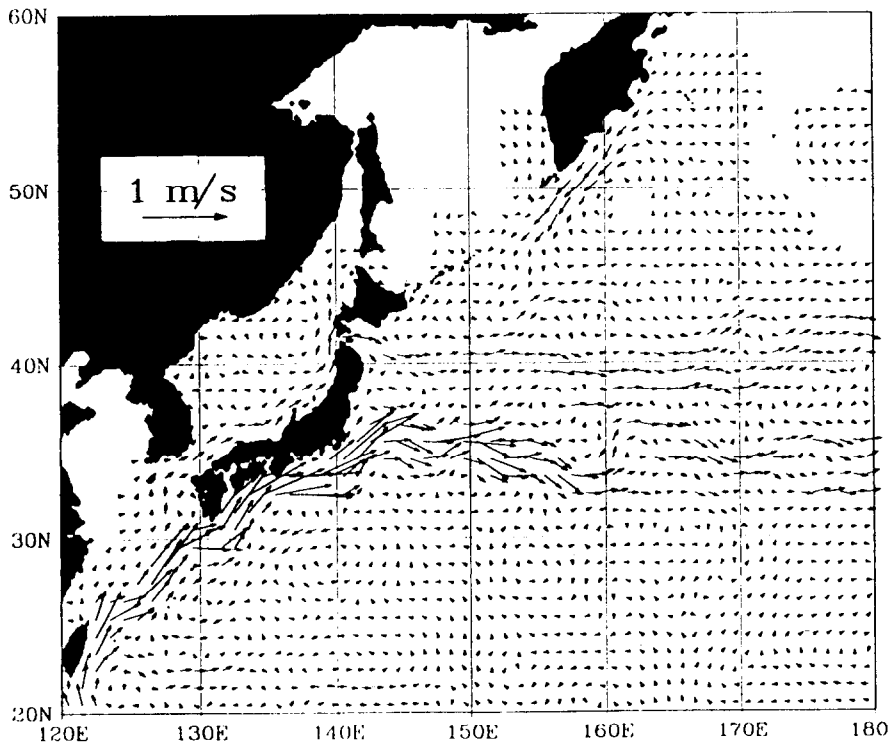


Fig.3. Mean velocity field, optimized with variational technique.

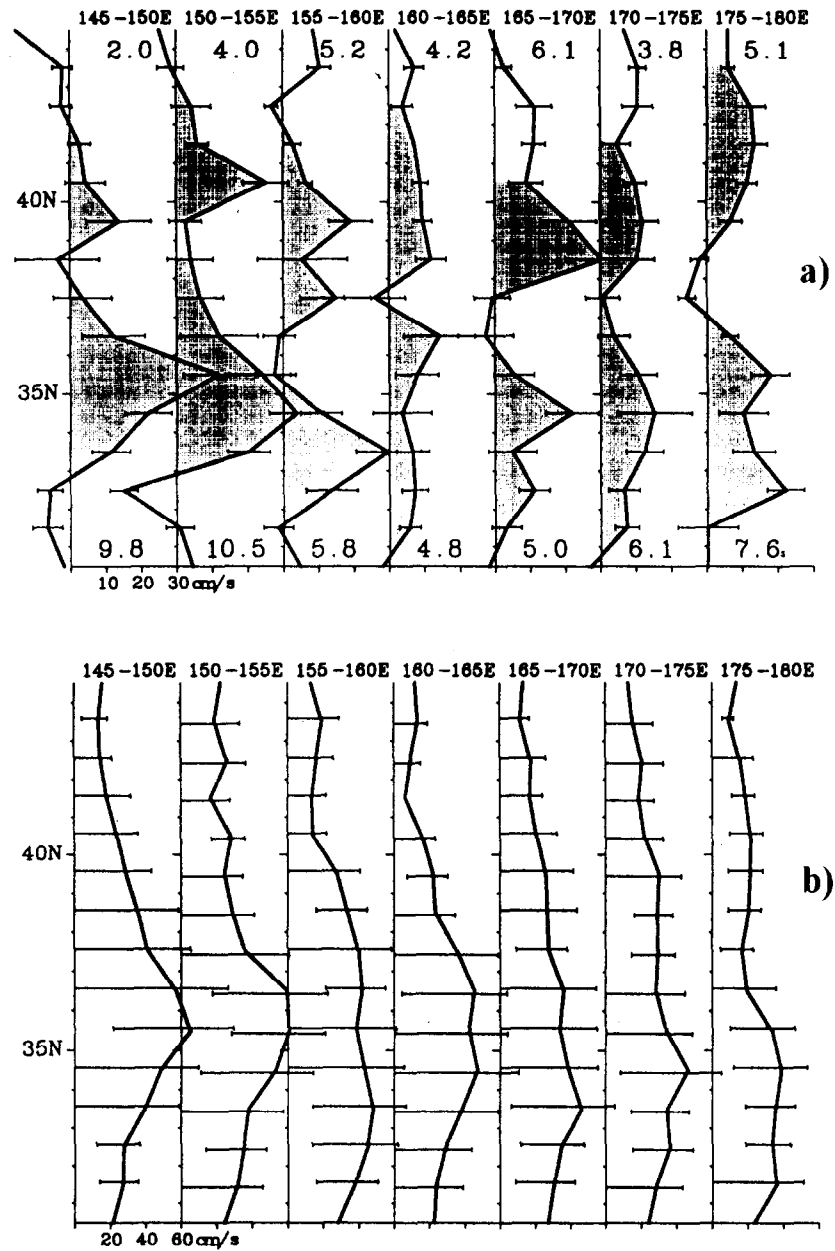


Fig.4. Mean velocities (a) and their variability (b), averaged within $1^{\circ}\text{N} \times 5^{\circ}\text{E}$ bins.

Limitation in data causes a high level of noise and errors in mean velocity estimates. To get more representative mean velocity field without oversmoothing by direct statistical methods (i.e. to remove uncorrelated noise in the central areas of large-scale gyres, poorly covered with drifter measurements, and to remain, at the same time, reliably observed and well-resolved narrow strong jets, like KE) we employed original variational interpolation technique. Main advantage of our scheme is the inclusion of advective nonlinear term into the cost function soft constraints. This idea is based on estimates of weakness of ageostrophic currents, obvious difference in cross- and along-stream decorrelation scales in the western

boundary currents and frontal areas, and, mathematically, results in a preference of along-stream velocity averaging, when cross-stream flow structure is mostly remained unchanged. Other terms of our cost function provided smoothness and non-divergence of the solution as well as its fitting averaged data. Results are shown in Fig.3. Indeed, optimized mean velocities not only keep main parameters of main jets, but even allow discussion of KE and SF interaction with Shatsky Rise and Emperor Seamounts.

Kuroshio Extension/ Subarctic Front region

To put more details in KE/SF region we calculated mean velocities and their variability within $1^{\circ}\text{N}\times 5^{\circ}\text{E}$ boxes, elongated nearly downstream of main jets. Mean zonal velocity field (Fig.4a) consists of two eastward jets (KE at $32\text{-}36^{\circ}\text{N}$ and SF at $37\text{-}43^{\circ}\text{N}$), when maximum of its variability (Fig.4b) is unique at every section and correlates well with KE location. By comparing Figs.4a and b, one can see that SF jet, being almost as fast as KE, is much more stable than the later. This can make difficulties for SF detection from satellite altimetry data.

Surprisingly, five of seven sections demonstrate also mean westward flow between KE and SF. "Wave-like" horizontal structure of velocity field in KE have been recognized before [4], but was attributed to eddy activity. Results of analysis of westward fragments of drifter trajectories, superimposed on the regions of westward mean velocities gives the idea of possibility of continuous mean westward flow in this area. When most of drifters demonstrate fast rotation in eddies of both signs, some others were advected smoothly through more than 10°E . The existence of this countercurrent should be clarified with more data and independent methods and measurements.

References

- [1] World Ocean Circulation Experiment implementation plan. Volume 1: Detailed requirements, 1988, WMO World Climate Research Programme, WCRP-11, WOCE International Planning Office, WOCE Report 20/88 (WMO/TD-No.242), 63pp.
- [2] D.V. Hansen and P.-M.Poulain, 1996, Quality control and interpolation of WOCE-TOGA drifter data. *J.Atmos.Oceanic Technol.*, 13, 900-909.
- [3] S.Aoki, S.Imawaki and K.Ichikawa, 1995, Baroclinic disturbances propagating westward in the Kuroshio Extension region as seen by satellite altimeter and radiometers. *J.Geophys.Res.*, 100, 839-855.
- [4] A.S.Vasilev and V.P.Makashin, 1993, Mesoscale dynamic structure of Subarctic frontal zone in the Pacific. *Meteorology and Hydrology*, 4, 60-68.

LABORATORY SIMULATION OF FRONTS BETWEEN THE VARIOUS WATER MASSES IN THE KARA SEA

T. A. Mc Climans¹, B. O. Johannessen² and J. H. Nilsen³

¹SINTEF CEE and NTNU, N-7034 Trondheim, Norway

thomas.mcclimans@civil.sintef.no

²Det Norske Veritas, 1322 Høvik, Norway

bjorn.olaf.johannessen@dnv.no

³HIST, Dept. of Computer Engineering, 7005 Trondheim, Norway

jan.h.nilsen@idb.hist.no

Abstract: A laboratory model of the eastern Barents and Kara seas has been built to simulate the transport and spreading processes in the region. Transports are forced by three inflows of Atlantic Water (1- Murman Current, 2- the flow between the Central and Great banks and 3- an underflow to the St. Anna Trough), buoyant coastal water along northern Russia, buoyant Polar Water past Franz Josef Land and three fresh water sources from the Pechora, Ob and Yenisei rivers. Diurnal tidal forcing is applied to simulate the tidal exchange in the Kara Strait that connects the Barents and Kara seas in the south. The results show strong topographic steering of the ocean currents and fronts, tidally rectified currents and long residence times of the large river plumes on the broad, shallow delta region to the north of the Ob and Yenisei estuaries. The main front of the region of fresh water influence (ROFI) is along the edge of the delta, probably held in place by the slope current.

The currents show good agreement with field measurements. The salinities over the delta agreed well with autumn field measurements, but show too low surface values in late winter, possibly due to brine rejection during freezing and southerly winter monsoon winds, which are not simulated in the model. A strong front between the inflowing coastal water and the basin water in the southwestern Kara Sea agrees well with field observations. A western flow through the northern part of the Kara Strait contains some of the inflow to the Kara Sea in the southern two thirds of the passage. Discharges in the Pechora River probably follow this route. The validations to field data show that flux, density and tide forcings are reasonable, and that the results should provide a good benchmark for testing numerical models.

Introduction

The purpose of the laboratory model of the Kara Sea is to study the transport routes of contaminants in the northern region (Barents and Kara seas). Emphasis is placed on the possible discharge of radioactive contaminants from the Ob and Yenisei catchments and containers dumped in the Kara Sea. The first objective of the model simulations was to inform the research vessel *RV H.U. Sverdrup II* of important locations to take field measurements of currents and hydrography to assess the transport rates and routes in the Kara Sea during late summer, 1995. This was done under the auspices of the Arctic Nuclear Waste Assessment Program, administered by the Office of Naval Research in Arlington, Virginia. Follow-on studies and reporting of the results were supported by the Norwegian Ministry of Foreign Affairs.

The simulations give new insight on the extent and transport routes of the various water masses. The present paper focuses on the fronts that separate the various water masses flowing through the Kara Sea.

Circulation in the Barents and Kara Seas

The general circulation in the Barents Sea [1], [2] was simulated in the laboratory without wind forcing, indicating that the flows are forced remotely by the ocean currents and pressure fields in the Norwegian Sea and the Arctic Ocean [3]. Details of the historical accounts of the circulation pattern in the Barents Sea are verified both by newer *in situ* measurements and model simulations [4], while the historical sketches of the circulation in the Kara Sea show much less detail and verification to newer measurements [5]. The forcing of the currents in the Kara Sea is greatly influenced by the oceanographic conditions in the eastern Barents Sea and the Arctic Ocean. Processes in the major passages to the north and south of Novaya Zemlya (Fig. 1) determine by and large the flow in the Kara Sea. The coastal water flowing eastward in the Pechora Sea is the dominant forcing of the (two-way) flow in the Kara Strait [6]. This flow is further forced by the dynamics of the Murman Current that holds the coastal current in place. In the north, there is a complicated interplay between the extensions of the Murman Current and the inflow of Polar Water past Franz Josef Land that forms the Persey Current in the northern Barents Sea. The seasonal variability of these forcing currents depends on thermodynamic forcing, regional winds and the seasonal runoff from land. There appears to be a down-slope pressure gradient to the east, during most of the year, while there is a reversal in late summer [7]. These circumstances, and earlier experience with the Barents Sea model, are used to formulate boundary conditions to force the circulation in the Kara Sea model.

Tidal forcing is not considered to be important for *persistent transports* except in shallow regions, along steep slopes and in narrow straits. The shallow delta region in the Kara Sea, with its steep slope, and the Kara Strait are particular regions of interest for tidal forcing.

Laboratory model

The extent of the laboratory model of the eastern Barents Sea and the Kara Sea is shown in Fig. 1, together with relevant information for the simulations. The gravitational Froude and rotational Rossby similitudes govern

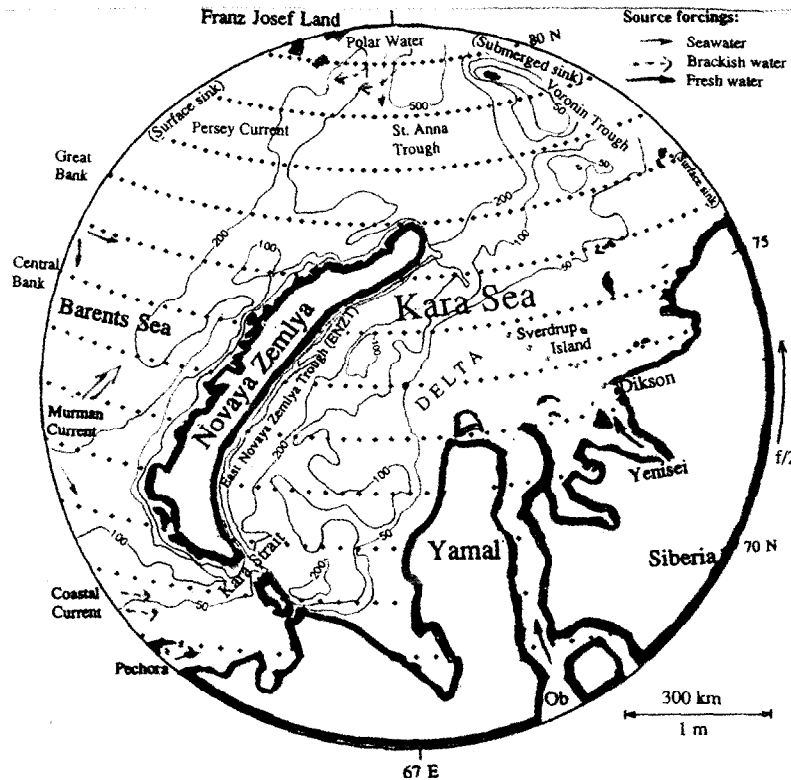


Figure 1. The laboratory model domain with the sources, sinks, bathymetry and relevant names noted.

large-scale motions in which the force balance is between the hydrostatic pressure field and the Coriolis term. These are compatible, and can be simulated accurately in a rotating basin [8]. The laboratory model boundaries are shown in Fig. 1. They are chosen to pass through regions that are either streamlines or sufficiently easy to control (the flux conditions). These conditions will be subjected to a validation. The 5 m diameter Kara Sea model simulates a geographical expanse of 1,500 km diameter, centered at 74°N, 67°E, thus, the ratio of horizontal lengths is

$$L_r = \frac{L_{nature}}{L_{lab}} = 300,000. \quad (1)$$

To avoid the effects of surface tension gradients, to secure that the dynamics of the fronts are dominated by buoyancy, or barotropic forcing, it is necessary to exaggerate the vertical scaling in the model [9]. This can be done as long as the vertical accelerations in the model do not contribute to the pressure balance (the flow in the model must also be hydrostatic). To model the depths of the region in a 50 cm deep basin, the vertical ratio of length scales must be

$$H_r = \frac{H_{nature}}{H_{lab}} = 1,000. \quad (2)$$

This gives a distortion of 300, which is typical for this type of model [3]. This satisfies the requirement for surface tension gradients for the Ob and Yenisei discharges, but the Pechora river discharge is so small that it is influenced significantly by an outward pull of the surface tension of the more saline water. However, it is expected that the river plume here is passive in the energetic coastal and tidal flows.

Due to the highly sub-critical flow speeds in the ocean (much less than tidal wave speeds), it is both necessary and sufficient that the simulation of the physics in the model simulations obey the densimetric Froude and Rossby model laws. This is necessary to model the ratio of buoyancy, inertial and rotational forces in a vertically distorted geometry, provided that the flow is approximately hydrostatic in the laboratory, and that *viscous* and surface tension effects are small [8]. The most significant frictional effect is wind shear, which is not simulated here.

Within the above framework, it is possible to tailor the buoyancy (or density) ratio

$$g'_r = \frac{g'_{nature}}{g'_{lab}}, \quad (3)$$

where g' is the so-called reduced gravity = $g(\rho - \rho_o)/\rho_o$, g is the acceleration of gravity, ρ_o is a reference density and ρ is the density which varies in space and time.

The densimetric Froude number is

$$F = \frac{u}{\sqrt{g' H}}, \quad (4)$$

where u is the flow velocity. For similitude, the ratio

$$F_r = \frac{F_{nature}}{F_{lab}} = 1 = \frac{u_r}{(H_r g'_r)^{1/2}}, \quad (5)$$

where $u_r = L_r/t_r$ and t_r is the time ratio $t_r = t_{nature}/t_{lab}$.

By choosing a convenient density scaling, we can tailor the time so that a day in nature is an integral number of seconds in model time to facilitate control of the monthly variable inflows. For the Kara Sea model, the choice is $g' = 1.74$, giving a time scale $t_r = 7,200$, for which a day is modeled in 12 s.

The Froude similitude above is compatible with the Rossby similitude

$$Ro_r = \frac{u_r}{f_r L_r}, \quad (6)$$

where f is the so-called Coriolis parameter ($= 2 \times$ rotation rate). Thus, $f_r = t_r^{-1}$. With this scaling, the volume flux scaling is

$$Q_r = L_r^2 H_r / t_r = 300,000^2 \cdot 1,000 / 7,200 = 1.25 \cdot 10^{10}. \quad (7)$$

A source flux of 1 Sverdrup ($1 \text{ Sv} = 10^6 \text{ m}^3/\text{s}$) in the ocean requires a model source flux of $80 \text{ cm}^3/\text{s}$ or $4.8 \text{ l}/\text{min}$. The model is constructed in a UTM 67 projection, which is exact along the 67°E longitude and has a maximum deviation of about 2 km at the eastern and western boundaries. Due to the rotation of the model, to simulate the geophysical flows, the water surface describes a paraboloid of revolution. This datum is taken into account in forming the bottom topography from sea charts. The rotating basin provides a constant Coriolis parameter $f = 2\Omega \sin \phi$, where Ω is the rotation of the earth and ϕ is the latitude. In nature, f varies with $\pm 2.7\%$ over the model domain, but only $\pm 1\%$ from its average value over the flat delta. Thus, the variations in depth dominate over the differences in Coriolis parameter when it comes to potential vorticity dynamics [10]. Key isobaths are noted in Fig. 1.

A crucial problem for simulating flows is obtaining accurate forcing data. In the present model, the main forcing is the density (salinity) and volume fluxes of 8 sources and the division of the downstream (outflow) into 3 paths. Monthly values of the forcing data are given in Table 1. These are based on the forcings used in the Barents Sea model study, the climatology of [11] and hydrological data from [12].

In addition to the advectively forced flows, the model is slightly tilted to simulate a tidal excitation of flow through the Kara Strait.

Table 1. Monthly flux boundary conditions in Sverdrups ($\text{Sv} = 10^6 \text{ m}^3/\text{s}$).

Source*	S	J	F	M	A	M	J	J	A	S	O	N	D
	(psu)												
MC	35	1.82	1.82	1.26	1.26	1.26	0.83	0.83	0.71	1.14	1.41	1.61	2.52
CBC	35	0.91	0.91	0.63	0.63	0.63	0.42	0.42	0.35	0.70	0.70	0.83	1.26
CC	33	0.45	0.35	0.21	0.21	0.40	0.55	0.60	0.55	0.95	0.65	0.60	0.50
PW	33	0.72	0.81	0.72	0.81	1.17	1.08	1.08	1.08	0.99	0.72	0.72	0.90
Y	0	.008	.008	.007	.008	.038	.096	.051	.020	.020	.016	.010	.008
O	0	.006	.006	.005	.006	.029	.071	.038	.015	.015	.012	.007	.006
P	0	.002	.002	.002	.002	.008	.021	.011	.004	.004	.003	.002	.002

* The source symbols are as follows: MC = Murman Current, CBC = Central Bank Current, CC = coastal current, PW = Polar Water, Y = Yenisei, O = Ob and P = Pechora. The eighth source, the underflow of Atlantic Water to the east of Franz Josef Land is held at a constant 1 Sv, for lack of better data. The river discharge was obtained from the GRDC archives [12], increased by 20% to account for ungauged runoff, and normalized to a common seasonal variation.

There are 3 outflows: an overflow weir accommodating most of the surface water in the region where the Persey Current flows west, a diversion of 0.25 Sv of the surface outflow to the northeast, toward Vil'kitsky Strait, and a deeper outflow under a broad skirt at 110 m depth in the north. The seasonal variability in Table 1 is run for 3 consecutive, identical years to obtain a *stationary* solution. This is based on estimates of residence times.

The instrumentation of the model is divided into *in situ* and remote sensing. Monthly *in situ* samples of salinity and fluorescent dye are withdrawn at a total of 32 stations to monitor the stratification on the delta and the spread of plume water. The sampling locations NW of Dikson are noted with small *s* in Fig. 1, and the results are shown later in Fig. 7.

The remote sensing is accomplished with video cameras, which include two sets of 3 super VHS cameras to quantify the 3 dimensional flow fields near the northern and southern ends of Novaya Zemlya. To achieve a good mapping and quantification of the flow, large surface buoys, smaller neutral (submerged) buoys and dye clouds are used at critical times and locations. A description of the photogrammetric method is given elsewhere [13]. Latitudes and longitudes are marked on the bottom for reference in positioning the particles and dye clouds. Totally there are 8 video cameras and a 35 mm Nikon F6 with a wide lens to view the entire region of interest.

Results and validations

Fig. 2 shows the surface transport routes in the laboratory model of the Kara Sea [14]. The circled letters on the figure refer to the following processes:

- A - The northwestern flow of the river plumes and fronts between the water masses.
- B - A return current of seawater to the mixing region in the estuaries at 10-15 m depth.
- C - Several circulation patterns to the east of Novaya Zemlya.
- D - The western outflow in the northern part of the Kara Strait forming the Litke Current.
- E - A coastal current front and internal tides with amplitudes up to 15 m to the east of the Kara Strait.

The above results are confirmed by several sets of field data [5], [15]. The western and northern flow of the river plumes was noted first by Fridtjof Nansen in 1893 [16] and the two-way flow in the Kara Strait has been known since early in this century [6]. However, recirculation of the coastal water, with Pechora discharge, through the Kara Strait appears to be a new result which has been verified only in part, due to a lack of available field data. The model simulations show that the currents to the east of Novaya Zemlya, where there are several ocean dump sites for radioactive wastes, are divided into many cells, with passive, diffusive fronts, unlike the through-flow depicted by [11], based on sparse, historical data. This suggests that the transport of contaminants from the Kara Sea to the fish habitats in the southeastern Barents Sea is less than earlier assumed.

Since there has not been any calibration, except for the tilt to force the tides through the Kara Strait, the comparison with available *in situ* velocity measurements is a validation of both the model and the forcing. The first comparison is with the current measurements along 60° E [17]. The field and laboratory data are compared in Fig. 3. The directions are good (< 20° deviation), but the strengths of the surface currents in the model are about twice those of the currents at 60 m depth in the field. It should be noted that the details of several current reversals in the historical charts are reproduced. The larger currents at the surface may, however, be reasonable for this region of moderate stratification. The density at 60 m depth is 1 kg/m³ higher than at the surface.

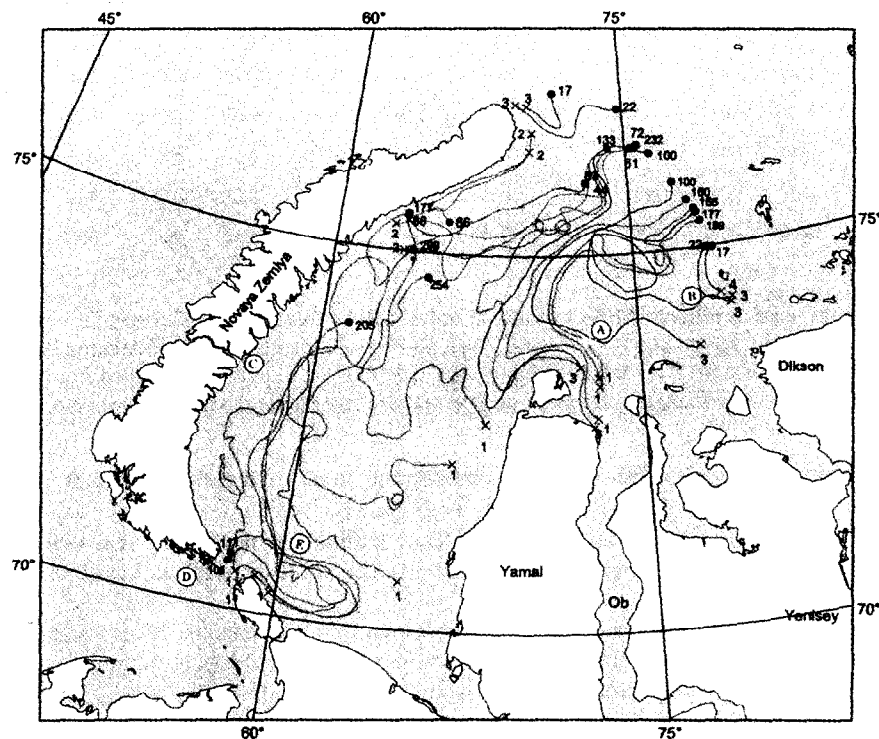


Fig. 2. Surface particle paths from the laboratory simulation of the ocean circulation in the Kara Sea. Numbers at the crosses denote start season (1 = Jan-Mar, 2 = Apr-June, etc), and numbers at the dots give the number of (simulated) days of travel. The circled letters refer to features discussed in the text.

The comparison of model velocities with field data from the Pechora Sea [1] and the Kara Strait [6] is shown in Fig. 4. Here too, the current directions are well validated. In particular, the Pechora Current and the origins of the Litke Current, in the northern third of the strait, are well documented. The current strengths are here on the same order of magnitude ($\frac{1}{2}$ knot), but there are significant advective accelerations that produce large differences over very short distances in this very rough topography. We claim that this is a reasonable validation, but with the disparate data in the north, it does not match the normalized standard deviation of about 25% of earlier laboratory validations.

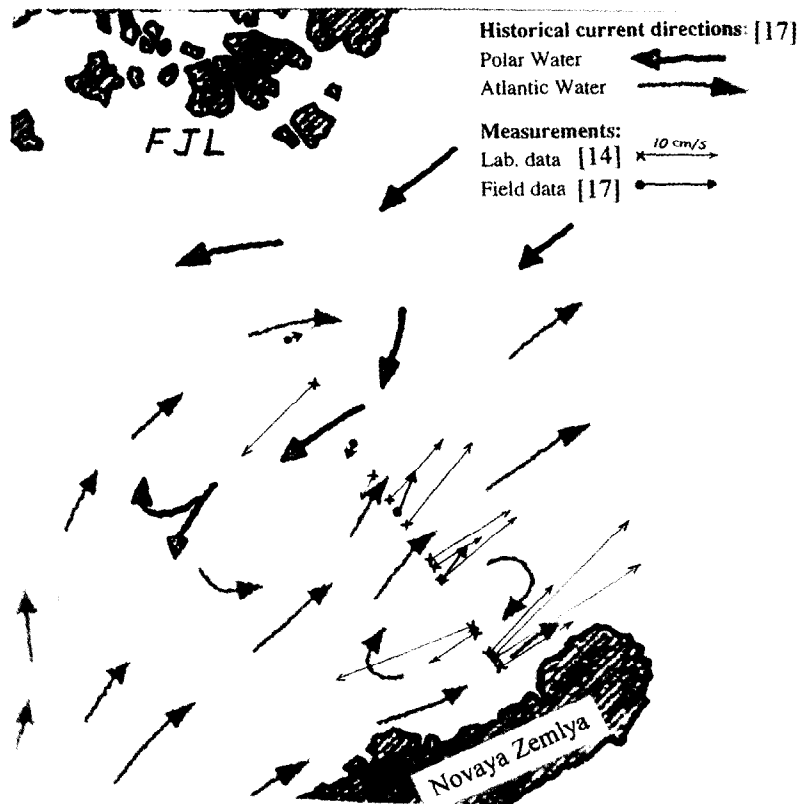


Fig. 3. Comparison of laboratory surface currents with the historical surface circulation and field measurements at 60–70 m depth.

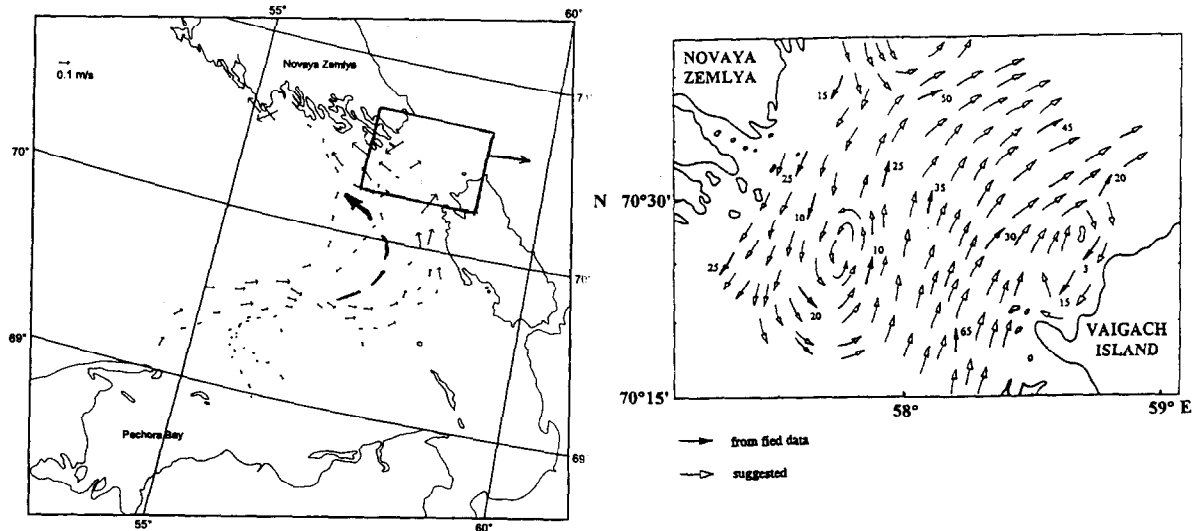


Fig. 4. Comparison of laboratory currents (left) with the current measurements of Maximov [6]. The dashed arrow superimposed on the laboratory data shows the path of the Pechora Current [1].

Frontal dynamics

The focus on the present study is to delineate the water masses and their transport routes. In Fig. 5, two particles following the coastal water at various depths are compared with the trajectory of a drogue at 15 m depth [18]. The vertical motions of the neutral buoys (right) show that there are significant internal tides just inside the Kara Sea, forced by the oscillating flow in the strait. These forced motions are within a Rossby radius of the coast and behave as internal Kelvin waves. Such disturbances have also been observed along the slopes of the delta [6].

The boundaries between the masses are distinguishable fronts, as mentioned above, each of which have their own peculiar form of dynamic balance. The coastal current is a baroclinic jet in this region. The inflow of coastal water through the Kara Strait meets the cold basin water in the ENZT and is diverted to the southeast along Vaigach Island. The flow properties in the dotted section noted in Fig. 5 are shown in Fig. 6.

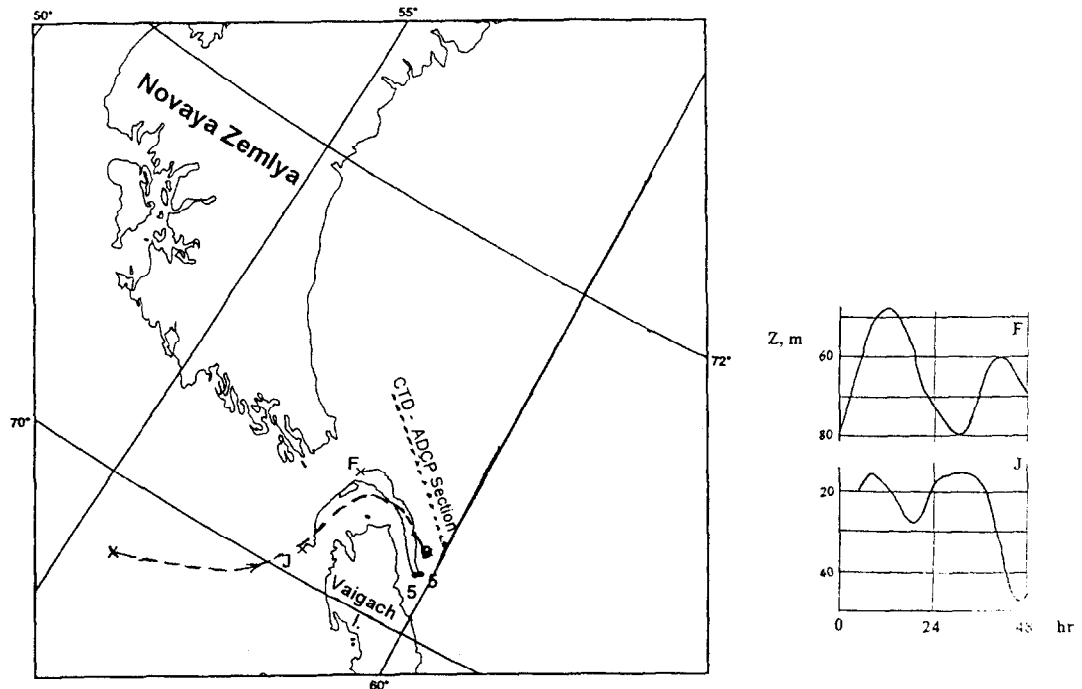


Fig. 5. Vertical excursions (right) of the two neutral buoys during the first 2 days of their 5-day trajectory (left) at intermediate depths between coastal water and ENZT water. The dashed line on the left is the path of a 15 m deep drogue observed by Føyen and Nikitin [18]. Results from the CTD-ADCP section [15] are shown in Fig. 6.

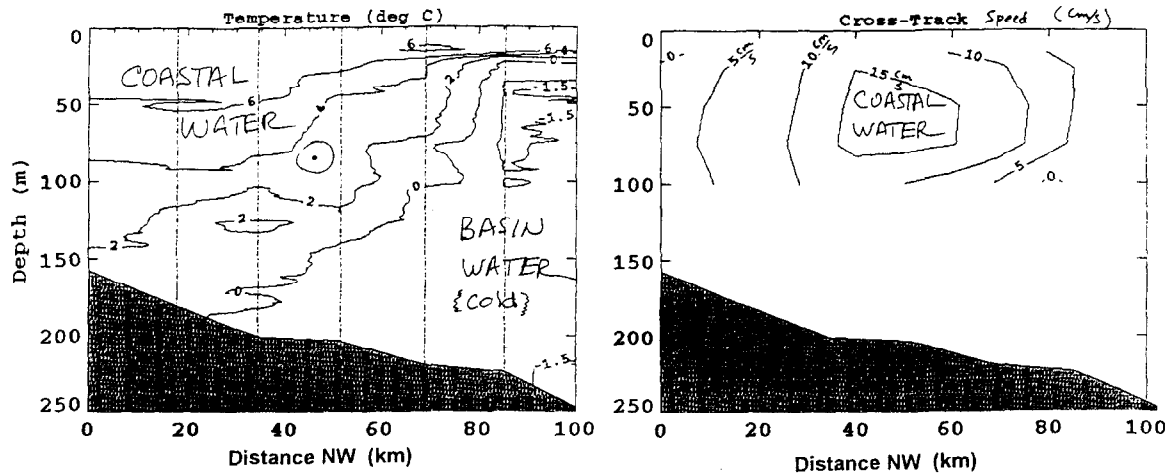


Fig. 6. Cross sections of temperature (left) and velocity through the coastal current inflow to the Kara Sea [15].

The front between the river plume and the coastal water (the Region Of Fresh Water, or ROFI front) is seen in the surface salinity distribution of Fig. 7 [5]. The currents in the coastal water help to contain this baroclinic front on the delta. At the edge of the delta there is another front between the coastal water and the ENZT water which appears to be stabilized barotropically by the bottom topography [7]. In the north, the slope current fronts the Polar Water which is advected by the underflow of modified Atlantic Water. There appear to be large eddies formed along the ROFI front [5]. These enhance the transport of river plume water to the outer region where it can mix more efficiently with the deeper water. This can precondition the water to winter convection [19].

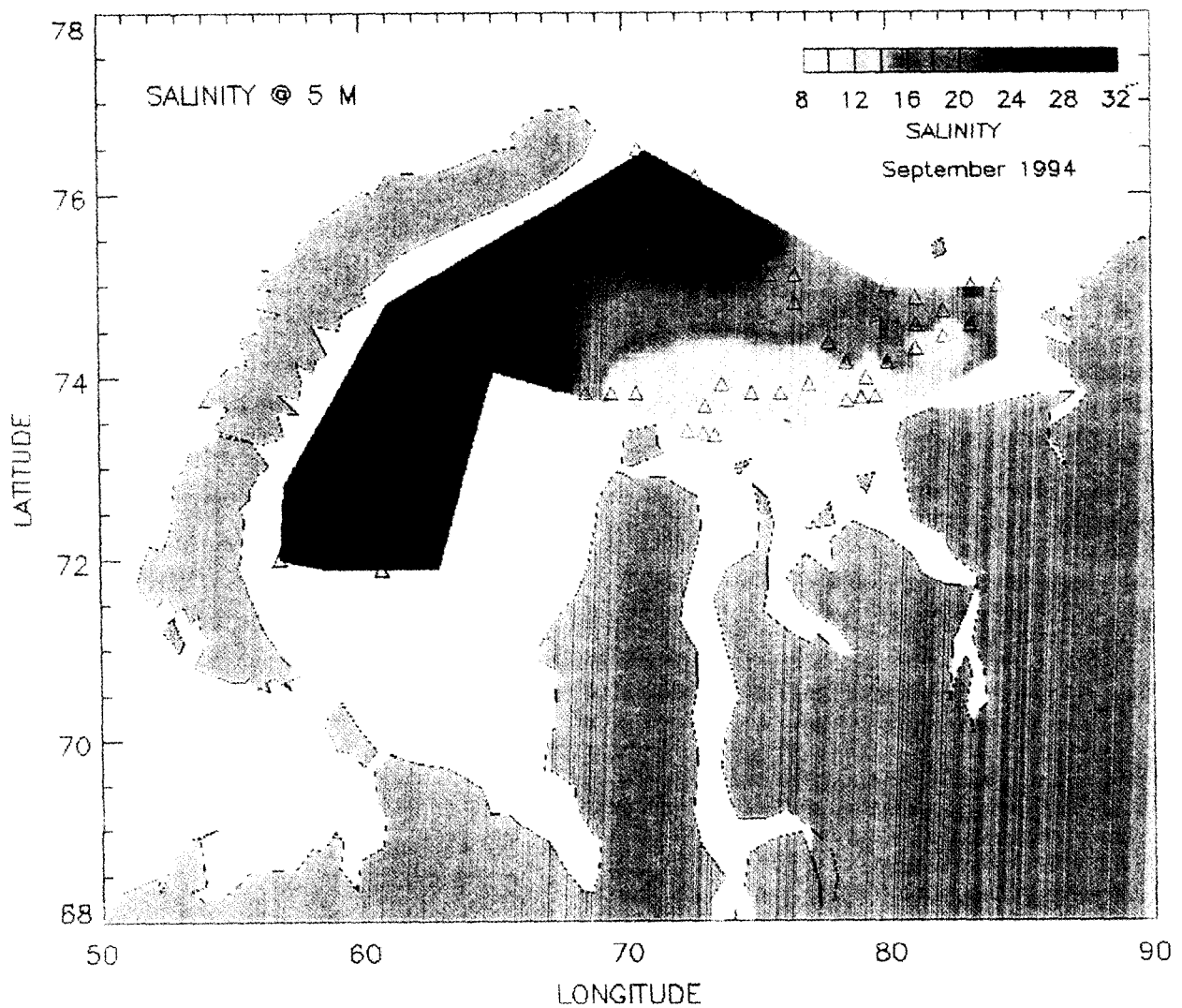


Fig. 7. Salinity field at 5 m depth from a CTD survey [5].

Summary and conclusions

The laboratory simulations of currents in the Kara Sea are in general agreement with newer field data [5], [15], [17], [18], [20], [21] and a reevaluation of historical data by [5]. They are, however, at variance with the general circulation pattern presented by [11], which was attributed largely to the prevailing winds. The laboratory results, *without wind*, show that the circulation pattern is much more complicated than the maps indicate, with both fine scale geographic and temporal variability. In the north, the historical details [17] are well captured. The circulation in the model domain is forced by controlling the volume fluxes from 8 sources, the dominant one being the Murman Current (up to 2.6 Sv). Without wind forcing, the topographic steering is quite dominant. On the delta, the residual currents are propelled somewhat by tidal forcing. This forces the major part of the river plumes to flow to the west and northwest toward the outer slope of the delta. Only a small part of the Yenisei outflow is steered east along the coast. Compensation currents to the estuaries, driven by density gradients at intermediate depths, are also simulated in the model.

Contaminants in the ENZT water will have a long residence time in the basin. Several recirculating gyres are seen above the smaller basins in the shelf topography. The through-flow of water from the Kara Strait and the Yamal region is quite tortuous. Effluents from most of the ocean dump sites to the east of Novaya Zemlya are expected to meander through this labyrinth and flow out along the slope toward the Voronin Trough. Effluents along the southernmost portion of the eastern coast of Novaya Zemlya may feed into the Litke Current along the southwest coast of Novaya Zemlya, entering the eastern Barents Sea.

Effluents in the river catchments will exit to the west, but find their way to the north and northeast, being confined by the delta slope current (front). The long-range fate of contaminants depends on how deep they penetrate the water column in the Kara Sea. Thermodynamics (freezing, brine rejection, convection, ice drift and melting) are important. For contaminants exiting in the north at the surface, the transport route is westward in the Percy Current, toward Svalbard. For contaminants at depth, in the modified coastal water, or modified Atlantic Water, the route will follow the bottom slopes to the north and east toward Alaska.

Southeast of the Kara Strait, the amplitudes of internal tides reach 15 m near the bottom slopes. The two-way transport in the Kara Strait is partially propelled by the tides. However, it is not established how much of the deeper water below the coastal water can be pumped over the 70 m deep sill at the Kara Strait.

Effluents from the Pechora River appear to be transported to the north along the southwest coast of Novaya Zemlya, either by breaching the Pechora Sea, on the Pechora Current, or first being transported east through the Kara Strait, and then being returned by the recirculation cell to the east of the strait. Part of the Pechora River water flows through the Kara Sea. These results are tenuous, since surface tension gradients give an extra pull of the river plume to the coastal current in the laboratory model. However, it is argued that the plume is passive in the strong coastal current, and follows its path across the Pechora Sea and through the Kara Strait.

The laboratory results show a system with long adjustment times for the water masses. Even on the shallow delta, the adjustments take more than two years, and approach the estimate of [22]. The tracer in the Ob discharge first reaches the outer delta after just 5 months, with a dilution of more than 10, but lingers on the delta for more than a year. Surface particles tend to move faster than the deeper tracer clouds. Several of the details are seen in the particle paths of Fig. 2. The tidal residuals over the rugged topography cause many regions of recirculation, like the anticyclonic circulation around Sverdrup Island. The residence times along the delta slope are short, compared with those of the deeper waters and on the delta. The residence times in the Pechora Sea are much shorter than in the Kara Sea. The underflow of coastal water is an effective transport mechanism here.

With the transport routes and time scales derived from the laboratory simulations, it is possible to comment on a cold core jet along the upper slope (70 m isobath) to the east of the northern tip of Novaya Zemlya, observed by Quadfasel *et al.* [23]. They argued that it could be either recirculated Polar Water along the rim of the St. Anna Trough or remnants from winter convection on the delta. The present results show that it could also be late winter water from the coastal current that is advected along the 50 m isobath around the delta.

The effects of meteorological/thermodynamic processes are not simulated in the laboratory. They are more amenable to simulation by computer models. Persistent winter southerlies appear to be responsible for the discrepancy between modeled and observed, late-winter surface salinities to the northwest of Dikson (Fig. 8). Both field and laboratory autumn data approach the delta front at an offshore distance of 220 km (see Fig. 7).

The present has improved our understanding of the physical cause-effect relationships governing the transport processes for the different water masses in the eastern Barents and Kara seas. Even with a good understanding of these governing physical processes, however, it is necessary to have reliable boundary conditions to be able to quantify the rates and routes, and predict the future. The pathways seem to be steered by topography and driven by tide-topography effects in some regions. Both are predictable. Judging from Fig. 3, the advective forcing may be too strong. More work is needed to determine how this is driven by the remote sea level variability.

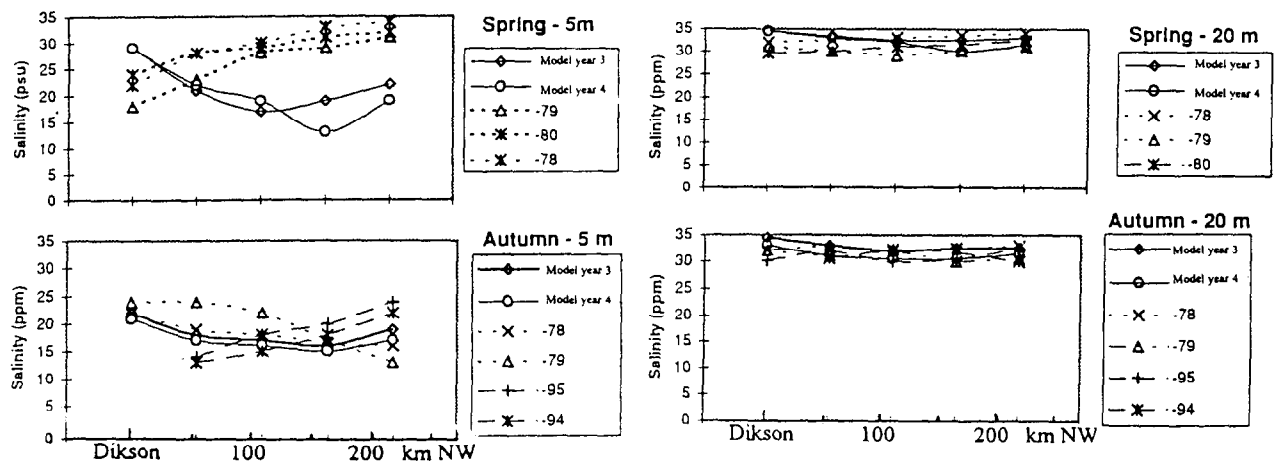


Fig. 8. Comparison between field and laboratory salinities [14] (field data from [24], [5] and [15]).

The present study is more exploratory than parametric. More systematic studies are needed to better quantify the validations to corresponding measures, and to study the sensitivity of the system to the boundary conditions, including the bottom topography. The degree to which the transports depend on local meteorological parameters (wind and heating) will determine the degree to which the fate of contaminants can be predicted. The sensitivity of the transport routes and times of travel to the governing processes is an important issue, since climatology can provide reasonable answers in many cases. Such a study should be made to determine how much of the spreading is affected by stochastic (unpredictable) events. The reasonable validation of the laboratory simulations to field data implies that the chosen boundary conditions are reasonable, and that they represent the dominating forcing.

The model simulations reported here have the nature of a complicated process study, and have provided a comprehensive, detailed description of the transport routes for contaminants from a variety of sources in the eastern Barents and Kara seas, for windless conditions. The present results can therefore, in principle, provide a benchmark to test idealized numerical models using the given forcings and no wind. In this way it will be possible to study the role of the separate advective forcings, and the artificial tidal excitation. Similar benchmarks have been provided by other laboratory models, e.g. [3] and [25].

Acknowledgements

The laboratory study was supported by the Office of Naval Research under Grant N-00014-95-1-1270 of the Arctic Nuclear Waste Assessment Program, and the Norwegian Ministry of Foreign Affairs.

References

- [1] P. V. Novitskiy, 1961, Permanent currents of the northern Barents Sea. U.S. Naval Oceanographic Office translation of *Trudy Gosudarstvennogo Okeanograficheskogo Instituta, Leningrad*, Vol. 64, pp 1 – 32, Washington, 1967.
- [2] H. Loeng, 1991, Features of the physical oceanographic conditions of the Barents Sea. *Polar Research* 10:5-18.
- [3] T. A. M^cClimans and J. H. Nilsen, 1993, Laboratory simulation of the ocean currents in the Barents Sea. *Dynamics of Atmospheres and Oceans* 19:3-26.
- [4] T. A. M^cClimans, 1997, Model validation of transport processes in the Barents and Kara Seas. AMAP International Symposium on *Environmental Pollution of the Arctic*. Tromsø, Norway, 1-5 June, 1997. Extended Abstract pp 244-246.

- [5] D. R. Johnson., T. A. M^cClimans, S. King and Ø. Grenness, 1997, Fresh water masses in the Kara Sea during summer. *J. Marine Sys.* 12:127-145.
- [6] V. K. Pavlov, L. A. Timohov, G. A. Baskakov, M. Yu. Kulakov, V. K. Kurazhov, P. V. Pavlov, S. V. Pivovarov and V. V. Stanovoy, 1994, The Kara Sea. Ch. 1 in *Hydrometeorological regime of the Kara, Laptev and East-Siberian seas*, Federal Service of Russia for Hydrometeorology and Monitoring of the Environment. AARI, St. Petersburg. Fig. 4 adapted from B. Aselme and J. Kögeler (1995) Transport processes in the Kara Sea. Paper presented at the Third Thematic Conference on Remote Sensing for Marine and Coastal Environments, Seattle WA, 18-20 September, 1995.
- [7] S. Li and T. A. M^cClimans, 1998, The effects of winds over a barotropic retrograde slope current. *Continental Shelf Research.* 18:457-485.
- [8] T. A. M^cClimans, 1990, The role of laboratory experiments and models in the study of sea straits. pp. 373-388 in *The Physical Oceanography of Sea Straits*. Ed. L.J. Pratt. Kluwer Academic Publishers.
- [9] T. A. M^cClimans and S. Sægrov, 1982, River plume studies in distorted Froude models. *J. Hyd. Res.* 20:15-27.
- [10] J. Pedlosky, 1979, *Geophysical Fluid Dynamics*, Springer-Verlag 624 pp.
- [11] V. K. Pavlov, M. Y. Kulakov and V. V. Stanovoy, 1993, Oceanographical description of the Kara and Barents Seas. Report to IAEA, St. Petersburg, Russia, 133 pp.
- [12] GRDC, 1995, Global Runoff Data Center, Koblenz, Germany.
- [13] J. H. Nilsen and I. Hådem, 1994, Photogrammetric tracking of tracer particles in modelled ocean flows. *J. Photogrammetry and Remote Sensing.* 49:9-20.
- [14] T. A. M^cClimans, B. O. Johannessen and J. H. Nilsen, 1997, A laboratory simulation of the ocean circulation in the eastern Barents and Kara seas. SINTEF CEE Report STF22 A97235, ISBN 82-14-00387-3, 1997.
- [15] S. E. King, D. R. Johnson and JoL. Carroll, 1996, EPOCA-95 Cruise report. Report NRL/MR/6616--96-7813, 51 pp.
- [16] F. Nansen, 1902, Oceanography of the North Polar Basin. In: F. Nansen (Editor), *The Norwegian north polar expedition, 1893-1896, scientific results*, Vol III, 427pp.
- [17] H. Loeng, H. Sagen, B. Ådlandsvik and V. Ozhigin, 1993, Current measurements between Novaya Zemlya and Franz Josef Land September 1991 - September 1992. Institute of Marine Research Department of Marine Environment Report No. 2 - 1993.
- [18] L. Føyn and A. Nikitin, 1994, The joint Norwegian/Russian expedition to the dump sites for radioactive waste in the Abrosimov Fjord and the Stepovogo Fjord, August-September 1994. Report from the expedition on board *R/V Viktor Buinitskiy*, with some preliminary results, 18 pp.
- [19] S. Martin and D. J. Cavalieri, 1989, Contributions of the Siberian shelf polynyas to the Arctic Ocean intermediate and deep water. *J. Geophys. Res.*, 94:12,725-12,738.
- [20] E. Nøst, 1995, Current data from KAREX-94. Paper presented at the scientific seminar "Nature conditions in the Kara and Barents Seas", St Petersburg, Russia.
- [21] M. Krosshavn., JoL. Carroll, T. Engøy, Ø. Grenness, A. Johnsen, D. R. Johnson, S. E. King and A. B. Ruud, 1998, Transport pathways of radionuclides and chemical contaminants in the Kara Sea. *Radiation Protection Dosimetry* 75:229-236.
- [22] D. Hanzlick and K. Aagaard, 1980, Freshwater and Atlantic Water in the Kara Sea. *J. Geophys. Res.*, 85:4937-4942.
- [23] D. Quadfasel, A. Sy and B. Rudels, 1993, A ship of opportunity section to the north pole: upper ocean temperature observations. *Deep-Sea Res. I*, 40:777-789.
- [24] J. Morison, 1997, A compilation of AARI hydrographic data. PSC/AARI web site <http://psc.apl.washington.edu>.
- [25] T. A. M^cClimans, J. Pietrzak, V. Huess, N. Kliem, J. H. Nilsen and B. O. Johannessen, 1998, A comparison of laboratory and numerical simulations of the ocean circulation in the Skagerrak. (Submitted to *Cont. Shelf Res.*)

Influence of the Indonesian Throughflow on the circulation of intermediate water in the Pacific Ocean

Julian P. McCreary, Jr. and Peng Lu

Oceanographic Center, Nova Southeastern University,
8000 N. Ocean Dr., Dania, FL 33004, USA
(e-mail: jay@ocean.nova.edu, lu@ocean.nova.edu)

Abstract: A $4\frac{1}{2}$ -layer model is used to study intermediate-water circulation in the Pacific Ocean. Each of the model's four active layers represents a different water-mass type, namely, surface water (layer 1), thermocline water (layer 2), North Pacific and South Pacific intermediate waters (NPIW and SPIW; layer 3), and Antarctic Intermediate Water (AAIW; layer 4). Across-interface flow between the layers parameterizes the processes of upwelling, subduction and diapycnal mixing. Solutions are obtained in a domain resembling the Pacific basin from 50°S to 55°N , and they are forced by annual-mean, climatological winds. They are also forced by an inflow of layer-4 water at the southwestern corner of the basin, and a compensating outflow in layers 1, 2 and 3 through the western boundary just north of the equator; this mass exchange simulates the Pacific interocean circulation (IOC), in which intermediate water enters the South Pacific and the same amount of upper-ocean water exits via the Indonesian Throughflow.

Solutions with and without forcing by the IOC are compared. With the IOC, SPIW fills the equatorial ocean and AAIW can spread into the subpolar region of the North Pacific. Without the IOC, however, NPIW fills the equatorial ocean, and AAIW is virtually confined within the South Pacific. Thus, the IOC is an important element of the Pacific general circulation, essentially determining much of the structure and water-mass properties of its intermediate-water flow.

1. Introduction

Recently, it has become clear that circulations in the tropical Pacific are not dynamically isolated, but rather are connected to the Pacific general circulation through meridional cells that extend to mid and higher latitudes. Indeed, because branches of these cells tend to converge in the western tropical Pacific, it is a place where a number of distinct water masses intermingle [1]. Figure 1 (adapted from [2]) illustrates the typical salinity field in the central tropical Pacific, and it indicates the presence of at least five water masses in the tropical ocean. Low-salinity (34.3–34.5 ppt) surface water centered near 10°N is formed locally in the vicinity of the Intertropical Convergence Zone (ITCZ). Northern and southern thermocline waters, formed by subduction in the subtropical oceans, are identifiable by tongues of high

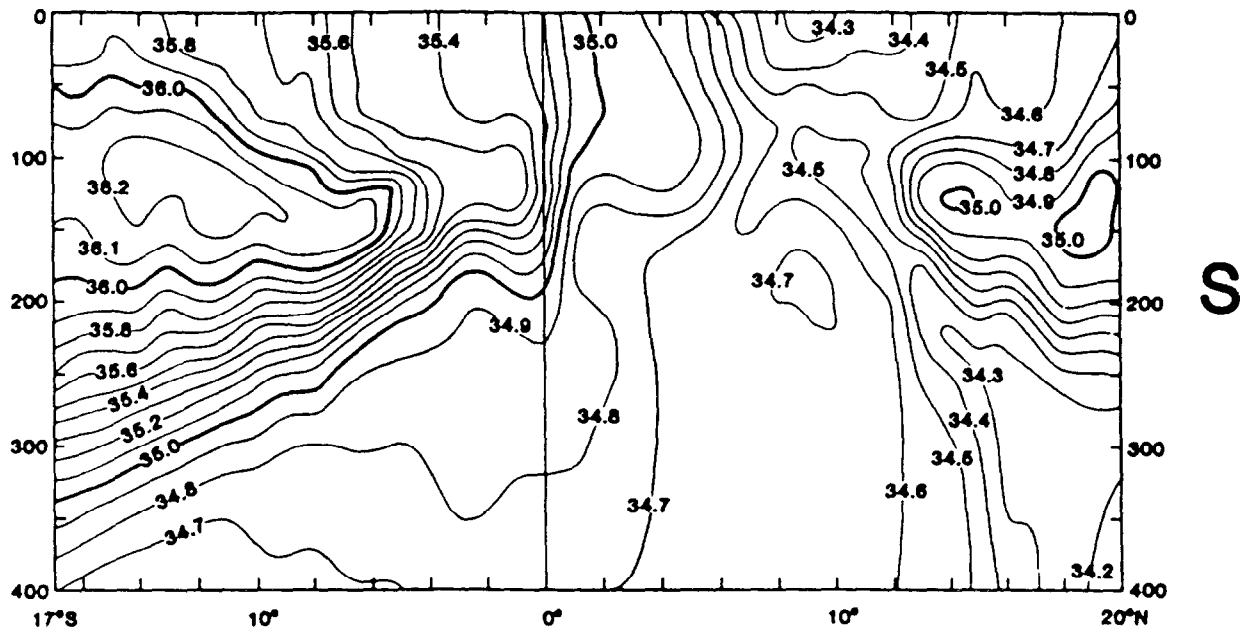


Figure 1: Mean distributions of salinity S between Hawaii and Tahiti near 155°W . The contour interval is 0.1 ppt. High-salinity tongues extend equatorward in both hemispheres to about 5°S and 12°N . At greater depths, a low-salinity tongue of NPIW extends upward and equatorward from the lower-right corner of the plot, and SPIW fills the tropical ocean to about 12°N . (Adapted from [2].)

salinity (maxima of 35.0 ppt for the northern tongue and 36.2 ppt for the southern one) that extend equatorward from the subtropics. At greater depths, low-salinity (34.6–34.9 ppt) water formed at high latitudes in the southern hemisphere, [3], [4], [5], spreads throughout the equatorial ocean to about 12°N . This water is a mixture of upper Antarctic Intermediate Water (AAIW), Subantarctic Mode Water and southern thermocline water, and we refer to it as South Pacific Intermediate Water (SPIW). Intermediate water with the lowest salinity (34.2–34.5 ppt) is located underneath the northern, high-salinity core; it is linked to North Pacific Intermediate Water (NPIW), which is primarily formed by mixing between the Kuroshio and Oyashio Currents during wintertime convection [6]. Note that NPIW can only spread to the latitudes of the ITCZ. At depths greater than displayed in Figure 1, AAIW fills the tropical Pacific and is detectable even in the far northeastern Pacific [7], [8].

Significant water exchange between the Pacific and Indian Oceans occurs in the Indonesian Archipelago, where the Indonesian Throughflow allows an outflow of upper-ocean water estimated to be 5–15 Sv [9], [10], [11]. This outflow appears to be balanced by an inflow of intermediate water associated with the Antarctic Circumpolar Current [12]. We define the Pacific Interocean Circulation (IOC) to be all the pathways that connect this southern inflow to the Indonesian outflow. Defined in this way, the IOC is the Pacific branch of the hypothesized global “conveyor belt” [9], and its deeper pathways are composed of AAIW and SPIW.

The above observations suggest several intriguing questions: Why does NPIW flow into the tropical ocean, but *not* into the equatorial region? Why instead does SPIW fill the equatorial region? Why does AAIW flow to the northeastern Pacific? In this paper, we investigate these questions using a $4\frac{1}{2}$ -layer model to simulate the circulation in the upper (≤ 1200 m) Pacific Ocean. In Section 2, we summarize the essential physics of the model. In Sections 3 and 4, we compare solutions with and without the IOC.

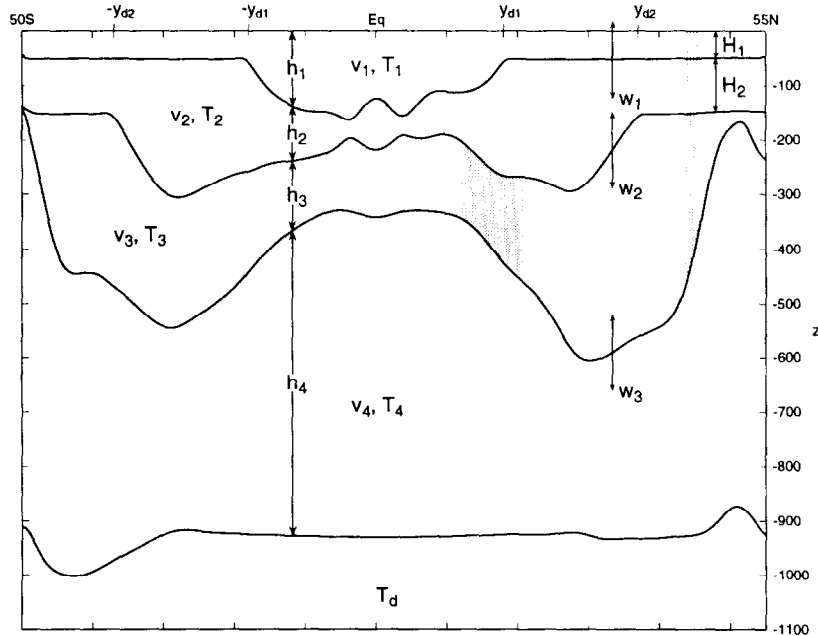


Figure 2: A section along 175°W for the solution forced by the IOC, illustrating the structure of the model. Various quantities are defined in the text. The shaded regions indicate locations of the NPIW that flows into the tropics.

As we shall see, the IOC is necessary for the model to be able to develop an intermediate circulation that resembles the observations.

The research reported here is an extension of the study by [13], who used a $3\frac{1}{2}$ -layer model to investigate the source waters of the Pacific Equatorial Undercurrent. The two studies are complementary in that the focus of the present one is on intermediate-water circulation, whereas that of the previous one is on the shallower circulations involving thermocline and surface waters.

2. Model Ocean

Figure 2 schematically illustrates the structure of the model, showing a meridional section at 175°W of the solution in Section 3. It consists of four active layers with thicknesses h_i , velocities v_i and temperatures T_i ($i = 1, 2, 3, 4$ is a layer index), overlying a deep, inert layer of temperature $T_4 = 0^\circ\text{C}$ where the pressure-gradient field vanishes. Each of the layers corresponds primarily to a single water-mass type, namely, surface water, thermocline water, SPIW and NPIW, and AAIW in layers 1, 2, 3 and 4, respectively. For convenience, the active layer temperatures T_i are kept fixed at the values 28, 20, 13 and 8°C . (It is, however, not necessary to fix layer temperatures in models of this type. See [14] for an example of a solution in which layer temperatures vary realistically.) The initial layer thicknesses are chosen to be $h_{1in} = 100$ m, $h_{2in} = 200$ m, $h_{3in} = 300$ m, and $h_{4in} = 600$ m. Water can move across the interfaces beneath the upper three layers at the velocities w_1 , w_2 and w_3 , but no exchange is allowed between layer 4 and the deep ocean or between layer 1 and the atmosphere. These velocities are a crucial part of the model's physics, because they represent all the vertical mixing processes in the model (*i.e.*,

entrainment, subduction and diapycnal mixing). For our purposes, w_2 and w_3 are particularly important because they determine the regions where intermediate water rises in the water column.

The across-interface velocity beneath layer 1 is given by

$$w_1 = \frac{(h_1 - H_1)^2}{H_1 t_1} [\theta(H_1 - h_1)\theta(y_{d1} - |y|) + S(H_1 - h_1)\theta(|y| - y_{d1})], \quad (1)$$

where θ and S are step and sign functions, respectively, $y_{d1} = 18^\circ\text{N}$, $H_1 = 50$ m, and $t_1 = 1$ day. According to (1), water located equatorward of $\pm y_{d1}$ will entrain into layer 1 ($w_1 > 0$) wherever h_1 becomes too thin ($h_1 < H_1$), a process that parameterizes the *upwelling* of layer-2 water into layer 1. Poleward of $\pm y_{d1}$, water can entrain into layer 1 but it also detrains into layer 2 if h_1 becomes too thick ($h_1 > H_1$), a process that parameterizes the *subduction* of layer-1 water into layer 2. Because both entrainment and detrainment occur poleward of $\pm y_{d1}$ and the adjustment time scale t_1 is so small, h_1 necessarily remains close to H_1 there (Figure 2). Poleward of $\pm y_{d1}$, then, layer 1 represents a mixed layer of constant thickness H_1 rather than a dynamically active layer.

The across-interface velocity beneath layer 2 is

$$w_2 = \kappa_2 \left(\frac{2}{h_2} - \frac{3}{h_3} \right) \theta(y_{d2} - |y|) + \frac{(h_2 - H_2)^2}{H_2 t_2} S(H_2 - h_2)\theta(|y| - y_{d2}), \quad (2)$$

where $y_{d2} = 37^\circ\text{N}$, $H_2 = 100$ m, $t_2 = 1$ day, and $\kappa_2 = 0.2$ cm²/s. According to (2), w_2 is determined by the second term poleward of $\pm y_{d2}$, which ensures that h_2 remains close to H_2 ; consequently, layers 1 and 2 together represent a mixed layer of constant thickness, $H_1 + H_2$, there (see Figure 2). Equatorward of $\pm y_{d2}$, w_2 is determined by the first term, which represents diapycnal mixing [13]. Note that $w_2 \neq 0$ wherever $h_3/h_2 \neq h_{3in}/h_{2in}$, that is, w_2 acts to relax layer thicknesses to their initial values when no force is imposed.

Finally, the across-interface velocity beneath layer 3,

$$w_3 = \kappa_3 \left(\frac{1}{h_3} - \frac{2}{h_4} \right), \quad (3)$$

is determined entirely by diapycnal mixing, where $\kappa_3 = 0.2$ cm²/s. Upward mixing is prominent where h_3 becomes thin near the southern and northern boundaries of the basin.

The model basin is illustrated in Figures 3 and 4 below. Closed, no-slip conditions are imposed on continental barriers (thick lines in the figures). In layer 4, boundary conditions along the western-boundary segment from 45°S to 50°S are

$$u_1 = 0, \quad u_2 = 0, \quad u_3 = \frac{M}{h_4 L_{w1}}, \quad v_{ix} = 0, \quad (4a)$$

where $M = 12$ Sv and $L_{w1} = 550$ km is the width of the segment. In layers 1, 2 and 3, boundary conditions from 4°N to 8°N , which represents the Indonesian passages in the model, are

$$u_1 = -\frac{1}{3} \frac{M}{h_1 L_{w2}}, \quad u_2 = -\frac{1}{3} \frac{M}{h_2 L_{w2}}, \quad u_3 = -\frac{1}{3} \frac{M}{h_3 L_{w2}}, \quad v_{ix} = 0, \quad (4b)$$

with $L_{w2} = 440$ km being the width of the segment. According to (4a) and (4b), a transport of 12 Sv enters the Pacific at the southwestern corner of the basin within layer 4, and the same amount leaves in layers 1, 2 and 3 via the Indonesian passages.

The wind stress that forces the model is a smoothed version of the annual-mean wind stress of [15], reduced by a factor of 0.7 because these winds are commonly believed to be too strong in the tropics. The inflow and outflow associated with M is the other forcing mechanism that drives the model.

Solutions are evaluated on a standard Arakawa C-grid with a resolution of $\Delta x = 1^\circ$, $\Delta y = 0.5^\circ$, and the equations of motion are integrated forward in time with a time step of $\Delta t = 72$ min. The solutions discussed in Sections 3 and 4 are obtained by integrating the model for 100 years from a state of rest, by which time they have adjusted to equilibrium.

3. Solution with the IOC

Here, we describe the solution with the IOC, that is, the one forced by both the wind and transport M . To focus attention on intermediate-water circulations, we only report layer-3 and layer-4 flow fields below. (See [13] for a discussion of the layer-1 and layer-2 currents.)

3.1. NPIW and SPIW

The upper panel of Figure 3 shows the layer-3 flow field. Five streamlines are plotted in the panel. Streamline E extends eastward and southward around the perimeter of the Subtropical Gyre, meanders into the eastern ocean, crosses the interior ocean near 15°N , and finally recirculates within the tropics; its defining characteristic is that no streamline located outside of E (that is, farther toward the edge of the Subtropical Gyre) enters the tropics, but instead intersects the eastern boundary near 30°N . Streamline E' is located near E , but does not meander eastward. Streamline B ends at 16.5°N on the western boundary, the bifurcation point of the Subtropical Gyre in this layer. Streamline C begins at 2°N on the western boundary at the point where northern- and southern-hemisphere waters converge, and hence it provides a dividing line between NPIW and SPIW. Streamline S illustrates a typical pathway for the flow of SPIW throughout the basin.

The NPIW is formed in the mixed-water region where the Oyashio and Kuroshio come together (*e.g.*, see [6]; trapezoidal region in the upper panel of Figure 3). The part formed north of E either moves into the subpolar ocean or upwells along the North American coast, and that formed south of B recirculates within the Subtropical Gyre. Only NPIW formed between E and B flows into the tropics, virtually all of it west of E' thereby bypassing the eastern ocean. As this “tropical NPIW” circulates around the Subtropical Gyre, its transport increases somewhat north of y_{d2} due to subduction (shaded region in upper panel of Figure 3) and south of y_{d2} due to upward mixing of AAIW from layer 4. By the time it reaches the Indonesian passages its transport is 4.5 Sv. Most of it (4.0 Sv) exits the basin via the Throughflow, the remainder turning eastward to flow back across the interior ocean. Outflow in the Indonesian Throughflow, then, is the reason why so little NPIW is present in the tropical ocean. The shaded regions in Figure 2 are bounded by the positions of streamlines E and B at 175°W , and hence indicate areas of tropical NPIW. Note that the region closest to the equator appears as a tongue rising toward the equator, consistent with the observed tongue of NPIW (Figure 1).

The primary source of SPIW is upward mixing of AAIW near the southern boundary (light-shaded region in the lower panel of Figure 3) where h_3 becomes very thin (Figure 2). In fact, most of this water first upwells into layer 1 there, and only then returns to layer 3 via subduction south of $-y_{d2}$ (light-shaded region in the lower panel of Figure 3). The SPIW circulates in the deep part of the Subtropical Gyre, and flows equatorward in a western-boundary current that includes the New Guinea Coastal Undercurrent [3], [8]. As it does, its transport increases somewhat due to upward mixing, and the amount that finally moves to the equator is 5.2 Sv.

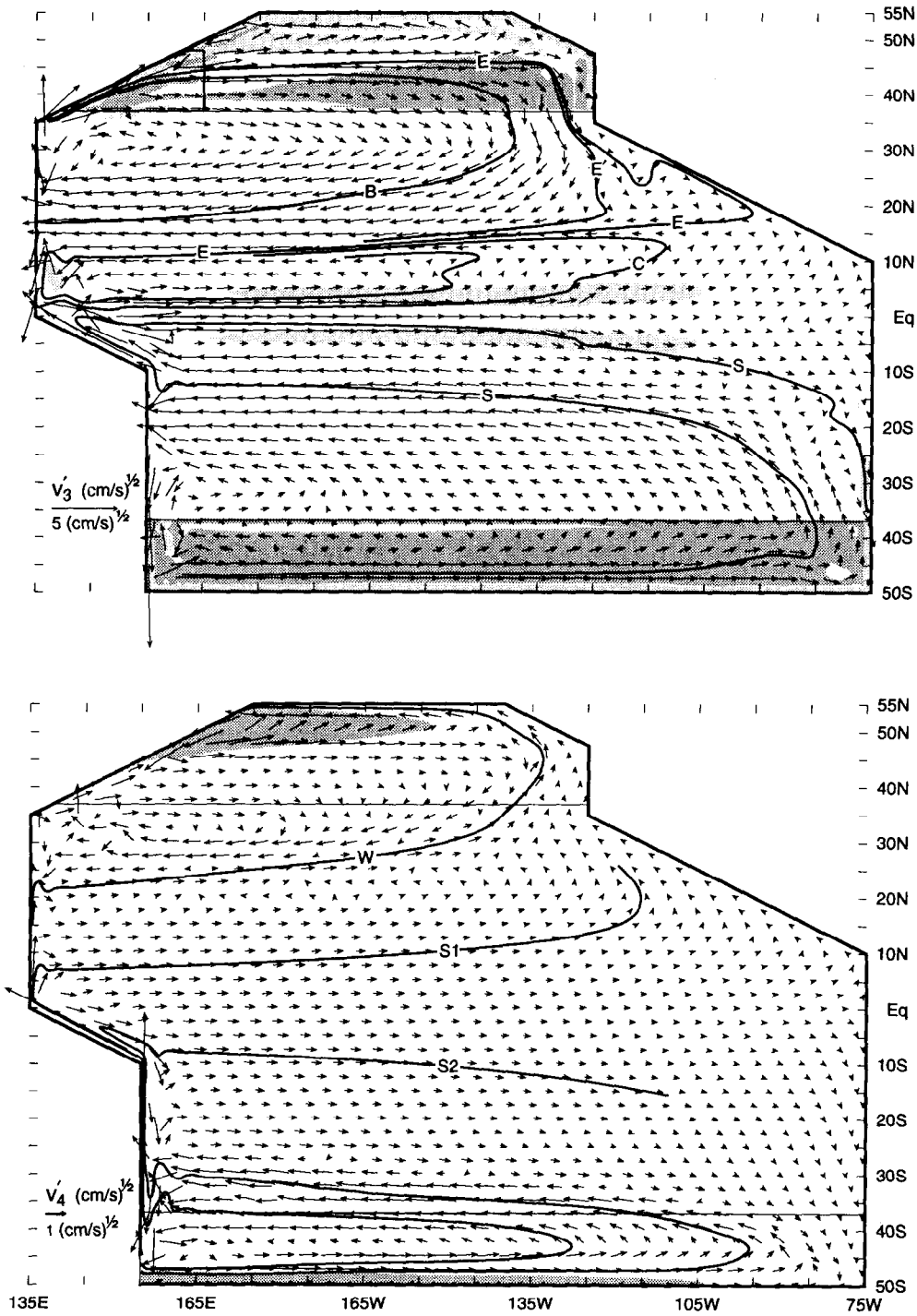


Figure 3: Horizontal distributions of \mathbf{v}_3 (upper panel) and \mathbf{v}_4 (lower panel) for the solution forced by the IOC. Current arrows are of the vector fields $\mathbf{v}'_i = \mathbf{v}_i/|\mathbf{v}_i|^{1/2}$ ($i = 3, 4$), which has the same direction as \mathbf{v}_i but an amplitude of $|\mathbf{v}_i|^{1/2}$; this modification enhances the strength of weak flows relative to stronger ones, allowing them to be more visible in each plot. In the upper panel, the dark (light) shading indicates regions where w_2 is significantly negative (positive). In the lower panel, the shading indicates where w_3 is significantly positive. The trapezoidal region in the upper panel indicates the mixed-water region where NPIW is mostly formed. Definitions of the various streamlines are provided in the text.

At the equator, much of the SPIW flows eastward, eventually filling the entire eastern tropical Pacific east of streamline C . Interestingly, when this eastward current enters the central Pacific, its maximum speeds are located at about $\pm 3^\circ$, and the cores shift away from the equator farther to the east (as indicated by streamlines C and S). These properties are reminiscent of the Tsuchiya Jets (TJs), which are permanent features of the observed Pacific circulation [16], [17], [18]. In this solution, however, the TJs are broader and weaker than the actual ones, likely due to the coarse resolution of the model's grid. Note also that the TJ pathways are not symmetric about the equator: The southern TJ extends to the eastern boundary where it upwells into layer 3 (as indicated by S), whereas the northern TJ recirculates in the tropical ocean from 2°N to 15°N (as indicated by C). These features are in agreement with the observations [17], as well as a solution from a high-resolution GCM (Ishida, 1998, priv. comm.).

Note that both streamlines C and E recirculate within the tropics. If they are extended further, they spiral inward to a central point, a consequence of upwelling of layer-3 water into layer 2 by Ekman pumping associated with the ITCZ. Thus, the area that is (nearly) enclosed by C (and E) is a recirculation region where NPIW and SPIW are necessarily well mixed.

3.2. AAIW

To illustrate the circulation of AAIW, the lower panel of Figure 3 plots \mathbf{v}_4 , together with shaded regions indicating where w_3 is significantly positive and three streamlines. Streamlines $S1$ and $S2$ start at the inflow port in the lower-left corner of the plot, and illustrate typical pathways for the spreading of AAIW throughout the basin. Streamline W extends across the interior of the North Pacific, and defines the dividing line between northward-spreading AAIW and “old” recirculating North-Pacific water.

Similar to the SPIW circulation, water imported into the South Pacific first flows eastward along the southern boundary, then circulates westward and northward within the deepest portion of the southern Subtropical Gyre to intersect the western boundary near 35°S , and finally flows north to the equator in a western-boundary current, consistent with the observed flow of AAIW [8].

When AAIW reaches the equator, most of it turns eastward to fill the tropical ocean, where it slowly mixes upward into layer 3 since $h_3 < 2h_4$. Part of it, however, continues to flow northward as a western-boundary undercurrent, consistent with the observed Mindanao Undercurrent [19], [20]. This western-boundary current turns offshore near 25°N , circulates eastward and northward across the interior ocean, and eventually moves into the subpolar ocean in the far-eastern ocean (streamline W). This interesting interior pathway is an across-gyre “window” that exists in a region where the zonal speed of second-baroclinic-mode Rossby waves vanishes [21], [22], [13]. The IOC water in this northern branch first upwells into layer 1 due to Ekman suction before departing the subpolar region [13].

4. Solution without the IOC

Figure 4 shows the layer-3 and layer-4 flow fields of the solution without forcing by the IOC (*i.e.*, with $M \equiv 0$). In layer 3 (upper panel of Figure 4), streamlines E , B , and C have the same meanings that they do in Figure 3. Streamline S begins at an eastern-boundary convergence point. In this case, NPIW fills the tropical ocean north of streamlines C or S , SPIW is confined entirely within the South Pacific, and there is a recirculation region where SPIW and NPIW are well mixed south of the equator. The layer-4 circulation (lower panel of Figure 4) is weak in this solution since it is not forced by M . Streamline C

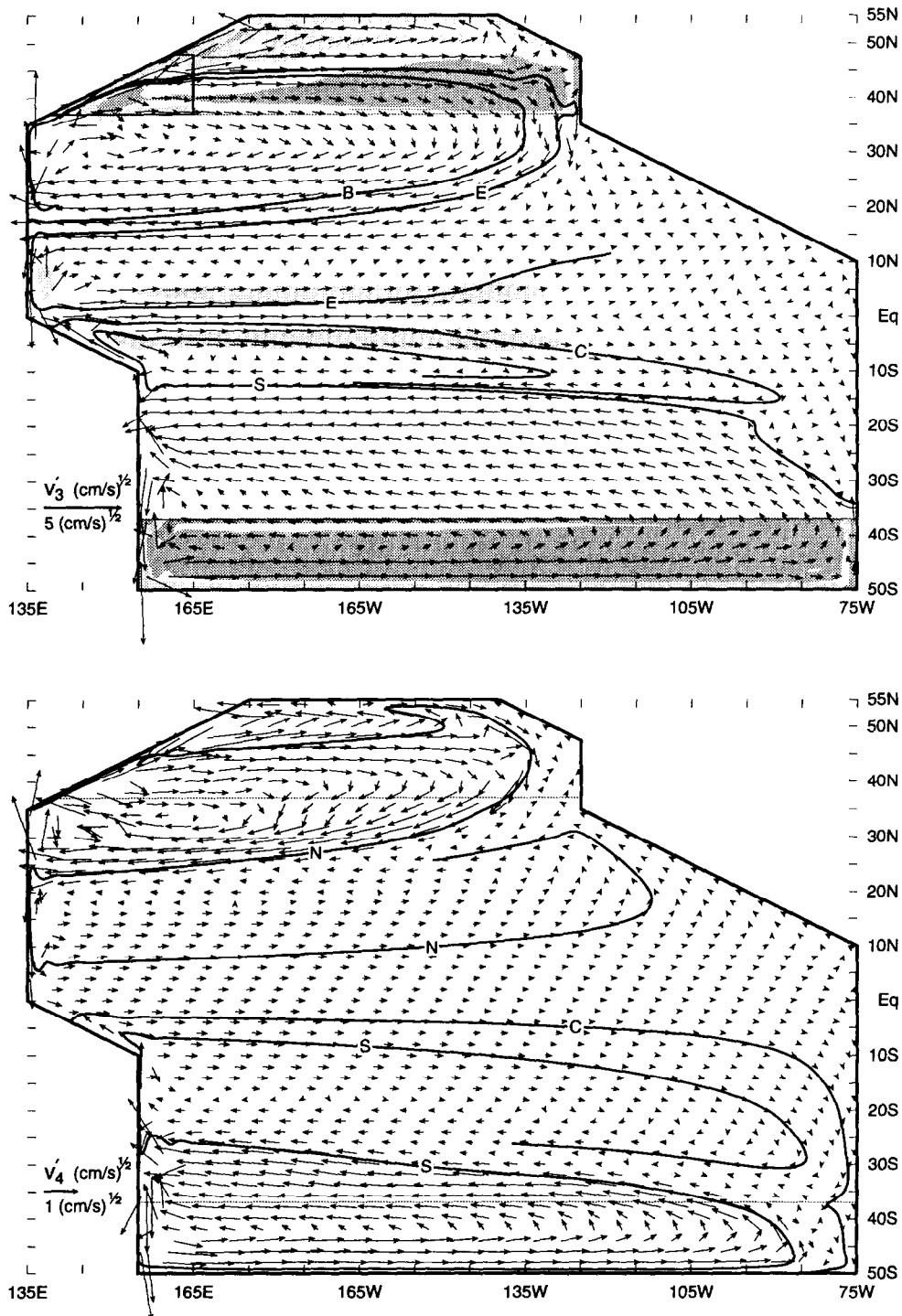


Figure 4: As in Figure 3, except for the solution without IOC and there is no shading in the lower panel. Definitions of the streamlines are provided in the text.

begins at 2°S on the western boundary where the northern and southern water masses converge. Thus, southern-hemisphere water does not spread into the northern Pacific at all.

5. Conclusions

The circulation of intermediate waters is very different in solutions with and without forcing by the IOC. With IOC forcing, nearly all of the NPIW that moves into the tropics exits the basin via the Indonesian Throughflow, SPIW fills much of the tropical ocean, and there is a recirculation region in northern tropics where NPIW and SPIW are well mixed. In addition, AAIW spreads throughout the North Pacific. These properties are all consistent with the observed circulation. Without IOC forcing, NPIW occupies most of the tropics to 20°S, and southern-hemisphere water in layer 4 does not flow north of the equator, properties that differ markedly from reality.

These results suggest that the Indonesian Throughflow is the reason why intermediate waters of southern-hemisphere origin fill the tropical Pacific Ocean and spread to high northern latitudes. Further observational and theoretical work is needed to confirm this conclusion. If proven true, it is a remarkable example of remote forcing, in which outflow in the Indonesian passages determines properties of the intermediate-water circulation throughout the entire Pacific Ocean.

Acknowledgments: This research was sponsored by the NSF grants OCE-95-03379 and OCE-95-21138. We thank Kevin Kohler for his programming assistance.

References

- [1] Bingham, F., and R. Lukas, 1995: The distribution of intermediate water in the western equatorial Pacific during January–February, 1986. *Deep-Sea Res.*, **42**, 1545–1573.
- [2] Wyrtki, K., and B. Kilonsky, 1984: Mean water mass and current structure during the Hawaii-to-Tahiti Shuttle Experiment. *J. Phys. Oceanogr.*, **14**, 242–254.
- [3] Tsuchiya, M., 1981: The origin of the Pacific equatorial 13°C water. *J. Phys. Oceanogr.*, **11**, 794–812.
- [4] McCartney, M.S., and L.D. Talley, 1982: The subpolar mode water of the North Atlantic Ocean. *J. Phys. Oceanogr.*, **12**, 1169–1188.
- [5] Toggweiler, J.R., K. Dixon, and W. S. Broecker, 1991: The Peru upwelling and the ventilation of the South Pacific thermocline. *J. Geophys. Res.*, **96**, 20,467–20,497.
- [6] Talley, L.D., 1993: Distribution and formation of North Pacific Intermediate Water. *J. Phys. Oceanogr.*, **23**, 517–537.
- [7] Reid, J.L., 1986: On the total geostrophic circulation of the South Pacific Ocean: Flow patterns, Tracers and transports. *Prog. Oceanogr.*, **23**, 101–147.
- [8] Tsuchiya, M., 1991: Flow path of Antarctic Intermediate Water in the western equatorial South Pacific Ocean. *Deep-Sea Res.*, **38** (Suppl. 1), s273–s279.
- [9] Gordon, A. L., 1986: Interocean exchange of thermocline water. *J. Phys. Oceanogr.*, **91**, 5037–5046.
- [10] Godfrey, J.S., 1989: A Sverdrup model of the depth-integrated flow for the World Ocean allowing for Island circulation. *Geophys. Astrophys. Fluid Dyn.*, **45**, 89–112.

- [11] Hirst, A.C., and J.S. Godfrey, 1993: The response to a sudden change in Indonesian Throughflow in a global GCM. *J. Phys. Oceanogr.*, **23**, 300–328.
- [12] Gordon, A. L., R.F. Weiss, W.M. Smethie, and M.J. Warner, 1992: Thermocline and intermediate water communication between the South Atlantic and Indian Oceans. *J. Geophys. Res.*, **97**, 7223–7240.
- [13] Lu, P., J.P. McCreary, and B.A. Klinger, 1998: Meridional circulation cells and the source waters of the Pacific Equatorial Undercurrent. *J. Phys. Oceanogr.*, **28**, 62–84.
- [14] McCreary, J.P., and P. Lu, 1994: Interaction between the subtropical and the equatorial ocean circulations: the Subtropical Cell. *J. Phys. Oceanogr.*, **24**, 466–497.
- [15] Hellerman, S. and M. Rosenstein, 1983: Normal monthly wind stress over the world ocean with error estimates. *J. Phys. Oceanogr.*, **13**, 1093–1104.
- [16] Tsuchiya, M., 1975: Subsurface countercurrents in the equatorial Pacific Ocean, *J. Mar. Res.*, **33**(suppl.), 145–175.
- [17] Johnson, G.C., and D.W. Moore, 1997: The Pacific Subsurface Countercurrents and an inertial model. *J. Phys. Oceanogr.*, **27**, 2448–2459.
- [18] Johnson, G.C., and M. McPhaden, 1998: Interior pycnocline flow from the subtropical to the equatorial Pacific Ocean. *J. Phys. Oceanogr.* (Under review.)
- [19] Hu, D., M. Cui, T. Qu and Y. Li, 1989: The western boundary current in the far-western Pacific Ocean. In: *Proceedings of Western Pacific International Meeting and Workshop on TOGA-COARE, May 24–30, 1989, Noumea*, 123–124.
- [20] Hu, D., 1995: Mindanao Undercurrent. In: *China Contribution to Global Change Studies*, Eds. D. Ye *et al.*, China Science Press, Beijing, 168–170.
- [21] Pedlosky, J., 1984: Cross-gyre ventilation of the subtropical gyre: An internal mode in the ventilated thermocline, *J. Phys. Oceanogr.*, **14**, 1172–1178.
- [22] Dewar, W.K., 1991: Arrested fronts. *J. Mar. Res.*, **49**, 21–53.

SIMULATION OF THE VARIABILITY OF THE SUBPOLAR FRONT AND JET IN THE JAPAN (EAST) SEA

Christopher N.K. Mooers¹ and HeeSook Kang¹

¹ Rosenstiel School of Marine and Atmospheric Science, University of Miami, 4600 Rickenbacker Causeway, Miami, FL 33149-1098, USA, cmooers@rsmas.miami.edu, hkang@rsmas.miami.edu

Abstract. Some of the properties of the variability of the Subpolar Front and Jet in the Japan (East) Sea (JES) are simulated with a mesoscale-admitting implementation of the Princeton Ocean Model (POM). A comparison of model output over Days 1,000 to 2,000 of a simulation (with steady atmospheric and throughflow forcing) to CREAMS current meter data in the Japan Basin indicates considerable agreement in the mesoscale band but not for mean values. The simulation indicates that the major JES circulation feature is a cyclonic recirculation gyre which interacts with the bottom topography of the deep Japan Basin and the Subpolar Front and Jet.

Introduction

The Japan (East) Sea (JES) is a semi-enclosed sea connected to adjacent regions by relatively shallow (ca. 200 m) straits [Korea/Tsushima Strait for the inflow (predominantly); Tsugaru and Soya Straits for the outflow (predominantly); and Tatarskii Strait, with negligible throughflow] and several relatively deep (ca. 3 km) basins (Japan, Yamato, and Ulleung Basins) (Fig. 1). Consequently, the upper several hundred meters of the southern half of the JES is stratified, and, in the upper ocean, the East Korean Warm Current (EKWC) flows along the Korean Coast to ca. 38N where it separates and flows eastward along the Subpolar Front as the Subpolar Jet, and the Nearshore Branch (NB) that flows along the Japanese Coast. Mesoscale variability is observed to be ubiquitous. The Subpolar Front is one of the loci of high mesoscale variability.

The Princeton Ocean Model (POM) [1] has been implemented for the JES with ca. 10 km horizontal resolution and 26 sigma-levels, which are concentrated in the surface and bottom boundary layers but are otherwise uniformly distributed in the interior. It is implemented with a smoothed version of DBDB5 bottom topography, and Levitus [2] temperature and salinity field climatologies are used to initialize the model. A variety of sensitivity studies have been accomplished [3] and early results have been summarized [4].

In this study, SOJ-POM is forced with climatological mean throughflow and wind-forcing [5], and relaxation to climatological mean surface temperature and salinity. With the climatological mean mass fields as initial conditions, SOJ-POM spins-up rapidly and considerable mesoscale variability develops, including a meandering, eddy-shedding Subpolar Jet and Front (SJF) system. Here, some of the simulated properties between Days 1,000 and 2,000 are examined. At this stage, the model has settled into a regime where the EKWC bifurcates with a branch that separates further north. First, aspects of the mean and variable fields are described. Second, the means, standard deviations, and spectra of simulated currents are compared with observed currents available in the interior of the deep Japan Basin (JB). Third, some features of the simulated SJF are examined. Finally, the results are summarized.

Mean Fields and Variability

For the interval of focus (Days 1,000 to 2,000), the mean and standard deviation of the seasurface height (SSH) and depth-integrated stream function (ISF) are examined (Fig. 2). The mean SSH field evidences the predominance of EKWC, NB, and SJF in the upper layer of the southern basin, while the Liman Current along the Russian Coast is part of a cyclonic flow in the northern basin, and there is a cyclonic gyre over the deep JB adjacent to the SJF. From the standard deviation SSH field, the variability is greatest near the separation point along the Korean Coast; other high variability zones are located off the Russian Coast and over the deep JB. From the mean ISF field, the cyclonic gyre over the deep JB is the major circulation feature, and that there is also a secondary cyclonic gyre over the southwestern JB. The standard deviation ISF field is dominated by variability over the deep JB that is centered on the mean cyclonic gyre.

The first two vertical EOFs of horizontal velocity components at three fiducial points (Fig. 1) in the JB are examined for the distribution of vertically coherent variability over the water column (Fig. 3). Points S4 and S6 (situated on opposite sides of JB) have very similar EOF1s for both the zonal and meridional velocity

components, both in terms of fractional variance and vertical structure. Their vertical structure is largely uniformly sheared in the upper 500 m and uniform and weak below 750 m, consistent with phase-locked barotropic and first baroclinic dynamical modes. However, the EOF1s for S5 (in the center of JB) are quite different: U1 is almost uniform (barotropic), while V1 is sheared in the lower as well as the upper layer; they also account for a substantially smaller fraction of the variance compared to S4 and S6. Together, EOF1 and EOF2 account for at least 90% of the variance at S4 and S6, but only 87% and 61% for U1 plus U2 and V1 plus V2, respectively, at S5. The exceptional case is U2 because it differs substantially at each point, and only U2 at S4 is similar to V2. Interestingly, U2 at S5 appears to be the first baroclinic mode. Recalling that U1 at S5 has almost a pure barotropic structure, then the barotropic and first baroclinic modes at S5 are not phase-locked in (only) the zonal component. Again, the vertical structure of V2 is very similar at S4 and S6, but rather different at S5; however, they all tend to vanish at the surface.

Comparisons of Model Output and Observations

To help validate the model simulation, comparisons of current time series are made at the location of current meters in moored arrays deployed as part of the CREAMS experiment [6]. The current meters were typically deployed at nominal depths of 1,000, 2,000, and 3,000 m. One year of common data (from AUG93 to JUL94) was used to compare mean and standard deviation profiles. The vertical profiles of mean currents compare poorly: while the observed values were generally less than 1 cms^{-1} , the simulated values were typically several cms^{-1} at the depths of the current meters. In contrast, the standard deviation profiles were largely isotropic and spatially homogeneous (with greatest values in the upper 500 m) and agreed quite closely with the observations, typically within 1 cms^{-1} for values of 1 to 4 cms^{-1} .

The longest observed (3 years) time series available are used to compare with spectra at two depths (2,000 and 3,000 m) (Fig. 5) for each velocity component at S5 (=M3). Overall, there is good agreement for the mesoscale band (10 to 100-day period); i.e., the spectral slopes and energy levels are similar. The observations have a strong inertial peak which is absent in the model output due to the steady forcing. Substantial energy from the "weather band" (1 to 10-day period) is also absent in the model output for the same reason.

Overall, the comparison to observations suggests that the model captures much of the mesoscale variability due to intrinsic dynamical instability, though the mean motions in the lower water column are suspect.

Subpolar Jet and Front

The EKWC bifurcates with the southern branch separating at ca. 38 N and forming the SJF along the southern edge of the JB, and the northern branch separating at ca. 43.5 N and forming a second eastward jet, Fig. 6. These zonal jets are baroclinic in the upper 500 m but penetrate to the bottom (at a depth of ca. 3 km), Fig. 7. While the major features of the circulation are persistent between Days 1,000 and 2,000, they undergo variation; for example, the cyclonic recirculation gyre of the JB intensifies and moves southwestward a few hundred km, Figs. 6 and 7.

Summary

Numerical simulations with SOJ-POM indicate that a cyclonic recirculation gyre over the deep JB is the major, persistent circulation feature in the JES, and it is the locus of maximum variability. Its southern limb is tangent with the SJF. The JB cyclonic recirculation gyre is baroclinic in the upper 500 m and barotropic throughout the water column below. With steady forcing, the intrinsic variability (due to internal dynamical instabilities) of the numerical simulations is comparable to observed values over the JB, especially in the mesoscale frequency band. The numerical simulations also give insight into the role of the JB cyclonic recirculation gyre, its density dome, and its interaction with bottom topography, in controlling the variability of the SJF system.

References

- [1] A.F. Blumberg and G.L. Mellor, in *Three Dimensional Coastal Ocean Models* (Ed., N.S. Heaps). *Coastal and Estuarine Sciences* 4, 1 (1987).

- [2] H.-S. Kang, *University of Miami Technical Report, No. RSMAS-97-008*, 173 (1997).
- [3] S. Levitus, *NOAA Prof. Paper*, 13 (1982).
- [4] C.N.K. Mooers and H.-S. Kang, in *Advanced Mathematics: Computations and Applications* (Eds. A.S. Alekseev and N.S. Bakhalov), NCC Publisher, Novosibirsk, 350 (1995).
- [5] J.-Y. Na, J.-W. Seo, and S.-K. Han, *J. Oceanol. Soc. Korea*, 27, 1 (1992).
- [6] M. Takematsu, Z. Nagano, A.G. Ostrovskii, K. Kim, and Y. Volkov, *J. Oceanog.* (In press).

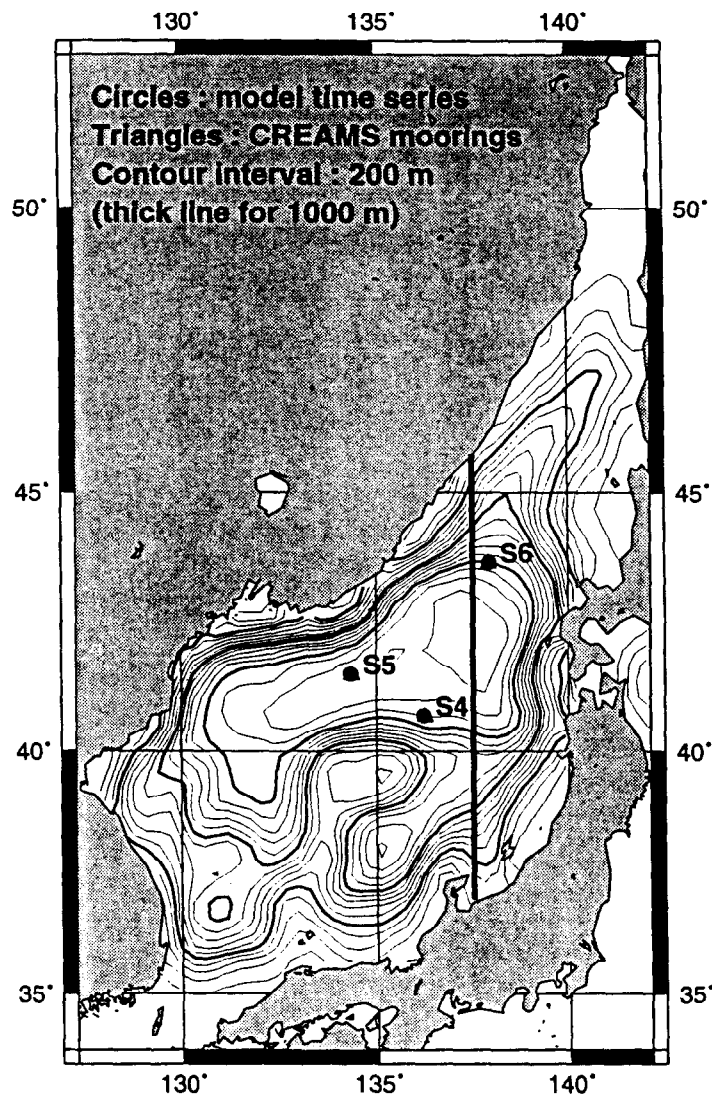


Figure 1. Bottom topography of JES used in SOJ-POM (fiducial points for analysis in Figs. 3, 4, and 5 and the meridional transect used in Fig. 7).

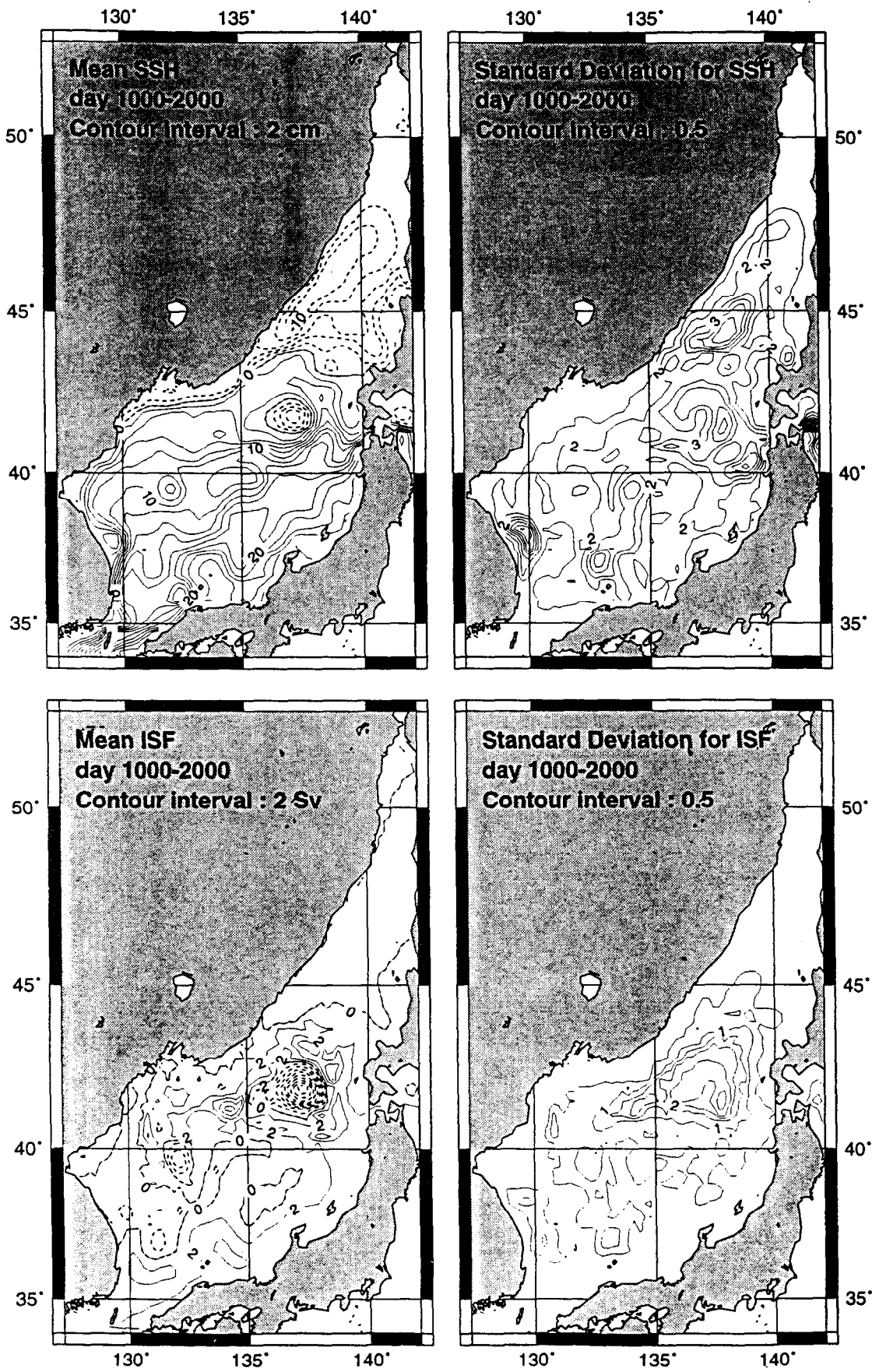
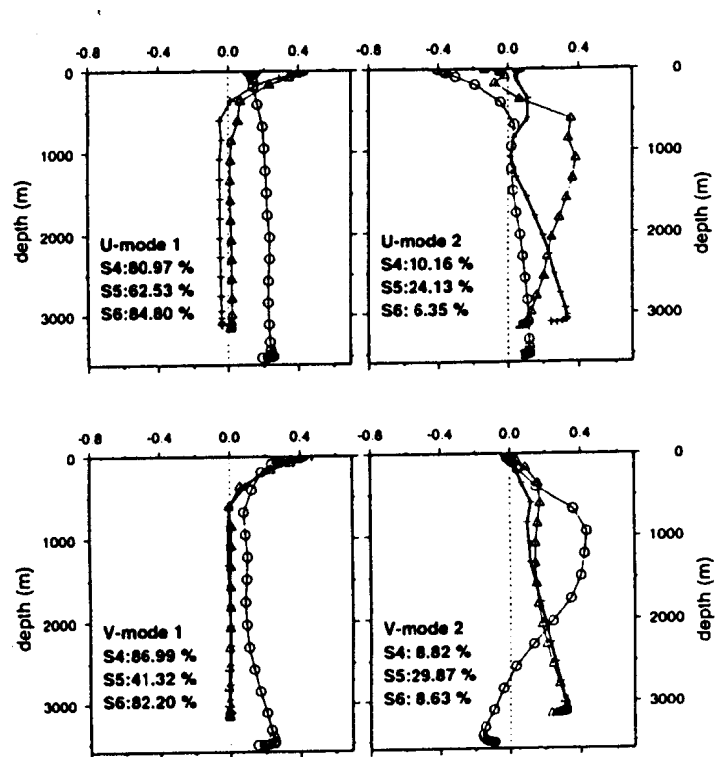


Figure 2. Mean and standard deviation of seasurface height (SSH) and depth-integrated streamfunction (ISF) fields for SOJ-POM from Days 1,000 to 2,000.

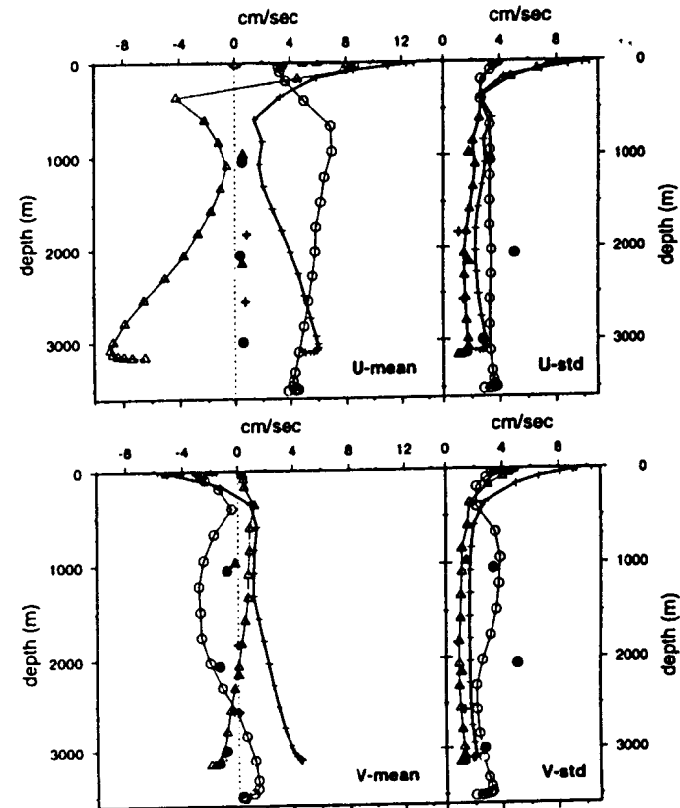


Vertical profiles of horizontal velocity components eigenfunction for the first two modes (P26)

Cross: at S4(136.2E, 40.7N; 3114.5 m)

Circle: at S5(134.4E, 41.5N; 3517.2 m)

Triangle: at S6(137.9E, 43.7N; 3162.6 m)



Vertical profiles of mean velocity and standard deviation

Circles for mooring data

Cross: at S4 (136.2E, 40.7N; 3114.5 m), M2

Circle: at S5 (134.4E, 41.5N; 3517.2 m), M3

Triangle: at S6 (137.9E, 43.7N; 3162.6 m), M1

CREAMS Mooring: Aug. 1993 to July 1994

Figure 3. First two empirical orthogonal functions (EOFs) for SOJ-POM horizontal velocity components at fiducial points over the deep Japan Basin.

Figure 4. Mean and standard deviation profiles of SOJ-POM horizontal velocity components compared to CREAMS current meter data (6) at fiducial points over the deep Japan Basin.

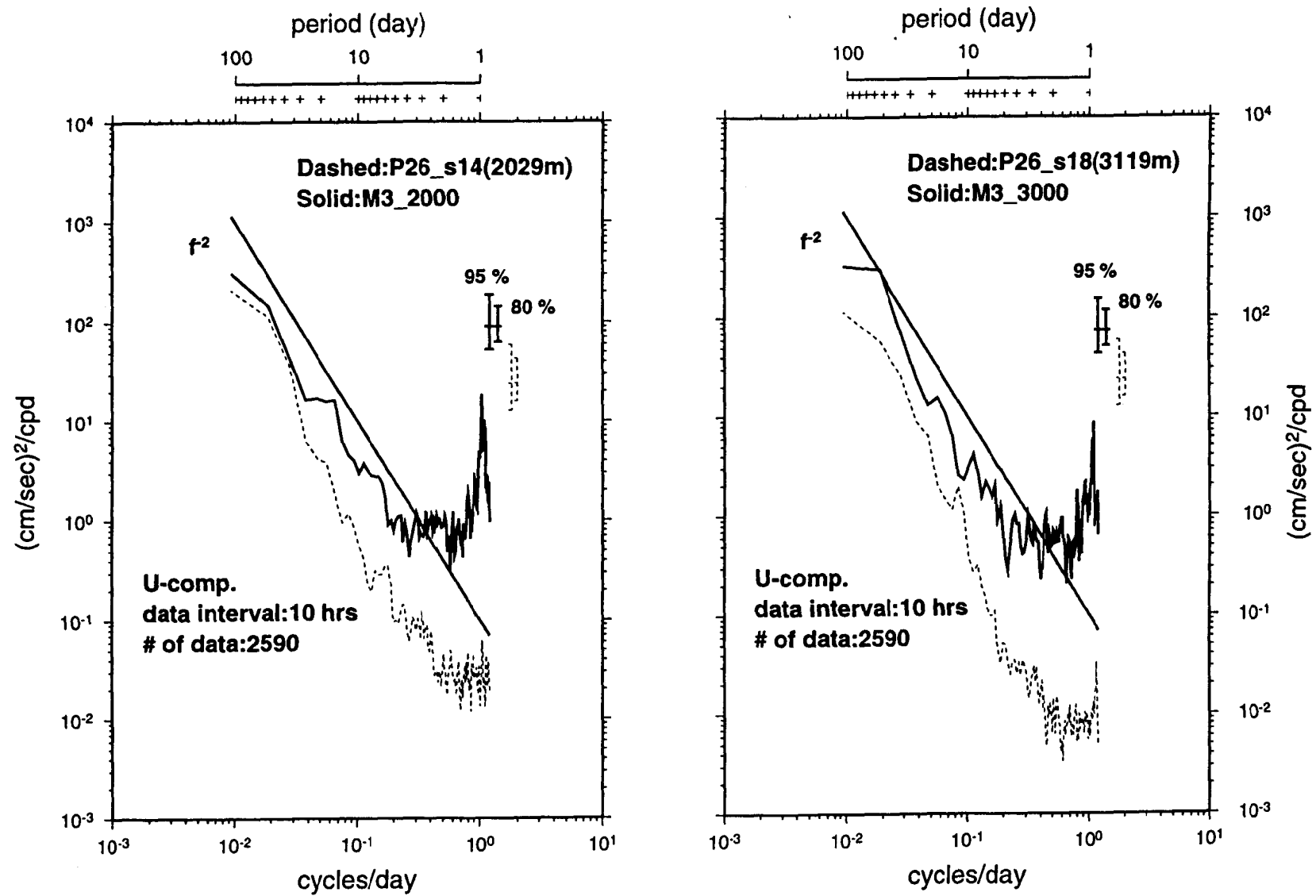


Figure 5. Energy spectra for the zonal component of velocity at S5 (=M3) (left panel: 2,000 m deep; right panel: 3,000 m deep) for ca. 1,000 days; energy spectra for the meridional component (not shown) are almost identical; solid lines: observed values and dashed lines: simulated values.

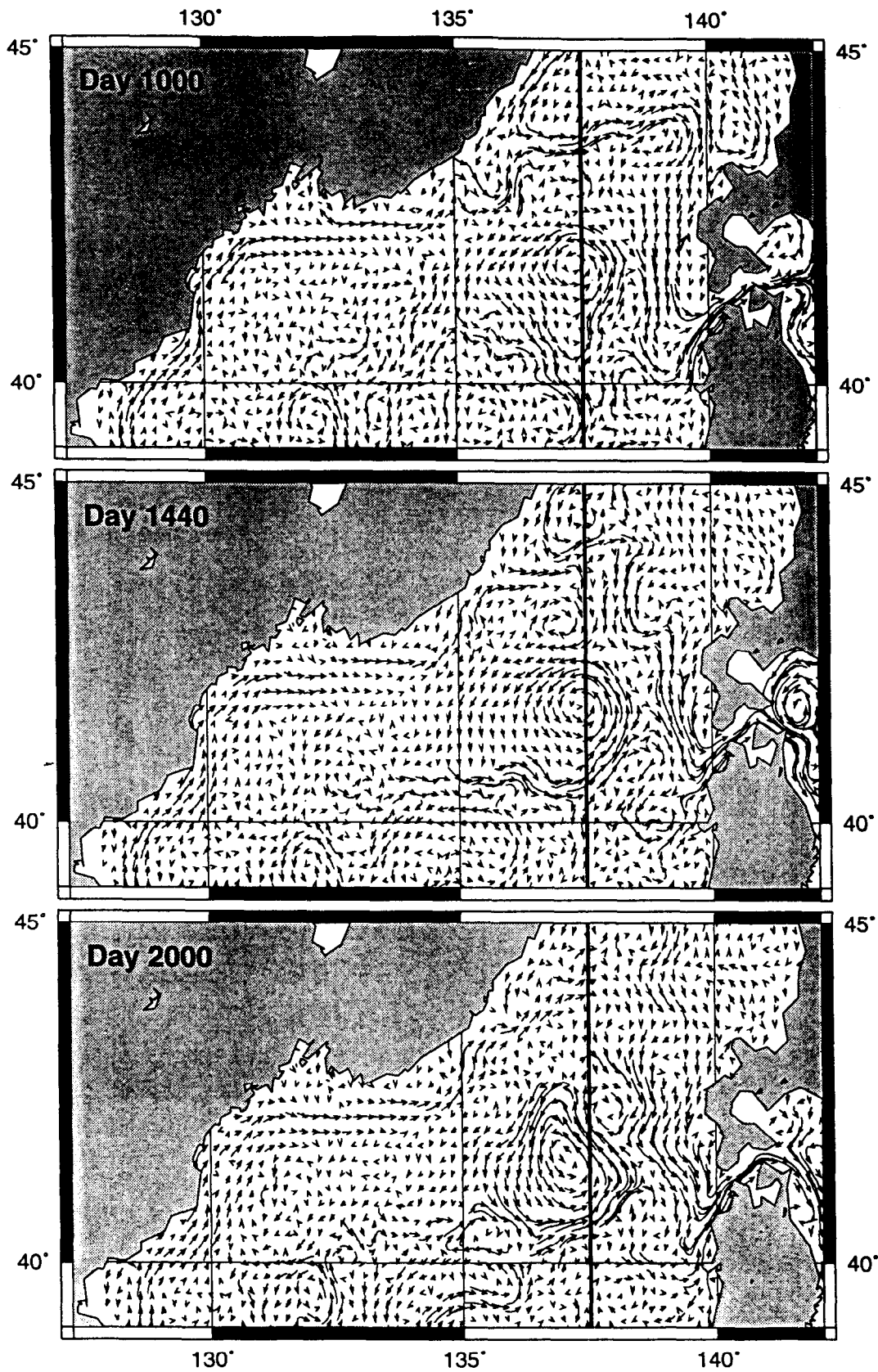


Figure 6. Synoptic surface (3 m) currents in the Japan Basin subdomain of JES on Days 1,000, 1,440, and 2,000. Bold meridian corresponds to locus of transects in Fig. 7.

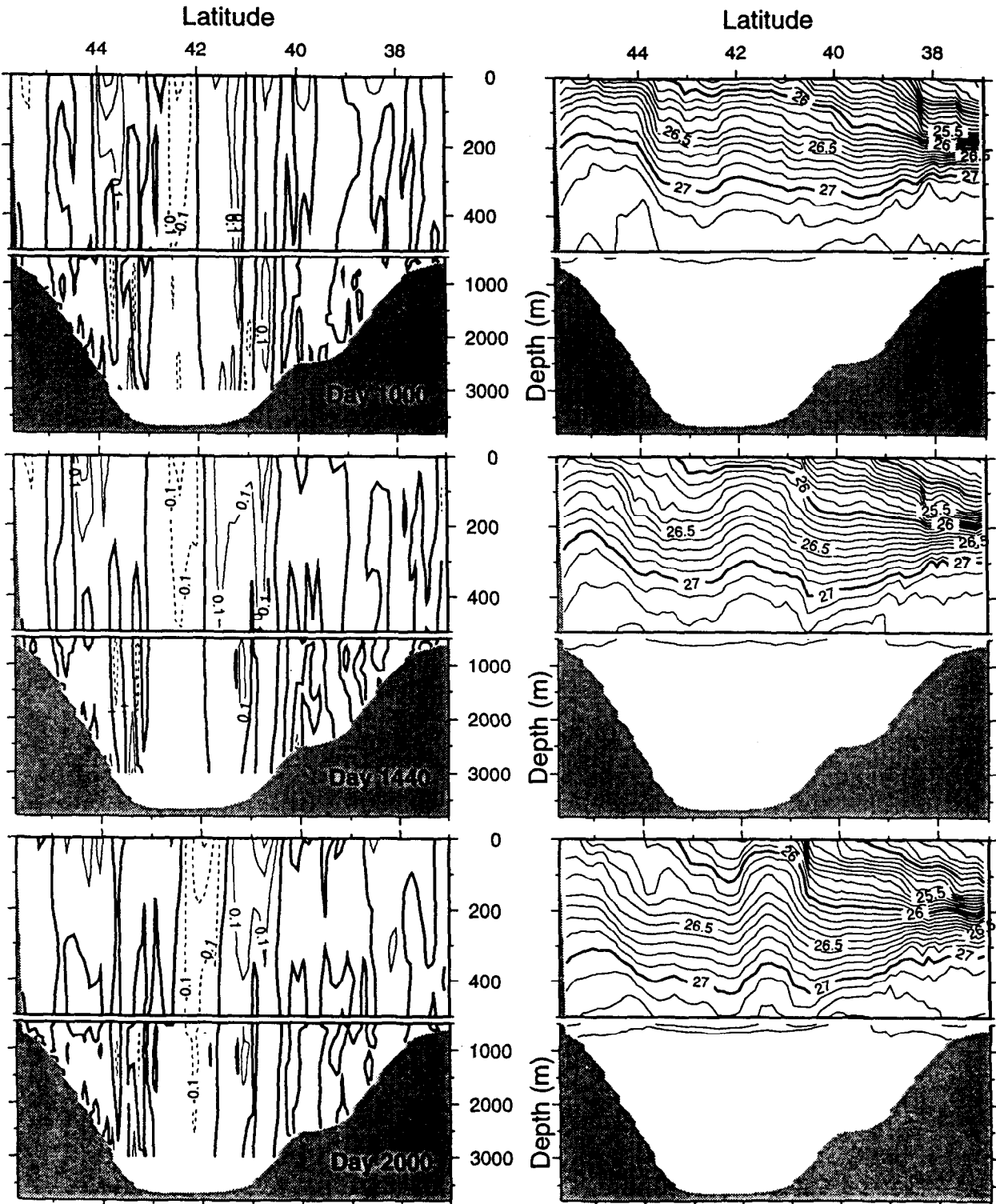


Figure 7. Meridional transects of zonal velocity (left panel) and density (right panel) at 137.5 E on Days 1,000, 1,440, and 2,000 (CI = 0.1 for zonal velocity and sigma-t).

INERTIAL MOTIONS AND INTERNAL WAVES IN THE OCEAN FRONTAL ZONES

V. V. Navrotsky and V. V. Novotryasov

Pacific Oceanological Institute
43 Baltiyskaya St., Vladivostok, 690041 Russia
E-mail: navr@online.vladivostok.ru

Abstract

Inertial motions are observed almost everywhere in the ocean, and distinct peaks in power spectra of velocity and temperature-salinity-density fluctuations are seen near the inertial frequency. The positive shift of maximum from inertial frequency dominates in many observations and leads to the possibility of direct exchange of energy between inertial and internal gravitational waves, especially in the regions of large horizontal gradients of density, that is, in frontal zones. We are analyzing different mechanisms leading to the blue shift, and our explanation is the effect of bottom or upper turbulent boundary layers.

Analysis and estimates

The dispersion relations for pure inertial waves, pure internal gravitational waves and inertia-gravitational waves are as follows:

$$\omega = f \cdot \cos \theta, \quad (1)$$

$$\omega = N \cdot \sin \theta, \quad (2)$$

$$\omega^2 = f^2 \cdot \cos^2 \theta + N^2 \cdot \sin^2 \theta. \quad (3)$$

Here ω is wave frequency, f - inertial frequency, N - Brunt-Vaisala frequency, θ - the angle between wave vector and vertical direction.

It is clear from these relations that f is a resonance frequency for both internal inertia-gravitational waves ($\omega \geq f$) and pure inertial waves ($\omega \leq f$). So it is natural to believe that spectra of velocity and scalar parameters (temperature, salinity) fluctuations will have maximum just at that frequency. But a great number of observations show, that in most cases very distinct energy peaks for current and temperature-salinity-density fluctuations are at frequencies $f \pm \delta$.

The observed values of δ are from 1-3% up to 15-25%, that is, they can be considerably higher than statistical uncertainties. One of interesting features of observational results is predominance of positive values of δ [1]. Here we are trying to explain just this feature and follow its consequences.

Let us look at several possible mechanisms for the frequency shift δ .

1) Generation of inertial motions by the wind tangential stresses [2] leads to the shift

$$\delta_1 = \pm \frac{N}{f} \frac{2\pi}{L} \sqrt{\frac{\mu}{f}}, \quad (4)$$

where N is Brunt-Vaisala frequency, L - horizontal wave-length, μ - effective coefficient of exchange. For general ocean conditions the value of δ_1 is rather small - 1-3%. Close to that value is the result of Gonella [3].

If we use the Pollard and Millard's [4] relation for the effective frequency of wind-generated inertial waves

$$f_e = f \left(1 + \frac{k^2 N^2}{f^2 n^2} \right)^{1/2}, \quad (5)$$

we can obtain as the first approximation for δ :

$$\delta_2 = \frac{1}{2} \frac{k^2 N^2}{f^2 n^2}. \quad (6)$$

Here n is the vertical wavenumber and k is the zonal wavenumber. For the typical ocean conditions we can estimate the positive value $\delta_2 = 3 - 5\%$.

2) Advection by currents (Doppler shift) can be estimated from the relation [5]:

$$\delta_3 = \pm u_0 k \quad (7)$$

and can reach the values 3-5%, the sign depending on current and inertial wave relative direction. But in many cases, where mean current velocity is considerably higher than inertial motion velocity, the positive shift will dominate.

3) Mean current vorticity $\omega = \partial v / \partial x - \partial u / \partial y$ gives for the effective local inertial frequency [6]:

$$f_e = \sqrt{f^2 + f\omega}, \quad \text{and} \quad \delta_4 \approx \omega / 2. \quad (8)$$

For some specific regions (equatorial currents, for example) the blue shift can dominate, but in general it has no preference comparing to the red shift.

Lately van Meurs [7] and Lee and Eriksen [8] have shown, that in frontal zones especially important are gradients of vorticity and Vaisala frequency, as large spatial variability of the vorticity and density fields is characteristic of these zones.

4) Space-time difference between the inertial motion generation and observation processes. Strong inertial oscillations can propagate more than 500 km during 5-10 days [9]. If that propagation is in direction up or down the latitude, the difference between observed and local inertial frequencies can be of order $\pm 10\%$. So, we will have rather stable blue shifts in regions with mean currents from low to high latitudes (western parts of the oceans) and red shifts in regions with mean currents from high to low latitudes (eastern parts of the oceans).

5) Boundary layers. If a boundary layer is produced by inertial and geostrophic currents, it serves to dissipate energy, and amplitude attenuation and frequency decrease are the result. But the feed-back of vertical fluctuations at the boundary of boundary layers is usually not taken into account. We can do that, if we find such velocity $u(x, y, t)$ that matches these vertical motions, produced by the small-scale turbulence in the boundary layer.

We are using the equations for the velocity in the boundary layer and continuity equation:

$$\frac{\partial u}{\partial t} - f v = -\frac{\partial p}{\partial x} + \frac{\partial}{\partial z} \left(\mu \cdot \frac{\partial u}{\partial z} \right), \quad (9)$$

$$\frac{\partial v}{\partial t} + f u = \frac{\partial p}{\partial y} + \frac{\partial}{\partial z} \left(\mu \frac{\partial v}{\partial z} \right), \quad (10)$$

$$\frac{\partial \mathbf{u}}{\partial x} + \frac{\partial \mathbf{v}}{\partial y} + \frac{\partial \mathbf{w}}{\partial z} = 0, \quad (11)$$

$$\mathbf{u} = \mathbf{v} = 0 \text{ for } z = 0, \quad \mathbf{u} = U, \quad \mathbf{v} = 0 \text{ for } z = h, \quad (12)$$

where $h \ll H$ is the boundary layer height, U is the velocity in the ocean interior (generally the sum of geostrophic current and inertial oscillations).

Using the nondimensional functions

$$\zeta = zf / U, \quad \varphi(\zeta) = u / U, \quad \psi(\zeta) = v / U, \quad (13)$$

we obtain the system, which can be easily integrated:

$$\frac{d}{d\zeta} \left(\mu \frac{d\varphi}{d\zeta} \right) - \psi = 0, \quad (14)$$

$$\frac{d}{d\zeta} \left(\mu \frac{d\psi}{d\zeta} - (\varphi - 1) \right) = 0, \quad (15)$$

$$\bar{w}_h = \int_0^\infty \nabla \cdot \bar{\mathbf{U}} \cdot d\zeta, \quad (16)$$

$$\varphi = \psi = 0 \quad \text{for } \zeta = 0, \quad (17)$$

$$\varphi = 1, \quad \psi = 0 \quad \text{for } \zeta \rightarrow \infty. \quad (18)$$

Integrating (16) with

$$\bar{\mathbf{u}} = \begin{vmatrix} \varphi(\zeta) - \psi(\zeta) \\ \psi(\zeta) \quad \varphi(\zeta) \end{vmatrix} \cdot \bar{\mathbf{V}}, \quad (19)$$

we obtain

$$\bar{w}_h = \frac{1}{f} \text{rot}_z \left\{ s_0 |\bar{\mathbf{V}}| \bar{\mathbf{V}} + s_1 |\bar{\mathbf{V}}| [\bar{\mathbf{k}} \times \bar{\mathbf{V}}] \right\}, \quad (20)$$

where $s_0 = \int_0^\infty \psi(\zeta) d\zeta$, $s_1 = \int_0^\infty (1 - \varphi) d\zeta$ are positive constants. Using these relations and (19), we

can obtain for the near-inertial velocity $\bar{\mathbf{V}}$ the equation:

$$\partial \bar{\mathbf{V}} / \partial t + \left(1 + \frac{s_1}{s_0} \frac{|\bar{\mathbf{V}}|}{D_0 f} \right) \cdot f \cdot (\bar{\mathbf{k}} \times \bar{\mathbf{V}}) = \frac{1}{\rho} \nabla(p + \phi) - \frac{1}{D_0} |\bar{\mathbf{V}}| \bar{\mathbf{V}}, \quad (21)$$

where $D_0 = H / s_0$.

We can see, that effective inertial frequency is augmented by the positive value

$$\delta_5 = \frac{s_1}{s_0} \frac{|\vec{V}|}{D_0 f}. \quad (22)$$

Our estimates show that due to the feed-back of boundary layers we can have always positive value of order 5-10% for the relative shift δ of inertial frequency.

Discussion

We know that a large amount of the Earth rotation energy is given to movements in the ocean and atmosphere. And we know from observations that internal gravity waves have maximum energy near the inertial frequency f . But modelling the direct excitation of IW by pure inertial motions is not possible because of peculiarities in the equations for both pure inertial oscillations and gravitational internal waves at frequency f .

Now we have shown that most of inertial oscillations should have frequencies a little higher than f because of interaction with turbulent boundary layers. Free inertia-gravitational internal wave have the widest range of eigen modes and corresponding wavenumbers near the inertial frequency. In this case horizontal inertial motions excited in zones with large horizontal gradients of density (that is, in zones with inclined isopycnals) will force vertical motions at frequencies $f + \delta$ and in such way generate internal gravity waves in the resonance regime just at frequencies, where maximum energy peaks are observed.

So, the frontal zones in the open ocean and along shelves should be and really are the zones with maximum energy of near-inertial internal gravity waves.

References:

1. K.V. Koniayev and K.D. Sabinin, 1992. Waves in the ocean interior. Hydrometeoizdat, St.-Pet., 272 p.
2. M. Tomczak, 1968. Uber interne Wellen in der Nahe der Tragheitsperiode. Deutsche Hydr. Zeif., 21, H. 4, 145-151.
3. J. Gonella, 1971. A local study of inertial oscillations in the upper layers of the ocean. Deep-Sea Res., 18, 775-778.
4. R.T. Pollard and R.C. Millard, 1970. Comparison between observed and simulated wind-generated inertial oscillations.. Deep-Sea Res., 17, 813-821.
5. W.B. White, 1972. Doppler shift in the frequency of inertial waves observed in moored spectra. Deep-Sea Res., 19, 595-19,600.
6. P.-M. Poulaine, D.S. Luther and W.C. Patzert, 1992. Jour. Geophys. Res., 97, C11, 17947-17959.
7. P. van Meurs, 1998. Interactions between near-inertial mixed layer currents and the mesoscale: the importance of spatial variability in the vorticity field. Jour. Phys. Oc., 28, 1363-1388.
8. C.M. Lee and Ch.C. Eriksen, 1997. Near-inertial internal wave interactions with mesoscale fronts: Observations and models. Jour. Geophys. Res., 102, C2, 3237-3253.
9. E. Firing, R.-Ch. Lien and P. Muller, 1996. Observations of strong inertial oscillations after the passage of tropical cyclone Ofa. Jour. Geophys. Res., 101, C2, 3317- 3322.

FORECAST POSSIBILITY OF THE KUROSHIO FRONT MEAN POSITION

Alexander D. Nelezin

Pacific Oceanological Institute, Far Eastern Branch, Russian Academy of Sciences,
Vladivostok, Russia (E-mail: alexander@poi.marine.su)

Abstract. Variability of the Kuroshio front mean position is studied in dependency on the subtropic gyre currents intensity. Principal possibility of the seasonal prediction of the front position is revealed.

Having stated the global climatic problems, the ocean climate and its variability shall be investigated. At the present stage of great concern are non-quasistationary multi - year climatic background but the tendencies of the background changes for some decades, such changes can occur even on local spatial scales. The ocean climate has been studied much worse if compared to the atmosphere one [5].

The process interdependence from the small scales to planetary ones has a great importance for the oceanic trend understanding in the climate changes. The temporal - spatial diagrams show that the atmosphere and the upper ocean layers are evidence of the rapid part of the Earth climatic system, but the deep sea layers are the slow ones [4]. The ocean is a basic mechanism of the longterm fluctuation in the system - ocean- atmosphere, therefore, to describe the climatic changes in an actual way its state shall be studied.

Thus, to obtain information required, to make a choice of averaging scales and providing of the fields in a form of the sum of the trend components and random "adds" we shall know the spectral structure of the ocean hydrophysic fields. To divide the fields as determined and random components is an equivalent to the fact that the field studied has in its composition a number of structures of the fixed scale.

The annual ocean surface temperatures averaged by the space under the condition of the long term set and the interannual changes smoothing are the ocean parameter of the climate significant.

Nevertheless, the processes investigation in the most upper ocean layer by the OST data is not enough basic for understanding of its role in the climatic system. The result analysis of the previous studies demonstrates that in some cases trend revealing problem has been solved rather strictly, however, in many examples the initial data have been distributed irregularly in time [2]. So, to discover the climatic tendencies we shall systematize (classify) the deep sea data being available and provide the observational system arrangement.

The north-west Pacific has enemas biological resources, the marine environmental monitoring shall be arranged for their right exploration [8]. A certain feature of the N-W Pacific is the Subarctic front, it is zone of the cold subarctic and warm Kuroshio waters contact. The spatial-temporal oceanic front variability is referred to a number of the basic indications [1], but on the Kuroshio front there is very little information. The basic difficulty for oceanic front problem decision is their non-stationary. The

ocean role understanding in the climatic system relates to a problem of the meridional transport correct estimation which is one of the essential mechanism in the Earth climate formation. In addition, monitoring of the current discharges has a special climatic meaning.

For the tendency of actual problem decision, we have considered variability of the North Trade current discharges in parallel with the Kuroshio one along 137° E in 1972-1991, an interaction of them has been determined in quantitative way, a systematic component of the temporal fluctuations has been revealed. Multi-year variations (1965-1991) of the Kuroshio front mean position (140-150° E) eastward the Honshu Island have been studied, in which the similar tendencies to the current discharge changes of the Pacific subtropical gyre have been discovered.

The vertical temperature section crossing the Subarctic front were constructed along the section of 145° E based on multi-year oceanographic data collected in February and August. The figure shows that the frontal zone transforms significantly from winter to summer in the upper oceanic layer, but it is well distinguished in the layer of 150-300 m.

The front position was marked on each longitude from 140° to 150° E, and then the value corresponding to the average front position eastward from the Honsu Island was calculated. To improve the accuracy of our calculations the characteristic isotherm (isohaline) in zone of maximal gradients was assumed as a criterion of the front.

The preliminary analysis suggested that the isotherm 13° C and isohaline 34.6 ‰ at the level of 200 m, located in the Kuroshio current zone, are the most informative for the Subarctic front within the region of 140-150°E. Therefore, for further investigations the term Kuroshio front was used appropriate to the chosen criterion.

The annual variability of the front position is characterized by the northeast displacement in December and by the southeast in April. During the cold period (December- April) the rapid front displacement southward is observed and then the relative smooth fluctuation of its northward movement occurs [6].

Interannual front position variations are one of the basic indicators of the ocean thermodynamic regime, but the shortage of information regarding this problems is obvious. To investigate the multi-year Kuroshio front variability, the mean front position (within the region of 140-150°E) and standard deviations were calculated using the seasonal mean temperatures at the level of 200 m from observational data collected in 1965-1991. The isotherm of 13°C was also assumed as a criterion of the front [6].

In 1965-1977 a tendency for the front to move northward from 35.5 to 37°N was observed, then in 1978-1986 the front shifted southward (to 35.2°N) and in the latter period the inverse shearing to 36.4°N (in 1991) occurred. The Kuroshio front was located in the extreme north and south positions in autumn of 1977 (37.6°N) and in summer of 1986 (34.7°N), respectively. The front meandering decreased in 1965-1977 and increased in 1978-1985.

The front meandering is a wave of the current track deviation (bending) which is a consequent of eddy detachment, and is considered as one of the basic reasons for the spatial front position variability. Apparently, it is under the influence of quasi-stationary meanders and Rossby waves, associated with the non-stationary Kuroshio. The quasi-stationary meanders were well distinguished by the averaged spatial front position for all four seasons for the period of study. The greatest meander amplitude was observed in winter, while in the warm period the front shear became more sloping.

Multi-year variability of the average front position is influenced by the water circulation intensity on the western periphery of the subtropical gyre [3]. Fig. 1 presents the calculation results of the arithmetic mean of the North Trade and Kuroshio currents discharges as well as the Kuroshio front mean position in 1972-91. The calculated correlation rate (0,52) is significant; the values of discharges were obtained in January, June, and front position - in May, November.

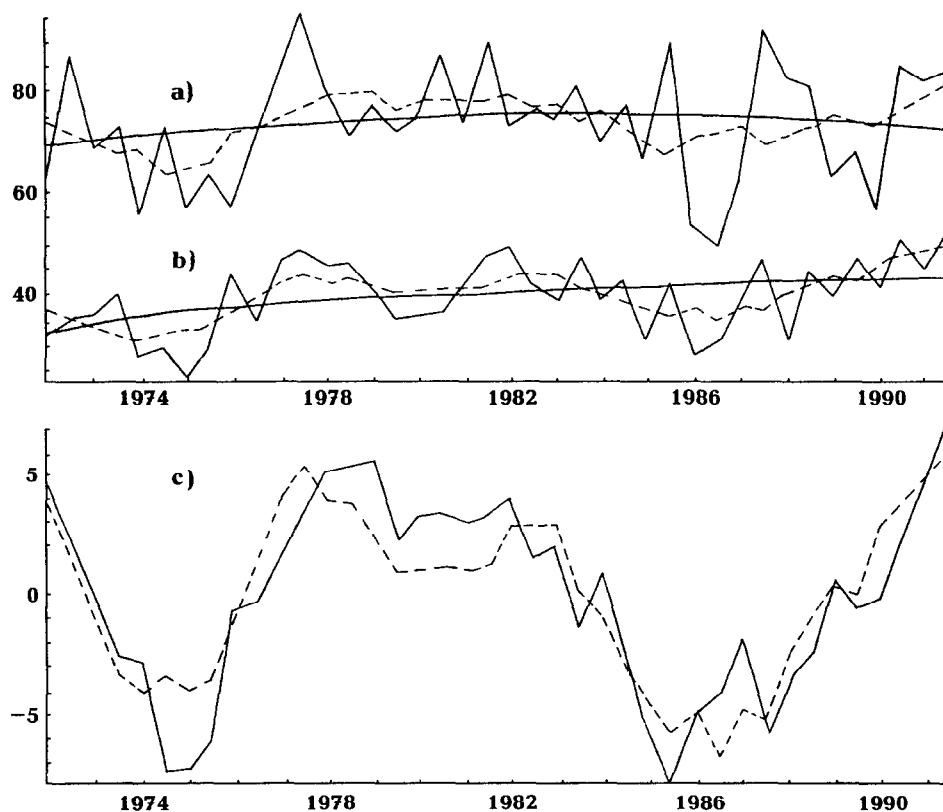


Fig. 1. Temporal variation of the subtropical gyre discharges (10 m/s) and the Kuroshio front mean position in 1972-1991 years the components smoothed by the trend parabolic model.

The physical base of the relation stated is evidence that the water circulation intensity on the western periphery of the north subtropical gyre determines the heat quantity removal from the Pacific tropical zone. The mean front position eastward the Honshu Island depends on the heat quantity incoming, so, the subtropics water gyre circulation has the more intensity, the Kuroshio front has location more northern. The cross-correlation function calculation showed the negative relation of 95 % level of significance with a maximal value within a shift of 4,5 years.

Taking into consideration the different directions of trends, the initial data sets filtration by the correspondent frequency filter has been fulfilled. The residual temporal variation sets are evidence of the high level relation (0.79) of multi-year changes within the range of mean discharge values of the subtropical water gyre and the Kuroshio front position (Fig. 2).

The quantitative dependence stated is a basis for the background forecast development, as by the discharge value known, a tendency of the Kuroshio front mean position variations can be determined.

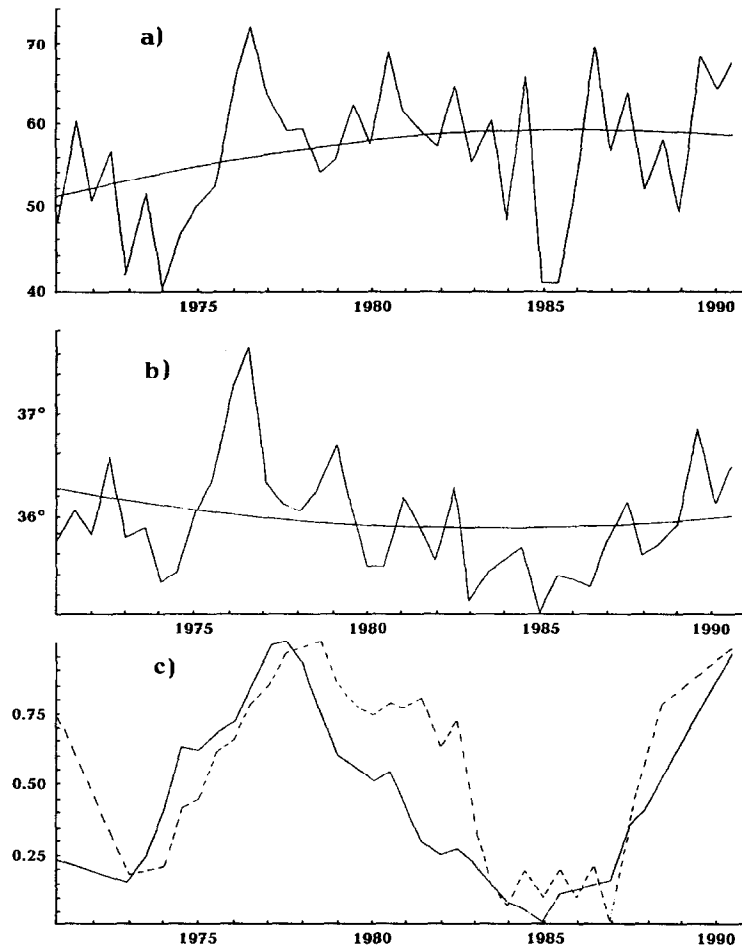


Fig.2. Temporal variations of the North Trade and Kuroshio currents discharges (a,) mean position of the Kuroshio front (b) in 1972-1991, residual curves (in relative scale) of mean values of the subtropic gyre discharges (dotted line) and the Kuroshio front position after filtration and removing trend components (c).

REFERENCES

1. Fedorov K. 1983. Physical nature and structure of ocean fronts. Gydrometeoizdat, 295 p. (in Russian).
2. Gulev, S., D. Kadaev, and I. Yashaev. 1988. Synoptic variability of sea water temperature in the Gulf Stream and the North Atlantic currents. *Oceanology*. 28(5): 721-727 (in Russian).
3. Kort, V. 1970. The large-scale ocean-atmosphere interaction (the North Pacific). *Oceanology*. 10(2): 222-240 (in Russian).
4. Mamayev O. On space-time scales of an ocean and atmosphere. *Oceanology*. 35(6): 805-808 (in Russian).
5. Monin A. 1993. About ocean climate. Report of Academy of sciences. 328(3): 395-398 (in Russian).
6. Nelezin, A. 1996. Variability of the Kuroshio Front in 1965-1991. PICES SCIENTIFIC REPORT. 6: 124-130.
7. Uda M. 1938. Researches on "Siome" or current rip the seas and oceans. *Geoph. Mag.* 2(4): 306-372.

Antarctic Circumpolar Wave and Oceanic Fronts

A. G. Ostrovskii^{1,2} and T. Setoh³

¹Research Institute for Applied Mechanics, Kyushu University 87, Kasuga 816, Japan

²P.P. Shirshov Institute of Oceanology, RAS, Nakhimovsky 36, Moscow 117851, Russia

³Graduate School of Earth Science & Technology, Kyushu University, Kasuga 816, Japan
(e-mail: sasha@king.riam.kyushu-u.ac.jp)

Abstract. The SST component of the Antarctic Circumpolar Wave (ACW) is extracted from the NMC SST data set by means of a wavelet technique as a wave-like disturbance, having the scales of 2.7 - 5.5 years and 1/4 - 1/2 of the zonal circle, that propagates eastward in the latitudinal belt between 40°S and 63°S. The wavelet analysis demonstrates deviations of the ACW propagation indicating that this phenomena is less regular than it was thought. There are indications that the ACW is modulated by the biennial processes. The ACW is confined to the South Polar Front Zone at the longitudes of 160°W - 20°E where the ACW and the SST meridional gradient are highly correlated. The ACW anomalies contribute significantly into zonal variations of the Polar Front in this region.

1. Introduction

Recently, White and Peterson [1] found an eastward travelling large-scale anomaly in the ocean-atmosphere system near South Pole: the monthly deviations from average annual cycles in the atmospheric pressure at sea level, the meridional wind stress, the sea surface temperature (SST), and the sea-ice extent propagate with speed of 0.06-0.08 m/s and period of 4-5 years, taking 8-10 years to encircle the pole. The wave-like pattern of this phenomena was called Antarctic Circumpolar Wave (ACW). Its cycle was described in terms of the EOF modes [1]. More recently, it has been hypothesized that the ACW as an entity represents the result of moving oceanic climate anomalies interacting with a spatially fixed atmospheric forcing pattern [2]. Here we focus on certain details of the SST variability related to ACW, which have not been discussed yet, namely relationships between the ACW and the variations of neighboring frequencies and wavenumbers, secular changes in the ACW, and interactions between the ACW and the fronts in the Southern Ocean.

2. Wavelet Analysis of the Sea Surface Temperature Data

We use the OISST product (NMC, NOAA) that comprises the high-resolution optimum interpolation analysis of the in situ (ship and buoy) data, satellite retrievals, and sea-ice coverage data [3]. The data are provided on a weekly basis over 1°x 1° global grid and the time series from October 1981 to December 1997 are available for this study.

For data analysis we chose a wavelet method, which is known to be powerful in detecting singularities such as regime shifts in climate time series (e.g. [4]). We use a harmonic wavelet technique [5] whose analyzing wavelet is constructed of trigonometric functions:

$$w(2^j x - k) = \{\exp(i4\pi(2^j x - k)) - \exp(i2\pi(2^j x - k))\} / i2\pi(2^j x - k), \quad (1)$$

where x is the time or space coordinate, $j = 0$ to ∞ is the level or scale index and $k = -\infty$ to ∞ is the position index. It is compact in Fourier space, acquiring the skills of a band-pass filter, though it is not completely compact in physical space. The spectrum of the harmonic wavelet is exactly like a box so that the magnitude of its Fourier transform is nil except for an octave band of frequencies. In other words, the wavelets of different levels have Fourier transforms that occupy different frequency bands.

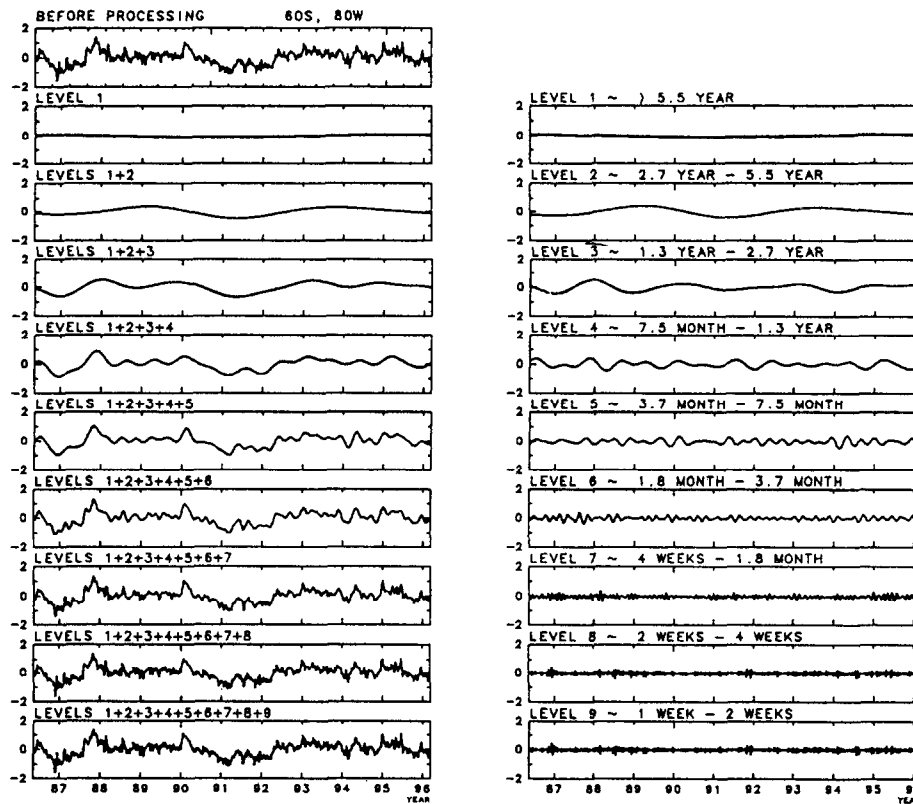


Fig. 1. The wavelet analysis of the SST anomaly time series at 60°S, 80°W. The original time series is shown at the top of the left half of the figure. The plots below the original time series represent sequential reconstructions. The individual wavelet components are shown in the right half of the figure. The vertical axes are for the temperature in °C.

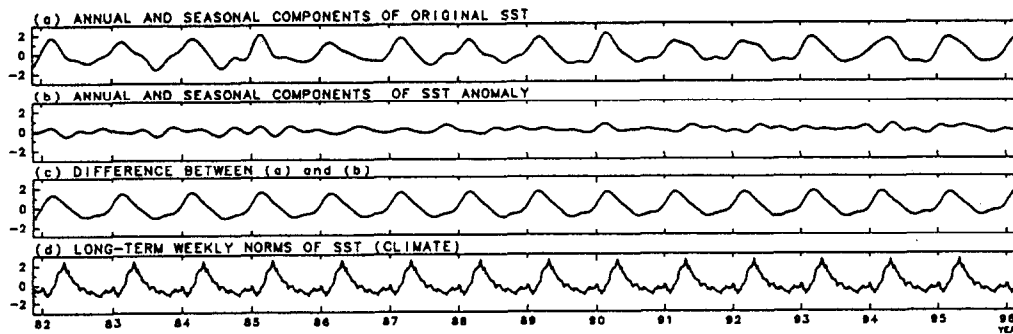


Fig. 2. (a) The wavelet reconstruction of the sum of the annual and seasonal modes of the SST variability at 60°S, 80°W. (b) The wavelet reconstruction of the sum of the annual and seasonal modes of the anomalous (nonseasonal) SST variability at 60°S, 80°W. (c) The time series received by subtracting (b) from (a). (d) The long-term weekly norms that were removed from the original time series to get the SST anomalies whose annual and seasonal modes were reconstructed as in (b). The vertical axes are for temperature in °C.

Numerical implementation of the harmonic wavelet transform is rather simple and a MATLAB code can be found in [5]. The method requires the data series of the length 2^n . In standard case, the signal is assumed to be periodic out of observational domain. Notably, the latitudinal belt of 56-62°S in the Southern Ocean is the only region of the World Ocean where it is possible to arrange the data along the zonal circles thus far satisfying the periodicity assumption. While analyzing the data, we compiled two overlapping time series each of 512 weekly observations. We use both 1D (in time) and 2D (along zonal circle and in time) wavelet analyses. The former

allows a description of the SST spatial patterns at different temporal scales of resolution, while the latter focuses on the SST ACW mode, which propagates zonally around Antarctica.

Fig. 1 shows results of the 1D decoding - encoding wavelet transform of the SST anomaly time series at 60°S, 80°W. The wavelet decomposition allows us to obtain the wavelet modes (Fig. 1b), i.e. oscillating signals of different wavelengths. The set of modes is defined on a dyadic grid of scales, called levels, where each scale is twice as long as the preceding one. The original time series can be reconstructed by summing up the individual modes as in Fig. 1a. Notice that the sum of the annual and seasonal modes (7.5 months - 1.3 year and 3.7 - 7.5 months, respectively) of the anomalous SST variability (Fig. 2b) indicates irregularity of the annual variation, for example an early onset of season in individual year.

3. Results

3.1. Variability at the Biennial and ENSO/ACW Time Scales

The variances at multiple time scales are computed from the wavelet modes such as those shown in Fig. 1b. Fig. 3 shows the contributions of the modes, having the biennial and ENSO time scales (1.3-2.7 years and 2.7-5.5 years respectively), to the SST anomaly (nonseasonal) variance over the Pacific Ocean. The ENSO contribution is highest, ~85%, near 7°S, 110°W. Other two regions of the enhanced loadings of the 2.7-5.5-year variations are the midlatitudes of 30°-50°N in the eastern North Pacific and the high latitudes of 50°-70°S in the eastern South Pacific. In the southern hemisphere, the ENSO contribution is high in the tropical region stretched from 0°S, 150°E to the South American coast between equator and 20°S; the maximum occurs near 5°S, 110°W.

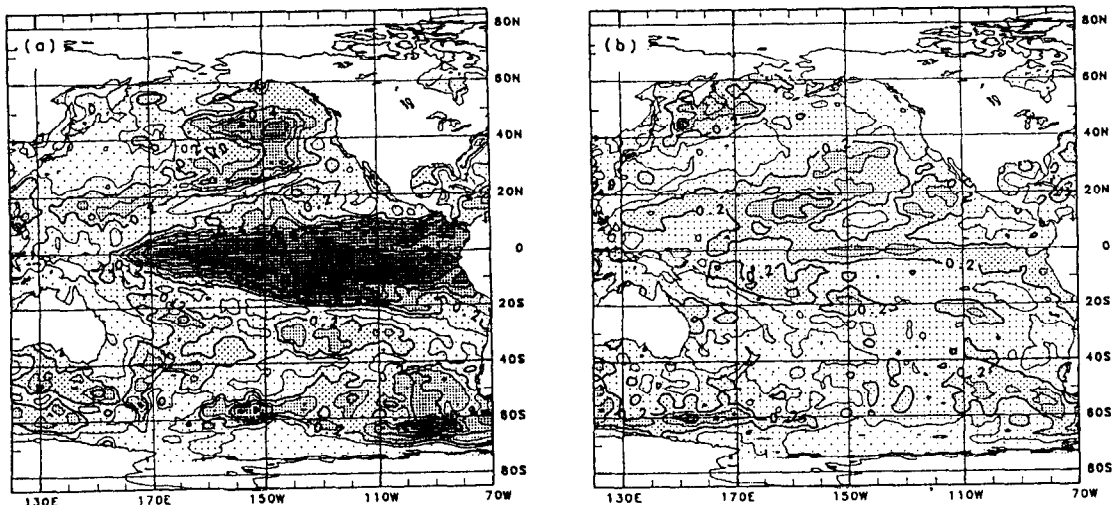


Fig. 3a. (a) The ratio of the SST variance, having the time scale of 2.7 - 5.5 years, to the SST anomaly variance over the Pacific Ocean, (b) the same but for the loading of the biennial (1.3 - 2.7 years) SST variance.

As to the biennial mode in the tropics, its local maximum is shifted northwestward, towards equatorial region at 125°-140°W, as compared with the off-equatorial maximum of the ENSO mode. To the north and to the south from the zonal belt of 10°N - 10°S, the biennial mode loadings are largest (up to 20-40%) beyond the areas where the ENSO dominates.

In the Southern Ocean, the modes, having the biennial and ENSO time scales, are in the 'seesaw' relationship, too: the biennial variability increases in the regions where the variability of 2.7-5.5 years tends to decline, for example contribution of the former to the SST anomaly variance shows local maximum of 50% south of Tasmania where the 2.7-5.5 year mode is rather weak.

Fig. 4 displays the wavelet wavenumber-frequency spectrum averaged over 6 individual spectra computed from the original (including the annual cycle) SST time series along 6 zonal circles between 56°S and 62°S. The spectrum in Fig. 4 shows energies of both standing and moving modes; notice that the standing modes are defined here as either spatial or temporal means.

Perhaps, the most interesting feature of Fig. 4 is an increase in energy at the periods less than 5 years and the wavenumbers of 1/2 of the zonal circle. Meanwhile, there is no individual maximum at the biennial scale, rather there is a broad maximum over the annual and biennial periods with two peaks at two wavelengths: the largest depicts a standing mode and the other indicates a moving mode with the spatial scale of about 1/4-1/2 of the zonal circle.

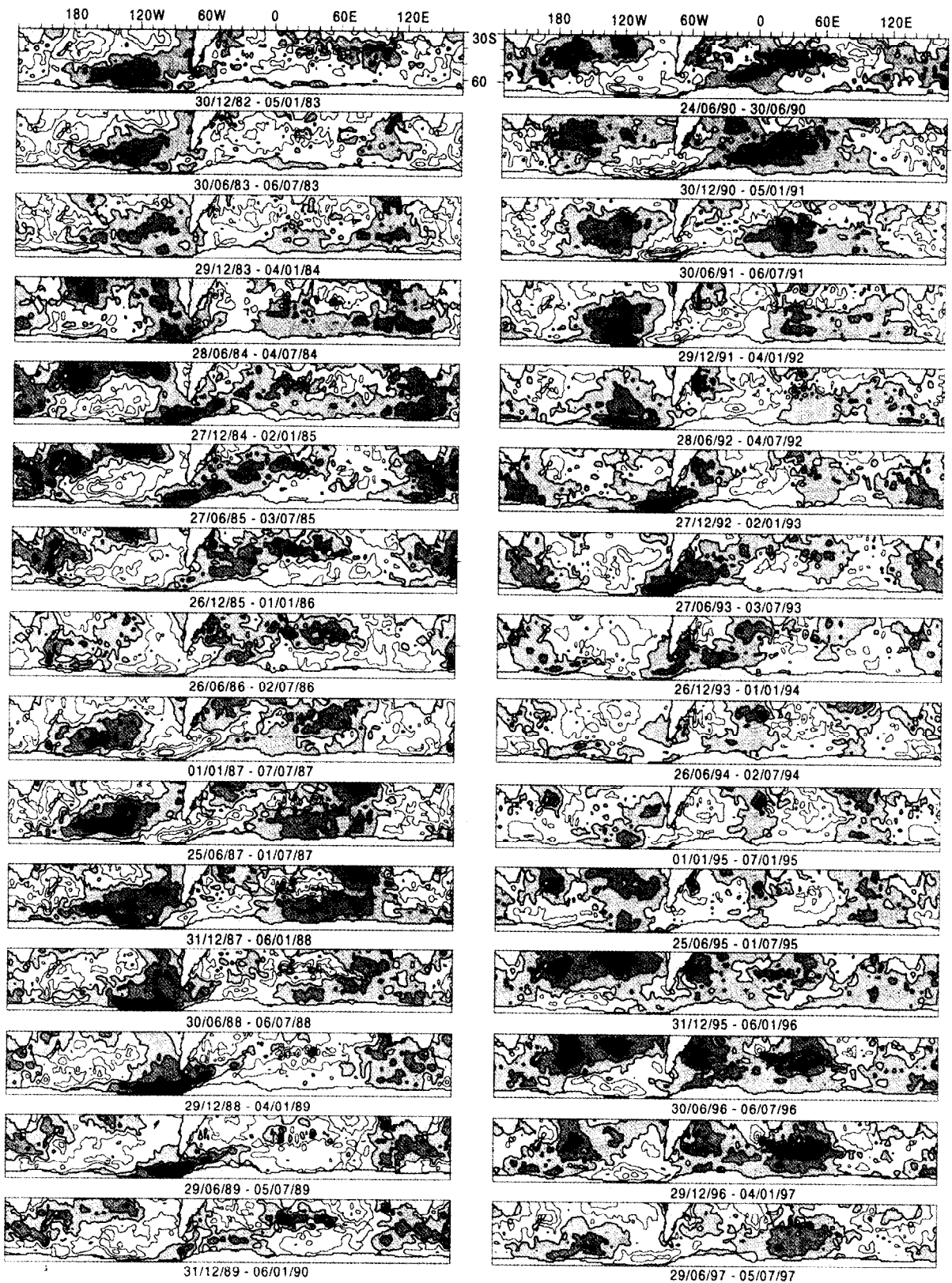


Fig. 6. The ACW SST variations of the time scales of 2.7-5.5 years in the zonal belt between 30S and 63S. One weekly snapshot is shown for every half year during 1982-1997.

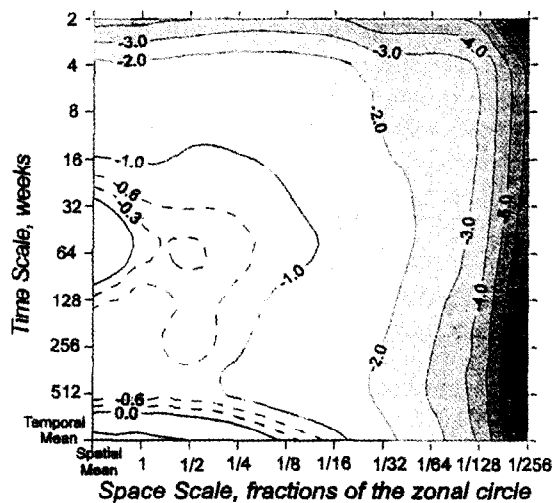


Fig. 4. The 2D energy spectra computed for the wavelet modes of the SST variability at the latitudinal band of 56 - 62S. The horizontal axis is for the wavenumbers and the vertical axis is for the periods. The spectrum is plotted in the logarithmic scale.

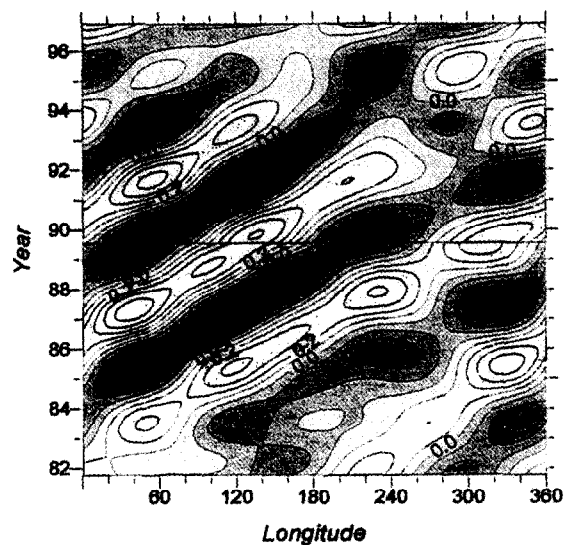


Fig. 5. The ACW mode of the SST variations along 56°S. At the horizontal axis, zero stands for the date-line.

The longitude-time diagram in Fig. 5 shows the ACW mode, having the time scales of 2.7-5.5 years and the spatial scales of 1/4-1/2 of the zonal circle, as it is derived by the 2D wavelet analysis from the SST data along the latitude of 56°S. Notice the horizontal axis starts from the date line. Clearly, usually there are two positive and two negative SST anomalies having the scales of 2.7-5.5 years in the Southern Ocean. The magnitude of such anomalies is largest in the Pacific and western Atlantic sectors with local maximum of 0.6-0.8°C found east of dateline in 1985-1988. The ACW mode propagates eastward along Antarctic Circumpolar Current, the propagation speed is about 0.09 m/s, quite in accord with the earlier study [1]. What is new in Fig. 5 as compared with the previous results, is that while propagating, the oceanic component of the ACW undergoes fluctuations. The most significant event was a bifurcation of this component in 1992-1993 at 60°-120°E. It is noteworthy that this event apparently coincided with the global climate regime shift in early 1990's.

3.2. Secular Changes in the ACW

To consider the spatial changes of the ACW in more detail, let us turn our attention again to the results of the 1D wavelet analysis, which does not stick to the particular set of wavelengths. Fig. 6 represents wavelet reconstruction of the 2.7-5.5-year variations in the latitudinal belt between 30°S and 63°S. The anomalies shown in Fig. 6 are significant and their magnitude often can be as high as 1.5°C. Remarkably, though here we deal with the frequency domain wavelet analysis, the reconstructed field is coherent in space clearly showing the familiar eastward propagating pattern.

Although here we reconstruct the low frequency oscillations, the ACW SST pattern often displays characteristic features of small spatial scale of few hundred kilometers. These features are often relevant to the oceanic fronts. For example, south of New Zealand, the ACW SST anomalies seem to be constrained by the Polar and South Subtropical Fronts [6]. At 70°E - 180°E, there often is a northward intrusion of the warm or cold ACW SST anomaly, which follows along the detour of the Subantarctic Front near the Campbell Plateau. Although the anomaly often expands substantially to the east, its core remains confined to the Polar Frontal Zone and bends southeastward near 150°W apparently following the Polar and Subantarctic Fronts.

Fig. 6 indicates the general anticlockwise circulation of the anomalies, having the 2.7-5.5-year scale, in the South Pacific. Particularly, in 1983, the warm anomaly occupied the high latitudes. It moved to the South American coast by early 1984. Then it separated into two parts: one penetrated through the Drake passage into the South Atlantic and the other moved northward along the eastern coast of the South Pacific. At latitudes of 30°-40°S, the later anomaly separated from the South America coast and propagated westward. At the second half of 1984, the warm anomaly emerged northeast of New Zealand and translated further southward to the latitudes of 50°-60°S where it coupled with warm anomaly arrived from the Indian Ocean in late 1985.

In the Atlantic sector, the ACW SST anomalies often drift both to the north along the ocean western boundary and to the west-west-north, towards the South Africa. In the former case, the drift can be associated with the Falkland Escarpment Front [7]. In the later case, the anomalies are partly disintegrated in the vicinity of the South Africa at 20°-40°E, 40°-45°S. The spatially mesoscale features dominate the variability in the Agulhas Front region well known for the eddy and Rossby wave activity. However in the higher latitudes south of Africa, the ACW mode spatial scale persists and the overall eastward drift continues.

Although the ACW propagation is remarkably regular in the SST field, certain distortions from the average cycle such as local westward drift in the Atlantic sector in 1984 could be also noticed. The most significant event was the aforementioned bifurcation of the warm SST anomaly in 1992-1993. The bifurcation seems to be originated from the Indian sector of the Southern Ocean where huge warm anomaly of the ACW scale appeared in 1991. It eventually split into two anomalies by the end of 1992: the stronger one emerged south of Australia while the second was localized in the western part of the Indian sector. As a result, three maximums of the 2.7-5.5-year scale anomalies were found in the Southern Ocean. All anomalies propagated eastward, though the propagation speed was relatively slow in the Indian sector. It is unclear whether this event led to temporal reversal of the ACW anomaly drift in the eastern part of the Pacific sector in 1994. It should be noted that the bifurcation of 1992/93 could not be reported by White and Peterson [1] because their analysis was limited by the period of 1982-1994, however, the figures given in [1] indicate partial collapse of the atmospheric component of the ACW in autumn 1993.

The ACW underwent biennial modulations. The biennial mode was particularly strong before and after the El-Nino events of 1982/83 and 1991/92 and led to the spatio-temporal variation of the warm SST anomaly west of the South America. Interestingly also, the near-surface warm anomaly occupied the eastern part of the southern Pacific during the El-Nino event of 1986/87. It may not be appropriate, however, to view the ACW modulations as a superposition of the 2.7-5.5-year and biennial variations and instead the nonlinear interactions in the coupled ocean-atmosphere system can be invoked.

In order to investigate the relationships between the ACW and the oceanic fronts in some more detail we compared the available data on locations of fronts identified from the *in situ* temperature and salinity profiles with the ACW passages. The fronts have been identified by I. Belkin (personal communication) at the depths of 200, 400, and 600 m along the meridional sections in the southern Indian Ocean (0-150E, 30-60S) from all available historical observations. Unfortunately our analysis did not show any significant relationships between the ACW SST anomalies and the fluctuations in the positions of the fronts in the Indian sector.

Finally, we estimated the correlation between the ACW SST variations and the SST meridional (north - south) gradient, which partly represents the near surface fronts. The correlation was found to be high (up to 0.9) near the Polar Front in the region of 160W - 20E, 50-63S. Furthermore, the correlation is negative north of the Polar Front and positive to the south. This implies that the ACW core usually stretches along the Polar Front and the ACW mode positive (negative) anomalies lead to weakening (strengthening) the meridional gradient on the northern side of the Polar Front. The ACW impact is opposite on the southern side of the front. The fluctuations of the SST meridional gradient were small at the ACW core. The conclusion is that the ACW contributes to the latitudinal variations in the near-surface position of the Polar Front in the eastern Pacific and western Atlantic sectors of the Southern Ocean.

References

- [1] W. B. White and R. G. Peterson, 1996, An Antarctic circumpolar wave in surface pressure, wind, temperature and sea-ice extent, *Nature*, 380, 699-702.
- [2] M. Christoph, T. P. Barnett and E. Roeckner, 1998, The Antarctic Circumpolar Wave in a coupled ocean-atmosphere GCM, *J. Climate*, 11, 1659-1672.
- [3] R. W. Reynolds and T. M. Smith, 1994, Improved global sea surface temperature analysis using optimum interpolation, *J. Climate*, 7, 1659-1672.
- [4] C. Torrence and G. P. Compo, 1998, A practical guide to wavelet analysis, *Bull. Amer. Meteor. Soc.*, 79, 61-78.
- [5] D. E. Newland, 1993, An introduction to random vibrations, spectral & wavelet analysis, Longman Scientific & Technical, UK, John Wiley and Sons, NY, USA, 478 p.
- [6] I. Belkin and A. Gordon, 1996, Southern Ocean fronts from the Greenwich meridian to Tasmania, *J. Geoph. Res.*, 101, 3675-3696.
- [7] Y. Ikeda, G. Siedler and M. Zweirz, 1989, On the variability of Southern Ocean Front locations between Southern Brazil and the Antarctic Peninsula, *J. Geoph. Res.*, 94, 4757-4762.

FORMATION AND DYNAMICS OF THE COLD INTERMEDIATE LAYER DETERMINING THE STATE OF THE BLACK SEA ECOSYSTEM

I.M.Ovchinnikov

Southern Branch of P.P.Shirshov Institute of Oceanology,
Russian Academy of Sciences, Gelendzhik, Russia
E-mail: kosyan@sdios.sea.RU

Abstract

As it is shown by the results of hydrophysical studies of the Black Sea, during the recent 15-20 years there were revealed and studied the foci of cold intermediate water (CIW) formation on the pycnocline domes in the centres of cyclonic gyres and the ways of these CIW spreading from the centre of the sea into the nearshore zone (1983-1985). Warm and freshened nearshore anticyclonic eddies (NAE; 1981 and 1987-89) which set off the whole sea over its perimeter, were found in winter. In early nineties, during the summer surveys on the CoMSBlack program, cold intermediate lenses were found which as if took the place of the winter NAE. In the same years in the Black Sea an active transfrontal water exchange through the violently meandering Main Black Sea Current was found out as well as many other features of the hydrological regime of this interior basin. All this required the new understanding of the role of many oceanographic processes in the hydrological regime of this isolated basin. The present work is dedicated to these problems.

Materials of oceanographic expeditions carried out mainly in winter seasons by the Southern Branch of the Institute of Oceanology RAS and the former Odessa Branch of SOIN for the last 15-17 years were assumed as a basis of our investigations of the hydrological regime of the Black Sea.

First of all we have to note that the intensification of water circulation in autumn-winter period results in increasing difference of the sea level between the nearshore convergence zone (NCZ) and the divergence zone in the open sea. That is why by the beginning of winter brackish and warm surface waters from the central regions of the Black Sea flow actively into the NCZ. Nearshore anticyclonic eddies (about 20 NAE) are formed there. They are filled with warm and less saline water penetrating to the depth of 150-200 m and deeper [8,13]. So the contaminants accumulated in the Black Sea surface waters for about a year, are concentrated in NAE along the NCZ, and with kinematic lowering of these waters they are buried within the deep waters and on the sea bottom.

With winter circulation increasing in autumn-winter period, kinematic rising of the deep waters in the centres of cyclonic gyres of the open sea becomes more active. But the deep waters saturated with hydrogen sulphide, meet with the main pycnocline on the way of their rising. There, at its lower and upper boundaries (about 200 m and 30-40 m), internal inertial waves are developed. Under their action oxygen is delivered from above with the surface water, and hydrogen sulphide arrives from below with the deep water. Therefore in the main pycnocline (in redox-zone) as at powerful chemical combine, the complete purification of oxygen in the rising deep waters takes place including transformation of the reduced forms of chemical compounds into the oxidized forms. Having passed through this original chemical filter, the clean deep waters enter the surface layer [10].

The active winter (January-March) interaction between the rising deep waters (3 000 km³) and the convectively mixing surface waters (18 000 km³) under the influence of internal waves on the pycnocline dome

is the main factor of the cold intermediate water formation (CIW, about 21 000 km³) in the centre of cyclonic gyres in the Black Sea [5,7].

These waters with increased density (to 15,0) which were formed anew in winter, are accumulated on the pycnocline domes in the centres of cyclonic gyres while within the NCZ (in NAE) the surface water density holds minimal. That is why between the gyres of different sign there arise well-defined conditions for baroclinity which favours development of the Main Black Sea Current. Therefore the cold intermediate layer (CIL) of high density after being accumulated on the pycnocline dome, slip isopycnally down the pycnocline steep slope; firstly "diving under" the Main Black Sea Current and then under the NAE, they reached the continental slope at the depths of 150-250 m. (Fig. 1).

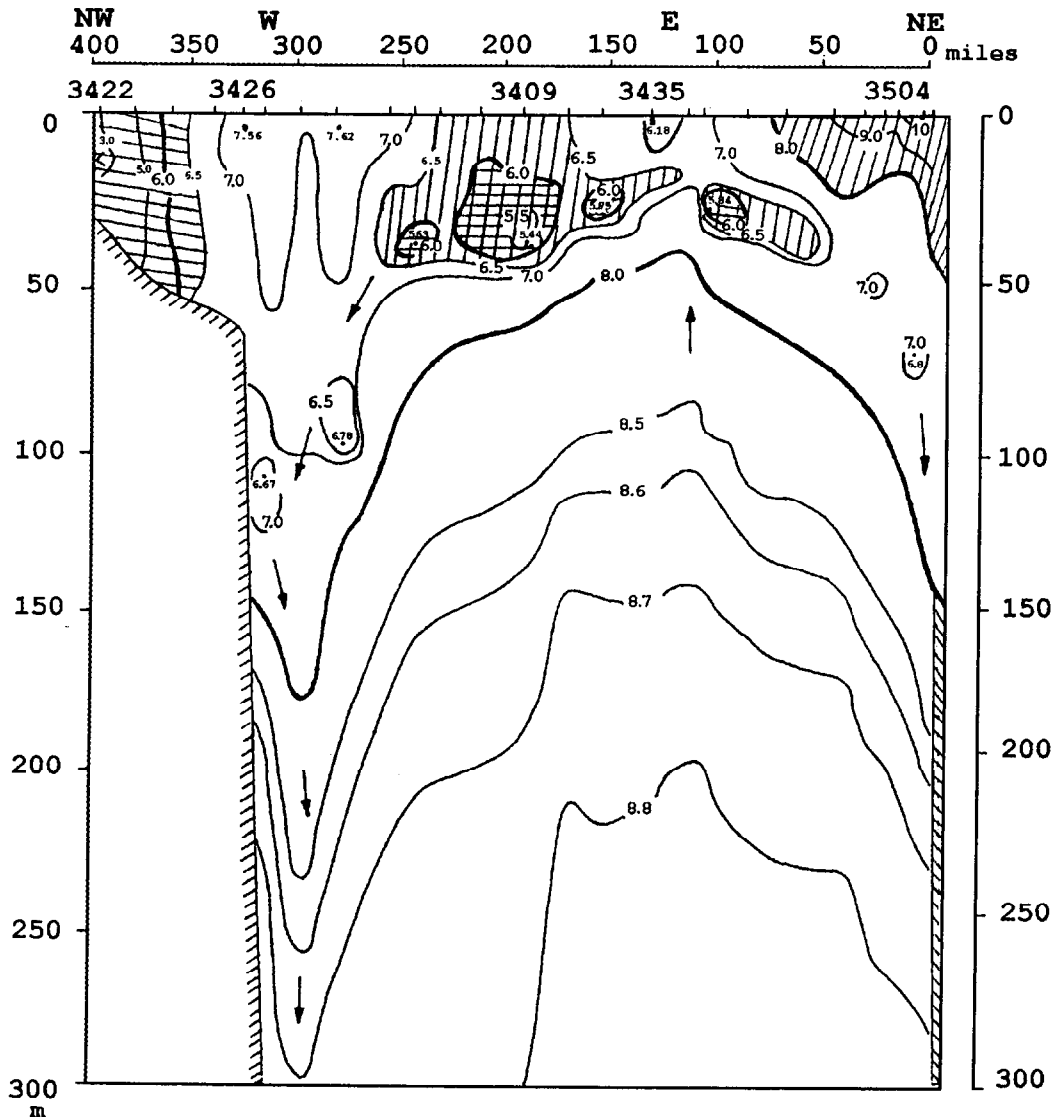


Fig. 1. Distribution of water temperature along the sublatitudinal section from the middle of the north-western shelf across the centres of the main cyclonic gyres to Novorossiisk according to the data of the 21-st cruise on board the r/v «Vityaz» in winter and spring 1991: 10.03-09.04.91.

Isopycnical slipping of the CIW into the NCZ favours the active lowering of about 3 000 km³ of mainly cold waters from the intermediate layer into the sea depths. The absence of accumulation foci of the CIW within the NCZ in February-March and the presence of oxygen intrusions within the main pycnocline

confirm an active interaction of cold intermediate and deep water there. In this case the kinematic lowering of more warm and brackish waters in the NAE turns to be inessential.

The cold intermediate waters lowering into the NCZ in the process of transverse circulation, pass a long and complex way of self-purification till their return into the centres of the main cyclonic gyres after 165 years (150-200 years). In so doing the renewal of hydrogen sulphide in the deep waters of the Black Sea takes place within nearly 75-100 years.

In severe winter conditions when the interaction processes between the cold intermediate waters and the deep water mass are more active, the Black Sea bioproductivity increases and recovers. So the CIL appears to be there a regulator of both bioproductivity of the Black Sea and its ecosystem recovering as a whole.

With spring heating of the surface waters and seasonal thermocline formation and also with the weakening of water circulation baroclinity in the Black Sea is notably decreased and replaced towards the continental slope. That is why as early as in April (Fig.2) the main mass of the CIW occurs at the depths from 30 m (in the centre) to 110 m (along the sea periphery) being located from the eastern continental slope to the western one (contrary to opinion of L.Ivanov et al., 1997)[2]. By July in the location of the CIL which consists of cold intermediate lenses under the thermocline (about 20 cold intermediate lenses only along the sea coast), the baroclinity disappears completely because the CIW core occurs everywhere at the depth of 30-60 m. In this case winter NAE with more warm and less saline water are gradually displaced towards the sea surface and then, being placed over the seasonal thermocline, they are included into the surface water structure forming their main bulk. In such a way under conditions which are close to mean perennial, the total volume of the CIL makes about 21 000 - 20 000 km³ [1,2] that is in good agreement with our estimations [7].

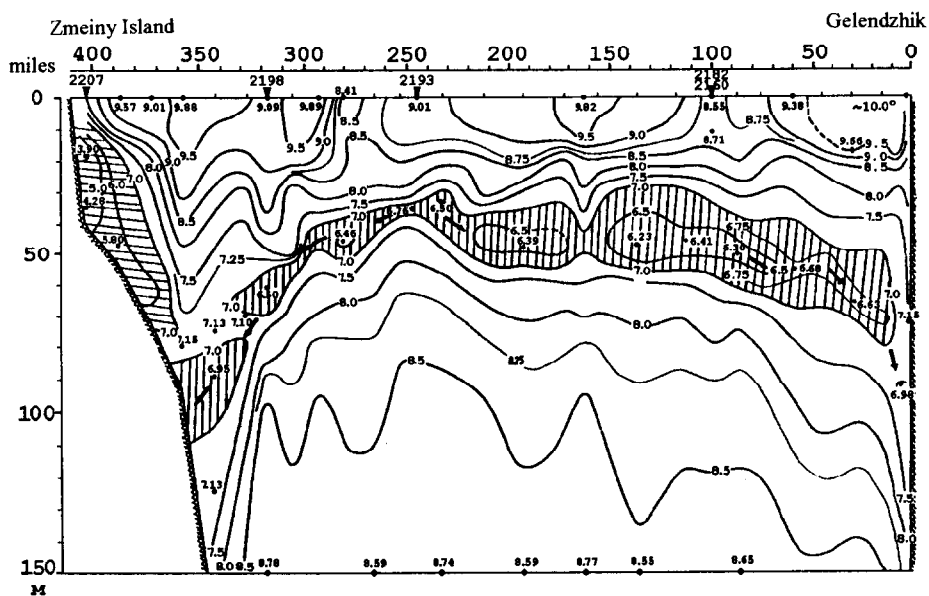


Fig. 2. Water temperature distribution along the sublittoral section from Zmeiny Island across the centres of the Western and Eastern cyclonic gyres to Gelendzhik. April 05-25, 1988.

In connection with prevailing fair weather and slight winds during summer-autumn season the Main Black Sea Current markedly weakens and undergoes vigorous meandering. It may even separate into some self-dependent cyclonic current systems. That is why the cold intermediate lenses in some sea areas (in the vicinity of Batumi, Sevastopol, Kertch etc.) may considerably strengthen. Overcoming the Main Black Sea Current in the process of transfrontal exchange, they penetrate into the central part of the Black Sea. Such superdeep anticyclonic eddies (to 750-1250 m and even deeper) exert an essential influence on the renewal of deep waters [3,4, 11].

In December-January the "old" CIL degenerates everywhere and gradually gives way to a homogenous convective layer. On the basis of homogenous convective layer, under favourable winter conditions, a new CIL is generated. These processes of the CIL formation and its dynamics over a year in the centres of cyclonic gyres and within the nearshore zone are well reflected in many our works [6].

In the north-eastern half of the Black Sea in winter (January-February) the oscillations of mean winter air temperature with the periods of 20 years (lunar-solar) and 60 years (saturnal) are particularly well

manifested. By way of example we have taken 125-year set of T^0 in the port of Novorossiisk (Fig.3) [9,12]. From 1870 till 1930 and then from the thirties to the nineties there were observed two cycles with three gradually rising 20-year temperature "waves". 60-year trend of mean winter air temperature equal to about $+1.5^{\circ}\text{C}$ in both cases passes across them. But in the thirties and nineties this trend is lowered abruptly also by -1.5°C . Stability of two 60-year cycles of mean winter air temperature gives us good grounds for its reliable long-term prognosis. At the same time it is possible to predict even such natural cataclysms which are present everywhere in changing 60-year temperature (saturnal) cycles. Their change may be expected in the fifties of the next century.

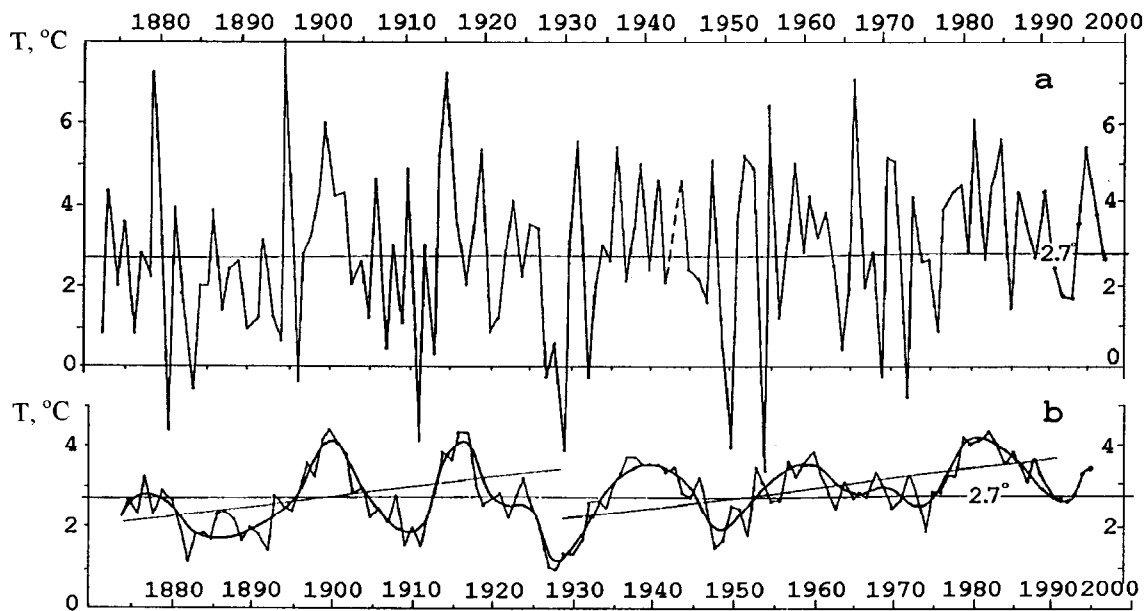


Fig. 3. a) Variation of mean winter temperature of air in Novorossiisk over the period from 1872 to 1994; b) Variation of mean winter temperature of air (T^0) smoothed by five-year sliding averaging of T^0 in Novorossiisk over the same period.

Conclusion

Performed investigations evidence that the rising of clear, rich in biogens deep waters in the centres of cyclonic gyres in the Black Sea under severe winter conditions determines most favourable conditions for development of the ecosystem of this interior basin. On the contrary, when winter conditions are anomalously warm, the Black Sea ecosystem turned out to be in a depressed state. That is why the knowledge of winter climatic regularities in this region allows to work out the reliable prognostic evaluations of the ecological state of the Black Sea for 60-120 years in advance.

References

1. German I.F., 1986, Thermohalinic structure and convective mixing of the Black Sea waters in the conditions of anthropogenous influence, Abstract of the candidate thesis, 23.
2. Ivanov L.I., Besiktepe S. and Ozsoy E., 1997, The Black Sea cold intermediate layer. E.Ozsoy and A.Mikaelyan (eds.), Sensitivity to Change: Black Sea, Baltic Sea and North Sea, 253-264.
3. Krivosheya V.G., Moskalenko L.V., Ovchinnikov I.M. and Yakubenko V.G., 1997, Peculiarities of water dynamics and hydrological structure in the north-eastern part of the Black Sea in autumn 1993, *Oceanology*, 37(3), 352-358.
4. Latun V.S., 1989, The role of anticyclonic gyres in interseasonal evolution of thermoahalinic structure and geostrophic circulation of waters, In Monograph: "Investigation and Modelling of Hydrophysical Processes in the Black Sea", Moscow, Gidrometeoizdat, 40-49.
5. Ovchinnikov I.M. and Popov Yu.I., 1987, Foramtion of the cold intermediiate layer (CIL) in the Black Sea, *Okeanologia*, 27(5), 739-746.

6. Ovchinnikov I.M., Osadchy A.S., Prokopov O.I. and Titov V.B., 1989, Some features of water dynamics and the cold intermediate layer in the north-eastern part of the Black Sea. In Monograph: "Investigation and Modelling of Hydrophysical Processes in the Black Sea", Moscow, Gidrometeoizdat, 60-67.
7. Ovchinnikov I.M. and Popov Yu.I., 1990, Peculiarities of the cold intermediate layer (CIL) formation in the Black Sea in extremal winter conditions, In: "Oceanology and Meteorology of the Atlantic Ocean", Trudi GOIN, 190, 132-151.
8. Ovchinnikov I.M. and Titov V.B., 1990, Anticyclonic vorticity of currents in the nearshore zone of the Black Sea, Dokl. Akad.Nauk SSSR, 314(5), 1236-1239.
9. Ovchinnikov I.M. and Osadchy A.S., 1991, Secular variability of climatic conditions determining the peculiarities of the Black Sea hydrological regime, In: "Variability of the Black Sea Ecosystem", Moscow, "Nauka", 8-25.
10. Ovchinnikov I.M., Popov Yu.I. and Titov V.B., 1993, Hydrophysical conception of a development of Black Sea ecological situation, Dep. VINITI, №278-V93, 35 p.
11. Ovchinnikov I.M., Titov V.B. , Krivosheya V.G. and Popov Yu.I., 1993, The main hydrophysical processes and their role in the ecology of the Black Sea, Okeanologia, 33(6), 801-807.
12. Ovchinnikov I.M. ,1998, Interaction between surface and deep waters in the process of transverse circulation of the Black Sea, In book: Ventilation of the Black Sea's anoxic waters. Liege, Belgium, 135-161.
13. Oguz T., Latif M.A., Sur H.I. and Unluata U., 1991, On the dynamics of the southern Black Sea, E.Isdar and I.Murray (eds.), in "The Black Sea Oceanography", 43-63.

THE BOSPHORUS STRAIT AND ITS SHELF OUTFLOW INTO THE BLACK SEA: EXPERIMENTS AND MODELLING

**Emin Özsoy¹, Michael C. Gregg², Hermann Föhrmann³
and Jan O. Backhaus⁴**

¹Institute of Marine Sciences, Middle East Technical University,
P. O. Box 28, Erdemli, Icel 33731 Turkey. e-mail: ozsoy@ims.metu.edu.tr

²Applied Physics Laboratory, College of Ocean and Fishery Sciences, University of Washington,
1013 NE 40th St., Seattle, Washington 98105-6698 USA. e-mail: gregg@apl.washington.edu

³Sonderforschungsbereich 313 der Universität Kiel,
Heinrich-Hecht-Platz 10, D-24118 Kiel, Germany. e-mail: hermann@sfb313.uni-kiel.de

⁴Institut für Meereskunde an der Universität Hamburg,
Tropelwitzstrasse 7, D-22529 Hamburg, Germany, e-mail: backhaus@dkrz.de

Abstract. We describe the exchange and mixing across the Bosphorus Strait and on the Black Sea continental shelf / slope, based on intensive measurements in 1994 and through modelling of the dense bottom current. The surface water entrains and mixes in the southern Bosphorus, while the lower layer entrains throughout its route, and is affected by topography. Its cascade along the continental slope increases the entrainment. Results from a reduced gravity model of the dense bottom current confirm the crucial importance of topographic features of the continental shelf. Sensitivity to environmental parameters and the Black Sea ambient is investigated.

The Measurements

The two-layer, hydraulically controlled, 'maximal exchange' [3] flows across the Turkish Straits System have direct influence on the environmental problems in the region, as well as on the fate of the Black Sea, through its role in the mixing and renewal of its waters [15, 7, 6, 8, 10, 11, 12, 14, 9, 13]. It is now clear, after extensive observations, that the Bosphorus, characterized with rapid along-strait variations in its geometry, its sharp stratification, nonlinear controls and temporary blocking of the flows in either direction, is driven by variable atmospheric pressure, wind set-up, sea level variations and water budgets in the adjacent basins [14, 2], displaying time dependence on daily to interannual time scales.

The above unique characteristics of Bosphorus Strait, as well as its sharp two-layer interface with high levels of turbulent dissipation and entrainment has motivated intensive collaborative studies in September 1994 carried out by APL/UW and IMS/METU on board the R/V BİLİM, using ADCP, CTD, the Advanced Microstructure Profiler (AMP), current meter, sea-level recorder instruments and acoustic backscatter imaging of the physical features. The measurements and their results will appear in forthcoming papers. Here we provide a short description of the main features of the temperature and salinity variations and entrainment/mixing along the Strait and describe observations and modelling of the flow of dense Mediterranean water along the Black Sea continental shelf.

Mixing in the Bosphorus and the Black Sea Exit

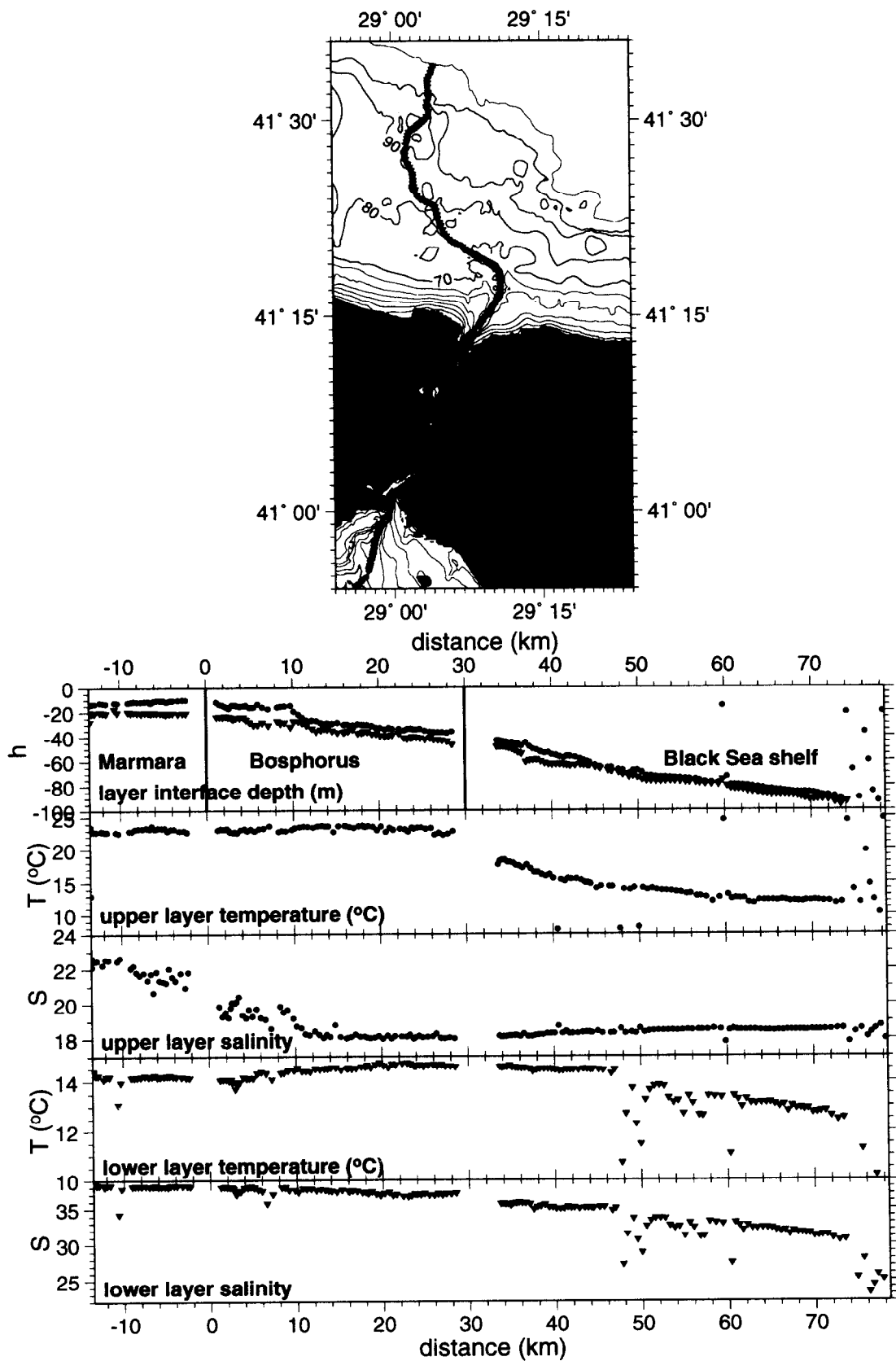


Figure 1: (a) A composite section of AMP drops across the Bosphorus Strait (179 profiles) during 13-19 September 1994. (b) Variation of upper and lower layer depths and average properties (temperature and salinity), along the same section.

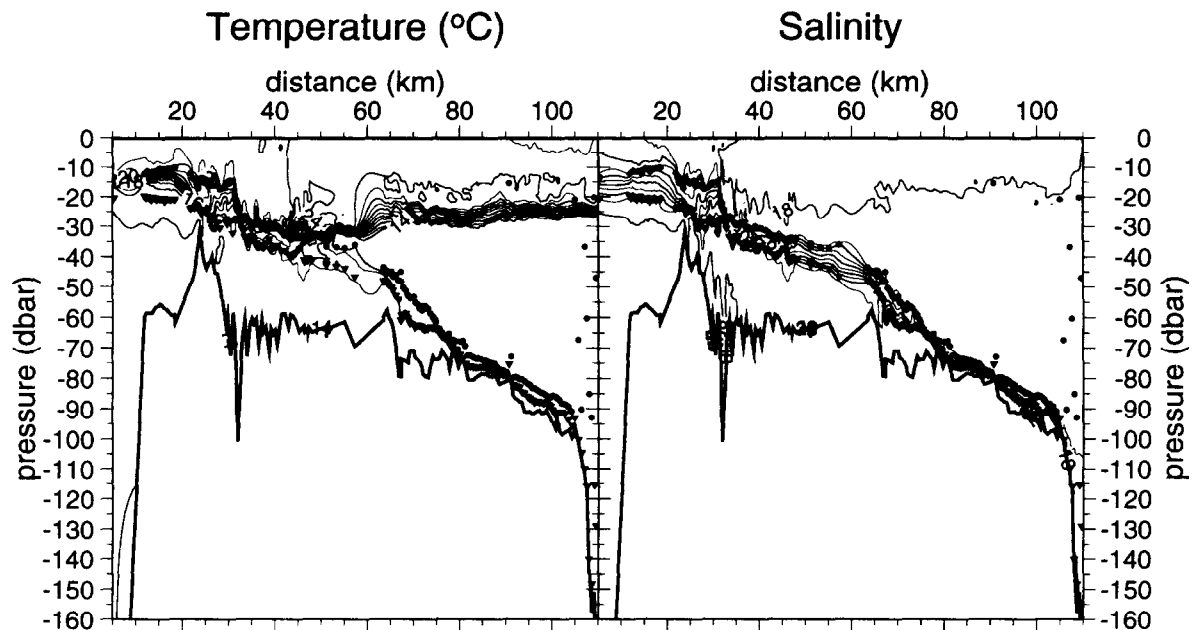


Figure 2: Contours of (a) temperature and (b) salinity along the transect in Figure 1 extending from the Marmara Sea to the Black Sea across the Bosphorus Strait, from a composite section during 13-19 September 1994.

The geographical locations of bursts of stations along the thalweg, the interfacial depths, and the upper and lower layer average properties are presented in Figure 1, with corresponding temperature and salinity cross-sections shown in Figure 2. The interfacial layer thickens and the upper layer salinity increases in the southern 10 km of the Strait, past the contraction where one of the two main hydraulic controls takes place. The interface also thickens past the northern sill in the Black Sea, where the other hydraulic control takes place, and finally becomes much thinner when the flow emerges on the flat shelf, when it emerges from a bottom channel extending of the exit.

The temperature in the upper layer does not appear to change much in the Bosphorus because of the high contrast of the warm mixed layer at the surface originating from the Black Sea, but a slight decrease as a result of entrainment is evident south of the contraction. The rapid decrease in temperature towards the the Black Sea results from the inclusion in the upper layer average of two different layers with variable depths: the surface mixed layer and the underlying layer of Cold Intermediate Water (CIW).

The lower layer temperature first rises as one proceeds north in the Bosphorus, by entrainment of warm water from the surface mixed layer in direct contact with it, and later decreases by entrainment of the overlying CIW in the northern Bosphorus and the Black Sea shelf. The salinity is perhaps a better indicator of entrainment for the lower layer, because it is more conservative with regard to sources, and relatively more uniform in the upper layer. The lower layer salinity decreases continuously from Marmara to the Black Sea, with changes of gradient in the different regions: In the northern Bosphorus where the interface stability is higher, the entrainment rate appears to be smaller than the southern part. In comparison to the Bosphorus, flow past the northern sill (about 35km from the southern end) on the Black Sea shelf has greater entrainment, and increases further when the flow exits the narrow northwestward bending channel topography and spreads on the flat shelf region (at 50km). Finally with the increased slope at the shelf edge, the bottom layer can only be identified with difficulty, but a few data points where it could be detected show that the entrainment has been increased by an order of magnitude there.

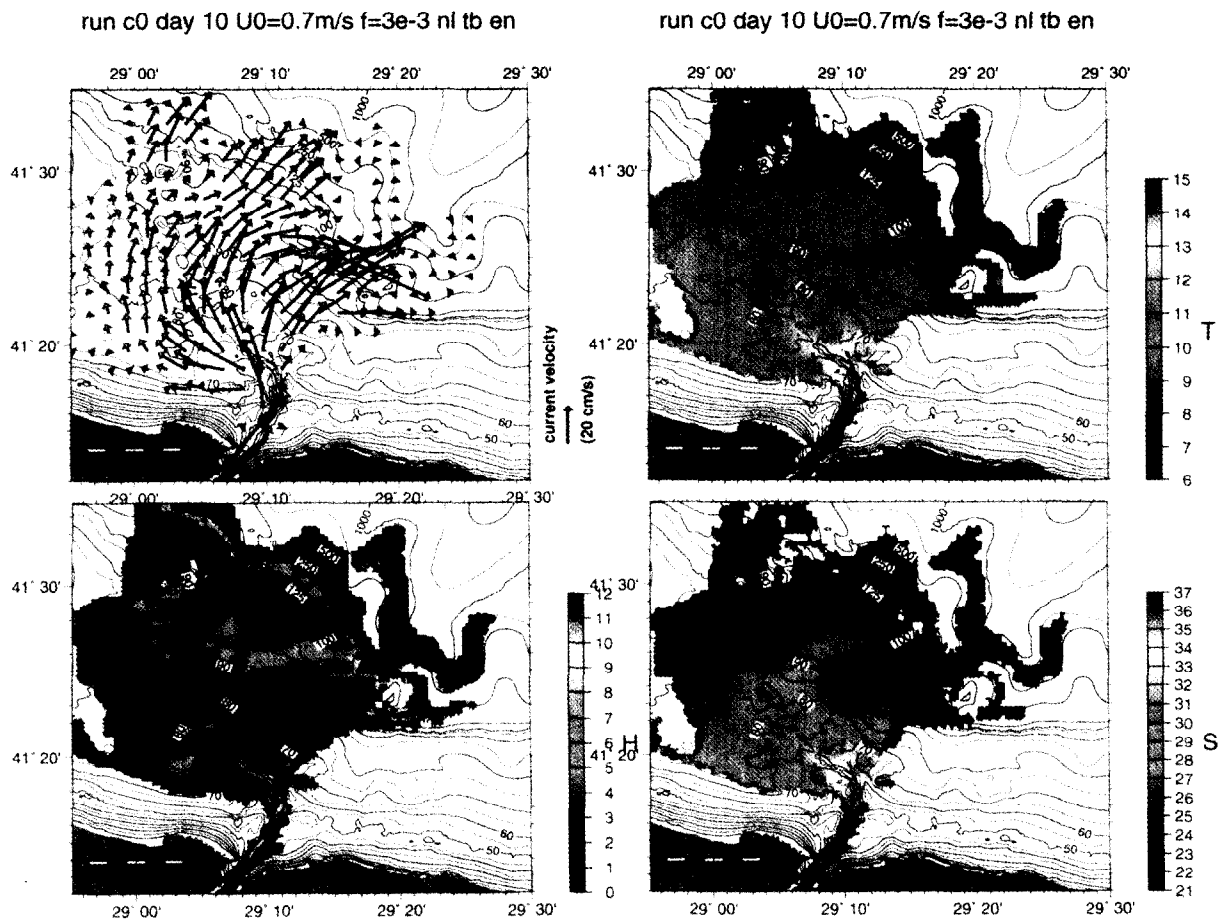


Figure 3: Model results for (a) flow velocity and (b) layer thickness 10 days after initialization. Run parameters are: $A_h = 150m^2/s$, $k = 0.003$ for the horizontal eddy coefficient and bottom friction respectively, and $u_o = 0.7m/s$, $S_o = 37$, $T_o = 14.5^\circ C$, $H_o = 40m$ for the initial conditions specified at the Black Sea exit of the Bosphorus.

Modelling of the Shelf Mixing and Spreading of Dense Water

We use the [5] model to study the Mediterranean plume in the Black Sea, incorporating the effects of the complex topography in the Bosphorus exit region. It is a reduced gravity single layer approximation to the primitive equations [4], including horizontal, bottom friction and entrainment. Either the Kochergin or the Pedersen entrainment parameterizations [5] can be chosen, taking into account the ambient property distributions, represented by realistic vertical profiles of temperature and salinity in the Black Sea.

A sample run with indicated set of parameters and initial conditions is shown in Figure 3. The bottom drag coefficient was found to be in the range of 0.003 to 0.015 from acoustical measurements of flow and dissipation over the sill [1], and we have selected the lower values of this range. The horizontal resolution of the model is 200m. The detailed bathymetry has been constructed from a weighted combination of adcp depth measurements, UNESCO digital bathymetric data and digitized hydrographic maps.

The model results are very sensitive to topographic details, the entrainment formulation, as well as variations of the parameters. The flow and property distributions reach a quasi-steady state on the shelf area after about 10 days from start-up. The flow along the continental slope is either in the form of a geostrophically adjusted motion along the bathymetric contours or the precipitous flow down hill to great depths, and continues to develop with time. The behaviour here is rather erratic because the

solutions reach the limits of validity of the model itself: the rapid entrainment at the steep slope produces a very thick, diluted layer with vanishingly small density contrast at the edges of the plume. On the other hand, the assumptions with regard to entrainment are also expected to break down in this steep region affected by other processes, such as the double diffusive convection [8, 9], and numerous small-scale canyon features probably not adequately resolved in the present topography.

There are competing or enhancing effects of friction, entrainment and initial parameters in the various runs. When the model is run without entrainment, the flow is steered more to the west along the bottom groove without being withdrawn into the deep canyon along the continental slope, and becomes arrested at a shallower depth. With alternative entrainment formulations, the results can differ significantly, especially along the slope.

Discussion

As part of ongoing effort to analyse the wealth of data obtained in the Bosphorus, and modelling of the outflow aimed at obtaining features better representing the observations, we have offered a glimpse of the expected results in this brief account. The regimes of mixing and entrainment in the Bosphorus and its Black Sea exit have complex nature which need further evaluations not attempted here. The results are important in their own right, but also have bearing on many applied problems, including the fate and conservation of the Black Sea and the Marmara Sea, the hydrology and climatic changes in these systems, and the regulation and safety of navigation through the Strait, which seems to be increasing rapidly in recent years.

References

- [1] Di Iorio, D. and H. Yüce (1998). Observations of Mediterranean Flow into the Black Sea, *J. Geophys. Res.*, (in press).
- [2] Ducet, N. and P. Y. Le Traon (1998). Response of the Black Sea Mean Level to Atmospheric Pressure and Wind Forcing, (submitted).
- [3] Farmer, D. M. and L. Armi (1986). Maximal Two-Layer Exchange over a Sill and Through the Combination of a Sill and Contraction with Barotropic Flow, *J. Fluid Mech.*, **164**, 53-76.
- [4] Jungclaus, J. H. (1994), Ein numerisches Modell zur Simulation dichter Bodenströmungen im Ozean mit Anwendung auf den "Overflow" durch die Dänemarkstraße, Ph.D thesis, Zentrum für Meeres-und Klimaforschung der Universität Hamburg, Institut für Meereskunde, Hamburg, Germany
- [5] Jungclaus, J. H. and J. O. Backhaus (1994). Application of a transient reduced gravity plume model to the Denmark Strait Overflow, *J. Geophys. Res.*, **99**, 12,375-12,396.
- [6] Latif, M. A., E. Özsoy, T. Oğuz and Ü. Ünlüata (1991). Observations of the Mediterranean inflow into the Black Sea, *Deep Sea Research*, **38**, Suppl. 2, S711-S723.
- [7] Oğuz, T., Özsoy, E., Latif, M. A., and Ü. Ünlüata, (1990). Modelling of Hydraulically Controlled Exchange Flow in the Bosphorus Strait, *J. Phys. Oceanogr.*, **20**, 945-965.
- [8] Özsoy, E., Ünlüata, Ü. and Z. Top, (1993). The Mediterranean Water Evolution, Material Transport by Double Diffusive Intrusions, and Interior Mixing in the Black Sea, *Progress in Oceanography*, **31**, 275-320.
- [9] Özsoy, E. and Ş. Beşiktepe, (1995). Sources of Double Diffusive Convection and Impacts on Mixing in the Black Sea, pp. 261-274, in: Brandt, A. and H. J. S. Fernando (editors), *Double-Diffusive Convection*, Geophysical Monograph 94, American Geophysical Union, 334 pp.

- [10] Özsoy, E., M. A. Latif, S. Tuğrul, and Ü. Ünlüata (1995a). Exchanges with the Mediterranean, Fluxes and Boundary Mixing Processes in the Black Sea, In: F. Briand, (editor), Mediterranean Tributary Seas, *Bulletin de l'Institut Océanographique, Monaco*, Special Number 15, CIESM Science Series No. 1, Monaco p. 1-25.
- [11] Özsoy, E., Latif, M. A., Beşiktepe, Ş. and A. F. Gaines (1995b). Fluorescent Dye Measurements of the Mixing and Transport of Wastewater Discharge in the Bosphorus, *Wat. Sci. Tech.*, **32**(2), 61-68.
- [12] Özsoy, E., M. A. Latif, H. İ. Sur and Y. Goryachkin (1996). A Review of the Exchange Flow Regimes and Mixing in the Bosphorus Strait, In: F. Briand, (editor), Mediterranean Tributary Seas, *Bulletin de l'Institut Océanographique, Monaco*, Special Number 17, CIESM Science Series No. 2, Monaco.
- [13] Özsoy, E. and Ü. Ünlüata (1997). Oceanography of the Black Sea: A Review of Some Recent Results, *Earth Science Reviews*, **42**, 231-272.
- [14] Özsoy, E., Latif, M. A., Beşiktepe, Ş., Çetin, N., Gregg, N. Belokopytov, V., Goryachkin, Y. and V. Diaconu (1998). The Bosphorus Strait: Exchange Fluxes, Currents and Sea-Level Changes, L. Ivanov and T. Oğuz, editors, Proceedings of NATO TU-Black Sea Project - Ecosystem Modeling as a Management Tool for the Black Sea : Symposium on Scientific Results, Crimea, (Ukraine), June 15-19, 1997.
- [15] Ünlüata, Ü., Oğuz, T., Latif, M. A., and E. Özsoy, (1990). On the Physical Oceanography of the Turkish Straits, in: *The Physical Oceanography of Sea Straits*, L. J. Pratt (editor), NATO/ASI Series, Kluwer, Dordrecht, 25-60.

PECULIARITIES OF THE FORMATION OF THE THERMOHALINE WATER STRUCTURE IN THE STOLPE CHANNEL OF THE BALTIC SEA.

V.T Paka¹, N.M. Stashchuk², V.I Vlasenko² and N.N.Golenko¹

1 Atlantic Branch of P.P. Shirshov Oceanology Institute, Mira Street 1, Kaliningrad, 236000, Russia,
e-mail: paka@ioran.kern.ru

2 Marine Hydrophysical Institute, Kapitanskaya Street 2, Sevastopol, 335000, Ukraine,
e-mail: vlasta@ukrcm.sebastopol.ua

ABSTRACT

Analysis of the in-situ measurements conducted in spring, 1993 in Stolpe Channel after the salty water inflow to the Baltic Sea through the Danish straits has shown the presence of an asymmetry of the hydrophysical fields across the channel. The narrowing and uprising of isohalines to a sea surface was clearly seen on the northern periphery of the channel. From the other side, the halocline was wide and deep in the southern part of the channel. It was supposed that the system of nearbottom currents generated during a salty water inflow was the reason of a formation of marked hydrophysical fields structure. The mathematical model was developed for calculation of a water circulation induced by an inflow. It was obtained that the North Sea waters moving eastward along the channel form a bottom boundary layer. The Ekman drift excited due to the Coriolis force generates the water transport across the channel in the bottom boundary layer. It can lead to a reconstruction of hydrological fields and formation of an asymmetrical across the channel structure of hydrophysical fields.

IN-SITU DATA ANALYSIS

The thermohaline structure the Baltic Sea waters in April, 1993 was investigated in different sites of the Stolpe Channel. The measurements were carried out by the undulating towed CTD-probe installed on the board of the R/V "Professor Shtokman". The preliminary results of the experiment was presented in [1]. Two cross channel sections of salinity in the central part of the Stolpe Channel are shown in Figure 1 as an example of obtained data. The asymmetry of the salinity fields (narrowing and lifting of the halocline to the surface in the northward direction and its deepening and widening southward) is clearly seen in this figure.

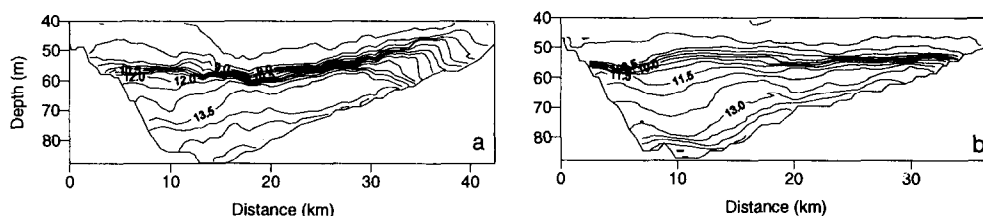


Figure 1. The cross-sections of salinity obtained in Cruise 29 of R/V "Professor Shtokman" in the stolpe Channel.

One of the possible mechanism of formation of the marked asymmetry due to the seiches oscillations was considered in [2]. The across basin seiches in the Baltic Sea have periods 13 h 43 min and 8 h 11 min. In situ

measurements were carried out continuously during three days. If the assumed in [2] periodical mechanism of the phenomenon is valid the tilting of the halocline would be changed its sign to the opposite one at least several times during the measurements. However, the qualitative behavior of the halocline (deepening and widening southward) remained during several days. All cross channel sections of the density and salinity qualitatively were identical. This fact permits to formulate an idea about the quasistationary character of the revealed phenomenon.

It is important that the measurements were carried out just after the North Sea water inflow to the Baltic Sea. The North Sea waters moving to the east form in the Stolpe Channel the bottom boundary layer. The Ekman drift, excited due to the Coriolis force generates the water transport across the channel in the boundary layer. It can lead to a reconstruction of hydrological fields and formation of an asymmetrical across the channel structure of temperature, salinity and density fields. This mechanism of formation of the cross-channel circulation (called the „pressure compensation“) was considered in [3]. The primary barotropic along channel flow is essentially modified by the Ekman cross-channel transport. The velocity of the flow in the bottom layer decreases and pressure is compensated by baroclinic component. The similar idea about reconstruction of hydrophysical fields in the upper layers due to the water transport in the bottom layer was formulated also in [4] and [5].

In the present paper it is assumed that the main reason of the formation of the asymmetrical structure of thermohaline fields in the Stolpe Channel is the bottom Ekman drift across the channel, generated by the inflow of the North Sea waters. This hypothesis was used for development of a mathematical model. The initial system of currents in the channel was two layered. The nearbottom current was directed eastward and modeled the inflow of heavy salty North Sea waters to the Baltic and the Baltic Sea fresh water outflow in the upper layer was directed westward.

MATHEMATICAL MODEL

The main purpose of the present study is to investigate the cross channel circulation generated during the inflow phenomenon. Thus, it is supposed that the distributions of hydrophysical fields along the channel are uniform and the following system of equations can be used for the modeling [6]:

$$\begin{aligned}
 \omega_t + J(\omega, \psi) - fv_z &= g\rho_0^{-1}(\rho)_x + a\omega_{xx} + A\omega_{zz}, \\
 v_t + J(v, \psi) + f\psi_z &= av_{xx} + Av_{zz}, \\
 S_t + J(S, \psi) &= mS_{xx} + MS_{zz}, \\
 T_t + J(T, \psi) &= mT_{xx} + MT_{zz}.
 \end{aligned}
 \tag{1}$$

Here ψ is the stream function ($\psi_z = u$, $\psi_x = -w$), u and v are the cross- and along-channel velocity respectively, w is the vertical velocity, $\omega = \psi_{zz} + \psi_{xx}$ is the eddy, J is the Jacobian, S and T are the temperature and salinity, ρ is the deviation of density from the stable state, ρ_0 is the mean density value, f is the Coriolis parameter, g is the gravity acceleration, a and A ($a=30\text{m}^2\text{s}^{-1}$, $A=10^{-4}\text{m}^2\text{s}^{-1}$) are the coefficients of horizontal and vertical turbulent viscosity, m and M ($m=30\text{m}^2\text{s}^{-1}$, $M=10^{-5}\text{m}^2\text{s}^{-1}$) are the coefficients of horizontal and vertical density diffusion.

At the sea surface the "rigid-lid" condition and the absence of velocity and eddy shears were used as the boundary conditions. For the salinity and temperature we putted the non-flux conditions at $z=0$. At the bottom the non-slip for v and non-flow for T and S conditions were used. The problem (1) was solved numerically [6].

RESULTS OF MATHEMATICAL MODELING

A model starts from the state characterized by the existence of an initial along-channel westward directed nearsurface outflow having velocity of 10cm/sec, and eastward directed nearbottom inflow. The value of velocity of the inflow current was calculated from the condition of a zero resulting discharge through the channel. The velocity changes its sign at the depth of 60m (position of the halocline center). The isotherms and isohalines were initially horizontal. The distributions $T(z)$ and $S(z)$ were built on the basis of in-situ data.

The evolution of the salinity field for the first four days after the beginning of motion is shown in Figure 2 (hereafter the time scale T is equal to 24 hours). During the first day after the beginning of the inflow the development of a wave motion with amplitudes of 15-20m caused by a shear current is clearly seen. These oscillations attenuate during the next two days due to the dissipation. By the end of the fourth day the salinity

field has quasistationary character. It is characterized by a widening and surfacing of the halocline northward and sinking and widening southward. Thus, the obtained structure is qualitatively similar to experimental one.

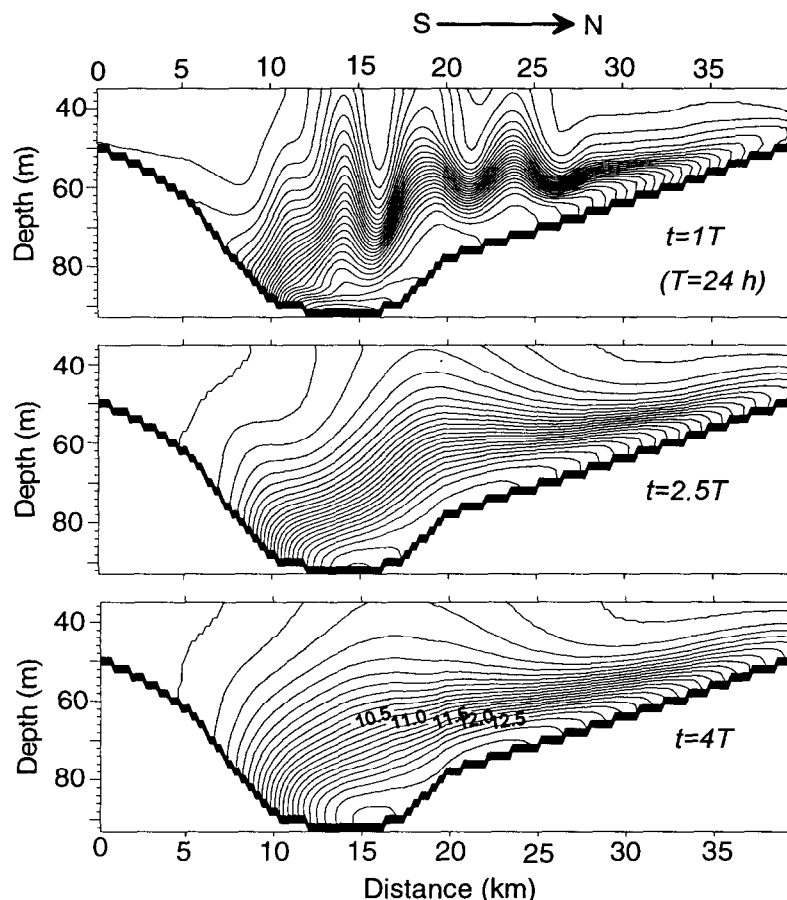


Figure 2. The model predicted evolution of the salinity field in the Stolpe Channel during the development of the North Sea water inflow.

The analysis of the currents fields at $t > 4T$ shows that in spite of the quasistationary character of thermohaline fields the velocities are not stationary. This fact is seen in the Figure 3 (the left panels represent the along-channel velocity and right panels - the cross channel velocity). The motion has oscillating character. The currents change their direction during a definite interval of time (compare Fig. 3b, 3c and Fig. 3e, 3f). Besides, in the central part of the channel the fluid moves in the opposite directions above and below halocline. Thus, the baroclinic character of motion is established.

The detailed quantitative and qualitative analysis of a temporal variability of current fields allows one to detach two main type of motions established in the channel. The first one is the inertial oscillations. The time dependencies of v and u velocities in different points of the channel are shown in Figure 4. The curves A-D in Fig. 4a were built for points A-D in Figure 3c respectively and lines A-F in Fig. 4b,c,d are the time dependencies of currents in points A-F in Fig. 3f respectively.

The periods of oscillations in points B, C in Fig. 3c (lines B, C in Fig. 4a) and also in points C, D in Fig. 3f (lines C, D in Fig. 4c) are very close to the nearinertial one. These oscillations attenuate with time due to the dissipation (amplitude reduces 1.5-2 times during 2 days). In the same time the mean currents predominate on the periphery of the channel. The analysis of Figures 3-5 shows that the along-channel motions of water in the shallow parts of the channel (for instance, points A, D Fig. 3c) attenuate slowly without essential oscillations (lines A, D Fig. 4a). The analogous character of a monotonous attenuation has the time dependencies of the across-channel velocity on the periphery of the channel (lines A, B, E, F in Figure 4 b, d).

Inertial oscillations discussed above are almost linear periodical motions. They are not able to influence essentially on a thermohaline structure of water. Thus, the another type of movement must exist in the basin to reconstruct the thermohaline fields. The procedure of filtration of inertial oscillation was carried out to obtain

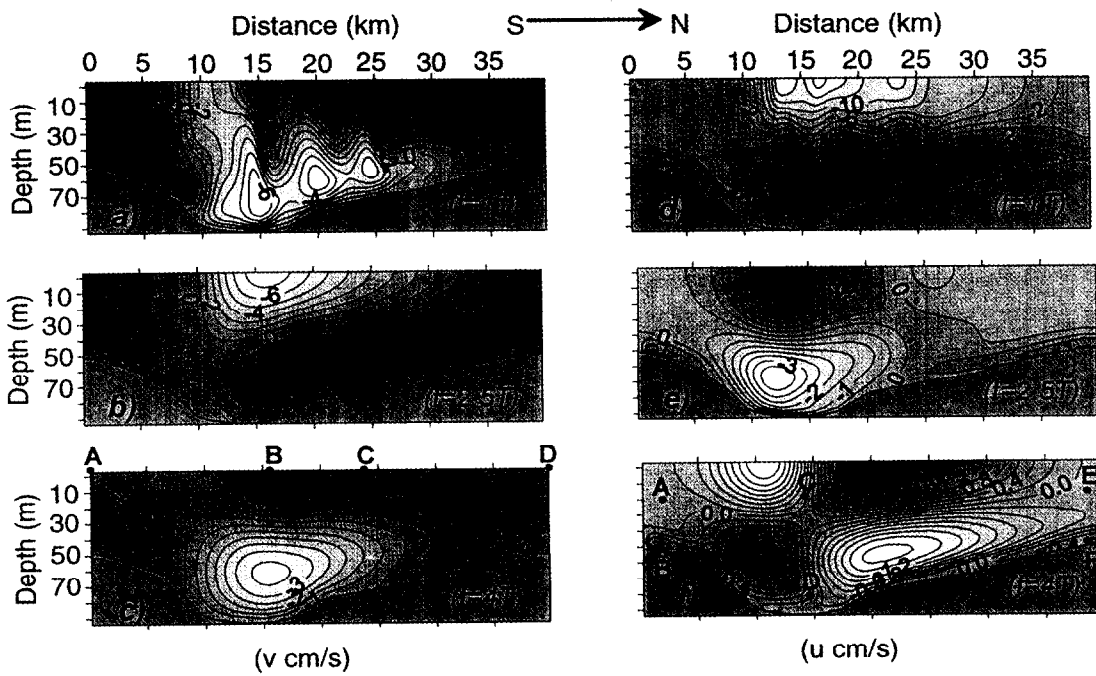


Figure 3. Along (left panels) and across channel (right panels) velocity fields in different moment of time after the beginning of the inflow (model results).

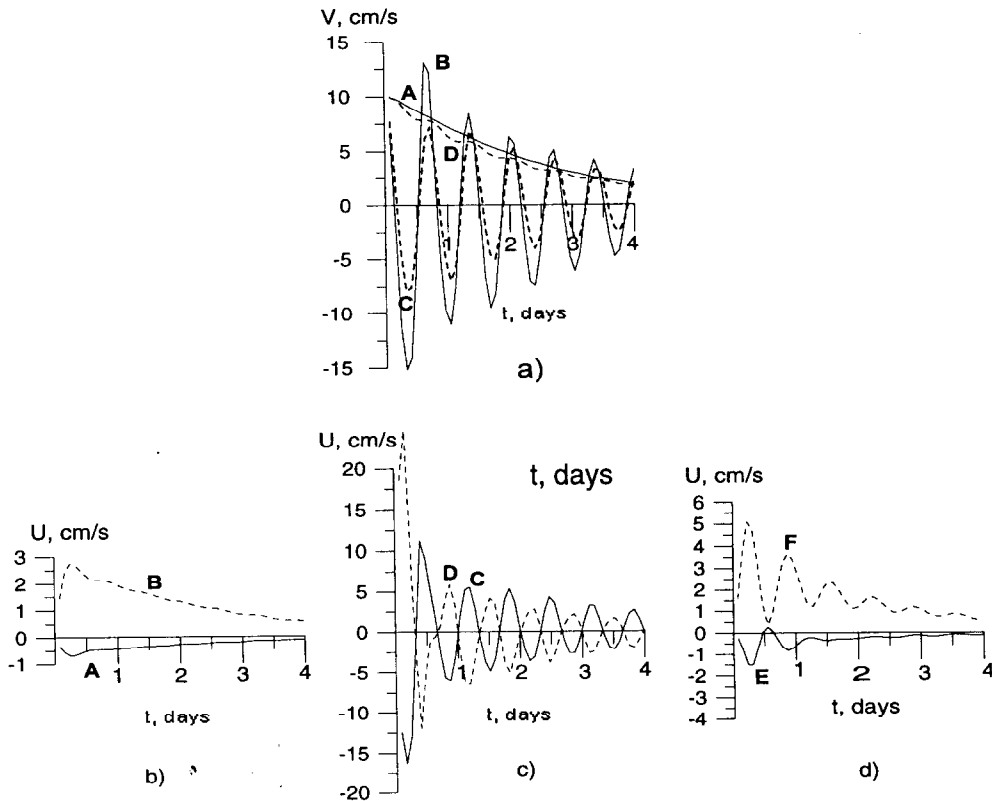


Figure 4. The time dependences of along (a) and across (b), (c), (d) channel velocities. Letters A-D in Fig.4a and A-F in Fig.4b-d correspond to the respective points in Fig.3c, 3f.

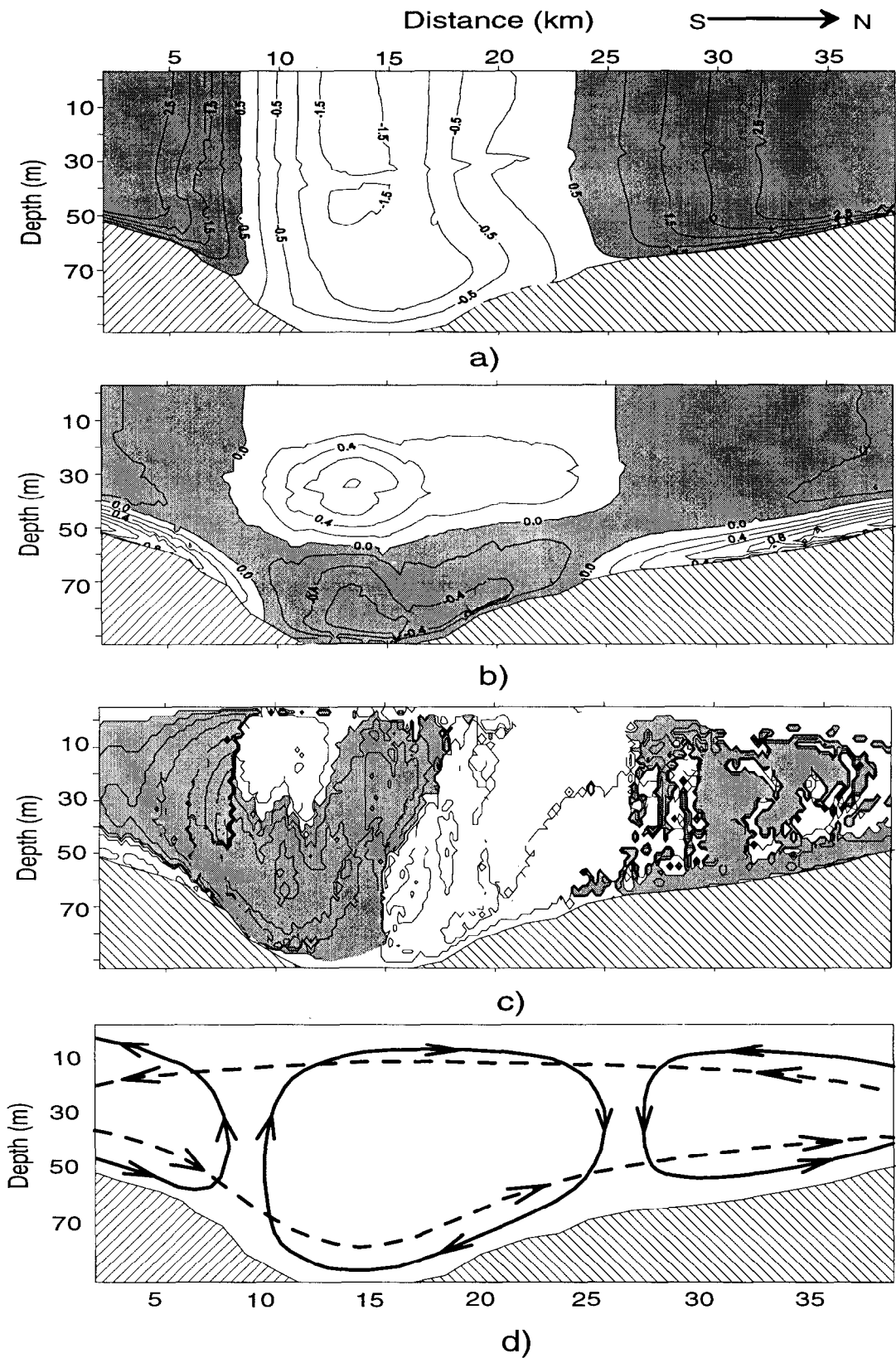


Figure 5. The results of the filtration procedure of inertial oscillation. Fig.5a,b,c are u , v and w fields respectively. Fig.5d is the schematic diagram of a cross-channel water circulation in the beginning (dashed lines) and in the end (solid lines) of the development of the inflow phenomenon.

the mean residual currents which lead to the formation of asymmetrical structure of thermohaline fields across the channel. The result of filtration of inertial oscillations is shown in Figure 5. Panels a, b and c present u , v and w velocities respectively. It is seen that the mean along-channel currents are directed to the Baltic Sea in the central part of the channel by the end of the processes of adjustment (Figure 5a). On the periphery of the channel water moves from the Baltic Sea. The vertical structure of the residual currents has the barotropic character. The values of velocities are almost constant from the surface to the bottom (if don't take into account the boundary bottom layer). In the cross-channel direction the more intensive near-bottom currents take place at the left and right slopes of the channel (Fig. 5b). These currents result in transport of water masses and lead to pinching and surfacing of the halocline on the northern slope of the channel and sinking and widening on the southern one. In the central part of the basin the along channel currents are two times less than on the periphery. Thus, the across channel transport here is much weaker.

The analysis of Fig.5b shows the existence of zones of convergence and divergence. At least two zones of water upwelling and downwelling can be detached in Figure 5b. Thus, the mean movement in the channel has a three-dimensional character. On the basis of Fig.5a-c the scheme of a cross-channel circulation can be drawn. It is presented in Fig.5d. Three vertical circulation cells are formed across the channel. Their boundaries coincide with the zero isopleth of the along-channel velocity. Such picture of the mean across-channel circulation (Fig.5d) is the result of the North Sea water inflow to the Baltic Sea.

CONCLUSIONS

The analysis of a water circulation in the Stolpe Channel obtained on the basis of numerical calculations allows to detach two types of predominant motions established in the channel during the process of the North Sea water inflow to the Baltic Sea: inertial oscillations and quasistationary currents.

On the first stage of the development of the inflow phenomenon the inertial oscillations are generated by the initial shear currents. These oscillations are the most intensive in the central part of the channel and attenuate during three days after the beginning of the inflow. They have a baroclinic character. In the central part of the channel the fluid moves in the opposite directions above and below halocline. On the periphery of the channel the inertial oscillations are essentially weaker. Here the mean westward currents are predominant.

The inertial oscillations develop on the background of the quasi-stationary currents established in the channel during the inflow event. They are the main reason of a reconstruction of the initial horizontally homogeneous thermohaline fields. The Ekman drift, excited in the bottom boundary layer due to the Coriolis force, generates the water transport across the channel. It leads to a reconstruction of hydrological fields and formation of an asymmetrical across-channel structure of thermohaline fields (pinching and surfacing of the halocline on the the northern slope of the channel and sinking and widening on the southern one). The mean along-channel currents are established in such manner that they are directed to the Baltic Sea in the central part of the channel and from the Baltic Sea on its periphery. These currents have basically a barotropic character with almost constant values of velocities from the surface to the bottom.

REFERENCES:

- [1] V.T. Paka, 1996, Thermohaline structure of water in the Stolpe Channel sections of the Baltic Sea in spring, 1993, *Oceanology* 36, 2, 207-217.
- [2] N.N. Kolchitskiy, A.S. Monin and V.T. Paka, 1996, About internal seiches in the Baltic Sea, *DAN*, 346, 2, 255-259.
- [3] G.L. Mellor, X.H. Wang, 1996, Pressure compensation and the bottom boundary layer, *J. of Phys. Oceanogr.*, 26, 10, 2214-2222.
- [4] C. Garrett, P. MacCready and P. Phines, 1993, Boundary mixing and arrested Ekman layers: Rotating stratified flow near a sloping boundary, *Annual Reviews of Fluid Mechanics*. 5, Annual Reviews, 291-325.
- [5] P. MacCready and P. Phines, 1991, Buoyant inhibition of Ekman transport on a slope and its effect on stratified spin-up, *J.Fluid Mech.* 223, 631-661.
- [6] V.I. Vlasenko, V.A. Ivanov and N.M. Stashchuk, 1996, Generation of quasi-inertial oscillations during upwelling event near the south part of Crimea, *Oceanology* , 36, 1, 43-51.

SOME ASPECTS OF THE HYDROPHYSICAL FIELDS FORMATION IN THE GOTLAND DEEP OF THE BALTIC SEA IN SUMMER

V.T Paka¹, V.I Vlasenko², N.M. Stashchuk² and N.N.Golenko¹

1 Atlantic Branch of P.P. Shirshov Oceanology Institute, Mira Street 1, Kaliningrad, 236000, Russia,
e-mail: paka@ioran.kern.ru

2 Marine Hydrophysical Institute, Kapitanskaya Street 2, Sevastopol, 335000, Ukraine,
e-mail: vlasta@ukrcom.sebastopol.ua

ABSTRACT

The thermohaline structure of the water masses in the area of the Gotland Deep of the Baltic Sea was investigated by undulating CTD-probe in Cruise N 29 of R/V "Professor Shtokman" in spring, 1993. The local widenings of a pycnocline with vertical scope of about 30 m and horizontal scale of 12-20 km were revealed at several cross-shelf tows near a shelf break. Two-days measurements had shown that the density disturbances were located at different distances from the 100 m isobath in different sites of the tested area. Two possible mechanisms of formation of the local pycnocline widenings are investigated in this paper by means of mathematical modeling. The first one explains the in-situ data as an "internal surf" phenomenon. The pycnocline inhomogeneities revealed at different distance from the shore are explained as a shoreward propagating two-dimensional internal wave. It is generated by barotropic seiches in the region of a steep continental slope near the Bornholm Island. Nevertheless, a comparison of the in-situ data with the results of mathematical modeling did not confirmed this hypothesis. The generation of observed inhomogeneities of hydrophysical fields due to a shear instability of baroclinic seiches is more realistic. It was obtained that baroclinic seiches oscillations in the conditions of a winter stratification can result in a formation of local zones of a shear instability. This leads to a widening of a pycnocline in zones of instability due to a mixing.

INTRODUCTION

The thermohaline structure of the Central Baltic waters ($57^{\circ}10'-57^{\circ}35'N$ and $20^{\circ}00'-20^{\circ}50'E$) was investigated by undulating towed CTD in March, 1995 during the Cruise N 29 of R/V "Professor Shtokman". The speed of towing was 2.2-2.6 m/s, the distance between two consistent probe immersions was 200-450 m, the maximal depth of measurements was 160 m. The numbers of tows, directions and the time of beginning and end of each towing along with the 100 m isobath are shown in Fig.1a.

Four cross-shore sections of the conventional density σ_t are presented in Fig. 1b. The numbers of towing are corresponded to ones in Fig.1a. The local inhomogeneities of the density field with horizontal scales of 12-20 km are clearly seen at a different distance from the shore for all sections. This paper is addressed to the question of the nature of revealed peculiarities and the mechanism of their generation and evolution.

There are several possible explanations of the inhomogeneities formation. These disturbances are interpreted in [1] as quasistationary eddies with horizontal scale of about 10 km. The alternative idea is followed from the qualitative analysis of horizontal and vertical structure of disturbances. The series of cross-sections in Fig.1b looks like the definite stages of evolution of a propagating internal wave. The hypothesis that internal wave propagates from the deep part of the sea to shallow one can be formulated from the fact of different distance of

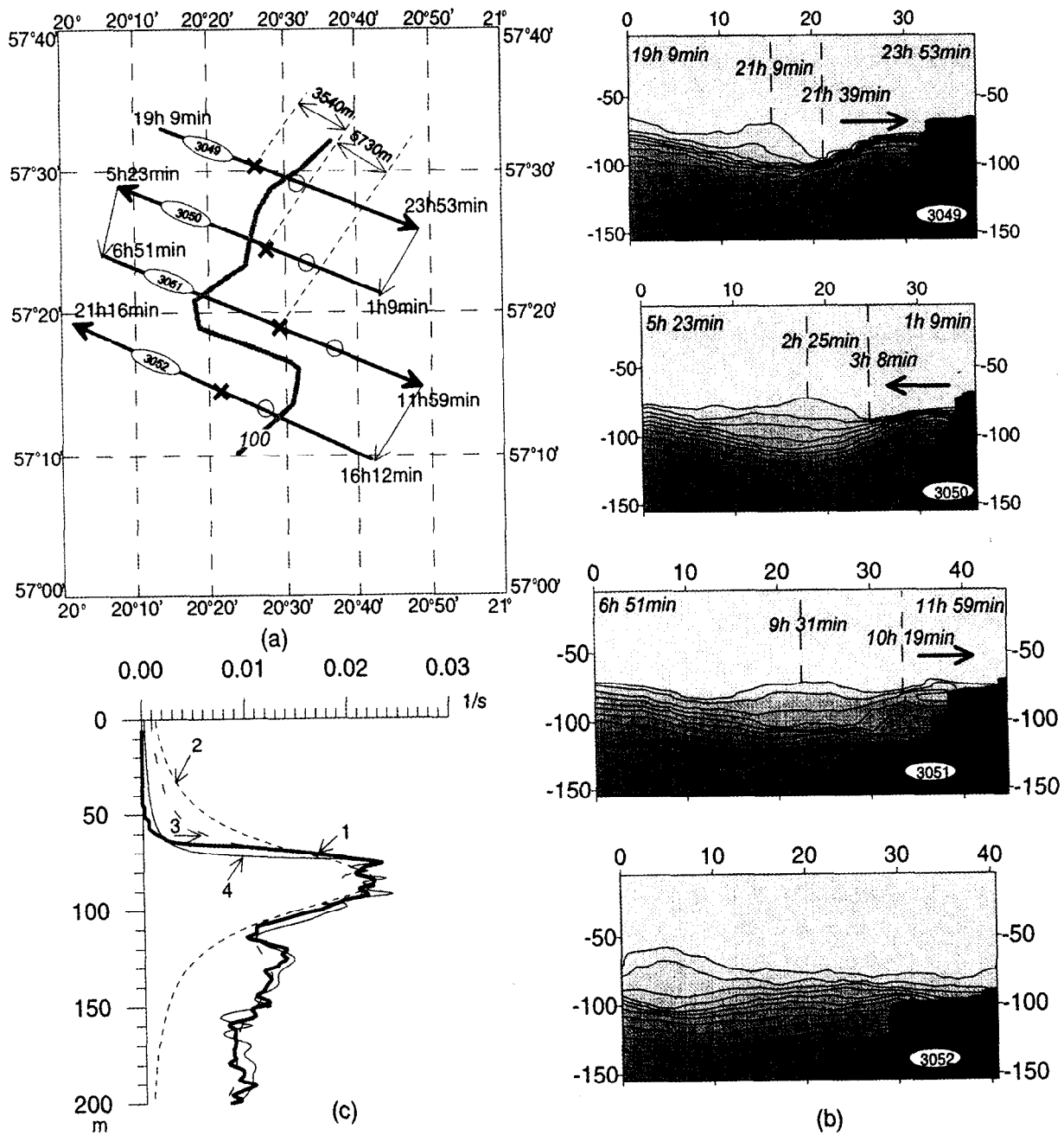


Figure 1. The results of CTD measurements fulfilled in Cruise 29 of the R/V "Professor Shtokman":
 (a) The scheme of ship tracks along with 100m izobath in the area of the Gotland Deep. 3049-3052 are the numbers of tows. The wave crests and troughs are marked by symbols \times and \circ respectively;
 (b) The cross-shore section of the conventional density σ_t for the tows 3049-3052;
 (c) The buoyancy frequency profiles. Line 1 is the experimental and lines 2-4 are the model profiles.

the disturbances from the shore at different moments of time. If the idea of the moving wave is accepted it is ought to pay attention to a few circumstances characterized this wave process:

1. The counterphase displacements of isopycnals above and below pycnocline are unusual for first baroclinic mode. They are inherent to higher baroclinic modes;
2. The rough estimations of the phase speed give the magnitudes of 0.17-0.21 m/s;
3. The location of the density disturbance during the towing 3052 contradicts the stated assumption. It locates far from the shore in comparison with towing 3051. If we assume the reflection of the previous wave from the slope or the existence of a new wave moving from the open part of the sea, the quasiperiodical character of the motion must be taken into account.

To describe this process the mathematical model was developed in the assumption of a quasiperiodical character of the motion. The main question is: what is the reason of a waves generation? The Baltic Sea is nontidal. Thus, probably seiches oscillations can cause vertical motions above the bottom topography and generate internal waves. The periods of the Baltic Sea seiches are: 48 h 13 min, 30 h 12 min, 24 h 03 min, 13 h 43 min, 8 h 11 min. Taking into account the value of the inertial period ($T_{in} \approx 14.3$ h), only seiches with periods 13 h 43 min or 8 h 11 min can generate internal waves. These period were used for modeling.

MATHEMATICAL MODEL

The system of equation describing the dynamics of baroclinic seiches in stratified fluid on a f-plane is expressed in terms of the stream function ψ ($\psi_z = u$, $\psi_x = -w$) and the eddy $\omega = \psi_{zz} + \psi_{xx}$ [2,3]:

$$\begin{aligned} \omega_t + J(\omega, \psi) - fv_z &= g\rho_o^{-1}(\rho)_x + a\omega_{xx} + A\omega_{zz}, \\ v_t + J(v, \psi) + f\psi_z &= av_{xx} + Av_{zz}, \\ \rho_t + J(\rho, \psi) + \rho_o \psi_x N^2(z) / g &= m\rho_{xx} + M\rho_{zz}, \end{aligned} \quad (1)$$

Here u and v are the cross- and along-basin velocity, w is the vertical velocity, J is the Jacobian, ρ is the wave disturbances of the density, ρ_o is the mean value of the density, $N(z)$ is the buoyancy frequency, f is the Coriolis parameter, g is the gravity acceleration, a , A , m , M are the coefficients of horizontal and vertical turbulent viscosity and density diffusion respectively.

The "rigid-lid" conditions, the absence of velocity shear and density fluxes were used at the sea surface:

$$\omega = 0; \quad \psi = 0; \quad \rho_z = 0 \quad \text{at } z = 0. \quad (2)$$

The non-slip and non-flow conditions were used at the bottom:

$$\psi = \psi_o \sin(\sigma t); \quad \psi_n = 0; \quad \rho_n = 0 \quad \text{at } z = -H(x). \quad (3)$$

Here ψ_o is the amplitude of the cross basin barotropic flux, σ is the wave frequency, n is the normal to the bottom. Boundary value of the eddy at the bottom is calculated from the formula $\omega = \Delta\psi$ [4], with the use of the stream function ψ on the previous temporal layer.

The problem (1)-(3) was solved numerically [2,3]. The used bottom profile was steep at the northern part of the sea (near the Bornholm Island) and gentle sloping at the southern part. The value of barotropic flow ψ_o was calculated from the condition of maximum velocity of 25 cm/s at the izobath 60 m.

MODELING OF THE "INTERNAL SURF" PHENOMENON

Before the considering of the obtained results let's discuss the peculiarity of a fluid stratification in region under study. The experimental profile of the buoyancy frequency is shown in Fig.1c (line 1). It characterized by an upper 60 m homogeneous layer. The pycnocline is located at a depth of about 85 m. Three model profiles of the buoyancy frequency are also shown in Fig.1c. The first one (line 2) is described by a formula:

$$N^2(z) = [c_1(z + c_2) + c_3]^{-2}. \quad (4)$$

The factors c_1 , c_2 , c_3 are defined by three constants: value of a buoyancy frequency maximum, the depth of pycnocline and its width. Lines 3 and 4 (Fig.1c) were obtained as a sum of several profiles (4).

The density sections for the first type of stratification are presented in Fig.2. At the first stage of the generation process the more intensive vertical displacements of a pycnocline are located near the steep northern slope. Being generated near the Bornholm Island the pycnocline perturbations are divided onto two waves propagating in

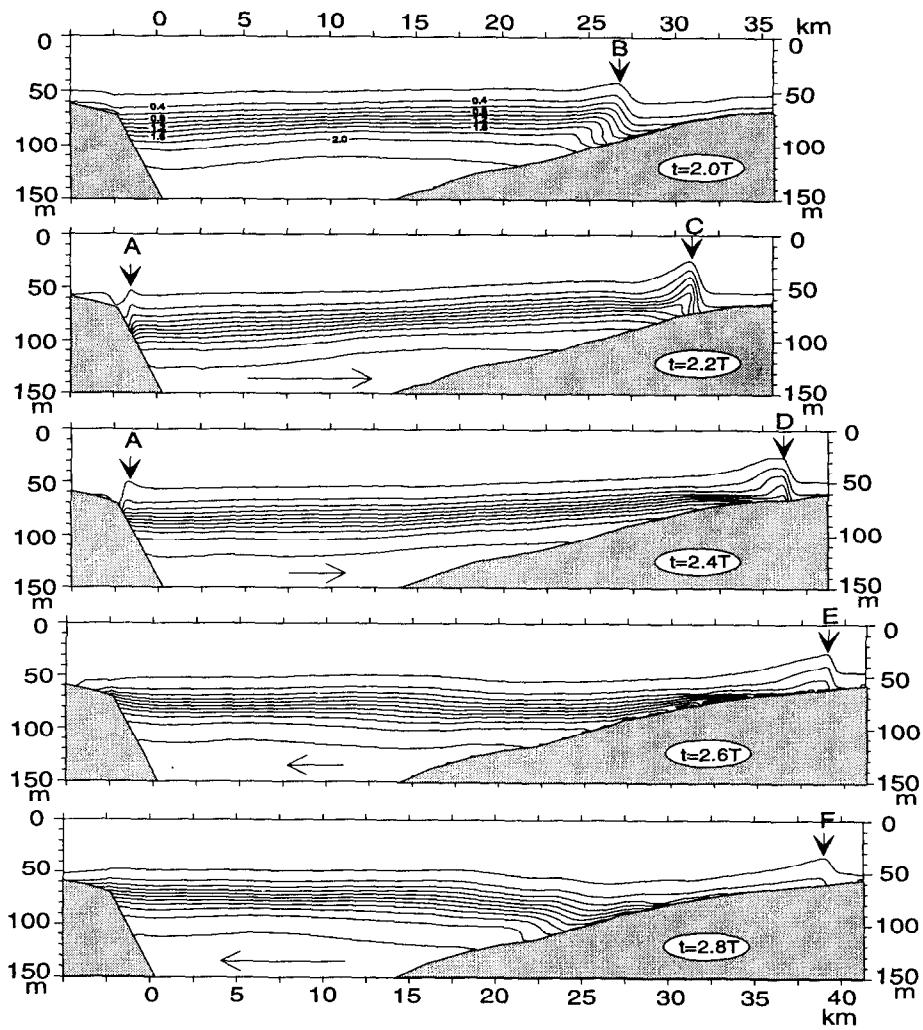


Figure 2. The process of development of the "internal surf" phenomenon obtained from the numerical modelling. Positions B, C, D, E and F represent the propagating internal wave.

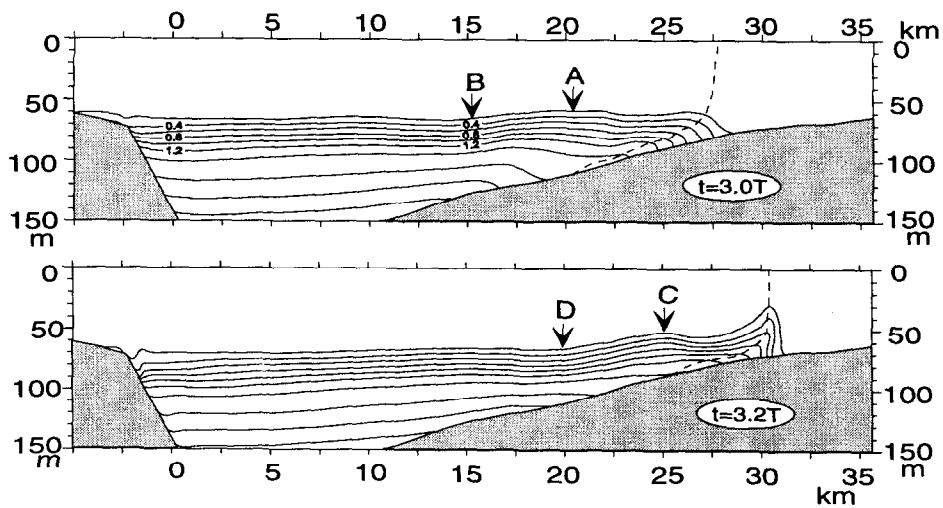


Figure 3. The model predicted cross-sections calculated for the buoyancy frequency profile 3 (Figure 1c). The manifestation of high baroclinic modes are presented by positions A, B, C, D.

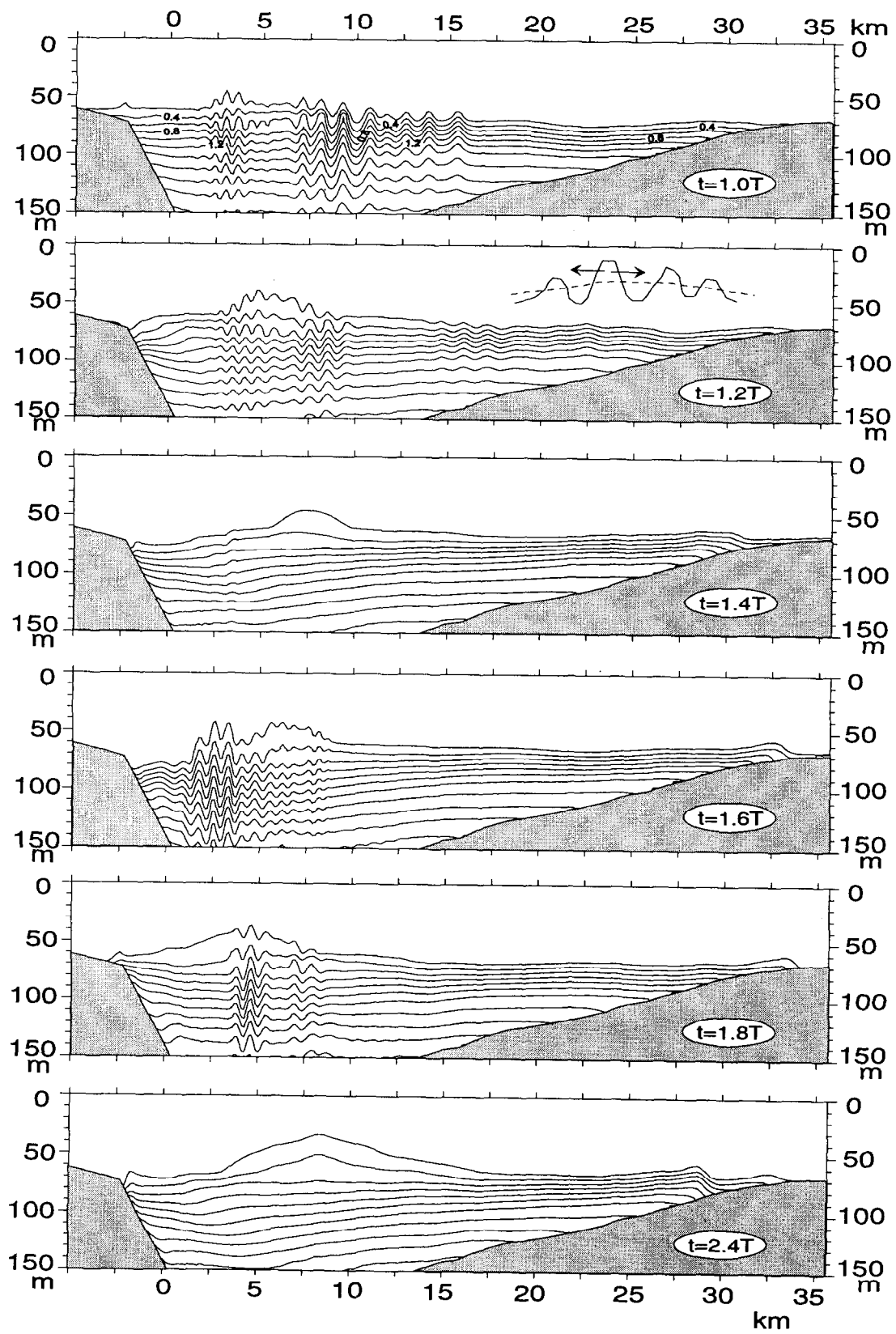


Figure 4. Development of the hydrodynamic instability obtained numerically for the buoyancy frequency profile 4 (see Fig 1c).

opposite directions. The wave moving northward reflects from a steep continental slope. Therefore the pycnocline disturbances near the Bornholm Island are negligible (position A in Fig.2). The main part of energy is reflected from the slope. The energy of a southward moving internal waves practically doesn't reflect from the gentle sloping bottom. The wave energy are concentrated in the leading wave which increases its amplitude in the shoreward direction due to the shoaling effect. The propagating wave forms so called "internal surf". This process is presented in Fig.2 by position B, C, D, E and F.

The comparison of the theoretical results (Fig.2) with in-situ data (Fig.1b) shows that the theoretical wave amplitude (~30-35 m) coincides with experimental one but the horizontal scale of experimental "wave" two-three times greater. Besides, the phase speed of experimental wave is equal to 0.17-0.21 m/s and theoretical wave propagates with the phase speed of 0.34 m/s. The next disagreement is that the experimental disturbances have the multimodal character, whereas the first mode is predominant in the theoretical wave.

The multimodal solution in the mathematical modeling can be obtained with the use of the buoyancy frequency profile 3 (Fig.1c), which differs from the previous one by existence of a stratified near-bottom layer. According to [6,7] this fact can result in generation of high modes. Two sections of density fields, obtained for profile 3 are shown in Fig.3. The counterphase isopycnal displacements are clearly seen in the positions A, B, C, D in Fig.3. Nevertheless, the comparison analysis of Fig.3 and Fig.1c has shown that the increase of stratification near the bottom didn't modify essentially the wave field.

MODELING OF A SHEAR INSTABILITY

Now lets consider the results obtained for the profile 4 (Fig.1c). The main difference between the profile 4 and considered above is the absence of the stratification in the upper 60-meter layer.

The density field for different moment of time is presented in Fig.4. The existence of short-wave disturbances in the central part of the basin at $t=1.0, 1.2, 1.6T$ can be explained by virtue of analysis of the eigen functions of the boundary value problem. For the stratification 4 the maximum of a velocity shear is located near the upper boundary of a pycnocline. Thus, a decrease of Richardson number below the critical value is possible at a definite stages of the wave process. As a result, a shear instability is developed ($t=1.0; 1.2; 1.6T$). Due to the periodicity of the motion the phase of instability amplification is changed by a phase of attenuation ($t=1.4; 2.4T$).

The presence of a horizontal turbulent diffusion leads to a widening of a pycnocline in zone of instability due to a mixing. The schematic diagram of this process is presented in Fig. 4. The comparison analysis of Fig.1b and 4 has shown that the parameters of experimental disturbances and theoretical ones coincide. In addition, the phenomenon of the "internal surf" also takes place for these type of stratification. But the wave amplitude near the shore in Fig. 4 is smaller then in Fig.2.

CONCLUSIONS

From two possible mechanisms of generation of hydrophysical fields inhomogeneities in the Baltic Sea in winter (the phenomenon of "internal surf" and shear instability) the latter more adequate explains the in-situ results obtained in Cruise 29 of R/V "Professor Shtokman". Nevertheless, the numerical calculations have shown that the phenomenon of "internal surf" can also take place in the Baltic Sea.

REFERENCES:

- [1] A.G. Novitski, 1995, On eddy disturbances in the Baltic Sea, *Oceanology*, 35, 5, 663-667.
- [2] V.I.Vlasenko, 1992, Nonlinear model for the generation of the baroclinic tides over extensive inhomogeneities of the seabed relief, *Sov. J. of Phys. Oceanogr.*, 3, 6, 9-16.
- [3] V.I.Vlasenko and L.V.Cherkosov, 1989, The generation of the baroclinic tides over steep bottom topography, *Sov. J. of Phys. Oceanogr.*, 1, 3, 161-169.

CHLOROPHYLL AND OTHER NATURAL ADMIXTURES CONCENTRATIONS ESTIMATION IN SEA WATER OF DIFFERENT TYPES FROM CONTACT AND REMOTE SENSING DATA

V. N. Pelevin and V. V. Rostovtseva

P.P. Shirshov Institute of Oceanology RAS,
36, Nahimovskii av., 117 851 Moscow, Russia
e-mail: pelevin@sio.rssi.ru

Abstract. An original method has been developed for estimating the concentrations of chlorophyll pigments, dissolved organic matter ("yellow substance") and suspended matter from the data of spectral vertical light attenuation coefficient and diffuse light reflection coefficient. The suggested method is valid for any ocean area including shelves. The proposed method has been applied to the sea waters of different types according to the effective numerical single parameter classification. This classification gives the possibility to restore the main characteristics of the light field in water in the open ocean using the only one parameter - *water type optical index m*. For *m* over the whole range of the open ocean waters the calculations have been carried out and the light absorption spectra of sea waters have been tabulated. Using these spectra the absorption models have been optimised and the main sea water admixtures concentrations estimated. By the help of these results the sea water composition in any area of the open ocean can be easily estimated if the only one parameter *m* is known for the aquatorium of interest. The value of *m* can be determined by direct measurements of vertical light attenuation coefficient or calculated from the remote sensing data using the given regressions.

1. Method of the main natural admixtures estimation from contact measurements data

The suggested method consists of two steps. At the first step the values of light absorption coefficient in water are calculated from measured values of the spectral coefficient of vertical light attenuation and coefficient of diffuse light reflection in the visible. At the second step an absorption model giving the closest possible approach to the obtained light absorption coefficient spectrum is developed. The parameters of such model are the values of the chlorophyll concentration and absorption coefficients of "yellow substance" and suspended matter.

As known, the divergence of the vector of light energy transfer \mathbf{H} is equal to the spatial density of light energy absorption by an elementary volume:

$$\operatorname{div} \mathbf{H} = -a E^{\circ}, \quad (1)$$

where a is the light absorption coefficient in water, E° is the spatial illumination of the given volume. Since horizontal gradients of optical properties of water in sea are much smaller than vertical ones (vertically stratified medium) and the scale of nonuniformity in surface illumination by daylight far exceeds the scale of vertical variability of light field in water, the horizontal gradients of \mathbf{H} can be neglected. The vertical component of this

vector H_z is equal to $(E_{\downarrow} - E_{\uparrow})$ where E_{\downarrow} is down- and E_{\uparrow} is up-illumination at a level z . Thus, (1) takes the form $d/dz (E_{\downarrow} - E_{\uparrow}) = -a E^0$ [1]. Dividing (1) by $(E_{\downarrow} - E_{\uparrow}) = E_{\downarrow} (1 - R)$, where R is the coefficient of diffuse light reflection by sea ($R = E_{\uparrow} / E_{\downarrow}$), and taking into account $K_d = -1/E_{\downarrow} (dE_{\downarrow}/dz)$ we derive the formula:

$$K_d \left\{ 1 + (dR/dz) / K_d / (1-R) \right\} = a E^0 / (E_{\downarrow} - E_{\uparrow}). \quad (2)$$

The diffuse light reflection coefficient R varies only slightly with depth. It was shown by processing of numerous experimental data that the second term in brackets is no more than 0.04, therefore, it can be ignored [1]. In the right-hand side of (2) there is the expression for the mean cosine of the angle of radiation incidence $\mu = (E_{\downarrow} - E_{\uparrow}) / E^0$. Then (2) takes the form

$$a = K_d \mu. \quad (3)$$

Special model experiments in artificial media and series of measurements carried out in the Indian Ocean [2] have shown the mean cosine of the angle of light incidence is highly correlated with the coefficient of diffuse reflection according to the regression

$$\mu = 1 - 0.185 \sqrt{R}. \quad (4)$$

The error in determining μ from this formula is rather small ($-0.03 < \Delta\mu < 0.04$). Thus, using measured values of K_d and R the water absorption coefficient can be estimated:

$$a = K_d (1 - 0.185 \sqrt{R}). \quad (5)$$

Since solar light field parameters K_d and R can be obtained in any aquatoria, a can be determined by this method both in open sea and shelf waters.

For the evaluation of the main natural admixtures concentration in sea water from the obtained absorption coefficient (the second part of the suggested method), let us assume that the light absorption coefficient depends mainly upon four factors:

$$a_{\lambda}^{mod} = a_{w,\lambda} + C_p a_{p,\lambda}^*(C_p) + a_{ys} \exp(-g(\lambda - \lambda_0)) + a_{sm}. \quad (6)$$

Here $a_{w,\lambda}$ is the coefficient of light absorption by clear sea water; C_p is the phytoplankton pigments concentration, mg/m^3 ; $a_{p,\lambda}^*(C_p)$ is the coefficient of specific absorption by phytoplankton pigments depending on the pigments concentration; a_{ys} is the coefficient of light absorption by "yellow substance" contained both in solution and in detrits at a wavelength λ_0 ; a_{sm} is the coefficient of light absorption by suspended particles excluding the absorption of phytoplankton pigments as well as the absorption of "yellow substance" in particles. The dependence of the coefficient of specific absorption by phytoplankton pigments on the chlorophyll concentration was taken into account using some empirical relations from [3] in the way suggested in [4]. The spectrum of "yellow substance" absorption was defined as exponential with the index equal to 0.015nm^{-1} [5]. The numerous measurements of its spectrum in the Indian and Pacific oceans ([6] pp.158-159) and in the Baltic Sea [7] confirmed its exponential character with the index values differ from 0.012 to 0.019nm^{-1} , 0.015nm^{-1} being the mean value. We suppose the absorption of the suspended matter a_{sm} is unselective since we included the absorption of pigments as well as the absorption of "yellow substance" contained in particles into the second and third terms of (6).

Now, if one obtains the spectra of vertical light attenuation and diffuse reflection coefficients for aquatorium of interest he can derive them into the set of light absorption coefficients using the procedure described above. Then the concentrations of the main water admixtures can be calculated by selecting the coefficients for the absorption model (6) in such a way to provide the closest approach of it to this set of empirical data using the optimisation algorithm [4].

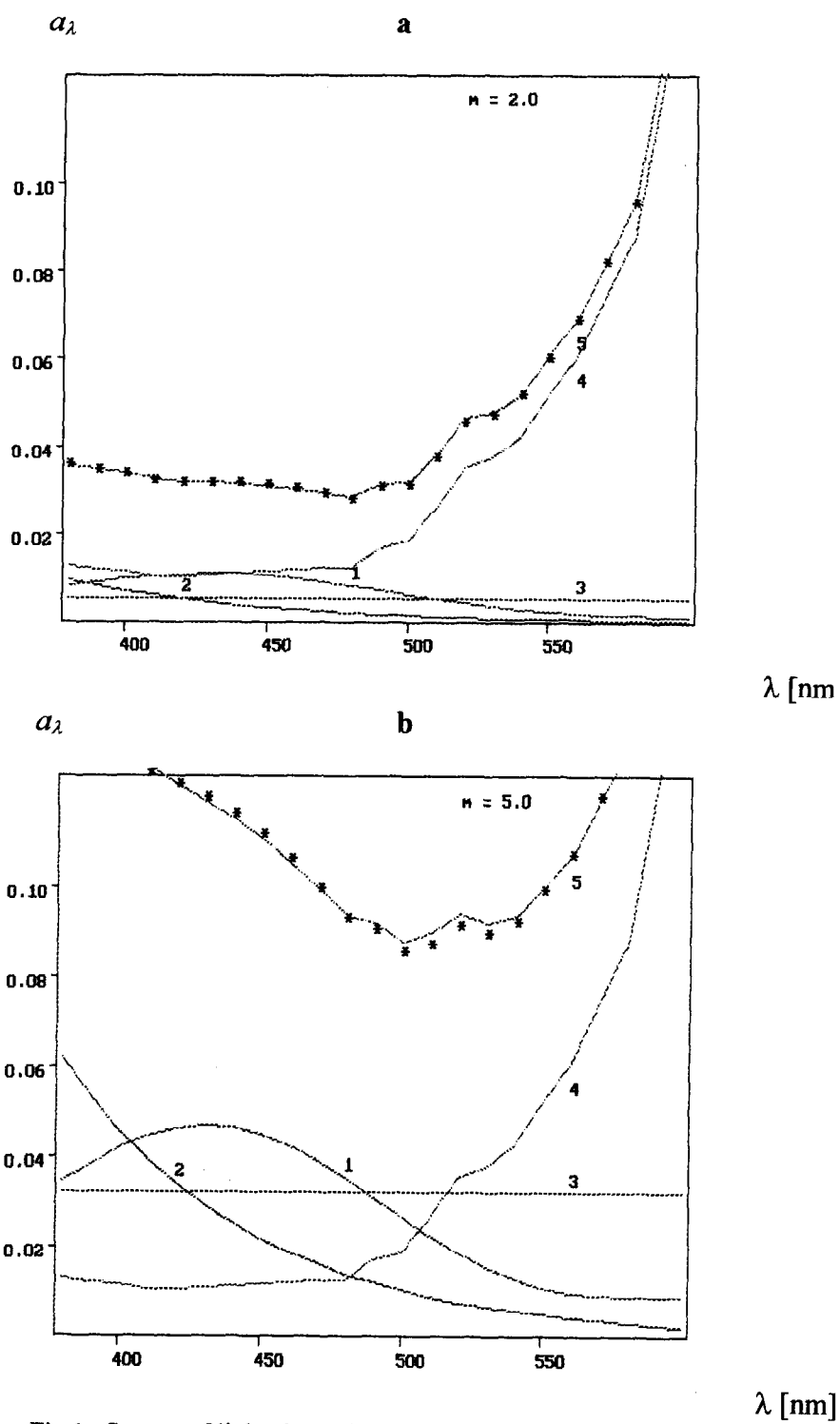


Fig.1. Spectra of light absorption obtained by optimisation procedure
 a) for some oligotrophic ($m=2$) and b) for some eutrophic ($m=5$) waters.

As an example the proposed technique is demonstrated for two cases: some oligotrophic and eutrophic waters (Fig.1). The spots give the input dataset of light absorption spectra. After the absorption model optimisation we obtained the optimal absorption spectra for the three main natural water admixtures: absorption by phytoplankton pigments (curve 1), absorption by "yellow substance" (curve 2), absorption by suspended matter without pigments and "yellow substance" in detrits (curve 3). Their sum plus the spectrum of pure sea water absorption (curve 4) make the model spectrum for water absorption (curve 5) which is the best approximation for these experimental values.

2. Main admixtures concentration for the whole range of sea-water types in open ocean

Let's calculate the concentration of phytoplankton pigments, "yellow substance" and suspended matter using the above suggested method for all kinds of waters in the open ocean (Case 1 according to Morel). There are several different water type classifications giving the possibility to characterise the sea water using the simple indices of water type (see for example [8-10]) or values of chlorophyll concentration [11,12]. But we chose the classification that enables one to restore the characteristics of the solar light field in sea-water using the only one parameter defined as water type optical index m [13]. This parameter is proportional to the vertical light attenuation coefficient at 500 nm:

$$m = 100 \lg e K_{d500} \cong 43.43 K_{d500}. \quad (7)$$

K_{d500} should be measured by the Sun altitude more than 35 degrees or by the sky overcast.

The least obtained value of m was measured in the central part of Pacific at the south-east of Cook Islands and turned to be equal to 1.15 [14]. We consider the optical properties of such water as the properties of pure sea-water. The values of m from 1.15 to 2 correspond to oligotrophic waters, the values from 2 to 5 correspond to mesotrophic ones, larger values characterise eutrophic waters. The distribution of m in Pacific, Indian and Atlantic Oceans obtained by numerous contact measurements are given in [15-17]. There are also the tables and nomograms there given for restoration of the spectra of vertical light attenuation coefficient and diffuse light reflection coefficient for given m . We carried out calculations of these spectra for the whole range of m in the open ocean. Now, using the above proposed method we can estimate the main natural admixtures concentrations.

The optimisation of the absorption models was carried out in the visible from 380 to 600 nm. The calculation results are given in Fig.2. Variations in input parameters within 10% together with the possible variations in other parameters used by the absorption model produce the error in estimation of C_p , a_{ys} and a_{sm} no more than 20 - 25% [4].

Numerous data obtained by the direct measurement of chlorophyll concentration from board the research vehicle "Vityaz" in the Atlantic Ocean in 1991 and averaged for every m fall within the above indicated error in estimation of the chlorophyll concentration (Fig.2). As for "yellow substance" concentration numerous data of its investigation in the open ocean give the value range for light absorption referred to 500nm from $0.0002m^{-1}$ to $0.02m^{-1}$ ([6] p.159-160). These values are in good accordance with the results obtained by our method.

3. Estimation of sea water admixtures concentrations by remote sensing

The obtained admixture concentration dependences can be used for estimating the water content in any open sea aquatorium of interest if the appropriate contact measurements of K_d are available. Moreover, they can be also used for the remote sensing of sea waters. In fact m can be estimated rather safely from some remote measurements too. It can be calculated from the ratio of sea radiance coefficients ρ_λ using the regressions [18]:

$$m = 1.0 + 3.7 \rho_{550}/\rho_{440} \quad \text{or} \quad m = 1.3 + 3.5 \rho_{560}/\rho_{430} \quad (9)$$

with standard deviations of 14% and 20%.

C_p, a_{ys}, a_{sm}

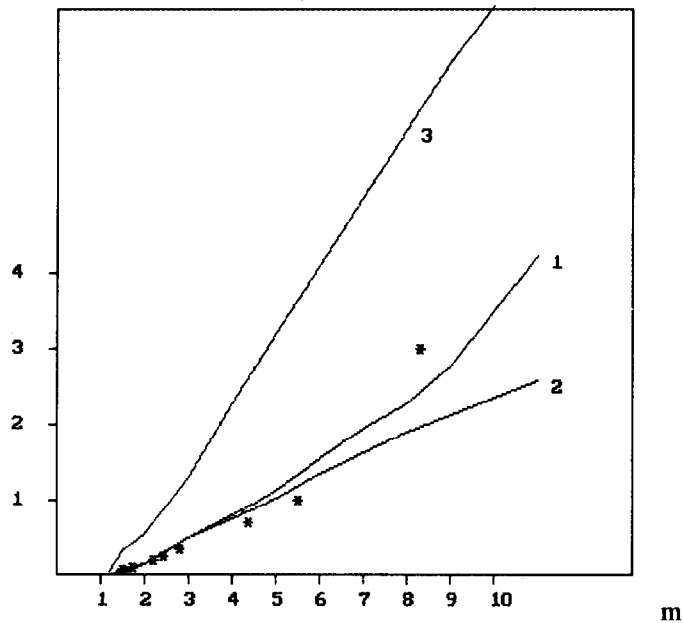


Fig.2. Chlorophyll concentration C_p in [mg/m^3] (1), "yellow substance" absorption coefficient $a_{ys} \cdot 100$ in [m^{-1}] (2) and suspended matter light absorption coefficient $a_{sm} \cdot 100$ in [m^{-1}] (3) as a function of water type optical index m . Spots - the data of the direct measurements of chlorophyll concentration in sea water.

Recently we suggested another method of determination of m from remote sensing data [19]: we revealed the strong correlation between the gradient of the sea surface spectral radiance in the band 490 - 510 nm and the optical index of water type m . Therefore the water type can be estimated from space using the new parameter slightly affected by the atmospheric conditions.

Thus, the obtained dependences of the three main natural sea-water admixtures concentrations upon the water type optical index m give the possibility of the water composition estimation in any open sea aquatorium if only m is measured there by contact or remote sensing methods.

References

- [1] Pelevin V.N., 1965. The measurement of the light absorption coefficient in the sea, *Izvestia Akademii Nauk SSSR, PhAO*, V.1, N5, 539-545.
- [2] Pelevin V.N. and Prokudina T.M., 1979. On the relation of parameters of deep radiance distribution upon P criterion, in: *Light fields in the ocean*, Publishing House of P.P.Shirshov Institute of Oceanology, USSR Academy of Sciences, Moscow, 34-38.
- [3] Wozniak B. and Ostrowska M., 1990. Composition and resources of photosynthetic pigments of the sea phytoplankton, *Oceanologia (Pol.)*, V.29, 91-115.
- [4] Pelevin V.N. and Rostovtseva V.V., 1995. Estimation of chlorophyll concentration in sea water from measurements of spectral index of vertical light extinction, *Atmospheric and Oceanic Optics*, V.8, N12, 989-992.
- [5] Jerlov N.G., 1968. *Optical Oceanography*, Elsevier, Amsterdam - London - New York, 222 pp.
- [6] Monin A.S., ed., 1983, *Oceanic optics, Vol.1. Physical optics of the ocean*, Nauka, Moscow, 372pp.
- [7] Pelevina M.A., 1979. The method and results of measuring the spectral absorption of light by dissolved organic "yellow substance" in the waters of the Baltic sea, in: *Light fields in the ocean*, Publishing House of P.P.Shirshov Institute of Oceanology, USSR Academy of Sciences, Moscow, 92-97.
- [8] Jerlov N.G., 1976, *Marine optics*, Elsevier, Amsterdam and New York, 231 pp.
- [9] Morel A. and Prieur L., 1977. Analysis of variations in ocean colour, *Limnol. Oceanogr.*, V.22, N4, 709-722.
- [10] Prieur L. and Sathindranath S., 1981. An optical classification of coastal and oceanic waters based on the specific spectral absorption curves of phytoplankton pigments, dissolved organic matter and other particulate materials, *Limnol. Oceanogr.*, V.26, N4, 671-689.
- [11] Baker K.S. and Smith R.C., 1982. Bio-optical classification and model of natural waters 2, *Limnol. Oceanogr.*, V.27, N3, 500-509.
- [12] Morel A., 1988, *Optical modelling of the upper ocean in relation to its biogenous matter content (case 1 waters)*, *J.Geophys.Res.*, V.93, N C9, 10749-768.
- [13] Pelevin V.N. and Rutkovskaya V.A., 1977, On the optical classification of the ocean waters by the spectral solar light attenuation, *Oceanology*, V.17, N1, 15-21.
- [14] Otchakovskii Yu.E., et al., 1978, Propagation of the natural radiation in the ocean, in: *Hydrophysical and hydrooptical investigations in the Atlantic and Pacific Oceans*, Monin A.S. and Shifrin K.S., eds., Nauka, Moscow, 166-190.
- [15] Pelevin V.N. and Rutkovskaya V.A., 1978, On the attenuation of photosynthetically active solar radiation in the Pacific waters, *Oceanology*, V.18, N4, 619-625.
- [16] Pelevin V.N. and Rutkovskaya V.A., 1979. On the attenuation of solar energy flux with depth in the waters of the Indian Ocean, in: *Light fields in the ocean*, Publishing House of P.P.Shirshov Institute of Oceanology, USSR Academy of Sciences, Moscow, 73-85.
- [17] Pelevin V.N., Rutkovskaya V.A. and Voitov V.I., 1982, Penetration of photosynthetic radiation in Atlantic waters, *Oceanology*, V.22, N3, 488-495.
- [18] Pelevin V.N., 1979. On the spectral characteristics of the solar radiation field in the sea and above the sea surface, in: *Light fields in the ocean*, Publishing House of P.P.Shirshov Institute of Oceanology, USSR Academy of Sciences, Moscow, 16-25.
- [19] Pelevin V.N., Rostovtseva V.V. and Matyuschenko V.A., 1998. Remote sensing determination of sea water type using the gradient of spectral radiance of sea surface, *Proceedings of International conference on Coastal Ocean and Semi-Enclosed Seas: Circulation, Ecology Modeling and Monitoring*, Moscow, 19.

Gravity currents over smooth and rough topography. Modelling study on the Mediterranean outflow in the Black Sea

E. L. Peneva and E. V. Stanev

Department of Meteorology and Geophysics, University of Sofia,
5 James Bourchier Str, 1126 Sofia, Bulgaria
e-mail: elfa@phys.uni-sofia.bg

Abstract.

Numerical simulations of Mediterranean outflow in the Black Sea using reduced gravity model have been carried to study the topographic control. In the reference experiment we use realistic topography and the model is tuned to adequately simulate the observed characteristics of gravity currents. Idealistic topography $H=H(y)$, consisting of Bosphorus exit, shelf, continental slope and abyssal plain, is constructed in such a way that the geometric parameters of topography elements (slope and length) are comparable to the real ones. In order to investigate the impact of roughness on the gravity current simulations are carried out with idealistic but rough topography with roughness characteristics similar to observed ones. The results demonstrate that the behavior of gravity currents under specified ambient stratification is strongly dependent on local topography slope and roughness. Entrainment velocity reaches maximum on the continental slope. The roughness affects both entrainment rates and dispersive properties of the model. It was also found that the presence of Bosphorus underwater channel extension is quite significant for the dynamics of gravity currents.

1. Introduction.

The gravity plumes in stratified oceans are recently addressed in number of studies where the transport by gravity currents is considered as a key mechanism of ocean water mass formation. Most of these studies are focused on the Mediterranean outflow [1], [2], [9] and on the outflows through the North Atlantic straits [4], [10]. A large variety of models (e. g. stream-tube models, reduced gravity models, $1\frac{1}{2}$ -D models or fully 3D models) is used in these studies. Here we address the Mediterranean outflow in the Black sea.

The Black Sea is a semi-enclosed basin where the limited exchange with Mediterranean Sea through the Bosphorus Straits is of great significance for deep water formation. The specific conditions in the outflow area, e.g. the extremely sharp salinity differences between Black Sea and Mediterranean Sea (18 psu versus 36 psu), the very strong vertical stratification (salinity at the surface about 18 psu versus 21.5 psu at 300 m depth), variable topography in the outflow area (shallow shelf of about 50 m and abrupt increase of bottom depth down to 1000 m in about 20 km) give a unique test case to study slope convection, internal mixing and the impact of bottom topography on gravity currents. The main questions that still need deeper elucidation are: (1) does the Mediterranean Sea Water (MSW) reach the bottom (as this occurs in the Weddel Sea) or can it be found at some specific depth interval (as this is the case with the Mediterranean outflow in Atlantic); (2) does the current turn to the right and propagate along the isobaths affected by Coriolis force, as this occurs after the outflow leaves the Gibraltar Straits; (3) what is approximately the area where the plume can be identified and the area where it loses its identity.

Observations in the Black Sea support the idea that the deep layers are formed long time ago and are currently unaffected by the sinking plume [7]. The pathway of Mediterranean outflow was investigated by Russian and Turkish oceanographers and it was shown that the current persistently takes North-West direction following a narrow underwater channel. After leaving the channel and reaching the continental slope, no pronounced turn to the right was observed [5], [6], [13], [16]. It is widely accepted that substantial part of the vertical mixing is caused by the entrainment of Black Sea Water (BSW) by the sinking plume [3], [11]. However, the results of observations give wide range of estimated ratios between the inflowing and entrained water that motivated some

recent numerical studies on this subject. The recent paper [12] (hereinafter SSP) investigates in detail the dynamics of Mediterranean outflow in the Black Sea using results of number of numerical experiments. The simulations described in this study give a good agreement with observations and prove that the shallow sinking of the outflow could be explained by the large entrainment on the shelf. This entrainment reduces the salinity of the plume and its density so that the depth of neutral buoyancy is reached at about 200-400 m. Another consequence of the large entrainment is the rapid decrease of temperature and salinity anomalies of the plume with increasing distance from the strait exit, thus the plume can not be identified in the open sea. It is demonstrated in the above study that the ambient stratification is of major significance for the depth of penetration of gravity currents.

Here we extend our previous analysis towards investigating the role of bottom topography for the propagation of the plume. We try to give answers to the following important questions: (1) What would be the pathways of density currents and their characteristics if the underwater channel was absent? (2) What are the differences between the currents on the shelf and on the continental slope? (3) How the slope of topography controls the gravity currents? (4) What is the impact of bottom roughness?

In our study we use reduced gravity model which allows better description of processes over realistic topography than in the stream-tube models and in the same time consumes much less computer resources than 3D models. This makes the integration with high resolution very efficient and manageable even on a single processor workstation.

With mass, buoyancy and momentum fluxes we can fully describe the propagation of the idealistic gravity plumes [14]. However, the dependence of acceleration on local topography under realistic conditions could perturb the main balance of forces. To better understand the key mechanisms controlling the Mediterranean outflow in the Black Sea and to answer the main questions addressed in the present study we will analyze simulations with idealized, simplified and realistic topography.

2. The numerical model.

The model consists of a turbulent lower layer (the plume) underlying an upper layer, Fig. 1. Bottom friction obeys quadratic drag law and the friction coefficient is set at $r=3 \times 10^{-2}$ after number of tuning experiments. The coefficients of turbulent exchange and diffusion are taken as $A_h=A_{hT}=50 \text{ m}^2\text{s}^{-1}$. Model entrainment velocity is parameterized in such a way that the exchange between the plume and ambience depends on Richardson number as

$$w_e = \frac{c_L^2}{S_m} \sqrt{\bar{u}^2 + \bar{v}^2 + \frac{g'H}{S_m}}, \quad (\text{Eqn. 1}),$$

where u, v are zonal and meridional component of velocity, g' is reduced acceleration rate, H is bottom depth, $c_L=0.0086$ and S_m is turbulent Schmidt number (for more details about the governing equations, parameterizations and numerics, see [4] and SSP).

The model domain is resolved with a horizontal grid step of 600 m. The model area has almost solid south boundary with a small opening where the characteristics of the strait outflow are prescribed. The other three boundaries are open with zero normal gradients of temperature, salinity, zonal and meridional components of velocity and interface depth. At the solid boundary the velocity components are set to zero. The initial width of the plume is limited by the strait opening (three grid elements). Its thickness at the exit of the Bosphorus Straits is specified in such a way that the simulated transport is comparable to the observed one ($10^4 \text{ m}^3\text{s}^{-1}$, [15]).

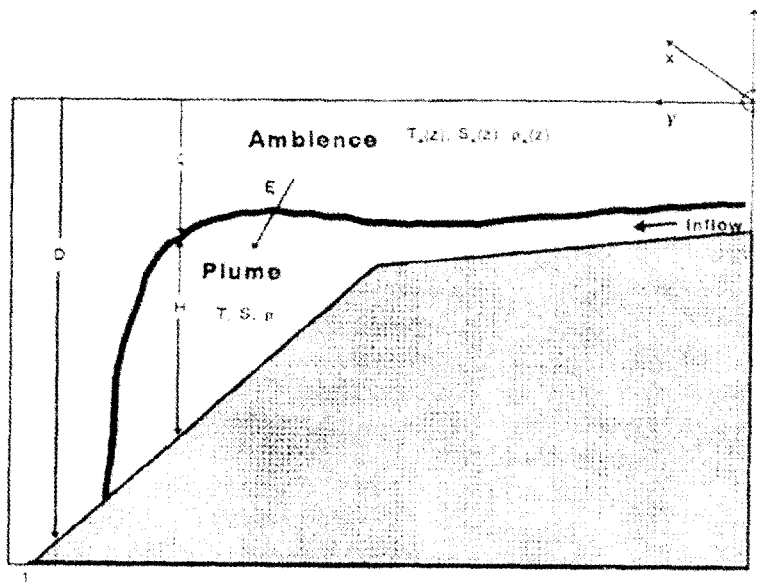


Fig. 1. Schematic view on the reduced gravity model.

3. Model scenarios.

We carry out several simulations with the only difference between them being the bottom topography. The Control Run (CR) has realistic topography (Fig. 2a) based on the bathymetric map of [5]. This experiment is described in [12] and is used here as reference one giving good agreement with the existing observations. The remaining simulations have idealistic topography. All forcing parameters (temperature and salinity differences between plume and ambient water, initial thickness of the plume, ambient stratification) and subgrid parameters (entrainment ratio and bottom drag coefficient) are kept unchanged as in the CR. In order to keep the forcing in all experiments almost identical, the configuration of the Bosphorus channel (governing the transport at the exit) is kept the same in all experiments. The idealistic topography $H=H(y)$ is constructed in such a way that some of the characteristics are similar to the ones in CR topography. In this experiment (we will use further the abbreviation IT-idealistic topography) the Bosphorus Channel exits on almost flat shelf part with small slope changing from 50 to 100 m at a distance of 20 km (Fig. 3a). After, the shelf reaches the steep continental slope where the depth increases from 100 m to 1000 m at a distance of about 16 km. The slopes are chosen to be comparable to the real ones (compare Fig. 2a with Fig. 3a). The flat bottom beyond the continental slope with a depth of 1000 m aims to represent the deep abyssal part of the outflow area. An important difference between CR and IT topography is the presence of underwater channel in the CR, which deflects the MSW in north-western direction thus gravity currents do not follow the line of largest slope (see Fig. 2a). To simulate the guidance of gravity current using the simplest possible bottom forms we design the experiment with Idealistic Topography and Wall (ITW). ITW topography is similar to IT but at the exit of the Bosphorus underwater channel a vertical underwater wall with a depth of 50 m is imposed on the shelf (Fig. 4a). The wall geometry (height, length and angle between the wall and the coast) is chosen to be comparable with the geometry of the channel extension (see Fig. 2a and Fig. 4a) thus we can expect that currents in ITW experiment will show more realistic behavior.

An important difference between topographies in the CR and in the idealistic experiments is the bottom roughness. Local topographic irregularities could induce accelerations, causing increase in entrainment velocity and as a consequence fast mixing with ambient water. In order to investigate the impact of the roughness factor we run two additional experiments - Idealized Rough Topography (IRT) and Idealistic Rough Topography and Wall (IRTW). We prescribe the bottom roughness using random number generator with variations in the interval $[-10,+10]$ m (except for the Bosphorus channel area, where the topography is not changed in order to avoid changes in the forcing at the outflow location). By comparing the results in IT and IRT experiments we aim to demonstrate the impact of bottom roughness on the plume characteristics. The IRTW experiment aims to combine both rough bottom and north-western deflection after the exit of Bosphorus channel, so the same wall as in the ITW is placed at the same location.

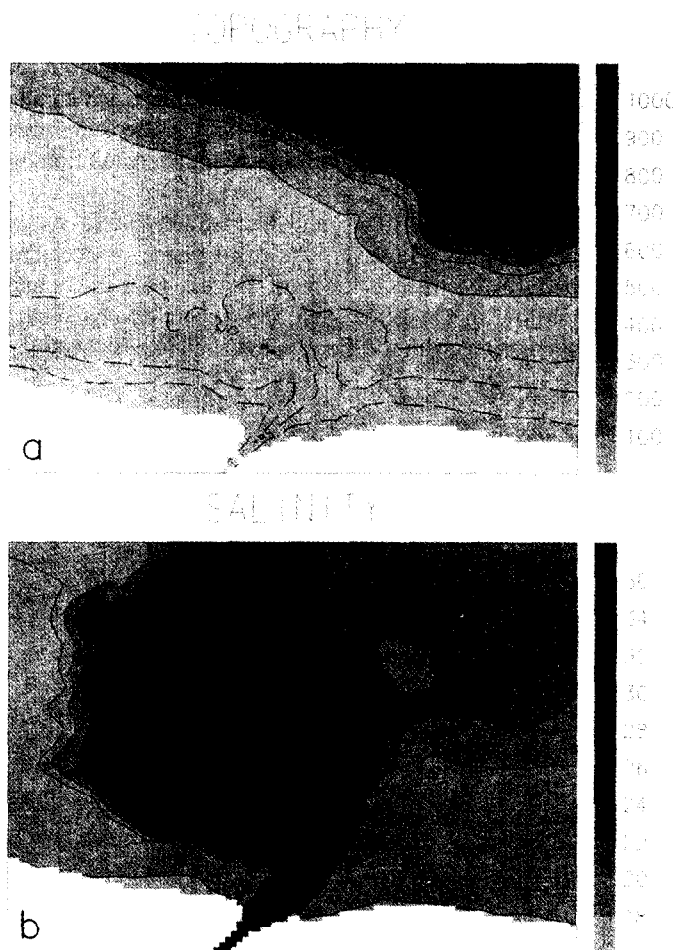


Fig. 2. CR experiment: (a) bottom topography [m], long-dash curves are the 40, 60 and 80-m isobaths. (b) bottom salinity [psu].

4. Analysis of the results.

The behavior of the plume is governed by the balance between different forces: reduced gravity, Coriolis force, bottom friction and horizontal mixing. The slope convection was studied in [10] where the configuration of model topography was similar to ours in IT experiment. It was found that depending on the ratio between buoyancy and bottom friction there were two cases of propagation: alongslope and downslope motion. The relative significance of friction increases for thin plumes (thinner than the thickness of bottom Ekman layer). Our simulations in IT and ITW experiments (Fig. 3b and Fig. 4b) show strictly downslope motion on the continental slope like in the case of thin plumes in [10], which clearly indicates the dominance of gravity force.

In the IT experiment the plume leaves the Bosphorus channel and flows down the continental slope. After reaching the flat bottom part it starts to propagate in all directions with slight preference to the east (Fig. 3b). The plume thickness on the continental slope is about 5 to 15 m which is comparable to the typical value for the depth of bottom Ekman layer 10 m. This result is in agreement with [10]. Our simulations show that BSW is entrained mostly over the steepest parts of topography [SSP] where the entrainment velocity (not presented here) reaches largest values. The explanation is that here the plume accelerates, the velocity increases, and the entrainment rate that is parameterised as a function of velocity and local topography (Eqn. 1) also increases (the steeper the slope, the larger the entrainment rate). The anisotropic spreading of the plume (right deflection on the abyssal plane) might be explained as resulting from the different balance of forces on the continental slope and in the flat area. On the continental slope the gravity acceleration is dominating and the horizontal scales are too small to see the influence of Coriolis force. Reaching the abyssal plane the plume decelerates, that strongly reduces the bottom friction. At the same time the buoyancy flux also decreases abruptly since the entrained ambient water on the continental slope is enough to substantially reduce the density difference between the plume and ambience [SSP]. Under such conditions the Coriolis force starts to dominate and we observe the right deflection.

The CR and IT experiments give quite different estimates about the broadening of the plume on the shelf. In the CR (Fig. 2b) the plume spreads over large part of shelf, the zonal gradients of salinity are small at the edges of the plume and the core of the plume stays close to the exit of Bosphorus channel. Differently, in the ITW experiment the plume is wider than in the IT (compare salinity in Fig. 3b and Fig. 4b) and the results in the ITW experiment show closer similarity to the ones of the CR. The conclusion here is that the north-western deviation of the current increases the horizontal mixing and enables the plume propagation in zonal direction.

Comparing the salinity in idealistic topography experiments and CR (see Fig. 2b, 3b, 4b) we find many differences but the main point is that the plume in the CR does not reach the abyssal plain, completely losing its identity on the continental slope. One possible reason could be the roughness of realistic topography that facilitates mixing between plume and ambient water. This conclusion is supported by the results from experiments with rough topography. The horizontal maps of salinity in IRT and IRTW experiments (Fig. 5a and Fig. 5b) show that the plume does not reach depths below 500 m. As the only difference between IT and IRT

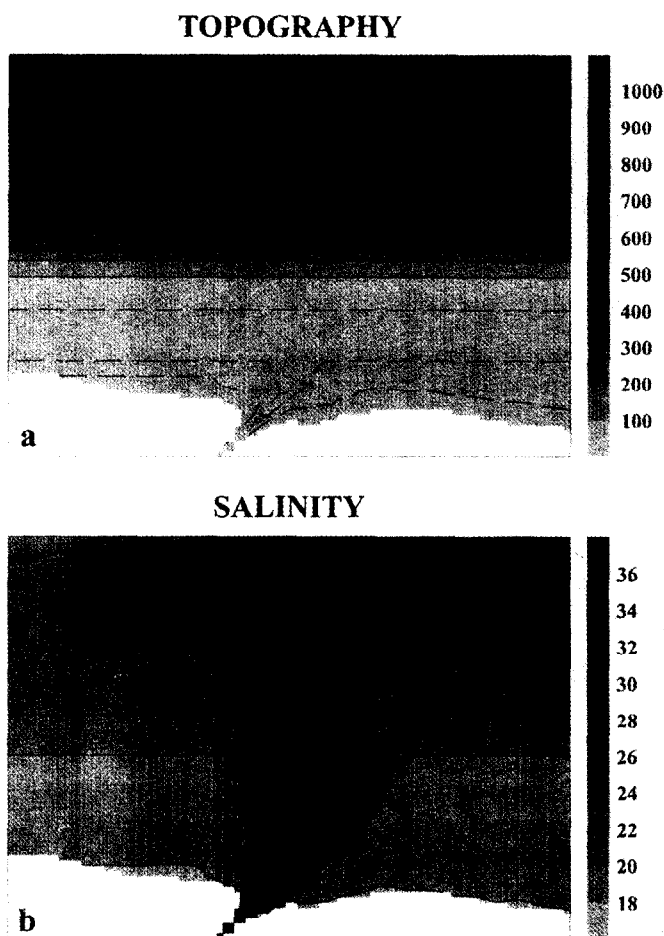
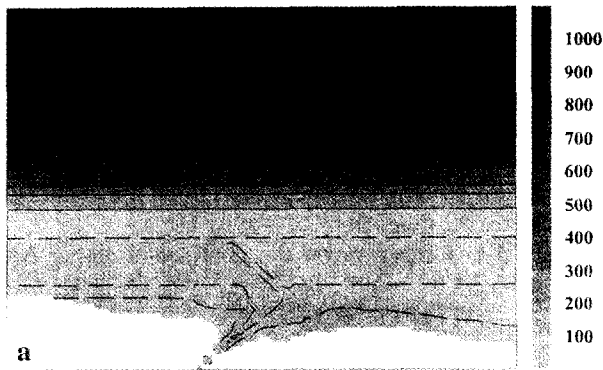


Fig. 3. IT experiment: (a) bottom topography [m], long-dash curves are the 60, 80 and 100-m isobaths. (b) bottom salinity [psu].

TOPOGRAPHY



SALINITY

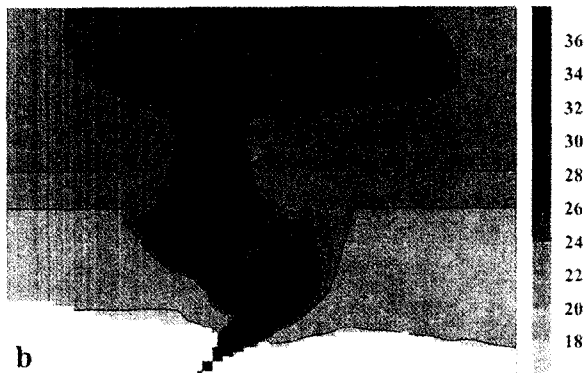


Fig. 4. ITW experiment: (a) bottom topography [m], long-dash curves are the 60, 80 and 100-m isobaths. (b) bottom salinity [psu].

Conclusions.

Numerical simulations of Mediterranean outflow in the Black Sea are carried out here using reduced gravity model. The results from experiments with idealistic topography show large entrainment rates on the continental slope where substantial part of mixing between BSW and MSW occurs. However, using simplified and smooth topography results in unrealistically small mixing in the shelf area, and as a consequence the current reaches the abyssal plain and flows in the deep sea. The latter is not supported by observations. It was found that the behavior of the gravity current under specified ambient stratification in the Black Sea is governed by the topography slopes and local roughness. More detailed discussions on about what are the magnitudes of bottom roughness that could be significant for the plume behavior and how the width of the shelf affects bottom currents will be addressed in the forthcoming paper.

Acknowledgements

This work has been supported by the CEC Contract IC15CT960113.

(respectively between ITW and IRTW) experiments is the random bottom roughness, the above comparisons demonstrate the impact of rugged topography on the mixing mechanisms. More detailed examination of the correlation of plume characteristics and bottom topography indicate that some of the “finger type” or other larger scale features are due to the small bottom forms with random distribution. This gives an illustration that very small (less than 10 m) bottom forms could contribute to specific guidance of the flow and might localize leakage of plume water into the deeper layers.

When comparing the IRT and IRTW simulations to the ones in CR (Fig. 5a, 5b to Fig. 2b) we see that features simulated in IRTW are more similar to the ones in CR than in IRT. This is explained by the combined effects of local topography roughness and substantial along-isobaths component of currents in the CR. Thus the plume propagates slower on the shelf than in the IT and ITW experiments, and mixes and entrains more ambient water than under idealistic conditions. This results in a rapid decrease of density contrasts between the plume and ambience and the current reaching the continental slope completely loses its identity due to the large entrainment rates.

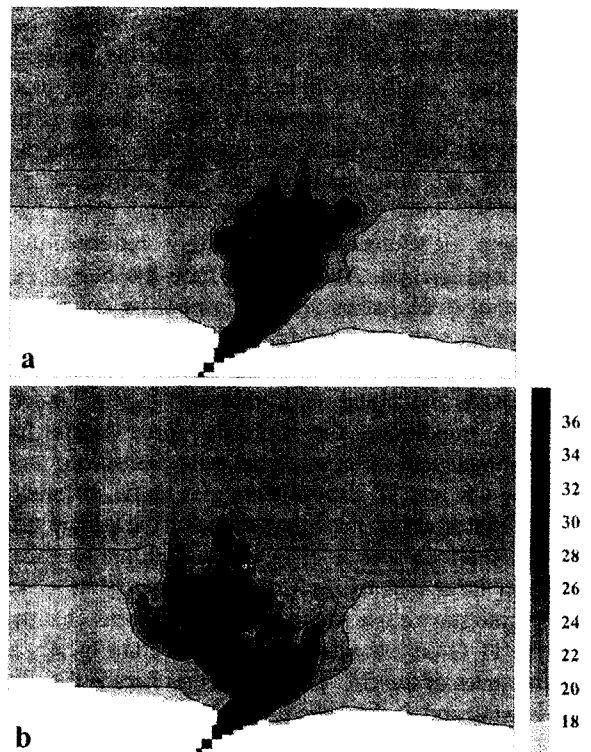


Fig. 5. Random topography experiments: (a) IRT bottom salinity [psu], (b) IRTW bottom salinity [psu].

References:

- [1] M. O. Baringer and J. Price, 1997a, Mixing and spreading of the Mediterranean outflow. *J. Phys. Oceanogr.* **27**, 1654-1677.
- [2] M. O. Baringer and J. Price, 1997b, Momentum and energy balance of the Mediterranean outflow. *J. Phys. Oceanogr.* **27**, 1678-1692.
- [3] K. Buesseler, H. Livingston and S. Casso, 1991, Mixing between oxic and anoxic waters of the Black Sea as traced by Chernobyl cesium isotopes, *Deep Sea Research* **38**, S725-S745.
- [4] J. H. JungCLAUS and J. Backhaus, 1994, Application of a transient reduced-gravity plume model to the Denmark Strait overflow, *J. Geophys. Res.* **99**, C6, 12375-12396.
- [5] M. A. Latif, E. Özsoy, T. Oguz and U. Unluata, 1991, Observation of the Mediterranean inflow into the Black Sea, *Deep Sea Research* **38**, Suppl. 2, S711-S723.
- [6] T. Oguz and L. Rozman, 1991, Characteristics of the Mediterranean underflow in the south-western Black Sea continental shelf/slope region, *Oceanologica Acta* **14**, 433-444.
- [7] E. Özsoy, U. Unluata and Z. Top, 1993 The evolution of Mediterranean water in the Black Sea: interior mixing and material transport by double diffusive intrusions, *Progress in Oceanogr.* **31**, 275-320.
- [8] J. F. Price and M. Baringer, 1994, Outflows and deep water production by marginal seas, *Prog. Oceanogr.* **33**, 161-200.
- [9] J. F. Price, M. Baringer, R. Lueck, G. Johnson, I. Ambar, G. Parrilla, A. Cantos, M. Kennelly and T. Stanford, 1993, Mediterranean outflow mixing and dynamics. *Science*, **259**, 1277-1282.
- [10] G. I. Shapiro and A. Hill, 1997, Dynamics of Dense Water Cascades at the Shelf Edge, *Journal of Phys. Oceanography*, **27**, 2381-2394.
- [11] J. V. Staneva, K. Buesseler, E. Stanev, H. Livingstone, 1998, Application of Isotope tracers to study ocean circulation. Validation of numerical simulations against weapon testing and Chernobyl Cs¹³⁷ and Sr⁹⁰ data (accepted manuscript).
- [12] E. V. Stanev, J. Simeonov, E. Peneva, 1998, Gravity plumes in stratified oceans. Test case for the entrainment of Black Sea water by the Mediterranean plume (submitted manuscript).
- [13] D. Tolmazin, 1985, Changing coastal oceanography of the Black Sea. Part II: Mediterranean effluent, *Progress in Oceanogr.* **15**, 277-316.
- [14] J. S. Turner, 1973, Buoyancy effects in fluids. Cambridge University Press, 368 pp.
- [15] U. Unluata, T. Oguz, M. A. Latif and E. Özsoy, 1990, On the Physical Oceanography of the Turkish Straits, *The Physical Oceanography of Sea Straits*, L. J. Pratt (editor), NATO/ASI Series, Kluwer, Dordrecht, pp. 25-60
- [16] H. Yuce, 1990, Investigation of the Mediterranean Water in the Strait of Istanbul (Bosphorus) and the Black Sea, *Oceanologica Acta* **13**, 177-186.

THE BARENTS SEA POLAR FRONT: TOPOGRAPHIC CONTROL AND SEASONAL VARIABILITY

A. J. Plueddemann¹, G. G. Gawarkiewicz¹, and C. L. Harris²

1. Department of Physical Oceanography, Woods Hole Oceanographic Institution, Woods Hole, Massachusetts, 02543-1541 USA
2. Scripps Institution of Oceanography, University of California, San Diego, La Jolla, California, 92093-0230 USA

Abstract

The Barents Sea Polar Front denotes the boundary between relatively warm, saline water of Atlantic origin and colder, fresher Arctic Water. Recent field work, numerical modeling, and historical data analyses have resulted in a revised view of frontal dynamics and the seasonal variability of hydrographic properties in the frontal region. Atlantic Water is assumed to enter the Barents Sea as a barotropic current, trapped to topography through the conservation of potential vorticity. The crucial concept is that this current splits into two branches at the sill between Sentral Bank and Nordkapp Bank. One branch flows into the eastern Barents Sea, while the other recirculates within the Bear Island Trough and Hopen Trench. The recirculating branch creates a topographically controlled, barotropic front between Sentral Bank and Bear Island. Topographic control is disrupted near the surface by the seasonal discharge of fresh water from melting ice to the north of the front. The meltwater pool creates a strong pycnocline in the upper 50 m and an associated geostrophic jet. Below this seasonal, baroclinic front the topographically controlled, barotropic front remains throughout the year. Regional water mass properties are strongly influenced by the fact that ice and fresh meltwater cross the front to overlie Atlantic Water in the Bear Island Trough and Hopen Trench.

Introduction

The Barents Sea Polar Front is the boundary between Atlantic Water and Arctic Water in the western Barents Sea. This boundary is in fact a frontal zone consisting of two principal components, an Atlantic Water front and a meltwater front [1, 2]. The topography near the frontal zone consists of several shallow banks surrounding the Bear Island Trough and Hopen Trench (Figure 1). A relatively uniform slope separates the banks from the trough between Bear Island and Sentral Bank. Observations of temperature at 50 m depth in the frontal zone [3] show that the Atlantic Water front is topographically trapped along the slope, but the trapping mechanism is not known. Geostrophic calculations indicate a southwest flow of Arctic Water over the Spitsbergen Bank [1, 4], and both northeast [1, 5] and southwest [4, 6] Atlantic Water flow along the slope. There are few reports of absolute velocities in the region, and the influence of the barotropic flow is difficult to assess.

A high-resolution survey of the frontal zone in the summer of 1992 has stimulated a modeling study and a retrospective analysis of some historical hydrographic data. The new observations indicated that the barotropic flow of Atlantic Water along the slope may be significant [5]. The modeling work showed that this barotropic circulation may be the key to understanding the topographic control of the Atlantic Water front [7]. Historical data analyses showed results consistent with these findings [8]. In this paper, these results are briefly reviewed with emphasis on topographic control of the Atlantic Water front and the seasonal variability of water mass properties near the frontal zone.

Observations of the Frontal Zone

High-resolution observations of hydrographic properties over the south flank of Spitsbergen Bank were made during the Barents Sea Polar Front Experiment (BSPFX) conducted from 6 to 26 August 1992 [5]. Of interest for this study are surveys conducted from the USNS *Bartlett* using a profiling Conductivity–Temperature–Depth (CTD) system and an underway Acoustic Doppler Current Profiler (ADCP). Repeated CTD/ADCP surveys were conducted within a 70 × 80 km box centered at 22.5°E,

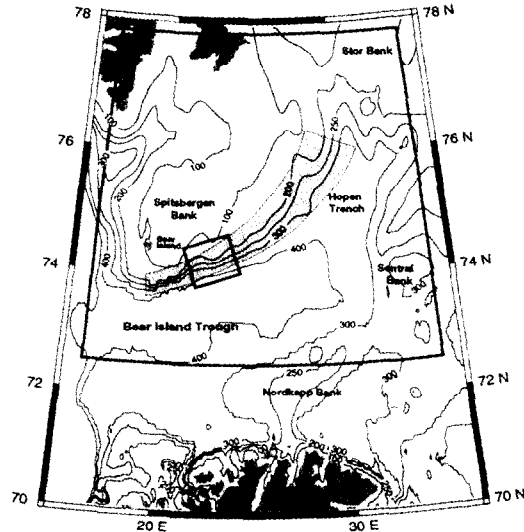


Figure 1: Plan view of western Barents Sea topography with a shaded region denoting the frontal zone. The small box is the study area of the Barents Sea Polar Front Experiment (BSPFX). The large box encloses the area included in the historical survey of National Ocean Data Center (NODC) hydrography.

complete. The three-minute average ADCP data had along-track resolution of 1 km and cross-track resolution set by the survey pattern (typically 10 km). Moorings with temperature sensors and current meters at depths of 20, 50, and 80 m were placed at three corners of the survey area.

Hydrographic sections revealed two thermohaline fronts: A subsurface Atlantic Water front and a surface-trapped meltwater front (Figure 2). Atlantic Water ($1 < T \leq 8^{\circ}\text{C}$; $35.0 < S \leq 35.2$ psu) was found throughout the water column in the deeper portion of each section. The Atlantic Water front, defined here by the the 35.0 psu isohaline, represents the northernmost boundary of Atlantic Water in the western Barents Sea. The spatial survey showed that the location of the front was approximately coincident with the 250 m isobath. The Atlantic Water front showed relatively little vertical structure below 50 m depth and was strongly T-S compensated, with a horizontal density gradient of less than 0.1 kg m^{-3} despite a temperature contrast of 3°C and salinity contrast of 0.3 psu. Arctic Water ($T \leq 0^{\circ}\text{C}$; $34.3 < S \leq 34.8$ psu) was found below 50 m and shoreward of the 150 m isobath.

The meltwater pool, delineated by the 34.4 psu isohaline, consisted of warm, fresh water produced from the melting of sea ice and was associated with strong ($\Delta\rho \approx 1 \text{ kg m}^{-3}$) horizontal and vertical density gradients. Geostrophic velocity calculations showed a surface-trapped jet over the shelf with maximum velocities (relative to 100 m) of $5\text{--}15 \text{ cm s}^{-1}$. Over the slope, the geostrophic flow was weaker ($2\text{--}4 \text{ cm s}^{-1}$) and directed towards the east.

The BSPFX data were particularly valuable due to the observation of absolute currents. A “snapshot” of the sub-tidal flow was produced using a least-squares fit to the combined ADCP and mooring data over the 20 day experimental period (Figure 3). The technique models the tide as the sum of harmonic functions at specific frequencies and allows a temporally steady (sub-tidal) flow to be extracted [9]. At 20 m depth the sub-tidal velocities over the shelf were consistent in magnitude and direction with the geostrophic velocities. Below 20 m the flow over the shelf was weak ($2\text{--}5 \text{ cm s}^{-1}$) and variable in direction. This indicates that the shelf was dominated by the baroclinic meltwater jet. The flow over the slope was strong ($8\text{--}15 \text{ cm s}^{-1}$) and persistently to the west. Note that the reduction of the observed westward flow from $10\text{--}15 \text{ cm s}^{-1}$ at 80 m to $8\text{--}10 \text{ cm s}^{-1}$ at 20 m is consistent with the surface-intensified geostrophic flow of $2\text{--}4 \text{ cm s}^{-1}$ to the east. Thus, the total flow of Atlantic Water at this point on the slope is strongly influenced by the barotropic component and is to the west at all depths.

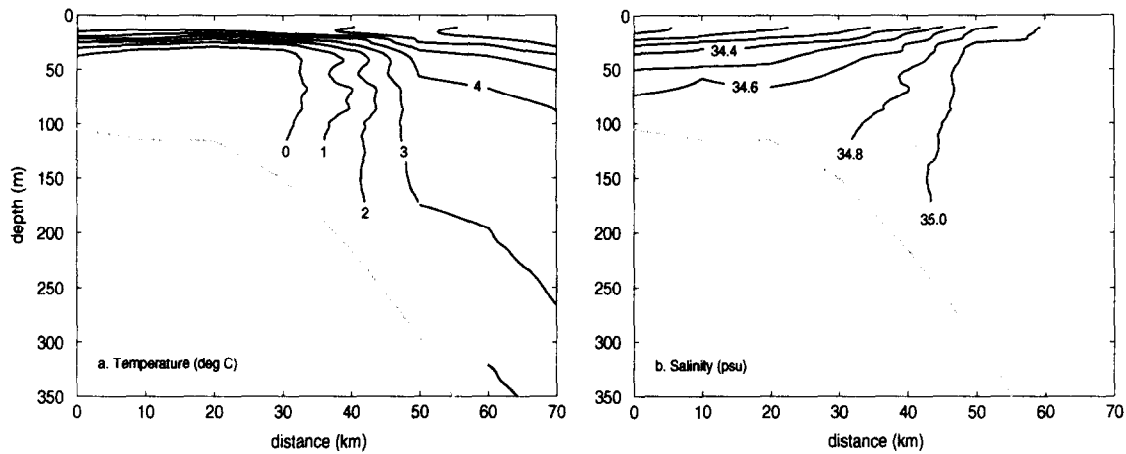


Figure 2: Cross-slope sections of (a) temperature and (b) salinity from the CTD survey conducted during BSPFX. The positions of the Atlantic Water front and the meltwater front can be defined by the the the 35.0 psu and 34.4 psu isohalines, respectively. Note that neither front is well defined by temperature at the surface.

Topographic Control

Based on the T-S structure and velocity field associated with the subsurface, Atlantic Water front observed in BSPFX a process modeling study was undertaken [7] which suggested a topographically controlled Atlantic Water recirculation within the western Barents Sea. This study presented a simple explanation for the recirculation: a barotropic flow of Atlantic Water enters the Barents along the southern side of Bear Island Trough and conserves potential vorticity by following topography. A topographic bifurcation at the Sentral Bank–Nordkapp Bank sill divides the Atlantic Water current into two branches. Shallow topography guides one branch into the eastern Barents Sea while deeper topography steers the other branch to recirculate within the Bear Island Trough–Hopen Trench system, eventually returning to the Norwegian Sea. Along the slope between Sentral Bank and Bear Island, the model suggests that the westward flowing Atlantic Water remains offshore of the 250 m isobath as a result of the upstream bifurcation in the topographically trapped flow.

Direct current measurements across the Bear Island Trough [6] are consistent with this concept in that they show westward velocities at all depths between 73°30'N and Bear Island, a region where recirculating Atlantic Water would be expected. However, the idea of a persistent westward flow of Atlantic Water over the southern flank of Spitsbergen Bank is at odds with another study [10] which suggests that Atlantic Water flows eastward over the slope throughout most of the year, reversing to flow westward only in summer. The number and duration of absolute velocity measurements presently available from the western Barents Sea are insufficient to resolve this issue.

The National Oceanographic Data Center (NODC) Global Ocean Temperature and Salinity Profiles and Oceanographic Station Profile Time Series were used to determine the geographic distribution of subsurface water masses in the western Barents Sea. Water mass definitions [9] and closely follow those of Loeng [1]. The geographic extent of the Atlantic and Arctic water masses is shown in Figure 4. The subsurface Atlantic Water was found mostly in waters deeper than 250 m. The subsurface Arctic Water extended into waters deeper than the shelfbreak (roughly the 100 m isobath) but tended to remain shelfward of the 250 m isobath. Both results are consistent with the topographic control concept, which predicts the Atlantic Water boundary to be aligned with the 250 m isobath.

Seasonal Variability

The vertical structure of temperature and salinity in the frontal region was examined to determine

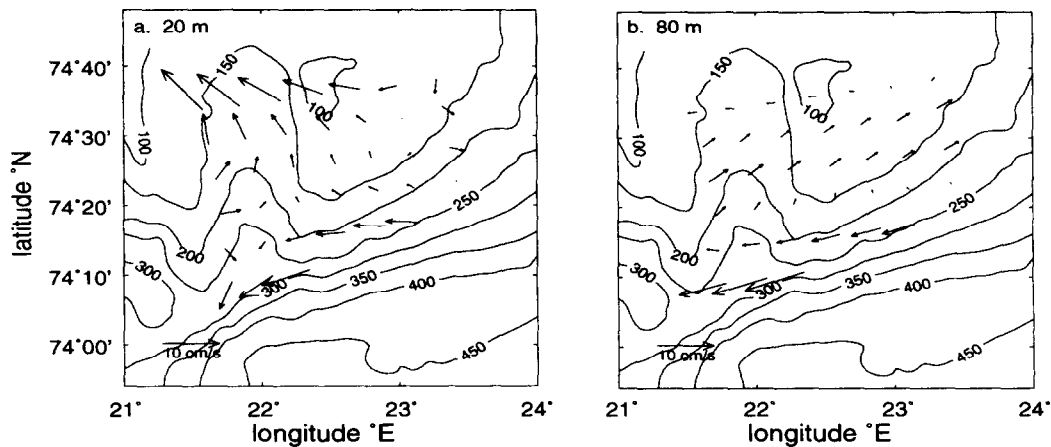


Figure 3: Sub-tidal velocity field at (a) 20 m depth and (b) 80 m depth during BSPFX estimated from the combination of the ADCP survey and moored current meter data.

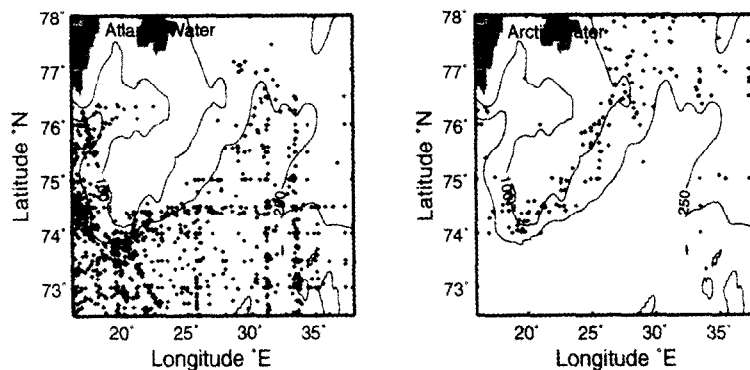


Figure 4: Geographic distribution of sub-surface (> 50 m) hydrographic data from the NODC database. (a) Atlantic Water and (b) Arctic Water are shown along with topographic contours at 100 m (the shelf break) and 250 m (the sill depth).

seasonal changes in stratification at the Polar Front. Vertical structure was characterized in a surface layer and a subsurface layer by computing two-point differences between 0–100 m and 100–200 m, respectively (Figure 5). The surface layer salinity field was vertically uniform from December through June with very low variability. From August to November, the typical salinity difference over the top 100 m was -0.5 psu, indicating that fresh water had overridden saltier water. The much larger variability during these months reflected the varying strength and horizontal extent of the meltwater pool. The vertical temperature structure in the surface layer showed that the thermocline developed several months before the halocline and reached a maximum strength of about 4°C in August. The subsurface salinity field was vertically uniform throughout the year and the temperature field showed only slight vertical stratification (maximum $\Delta T \approx 1^{\circ}\text{C}$). Thus, the frontal region was nearly vertically uniform during the winter months. Under these conditions, the critical simplifying assumption of the topographic control concept, barotropic Atlantic Water flow, may be considered valid. In the summer, the situation is more complex since a seasonal thermocline and halocline are present in the upper 100 m. However, the subsurface layer remains nearly vertically uniform throughout the year, apparently decoupled from the seasonal cycle in the surface layer.

The densest water in the NODC data set was found along the slope between Bear Island and Sentral

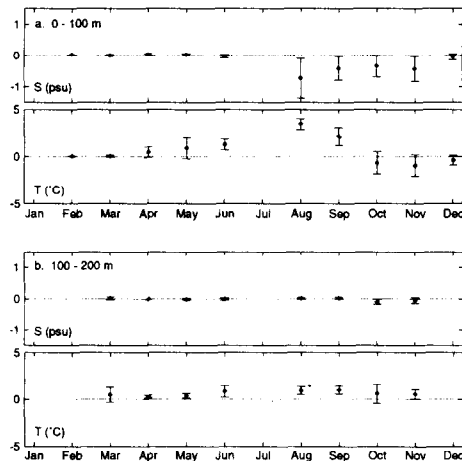


Figure 5: Vertical gradients, presented as two-point differences, from NODC data in the frontal region. (a) Salinity (upper) and temperature (lower) differences for the surface layer (0–100 m depth). (b) Salinity (upper) and temperature (lower) differences for the lower layer (100–200 m depth). Circles represent mean differences, vertical bars denote one standard deviation.

Bank, predominantly between the 100 m isobath and the deepest part of Bear Island Trough. This water mass was a cold, fresh end member of Atlantic Water, denoted Modified Atlantic Water ($T \leq 1^\circ\text{C}$; $34.95 < S \leq 35.10$ psu). Modified Atlantic Water was often found throughout the water column in late winter, whereas a surface layer of relatively fresh water, presumed to have as its source the meltwater on Spitsbergen Bank, was found throughout the western Barents Sea in summer. Thus, Modified Atlantic Water was probably formed by the convective mixing of Atlantic Water with overlying meltwater. The large wintertime surface heat loss in the region [11] would be sufficient to cool the water column by 4°C [8] and the meltwater would cause a slight freshening. For example, a 30 m deep meltwater layer ($S = 34.5$ psu) mixed with 270 m of 35.0 psu Atlantic Water would form water with salinity of 34.95 psu, the lower bound for Modified Atlantic Water (the same salinity would result from 0.4 m of ice ($S = 5.0$ psu) mixed with 250 m of 35.0 psu Atlantic Water).

Conclusions

The Barents Sea Polar Front is a frontal system consisting of two principal components, an Atlantic Water front and a meltwater front. The Atlantic Water front represents the northern edge of North Atlantic water which enters the Barents Sea in the Norwegian Atlantic current. The Atlantic Water front is well defined year-round below about 50 m depth and exhibits a strong relationship to the underlying topography. The meltwater front is a result of the spring ice melt over the Spitsbergen shelf. The meltwater front shows significant seasonal variability, typically being established in June and persisting until October. The meltwater front does not show a strong relationship to topography, and there is evidence that either ice, meltwater, or both move southward off of Spitsbergen Bank to overlie Atlantic Water within the Bear Island Trough and Hopen Trench.

The temperature and salinity structure of the frontal zone found during BSPFX was completely consistent with Loeng's description of summer water mass distributions on the Spitsbergen Bank [1]. However, a new element was introduced by the direct observation of velocity. In particular, the absolute velocity in the Atlantic Water core was found to be towards the west at all depths.

Topographic control of the Atlantic Water front can be explained by a recirculating branch of the Norwegian Atlantic Water inflow. The Norwegian Atlantic Current is presumed to enter the Barents Sea as a predominantly barotropic flow which conserves potential vorticity, and thus is strongly constrained to follow the topography of the western Barents Sea. A topographic bifurcation (saddle point) at the Sentral Bank–Nordkapp Bank sill divides the current into two branches. The inshore edge of the recirculating

branch remains at the sill depth, about 250 m, thereby setting the position of the Atlantic Water front along the slope between Sentral Bank and Bear Island. Historical data are consistent with this concept in that the boundary between Atlantic Water and Arctic Water is found near the 250 m isobath.

The frontal zone is strongly influenced by seasonal variability. In winter the water column is well-mixed vertically and water mass variability is dominated by horizontal property gradients associated with the Atlantic Water front. In summer strong vertical gradients of temperature and salinity are found in the upper 50 m, associated with solar heating and the melting of sea ice over the shelf. Low salinity water presumed to have its origin on the Spitsbergen shelf is found throughout the western Barents Sea in summer. This surface water appears to be an important component in the formation of a dense water type, denoted Modified Atlantic Water, along the slope between Sentral Bank and Bear Island. Modified Atlantic Water is the densest water found in the western Barents Sea in the 40 year NODC data set, and is clearly distinguishable from brine-enhanced, dense bottom water found elsewhere in the Barents Sea.

Acknowledgments. The Barents Sea Polar Front Experiment was conducted by R. Bourke, C.-S. Chiu, J. Lynch, J. Miller, R. Muench, A.R. Parsons, and R. Pawlowicz. This work was supported by the Office of Naval Research through contracts N00014-90-J-1357 (AJP and CLH) and N00014-93-1-0180 (GGG) and a Department of Defense Science and Engineering Graduate Fellowship (CLH).

References

- [1] Loeng, H., 1991. Features of the physical oceanographic conditions of the Barents Sea, *Polar Research*, 10, 5–18.
- [2] Chvilev, S.V., 1991. Frontal Zones of the Barents Sea, *Soviet Meteorology and Hydrology*, 11, 89–95.
- [3] Johannessen, O.M. and L.A. Foster, 1978. A note on the topographically controlled oceanic polar front in the Barents Sea, *Journal of Geophysical Research*, 83(C9), 4567–4571.
- [4] Pfirman, S.L., D. Bauch and T. Gammelsrød, 1994. The northern Barents Sea: Water mass distribution and modification, in *The Polar Oceans and Their Role in Shaping the Global Environment*, edited by O. M. Johannessen, R. D. Muench and J. E. Overland, pp. 77–94, AGU, Washington, D.C., 1994.
- [5] Parsons, A.R., R.H. Bourke, R.D. Muench, C.-S. Chiu, J.F. Lynch, J.H. Miller, A.J. Plueddemann and R. Pawlowicz, 1996. The Barents Sea polar front in summer, *Journal of Geophysical Research*, 101(C6), 14,201–14,221.
- [6] Blindheim, J., 1989. Cascading of Barents Sea bottom water into the Norwegian Sea, *Rapports et Proces-Verbaux des Réunions*, Conseil International pour l'Exploration de la Mer, 188, 49–58.
- [7] Gawarkiewicz, G.G. and A.J. Plueddemann, 1995. Topographic control of thermohaline frontal structure in the Barents Sea Polar Front on the south flank of Spitsbergen Bank, *Journal of Geophysical Research* 100(C3), 4509–4524.
- [8] Harris, C.L., A.J. Plueddemann and G.G. Gawarkiewicz, 1998. Water mass distribution and polar front structure in the western Barents Sea, *Journal of Geophysical Research*, 103(C2), 2905–2917.
- [9] Harris, C.L., A.J. Plueddemann, R.H. Bourke, M.D. Stone and R.A. Pawlowicz, 1995. Collection and processing of shipboard ADCP velocities from the Barents Sea Polar Front Experiment, Woods Hole Oceanog. Inst. Tech. Rept, *WHOI-95-03*, 71 pp.
- [10] Li, S. and T. A. McClimans, 1998. The effects of winds over a barotropic retrograde slope current, *Cont. Shelf. Res.*, 18.
- [11] Häkkinen, S. and D.J. Cavalieri, 1989. A study of oceanic surface heat fluxes in the Greenland, Norwegian, and Barents seas, *Journal of Geophysical Research*, 94(C5), 6145–6157.

**Low-frequency climate variability over the Eastern Europe as a result of
the North Atlantic and Pacific changes**

Polonsky, A., and Voskresenskaya, E.

Marine Hydrophysical Institute, Sevastopol, 2 Kapitanskaya St., the Crimea, UKRAINE

Introduction

The goal of present work is to discuss the interannual and interdecadal variability of the air temperature, precipitation over the Crimea, and sea temperature, rivers' run-off, salinity and vertical stability of the upper sea layers in the Northwestern Black Sea associated with the North Atlantic changes. It was shown earlier (Simonov and Altman, 1991; Polonsky e.a., 1997) that the natural changes of the Black Sea river discharges and coastal variability of the hydrographic fields prevail in spite of the strong run off artificial regulation. They are due mostly to low-frequency variability of the coupled ocean-atmosphere system over the North Atlantic and Equatorial Pacific. The present results obtained using the additional hydrometeorological data confirm that.

Data and Processing Procedure

We used historical data of temperature and salinity at 0 and 20 m in the N.W. Black Sea from 1924 till 1994 monthly averaged over regular mesh 40 by 40 miles., monthly river discharges from January 1921 to December 1992, assessment of the annual discharges of Danube and Dnieper from 1855 to 1994 using published data, and monthly magnitudes of the sea level pressure (SLP) and Rossby index (RoI) from 1891 to 1990 (Polonsky and Sizov, 1991). The RoI was calculated as a difference of the SLP in the Azores High and Iceland Low. The monthly position of Azor High an Iceland Low and SLP magnitudes after 1891 were received from (Monthly data sets, 1988 and Monthly synoptic bulletins, 1986/1991). Regional hydrometeorological data sets, including observations in Sevastopol, Yalta, Feodosiya and Odessa and global hydrometeorological archive of the Russian Hydrometeorological Center for XX century including the North Atlantic and Southern Oscillation Indices (NAOI and SOI) were used.

Results and Discussion

VARIABILITY IN THE NORTHWESTERN BLACK SEA

Spatial distributions of r.m.s. of the surface fields show the strong variability of hydrographic parameters especially in the coastal zone. The r.m.s. is at a maximum during spring when the discharge changes of Dnieper and Danube increase. For instance, total May r.m.s. of sea surface temperature and salinity (SST and SSS) reach about 3.0°C and 4.4 psu, respectively, while the r.m.s. of SST and SSS are of about 1.4/2.4°C and 2.5/4.0 psu in the vicinity of the rivers' inflow in February and November, respectively. The r.m.s. of SST and SSS due to annual harmonic reach there about 7°C and 2.2 psu. So, the r.m.s. due to the average annual cycle and r.m.s. due to variability at the other space-time scales are of the same order. About 50% of total r.m.s. after deseasonalization are due to interannual and interdecadal variability. Low-frequency variability of the surface density in the N.W. Black Sea and of vertical stability (stratification) of the upper layer are due mostly to SSS change. There are two typical scale of low-frequency variations of the hydrographic fields in the N.W. Black Sea: from 10 to 20 years and from 2 to 7 years. Each of them is responsible for 30 to 45% of total variance of monthly salinity and density fields in 1955 to 1994. Cospectra of the river discharges and SSS show two or three significant peaks. The typical

periods of these coherent variations are as follows: 2 to 3 years, around 4 years and around 15 years. Significant trends of temperature, salinity, density and stratification in the N.W. Black Sea in 1955 to 1994 are absent in spite of strong artificial regulation of Dnieper and Dniester run-off (Polonsky e.a.,1997). Thus, the hydrographic fields of the N.W. Black Sea are characterized by strong natural year-to-year and decade-to-decade variability due to changes of the river discharges. The same variability was found in all analyzed hydrometeorological parameters in Yalta, Feodosiya, Sevastopol and Odessa (e.g., Fig.1, curves 2 and 3). As shown below these changes are due mostly to processes in the coupled ocean-atmosphere system over the North Atlantic and Equatorial Pacific.

VARIABILITY OF SEA-AIR INTERACTION IN THE NORTH ATLANTIC OCEAN AND ASSOCIATED CLIMATE ANOMALIES OVER THE EASTERN EUROPE

There are two distinct temporal scales of interdecadal and interannual variability of hydrometeorological fields in the North Atlantic. Both are due to natural fluctuations of the atmosphere-ocean system. Their typical time scales are from one to several decades and from 2 to 7 years, respectively.

The first type of variability looks like the trend or quasi-harmonic signal if the analyzed data sets cover a few decades. The decadal signal is the most prominent one (e.g., Figure 1, curve 1). Variability of "conveyor belt" is the possible cause of the natural decadal to multidecadal changes of the coupled system. North Atlantic plays the crucial role in their generation (Stocker, 1994). The SLP changes over North Atlantic Ocean associated with the low-frequency variability of the coupled system are the most interesting from point of view of the present study. On the decadal scale, the intensification of Azores High and Iceland Low is accompanied by their shift to the North by the several hundreds km. As a result there is a significant correlation of decadal anomalies of the Black

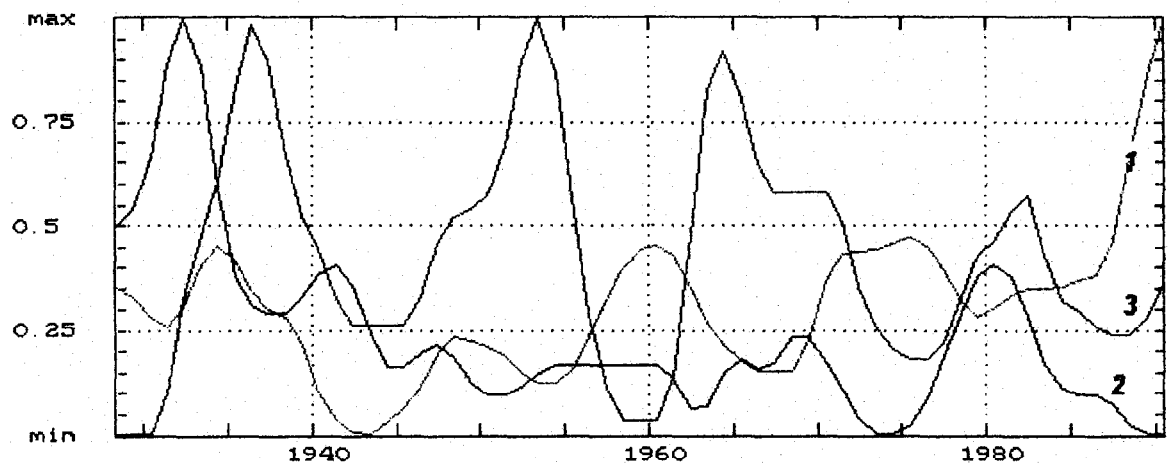


Fig.1. Variability of annual NAOI (1), Dnieper run-off (2) and February precipitation in Sevastopol (3) in 1928 to 1990. Relative Y scale is used. Series were smoothed using 7yr cut-off filter.

Sea hydrometeorological parameters, Dnieper discharge and SLP over the North Atlantic. The coefficient of correlation is at a maximum between winter/spring RoI and spring Black Sea parameters. It reaches about 0.7. So, there is the significant lag between North Atlantic and Black Sea variabilities. The same magnitude of correlation coefficients is between concurrent series of RoI and of sea level temperature. The role of the Pacific anomalies is not important at this scale (Figures 1, 2; Table 1). On the multidecadal scale Azores High and Iceland Low shift to the South-West and South when SLP rises and drops, respectively (Kushnir, 1994; Polonsky e.a., 1997).

The second type of low-frequency changes looks like a quasi-periodical random signal due to

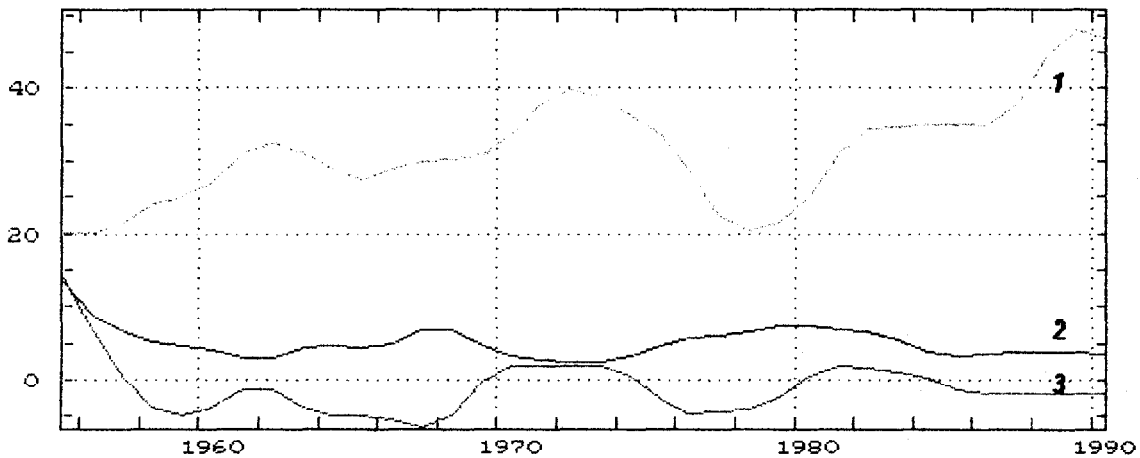


Fig.2. Variability of January RoI (1,mba), May Dnieper run-off (2,cubic km) and January SOI (3) in 1955 to 1990. Series were smoothed using 7 yr cut-off filter.

interannual fluctuations in the coupled system on the globe. El Nino-Southern Oscillation (ENSO) and NAO are the main manifestations of these fluctuations. The global ENSO-events manifest usually in the Atlantic fields as follows (Hastenrath, 1991; Polonsky & Sizov, 1991). Anomalous conditions develop in the North/Tropical Atlantic and in the Equatorial Pacific simultaneously (in accuracy of a season). Before the typical ENSO-event (in winter), the atmosphere shift to the North or to the North-East and the atmosphere circulation intensifies in the North Atlantic. Concurrently, the negative and positive SSTA are generated over the eastern tropical and subtropical/mid-latitude North Atlantic, respectively. After the ENSO-event start, the atmosphere circulation weakens in the North Atlantic simultaneously with a displacement of the Atlantic atmosphere centers to the South-West or South. Before the ENSO-event beginning, the storm tracks shift to the North-East by about 800 km (Figures 3,4). As a result there is a significant correlation of monthly (high-passed filtered) anomalies of the Black Sea hydrometeorological parameters, Dnieper discharge and SLP over the North Atlantic (Table 1).

Geophysical mechanism of discussed correlations associates with a long-term memory of the Ocean and feedbacks in the coupled system. Simultaneously with anomalous warming of the Subtropical Atlantic and cooling of high latitudes, the low-troposphere zonal circulation is intensified in the subtropical latitudes. This leads to increase of the RoI magnitude to change of position of Azores High/Island Low and cyclonetrajectories. As a result the snow cover and precipitation over the Central and Eastern Europe decrease, while the air temperature increases. The negative anomalies of the river discharges increase with some lag after that. Thus, it seems the positive feedbacks in the coupled Atlantic system support the large-scale anomalies initially generated in the Equatorial Pacific.

Conclusions

High-amplitude low-frequency fluctuations of all time series occurred during analyzed period. They are due mostly to low-frequency variability of the coupled ocean-atmosphere system over the North Atlantic. The typical temporal scales of these changes are of about 2-7 and 10-20 years. First of them is due mostly to the Equatorial Pacific processes, while the second one is due to inherent variability of the coupled system in the North Atlantic.

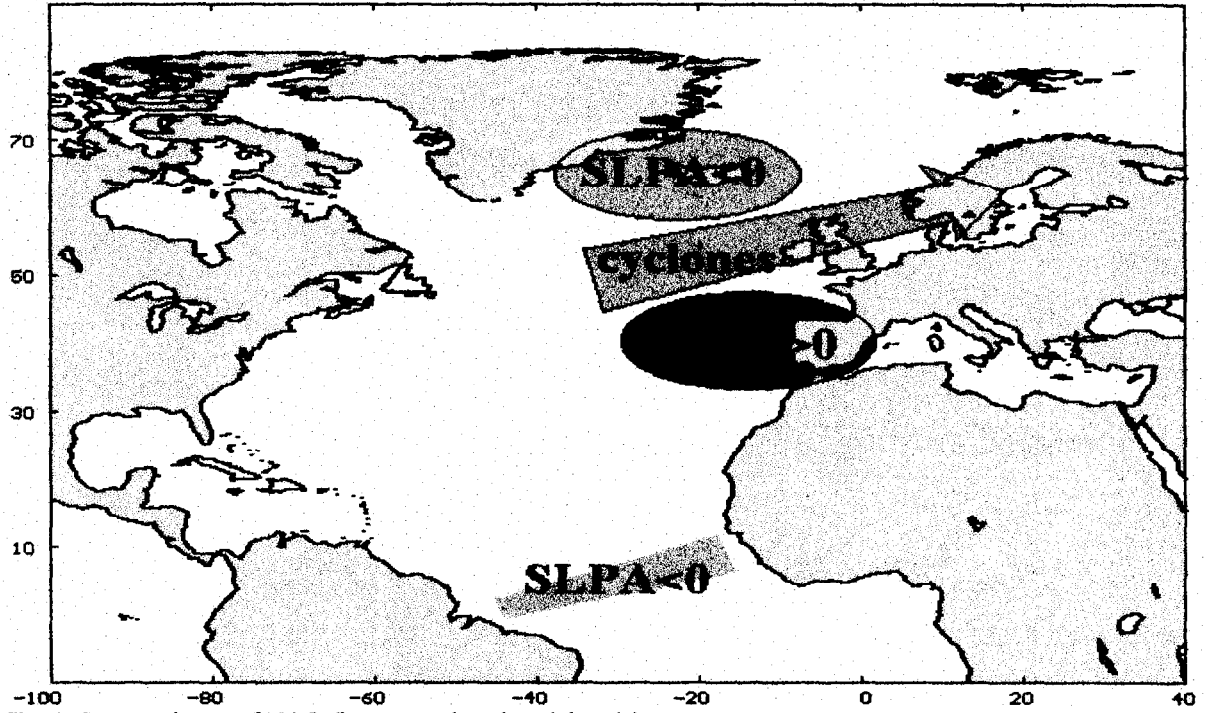


Fig. 3. Strong phases of NAO (interannual to decadal scale).

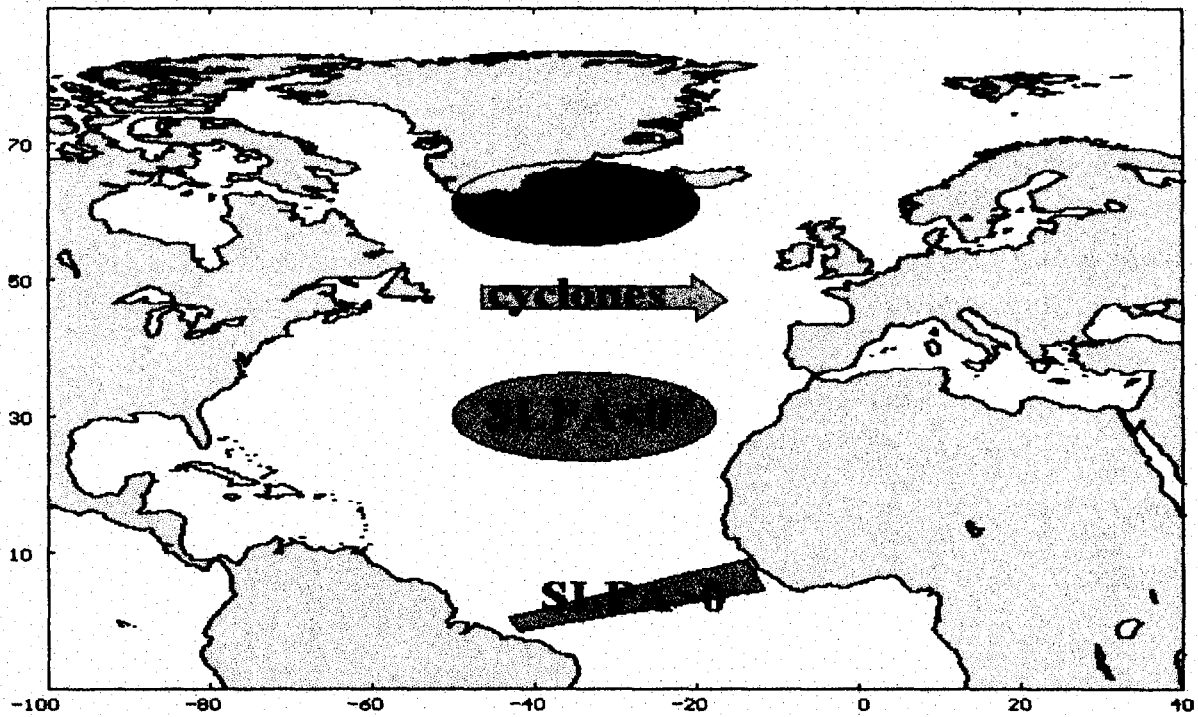


Fig. 4. Weak phases of NAO (interannual to decadal scale).

TABLE 1. Correlation matrix of RoI and SOI with Dniepr discharges and vertical salinity stratification (DS) in the upper 20m layer in the vicinity of Dnieper inflow. January and May data sets for 1955 to 1990 were used. Left, central and right magnitudes show the correlation without filtering, after high-passed 7 yr cut off, and low-passed 7 yr cut off filtering, respectively (multiplied by 100). Significant magnitudes (95% confidence level) are underlined.

	RoI/Jan	SOI/Jan	Dniep/May	DS/May
RoI/Jan	100			
SOI/Jan	3/-15./-5	100		
Dniep/May	2/-10/ <u>-67</u>	<u>23</u> / <u>-19</u> /53	100	
DS/May	2/ <u>-22</u> / <u>-61</u>	<u>21</u> / <u>-9</u> /47	<u>63</u> / <u>53</u> / <u>88</u>	100

References

- Hastenrath, S. (1991). *Climate Dynamics of the Tropics*. Kluwer Academic Publishers. Dordrecht/Boston/London. 488p.
- Kushnir, Y. (1994). The Change in Atmosphere Circulation Associated with North Atlantic Interdecadal SST Variability. AGS 1994 Spring Meeting (23-27 May, Baltimore, Maryland). Suppl. to EOS, 90.
- Monthly data sets on centers of action of the atmosphere. (1985). Obninsk. 395p.
- Monthly synoptic bulletin. (1986/1991) Part 2. Obninsk.
- Polonsky, A., and Sizov, A. (1991) Low-frequency North Atlantic variability associated with Pacific ENSO events. Obninsk, 247p.
- Polonsky, A., Voskresenskaya, E, and Belokopytov, V. (1997). Variability of Northwestern Black Sea Hydrography and River Discharges as Part of Global Ocean-Atmosphere Fluctuations. In book: *Sensitivity to Change: Black, Baltic and North Sea*. Kluwer Academic Publishers, 11-24.
- Simonov, A.I., and Altman, E.N. (1991). *Hydrometeorology and hydrochemistry of the USSR seas, v.4 (Black Sea), is.1 (hydrometeorological conditions)*. Hydrometeoizdat. St.Peterburg, 230p.
- Stocker, T.F. (1994) The variable ocean. *Nature*, v.367, No.6460, 221-222.

ON A DECADAL VARIABILITY IN THE COUPLED OCEAN-ATMOSPHERE SYSTEM OVER THE NORTH ATLANTIC OCEAN

Alexander POLONSKY and Eugeny OSTROVSKY

Marine Hydrophysical Institute., 2 Kapitanskaya St.,
335 000 Sevastopol, the Crimea, Ukraine. ocean@mhi2.sebastopol.ua

ABSTRACT

The aim of this paper is to discuss the mechanism of the decadal-scale climate variability in the North Atlantic Ocean. It is argued that decadal-scale climate variability stems from a coupled ocean-atmosphere mode generated in the North Atlantic. Evaluation of historical observations and simplified box model indicate the importance of changes in the tradewinds over the tropical Atlantic and ocean-atmosphere coupling in the entire basin in generating the self-sustained decadal-scale mode.

INTRODUCTION

Ocean variability is a crucial factor in regulating the long-term (interdecadal to multidecadal) changes in the coupled ocean-atmosphere system. The role of the North Atlantic Ocean merits particular attention in this context (1,2,3,4). Changes of the meridional circulation in the Atlantic Ocean are a plausible mechanism for generating long-term variability in the coupled ocean-atmosphere system (4). Concurrently there is a high-amplitude decadal mode in the North Atlantic Ocean. The magnitudes of the decadal and multidecadal modes are of the same order (2,5).

There are following ocean-related candidates for generating low-frequency (including decadal) climate changes (4):

- a) internal ocean (quasi)-periodical oscillations;
- b) abrupt transitions from one quasi-steady climate state to another;
- c) coupled (including ENSO induced) modes.

Let us consider briefly each of these candidates using selected published results.

a) According to simulations (6), the oceanic decadal mode is due to inherent feedback between thermohaline advection within the subsurface subtropical layer and convection in the Northern Atlantic Ocean. Chen and Ghil and Weaver et al (7) showed that about 20 year oscillations over the North Atlantic can be generated as a result of feedback between the rate of the high-latitude convection and value of the meridional heat flux (MHF) in the ocean. They point out that these inherent oceanic oscillations can exist without salinity changes and ocean-atmosphere coupling. The authors of both references emphasize the advective origin of decadal to interdecadal oscillations.

b) Ruhmstorf (8) developed Stommel's idea (9) concerning multi-regime of the oceanic circulation in the scope of the simplified (especially in its atmospheric part) coupled model. He argued that about 20 year oscillation can be a manifestation of the limit cycle during bifurcations of the meridional thermohaline circulation in the North Atlantic Ocean. He believed that even moderate changes in the freshwater input into the high latitudes can induce transitions between different equilibrium states. However, more complete coupled models (see e.g., ref.10) show that transitions claim more intense freshwater input anomalies.

c) The ENSO-induced coupled decadal variability in the Pacific Ocean was analysed in ref.(11). The authors showed that the planetary waves exiting in the ocean by the ENSO-events play the crucial role in the decadal-scale variability of the coupled system. At the same time Latif and Barnett (12) argued the importance of the mid-latitude ocean-atmosphere coupling in generating the self-sustained decadal mode over the North Pacific and North Atlantic Ocean. They showed that the period of the oscillations is controlled by the subtropical gyre adjustment which is determined by the speed of the gravest Rossby waves at the coupling latitudes and by the basin geometry. Stochastic atmospheric variability causes the additional red shift in the oceanic spectra with a broad peak at decadal scales superimposed (see, e.g., ref.13). Zhang et al.(14) also emphasized the coupled origin of the decadal mode. They drew attention to the feedback between MHF, ice conditions and sea surface heat fluxes (SSF) over the Northern Atlantic.

Thus, the recent results show the crucial role of the meridional oceanic circulation and MHF in generating the decadal mode. The role of coupling and tropical-extratropical connection is not so clear.

The aim of the present note is to discuss the mechanism of the coupled decadal mode over the North Atlantic Ocean. The importance of the trade-wind change over the tropical Atlantic, SST and MHF variability, and ocean-atmosphere coupling over the whole basin in generating the self-sustained coupled decadal mode will be shown using historical data sets, our earlier results (5,15) and simplified box model.

DATA AND PROCESSING PROCEDURE

The following datasets were used:

- monthly sea level pressure (SLP) in the vicinity of the Azores High (SLPaz) and Iceland Low (SLPisl) and monthly coordinates of their centers in 1891 to 1990 defined from the monthly maps (5);
- routine marine data from the volunteer observing system in 1957 to 1990 monthly averaged over 5 by 5 degree squares in the North Atlantic Ocean in the Russian Hydrometeorological Center (5); in fact this is the Russian analog of the well-known hydrometeorological archive file COADS (16);
- COADS after the Second World War (WW-II);
- SLP in 1930 to 1990 monthly averaged over 5 by 10 degree squares in the Northern Hemisphere in the Russian Hydrometeorological Center (15);
- subsurface historical temperature after the WW-II monthly averaged on the standard levels in upper 1000m layer in the World Oceanographic Data Center (15).

Low-frequency variability of the Rossby index ($RoI = SLP_{az} - SLP_{isl}$) was studied using the first dataset. The coefficient of correlation of RoI with the North Atlantic Oscillation Index (NAOI) defined from normalized SLP anomalies over the Azores and Iceland varies from 0.54 to 0.77 for different months. It is at a maximum in winter. Coefficient of correlation for the annual values is equal to 0.65. Monthly SSF, Ekman meridional and Sverdrup transports over the North Atlantic Ocean were evaluated using the second dataset. The third/fourth and fifth datasets were used to find the regions with the maximum low-frequency (decadal to interdecadal) surface and subsurface changes, respectively (for details, see refs.5 and 15).

EXPERIMENTAL RESULTS

We summarise below some results of data processing and selected published results demonstrating the coupled character of the decadal mode and the importance of the tropical-extratropical interaction.

1. The mutual compensation of northward Ekman transport and southward flow of the North Atlantic Deep Water (NADW) is a principal mechanism of the quasi-steady overturning over the North tropical Atlantic (17,18). The MHF due to transient processes in this region was evaluated in the refs.(19) and (20) as 10 to 15 % and about 20 % of total average oceanic MHF there, respectively. Recently (21), we revised published results and confirmed the crucial role of the quasi-steady overturning over the North tropical Atlantic due to northward Ekman/southward NADW in the meridional heat transport. In the subtropical and mid-latitudes, the MHF within the western boundary layer is a crucial share of total oceanic MHF (17).

Intense decadal-scale variability of the meridional Ekman transport (Q_y) occurs in the North Atlantic Ocean. The portion of r.m.s. due to this variability in total Q_y r.m.s. in the range of temporal scales from 2 to about 35 years reaches 40 to 50 %. A typical magnitude of the decadal changes of the meridional Ekman transport in the North tropical Atlantic is about 1 Sv. These changes strongly correlate with the low-frequency changes of the Sverdrup transport (especially in the subtropics and mid-latitudes), NAOI/RoI and SST over the North Atlantic Ocean. High-amplitude low-frequency changes of the Ekman transport in the tropical Atlantic were found also in ref.(22).

The mutual compensation of the northward Ekman transport and southward NADW transport over the North tropical Atlantic is expected on a decadal time scale because a typical temporal scale of the baroclinic adjustment of the North Atlantic Ocean due to thermohaline forcing in the Northern latitudes does not exceed one decade (23). The same compensation of the Gulf Stream and NADW transports is expected in the mid-latitudes. If so, the low-frequency changes of the NADW transport in the North tropical Atlantic should exist also. Our results (see below) confirm in part this conjecture.

2. Interannual to multidecadal variability of the SLP over the Northern Hemisphere is at a maximum in the vicinity of Greenland and in the polar region. In other words, SLP varies strongly over the regions of the NADW origin (24). The SLP r.m.s. due to these changes exceeds 20 to 25 mbar there. The SLP variance tends to be larger also in the vicinity of Iceland Low and Azores High. Decadal variability takes up to 30 % of total year-to-year variance over the North Atlantic Ocean in the range of temporal scales from 2 to about 60 years. Low-

frequency variability of the oceanic temperature within the upper 1000 m layer is at a maximum in the vicinity of the strong boundary currents and over the region of the NADW sinking (15).

3. Decadal meridional Ekman transport and, hence, decadal zonal circulation in the atmosphere boundary layer intensify concurrently over the whole North Atlantic. In that time, the sea surface becomes warmer (cooler) by about 1 to 2°C in the subtropical/mid-latitude (subarctic/equatorial) regions. Advection within the upper mixed layer is a principal cause of these changes in the subtropics/mid-latitudes, while convection is a crucial factor in the subarctic region. Intensified equatorial upwelling causes the sea surface cooling in the vicinity of the equator. During these periods the Azores High became deeper and shifted to the North or North-East (15). In other words there is a positive feedback between SST and SLP anomalies (SSTA and SLPA) (see also, ref.25). It should be noted that strong positive decadal-scale correlation between subtropical/mid-latitude SSTA and SLPA occurred only during long-term intensification of the zonal atmospheric circulation resulting in deepening of Azores High and Iceland Low (Fig. 1). In other words there is an interaction between decadal-scale and multidecadal modes.

So, above results show the principal importance of coupling and tropical-extratropical interaction in the decadal changes in the North Atlantic Ocean. Variability of the Ekman meridional transport in the Northern tropical/subtropical Atlantic is especially important. This permits to formulate the simplified box model demonstrating the possible generating mechanism of the decadal-scale mode.

BOX MODEL

We postulate the following 3-box ocean structure with simple feedback with the atmosphere (Fig. 2). There are two upper (tropical and mid-latitude) boxes and low box. Trade wind is responsible for the northward transport from Box 1 to Box 2. Salinity is constant. The governing eqs. system is as follows:

$$V_1 T_1' = U(T_3 - T_1) + R, \quad (1)$$

$$V_2 T_2' = U(T_1 - T_2) - R, \quad (2)$$

$$V_3 T_3' = U(T_2 - T_3). \quad (3)$$

Where: V_i , T_i are the volume and temperature of the i^{th} box; R is the surface heat flux.

Feedback in the coupled system is prescribed as follows: $U=U_0-Q(T_1-T_2)$, $Q>0$; that implies $\Delta P_a \sim \Delta T$, (where P_a is a sea level pressure).

We analyse a solution of the eqs (1-3) in the vicinity of the steady state, that fits to eq.: $\bar{U} \cdot \Delta T = R$, where $\bar{U} = (U_0 - Q\Delta T)$, $\Delta T = \bar{T}_1 - \bar{T}_2$.

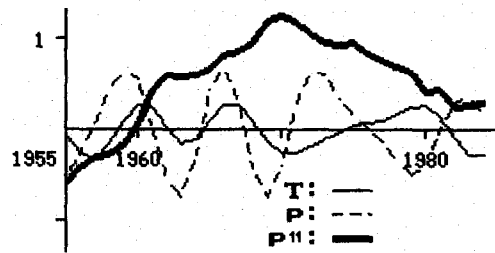


Fig.1 Time series of SLP (P) in the Azores High and SST (T) in its vicinity (five COADS 2°by2° squares centered at 35°N, 29°W). Series were filtered using band-passed (5 to 20 yr) filter. Thick line (P¹¹) shows the low-passed (11 yr cut off) filtered SLP in the Azores High.

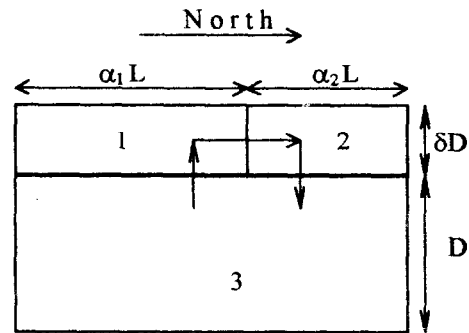


Fig. 2. Schematic structure of the ocean box model.

Box 1 is placed between Equator and North Tropic. Box 2 spreads to 50°N. Both boxes are shallow. Box 3 is deep. It consists of the NADW. Arrows show the direction of integral circulation. It can intensify or weaken due to temperature changes and associated variability of the Ekman transport. The relation between temperatures of the upper boxes and Ekman transport is prescribed through the postulated positive feedback between sea level pressure and sea surface temperature. It leads to the simple connection between meridional Ekman transport and temperatures of the upper boxes because zonal wind stress depends on the meridional gradient of sea level atmosphere pressure. The background meridional ocean circulation is implied to be governed by slow global meridional thermohaline overturning and can be postulated as a constant on the analysed decadal scale.

Linear analysis. Conventional linear analysis near steady state leads to following dimensionless characteristic equation: $\lambda^2 + 2(1 - \varepsilon + \delta\eta)\lambda + 4\eta(1 - \varepsilon)(1 + \delta) = 0$. The time scale is: $2\eta(V_1 + V_2)/\bar{U}$. $\eta = \alpha_1\alpha_2$, $\alpha_1 + \alpha_2 = 1$ and δ are the geometric characteristics. Dimensionless parameter $\varepsilon = QR/\bar{U}^2$ expresses the effect of coupling. The asymptotic stability occurs when $\varepsilon < 1$. Besides a solution is oscillated if $(1 - (\sqrt{1 + \delta} + 1))^2 \eta < \varepsilon < 1 - (\sqrt{1 + \delta} - 1)^2 \eta$

For fixed δ the minimal amplitude damping decrement $d_A = 2\pi |\text{Re}\lambda/\text{Im}\lambda|$ is reached when $\varepsilon = 1 - \delta\eta$ and equals to $2\pi\delta^{1/2}$. A correspondent period is equal to $2\pi\delta^{-1/2}(V_1 + V_2)/\bar{U} = 2\pi\delta^{1/2}V_3/\bar{U}$ and varies from 10 to 20 years approximately for the following typical magnitudes of the basic parameters: $\delta = 0.01$, $V_3 \approx 10^{16} \text{ m}^3$ and mean transport ranging from 18 to 9 Sv. The amplitude decaying rate per one period of an oscillation ($\exp d_A$) depends on two parameters: δ and $k = (1 - \varepsilon)/\eta$ (see Fig. 3). If e.g., $\delta = 10^{-2}$ the minimum decaying rate is ≈ 1.87 .

If the coupling is neglected oscillations may also exist when $(\alpha - 1/2)^2 < 1/4 - (\sqrt{1 + \delta} + 1)^{-2}$. However, in this case $d_A \approx 2\pi (2/\delta)^{1/2}$ and very fast decay of the oscillations occurs.

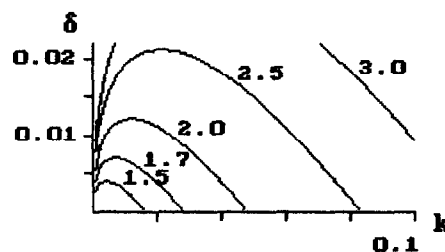


Fig. 3. The amplitude decaying rate per one period of an oscillation versus dimensionless parameters k and δ .

DISCUSSION

Thus, our results show a principal importance of decadal changes of the meridional Ekman transport (especially in the Northeast trade wind region) and associated SST/SLP changes in generating the decadal variability in the coupled system. Certainly the role of thermohaline circulation is not passive on this scale. Moreover, the simulation results (6,7,23) argue the active role of meridional thermohaline advection in generating the decadal to multidecadal mode. The sea surface cooling in the high-latitudes is especially important because it generates the fast anomalous convection and decadal oceanic response. In fact, the atmospheric thermodynamics and the law of mass conservation in the ocean (both) require the trade wind intensification after the sea surface cooling in the high-latitudes on the decadal scale. That is why we agree with the authors of ref.(12) and believe this is a coupled mode. We would like also to emphasize the importance of the tropical-extratropical interaction on this scale. The coherent decadal changes of the Ekman transport (mostly associated with the change of the trade wind in the Northwest tropical Atlantic), of the Sverdrup transport in mid-latitudes, of the SLP over the Azores High and Iceland Low, of the SST and SSF (and, hence, the rate of convection) over the North Atlantic confirm this conclusion.

The plausible generating mechanism of decadal mode is as follows.

At the first (intense) stage of the decadal oscillation, the positive feedback between SST and SLP anomalies (SSTA and SLPA) in the mid/high latitudes supports this intensification. Then, the negative SSTA generated over the equatorial Atlantic by intensified trade wind spread over the subtropics and mid-latitudes, while the positive SSTA are advected from the subtropics/mid-latitudes to the high latitudes. This weakens the atmospheric circulation and hence reduces the MHF magnitude. As a result, new SSTA are generated over the North Atlantic. They are positive over the equatorial zone and negative over the mid/high latitudes. This again intensifies the atmospheric circulation. Thus, this is a self-sustained coupled oscillation with more abrupt intense phase and strong tropical-extratropical interaction.

It seems the coupled mode is faster than the pure oceanic one. In both cases, the typical temporal scale depends on the time of baroclinic adjustment of the North Atlantic Ocean or the typical time of advective processes. In the ocean-only coarse-resolved models with the flat bottom (e.g.,(7)) this time is due to the traveling time for the Kelvin (around the basin) and the long Rossby (from the East to the West coastline) waves generating initially at the 60 to 70°N or at the surface (if one includes into consideration the bottom relief the topographic mode plays an important role in the adjustment, see ref.23). In the coupled case, the oceanic waves are generated also by the low-frequency atmosphere forcing all over the basin. Moreover, the recent observations show that the phase speeds of the Rossby waves exceeds those predicted by standard linear theory (typically twofold) as a result

of influence of the bottom relief and average circulation (26). That is why in the real coupled system, the decadal changes of the high-latitude SST and of the meridional Ekman transport over the tropical Atlantic are in phase, while in the ocean-only coarse-resolved models they are out-of-phase.

Thus, the observations and simple box modeling confirm the coupled character of the decadal oscillations. The absence of robust atmospheric decadal-scale signal associated with extratropical SST fluctuations in some coupled models (e.g., ref.27) can be result (at least, in part) of coarse resolution, poor parameterization of the convective processes, model drift, etc. It is clear on the other hand, the different mechanisms are responsible for the long-term variability of the coupled system. The stochastic component of the atmospheric forcing is one of them. Therefore, necessary to perform precise global observations (WOCE/TOGA-TAO-type and satellite) during at least a few decades and to develop coupled models with improved parameterization of the small-scale (sub-grid) processes and using recent techniques (e.g., assimilation procedure, ensemble averaging, etc). Only in this case, a further progress in study and predictability of the long-term climatic variability can be expected.

CONCLUSIONS

It seems the tropical-extratropical interaction and coupling are the important possible mechanism generating the coupled decadal mode over the North/Tropical Atlantic Ocean. The coherent decadal changes of the trade-wind over the tropical Atlantic, of meridional circulation (and, hence, MHF) over the whole basin, of mid/high-latitude SLP/SST and equatorial SST confirm such conclusion. Equilibrium of the oceanic circulation over the North Atlantic Ocean on the decadal scale, importance of the Ekman meridional transport over the North tropical Atlantic and feedbacks in the coupled system are the principal reasons for that. In principle, a quasi-periodical decadal mode can be generated by abrupt high-latitude thermal convection without salinity variability and catastrophic transition from one quasi-steady climate to another.

REFERENCES

1. Bjerknes, J. Atlantic air-sea interaction. *Adv. Geophys.*, **10**, 1 (1964).
2. Deser, C., and Blackmon, M.L. *J. Climate*, **6**, 1743 (1993);.
3. Kushnir, J. *J. Climate*, **7**, 141 (1994).
4. CLIVAR (A study of climate variability and predictability). Science plan.WCRP-89, WMO/TD, No.690, 157p.(1995).
5. Voskresenskaya, E.N., and Polonsky, A.B. *Meteorology and Hydrology*, *No.11*, 73 (1993); *No.9*, 48 (1994) (in Russian).
6. Yin, F.L., and Sarachik, E.S. *J. Phys. Oceanogr.*, **25**, 2465 (1995).
7. Chen, F and Ghil, M. (1995). *J. Phys. Oceanogr.* **25**, 2547 (1995); Weaver, A.J., Aura, S.M., Myers, P.G. *J. Geophys. Res.*, **99**, 12,423 (1994).
8. Rahmstorf, S. *Nature*, **378**, 145 (1995).
9. Stommel, H. *Tellus*, **13**, 224 (1961).
10. Delworth, T., Manabe, S., and Stouffer, R. Workshop on Atlantic Ocean Climate Variability (Moscow, Russia, 13-17 July 1992). IOC., Workshop Report, *No.84*, 5 (1992); Manabe, S., Stouffer, R.J. *Nature*, **378**, 165 (1995).
11. Jacobs, G.A. et al., *Nature*, **370**, 360 (1994).
12. Latif, M., and Barnett, T. *Science*, **266**, 634 (1994).
13. Munnich, M., Latif, M., and Marie-Reimer, E. *Annales Geophysicae*, Suppl. II to v.15, P.II, 475 (1997).
14. Zhang, S., Lin, C.A., Creatbatch, R.J. 1995. *J. Marine Res.*, **53**, 79 (1996).
15. Polonsky, A.B., and Kazakov, S.I. Proceedings of Regional Workshop on Climate Variability and Climate Change Vulnerability and Adaptation. (PRAHA, September 11-16 1995), 54 (1995); Polonsky, A.B., and Voskresenskaya, E.N. *Meteorology and Hydrology No.7*. 89 (1996) (in Russian).
16. Woodruff, S.D., Slutz, R.J., Jenne, R.L., Seurer, P.M. *Bull. Amer. Meteorol. Soc.* **85**, 1238 (1985).
17. Bryan, K. *Ann. Rev. Earth Planet*, **10**, 15 (1982).
18. Polonsky, A.B. *Marine Hydrophysical Journal*, *No.1*, 58 (1985) (in Russian); Kraus, E.B., and Levitus, S. *J. Phys. Oceanogr.*, **16**, 1479 (1986); Friedrichs A.M., and Hall M.M. *J. Marine Res.*, **51**, 697 (1993).
19. Polonsky, A.B., and Bulgakov, N.P. Report on the Atlantic Panel of CCCO, Kiev, 31 (1989).
20. Richardson, Ph., and Schmitz, W.J. *J. Geophys. Res.* **98**, 8371 (1993); Schott, F., Fischer, J., Reppin, J., Send, U. *J. Geophys. Res.* **98**, 14,353 (1994).
21. Dzhigashin, G.F., and Polonsky, A.B. *Marine Hydrophysical J. No.4*, 27; *No.6*, 39 (1996) (in Russian).

22. Baev, S.A., Bulgakov, N.P., Polonsky, A.B. *Marine Hydrophysical Journal*, No.6, 29 (1988) (in Russian).
- Adamec, D., Rienecher, M.M., Vuhovich, J.M. *J.Phys. Oceanogr.*, **23**, 2704 (1993);
23. Doscher, R., Boning, C.W., Herrmann, P. *J. Phys. Oceanogr.*, **24**, 2306 (1994).
24. Dickson, R., and Brown, J. *J. Geophys. Res.*, **99**, 12,319 (1994).
25. Trenberth, K.E., and Hurrell, J.W. *Climate Dynamics*, **9**, 303 (1994).
26. Killworth, P., and Blundell, J. Poster at WOCE Conference (Halifax, Canada, 25-29 May 1998) (1998).
27. Zorita, E., and Frankignoul, C. *J. Climate*, **10**, 183-200 (1997).

REGULAR DYNAMIC STRUCTURES IN THE JAPAN /EAST SEA

Vladimir I. Ponomarev and Olga O. Trusenkova

Pacific Oceanological Institute, Far-Eastern Branch of Russian Academy of Sciences,
43 Baltiyskaya St., Vladivostok, 690041, Russia
(e-mail: ponomarev%dan86@poi.marine.su, archer@linkor.ru)

Abstract. The research was initiated by data analysis. The observational evidence for synoptic scale regular structures as well as strong topographic effects over the continental slope, sea mounts and rises in the Japan/East Sea is highlighted. To study the influence of buoyancy and wind forcing on generation of the regular structures the quasi-isopycnal ocean circulation model developed by Naum Shapiro [1,2] in Marine Hydrophysical Institute (MHI, Sebastopol, Ukraine) is adapted to the realistic Japan/East Sea geometry, bottom topography and external conditions. We set vertical resolution of 7 layers and 7-14 km horizontal resolution in numerical experiments which permits us to simulate main currents and fronts, gyres and eddies over sea basins and rises. The numerical solutions with and without wind forcing as well as with closed and open straits are compared and analyzed. The results show that both general circulation patterns and regular structures of different origin can be simulated by the MHI quasi-isopycnal model. In particular, taking into account buoyancy forcing due to heat flux through the sea surface and inflow of warm saline water through the Korea Strait, the rings separated from a frontal jet, chains of anticyclonic eddies, streamers and mushroom-like structures are revealed in numerical experiments. Taking into account synoptic wind forcing, topographic eddies near sea mounts and eddy structure of upwelling over continental slope caused by wind jets are also demonstrated.

1. Introduction

The Japan/East Sea is a deep marginal sea connected to the Pacific ocean, East-China and Sea of Okhotsk by shallow straits. The transformed warm and saline water of the Kuroshio branch is directly transported in the upper layers through the Sea of Japan from the Korean/Tsushima Strait (50m) to the Tsugaru (100m) and Laperus/Soya (100m) Straits. The main pycnocline is about 250-300m in the south Japan/East Sea and 50-70m in the north where it is approximately in line with the seasonal one. The isopycnal surface of 27.0 lifts up from the lower boundary (depth of 150-200m) of the subtropical salinity maximum layer in the southern area to the depth of seasonal pycnocline (30-50m) in the north-western sea area. This isopycnal surface is associated with the main frontal surface which separates two of the most important sea layers of different mean density and thickness. In the central sea area where the isopycnal surface of 27.0 approaches the seasonal pycnocline the subarctic (polar) front is stretched along 39-40°N. As pycnocline thickness and, therefore, Rossby deformation radius, decrease when passing the subarctic (polar) front from south to north, typical sizes of synoptic scale eddies decrease, too. In our opinion, the appropriate tool for simulating synoptic scale structures and frontal dynamics in the Japan/East Sea is quasi-isopycnal circulation model with free sea surface [1].

2. Observation data

Data analysis was based on the oceanographic observations of temperature, salinity, dissolved oxygen and silicate measured in following cruises: R/V "Vityaz" 3rd cruise in January - February 1950, expedition of Russian Academy of Sciences, 124 oceanographic stations; R/V "Akademik Vinogradov", KEEP-MASS Joint Russian-Taiwan expedition, 23rd cruise in July 1992, 3 sections across the Japan/East Sea basins, 14 oceanographic stations; R/V "Akademik Lavrentyev" 26th cruise in November - December 1995, 10 stations on the Niigata-Vladivostok section and 6 stations over the Pervenets Rise; R/V "Borey" cruise in late October 1990, section along 132°E in the Peter the Great Bay and adjacent area over the continental slope.

The observation data shows the synoptic scale eddies and meso-scale disturbances over the continental slope and slopes of Pervenets, Bogorov, Yamato Rises, Korean Plateau as well as multifrontal structure of the Japan/East Sea main pycnocline. During the cruise of R/V "Vityaz" the most complete hydrochemical and oceanographic observations were implemented in the vicinity of above mentioned topographic features. Most of measured parameters (temperature, salinity, oxygen, silicate) showed extremal values and maximal gradients there which indicated pairs of eddies of opposite vorticity [3]. During more recent cruises detailed CTD and hydrochemical observations were performed. Maximal horizontal gradients of potential temperature and oxygen were found in deep layers near the Korean Plateau and Pervenets Rise. Cross-frontal sections showed that temperature and salinity fronts were separated in the East-Korean Current area.

We also used the AVHRR NOAA satellite data in late October 1990 and more recent data in the fall of 1993, 1996, 1997 and spring of 1997. Satellite and CTD observations in October 1990 revealed the eddy structure of upwelling in the Peter the Great Bay adjacent area over the shelf and continental slope [4]. We simulated the upwelling eddy structure in this area using the numerical model. High resolution satellite images of 1993, 1996 and 1997 showed synoptic scale multiple fronts, streamers and eddies both in southern and northern sea areas [5, 6]. We obtained some of these features in numerical experiments.

3. The Japan/East Sea circulation model

Findings based on observation data analysis were confirmed and developed by numerical simulation of the structures considered. We adapted the nonstationary quasi-isopycnal circulation model developed by Naum Shapiro and Eleonora Mihaylova, MHI, Sebastopol, Ukraine [1,2] to the Japan/East Sea. This model was earlier used to simulate the eastern ocean boundary undercurrent and Kelvin wave during upwelling as well as the general circulation in the Black Sea and Atlantic ocean but never applied to the Japan/East Sea. The model is close to known layered isopycnal models, for example [7-10].

The model [1] is based on the primitive equations with free surface boundary condition. It consists of upper mixed layer, seasonal pycnocline (like in [8]) and quasi-isopycnal inner layers. Temperature, salinity and buoyancy in every layer are functions of horizontal coordinates and time. Interfaces between layers can move vertically and lift up to the sea surface or descend down to the bottom. The so-called "base stratification", typical for the sea is postulated in the model. If buoyancy in a certain layer gets out of limits determined by base stratification the layer degenerates and its thickness becomes negligible. The model has slip boundary conditions on the coastal boundary and bottom. In a case of unstable density stratification, mixing is produced by traditional convective adjustment scheme.

We adapted the model to the realistic Japan/East Sea geometry, bottom topography and external conditions. The vertical resolution of 7 layers and 1/8° horizontal resolution of 7-14 km was set up in numerical experiments. Isopycnal lateral mixing coefficient was set up as 10^2 - 10^3 m²/c depending on bottom topography smoothing. Diapycnal mixing was taken into account only on the upper mixed layer lower boundary, with vertical exchange through inner layers interfaces being neglected.

4. Numerical experiments.

Two series of numerical experiments were performed, initial & external conditions described in the Table.

INITIAL CONDITIONS AND EXTERNAL FIELDS FOR THE NUMERICAL EXPERIMENTS

	EXPERIMENT I, CASE 1	EXPERIMENT I, CASE 2	EXPERIMENT II
Temperature in 1st-7th layers ($^{\circ}\text{C}$)	Levitus climatology as a function of horizontal coordinates	12, 12, 6, 3, 2, 1, 0.06 in the internal sea area, 13-16 in annual cycle for the Tsushima Strait inflow water	
Salinity in 1st-7th layers (ppt)	33.5, 33.5, 34.0, 34.02, 34.05, 34.06, 34.077 in the internal sea area, 34.6 for the Tsushima Strait inflow water		
Interfaces depths (m)	10, 50, 100, 150, 250, 500, 2500		
Wind	Averaged wind affecting only upper mixed layer turbulent heat fluxes		Synoptic NNW1 wind
Straits	Annual mean volume transport through the Tsushima (Korean), Tsugaru, Laperus (Soya) Straits		Closed
Precipitation - evaporation residuals	Neglected		
Short-wave radiation	Annual cycle as climatological monthly norms		
Surface air temperature	Annual cycle as climatological monthly norms		
Starting date	The 1 st of June		The 1 st of October
Time step (sec)	360-1200		360

It should be noted that for the initial condition in the Experiment I, Case 1 the Levitus climatology was taken into account only for temperature field. It is quite sufficient for the Sea of Japan because density stratification is mostly maintained with temperature profile there.

The findings concerning eddy dynamics were obtained under rather rough horizontal and vertical resolution with artificially amplified horizontal exchange and the depth of the main pycnocline and smoothed bottom topography. These factors result in overestimation of the eddy horizontal scale.

5. Results

Starting numerical experiment from Levitus climatology initial conditions is the most typical for model application to the Sea of Japan. We set our Experiment I, case 1 in the same way but without wind influence on sea currents (averaged wind affecting only upper mixed layer turbulent fluxes was applied).

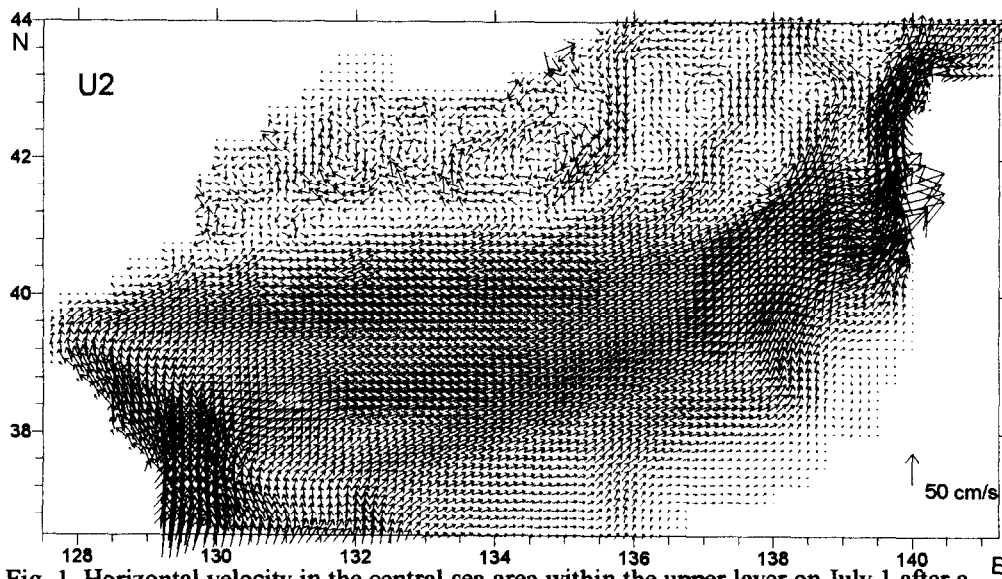


Fig. 1. Horizontal velocity in the central sea area within the upper layer on July 1 after a month of integration from Levitus climatology initial conditions. (Experiment I, case 1).

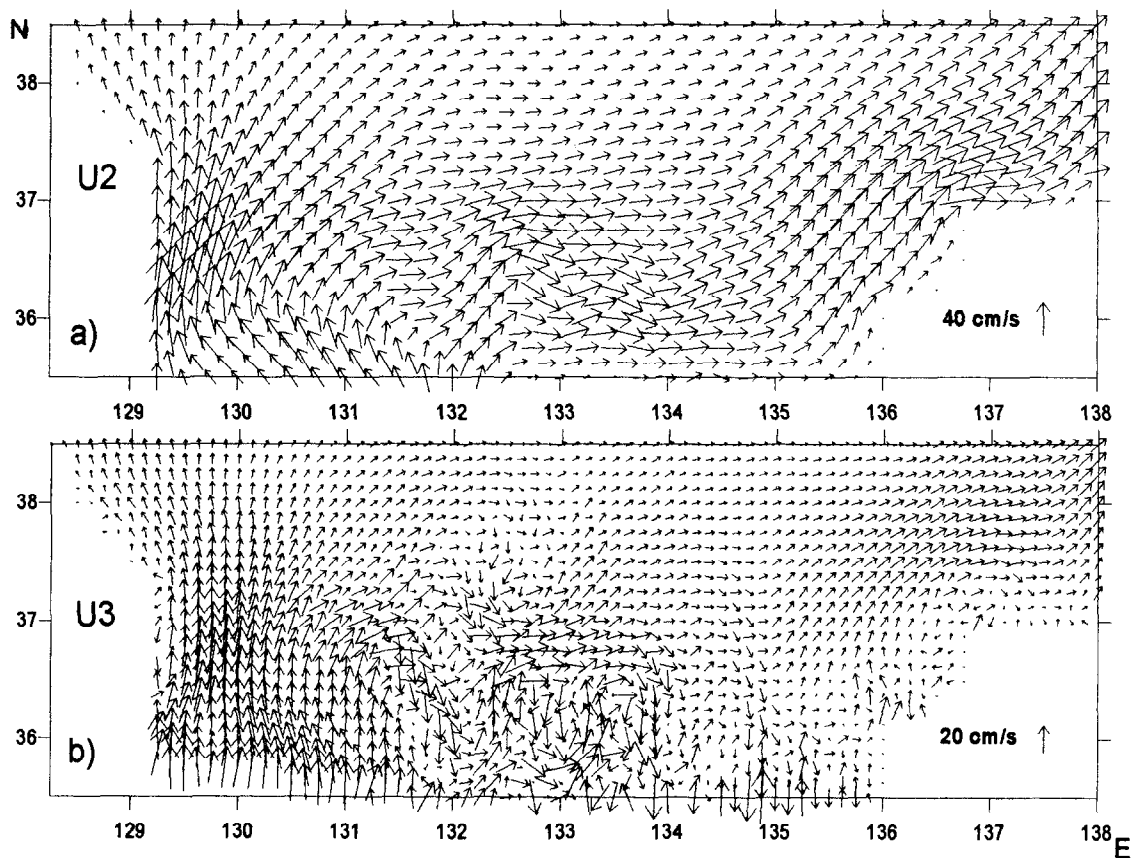


Fig. 2. Horizontal velocity in the area adjacent to the Tsushima/Korean Strait within the upper layer (a) and layer of subtropical water (b) on October 2 after 124 days of integration. (Experiment I, case 2).

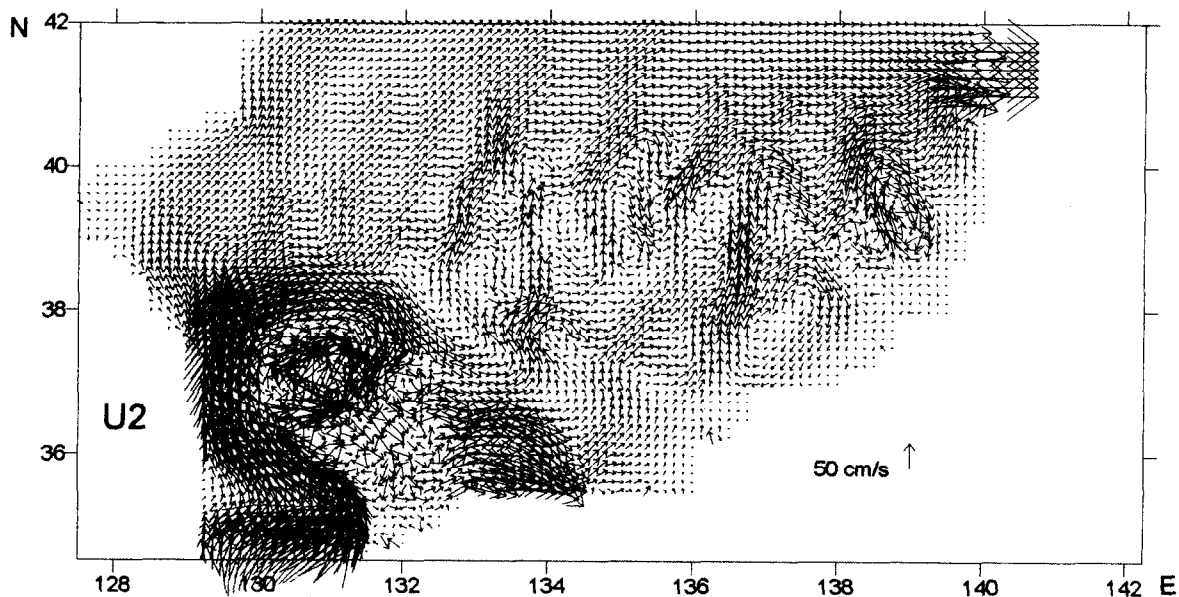


Fig. 3. Horizontal velocity in the upper layer on August 24 after 419 days of integration from horizontally homogeneous initial conditions (Experiment I, case 2).

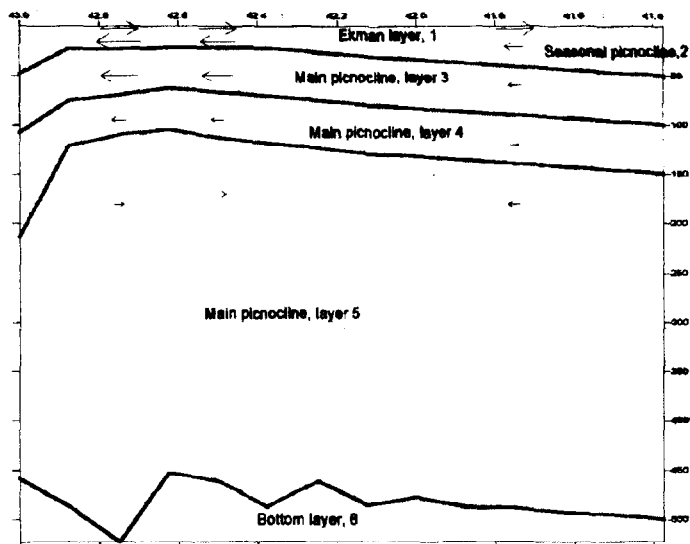


Fig. 4. Experiment II. Vertical section of layer interfaces and longitude current velocity component in the cyclonic eddy in the Peter the Great Bay along $132^{\circ}37'30''$ after 5 days of integration in time.

conditions but for inflow water in the Tsushima/Korean Strait (see Table). The subarctic (polar) front was being formed in the time integration process due to inflow of warm saline water through the Tsushima/Korean Strait and heat exchange through the sea surface in annual cycle. With increase of temperature and density gradients eddies were being formed in the 3rd layer with maximal vertical density gradients in the frontal zone of the Tsushima Warm Current. The 3rd layer represents the most of the main pycnocline in the southern sea area and corresponds to the saline subtropical water propagating in the Sea.

Fig. 2a shows meandering and branching of the Tsushima/Korean Current in the upper layer. In the lower, 3rd layer (Fig. 2b) steamers and eddies of alternative vorticity similar to mushroom-like structures were formed. In a few days the eddies and steamers occupied also the upper mixed and seasonal thermocline layers and the 4th layer.

At the end of the first year the strong western boundary meandering current, corresponding to the East Korean Current, was formed. By the 419 day of integration in time the anticyclonic ring was formed and separated from the jet (Fig. 3). It is similar to one obtained by [10] with the use of climatological wind forcing. In the same time, the second temperature front was being formed in the upper layers approximately along the $39-40^{\circ}\text{N}$ in summer. The Fig. 3 also shows regular dynamic structures - steamers and eddies, mainly of anticyclonic vorticity, associated with dynamic processes above rough bottom topography in the central sea area. When lateral isopycnal coefficient decreased down to $10^2 \text{ m}^2/\text{s}$, the Experiment I, cases 1,2 showed the near-shore current branching obtained in [11]. Traditional smoothed general circulation gyres were obtained with high values of lateral isopycnal coefficient (more than $10^3 \text{ m}^2/\text{s}$).

The second series of numerical experiments was performed under forcing of synoptic north-north-western (NNW1) wind characterized by strong jets, one directed along the axis of the Peter the Great Bay (along 132°E) and another, over the entire sea, directed approximately from the Olga Bay and Vladimir Bay to the Tsugaru Strait. Steady baroclinic dipole structures were obtained in areas of jet wind forcing, associated with strong upwelling in the cyclonic eddy and downwelling in the anticyclonic one. The section along $132^{\circ}37'30''\text{E}$ across the upwelling of the Peter the Great Bay adjacent area (Fig. 4) shows upwards bending of the layers interfaces typical for upwelling as well as horizontal velocities in layers. Earlier, observational evidence for similar structures over the continental slope near the Peter the Great Bay and Vladivostok was revealed from the AVHRR satellite data in late October 1990 [4]. The atmospheric jet in the Olga Bay adjacent area produced the strong dipole structure near the Bogorov Rise and Primorye continental slope. Evidence for these structures was revealed from the R/V "Vityaz" observation data back in winter 1950 [3].

These results were obtained under neglected vertical diapycnal mixing, possible with layered models. Under condition of high resolution in space and time a layered model can describe longwave eddy dynamics caused by Rossby and topographic (Rossby and Kelvin) waves affecting formation of regular structures.

The integration time was about 9 months. We obtained characteristic general circulation similar to [10-12]: the Tsushima and East-Korean Currents in the southern sea area as well as cyclonic gyre over western Japan basin corresponding to the Primorskoje Current and a strong jet carrying transformed subtropical water to the Tatar Strait. The specific features of our solution are multiple jets in the frontal zone and main current branching both in the southern sea area and in the cyclonic gyre mentioned above (Fig. 1), despite the smooth initial conditions of Levitus climatology. Fig. 1 also shows synoptic eddies and jets in the Primorye adjacent area over the bottom slope and current branching in the southern sea area. The current pattern shown in Fig. 1 is similar to that obtained in [6] based on satellite and drifter data.

The Experiment I, case 2 was started from horizontally homogeneous initial conditions

but for inflow water in the Tsushima/Korean Strait (see Table). The subarctic (polar) front was being formed in the time integration process due to inflow of warm saline water through the Tsushima/Korean Strait and heat exchange through the sea surface in annual cycle. With increase of temperature and density gradients eddies were being formed in the 3rd layer with maximal vertical density gradients in the frontal zone of the Tsushima Warm Current. The 3rd layer represents the most of the main pycnocline in the southern sea area and corresponds to the saline subtropical water propagating in the Sea.

Fig. 2a shows meandering and branching of the Tsushima/Korean Current in the upper layer. In the lower, 3rd layer (Fig. 2b) steamers and eddies of alternative vorticity similar to mushroom-like structures were formed. In a few days the eddies and steamers occupied also the upper mixed and seasonal thermocline layers and the 4th layer.

At the end of the first year the strong western boundary meandering current, corresponding to the East Korean Current, was formed. By the 419 day of integration in time the anticyclonic ring was formed and separated from the jet (Fig. 3). It is similar to one obtained by [10] with the use of climatological wind forcing. In the same time, the second temperature front was being formed in the upper layers approximately along the $39-40^{\circ}\text{N}$ in summer. The Fig. 3 also shows regular dynamic structures - steamers and eddies, mainly of anticyclonic vorticity, associated with dynamic processes above rough bottom topography in the central sea area. When lateral isopycnal coefficient decreased down to $10^2 \text{ m}^2/\text{s}$, the Experiment I, cases 1,2 showed the near-shore current branching obtained in [11]. Traditional smoothed general circulation gyres were obtained with high values of lateral isopycnal coefficient (more than $10^3 \text{ m}^2/\text{s}$).

The second series of numerical experiments was performed under forcing of synoptic north-north-western (NNW1) wind characterized by strong jets, one directed along the axis of the Peter the Great Bay (along 132°E) and another, over the entire sea, directed approximately from the Olga Bay and Vladimir Bay to the Tsugaru Strait. Steady baroclinic dipole structures were obtained in areas of jet wind forcing, associated with strong upwelling in the cyclonic eddy and downwelling in the anticyclonic one. The section along $132^{\circ}37'30''\text{E}$ across the upwelling of the Peter the Great Bay adjacent area (Fig. 4) shows upwards bending of the layers interfaces typical for upwelling as well as horizontal velocities in layers. Earlier, observational evidence for similar structures over the continental slope near the Peter the Great Bay and Vladivostok was revealed from the AVHRR satellite data in late October 1990 [4]. The atmospheric jet in the Olga Bay adjacent area produced the strong dipole structure near the Bogorov Rise and Primorye continental slope. Evidence for these structures was revealed from the R/V "Vityaz" observation data back in winter 1950 [3].

These results were obtained under neglected vertical diapycnal mixing, possible with layered models. Under condition of high resolution in space and time a layered model can describe longwave eddy dynamics caused by Rossby and topographic (Rossby and Kelvin) waves affecting formation of regular structures.

6. Conclusions

The main baroclinic currents and fronts of the Japan/East Sea are formed due to the seasonal cycle of heat and water exchange through the straits and sea surface during model integration from both Levitus climatology and horizontally homogeneous initial conditions.

The basic features of the synoptic dynamics such as current branching, baroclinic instability of jets, ring and eddy formation in frontal zones over rough bottom topography can be successfully simulated by the MHI quasi-isopycnal model.

The following synoptic regular structures were obtained in numerical experiments:

a) taking into account buoyancy forcing due to heat flux through the sea surface and inflow of warm saline water through the Tsushima Strait:

- current branching and mushroom-like structures formed in the East Korea & Tsushima Currents frontal zones,
- streamers and chains of anticyclonic eddies caught by bottom topography in the central sea area,
- rings formed and separated from a frontal jet;

b) taking into account synoptic wind forcing:

- eddy dipoles and upwellings caused by wind jets over basin slopes,
- topographic dipoles and more complicated eddies over sea mounts and rises.

Acknowledgments: This study became feasible due to courtesy of Prof. Naum Shapiro and Dr. Eleonora Mikhaylova who provided us with the model. We would like to thank Prof. N. Shapiro, Drs. E. Mikhaylova and Yu. Ryabtsev for consulting with the model source texts. We are grateful to Prof. Chris Garret and Prof. Young J. Ro for valuable remarks during the poster session at the Constantine Fyodorov Memorial Symposium, 18-22 of May 1998, St.-Petersburg, Russia.

References

- [1] Shapiro N.B. 1998. Formation of circulation according to quasi-isopycnal model of the Black Sea considering stochastic wind stress. *Marine Hydrophysical J.* (in press).
- [2] Mikhailova, E.N., and N.B. Shapiro. 1992. Quasi-isopycnal multilayer model of large-scale ocean circulation. *Marine Hydrophysical J.*, 4, Sebastopol, 3-13.
- [3] Ponomarev, V.I., A.N. Salyuk, and A.S. Bychkov. 1996. The Japan Sea water variability and ventilation processes. *Fourth CREAMS Workshop Proc., R/V OKEAN, Vladivostok, Feb. 12-13, 1996*, 63-69.
- [4] Goncharenko, I.A., V.G. Federyakov, A.Yu. Lazaryuk and V.I. Ponomarev. 1993. Thematic processing of the AVHRR data illustrated by the example of studying the coastal upwelling. *Issledovaniya Zemli iz kosmosa*, 2, Moscow, 97-108.
- [5] Danchenkov, M.A., V.B. Lobanov, and A.A. Nikitin. 1997. Mesoscale eddies in the Japan Sea, their role in circulation and heat transport. *Proc. CREAMS'97 Int. Symp., Fukuoka, Japan, 28-30 Jan., 1997*, 81-84.
- [6] Gingzburg A.I., A.G. Kostianoy, and A. Ostrovskii. 1998. Surface circulation of the Japan Sea (satellite information and drifters data). *Issledovaniya Zemli iz kosmosa*, 1, Moscow, 66-83.
- [7] Huang R.X., and K. Bryan. 1987. A multilayer model of the thermohaline and wind-driven ocean circulation. *J. Phys. Oceanogr.*, 17, 11, 1909-1924.
- [8] Bleck R., H.P. Hanson, D. Hu, and E.B. Kraus 1989. Mixed layer-thermocline interaction in a three-dimensional isopycnal coordinate model *J. Phys. Oceanogr.*, 19, 10, 1417-1439.
- [9] Oberhuber J.M. 1993. Simulation of the Atlantic circulation with a coupled sea ice-mixed layer-isopycnal general circulation model. Part 1: Model description. *J. Phys. Oceanogr.*, vol.23, N.5, 808-829.
- [10] Hogan P.J., and H.E. Hurlburt. 1997. Sea of Japan circulation dynamics via the NRL layered ocean model. *Proc. of the CREAMS'97 Int. Symp., Fukuoka, Japan, 28-30 Jan. 1997*, 109-112.
- [11] Yoon J.-H. 1982. Numerical experiment on the circulation in the Japan Sea. Part 3. Mechanism of near-shore branching of the Tsushima Current. *J. Oceanogr. Soc. Japan*, v.38, 125-130.
- [12] Mooers, C.N.K., and H.S. Kang. 1997. On the 26-sigma level POM model for Japan (East) Sea circulation. *Proc. of the CREAMS'97 Int. Symp., Fukuoka, Japan, 28-30 Jan. 1997*, 15-17.

PECULIARITIES OF THE THERMOHALINE STRUCTURE AND VARIABILITY OF THE ST. PAUL ISLAND COASTAL FRONT (THE BERING SEA)

S.G. Poyarkov, M.V. Emelianov

P.P. Shirshov Institute of Oceanography, 36, Nakhimovsky Pr., Moscow 117851, Russia
E-mail: zatselin@glasnet.ru

Abstract. The coast frontal zone is known as an important agent of the near shore energy and matter transfer processes in the World Ocean [1]. The analysis of the thermohaline structure and variability of the St. Paul island coastal front is considered on the basis of two identical hydrophysical surveys with the time interval 1.5 months one after another. It is shown, that the observed difference in the structure of the frontal zone between these two surveys is conditioned by the seasonal change of thermal state of surrounding waters. The peculiarities of the crossfrontal exchange in the cases of different structure of the frontal zone are discussed. The generalised characteristics of the coastal front are given.

Brief hydrophysical survey results.

A detailed survey of the coastal front was repeated twice during the 5.5 weeks period on 11th-12th June and 20th-21st July 1994. The surveys covered the same relatively small area (11×4 miles) south-westwards from the St. Paul Island (Fig. 1). Both surveys have been done during nearly the same phase of tidal cycle. According to NWS St. Paul for Village Cove, average tidal mark during the June survey reached +2.1 feet and +2.9 feet in July with the average 11 hours duration. Each survey contained 3 sections. General features of the coastal front south-westwards from the St. Paul Island are given in the Table.

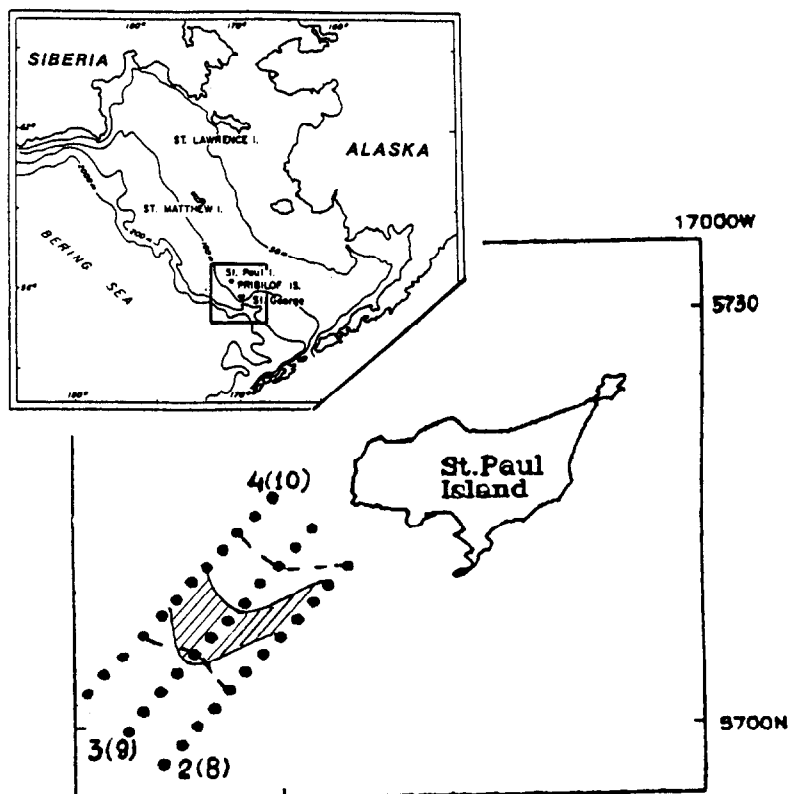


Fig. 1. Coastal front surveys area.

- - CTD casts;
- front position boundaries in:
(—) - June, (- - -) - July.

Table

Features of the Coastal Front South-Westwards from the St. Paul Island

Date	Section #	Level, metres	Distance from the shore, miles	Width, miles	Gradient		
					T, °/mile	S, psu/mil e	
11 th -12 th June	2	surface	5 - 8	3	0.25		
		20	10.5 - 11.5	1	1.00	0.13	
		bottom	8 - 9.5	1.5	0.40	0.20	
	3	surface	8.5 - 11.5	3	0.13		
		20	10 - 12	2	0.40	0.10	
		bottom	6 - 8	2	0.30	0.10	
	4	surface	8 - 10.5	2.5	0.17		
		25	6 - 8	2	0.80	0.13	
		bottom	5.5 - 6.5	1	0.60	0.10	
	20 th -21 st July	8	surface	4 - 11	7	0.20	
			30*	9 - 11	2	0.40	0.15
			bottom	7.5 - 9.5	2	0.40	0.10
9		surface	6 - 11	5	0.16		
		30*	7 - 12	5	0.30	0.05	
		bottom	7.5 - 9.5	7	0.22	0.04	
10		surface	6 - 12	6	0.17		
		30*	7.5 - 12	4.5	0.18	0.05	
		bottom	5 - 9	4	0.15	0.06	

* Below the thermocline

Results discussion.

At the beginning of the first decade of June the front separated cool (1.4 -1.8 °C), less saline (below 31.8 psu) and vertically homogeneous near island waters from the warmer (2.8 -3.2 °C), more saline (over 32.0 psu) stratified shelf waters. The coastal front clearly divided this two water masses. So, the near island water was sharply contrasted as:

- the most cold, because of direct cooling during abnormally cold spring;
- low saline, resulting from the inland snow melting;
- density homogeneous water column, due to tidal and wind mixing forced by winter vertical convection.

The near island coastal front in June was most clearly pronounced in the field of temperature (Fig.2). It could be traced across the entire water column. At the surface the front was observed 5 to 11.5 miles away from the shore in different sections of mesoscale survey. The average crossfrontal extent reached 3 and 1-2 miles in the surface and bottom layers respectively (Table). The front inclination became visible starting from subsurface levels below 10-15 metres (Fig.2). According to the conducted survey, significant changes were found both in the location and the inclination angle of the front. Sections 3 and 4 showed 3-5 miles shift of the coastal front seawards as compared to Section 2 data. On the contrary, near the bottom the front was detected 1-2.5 miles closer to the Island (Table). The observed displacements of the coastal front in the opposite directions corresponds to the decrease of its inclination angle. It is interesting to note, that in the plane of the section the coastal front rotated around an "axis", which could be imagined at the 15-20 metres depth. Just at that depth the thermocline emerged due to summer heating later on.

The most intensive crossfrontal exchange was observed in the 10-15 metres surface layer, where low-saline waters spread outwards from the shore. This water used to warm up rapidly. The "permeability" of the coastal front in the surface layer was observed in all sections of the June survey (Sections 3,4) and was proved by distributions of dissolved oxygen and nutrients (Section 1, Fig.3). In the bottom layer, a trend for "backing" the coastal front with shelf waters was clearly traced. Section 3 even showed their penetration through the front along the bottom. The possibility of shelf water penetration into the near island area was defined, in particular, by the weakness of horizontal near-bottom gradients (Table) and was proved by distributions of phosphates and nitrates near the bottom at Section 1 (Fig.3).

In the July survey, the situation at the coastal front south-westwards from the St. Paul Island had changed dramatically (Table, Fig.2, 3). The ongoing warming and intensive wind and tidal mixing over low depths were responsible for the coastal front link with gradient layer in pelagial. The layer was found beyond the 12-mile belt, 15-30 metres deep and constituted a thermo- halo and pycnocline in the structure of shelf waters. 5-10 miles away from the Island the gradient layer has been split: which partially appeared on the surface and partially sank down to the bottom, forming the coastal front in July. The coastal front at the time was marked with surface and bottom partition fronts in the fields of properties. Now, the front separated the well mixed coastal water, already warmed up to 4.8 - 5.2 (°C) but still desalted below 31.8 psu from the adjacent warm (up to 6.8 °C) and saline (over 31.8 psu) shelf water in the upper 15-20 metres layer. Under the thermocline the shelf water was significantly cooler (3.6 - 3.8 °C) and more saline (32.1-32.2 psu) (Fig.2).

The coastal front in July became wider from the surface to the bottom than in June, reaching the values of 5-7 and 4 miles respectively. Near the bottom, horizontal gradients of properties in July significantly decreased from Section 8 to Section 10, i.e. from south to north (Table, Fig.2).

The crossfrontal exchange at the beginning of the 3 decade of July was detected in the 15-20-metres surface layer. Contrary to the situation in June, the layer exhibited penetration of warm and relatively saline shelf water, located above the thermocline, into the coastal front area. On the other hand, below the thermocline the trend for expansion of shelf waters into the near island area through the coastal front preserved, as in June. The "permeability" of the coastal front near the bottom was especially visible in Section 10 (Fig.2). This was also proved by distributions of phosphates and silicate at Section 7, done one day before along the same direction from the St. Paul Island (Fig.3). It should be noted, that the frontal dynamics in the shallow water

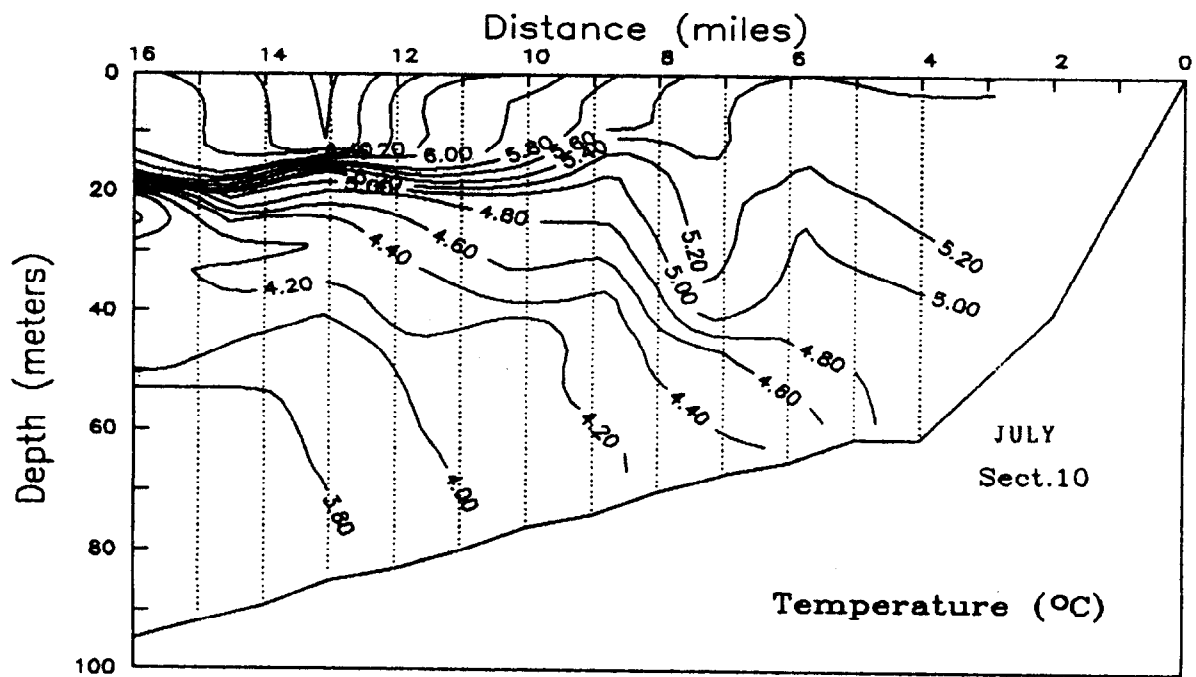
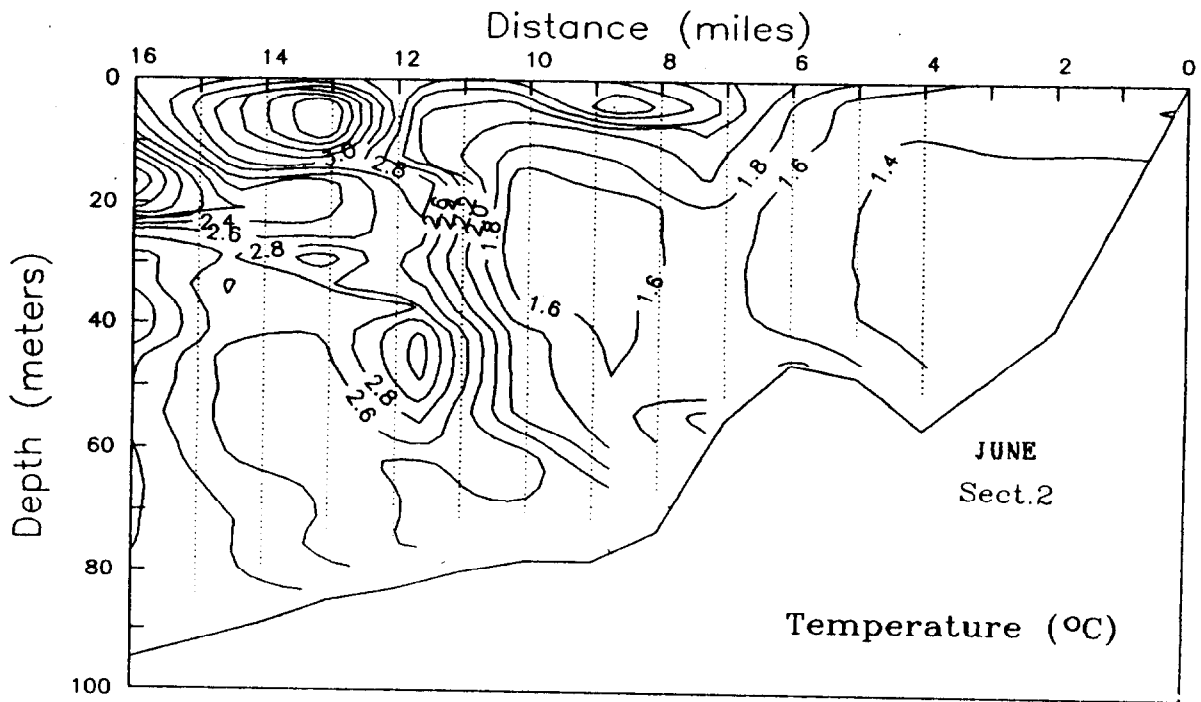


Fig. 2. Crossfrontal Temperature sections.

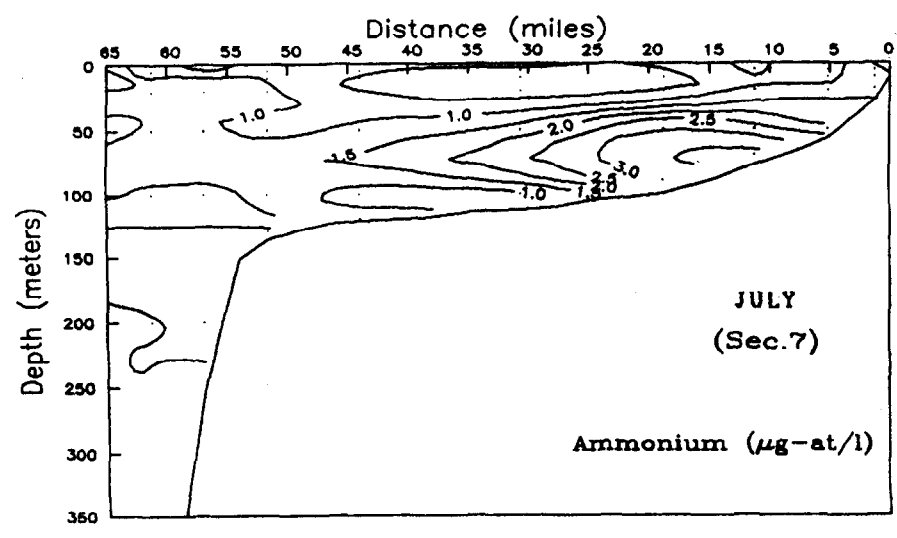
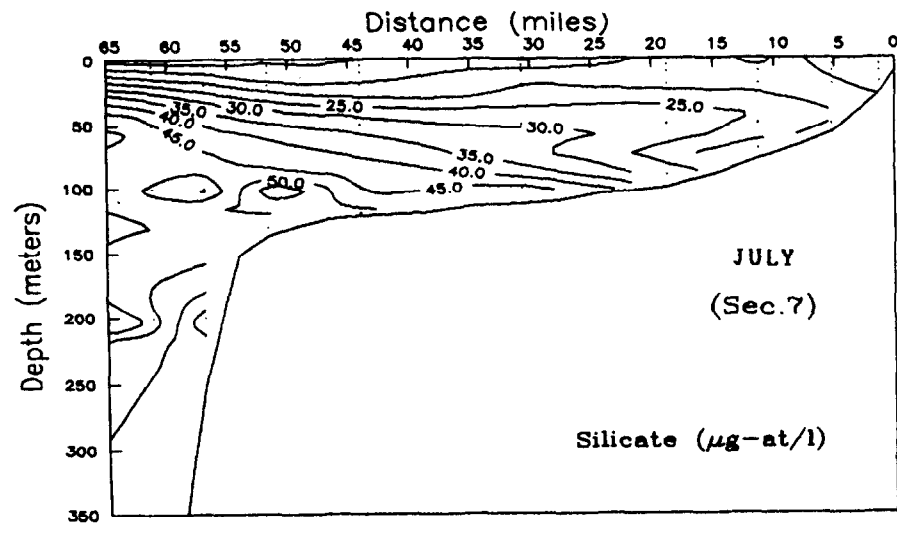
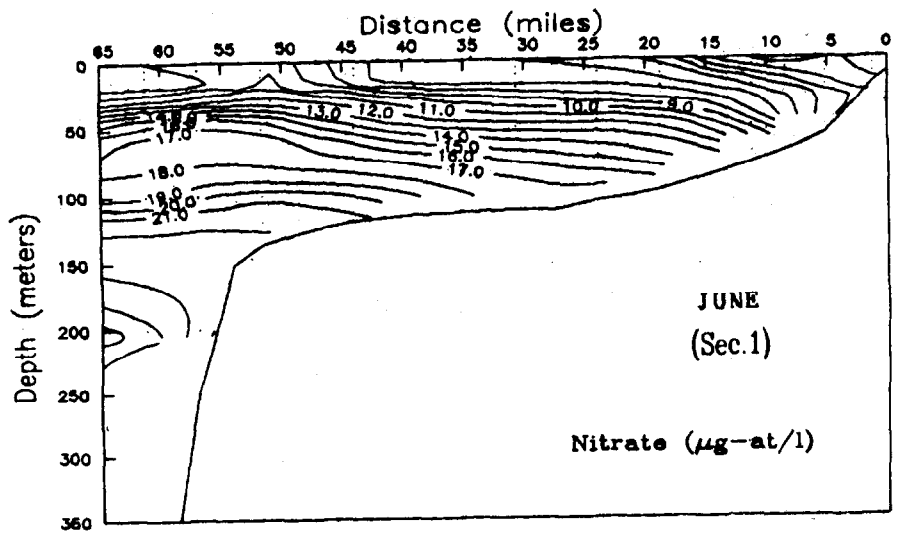


Fig.3. Distribution of nutrients toward the shelf edge along sections 2, (8).

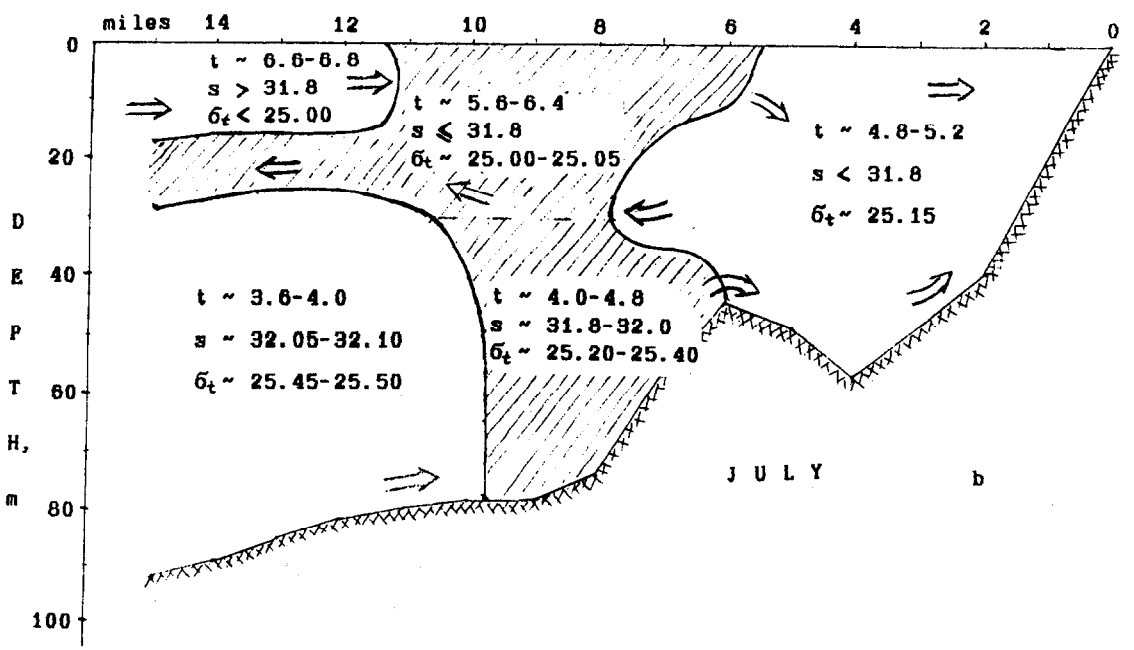
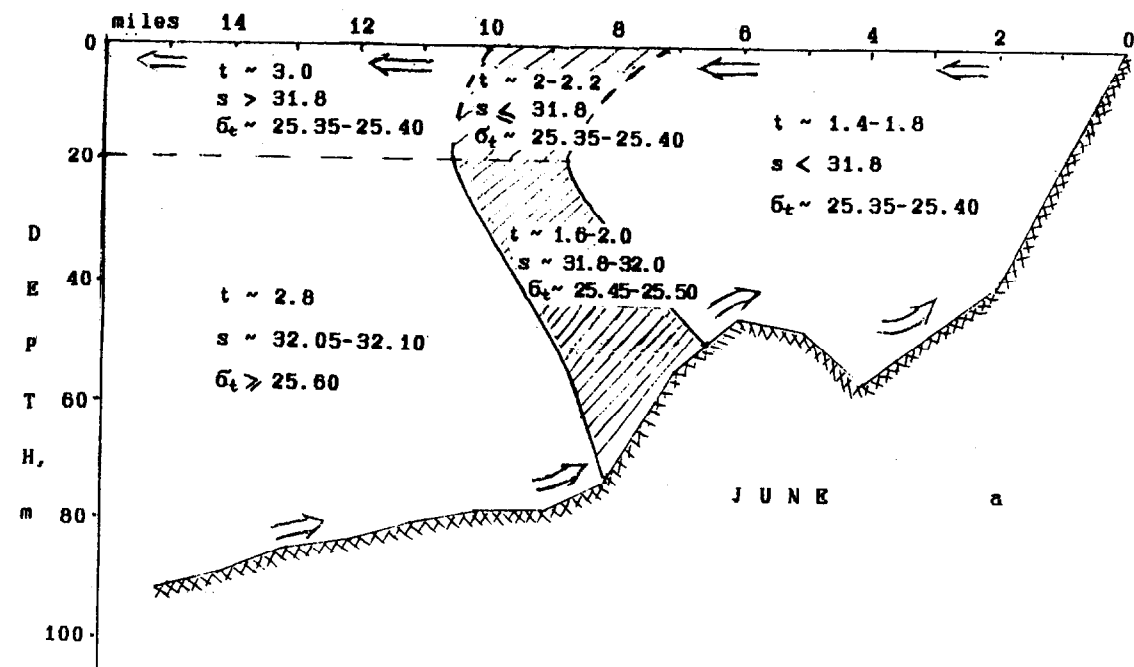


Fig.4. The coastal front structure schemes. (\Rightarrow) - flux direction of the properties exchange.

under the seasonal cycle action, observed in different geographic regions, is very much in common with the above mentioned results [2].

The fine thermohaline water structure is usually observed in the Pribilof Islands region [3]. During the July survey the intrusion of the low saline coastal water has been observed penetrating on its equal density level through the coastal front into the stably stratified shelf water. A good illustration of the intrusive water flow from the near island area may be seen in the nitrites and ammonia distributions at Section 7 (Fig.3).

The general view of the typical coastal front structures and exchange processes involved is presented on Fig.4

To conclude, the analysis of two oceanographic surveys in June and July 1994 of the coastal front area south-westwards from the St. Paul Island showed different thermohaline and dynamic structures mainly due to the change in thermal conditions. Seasonal warming during the whole period of observation defined local peculiarities of circulation and those of crossfrontal water exchange.

This paper is supported by Grant RFBS # 98-05-64773.

References

- [1]. Fedorov K.N., 1983, Physical Nature and Structure of Oceanic Fronts, Len.Gidromet., 296p. (in Rus.)
- [2]. Simpson J.H., Pingree R.D., 1978, Shallow Sea Front Produced by Tidal Stirring // in: Oceanic Fronts in the Coastal Processes. M.Bowman, W.Esaia (Eds.). Springer-Verlag. pp.29-42.
- [3]. Investigation of the Pribilof Marine Ecosystem. Third Year. Significance of Oceanographical and Biological Processes at the Shelf Break, Outer Domain, and Middle Front for Biological Productivity of the Pribilof Region, the Eastern Bering Sea. Oceanographical Conditions and Plancton Communities in the Coastal Zones and coastal Fronts of the St.Paul and St.Georges Islands (May 28-August12, 1994). / M.V.Flint (Ed.). Moscow.1996. P.P.Shirshov Inst. Oceanol. 665pp.

MESOSCALE FRONTAL STRUCTURE IN THE PRIBILOF REGION OF THE EASTERN BERING SEA SHELF

S.G.Poyarkov

P.P.Shirshov Institute of Oceanography, 36, Nakhimovsky Pr., Moscow117851, Russia
E-mail: zatsepin@glasnet.ru

Abstract. A relatively small Pribilof area, as compared to the vast shelf, hosts the principal elements of macroscale oceanographic structure of the eastern Bering Sea. These are the middle and the outer shelf domain with the bordering middle front, the shelf break front and the adjacent oceanic domain. The existence of specific features in the structure of shelf waters in the Pribilof area on the eastern Bering shelf are due to the local bottom topography -- the presence of the islands.

Introduction.

The Pribilof Islands lay on the southern periphery of the eastern Bering Sea shelf, close to its outer boundary -- the shelf break. Hydrophysical and hydrochemical survey conducted in 1993 highlighted mesoscale peculiarities of waters' structure in the vicinity of the Pribilof Islands on the background of the large-scale oceanographic structure typical to the eastern Bering sea [1]. The survey of 1994 proved the stable existence of various water types and fronts around the Islands, which were observed in 1993. This establishes more clear and detailed relationship between the local near-island and the shelf macroscale oceanographic structures over the Pribilof area [2]. So, the existence and the quasistationary condition of the oceanographic structure on the eastern Bering shelf is generally due to a set of climatic factors and peculiarities of the bottom topography.

Oceanographic description of the multifrontal zone in the Pribilof islands region.

1. Coastal and Shelf break fronts.

The local mesoscale oceanographic structure of shelf waters in the Pribilof area in general proved to be similar to the macroscale frontal structure of the eastern Bering shelf water, known from the previous studies [2,3]. A coastal front appears around each of the two major islands of the Archipelago, which borders almost homogenous, less saline and well aerated near-island water (Fig.1) from the surrounding shelf water, stratified across the entire water column. This frontal zone is a strict partition between two different water masses. The coastal front, an essential element of near-island waters' structure, is maintained by processes of dissipation of kinetic energy of tides and wind, which take place over the near island shelf. The coastal front appears in the area where layers of tidal and wind friction fall apart along the vertical axis owing to increasing depth. Similar conditions facilitate existence of the inner macroscale front near the continental shore, that separates low-saline homogenous waters of the inner domain from stratified waters of the middle domain [2]. Similarity of coastal fronts formation near the continent and near the islands is hinted by equal widths of the macroscale inner front and of the mesoscale near-island coastal front (Table 1). Therefore coastal frontal zones found around each of the Pribilof Islands are by their nature similar to the inner front located along the Alaska coast.

According to observations of 1993-94, the coastal front around the St. Paul Island was found 4-6 to 10-12 miles away from the shore over the depths of 40-50 to 60-80 metres depending upon the direction from the Island. The transversal extent of the front, according to the data obtained, was equal to average 5-6 miles. Nevertheless, special survey of the front's part to the south-west from the St. Paul Island conducted in June-July of 1994, showed the coastal front's transversal extent in the water column varies within a more wide range from 1-2 to 7 miles. The coastal front around the St. George Island, due to the Island's own steep shelf and the corresponding sharp increase in depth, was observed over somewhat higher depths of 80-110 metres but

Table 1 The eastern Bering Sea shelf (Kinder, Schumacher, 1981) and Pribilof area waters' structure(1993-1994)

The Eastern Bering Sea Shelf			The Pribilof Area				
Oceanographic domains and fronts	Distance from the mainland, miles	Width, miles	Waters' types and fronts	St. Paul Island		St. George Island	
				Distance from the island, miles	Width, miles	Distance from the island, miles	Width, miles
Coastal Domain	0 - 110	110	Near Island Waters	0 - 7	7	0 - 2	2
Inner Front	110 - 115	5	Coastal Front	7 - 12	5	2 - 6	4
Middle Domain	115 - 200	85	Interior Shelf Wat.	12 - 26	14	6 - 16	10
Middle Front	200 - 225	25	Shelf Partition Front	26 - 32	6	16 - 21	5
Outer Domain	225 - 290	65	Exterior Shelf Waters	32 - 46	14	21 - 26	5
Shelf Break Front	290 - 315	25	Shelf Break Front	46 - 53	7	26 - 29	3
Oceanic Domain	> 315		Oceanic Waters	> 53	-	> 29	-

Table 2
Water Types in the Pribilof Area

Water Types	Distance from the islands, n.miles					
	1993			1994		
	June	July		June		July
	St.P.	St.P.	St.G.	St.P.	St.G.	St.P.
Near island waters (Fig.1)	0-6	0-7	0-2	0-7	0-3	0-8
Coastal front	6-11	7-13	2-6	7-12	3-7	8-13
S H E L F W A T E R S Interior shelf waters (Fig.2)	11-26	13-26	6-19	12-24	7-14	13-26
Shelf partition front	26-31	26-30	19-22	24-33	14-19	26-32
Exterior shelf waters (Fig. 3)	31-48	30-46	22-	33-48	19-26	32-43
Shelf break front	48-54	-	-	48-53	26-29	43-53
Oceanic waters (Fig. 4)	>54	-	-	>53	>29	>53

much closer to the island's shore from 1.5-2.0 to 5-7 miles as far. The transversal extent was everywhere narrower than around the St. Paul Island by 1-2 miles (Table 2).

The outer domain waters of the eastern Bering Sea shelf are separated from the oceanic waters of the deep-water basin by the macroscale shelf break front. The conducted survey proved the shelf break front being an element of the local coastal frontal system of the Pribilof Islands. The processes within the front greatly affect structure of waters between the outer shelf border and the coastal fronts of the Islands. As the principal productive area of the whole Bering Sea ecosystem [4] the front strongly influences formation of biological productivity in the entire near-island region. The frontal zone exists due to interaction between the Bering Sea Slope current, which is a part of large-scale cyclonic circulation in the Bering Sea, with the slope of the eastern shelf. At the south-western direction from the St. Paul Island the shelf break front locates some 50 miles as far from the island's shore over the depths of 120-150 metres. The transversal extent typically equals to 5-6 miles, though in July 1994 reached 10 miles. To the south off the St. George Island the front can be found nearly 30 miles away from the Island where depths exceed 300 metres. Here it is about twice as wide compared to that near the St. Paul Island.

2. Subsurface shelf partition front.

Shelf waters between the shelf break front and the coastal fronts around the Islands are divided by the subsurface shelf partition front and fall apart into the interior and the exterior shelf waters with respect to the island. The waters differ by vertical stratification. Two-layer vertical structure of the interior shelf water presents a high-gradient layer that separates quasihomogeneous surface water from underlying stratified one (Fig.2). The type of vertical stratification makes these waters similar to the middle domain water lying beyond the Pribilof Islands region. Regional-specific features in distribution of observed properties in the interior shelf water arise due to apparent influence of the near island water.

Vertical structure of the exterior shelf water exhibits specific features: here the thermocline expands vertically and divides into thermohaline fine-structure layers in its lower portion (Fig.3). The exterior shelf water was found to be under the influence of the oceanic waters and presented no significant difference from the outer domain areas on the eastern shelf.

The interior shelf water near the St. Paul Island can be found 10-25 miles away from the shore; to the south of the St. George Island the distance reduces down to 6-19 miles. The exterior shelf waters south-westwards from the St. Paul Island located 30-40 miles as far, those to the south off the St. George Island were found 20-25 miles away from the shore.

The shelf partition front plays a very important role in the mesoscale oceanographic structure of the Pribilof region. The front generally does not appear at the surface though it is well pronounced in all observed fields of properties underneath the gradient layer. Only in few cases the sea surface in the frontal zone presented 'spots' in distribution of salinity and the consequent growth of the horizontal gradients. The shelf partition front was a 'border of influence' from the Island on shelf waters structure, as no structural inhomogeneities caused by presence of the island were traced beyond the front border. For example, 'tongues' stretching outwards to the sea, where influence of the near-island waters was apparent, were generally restricted by the shelf partition front. From the side of the shelf break, the shelf partition front in some cases was also a border of oceanic waters from spreading on the shelf along the bottom. Specific structure of fields of properties within the frontal zone reflected its connection with waters' dynamics. In particular, convergence in the shelf partition frontal zone to the south-west off the St. Paul Island was due to generally anticyclonic circulation of shelf waters in the Pribilof islands area [5]. Surveys of 1993-94 found enough reason to consider the macroscale middle front plays a part in formation of own mesoscale frontal systems around each of the major Islands.

One of the key results achieved in the survey was the detection of the shelf partition front to the north-eastward from the St. Paul Island towards the middle shelf. At this side of the Island the shelf partition front had divergence attributed to it, which was linked to a stationary flow along the Island's shore south-eastwards. Therefore, the shelf partition front here looks like more a dynamic formation rather than mere a border of different water types. Analysis of the original data and its comparison with the earlier results [5] enable a reasoned assumption that the shelf partition front is a mesoscale analogue of the macroscale middle front. The fact that the former is found at the both sides of the St. Paul's Island most likely prompts on its close connection with the circulation of waters in the Pribilof region. In other words, the mesoscale frontal system

Typical pattern for the Near Island waters (st. 23)

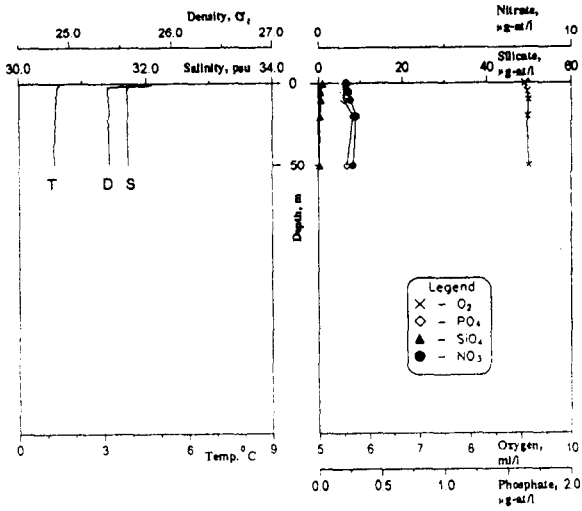


Fig. 1.

Typical pattern for the Interior Shelf waters (st.116)

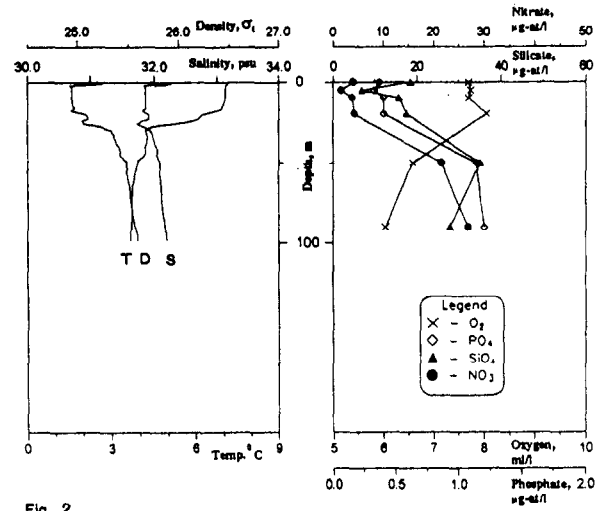


Fig. 2.

Typical pattern for the Exterior Shelf waters (st.112)

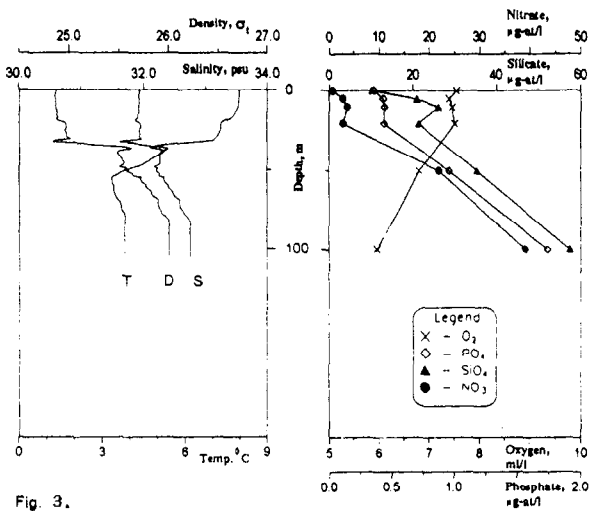


Fig. 3.

Typical pattern for the Oceanic waters (st.102)

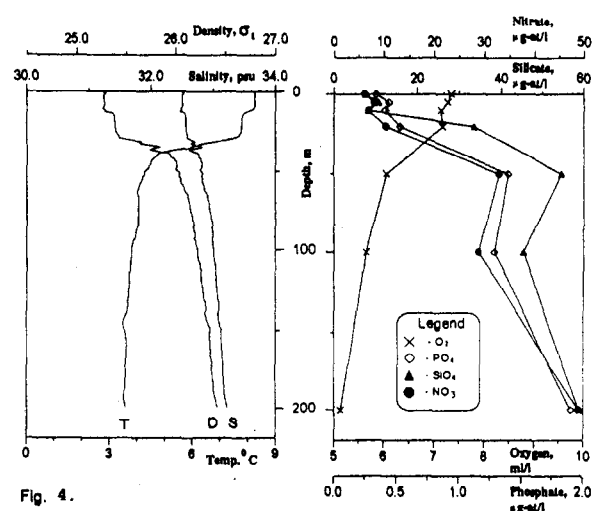


Fig. 4.

described above may be considered as a dynamic disturbance of the macroscale middle front, which exists on the background of the local bottom topography around the Islands.

The shelf partition front to the south-west off the St. Paul Island towards the shelf break is found 20 to 38 miles as far over the depths of 100-115 metres. According to the 1993 survey at the north-western side of the Island it was found 20-25 miles as far over the depth of some 60 metres. To the north-east from the St. Paul Island towards the middle shelf the shelf partition front was observed 19-35 miles as far where the depth reaches some 70 metres. The average transversal extent of the front near the St. Paul Island equalled to 4-5 miles, though in July 1994 reached even 9 miles. At the southern side of the St. George Island towards the shelf break the shelf partition front was indicated some 15-20 miles as far being 3-5 miles as wide. Because of steep slope of the Island's own shelf the front located over the depths of more than 200 metres. The data of the mesoscale survey are contrast with [2,3], where it was reported that the macroscale middle front attributed to the 100-metres isobath and 25 miles as wide.

Therefore, the interior and the exterior (with respect to the Islands) shelf waters as well as shelf partition front outlined as parts of the local spatial structure of the waters in the Pribilof area can be referred to as mesoscale disclosures of the middle domain, the outer domain and the middle front respectively, which are typical for macroscale oceanographic structure of the eastern Bering sea. It should be emphasised, that the outer domain in the Pribilof region is dramatically narrower (4-5 times at the least) than that in other regions of the eastern Bering Sea shelf (see Table1). That is why physical, chemical and biological processes in deep-water areas of the basin can immediately affect structure and productivity of the middle domain ecosystem in the Pribilof Islands area.

It should be noted that vertical distributions of properties in the outlined mesoscale elements of water structure in the Pribilof region (Fig.1-4) are virtually the same as in the macroscale domains on the eastern Bearing Sea shelf (Fig.5). Their similarity and comparison of the transversal extents are presented in Tab. 1.

Water mass exchange process in a multifrontal Pribilof islands area.

Water exchange processes are playing an important role in the Pribilof coastal ecosystem, both between mesoscale elements of the oceanographic spatial structure and within them. The exchange defines how clearly borders between pelagic communities will be pronounced, the level of interaction between them, inflow of nutrients on the shelf from the deep sea and their involvement into local production cycles. Processes of water exchange between mesoscale domains also define levels of isolation for specific near-island biotops and other important features of the ecosystem. The surveys of 1993-94 revealed the basic mechanisms of water transfer on the shelf within the 'deep sea -- shelf -- coastal zone' system [1,6], (Fig.5). Field data analysis showed processes in the shelf break front were the key link interaction between deep and shelf waters. The frontal zone is not merely a part of the spatial water structure, but an element of the three dimensional field of motion.

The shelf break front is attributed to the outer shelf border and is related to the processes in the Bering Sea Slope current, which is found below 50-70 metres as deep and has the nature of the eastern boundary current. At the deep sea side of the current waters descend, at the side of the slope -- ascend up to the lower border of the thermocline at the least. The vertical component of the water transfer in the frontal zone brings relatively rich in nutrients oceanic waters onto the shelf and 'feeds' the shelf domains (Fig.5). For example, to the south off the St. George Island within the shelf break frontal zone waters ascend from the depths over 300 metres and subsequently spread on the shelf within the near-bottom layers. Oceanic waters could be traced in nearly all outlined types of waters' structures during field periods of 1993 and 1994 [1,6]. Coming through all mesoscale spatial shelf structures the waters may even reach coastal frontal zones near the Islands.

It should be noted that in spite the coastal front seems "rigid or tight", oceanic water is frequently observed within the frontal zone, occasionally breaking the front near the bottom. The ocean water inflow to the near-shore area was, for instance, clearly detected in the late May 1993 at the south-western side of the St. Pauls Island [1].

The most favourable conditions for crossfrontal exchange through the coastal front, on the background of the observed seasonal differences in its structure, can be found in the surface 10-20 metres layer. In July 1994, when the thermocline was well developed, inflow of relatively warm and more saline water above the thermocline into the frontal zone was observed from the interior shelf zone. To the contrary, in June 1994 at the early stage of seasonal warming in absence of thermocline, light low salinity waters from the near-island zone entered within the surface layer through the coastal front into the surrounding shelf areas.

Spreading of the near-shore waters within a thin surface layer towards the open sea, observed at the south-western side of the St. Paul Island during field periods of 1993 and 1994, was generally constrained by the shelf partition front. In certain cases (observed in the early June 1993 [1]), the very same partition front was also the border for oceanic waters spreading on the shelf within the near-bottom layers. Appearance of oceanic waters within the surface 5-10-metres layer in the interior shelf area, observed in 1993-94, was likely due to vertical transfer in the shelf partition front, which was discussed above.

Special attention should be paid to a possibility of penetration of oceanic waters beyond the Pribilof Islands into the middle domain. In particular, to the north-west from the Island off High Bluffs and to the north-east towards middle shelf the oceanic waters were traced in the interior shelf area and in the shelf partition front, 10 to 30 miles as far from the Island. In these shelf areas transgression of oceanic waters along the bottom was best visible in distribution of nutrients. We made an assumption [1] that in the vicinity of the St. Paul Island a stationary current existed at the depth over 35-40 metres which brought oceanic waters along the bottom to the shelf area beyond the Island. This was proved later in May-November 1995, when a group of neutral buoys floating at the 40 meters depth have been traced from the satellite and the water flow velocity around Archipelago was estimated about 8-10 cm/s (Stabeno P.J., personal communication). This flow can bring oceanic waters, rich in nutrients, to the middle shelf area beyond the Island. It is well pronounced in the interior shelf water area and its border is most likely attributed to the shelf partition front. This data, along with the discussion on the nature of the shelf partition front, given above, enable a conclusion on a close relation between the macroscale middle front with water dynamics in the region and, in particular, with anticyclonic circulation of waters around the Pribilof Islands (Fig.6).

Despite significant differences in temperature conditions (close to the maximum known for the eastern Bering Sea [7]) during spring-summer periods of 1993 (relatively warm) and 1994 (with abnormally cold winter and spring) the mesoscale oceanographic structure of the Pribilof region did not change qualitatively. This largely concerns the presence of all components of frontal structure (the coastal, shelf partition and shelf break front) and their constant spatial position both in 1993 with and in 1994 [1,6].

Quantitatively, water properties, such as heat and salt capacity, vary significantly within a certain type of structure. For example, the specific conditions in winter and spring of 1994 resulted in formation of a lens of over-cooled water near the bottom (the absolute minimum within was -0.73°C) to the north-east off the St. Paul Island in the proximity of the shore. Significant variance in concentrations of nutrients in oceanographic domains of the Pribilof region, observed both on yearly and seasonal scales, were mainly due to variance in their inflow on the shelf from the open deep-water sea areas. 'Feeding' shelf areas with waters rich in nutrients is controlled by processes at the outer shelf border -- the shelf break front. Therefore, it is obvious that changes in the 'Bering Sea Slope current -- shelf break front' system promoted by climatic variations in the Bering Sea as a whole dramatically affect local variability of abiotic parameters of the Pribilof ecosystem [4].

The general view of the mesoscale frontal structures and water circulation around Archipelago on the background of the Eastern Bering Sea shelf macroscale fronts is presented on Fig.6.

This work is partly supported by Russian Ministry of Science and Technologies and Grant RFBS # 98-05-64773.

References.

- [1]. Investigation of the Pribilof Marine Ecosystem. Second Year. Study of the Marine Ecosystem in the Vicinity of the Pribilof Islands for General Ecological Evaluation and Elucidation of the Most Valuable Ecological Zones (April 30-August 8, 1993). / M.V.Flint (Ed.). Moscow: 1994. P.P.Shirshov Inst. Oceanol. 504pp.
- [2]. Kinder T.H., Shumacher J.D.,1981, Hydrographic structure over the continental shelf of the southeastern Bering Sea. in: The Eastern Bering Sea Shelf: oceanography and resources, Vol.1, (D.W. Hood and J.A. Galder, editors), OMPA/NOAA, University of Washington Press, Seattle, WA, pp.53-75.
- [3]. Coachman L.K.,1986, Circulation, water masses and fluxes on the South-eastern Bering Sea shelf. Continental Shelf Research, 5, pp.23-108.

[4]. Springer A.M., McRoy C.P., Flint M.V., 1996, The Bering Sea Green Belt: shelf-edge processes and ecosystem production. *Fisheries Oceanography*, Vol.5, N 3/4, pp.205-233.

[5]. Coyle K.O., Cooney R.T., 1993, Water Column Sound Scattering and Hydrography around the Pribilof Islands, Bering Sea // *J. Plankt. Res.* 1993. V13. pp.802-827.

[6]. Investigation of the Pribilof Marine Ecosystem. Third Year. Significance of Oceanographical and Biological Processes at the Shelf Break, Outer Domain, and Middle Front for Biological Productivity of the Pribilof Region, the Eastern Bering Sea. Oceanographical Conditions and Plancton Communities in the Coastal Zones and coastal Fronts of the St.Paul and St.Georges Islands (May 28-August12, 1994). / M.V.Flint (Ed.). Moscow.1996. P.P.Shirshov Inst. Oceanol. 665pp.

[7]. Azumaya T., Ohtani K., 1995, Effect of winter meteorological conditions on the formation of the cold bottom water in the Eastern Bering Sea Shelf, *J. of Oceanography*, Vol.51, pp.665-580.

EXPERIMENTAL STUDY OF THE STABILITY CONDITIONS FOR AN UNDERWATER CURRENT

D. Renouard, J.-M. Baey

LEGI/Coriolis, B.P. 53, 38041 GRENOBLE Cédex 9, France (coriolis@hmg.inpg.fr)

Abstract- To study the behaviour of an underwater current, a large number of experiments are conducted in the 13 m diameter LEGI « Coriolis » rotating tank. The intermediate current is introduced at the level of the interface of a two-layer system initially at rest in solid body rotation in the tank. The density and the volume flow rate of the current as well as the total volume of water in the tank are kept constant during each experiment. We checked that the flow is effectively in geostrophic balance and that, as predicted by the model, the geometric aspect ratios have little or no influence. The flow regime is highly deterministic and is fixed by the initial (injector) values of the Rossby (or Burger) and Ekman numbers. We observe five typical flow regimes: (1) a stable current for large Rossby and Ekman number and a significant evolution of the current when these numbers decrease with (2) a serie of cyclonic vortices attached at the outer edge of the current, with an upstream stable current, (3) an anticyclonic instability which remains attached to the current, (4) dipoles shed from the current and at last, for the smallest values of Rossby and Ekman numbers, (5) generation of anticyclonic lenses of intermediate water, alike "Meddies". The predicted instability wavelengths agree very well with the observed instability wavelengths, although in the lense formation case there are some discrepancies which can be linked to nonlinearity which is not taken into account in the model. The model also enables us to compute the energy transfers between the mean flow and the perturbations. The instability is thus proved to be always a mixed barotropic and baroclinic instability, predominantly baroclinic in the lense formation cases, which is fully consistent with the observations, and predominantly barotropic in the cases when the current is either stable upstream or fully stable. In the case of a stable current, the Ekman pumping is responsible for a significant inflow of intermediate water at the interface level, outside the current.

1- Introduction

Intermediate water currents are observed in various part of the world ocean since about thirty years, e.g. [1], [2], [3]. Such currents are known to play a major role in the exchanges between sea basins and they may lead to isolated eddies such as the Mediterranean Eddies (or Meddies) in the Atlantic Ocean [4] [5], or the Levantine Intermediate Water (or Leddies) South of Sardinia [6]. However very little is known about the detailed behaviour of such an underwater current flowing along a plane vertical wall and the present study is an attempt to provide an extensive parametric study of such a flow and to compare the experimental data with a Shallow-Water model that we developed.. Several previous experimental studies were devoted to surface gravity flows either in rotating channels [7] or in rotating tanks [8] [9] but, to our knowledge, there was no systematic study of the intermediate water current. In [10] we presented some preliminary results and showed that an underwater current has a very deterministic behaviour which can be predicted when knowing the initial (stratification and rotation parameters) and the boundary (volume flow rate of injected intermediate water) conditions. Here we present the results of a comprehensive parametric study which was performed in the 13 m diameter LEGI-Coriolis rotating tank and compare the data with a Shallow Water model [11]. Such a model allows interfaces to intersect, which is *a priori* the case when an intermediate water current flows along a wall at the interface of a two-layer system.

2- Physical system and parameters

Let us consider a constant volume flow rate underwater current propagating along a plane vertical wall, at the interface of a two layer system of fresh and salted water, initially at rest in solid body rotation. Let us assume, as a first order approximation, that there is no movement outside the underwater current, i.e. in the upper and lower layer. Then a straightforward dimensional analysis shows that such a flow is characterized by the following nondimensional parameters: H/L , $RG1 = H/H_1$, $RG2 = H/H_3$, geometrical aspect ratios, $Fr_{12} = U/(g'_{12}H)^{1/2}$ and $Fr_{23} = U/(g'_{23}H)^{1/2}$, Froude numbers for the upper and lower interfaces respectively, $Ro = U/f.L$, Rossby number, and $Re = UH/\nu$, Reynolds number, where H_1 , H_3 and H are respectively the upper and lower layer thickness of the undisturbed stratified system, i.e. far from the current, and intermediate water thickness at the wall; U is the characteristic velocity of the intermediate water current, and L is its characteristic width. The kinematic viscosity, ν , is assumed identical for all layers; f is the Coriolis parameter; and $g'_{12} = g(\rho_2 - \rho_1)/\rho_2$ and $g'_{23} = g(\rho_3 - \rho_2)/\rho_2$ are the reduced gravity accelerations characterizing the upper and lower interfaces of the intermediate water current. Now for some experimental conditions, it may be more useful to use $Ek = Re^{-1}.Ro.(H/L)^{-1}$, Ekman number, $Bu_{12} = g'_{12}H/f^2L^2$ and $Bu_{23} = g'_{23}H/f^2L^2$, Burger numbers for upper and lower interfaces. When we assume geostrophic equilibrium, we find that $H = f L U (1/g'_{12} + 1/g'_{23})$ and then $Ro = Fr_{12}^2 + Fr_{23}^2$. If we choose $g'_{12} = g'_{23}$, which will be the case for all experiments, we will have a further simplification. Let us note that, for practical reasons, it may be easier to characterize the intermediate water flow by its properties at the injector level, i.e. H_0 , L_0 and U or rather the injected volume flow rate $Q = U H_0 L_0/2$ (then all parameters computed using these values will be with a 0 subscript).

3- Experimental set-up and techniques

For the experiments we use the LEGI-Coriolis 14 m diameter rotating platform which is equipped with a 13 m diameter and 1.2 m deep tank. The rotating tank is filled with a two-layer system of salt and fresh water. The rotation period (T) and the upper and lower layer densities (ρ_1 and ρ_3) and thicknesses (H_1 and H_3) can be adjusted to cover a wide range of variations of the parameters of the problem. Before introducing the intermediate current, the two layers are at rest in solid body rotation. The intermediate water is introduced into the rotating tank directly at the interface level between the lower and upper layers. The density (ρ_2) and the volume flow rate (Q) of the underwater current can be adjusted; for a given experiment, they are constant with time during the whole duration of the experiment. For the sake of simplicity, the density of the intermediate water current is chosen so that $(\rho_2 - \rho_1) = (\rho_3 - \rho_2)$. The flow of intermediate water is uniform and constant with time.

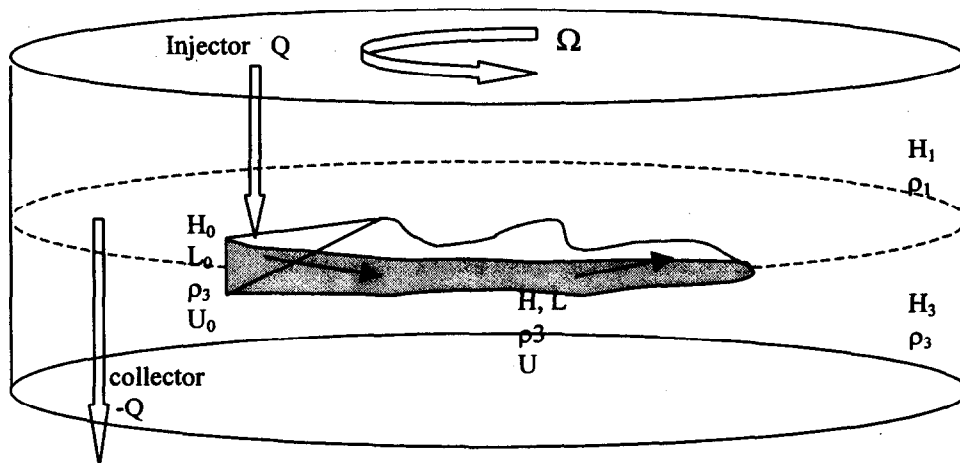


Fig. 1- Scheme of the experimental facility and notation used.

Its depth is adjustable so that the intermediate current is injected exactly at the interface level and the upper and lower slopes of the injector are equal to the mean upper and lower underwater current slopes, assumed to be in geostrophic balance, for all experiments. Immediately downstream of the injector we set a 2 m plastic sheet which can be adjusted for each experiment so that it corresponds to the lower underwater interface assumed to be in geostrophic balance. In order to have a constant volume of water in the tank and to avoid the intermediate water to come back in the injector region after propagating over the whole tank wall, we placed a collector a few distance upstream the injector (upstream and downstream for an observer looking in the current's direction and so having the wall at his right hand side). Hence the underwater current can move freely along 35 m between the injector and the collector. Fig. 1 is a sketch of the facility. The density profiles along several vertical lines in a plane perpendicular to the wall are measured with ultra-sonic probes (recording the variations of the propagation time of an acoustic signal between two small sensors placed horizontally 2 cm away and moved vertically at a constant speed). Thus we can draw the upper and lower layer interfaces of the current. Dye is injected along horizontal lines at several depths and we record the deformations of the dye streaks. Usually one streak is in the upper fluid, one in the lower fluid and one in the underwater current at the initial level of the interface of the upper and lower fluid (i.e. when they are in solid body rotation before the start of the experiments).

4- Parametric study of the stability of an underwater current

Preliminary experiments [10] showed that a very distinctive feature of the underwater current is that its stability is determined by the adimensional parameters' values at the injector level. The present set of experiments fully confirms it and, from all observations, it is possible to plot a flow regime diagram in one or the other of the parameter spaces.

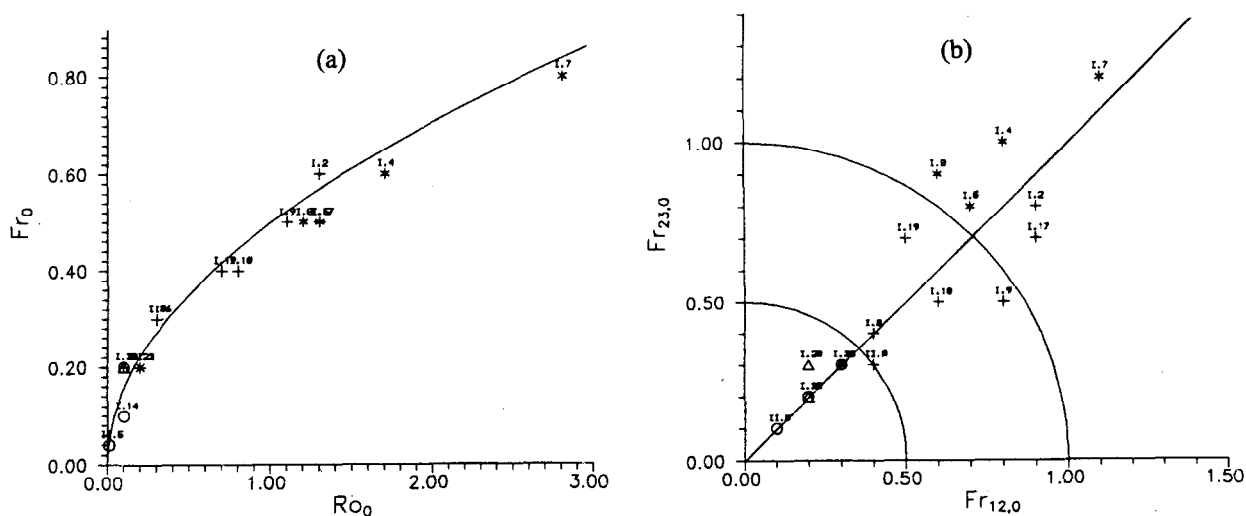


Fig. 2- (a) Flow regime diagram in the Ro_0 - Fr_0 space ; (b) Flow regime diagram in the $Fr_{12,0}$ - $Fr_{23,0}$ space ; * stable current ; + frontal cyclonic instability ; x anticyclonic instability ; Δ dipole ; O anticyclonic lenses ; \oplus quadrupole.

First in the $(Ro_0$ - $Fr_0)$ space (Fig. 2a), it is possible to check that all the parameter values computed from the observed characteristics of the current at the injector are very close to the $Fr_0 = 4 \cdot Ro_0^2$ curve corresponding to an underwater current in geostrophic balance when $(\rho_2 - \rho_1) = (\rho_3 - \rho_2)$. Therefore the injector effectively enables us to input a flow which is in geostrophic equilibrium and which has a constant volume flow rate. In the $(Ro_0$ - $Ek_0)$ or $(Bu_0$ - $Ek_0)$ spaces (not shown), it is possible to see that the higher values of both Ro_0 (or Bu_0) and Ek_0 correspond to a stable flow progressing smoothly all along the vertical sidewall of the tank. Then the current's velocity decreases from upstream to downstream and, at a given location, the dye experiments show a slow increase in current width with time. If we now keep the Ekman number constant and decrease the Rossby (or Burger) number, we first find, for $Ro < 1$, a regime when the upstream part of the current is stable whereas the downstream part of the current exhibits a sequence of cyclones which are regularly spaced along the tank wall. These cyclones are located at the outside edge of the current and they are slowly advected by the current. Also, above the underwater current, in the upper layer, there are cyclones regularly spaced along the wall. For

$Ro_0 \sim 0.3-0.4$ (or more precisely at $Bu_0 \approx 1$) meanders appear and an anticyclonic vortex may develop. The latter remains attached to the current and is associated to a larger diameter cyclone. They both are attached to the current while being slowly advected by it. Usually only one such pair is observed along the current. For $Ro_0 \sim 0.2$ the cyclone and the anticyclone pairs appear in several locations along the sidewall and these dipoles separate from the current. Their trajectory is first roughly normal to the wall before being advected by the residual current which is linked to the wind stress acting at the free surface. Once, for a small Ekman number, we even observed a quadrupole which was stable for a significant period of time. For $Ro_0 \sim 0.1$ anticyclonic vortices are regularly formed and shed from the current. This anticyclonic lenses formation is periodic both in space and time, for once a lense is fully detached from the wall another meander appears and develops into an anticyclonic vortex. The lifetime of the detached lense is at least thirty to forty inertial periods and their spin-up time is approximately eight inertial periods. The apparent diameter of the lenses is twice the characteristic Rossby radius of deformation associated with the current $R_0 = (g_{12} H_0 / 2)^{1/2} / f$. At the start of the lense generation process we always observe a small anticyclonic vortex located in the intermediate water current along the wall. It initiates a meandering process and as soon as the meander starts developing there is an associated cyclone, both in the upper and lower layer. The cyclone diameter increases as the meanders grows and reaches approximately the same diameter as the intermediate water lense when the latter detaches from the current. It seems that the lifetime of these cyclones is shorter than the anticyclone lifetime. Therefore it appears very clearly that no topographical effect (e.g. cape or canyon) is required for an underwater current to generate anticyclonic lenses since an instability of the current can lead to such anticyclone generation. At last, in the $(Fr_{12,0} - Fr_{23,0})$ space (Fig. 2b) three distinct regions appear : (i) for $Fr_{12,0}^2 + Fr_{23,0}^2 > 1$ the flow is stable all along the tank sidewall, (ii) for $0.25 < Fr_{12,0}^2 + Fr_{23,0}^2 < 1$ the flow exhibits cyclonic eddies at the edge of the current and (iii) for $Fr_{12,0}^2 + Fr_{23,0}^2 < 0.25$ we find all experiments for which there is an anticyclonic instability observed. It seems that, using the values measured at the injector, the flow behaviour is independent of the geometric ratios H_0/H_1 , H_0/H_3 and H_0/L_0 . Rather than using the flow characteristics at the injector, it is interesting to compute the same adimensional parameters using the flow characteristics immediately upstream an instability. It appears that, in the $(Fr-Ro)$ space, the experimental data are still close to the curve corresponding to the geostrophic balance, although with more scattering than at the injector. The plots in the $(Ro-Ek)$, $(Bu-Ek)$ and $(Fr_{12}-Fr_{23})$ spaces lead to the same conclusions as above, however, the critical values between regimes are not as clear except in the latter where all unstable flows occur for $Fr_{12}^2 + Fr_{23}^2 < 0.25$. It is only in the $(H-L)$ space that it appears that the largest H/L ratios correspond to the lense and dipole formation regimes, whereas the smallest values correspond to the cyclone regime.

5- Discussion and conclusion

Let us first focus upon the stable flows. The dye measurements enable us to measure the along-wall velocity component of the underwater current and the ultra-sonic density profilers give the upper and lower interface profiles of the current. From the latter and assuming that the flow is in geostrophic balance, it is possible to compute the « geostrophic » current corresponding to the observed interfaces and to compare it with the actual current. At stations $x = R_0, 5.R_0$ and $10.R_0$ from the injector, the agreement is quite satisfactory : the current width and the location of the current maximum velocity are almost identical for the computed and the measured velocities. However, for station $x = 20.R_0$, there is a clear discrepancy and the computed current seems shifted away from the wall. It is also worth noting that the upper and lower interfaces exhibit an inflection point at $x = R_0, 5.R_0$ and possibly $10.R_0$, which corresponds to the distance from the wall where the current is equal to zero (i.e. to the current width). At station $x = 20.R_0$ the interface between the upper and lower layer outside the current is almost as thick as the current itself, whereas closer to the injector the current is significantly thicker than the interface outside the current. Thus, as we move away from the injector, there is both a weakening of the current maximum velocity, a slight increase in current width and a significant increase in the interface thickness between the upper and lower layer outside the current. The volume flow rate in the current also decreases by about 40 % between station R_0 and $20.R_0$. At a given station, the underwater current is in geostrophic balance almost since the start of the experiment and its width is constant with time. However, even close to the injector, it is clear that the interface between the upper and lower interface outside the current tends to widen with time, thus suggesting that there is an intrusion of water from the intermediate current into the interior region, at the interface level. From the vertical density profiles in the current region, it appears that it is possible to relate the increase in thickness of the current upper interface with time with mixing associated with a Kelvin-Helmost instability. But the main mechanism for the intrusion of intermediate water at the interface level is most likely

linked with the Ekman transport in the upper and lower interfaces of the current. The vertical laser visualization of the current distinctly shows that there are weak but noticeable jets, normal to the wall, confined in the upper and lower interfaces of the current, impinging upon each other at the level of the interface between the upper and lower layer and resulting into a (quasi-)horizontal jet. A simple estimate of the Ekman transport in the two active interfaces of the current shows that such a transport is of the same order of magnitude as the loss of volume flow rate in the current and thus that the Ekman transport is likely responsible for this lateral transport of intermediate water and the subsequent thickening of the interface.

Let us now turn to the unstable flows. [11] developed a shallow water instability model and for varying Rossby number Ro , it is possible to compute the growth rate of a perturbation of given adimensional wavelength λ/L . It appears that the growth rate is maximum (> 3) for the smallest values of both Ro and λ/L and that the lense formation case corresponds to these highest growth rates. The growth rate decreases quickly as Ro increases, being less than 0.25 for $Ro > 0.4$ and less than 0.08 for $Ro > 1$. This corresponds very well with the experimental observations: stable currents for $Ro > 1$, apparition of meanders and other anticyclonic instabilities for $Ro \leq 0.4$, then dipole formation and isolated lense formation. For the most unstable cases (smallest Ro values), the wavelength of the instability is of the same order as the current width. For each unstable flow, using the exact geometric ratios and experimental conditions, we can compute the theoretical instability wavelength and we can also estimate, within ± 10 cm, the wavelength of the instabilities when they first appear along the current. Fig. 3 shows that the agreement between the predicted and the measured wavelength is very good for the attached anticyclonic instability and the dipole cases, and even for some of the isolated lense cases.

Fig. 3- Comparison of the predicted and measured instability wavelengths normalized by the current width; x anticyclonic instability; Δ dipole; \circ anticyclonic lenses; \oplus quadripole.

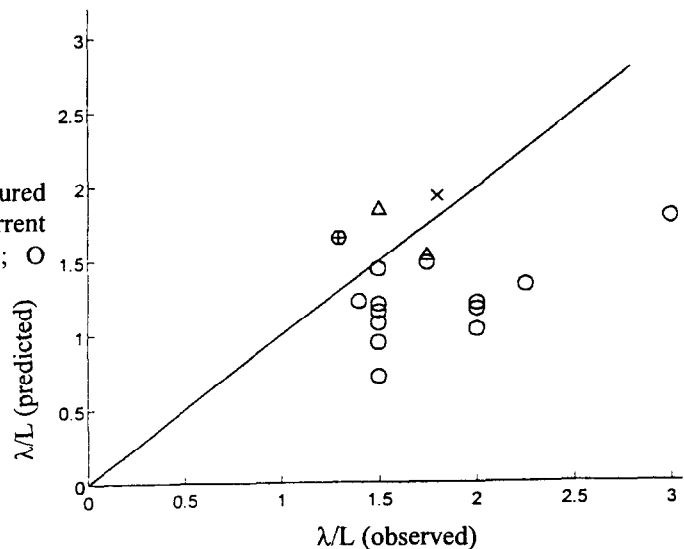
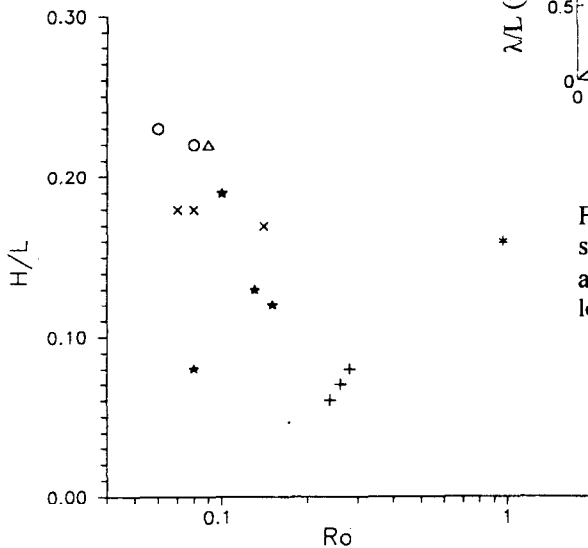


Fig. 4- Flow regime diagram in the Ro - H/L space; * stable current; + frontal cyclonic instability; x anticyclonic instability; Δ dipole; \circ anticyclonic lenses; ★ meander.

For most of the isolated (anticyclonic) lense cases, the observed wavelengths are smaller than the predicted wavelength but then the current is so unstable that the wavelength is difficult to measure and it is most likely that the process is strongly nonlinear, hence a deviation from our linear estimates is to be expected. For a given Rossby number, the model shows that the growth rate of the instabilities is practically independent from the

geometric aspect ratios, as is observed experimentally. From the dye measurements it is possible to compute the gradient of potential vorticity along a line perpendicular to the sidewall of the tank. Then it is possible to check that this gradient is always positive in the case of a stable current but that it changes sign in the case of an unstable current. Hence the necessary condition for instability is fulfilled [12]. [11] shows that the instability is always a mixed barotropic and baroclinic instability. The flow is predominantly baroclinically unstable in cases when we observed lense formation and that, as Ro increases, the flow is less and less baroclinically unstable. The predominantly baroclinic nature of the instability in the lense formation cases is consistent with the observations, for we mentioned above that, in the lense formation cases, (i) during the formation process, a cyclone appears in both the upper and the lower layers (but not in the intermediate current itself), immediately upstream the growing anticyclone, which is typical of a baroclinic instability, and (ii) that these experiments correspond to the highest H/L ratios (Fig. 4), that is when the maximum potential energy is available from the mean current. The horizontal shear along the vertical wall provides the source of barotropic instability.

Although it is quite difficult to have the exact values of the Ekman and Rossby (or Burger) numbers in an oceanic undercurrent, it is nonetheless possible to have estimates from the various available published data. For instance, South of Sardinia seems to be a possible place for dipole or meander formations for the flow of Levantine Intermediate water ($Bu \approx 0.8$ and $Ro > 0.1$) which may be related to the observed Leddies (Levantine Intermediate Water Eddies), whereas the flow of Mediterranean water in the Gulf of Cadix seems to be unstable (both for the upper and lower core of Mediterranean water, with a slightly more unstable upper core ; $Bu \approx 0.06$ and $0.05 \leq Ro \leq 0.08$). Along the Portuguese coasts the Mediterranean water current can also be unstable ($Bu \approx Ro \approx 0.05$). The rotation period of the experimental lenses is consistent with the observed rotation periods for the Meddies. Thus, from the conclusions of our experimental study and the estimated Ro and Bu values, it seems that the current can itself be unstable in the regions where such lenses are actually observed in the ocean. Such conclusions are consistent with observations of salt lense production in the Iberian Basin [13] [14] [15] which, from the locations of the Meddies they observed, concluded that they could be generated through a baroclinic instability mechanism either in the Gulf of Cadix or along the Portuguese coast North of Cape Saint Vincent.

References

- [1] G. Wust, 1961. On the vertical circulation of the Mediterranean Sea. *J. Geophys. Res.*, 66, 3261-3271.
- [2] M.R. Howe, 1984. Current and hydrographical measurements in the Mediterranean undercurrent near Cape St Vincent. *Oceanol. Acta*, 7, 41-50.
- [3] N. Daniault, J-P Mazé, M. Arhan, 1994. Circulation and mixing of Mediterranean Water west of the Iberian Peninsula. *Deep-Sea Res.*, 41, 11/12, 1685-1714.
- [4] J.C. Swallow, 1969. A deep eddy off Cape St. Vincent. *Deep Sea Res.*, 16, 285-295.
- [5] A. Bower, L. Armi and I. Ambar, 1997, Lagrangian observations of Meddy formation during a Mediterranean Undercurrent seeding experiments, *J. Phys. Oceanogr.*, 27, 2545-2575.
- [6] C. Millot, 1991, Mesoscale and seasonal variabilities in the Algerian Basin. *J. Geophys. Res.*, 92, C-8, 8265-8276.
- [7] A. Vinger and T.A. McClimans, 1980. Laboratory studies of baroclinic coastal currents along a straight, vertical coastline. River and Harbour Laboratory Report. STF60 A80081, Tromdheim (Norway).
- [8] R.W. Griffiths and P. Linden, 1982, Laboratory experiments on fronts ; Part I : density-driven boundary current. *Geophys. Astrophys. Fluid Dyn.*, 19, 159-187.
- [9] D. Obaton, 1994, Etude expérimentale de la stabilité d'un courant de gravité ; application au Courant Algérien. PhD Dissertation, UJF-Grenoble I.
- [10] J-M Baey, D. Renouard and G. Chabert d'Hières, 1997, Preliminary results about the stability of an intermediate water current. *Deep-Sea Res.*, 42, 2063-2073.
- [11] J-M Baey, D. Renouard and Y. Morel, 1998, Instabilities of an intermediate water current, *submitted to J. Mar. Res.*
- [12] J. Pedlovsky, 1983, Baroclinic instability in two-layer systems, *Tellus*, 15, 20-25
- [13] R. Kaese, A. Beckmann and H.-A. Hinrichsen, 1989, Observational evidence of salt lense formation in the Iberian Basin. *J. Geophys. Res.*, 94, C-4, 4905-4912.
- [14] R. Pingree and B. Le Cann, 1993, A shallow Meddy (a Smeddy) from the secondary Mediterranean salinity maximum. *J. Geophys. Res.*, 98, C-11, 20,169-20,185.
- [15] M. Prater and T. Sanford, 1994, A Meddy off Cape Saint Vincent. Part I : Description. *J. Phys. Oceanogr.*, 24, 1572-1585.

THE RESPONSE OF THE UPPER OCEAN TO SYNOPTIC VARIATIONS OF ATMOSPHERIC FORCING: IMMEDIATE AND INDIRECT MANIFESTATIONS

Yu. D. Resnyansky¹ and A. A. Zelenko¹

¹Hydrometeorological Research Centre of the Russian Federation, 9-13 Bolshoi Predtechensky per., Moscow 123242, Russia, E-mail: resn@mskw.mecom.ru

Abstract. *The twofold effects in the ocean response to synoptic variations of atmospheric forcing (AF) are considered basing on numerical experiments with a low resolution general circulation model. A direct response is seen as variations of the ocean variables in the frequency range of AF. Indirect effects resulting from the nonlinearity of the ocean dynamics/thermodynamics manifest themselves as longer term changes of sea water temperature and as an increase of the kinetic energy mean level. The indirect effects seem to be seasonally and geographically dependent. The longer term temperature changes originated due to the AF synoptic variations are most pronounced in mid latitudes and during the heating season.*

Introduction

There is abundant evidence (e.g. [8]) that large-scale features of the upper ocean fields are largely formed in response to atmospheric forcing (AF), the latter expressed as momentum, heat and fresh water fluxes at the water surface. One of the pronounced variation modes in the AF continuous frequency spectrum are the synoptic variations. They are produced due to changes of weather conditions in a sequence of propagating cyclonic/anticyclonic disturbances generated predominantly in middle latitudes, where the AF power spectrum level within the synoptic frequency range (characteristic time scale of several days) is one or two orders of magnitude greater than, for example, in near equatorial region (fig. 1a). Storm events are one of the essential contributor to these variations [2].

Due to nonlinear nature of the dynamic/thermodynamic processes governing the upper ocean evolution its response to AF involves not only the immediate ocean changes in the corresponding synoptic frequency range, but some indirect effects for longer term ocean changes as well.

These effects have been thoroughly studied from theoretical principles of stochastic climate models introduced by Hasselmann [4] and subsequently developed in a number of further works (e.g. [9] as a summary). The estimates of the indirect constituent of the twofold ocean response to AF short term variations based on a simple one-dimensional mixed layer model have been presented in [10]. In the present paper the direct and indirect manifestations of the ocean response to the AF synoptic variations will be considered basing on numerical experiments with an ocean general circulation model (OGCM).

Ocean Model and Design of Numerical Experiments

The OGCM used for this purpose is based on primitive equations written in spherical coordinates [12]. Finite differencing is similar to that of [1] and devised within the framework of the so-called box-method.

The small scale mixing in the upper ocean is parameterized using the concept of a well mixed layer (ML) [6] with updated formulation of the turbulent kinetic energy budget and employment of a special algorithm

for embedding ML into OGCM [11]. In addition to inclusion of ML processes the convective adjustment is performed at every time step and at any depth when static instability emerges.

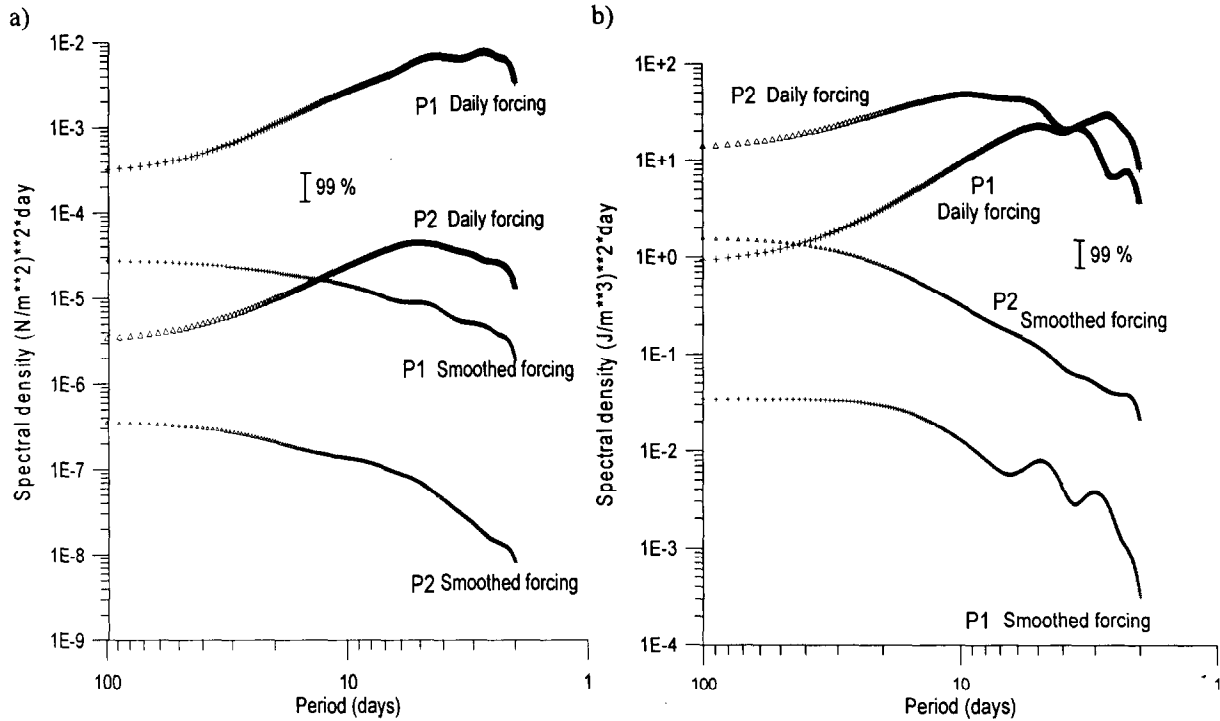


Fig. 1. Spectral densities of the wind stress module estimated from ECMWF daily time series over 1985-1990 (a) and of the depth mean kinetic energy estimated from OGCM simulations (b) in two ocean regions: in the North Atlantic (point P1, $\varphi = 52.6^\circ \text{ N}$, $\lambda = 22.5^\circ \text{ W}$) and in the equatorial zone (point P2, $\varphi = 2.8^\circ \text{ N}$, $\lambda = 29.4^\circ \text{ W}$). Spectral densities were computed by smoothing the periodograms with the Parzen window (spectral window parameter = 20). Time series prior to estimating the spectral densities have been detrended by applying the first differences filter. Curves labeled as “daily forcing” correspond to run A01, and curves labeled as “smoothed forcing” to the A30.

The boundary conditions at the water surface involve a rigid lid condition as well as specified momentum, heat and fresh water fluxes. They are essentially the atmospheric forcing which effects are to be considered.

The particular realization of the OGCM used in the numerical experiments was defined for the multiply connected world ocean domain, North Polar Basin being excluded. Coefficients of lateral turbulent viscosity A_M and diffusion A_H have been selected rather large, $A_M = 2 \cdot 10^6 \text{ m}^2 \text{ s}^{-1}$, $A_H = 10^4 \text{ m}^2 \text{ s}^{-1}$, compatible with a relatively low resolution of this particular model realization: 64×32 grid points over the globe with grid step of about 5.5° . Vertical structure was represented by 15 unevenly spaced levels. Bottom topography has been fitted to the model grid from $1^\circ \times 1^\circ$ data set. Time step is 2 hours.

For the equation of state the UNESCO form was approximated by the 3rd order polynomial, as suggested by Winton and Saraschik [13].

To specify the boundary conditions at the water surface, the global flux data, supplied by ECMWF on the TOGA CD-ROMs [3] were used. The flux data include 6 hourly global fields of wind stress, net heat flux and evaporation rate (derived from latent heat flux). The AF was formed from these data as daily averages for each day of the 1986-1990 time interval. The climatological data on precipitation [5] were also involved to compute fresh water fluxes.

The design of numerical experiments aimed to assess the ocean response to synoptic AF involved the preliminary 6 year spin-up integration (started from the state of no motion and climatological temperature/salinity distributions [7]). The ocean was driven at this stage by daily AF specified by 1986-1990 ECMWF data. The spin-up run was followed by two 2 years integrations, each of them started from the final stage of the spin-up run. In the first of the by pair runs (hereafter referred to as “run A01”) the ocean was driven by daily AF from ECMWF data for 1986-1987 and in the second run (referred to as “run A30”) by filtered AF for the same time interval. The filter applied was 30 days running average, which almost entirely eliminated synoptic variations. This can be clearly seen from comparing spectral densities of the wind stress module in Fig. 1a: curves labeled as “daily forcing” (run A01) and “smoothed forcing” (run A30). The inferences on the direct and indirect manifestations of the ocean response to synoptic variations of AF were made through the intercomparison of the ocean evolution driven by daily and filtered AF.

Results of Simulations

The dynamic response of the ocean may be considered in terms of the kinetic energy (KEN) generated in the model under different forcing.

Time series of globally averaged KEN for the whole set of simulations (spin-up, A01, A30) are shown in Fig. 2. Both of the twofold effects of synoptic forcing are clearly seen in this plot. Day to day fluctuations of KEN are generated in the A01 run as a consequence of the direct response. These fluctuations are most pronounced in the uppermost layer, where the variations of KEN are two orders of magnitude more intense than in the underlying layers. Spectral density functions of the KEN time series (Fig. 1b) are similar to that of the wind stress (Fig. 1a) though the differences in the spectral level between mid latitude and equatorial regions tend to decrease as compared to differences in AF.

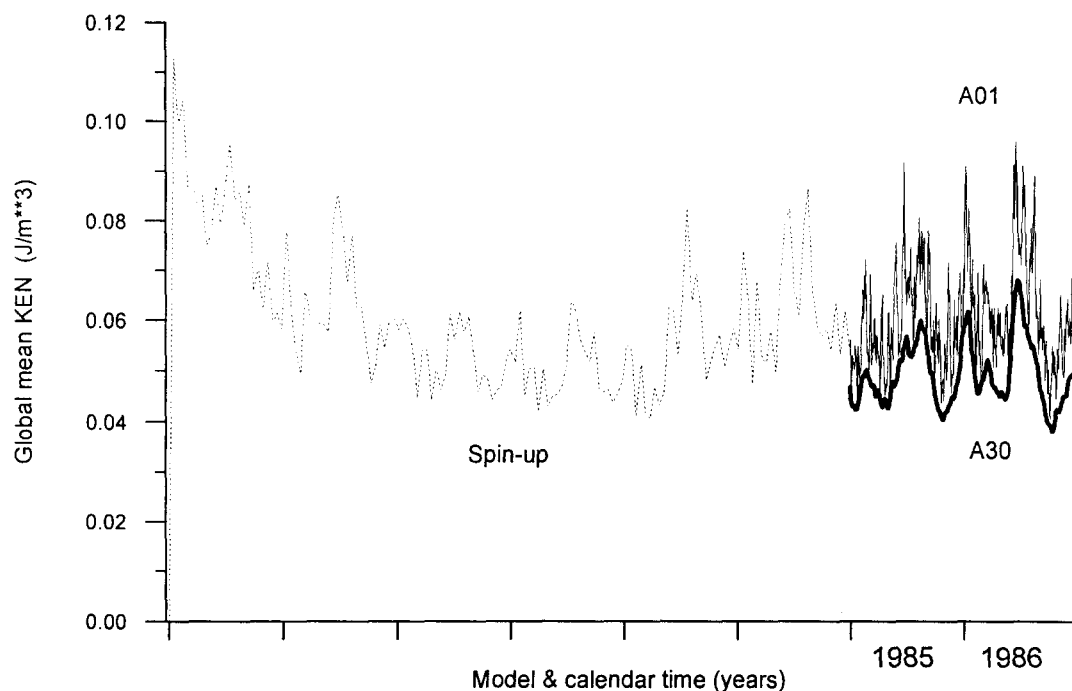


Fig. 2. Global volume mean kinetic energy for three runs. Time discrete intervals for ‘history’ file (and for respective curves in the figure) are: 15 days in run Spin-up and 1 day in runs A01 & A30.

The indirect consequences of the dynamic response manifest themselves as an increase of the mean kinetic energy level in run A01 being compared to the case of filtered forcing in run A30. In geographical context that increase is the most distinct in mid latitudes, characterized by a developed synoptic activity, and in the Indian Ocean acted upon by seasonal monsoons.

Similar features are observed in the thermal response characterized by day to day fluctuations of sea water temperature in run A01, though the spectral density of SST variations (Fig. 3b) is somewhat different from those of the AF (wind stress and net heat flux) and of the kinetic energy. The main difference, originated due to thermal inertia of the ocean water, appears in the redistribution of variance to low frequencies, which is typical for red noise random processes, in accordance with stochastic theories of SST variability [4].

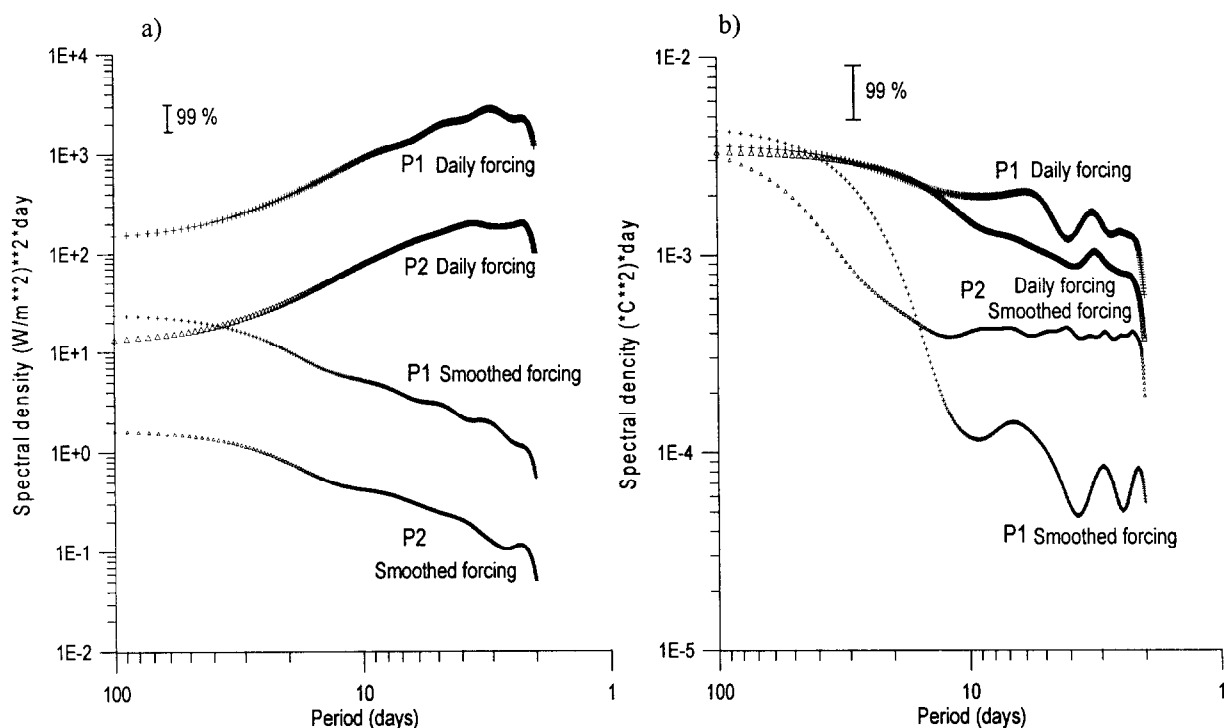


Fig.3. Spectral densities of the surface net heat flux estimated from ECMWF daily time series over 1985-1990 (a) and of the upper 20 m ocean layer temperature estimated from OGCM simulations (b) in two ocean regions: in the North Atlantic (point P1, $\phi = 52.6^\circ \text{ N}$, $\lambda = 22.5^\circ \text{ W}$) and in the equatorial zone (point P2, $\phi = 2.8^\circ \text{ N}$, $\lambda = 29.4^\circ \text{ W}$). Curves labeled as “daily forcing” correspond to run A01, and curves labeled as “smoothed forcing” to run A30.

The indirect consequence of the synoptic forcing manifest itself as a decrease of the upper layer temperature under daily forcing (run A01) as compared to filtered forcing (run A30). The greatest changes are observed in mid latitudes (Fig. 4), as was the case for the kinetic energy. This decrease is accompanied by the increase of temperature in underlying layers, that is the synoptic AF variations contribute substantially to vertical heat redistribution from the upper layers to deeper ones. One of the redistribution mechanisms is a deep convection appearing in abrupt changes of temperature at great depth (Fig. 5).

In the seasonal context the temperature decrease is enhanced during the heating season, while in winter the accumulated effects diminish.

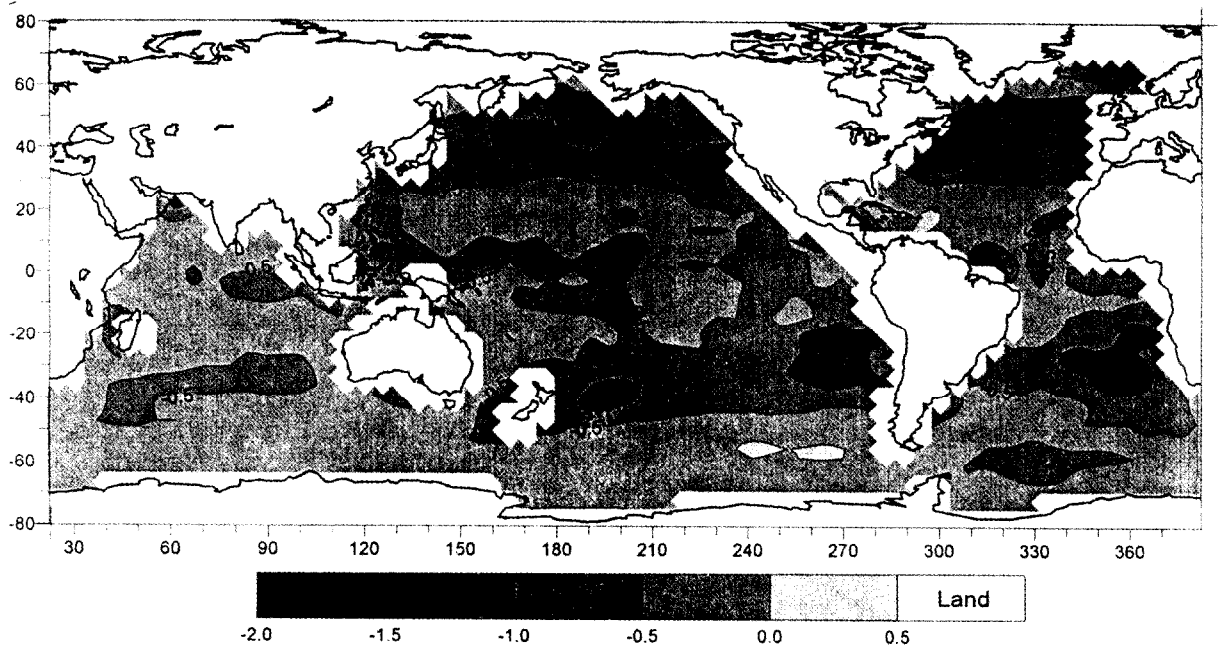


Fig. 4. Differences of the mean annual temperatures in the upper model layer (0—20 m) between two runs: A01 (daily forcing) minus A30 (smoothed forcing). Smoothing of atmospheric forcing leads to overestimation of the upper layer temperatures almost through out the World ocean.

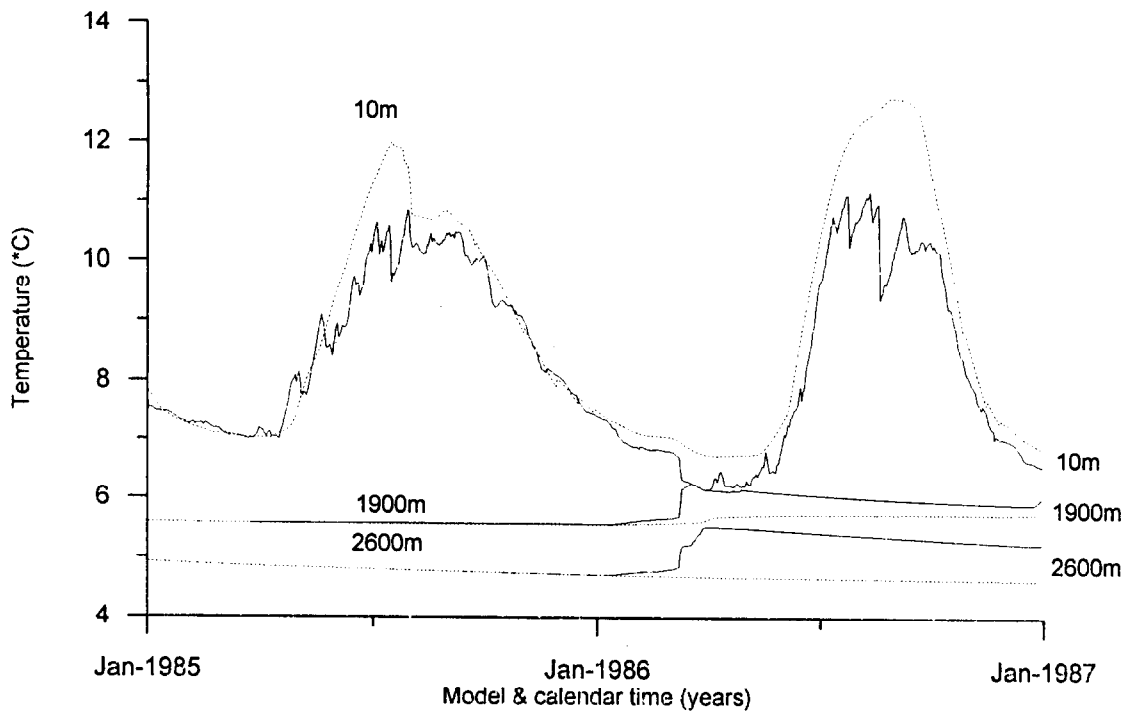


Fig.5. Time series of the water temperature at selected model levels for a grid point in the North Atlantic ($\phi=52.6^\circ$ N, $\lambda=22.5^\circ$ W) for two runs: A01 — daily forcing (solid curves) and A30 — smoothed forcing (dash). Smoothing of atmospheric forcing suppresses deep convection as is indicated by curves for levels 1900 and 2600 m (over the first year solid and dash curves are almost coincident).

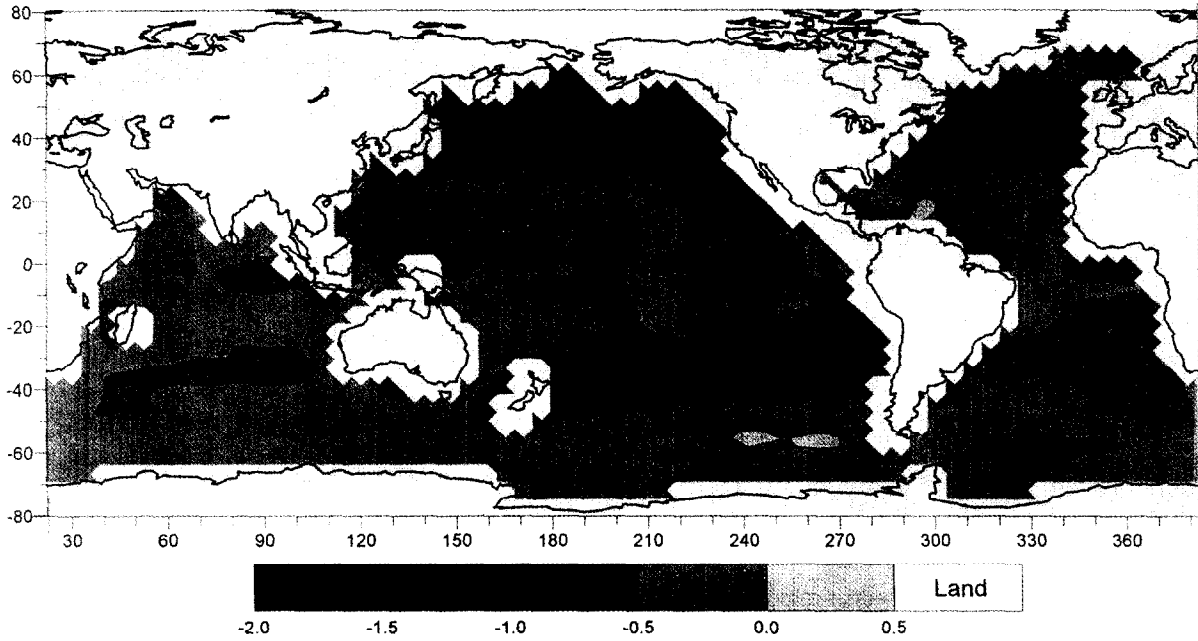


Fig. 4. Differences of the mean annual temperatures in the upper model layer (0—20 m) between two runs: A01 (daily forcing) minus A30 (smoothed forcing). Smoothing of atmospheric forcing leads to overestimation of the upper layer temperatures almost through out the World ocean.

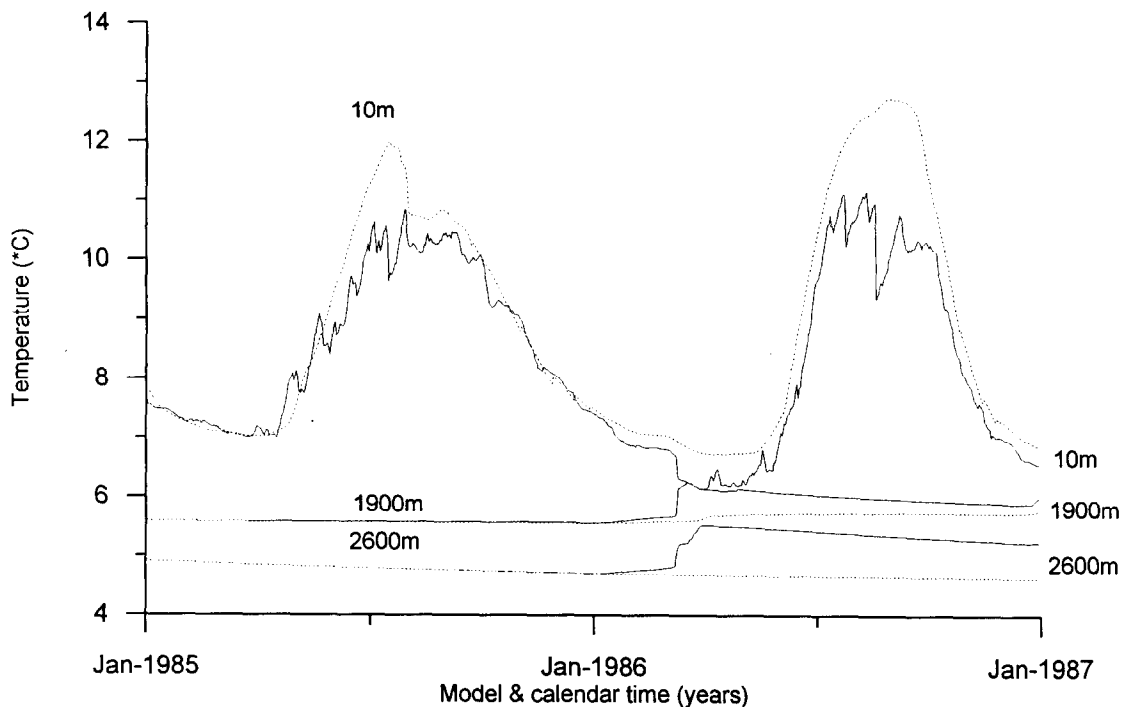


Fig.5. Time series of the water temperature at selected model levels for a grid point in the North Atlantic ($\phi=52.6^\circ$ N, $\lambda=22.5^\circ$ W) for two runs: A01 — daily forcing (solid curves) and A30 — smoothed forcing (dash). Smoothing of atmospheric forcing suppresses deep convection as is indicated by curves for levels 1900 and 2600 m (over the first year solid and dash curves are almost coincident).

Conclusions

1. Synoptic variations of atmospheric forcing at the ocean surface exert a twofold effect:
 - produce directly the variations of the ocean state dynamic and thermodynamic variables in the corresponding frequency range;
 - have accumulative influence on longer changes, as a consequence of nonlinearity of the governing processes.
2. The accumulative influence is the most distinct in the upper ocean layers, but its evidence may extend to rather great depths through the dependence of convective events on the short-term AF variations.
3. Evidences of the accumulative effects seem to be seasonally dependent. In the field of the upper ocean temperature these effects accumulate primarily during a heating season, while during a cooling season they tend to decay.
4. Hence, simulations of low-frequency variability with ocean general circulation models turn out to be closely dependent on the allowance for synoptic variations of atmospheric forcing.

Acknowledgements. This work was partly supported by RFBR grant No 97-05-64894. OGCM simulations were performed using the data supplied by ECMWF on the TOGA CD-ROM.

References

- [1] K. Bryan K., 1969, A numerical method for the study of the circulation of the world ocean, *J. Comput. Phys.*, **4**, 347-376.
- [2] R.L. Elsberry and N.T. Camp, 1978, Oceanic thermal response to strong atmospheric forcing. I. Characteristics of forcing events, *J. Phys. Oceanogr.*, **8**, 206-214.
- [3] C.J. Finch, 1994, TOGA CD-ROM Users' Guide. Physical Oceanography DAAC, JPL, Calif. Inst. Technology, 126 pp.
- [4] K. Hasselman, 1976, Stochastic climate models. Part I. Theory, *Tellus*, **28**, 473-485.
- [5] L. Jaeger, 1976, Monatskarten des Niederschlags für die Ganze Erde. Berichte des Deutschen Wetterdienstes. Nr. 139 (band 18), Offenbach.
- [6] E.B. Kraus and J.S. Turner, 1967, A one-dimensional model of the seasonal thermocline. II. The general theory and its consequences, *Tellus*, **19**, 98-105.
- [7] S. Levitus, R. Burgett and T.P. Boyer, 1994, World Ocean Atlas 1994: Vol. 3 (Salinity), Vol. 4 (Temperature). NOAA Atlas NESDIS 3 and 4, US Dept. Commerce, Washington, DC.
- [8] A.S. Monin, V.M. Kamenkovich and V.G. Kort, 1974, Variability of the World Ocean (in Russian), Leningrad, Gidrometeoizdat, 262 pp.
- [9] L.I. Piterbarg, 1989, The Dynamics and Prediction of the Large Scale Sea Surface Temperature Anomalies (Statistical Approach) (in Russian), Leningrad, Gidrometeoizdat, 200 pp.
- [10] Yu.D. Resnyansky, 1990, The heating of the upper ocean under cyclic atmospheric forcing, *Izvestiya Akademii Nauk SSSR, Fizika Atmosferi i Okeana (Izvestiya of Academy of Sciences, USSR. Atmospheric and Oceanic Physics)* (in Russian), **26**, 227-233.
- [11] Yu.D. Resnyansky and A.A. Zelenko, 1991, Parameterization of the upper mixed layer in the ocean general circulation model, *Izvestiya Akademii Nauk SSSR, Fizika Atmosferi i Okeana (Izvestiya of Academy of Sciences, USSR. Atmospheric and Oceanic Physics)* (in Russian), **27**, 1080-1088.
- [12] Yu.D. Resnyansky and A.A. Zelenko, 1992, Numerical realization of an ocean general circulation model with parameterization of the upper mixed layer. *Trans. Hydrometeorological Centre of the Russian Federation* (in Russian), Is. 323, 3-31.
- [13] M. Winton and E.S. Sarachik, 1993, Thermohaline oscillations by strong steady salinity forcing of ocean general circulation models, *J. Phys. Oceanogr.*, **23**, 1389-1410.

Thermohaline and Current Structures of the Polar Front along 134° E in the East (Japan) Sea

Young Jae Ro¹ and Jae Chul Lee²

1: Dept of Oceanography, Chungnam Natl. Univ., Taejon, Korea

2: Dept of Oceanography, Pukyong Natl. Univ., Pusan, Korea

(ryj@rsense.chungnam.ac.kr, jaechul@dolphin.pknu.ac.kr)

Abstract

The field observation program was developed by POFSE/KIOS group to characterize the oceanographic characteristics around the polar frontal region of the East Sea from 1995 to 1997. In this paper, detailed descriptions of the hydrographic and current structures along the line of 134° E are presented. Year-to-year variation was remarkable due to the development of the meso-scale eddies, which had significant influences on the hydrographic and current fields in the East Sea. Cross-sectional distributions of DO showed local processes such as sinking and mixing clearly and was very useful in identifying water masses. Current structures measured was in good agreement with geostrophic computations and revealed cyclonic and anti-cyclonic eddying motions.

Introduction

The East Sea, enclosed by the Korean Peninsula and Japanese Islands is drawing keen attentions as an important "natural laboratory for examining many physical processes including wind- and buoyancy-driven effects, sea ice processes, western boundary currents, fronts, mesoscale eddies, topographic effects, flow through narrow straits, deep convection, and many others that are ubiquitous in other marginal seas and the global ocean." [1]. Pronounced mesoscale eddies are readily observable year-round on satellite images (Plate I) near sharp polar front [2], [3]. These eddies are exhibiting natural beauty (I would call the flowers of sea) and provide with opportunities for research subjects of eddy dynamics associated with polar front. Many people [4]

start to call the East Sea as mini-ocean for its oceanlike behaviors in which gyre circulation is observed with the east Korea Warm Current (EKWC) as western boundary current and North Korea Cold Current (NKCC) forming cyclonic gyre north of the polar front where these two different water masses are colliding. One of the

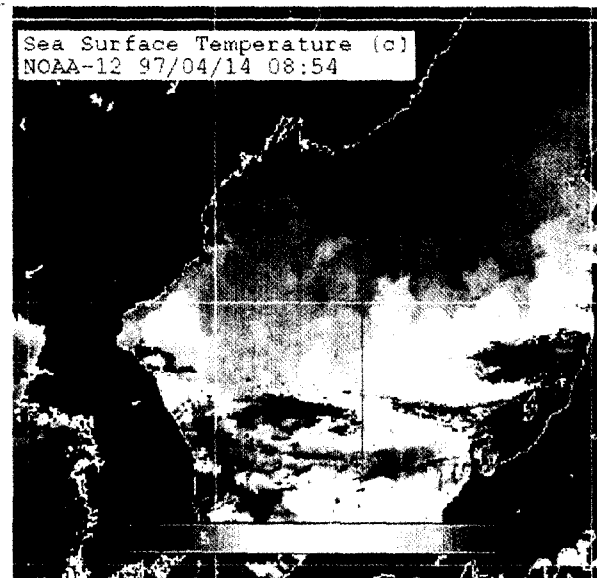
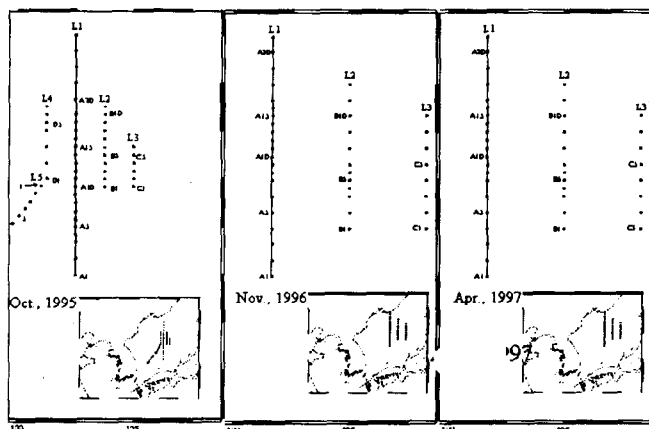


Plate I. Remotely sensed SST image in the East Sea where line along 134° E is marked.

Fig. 1 CTD stations for the Polar Front Study in Oct., 1995, Nov., 1996 and Apr., 1997.



most important features in the East Sea circulation is the polar front and accompanying eastward subpolar jet transporting the water volume out of the East Sea through the Tsugaru Strait.

The scientific attentions focusing on the East (Japan) Sea are increasing in these years generating a few international research activities and groups. Among those, POFSE/KIOS and CREAMS [1] are noteworthy. Field observations of the polar front and meso-scale eddies in the East (Japan) Sea so far were rather scarce despite of its long historical recognition. Through CREAMS activities, many new findings and measurements are being added [4], [5], [6]. On the other hand, the KIOS research groups for the Polar Front Study in the East Sea (POFSE) was formed in 1995 to carry out field observation program for three years. Interested readers can refer to reports [7] in which the characteristics of the polar frontal regions are described in details in four major disciplines.

In this paper, we describe only part of the physical oceanographic characteristics in terms of the cross-sectional distributions of thermohaline and current structures along 134° E.

Field Observations

The polar frontal region was investigated by three cruises in Oct., 1995, Nov., 1996 and Apr., 1997 by using CTD (Sea Bird 911) profilings and ADCP (RDI) trackings. Total of 13 lines with 164 CTD stations (5 lines with 59 st. in 95; 3 lines with 41 st. in 96; 5 lines with 64 st. in 97) were covered and profiled. Detailed description can be referred to [7]. The CTD stations are seen in Fig. 1 and the reference line along 134° E was a major line from 37° N to 41.5° N.

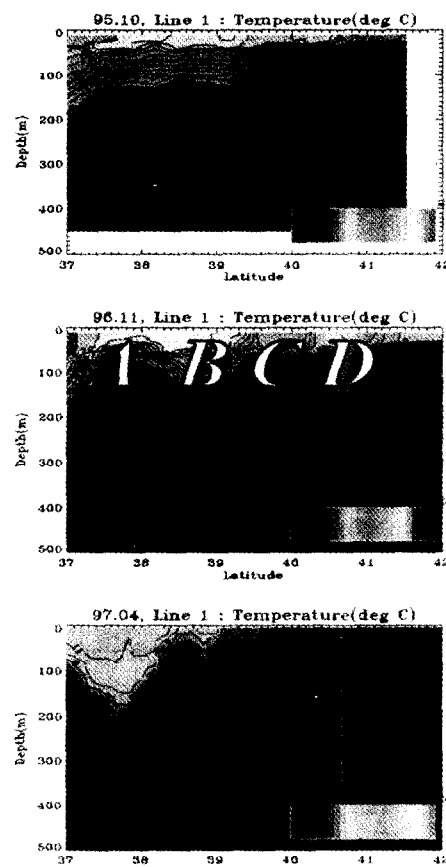


Fig. 2. Cross-sectional distributions of the temperature along 134° E in Oct., 1995, Nov., 1996 and Apr., 1997.

Cross-sectional Structures of Thermohaline, DO and Current Fields

1) Temperature Field

Cross-sectional distributions of temperatures along 134° E in 1995, 1996, and 1997 are seen in Fig. 2. In general, the thermocline depths are getting shallower gradually from south to north, while two areas around 37° and 39° N showed abrupt changes of the thermocline depths. The strong gradients of the thermocline depths are associated with the warm meso-scale eddies areas, where the polar front is located. Below surface mixed layer (50 m), there exist very strong stratifications which distinguish the intermediate Korean Proper Water underneath the overlying Tsushima warm and saline water mass. From Oct., 1995 to Nov., 1996, we could observe the dramatic changes of the hydrographic profiles due to the presence of meso-scale warm eddies at least in four areas designated as A, B, C, D in Fig. 2. These eddies are in cylindrical and/or conic shape depending on their mature stages. The eddy A is believed to be in growing stage, while the eddies B and C are merging, yet weakening based on their sizes and intensities and the eddy D is slowly decaying. In such a short period of five months from Nov., 1996 to Apr., 1997, the eddy A exhibits very energetic evolving structures. The axis of the eddy A moved toward north with its size increasing to more than 150 km in radius. In addition, it penetrated much deeper (down to 350 m) through wintering process (severe vertical mixing). This incident dictates well the influence of the meso-scale eddies on the hydrography and the importance of their roles in distributing energetics in the East Sea.

2) Salinity Field

The distribution patterns of salinities (not presented) are very similar to that of temperatures, since high salinity corresponds to high temperature in Tsushima water mass. Yet, they are comparatively simpler than the temperature distributions, except the upper surface layers where fresher water (< 33.5 psu) derived from land mass. The core of the salinity minima was observed in the eddy D between 40° and 41° N which corresponds to the DO rich water in Fig. 3.

3) DO Field

Cross-sectional distributions of DO along 134° E in 1995, 1996, and 1997 are seen in Fig. 3. The DO distributions are quite different from the thermohaline ones. In fact, they betrayed many more complicated structures and very strong year-to-year variation. Most striking features are localized subsurface maxima seen in three years. In 1995, the thin layer of the subsurface maxima (> 7.5 ml/l) was observed between 40.5° and 41.5° N at the depth of 50 m indicating the intrusion of cold and less-saline water

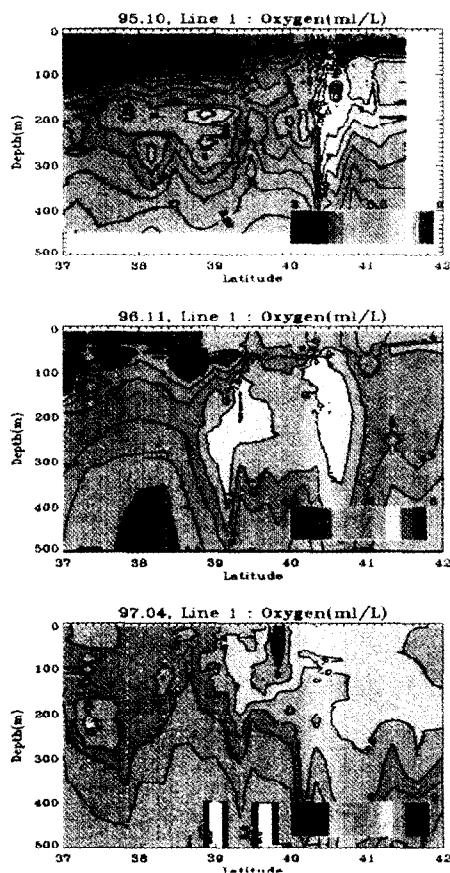


Fig. 3. Cross-sectional distributions of the DO along 134° E in Oct., 1995, Nov., 1996 and Apr., 1997.

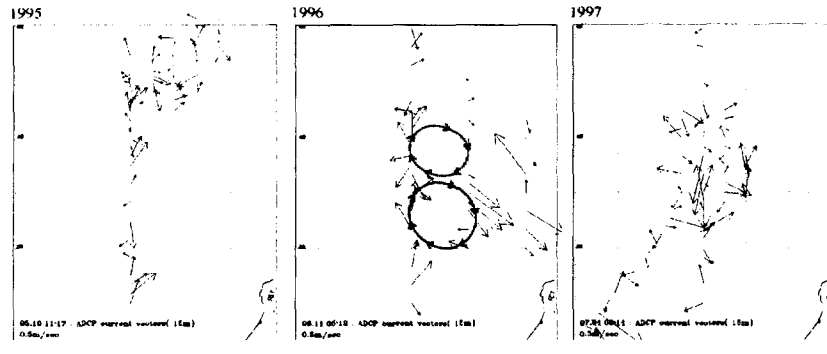


Fig. 4. Horizontal distributions of the surface current field in Oct., 1995, Nov., 1996 and Apr., 1997.

under the surface mixed layer from north. The DO rich layer further penetrated down to 400 m forming a narrow core with the wall-like sharp boundary around 40.3° N. This is considered as another indication of sinking water. In the area south of 39° N, subsurface minima of DO (< 4.5 ml/l) were observed around the depth of 100 m in 1995 and 1996. The DO minima were originated from the Tsushima water mass. In 1996, the DO rich waters were extending further southward occupying the water column from 100 to 400 m depths and over the vast area between 39° and 41° N where meso-scale eddies B and C were identified in Fig. 2. In Apr., 1997, it also shows the very high DO (> 8 ml/l) in localized area around 40° N down to the depth of 150 m. It is suspected that in addition to the wintertime mixing, sinking and/or downwelling processes are responsible for this localized subsurface DO maxima. These facts assures that DO is a much more useful tracer for the study of water mass and the circulation in the East Sea.

4) Structures of Currents Fields

Fig. 4 show the horizontal distributions of the ADCP current vectors observed in Oct., 1995, Nov., 1996 and Apr., 1997. They are very complicated at first glance due to the presence of anticyclonic meso-scale eddies in 1996 and 1997. In Fig. 4,

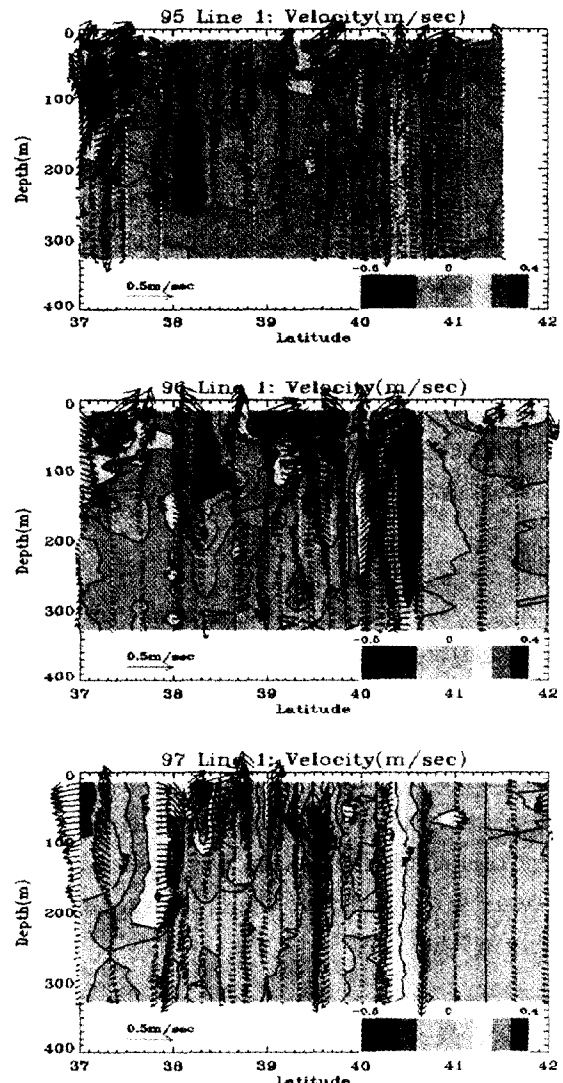


Fig. 5. Cross-sectional distributions of the ADCP-measured current overlapped on geostrophic current along 134° E in Oct., 1995, Nov., 1996 and Apr., 1997.

schematic ellipses are drawn to indicate the presence of eddies corresponding to the eddies B and C in Fig. 2. Fig. 5 show the vertical profiles of the ADCP currents compared to the geostrophic currents which are in excellent agreement. The speeds of the currents are less than one knot in general, while local maximal currents flew over the area where the axis of eddies existed. The vertical profiles of the ADCP-measured currents exhibited strong vertical gradients with some locations flowing in the lower layer opposite to surface current. This confirms that the current field is very baroclinic, yet geostrophic. The observed currents were compared to recent results of numerical experiments very favorably [8] where cyclonic and anti-cyclonic eddies were successfully reproduced in Fig. 6.

Concluding Remarks

The thermohaline and current structures along the cross-section of 134° E in the East (Japan) Sea are described. Following points are drawn: 1) Year-to-year variation of hydrographic conditions are remarkable due to the presence of the meso-scale eddies in the East (Japan) Sea. 2) Two areas around 37° and 39° N showing abrupt changes of the thermocline depths is associated with the warm meso-scale eddies. 3) In a short period of five months from 1996 to 1997, the eddies showed very energetic evolving structures depending on their mature stages. 4) The distribution patterns of salinities are very similar to that of temperatures, since high salinity corresponds to high temperature in Tsushima water mass, yet, they are comparatively simpler than the temperature distributions. 5) The DO distributions are quite different from the thermohaline ones with many more complicated structures and stronger year-to-year variation. Striking features such as localized subsurface maxima and minima were observed. 6) In 1995, the thin layer of the subsurface maxima (>7.5 ml/l) was observed between 40.5° and 41.5° N at the depth of 50 m indicating the intrusion of cold and less-saline water under the surface mixed layer from north. In 1996, the DO rich waters were extending further southward occupying the deeper depths and over the wider area. 7) The vertical profiles of the ADCP currents are compared to the geostrophic currents in excellent agreement. The vertical profiles of the ADCP-measured currents exhibited strong vertical gradients indicating the current field very baroclinic, yet geostrophic.

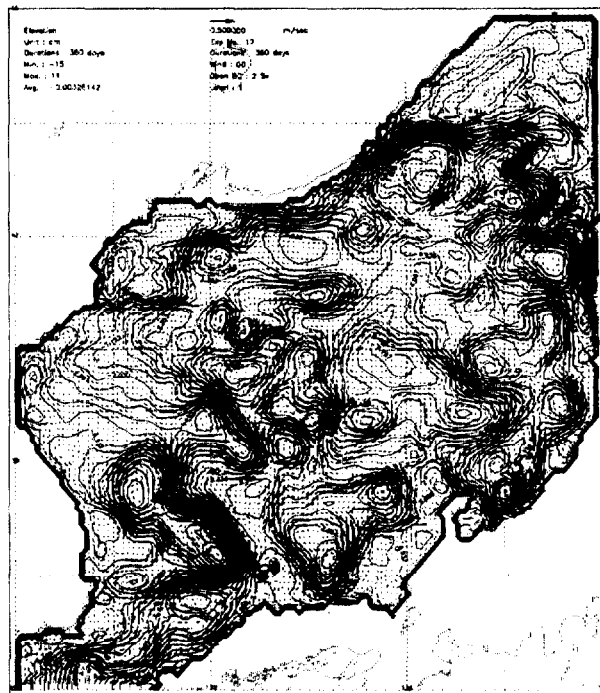


Fig. 6. An example of numerical experiments showing the meso-scale eddies reproduced in the East (Japan) Sea.

Acknowledgements

This research was sponsored by the Korean Ministry of Education via KIOS through 1995-1997.

References

- [1] Riser, S. R. and S.C. Ramp, 1996. THE OCEANOGRAPHY OF THE JAPAN/EAST SEA. Report of a Workshop Held in Honolulu, Hawaii 25-27 June, 1996.
http://www.onr.navy.mil/sci_tech/ocean/info/ramp1/workshop.htm
- [2] Isoda, Y., S. Saitoh, and M. Mihora (1991). SST structure of the polar front in the Japan Sea. In: Oceanography of Asian Marginal Seas (Ed., K. Takano) Elsevier Oceanography Series, 54: 103-112.
- [3] Ro, Y.J., A. Alexanin, and A. Kazansky, 1997. Synoptic Approach to Estimation of Sea Surface Current Fields from Sequential Satellite Images: Improved Technique and Validation Study, J. Korean Soc. of Remote Sensing, 13(3):203-222.
- [4] Kim, K.-R. and K. Kim, 1996. What is happening in the East Sea (Japan Sea)? : Recent Chemical observations during CREAMS 93-96. J. Kor. Soc. of Oceanogr., 31(4): 164-172.
- [5] Kim, K., K.R. Kim, Y.-G. Kim, Y.-K. Cho, J. Y. Chung, B. H. Choi, S.-K. Byun, G.-H. Hong, M. Takematsu, H.H. Yoon, Y. Volkov and M Danchenkov, 1996. New findings from CREAMS observation: water masses and eddies in the East Sea. J. Kor. Soc. of Oceanogr., 31(4): 155-163.
- [6] Kim, Y.-G., 1996. A study on the water characteristics and circulation of the intermediate and deep layer of the East Sea, Ph.D. Thesis, Seoul National University, pp 111.
- [7] Kim, D.C., Y.J. Ro, K.H.Kim, J.K. Choi, C.H. Moon, 1997. Oceanographic Characteristics of the Polar Frontal Regions in the East Sea, report submitted to the Ministry of Education, and prepared by the Korea Inter-university Institute of Ocean Science, Pukyong National University 526 pp, in Korean with English abstract.
- [8] Ro, Y.J. and K. Wang, 1998. Numerical experiments of the meso-scale eddy activities in the East (Japan) Sea, to be submitted to J. of Korean Oceanogr. Soc.

NEAR-BOTTOM AND INTERMEDIATE STRATIFIED CURRENTS.

Samolyubov B.I., Kremenetskiy V.V., Moya A.A.

M.V.Lomonosov Moscow State University, Chair Physics of Sea and Inland Waters.

Moscow 119899, Russia, e-mail: sambis@flow.phys.msu.su

Abstracts. On the basis of natural measurement data the processes of stratified current evolution are explored. The near-bottom gravity and circulating currents as well as intermediate flows at the pycnocline are under investigation. Special attention is paid to the study of these currents and internal wave influence on the water quality parameter distributions. Mechanisms of formation and development of circulating current and intermediate flow are proposed taking into account the influence of wind, bottom relief and internal waves on the water dynamics and on the diffusion of admixtures.

Introduction.

Density currents under investigation were formed and evolved under the strong influence of internal waves, meteorological and topographical factors. Presented results of complex natural investigations of stratified current dynamics and structure are obtained at the plane Mozhaisk reservoir. This reservoir was created at the upper part of the Moscow river. The length of this basin is 28 km, width and depth are up to 2.6 km and 23 m consequently, mean bottom slope is $5 \cdot 10^{-4}$. Vertical profiles of current velocity U , water temperature T , electroconductivity k_e , concentration of suspended material C_s and dissolved oxygen O_2 were registered simultaneously by means of specially constructed equipment. Our measurements were carried out at the longitudinal crossings and at the term stations. There were observed density gravity flow, circulating near-bottom stratified current and jet flow at the thermocline [1, 2].

Goals of our researches: 1. The revelation of stratified flows formation and evolution mechanisms taking into account an influence of internal waves, meteorological conditions and topography upon the currents development. 2. The elaboration of such currents mathematical models for the prediction of these flows action on the water quality.

Near-bottom density currents.

The observed gravity and circulating near-bottom currents are characterised by velocities up to 15 cm/s, that are high for the plane reservoir with low water-exchange (mean water-exchange coefficient is 1,8 year⁻¹). Typical parameters of the near-bottom density currents are following:

flow height z_u	4–6 m
current velocity \bar{U} (averaged over the height z_u)	7 cm/s ($\pm 13\%$)
water density difference in the flow and above it $\bar{\Delta\rho}$ (averaged over the height z_u)	$(4-7) \cdot 10^{-4} \text{ g/cm}^3$
integral Richardson number $Ri_U = g\bar{\Delta\rho}z_u / \rho\bar{U}^2$	4–8
roughness height $\langle z_0 \rangle$ (averaged over the time of measurements)	3 cm
friction velocity U_*	0.2–1 cm/s

Vertical profiles of current velocity U , water density difference $\Delta\rho$, electroconductivity k_c , concentrations of the dissolved oxygen O_2 and of the suspended material C_s , shown at fig.1, were obtained during the circulating flow investigation. The value of $\Delta\rho$ in this current is quantified mainly by the thermal stratification.

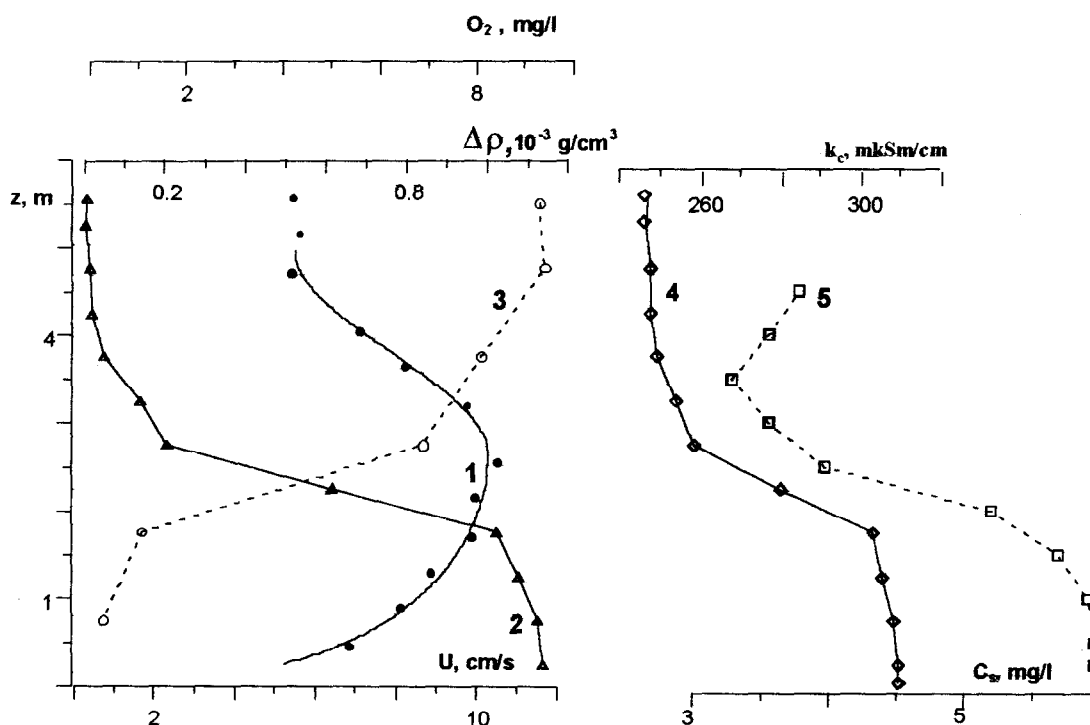


Fig.1. Vertical profiles of U (1), $\Delta\rho$ (2), O_2 (3), k_c (4) and C_s (5).

The distributions of U , $\Delta\rho$ in this flow and in the gravity current were similar. However in contrast to the gravity current the circulating flow propagated upslope. It was found out that a circulation inside a pool causes

this current appearance and provides an exchange between deep and shallow parts of the pool. The analysis of obtained results showed that not only drift circulation but also stable density stratification belongs to the main factors inducing the revealed current. The essential motive force for such flow is longitudinal pressure gradient that is connected with wind velocity and with longitudinal gradients of $\overline{\Delta\rho}$ and z_u . One of the principle differences of this current from gravity flow consists in the form of dependence of \overline{U}^2 from the excess liquid mass per unit of the flow width $\overline{\Delta\rho z_u}$. In the upslope moving current $\overline{U}^2 \cong 0.23g[(\overline{\Delta\rho z_u})_M - 0.8\overline{\Delta\rho z_u}]$, where $(\overline{\Delta\rho z_u})_M$ is the maximum of the $\overline{\Delta\rho z_u}$ value, obtained during the measurements at the term station.

The influence of density stratification on turbulence in the near-bottom current is characterised by the semi-empirical expression $(U_* / \overline{U})^2 = 1.6 \cdot 10^{-2} / (1 + 4Ri_U)$. The stratification stability growth limited the gas exchange between density current and upper waters. For this reason O_2 concentration in the flow was proportional to Ri_U .

Jet-type stratified flow.

Stratified jet flow in the thermocline was formed only in presence of the drift current and internal wave. Profiles of such current velocity $U(z)$ and square buoyancy frequency N^2 presented at fig.2 correspond to the typical distributions of U and N^2 registered during 16-hours set of measurements.

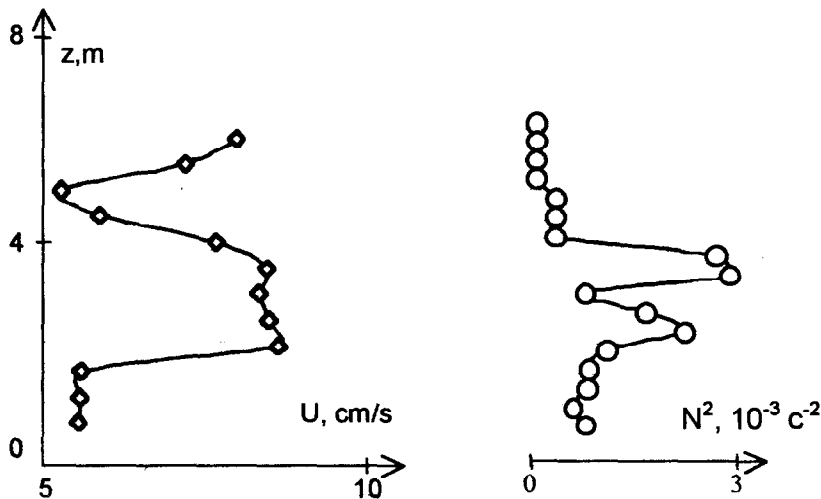


Fig.2. Vertical profiles of U and N^2 in the jet-type stratified current.

The essential parameters of the current are following:

current thickness δ_f	3–3.5 m
jet flow velocity \bar{U} (averaged over the δ_f)	1–4 cm/s
water density difference in the flow and above it $\bar{\Delta\rho}$ (averaged over the δ_f)	$(4-7) \cdot 10^{-4} \text{ g/cm}^3$
density Froud number $Fr_\Delta = \bar{U} / (g(\bar{\Delta\rho} / \rho)\delta_f)^{1/2}$	0.5–3.5.

The drift flow energy is transferred into the pycnocline by the internal wave of seiche origin (fig.3). Wave velocity disturbance amplitudes are proportional to the drift current velocity. These disturbances

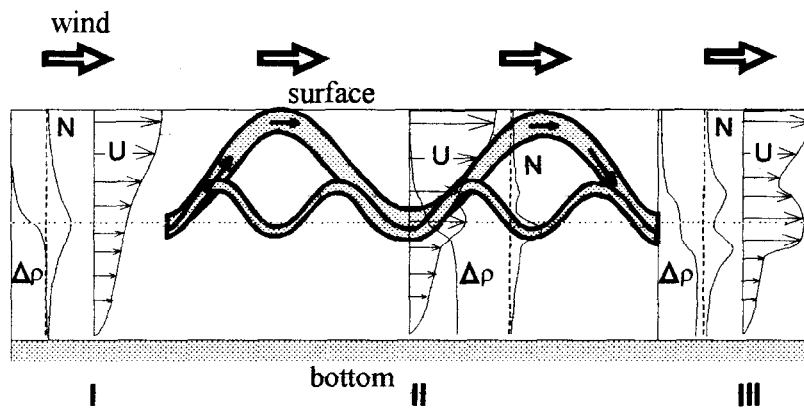


Fig.3. Scheme of the intermediate jet current formation process. Shaded area corresponds to the zones of positive wave disturbances of the flow velocity.

propagation from the surface down to the pycnocline leads to the appearance of the jet-type velocity profile (fig.3). Due to such mechanism the vertically averaged jet-flow velocity $\bar{U}(t)$ is proportional to the wind velocity $U_w(t - \Delta t)$ with the time shift $\Delta t = 1\text{h}$ (fig.4).

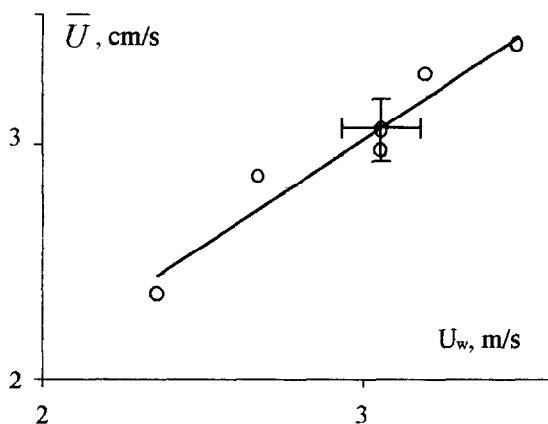


Fig.4. Diagram of the dependence of the vertically averaged intermediate flow velocity $\bar{U}(t)$ upon the wind velocity $U_w(t + \Delta t)$, measured at height 2m above the water surface ($\Delta t = 1\text{h}$).

At the boundaries of this jet flow the maxima of water density gradient appear. It provides the current stability until the next energy supplying by the internal wave. Figure 5 shows that the growth of the wind velocity leads to the increase of the density Froud number for the jet flow at the range of this number values: $Fr_{\Delta} \leq 2.5$.

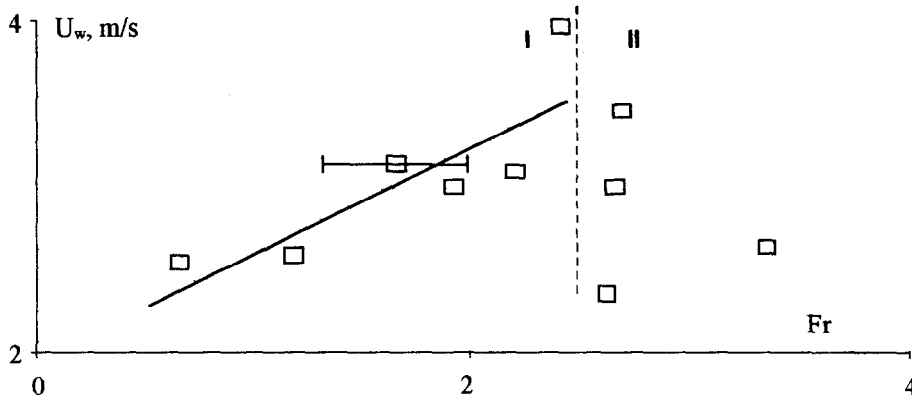
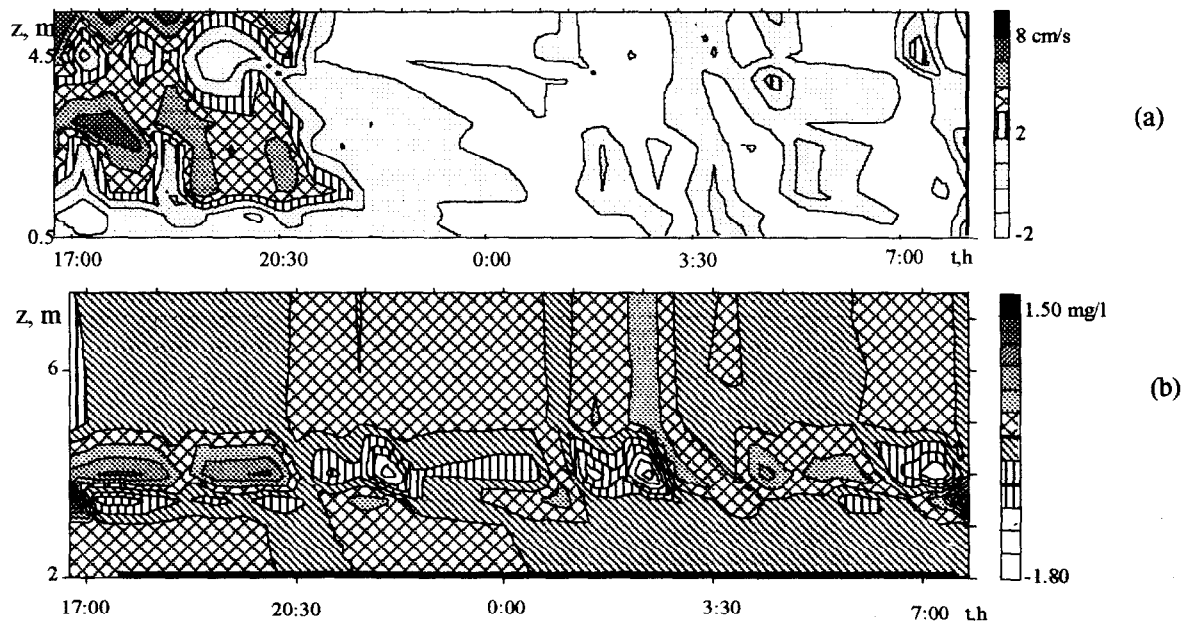


Fig.5. The diagram of the dependence of the Froud number for the jet-flow upon the wind velocity U_w . Numbers I and II denote ranges of the current stability and instability correspondingly, vertical dotted line indicates the boundary between these ranges.

According to these results jet flow loses its hydrodynamic stability if the Froud number reaches values more then critical one that is about 3. Both currents (drift and intermediate) calmed down simultaneously with the wind.

The comparison of measured vertical distributions of U and O_2 with the profiles, averaged for the calm period, allowed to obtain the fields of U and O_2 disturbances (fig.6a and 6b) and to reveal the evolution of these field structures under the influence of the internal wave.



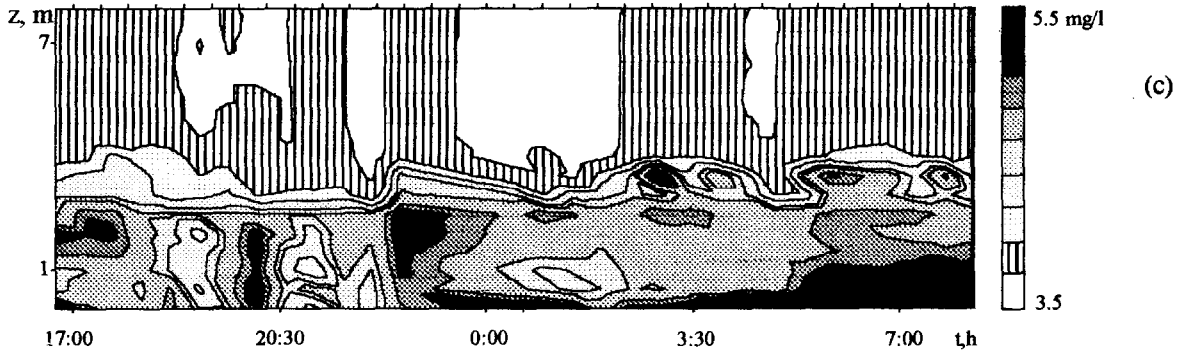


Fig.6. The distributions of current velocity and dissolved oxygen concentration disturbances U_d and $(O_2)_d$ (a), (b) as well as the suspended material concentration C_s (c) in time t and over the height z above the bottom.

On the left at fig.6a there are clearly seen the jet-flow and its velocity field perturbations at the range $t < 22h$ until the wind calmed down. Its are typical for an influence of the second mode of internal wave on the current. The same structures present in the field of $(O_2)_d$ (fig.6b) at the pycnocline. Field of C_s (fig.6c) indicates the presence of “turbid columns”, that reach the water surface with the period from 2 up to 3 h. At the time interval after 2h there are observed two “clouds of turbidity” under the foot of each column. The pointed clouds correspond to the second wave mode influence upon the structure of the suspended material concentration field.

Perturbations of suspended material concentration field during the 16-hours natural experiment are characterised by injection of this material from hypolimnion to epilimnion under the internal wave action. Horizontal scales of the formed turbid plumes were 0.3-0.6 km. In presence of the wind the O_2 concentration within the intermediate jet influence zone was 30% higher than average one for the period of the term station.

The discovered effects are of great interest, as they belong to the processes of formation and development of stratified currents widespread in nature. The obtained information about the mechanisms of such near-bottom and intermediate density flows evolution can be useful for the simulation of the similar phenomena in oceans, seas, lakes and reservoirs.

Literature.

1. Kremenetskiy V.V., Rykunov L.N., Samolyubov B.I. Circulating Density Current // Academy of Sciences / Earth Science Section, 1998. V. 357. N4. P.539-541.
2. Samolyubov B.I. Kremenetskiy V.V., Moya A.A. Near-bottom density flows induced by drift currents and internal waves. // Inter. Symp. “Oceanic Fronts and Related Phenomena”. Sankt-Petersburg, Pushkin, 1998, abstr. of the rep. P. 157-158.

HEAT AND SUSPENDED PARTICLES TURBULENT TRANSFER IN DENSITY CURRENTS

Samolyubov B.I., Silaev A.V., Silaeva L.V.

M.V.Lomonosov Moscow State University, Chair Physics of Sea and Land Waters
Moscow 119899, Russia, e-mail: sambis@flow.phys.msu.su

Abstract

The turbulent diffusion of heat, pulse and suspended particles in a near-bottom density flow is investigated. The calculation techniques of account of distributions of turbulent transfer coefficients for heat and suspended particles are described. The experimental and calculated distributions of the appropriate coefficients are compared and the vertical structures of Prandtl and Schmidt numbers are received. The influence of suspended particles on the heat transfer is analyzed and described by semi-empirical expression of Prandtl number with taking into account hydrodynamic stability and the origin of stratification in the cold near bottom flow with internal wave.

Introduction

Thermally stratified density currents with suspended particles (turbidity flows) play an important role in mass-transfer in the near-bottom layers of oceans, seas, lakes and reservoirs. The forecast of the hydrosphere pollution by the admixtures transported by density currents includes the determination of the pollution zones. To elaborate the theoretical description techniques of the admixture diffusion in density currents it is necessary to take into account the specifics of the turbulent exchange coefficient profiles. The problem is essentially complicated at conditions of strong influence of the admixture of one type on the transfer of another. It is especially important in case of the suspended sediment action on the energy and heat transfer. The results of these effects investigations including the suspended particle size spectra transformations are presented in this article.

The distributions of turbulent exchange coefficients.

The main part of the introduced results was obtained in the expeditions of the Moscow State University. Characteristics of the near-bottom current investigated during these expeditions (velocity up to 70 cm/c and height 15÷30 m) were of the same order as the parameters of similar flows observed at the sea and oceanic conditions and also at the lakes and reservoirs. Such a density current was discovered during the searching investigations at the Nurek reservoir (Tadjikistan). The typical concentration, velocity and water temperature vertical distributions in the formed near bottom density current are presented at fig.1. These figure shows also the profiles of exchange coefficients of heat K_h , pulse K_T and suspended particles K_s .

The turbulent diffusion coefficients were calculated by applying the turbulent diffusion equation

$$\frac{d\varphi}{dt} - w_\varphi \frac{\partial \varphi}{\partial z} = \frac{\partial}{\partial z} \left(K_\varphi \frac{\partial \varphi}{\partial z} \right), \quad (1a)$$

where $\varphi = S_i, T$; $\frac{d\varphi}{dt} = \frac{\partial \varphi}{\partial t} + u \frac{\partial \varphi}{\partial x} + w \frac{\partial \varphi}{\partial z}$ (for the plane task), w denotes vertical component of the time

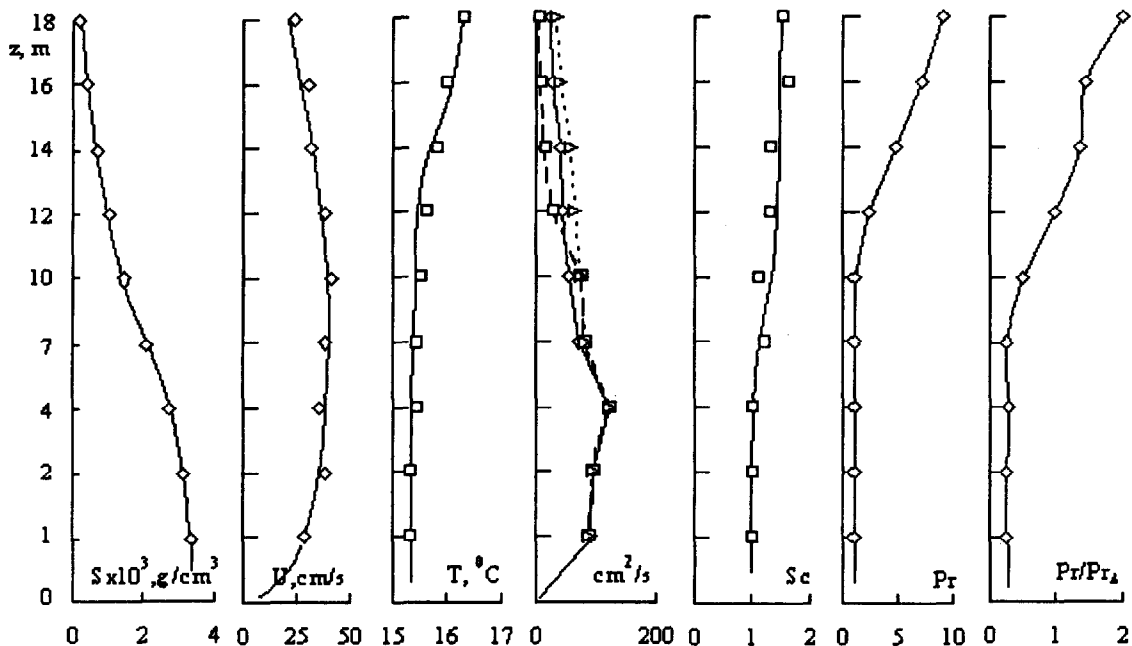


Fig. 1. The vertical distribution of concentration S , velocity U , temperature T , transfer coefficient of pulse K_T (striped line), suspended particles K_S (solid line), heat conductivity K_h (dashed line), Schmidt Sc and Prandtl Pr numbers, and ratio Pr/Pr_Δ , where Pr_Δ is average in the mixing layer.

average current velocity, $\omega_\varphi = \omega_{fi}$ at $\varphi = S_i$ and $\omega_\varphi = 0$ at $\varphi = T$, $K_\varphi = K_{si}, K_h$, (K_{si} is turbulent diffusion coefficient of particles with size a_i), t is a time, x denotes distance along the flow, z is height above the bottom.

The distribution of exchange coefficient K_h was calculated (1a). According to the estimates on the direct measurements base in studying flow are correct non-equations:

$$w \ll \omega_f, \quad U \partial T / \partial x + w \partial T / \partial z \ll \partial T / \partial t. \quad (2)$$

From (1a) after integrating with condition (2) follows expression of K_h

$$K_h = \left[\int_{z_k}^z \partial_i T \quad dz + C_H \right] / \partial_z T, \quad (3)$$

where $C_H = const$, $z_k \cong 0,05 z_u$ is the nearest to bottom (on measurements data) T registration level. To determinate C_H it is necessary to set equation (1a) parameters values on one of the flow boundary.

The correctness of $K_h(z)$ found from (3) can be checked by comparing the measured profiles $T(z, t)$ and the calculated ones (from (1a) with found distribution $K_h(z)$).

The collation of calculated profiles $T(z)$ and measured ones testifies to suitability of suggested technique. The deviations of theoretical $T(z)$ distributions from measured ones are caused mainly by the effects of non-stationarity which period is of the same order as the time of the profile $T(z)$ measurements.

The coefficient K_S (fig.2b, 1) was obtained from the equation (1a) for the mix of particles of different

fractions with the concentration $S = \sum_{i=1}^{\Phi} S_i$ in approaches of quasi-stationarity and horizontal quasi-homogeneity of the current with $W \ll \omega_f$.

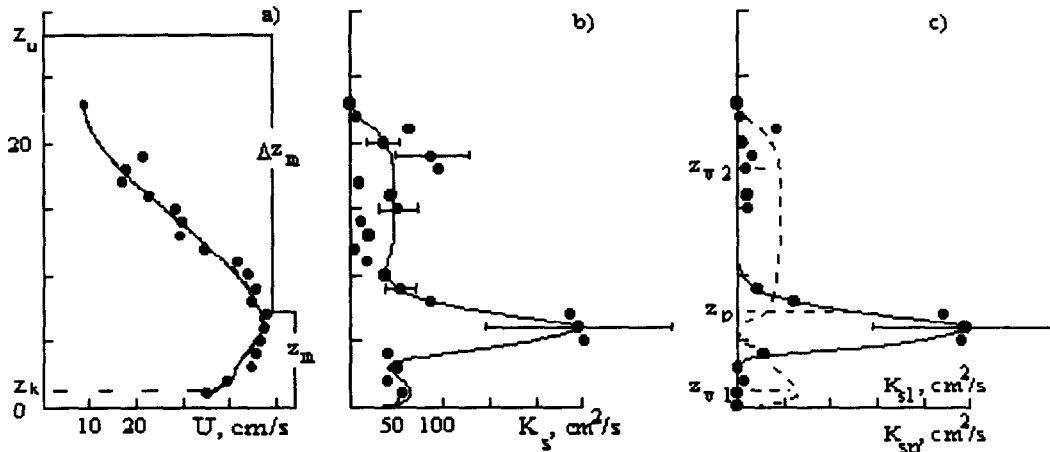


Fig. 2. The vertical distribution of a) velocity U : measured (points) and calculated by model [1] (solid line); b) diffusion coefficient K_s ; c) components K_s : penetrating K_{sp} (solid line and points) and shear K_{sl} (dashed line).

In the same approaches from the turbulent energy balance equation the expression K_s is received [1] as

$$K_s = K_{sl} + K_{sp}, \quad (4a)$$

where

$$K_{sl} = Sc^{-1} l^2 \left| \frac{dU}{dz} \right| \quad \text{and} \quad K_{sp} = (K_{sp})_m F_{ln} \quad (4b)$$

are components of K_s : shear with two maxima arranged in the near-bottom area and in the mixing layer and "penetrating" one dominant in a core of the current (third maximum, fig.2c). Such structure belongs to the distribution of type "diffusion triplet"[1]. In (4) $Sc(z)$ denotes Schmidt number, l is mixing length,

$(K_{sp})_m \cong \omega_f z_u (\pm 20\%)$ is value K_{sp} at $z = z_p$, $F_{ln} = \frac{z_p}{z} \exp \left[\frac{1}{2\sigma_p^2} \left(\ln \frac{z}{z_p} \right)^2 \right]$ is probability density

function of log-normal distribution with a mode $z_p = 0,3z_u (\pm 17\%)$ and dispersion $\sigma_p = 0,5 (\pm 15\%)$.

The physical interpretation of diffusion triplet structure is bound up with two factors (fig.2c):

1. Appearance of the component K_{sl} due to the shear turbulence in mixing and near-bottom layers.
2. Origination of the central component K_{sp} , that is determined mainly by vortexes penetrating through the core area. The vertical axes projections of this vortexes are distinguish from zero that is stipulated by the following reasons:

a). By impenetrability of a plane $z = z_m$ for vortexes with horizontal axes which orientation is determined by a sign of $\frac{dU}{dz}$.

b). By the absence of the suppression influence of stratification on the orbital velocity component of vortexes with vertical axes.

The basic deflection between the profiles K_h , K_T , K_s are observed in the current mixing layer (at $z > 7$ m). This distinctions are characterized by distributions of Schmidt $Sc(z)$ and $Pr(z) = K_T/K_h$ numbers which are analyzed further on.

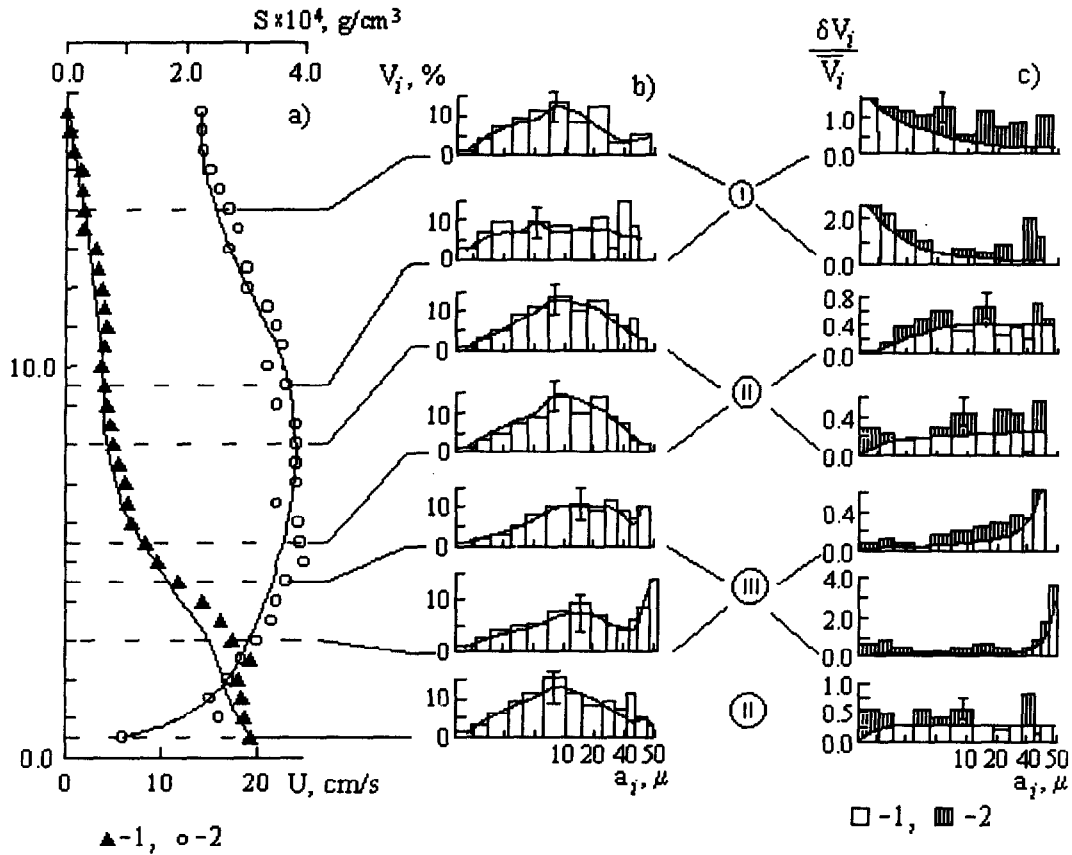


Fig. 3. The distributions of: a) suspended particle concentration S -1 and velocity U -2 on height z above bottom; b) volume content of particles V_i with its size a_i on different levels z , c) deviation $\frac{\delta V_i}{\bar{V}_i}$ of local spectra $V_i(z)$ from average on thickness of flow ($\delta V_i = V_i - 0,8 \bar{V}_i$). The solid line on a) is theoretical, dotted line is profile $U(z)$ restored by $S(z)$. The lines on b), c) correspond to approximation of V_i and deviation $\frac{\delta V_i}{\bar{V}_i}$ of types I, II, III. On c) the 1 is basic components δV_i of I, II and III types; the 2 (hatched area) is additional deviations of types II at $z = 14 \text{ m}$, III at $9,5 \text{ m}$, I and III at $5,5 \text{ m}$, I at $0,5 \text{ m}$.

Suspended particle size spectra

Typical particle size spectra $V_i(a_i)$, are submitted at fig.3 together with the simultaneously obtained profiles of current velocity $U(z)$. To research spectra $V_i(a_i)$ (fig.3b) the distributions $V_i(a_i, z)$ were compared with \bar{V}_i (averaged on of current height z_u). The deviations δV_i of the curves V_i from \bar{V}_i are characterised by types of I, II, III or by their combinations (fig.3c) connected with perturbations of the mass-exchange mechanisms in a flow over its height z .

The description of the V_i spectra changes in the near-bottom current is carried out on the basis of the solution of the equation (1a) in a boundary layer assumption for the two-dimensional currents. Integration of (1a) gives after a number of transformations the following function $V_i = \frac{S_i}{S}$ [1]

$$V_i(a_i) = k_0 V_0 + k_I V_I + k_{II} V_{II} + k_{III} V_{III}, \quad (5)$$

where $k_0, k_I, k_{II}, k_{III}$ are coefficients, dependent on the properties of the current and of the suspended sediments, $V_0, V_I, V_{II}, V_{III}$ denote functions of the particles size value a_i .

The component $k_0 V_0$ is determined by the influence of turbulent exchange on the $V_i(a_i)$ distribution. Other three components in (5) are bound up with the following mass-exchange mechanisms (fig.3c):

1. The falling down function $k_I V_I$ dominates in (5) if the process of gravitational sedimentation of particles prevails over turbulent suspending.
2. The probability of suspending particles of the largest fractions rises with the increase of intensity and scales of turbulent exchange that conducts to occurrence of features of type II (fig.3c). The function V_{II} is bound up with the influence of advective processes and turbulent exchange on V_i .
3. The component $k_{III} V_{III}$ belongs to type III (fig.3c) and is stipulated mainly by non-stationary processes.

The influence of stratification stability and suspended particles concentration on the turbulent heat transfer

The typical Prandtl and Schmidt number profiles are presented at fig.1 as well as averaged in time relation Pr/Pr_Δ , where Pr_Δ is value average over the mixing layer. To take into account the influence of stratification stability on Prandtl number semi-empirical expression $Pr(Ri_\Delta)$ is usually applied. Here

$$Ri_\Delta = \frac{g \Delta\rho_m \Delta z_m}{\rho \Delta U_m^2}$$

is integral Richardson number.

The results of the qualitative analysis of function $Pr(Ri)$ for stratified currents are systematized below.

The regularities of simultaneous changes of Pr number and the stratification stability are come to the following:

1. Number Pr grows with increase of the stratification stability, and the view of function $Pr(Ri)$ depends on area of values Ri .
2. With a combination of the turbulent exchange with wave the value $\partial Pr/\partial Ri$ is increased. As a rule, in case of influence amplification of internal waves on the mass exchange the higher values Ri were observed than by the turbulent transfer.

The analysis of the view of dependencies $Pr(Ri)$ was carried out also in [2,3,4]. Proceeding from these results, it is possible as the first approximation to present semi-empirical dependence $Pr(Ri)$ as

$$Pr = 1 + A_\rho Ri. \quad (6)$$

In a turbidity flow besides the specified factors influencing to the ratio K_u/K_T it is necessary to take into account the sediment influence on heat exchange. For this purpose it was executed the research of parameter A_ρ from (6) dependence on the

density Turner relation $R\rho_s = \frac{\Delta\rho(S)}{\Delta\rho(T)}$ which characterizes the

alignment of the suspension and thermal stratification contributions in a density layering of water. In according with our data (fig. 5) in the flow with the mixed stratification $A_\rho = A_\rho(R\rho_s, Ri)$. We assumed the expression

$$A_\rho = A_S(R\rho_s) + A_R(Ri_\Delta), \quad (7)$$

where $A_S = 2(1 - 0,06R\rho_s)$, $A_R = -1,3/Ri_\Delta$, $R\rho_s = 4 + 12, Ri = 0,5 + 5$. At $Ri = 5 + 7$ the terms from (7) are defined as $A_S = 0$, $A_R = 4(1 - 4,5Ri_\Delta^{-1})$. According to fig. 4a the values

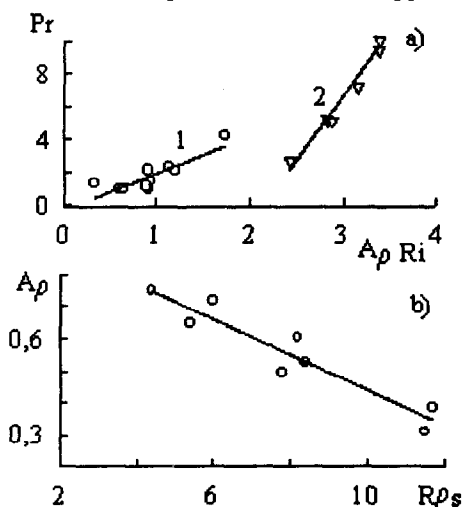


Fig. 4. The diagrams of dependencies $Pr(A_\rho Ri_\Delta)$ (a), $A_\rho(R\rho_s)$ (b).

Pr found by profiles K_T , K_h correspond to calculated ones by (6), (7). The factor A_ρ depends on the Turner parameter in contrast to function $Pr(Ri_\Delta)$ from [3,4,5].

The division into two groups of points in a fig. 4 corresponds to two various modes of mass exchange in a flow. The analysis of the temperature field evolution in time during measurements has shown that the maximal values $Pr = 3 \div 10$ are registered at the moment of the internal wave fronts passing through observed vertical line. At these moments the internal wave velocity vertical component has maximal value. Therefore

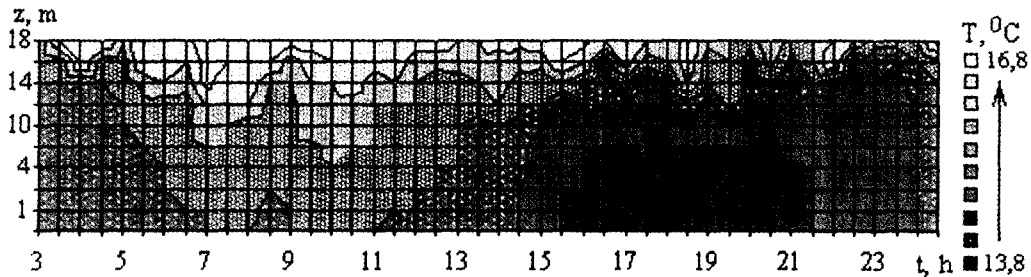


Fig. 5. The evolution of temperature during the cycle of measurement.

K_T essentially increases at small changes of K_h . The interpretation of this effect was given in [6]. The line 1 (fig. 4a) corresponds to the moments of the internal wave crests and foets passing through the point of measurements. At this moments the vertical component of the internal waves velocity is close to zero and the turbulent exchange dominates in the flow. Precisely in this mode there is dependence Pr on $R\rho_s$.

According to the revealed interdependence of Pr , $R\rho_s$, Ri the Pr number growth in the process of current stability (Ri) increase is slowed down at the rise $R\rho_s$ due to the influence amplification of the suspension stratification on a density layering of water. The diagram of dependence A_ρ on $R\rho_s$ (fig.4b) illustrates this process. For the investigated turbidity flow with $R\rho_s = 4 \div 12$, $i_s = 3 \times 10^{-3}$ and $Ri_\Delta = 0,5 \div 5$ the marked above effect is connected to dual character of sediment influence on the current: on the one hand growth $\Delta\rho(S)$ leads to increase of the flow stability and reducing of turbulent exchange. On the another hand increase $\Delta\rho(S)$ leads to the current acceleration above an inclined bottom and to the turbulence intensity growth. The last effect is taken into account by dependence $A(R\rho_s)$ in (6), (7). Therefore the increase $R\rho_s$ due to $\Delta\rho(S)$ at the conservation of the value Ri results in reduction Pr , that characterizes intensification heat exchange in a flow accelerated above an inclined bottom.

References

1. Samolyubov B.I., Silaeva L.V. Turbulent Diffusion and Suspended Particle Size Spectra in Turbidity Current. // Izvestiya, Atmospheric and Oceanic Physics. 1998. V.34. №2. P. 274-281.
2. Jungclaus J.H., Backhaus J.O., A model for the Denmark strait overflow. // J. Of Geoph. Res.. 1994. C. v. 99. № 6. p.12,385-12,396.
3. Stacey M.W., Bowen A.J. The vertical structure of density and turbidity currents: theory and observation. // J. of Geophys. Res. 1988. v.93. № C4. p.3528-3542.
4. Bowden K.F. Turbulent mixing in Estuaries. // Ocean Management. 1981. v.6. № 2/3. p. 117-135.
5. Erjemina E.R., Karlin L.N. The model of water vertical structure of stratified estuaries. // Intrusive currents: Theory and experiment. (Сборник научных трудов). Kaliningrad. 1997. p.30-38.
6. Lozovatsky, R.V. Ozmidov On the relation between small-scale turbulence characteristics and water stratifications parameters in the ocean. // Oceanology. 1979. V.19. N6. P.982-991/

SECONDARY IGNITIVE FLOWS AND INTERNAL WAVES IN DENSITY CURRENT

B. I. Samolyubov, M. V. Sluev

M. V. Lomonosov Moscow State University, Chair Physics of Sea and Inland Waters
Moscow 119899, Russia, e-mail: sambis@flow.phys.msu.su.

Abstract. The results of the near-bottom density current natural investigations including our last expedition data are introduced in complex with the mathematical modelling. The mathematical model of the density flow was elaborated and verified using the conclusions of the experimental data analysis. The current velocity field is described taking into account the influence of density stratification, bottom slope, as well as the erosion and deposition processes on the main and secondary flows. On obtaining these theoretical results the current velocity disturbances field structure was revealed. It allows us to discover the main regularities of the internal wave propagation lengthwise and over the flow height. The dispersion relation was obtained for this wave in the density current flowing in the moving surrounding water.

Expedition Data Analysis.

The density currents under investigation were formed in reservoirs (mountain and plain) due to the intrusion of the cold, turbid river water in to the receiving basins. Expeditional investigations were performed at the mountain Nurek reservoir at the Vahsh river and at the plane Mozhaisk reservoir at the Moscow river. These currents velocities were from 15 to 70 cm/s (Fig. 1), flow height was up to 30 m, the water density difference in the near-bottom density current and above it was up to $5 \cdot 10^{-3}$ g/cm³, bottom slopes were up to 10^{-2} and suspended particles sizes were up to 70 mkm. The points at the current velocity profiles correspond to the measurement data and curve respect to the theoretical distributions. These theoretical distributions are obtained by applying specially elaborated mathematical model presented in the second section. The analysis of the expedition measurements data showed that the flow dynamics and structural perturbations are mainly determined by the interaction of primary density current with the secondary near-bottom flow and internal waves: $U=U_g+u+U_d$ (see fig. 2).

The origin of the discovered secondary flows is connected with the suspended particles concentration growth due to the bottom erosion. This effect was observed not only at the steep bottom slopes but also at the plateau in consequence of the current acceleration under the action of internal wave [Monin A. S., 1988; Samolyubov B.I., Sluev M.V., 1996, 1997, 1998]. The secondary flows of such origin existed at the short intervals

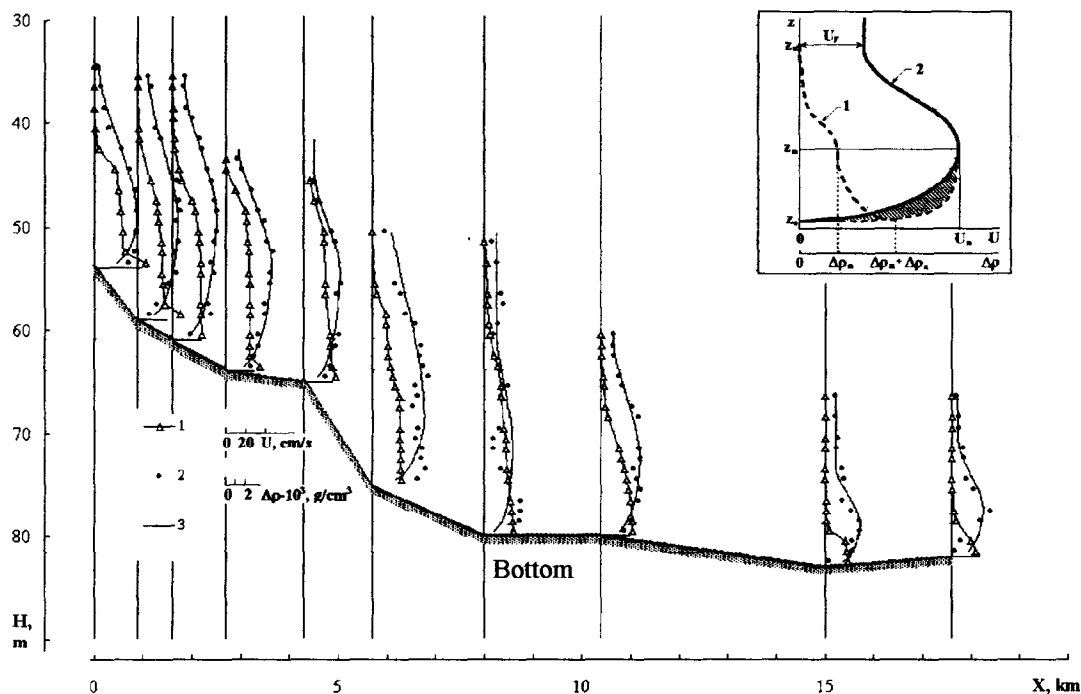


Fig. 1. Distributions of depths H (bottom relief), water density difference (1) and current velocity (measured (2) and theoretical (3)) along the near-bottom density flow propagation axes at the crossing in the Nurek reservoir. On insertion: the scheme of vertical distributions of the density difference of $\Delta\rho(z)$ and velocity $U(z)$ in density current (1 and 2). The explanations are in the text.

of the main gravity current length. The local increments of the near-bottom current velocities may arrive 150% of their undisturbed values due to the action of these ignitive secondary flows.

To investigate the influence of the suspended particles transport processes on the stability of the density current the longitudinal distributions of the Richardson number were analysed in the shear layers of the turbidity flows and of the thermally stratified currents. These results were compared with distributions of the bottom sediment entrainment function E_s and with the volumetric concentration of suspended particles near the

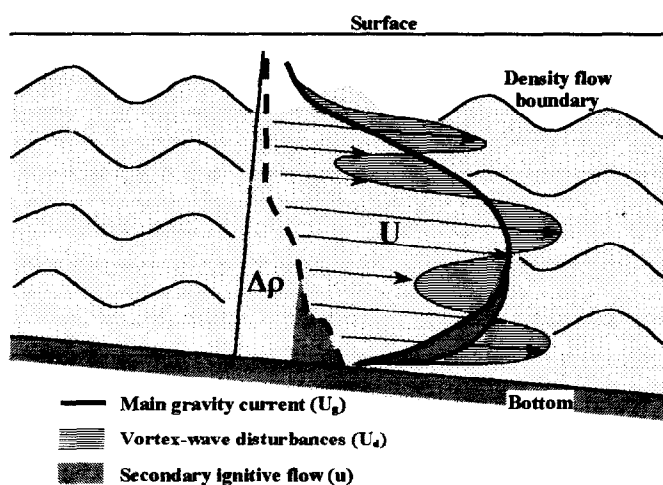


Fig.2. Conceptual schema of the near-bottom density current with secondary gravity flow and internal wave.

bottom S_k/ρ_s (fig.3). The flow stability in the near-bottom boundary layer Ri_a decreased at the intervals of bottom erosion ($E_s > \rho_s$) and increased in the regions of current decay.

At the intervals ΔX where density current loses its stability ($Ri_a < Ri_{cr}$) the internal secondary current practically disappears (fig.3). The theoretically calculated vertically averaged velocities of ignitive flows \bar{u} fall at these intervals up to the values less than 1 cm/s. The acceleration of the secondary gravity flows takes place in regions of the active interaction between density current and bottom due to the erosion and sedimentation processes ($E_s > S_k/\rho_s$ and $E_s < S_k/\rho_s$ at fig.3).

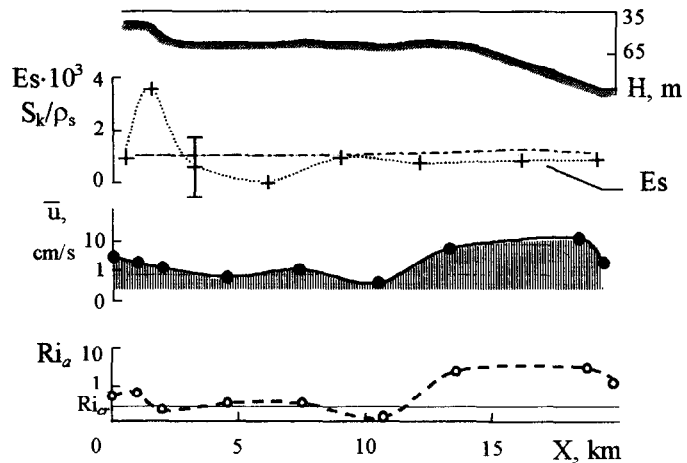


Fig.3.

The mathematical model of the density flow was elaborated and verified using the conclusions of the experimental data analysis. This model allowed obtaining theoretical distributions of current velocity lengthwise and over the height of the flow in the analytical form. The current velocity field is described with taking into account the influence of density stratification, bottom slope, erosion and deposition on the main and secondary flows. On obtaining these theoretical current velocity distributions the current velocity disturbances field structure was revealed (fig. 3). This structure has typical wave character. Such perturbations of the current velocity field are caused by the forced internal wave action on the density flow. The origin of the discovered wave is connected with glacial nature of the river, providing the non-stationary intrusions of the cold turbid water in reservoir.

The dispersion relation for this internal wave $k_z = C_R N / (U - c_f)$ was verified [Monin A.S., 1988]. In this relation coefficient C_R is dependent on Ri ; k_z denotes the vertical wave number, $N = ((g/\rho) |\partial_z \rho|)^{1/2}$ is the Vaisala-Brent frequency, c_f quantifies phase velocity of the internal wave. The wave phase velocities were evaluated in the near-bottom boundary layer and in the mixing layer of stratified current. These velocities are connected with the density flow mean velocity \bar{U} by the expression $c_f \approx 0.7 \bar{U}_0 (\bar{U} / \bar{U}_0 - 0.2)$, where $\bar{U}_0 = \bar{U}|_{x=0}$.

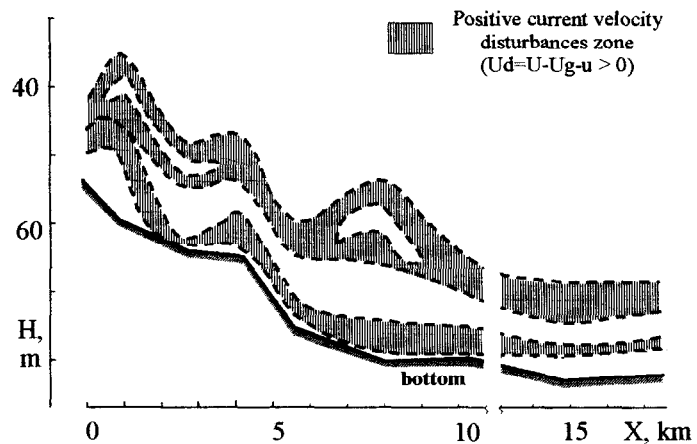


Fig. 4.

Theoretical Description of the Density Current Structure.

The structure of the current velocity profile $U(z)$ is schematically represented on insertion (fig. 1). On the scheme: $\Delta\rho = \rho(z) - \rho(z_u)$, $\Delta\rho_m = \Delta\rho(z_m)$, $\Delta\rho_a = \rho(z_o) - \rho(z_m)$, $z_o = \zeta_o z_m$ is roughness height, z_u denotes the current height, z_m quantifies the level of the current velocity maximum $U_m = U(z_m)$, $U_F = U(z_u)$ is the following current velocity.

The simulation of current is carried out in approximations of a boundary layer for the two-dimensional (plain) flow. The set of equations of the flow dynamics and of the turbulent energy balance of density current can be written as:

$$\left\{ \begin{array}{l} \frac{\partial U}{\partial t} + \frac{\partial U^2}{\partial x} + \frac{\partial}{\partial z}(UW) = \frac{g}{\rho} \Delta\rho i_s - \frac{1}{\rho} \frac{\partial p}{\partial x} + \frac{1}{\rho} \frac{\partial \tau}{\partial z} + \nu \frac{\partial^2 U}{\partial z^2}, \end{array} \right. \quad (1.1)$$

$$\left\{ \begin{array}{l} 0 = -g\Delta\rho - \frac{\partial p}{\partial z}, \end{array} \right. \quad (1.2)$$

$$\left\{ \begin{array}{l} \frac{\partial U}{\partial x} + \frac{\partial W}{\partial z} = 0, \end{array} \right. \quad (1.3)$$

$$\left\{ \begin{array}{l} \frac{\partial b}{\partial t} + U \frac{\partial b}{\partial x} + W \frac{\partial b}{\partial z} = U_\tau^2 \left| \frac{\partial U}{\partial z} \right| - \frac{g}{\rho} \langle \rho' W' \rangle - D - \varepsilon. \end{array} \right. \quad (1.4)$$

The axes x and z are directed correspondingly downwards along the bottom slope and towards to the open surface; ρ , U , W and ρ' , U' , W' are average and pulsing values of water density and components of current velocity (longitudinal and vertical); p denotes pressure; $\tau = -\rho \langle U'W' \rangle$ is turbulent stress; $i_s \ll 1$ is bottom slope; ν denotes molecular viscosity; b is specific (per unit of water volume) turbulent energy; $U_\tau = (\tau/\rho)^{1/2}$ is shear velocity; $U_\tau^2 |\partial_z U|$, D , ε and $\frac{g}{\rho} \langle \rho' W' \rangle$ are production, diffusion, dissipation of energy b and energy losses connected with turbulent vertical mass-exchange.

The distributions $U(z)$ presented at fig. 1 are obtained from a system (1) in approximations of the local quasi-stationary and horizontal homogeneity of the current. This analytical solution was found for low density turbidity and thermally stratified currents ($\Delta\rho/\rho \leq 3 \cdot 10^{-3}$) [Samolyubov B. I., Sluev M. V., 1996, 1997, 1998]. For regime of dynamically rough bottom in the flow eddy viscosity $\bar{\nu}_T = (\tau/\rho \partial_z U) = (10^3 \div 10^5) \nu$, the current velocity vertical distribution is:

$$U = \left\{ \begin{array}{l} \frac{1}{\kappa} \left[\int_{\zeta_o}^{\zeta} \frac{U_\tau}{\zeta} d\zeta + \frac{z_m}{L_a} \int_{\zeta_o}^{\zeta} U_\tau d\zeta \right], \quad \zeta = \zeta_o \div 1, z = z_o \div z_m, \end{array} \right. \quad (2.1)$$

$$\left\{ \begin{array}{l} U_F = U_F + \Delta U_m f_u, \quad f_u = 1 - 3\xi^2 + 2\xi^3, \quad z = z_m \div z_u, \end{array} \right. \quad (2.2)$$

Where $\xi = |z - z_m|/\Delta z_m$ and $\zeta = z/z_m$ are dimensionless ordinates, $\Delta z_m = z_u - z_m$, $\Delta U_m = U_m - U_F$. Expression (2.1) is integral of equation (1.4) at the interval of the local quasi-stationary and horizontal homogeneity of the current ΔX_q (at zero left part) in range $z \leq z_m$ by $U(z_o) = 0$. The similarity assumption is applied only in the mixing layer ($z_m \div z_u$) for obtaining (2.2).

In (2.1) $\kappa = 0.4$; L_a is integral scale of turbulent exchange: $L_a(\zeta) = \int_{\zeta_0}^{\zeta} U_\tau d\zeta / \int_{\zeta_0}^{\zeta} L_e^{-1} U_\tau d\zeta$, where

$L_e = U_\tau^3 / \left[\frac{g}{\rho} \langle \rho' w' \rangle + D + \varepsilon_\delta \right]$ denotes the scale of turbulence similar to the Monin-Obuchov scale;

$\varepsilon_\delta = \varepsilon - U_\tau^3 / \kappa z$ is deviation ε from $U_\tau^3 / \kappa z$ corresponding to the energy losses connected with diffusion D and

mass-exchange $\frac{g}{\rho} \langle \rho' w' \rangle$ [Eldsvic K., Brors B., 1989]; $U_\tau^3 / \kappa z$ is the dissipation component, that is equal ε under

the condition of balance production = dissipation in (3.4) for the near bottom part of the current ($z < z_m$). From

(1.1), (1.2) at $\tau(z_m) = 0$ and $\partial_x p = \partial_x p|_{z=z_m}$ the expression U_τ^2 in range $z \leq z_m$ (at ΔX_q -interval with

$g \partial_x \int_z^{z_m} \Delta \rho dz \ll \partial_x p|_{z=z_m}$ is received, when the value $v \partial_z^2 U$ in (1.1) at $z \geq z_0$ is negligibly small):

$$U_\tau^2 = g i_s \frac{z_m}{\rho} \int_{\zeta}^1 (\rho - \rho_m) d\zeta + \frac{z_m}{\rho} \left(g i_s \Delta \rho_m - \frac{\partial p}{\partial x} \right) (1 - \zeta). \quad (3)$$

The distributions (2), (3) were tested by comparison of theoretical current velocity profiles with measured ones in density currents with typical parameters: $\bar{\Delta \rho} \leq 3 \cdot 10^{-3} \text{ g/cm}^3$, $z_0 = (0.2 \div 20) \cdot 10^{-3}$, $Ri_a = g \Delta \rho_a z_m / \rho U_m^2 \leq 3$, $L_a \geq 0.2 z_m$.

In accordance with (3), in the current with a quasi-homogeneous water density difference profile $\Delta \rho(z)$ (when $\rho - \rho_m \ll \Delta \rho_m$) at range $z < z_m$ the shear velocity normalized distribution is $U_\tau / U_* (1 - \zeta)^{1/2}$, where U_* is friction velocity. In such conditions the evaluations reliably testify that the contribution of the 2-nd term from (2.1) in value $U(z)$ don't exceed 25 % for $L_a \leq 0.2 z_m$. Deviations of $L_a(\zeta)$ from \bar{L}_a (averaged in layer $\zeta \leq 1$) are less than 40%. It enables us to use in (2.1) \bar{L}_a instead of $L_a(\zeta)$ with accompanying error of definition U up to 10%. Then from (2.1) at $U_\tau / U_* = (1 - \zeta)^{1/2}$ the velocity distribution can be expressed as:

$$U_g = \frac{U_*}{\kappa} \left[\ln \left| \frac{(1 - \zeta)^{1/2} - 1}{(1 - \zeta)^{1/2} + 1} \right| + 2(1 - \zeta)^{1/2} - \frac{2\kappa z_m}{3L_a} (1 - \zeta)^{3/2} \right] \Bigg|_{\zeta_0}^{\zeta}. \quad (4)$$

Scale L_a is evaluated by applying (4) under condition of $U|_{\zeta=1} = U_m$ and expressed as

$$L_a \cong L_a|_{\zeta=1} = \left[\frac{2}{3} \kappa z_m (1 - \zeta_0)^{3/2} \right] / \left[\frac{\kappa U_m}{U_*} + 2(1 - \zeta_0)^{1/2} - \ln \left(\frac{(1 - \zeta_0)^{1/2} + 1}{(1 - \zeta_0)^{1/2} - 1} \right) \right]. \quad (5)$$

The integration (6) on ζ in limits $z_0 \div 1$ with L_a from (5) gives expression z_0 :

$$\zeta_0 = 0.1 \exp \left[\frac{\left(\bar{U}|_{z \leq z_m} - U_m \right)}{U_*} \right], \quad (6)$$

Where $U|_{z \leq z_m} = \int_{z_0}^z U d\zeta$. With an error up to 10 % the replacement $\bar{U}|_{z \leq z_m} \cong 0.8U_m$ verified at typical values $U = (0.04 \pm 0.1)U_m$, $U|_{z \leq z_m} = (0.7 \pm 0.9)U_m$ is allowable.

According to the theoretical conclusions of [Stacey M., Bowen A. A., 1990, Samolyubov B. I., Sluev M. V., 1998]: $U_*^2 \sim \frac{g}{\rho} \bar{\Delta\rho} z_u \omega_f / \bar{U}$. This interdependence is based on the results of measurements in 9 density currents with $i_s = 10^{-3} \pm 10^{-2}$, $\bar{\Delta\rho} = 10^{-4} \pm 10^{-2}$ g/cm³, $z_u = 5 \pm 40$ m: $\omega_f / \bar{U} \sim i_s^{1/2}$. Therefore, $U_*^2 \sim \frac{g}{\rho} \bar{\Delta\rho} z_u i_s^{1/2}$. This proportionality is valid for the given (fig. 1) and for the other similar currents on the intervals ΔX with $i_s = \text{const}$ at $i_s \geq 10^{-3}$. The corresponding expression U_*^2 at $i_s < 10^{-2}$:

$$U_*^2 = \begin{cases} C_* \frac{g}{\rho} \bar{\Delta\rho} z_u i_s^{1/2}, & i_s \geq 10^{-3} \\ 1.6 \cdot 10^{-2} C_* \frac{g}{\rho} \bar{\Delta\rho} z_u, & i_s < 10^{-3} \end{cases}, \quad (7)$$

where $C_* \cong 2.8 \cdot 10^{-3} (\rho / \bar{\Delta\rho}_0)^{1/2}$, $\bar{\Delta\rho}_0$ is value $\bar{\Delta\rho}$ at the beginning of an interval ΔX with $i_s = \text{const}$ [Samolyubov B. I., Sluev M. V., 1998]. At $i_s = C_*^2$ the formula (9) passes in to the expression $U_*^2 = \bar{U}^2 Ri_u i_s$ well known for density currents at ΔX_i -intervals [Chikita K., 1989, Fukushima Y., Parker G., Pantin H., 1985]. In contrast to this expression the formula (7) allows to take into account the nonlinearity of the function $U_*^2(i_s)$.

The input parameters of (4.2), (6 - 7) are i_s , U_F , z_u , $\bar{\Delta\rho}$, U_m , z_m . The values z_u , $\bar{\Delta\rho}$ can be found by applying one-dimensional model of current propagation; parameters U_m , z_m can be evaluated as $U_m = 14U_* (\pm 15 \%)$, $z_m = 0.4z_u$ [Samolyubov B. I., Sluev M. V., 1996, 1997, 1998]. The structures U at fig. 1 are obtained from (4.2), (6), with L_b , z_0 , U_* found from (7), (8), (9) for a given initial values of the model parameters. The deviations of theoretical curves from the measured values U are stipulated by the effects not discounted in a model: current non-stationarity and water density growth with depth in range $z < z_m$.

References

- [1] Chikita K., 1989, A Field Study of Turbidity Currents Initiated from Spring Runoffs, J. Water Resour. Res., vol. 25, no 2, p. 257-271.
- [2] Eldsvic K., Brors B., 1989, Self-accelerated Turbidity Current Prediction Based upon (k-ε) Turbulence, Contin. Shelf Res., vol. 9, no 7, p. 617-627.
- [3] Fukushima Y., Parker G., 1985, Pantin H. Prediction of Inertive Turbidity Currents in Scripps Submarine canyon, Mar. Geol., vol. 67, no 1-2, p. 55-81.
- [4] Monin A. S. 1988, Theoretical foundations of the geophysical hydrodynamic, L.: Hydrometeoizdat, ch. 5, p.189-223.
- [5] Samolyubov B. I., 1986, Interaction of shear layers and formation of inversion structure of near-bottom stratified flow, Oceanology, vol. 26, no. 6, p. 920-930.
- [6] Samolyubov B. I., Sluev M. V. and other, 1997, Evolution of the velocity field and distribution of the diffusion coefficient in density current. Collection of scientific works. Kaliningrad State Technical University, Kaliningrad, p. 39-48.
- [7] Samolyubov B. I., Sluev M. V., 1996, About the structure of the near-bottom stratified flow, Meteorology and Hydrology, no. 1, p. 94-100.
- [8] Samolyubov B. I., Sluev M. V., 1998, Evolution of Internal Wave and Secondary Flows in Turbidity Current // Oceanology, 1998, Vol. 38, No. 6, p. 620-628.
- [9] Stacey M., Bowen A. A., 1990, Comparison of an Autosuspension Criterion to Field Observations of Five Turbidity Currents, J. Sedimentology, vol. 37, no 1, p.1-5.

This work was supported by RFBR (grants no. 96-05-65856, 96-05-01118).

SPATIAL AND TEMPORAL VARIABILITY MEASUREMENTS IN THE ICELAND-FÆROES FRONTAL ZONE USING TOWED DISTRIBUTED SENSORS AND REMOTE SENSING

John C. Scott, Tim Sawyer and Kate Kelly

Defence Evaluation & Research Agency, Winfrith Technology Centre, Winfrith Newburgh, Dorset DT2 8XJ,
UK [EMail: jcscott@dera.gov.uk]

Abstract

A total of eight small-scale measurement surveys took place in the Iceland-Færoes Frontal Zone in the period 1985-1992, using a towed thermistor chain carrying 100 temperature sensors and some conductivity-temperature-depth sensors. The surveys covered the seasonal variability in the region and also allowed assessment of temporal variability on time-scales down to daily. Rapidly developing mesoscale features with length scales $O(10\text{km})$ were tracked and observed to develop. The measurements were often supported by coincident satellite infra-red images; these allowed real-time adaptation of the survey tracks, and the movement and development of frontal and eddy features could thereby be followed. The observations allowed the detection of a large number of structures that are characteristic of this region. Those summarized in this brief account include: the large 'warm intrusion' region; a spring/summer low salinity contribution to the structure of the major frontal boundary, in the form of a narrow surface jet of Icelandic Shelf Water; and the role of this jet in the structure of cold eddies generated at the boundary.

Introduction

The Iceland-Færoes Frontal Zone (IFFZ) is one of the world's most dynamic ocean regions, occurring at the confluence of the northwards-flowing warm saline Atlantic Water of the Gulf Stream extension with the cold saline waters of the Iceland Sea. The system of sub-sea ridges that connect Greenland with the European Continental Shelf, via Iceland and the Færoe Islands effectively blocks the southward transport of deep cold water masses of Arctic origin, except at the western side of the Denmark Strait. Cold water overflows between Iceland and the Færoes, and between the Færoes and the Shetland Islands are much less significant, and largely intermittent [1]. Figure 1 shows schematically the arrangement of water mass features in the region.

The region has been the subject of a large number of surveys since 1950, involving increasingly sophisticated techniques. Steele reported CTD stations at approximately 10km intervals in 1959 [2], and Koltermann, Meincke and Muller [3] reported CTD data from 1973, with similar spatial resolution, but including repeated sections which gave some indications of the temporal variability. These data gave indications of the overall structure of the frontal zone and estimates of the cold overflow [4]. Smart [5] reported a series of near-synoptic surveys in 1980-81 using extensive patterns of air-dropped expendable bathythermograph (AXBT) probes, and for the first time used surface thermal images from satellite infra-red sensors to aid the interpretation of the data. These data were the first in which temporal variability during the measurements was removed as a variable, although the AXBT data were still coarsely sampled ($\sim 40\text{km}$), and the satellite data, though truly synoptic, only represented the surface condition, and gave little indication of the deeper structures. The measurements showed large changes between surveys, but failed to resolve important details of eddies and frontal structure.

In all of these investigations, it proved impossible to separate the influences of temporal and spatial variability in the interpretation of the data. CTD surveys are limited by practical considerations to relatively slow progress along measurement tracks, even for coarse spatial sampling. Aircraft surveys, though faster, are also limited to

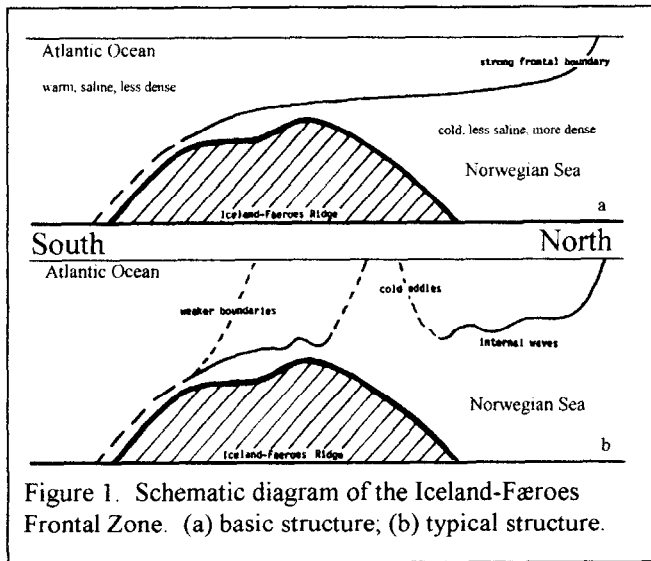


Figure 1. Schematic diagram of the Iceland-Færoes Frontal Zone. (a) basic structure; (b) typical structure.

coarse sampling. Satellite infra-red images resolve details spatially, but are so limited by cloud cover here that they under-sample in time; correlation of individual features to determine their dynamics has rarely been possible, even when their sub-surface structures are relatively well understood. It was only in the 1980s that it became possible to measure the detailed structure of the frontal zone and to attempt to separate the effects of temporal and spatial variability. This needed towed chains and vertically undulating towed sensors, supplemented by satellite infra-red imagery and also by precision satellite altimetry. Investigations such as the towed thermistor chain surveys summarized in this paper [6,7] and those using the Seasoar undulating towed CTD [8,9], supported by the acoustic Doppler current profiler (ADCP) coincided with the publication of the monograph of Fedorov [10],

which largely confirmed the region as one of the most vigorous in the World's oceans. Fedorov also clarified the distinction between a front and a frontal zone, which is particularly relevant to complex regions such as Iceland-Færoes. A third survey approach, using AXBT probes together with infra-red images, was reported by Niiler et al. [11], and a fourth approach, using a combination of AXBT measurements and altimeter data, was reported by Robinson et al. [12]. This paper will review recent advances in the current state of knowledge regarding the structure of this frontal zone, concentrating on new techniques and combination of their data.

Experimental and Sampling Considerations

The past two decades have seen a dramatic increase in the number and variety of techniques for observing processes in frontal zones. Understanding of the Iceland-Færoes frontal zone requires consideration of what each of these tells us and what each of them is likely to miss. Although those carrying out the earliest surveys will have realised that standard CTD and AXBT sections and grids were undersampling the spatial and temporal variability it was not then possible to assess neither the extent of this undersampling nor its consequences for monitoring the dynamic structures present.

Towed undulating CTDs, able to collect km-scale data along tracks at about 10 knots, are a major advance on standard CTD measurements. However, it may be shown that the gentle inclination of the profiling sensor leads to problems in sensing frontal features, which here can have *vertical* boundaries with 100m horizontal length scales, and also coastal water filaments, which may only be a few km wide. Towed sensor chains are necessary to resolve these features, and although these are normally limited to much lower speeds their contribution in this sense cannot be otherwise matched. Although ideally a chain would have C,T or C,T,D sensors at each location, we have found that the T sensors are most important, needing the greatest vertical density. A relatively small fraction of co-located C (S) sensors allows the deduction of a T,S relationship adequate for most purposes of deducing density and sound speed structures; an even smaller proportion of D sensors allows inference of the whole chain shape. The cost of the overall chain can be reduced to give a performance better than that of a simple thermistor chain. The *thermotrawl* system, developed and used by Russian oceanographers [12], carries the same principles further, using relatively inexpensive sensors for the majority of the water column.

ADCPs provide a valuable enhancement to both towed chains and undulating systems, in providing estimates of vertical variation of current on scales of a few hundred metres. Knowing that structural variability may be on shorter length scales, however, gives interpretation problems for these data which are worse for undulators than for the lower speeds of chains. However, inclined boundaries appear in ADCP data as shear layers with reliable local current variations, giving important information in support of the thermal or T,S data being collected, as the current data may be compared that that expected from the measured slope of the density boundary.

The combination of ADCP and either towed chain or undulating profiler is the current optimum for assessing the structure and dynamics of active frontal zones such as that of Iceland-Færoes. However, it is unlikely that investigations will progress effectively unless they are supported by satellite remote sensing data. These essentially synoptic data not only allow the establishment of the spatial context of line and grid in-water data, but

they are able to support survey direction and planning. High resolution satellite data, even of many megabytes, can now be supplied to ships at sea via satellite data links. Although this situation applies principally to infra-red image data it is now also possible for very high resolution digital synthetic aperture radar (SAR) data.

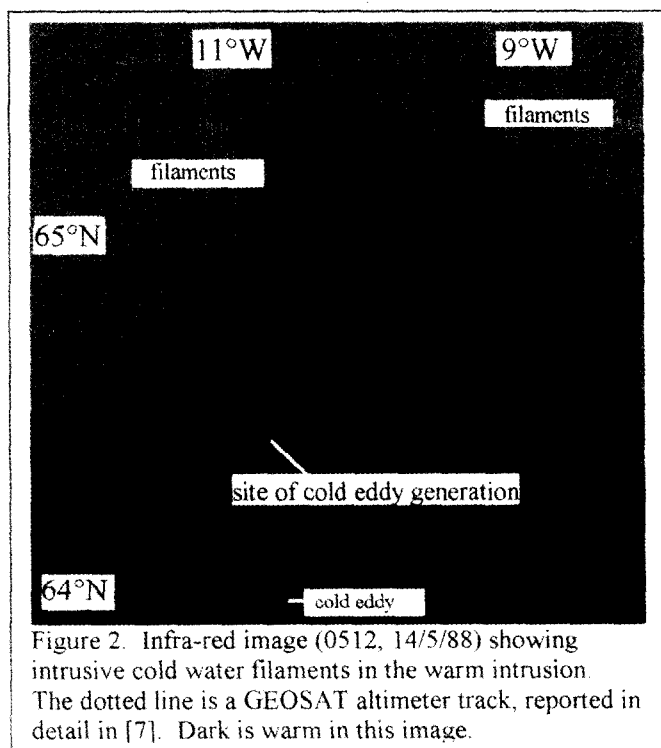
Satellite infra-red images show the detailed structure of these structures at the sea surface, at ~1km resolution, and they are potentially capable of allowing a perfect understanding of the region. However, they are seriously limited by cloud - the best months for cloud-free observation here are April and May - and overall surface warming reduces the value of images in July and August. Cloud cover is so continuous here that it is rare for a sequence of images to last long enough for significant changes in structure to be seen. We are limited to occasional glimpses, and although these often demonstrate remarkable similarity in the structures they show it is clear that they are grossly undersampled in time. The 2½-day image sequence partly reported by Scott & McDowall [7] from May 1988 is unique so far in being supported by thermistor chain and altimeter data; they clearly show the processes of cold eddy generation and development.

SAR images, notably from the European Space Agency (ESA) ERS satellites penetrate cloud, and are therefore of potentially greater value. However, since radar images of the sea are formed by spatial variations in wind-driven surface roughness they are hard to interpret, being influenced by wind structures and surface films as well as by surface current shears and convergences. It is likely that this source of data will improve in future, as more sophisticated radars are developed, with better coverage, and interpretation skills are improved. However, SAR can already play a major part in at-sea survey direction. The ESA radars are relatively limited in swath, at 100km, compared with current infra-red imagers, and this gives relatively little data at a given site; for Iceland-Færoes a useful image can be obtained from a single satellite about every three days. Future radars are expected to follow the Canadian Radarsat in having wider (and adaptable) swaths, giving improved temporal sampling.

Each of the data sources reviewed here is unique set in its sampling characteristics, trading spatial and temporal

resolution and giving varying degrees of flexibility for survey planning. A survey may adopt either a 'grid survey' [5,9] or a 'feature-tracking' approach [6,7]. The main benefit of the former is that its data may be contoured to represent a large area, but it needs to cover an area large compared with the mesoscale, making interpretation of the data as 'synoptic' increasingly questionable for larger areas. Further, it does not provide information on local changes during the period, or indeed the effects of such changes on the interpretation of the results as 'synoptic'. Feature tracking assesses the time development of a relatively small part of the frontal zone, following specific features and adapting measurements to monitor movement and changes. Information on the overall picture comes only from satellite images (when available), but feature tracking does give information on the detailed depth structure of any features found in images, and also shows the speed and nature of changes.

The complementarity of the two approaches will be made clear in the following descriptions of specific components of the frontal zone.



The structure of the warm intrusion

A large northwards bulge of the frontal zone is frequently seen between 9°W and 11°W, sometimes extending north as far as 66°N, when the majority of the major frontal activity is between 64°N and 64°30'N. This region is shown in figure 2, adapted from [7]. This is a reasonably typical image of this large permanent feature of the frontal zone, which comes from the movement of warm, high salinity Atlantic upper layer water northwards over the Ridge, ~300-400m deep at this location. The warm layer is typically 150m to 300m deep, becoming

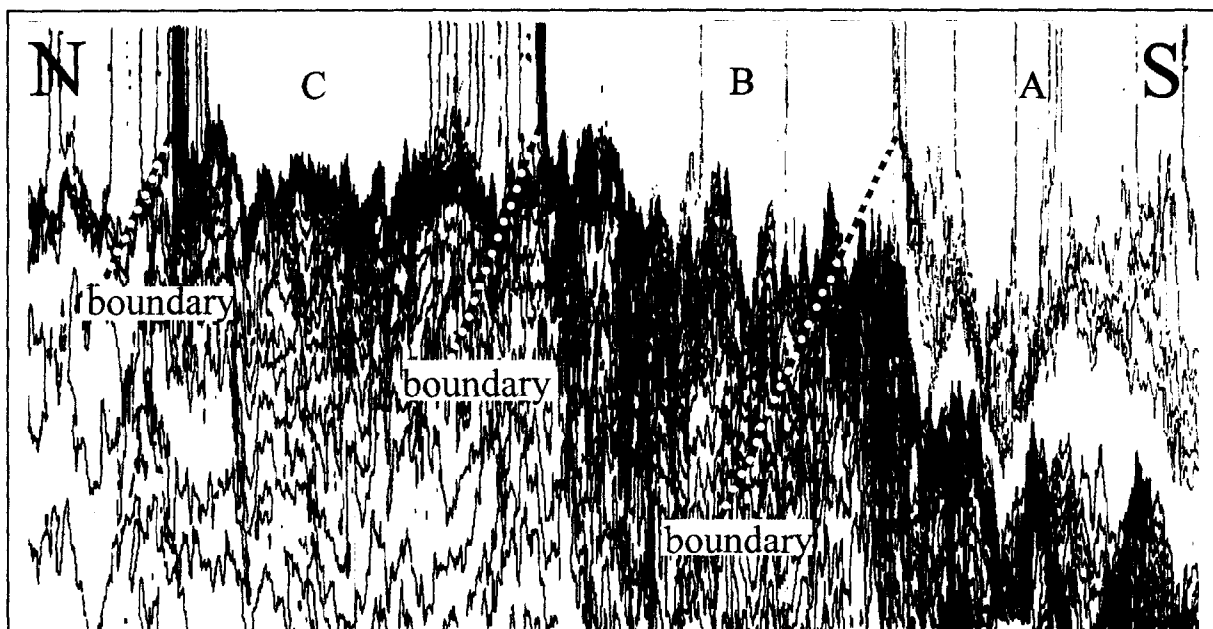


Figure 3. Representation of 0.2°C temperature contours, over at 250m water depth, along a 190km section through the warm intrusion, near 10°30'W. Three distinct warm regions are seen, here marked A,B,C, with sharp frontal boundaries, indicated using dotted lines. The cold region north of the B-C boundary appears to be a cold filament entering the intrusion from outside. The A-B boundary, here showing a 1°C temperature difference, is close to 64°30'N. Here, all upper layers are well mixed following an extended period of gale force winds. The data were collected on 19/5/88, shortly after the image shown in figure 2.

shallower further north, but often with a sharp lower boundary with the underlying cold, lower salinity Norwegian Sea water. Figure 2 shows cold water filaments intruding into this warm water mass from both eastern and western boundaries; these are typical of the warm intrusion. The 2½-day time sequence of images at this time showed no overall circulation of the warm intrusion.

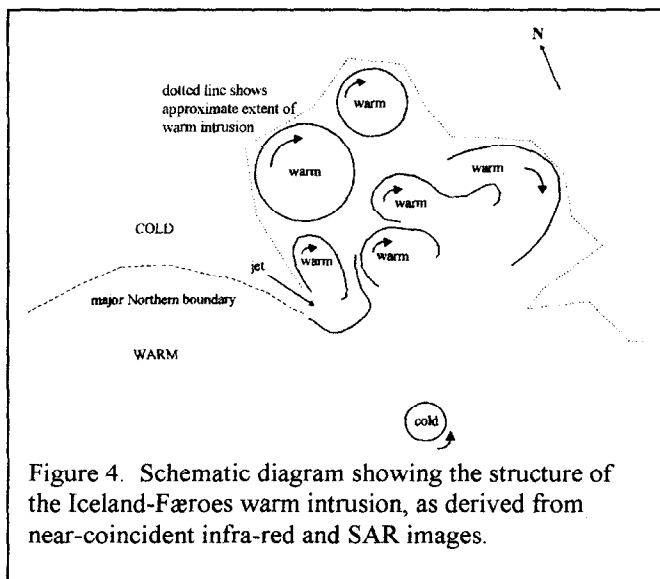


Figure 4. Schematic diagram showing the structure of the Iceland-Faeroes warm intrusion, as derived from near-coincident infra-red and SAR images.

Successive surveys of this region have allowed an accumulation of evidence relating to the formation and development in time of the warm intrusion. Firstly, the data indicate that the similarity in surface temperature between the warm intrusion and the Atlantic water to the south – seen in typical thermal images – does not always indicate a similar sub-surface structure. A frontal boundary is often seen at the southern end of the intrusion that is approximately aligned with the main boundary east of Iceland, around 64°20'N – 64°40'N. This boundary separates the weakly stratified Atlantic water and a more strongly stratified layer formed of Atlantic water modified by mixing with the underlying and adjacent Norwegian Sea water. This boundary changes significantly, both between surveys and during a survey lasting a few weeks, as the modification takes place. As well as this southern boundary, further boundaries are seen further north in the warm intrusion, each

transition leading to a shallower layer which has undergone greater modification. Figure 3 shows a north-south section through the intrusion, showing this thinning of the warm layer, including the appearance of the frontal boundaries which separate the warm water regions.

The origin of the warm intrusion was discovered during surveys of its southern boundary, carried out using zig-zag tracks progressing east-west along it. It was occasionally found during a northwards section of this zig-zag failed to find the boundary, and experienced a northwards-going strong warm current. Continuing northwards to map the extent and progress of this current, evidence was obtained that it quickly formed an anticyclonic circulation in the warm intrusion region. Such current patterns can be seen occasionally in infra-red images, and figure 4 shows the reconstruction of a pattern obtained using a combination of near-coincident infra-red and SAR images [14]; the circulation information comes from observations of the backscatter variations in the SAR images of the eddies. The warm jets are typically 20-50km wide, and form circulations of diameter 20-50km. It is likely that these warm inflows are episodic, perhaps related to pulses of the strong tidal flows in the region.

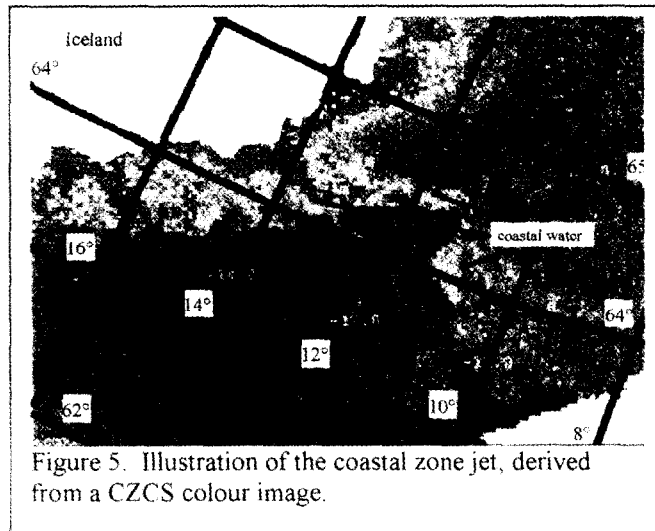


Figure 5. Illustration of the coastal zone jet, derived from a CZCS colour image.

These observations show that the warm intrusion is formed by a number of these warm anticyclonic eddies, separated from each other by regions of strong cyclonic shear. Eddies are forced northwards by new inflows of warm water, and they are quickly modified, both by the underlying cold water and by the cold filaments intruding at their boundaries, seen in figure 2. Evidence for the cold filaments separating the warm eddies also appears in figure 3.

This picture of the region differs from that deduced by Allen et al. [9], on the basis of a grid survey with ADCP and undulating CTD. Allen et al. concluded that the warm intrusion as a whole had anticyclonic circulation, and although this is consistent with its overall density structure, the smaller scale observations indicate the existence of the smaller anticyclonic eddy circulations which resolve this apparent anomaly.

This conclusion is supported by the observation, reported above, that the intrusive cold filaments do not become distorted in a 2½-day period, as they would if the whole region were rotating. These conclusions demonstrate the value of the feature tracking mode of survey, as a complement to the grid survey mode. Consideration of all of the available data indicates that neither approach manages to capture the spatial and temporal variability perfectly, but that the ability of a towed sensor chain to detect narrow boundaries significantly improves the understanding of this complex region.

The contribution of low-salinity water to cold eddy generation

Further analysis of the complete dataset has also modified the conclusions offered by Scott & McDowall [7] on the generation of cyclonic cold eddies at the south-western corner of the warm intrusion. The generation of these eddies at a particular geographical location, 64°30'N, 11°00'W (figure 2) is a striking feature of the western end of the Iceland-Færoes frontal zone. Analysis of several of the datasets has shown that, in the spring and early summer, a narrow jet of cold, very low salinity water runs eastwards from the coastal zone along the major frontal boundary.

Survey	Width km	Mean Temperature	Mean Salinity
July	2.6	4.7°C	34.48ppt
August	2.5	5.6°C	34.62ppt
September	4.7	6.1°C	34.39ppt

Table 1. Indications of variability of the coastal zone current jet in the Iceland-Færoes major boundary.

This jet is only a few km wide, but its distinctive T,S characteristics can be traced as far as the cold eddy generation site, and the same water has also been detected around the periphery of cold eddies generated here. The coastal zone

origin of this water can be seen in ocean colour images from the CZCS satellite, as a result of the high sediment load it often contains. Figure 6 illustrates this information, and table 1 indicates the observed variations of the water mass characteristics. Figure 6 also shows the generation of a cold eddy at the location indicated in figure 2, and provides an illustration of the entrainment of the coastal zone water around the eddy.

These results have provided further evidence of the value of the feature-tracking survey mode, and also of the value of towed chains compared with undulating sensors. Undulator data does show indications of low salinity water, but its coarse horizontal sampling gives no clear indication of this current.

Summary

The large volume of related data obtained from eight surveys of the Iceland-Færoes region contain information on the many water mass features that are characteristic of this complex frontal zone. The data, obtained using a variety of in-water and remotely sensed techniques, have been found to be complementary in several senses: in the synergy of the various kinds of in-water data with each other and also with the different kinds of remotely sensed data; and further, in the support provided by successive re-visits to the region, both during each survey and between surveys at different seasons in a multi-year period. It has been concluded that the high levels of spatial and temporal variability of this dynamic region make its adequate surveying impossible using any single survey technique. A combination of data – from several repeated, time-separated surveys - from a detailed towed sensor chain, an on-board ADCP, infra-red satellite images and colour satellite images gave a combined analysis potential which would have been significantly reduced by the absence of any one of these sources. Similarly, it is estimated that no carrying out less than four or five of the eight surveys would also have seriously degraded the final understanding of the region.

Acknowledgements

A measurement programme of the extent reported here inevitably involves many people in its planning, execution and analysis; they cannot all be given due acknowledgement. However, the parts played by Nichola Lane and by Norman Geddes throughout the period concerned were both essential, and due recognition is given. The part played by Will Spooner in identifying the jet of coastal water is also gratefully acknowledged.

References

- [1] T.S.Hopkins, 1991, 'The GIN Sea – A synthesis of its physical oceanography and literature review 1972-1985', *Earth-Science Reviews*, 30, 175-318.
- [2] J.H.Steele, 1959 'Observations of deep water overflow across the Iceland-Færoe Ridge', *Deep-Sea Research* 6, 69-72.
- [3] K.P.Koltermann, J.Meinke and T.Muller, 1976. 'Overflow '73 - Data Report 'Meteor' and 'Meerkatze 2'', *Berichte aus dem Institut für Meereskunde, Kiel, Nr 23*.
- [4] B.Hansen and J.Meinke, 1979, 'Eddies and meanders in the Iceland-Færoes Ridge area', *Deep-Sea Research*, 26, 1067-1082.
- [5] J.H.Smart, 1984. 'Spatial variability of major frontal systems in the North Atlantic-Norwegian Sea area: 1980-81', *Journal of Physical Oceanography*, 14, 185-192 (1984).
- [6] J.C.Scott, N.R.Geddes, N.M.Lane and A.L.McDowall, 1988. 'Thermal structure and remote sensing measurements in a major frontal region', *Advances in Underwater Technology, Ocean Science and Offshore Engineering*, 16, 59-68.
- [7] J.C.Scott and A.L.McDowall, 1990. 'Cross-frontal cold jets near Iceland: In-water, satellite infrared and Geosat altimeter data', *Journal of Geophysical Research* C10, 18005-18014.
- [8] W.J.Gould, J.F.Read and J.Smithers, 1987. 'Seasoar profiles in the Iceland-Scotland area', *IOS Report No.253, Institute of Oceanographic Sciences, UK*.
- [9] J.T.Allen, D.A.Smeed and A.L.Chadwick, 1994. 'Eddies and mixing at the Iceland-Færoes front', *Deep-Sea Research*, 41, 51-79.
- [10] K.N.Fedorov, 1986. 'The Physical Nature and Structure of Oceanic Fronts', Springer-Verlag, Berlin, 333pp (1986) ISBN 3-540-96445-2.
- [11] P.P.Niiler, S Piacsek, L.Neuberg and A.Warn-Varnas, 1994. 'Sea surface temperature variability of the Iceland-Færoe front', *Journal of Geophysical Research*, C, 97, 17777-17785.
- [12] A.R.Robinson, L.J.Walstad, J.Calman, E.B.Dobson, D.W.Denbo, S.M.Glenn, D.L.Porter and J.Goldhirsh, 1989. 'Frontal signals East of Iceland from the GEOSAT altimeter', *Geophysical Research Letters*, 16, 77-80.
- [13] N.N.Golenko and Y.V.Kol'tsova, 1985. 'Vertical mode structure of internal waves from the data of a towed thermotrawl', *Oceanology*, 25, 586-588.
- [14] N.Stapleton, A Dawson, J.Scott and C.Brownsword, 1997. 'Combined IR and SAR observations of the Iceland-Færoes frontal zone', *Proceedings of 'Monitoring the Oceans in the 2000s: An integrated approach', Biarritz, France 15-17 October 1997, CNES/NASA*.

FLOW EXCHANGE AND TIDALLY INDUCED DYNAMICS IN THE STRAIT OF GIBRALTAR DERIVED FROM A TWO-LAYER, BOUNDARY-FITTED COORDINATE MODEL

D. V. Sein¹, J. O. Backhaus², P. Brandt², A. Izquierdo³, B. A. Kagan¹, A. Rubino² and L. Tejedor³

- 1 St. Petersburg Branch of the P. P. Shirshov Institute of Oceanology, Russian Academy of Sciences, Pervaya Liniya 30, St. Petersburg 199053, Russia
- 2 University of Hamburg, Institute of Oceanography, Troplowitzstr. 7, D-22529 Hamburg, Germany
- 3 Universidad de Cadiz, Departamento de Fisica Aplicada, C.A.S.E.M., 11510, Puerto Real, Cadiz, Spain

Abstract. A two-dimensional, two-layer, boundary-fitted coordinate model based on the hydrostatic nonlinear shallow-water equations on an f -plane is employed for the simulation of the hydrodynamics of the Strait of Gibraltar. The model is forced by imposing mean interface depths, mean surface displacements, and diurnal and semidiurnal tidal surface displacements at the Atlantic and Mediterranean open boundaries. The model predicts (1) the existence of a hydraulically controlled exchange flow between the Atlantic and the Mediterranean, (2) the generation of eastward propagating internal bores due to the interaction of the semidiurnal tidal flow with the Camarinal Sill, and (3) their diurnal and fortnightly variability. The locations of internal bores as function of the semidiurnal tidal phase as obtained by the numerical simulations are compared with those inferred by the analysis of synthetic aperture radar data.

Introduction

The Strait of Gibraltar connects the Atlantic Ocean with the Mediterranean Sea. The vertical density distribution in the oceanic region of the Strait of Gibraltar is characterized by the presence of an upper layer of Atlantic water and of a lower layer of denser Mediterranean water. The mean circulation through the strait is composed of two counterflowing currents: In the upper layer Atlantic water flows eastward, toward the Mediterranean, and in the lower layer Mediterranean water flows westward, toward the Atlantic. The resulting mean exchange flow is mainly modulated by tidal currents and by currents induced by wind and atmospheric pressure variations.

Armi and Farmer [1] performed a detailed analysis of different hydraulic phenomena occurring in the Strait of Gibraltar and of their influence on the exchange flow, which revealed the existence of locations where the flow is hydraulically controlled. These locations are situated inside the Strait of Gibraltar at the Tarifa Narrows, at the Camarinal Sill, and at the Spartel Sill, and outside the Strait of Gibraltar, west of the Spartel Sill. The mean exchange flow through the Strait of Gibraltar was estimated by Bryden et al. [2] by analyzing data from current meter moorings deployed in the strait over almost one year.

In the Strait of Gibraltar, due to the interaction of the semidiurnal tidal flow with prominent topographic features, internal disturbances are generated. Among these, the most frequently observed are quasi-stationary internal disturbances near the Camarinal Sill and eastward propagating internal waves, often ranked in trains of internal solitary waves [3]. As internal waves modulate the sea surface roughness via wave-current interaction, they can also be detected by remote sensing [4]. By analyzing synthetic aperture radar (SAR) data acquired during two flights with an aircraft over the Strait of Gibraltar, Richez [5] was able to observe the evolution of two eastward propagating internal waves. In particular the analysis of the SAR data revealed the existence of strong differences

in several characteristics of the internal waves like, e. g., wave location as function of the semidiurnal tidal phase and wave phase speed, which were ascribed to diurnal inequalities in the semidiurnal tidal currents.

The numerical modeling of the hydrodynamics of the Strait of Gibraltar has been carried out by using, e. g., three-dimensional hydrostatic general ocean circulation models [6] as well as two-dimensional hydrostatic barotropic models [7]. Using a three-dimensional hydrostatic general ocean circulation model, Wang [6] was capable of describing several aspects of the barotropic and baroclinic semidiurnal tidal flow in the Strait of Gibraltar including its diurnal variability and fortnightly modulation. Tejedor et al. [7] carried out numerical simulations aimed at describing the barotropic semidiurnal tides in the Strait of Gibraltar by using a high-resolution, boundary-fitted coordinate model. As a result of this model, detailed cotidal charts and charts of tidal current ellipse parameters were constructed which are in good agreement with observations. In the present paper we investigate the two-layer exchange flow between the Atlantic Ocean and the Mediterranean Sea as well as the barotropic and baroclinic semidiurnal and diurnal tides in the Strait of Gibraltar by using a high-resolution two-layer boundary-fitted coordinate model.

Model

The model used for the description of the hydrodynamics of the Strait of Gibraltar is a two-layer model. The equations which constitute the model are the nonlinear, hydrostatic, shallow-water equations on an f -plane which include interface and bottom friction terms. In the following we denote the vertically averaged velocity and transport vectors by \mathbf{u}_i and $\mathbf{U}_i = \mathbf{u}_i h_i$ ($i = 1, 2$) respectively. The subscripts $i = 1$ and $i = 2$ refer to the upper and lower layer respectively. For the upper layer, the momentum and the continuity equations read:

$$\frac{\partial \mathbf{U}_1}{\partial t} + \nabla \cdot (\mathbf{u}_1 \otimes \mathbf{U}_1) + \mathbf{F} \cdot \mathbf{U}_1 = -g h_1 \nabla \eta_1 - \frac{\kappa_1}{\rho_1} (\mathbf{u}_1 - \mathbf{u}_2) |\mathbf{u}_1 - \mathbf{u}_2|, \quad (1)$$

$$\frac{\partial h_1}{\partial t} + \nabla \cdot \mathbf{U}_1 = 0, \quad (2)$$

while for the lower layer they read:

$$\frac{\partial \mathbf{U}_2}{\partial t} + \nabla \cdot (\mathbf{u}_2 \otimes \mathbf{U}_2) + \mathbf{F} \cdot \mathbf{U}_2 = -g \frac{\rho_1}{\rho_2} h_2 \nabla \eta_1 - g' h_2 \nabla \eta_2 + \frac{\kappa_1}{\rho_2} (\mathbf{u}_1 - \mathbf{u}_2) |\mathbf{u}_1 - \mathbf{u}_2| - \frac{\kappa_2}{\rho_2} \mathbf{u}_2 |\mathbf{u}_2|, \quad (3)$$

$$\frac{\partial h_2}{\partial t} + \nabla \cdot \mathbf{U}_2 = 0. \quad (4)$$

Here ∇ denotes the horizontal Nabla operator, \cdot the scalar product, and \otimes the tensor product. The two-dimensional Coriolis matrix \mathbf{F} is defined as:

$$\mathbf{F} = \begin{pmatrix} 0 & -f \\ f & 0 \end{pmatrix},$$

where f is the Coriolis parameter, h_1 and h_2 are the thicknesses of the upper and lower layer respectively, η_1 is the sea surface displacement, and η_2 the opposite of the distance of the interface from the undisturbed sea surface, ρ_1 and ρ_2 are the water densities in the upper and lower layer respectively, $g' = g(\rho_2 - \rho_1)/\rho_2$ is the reduced gravity, where g denotes the acceleration of gravity, and κ_1 and κ_2 are the interface and bottom friction coefficients, respectively. Note that the densities ρ_1 and ρ_2 , as well as the coefficients κ_1 and κ_2 are assumed to be constant in our model.

The equations, which are discretized on a staggered Arakawa C-grid, are solved by employing an alternating-direction method and a semi-implicit Crank-Nicolson scheme in boundary-fitted curvilinear coordinates. The advective terms are calculated by means of a directional upstream algorithm. For further details about the numerical methods used in this model the reader is referred to the work of Tejedor et al. [7]. In Fig. 1, which refers only to a part of the model domain including the region of the Strait of Gibraltar, the curvilinear grid as well as the bottom topography used in the numerical simulations are presented. The actual Atlantic and Mediterranean open boundaries of the model domain (not shown in Fig. 1) are located approximately at 6.5°W and 3°W respectively. Along these open boundaries, the model is forced by prescribing the sea surface elevation caused by the semidiurnal (M_2 and S_2) and the diurnal (O_1 and K_1) tidal constituents. Radiation conditions for the upper and lower layer transports are moreover employed to minimize reflection. At the closed boundaries a free

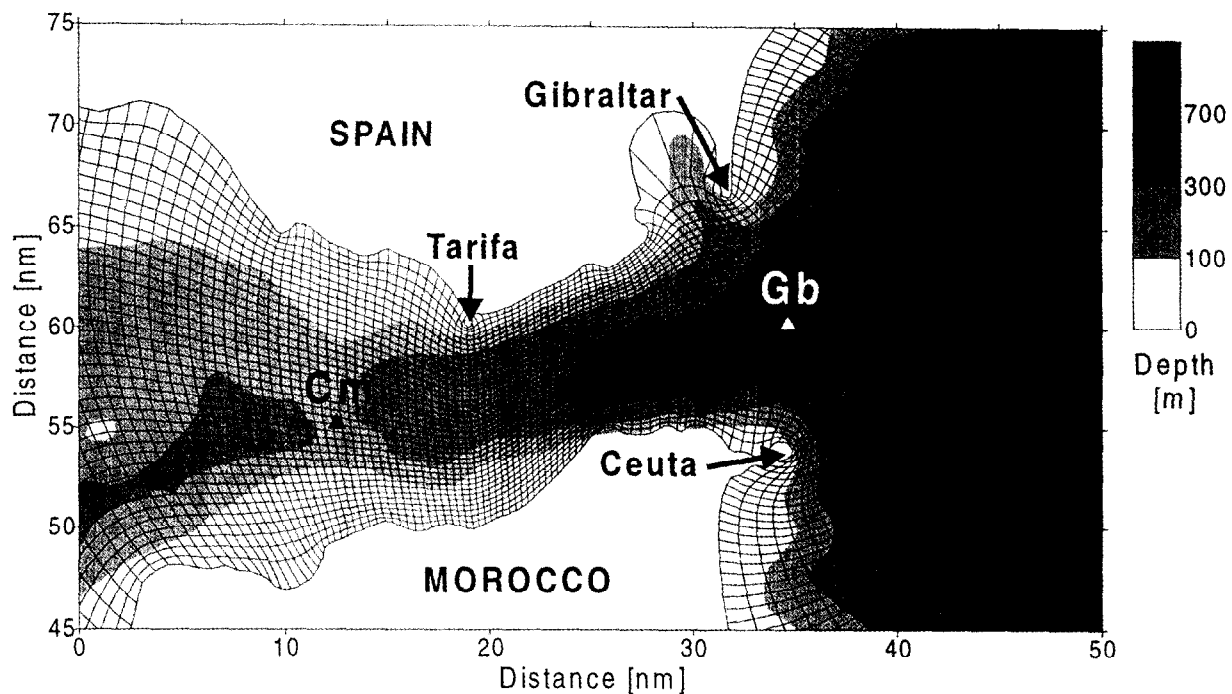


Fig. 1. Bottom topography and computational grid used in the numerical simulations. The gray levels indicate the water depth. The points Cm and Gb mark the locations to which the model results shown in Fig. 4 and Fig. 5 refer.

slip condition for the velocity is applied. The complex hydrodynamics of the Strait of Gibraltar can lead to a local surfacing of the lower layer as well as to a change in the extension of the regions where this layer is present. In this model a special technique for the numerical treatment of movable lateral boundaries is thus implemented, which allows for the description of the temporal and spatial evolution of localized water layers: A layer whose thickness is larger (smaller) than a critical value ϵ (typically a few centimeters) in a certain grid point is considered active (inactive), i. e., the momentum equations are solved (not solved) there. The water column is thus considered as composed of stratified water for those points where two active layers are present and of merely Mediterranean (Atlantic) water for those points where one active lower (upper) layer and one inactive upper (lower) layer are present.

Steady two-layer exchange flow

In this section we present the results of numerical simulations carried out by using the numerical model described in the previous section which are aimed at simulating the main characteristics of the non-tidal exchange flow through the Strait of Gibraltar. For these simulations we used the following model parameters: $\kappa_1=0.5 \text{ kg/m}^3$ and $\kappa_2=5 \text{ kg/m}^3$. We initialized the model by assuming a dam-break setup: The western part of the model domain is filled with Atlantic water ($\rho_1=1027 \text{ kg/m}^3$), its eastern part with Mediterranean water ($\rho_2=1029 \text{ kg/m}^3$). Both water masses, which are separated by a lock, are initially at rest and the sea surface is level. Once the lock is lifted, the light Atlantic water flows as a near-surface jet toward the Mediterranean and the heavier Mediterranean water flows as a bottom-arrested current toward the Atlantic. At the two open boundaries, radiation conditions are implemented which prescribe reference levels for the sea surface displacement as well as for the interface depth. For the sea surface displacement, the reference level is set to zero at both boundaries; for the interface depth, it is set to 450 m at the Atlantic boundary and to 20 m at the Mediterranean boundary. Sensitivity experiments indicate that, as long as during the adjustment phase counterflowing currents evolve which are able to reach the open boundaries, very similar steady states are attained, when realistic values for the reference levels are imposed.

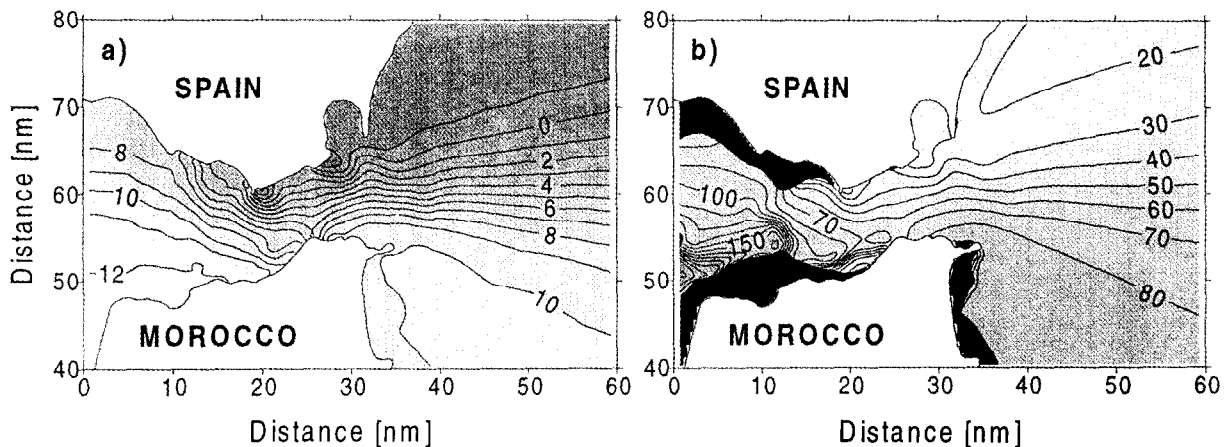


Fig. 2. Steady sea surface displacement (a) and interface depth (b) as simulated by our numerical model. The black areas mark the regions where no lower layer is present. The values of the sea surface displacement are given in centimeters, those of the interface depth in meters.

In Fig. 2 the steady sea surface displacement (a) and the steady interface depth (b) in the Strait of Gibraltar obtained by our model are presented. Along the strait, the mean sea surface elevation decreases toward east, the difference between Cadiz and Malaga (not shown) being about 10 cm. Across the strait, the mean sea surface displacement increases toward south, the difference between the northern and the southern shore being about 5 cm at the western mouth of the Strait of Gibraltar and about 11 cm at the eastern mouth. The steady interface depth decreases toward east and increases toward south. Note the dramatic change in the interface depth near the Camarinal Sill which is an observed feature of the hydrodynamics of the Strait of Gibraltar [1].

In Fig. 3 the steady upper layer (a) and lower layer (b) velocity field are shown, together with the regions where the water flow is supercritical, i.e., where the composite Froude number $G^2 = \mathbf{u}_1^2 / g'h_1 + \mathbf{u}_2^2 / g'h_2$ is larger than 1. The steady velocity field is characterized by the presence of a water flow toward the Mediterranean in the upper layer and toward the Atlantic in the lower layer. The absolute values of the total transport associated with these flows are about $0.7 \times 10^6 \text{ m}^3/\text{s}$ in both layers which closely agrees with the estimates of Bryden et al. [2]. Note that, in several locations within the Strait of Gibraltar, the flow is hydraulically controlled, i.e., $G^2 = 1$. The model results show that these locations are, in general, disconnected. In particular, it is not possible to identify a strait cross-section through which the steady exchange flow is hydraulically controlled across the whole strait.

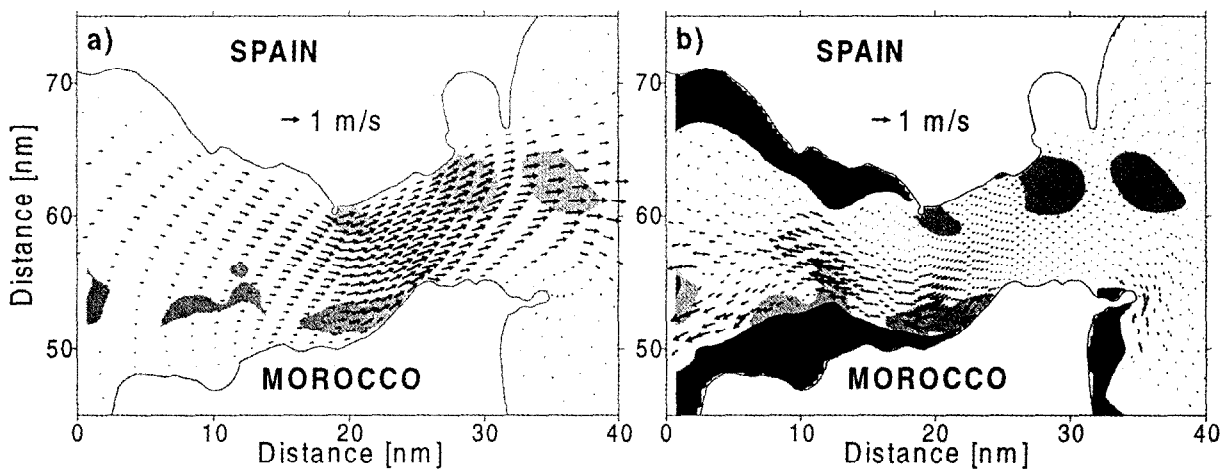


Fig. 3. Steady upper (a) and lower (b) layer velocity. The black areas mark the regions where no lower layer is present. The gray shaded areas mark the regions where the flow is supercritical, i. e., where the composite Froude number is larger than 1.

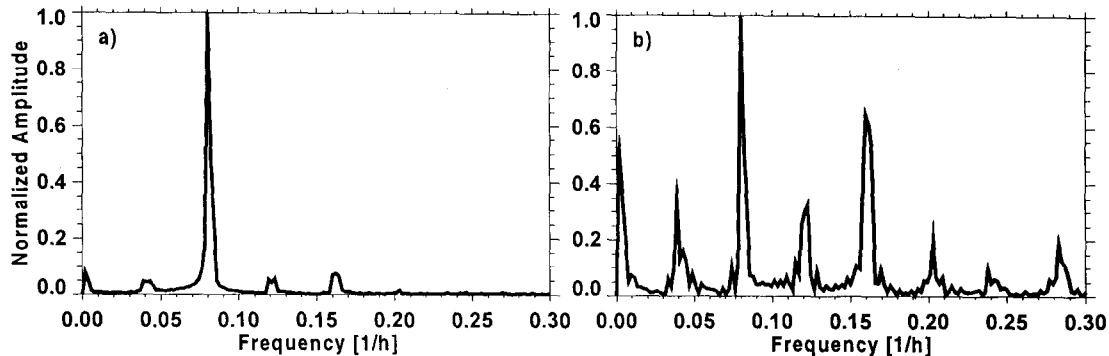


Fig. 4. Fourier transform of the time series of the surface displacement (a) and of the interface depth (b) of a point at the Camarinal Sill (point Cm in Fig. 1).

Tidally induced dynamics

In order to investigate the peculiar features of the hydrodynamics in the Strait of Gibraltar induced by the semidiurnal and diurnal tides we carried out numerical simulations over a neap-spring tidal cycle. The model was initialized by imposing the steady two-layer exchange flow described in the previous section and forced by prescribing the tidal elevation of the sea surface at the two open boundaries. Fig. 4 shows the Fourier transform of the time series of the sea surface displacement and of the interface depth for a point at the Camarinal Sill (point Cm in Fig. 1). While in the time series of the sea surface displacement the semidiurnal signal largely exceeds the other signals, in the time series of the interface depth this signal is of the same order as the fortnightly, the diurnal, the terdiurnal, and the quarter-diurnal ones. The presence of a strong fortnightly signal is a consequence of the fact that, while during neap tide the diurnal average of the interface depth is larger than the mean interface depth, during spring tide it is smaller, their difference being approximately 30 m. The presence of a strong quarter-diurnal signal results from the fact that, within a semidiurnal tidal cycle, an elevation of the interface depth is produced at the Camarinal Sill during maximum westward tidal flow as well as during maximum eastward tidal flow.

Fig. 5 shows the Fourier transform of the time series of the upper and lower layer along-strait velocity component for a point at the eastern mouth of the Strait of Gibraltar (point Gb in Fig. 1). In this case, while in the time series of the lower layer velocity the semidiurnal signal largely exceeds the other signals, in the time series of the upper layer velocity the main signal is the diurnal one. These findings of our numerical simulations are in good agreement with experimental evidence [8].

The diurnal inequalities, which are known to exert a profound influence on the tidally induced internal dynamics in the Strait of Gibraltar [8] are captured by our numerical model. They are particularly evident in the difference between the simulated evolution of two consecutive eastward propagating internal bores as well as in the hydraulics of the region of the Camarinal Sill and of the Tarifa Narrows. The distance traveled by two numerical simulations for spring tide and results obtained from the analysis of the SAR data of Richez [5], which also refer to spring tide, agree reasonably well: In both cases, the difference in the time of release of two consecutive

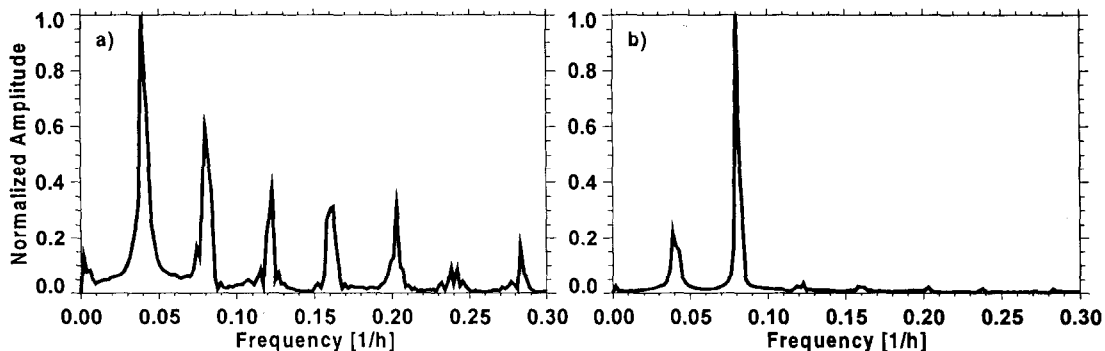


Fig. 5. Fourier transform of the time series of the upper (a) and lower (b) layer along-strait velocity component of a point at the eastern mouth of the Strait of Gibraltar (point Gb in Fig. 1).

consecutively generated eastward propagating internal bores as a function of the semidiurnal tidal phase for spring tide and for neap tide is depicted in Fig. 6. In this figure, the main difference between two consecutively internal bores is approximately 2 h and the difference in the time of their arrival at a certain point west of the Camarinal Sill increases slightly with the distance from the Camarinal Sill. The stars in Fig. 6 refer to generated eastward propagating internal bores consists in the time of their release from the Camarinal Sill and, therefore, in the time of their arrival at the eastern mouth of the strait. A comparison between the results of our data obtained from ERS 1 SAR images which were acquired during different phases of the neap-spring tidal cycle. From these data, a large variability in the tidally induced internal wave field in the Strait of Gibraltar can be inferred, part of which is also found in the results of our numerical model as a consequence of the diurnal variability and fortnightly modulation.

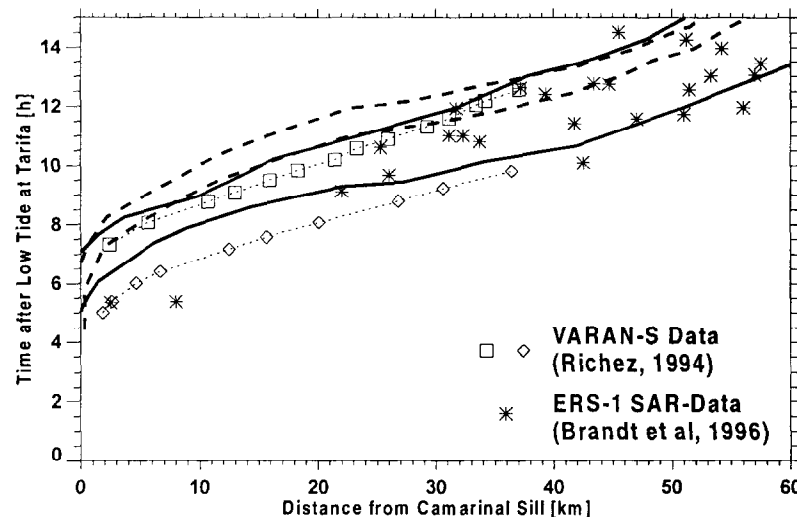


Fig. 6. Space-time diagram delineating the eastward propagation of the leading edge of eastward propagating internal bores through the Strait of Gibraltar. The dotted lines are derived from experimental data obtained from airborne SAR measurements during spring tide [5], the stars denote data obtained from ERS 1 SAR measurements during different phases of the neap-spring tidal cycle [3]. The solid lines refer to the propagation of two consecutive internal bores during spring tide, the dashed lines to the propagation of two consecutive internal bores during neap tide as simulated with our numerical model.

Acknowledgements. This work was partly supported by INTAS, under contract N96-1875, and by the European Commission, under contract MAS3-CT95-0027.

References

- [1] L. Armi and D. M. Farmer, 1988, The flow of Mediterranean water through the Strait of Gibraltar, *Prog. Oceanogr.*, **21**, 1-105.
- [2] H. L. Bryden, J. Candela and T. H. Kinder, 1994, Exchange through the Strait of Gibraltar, *Prog. Oceanogr.*, **33**, 201-248.
- [3] P. Brandt, W. Alpers and J. O. Backhaus, 1996, Study of the generation and propagation of internal waves in the Strait of Gibraltar using a numerical model and synthetic aperture radar images of the European ERS 1 satellite, *J. Geophys. Res.*, **101**, 14,237-14,252.
- [4] W. Alpers, 1985, Theory of radar imaging of internal waves, *Nature*, **314**, 245-247.
- [5] C. Richez, 1994, Airborne synthetic aperture radar tracking of internal waves in the Strait of Gibraltar, *Prog. Oceanogr.*, **33**, 93-159.
- [6] D.-P. Wang, 1993, The Strait of Gibraltar model: internal tide, diurnal inequality and fortnightly modulation, *Deep Sea Res.*, **40**, 1187-1203.
- [7] L. Tejedor, A. Izquierdo, B. A. Kagan and D. V. Sein, 1998, Simulation of the semidiurnal tides in the Strait of Gibraltar, *J. Geophys. Res.*, in press.
- [8] J. Candela, C. Winant, and A. Ruiz, 1990, Tides in the Strait of Gibraltar, *J. Geophys. Res.*, **95**, 7313-7335.

SOME ASPECTS OF SST FRONTS DYNAMICS IN THE SOUTHWESTERN ATLANTIC

D. N. Severov ¹, V. A. Severova ², and M. Blanco ³

Facultad de Ciencias, Universidad de la Republica, Igúa 4225, 11400-Montevideo, Uruguay
E-mail: dima@fcien.edu.uy

Abstract- SW Atlantic SST fronts dynamics are studied from three satellite SST data bases: "METEOR" (1989-1994), "ds277" -Reynolds (1982-1995), and NOAA-AVHRR (1996-1998). SST fronts are analysed and classified: Brazil Current Subtropical Front (20°C), Principal Subtropical Front (18°C), North Subtropical Front (15°C), Subtropical Surface Front (12°C), South Subtropical Front (10°C), Subantarctic Surface Front (7°C), Circumpolar Subantarctic Front (5°C) and Polar Front (3°C). The influence of the atmospheric processes on the formation of mesoscale cyclonic eddies on fronts of the BMC is determined.

1-Introduction

Southwestern Atlantic (SWA) and, first of all, the Brazil-Malvinas (Falkland) currents confluence zone (BMC) is the world ocean western currents extension zone. According to [1], "the South Atlantic stands out as having numerous exceptional features". After [2], the study of water dynamics and fronts in the SWA by satellite data has been widely accepted. Several approaches have been used: [3], [4], and [5] analyzed the variability of temperature fields, [6] analyzed the variability of time and place of SST anomalies, [7] investigated satellite data for the determination of boundary sharp change of color of waters and phytoplankton pigment concentration, [8] analyzed altimetry data for the determination of zones of sharp changes of sea level and currents connected to them, [9], [3], and [10] analyzed the trajectories of surface and deep currents using different buoy systems. The following criteria for the identification of surface SWA fronts by different authors are shown on Fig. 1:

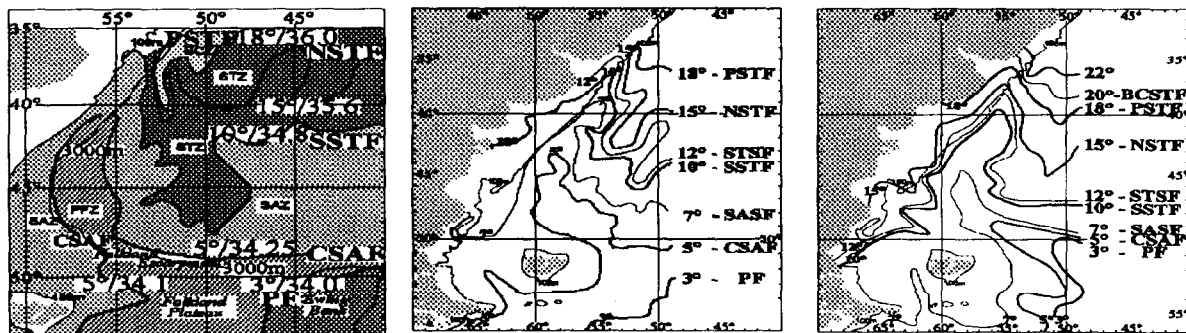


Fig.1 - Schematic representation of the front and interfrontal zone positions in the SWA. Developed from the original scheme presented by [14] (a); Climatic isotherms (b-winter, c-summer) indicating the position of the SST fronts.

1. BCF - Brazil Current Front is the northern boundary of the BMC; it coincides with the Brazil Current Return Flow to the west of 46°-50°W, characterized by [2], [3], [11] [12], and [13] as 21°-22°C, 21°C, 19°-20°C, and 20°C SST, respectively.
2. NSTF - North Subtropical Front coincides to the east of 41°-42°W with the eastern extension of the Brazil Current. This front is designated as BCF on the schemes presented by [11] [12], [14], and as North Subtropical Front by [15]. The characterization of this front agrees with [11] [12]: near 15°C SST and 35.6 salinity in the 0-100 m layer, and the position of the 10°C isotherm and 34.8 isohaline between 300 and 500 m.
3. SSTF - South Subtropical Front as described by [16], [17], [11] [12], and [3], coincides with the northern boundary of the Subantarctic Zone. By [13], it is named as Falkland Escarpment Front (FEF), while [14] and [19], call it STF, and [15] name it South Subtropical Front. This front was characterized by [16] as 9°-10°C SST, and by [11] [12] "the outcrop or near outcrop of the 10°C isotherm at the 9°-11°C temperature range, and very close to the surface 34.8 isohaline at the 34.5-35.1 salinity range".
4. CSAF - Circumpolar Subantarctic Front coincides with the southern border of SAZ and with the northern boundary of PFZ. In the documents of WCRP [19], it has the name of the circumpolar SAF, and on the schemes by other authors it is named SAF. For [20], this front belongs to the ACC system and it is identified by the 4°C isotherm position at 200 m depth. For [21] and [22], the front can be established by the subsurface horizontal temperature gradient change between the 3° and 5°C isotherms.
5. PF - Polar Front coincides with the core of the Antarctic Circumpolar Current and is characterized by the surface 2° -3°C isotherm by [6] and the 34.00 isohaline position by [23].

2- Results

To study SWA thermal fronts we used three independent sources of information: i) monthly composition of satellite SST charts from the Russian "Meteor" system for the period 1989-1994 (60 monthly charts), ii) monthly "ds 277" Reynolds data for the period 1982-1995 (168 monthly charts), and iii) daily NOAA (RSMAS) satellite SST data for the period 1996-1998. The horizontal SST gradients on the basis of the first two data bases, for the region 34°-56°S and 48°-70°W, and for the centres of squares with a 30' step were calculated. The identification of frontal zones and fronts we made by choosing the maximum values of the horizontal SST gradients ($> 1^{\circ}\text{C}/100\text{ km}$ and $> 1.5^{\circ}\text{C}/100\text{ km}$, respectively) when the horizontal SST gradients followed the courses of SST isotherms. To determine concordance, space-time analysis was performed for the 60-monthly distributions of the SST gradients on "Meteor" data and the 168- monthly distributions of the "Reynolds data", separately for the spectrum of gradient values from $0.5^{\circ}\text{C}/100\text{ km}$ up to $4.0^{\circ}\text{C}/100\text{ km}$. The daily NOAA (RSMAS) satellite data using the criterion of the position of the thermal fronts and interfrontal zones for 1996-1998 were investigated.

Here we analysed details of the formation of cyclonic and anticyclonic mesoscale eddies, the atmospheric processes, and discharge of low salinity shelf waters, related with and front dynamics previously defined in the Brazil Current Frontal System. One of the goals of this study is to adapt the use of satellite SST for the identification of thermal fronts. Therefore, the criteria chosen here for the identification of fronts and frontal zones based on satellite SST data, are in accordance with previously published values of horizontal gradients of SST(Gt). According to [24], [12], and [26], (Gt) on the fronts of the Subantarctic Frontal Area, and the Brazil-Malvinas Frontal Area (BMC) are between $1.42^{\circ}\text{C}/100\text{ km}$ and $4.65^{\circ}\text{C}/100\text{ km}$ up to $10^{\circ}\text{C}/100\text{ km}$ ($10^{-4}\text{C}/\text{m}$). Based on monthly "METEOR satellite SST data and "ds277" - Reynolds data, for the location of the frontal zone and front values (Gt) we calculated $> 1^{\circ}\text{C}/100\text{ km}$ and (Gt) $> 1.5^{\circ}\text{C}/100\text{ km}$, respectively. This criterion coincides with the one postulated by [25]: the value of (Gt) for frontal zones must be one order of magnitude greater than the average meridional climatic gradient of temperature ($< 0.002^{\circ}\text{C}/\text{km}$). The isotherms near to which the maximum horizontal SST gradients are formed, were determined statistically on the basis of the two independent data bases Fig. 2. The spatial-time analysis was carried out for various horizontal gradients (Gt) values: $> 0.5^{\circ}\text{C}/100\text{ km}$, $> 1^{\circ}\text{C}/100\text{ km}$, $> 1.5^{\circ}\text{C}/100\text{ km}$, $> 2^{\circ}\text{C}/100\text{ km}$, $> 2.5^{\circ}\text{C}/100\text{ km}$, $> 3^{\circ}\text{C}/100\text{ km}$, and $> 4^{\circ}\text{C}/100\text{ km}$. Histograms and charts of the gradient distribution show the conformity of the horizontal gradients to the determined isotherms position only for the (Gt) values from $1^{\circ}\text{C}/100\text{ km}$ to $2^{\circ}\text{C}/100\text{ km}$ and more. For smaller values, the (Gt) identifies the uniform frontal zone for the BMC, and Malvinas and Antarctic Circumpolar currents. For high values, the (Gt) identifies only the convergence of the different values of the

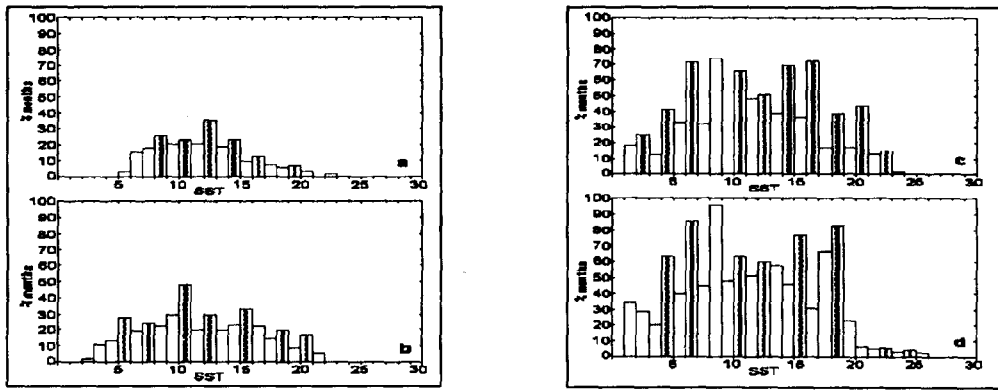


Fig. 2 - Histogram of distribution of horizontal gradients SST $> 2^{\circ}\text{C}/100\text{ km}$ - (a), (b) and $> 1^{\circ}\text{C}/100\text{ km}$ - (c), (d), based upon the "Meteor" satellite data (a, c) for the period 1989-1994 (60 months), and "ds 277"-Reynolds (b, d) for the period 1983-1996 (168 months).

SST isotherms at BMC. For horizontal SST gradient values $> 1.5^{\circ}\text{C}/100\text{ km}$, the values of temperatures for thermal fronts in SWA are established. The agreement of the thermal fronts with the 20, 18, 15, 12, 10, 7, 5 and 3°C isotherms, independent of time, is found. Fig. 1b,c shows these values for climatic isotherms and their positions characterize SST fronts in the SWA in winter (1b) and in summer (1c): Brazil Current Subtropical Front (BCSTF- 20°), Principal Subtropical Front (PSTF- 18°), North Subtropical Front (NSTF- 15°), Subtropical Surface Front (STSF- 12°), South Subtropical Front (SSTF- 10°), Subantarctic Surface Front (SASF- 7°), Circumpolar Subantarctic Front (CSAF- 5°), and Polar Front (PF- 3°). Depending on season, we suggest the Brazil Current Front can be any of the subtropical fronts: BCSTF, PSTF, and NSTF or some of them can overlap.

The spatial-temporal analysis of dynamics of the SST fronts: PSTF- 18°C , NSTF- 15°C , STSF- 12°C , SSTF- 10°C , SASF- 7°C , and CSAF- 5°C was carried out using monthly mean values. In this paper it is possible present the most general characteristics of the SST front dynamics only. Fig. 3 indicates the variability of positions of the three SST fronts (PSTF- 18°C , SSTF- 10°C , and CSAF- 5°C) inside their respective front zones. Maximum northern and southern limits of these zones for the studied area of the Southwestern Atlantic

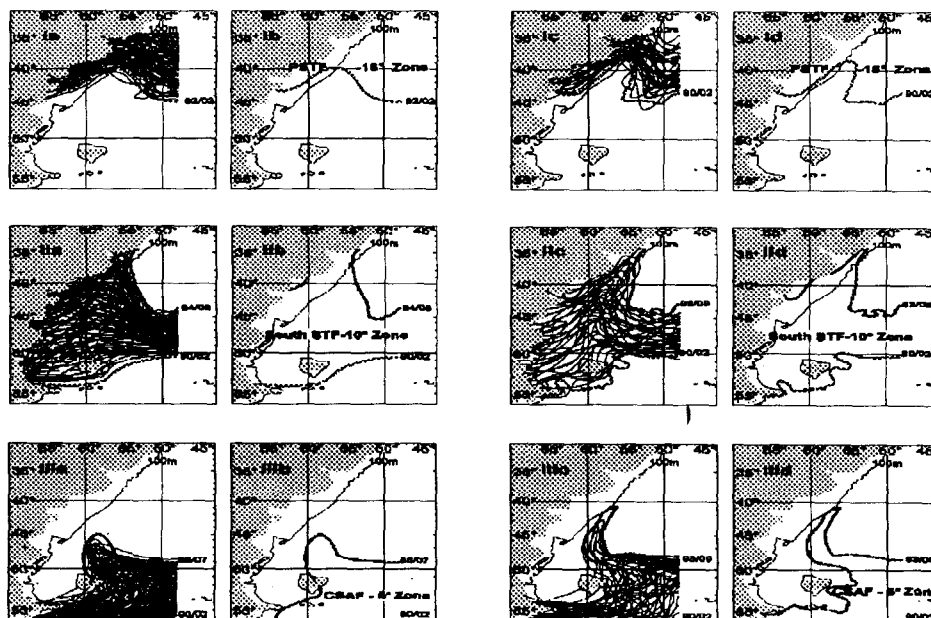


Fig.3 - Dynamics of the PSTF- 18°C (Ia), SSTF- 10°C (IIa), and CSAF- 5°C (IIIa), and position of the PSTF (Ib), SSTF (IIb), and CSAF zones (IIIb), from "ds 277"-Reynolds (a, b), and SST "Meteor" (c, d) data.

(34-56°S, and 48-70°W) are marked by positions of SST fronts by specific dates (year/month). The position of the fronts and their critical sites are shown using both data bases. Some differences of positions and dates can be explained by the varying data periods and by the processing methods applied. Annual and interannual variability of the position of the SST fronts, is accompanied by significant spatial-temporal changes of the SST gradients. Three quasi-constant areas with the maximum gradients exist: BMC, over the slope of Patagonian and Malvinas Islands shelves, and eastward of 55°W between 42-52°S. Depending on the season, these areas are formed on various subantarctic and subtropical fronts. It was established that the maximum values of the SST gradient ($>5^{\circ}\text{C}/100\text{ km}$) correspond to the Brazil Current Front and it can be any of the subtropical deep fronts. In summer, it can be either BCSTF-20°C, or PSTF-18°C, or NSTF-15°C, or some of them can overlap. In winter, the BCF can be formed on PSTF-18°C, or NSTF-15°C, or STSF-12°C, or some overlap can be seen.

Aiming to classify the SST fronts, the formation of some meso-scale peculiarities of dynamics of waters in the SWA was studied for 1996-1998. Fig. 4 shows a IR image (4a) of SST data (06.20.1996), and in relation with

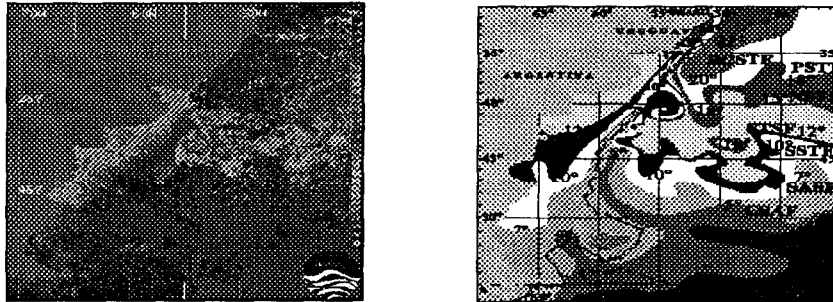


Fig. 4 – Position of a cyclonic eddy (a) on the Malvinas side of the BMC (RSMAS data for 06.20.1996), and (b) a 7-day (from 06.19 to 06.26) schematic composition of the SST fronts and frontal zones positions.

it a composition scheme (06.19 and 06.26.1996) of the SST front and interfrontal zone positions (4b). On the image and scheme, the cold eddy, formed in the Malvinas part of the BMC and on shallow SST fronts, is shown: STSF-12°C and SSTF-10°C. The generation of cyclonic eddies must be accompanied by sharp increase of the surface current velocities and by formation of eddy system of "fungous" (mushroom-like) structure [27]. We suppose the fungous vortices are forced by atmospheric processes, which are expressed in winter. These eddy systems can contribute to an increase of subantarctic water transport, penetration of the Malvinas current to the north, and to growth of discharge of the low salinity water to the open ocean. During the duration of the eddy (8 days), the eastward displacement of the BMC was about 200 miles, and the horizontal SST gradients increased from 3-4°C up to 7-10°C/100 km. In agreement with [8], such zone shifts of the BMC must be accompanied by the formation of the northward extension of the Malvinas Current and fast displacement of current to the southern coast of Brazil. SST front dynamics shows that such displacement during the existence of the cyclonic eddy was about 350 miles.

[28] have shown, that after the passage of powerful atmospheric polar fronts, the period of formation of cyclonic cold eddies in the Malvinas part of the BMC in June 1996 (Fig. 5) and June 1997, were accompanied by a complete reversal of the wind direction (northward/southward). We suppose the atmospheric circulation forces the ocean near-surface dynamics when the strong wind of average velocity higher than 10 m/s blows in the low atmosphere for more than 5-6 days. In 1996 and 1997, cyclonic eddies were generated in the confluence zone at the same month (June). In 1998, the cold eddies were formed on the BMC by active atmosphere processes in August- September.

The coastal observations for the same period indicate a sharp decrease of the salinity of the shelf waters (i.e. on station Isla de Flores at the Rio de la Plata, salinity decreased from 20 to 1.00 ‰). The mechanism of the low salinity water discharge from the Rio de de la Plata to the shelf, and from there to the open ocean has not yet been investigated. The influence of these waters in the thermohaline processes in the Brazil-Malvinas Confluence Zone are poorly known. On the other hand, the increase of the thermohaline gradients on fronts should strengthen the western boundary extension [8], and the advection of the low salinity shelf water on the BMC. The dynamics of the SST fronts become a necessary component of the study of the redistribution and transport of the low salinity water in coastal, shelf, and oceanic subregions of the Brazil Current Frontal

System. A number of authors presented data on the formation of anticyclonic meanders and warm eddies on Brazil Current West Branch (BCWB) [2], [11] [12], [3], [24], [29], and [30]. They observed warm core eddies are formed at the southern boundary of the meander at approximately one week-intervals. The life cycle of the eddies at mesoscale, from 120-180 km up to 300-400 km, is between several weeks and 1-2 months.

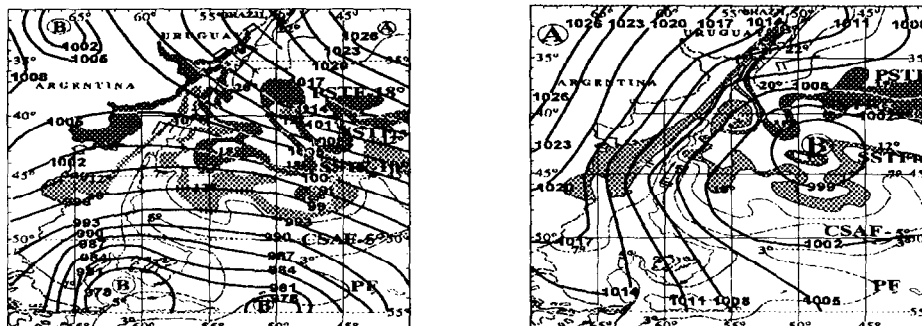


Fig. 5 – Synoptic situation before (a) and after (b) the cold eddy formation on the BMC fronts.

[29] showed two warm eddies ("Asp", and "Anthony"), limited approximately by the SST isotherm 12°C and isohaline 35.1, corresponding to the characteristics of the Subtropical Surface Front (STS-12°C) according to our terminology. If the thermocline depth is accepted as a rough estimate of the eddy depth, outside of BCWB such a shallow front will limit warm eddies up to 300-400 m [29]. Fig. 5b presents such a warm eddy: it was separated from the southern boundary of the meander (06.13.1996) a week before a cyclonic eddy was observed in the Malvinas part of BMC. Over almost three weeks, the boundary of the warm eddy was NSTF-15°C, which is characterized by a depth thermohaline frontal section up to 500-600 m [11] [12]. The different values of the depths of frontal sections of the SST fronts could be used as indicators of the vertical sizes of eddies. Thus, the transport of heat and salt by such eddies can be roughly estimated by satellite SST information.

3- Summary

We tried to show that indicators of the SST fronts are determined analyzing the data published by many authors and the reported results are coherent with the most important previously published data and satellite information. We suggest a nomenclature for SST fronts in the SWA. The usefulness of the satellite NOAA-AVHRR data for the construction of composite serial schemes of SST fronts and interfrontal zones is demonstrated. Based on these schemes, we suggest the analysis of the front, frontal and interfrontal zones time-space dynamics. The present investigation describes an example of atmospheric forcing on ocean dynamics, in the BMC region. A more systematic approach is need, in order to characterize the phenomenology and dynamics of the ocean-atmosphere coupling. It seems clear that the kind of event described, even if it could be exceptional for its characteristics, constitutes one of the mechanism that promotes low salinity water flow from the Río de la Plata estuary. The formation of a cyclonic eddy in the BMC zone is an important product of this interaction, with consequences on the fluxes of materials from the shelf water to the open ocean. The depths of the fronts can be used for a rough estimation of the vertical and horizontal structure of eddies having no longer contact with BMC. The reported results are being used in order to develop an automated monitoring system of the water dynamics and fisheries in the SWA.

References

- [1] A. L. Gordon, 1994. South Atlantic's role in the Global Circulation. The South Atlantic: Present and Past Circulation. Symposium, Bremen, Germany, 52, 55.
- [2] R. Legeckis and A. L. Gordon, 1982. Satellite observations of the Brazil and Falkland Currents - 1975 to 1976 and 1978. Deep Sea Res., 29, 375-401.
- [3] D. B. Olson, G. P. Podestá, R. H. Evans and O. B. Brown, 1988. Temporal variations in the separation of Brazil and Malvinas Currents. Deep Sea Res., 35, 1971-1990.

- [4] G. P. Podestá, O. B. Brown and R. H. Evans, 1991. The annual cycle of satellite-derived sea surface temperature in the Southwestern Atlantic Ocean. *J. Clim.*, 4, 457-467.
- [5] C. Provost, O. Garcia and V. Garçon 1992. Analysis of Satellite Sea Surface Temperature Time Series in the Brazil-Malvinas Current Confluence Region. *J. Geophys. Res.*, 97, 17841-17858.
- [6] W. B. White and R. G. Peterson, 1996. An Antarctic Circumpolar wave in surface pressure, wind, temperature, and sea ice extent. *Nature*, 380, 699-702.
- [7] D. B. Olson, G. L. Hitchcock, A. J. Mariano, C. J. Ashjian, Ge Peng, R. W. Nero and G. Podesá, 1994. *Oceanogr.*, 7, 2, 52-60.
- [8] G. Goni, S. Kamholz, S. Garzoli and D. Olson, 1996. Dynamics of the Brazil-Malvinas Confluence based on inverted echo sounders and altimetry. *J. Geophys. Res.*, 101, C7, 16273-16289.
- [9] A. R. Piola, H. A. Figueroa and A. A. Bianchi, 1987. Some aspects of the surface circulation south of 20°S revealed by First GARP Global Experiment drifters. *J. Geophys. Res.*, 92, 5101-5114.
- [10] N. G. Hogg, 1997. The deep Basin experiment-status and accomplishments, WOCE Atlantic Workshop, France.
- [11] G. I. Roden, 1986. Thermohaline fronts and baroclinic flow in the Argentine Basin during the austral spring of 1984. *J. Geophys. Res.*, 91, 5075-5093.
- [12] G. I. Roden, 1989. The vertical thermohaline structure in the Argentine Basin, *J. Geophys. Res.*, 94, 877-896.
- [13] Y. Ikeda, G. Siedler and M. Zwierz, 1989. On the variability of Southern Ocean front location between southern Brazil and the Antarctic Peninsula. *J. Geophys. Res.*, 94, 4757-4762.
- [14] L. Stramma and R. G. Peterson, 1990. The South Atlantic Current. *J. Phys. Oceanogr.*, 20, 846-859.
- [15] I. M. Belkin, 1994. Frontal Structure of the South Atlantic. *The South Atlantic: Present and Past Circulation, Symposium, Bremen, Germany*, 52, 19.
- [16] H. U. Sverdrup, M. V. Johnson and R. H. Fleming, 1942. *The Oceans, Their Physical Chemistry and General Biology*. Prentice-Hall, New York, 1087 pp.
- [17] M. S. McCartney, 1977. Subantarctic Mode Water, in: *A Voyage of Discovery*, edited by M. Angel and Elmsford, pp. 103-109, Pergamon Press.
- [18] R. G. Peterson and L. Stramma, 1991. Upper-level circulation in the South Atlantic Ocean. *Prog. Oceanogr.*, 26, 1-73.
- [19] World Climate Research Program (WCRP), 1985. *General Circulation of the Southern Ocean: Status and Recommendations for Research*, WCP-108, WMO/TD, 26, Geneva.
- [20] R. G. Peterson and T. Whitworth, 1989. The Subantarctic and polar fronts in relation to deep water masses through the Southwestern Atlantic. *J. Geophys. Res.*, 94, 10817-10838.
- [21] H. A. Sievers and W. J. Emery, 1978. Variability of the Antarctic Polar Frontal Zone in Drake Passage-summer 1976-1977, *J. Geophys. Res.*, 83, 3010-3022.
- [22] J. R. E. Lutjeharms and H. R. Valentine, 1984. Southern Ocean thermal fronts south of Africa, *Deep Sea Res.* 31, 1461-1475.
- [23] A. L. Gordon, D. T. Georgi and H. W. Taylor, 1977. Antarctic Polar Front zone in the Western Scotia Sea - Summer 1975. *J. Phys. Oceanogr.* 7, 309-328.
- [24] S. Garzoli and A. Bianchi, 1987. Time-space variability of the local dynamics of the Malvinas-Brazil Confluence as revealed by inverted echo sounders. *J. Geophys. Res.*, 92, 1914-1922.
- [25] K. N. Fedorov, 1983. Physical nature and structure of the ocean fronts, *Hidromet*, (in Russian), 295 pp.
- [26] A. A. Bianchi, C. F. Guilivi and A. R. Piola, 1993. Mixing in the Brazil-Malvinas Confluence. *Deep Sea Res.*, 40, 7, 1345-1358.
- [27] K. N. Fedorov, A. I. Ginzburg and A. G. Kostianoy, 1989. Modelling of "mushroom-like" currents in a laboratory tank with rotating homogeneous and stratified fluids. *Proc. 20, Int. Liege Colloq. Ocean Hydrodyn. "Mesoscale/synoptic coherent structures in geophysical turbulence"*, J. C. J. Nihoul, B. M. Jamart (Eds.), Amsterdam, Elsevier, 691-700.
- [28] V. A. Severova and D. N. Severov, 1997. On aspect of the fresh water discharge in the Río de la Plata estuary to the open ocean, VII COLACMAR, São Paulo.
- [29] A. L. Gordon, 1989. Brazil-Malvinas Confluence-1984. *Deep Sea Res.*, 36, 359-384.
- [30] S. Garzoli and Z. Garraffo, 1989. Transports, frontal motions and eddies at the Brazil-Malvinas Currents confluence, *Deep Sea Res.*, 36, 681-703.

Transport of Fine Suspended Matter in the Coastal Zone by Mesoscale Currents

G.I.Shapiro, T.M.Akivis, N.N.Pykhov and S.M.Antsyferov

P.P.Shirshov Institute of Oceanology,
117851, Moscow, Russia, Nakhimovsky prospect, 36,
(e-mail: shapiro@sio.rssi.ru)

Abstract: A semi-analytical model is developed for simulating the transport of fine suspended particulate matter (SPM) in the shelf/slope zone by mesoscale currents in the bottom boundary layer (BBL). The model takes into account multiple deposition/resuspension events and is forced by the current that is prescribed outside the BBL. Vertical profiles of horizontal velocity and SPM concentration are calculated analytically in a zero order approximation, i.e. by neglecting horizontal inhomogeneities within the BBL in comparison to vertical variability of parameters. Then these profiles are used to calculate horizontal fluxes for the depth integrated advection-diffusion problem that is solved numerically. The erosion/resuspension flux at the bottom is taken in the form $E = M(\tau - \tau_0)$, where $\tau = \tau(x, y, t)$ is variable bottom stress, M and τ_0 are empirical constants. The model is run to simulate SPM transport by various types of mesoscale currents including cyclonic and anticyclonic eddies and a meandering along-shore current. It was found that because of strong non-linearity of the problem a small variability in the strength of the current results in a great difference of erosion and sedimentation rates. Mesoscale eddies moving along the continental slope produce deposition and erosion zones extended in the direction of their propagation. This mechanism produces both downslope and upslope migration of sediments.

1. Introduction

It is expected that human activity related to raw material exploitation on the sea floor could introduce some changes in the natural process of sedimentation. The situation in the oil and market forces the exploration and exploitation of hydrocarbon deposits in the ocean at greater and greater depths. A good example is future development of oil industry in the East-South Barents Sea [1]. Another example of industrial activity is arranging long pipelines across the Black Sea. Present oil prices economically limit the feasibility of large-scale industrial activity in the Arctic. This stagnation phase gives time for carrying out research on precautionary outer shelf/continental slope environmental protection. From environmental point of view it is especially important to be able predicting sediment and related pollutant transport in the onshore-offshore direction.

Processes of sand migration and beach erosion under action of wind waves have been widely studied in the surf zones within the typical water depth range 0-15 m [2,3,4]. Despite some progress in recent years [5,6,7], transport of suspended particulate matter (SPM) at greater depths is much less understood. Further of the coastline the bottom is mainly covered by fine sediments rather than by sand. It is too deep for wind waves to penetrate to the bottom in intermediate and outer shelf and continental slope. Large-scale currents flow mainly along contours of constant depth and are not able to cross the shelf edge because of geostrophic constraints. Other physical process could be responsible for sediment migration in these regions. Potential carriers are mesoscale currents such as eddies and meanders of along slope current, tides, swell and internal waves.

This paper focuses on transport effects by mesoscale currents. Typical examples are mesoscale eddies that have been repeatedly observed both on shelves [8] and continental slopes [9]. These eddies have maximum orbital velocities of the order of 20 cm/s and diameters of about 10-30 km. In the following sections, a model is

developed that describes both horizontal fluxes of SPM and deposition/erosion processes on the sea floor. There is a great variety of physical characteristics that influence erosion of sediments. Many of them are unknown and need specialist experiments to be quantified. The aim of this paper is to reveal main features of the SPM transport in the bottom boundary layer. For this reason the model is constructed as simple as possible to provide adequate description of the main parameters rather than to go in much details which are related to a specific region or a season of the year.

2. Model description

The model simulates erosion, propagation, and deposition of fine sediments forced by mesoscale currents in the Bottom Boundary Layer (BBL). While the model predicts 3D parameters of suspended particulate matter (SPM) plume, emphasis is made on evolution of bulk properties such as depth integrated SPM mass, total bottom sediment flux and total mass of eroded or deposited matter. Boundary layer approximation is used that implies that vertical gradients of parameters are much greater than horizontal ones. The influence of vertical density stratification within BBL on near bottom currents is neglected.

Taking into account that inertial forces in the BBL are small compared to Coriolis force and friction, the momentum equations in the BBL are written as follows

$$\frac{\partial u}{\partial t} - fv = -\frac{1}{\rho} \frac{\partial p}{\partial x} + K_z \frac{\partial^2 u}{\partial z^2}, \quad (1)$$

$$\frac{\partial v}{\partial t} + fu = -\frac{1}{\rho} \frac{\partial p}{\partial y} + K_z \frac{\partial^2 v}{\partial z^2}. \quad (2)$$

The equation for the distribution of suspended matter is

$$\frac{\partial c}{\partial t} + \frac{\partial uc}{\partial x} + \frac{\partial vc}{\partial y} + \frac{\partial (w - w_s)c}{\partial z} = K_c \frac{\partial^2 c}{\partial z^2}, \quad (3)$$

where f is Coriolis parameter, K_z and K_c are turbulent vertical friction and diffusion coefficients. Boundary conditions at the bottom are

$$u = v = w = 0, \quad \tau = C_d(u_f^2 + v_f^2), \quad F_{zc} = E - D, \quad \text{at } z = b(x, y) \quad (4)$$

where $F_{zc}(x, y, z, t) = (w - w_s)c - K_c \frac{\partial c}{\partial z}$ is the vertical component of the SPM flux, E is the erosion rate $E(x, y, t) = M(\tau(x, y, t) - \tau_0)$ at $\tau > \tau_0$, $E = 0$ at $\tau < \tau_0$ [10], $D(x, y, t) = w_s c_b$ is the deposition rate, M and C_d are constants, c_b is the near-bottom SPM concentration, $\tau = K_z \left[\left(\frac{\partial u}{\partial z} \right)^2 + \left(\frac{\partial v}{\partial z} \right)^2 \right]$ is the bottom stress due to near-bottom current, τ_0 is the erosion/resuspension threshold stress, w_s is the settling velocity, $z = b(x, y)$ is the bottom elevation above a reference plane.

The model is forced by the current above the BBL so that the current velocity (u_f, v_f) or its geopotential $\Phi(x, y, t, z_f)$ at a depth level z_f above the BBL are prescribed. Above the BBL the SPM flux is taken zero:

$$F_{zc} = 0 \text{ at } z \geq z_f. \quad (5)$$

For mesoscale currents the typical evolution time is greater than the pendulum period $1/f$ so that the first term in Eqs. (1,2) can be neglected and the reduced Eqs. (1,2) have an analytical Ekman-style solution

$$u + iv = \frac{i(\Phi_x + i\Phi_y)}{f} \left[1 - \exp\left(-\frac{(1+i)(z-b(x,y))}{h_E}\right) \right], \quad (6)$$

where Φ_x, Φ_y are horizontal derivatives of the geopotential, $h_E(x,y,t) = \frac{2K_z}{f}$ is Ekman scale,

$i = -1$. The value of Ekman scale is calculated from the second equation (4) yielding $h_E = 2(u_f^2 + v_f^2)C_D / f$. We assume the following relation between vertical diffusivity and friction coefficients $K_c = rK_z$, $r = \text{const}$.

Integration of Eq (3) over vertical from the bottom to z_f yields

$$\frac{\partial}{\partial t} \int c dz + \frac{\partial}{\partial x} \int u c dz + \frac{\partial}{\partial y} \int v c dz = M(\tau - \tau_0) - w_s c_b, \quad (7)$$

where c_b is the SPM concentration immediately above the bottom.

To complete the equations we need to express the vertical distribution of SPM in terms of its bottom concentration that can be obtained in different ways. For the present study we use the fact that under mesoscale currents the balance of SPM concentration in the BBL is governed mainly by upward-downward vertical fluxes. In the zero order approximation we neglect temporal and horizontal derivatives in Eq.(3) and use the boundary condition (5) to obtain

$$c(x, y, z, t) = c_b(x, y, t) \exp\left(-\int_b^z \frac{(w_s - w)}{K_c} dz\right). \quad (8)$$

If we adopt a widely used assumption $w_s \gg w$ (see e.g. [6]) then integrals in Eq.(7) are rewritten in terms of m , the total mass of SPM over a unit bottom square, as follows

$$\begin{aligned} \int_b^{z_f} u c dz &\approx -\frac{m}{f} A[\Phi_x + (2\beta + 1)\Phi_y], & \int_b^{z_f} v c dz &\approx \frac{m}{f} A[\Phi_x(2\beta + 1) - \Phi_y] \\ \int_b^{z_f} c dz &\approx c_b h_d = m, & A &= \frac{\beta}{[(\beta + 1)^2 + \beta^2]}, & h_d(x, y, t) &= \frac{K_c}{w_s}, & \beta(x, y, t) &= \frac{h_d}{h_E}. \end{aligned} \quad (9)$$

In deriving Eqs(9) it is taken into account that both Ekman scale, h_E , and vertical diffusion scale, h_d , are smaller than the total water depth, the thickness of the BBL is $h_{BBL} = \max(h_E, h_d)$, and free stream depth level, z_f , is located above the BBL: $z_f - b > h_{BBL}$. Substitution of Eqs. (9) into (7) yields one diffusive-advective equation for one unknown variable, m .

$$\frac{\partial}{\partial t} m - \frac{1}{f} \frac{\partial}{\partial x} \{m A[\Phi_x + (2\beta + 1)\Phi_y]\} + \frac{1}{f} \frac{\partial}{\partial y} \{m A[\Phi_x(2\beta + 1) - \Phi_y]\} = E - w_s \frac{m}{h_d}. \quad (10)$$

The right hand side of eq (10) is the total SPM flux at the bottom, positive values corresponding to

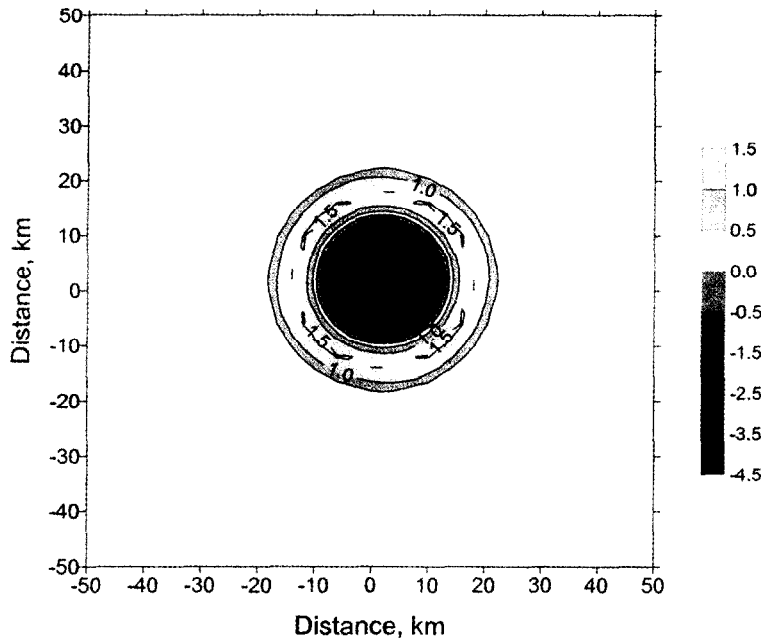


Fig.1a. Near bottom vertical SPM flux, $E-D$, produced by a stationary cyclone. Units are $10^{-6} \text{ g}/(\text{cm}^2 \text{ sec})$.

$2 \cdot \text{s}^{-1}$. As the thin surface layer of such sediments is usually poorly consolidated it is reasonable to take τ_0 and $M\tau_0$ for calculation close to the lower end of the ranges. The following constants were taken throughout:

$$C_D = 2.5 \cdot 10^{-3},$$

$$f = 1.0 \cdot 10^{-4} \text{ sec}^{-1}, \quad \tau_0 = 1.1 \text{ din} \cdot \text{cm}^{-2}, \quad w_s = 5 \cdot 10^{-3} \text{ cm} \cdot \text{s}^{-1},$$

$$M\tau_0 = 5 \cdot 10^{-6} \text{ g} \cdot \text{cm}^{-2} \cdot \text{s}^{-1}$$

[12,13,14]. The model was forced by idealised currents whose parameters were taken typical for mesoscale eddies e.g. in the Black Sea.

(i) Non-moving stationary cyclonic eddy. Geopotential in the free stream above the Ekman layer has a Gaussian shape. Maximal orbital velocity is 25.5 cm/s at radius of 20 km. The values of the Ekman scale and vertical diffusion length scale depend on distance from the centre of the eddy and range from zero at the periphery to 9 m (Ekman scale) and 8.2m (diffusivity scale).

prevailing erosion. After solving this equation numerically, vertical distribution of concentration is calculated from (9) and (8). The total mass of eroded/deposited material is obtained by integration the RHS of eq (10) over time. Numerical code used for solution of eq. (10) is similar to that described in [11] and is based on direction splitting method and enhanced Lax-Vendroff scheme for advection.

3. Results

A few model cases were considered that differ mainly in the forcing current pattern: (i) non-moving cyclone, (ii) non-moving anticyclone, (iii) meandering stream current, and (iv) an anticyclonic eddy embedded in an along-slope current. For natural fine sediments the values of τ_0 and $M\tau_0$ are in the range of $\tau_0 = 1 \div 16 \text{ din} \cdot \text{cm}^{-1}$ and $M\tau_0 = 10^{-6} \div 5 \cdot 10^{-5} \text{ g} \cdot \text{cm}^{-2}$

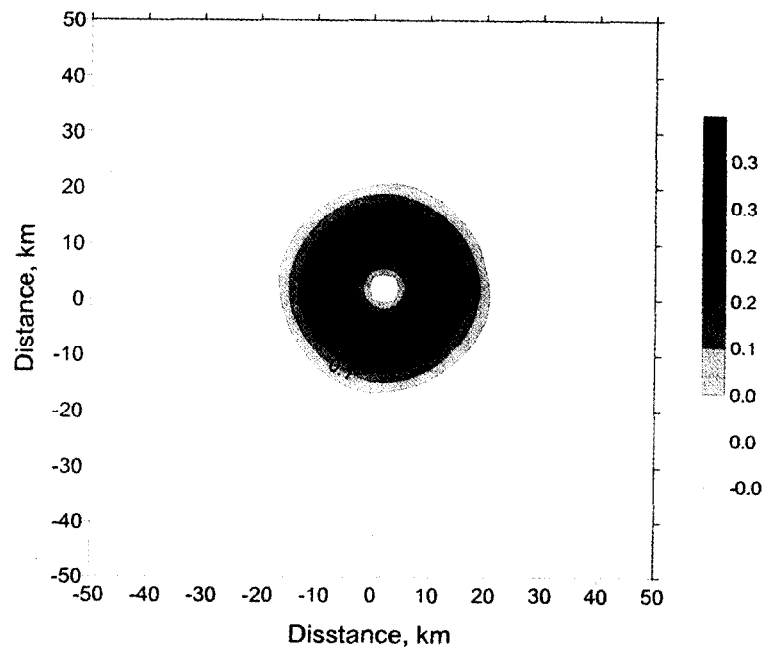


Fig.1b. Mass of SPM, m , over unit square produced by a stationary cyclone. Units are g/cm^2 .

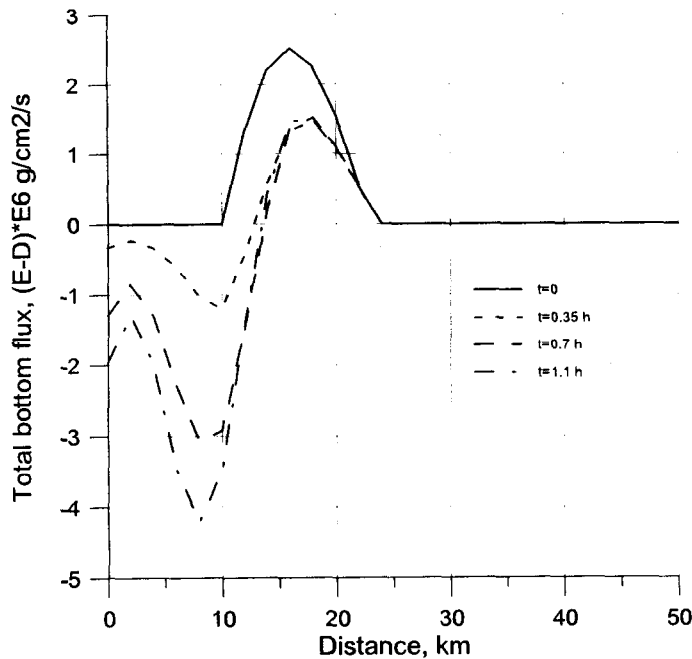


Fig.1c. Contour plot of total near bottom SPM flux, $E-D$, at different times for a cyclone.

The eddy starts rotating in the fluid with zero SPM concentration so that the only source of SPM is the resuspension of sediments from the bottom. Erosion is most intensive in the regions where free stream velocities are highest. Because of frictionally induced secondary circulation, the fluid particles in the bottom Ekman layer deviate from the circular anticlockwise rotation to the left. The horizontal flux of SPM has an inward component, and maximum concentration of SPM is found at a smaller radius than maximum velocity. The SPM particles fall onto the bottom in the inner area of the eddy. They are not resuspended there because the actual shear stress at the bottom is less than the threshold value. At the initial stage the total amount of SPM increases because of prevailing bottom erosion, then deposition becomes more intensive and an equilibrium between overall erosion and deposition is reached at $t=3$ days.

Fig.1a shows a contour plot of total (erosion - deposition) vertical SPM flux at the bottom. Dark grey areas mark downward total flux and the light grey areas are related to the upward flux. Deposition is prevailing in the inner area of the eddy while erosion corresponds to the area of the fastest free stream velocities. Fig.1b depicts the total mass of SPM in a water column over a unit square, m , after a steady state distribution of SPM concentration is reached. It is shifted towards the eddy centre. Fig.1c shows the line plots of bottom SPM flux vs radius at successive times during the initial stage of development of erosion.

(ii) Fig. 2 shows equilibrium bottom SPM flux for the anticyclonic eddy that has the same parameters as in the above case except the direction of rotation. In this case SPM flux has an outward component and the area of deposition is shifted to periphery of the eddy.

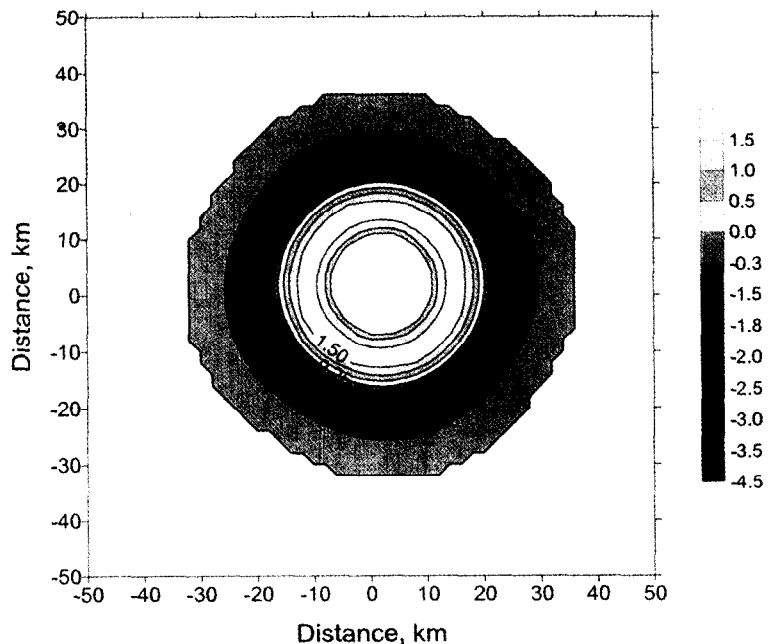


Fig.2. Near bottom vertical SPM flux, $E-D$, produced by a stationary anticyclone. Units are $10^{-6} \text{ g}/(\text{cm}^2 \text{ sec})$

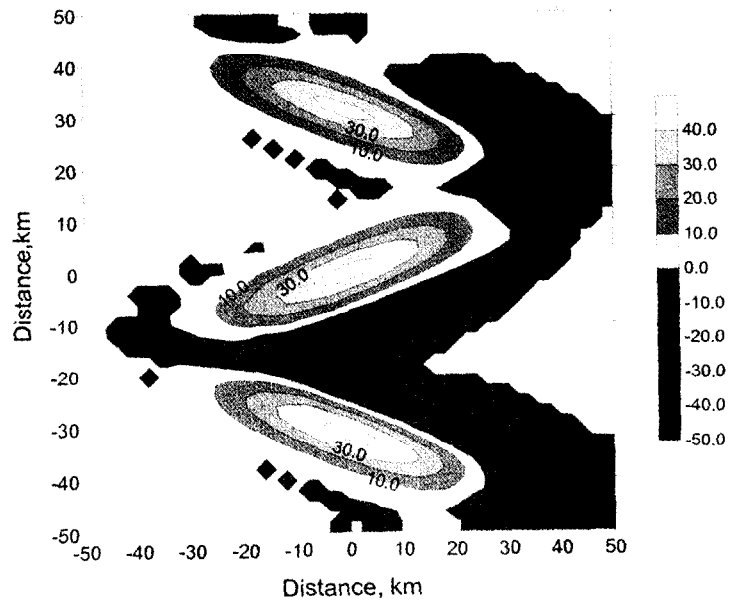


Fig.3. Near bottom vertical SPM flux, $E-D$, produced by a stationary meandering current. Units are $10^{-6} \text{ g}/(\text{cm}^2 \text{ sec})$. The flow is directed from the top of the panel to the bottom.

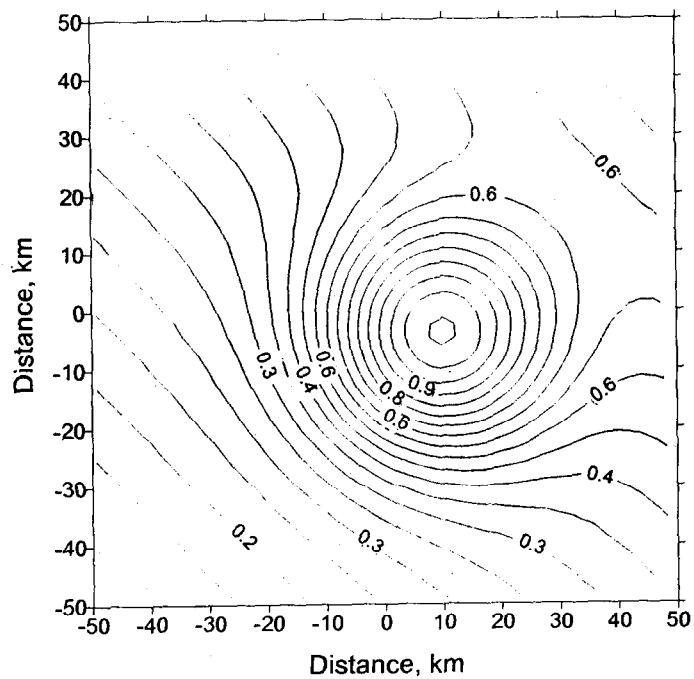


Fig.4a. Contour plot of geopotential for a moving anticyclone at an intermediate time. Units are $10^4 \text{ cm}^2/\text{sec}^2$.

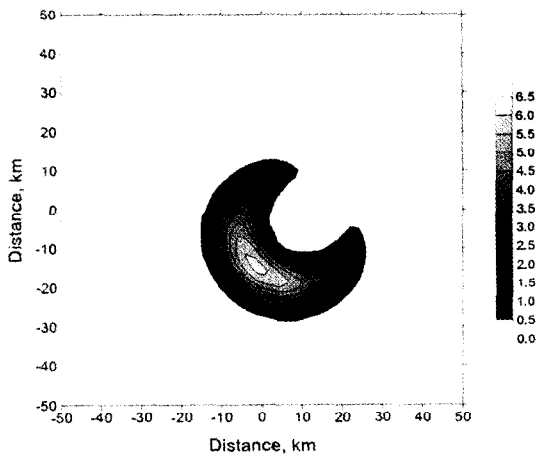


Fig.4b. Near bottom vertical SPM erosion flux, E , produced by a moving anticyclone. Units are $10^{-6} \text{ g}/(\text{cm}^2 \text{ sec})$.

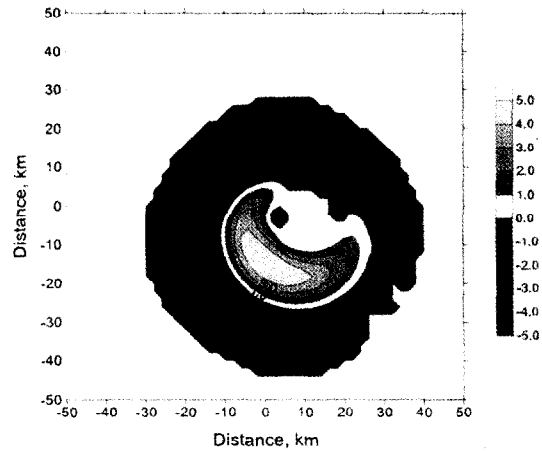


Fig.4c. Near bottom vertical SPM flux, $E-D$, produced by a moving anticyclone. Units are $10^{-6} \text{ g}/(\text{cm}^2 \text{ sec})$.

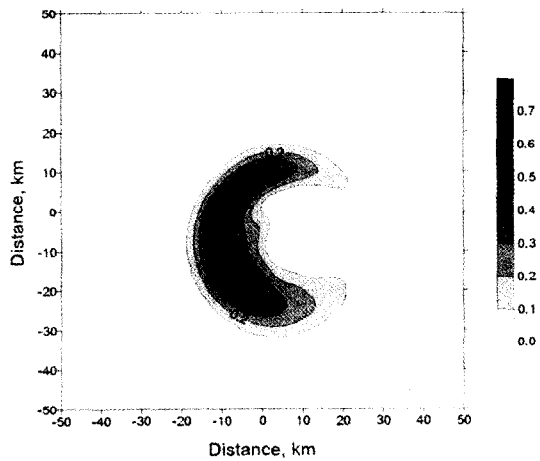


Fig.4d. Mass of SPM, m , over unit square produced by a moving anticyclone. Units are g/cm^2 .

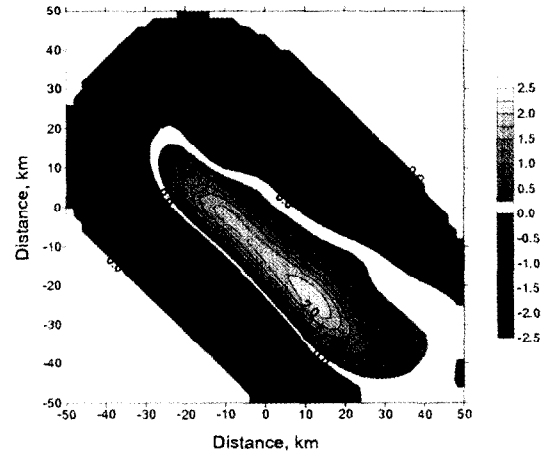


Fig.4e. Total amount of eroded/deposited sediments after passing the eddy. Units are g/cm^2 .

(iii) Fig.3 shows the bottom flux distribution for a meandering current. Maximum free stream velocity is $66 \text{ cm}/\text{sec}$. This flow generates both cyclonic and anticyclonic turns. Accordingly the areas of deposition (dark grey) occur inside or outside the meander.

(iv) Fig. 4 illustrates the SPM transport produced by an anticyclonic vortex which is advected by an along-slope current. The parameters of the eddy are identical to the case (ii). The ambient current flows uniformly to North-West and has a speed of $5.6 \text{ cm}/\text{sec}$. This case simulates propagation of Coastal Anticyclonic Eddies in the Black Sea [9Titov]. Figs 4a, 4b, 4c and 4d show the contour plots of velocity geopotential, erosion bottom flux, total bottom flux, mass of SPM in a water column over a unit bottom area at the same intermediate time. Fig.4e shows the distribution of amount of eroded and deposited sediments after the eddy crossed model area.

4 Discussion

Strong non-linearity in SPM transport introduced mainly because of two reasons. Firstly, the bottom stress depends non-linearly on the free stream velocity. Secondly, there is a threshold stress for erosion and resuspension of SPM. Transport of SPM by mesoscale currents differs in some important details from the transport by high frequency currents generated by waves. It is well known [2,3] that in case of surface waves the direction of SPM transport coincide with the direction of the wave phase velocity. In case of mesoscale currents the direction of SPM flux does not coincide with the direction of the free stream velocity because of frictionally induced secondary circulation in the bottom boundary layer at time scales compared to pendulum day and longer. This effect leads to essentially 3D pattern of SPM fluxes. One of the results illustrated in Fig. 4e is that an along slope current containing an eddy could redeposit sediments both off-shore and on-shore. This effect provides a mechanism of suspended matter exchange between the shelf and the open ocean.

5 Acknowledgements

This research was supported by Russian Foundation for Basic Research under grant 97-05-65635, Russian Ministry of Science and Technology through the program "Coastal zone: theoretical study of physical processes" and The Royal Society (UK) through the project "Cascading".

6 References

- [1] Nikitin B.A., Vovk V.S. 1997: The concept of exploitation of hydrocarbon resources in the Pechora sea. *Proc. III-d Int. conf. «Development of the Russian Arctic offshore»*, 23-26 Sept 1997, SPb, 4-5.
- [2] Kos'yan R.D. and N.V.Pykhov, 1991: Hydrogenous sediment shift in the coastal zone. M., "Nauka", 280pp.
- [3] Antsyferov S.M. and R.D.Kos'yan, 1986: Suspended sediments on the upper shelf. M., "Nauka", 224 pp.
- [4] Nielsen P., 1992: Coastal bottom boundary layer and sediment transport. World Sci.Publ.Co., Singapore, 324 pp.
- [5] Lang G.et al., 1989: Data interpretation and numerical modelling of the mud and suspended sediment experiment. *J. Geophys. Res.*, **94**, C10, 14381-14393.
- [6] Sanford L.P. and J.P.Halka, 1993: Assessing the paradigm of mutually exclusive erosion and deposition of mud, with examples from upper Chesapeake Bay. *Marine Geology*, **114**, 37-57.
- [7] Jankovski J.A., A. Malcherek and W.Zielke, 1996: Numerical modelling of suspended sediment due to deep-sea mining. *J. Geophys. Res.*, **101**, C2, 3545-3560.
- [8] Fedorov K.N. and A.I. Ginzburg, 1989: Multiple forms of coherent motions in marginal ice zones (from remotely sensed data). *Study of Earth from Space*, 3, 3-13.
- [9] Krivosheya, V.G., I.M.Ovchinnikov, V.B.Titov, V.G.Yakubenko, and A.Yu.Skirta, 1998: Meandering of the main Black sea current and eddies formation in the North-Eastern part of the Black sea in summer 1994. *Oceanology*, **38**, 4, 546-553.
- [10] Mehta A.J., 1988: Laboratory studies of cohesive sediment deposition and erosion. In *Physical processes in Estuaries*, ed. by J.Dronkers and W.van Leussen, Shpringer-Verlag, N.Y., 427-445.
- [11] Shapiro G.I. and A.E.Hill, 1997: Dynamics of dense water cascades at the shelf edge. *J. Phys. Oceanogr.*, **27**, 11, 2381-2394.
- [12] Villaret C. and M.Paulic, 1986: Experiments on the erosion of deposited and placed cohesive sediments in an annual flume and a rocking flume. *Rep. UFL/COEL-86/007, Coastal and Oceanogr. Eng.Dep.*, Univ. of Florida, Gainesville.
- [13] Uncles R.J. and J.A.Stephens., 1989: Distribution of suspended sediment at high water in a macrotidal estuary. *J. Geophys. Res.*, **94**, 14395-14405.
- [14] Van Rijn L., 1993: Principles of sediment transport in rivers, estuaries and coastal seas. Aqua Publ., 720 pp.

NEW POSSIBLE MECHANISMS OF THE NORTH PACIFIC INTERMEDIATE WATER FORMATION

A.Yu. Shcherbina¹ and N.A. Maximenko²

¹Moscow Institute of Physics and Technology, 9 Institutskii per., Dolgoprudny 141700, Russia

²P.P.Shirshov Institute of Oceanology, 36 Nakhimovsky Prospekt, Moscow 117851, Russia

E-mails: shcher@sio.rssi.ru, maximen@sio.rssi.ru

Abstract. Several new mechanisms of the North Pacific Intermediate Water (NPIW) formation have been investigated. Specially stressed was the importance of processes of large-scale vertical momentum transfer in the dynamics of intermediate waters. The effect of vertical momentum transfer from the Kuroshio Extension to NPIW was estimated from climatological and drifter data. Processes of geostrophic adjustment in the Kuroshio-Oyashio confluence zone and their effect on NPIW are also discussed.

Overview

North Pacific Intermediate Water (NPIW) is usually defined as a salinity minimum observed in the North Pacific. Throughout the decades of investigations, spatial distribution of NPIW was thoroughly studied [1], but only a few ideas of physical mechanisms of its formation were forwarded. According to the traditional approach [2], NPIW is formed by the Okhotsk sea water that penetrates to the Mixed Water Region by means of the Oyashio current, and subsequently intrudes into the Subtropical Gyre due to isopycnal mixing.

Data of numerous sections across the Kuroshio Extension (KE) as well as observations in the warm core rings of Kuroshio indicate on the regular equatorward drift of NPIW layer. However, studies of Ichiye [3] showed the absence of zonal geostrophic flow at NPIW depth. In this study we made an attempt to investigate a number of mechanisms that could possibly produce ageostrophic drift and thus be responsible for NPIW formation.

Density-driven penetration of the Oyashio water into the Subtropical Gyre.

Hereafter we discuss the mechanism of NPIW formation analogous to that of the Mediterranean Intermediate Water in the North Atlantic. We calculated the weight of water column confined by a pair of isopycnals (26.8 and $26.9 \sigma_\theta$) as an indicator of watermass intrusion driven by gravitational and frictional forces (Fig. 1). In general, this weight decreases southward, as if the source of NPIW were located at the Oyashio. However, zonally elongated local minimum is observed along the northern edge of KE. At the same time, a local maximum in the layer weight is located just to the south of KE. It might be possible to attribute this peculiarity to the intrusion of the Oyashio water into the Subtropical gyre east of 148°E with its westward recirculation south of KE, but analysis of seasonal mode at $26.8 \sigma_\theta$ surface (not shown in figures) demonstrates that seasonal perturbations propagate from the Mixed Water Region omnidirectionally, crossing KE southward at any longitude east of Honshu. Such weight distribution suggests some kind of local forcing existing in KE, that will be investigated in the following chapters.

Momentum transfer

It is quite common to distinguish between small- and large-scale horizontal friction (or process of momentum transfer). However, small-scale turbulence alone is still believed to be responsible for the vertical friction at any scale. Recently some indications on the importance of mechanisms of direct momentum transfer in vertical direction on large scales appeared. Among this mechanisms we can accentuate the attenuation of waves, emitted by a moving layer, inside another motionless viscose layer, and interaction of baroclinic perturbations (such as meanders, eddies etc.) with the vertically sheared flow. The latter mechanism seems to be the most credible. In either case, momentum, “emitted” by moving upper layer (Fig. 2), being absorbed by the lower layer, exert a force on it that, similarly to windstress at the seasurface, results in an ageostrophic drift of the lower layer. Unfortunately, we can not measure this drift directly. Yet, it is possible to evaluate the loss of geostrophical momentum by the upper layer.

We used Levitus climatology data to calculate 3D-distribution of isopycnal geostrophic velocities referenced to 1000dbar level. Momentum loss in a fluid volume ε can be defined as

$$\frac{1}{\varepsilon} \frac{d\vec{M}}{dt} = \rho_0 \frac{d\vec{V}}{dt} = \rho_0 (\vec{V}\nabla)\vec{V}. \quad (1)$$

Provided that the momentum is transferred downward, we can infer that the force exerted on the lower layer and equivalent to this momentum transfer, is determined as

$$\vec{F} = -\frac{\rho_0}{H_2} \int_0^{H_1} \frac{d\vec{V}}{dt} dz, \quad (2)$$

where H_1 is the thickness of the upper layer and H_2 is the thickness of the lower one. Since we considered

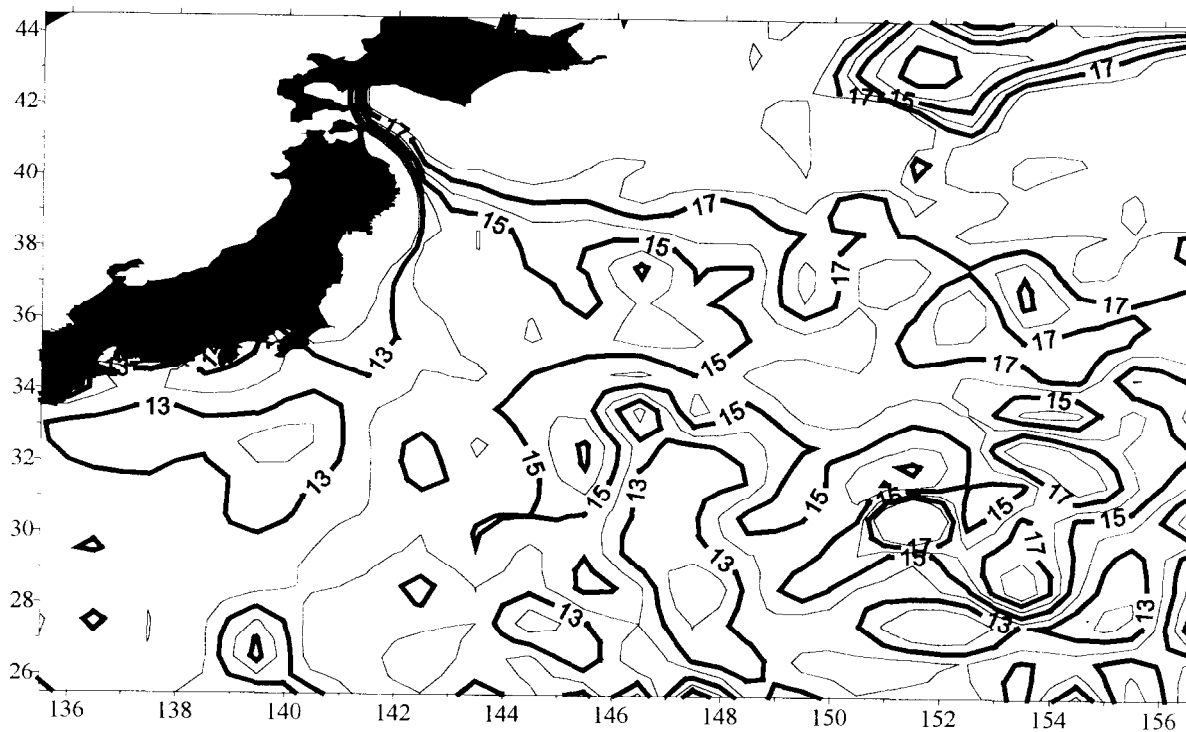


Fig. 1. Weight anomaly of water column between 26.8 and $26.9 \sigma_{\theta}$.

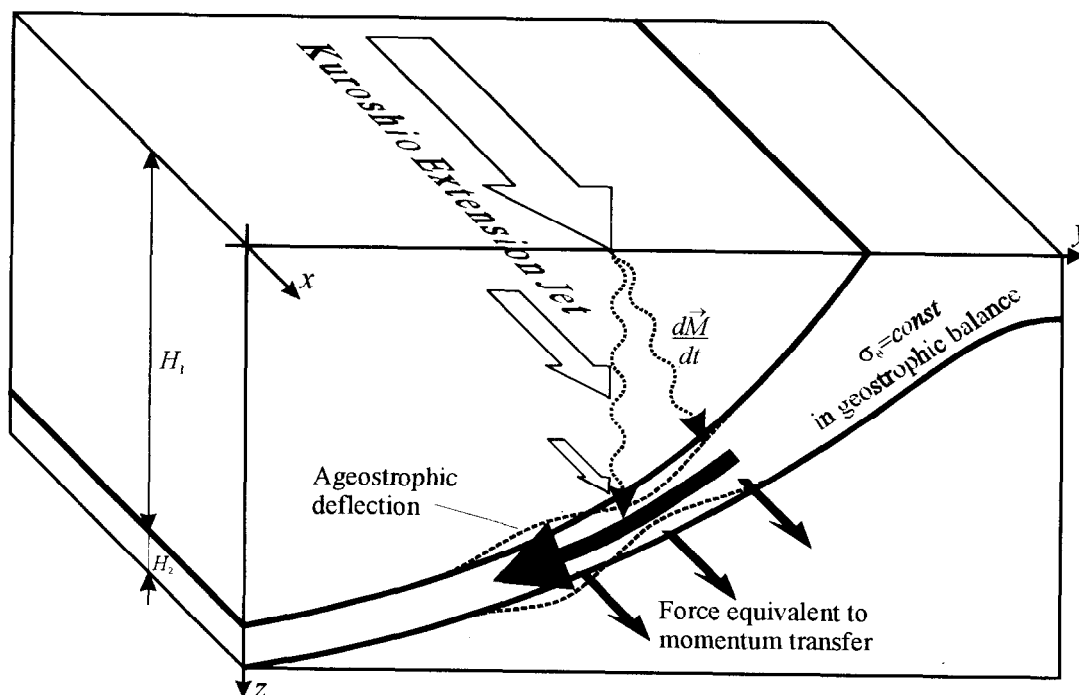


Fig. 2. Scheme of NPIW meridional drift due to momentum "radiation" from the upper layers.

the $26.8 \sigma_\theta$ isopycnal to be the lower border of the upper layer, H_1 is determined as the depth of this isopycnal.

For the meridional velocity of stationary ageostrophic drift of the lower layer we get

$$\tilde{v}_2 = -\frac{1}{\rho_0 f} F^x, \quad (3)$$

where F^x is the zonal component of the force (2).

Employment of smoothed climatological data resulted in the underestimation of geostrophic velocities. In order to take into account such underestimation we compared the trend of variation of velocity in the mainstream of KE derived from climatology data with that obtained from drifter observations (Fig. 3). In the following table summarized are some characteristic values.

	U , cm/s	U_x , s^{-1}	U_t , cm/s^2
Levitus	15	$4 \cdot 10^{-8}$	$6 \cdot 10^{-7}$
Drifters	50	$2 \cdot 10^{-7}$	10^{-5}

Here U_x is the derivative of zonal velocity U along the curvilinear path of KE mainstream and $U_t = dU/dt$ is Lagrangian time derivative of U . After the correction we get

$$v_2 = \frac{(U_t)_{Drifters}}{(U_t)_{Levitus}} \tilde{v}_2. \quad (4)$$

Results of estimation of v_2 with H_2 equal to the typical thickness of NPIW $\sim 100m$ is shown in Fig. 4.

We can also estimate the net ageostrophic NPIW transport Q across KE mainstream at $144.5-170.5^\circ N$,

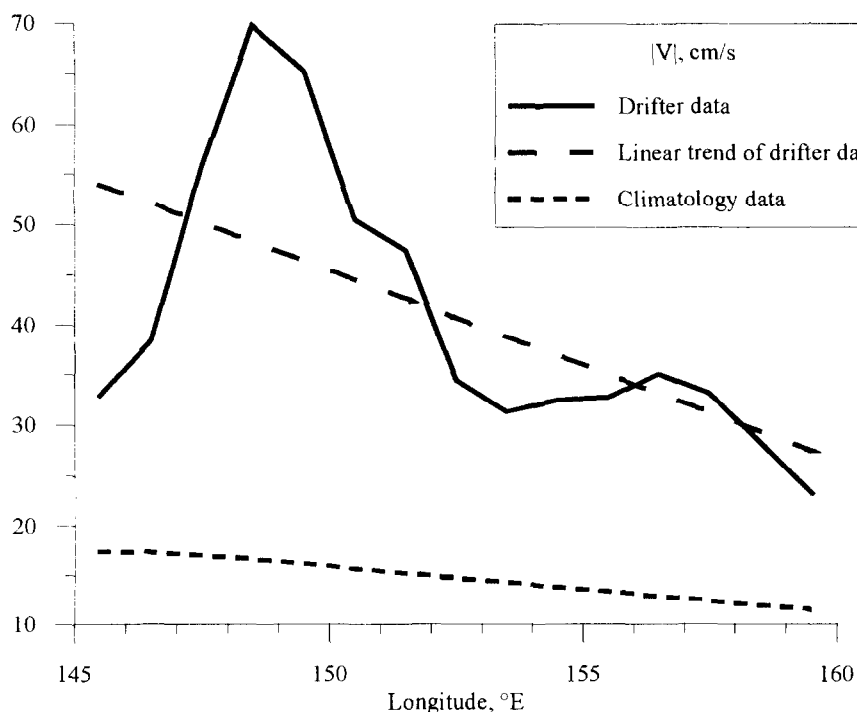


Fig. 3. Mean Kuroshio Extension (KE) speed along its mainstream, calculated from drifter and climatology data.

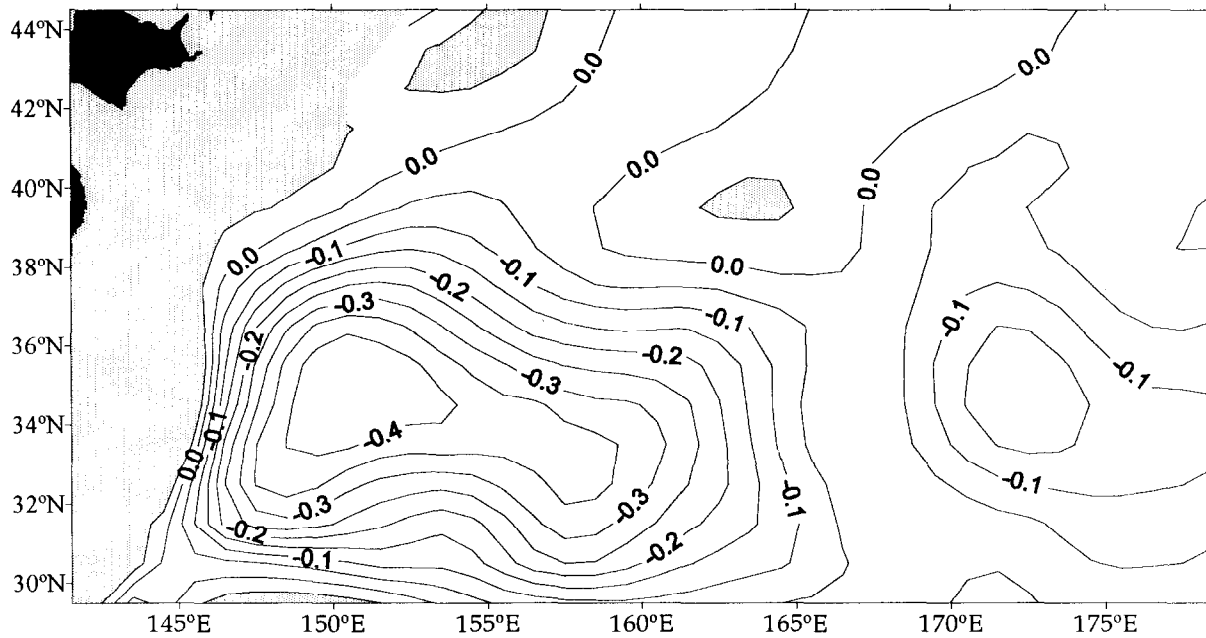


Fig. 4. Velocity of ageostrophic drift of NPIW induced by momentum transfer from upper layers. Shaded are the regions with positive velocities.

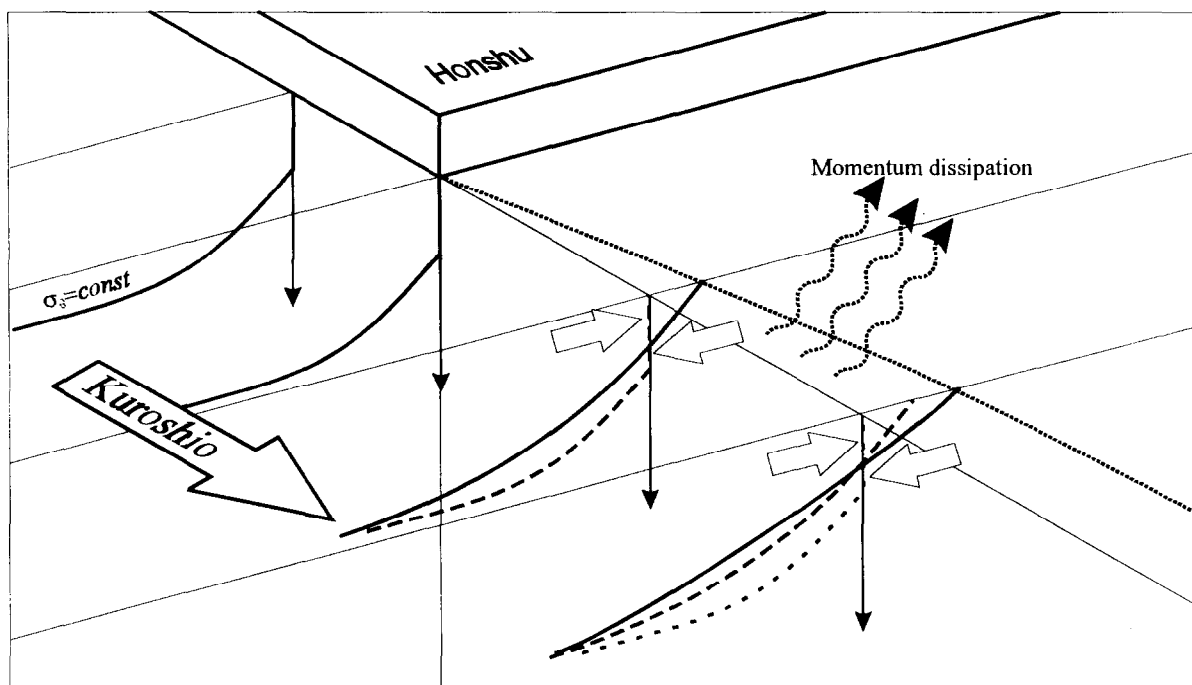


Fig.5. Scheme of geostrophic adjustment upon Kuroshio detaching from the coast..

We can also estimate the net ageostrophic NPIW transport Q across KE mainstream at 144.5-170.5°N, the latter being defined as the line of maximal velocity ($s: y(x)=y(u=u_{\max})$):

$$Q = H_2 \int_s v_2 ds = \frac{1}{f} \int_s \int_0^{H_1} \frac{du}{dt} dz ds \sim 5 \cdot 10^{11} \text{ cm}^3/\text{s}, \quad (5)$$

and the time of ventilation of entire NPIW layer in the North Pacific by this mechanism as 100 years.

Though our estimates agree with the results of some studies of chemical tracers [5,6], still our scheme either underestimates NPIW production rate or allows for a number of other physical mechanisms to coexist with the described one.

Geostrophic adjustment in the Kuroshio-Oyashio confluence zone and in the decaying Kuroshio Extension.

One such mechanism can be due to a geostrophic adjustment occurring east of Honshu in the Kuroshio-Oyashio confluence zone. The vertical structures of the Kuroshio and Oyashio water masses are initially completely different. This calls for geostrophic adjustment during the confluence process. Existence of such an adjustment is also confirmed by the results of isopycnal analysis that reveals abrupt changes of NPIW characteristics just east of Izu islands. The subtropical watermass is forced to float while expanding northward, as Oyashio water subsides under it. This process continues in KE as the latter decays eastward.

References

- [1] L. D. Talley, 1993, Distribution and Formation of North Pacific Intermediate Water, *J.Phys.Oceanogr.*, 23, 517-537.
- [2] J. L. Reid, 1965, Intermediate Waters of the Pacific Ocean, *The Johns Hopkins Oceanographic Studies*, 2, 85 pp.
- [3] T. Ichiye, 1962, On formation of the Intermediate Water in the Northern Pacific Ocean, *Geofis. pur. appl.*, Milano, 51.
- [4] S.Watanabe, N.Higashitani, N.Tsurushima, and S.Tsunogai, 1995, Methane in the Western North Pacific, *J.Oceanogr.*, 51, 39-60.
- [5] S.Tsunogai, S. Watanabe, M.Honda, and T.Aramaki, 1995, North Pacific Studied Chiefly with Radiocarbon, *J.Oceanogr.*, 51, 519-536.

CLASSIFICATION, PHYSICAL NATURE AND STRUCTURE OF FRONTS ON LAKE BAIKAL

P.P.Sherstyankin, V.V.Khokhlov, L.N.Kuimova, N.G.Melnik

Limnological Institute SD RAS, P.O.Box 4199, Irkutsk 664033 Russia E-mail: ppsherst@lin.irk.ru

Abstract. Fronts existing on Lake Baikal correspond practically completely to the classification of oceanic frontal zones and fronts detailed by K.N. Fedorov [1], but there are also some differences. Since there are no tides fronts on Lake Baikal, and no run-off and estuarine fronts in the ocean, this is a case when river waters have a higher density than oceanic one due to a low probability of the latter. On Lake Baikal, inflowing rivers may have water density and salinity both more and less than for the waters of open lake. For example, the first case is represented by Selenga River. In this very case frontal structure caused by intensive vertical mixing is observed at the major part of Selenga shallow water during all a year [2, 3 etc.]. The most complete characteristic of fronts of oceanic type on Lake Baikal spread practically from surface to bottom, is given. The characteristics of such fronts were discussed in detail at Konstantin Fedorov Memorial Symposium [4, 5, 6, 7].

Peculiarities of physical nature and structure, as well as ones of Baikalian fronts ecology representing an interest both for limnologists and for oceanologists, are considered.

Introduction

By its hydrophysical, hydrodynamical and other processes, deep water Lake Baikal is a small ocean. This becomes obvious when studying its fronts. Some phenomena, fronts being one example, are much more easily and conveniently studied in Lake Baikal, e.g. oceanic type fronts under ice, but this is complicated by the fact that differences in water density, variations in water temperature and salinity, playing major roles in the processes of mixing of lake waters in Lake Baikal, are insignificant on the oceanic scale. Various density relationships between waters that mix are discussed.

II. The main Aim and Methodology

The purpose of this paper is to work out study of processes of mixing and front genesis of fresh deep waters on Lake Baikal. We employ the experimentally theoretical approach.

The fronts appearing due to water masses of equal [1, 8, 9] and unequal density mixing (inflow fronts near large rivers delta) are discussed. First descriptions of fronts on Lake Baikal (thermal bar type and oceanic type) were done by [2, 10, 11].

III. Results and discussions

Classification of Fronts on Lake Baikal.

The Brief theory. Let us propose one of the most common schemes of fronts classification based on their origin, i.e., taking into account the density of parents waters A, B and ones obtained due to mixing C. One can immediately present all possible classes of mixing (Table 1):

Table 1.

The classes of mixing for different density of parents waters ρ_A , ρ_B and mixed water ρ_C .

	Class I: $\rho_A = \rho_B$		Class II: $\rho_A \neq \rho_B$	
1	$\rho_A = \rho_B$	$\rho_C > \rho_A$ and ρ_B	$\rho_A > \rho_B$	$\rho_A > \rho_C > \rho_B$
2	$\rho_A = \rho_B$	$\rho_C < \rho_A$ and ρ_B	$\rho_A < \rho_B$	$\rho_A < \rho_C < \rho_B$
3	$\rho_A = \rho_B$	$\rho_C = \rho_A = \rho_B$	$\rho_A = \rho_B$	$\rho_C = \rho_A = \rho_B$

Mixing and stirring (class I and II) may result (or not result) in front genesis. Let us consider it in more detail.

Class I. Under initial conditions, we suppose that waters with equal density and different temperature and salinity take part in the mixing which becomes more density at cabbeling than parents waters [1, 9].

The case class I.1. Let us consider which conditions in this case may cause a front genesis. The front genesis conditions must be presented as:

$$\rho_A - \rho_B = \Delta\rho = 0 \quad \text{a.}; \quad \Delta\rho_{AB} \text{ or } \Delta\rho_{cab} > 0 \quad \text{b.}, \quad (1)$$

where is $\Delta\rho_{cab}$ value cabbeling. We take ρ_{cab} in the form by Kilmatov, Kuzmin [12]. All possible variants of the condition (1) are considered in more detail by Sherstyankin, Kuimova [9]. Theoretically four types of water mixing are possible: at constant S or T, or ρ , and, finally, different mixed variants are possible. Let us consider them in detail.

The class I.1.a. At $S = \text{Const}$. This is an isohalinic mixing. The condition of front genesis (1) is written in the form of:

$$\Delta\rho = \rho_t \Delta T = 0 \quad \text{a.} \quad \text{and} \quad \Delta\rho_{cab} = -(\rho_{tt} \Delta T^2 / 8) > 0 \quad \text{b.}, \quad (2)$$

where the lower index in ρ means differentiation. The condition (2 a.) is fulfilled only when ρ_t vanishes. It occurs at temperature of maximal density $T = T_{md}(S, P)$. The front which appears under such conditions is called a thermal barrier or thermal bar.

The class I.1.b. At $T = \text{Const}$. This is isothermic mixing. The conditions of front genesis (1) are written in following way:

$$\Delta\rho = \rho_s \Delta S = 0 \quad \text{a.} \quad \text{and} \quad \Delta\rho_{cab} = -(\rho_{ss} \Delta S^2 / 8) < 0 \quad \text{b.} \quad (3)$$

I.e., the case of class I.1.b. pass into class I.2.

From the analysis of the expression (3) it appears that $\rho_s > 0$ and never vanishes. $\Delta\rho_{cab}$ is everywhere < 0 , i.e. the conditions of front genesis are not now here realized at any T, S and P.

The class I.1.c. At $\rho = \text{Const}$. This is isopycnic mixing. The conditions of front genesis (1) are written in following way:

$$\Delta\rho = \rho_t \Delta T + \rho_s \Delta S = 0 \quad \text{a.} \quad \text{and} \quad \Delta\rho_{cab} = -(\rho_{tt} \Delta T + 2\rho_{ts} \Delta S) \Delta T / 8 > 0 \quad \text{b.} \quad (4)$$

It is seen that the fulfillment is possible within the whole range of T,S-diagram at any P, and can lead to an unlimited number of appearance of front genesis. At unrestricted changes of T, S and P. This is the most common case.

At long-term mixing a complete densities leveling occurs, and the case class I.3 realizes.

Class II. The fronts of this class appear when mixing waters have an unequal density, when $|\rho_A - \rho_B| \neq 0$ (conditions II.1 and II.2 in the Table 1). Such situations appear usually when river flow into a sea in near-mouth sites [1, 9], when due to a low salinity of river waters they are easily.

At long-term stirring and mixing complete densities leveling and transition to class II.3 or I.3 occur, but multiple realization of classes I.1 and I.2 is not excluded.

Among fronts classes established by K.N. Fedorov [1] the majority of fronts belongs to the class I (Table 1); as for class II, only run-off fronts, in particular, estuarine ones, can be classified as belonging to it for sure.

On Lake Baikal both cases are realized. The littoral waters of Lake Baikal are influenced by the flow of large rivers with salinity, changing from 50 to 300 mg/l and with 96.5 mg/l. more at mean salinity of the waters of open Baikal [14]. In Selenga shallow water area there is mixing of denser waters (higher turbidity, salinity) with open Baikal waters, and a frontal structure appears. This structure suggests that mixing occurs in all water column from the surface to the bottom, as it follows from spatial distribution of temperature attenuation coefficient, Fig.1, [3]. The observations show that mixed Selenga River waters are spread in Lake Baikal in several ways: along an

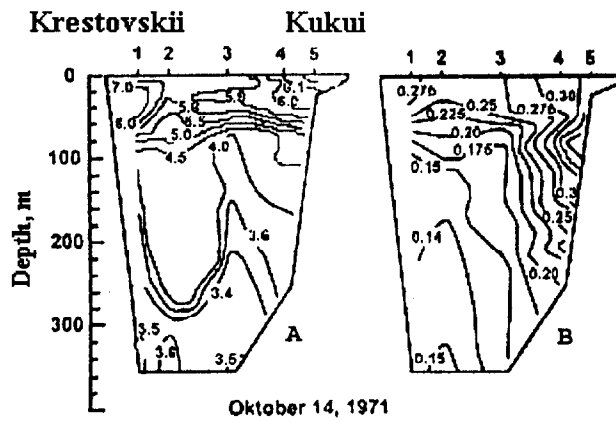


Fig.1. The spatial distribution of (A) temperature T , $^{\circ}\text{C}$, and (B) attenuation coefficient C , m^{-1} , arb.un., on the Selenga shallow water. The transect Cape Krestovskii - settlement Kukui in Selenga delta. The location of this transect on Lake Baikal see on Fig. 2.

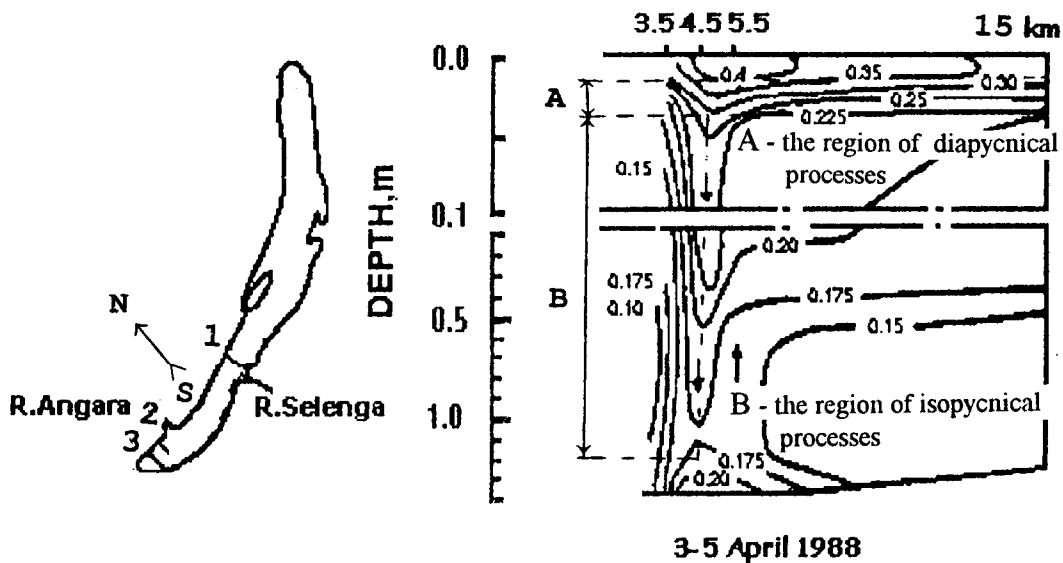


Fig.2. The simple diagram of formation a convergent zone and the front appearing center on Lake Baikal. It is the real example of fragmentary spatial distribution attenuation coefficient, $C \text{ m}^{-1}$, near Cape Ivanovskii. One can see the reason of frontal paradox by K.N.Fedorova and the key to its. Transects on Lake Baikal: 1 - Cape Krestovskii - Settlement Kukui (The Northern part of Selenga delta), 2 - from Cape Ivanovskii and 3 - Maritui - Solzan.

underwater slope (Fig.1), in lake water column [2] and in surficial layers only during the period of summer warming up maximum.

In the seas similar cases occur very seldom because practically always ρ and S of river waters are less than for marine ones. Near inflow fronts lenses of lighter fresh waters on sea surface ρ_B (case II.1 in the Table 1) or lenses of primary heavier waters ρ_A appear [13]. Fronts are classified on the base of a conception of K.N.Fedorov [1] taking into account front genesis and vortices genesis on Lake Baikal. Front genesis areas on Lake Baikal are closely connected with the gyre around Lake Baikal, inner basin vortices, near-coastal currents and run-off of large rivers.

Finally, long stirring or mixing with the fronts of the II class can results in the fronts I and, as a final result, in full mixing (cases I.3 and II.3).

Practically all the types of oceanic fronts with some exceptions (e.g., tidal front) can realize on Lake Baikal, therefore the lake is a natural laboratory to study them.

Front zones on Lake Baikal are divided into: 1. Climatic ones connected with nowadays and paleo-planetary processes on whole Lake Baikal and in its basins; and 2. Synoptic ones connected with synoptic processes in the lake and in the atmosphere.

Front sections and fronts are divided into geostrophic ones (small values of Kibel-Rossby frontal number K_{if}) and ageostrophic ones (great values K_{if}). The first ones consist of climatic fronts in whole the lake and in its basins which are also circulation-topographic, and of synoptic fronts with a scale of whole a basin and less. Second ones are synoptic fronts appearing, as a rule, due to storms and after them with a scale of whole the lake and less. Fronts of spring and autumn thermal bars are also synoptic ones.

There are fronts appearing in the conditions of unequal density which are considered apart. These are inflow fronts forming near large rivers inflow the waters of which have a different salinity S and turbidity. For example, on Lake Baikal, these are the largest tributaries Selenga, Barguzin with a higher S and Snezhnaya with a lower S than in Lake Baikal [14]. Inflow front on Selenga River in near delta boundaries [2] and denser waters of Selenga and Barguzin rivers penetrate Lake Baikal via near-bottom areas and canyons, Fig.1.

Peculiarities of Nature and Structure of Fronts on Lake Baikal.

The thermal bar as a lacustrine phenomenon was described at the end of last century and in the beginning of this one by Forel [15]. Two processes are in the base of the fronts considered: mixing of waters of equal density [1, 9] and cabbelling .

Due to optical observations, deep-water fronts (beam Attenuation Coefficient, C) were discovered on Lake Baikal (Southern part, in the area of neutrino telescope installation by DUMAND project) in winter at the depth about 1400 m in observation site [10]. By that time thanks to the observations from the surface to the bottom optical structures of Baikal waters were described; they were composed of upper zone (0 - 300 m) with high C values, of deep one with the greatest vertical gradients of C , with the highest water transparency and small, with negligibly low C gradients ($\approx 300 - 1200$ m) and of near-bottom one with increased C and their gradients values [16]. More detailed (each 1 km) observations showed the existence of very thin and more turbid vertical water layers about 1 km thick and spread almost from the surface and practically to the very bottom and having nature and structure of oceanic fronts by K.N. Fedorov [1]. In 1988 one of the authors (P.P.Sherstyankin) agreed with K.N. Fedorov to meet to discuss materials on baikalian fronts but unpredictable and sad circumstances have prevented this from happening.

In order to understand clearer the nature and the structure of fronts, some of them appearing at the equal density [1, 8, 9] and at stationary state are considered. The best conditions for the study of such fronts are realized in winter under the ice on Lake Baikal [10, 11].

The main peculiarities of Baikalian fronts (at the depth about 1400 m):

1. A frontal section (convergent zone) is very steep, almost vertical; it is due to insignificant difference in water densities $\Delta\rho$ (some units per 10^{-6} g/cm³);
2. Convergent zone width about 1 km;
3. If in upper layers there is a pycnocline above the convergent zone, so, in the upper part of leap layer there is a significant change of T , C and ρ , causing «a hydrostatically stable layer of oceanic pycnocline» (the basis of frontal exchange paradox by K.N. Fedorov (his words are in the quotation marks)), and in the lower part leap layer, a pycnocline is destroyed almost completely, a convergent zone (front appearing center) begins, it creates «the most effective mixing and heat and salt transfer mechanism» (answer to Fedorov's paradox) (Fig.2);
4. On the flanks from front appearing center an isopycnic income of water from leap layers into convergent zone takes place, but water income cannot remain isopycnic long time, so, it becomes diapycnic (fine structures area);

5. Below front appearing center water from convergent zone reaches deep area, cross it and flow near the bottom. We fixed the increase of turbulence in convergent and near-bottom zones. Probably, the oceanic effects described in [7] are connected with such phenomena.

6. Assessments of the values of vertical rate W by the formula given by K.N. Fedorov [1] for winter conditions are $W \approx 0.07$ cm/s or near 70 m/24 h or 22 km/year.

7. Fine T, S and C structure appearing near the front is a consequence and occasional coincidence of water jets running and compensating the running to convergent zone. A fine optical structure on Lake Baikal was observed in 1971 and described in 1979 [11].

Fine structure nature (T, S, C) is due to water income into convergent zone, therefore it is clear why it may be manifested near the fronts.

When the center of front genesis is on the water surface (classic thermal bar) lighter particles floating on the water surface (e.g., foam etc.) are attracted towards the thermal bar line. It is caused by cross currents appearing with a front. It is interesting to notice that in calm weather Research Vessels which stay near (in front or behind) thermal front line are later on the thermal front line. It is not occasional, but a regular phenomenon (crossing and directed towards each other frontal currents).

Analogous phenomenon is observed when the center of front appearance is under the surface, a water area with a higher C formed above it, and these waters are warmer (lighter) in summer and have a higher pycnocline. It is caused by a lateral flow of the water towards the convergent zone in the lower part of pycnocline both from the coast and from the central lake area.

Vertical velocity W was determined by Fedorov's formula

$$W = K_1 H / (2 B^2), \quad (5)$$

where K_1 is the factor of horizontal exchange, H is the depth and B is the width of convergent zone. For the period of reversal temperature stratification close to the autumn homothermy the diffusion rate p equal to 0.2 cm was determined in experimental way using [18] formula, and $K_1 = pr/2$, where r is the horizontal scale, was found by this formula [19]. For the baikalian condition indicated from (5) the following formula was obtained:

$$W[\text{m/s}] = 0.05 H/B,$$

where H and B are expressed in the same length units [10, 11].

About Thermohalinal Nature of Fronts on Lake Baikal.

Spatial distribution of temperature T , salinity S (in reality - conductivity), attenuation coefficient of light radiation (transparency) C , O_2 concentration at the section Maritui-Solzan on October 21, 1994 were analyzed at the qualitative level. Measurements were made with CTD-Probe SBE-9 [7]. It was supposed that conductivity in a narrow range of changes is proportional to S , and this is enough for T, S -analysis at the qualitative level.

The Fig.3 (A-C) shows that in the site of front genesis T and S are in accordance, as required during isopycnic transition. Where T increases ($T > T_{md}$, where T_{md} is the temperature of maximum density), it corresponds to decreases of water ρ , salinity S and ρ increase, and vice versa. Front genesis is well observed only by C , by T and S it is not evident due to some changes. It is also observed by even isolines, although one of main front genesis conditions - a significant increase of horizontal gradients in the front area in comparison with spatial averages - is observed. The most sensitive front index is optical one - transparency, established for Lake Baikal before [11]. The front is also observed by oxygen content. One can believe that all fronts described before by their optical indices [10, 11, 20], are also thermohaline. C isolines on the graphs with T , S and O are shown by dash lines, Fig.3.

C isolines suggest that: 1. A front appears at the depths 50 to 200 meters; 2. Convergence zone width does not extend 1 km; 3. Convergent zone is practically vertical from the site of its appearing (depths 50-200 m at the station in 5 km from the shore) to near-bottom layers where turbidity increase is observed like in the upper layers.

Dynamic activity increase in the oceans just in these layers of frontal section was noted by K.N.Fedorov, N.P.Kuzmina [21].

On the Fig. 3 T and O from all the stations of Maritui-Solzan section are put on the same graph, and it makes two peculiarities of convergent zone trustworthy: the waters of convergent zone are the most turbid (great C values) in comparison with adjacent stations (practically full similarity with C data for April 3-5, 1988, [5]), and the content (concentrations) of O is minimal. Increased oxygen consumption on pre-coastal stations was noticed

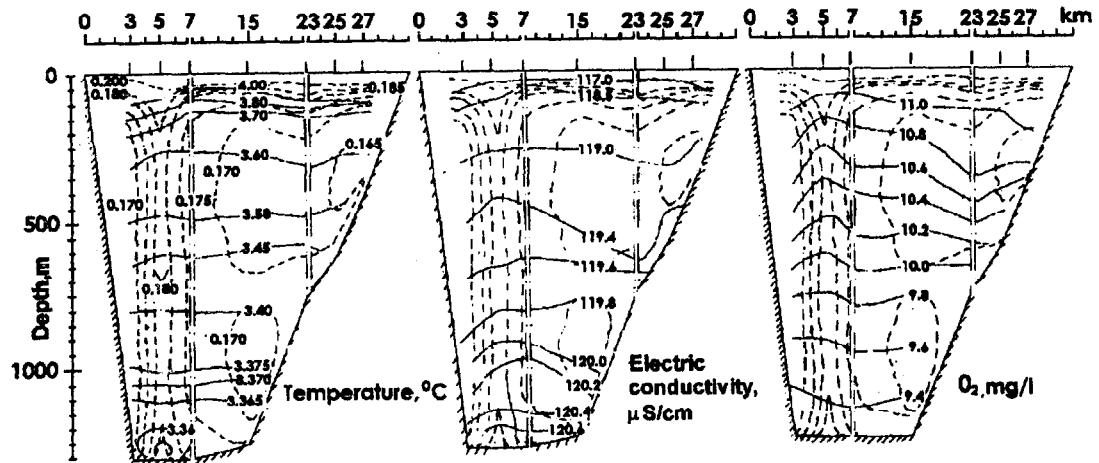


Fig.3. Temperature, °C; electric conductivity (analogy with salinity), $\mu\text{Sm}/\text{cm}^2$; dissolved oxygen concentration O_2 , mg/l; Attenuation coefficient (the dashed line), m^{-1} , measured on the Maritui-Solsan transect on October 21, 1994 [7].
The location of this transect on Lake Baikal see on Fig. 2.

before by V.A. Tolmachev [22]. For convergent zones such an effect is noticed for the first time and suggest an increased biological activity of convergent zones.

Practically vertical C isolines way must be connected with small changes of potential density, it corresponds completely to Margules formula (The less the difference of water density is, the higher is the slope of frontal bound), as well as isopycnic exchange character.

Ecological Role of Fronts in the Ecosystem of the Lake Baikal.

Fronts as a purely hydrological phenomenon constitute a part of abiotic background for waterbody ecosystem and are primarily responsible for near-bottom water ventilation. Hydrologists, hydrobiologists, and other oceanologists have for a long time known this phenomenon [23, 24 etc.], they just termed it differently. Let us consider, on the example of Lake Baikal, the physical properties of these fronts that can be useful for the existence and development of ecosystems with deep water biota [10, 11, 20, 25].

Principal among those properties are related to the genesis and existence of the fronts' convergent zone. Let us consider these properties and peculiarities: a) The place where fronts originate may be from surface down to 200-250 m; where pycnocline water comes rich in seston, fresh organic matter etc.; b) With width 1 km and less the convergent zone penetrates all the deep water zone, reaches bottom area (up to 300 m high) and spreads out to central and coastal parts of the lake; c) Downward movement of the water in the convergent zone has a turbulent character. The fronts are productive zones and areas of location of biotic aggregations, in general biologically active zones [26, 27, 28].

Thus, the fronts deliver into deep water (within the convergent zone) and bottom zones oxygen-, nutrient-, etc. rich surface waters for deep water biota, thus providing for a moving, flowing character of water and destroying standstill areas everywhere, including immediately at the bottom. At convergent zone boundaries, a gradient-type distribution of physical and biological properties of water environment is created, which is of extreme importance for the existence, sustenance and conception of life [29]. Remarkably, the fronts exist even under ice, in the absence of surface-roughing by winds, and are capable of providing in such conditions for a quadruple water exchange, creating in hydrodynamically isolated nuclei relatively still zones in deep water zones [25] having an 8 to 11-year-long water exchange [30].

Turbulent type of water movement (sinking) in the convergent zone is indirectly confirmed by the character of the record of light attenuation coefficient on an XY-recorder Fig.1. While working in the convergent zone the record is a wide trembling line in comparison with a quieter 1 km record. Knowing characteristics of transparency measurer (the length of the base of transparency measurer is 1 m), one can assess the scale of turbulent water movement by fractions of meter. This record effect is observed from surface to bottom.

Let us notice another interesting effect. Synchronous C and O_2 measurements in the convergent zone show that C increase is accompanied by O_2 values decrease [7] (Fig.2). It indicates directly an increased biological activity in

the convergent zone due to the formation of convergent zone waters by waters from pycnocline which are rich in high suspended and organic matter etc. content. When average velocity of waters movement (sinking) in the convergent zone is 70 m/24 h [11], the time of staying there is estimated in two weeks, it is probably sufficient for oxidation processes manifest.

Minima of O₂ content in near-shore areas under steep Northern and North-Western Baikal shore are noticed as well by other authors.

The influence of near-bottom waters (fronts) ventilation on very important biotic processes in oceanic and lacustrine ecosystems was noticed by hydrobiologists and oceanologists long ago [1, 23, 24], and their contribution to the study of this problem is hard to overestimate.

Another ecological property is added to the most interesting properties of fronts, which, from the point of view of oceanic (limnetic) turbulence, represent a double cascade [1], namely, ecologically active abiotic background in deep water bodies.

Conclusions

Many fronts properties and peculiarities which are difficult to be observed in the oceans are more accessible for the observations on Lake Baikal in winter, so, it is necessary to perform (maybe, regularly) Lake Baikal expeditions.

The Lake Baikal is Natural Laboratory for investigations deep water fronts and related phenomena.

Acknowledgements

The work was supported by Russian Foundation of Basic for Researches (Grants No.96-05-65850, No.96-05-65997, No.97-04-96243 and No.97-05-96521. The authors would like to express their gratitude to M.N.Shimaraev, R.Yu.Gnatovsky, V.V.Tsekhanovsky, A.A.Zhdanov, R.Hohman, R.Kipfer for theirs help by our preparation at Konstantin Fedorov Memorial Symposium.

References

- [1] K.N.Fedorov, 1983, Physical nature and structure of oceanic fronts. Gidrometeoizdat, Leningrad, 296 (in Russian).
- [2] P.P.Sherstyankin, 1964, Water Dynamics of Selenga Shallow Water in Early Summer from Date on the Distribution of Optical Characteristics and Water Temperature. Trudy Limnol. Inst., Vol.5(25), 20-57 (in Russian).
- [3] P.P. Sherstyankin, 1993, Optical Structure Waters, in BAIKAL-ATLAS, SD RAS, 82-83 (in Russian)
- [4] P.P.Sherstyankin, 1998, Classification of fronts on Lake Baikal. Oceanic Fronts and Related Phenomena Konstantin Fedorov Memorial Symposium, May 18-22, 1998. Sankt-Petersburg, 172-173.
- [5] P.P.Sherstyankin, L.N.Kuivmova, 1998, Peculiarities of nature and structure of Baikalian fronts, *ibid.*, 173-174.
- [6] P.P.Sherstyankin, N.G.Melnik, 1998, Ecological role of fronts in the ecosystem of the Lake Baikal. *Ibid.*, 174-175.
- [7] P.P.Sherstyankin, M.N.Shimaraev, R.Yu.Gnatovsky, V.V.Khokhlov, V.V.Tsekhanovsky, A.A.Zhdanov, R.Hohmann, R.Kipfer, 1998, About thermohalinic nature of fronts on Lake Baikal, *ibid.*, 175-177.
- [8] C.Garrett, and E.Horne, 1978, Frontal circulation due to cabbeling and double diffusion, *J.Geoph.Res.*, 83,4651-4656.
- [9] P.P. Sherstyankin, L.N. Kuimova, 1995, Frontogenesis in deep reservoirs of Lake Baikal. *Dokl. RAS*, 344, 247-251, in Russian; 1997, 2nd Workshop on «Physical in natural Waters» 2-3 Nov 1997, JRC, Ispra, Italy 84-88.
- [10] P.P.Sherstyankin, 1991, Slope Fronts of the Light Attenuation Coefficient in Lake During Winter, *Dokl. AN SSSR*, 321, 1987-1090 (in Russian).
- [11] P.P.Sherstyankin, 1993, Optical Structures and Fronts of Oceanic Type in Lake Baikal, *Doct. Diss. Phys.&Math. Sci. Shirshov's Institute Oceanology, Moscow*, 37 p. *Suppl.*, 6 p. (in Russian.).
- [12] T.R.Kilmatorov, V.L.Kuzmin, 1991, Cabbeling at mixing in sea waters and its seasonal motion on Pacific Subarctic Front, *Izv. AN SSSR, FAO*, 27, 883-887 (in Russian).
- [13] K.N.Fedorov, 1981, Diverse coexistence of salt and fresh waters, *Priroda*, No.8, 46 -56, (in Russian)
- [14] K.K. Votintsev, I.V. Glazunov, A.P. Tolmacheva, 1965, Hydrochemistry of rivers of Lake Baikal basin. *Izd. AN SSSR, Moscow*, (in Russian).
- [15] F.A.Forel, 1895., *Le Lemane: monographie limnologique. Lausanne*, Vol.2. Mecanique, chimie,thermique, optique, acoustique, 651,

- [16] M.E.Lee, G.G.Neuimin, P.P.Sherstyankin, 1970, Some Features of Dynamics of Lake Baikal Water According to the Data of Hydro-optical Observations. in *Techeniya i Diffusiya Vod Baikala*. «Nauka»: Leningrad, 136-145 (in Russian).
- [17] N.N.Golenko, A.C.Monin, V.T.Paka, 1991, On frontal intrusions in ocean, *Dokl. AN SSSR*, **319**, 1449-1452 (in Russian).
- [18] J.Joseph, G.Sendner, 1958, Uber die horizontale Diffusion im Meere. *Deut. Hydrogr Z.*, **11**, Hf.2, 49-77
- [19] P.P.Sherstyankin, 1970, Investigation of Horizontal Diffusion in the South Basin of Lake Baikal by Fluorescence Patching. in *Techeniya i Diffusiya Vod Baikala*. «Nauka»: Leningrad, 136-145 (in Russian).
- [20] P.P.Sherstyankin, 1992, Front Genesis at Lake Baikal by the Materials of Optical Observations. *Dokl. RAN*, **326**, 336-340 (in Russian).
- [21] K.N.Fedorov, N.P.Kuzmina, 1979, Fronts in ocean (Review). in: *Resume of Science. VINITI* (in Russian)
- [22] V.A.Tolmachev, 1957, About Seasonal Changes of dissolved Oxygen in deepwater on Baikal. *DAN*, **113**, 395-398 (in Russian).
- [23] N.N.Zubov, 1930, On Question about Ventilation of the Bottom Waters in Sea, *Researches seas USSR*, Issue 12 (in Russian).
- [24] L.Zenkevich, 1932, On the Aeration of the Bottom Waters through Vertical Circulation, *Bulletin of the State Oceanographical Institute*, Issue 5, 3-22.
- [25] P.P.Sherstyankin, 1994, Transfrontal Mechanism of Water Exchange in Lake Baikal, in: *Baikal as Natural Laboratory for Global Change*, Irkutsk, May 11-17, 1994. Vol.6, .30.
- [26] M.Yu.Beckman, V.K. Nagorny, 1985, Summer concentration and distribution of macroplankton in slope region on Baikal. in: *Circulation of substance and energy in resrvoice. Absracts YI All-Union Limnological Conference. Listvenichnoe on Baikal*, 4-6 Sept. 1985. Issue 3, .61-62 (in Russian).
- [27] N.G.Melnik, O.A.Timoshkin, V.G.Sideleva, 1995 Distribution of *Macrohectopus branickii* and some peculiarity its ecology, in *Guide and key to palagic animals of Baikal (with ecological notes)*. Novosibirsk: Nauka, 511-522 (in Russian).
- [28] V.V.Smirnov, 1997, Ecology of Baikalian Omul *Coregonus Autumnalis Migratorius* (Georgy), Doctoral Thesis, Ekaterinburg, 42 p, (inRussian).
- [29] I.Prigogin, I.Stengers I, 1984, *Order out of Chaos. Man's new dialog with nature*. Heinemann. London, 432
- [30] R.F.Weiss, E.C.Carmack, V.M.Koropalov, 1991, Deep-water renewal and biological production in Lake Baikal. *Nature*, **349**, 665-669.

**THE COMBINED HYDROPHYSICAL AND ACOUSTIC STUDY OF
THERMOHALINE FINE STRUCTURE IN THE ATLANTIC OCEAN**

V. E. Sklyarov and A. V. Berezutskii

P.P.Shirshov Institute of Oceanology, Nakhimovskii pr. 36, Moscow 117851, Russia

Abstract. We present the results of combined acoustic and CTD measurements of thermohaline fine structure which was observed under a large-scale tongue of Mediterranean Intermediate Water (MIW) in the central Atlantic. A horizontal intermittency was a significant feature of the MIW spreading. Several types of thermohaline vertical fine structure were observed by CTD data within the areas of local intensity maxima of intermediate water. A classification of acoustic images and features of hydrophysical parameters distributions was made to reveal a connection between CTD and acoustic data. The observed relationship between the thermohaline structure and sound-scattering properties of MIW showed the high potential of the remote acoustic sensing technique for investigation and monitoring of MIW structure and dynamics in the Atlantic ocean.

The main purpose of this note is to demonstrate that the use of acoustic sensing in combination with oceanographic measurements is a good tool to study the structure and dynamics of Mediterranean Intermediate Water (MIW) in the Atlantic [1,2]. A set of directed studies was carried out on the spatial-temporal variability in characteristics of MIW and its effect on the structure of the field of volume sound scattering (VSS) in one of the regions of the central Atlantic (29°N-35°N and 20°W-26°W). Measurements were made at 44 oceanographic stations during the period of observations [3]. Each station included a CTD cast and simultaneous narrowbeam acoustic sensing from a board of the ship at frequencies of 12 kHz and 24 kHz down to 2000 m.

Results of the hydrographic analysis showed that the central part of the study area (Fig.1) exhibited intermittent regions of elevated values for temperature (T) and salinity (S) anomalies with a depth maximum in the 1000-1100 m layer. The horizontal intermittency resulted in spatial variability of vertical thermohaline fine structure. Based on the formal method five types of vertical fine structure were revealed. Parametrization of the fine structure was performed for all hydrophysical data collected for the study area. 17 parameters were calculated for characteristic types of stratification encountered during the period of observation (see Table 1).

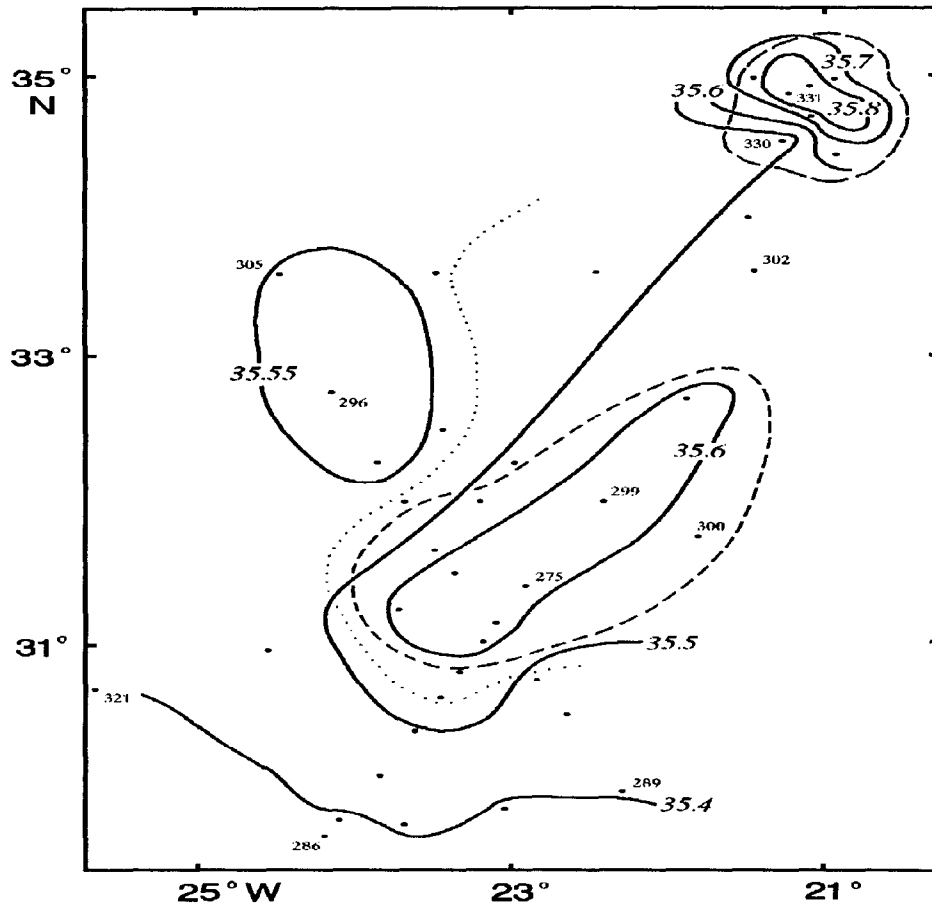


Figure 1. Map of salinity distribution at depth of 1100 m. The areas of "inversion" and "staircase" fine structure are contoured by dotted and dashed lines.

Table 1. Parameters of fine structure layering of waters

	1400-1800 m "stairs"	1400-1800 m no "stairs"	600-1200 m strong intrusive layering	600-1200 m weak layering	200-500 m, "stairs" with lateral advection
$T_z, ^\circ\text{C}/\text{m}$	$-(4-6)\times 10^{-3}$	$-(3-8)\times 10^{-3}$	$-(2-6)\times 10^{-3}$	$-(6-8)\times 10^{-3}$	$-(6-8)\times 10^{-3}$
$S_z, \text{‰}/\text{m}$	$-(5-8)\times 10^{-4}$	$-(2-8)\times 10^{-4}$	$-(1-9)\times 10^{-4}$	$-(1-2)\times 10^{-4}$	$-(2-4)\times 10^{-4}$
$N, 10^{-3}\text{C}^{-1}$	1,1-1,3	0,5-1,5	2,9-3,4	3,2-3,4	3,1-3,3
R_p	1,3-1,7	1,3-1,7	usually $-(1-10)$	usually $-(8-20)$	usually $-(5-20)$
r	1,2-1,5	0,95-1,15	0,9-1,05	1,0-1,5	1,5-2,0
H, m	20-60	various	20-60	10-40	15-60
K_{ts}	0,90-0,95	0,80-0,95	0,85-0,95	0,5-0,9	0,5-0,9
K_{tp}	$-(0,3-0,7)$	$-(0,1)-0,4$	$-(0,5)-0,5$	$-(0,1-0,8)$	$-(0,7-0,8)$
δ	0,5-1,0	0,05-0,30	$-0,03-0,03$	0-0,3	0,3-0,7
a_p	0,4-1,0	various	0,1-0,5	0,1-0,3	0,1-0,2
$ a_t $	0,8-1,5	1	1-10	0,3-1,0	0,3-0,8
$ a_t R_p $	1-3	2	large	10	5
$ a_s $	1-2	0,5-3	1-20	1-20	1-4
AT_i/AS_i	0,2-0,4	0,05-0,25/0,1-0,4	0,1-0,3/0,03-0,1	0,05-0,15/0,2-0,3	0-0,1/0,2-0,05
AT_{si}/AS_{si}	0,1-0,3/0,05-0,15	0,02-0,15	0,02-0,05	0-0,05	0-0,05
AT_l/AS_l	0,55-0,75	0,55-0,65	0,05-0,06/0,45-0,6	0,45-0,65	0,5-0,65
AT_s/AS_s	0,2-0,6/0,1-0,3	0,05-0,3	0,04-0,10	0,04-0,12	0,04-0,12

When analysing the features of the thermohaline structure of MIW, one should note the following. Near the most clearly expressed anomalies of T and S a strong developed fine structure was observed. In the layer between horizons 1200-1300 m and 1700-1900 m “staircase” fine structure was found. Vertical dimensions of the stairs were 40-60 m with temperature changes on the order of 0.3°-0.5°C and salinity of 0.05-0.15 ppt. Some profiles contained up to 20 stairs. The estimates of characteristics of fine structure – vertical density ratio R_ρ and temperature-density correlation δ - yielded values of 1.3-1.7 and 0.5-1.0, respectively. Such values for these parameters are typical for the double diffusion “salt finger” mechanism of these stairs’ formation. The significant share of low-gradient layers confirmed their double diffusion convective origin. For vertical profiles, in which stairs were not observed, the values of R_ρ were 1.3-1.7 and the values of δ were 0.05-0.3, which corresponded to domination of “intrusions” type of fine structure. An intensive layering of the “inversions” type was observed under the large core of MIW at depths of 600-1200 m approximately 100 km around 32°N, 22°W. The most intensive one was at the same depths at the boundary of the meddy. The typical values of the temperature and salinity inversions were about 0.2°C and 0.07 ppt, respectively. The typical thicknesses of the most intensive intrusions were from 15 m up to 50 m. Small-scale (less than 15 m thickness) intrusions were also observed.

Propagation of the MIW layer was spatially nonuniform. It was characterized by the existence of regions with maximal intensity of the layer and strong stairs stratification below it, and regions where it was not expressed and stairs were absent. The regions of minima and maxima of layer intensity were separated by zones of elevated gradients. These zones were characterized by a significant degree of the thermoclinicity, so the isopycnals were approximately horizontal. The formation at thermohaline stairs of intrusive structures propagating across the frontal zones were detected at horizons 1400-1800 m. The horizontal scales of such structures were on the order of several tens of km. It seems the transformation was caused by isopycnal advection processes.

An important aspect of the research under discussion here was the link established between the structure of the field of volume sound scattering (VSS) at frequencies of 12 kHz and 24 kHz, and the thermohaline structure at depths of 600-1900 m. The results showed that at horizons of MIW a complex pattern of VSS was observed. Nevertheless, analysis of the acoustic images revealed a trend toward increased intensity of scattering in the depth range of 1000-1200 m upon approach to the maxima of T,S layer intensity (Fig.2). It also showed the possibility of acoustically monitoring the top boundaries of both meddies and of large-scale MIW tongues.

The acoustic data analysis revealed the layered structure of VSS at depths of 700-1800 m. It was the significant feature of the observed scattering. At these depths a system of scattering layers of different thicknesses usually existed. The layers thickness varied from 0.75 m (the range resolution of the acoustic units) up to tens of meters. The range between two neighboring layers had lower scattering levels. Thus our data also showed existence of fine structure of volume sound scattering at MIW spreading depths. The comparison of the acoustic sensing results and the features of hydrophysical parameters distributions revealed the connection between the layered structure of VSS and the fine structure of MIW. Thicknesses of the most thin sound scattering layers didn't exceed the range resolution of the sonar tools. The data analysis revealed the connection between the locations of these thin layers and the gradient zones of fine structure. The connection was seen most

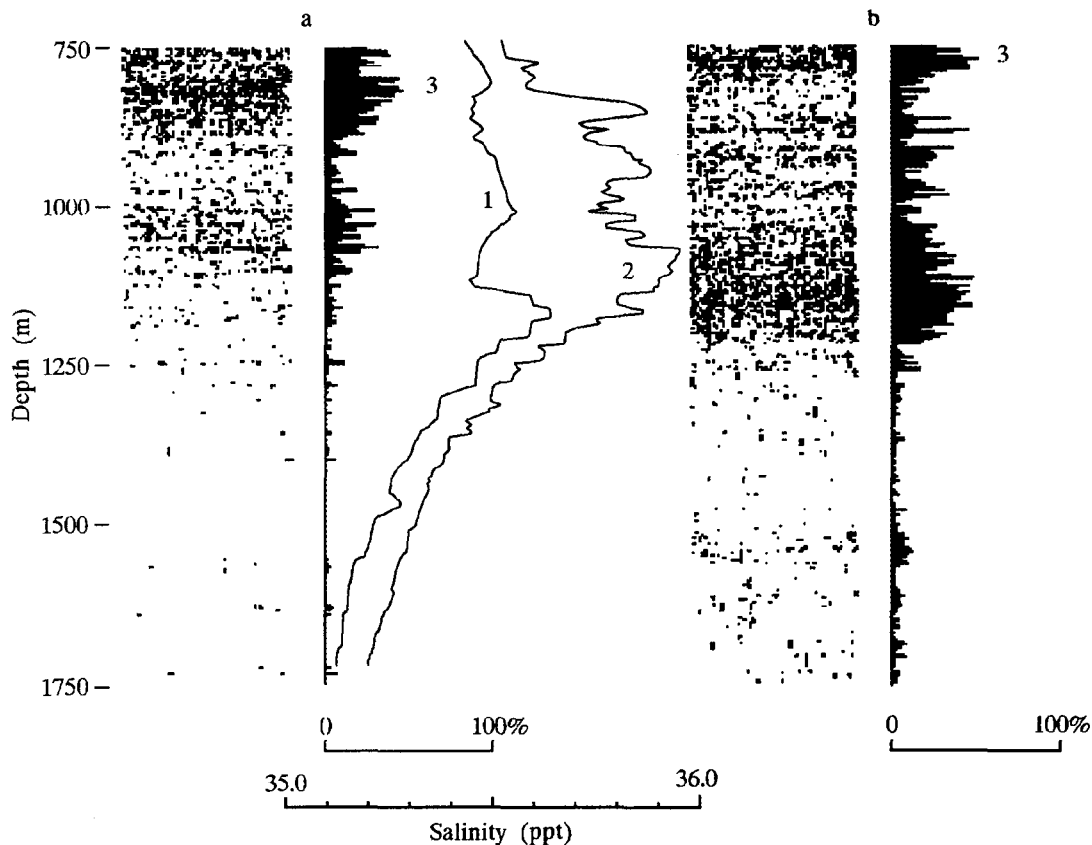


Figure 2 (top). Acoustic images, showing the intermittency of the MIW structure. a – outside the meddy, b – meddy central part. Frequency of 12 kHz, sound-backscattering range from -85 to -79 dB. Profiles 1 and 2 are salinity profiles outside and inside the meddy, respectively (profile 2 is shifted to the right by 0.01 ppt); 3 indicates the top boundaries of MIW.

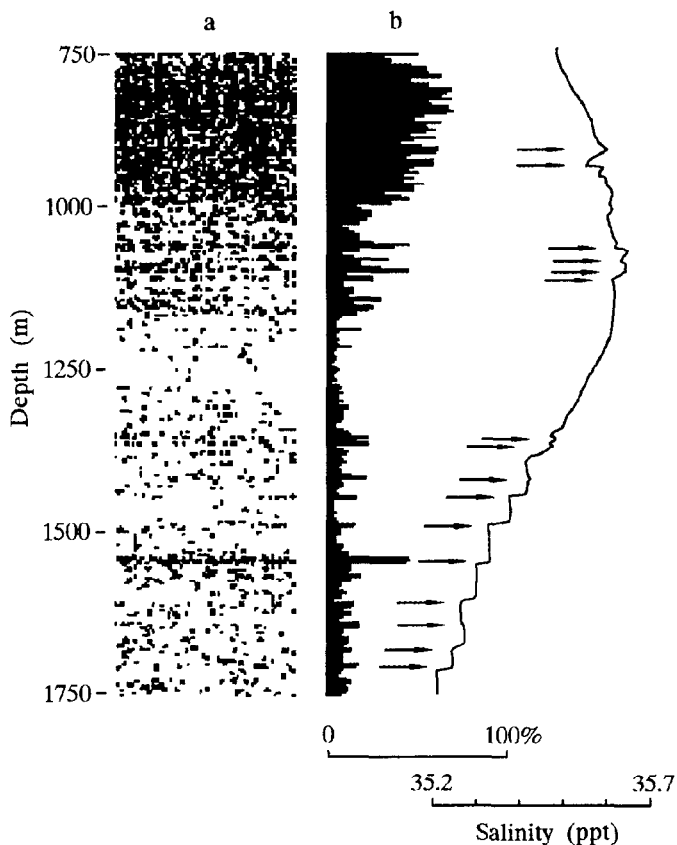


Figure 3 (left). Acoustic image (a) of a staircase fine structure of MIW and vertical statistical distribution (b) of scattering strength. Arrows show the consistency between the acoustic and in situ observations. Frequency of 12 kHz; sound-backscattering range from -85 to -79 dB.

distinctly at stations where the staircase fine structure was developed (Fig.3). This acoustic image demonstrates the consistency between the remote and in situ observations. On the other hand, it shows those peculiarities of the thermohaline structure and dynamics, which could not be traced on the basis of the CTD data only. These are: (i) significant changes in thicknesses of quasi-homogeneous layers under conditions of both variation and conservation of their middepth, (ii) - changes in depths of layers but conservation of their thicknesses, (iii) - variations in gradient zones thicknesses and, as a consequence, variations in values of thermohaline gradients and backscattering intensity. These peculiarities indicate both the complex pattern of thermohaline fine structure dynamics and the variety of its formation processes. The connection between the acoustic and thermohaline finestructures was also found for the stations where some stairs were transformed into inversions by isopycnal advective moving. Although the nature of VSS was not exactly revealed during our pilot investigations, the coincidence of the positions of the scattering layers with the gradient thermohaline stairs implies that the action of microstructure scattering mechanism should be take in to account.

Conclusions. The comprehensive CTD and acoustic studies revealed and examined the intermittent nature of spreading of MIW and the spatial structure of the field of volume sound scattering. Remote acoustic diagnostics of areas with higher and lower temperature and salinity anomalies at horizons of propagation of intermediate waters was found to be possible, due to the existence of the spatial variability of sound-scattering properties of MIW. The upper boundaries of thermohaline stairs observed under the areas with local increases in temperature and salinity were clearly recorded by acoustic tools. A connection between positions of thin sound scattering layers and step boundaries was found. The typical values of sound scattering strength of these layers were of the order of $-82 \dots -76$ dB. Statistical analysis of CTD data revealed five types of thermohaline fine structure. It showed the uniqueness of the studied region of the central Atlantic, which may serve as an excellent area for investigating the various types of fine structure and forms of deep water convection under conditions of propagation of intermediate waters with an intermittent nature. A link found between the thermohaline structure of the layer of MIW and the field of volume sound scattering indicates the expediency of using the method of echosound diagnostics for studying the structure and dynamics of intermediate waters of the Atlantic.

References.

1. L. Armi and W. Zenk, 1984, Large lenses of highly saline Mediterranean water, *J. Phys. Oceanogr.*, 14, 1560-1576.
2. K. N. Fedorov (edited), 1986, *Intrathermocline Edies in the Ocean*, P. P. Shirshov Institute of Oceanology, Moscow, USSR.
3. A. V. Berezutskii, S. E. Maximov, V. B. Rodionov and V. E. Sklyarov, 1994, Mediterranean water structure in the central Atlantic: Results of remote acoustic and conductivity-temperature-depth measurements, *J. Geophys. Res.*, 99, C10, 20375-20379.

Wind Forcing and Deep Circulation in the Japan Sea

M. Takematsu, A. Ostrovskii and Z. Nagano

Research Institute for Applied Mechanics, Kyushu University Kasuga, 816-8580, Japan
(takematu@hikari.riam.kyushu-u.ac.jp)

Abstract. As an unanticipated result of recent moored observations, strong quasi-barotropic currents with marked seasonal variation were found in the highly homogeneous deep water of the northern Japan Sea. In this paper, the observed deep currents are discussed in comparison with the ECMWF wind data, surface current data from a moored ADCP and remotely sensed data (sea surface temperature and drifter tracks). The observed deep currents significantly differed in temporal variability from site to site despite the rather small spacings of the mooring array. It is suggested that none of the observed current features can be accounted for in terms of the wind forcing only.

1- Introduction

It has been conjectured from hydrochemical analyses that the deep circulation in the Japan Sea is generally sluggish and non-seasonal as is the case in the world ocean. However, our recent moored current measurements [1] demonstrated that this is not true in the Japan Sea. The current measurements were made at selected seven sites (Fig.1) in the northern Japan Sea as a part of an international research program CREAMS (Circulation Research of the East Asian Marginal Seas). As an unanticipated result, we found that there exist strong, quasi-barotropic deep currents with strong seasonal dependence even in the interior region far from the western boundary of the basin. This suggests that the deep circulation of the Japan Sea is driven annually by atmospheric forcing in contrast to the conventional view that the present circulation was generated by deep convection events in exceptionally severe winters before 1969. Then, what is the major driving factor for the observed deep currents, wind forcing or thermohaline

processes? In this article, we examine the effect of wind forcing by comparing the observed current features with available wind data and surface current data from an upward-looking ADCP deployed at a representative site during the CREAMS program field observation phase.

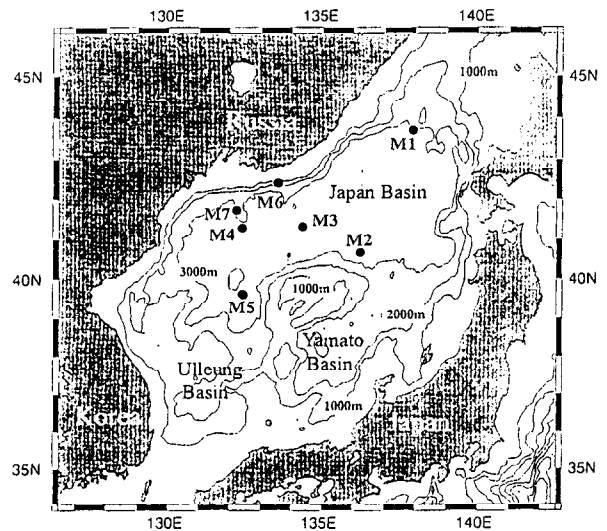


Fig. 1. Sites of moorings deployed during CREAMS field experiment of 1993-96.

2- Observations of the Japan Sea Circulation During the CREAMS Project

In August 1993, during the first CREAMS cruise of R/V Professor Khromov, the international team of scientists deployed three moorings M1-M3 equipped with 9 current meters to start the survey of the intermediate and deep circulation in the north Japan Sea (see Table 1 for details about distribution of instruments). The moorings M1 and M2 aimed at yearly survey in the eastern part of the Japan Basin. M3 was deployed in the

central north Japan Sea. It was redeployed twice and was finally recovered in August 1996 providing us with a unique 3-year series of current meter data for the Japan Basin interior. Other four moorings, carrying 12 current meters, a sediment trap and an upward-looking Acoustic Doppler Profiler (ADCP), operated in the western part of the Japan Basin in 1994-96. M4, M6, and M7 were deployed for one year near the Primorye coast; M6 measured currents over the continental slope whereas M4 and M7 worked off shore. M5 operated during two years in the Subpolar Front region west of Yamato Rise.

The network of moorings covered the deep part of the Japan Basin. Its overall design intended to capture general cyclonic circulation that was conventionally thought to persist in the Japan Basin (e.g. [2] among others). At the site M7, the ADCP (RD Instruments) was used on top of the mooring (330 m depth), aiming to observe a response of upper ocean to northwesterly wind. The Aanderaa RCM8 current meters were deployed basically at the 1000, 2000, and 2500 or 3000 m depths, so as to resolve probably weak vertical shear of horizontal currents in the nearly homogeneous deep water (e.g., [3,4]). The current meter records of originally 1 hour sampling period were low-passed with a tide-killer filter of 24 hours and sub-sampled once per day.

In between the deployment/recovery cruises the attempts were made to monitor the near-surface circulation by means of the satellite infrared imagery. The NOAA high resolution infrared images were acquired by TeraScan system (Sea Space) and processed with Multichannel Sea Surface Temperature method. Finally we had the sea surface temperature (SST) data on the Mercator grid of approximately 1.1. km resolution covering the whole Japan Sea. To complement the current measurements we selected several series of the satellite imagery when the atmosphere was partly free of clouds and the water vapor content was rather low in the air above the northern Japan Sea as in the cold season.

To obtain the near-surface velocities we analyzed data of the WOCE Surface

Velocity Programme Lagrangian drifters, with the drogues centered at 15 m depth, which could complement the satellite

Mooring	Latitude(° N) and longitude(° E)		Instrument		Date of observations	Mean current (cm/s)	
	depth (m)	depth (m)	type	E-W		N-S	
M1	43° 43.0'	137° 54.7'	1000	3000	RCM8 18 Aug,1993	-0.10	-0.27
			2000		RCM8 - 11 Jul,1994	Data Missing	
			2500		RCM8	0.14	-0.42
M2	40° 41.5'	136° 14.5'	1000	3000	RCM8 20 Aug,1993	Data Missing	
			2000		RCM8 - 13 Jul,1994	0.11	-0.14
			2500		RCM8	0.18	-0.14
M3	41° 29.7'	134° 21.4'	1000	3500	RCM8 22 Aug,1993	-0.40	-0.38 *
			2000		RCM8 - 3 Aug,1996	-0.25	-0.47
			3000		RCM8	-0.19	-0.29
M4	41° 18.0'	132° 24.0'	1300	3000	RCM8 17 Jul,1994	-1.06	-2.97
			2100		RCM8 - 4 Aug,1995	-0.76	-2.77
			2900		RCM8	-0.82	-2.17
M5	39° 38.0'	132° 25.0'	900	3100	RCM8 18 Jul,1994	-3.93	-0.44
			1500		RCM8 - 9 Aug,1996	-5.59	-0.70
			2400		RCM8	-4.00	0.31
M6	42° 24.9'	133° 33.8'	800	2900	RCM8 1 Aug,1995	-3.28	0.50
			1800		RCM8 - 4 Aug,1996	-1.73	0.12
			2400		RCM8	-0.60	0.27
					Sediment Trap		
M7	41° 45.0'	132° 13.0'	330	2200	SCADCP 4 Aug,1995		
			1300		RCM8 - 7 Aug,1996	-0.07	0.13
			2000		RCM8	-0.03	0.04

* The data was missing during July 1994 - July 1995.

Table 1. Mooring characteristics and mean currents.

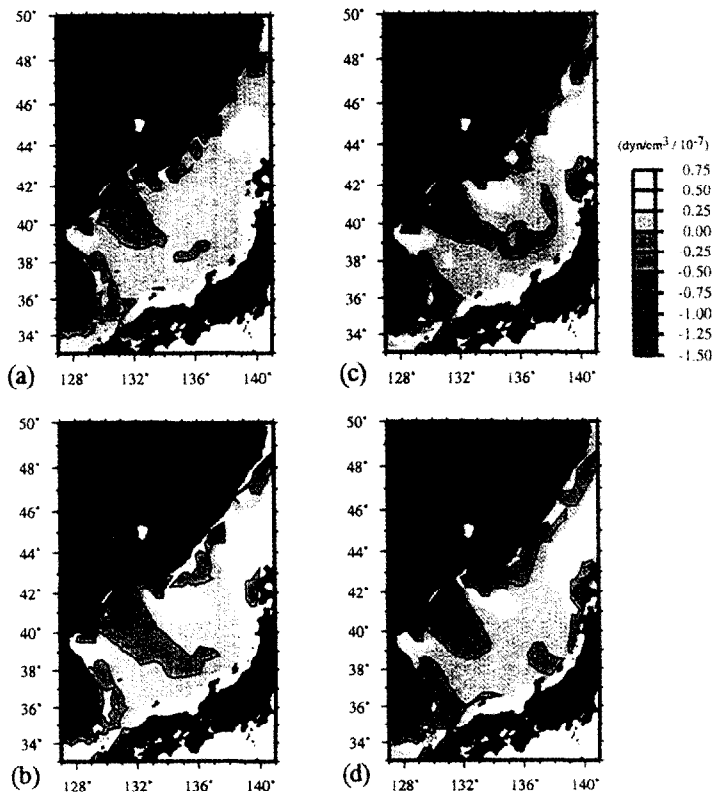


Fig. 2. The ECMWF surface wind stress curl over the Japan Sea: (a) annual mean for 1991-98, (b) mean for the winter 1993/94, (c) mean for the winter 1994/95, (d) mean for the winter 1995/96.

infrared imagery. Fortunately, we found two trajectories of the buoys lunched in 1996 that entered the interior of the Japan Basin in the vicinity of M3 and happened to be trapped by the eddies, which in turn could be traced in the satellite images.

In order to examine relationship between the sea circulation and the atmospheric wind forcing, we used the ECMWF daily surface wind stress for the period of 1991-98. An advantage of this data is higher resolution, particularly in space, i.e. $0.56 \times 0.56^\circ$, as compared with the data used in previous analyses [5,6]. The annual and seasonal mean wind stress curl was computed for individual years and considered vs the current features found in the Japan Basin. The results of this analysis are briefly given in the next section.

3- Results and Discussion

The annual mean wind stress is largely set up by the Asian Winter Monsoon, which blows from Siberia. The annual mean wind stress curl shows pattern very similar to that of the winter season alone (Fig.2). The anticyclonic curls appear in the region southwest of Vladivostok between the East Korea Bay and the Primorye coast. The tongue of anticyclonic curls stretches to the southeast towards the Yamato Basin. The wind stress curls are positive over the East Korea Bay, near the Hokkaido Island, and over the coastal zone east of Vladivostok. This pattern generally agrees with the surface wind stress curl pattern obtained by Na et al. [5] except in the region southwest of Vladivostok where an anticyclonic curl was identified here.

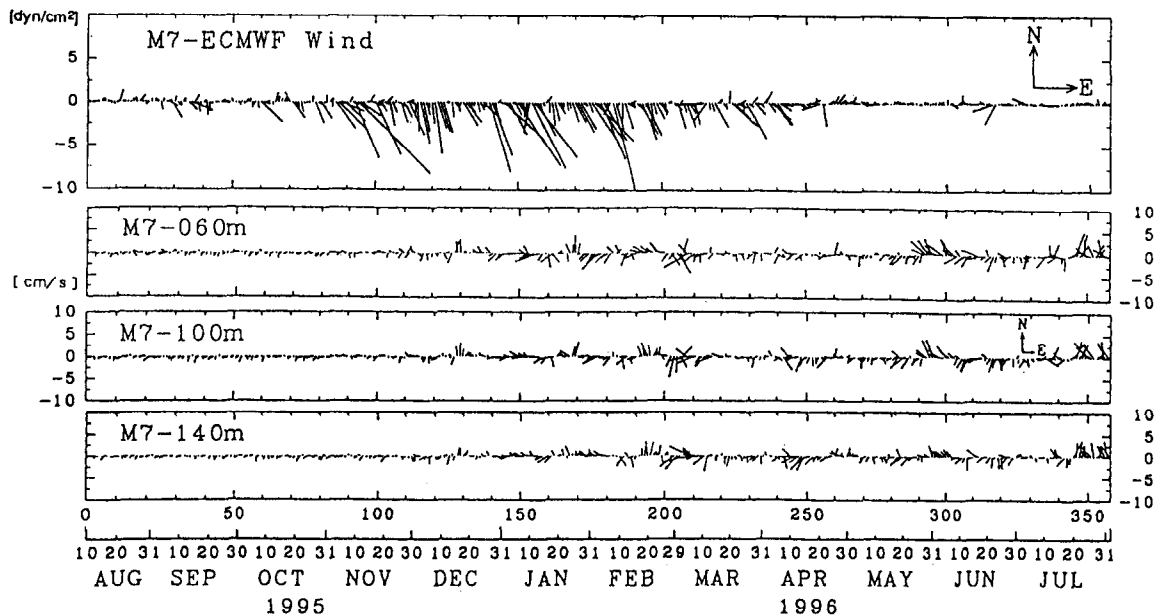


Fig. 3. The ECMWF surface wind stress and the ADCP current velocities at M7.

Surprisingly, despite the mean strong negative wind stress curl near M7, we did not find any evidence of persistent strong currents or eddies in the sea upper layer at M7. Fig. 3 shows the daily surface wind stress near M7 and the sea currents in the upper layer between 60 m and 300 m measured by ADCP at M7 in August 1995-July 1996 (the upward-looking ADCP was deployed too deep to observe the surface Ekman transport). Apparent in Fig.3 is huge annual variation of the surface wind with strong northwesterly prevailing in November - March and very weak wind in the warm season. The southeastward currents of less than 0.02 m/s were observed in the subsurface layer in August - November 1995. The current intensified in December demonstrating 10-day fluctuations of up to 0.07 m/s amplitude, which can be associated with the near-surface turbulence. These high frequency variations continued until recovery of M7, i.e. through July 1996, though the northwesterly wind vanished in May. Noticeably, there was no persistent flow that could be anticipated from rather stable wind stress curl of the cold season. Also, the current meter data of M7 show neither stable currents nor eddies all the year around through the entire water column at the site.

The site M6 was located in the Liman Current region near the Primorye coast. Low-passed current records from the top instrument at M6 are shown in Fig.4, demonstrating that the westward flowing Liman Current was clearly recognizable at the depth of 800 m. The westward current had an apparent vertical shear and was less stable at greater depths, but the westward transport dominated even at 2400 m (500 m above the sea floor).

It is of interest to compare the vector plot in Fig.4 with the wind vector plot at M7 located not far from M6 (Fig. 3). Amazingly there is no similarity between the two vector plots: The deep Liman Current exhibits little seasonal variation in spite of the marked annual variation of the wind forcing over the site. If the Liman Current is essentially wind-driven as has generally been believed, there must be some buffer mechanism to smooth out the Liman Current response to the strong annual variation of wind forcing.

Stick vector plots of low-passed deep current velocities at M5 are shown in Fig. 5. Visual similarity between the two between the two plots in Fig. 5 is apparent, indicating that the deep current at M5 is quasi-barotropic throughout the instrumented depths. Unanticipatedly the deep current in the interior region exhibited strong seasonal variation in contrast to the Liman Current. The seasonal variability of the deep current is similar to that of the surface wind though there is 3-4 month phase lag between the two variability's. The overall circulation of the Japan Basin is thought to be cyclonic at least in the upper few hundred meters in response to the cyclonic nature

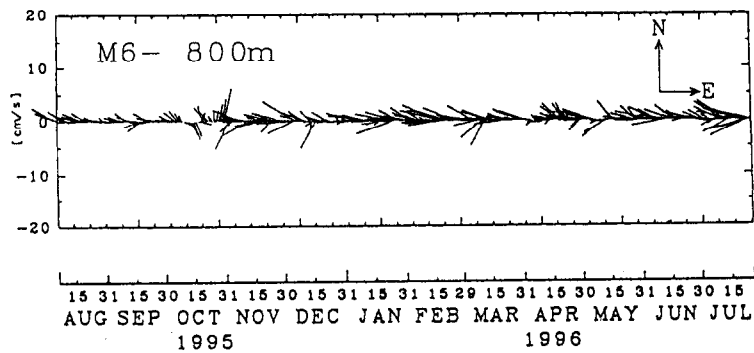


Fig. 4. The current velocities at the depth of 800 m at M6.

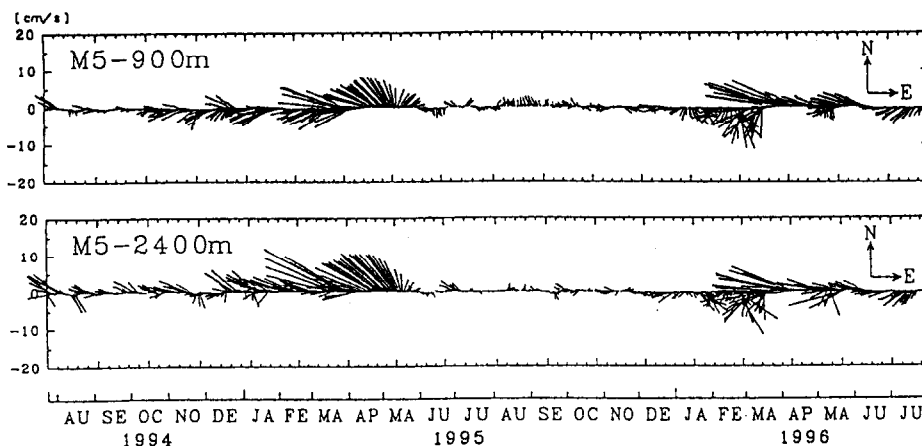


Fig. 5. The current velocities at M5.

of wind forcing. However, the strong deep current at M5 was predominantly westward in contradiction to a cyclonic circulation in the Japan Basin. As it is thus far believed, the Subpolar Front is stretched zonally along 40 N and at the latitude of the mooring site M5 the along-frontal current should be directed eastward in the sea upper layer. If this argument is valid, then the deep westward flow found at M5 appears to be a counter current.

Similar quasi-barotropic deep currents were observed also at M4 and M3. As is illustrated in Fig. 6, there was predominantly southward strong current at M4 while there was no appreciable current at all at the adjacent site M7. It seems reasonable to conjecture that the southward deep current reached M4 passing through the eastern side of the sea mount (see Fig.1): The current must have originated from the slope region around M6, where the steady Liman Current is flowing, and continues southward to M5. Notably, however, temporal variation of the current at M4 is quite dissimilar to that of the currents at M5 and M6 as well as of the surface wind.

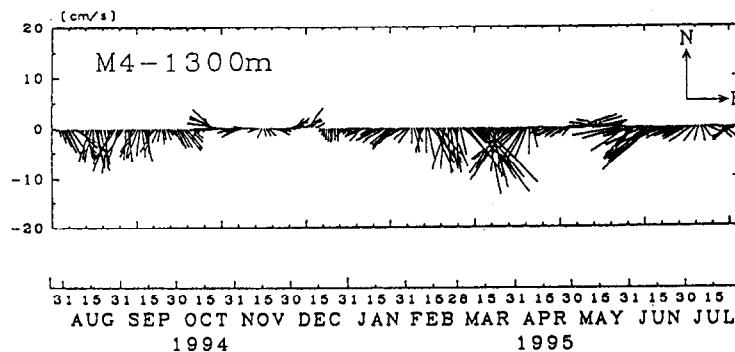


Fig. 6. The current velocities at M4.

Temporal variation of the quasi-barotropic current at M3 is illustrated in Fig.7. The current at M3 was highly eddy-like having almost negligible mean velocities (less than 0.01 m/s) in sharp contrast to the currents at M4 and M5. Indeed the current pattern is reminiscent of the passage of mesoscale eddies. However, the eddy-like current in the Japan Sea shows strong seasonal variation unlike ordinary mesoscale eddies in the world ocean. This specific eddy feature in the central region of the Japan Basin is discussed in a separate paper [7] by comparing the moored current meter records with near-surface eddy currents inferred from satellite infrared images and ARGOS drifter tracks. As is exemplified in Fig.8, the deep eddy-like current is found to be well correlated to isolated anticyclonic eddies emanating in cold seasons from the Subpolar Front zone south of M3. Thus it was concluded that the seasonal deep current at M3 was due to anticyclonic and barotropic eddies with the diameter of 60-70 km. In view of the relatively small eddy size and the uni-rotational (anticyclonic) nature, it seems unlikely that the eddies are a direct consequence of wind forcing.

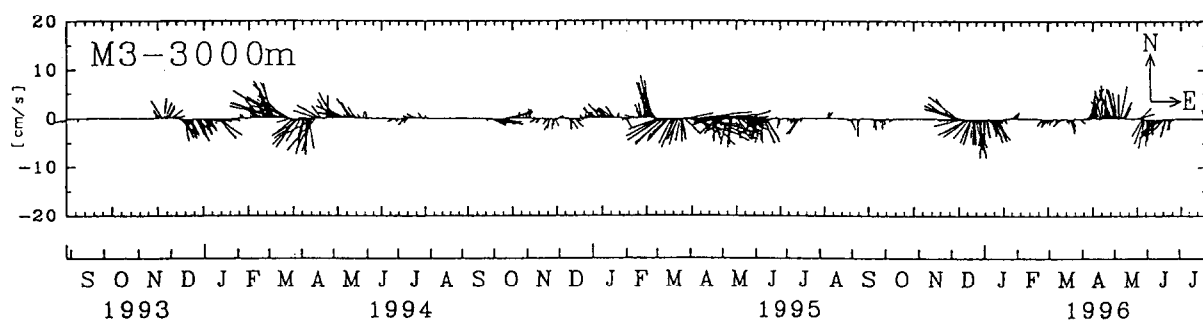


Fig. 7. Stick vector plots of the current velocities at M3.

Current meter data from the moorings at M1 and M2 showed that there were no appreciable deep currents all through the year in the eastern rim of the Japan Basin. The deep layer of the eastern Japan Basin seems to be almost inert to both the wind forcing and other thermohaline forcings.

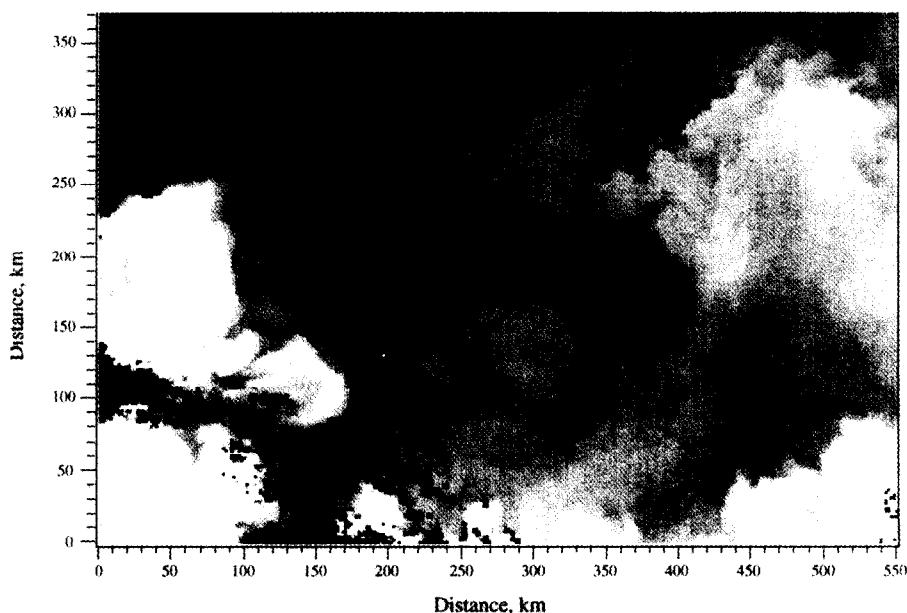


Fig. 8. The NOAA-10 AVHRR MCSST image of the north Japan Sea on December 23, 1993. The location of the M3 mooring site is shown by circle and stick represents the current vector at the depth of 2000 m. The lower temperatures are dark gray. The Primorye coast and clouds are black. The vertical axis is directed northward.

4- Conclusions

The CREAMS observations revealed some unanticipated current features in the deep water of the northern Japan Sea. There were strong deep currents in the interior region (M3, M4, M5) of the Japan Basin as well as in

the Liman Current region (M6) along the northern shelf slope. Temporal variability of the deep currents differed significantly from site to site in spite of rather small spacings (less than 300 km) of the mooring array. Curiously, the Liman Current showed little seasonal variation, while the deep currents at M5 and M3 had strong variation of the seasonal means similar to that of the wind forcing but with 3-4 month phase lag behind the wind change. The current pattern at M4 was quite unrelated to those at M5 and M3 as well as to the wind pattern. The wintertime wind forcing was particularly strong over site M7 nevertheless the entire water column below the surface Ekman layer at M7 was almost stagnant all the year round.

In conclusion, none of the observed current features can be directly related to the wind forcing. The deep currents in the Japan Basin must be affected not only by the wind forcing but also thermohaline processes such as the wintertime open-ocean convection and dense water cascading down the shelf slope. The bottom geometry may be also important in specifying the spatial variability of the currents.

References

- [1] M. Takematsu, A. G. Ostrovskii, and T. Kitamura. 1994, Current features in the Japan Sea Proper Water, Proc. 3rd CREAMS Workshop, 1-4.
- [2] V. G. Yarichin, 1980, Steady state of the Japan Sea circulation, In Problems of Oceanography, Ed. by V. Pokudov, 46-61 (in Russian).
- [3] T. Senjyu, and H. Sudo, 1993, Water characteristics and circulation of the upper portion of the Japan Sea Proper Water, J. Mar. Sys., 4, 349-362.
- [4] T. Senjyu and H. Sudo, 1996, Interannual variation of the upper portion of the Japan Sea Proper Water, J. Oceanogr., 52, 61-73.
- [5] J.-Y. Na, J.-W. Seo and S. K. Han, 1992; Monthly mean sea surface wind over the adjacent seas of the Korea Peninsula, J. Oceanol. Soc. Korea, 27, 1-10.
- [6] P. C. Chu, Y. Chen and S. Lu, 1998, Temporal and spatial variabilities of the Japan Sea surface temperature and atmospheric forcing, J. Oceanogr., 54, 273-284.
- [7] M. Takematsu, A. G. Ostrovskii and Z. Nagano, 1999, Observation of eddies in the Japan Basin interior, J. Oceanogr.: CREAMS special issue (revised).

THREE-DIMENSIONAL MODELLING OF BOTTOM DENSE LENS EVOLUTION

Tsarev V.

Russian State Hydrometeorological University,
St.-Petersburg, 195196, Malookhtinsky Av. 98, Russia

Abstract

A three-dimensional model simulating dense lens bottom evolution is developed. The model includes equations of three components of vorticity, equations of three components of vector potential, expressions of three velocity components through vector potential, equation of salt transfer and equation of state. The model was used for simulation of dense lens evolution near horizontal and inclined bottom. The results of the model application are presented and discussed.

The existence of bottom dense eddies and their key role in the bottom dynamics of ocean and many coastal seas are now evident. It stimulated the theoretical, laboratory and field investigations of such phenomena. Models of dense lens motion on a sloping bottom in rotating fluid were given by [2, 4–6]. Additional insights into such problem were obtained by laboratory experiments by [3, 7]. Bottom dense eddies were also observed in field study by [1]. First theoretical investigations focused on dense bottom lens behaviour and main features of dense lens motion on a sloping bottom. It was considered the case of dense lens on a sloping bottom beneath an infinitely deep and motionless upper layer. From these models it was established that the bottom dense lens spreading radially generates anticyclonic vortex. Its radial spreading continues until geostrophic equilibrium is reached. The second type of lens motion is its translation along isobathes governed by the bottom inclination and lens density excess over ambient water. From two layer models with ambient lighter water of finite depth it was shown that besides the cyclonic vortex surrounding by dense bottom lens because of its interaction with ambient water the lens radial spreading becomes a reason of the generating of cyclonic vortex over the lens. The intensity of this vortex was found to be more intensive than of lens vortex. Observations show that vertical distribution of cyclonic vortex intensity is not homogeneous. The much intensity was observed close over the lens and it decreased upward with distance. Obtained results made it clear that it is desirable to use three dimensional models which are free of assumptions of water property homogeneity into lens and surrounding layer that is used in two layer models. The main aim of the article is to present one of the possible such model and discuss results of its application.

For simulation bottom dense water flow use nonhydrostatic, three-dimensional model including Reynolds motion equation, equations of mass and salinity conservation and equation of state. Equations of motion and mass conservation can be presented in form of equations of vorticity and vector potential

$$\frac{\partial \Omega_x}{\partial t} + u \frac{\partial \Omega_x}{\partial x} + v \frac{\partial \Omega_x}{\partial y} + w \frac{\partial \Omega_x}{\partial z} = l \frac{\partial u}{\partial z} + g \frac{\partial \rho}{\partial y} + k \frac{\partial^2 \Omega_x}{\partial z^2}, \quad (1)$$

$$\frac{\partial \Omega_x}{\partial t} + u \frac{\partial \Omega_x}{\partial x} + v \frac{\partial \Omega_x}{\partial y} + w \frac{\partial \Omega_x}{\partial z} = l \frac{\partial u}{\partial z} + g \frac{\partial \rho}{\partial y} + k \frac{\partial^2 \Omega_x}{\partial z^2}, \quad (2)$$

$$\frac{\partial \Omega_x}{\partial t} + u \frac{\partial \Omega_x}{\partial x} + v \frac{\partial \Omega_x}{\partial y} + w \frac{\partial \Omega_x}{\partial z} = l \frac{\partial u}{\partial z} + g \frac{\partial \rho}{\partial y} + k \frac{\partial^2 \Omega_x}{\partial z^2}, \quad (3)$$

$$\nabla_x^2 \psi_x - \frac{\partial}{\partial x} \left(\frac{\partial \psi_z}{\partial z} + \frac{\partial \psi_y}{\partial y} \right) = \Omega_x, \quad (4)$$

$$\nabla_x^2 \psi_x - \frac{\partial}{\partial x} \left(\frac{\partial \psi_z}{\partial z} + \frac{\partial \psi_y}{\partial y} \right) = \Omega_x, \quad (5)$$

$$\nabla_x^2 \psi_x - \frac{\partial}{\partial x} \left(\frac{\partial \psi_z}{\partial z} + \frac{\partial \psi_y}{\partial y} \right) = \Omega_x, \quad (6)$$

$$u = \frac{\partial \psi_z}{\partial y} - \frac{\partial \psi_y}{\partial z}, \quad u = \frac{\partial \psi_z}{\partial y} - \frac{\partial \psi_y}{\partial z}, \quad u = \frac{\partial \psi_z}{\partial y} - \frac{\partial \psi_y}{\partial z}, \quad (7)$$

$$\frac{\partial s}{\partial t} + (\mathbf{u} \cdot \nabla) s = k_z \frac{\partial s}{\partial z} + k_l \nabla_l s, \quad (8)$$

$$\rho = \rho_0 + \alpha_s s, \quad (9)$$

where $\Omega_x, \Omega_y, \Omega_z$ are x, y, z components of vorticity; Ψ_x, Ψ_y, Ψ_z are x, y, z components of vector potential; α_s is water contraction due to salinity; $\nabla_x^2 = \frac{\partial^2}{\partial y^2} + \frac{\partial^2}{\partial z^2}$, $\nabla_y^2 = \frac{\partial^2}{\partial x^2} + \frac{\partial^2}{\partial z^2}$; $\nabla_z^2 = \frac{\partial^2}{\partial x^2} + \frac{\partial^2}{\partial y^2}$;

Boundary conditions for Ω components.

Neglecting for simplicity wind stress we can obtain for the free surface

$$\Omega_x = \frac{\partial w}{\partial y} - \frac{\partial v}{\partial z} = 0, \quad \Omega_y = \frac{\partial u}{\partial z} - \frac{\partial w}{\partial x} = 0, \quad \frac{\partial \Omega_z}{\partial z} = \frac{\partial}{\partial z} \left(\frac{\partial v}{\partial x} - \frac{\partial u}{\partial y} \right) = \frac{\partial}{\partial x} \left(\frac{\partial v}{\partial z} \right) - \frac{\partial}{\partial y} \left(\frac{\partial u}{\partial z} \right) = 0. \quad (10)$$

For the bottom $\frac{\partial w}{\partial x} \gg \frac{\partial w}{\partial y}$ are much less compared with $\frac{\partial u}{\partial z} \gg \frac{\partial v}{\partial z}$ and can be neglected. The current velocity derivative with respect to z can be expressed through the quadratic drag law for the bottom stress

$$\Omega_x = -\frac{c_0 \sqrt{u^2 + v^2}}{k_z \rho_0} u, \quad \Omega_y = -\frac{c_0 \sqrt{u^2 + v^2}}{k_z \rho_0} v, \quad \frac{\partial \Omega_z}{\partial z} = \frac{\partial}{\partial z} \left(\frac{\partial v}{\partial x} - \frac{\partial u}{\partial y} \right) \cong -\frac{c_0 \sqrt{u^2 + v^2}}{k_z \rho_0} \Omega_z. \quad (11)$$

For the side solid boundary the boundary conditions are proceeded from assumption of no normal flow and zero friction. In this case the tangent to solid side boundary vorticity component Ω_l is

$$\Omega_l = \mathbf{l} \cdot \boldsymbol{\Omega} = \mathbf{l} \cdot \nabla \times \mathbf{u} = -\nabla \cdot (\mathbf{l} \times \mathbf{u}) = -\frac{\partial u_m}{\partial n} - \frac{\partial u_n}{\partial z} = 0, \quad (12)$$

where \mathbf{l}, \mathbf{m} , are tangent and \mathbf{n} is normal to the side boundary unit vectors, u_m, u_n - \mathbf{m} and \mathbf{n} current velocity components in local co-ordinate system. For the vertical side boundaries \mathbf{m} is usually used aligned with \mathbf{z} . In this case instead of u_m can be used u_z .

The boundary condition for Ω_z can be obtained in the similar way

$$\Omega_z = 0. \quad (13)$$

Find derivative of normal vorticity component to the side with respect to n

$$\Omega_n = \frac{\partial}{\partial n} (\mathbf{n} \cdot \boldsymbol{\Omega}) = \frac{\partial}{\partial n} (\mathbf{n} \cdot \nabla \times \mathbf{u}) = -\nabla \cdot \left(\frac{\partial}{\partial n} (\mathbf{n} \times \mathbf{u}) \right) = -\frac{\partial}{\partial l} \left(\frac{\partial u_z}{\partial n} \right) + \frac{\partial}{\partial z} \left(\frac{\partial u_l}{\partial n} \right) = 0. \quad (14)$$

If \mathbf{l} is aligned with \mathbf{x} of main co-ordinate system then

$$\Omega_z = \frac{\partial v}{\partial x} - \frac{\partial u}{\partial y} = 0, \quad \Omega_y = \frac{\partial u}{\partial z} - \frac{\partial w}{\partial x} = 0, \quad \frac{\partial \Omega_x}{\partial x} = \frac{\partial}{\partial x} \left(\frac{\partial w}{\partial y} - \frac{\partial v}{\partial z} \right) = \frac{\partial}{\partial y} \left(\frac{\partial w}{\partial x} \right) - \frac{\partial}{\partial z} \left(\frac{\partial v}{\partial x} \right) = 0. \quad (15)$$

For the liquid side boundary we can use following expressions

$$\frac{\partial \Omega_i}{\partial n} = 0, \text{ where } i=l, n, z.$$

The boundary conditions for vector potential components at solid side boundary are proceeded from the condition of vanishing normal flow. This condition can be full-filled if to except that at the solid boundary

$$\Psi_l = 0, \Psi_z = 0. \quad (16)$$

were Ψ_1, Ψ_2 – tangent to the solid side boundary components of the vector potential.

The boundary condition for the normal vector potential component can be used in

$$\frac{\partial \Psi_n}{\partial n} = 0, \Psi_x = 0, \Psi_y = 0, \frac{\partial \Psi_z}{\partial z} = 0. \quad (17)$$

The boundary conditions has the most simple form in the case when the boundary is perpendicular to any main system co-ordinate vector. In another case vector potential components of local system of co-ordinate can be expressed through that components of main system. As for the side boundary $\mathbf{m} = \mathbf{z}$ then

$$\Psi_m = \Psi_z. \quad (18)$$

The boundary conditions for this salinity are given by

$$s(0, x, y) = s_0; \text{ (at the free surface),} \quad (19)$$

$$\frac{\partial s}{\partial z} = 0; \text{ (bottom),} \quad (20)$$

$$s = s(x, y, z) \text{ (at the open sea boundary and at the free surface);} \quad (21)$$

$$\frac{\partial s}{\partial n} = 0; \text{ (coastal boundaries).} \quad (22)$$

The initial salinity is taken 6 pml for almost all area except some small bottom volume located near open boundary area with high salinity. For this volume initial salinity is 16 pml. The volume size is 20 km in horizontal and 10 m in vertical directions the salinity.

The vertical diffusivity coefficients are taken as $k_z = 10^{-5} m^2 s^{-1}$, $k_l = 10 m^2 s^{-1}$.

Equations of the model (1)–(9) are integrated numerically with finite difference method.

The advection terms in equations replaced with Leth's method and the diffusion operator by the central finite difference expression. and are calculated with explicit method. Elliptic equations for vector potential components are solved with Gauss-Seidel iterations method. To increase a rate of convergence the first step of iterations is obtained with Tom's algorithm in z direction. Currents velocity components are calculated with central finite difference expression.

A model area was covered by the grid of size 41x81 in lateral and 30 points in vertical directions. Horizontal steps are 5 km. In the vertical direction upward from the bottom fist ten steps are of 2 m. In the upper layer it is equal to $(H-h_b)/19$, where H, h_b – total depth and near bottom layer thickness respectively.

Numerical experiments were performed to study the model applicability for simulation of dense water lens motion near an inclined bottom. The initial dense water vellum had in plan the square form with 20000 m of side size. In centre its height was 12 m from the bottom which decreased to 8 m at the sides. The initial conditions for these experiments were a zero vorticity. The dense water salinity was held constant at 16 psu. The surrounding

water salinity was 6 psu. The water density was accepted to be caused by salinity only. The bottom inclination was $0.2 \cdot 10^{-3}$ in x -direction.

Calculations were continued for a period of 20 Rossby periods ($T_R = l/f$) simulating time variations of the three-dimensional fields of vorticity, vector potential, currents velocity components, and salinity. To study the structure of the lens motion in addition to that the mean for the lens as a coherent body displacement velocity and local velocity relative to the lens mean velocity were calculated. The first was obtained by averaging of previously calculated numerical horizontal velocity components over the lens area. The second one was performed as a subtraction of the mean lens velocity from the numerical values for grid points located in the lens. The results illustrated in fig.1a and fig.1b show that during the time of $6T_R$ lens mean x and y velocity components (u_r and v_r respectively) perform decreasing periodic oscillations. After ones become equal to 5 and 20 cm s^{-1} respectively. It means that after establishment the lens moves across bottom inclination mostly. The obtained y (along slope) component is close to the Nof velocity for used bottom inclination and density difference [6]. During period of establishment in time from 2 to $3 T_R$ u_r has negative value. It means that in that period the lens moves in up-slope direction. Relative lens velocity components obtained have clockwise rotation mostly and reach rather large values close to 45 cm s^{-1} . That is connected with vorticity generating during the lens radial spreading.

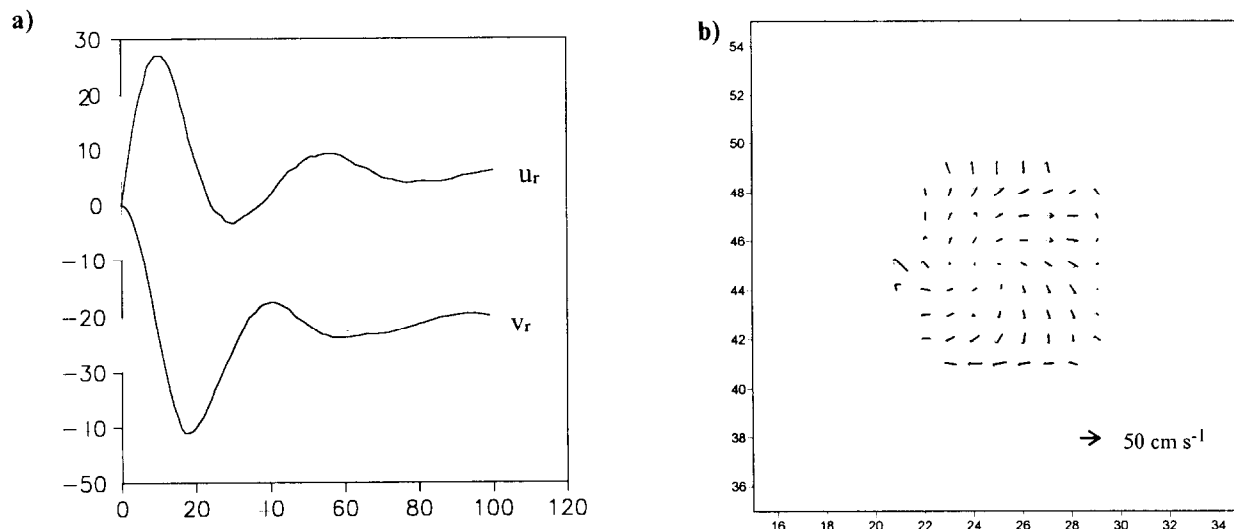


Fig.1. Time variation of averaged lens horizontal flow components/ (a) and relative velocity in T_R two meters above the bottom (b) .

Resulting currents velocity in vicinity of the lens are the sum of presented above components. That's why its velocity varies over the lens along the y axis from down-slop to along-slop directions (fig.2)

In spite of that the resulting the lens translation coincides with the lens mean velocity. Obviously such translation in the lens depends on the lens thickness. As a result it causes the lens form transformation which is characterised by increasing of the lens thickness front part compared with its left one (fig.3).

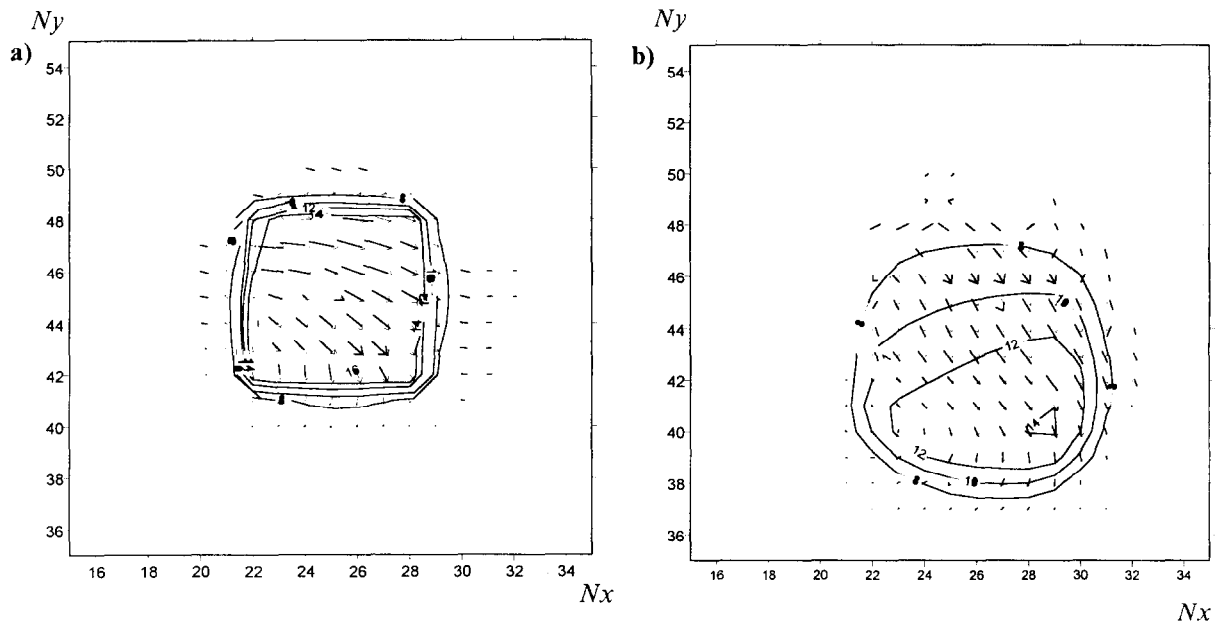


Fig. 2. Velocity and salinity distributions in T_R (a) and in $10 T_R$ (b) two meters above the bottom time (N_x, N_y – grid points numbers along x and y axis respectively).

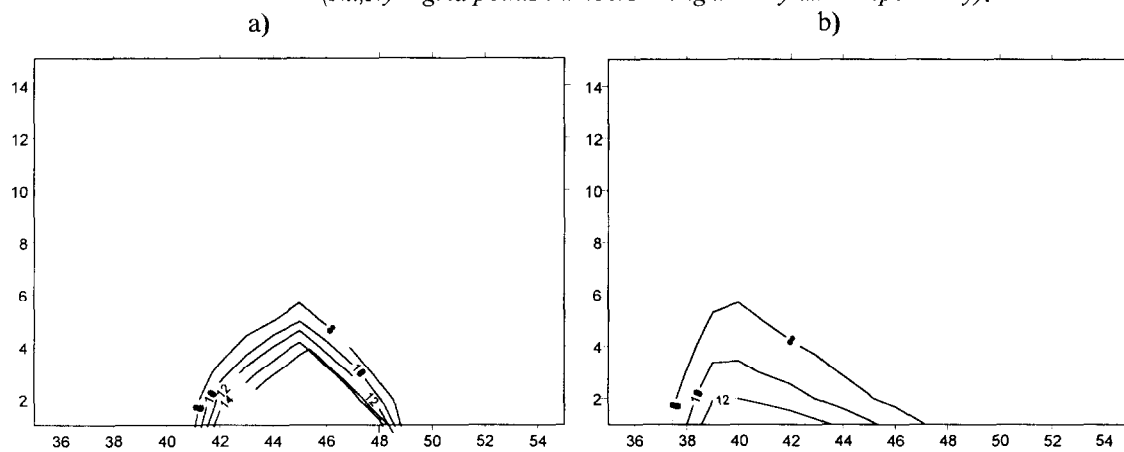


Fig.3. Salinity distributions (psu) along y - z section with $N_x=25$ in $t=T_R$ (a) and in $t=10 T_R$ (b)

References

1. Bignami F., Solusti E., Schiarini S. 1990 Observations on a bottom vein of dense water in the southern Adriatic and Ionian seas // J. Geophys. Res., № C5, 7249-7259.
2. Killworth, P. D. 1983 On motion of isolated lenses on beta-plane.// J. Phys. Oceanogr. 13, 368-376.
3. Mory, M. 1985 Integral constraints on bottom and surface isolated eddies. // J. Phys. Oceanogr. 15, 1433-1438.
4. Nof D. 1983 The translation of isolated cold eddies on a sloping bottom. // Deep-Sea Res. 30,171-182
5. Nof, D. 1984 Oscillatory drift of deep cold eddies.// Deep-Sea Res. 31,1395-1414.
6. Nof, D. 1985 Joint vortices, eastward propagating eddies and migratory Taylor columns. // J. Phys. Oceanogr. 15, 1114-1137.
7. Whitehead J., Stern, M., Flierl, G., Klinger, B. 1990 Experimental observations of Baroclinic eddies on a sloping bottom. // J Geophys. Res., v.95, № C6, 9585-9610.

HYDROLOGICAL AND DYNAMICAL CHARACTERIZATION OF MEDDIES IN THE AZORES REGION : INTERACTION WITH THE AZORES CURRENT

A. Tychensky and X. Carton

SHOM, LEGOS-BRESM, 14, Av. Edouard Belin, 31401 Toulouse, FRANCE
SHOM-Centre Militaire d'Océanographie, 13, rue du Chattelier, 29200 Brest, FRANCE

Abstract

During the Semaphore experiment, hydrological data, currentmeter recordings and float trajectories were collected over a 6-month period (june-november 1993), in a $500 \times 500 \text{ km}^2$ domain south of the Azores. This data exhibits three intrathermocline eddies of Mediterranean water (meddies). We quantify their hydrological and dynamical properties on isopycnic surfaces. Intense temperature and salinity anomalies (up to 4°C and 1 psu), vertically ranging over 1000 m and centered around 1000 dbar, are associated to these meddies. Horizontally, these anomalies spread out to radii of 50 to 60 km, though the maximum azimuthal velocities lay at around 35 km. These meddies followed bent trajectories, with drift velocities up to 10 cm/s, under the influence of the neighboring mesoscale features (companion cyclones or jet meanders). One of them was coupled to a subsurface anticyclone, forming an aligned vortex. It later interacted with the Azores front, creating a large-amplitude northward meander by vertical alignment of vorticity. South-east of the front, another meddy was horizontally sandwiched between an Azores front meander and a cyclone of large vertical extent. This cyclone later interacted with a stronger cyclone and underwent a partial merger. To explain the meddy interactions with the Azores jet, we use a simple quasi-geostrophic model in which analyses can be performed with a finer time-sampling.

1. Introduction

During the "Semaphore" experiment, which has been carried out over a 6-month period in an area located between the Azores and Madeira islands (Fig.1), 3 large meddies have been detected and studied .

The Azores-Madeira region possesses particularly rich mesoscale dynamics and specific hydrological conditions. It is characterized by the presence of the Azores Current (AC)[1,2] and of the Mediterranean water tongue (between 800 and 1300m), which spreads westward from its origin at the Strait of Gibraltar and strongly alters at large scales the vertical hydrological structure of the Northeast Atlantic Basin.

The semaphore experiment permitted to follow for a 6 month-period the trajectories of these meddies. A strong evolution of the frontal structure of the AC has been observed, which seems

to be directly related to the proximity of the meddies with the AC.

2. Observations

The intensive in-situ measurements focused on the study of the mesoscale circulation [3]. The experiment consisted in 3 hydrographic surveys, which consecutively sampled the domain with XBT and CTD stations. Leg 1 was carried out in July, leg 2 in August-September and leg 3 in October-November 93. A coherent XBT/CTD dataset was generated for each leg and optimally estimated maps of temperature (T), salinity (S) and geostrophic velocities were then obtained by an objective analysis (OA). The in-situ data also included Eulerian and Lagrangian current measurements. In particular, 47 Surdrifts, surface drifting buoys, drogued at 150 dbar to follow the subsurface geostrophic circulation, were regularly deployed during the 3 legs. Absolute velocity maps at 150 dbar were then computed by OA of the drifters velocities, which permitted to complement the hydrographic dynamic description of the meddies [4].

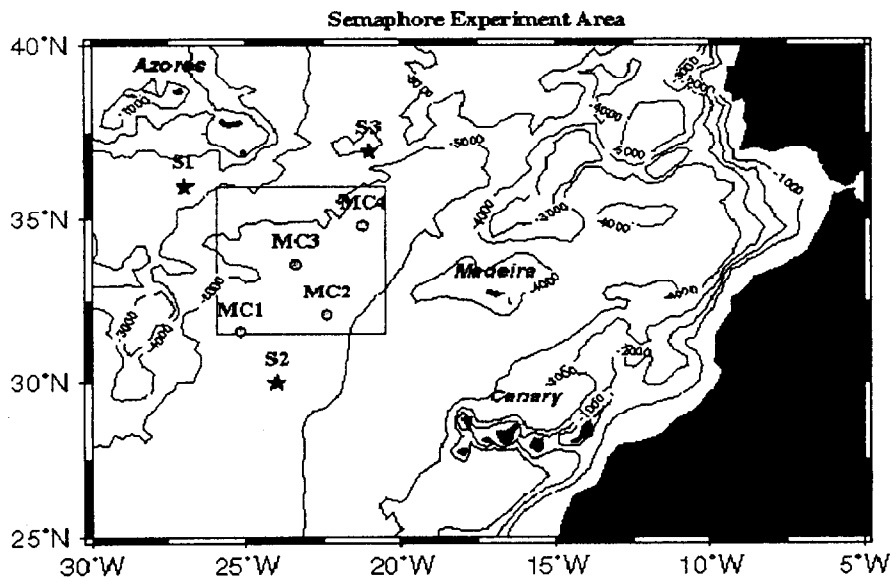


Fig.1: The Semaphore experimental area (square box), located in the Azores-Canary basin. The 4 current meter moorings are represented by gray circles, the three acoustic sources by black stars.

3. Meddy positions and hydrological structures

The analyzed T fields at 200 and 1000 dbar (Fig.2) present a synthetic view of the initial and following positions of the meddies observed in the Semaphore domain [5].

We first observe the thermohaline signature of the AC and its evolution during the consecutive 3 legs (Fig.2a,c,e). The 1st meddy, a very big structure called **Hyperion**, was observed west of the domain during leg1 (Fig2.b). A smaller meddy, called **Ceres**, was also found during leg1,

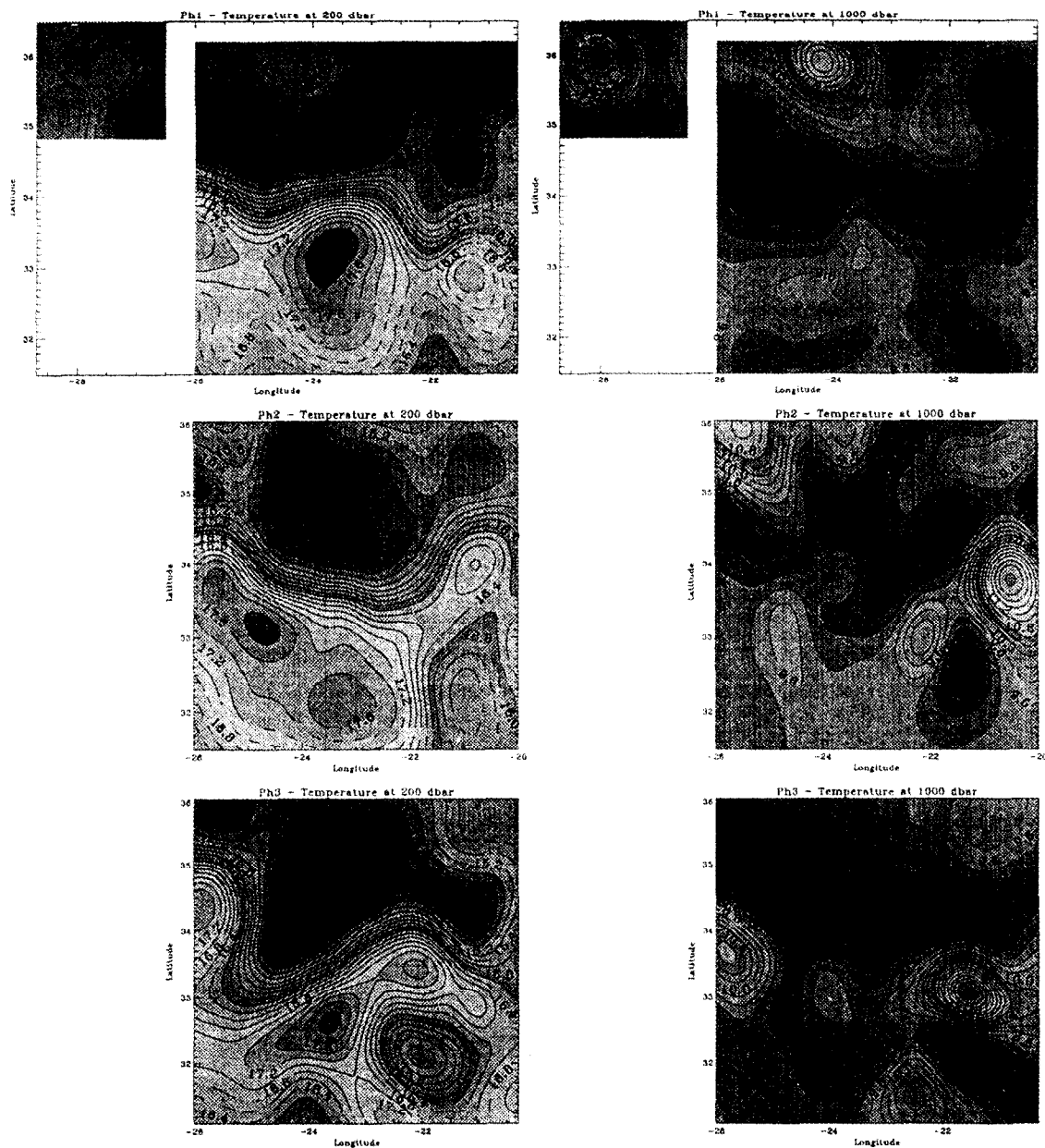


Fig.2: Horizontal maps of temperature at 200 and 1000 m depth estimated by OA. Phase 1, Hyperion (M1) is located outside of the Semaphore area, Ceres (M2) is on the northern boundary (see Fig.3 for localisation of M1-M3, E1-E3). A warm feature (E1) is overlying Ceres. Phase 2, Ceres (M2) is on the northwestern corner and Encelade (M3) enters the domain from the eastern boundary. The warm eddy (E1), which is found again above Ceres, has propagated at the same speed and in the same direction as Ceres. A cold and fresh anomaly (E3) is found south of Encelade. The thermohaline signature of this feature extends deeply vertically. Phase 3, Ceres (M2) is on the western boundary and Encelade (M3) in the southeastern part of the domain. E1 and E3 are again found above Ceres and south of Encelade respectively.

north of the average zonal axis of the AF. Near the sea surface at 200 dbar, located just above meddy Ceres, we observe a coherent warm and salty signal (Fig.2d). Ceres was relocated during leg2 in the northwestern corner of the experimental domain, as well as the subsurface warm anomaly at 200 dbar.

The 1000 dbar T field of the 2nd hydrographic survey evidences another huge and energetic meddy east of the domain, which we called **Encelade**. As for meddy Ceres, we observe a warm and salty water anomaly above Encelade. This surface structure is in fact formed by an anticyclonic meander of the AF. South of meddy Encelade, we notice a cold anomaly. This patch of cold and fresh water probably formed north of the front, as we will see later. During leg3, meddy Encelade was relocated (Fig.2f). The observation of the frontal area between legs2 and 3 reveals a strong meander and the AF completely encircled Encelade. The cold anomaly, already previously observed, has clearly intensified and now forms with the meddy a coherent dipole observable from the sea surface down to at least 1800 dbar (Fig.2e.f). Meddy Ceres is now detected on the western boundary of the domain, surprisingly exhibiting an abrupt turn to the south, after propagating westward between the first two legs; this change in direction was later confirmed by RAFOS float trajectories.

4. Dynamical characterization

We derived the geostrophic velocities from the hydrological density field (Fig.3). A reference level of no motion was chosen at 2000 dbar. We now concentrate on Ceres and Encelade due to their proximity with the AC and surface mesoscale structures. The presence of the warm and salty anomaly, associated with an anticyclone, above meddy Ceres results in a nearly barotropic signal extending from the surface down to 2000 m. At the depth of the meddy core, the maximum anticyclonic velocity is 12 cm/s at a radius of 35 km from the central axis. For meddy Encelade, under the influence of its cold cyclonic companion, located south of it, and of the Azores anticyclonic meander located above it, the meddy is strained, sheared and elongated in an elliptical form. Maximum geostrophic velocities reached 25 cm/s at roughly 40 km from the center. At the depth of the meddy-center, maximum azimuthal velocities of this cyclone were only 8 cm/s at 25 km from its central axis. The fluid column composed of the meddy with the anticyclonic meander and the neighbouring cyclone form a very intense dipole, whose dynamical signal extended from the surface down to very deep levels, at least 2000 m depth. In fact, a currentmeter mooring located in the southern part of the meddy, revealed that it extended well more deeply down to 4000 dbar, where significant velocities ($v \approx 5$ cm/s) were still recorded.

5. Dynamical evolution of the meddies, associated eddies and interactions with the Azores jet

5.1. Analysis of the meddy trajectories from observations

Figure 3 shows the geostrophic velocity fields at 200 and 900-950 dbar for the 3 legs of the experiment. We first observe that the jet meanders amplify with time, sometimes as a consequence of their interaction with the neighbouring meddies. Meddy Ceres, originally located 2 degrees north of the Azores jet axis, drifts westward at 2.5 km/day until leg 2. It is then found in the northwestern corner of the experimental domain. In fact meddy Ceres certainly moves

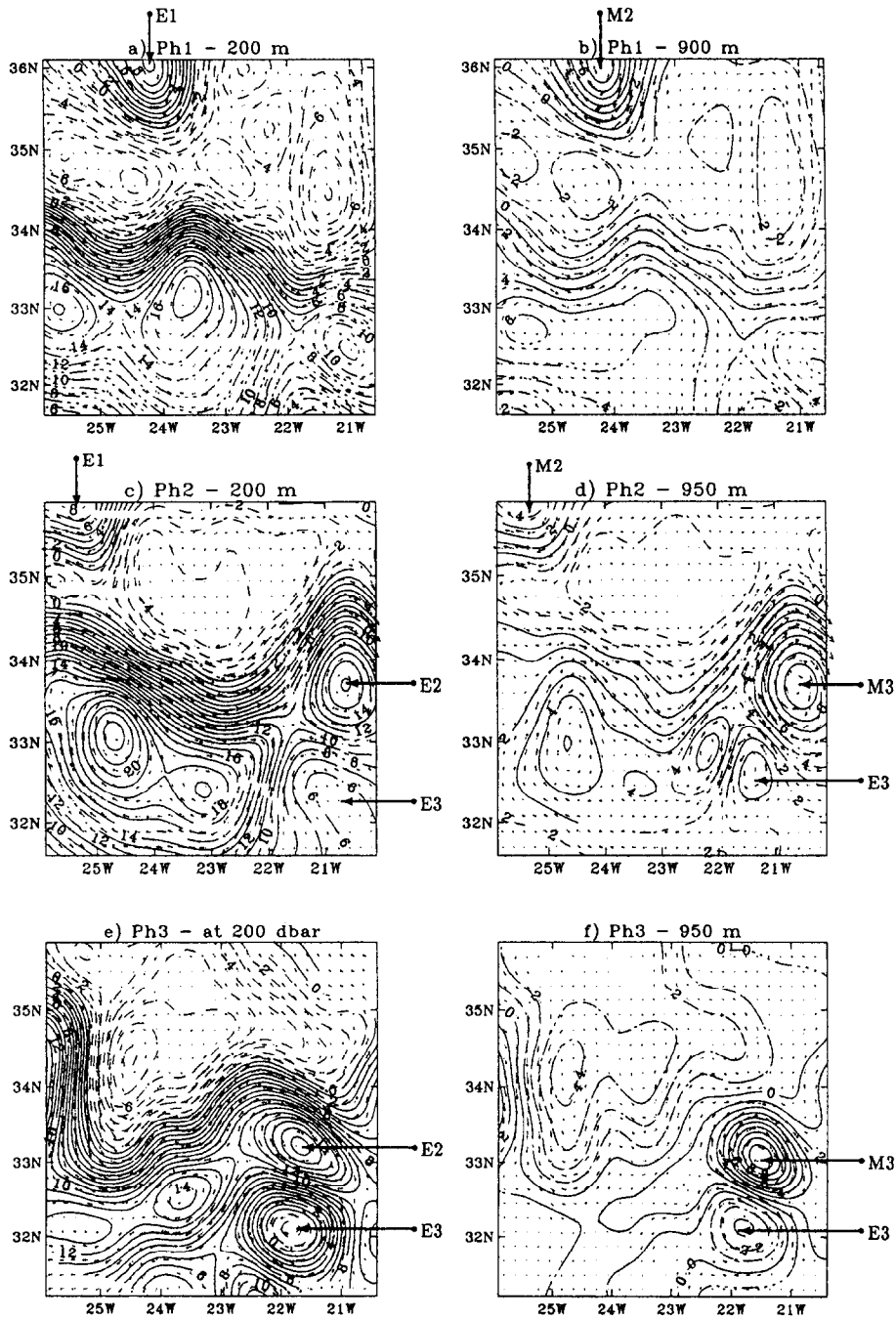


Fig.3: Horizontal maps of dynamic height anomaly at 200 m and at the depth of maximum anomaly in the meddies, for each phase. These maps were computed by OA with a 2000 m reference level. The negative and positive anomalies are plotted in dotted lines and solid lines respectively. An error field larger than 20% is displayed in mixed lines. Superposed is the vector field of horizontal geostrophic velocities computed with the same reference level. Vector lengths are proportional to the velocity magnitude.

by self-propagation, either induced by the beta-effect or by the meridional slope of isopycnals associated with the zonal baroclinic front [6,7].

During leg2, meddy Ceres comes close enough to the northward jet meander to interact with it. This anticyclonic meander is accompanied by cyclonic vorticity in the trough on its eastern flank. The effect of both positive and negative vorticity poles is to draw the meddy southward [8]. The full interaction is observed during leg 3, when Ceres aligns vertically under the meander, and thus undergoes a southward translation, at an average velocity of 6.5 km/day. Such a change in the velocity magnitude and direction, can be explained for by the merger of the anticyclone overlying the meddy with the AC meander. Rafos floats seeded in meddy Ceres at 1000 dbar confirm this geostrophic estimate [9].

Meddy Encelade enters the experimental domain through its eastern boundary during leg 2. It is already crossing the AC axis at this time and is inducing a northward meander on the jet. From leg 2 till leg 3, Encelade propagates southwestward at a velocity of about 2.7 km/day. Again, this motion can be attributed to self-propagation mechanisms and to the dipolar coupling with its cyclonic companion.

Subsurface velocity maps at 150 dbar, obtained from an OA of the Surdrift trajectories every 15 days from the beginning of october to mid-December (Fig.4) allow us to infer the further evolution of the meddies from the sea surface signature of their overlying anticyclonic structures. Ceres slowly drifts southward with a progressive shrinking of the surface meander till november, confirmed by the Rafos float. Meddy Encelade has a richer behavior: it propagates westward with its cyclonic companion at a velocity of 1.8 cm/s; then the dipole axis rotates anticyclonically, indicating that the strength of the meddy dominates that of the cyclone, in agreement with their respective potential vorticity. This cyclonic companion is observed during more than a month, and finally disappears around the end of november. This disappearance can be attributed to a partial merger and straining out, first with another cyclone located south of the domain at that time, and second another part of the cyclone then merged with the southward meander of the Azores front.

5.2. Idealized modeling of surface jet - deep vortex interaction

In order to to qualitatively support our interpretation of meddy-jet interaction, we present a few results from numerical experiments with a β - plane QG model. The model was set up on the stratification of the Azores region, with 3 layers of respective thickness 800, 800 and 3400m, flat bottom and rigid lid, deformation radii of 32 and 15 km, periodic zonal boundary conditions. The model was initialized in the upper layer with a **zonal jet of Gaussian meridional velocity profile** (with a 50 km width). The velocity on the jet axis is $25\text{cm}\cdot\text{s}^{-1}$. In the middle layer, the meddy is idealized as a **Gaussian vortex in streamfunction**. Its max. velocity is $20\text{cm}\cdot\text{s}^{-1}$ at a radius of 35 km. The bottom layer starts from rest. We use an initial distance of 25 km between the meddy and the jet.

Time-series of PV maps in the first 2 layers (fig.5) are presented here for a 2-month experiment. The meddy has a clear surface expression from the beginning. It advects the jet northward on its western side, and southward on its eastern side. In turn, the meddy is sheared and elongated in the NW-SE direction. Then, two effects contribute to the asymmetry of the cyclonic and anticyclonic meanders: the meddy drifts southward on the β -plane, and it is also advected southward by both cyclonic and anticyclonic meanders. Then southward deformations of the jet prevail. Two weeks after the beginning of the experiment, the vertical phase shift between the meddy and the upper layer positive vorticity anomaly results in a baroclinic dipole, which

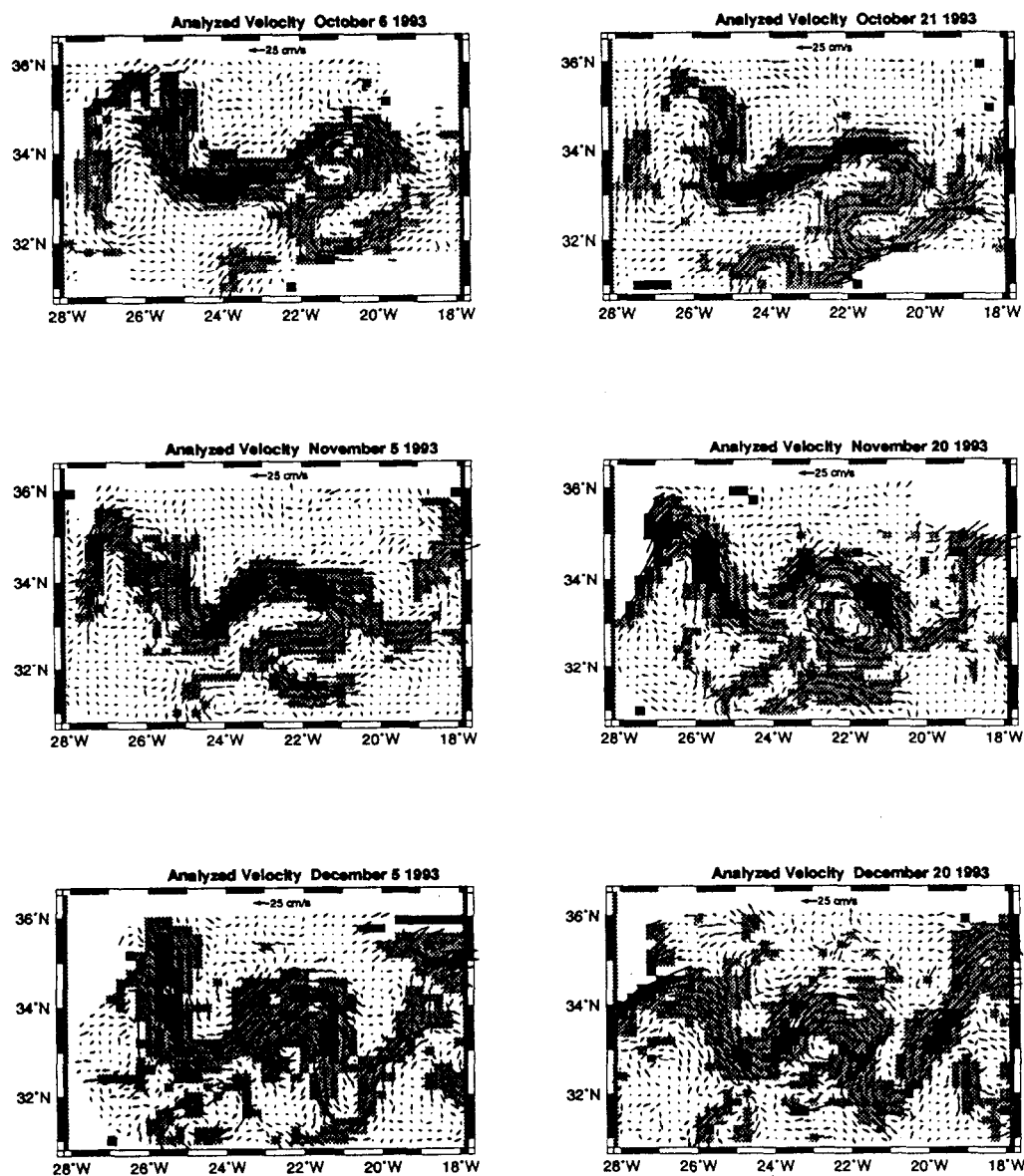


Fig.4: Time-series of velocity maps at 150 m estimated every two weeks by multivariate objective analysis from the surface drifter trajectories. Velocities are larger than 15 cm.s⁻¹ in the light grey boxes and larger than 30 cm.s⁻¹ in the dark grey ones. Dark circles materialize the successive positions of the anticyclonic eddy overlying meddy Encelade. White circles represent the cyclonic cold companion of meddy Encelade.

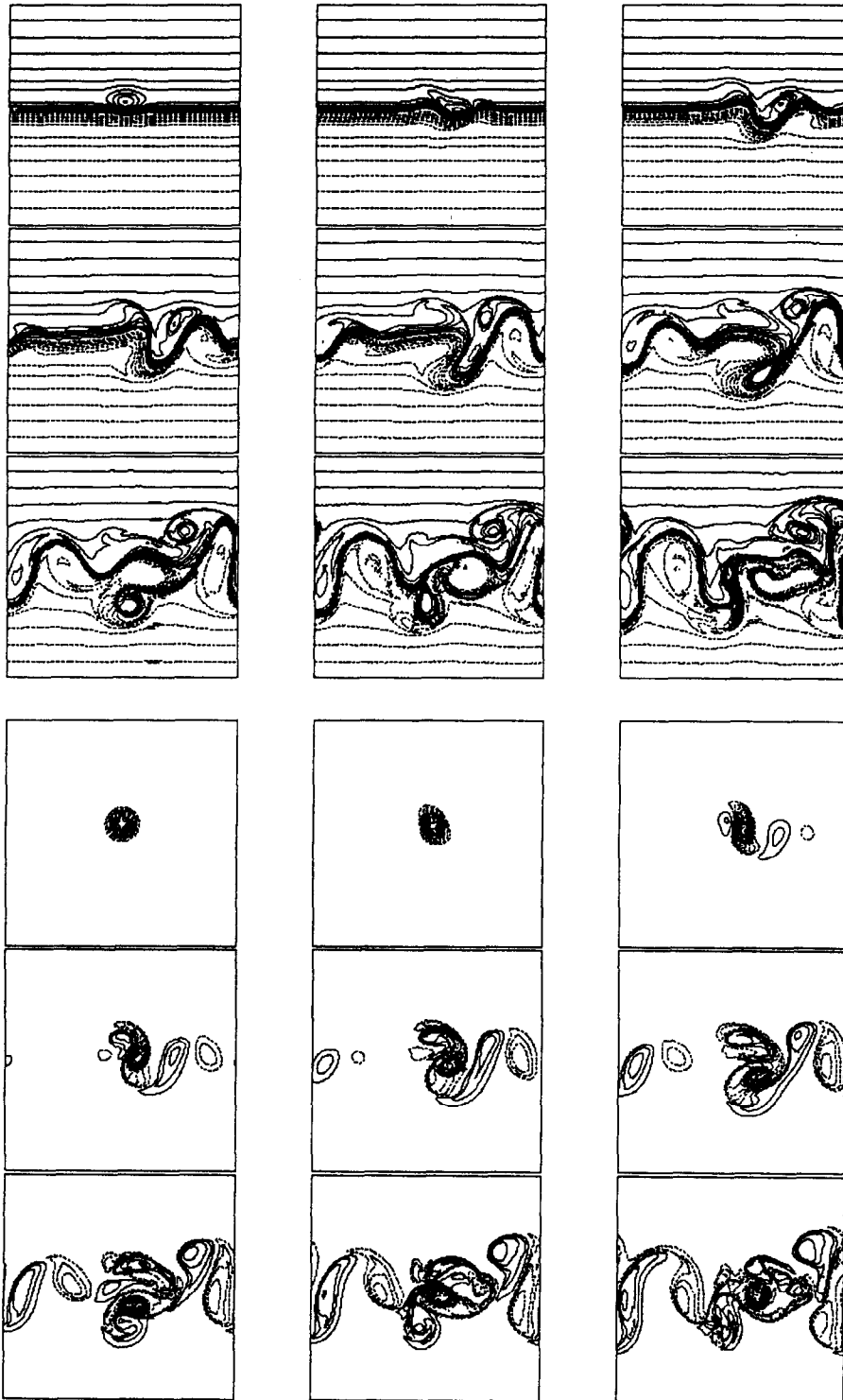


Fig.5: Time-series of potential vorticity in the upper, middle layers of the β -plane quasi-geostrophic model for the pivot experiment. Time intervals are 7 days (frames from left to right and from top to bottom).

propagates southward (the negative pole lies west of the positive one). During the following 3 weeks, the meddy is sheared by the neighboring positive PV poles, and filamentation ensues; the cyclone detaches via meander occlusion. Then the dipole travels eastward south of the jet. Under the effect of this interaction mechanism, the meander formation was much more energetic than that resulting from pure baroclinic instability, and the meddy propagation faster than that due to beta-effect solely.

6. Discussion

The interaction of the meddies with the AC constitute one of the main features of this campaign. Our study has focused on the horizontal and vertical coupling between different eddy structures. Firstly, meddies Ceres and Encelade were coupled to anticyclonic surface features (eddy and meander), yielding an indirect surface signature in T, S and potential density. Meddy Encelade was also coupled to a strong, nearly barotropic (strongly surface-intensified) cold cyclone, and propagated as a dipole.

Even though our numerical model was quite idealized it well reproduced the essential features of meddy-jet interaction observed during the Semaphore experiment: - rapid induction of a large meander by the approaching meddy, - cyclone formation, - meddy deformation - and fast propagation. This numerical experiment was only a short application of F. Vandermeirsch's on-going work [10,11,12] on eddy-jet interaction. Further work is now needed to determine if this dipolar coupling can help identify undoubtedly the crossing of a meddy. We hope this will provide operational criteria for meddy detection, and help forecast their evolution from sea surface measurements.

References

- [1] G. Siedler, W. Zenk and W.J. Emery, 1985, Strong current events related to a subtropical front in the Northeast Atlantic, *J. Phys. Oceanogr.*, 15, 885-897.
- [2] R.H. Käse, T. Zenk, B. Sandford and W. Hiller, 1985, Currents, fronts and eddy fluxes in the Canary basin, *Progress in Oceanography*, 14, 231-257.
- [3] L. Eymard et al., 1995, Study of the air-sea interactions at the mesoscale: the Semaphore experiment, *Ann. Geophysicae*, 14, 986-1015.
- [4] A. Tychensky, P.Y. Le Traon, F. Hernandez, D. Jourdan, 1997, Structural and temporal evolution of the Azores current during the Semaphore 93 experiment, in press in *J. Geophys. Res.*
- [5] A. Tychensky and X. Carton, 1997, Hydrological and dynamical characterization of meddies in the Azores region: a paradigm for baroclinic vortex dynamics, in press in *J. Geophys. Res.*
- [6] P.D. Killworth, 1982, On the motion of isolated lenses on a beta-plane, *J. Phys. Oceanography*, 23, 368-376.
- [7] Y. Morel, 1995, Etude des déplacements et de la dynamique des tourbillons géophysiques : application aux meddies, thèse de Doctorat de l'Université J. Fourier, Grenoble, France.
- [8] L.M. Polvani, 1991, Two-layer geostrophic vortex dynamics, Part 2: Alignment and two-layer V-States, *J. Fluid Mech.*, 225, 241-270.
- [9] P.L. Richardson and A. Tychensky, 1997, Semaphore meddy trajectories, in press in *J. Geophys. Res.*
- [10] M.E. Stern and G.R. Flierl, 1987, On the interaction of a vortex with a shear flow, *J. Geophys. Res.*, 92, C10, 10,733-10,744.
- [11] F. Vandermeirsch, 1995, Etude de la stabilité linéaire de jets; interaction d'un jet et d'un

tourbillon à partir d'un modèle quasi-geostrophique, Rapport final convention SHOM-CNRS 18/94, EPSHOM, Brest, France.

[12]F. Vandermeirsch, 1995, Etude de l'interaction jet-tourbillon à partir d'un modèle quasi-geostrophique; critère de traversée du tourbillon dans le jet. Rapport final convention SHOM-CNRS 2/96, EPSHOM, Brest, France.

SST FRONTS IN WINTER OFF THE EAST COAST OF NORTH AMERICA

D. S. Ullman, P. C. Cornillon, and T. P. Mavor

Graduate School of Oceanography
University of Rhode Island
Narragansett, RI 02882, USA
email: dave@fronts.gso.uri.edu

The distribution and variability of sea surface temperature (SST) fronts, over the continental shelf along the east coast of North America from Cape Hatteras to Nova Scotia, are studied using a 12 year time series (1985-1996) of Advanced Very High Resolution Radiometer (AVHRR) images. After the masking of cloud contaminated pixels, an edge detection algorithm identifies surface temperature fronts in each image. Statistical analysis of the detected fronts indicates that south of Cape Cod during spring-autumn, fronts are rarely observed over the continental shelf. In winter, however, fronts are common over the inner and middle shelf from Cape Hatteras to the Bay of Fundy. The occurrence of these fronts peaks during January-March. They are characterized by cold SST on their inshore (shallow) side and are found in progressively deeper water through the winter. They appear to result from the influence of surface cooling on shallow nearshore waters. XBT sections across the shelf during winter show that in the Mid-Atlantic Bight, the water column inshore of a mid-shelf temperature front can be vertically stratified with cold, fresh water overlying warm, salty water. This suggests the potential importance of riverine discharge on the formation of winter SST fronts.

Introduction

Fronts in the ocean are relatively narrow zones of enhanced horizontal gradients of physical, chemical and/or biological properties. Surface thermal fronts are ubiquitous in the ocean with spatial scales ranging from $O(1)$ to $O(1000)$ km [1]. Frontal zones can be dynamically very active and may be locations in which the transfer of energy from large scales to small scales is most intense. Internal wave generation and breaking, water mass interleaving, and wind driven transient upwelling are examples of processes occurring at fronts that contribute to vertical exchange of water properties. As a result of vertical fluxes of essential nutrients, high biological productivity often occurs in frontal zones [2, 3]. Coastal fronts in particular have also been shown to control the mixing of nearshore and offshore waters [4].

Identification of fronts from satellite imagery can provide a large scale perspective that can complement *in situ* observational studies. The spatial (~ 1 km) and temporal (≥ 2 images/day) resolution of sea surface temperature (SST) fields from the National Oceanic and Atmospheric Administration's (NOAA) polar orbiting satellites makes these data well suited to the identification of thermal fronts. The development of an automated edge detection algorithm [5] has provided the ability to objectively locate SST fronts in Advanced Very High Resolution Radiometer (AVHRR) images.

We have applied the edge detection algorithm to all available SST images of the shelf and slope from Cape Hatteras to Nova Scotia (Figure 1) during the period 1985 through 1996. A detailed description of the seasonal cycle in the occurrence and strength of fronts in this region is given by Ullman and Cornillon [6]. The present paper focuses on a description of the SST fronts observed in winter, when front occurrence peaks on the continental shelf.

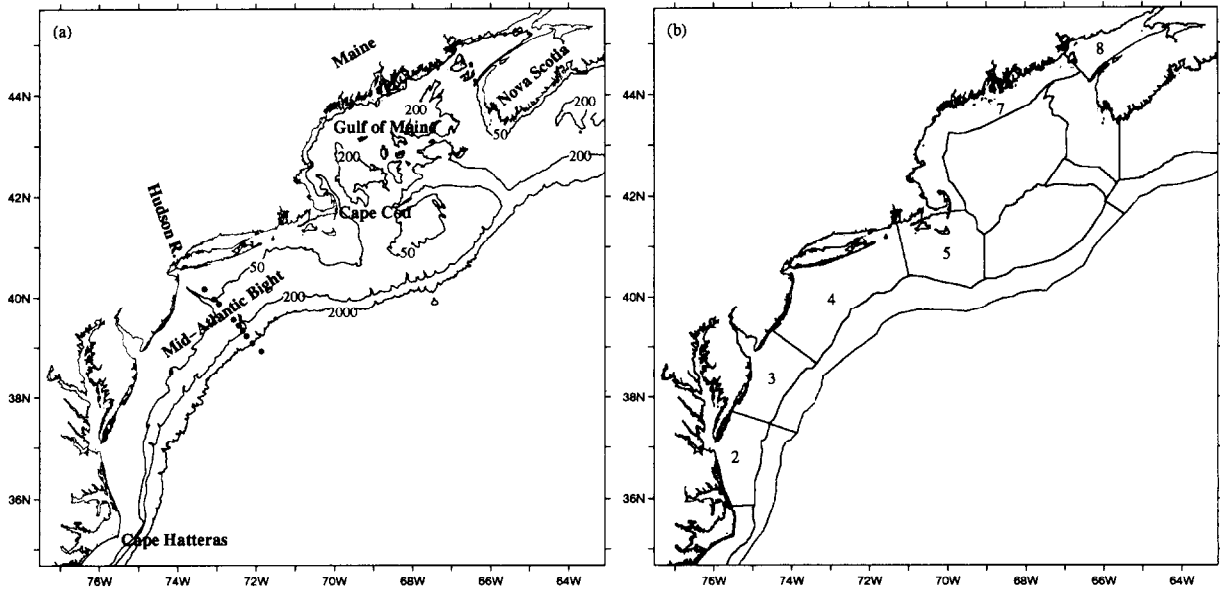


Figure 1: (a) Hatteras to Nova Scotia remap zone showing the 50, 200, and 2000 m isobaths. The black circles are the locations of XBT stations from February 20-21, 1985. (b) Coastal subregions (2-5, 7, 8) used in the analysis of front statistics.

Methods

SST fields for the coastal region extending from Cape Hatteras to Nova Scotia (Figure 1a) for 1985 through 1996 were derived from AVHRR measurements made from NOAA polar orbiting satellites. The radiometers carried aboard the satellites NOAA-9, NOAA-11, and NOAA-14 measure radiance in five spectral bands ranging in wavelength from $0.55\mu\text{m}$ to $12.5\mu\text{m}$. SST is calculated from the infrared channels 4 ($10.3\text{-}11.3\mu\text{m}$) and 5 ($11.5\text{-}12.5\mu\text{m}$) using the algorithm developed under the National Oceanic and Atmospheric Administration (NOAA)/National Aeronautics and Space Administration (NASA) Pathfinder program [7]. Each satellite pass, with a spatial resolution of 1.1 km at nadir, was manually navigated to an accuracy of approximately one pixel. A total of 13,191 passes covering at least part of the region were available over the 12 year period. These were remapped to an equirectangular projection with a pixel size of 1.2 kilometers at the image center.

Cloud contaminated pixels in each SST image were identified and masked using a declouding algorithm developed at the University of Rhode Island. A brief description of the method can be found in [6]. The declouded images were then analyzed for the presence of fronts using the multi-image edge detection algorithm developed by Cayula and Cornillon [5]. An analysis of the properties of the fronts found by this algorithm was carried out by Ullman and Cornillon [6].

The number of fronts detected in an SST image depends in part on the amount of the image that is not cloud covered. For this reason, in the presentation of our results, we attempt to correct for variations in cloud cover by computing the probability of detecting a front. This is performed on both a pixel by pixel basis and averaged over an entire region (see figure 1b for the regions). The probability of detecting a front at a particular pixel is calculated by dividing the number of times the pixel was an edge pixel by the number of times it was clear. Similarly for the probability of detecting a front averaged over a region, we divide the number of frontal pixels within the region by the number of clear pixels.

SST fronts in satellite imagery can be characterized by the temperature gradient across the front. In particular, the direction of the gradient vector can provide information as to the formation mechanism of the front. In this study, we classify fronts based on the direction of the temperature gradient at the front relative to the direction of the bathymetric gradient. We refer to fronts across which a temperature increase (decrease) is associated with a decrease in water depth as warm (cold) fronts. Note that these definitions are based only on the SST at the front and are not based on the subsurface frontal structure as is the case with previous classification schemes (e.g. [8]).

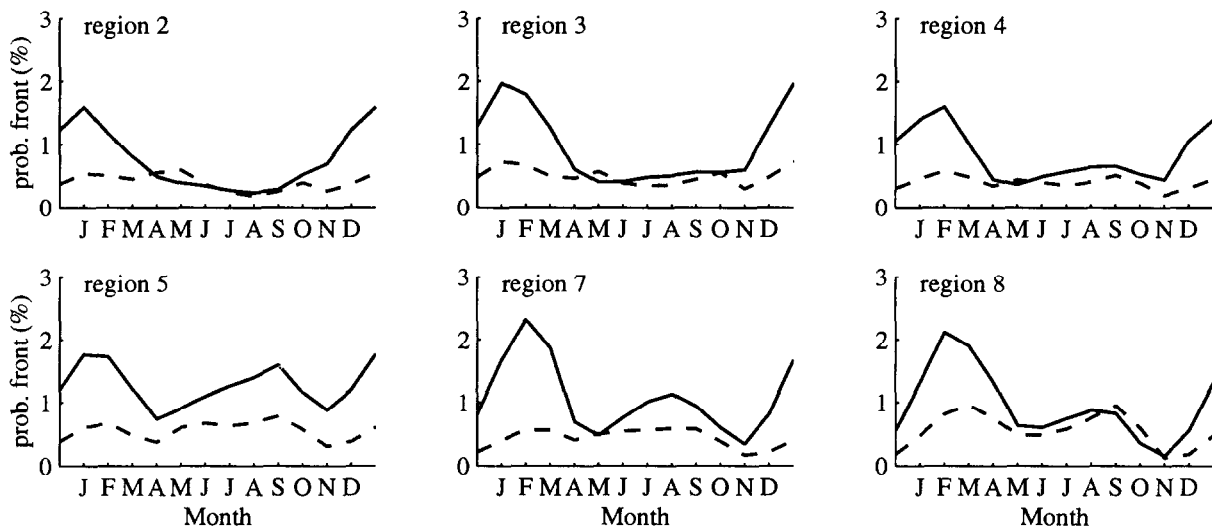


Figure 2: Seasonal cycle in mean monthly front probability for each of the regions shown in Figure 1b. The solid line represents cold front probability and the dashed line warm front probability. Mean monthly probabilities were computed for each month by summing the number of warm or cold frontal pixels within a region over 1985-96 and normalizing by the number of clear pixels within the region over the same time period.

Results

The mean seasonal cycle in front detection probability for each of the coastal regions labeled in Figure 1b is presented in Figure 2 as time series of mean monthly probability. Mean monthly probability refers to the probability computed by summing frontal pixels and clear pixels for a particular month from a region over the entire 12 years of data. We compute separate probabilities for warm and cold frontal pixels. All of the regions experience peak cold front probability in winter (January-February), with maximum probability of 1-2%. In early spring, cold front probabilities decrease, and in the three southern regions (2-4) remain low through summer. In the northern regions (5, 7, 8) cold front probabilities exhibit a secondary peak in late summer (August-September) before decreasing in autumn. Warm front probabilities are generally lower than cold front probabilities and exhibit less seasonal variability especially in the southern coastal regions.

Figure 3 depicts the pixel-by-pixel probability of detecting a front (warm or cold front) for the winter period averaged over 1985-1996. During this period, fronts occur in bands aligned predominantly with the bathymetry. We observe highest probabilities ($\approx 10\%$) in a narrow band along the 50 m isobath in the Gulf of Maine and along Cape Cod. In the Mid-Atlantic Bight probabilities are lower ($\approx 5\%$), but again fronts seem to be associated with the 50 m isobath. In the southern Mid-Atlantic Bight, the 50 m isobath frontal band appears to merge with the shelfbreak front, here observed as a moderately high probability band along the 200 m isobath. There is also evidence, in the Mid-Atlantic Bight, of a second, weaker frontal band inshore of the 50 m isobath. Figure 2 suggests, and examination of individual images confirms, that most of these winter shelf fronts have colder water on their inshore sides.

To investigate further the nature of winter cold fronts, we study next the occurrence of these fronts as a function of water depth. All pixels within a region were separated into bins based on the water depth at that pixel. Within each bin, we computed the front detection probability (cold fronts only) for each month over the entire 12 years. Figure 4 presents the results of this computation for regions 4 (Mid-Atlantic Bight) and 7 (Gulf of Maine coast) for December-March. In both regions, a clear shift into deeper water is observed in the probability distributions. In region 4, water depths of approximately 50 m are a preferred location for cold SST fronts throughout the winter. Early in winter (December), fronts are commonly detected in shallower water while late in winter (March) more fronts occur in deeper water. In February, in addition to the peak at 50 m, high probability also occurs at depths of 90-95 m. In region 7, maximum probability occurs at slightly deeper depths than in region 4. From January-March this depth is approximately 70 m. As in region 4, the probability histograms are skewed toward shallow water in December and toward deeper water in late winter (February-March).

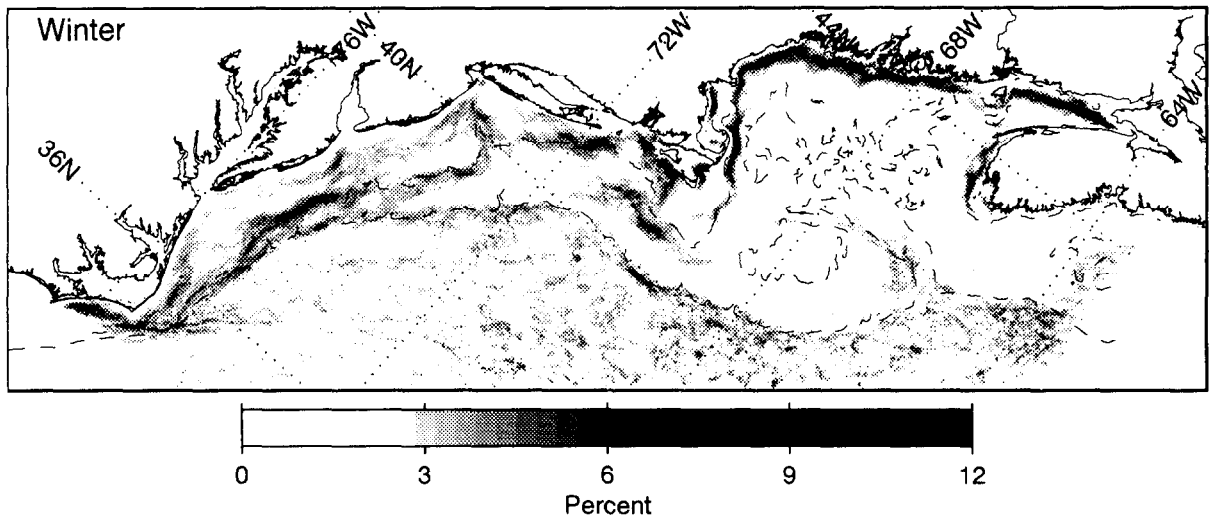


Figure 3: Front detection probability for winter (January-March) averaged over 1985-1996. The probability (expressed in percent) is the ratio of the number of times a pixel was a frontal pixel to the number of times the pixel was clear. For clarity, probabilities < 3% are not shown. The dashed lines are the 50 m and 200 m isobaths.

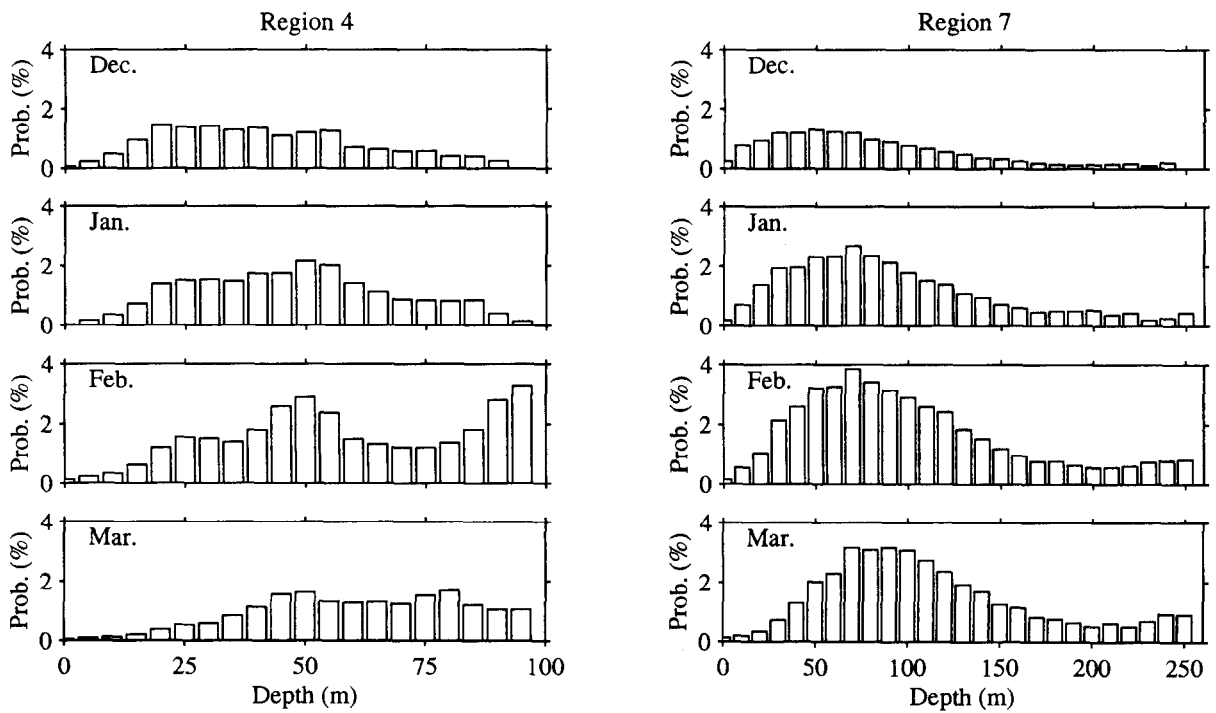


Figure 4: Cold front detection probability as a function of water depth for December-March in regions 4 and 7.

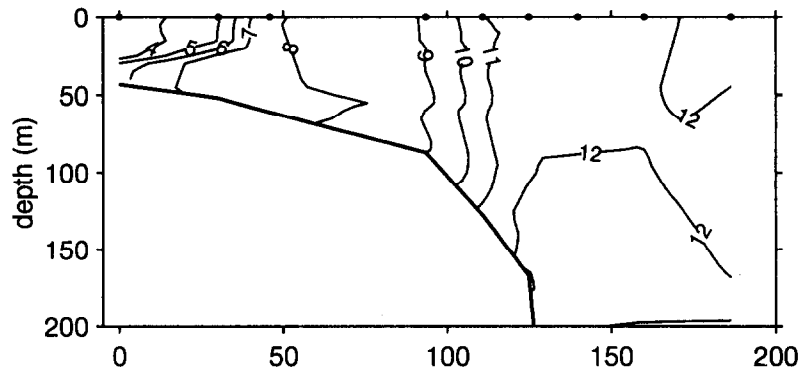


Figure 5: Temperature ($^{\circ}\text{C}$) versus depth and distance from XBT drops at stations shown in Figure 1 on February 20-21, 1985. Distances are relative to the first station. The positions of the XBT drops are indicated by the black circles.

Discussion

The winter SST fronts over the shelf, with cold water on their inshore sides, are likely caused by strong cooling at the surface. This process has been described for the shelf/slope region around the Bahama Banks by Garwood *et al* [9]. Their model predicts the formation of an SST front at the shelfbreak, due to surface cooling, when the depth of wind mixing is greater than the shelf depth. The fronts observed in our study occur over the middle shelf, with the zones of highest probability in regions 4 and 7 (≈ 50 m water depth in region 4 and $\approx 50 - 100$ m in region 7) approximately coincident with zones of rapid depth change [6].

Examination of XBT sections that cross the Mid-Atlantic Bight shelf in winter (extracted from the National Oceanographic Data Center's World Ocean Database) shows that the shelf can be vertically well-mixed at certain times. At these times, an SST front is often observed over the middle shelf, in agreement with our satellite observations. On other occasions, however, the inner shelf is not well-mixed, as Figure 5 illustrates (see Figure 1 for the location of the XBT stations). In this figure, we see that the outer shelf is well mixed with a distinct shelfbreak front separating shelf water from warm slope water. The inner shelf is vertically stratified, with cold water overlying warm water and a temperature front located at a water depth of approximately 50 m. The apparent instability implied by the presence of cold water over warm water can only occur if the cold water is also less saline, with salinity making the dominant contribution to density. The source of the low salinity water is presumably the Hudson River discharge into the apex of the Mid-Atlantic Bight.

The presence of a surface trapped plume of fresher water over the inner shelf implies a shallower surface mixed layer there than over the outer shelf where temperature is vertically uniform. Because of the shallower mixed layer, the results of Garwood *et al* [9] can be extended to suggest that the imposition of surface cooling should result in more rapid cooling of the plume relative to the shelf waters offshore. The result would be a strong temperature contrast between the plume and the adjacent shelf water. The fact that the cooling process weakens the stability of the water column suggests, however, that this can not continue indefinitely. Eventually sufficient cooling will cause overturning or at least allow wind mixing to destroy the vertical stratification.

Summary

Over the continental shelf off the east coast of North America, SST fronts are most common in winter. These fronts are predominantly cold fronts with cold water found on the shallow water side (inshore) of the front. They are not uniformly distributed over the shelf, but rather occur preferentially in alongshore bands parallel to the local bathymetry. In the Mid-Atlantic Bight (region 4) fronts are highly probable in water depths of approximately 50 m throughout the winter. Early in winter they also occur in shallower water, while late in winter, deeper depths appear to be favored. Along the Maine coast (region 7), fronts behave similarly, although the depth at which peak front detection probability occurs is somewhat greater (≈ 70 m). Preliminary analysis of historical XBT data in the Mid-Atlantic Bight shows that the shelf in winter is not always vertically well mixed. At such times, the presence

of a lens of cold water trapped near shore suggests that density is controlled by salinity. Thus some of the SST fronts we observe may actually be salinity fronts resulting from river discharge. Why these tend to occur most often at depths of about 50 m is a question that needs to be addressed.

Acknowledgments

This research was supported by the National Oceanographic and Atmospheric Administration's (NOAA) Sea Grant program (NA66RG0303), and the GLOBEC program jointly funded by the National Science Foundation (NSF) and NOAA (NA57FE0542). Salary support for P. Cornillon was provided by the State of Rhode Island and Providence Plantations. The software used for image processing was developed by R. Evans, O. Brown, J. Brown, and A. Li of the University of Miami. Their continued support is greatly appreciated.

References

- [1] Fedorov, K. N., 1986, *The Physical Nature and Structure of Oceanic Fronts*, Springer-Verlag, New York.
- [2] Fournier, R. O., 1978, Biological aspects of the Nova Scotian shelfbreak fronts, in *Oceanic Fronts in Coastal Processes*, edited by M. J. Bowman and W. E. Esaias, pp. 69-77, Springer-Verlag, New York.
- [3] Pingree, R. D., P. M. Holligan, and G. T. Mardell, 1978, The effects of vertical stability on phytoplankton distributions in the summer on the northwest European shelf, *Deep Sea Res.*, 25, 1011-1028.
- [4] Blanton, J. O., 1986, Coastal frontal zones as barriers to offshore fluxes of contaminants, *Rapp. P.-V. Cons. Int. Explor. Mer*, 186, 18-30.
- [5] Cayula, J. F. and P. Cornillon, 1995, Multi-image edge detection for SST images, *J. Atmos. Oceanic Technol.*, 12, 821-829.
- [6] Ullman, D. S. and P. C. Cornillon, 1998, Surface temperature fronts off the east coast of North America from AVHRR imagery, submitted to *J. Geophys. Res.*
- [7] Smith, E. A., J. Vazquez, A. Tran, and R. Sumagaysay, 1996, Satellite-derived sea surface temperature data available from the NOAA/NASA Pathfinder Program, *American Geophysical Union*, Electronic publication, 95247e.
- [8] Mooers, C. N. K., C. N. Flagg, and W. C. Boicourt, 1978, Prograde and retrograde fronts, in *Oceanic Fronts in Coastal Processes*, edited by M. J. Bowman and W. E. Esaias, pp. 43-58, Springer-Verlag, New York.
- [9] Garwood, R. W. Jr., R. W. Fett, K. M. Rabe, and H. W. Brandli, 1981, Ocean frontal formation due to shallow water cooling effects as observed by satellite and simulated by a numerical model, *J. Geophys. Res.*, 86, 11000-11012.

NUMERICAL AND EXPERIMENTAL MODELING OF A PATTERN OF INTERNAL WAVES INDUCED BY A DRIFTING ICEBERG

V. V. Vasilieva¹, O. D. Shishkina²

1 State Marine Technical University, 3 Lotsmanskaya st., St.-Petersburg, 190008, Russia

2 Institute of Applied Physics, Russian Academy of Sciences,

46 Uljanov st., Nizhny Novgorod, 603600, Russia. E-mail: ols@hydro.appl.sci-nnov.ru

Abstract. Natural conditions of iceberg drift - stratification parameters ($\Delta\rho = 1\text{-}3 \text{ kg/m}^3$) at the depth of 20-100 m), iceberg dimensions (the draught of 40-250 m) and drift velocities (0.1 - 0.5 m/s) - provide physical conditions for intensive internal wave (IW) generation [1]. Results of theoretical and experimental modeling of internal disturbances induced by an iceberg drifting in a stratified finite-depth fluid are presented.

1. Problem statement

A solution for amplitude-phase internal wave parameters in case of a solid body motion in the neighbourhood of an interface between liquids of different densities ρ_1 and ρ_2 ($\rho_1 < \rho_2$) was obtained.

The solid body influence was modeled by two coupled pressure pulses positioned both at the free surface and the interface, where vortex disturbances are supposed to be concentrated. The homogeneous water layers Ω_1 and Ω_2 were considered to be vortexfree. A linear three-dimensional problem was solved. The zero of the $OXYZ$ co-ordinates is at the undisturbed interface, the OZ axis is directed upwards:

$$\rho = \begin{cases} \rho_1 & \text{for } \Omega_1 = (x, y, z): |x| < \infty, |y| < \infty, 0 \leq z \leq h_0; \\ \rho_2 & \text{for } \Omega_2 = (x, y, z): |x| < \infty, |y| < \infty, -\infty < z \leq 0. \end{cases} \quad (1)$$

Potentials of induced velocities $\varphi_{1,2}(x, y, z, t, \rho)$ in the upper and the lower layers should satisfy:

(i) the Laplace equation

$$\Delta\varphi_1 = 0, (x, y, z) \in \Omega_1; \quad \Delta\varphi_2 = 0, (x, y, z) \in \Omega_2 \quad (2),$$

(ii) the boundary conditions

$$\Im\varphi_1 = 0 \quad \text{for } z = h_0, \quad (3)$$

$$\frac{\partial\varphi_1}{\partial z} = \frac{\partial\varphi_2}{\partial z} \quad \text{for } z = 0, \quad (4)$$

$$\rho_1 \Im\varphi_1 = \rho_2 \Im\varphi_2 \quad \text{for } z = 0, \quad (5)$$

$$\begin{aligned} \mathfrak{S} &= \frac{\partial^2}{\partial t} + g \frac{\partial}{\partial z} \\ \nabla \varphi_i &\rightarrow 0 \quad \text{for } r_1 = \sqrt{x^2 + y^2 + z^2} \rightarrow \infty \\ \varphi_2 &\rightarrow 0 \quad \text{for } z \rightarrow -\infty \end{aligned} \quad (6)$$

(iii) the initial conditions

$$\begin{aligned} t = 0; z = 0; \varphi_1 = \varphi_2 = F_2(r) + F_1(r)e^{-kh_0}; \frac{\partial \varphi_2}{\partial t} = \frac{\partial \varphi_1}{\partial t} = 0 \\ t = 0; z = h_0; \varphi_1 = F_1(r) + F_2(r)e^{-kh_0}; \frac{\partial \varphi_1}{\partial t} = 0. \end{aligned} \quad (7)$$

The boundary conditions (ii) of the linear problem mean respectively constant pressure at the free surface (3), continuity of the vertical velocity component (4) and of the pressure at the interface (5) and the infinity conditions (6). The initial conditions (7) take into account sources of surface and internal waves - the initial pressure pulses $F_1(x,y)$ at the free surface $z=h_0$ and $F_2(x,y)$ at the interface $z=0$, as well as the absence of initial deformation at both boundaries.

2.Solution

The unknown induced velocities potentials are tried in the form of the wave frequency spectrum:

$$\begin{aligned} \varphi_1 &= \int_0^{\infty} (A(k)e^{kz} + D(k)e^{-kz}) I_0(kr) \cos(\sigma t) dk, \\ \varphi_2 &= \int_0^{\infty} C(k)e^{kz} I_0(kr) \cos(\sigma t) dk \end{aligned} \quad (8)$$

where σ is the surface and internal waves frequency, k is the wave number, $I_0(kr)$ is the Bessel function, and $r_1 = \sqrt{x^2 + y^2}$. The potential functions (8) meet the boundary conditions (6). The values of the amplitude multipliers A, D, C are obtained from the boundary conditions (3)-(5). The boundary conditions system has a nontrivial solution for two dispersion relations:

$$\begin{aligned} \sigma_{j=1} &= \sqrt{gk}, \\ \sigma_{j=2} &= \sqrt{\frac{1-\bar{\rho}}{1+\bar{\rho}th(kh_0)} gkth(kh_0)}; \bar{\rho} = \frac{\rho_1}{\rho_2}. \end{aligned} \quad (9)$$

When solving the system (3)-(5) and taking into account (9) the induced velocities potentials for two homogeneous layers from two pressure pulses may be written as:

$$\begin{aligned} \sigma_{1j} &= -\frac{1}{g} \frac{\partial \varphi_{1j}}{\partial t} \quad \text{for } z = 0, \\ \sigma_{2j} &= -\frac{1}{g(\rho_2 - \rho_1)} \left(\rho_2 \frac{\partial \varphi_{2j}}{\partial t} - \rho_1 \frac{\partial \varphi_{1j}}{\partial t} \right) \quad \text{for } z = h_0, \end{aligned}$$

$$\sigma_{ij} = \frac{\rho}{2\pi\rho_2} \sigma_j(k_0) \sqrt{\frac{k_0}{r \left| \frac{\partial^2 \sigma_j}{\partial k^2} \right|_{k=k_0}}} M_{ij} \sin(k_0 r - \sigma_j t),$$

where k_0 is a root of the equation $\frac{\partial}{\partial k}(k_0 r - \sigma_j t) = 0$.

$$U dt \cos \theta = dr; k_0 \frac{dr(t)}{dt} - \sigma_j(k_0) = 0$$

$$m = \frac{1-\bar{\rho}}{1+\bar{\rho}}; T = \frac{1+\bar{\rho}}{1+\bar{\rho}th(kh_0)};$$

$$M_{1j} = \frac{gk(1-sh(kh_0)) + \sigma_j^2 ch(kh_0)}{\sigma_j^2 ch(kh_0) - gksh(kh_0)}; M_{2j} = \frac{1}{1-\bar{\rho}} M_j (1-\bar{\rho}K_j);$$

$$M_j = \frac{gk(1-sh(kh_0)) + \sigma_j^2 ch(kh_0)}{gk}; K_j = \frac{gkch(kh_0) + \sigma_j^2 ch(kh_0)}{\sigma_j^2 ch(kh_0) - gksh(kh_0)}.$$

Study of the internal wave parameters obtained for the vortical interface showed that critical phase velocities of internal modes are smaller than for the potential theory. And an almost plane induced wave system past a body moving with relatively small velocities, typical of iceberg drift, is observed.

$$U_g = \frac{1}{2} C_{ph} \left(1 + \frac{2kh_0}{sh(2kh_0)} - \frac{\bar{\rho}kh_0}{ch^2(kh_0)(1+\bar{\rho}th(kh_0))} \right); C_{ph} = \sqrt{\frac{g}{k} m T th(kh_0)};$$

$$C_{ph}^* = \sqrt{mgh_0 \frac{1+\bar{\rho}}{1+\bar{\rho}kh_0}} \cong \sqrt{mgh_0}; U_g = C_{ph}^* \left(1 - \frac{0.5\bar{\rho}kh_0}{1+\bar{\rho}kh_0} \right).$$

The constant phase lines calculated for some natural values of $h_0, \bar{\rho}$ and U showed that the propagation angle of induced internal waves is in the range $\frac{\pi}{4} \leq \beta \leq \frac{\pi}{2}$.

3. Experimental study

Numerical results were compared with experimental data obtained in a thermally stratified tank with overall dimensions $L \times B \times H = 18 \times 4 \times 2 \text{ m}^3$. The horizontally homogeneous stratification was created in fresh water providing a scale model ($K_L = 1:100$) of the seasonal ocean thermocline ($\Delta\rho = 2 \text{ kg/m}^3$).

The vertical cylinder of diameter $D = 0.4 \text{ m}$ had different draughts T close to the thermocline's depth of $h' = 0.6 \text{ m}$. Towing velocities U were in the range of limiting phase velocities of the first and the second internal wave modes ($K_U = K_L^{1/2}$).

Indications of the vertical chain of sensors allow one to determine temperature oscillations related to different internal wave modes. A spatial pattern of internal wave fronts was reconstructed using indications of horizontally arranged sensors. A phase picture for the working range of the body's velocities was almost plane with divergence angles $60^\circ < \beta < 90^\circ$. The amplitude decrease observed was about 30% at a distance of $3D$.

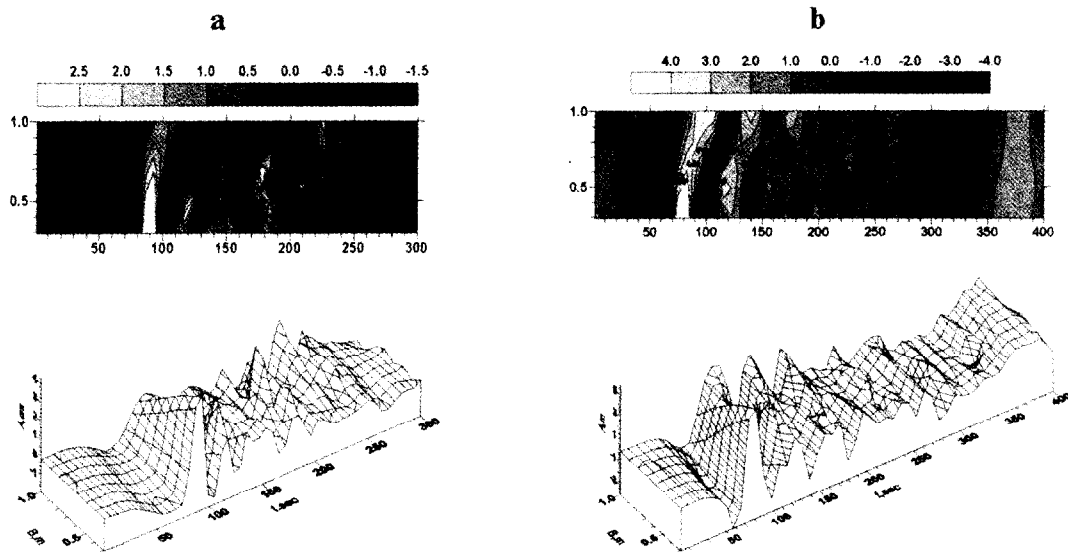


Fig. 1. Stationary internal wave pattern for $T/h' = 1$: a - $U/C_1=1$, b - $U/C_1=2$.

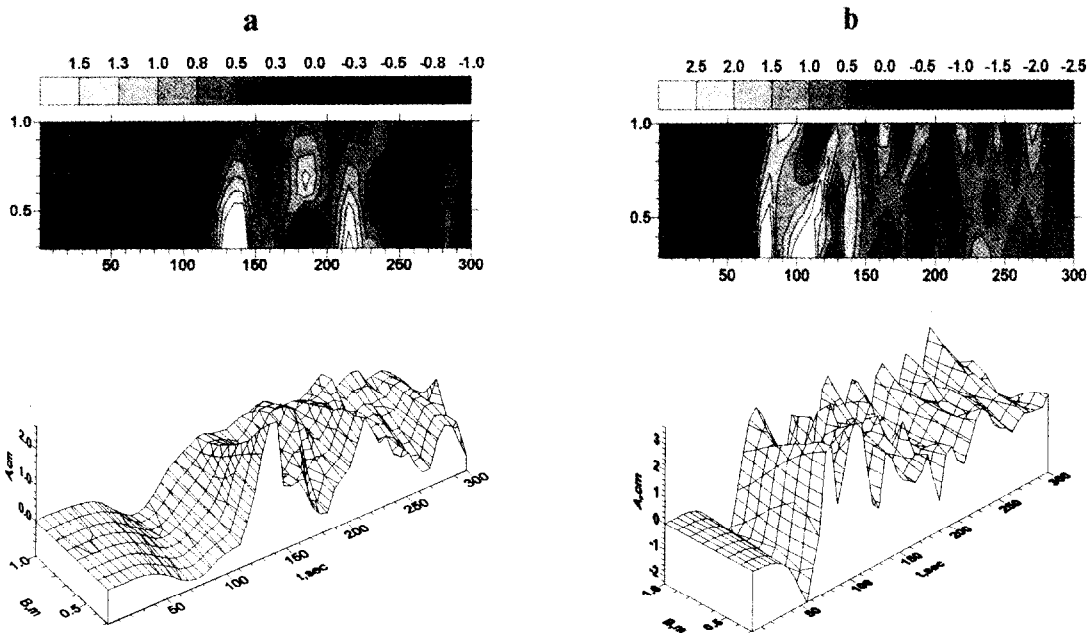


Fig. 2. Stationary internal wave pattern for $T/h' = 1.44$: a - $U/C_1=1$, b - $U/C_1=1.5$.

Induced *IW* amplitude investigations showed that the most intensive first-mode *IW* is observed in the Froude number range $Fr = 0.06$ (taking into account the density difference, the "internal" Froude number $Fi = U/(N_{max} T) = 0.67$ (here, $N_{max} = \left(-\frac{g}{\rho} \frac{d\rho}{dz}\right)^{1/2}$ is the maximum natural frequency for the density profile $\rho(z)$, T is the body's draught).

Numerical calculations [2] for the velocity range when only *IW* are generated showed that the wave-drag coefficient is less in case the body crosses the interface $T/h_0 > 1$. And experiments confirm this result. Behaviour of the normalised *IW* amplitudes (Fig. 3.) is similar to the drag coefficient dependence versus T/h_0 : the maximum thermocline disturbance occurs for $T/h_0 \approx 1$ and decreases for $T/h_0 > 1$. The Froude numbers for A_{max} depend, other conditions being equal, on T/h_0 .

the maximum thermocline disturbance occurs for $T/h_0 \approx 1$ and decreases for $T/h_0 > 1$. The Froude numbers for A_{max} depend, other conditions being equal, on T/h_0 .

For relatively low body velocities $U \sim C_2^*$ (where C_2^* is the limiting linear phase velocity of the second-mode IW) the waves amplitude is almost independent of the body's draught. For $U \sim C_1^*$ the thermocline disturbance is greater in case $T/h_0 > 1$ (e.g. for $U \sim C_1^* = 0.8$, twice relatively to $T/h_0 < 1$). For the velocities $U \gg C_1^*$ the function $A(U)$ also depends on T/h_0 . In case $T/h_0 < 1$, the waves amplitude increases versus growing velocities and has weak velocity dependence for $T/h_0 > 1$.

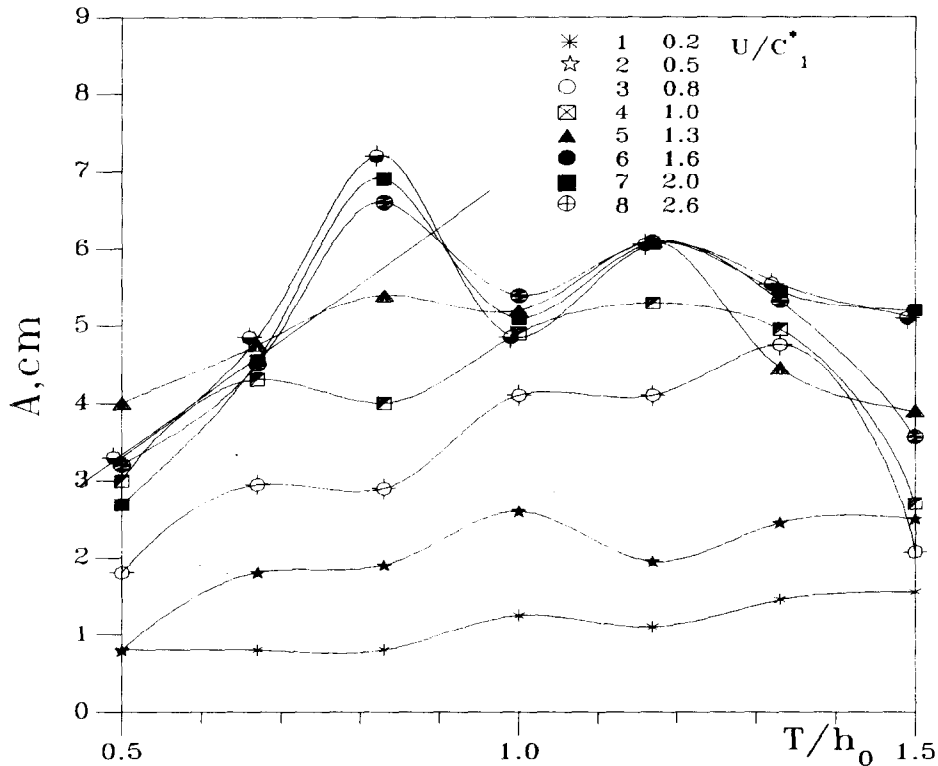


Fig.3. Induced internal waves amplitude vs. cylinder's draught.

This work was supported by the RFBR (grants no. 96-05-64457, 96-05-64476) and INTAS (grant no. 94-4057).

References

- [1] V. V. Vasilieva, L. G. Pisarevskaya, O. D. Shishkina, 1995, Generation of internal waves by a drifting iceberg. *Izvestiya Akademii Nauk, Atmospheric and Oceanic Physics*, 31(6), 842-851.
- [2] V. Bertram, V. V. Vasilieva, V. G. Korostelev, L. G. Pisarevskaya, O. D. Shishkina, 1998, A study of internal waves field generated by an iceberg in a pycnocline. *Izvestiya Akademii Nauk, Atmospheric and Oceanic Physics* (in press).

CYCLONIC AND ANTICYCLONIC VORTICES IN THE EASTERN INDIAN OCEAN DURING THE SUMMER MONSOON

P. N. Vinayachandran¹ and Toshio Yamagata^{1,2}

¹Institute for Global Change Research, Frontier Research System for Global Change, Seavans-N, 7F, Shibaura 1-2-1, Tokyo 105-6791, Japan. (e-mail: vinay@frontier.esto.or.jp)

²Department of Earth and Planetary Physics, Graduate School of Science, University of Tokyo, Tokyo 103-0033, Japan. (e-mail: yamagata@geoph.s.u-tokyo.ac.jp)

Abstract

The monsoon circulation in the eastern Indian Ocean is studied using an ocean general circulation model and TOPEX/POSEIDON data. The upper layer circulation in the southern Bay of Bengal consists of a cyclonic gyre east of Sri Lanka (Sri Lanka Dome), a large anticyclonic vortex south of Sri Lanka (Sri Lanka Anticyclone), an anticyclonic eddy east of Sri Lanka and a cyclonic meander near the coast of Sumatra. The model results are in good agreement with the sea surface height anomaly measurements from the altimeter on board the TOPEX/POSEIDON and climatological temperature data. The ocean circulation in this region is driven locally by monsoon winds as well as remotely by Rossby waves associated with the reflection of the spring Wyrтки jet from the eastern boundary of the Indian ocean. The Sri Lanka Dome is forced by the strong cyclonic wind stress curl east of Sri Lanka. The anticyclonic vortices form due to the interaction of the wind driven eastward monsoon current with a Rossby wave radiated from the eastern boundary.

1. Introduction

The Bay of Bengal is a semi-enclosed tropical ocean basin influenced by seasonally reversing monsoon winds and large quantity of freshwater, the latter in the form of river discharge and rainfall. In addition, the Bay is influenced by remotely forced planetary waves from the equatorial Indian Ocean [1] triggered off by the spring and fall Wyrтки jets [2]. The upper layer circulation in the Bay of Bengal is characterized by a distinct seasonal cycle [3]. The circulation consists of an anticyclonic gyre with a poleward western boundary current during spring and a cyclonic gyre with an equatorward western boundary current during early winter. The summer monsoon circulation does not show any well-organized pattern. The western

boundary current is made up of two opposing flows, southward in the north and northward in the south [4]. South of Sri Lanka the Southwest Monsoon Current (SMC) flows eastward but east of Sri Lanka the SMC curves around Sri Lanka and flows into the Bay of Bengal [5]. The monsoon circulation south and east of Sri Lanka consists of several vortices. East of Sri Lanka there exists a cyclonic gyre termed as the Sri Lanka Dome (SLD) [6]. East of the SLD there is an anticyclonic eddy and south of Sri Lanka a large anticyclonic vortex is embedded in the SMC. In this article these vortices are discussed using an ocean circulation model and TOPEX/POSEIDON data. The model and data are briefly discussed in the next section. Section 3 presents the results, and a discussion of the forcing mechanisms is given in the last section.

2. The model and the TOPEX/POSEIDON data

We use an ocean general circulation model based on the GFDL Modular Ocean Model version 2.2 β [7]. Our model domain is the Indian Ocean (30°S-30°N; 30°E-100°E) with a uniform spatial resolution of 0.33° in both latitude and longitude. There are 25 vertical levels in the model of which 8 are in the upper 100m. The model has realistic coastline and topography derived from ETOPO5 data set. Lateral eddy viscosity and diffusivity are $2 \times 10^7 \text{ cm}^2 \text{ s}^{-1}$ and $1 \times 10^7 \text{ cm}^2 \text{ s}^{-1}$ respectively. The vertical mixing is parameterized using a Richardson number dependent scheme [8]. The model is started from the state of rest and Levitus temperature and salinity for the month of January and spun-up for a period of five years by climatological monthly mean winds [9]. After the spin-up the model is forced by Florida State University winds [10] for the period 1990-96. Surface salinity is relaxed to monthly climatological value with a time scale of 1/30 days and surface heat flux is parameterized using a scheme that combines climatological heat flux with the sea surface temperature using a damping coefficient equivalent to 1/30 days.

The model results are corroborated with sea surface height anomalies derived from the altimeter measurements on board the TOPEX/POSEIDON. Sea level anomaly data, available at 10-day intervals with a spatial resolution of 0.5°X0.5° obtained from the CLS Space Oceanography Division (France) are used in this study. These anomalies are calculated from the mean values for the period from January 1993 to January 1996 [11].

3. Results

Figure 1 shows the model currents at a depth of 35m (level 4 in the model). East of Sri Lanka the model results show a cyclonic gyre called the SLD. The SLD forms first during May and fully develops by July. This gyre is featured by intense upwelling and hence brings cool subsurface waters to the near-surface layers enhancing the productivity of the waters in the region. The decay of the SLD begins in September when the northward flow that marks the eastern edge of the SLD moves westward and the cold water associated with the moves northward.

The most striking feature of the upper layer circulation in the southern Bay of Bengal is a large anticyclonic vortex (henceforth referred to as Sri Lanka Anticyclone, SLA) located south of Sri Lanka. In the model results for 1995, the SLA forms during June southeast of Sri Lanka. It later intensifies and moves westward. It has a near-circular shaped during June, and this shape gets distorted and finally disappears as it

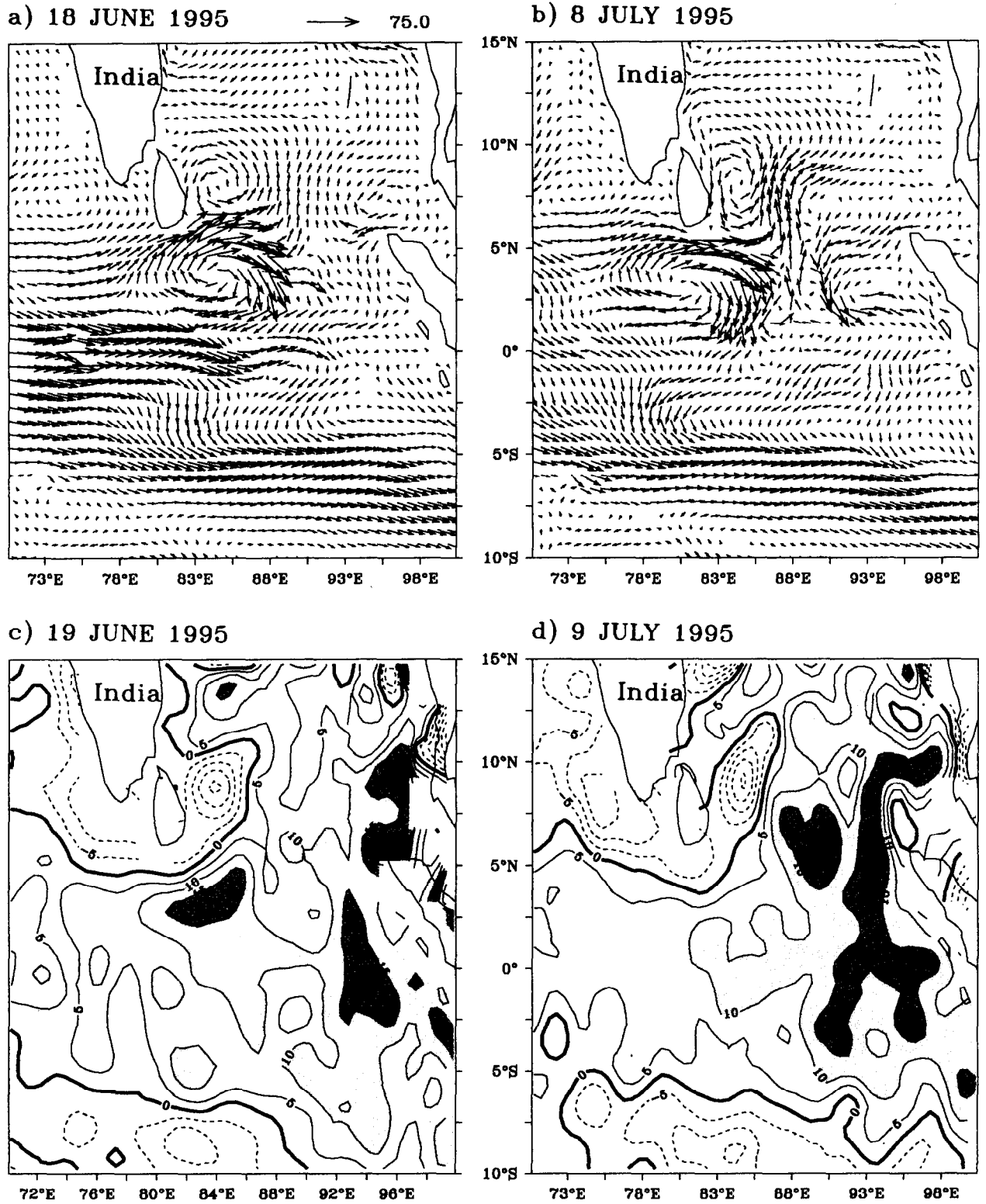


Figure 1. Upper panels: Model currents (cm/sec) at a depth of 35m. Lower panels: Sea surface height anomalies from TOPEX/POSEIDON. Negative anomalies are drawn in dashed contours. Positive anomalies greater than 10cm are shaded.

propagates westward beyond Sri Lanka. The SLA has a radius of about 500km and its center propagates westward at a speed of about 13 cm/sec.

East of the SLD, during June there is a fairly broad band of northeastward flow. This is identified here as the manifestation of the Rossby wave associated with the reflection of the Kelvin wave associated with the spring Wyrтки jet in the equatorial Indian Ocean. Near the eastern end of this band there is an anticyclonic eddy. As the season progresses this Rossby wave along with the anticyclonic eddy propagates westward. Due to the presence of the SLD the propagation slows down in the western part of the Bay.

Lower panels of Figure 1 shows the sea surface height anomaly from TOPEX/POSEIDON. The large negative sea level anomaly east of Sri Lanka indicates the cyclonic circulation associated with the SLD. The large positive sea level anomaly located south of Sri Lanka indicates the anticyclonic circulation associated with the SLA. Direct current measurements by moored current meters along 80°E [12] also indicates the presence of an anticyclonic vortex. The climatological temperature data [13] shows the upwelling of isotherms above a depth of about 200m confirming the presence of the SLD. The sea level anomalies from T/P do show a high value east of SLD suggesting the presence of an anticyclonic eddy there.

4. Discussion

Studies in the past have identified that the summer monsoon circulation in the Bay of Bengal is forced by winds over the bay and the remote effects from the equatorial Indian Ocean [14]. The latter is associated with Rossby wave radiation consequent to the reflection of the spring Wyrтки jet from the eastern boundary of the Indian Ocean. Figure 3 shows the wind stress and curl of the wind stress during June. The winds over the Bay of Bengal are southwesterly during the summer monsoon (May-September). East of Sri Lanka these winds have large cyclonic curl during May-September. This large cyclonic winds stress curl generates the thermal dome associated with a cyclonic gyre east of Sri Lanka [6]. The upward Ekman pumping induced by this cyclonic curl brings cooler subsurface water to the surface layer. The decay of the SLD coincides with the arrival of a warm Rossby wave (Figure 3). This Rossby wave originates from the eastern boundary and it is strengthened by the monsoon winds in the central part of the Bay of Bengal.

The anticyclonic vortices do not appear to be directly driven by local winds. A possible mechanism that can generate the anticyclonic vortices is the interaction of the eastward SMC with the westward propagating Rossby waves [15]. Greatbatch [15] noted that in the equatorial ocean a Rossby wave, when propagate against an eastward zonal current, can break into a series of vortices. The pattern seen here is remarkably similar to that simulated by Greatbatch. The slower phase speed in comparison to the theoretical value is in support of this argument. The three non-dimensional parameter that govern the shallow water equation on a β -plane (i.e., beta parameter, Rossby number and stratification parameter) estimated from the model results suggest that the anticyclonic eddy east of the SLD falls into a class of motion known as the intermediate geostrophic regime [16]. The large anticyclonic vortex, on the other hand, falls in the planetary geostrophic regime. Further studies are needed to understand the mechanism of generation of the anticyclonic vortices and their dynamics; future observational programs should verify their existence and three-dimensional evolution.

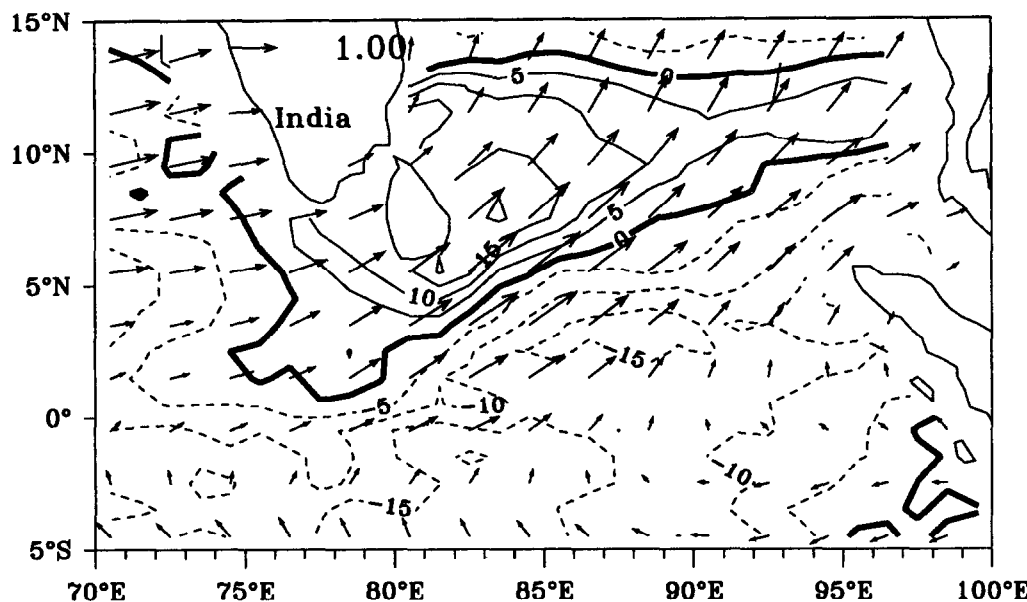


Figure 2. Wind stress vectors (dynes cm^{-2}) and curl of the wind stress (contours) during June, 1995. Negative values are shown by dashed contours. Contour interval is dynes cm^{-3} .

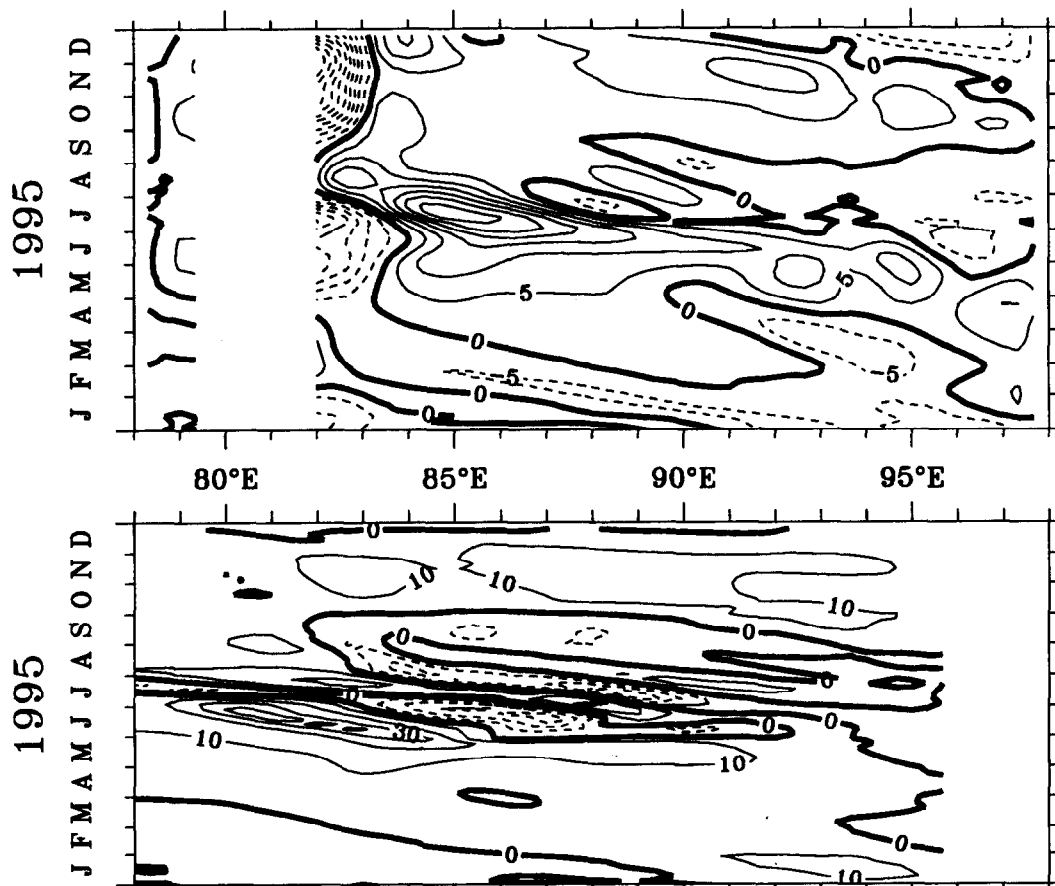


Figure 3. Meridional component of the velocity from the model at a depth of 55m along 8°N (upper panel) and 4°N (lower panel). Southward flow is shown as dashed contours.

References

- [1] J. P. McCreary, W. Han, D. Shankar and S. R. Shetye, 1996, Dynamics of the east India coastal current 2. Numerical solutions, *J. Geophys. Res.*, **101**, 13,993-14,010.
- [2] K. Wyrtki, 1973, An equatorial jet in the Indian Ocean, *Science*, **181**, 262-264.
- [3] A. N. Cutler and J. C. Swallow, 1984, Surface currents of the Indian Ocean (to 25°S, 100°E): Compiled from historical data archived by the meteorological office, Bracknell, UK, Rep. 187, Institute of Oceanographic Sciences, Wormley, UK., 8pp and 36 charts.
- [4] S. R. Shetye, S. S. C. Shenoi, A. D. Gouveia, G. S. Michael, D. Sundar and G. Nampoothiri, 1991, Wind-driven coastal upwelling along the western boundary of the Bay of Bengal during the southwest monsoon, *Cont. Shelf Res.*, **11**, 1397-1408.
- [5] P. N. Vinayachandran, Y. Masumoto, T. Mikawa and T. Yamagata, Intrusion of the Southwest Monsoon Current into the Bay of Bengal, *J. Geophys. Res.*, (accepted).
- [6] P. N. Vinayachandran and T. Yamagata, 1998, Monsoon response of the sea around Sri Lanka: Generation of thermal DOMEs and anticyclonic vortices, *J. Phys. Oceanogr.*, **28**, 1946-1960.
- [7] R. C. Pacanowski, 1996, MOM2.2β: Documentaion, user's guide and reference manual, GFDL Ocean Technical Report 3.2, 392pp.
- [8] R. C. Pacanowski and S. G. H. Philander, 1982, Parameterization of vertical mixing in numerical models of the tropical ocean, *J. Phys. Oceanogr.*, **11**, 1442-1451.
- [9] S. Hellerman and M. Rosenstein, 1983, Normal monthly wind stress over the world ocean with error estimates, *J. Phys. Oceanogr.*, **13**, 1093-1104.
- [10] D. M. Legler, I. M. Navon and J. J. O'Brien, 1989, Objective analysis of pseudo-stress over the Indian Ocean using a direct-minimization approach, *Monthly Weather Rev.*, **117**, 709-720.
- [11] P. Y. Le Traon, F. Nadal and D. Ducet, 1998, An improved mapping methos of multisatellite altimeter data, *J. Atmos. Ocean. Tech.*, **15**, 522-534.
- [12] F. Schott, J. Reppin, J. Fischer and D. Quadfasel, 1994: Currents and transports of the monsoon current south south of Sri Lanka, *J. Geophys. Res.*, **99**, 25,127-25141.
- [13] S. Levitus and T. P. Boyer, 1994: World ocean atlas 1994, Volume 4, Temperature, *NOAA atlas NESID 4*, U. S. Govt. Print. Off. Washington, D. C., 117pp.
- [14] L. Yu, J. J. O'Brien and J. Yang, 1991, On the remote forcing of the circulation in the Bay of Bengal, *J. Geophys. Res.*, **101**, 12,465-12,473.
- [15] R. J. Greatbatch, 1985, Kelvin wave fronts, Rossby solitary waves and nonlinear spin-up of the equatorial oceans, *J. Geophys. Res.*, **90**, 9097-9107.
- [16] T. Yamagata, 1982, On nonlinear planetary waves: A class of solutions missed by the traditional quasi-geostrophic approximation, *J. Oceanogr. Soc. Japan*, **38**, 236-244.

DRIFTING SAND RIPPLES AND BURIAL OF COBBLES IN NEAR-SHORE ZONES

S.I. Voropayev^{1,2}, G.B. McEachern¹, D.L. Boyer¹ and H.J.S. Fernando¹

¹Arizona State University, Tempe, AZ 85287-6106, USA

²Institute of Oceanology, Russian Academy of Sciences, Moscow, 117851, Russia.

E-mail: s.voropayev@asu.edu

Abstract. The purpose of this communication is to present the results of experiments on the dynamics of sand ripples and the influence of this process on the behavior of large bottom particles (cobbles). This problem is closely related to the migration and burial/scouring of isolated cobbles and anti-tank mines on a sandy beach in an oscillatory flow such as occurs in coastal waters beyond the region of wave breaking. The oscillatory flow was created in a long tank using standing waves of large amplitudes. Model cobbles were placed on the sandy bed and their evolution, changes in the bottom topography and velocity field in water were studied. The main findings include: (i) large-time changes of the bottom topography, which lead to the periodical burial of relatively large solid objects in intensive oscillatory flow and (ii) scouring of cobbles in relatively weak oscillatory flow. An explanation of the results is given.

1. Introduction

Cobbles are classified [1] as large particles with diameters $D = 6.4 - 25.6$ cm. Typical anti-tank mines have a similar size [2]. Under the action of external forcing cobbles can: (i) migrate along the shoreline, (ii) move or experience quasi-steady oscillations in the onshore/offshore direction, (iii) be buried in a movable sandy bed in intensive oscillatory flow or (iv) experience scour in relatively weak oscillatory flow. The along-shore migration occurs when a mean current exists and this process is hardly possible to reproduce correctly in relatively small-scale laboratory experiments. The mean motion and quasi-steady oscillations of cobbles in the onshore/offshore direction on solid impermeable bottom were studied in [3,4]. In the present study we reproduced the behavior of cobbles at movable sandy bed in a wave-induced flow.

The main difference between a solid impermeable bottom and a sandy bed is that when the fluid velocity exceeds some critical value, ripples can be formed at initially flat sandy bed. Because of the complexity of the problem, the mechanism of ripple formation is understood only qualitatively [1,5,6]; the quantitative theory is not developed and only linear analysis was done recently [7,8] for small rolling-grain ripples. With time the height of the rolling-grain ripples increases and flow separation becomes possible. As a result, vortex ripples with significant height may be formed. The theory for such ripples is not developed but different empirical and semi-empirical models are in broad use [1,9]. In contrast, the behavior of large bottom particles on a sandy bed in oscillatory flow remains practically unstudied and this topic forms the main purpose of the present study.

2. Experimental installation and method

At present at least two main experimental methods are in a broad use in studies related to the sediment transport in oscillatory flow. In the first method a platform loaded with sediment oscillates horizontally in a large tank filled with water. In the second method the oscillatory flow is generated in a closed water tunnel which has the shape of large vertical U-tube and sediment is placed in the horizontal section of the tunnel. Both methods have some advantages and some disadvantages. The platform in the first method may oscillate with variable amplitude and velocity, but at relatively high rates of sediment transport, most of the sediment falls down from the platform with time, making long duration experiments impossible. Besides, for large particles, such as cobbles,

the inertia forces may be significant in such geometry. In the second method the frequency of oscillations is usually fixed (or may be changed by two times) and the velocity is changed usually by changing the cross section of the working section of U-tube. The main disadvantage of such a device is that the working section must be closed. This makes problematic regular access to the sediment and cobbles and makes practically impossible the use of e. g., sonic probe, with the purpose of measuring the velocity at different points.

Taking these into account, it was decided to use standing waves with variable amplitude to reproduce horizontal oscillatory motion in a large tank with water. The experimental installation used in the present study was similar to that used in [3]. To produce an oscillatory flow standing waves were induced in a large tank (Fig. 1). The tank (length $L^* = 366$ cm, height 122 cm, width 61 cm) was filled with water to a depth of $h^* = 60-80$ cm. A layer of sand (density $\rho_s = 2.6$ gmcm⁻³, mean size $d = 0.04$ or 0.1 cm, depth 15 cm) was placed at the bottom. A vertical paddle connected through a mechanical drive to precision motor, forces the waves. In shallow water, if the oscillation frequency is chosen as

$$\omega = 2\pi/T = 2\pi(gh^*)^{1/2}/L^*,$$

where g is the gravity acceleration, one obtains the first standing wave mode with the wave length $\lambda = 2L^*$. If the amplitude, ϵ , of the horizontal excursion of fluid near the center of the tank is small, $\epsilon \ll L^*$, then the vertical velocity near the central part of the tank ($x = L^*/2 \pm \epsilon$) is also small, while the horizontal velocity u is practically depth independent:

$$u = U_0 \sin \omega t,$$

were $U_0 = \epsilon\omega$ and t is time. The velocity was measured using a three-component acoustic Doppler velocimeter (ADV) with a low noise level and small measurement volume (≈ 0.1 cm³) and data collection frequency 25 Hz [10]. Besides the velocities, the ADV probe can measure with good accuracy (± 0.05 cm) the distance to the sound reflecting surface, and using this effect the vertical position of the cobble from fixed horizontal level was also measured periodically. The evolution of initially flat bottom and the behavior of the cobble were videotaped using a high resolution SVHS video camera.

3. Results of observations

3.1. Ripple formation

When standing waves were initiated, initial rolling grain sediment transport was observed. As a result of the instability mentioned above, small (typical height $h = 0.5$ cm) three-dimensional ripples (typical horizontal

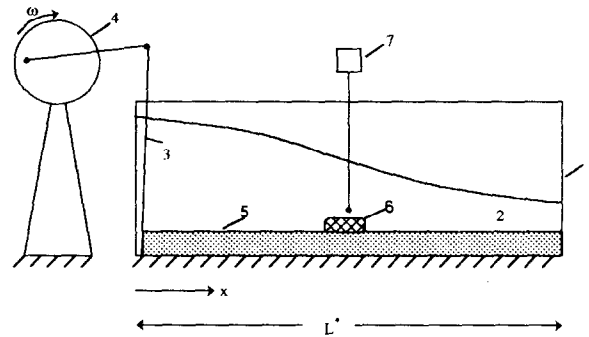


Figure 1. Schematic of the experimental system: 1 - tank, 2 - water, 3 - paddle, 4 - eccentric drive mechanism, 5 - layer of sand, 6 - cobble, 7 - ADV probe.

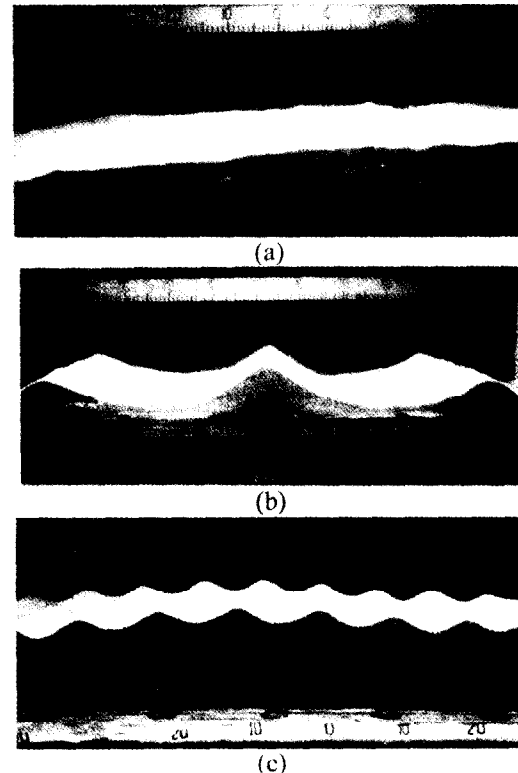


Figure 2. Side view photographs showing: (a) initially flat sandy bottom, (b) large and (c) moderate quasi-steady ripples formed after approximately 1 hour in steady oscillatory flow: $\omega = 2.13$ s⁻¹ (b, c), $d = 0.04$ cm, $\epsilon = 28$ cm, $U_0 = 60$ cms⁻¹ (b), 0.1, 10, 21 (c). Scale is given in cm.

spacing $L = 4\text{--}5$ cm) were generated at the bed. With time the height of these 3D ripples increased and vortices were formed in the lee of the ripples. This leads to the increase of the suspended sediment transport and subsequent increase in the number of small 3D ripples, which start to merge together forming two-dimensional vortex ripples directed across the flow (Fig. 2). Initially, 2D ripples have a relatively small L and h , but with time, t , the size of ripples increases and after some adjustment period it reaches equilibrium quasi-steady value with typical h_0 and L_0 , which depend on U_0 and d . Typical dependencies of $L(t)$, as measured in four different experiments, are shown in non-dimensional form by symbols in Fig. 3. Here

$$\tau = c/\omega\psi^{1/2}$$

and 2τ gives a characteristic time of the ripple formation,

$$\psi = U_0^2/g(\rho_s/\rho_w - 1)$$

is the mobility parameter, g is the gravity acceleration, ρ_w is the water density and $c = 2500$ is the empirical constant. The parameterization

$$L/L_0 = 1 - \exp(-t/\tau)$$

is proposed to describe the experimental data. Similar result was obtained for $h(t)$.

The measured equilibrium height h_0 and length L_0 of ripples were compared with the estimates obtained from semi-empirical formulas based on ψ and Shields parameter, θ (see, e.g., [1,9])

$$L_0 = \varepsilon(2.2 - 0.345\psi^{0.34}),$$

$$h_0 = L_0(0.182 - 0.24\theta^{1.5}).$$

Here, $\theta = \tau^*/(\rho_s - \rho)gd = \psi f_w/2$, where $\tau^* = \rho f_w U_0^2/2$ is the peak bed shear stress and f_w is the wave friction factor, which depends on the wave Reynolds number $Re = \varepsilon^2\omega/\nu$ and the relative bed roughness ε/d [9].

3.2. Velocity measurements

The velocity field (all three components) was measured at different heights above the ripple crest and trough. The data was obtained for established ripples using time records, which were phase averaged over 40-50 oscillation periods. Detailed information on mean characteristics (including weak secondary circulation cells, which are responsible for the large time ripples drift) and turbulent characteristics of the flow above the formed ripples were obtained and compared with some previous results [11], where two-component laser-Doppler-anemometer was used.

3.3. Dynamics of formed ripples

The most interesting result on the formed ripples is related with the large time changes of the bottom topography. Although on average the ripple parameters h_0 and L_0 do not change

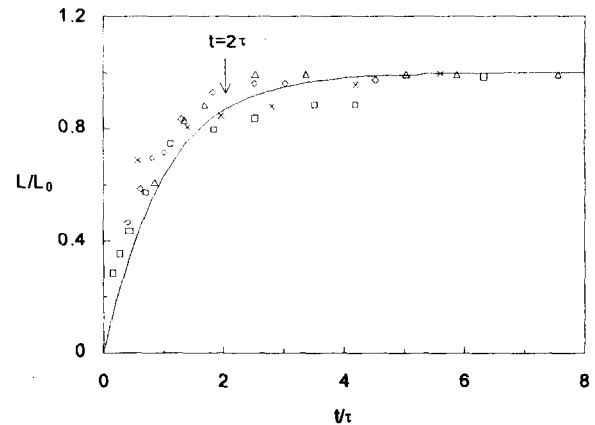


Figure 3. Non-dimensional ripple lengths L/L_0 as functions of non-dimensional time t/τ for four different experiments (symbols). Solid line shows the approximation function (3).

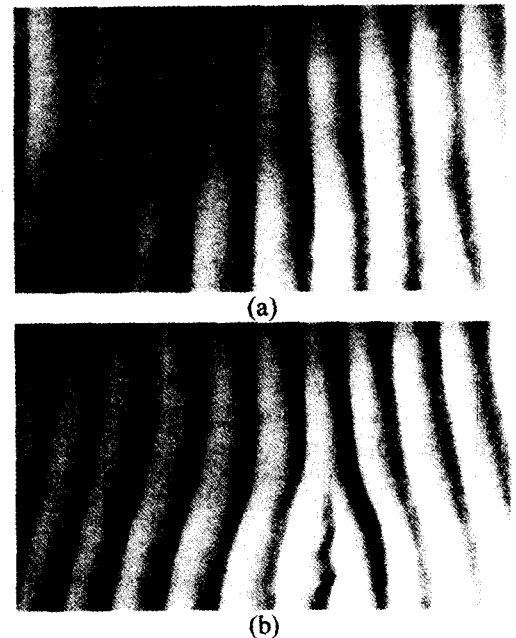


Figure 4. Top view photographs showing the large time instability and formation of a new ripple. With time the newly formed ripple spreads across the flow and initiates small mean drift of the surrounding ripples: $d = 0.04$ cm, $U_0 = 15$ cm s^{-1} , $L_0 = 15$ cm, $h_0 = 1.3$ cm.

significantly after the adjustment time 2τ , the bottom topography itself never reaches an exact steady state. While the frequency and the amplitude of the flow oscillations remain with very good accuracy constant, the formed ripples are not stable. Periodically the distance between two nearest ripples may slowly increase/decrease. This leads to the formation of a new ripple or merger of two old ripples. This process may start near the wall as well as away from the wall and a typical example of such instability is shown in Fig. 4. With time the new/merger ripple spreads across the flow. Because the typical spacing between ripples decreases/increases during this process, the whole system of ripples starts to migrate with some typical velocity U_d and with time a new quasi-steady state with approximately the same typical spacing L_0 is established. This process resembles the appearance of some kind of dislocation in an initially regular picture of the ripple pattern (see Fig. 4), and this dislocation induces the migration of the nearest ripples, which in their turn initiate the motion of the next ripples and so on (domino effect).

The mechanism of such instability is unclear and it may be rather complicated, but mentioned above weak mean secondary circulation between ripples may play an essential role in this process. The migration velocity U_d of ripples was determined by measuring periodically the mean absolute value of the displacements of the ripple crests and dividing this displacement by the time between measurements. Using these data, the mean over large time interval (5-6 hours) values for the drift velocity U_d were determined for different sand diameters d and different values of U_0 . To explain the results, a simple model is proposed and the following estimate derived:

$$U_d = L_0/8\tau = U_0\psi^{1/2}(2.2 - 0.345\psi^{0.34})/8c,$$

where the estimates for τ and L_0 , which are given above, are used.

3.4. Scouring around a cobble

Solid objects placed at the bottom causes diversion of streamlines and acceleration/deceleration of water around the object, which in turn causes scour or erosion. In the experiments, the value of U_0 was chosen in such a way that the mobility parameter ψ was near its critical value and only small-scale rolling-grain ripples could be formed. Because the flow velocity in the vicinity of cobble exceeds (approximately by two times) the free stream velocity, the mobility parameter becomes relatively large here and noticeable sediment transport can be observed around a cobble. Initially the scour occurs on the sides of the cobble where two cavities are formed. With time small scale rolling-grain ripples are generated at the bottom away from cobble and the scour pattern around the cobble takes the form of three under developed ripples which spread symmetrically relative to the cobble across the flow. After the scour pattern reaches this steady state it does not change significantly. During the scour formation the cobble dips into the sand. The maximum subsidence of the cobble, as measured using the ADV probe, practically does not depend on the cobble density ($\rho_c = 1.6-2.5 \text{ gcm}^{-3}$) and height ($H = 3-8 \text{ cm}$), but depends mostly on the cobble diameter ($D = 5-15 \text{ cm}$) and is approximately equal to:

$$S = 0.15 D.$$

3.5. Periodical burial of cobble

If the velocity amplitude U_0 increases such that the mobility parameter exceeds significantly its

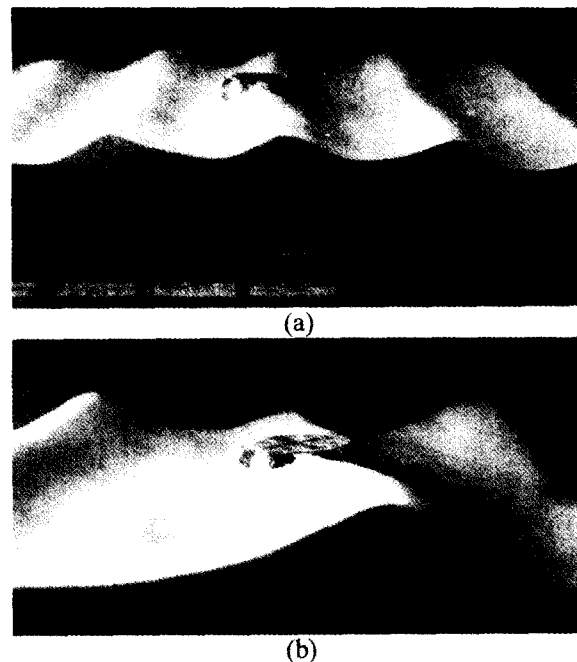


Figure 5. Side view photographs showing cobble on sandy bed in oscillatory flow: (a) after time $t \approx \tau$ a regular system of relatively small ripples, the size of which slowly increased with time (see fig. 4), develops on initially flat bottom with one ripple across the cobble, (b) initiation of large-time instability (close view). Experimental parameters: $U_0 = 60 \text{ cms}^{-1}$, $d = 0.04 \text{ cm}$.

critical value, then the formation of the vortex ripples becomes possible. In this case when the cobble is placed at a flat bottom, the initial evolution is very similar to the case discussed above with noticeable scour and small-scale rolling grain ripples. Later, however, three under developed ripples, which are formed symmetrically relative to the cobble, spread across the whole width of the tank and initiate rapid formation of the nearest vortex ripples, and soon (at $t \approx \tau$) the whole bottom is covered by a regular rippled pattern with one ripple crossing the cobble (Fig. 5a).

Thus the cobble appeared to be partly buried in sand. At this time ($t \approx \tau$) the depth of the burial h_b of a cobble, which was initially on the flat bottom, may be estimated as $h_b = h_0/2 + S = h_0/2 + 0.15 D$ (see Fig. 6b). At larger times $t > \tau$, however, the formed ripples demonstrate the large-time instability discussed above (see also Fig. 5b, showing horizontal displacement of two ripples near the cobble and the initiation of such instability). As a result, the whole system of ripples starts moving with small but finite mean drift velocity U_d relative to a still cobble and after the time, equal approximately to $t \approx \tau + L_0/2U_d = 3\tau$, the cobble appeared to be in a valley between two adjusted ripples (Fig. 6c). At this time the lower horizontal boundary of cobble, which was initially at the level $z = 0$ (Fig. 6a), will sink down to the height $(h_0/2 + S)$ below this level (Fig. 6c) and will be subsided on the depth S into the sand because of the scour. For a heavy cobble the gravity force exceeds the buoyancy force and the cobble does not move upward when at time $t \approx 3\tau + L_0/2U_d = 5\tau$ a ripple crest arrives (Fig. 6d). As a result the cobble appeared to be completely (if $H < h_0 - S$) or partly (if $H > h_0 - S$) buried in a sand during the time interval of the order of 5τ . Then a ripple trough arrives and the process repeats itself.

Thus, a heavy disk-shaped cobble of diameter D , which is placed on initially flat or rippled sandy bottom in a steady oscillatory flow, will be periodically buried with a typical time interval 8τ . The minimum burial depth is determined mostly by a maximum subsidence S , because of a local scour, while the maximum burial depth may be estimated as

$$h_b = h_0 + S = h_0 + 0.15 D.$$

4. Conclusions

The behavior of large disk-shaped bottom particles of diameter D and height H placed on a sandy bottom in oscillatory flow was studied experimentally. This problem is closely related to the migration and burial/scouring of isolated cobble and anti-tank mines on a sandy beach in an oscillatory flow such as occurs in coastal waters beyond the region of wave breaking. It is shown that when the background velocity is just below its critical value, small-scale rolling grain ripples develop at an initially flat bottom and noticeable scour around the cobble occurs. At large time the scour pattern reaches steady state and the resulting maximum subsidence becomes equal to S . When the background velocity exceeds its critical value, the vortex ripples start to form. Typical time τ of ripple formation depends on the wave frequency and the mobility parameter as given above. After that time a regular quasi-steady system of ripples is formed with one ripple across the cobble and the cobble appeared to be partly or completely buried (depending on the ripple size and cobble height). At larger times the system of ripples is not

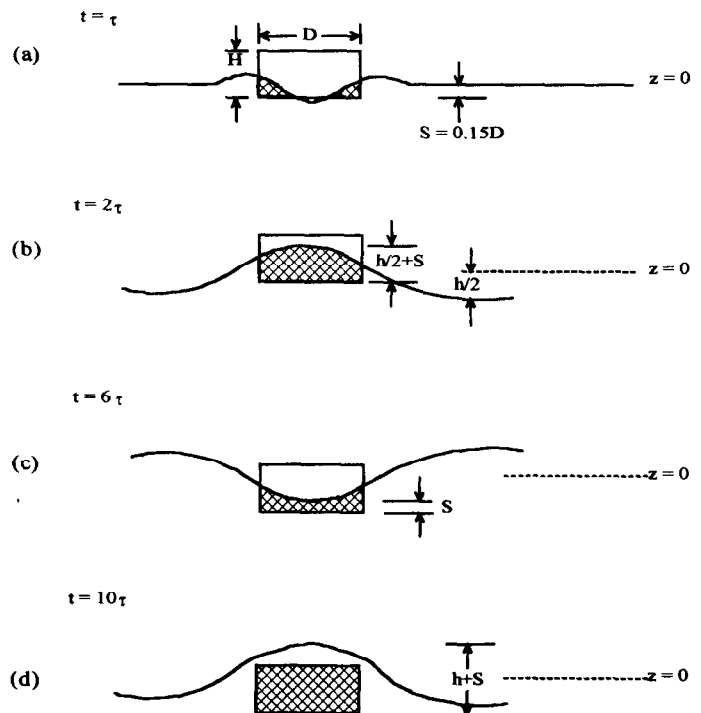


Figure 6. Schematic showing the time behavior of cobble, which was placed at flat sandy bottom in a steady oscillatory flow: (a) local scour and subsidence of cobble at relatively short time, (b-d) periodical burial of cobble at large time.

stable and every ripple slowly migrates with some mean drift velocity. As a result a heavy cobble appeared to be periodically near the crest or valley of a ripple thus being buried periodically.

Based on the results of experiments, some estimates for the oceanic case may be obtained. Let a cobble of diameter $D = 20$ cm, height $H = 10$ cm and density $\rho_c = 1.8 \text{ gmcm}^{-3}$ be placed in shallow water of depth 10 m at sandy beach with small slope beyond the region of wave breaking. The sand diameter $d = 0.1$ cm, density $\rho_s = 2.6 \text{ gmcm}^{-3}$. The waves are of amplitude 1 m, period 10 s approaching a beach and the mean current is negligibly small. Then a shallow water wave theory (see, e.g., [13]) gives for the amplitude of the horizontal water displacement $\epsilon \approx 1$ m and for the amplitude of the horizontal velocity $U_0 \approx 1.5 \text{ ms}^{-1}$. This gives $\psi \approx 150$ and using simple formulas above, one obtains the estimates: $L_0 \approx 70$ cm, $h_0 \approx 12$ cm, $S \approx 3$ cm, $8\tau \approx 240$ min and $h_b \approx 15$ cm. Thus one may expect that at such conditions the cobble may be completely buried after a typical time on the order of 4 hours. For more details see [14].

Acknowledgements

This study was supported by the Office of Naval Research.

References

- [1] Sleath, J.F.A. 1984. *Sea Bed Mechanics*. Wiley.
- [2] Dill, R.F. 1956. The burial and scouring of ground mines on a sand bottom. *Res. Report, 86*, US NAVY electronic laboratory, San Diego.
- [3] Voropayev, S.I., Roney, J., Boyer, D.L., Fernando, H.J.S., Houston, W.N. 1998. The motion of large bottom particles (cobbles) in a wave-induced oscillatory flow. *Coastal Eng.*, in press.
- [4] Luccio, P.A., Voropayev, S.I., Fernando, H.J.S., Boyer, D.L and Houston, W.N. 1998. The motion of cobbles in the swash zone on an impermeable slope. *Coastal Eng.*, **33**, 41-60.
- [5] Sleath, J.F.A. 1976. On rolling grain ripples. *J. Hydraul. Res.*, **14**, 69-81.
- [6] Sleath, J.F.A. 1995. Sediment transport by waves and currents. *J. Geophys. Res.*, **100**(C6), 10977-1098
- [7] Blondeaux, P. 1990. Sand ripples under sea waves. Part 1. Ripple formation. *J. Fluid Mech.*, **218**, 1-17.
- [8] Vittory, G., Blondeaux, P. 1990. Sand ripples under sea waves. Part-2. Finite-amplitude development. *J. Fluid Mech.*, **218**, 19-39.
- [9] Nielson, P. 1992. *Coastal Bottom Boundary Layers and Sediment Transport*. World Scientific.
- [10] Snyder, W.H., Castro, P.I. 1998. Acoustic- Doppler-velocimeter evaluation in a stratified tank. 1998 (submitted).
- [11] Toit, C.G., Sleath, J.F.A. 1981 Velocity measurements close to rippled beds in oscillatory flow. *J. Fluid Mech.*, **112**, 71-96.
- [12] Herbich, J.B., Sciller, R.E., Watanaber, R.K., Dunlap, W.A. 1984.. *Seafloor Scour*. Marcel Dekker, Inc.
- [13] Dean, R.G., Dalrymple, R.A. 1994. *Water Waves Mechanics for Engineers and Scientists*. World Scientific.
- [14] Voropayev, S.I., McEachern, G.B., Boyer, D.L., Fernando, H.J.S. 1998. Dynamics of sand ripples and burial/scouring of cobbles in oscillatory flow. Submitted to *Appl. Ocean Res.*

STERN-RADKO SELF-PROPAGATING EDDY

S.I. Voropayev^{1,2} and G.B. McEachern¹

¹Arizona State University, Tempe, AZ 85287-6106, USA

²Institute of Oceanology, Russian Academy of Sciences, Moscow, 117851, Russia
E-mail: s.voropayev@asu.edu

Abstract. The aim of this short contribution is to present the results of laboratory experiment on the dynamics of compact self-propagating quasi-monopolar vortex produced in a homogeneous rotating fluid of constant depth (f-plane). Recently Stern and Radko [1] considered theoretically and numerically a symmetric barotropic eddy, which is subject to a relatively small amplitude disturbance of unit azimuthal wave number on the f-plane. They predicted that such an eddy remains stable and could propagate significant distance away from its origin. This effect may be of importance for oceanographic application and we decided to reproduce such an eddy in laboratory experiment with the purpose of verifying theoretical predictions.

1. Introduction

Recent results, based on the high resolution satellite data [2], demonstrate that a significant dipolar component is present, for example, in most of the Gulf Stream rings and the long-held models of complete monopolar rings is now questioned. Taking into account the importance of rings and other quasi-monopolar eddies in large scale mixing in the ocean, the need for the development of models for compact self-propagating vortices becomes obvious. In [1] an attempt was made in this direction and some basic properties of single self-propagating quasi-monopolar vortex were predicted theoretically and numerically. Before moving further in developing models for merging and more complicated interactions of such eddies, these predictions must be verified. At present detailed field data are still absent, and the only way to verify the model prediction is to conduct a laboratory experiment.

Previous experiments on barotropic or baroclinic vortices which are non-compact and strictly monopolar indicate that merger only occurs for closely separated vortices. In the case of isolated self-propagating quasi-monopolar vortices the merger may occur for distant vortices and this is one of the main and important differences from previous studies. For a detailed discussion on this topic we refer the reader to [1,3]. The main aim of this brief communication is (i) to present the results of laboratory experiment on the formation and dynamics of self-propagating quasi-monopolar eddy, which was generated in a homogeneous rotating fluid of constant depth (f-plane) and (ii) to make a comparison with the theoretical predictions [1].

2. Experimental method

The experiment was conducted in a square Plexiglas tank (75 x 75 x 10 cm) mounted on a turntable rotating at a constant rate $\Omega = 2\pi/T = 0.75 \text{ s}^{-1}$, where T is the period of rotation (Fig. 1a). The working fluid was distilled

water at room temperature. The quasi-monopolar flow was generated using a stirring technique. For this purpose a heavy bottomless copper cylinder (diameter $D = 10$ cm) with thin walls (thickness 0.1 cm) was introduced into the tank approximately at the half-distance between the tank center and one of the corners. The fluid inside the cylinder was stirred by a small motor with a propeller during a fixed time interval and then the propeller was taken away. To reduce the effect of the centrifugal instability (see, e. g., [4]), the cyclonic direction of stirring was used. For the same reason, the fluid in the cylinder was free to rotate with the angular velocity Ω_0 (≈ 2 s⁻¹ near the cylinder center) during the period of time equal to $4T$. This time was needed to adjust the initial radial profile of the azimuthal velocity in the cylinder to the state when the flow will be stable (see, e. g., [5]) after the cylinder was taken out. Then the cylinder was pushed forward with small horizontal velocity U_0 (≈ 0.5 or 1 cm s⁻¹) in the direction of the opposite tank corner and at the same time the cylinder was smoothly lifted up vertically from the water. This procedure was made using an electric motor connected via thin wires with a cylinder,

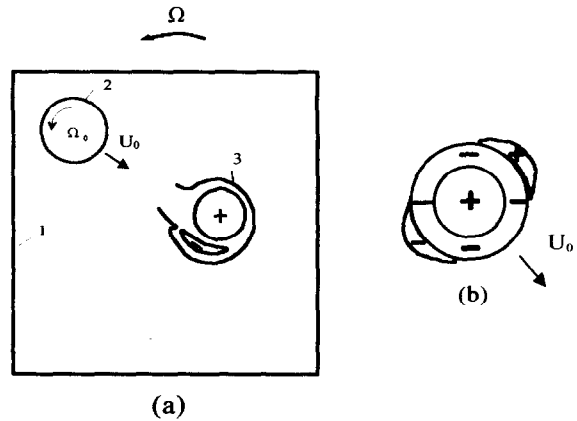


Figure 1. Schematic diagrams of the experimental set-up (a): 1 – rotating tank filled with water, 2 - bottomless cylinder with cyclonically rotating fluid, 3 - - resulting vortex which is formed with time after a cylinder was moved horizontally with small velocity U_0 and simultaneously lifted up from the water; initial vorticity distribution created at $t = 0$ (b).

The flow induced by this method presents a combination of an isolated monopole with relatively large net angular momentum M ($\propto \rho D^4 \Omega_0$) and a dipole with relatively small linear momentum P ($\propto \rho D^2 U_0$) per unit depth (ρ is the fluid density). The initial vorticity distribution produced by this method is shown schematically in Fig. 1b. In the experiment the ratio $DP/M \propto U_0/D \Omega_0$ ($= 0.02-0.05$) was relatively small. This ratio is equivalent to a small parameter $\epsilon/D \ll 1$, used in a theory by Stern and Radko [1], who scaled the eddy propagation velocity as $U_0 \propto \epsilon \Omega_0$. Note that only when this ratio was small, but finite, the resulting eddy in the experiment was a compact self-propagating quasi-monopole with a typical size approximately equal to the diameter of a cylinder. In the opposite case (larger ratio), relatively large slightly asymmetric dipole was generated, while for the case of $\epsilon/D = 0$ the resulting structure is a non-propagating ($U_0 = 0$) unstable monopole, studied in [6]. Note also that for a typical oceanic eddy this ratio is small (e. g., for an eddy with $D = 200$ km, $U_0 = 10$ cm s⁻¹ and azimuthal velocity on the periphery 50 cm s⁻¹ this gives $\epsilon/D = 0.1$).

The flow was visualized by using a thymol-blue pH-indicator (e.g., see [7]). The tank was illuminated by an array of fluorescent lights beneath the tank. The flow patterns were recorded from above using a high-resolution super-VHS video camera mounted on a frame attached to the turntable. To obtain information on the motion field, small neutrally buoyant particles (Pliolite) with high reflectivity were introduced into the working fluid. The particles were illuminated at the mid water level by a horizontal light sheet with a thickness of 0.5 cm and videotaped by the same video camera. After the run, standard digital image procedure was used to obtain pictures with dyed flow patterns from the video. Particle tracking was carried out using DigImage processing package [8]. With this technique it is possible to determine the position and velocities of a large number of tracer particles and

interpolate them onto a rectangular grid in order to calculate the velocity and vorticity fields in the flow.

The limiting cases of symmetric barotropic dipole ($\Omega_0 = 0, U_0 \neq 0$) and of momentumless isolated monopole ($\Omega_0 \neq 0, U_0 = 0$) were studied previously in [6,9,10,11] and below only the case when both U_0 and Ω_0 are non zero and the ratio $PD/M \propto U_0/D\Omega_0$ is small is considered.

3. Experimental results

Photographs in Fig. 2 show typical evolution of the flow patterns as visualized by pH- indicator. In this experiment $U_0 = 0.5$ cm. Initially (Fig. 2a), a volume of water, which was released from the cylinder, has approximately cylindrical shape with a diameter (≈ 12 cm) somewhat larger than a cylinder. This volume rotates anti-cyclonically with angular velocity approximately two times larger than the surrounding fluid and propagates forward with velocity of order 0.5 cm s^{-1} . With time (Fig. 2b) significant portion of eddy has a tendency to separate from the main cyclone and to form an anti-cyclonic structure. As was mentioned above, if the ratio of PD/M is not small (initial U_0 is relatively large or Ω_0 is small), the separation occurs and large (with a diameter 2-3 D) slightly asymmetric dipole forms.

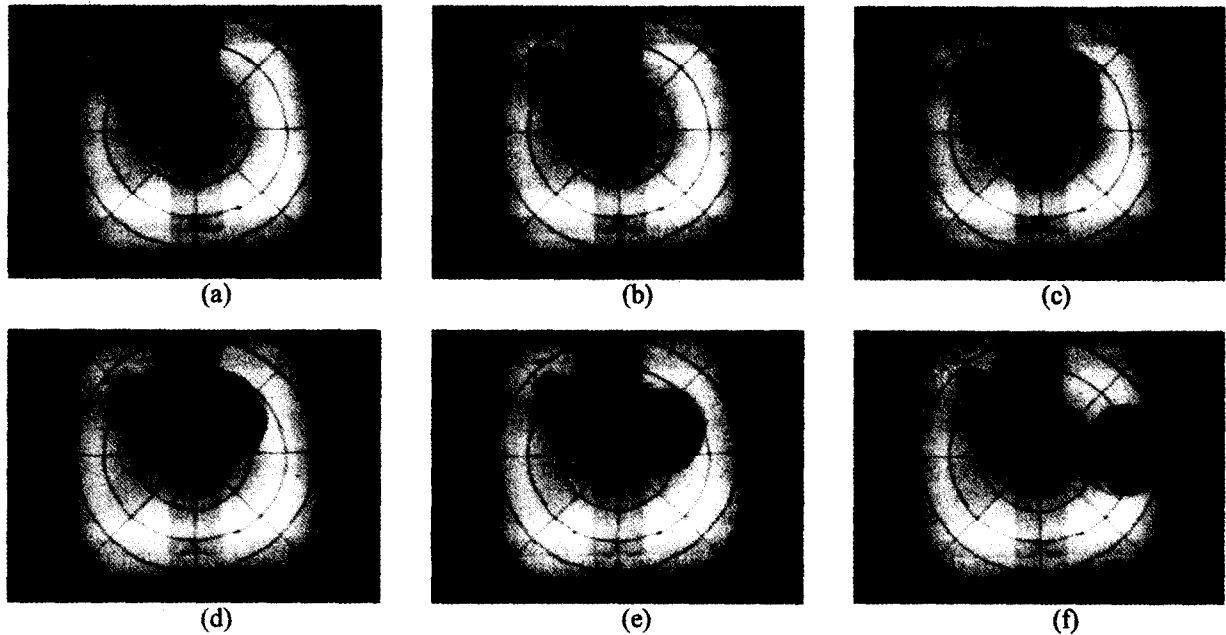


Figure 2. Top-view photographs (digitized images from video) showing formation and propagation of compact quasi-monopole visualized by thymol-blue indicator. The photographs were taken at (a) 1s, (b) 16, (c) 33, (d) 40, (e) 50, (d) 95 after the cylinder was taken out. Distance between circles at the bottom – 5 cm, $U_0 = 0.5$ cm s^{-1} and period of tank rotation $T = 7.4$ s.

In the case shown in Fig. 2, the ratio PD/M is relatively small and anti-cyclonic rider does not separate significantly; it appeared to be attached to the main cyclone. As a result, a compact self-propagating quasi-monopolar eddy is formed (Fig. 2d), which propagates forward, while a small rider slowly rotates around the main cyclone. The resulting eddy remains stable during a relatively large time interval and propagates a significant distance from the origin (Fig. 2f).

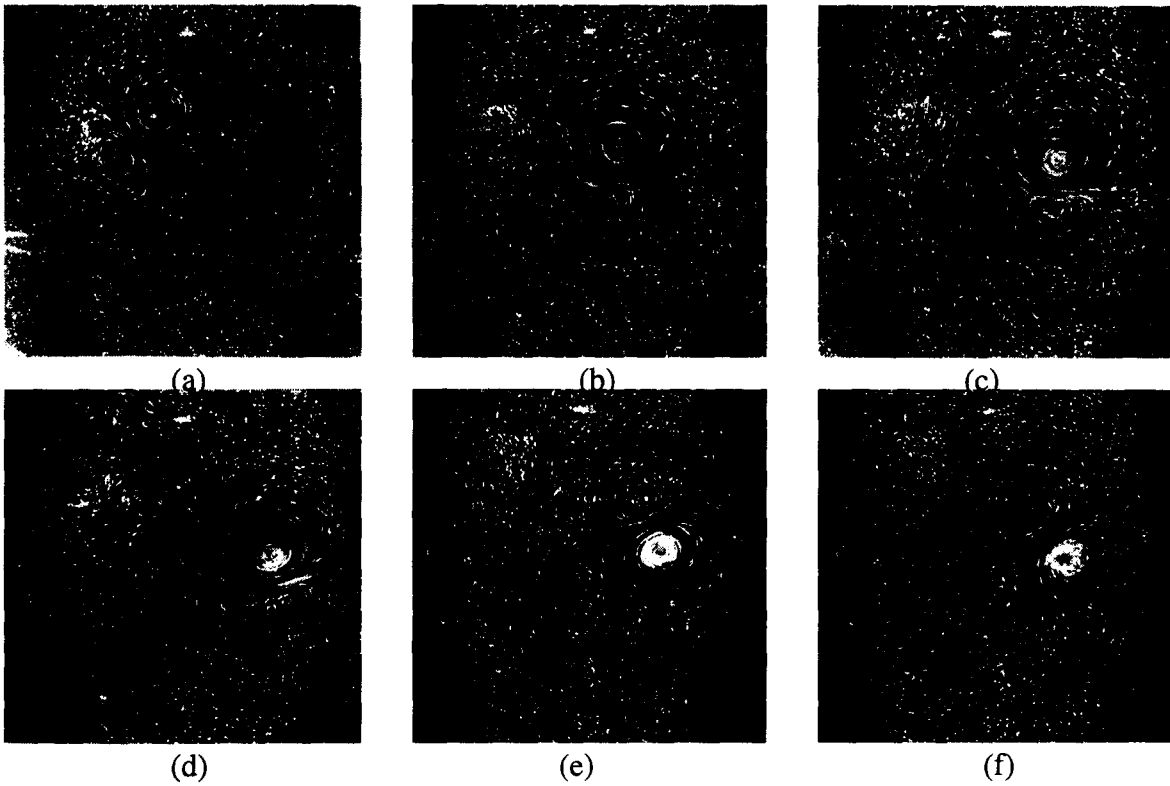


Figure 3. Particle streak photographs showing propagation and collision of compact quasi-monopole with vertical wall of the tank, which is at the right side of the photographs. The photographs were taken at (a) 15 s, (b) 30, (c) 37, (d) 45, (e) 60, (d) 95 after the cylinder was taken out. In this experiment $U_0 = 1 \text{ cms}^{-1}$, $T = 7.4 \text{ s}$. Exposure time is approximately 3-4 s.

Streak photographs (Fig. 3) give the general impression on the velocity field in the experiment conducted with the same initial conditions as shown in Fig. 2, but with a larger U_0 ($\approx 1 \text{ cms}^{-1}$). The sequence of events here in general is very similar to the previous case but with one difference. Because the propagation velocity of the vortex is now two times larger than in the previous case, the vortex crosses the tank and then reaches (Fig. 3d) the right wall of the tank. Here the vortex collides with a vertical wall and reflects, starting to move in the opposite direction (Fig 3e). The process of collision is non-elastic, because the no-slip condition at the wall and production of the secondary vorticity are important here. These effects were studied in detail previously for the case of symmetric dipoles [7,12,13] and qualitatively the mechanism of interaction is more or less clear. Schematically this process is shown in Fig. 4. Approaching the wall, the

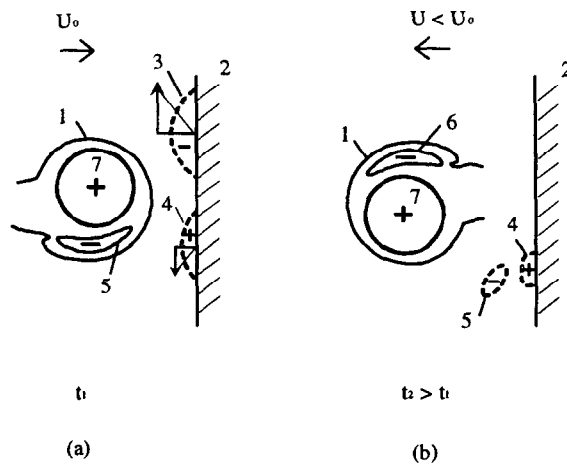


Figure 4. Sketch of the head-on collision of compact quasi-monopole (1) with a vertical wall (2). Secondary vortex patches (3, 4) are created in the boundary layer at the wall by the flow induced by the primary vortex (a). Initial relatively weak anti-cyclonic rider (5) dissipates near the wall (b), while a new small rider (6) is formed from the opposite side of relatively strong cyclonic eddy (7). Arrows parallel to the wall show the direction of the velocity induced by a monopole (a).

initial relatively weak anti-cyclonic rider generates at the wall an opposite sign vorticity patch and eventually dissipates near the wall. In contrast, the relatively strong cyclonic eddy produces here an anticyclonic vorticity patch. In the velocity field induced by a large cyclone this patch has a strong tendency to be detached from the wall. As a result, a new anticyclonic rider is formed and our quasi-monopole starts moving from the wall (Fig. 4e). Because the collision is non-elastic with significant loss of the linear momentum, the propagation velocity of the resulting vortex rapidly decreases and eventually it practically stops (Fig. 4f).

By using the particle tracking technique, it was possible to reconstruct the velocity field in the flow and calculate the distributions of the vorticity. To make some comparison with the Stern-Radko predictions for a steady motion, the data was taken at the moments when the vortex was formed but did not reach the vicinity of the wall. The results are shown in graph in Fig. 5. The data from which this graph was constructed was taken in the same experiment as shown in Fig. 4. Arrows of different length in Fig. 5 show the velocity vectors, while shadows of different grade give the vorticity distribution. Comparison of Fig. 5 with the correspondent solution for the vorticity ([1], Figs. 9b-d) shows satisfactory agreement, in spite of rather different initial conditions used in our experiment and in the theory. Initial distribution of the vorticity in the experiment is shown schematically in Fig. 1b, and only later, after some adjustment period, this distribution was transformed significantly into a quasi-monopolar distribution, shown in Fig. 5. In their numerical calculations Stern and Radko have used a simplified analytical solution for a steady quasi-monopole as the initial conditions, and demonstrated analytically and numerically that the resulting solution is a stable quasi-monopole. Thus we can conclude, that the details of the initial conditions are not very important in the experiment. When relatively large angular momentum and relatively small linear momentum are introduced locally into a rotating fluid, the resulting flow asymptotically tends to a quasi-monopolar vortex similar to that analyzed by Stern and Radko.

4. Conclusions

When a relatively large amount of angular momentum and small amount of linear momentum are introduced locally into a rotating homogeneous fluid, the resulting compact and self-propagating quasi-monopole is formed. The experiments show that such eddy (i) can be easily generated, (ii) is stable and can propagate significant distance from the origin, (iii) survives after a non-elastic collision with a vertical wall and (iv) its inner structure is very similar to that predicted by Stern and Radko [1].

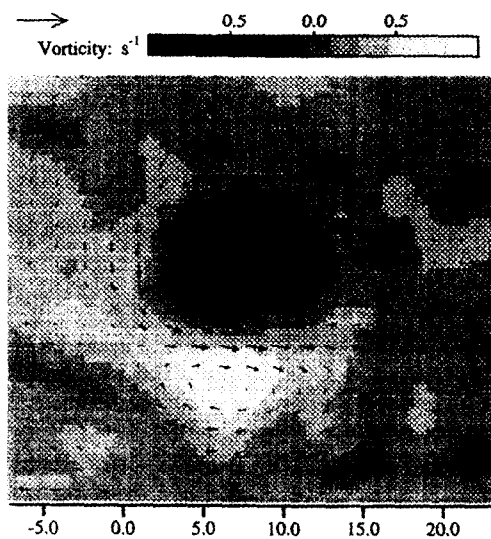


Figure 5. Instantaneous velocity field for the steady moving compact quasi-monopole is shown by arrows while the corresponding vorticity distribution is given by a black-white background. Intensity of shadow is proportional to the vorticity value. The particle tracking was made in the same experiment as shown in Fig. 4. Time after the cylinder was taken out - 30 s. Large arrow in the upper left part shows the velocity scale (5 cm s^{-1}), vorticity scale is given in the upper right part and numbers at the bottom show distance in cm.

Acknowledgements

We are grateful to Melvin Stern for very useful comments. This study was supported by the National Science Foundation.

References

- [1] Stern, M.E. and Radko, T. 1998: The self-propagating quasi-monopole vortex. *J. Phys. Oceanogr.*, **28**, 22-39.
- [2] Hooker, S.B., Brown, J.W., Kirwan, A.D., Linderman, G.L. and Mied, R.P.: 1995. Kinematic of warm-core dipole ring. *J. Geophys. Res.*, **100**, 24797-24809.
- [3] Radko, T. and Stern, M.E. 1998. On the propagation of mesoscale eddies. To be submitted.
- [4] Hopfinger, E.J. and van Heijst, G.J.F. 1993. Vortices in rotating fluids. *Ann. Rev. Fluid Mech.*, **25**, 241-289.
- [5] Flierl, G.R. 1987. Isolated eddy models in geophysics. *Ann. Rev. Fluid Mech.*, **19**, 493-530.
- [6] Kloosterziel, R.C. and van Heijst, G.J.F. 1991. An experimental study of unstable barotropic vortices in a rotating fluid. *J. Fluid Mech.*, **223**, 1-24.
- [7] Voropayev, S.I. and Afanasyev, Ya.D. 1992. Two-dimensional vortex dipole interactions in a stratified fluid. *J. Fluid Mech.*, **236**, 665-689.
- [8] Dalziel, S. 1992. *DigImage. Image Processing for Fluid Dynamics*. Cambridge Environmental Research Consultant Ltd.
- [9] Flierl, G.R., Stern, M.E. and Whitehead, J.A. 1983. The physical significance of modons: Laboratory experiments and general integral constraints. *Dyn. Atmos. Oceans*, **7**, 233-263.
- [10] Couder, Y. and Basdevant, C. 1986. Experimental and numerical study of vortex couples in two-dimensional flows. *J. Fluid Mech.*, **173**, 225-251.
- [11] Voropayev, S.I., Zhang, X., Boyer, D.L., Fernando, H.J.S. and Wu, P.C. (1997) Horizontal jets in a rotating stratified fluid. *Physics of Fluids*, **9**(1), 115-126.
- [12] van Heijst, G.J.F. and Flor, J.B. 1989. Dipole formation and collisions in a stratified fluid. *Nature*, **340**, 212-215.
- [13] Orlandi, P. 1990. Vortex dipole rebound from a wall. *Phys. Fluids*, **A2**, 1429-1436.

THE ARCTIC FRONT: STRUCTURE AND CROSS-FRONTAL TRANSPORT PROCESSES

Waldemar Walczowski

Institute of Oceanology Polish Academy of Sciences, 81-712 Sopot, Powstancow Warszawy 55,
POLAND
Walczows@iopan.gda.pl.

Abstract. The Arctic Front thermohaline structure is described on the basis of the hydrographic data obtained by the Institute of Oceanology Polish Academy of Sciences. Data from the period 1993-1996 were collected during summer expeditions of r.v. 'Oceania' to the European Arctic Seas. Investigations were conducted on two polygons in the border zone between the Norwegian Sea and the Greenland Sea, above the Mohna Ridge. Mesoscale eddies broken from frontal meanders were recognised as a primary process of transfrontal transport. Front meandering and eddy generation were caused primarily by baroclinic instability and topographic effect. Volume of several eddies was calculated. Transfrontal fluxes and total eddy transfrontal volume, heat and salt transport were calculated.

1. INTRODUCTION

The Arctic Front called also Polar Ocean Front [10] is Atlantic - Arctic water contact zone [17]. It is situated in the GIN Sea - Greenland-Iceland-Norwegian Sea basin. This bottom topography steered, 800 km long, climatic front extends from Jan Mayen Island towards NE over the Mohna Ridge, turns towards North over the Knipovitch Ridge. The northern end of the front is located in the NW direction from the southern part of Spitsbergen (Figure 1). The Arctic Front divides waters of Atlantic origin carried by the western branch of Norwegian-Atlantic Current and cold, low saline Arctic Waters transported by the Jan Mayen Current and cyclonic Greenland Sea Gyre [8].

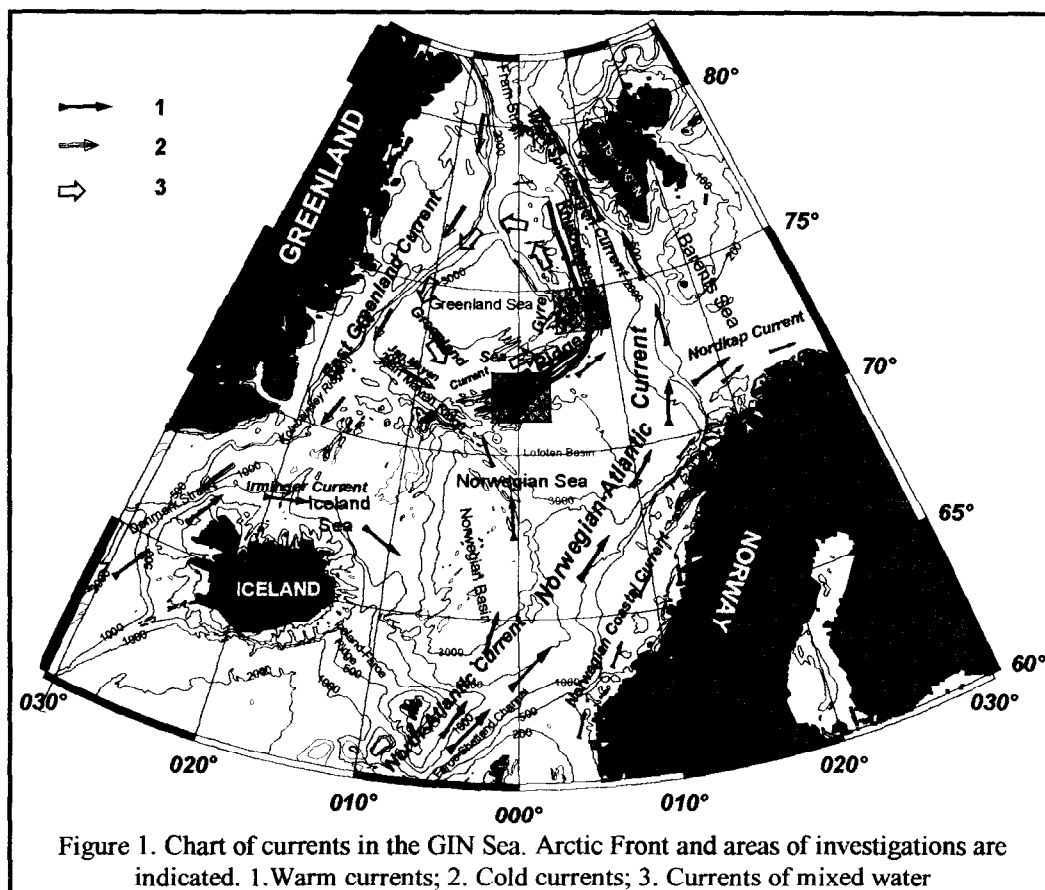
The importance of this front is linked with the significance of the GIN Sea for the World's climate system. Global thermohaline circulation - Conveyor Belt Circulation ends here its surface part. Warm, saline water is provided from Gulf Stream system by the North Atlantic and Norwegian-Atlantic Currents. Portion of this water after winter cooling and mixing sinks and initiates deep circulation. The intensity and northern extension of deep convection processes determine Conveyor Belt Circulation strength, heat redistribution and indirectly, northern hemisphere climate [1].

The Greenland Sea salt and heat budget is very important for deep convection. More saline Atlantic Water is necessary to initiate and provide salt to this process which occurs in the Arctic domain - central part of the Greenland Sea [16]. Transfrontal transport across the Arctic Front plays therefore a unique role for World's climate, the Arctic domain is an oceanic regime potentially sensitive to climatological variations [17].

2. INVESTIGATIONS

During summer expeditions of r.v. 'Oceania', the Arctic Front has been crossed and investigated since 1987. More detailed investigations were conducted in 1993 - 1996 period. The areas of measurements are indicated on the map (Figure 1). More than 320 deep CTD stations were made. In addition several high

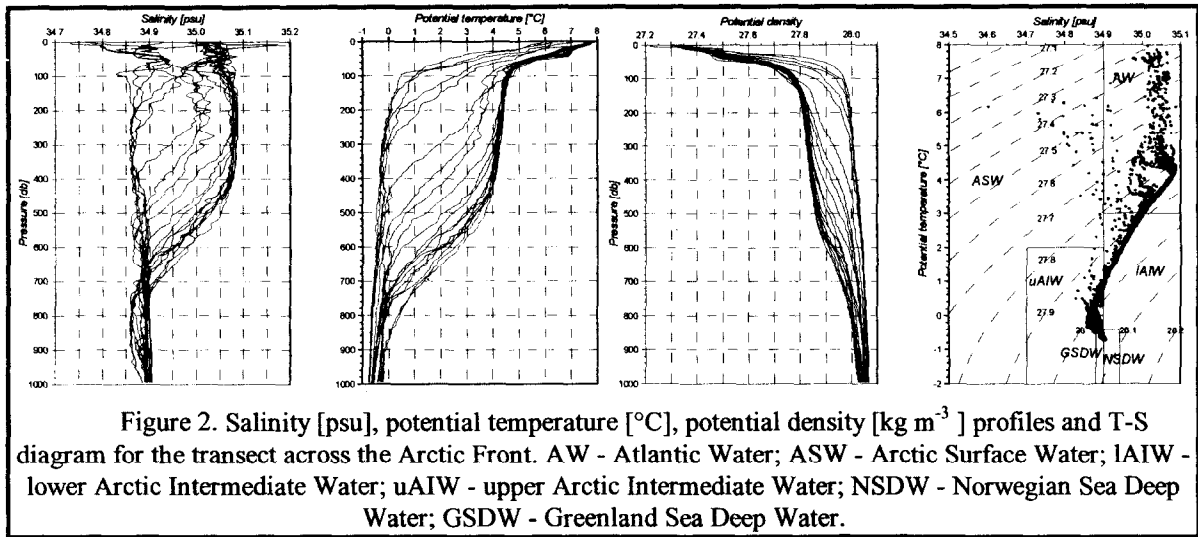
resolution CTD transects were made using towed probe. Vertical transects and synoptic maps of salinity, temperature, density, dynamic topography, geostrophic velocity and potential vorticity were calculated. The structure of hydrological fields and geostrophic flows related to the front have been well discerned. The baroclinic component of transport by the western branch of the Norwegian-Atlantic Current was estimated as 3.9-5.0 Sv at 72°N (for reference level of no motion 1000 dbar). Areas of intensive activity of meanders and mesoscale eddies have been found. The observed eddy circulation is both, cyclonic and anticyclonic. Diameters of the eddies are two to three times the Rossby radius of deformation.



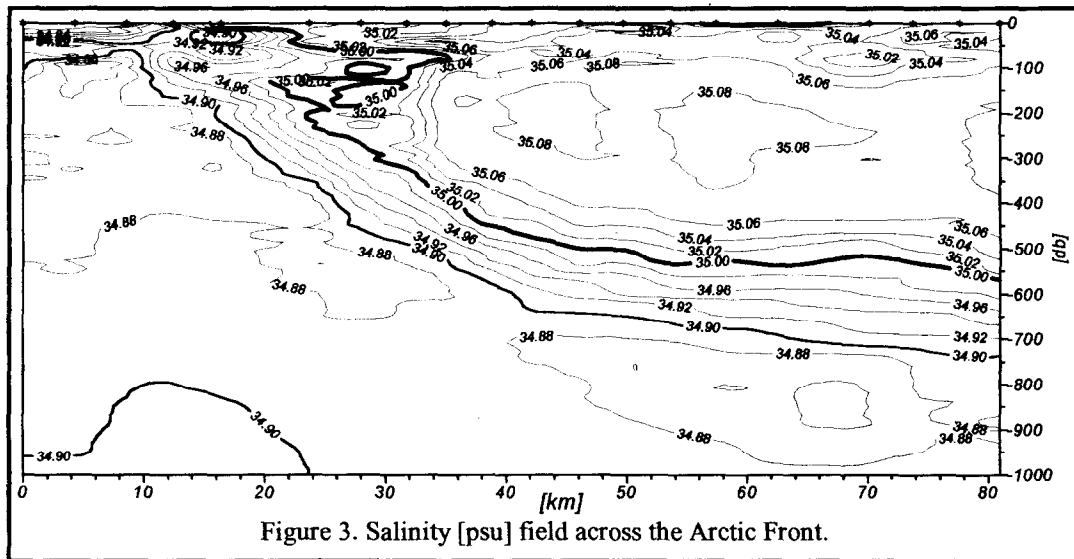
3. STRUCTURE OF THE ARCTIC FRONT

The Arctic Front is formed by the confluence of Arctic and Atlantic water masses. It is a 800 km long, 40 km wide zone of higher horizontal and vertical gradients of all properties. Arctic Waters are cold, less saline and more dense. At 300 m temperature varies from 0°C to 4°C, salinity from 34.85 to 35.08 psu and potential density from 27.82 to 28.01 kg·m⁻³ between Arctic and Atlantic sides of the front (Figure 2). Changes in salinity and temperature across the front partly compensate each other and the resulting horizontal density gradient is due to temperature differences between Arctic and Atlantic Water. Significant horizontal gradients of all properties occur under surface mixed layer, at 100 - 700 m. Maximal horizontal gradients are at 300 m, but even here they are rather weak in comparison with other climatic fronts [5]: the temperature gradient is 0.30-0.40°C·km⁻¹, salinity gradient 0.02-0.03 psu·km⁻¹, and density gradient 0.015 kg·m⁻³·km⁻¹. The weak density gradient may be a reason of frontal instability and meandering [9].

Vertical stability of the water column in the Arctic domain is lower than in Atlantic one. The Atlantic Water column stability is caused by the temperature vertical gradient, inversion of salinity occur. These properties of the Arctic Front - weak horizontal density gradient and temperature dependent stability of the Atlantic Water are very important for processes of deep convection.



Distinct water masses are clearly seen in the vertical distributions of temperature, salinity and density across the front as well as in the TS-diagram (Figure 2). Deep Water is the last stage of water transformation during deep convection processes. Atlantic Water, in spite of higher salinity, is less dense than Arctic waters because of high temperature. Portion of Atlantic Water, after crossing the Arctic Front, during winter cooling period reaches density higher than surrounding, homogenous waters. It leads to mixing and initiation of deep convection. [2,4,7,18]. This process takes place in the Greenland Sea, where heat fluxes from the sea to atmosphere are about 500 Wm^{-2} [7,12]. During extreme conditions, the total heat flux can be more than 1000 Wm^{-2} [11].



Salinity field at the transect across the Arctic Front is presented in Figure 3. This transect is situated at the southern polygon, at the latitude 72°N . The wedge of saline Atlantic Water is distinctly visible. Maximal thickness of AW layer is 750 m. Salinity of AW is more than 35 psu, but in the case of GIN Sea it can be lower, to 34.90 psu [17]. The Arctic Front is the slope zone of high horizontal gradients of all properties. In nature the angle of this slope is about 1° . Under the front the intermediate and deep waters are present. At 100 m depth one can see isopycnal intrusion associated with the advection of less saline Arctic Water towards Atlantic domain. Downwelling of the waters under the front caused by the densification on mixing (cabelling) is also visible.

4. MESOSCALE FEATURES

Instability of the front causes meandering with the specific wave length. Unstable meanders can produce eddies - warm, salt meanders produce anticyclonic eddies which migrate to Arctic domain carrying salt and heat [4,18]. During 4 years of the Arctic Front study meanders and eddies were investigated. In places of specific bottom topography (underwater mountains) meanders occurred every year, during our 4-year study. Some of the investigated eddies has been observed before and described in literature [9].

Figure 4 shows salinity fields at the northern polygon in 1996. A couple of fresh-salt (cold-warm) meanders are present at the latitude 73°40' - 74°00'N. Another pair is situated 40 nautical miles (74 km) northward. Northern, salty, anticyclonic meander (with centre at 74°20'N, 008°00'E) is unstable, nearly separated, 'young' eddy. The maximal diameter of the eddy is about 50 km, depth 450 m.

The fresh, cold meander at the right side of the 'young' eddy is very important. It helps in creating the warm eddy by separating it from the front. This meander moves upstream, against the main flow. It probably will never cross the front to become independent cyclonic eddy.

Meandering of the front, growth and expansion of the cyclonic meanders is possible due to Available Potential Energy (APE), that is released and

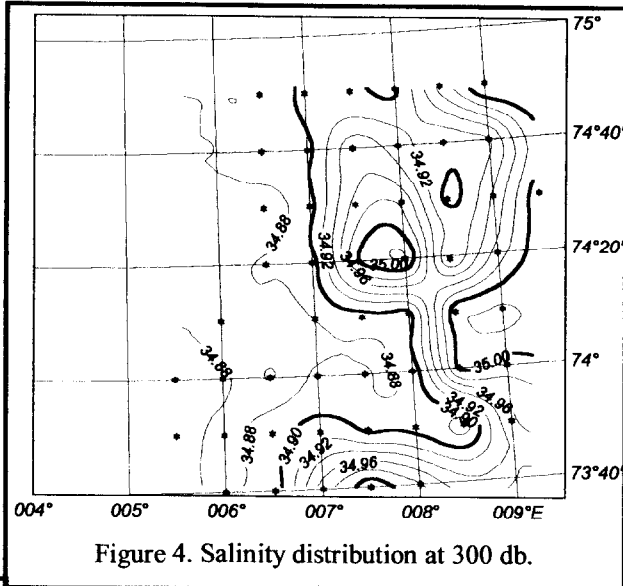


Figure 4. Salinity distribution at 300 db.

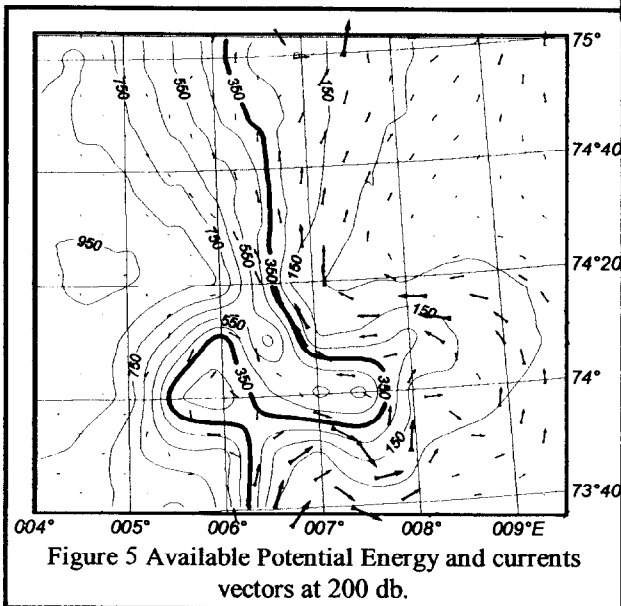


Figure 5 Available Potential Energy and currents vectors at 200 db.

transformed into kinetic energy. Value of the APE in the Arctic domain is bigger than in the Atlantic one, because the same density water parcels are elevated higher in the Arctic domain. Available Potential Energy at the Arctic side reaches up to 900 Jm^{-3} .

Figure 5 shows horizontal distributions of the APE in the northern polygon in 1995, at the level of 200 dbar. Geostrophic currents vectors are added. Correlation of APE with front structure is evident. Expansion of zones with high APE (more than 350 Jm^{-3} , bold line) is visible. Cyclonic meander moves against the main flow and isolates a warm eddy with centre at 74°N, 006°E. Our calculations indicate that up to 16 % of APE can be converted to kinetic energy. It means that the main source of the Arctic Front meandering is baroclinic instability.

Large changes in the thickness of the layer between different isopycnal surfaces and the different sign of the thickness gradients in the layers confirm

that baroclinic instability may occur [3,14].

The second cause of the front meandering is bottom topography effect and potential vorticity conservation [14]. Over underwater mountain structure of the flow is modified, isopycnal surfaces are deformed and compressed. To compensate an increasing stratification, water take on an anticyclonic circulation. This effect occur in 73°40' N, 07°10'E, over the Schultz Bank.

Other mesoscale features observed at the front were intrusions (Figure 3). Advection of less saline, cold waters towards the Norwegian Sea is more evident, intrusions penetrate Atlantic Waters 30 km from the frontal interface. Due to salt fingers in its top layer, fresh intrusions lower and sink. Also we observed an interesting and rather rare phenomenon, breaking-off lenses of water from intrusions - calving of intrusion [5].

5. TRANSFRONTAL TRANSPORT

Calculations of eddy salt and heat transport were done by modelling of the salinity and temperature anomalies on isobaric surfaces, using a Gaussian distribution centred on the vertical axis of the eddy. Gaussian curves describe salinity and temperature anomaly across the eddy (Figure 6.).

Properties of 3 eddies are presented in Table 1. Maximal diameter of eddy is about 50 km, depth from 450 to 650 m. Volumes of eddies calculated in reference to the isohaline surface 34.89 psu (V1, column 3) vary from 560 to 980 km³. After calculations it gives possible production of GSDW (V2, column 4). Interesting result is the statement, that the volume of GSDW is about 3.5 times more then the volume of warm eddy crossing Arctic Front and providing salt needed for production GSDW.

The wavelength of the meanders was estimated at 70 km. Estimation of the eddy production rate was the most difficult. Using 2-layers models [3,13] we found that 5-7 days are needed for production of one eddy. In this scenario a hypothetical eddy heat transport across the Arctic Front causes rapid heating of the Greenland Sea. Finally, the production rate of eddies was estimated based on literature [4,6] and field observations. In this case the mean time needed to create an eddy was approximately 40 days.

Calculated cross frontal transport from Norwegian to Greenland Sea, due to the eddies is presented in Table 2. Transfrontal volume eddy transport across all 800 km long Arctic Front is 2.1 Sv, transport of Atlantic Water with salinity more than 35.0 psu is 0.17 Sv. This transport can provide salt needed for the production rate 6.8 Sv of Intermediate and Deep Water. At this point it is only a hypothetical possibility because Greenland Sea salt budget is not so simple.

Heat and mass fluxes due to intrusions are smaller, but significant too. Water volume transport from the Greenland to Norwegian Sea is about 1 Sv. Heat transport is about 5 times lower than eddy transport. Crossfrontal transport due to intrusions has rather local significance but plays a role in frontolysis processes.

5. CONCLUSIONS

- The Arctic Front is an important phenomenon for the global climate system.
- Transfrontal transport across the Arctic Front occurs primarily as a consequence of mesoscale anticyclonic eddy activity.

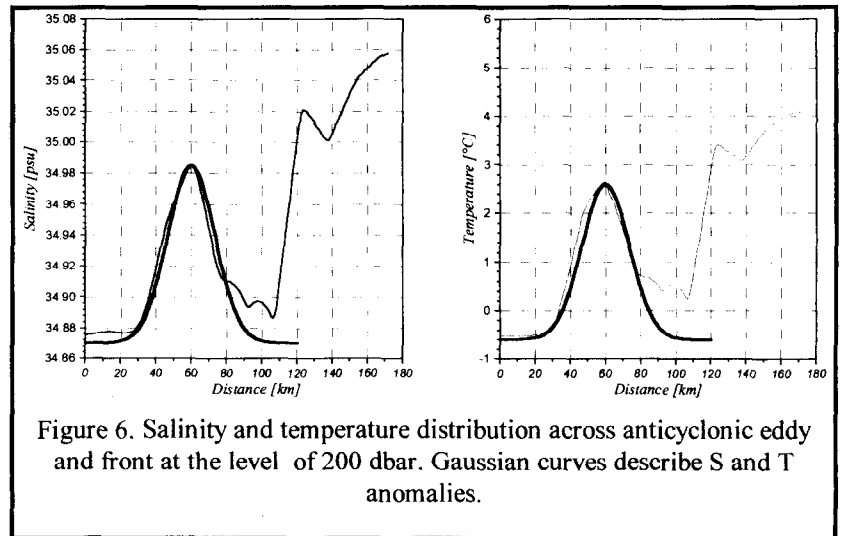


Figure 6. Salinity and temperature distribution across anticyclonic eddy and front at the level of 200 dbar. Gaussian curves describe S and T anomalies.

Eddy diameter [km]	Eddy depth [m]	V1 volume S>34.89 [km ³]	V2 GSDW S=34.89 [km ³]	V2/V1	Salt transport per eddy volume unit [10 ³ T km ⁻³]
50	450	560.86	1892.6	3.37	40.37
55	650	977.8	3960.1	3.74	45.70
50	450	717.9	2225.0	3.10	44.56

Transport type	Unit	Symbol	Value
Volume transport	[Sv]	Q _V	2.11
Salt transport	[kg · s ⁻¹]	Q _{Sal}	1.88 · 10 ⁵
Heat transport	[W]	Q _Q	1.77 · 10 ¹³
Atlantic Water transport (S>=35.0 psu)	[Sv]	Q _{V/S>=35}	0.17
Salt transport in water S>34.89	[kg · s ⁻¹]	Q _{Sal/S>34.8}	9.0 · 10 ⁴

- The baroclinic instability is the first reason of the Arctic Front destabilisation, meanders and eddies creation. The second one is topographic effect.
- After crossing of the Arctic Front, the anticyclonic eddies can stay in the Greenland Sea till winter and after intensive cooling and mixing processes they sink and form intermediate and deep water.
- Each eddy can provide salt necessary for the production of the volume of the Greenland Sea Deep Water which is 3.5 times higher than the eddy volume calculated in reference to the isohaline surface 34.89 psu.
- Hypothetical production rate of Intermediate and Deep Water is 6.8 Sv.
- Crossfrontal heat flux ($\sim 2.8 \cdot 10^4 \text{ W} \cdot \text{m}^{-2}$) and transport ($\sim 1.8 \cdot 10^{13} \text{ W}$) is in good agreement with the Greenland Sea heat budget.
- Intrusions are also an important phenomenon. Less saline, cold intrusions could play a significant role in the front destabilisation. Due to salt fingers activity, the intrusions change density and sink, releasing Available Potential Energy.

REFERENCES

1. Aagaard K., Carmack E. C., 1994, The Arctic Ocean and Climate: A Perspective, In: *The Polar Oceans and Their Role in Shaping the Global Environment*, American Geophysical Union, 5-20
2. Alekseev G.V., Ivanov V.V., Korablev A.A. (1995) Deep Convection in the Greenland Sea: Oceanographic Preconditions, Mechanisms and Interannual Variability, *Symposium „Nordic Seas”. Extended Abstracts*, 13-16.
3. Allen J.T., Smeed D.A., Chadwick A.L., 1994, Eddies and mixing at the Iceland-Faeroes Front, *Deep-Sea Research*, Vol. 41, No.1, 51-97.
4. van Aken H.M., Budéus G., Hähnel., 1995, Eddy Transport across the Arctic Frontal Zone in the Greenland Sea, *Symposium „Nordic Seas”, Extended Abstracts*, 9-12.
5. Fedorov K.N., 1983, The Physical Nature and Structure of Oceanic Fronts, Springer-Verlag, Berlin
6. Hart J.E., Kilworth P.D., 1975 On open ocean baroclinic instability in the Arctic, *Deep-Sea Research*, Vol. 23, pp 637-645.
7. Häkkinen S., Mellor G.L., Kantha L.H., 1992 Modelling Deep Convection in the Greenland Sea, *Journal of Geophysical Research*, Vol. 97, No. C4, 5389-5408.
8. Hopkins T.S., 1991, The GIN Sea - A synthesis of its physical oceanography and literature review 1972-1985. *Earth-Science Reviews*, No. 30.
9. Iwanow V., Koroblew A. (1994) *Struktura i dynamika gidrologiczeskich frontow*, [w:] *Zakonomiernosti krupnomassztabnych processow w Norweżskoj Energoaktywnej Zonie i prilegajuszczich rajonach*. Sankt-Petersburg Gidrometeoizdat 1994.
10. Johannessen O.M., 1986, Brief overview of the physical oceanography, in: *The Nordic Seas*, edited by B.Hurdle, Springer-Verlag, New York, 103-127.
11. Johannessen O.M., Sandven S., Johannessen J.A., 1991, Eddy-related winter convection in the Boreas Basin, in *Deep convection and deep water formation in oceans*, ed. P.C. Chu, J.C. Gascard, Elsevier Oceanography Series, 57, 87-105.
12. Nikołajew J.W., Aleksiejew G.W. (1989) *Struktura i izmieniowosc krupnomassztabnych okieanologiczeskich processow i polej w Norweżskoj Energeticzeskiej Zonie*, Gidrometeoizdat, Leningrad.
13. Oey L-Y., 1987, A Model of Gulf Stream Frontal Instabilities, Meanders and Eddies along the Continental Slope, *Journal of Physical Oceanography*, Vol. 18, 211-229.
14. Pedlosky J. 1987 *Geophysical Fluid Dynamics*, Springer-Verlag.
15. Piechura J., Walczowski W., 1995, The Arctic Front: structure and dynamics, *Oceanologia*, 37, 47-73.
16. Smith W. O. Jr., 1993, Physical Science, In: *Polar Oceanography*, Academic Press In .
17. Swift J.H., 1986, The Arctic Waters. In: *The Nordic Seas*, editor B.G.Hurdle, Springer-Verlag, New York, 129-153.
18. Walczowski W., 1995, The Arctic Front - results of the latest investigations, *Symposium „Nordic Seas”. Extended Abstracts*, 215-218 .

PARTICULATE MANGANESE AS A BASIC FACTOR OF OXIDATION OF HYDROGEN SULFIDE IN REDOX ZONE OF THE BLACK SEA

E.V.Yakushev ¹, E.I.Debolskaya ²

1- P.P.Shirshov Institute of Oceanology of RAS, 36, Nakhimovskiy pr., Moscow, 117218, Russia, e-mail:

yakushev@fadr.msu.ru

2- Institute of Water Problems of RAS, 3, Gubkina St., Moscow, Russia, e-mail: elena@iwapr.msk.su

Abstract. The transition zone between oxic and anoxic waters in the Black Sea is characterised by the absence of direct contact of significant concentrations of oxygen and hydrogen sulfide, that puts under doubt a reality of reactions of their direct interaction. The goal of this work is to estimate the role of particulate Mn in oxidation of the deep hydrogen sulfide in connection with influence of formation and dissolution of this oxidiser on the density of detrital particle and therefor on the vertical downward transfer of particulate Mn.

Introduction

Nowadays there are two points of view on the description of the phenomenon of absence of direct contact of significant concentrations of oxygen and hydrogen sulfide (H₂S) in the Black Sea. In the frames of the first one [1,2,3] this is a zone of oxygen deficiency that starts from the concentrations of O₂ < 20µM, which below top border of hydrogen sulfide is submitted by a layer of O₂ and H₂S coexistence with thickness about 10-15m [1, 3]. On the other point of view [4], this is a suboxic zone, in which both H₂S and oxygen are absent, as though the authors do not deny that in this layer the concentration of oxygen from 2 up to 10 µM [4] are measured. It is necessary to note, that a zone of oxygen – deficiency in accordance with the first classification and suboxic zone in accordance with the second one practically coincide in a field of depth and field of density.

The problem consists that the concentration and vertical gradient of oxygen, observed in this layer are too small to accomplish oxidation of H₂S, which gradient at the top border changes from 0.4 up to 1.0 µM/m and on the average is equal 0.71 µM/m [5]. At the same time the gradient of O₂ at the bottom border of a oxycline layer (4.5 µM/m) considerably exceeds the value necessary for oxidation not only H₂S, but also other reduced compounds (NH₄⁺, Mn²⁺, Fe²⁺, CH₄), supplying from hydrogen sulfide zone of the sea. By virtue of these circumstances the mechanisms of not direct interaction of oxygen and H₂S are discussed.

The investigation of chemical processes in the redox-layer permits to conclude, that ammonia, dissolved manganese and dissolved iron can be oxidized by dissolved oxygen only. At the same time hydrogen sulfide can be oxidized by dissolved oxygen, nitrates (during the thiodenitrification), particulate manganese (particulate Mn) and particulate iron. Though the existence of thiodenitrification in the Black sea is proved, the data of observations show that the nitrates disappear approximately about 15 m above the depletion level of deep H₂S and therefore nitrates, apparently, cannot play an essential role.

Both particulate Mn, and particulate iron can oxidise H₂S, and their maxima (30-1000 nM of Mn and 1-10 nM - of Fe) are located directly at the same depth, where deep H₂S depletes. However, in comparison with the H₂S concentrations, the content of the particulate Mn is very small, and it is impossible to explain, how the compound can stop a flux of deep H₂S, if their vertical transfers are based on the same hydrophysical mechanism of turbulent exchange.

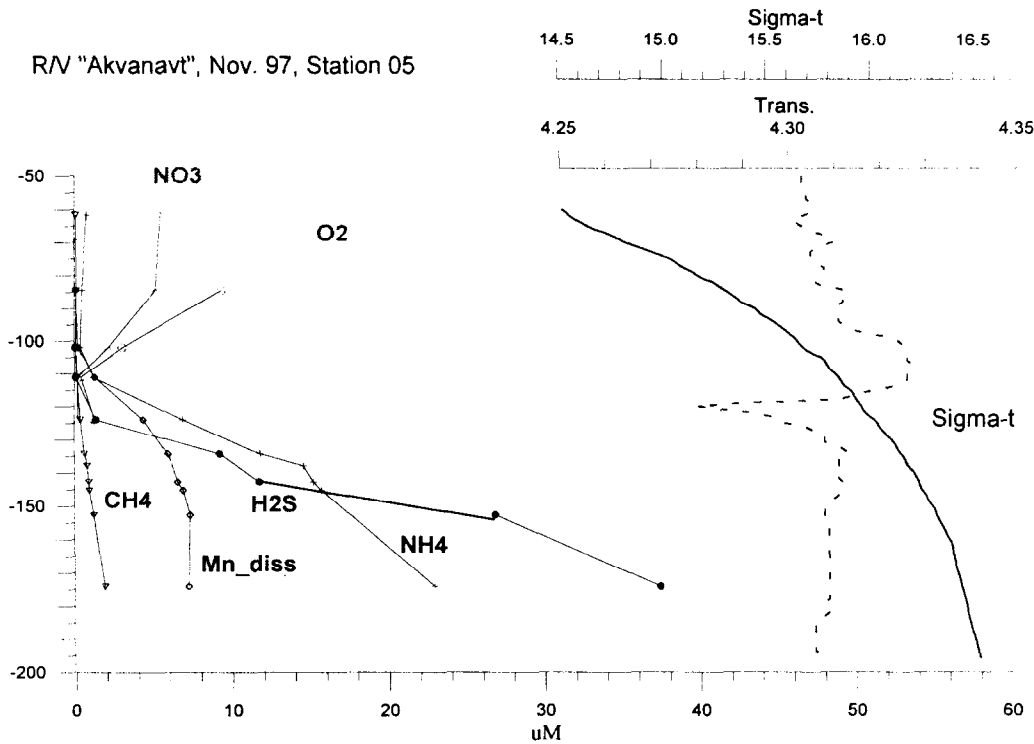


Fig. 1. Hydrochemical structure of redox layer (left) and transparency (right dotted line) as an example of Station 7 (r/v "Akvanavt", November, 1997). All concentrations are micromolar.

The absence of dominant oxidiser near the H₂S boundary distinguishes suboxic zone in water from suboxic zone allocated in the sea sediments, where an obvious dominant oxidiser is the iron. In the Black Sea the special feature of the a transition redox-zone from oxic conditions to anoxic ones is the deep fine particle layer, which can be named Nepheloid Redox Layer (NRL) [5]. The data of the observations show, that the top boundary of NRL practically coincides with transition of oxycline to a layer of oxygen deficiency, the bottom boundary settles down on 10-12 m below depletion horizon of deep hydrogen sulfide. However, the fields studies in 1994 demonstrated that the distributions of optical parameters (amplitude, thickness depth) are rather patchy (F.Nyffeler, personal communication, 1998). The capacity and degree of expressiveness of NRL varies depending on season, area of an arrangement of station relatively RIM current, eddies activity etc.

On modern representations a dominant part of NRL is the particulate organic matter. Among the inorganic elements of NRL the particulate manganese as MnO(OH)₂ is the most important [6,5]. The data of the observation show, that the share of the particulate Mn in NRL can achieve 11 % [7] or 40 % [6] of dry weight. The thin film of the Mn covering detrital particles of a various origin can be allocated.

Up to now the data on vertical distribution of the particulate Mn are not numerous. According to the observations, the thickness of layer of particulate Mn is about 30-80 m with the brightly expressed maximum, which is located on the top border of NRL. The concentrations of the particulate Mn are 0.04-1.0 uM [6]. The extremely high content of - 2 -6 uM was marked in is abnormal NRL in area of a canyon Sakarya in July, 1997 [8].

The mechanism of formation of the particulate Mn is the following (Fig. 2). In an oxic zone a process of oxidation of the dissolved reduced Mn^{2+} occurs, therefore particulate Mn (as $MnO(OH)_2$) will be formed and being sorbed on the detrital particles. After the Mn-covered particles are lowered to the H_2S layer, the reaction of particulate Mn with H_2S occurs, and the particles density decreases quickly and it can become the reason of their weighing or even emerging to the higher levels.

Therefore it is possible to assume existence of the additional mechanism of mixing connected with the processes of oxidation and reduction of Mn. The intensity of this mixing should be connected with the size of particles, their amount and features of the Mn cycle. The experimental data [9, 6] show, that specific speeds of oxidation and restoration of Mn are high and have the order $0.01-1.0 \text{ day}^{-1}$.

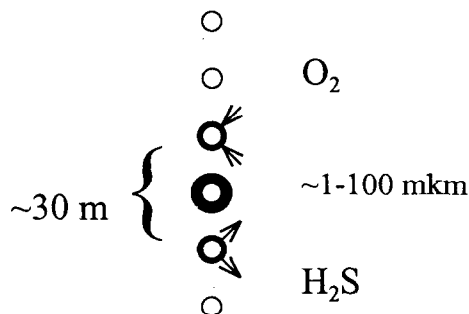


Fig. 2. The scheme formation and dissolution of the particulate Mn.

Model

The following formula is being used to describe the balance of matter in particulate or dissolved form:

$$\frac{\partial C}{\partial t} = \frac{\partial}{\partial z} \left(A_z \frac{\partial C}{\partial z} \right) - w \frac{\partial C}{\partial z}, \quad (1)$$

In all existing models [6, 10, 11] the rates of sedimentation w are accepted to be constant with depth. This assumption means that density of particles varies the same way as in oxic pools of oceans, i.e. exceeds density of water or in regular intervals smoothly grows following the sedimentation. However, in case of formation of the particulate Mn and its sorption on a surface of particles there should be a sharp increase of particles density, as the density of the $MnO(OH)_2$ in 5 times exceeds density of water. This effect was investigated neither experimentally, nor theoretically.

The sorption of Mn on a particle on the top border of this parameter maximum layer causes the increase of its weight and rate of sedimentation. The thickness of a film should depend on amount and size of the weighed particles, and also from density of manganese and organic substance. The observed concentrations of the particulate Mn have sharp maximum near the top border of NRL and should correspond to the film thickness. The sedimentation of particles can be described by the equation of a movement of particles in a liquid with various assumptions reflecting its basic features. From this equation describing the balance of hydrodynamical resistance and external potential forces it is possible to receive required expression for dependence of sedimentation speed of organic particles from depths containing as parameters their size and density, changing in depend of processes of oxidation and restoration of manganese:

$$w = \left(\frac{2A_1}{A_2 \bar{C} \rho_w} dg \right)^{\frac{1}{2}} |\rho - \rho_w|^{\frac{1}{2}} \text{sign}(\rho - \rho_w), \quad (2)$$

where ρ and d are density and linear size of an organic particle surrounded with a film of manganese consequently, A_1 is first factor of the form. A_1 is equal to the relation of particle volume to a diameter of equivalent sphere in the third degree. A_2 is second factor of the form. A_2 is equal to the relation of the area of

greatest section, normal direction of a movement, to a square of a diameter of equivalent circle. For a sphere $A_1/A_2 = 2/3$. \check{C} is factor of resistance dependent on the form of a particle and conditions of movement. In a rather large range of Reynolds numbers its value is close to $\check{C} = 0.44$, ρ is density of water, g is acceleration of gravity.

The natural observations and the numerical experiments allow to accept an assumption that in the layer under consideration the vertical distribution of organic matter concentration is uniform in absence of the particulate Mn. That is a consequence of neutral float ability of particles having the prevailing sizes and insignificant turbulent mixing. From this assumption it is easy to receive dependence of an organic particle size on change of its density varied on depth:

$$d = d_0 \left(\frac{\rho_{org}}{\rho_{org}^0} \right)^{-\frac{1}{3}}, \quad (3)$$

where d_0 is linear size of an organic particle on the top border of a layer.

Relative increase of particle size at the expense of Mn film formation $d = \Delta d/d$ and expression for density of such particle can be received from enough simply connections between concentration, density and sizes of a particle and geometrical ratios:

$$\delta = \frac{\Delta d}{d} = \frac{C_{Mn} \rho_{org}}{3C_{org}^0 \rho_{Mn}} = \frac{C_{Mn} \rho_{org}}{4\pi \rho_{org}^0 n d_0^3 \rho_{Mn}}, \quad (4)$$

where ρ_{org} is density of organic substance, ρ_{org}^0 is density of organic substance on the top border of a layer.

The non-stationary equation of turbulent diffusion of an impurity with use of the received expression for sedimentation speed (2) was solved numerically. The turbulent exchange coefficient A_z was determined from the dependence [6]:

$$A_z = a_0 \left(\frac{g}{\rho_w} \frac{\partial \rho_w}{\partial z} \right)^{-1/2} \left(a_0 = 0.0004 \text{ cm}^2 \text{ c}^{-2} \right).$$

Discussion

The numerical experiments with different concentrations of particulate Mn, sizes of particles, and their amount in unit of volume of a liquid were provided. The curves of vertical distribution of the particulate Mn were set as generalised functions reflecting the basic features of an observable picture [6, 7] with maxima in 200 nM (Fig. 3A) and 100 nM (Fig. 3B, 3C). The amount of particles on the submitted results is 100000/ml and 10000/ml, that corresponds with estimations [12] about the number of bacteria. The thickness of manganese film obtained from model calculations changed from decimals to several tens of angstroms.

The results of calculations are submitted in Fig. 3., which demonstrates the distribution of the particulate Mn with the maxima 200 nM and 100 nM, curves of changes of sedimentation rate w and relative concentration of organic substance particles (C/C_0 , C_0 is organic substance concentration on the top border of a layer) with the initial sizes 0.5 μm , 1 μm , 5 μm . Amount of particles in unit of liquid volume for Fig. 3A and Fig. 3B is $n = 10000/\text{ml}$, for Fig. 2C - 100000/ml.

On the data of numerical experiments, sorption and desorption of the particulate Mn results in anomalies of sedimentation rate w , which grows with the increase of particulate Mn concentrations, reduction of amount of particles and increase of their size from 5 m/day (at 100 nM, $n = 100000$, 1 μm) up to 400 m/day (at 200 nM, $n = 10000$, 5 μm).

The anomalies of vertical particles amount distribution (curves in the right part Fig.3) appeared most significant for fine particles (0.5 μm) and were more precise at higher concentrations of the particulate Mn.

Consequently sorption and desorption of the particulate Mn is one of the factors of vertical transfer of sediment particles and formation of a fine particle layer, that it is necessary to take into account in balance and mathematical models for the analysis of chemical structure of the Black Sea.

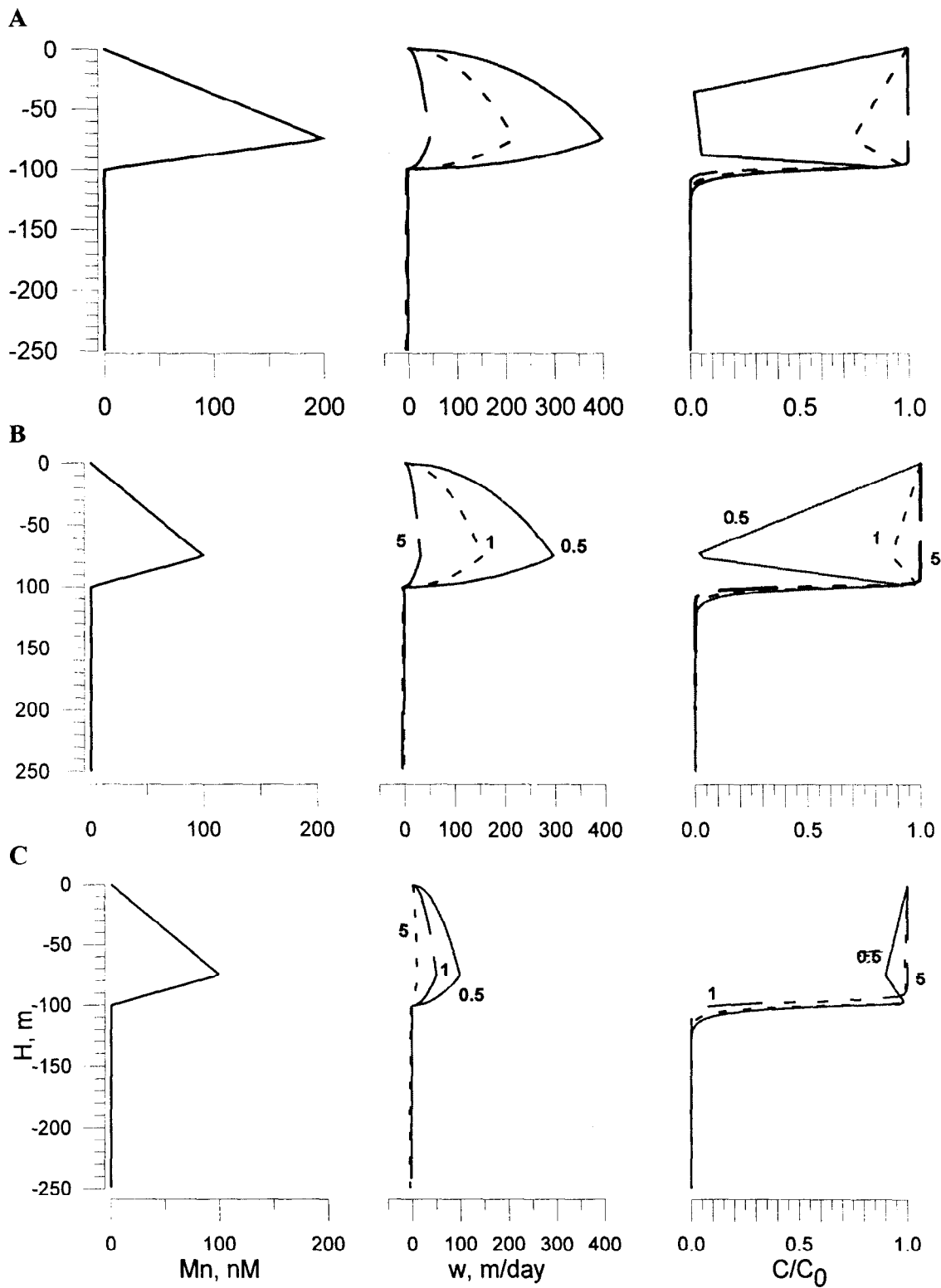


Fig. 3. Results of numerical experiments on the influence of particulate Mn on the rate of sedimentation (w) and vertical distribution of particles (C/C_0). A – at quantity of particles 100000/ml, B - at quantity of particles 10000/ml, C - at quantity of particles 10000/ml. The figures near to curves designate the size of particles (μm).

Conclusion

- a key role in the features of hydrochemical structure of redox zone belongs to a Mn cycle connected, first of all, with phase transitions and formation of heavy detrital particles, that accelerates the transport of this oxidiser to the deeper layers;
- particulate Mn can be the basic oxidiser of deep hydrogen sulfide on horizon of its disappearance. The intensive consumption of this oxidiser is compensated by its intensive flux of this oxidiser in particulate form;
- between a layer of oxygen-deficiency and actually hydrogen sulfide zone a layer, with a particulate Mn as a dominant oxidiser can be allocated.

Acknowledgement

This work was conducted with the financial support of the Russian Foundation for Basic Research, grants 96-05-66169, 97-05-65151 and 96-15-98440.

References

1. M.E Vinogradov and Yu.R. Nalbandov, 1990 Influence of changes of density of water on distribution of the physical, chemical and biological characteristics экосистемы пелагиали of the Black sea, *Oceanology*, 30, 5, 769-777.
2. Yu.F. Lukashev et al, 1990, On the layer of coexistence of oxygen and hydrogen sulfide in a deep-water part of the Black sea, *Doklady Akademii Nauk SSSR*, 314, 2, 23-29.
3. A.A.Bezborodov and V.N.Eremeev, 1993, Black sea. A zone of interaction of aerobic and anaerobic waters, MHI NASU, Sevastopol, 299 .
4. J.W.Murray, L.A. Codispoti and G.E. Friederich, 1995, The suboxic zone in the Black Sea, in *Aquatic chemistry: interfacial and interspecies processes*, edited by C.P.Huang, R.O'Melia and J.J.Morgan, American Chemical Society, 157-176.
5. I.I.Volkov, E.A.Kontar, Yu.F.Lukashev, L.N.Neretin, F.Nyffeler and A.G.Rozanov, 1997, The top border of hydrogen sulfide and the nature of Nepheloid Redox Layer in waters of a Caucasian slope of the Black sea, *Geochemistry International*, 6, 618-629.
6. B.L.Lewis and W.M.Landing, 1991, The biogeochemistry of manganese and iron in the Black Sea, *Deep Sea Res*, 38 (2A), S773-S803.
7. A.G.Rozanov, 1995, Redox stratification of waters of the Black Sea, *Oceanology*, 35, 4, 544-549.
8. O.Basturk, I.I.Volkov, S.Gokmen, H.Gungor, A.S.Romanov and E.V. Yakushev E.V, 1998, International expedition on r/v "Bilim" in July 1997 in the Black Sea, *Oceanology*, 38,3, 1-4
9. B.M. Tebo, 1991, Mn (II) oxidation in the suboxic zone of the Black Sea, *Deep Sea Res.*, 38, S883-S906.
10. V.I.Belyaev, E.E.Sovga and S.P.Lyubartseva, 1997, Modeling the hydrogen sulfide zone of the Black Sea, *Ecological Modelling*, 96, 51-59.
11. E.V.Yakushev, 1998, *Mathematical Modelling of Oxygen, Nitrogen, Sulfur and Manganese Cycling in the Black Sea* In: 'NATO TU-Black Sea Project Ecosystem Modeling as a management tool for the Black Sea. Symposium on scientific results', L.Ivanov & T.Oguz (eds.) Kluwer Academic Publishers, V.1, 373-384
12. Yu.I.Sorokin, 1982, *The Black Sea*. Moscow., Nauka, 1982, 216.

MODELING OF FINE HYDROCHEMICAL STRUCTURE OF THE ZONE OF CONTACT OF OXIC AND ANOXIC WATERS IN THE BLACK SEA

E.V. Yakushev

P.P. Shirshov Institute of Oceanology of RAS, 36, Nakhimovskiy pr., Moscow, 117218, Russia, e-mail:
yakushev@fadr.msu.ru

Abstract. An O-N-S-Mn model is considered to describe the biogeochemical sources. Rates of biochemical processes mediated by bacteria are described by first-order equations using semiempirical functions of O_2 concentration. The processes of turbulent diffusion, sedimentation, and biogeochemical transformation of compounds were parameterized in the frames of one-dimensional model. The model was calibrated using data observed for the vertical distribution of compounds in the Black Sea. The calculated spatial distributions of nitrogen compounds (organic nitrogen, ammonium, nitrate, nitrite), inorganic reduced sulfur compounds (hydrogen sulfide, elemental sulfur, thiosulfate, sulfate), dissolved and particulate Mn, as well as dissolved oxygen agree reasonably well with the observations. The model demonstrated that particulate Mn can be a main oxidiser of H_2S because of intensive vertical transport of detrital particles covered with particulate Mn.

Introduction

Hydrochemical structure of the zone of contact between oxic and anoxic waters of the Black Sea is characterised by absence of direct contact between significant concentrations of dissolved oxygen (O_2) and hydrogen sulfide (H_2S) (see Fig.1 in [1]). In this layer reduced and oxidised forms of several elements (N, S, C, Mn, Fe) can be observed [2,3,4,5,6,7,8], that reflects the complexity of processes occurring in this zone.

In contrast with modelling devoted to other oceanographic problems, modelling of the oxic/anoxic contact zone can provide more than just quantitative results but also insights into the qualitative nature of the zone, about which relatively little is currently known. In anoxic conditions, every element cycle plays its own geochemical role because the oxidation of organic matter occurs in different stoichiometric reactions. Modelling of oxic/anoxic transformation therefore requires the simultaneous parameterization of cycles of several elements.

The goal of this version of model is to study an effect of increasing of density of particles connected with particulate Mn formation on the vertical flux of this oxidiser and therefore on the peculiarities of the fine hydrochemical structure of the zone of contact of oxic and anoxic waters in the Black Sea.

Chemical-biological sources parameterization

The model (Fig. 1) computes the content of hydrogen sulfide (H_2S), total elemental sulfur ($S^0+S_n^{2-}$), thiosulfate (and sulfites) ($S_2O_3^{2-}+SO_3^{2-}$), sulfate (SO_4^{2-}), total organic nitrogen (N_{org}), ammonium (NH_4^+), nitrite (NO_2^-), nitrate (NO_3^-), dissolved manganese (Mn^{2+}), particulate manganese (Mn^{4+}) and dissolved oxygen (O_2).

The transformation of sulfur occurs as a result of hydrogen sulfide oxidation and sulfate reduction. Nitrogen transformation occurs as a result of ammonification, nitrification, nitrate reduction (denitrification), thiodenitrification and ammonium assimilation. In addition, the processes of manganese oxidation and reduction are also considered.

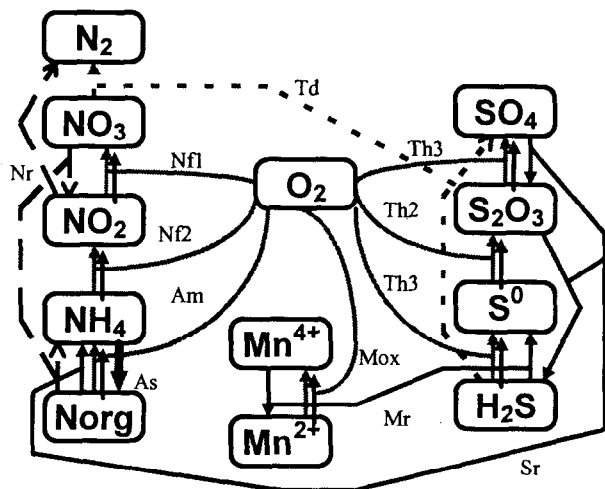
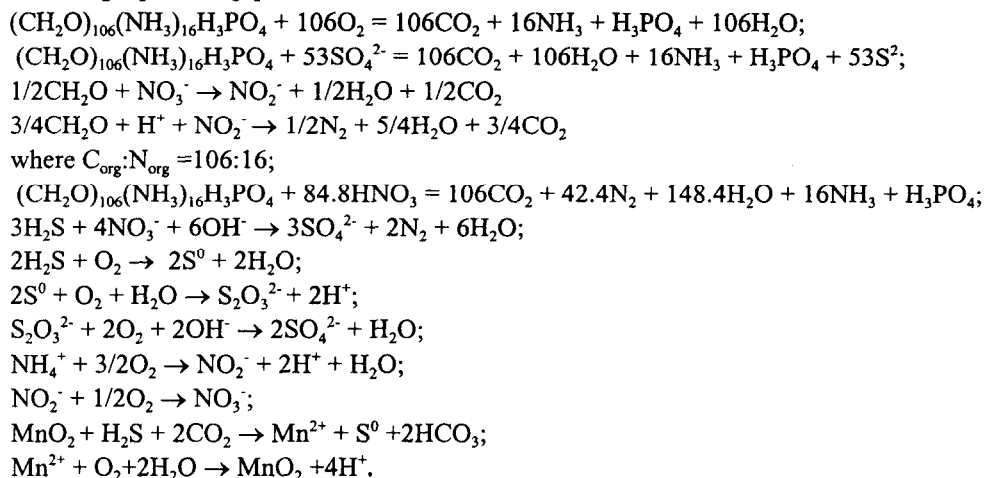


Fig 1. Diagrammatic representation of the coupled model of sulfur, nitrogen, manganese and oxygen cycling showing the compartments and the modeled rates of transformation processes.

To describe the transformation of matter between the model compartments carried out by microbiological or chemical means, first order equations were used. Stoichiometric coefficients m_i were calculated according to the following equations [9]:



The majority of these reactions like other redox-zone processes are mediated by bacteria [2,6,10].

Instead of considering special compartments for describing bacteria biomass dynamics, we describe the ammonia to organic nitrogen assimilation in relation to the intensity of the microbiological processes (chemosynthesis in nitrogen units).

$As = p_1 Th1 + p_1 Th2 + p_1 Th3 + p_2 Nf1 + p_2 Nf2 + p_3 Td + p_4 Nr1 + p_4 Nr2$ - where p_i - the quantity of consumed nitrogen of NH_4^+ in units of consumed substrate (S^{2-} , S^0 , $\text{S}_2\text{O}_3^{2-}$, NH_4^+ , NO_2^-). This assumption can be made because the main objective of this study is to describe the chemical structure of the redox layer, and not detailed modelling of its bacterial ecosystem.

Therefore the chemical sources of the model are the following:

$$\begin{aligned}
 R_{N_{\text{org}}} &= -Am - m_2 Nr1 - m_3 Nr2 - m_5 Sr1 + As \\
 R_{NH_4^+} &= Am + m_4 Nr1 + m_5 Sr1 - Nf1 - As \\
 R_{NO_2^-} &= Nf1 - Nf2 + Nr1 - Nr2 \\
 R_{NO_3^-} &= Nf2 - Nr1 - m_6 Td
 \end{aligned}$$

$$\begin{aligned}
R_{H2S} &= -Th1 + Sr2 - Td - m_{13}Mr \\
R_{S0} &= Th1 - Th2 \\
R_{S2O32-} &= Th2 - Th3 + Sr1 - Sr2 \\
R_{SO42-} &= Th3 - Sr1 + Td \\
R_{O2} &= -m_7 Th1 - m_8 Th2 - m_9 Th3 - m_{10} Nf1 - m_{11} Nf2 - m_{12} Am - m_{14} Mox, \\
R_{Mn2+} &= Mr - Mox; \\
R_{Mn4+} &= Mox - Mr;
\end{aligned}$$

where m_i ($i = 2-12$) - stoichiometric coefficients of the model.

The values of the coefficients used are the values presented in Table 1.

Table 1. Model coefficients [7]

Name	Symbol, units	Value, Source
Constant of ammonification	K_{Am} , day ⁻¹	0.01
Constant of ammonium oxidation	K_{Nf1} , day ⁻¹	0.1
Constant of nitrite oxidation	K_{Nf2} , day ⁻¹	0.3
Constant of nitrate reduction	K_{Nr1} , day ⁻¹	0.16
Constant of denitrification	K_{Nr2} , day ⁻¹	0.22
Constant of thiodenitrification	K_{Td} , day ⁻¹	0.006
Constant of hydrogen sulfide oxidation	K_{Th1} , day ⁻¹	0.45
Constant of elemental sulfur oxidation	K_{Th2} , day ⁻¹	0.7
Constant of thiosulfate oxidation	K_{Th3} , day ⁻¹	0.4
Constant of the first stage of sulfate reduction	K_{Sr1} , day ⁻¹	0.001
Constant of thiosulfate reduction	K_{Sr2} , day ⁻¹	0.004
Constant of manganese oxidation	K_{Mox} , day ⁻¹	0.10
Constant of manganese reduction	K_{Mr} , day ⁻¹	0.75
Ammonium assimilation coefficients for:		
thiobacteria	p_1 , $\mu\text{M(N)}/\mu\text{M(S)}$	1.0
nitrifiers	p_2	0.2
thiodenitrifiers	p_3	0.2
denitrifiers	p_4	0.2
Percentage of total organic nitrogen that is particulate	a , %	10
Specific rate of organic matter sedimentation	W , m day ⁻¹	2
Coefficient of the vertical turbulence diffusion	K_{z2} , cm ² s ⁻¹	0.4

For the dependence of processes considered on oxygen content, the following linear functions were proposed (Table 2).

1D Vertical distribution modeling

For 1D modelling we considered a column of water with a depth range from 50 m (lower boundary of the euphotic zone) to 150 m.

The following was used as the basic equation for dissolved components:

$$\frac{\partial C_i}{\partial t} = \frac{\partial}{\partial z} K_z \frac{\partial C_i}{\partial z} + R_{Ci}, \quad (1)$$

where R_{Ci} - sources and sinks of a substance (rates of transformation), C_i - concentration of nitrogen compounds (NH_4^+ , NO_2^- , NO_3^-), sulfur compounds (H_2S , S_0 , $\text{S}_2\text{O}_3^{2-}$, SO_4^{2-}), dissolved manganese (Mn^{2+}), and dissolved oxygen (O_2). K_z - vertical turbulent diffusion coefficient. We assume K_z to be a model constant with the value of $0.3 \text{ cm}^2/\text{s}$.

The total organic nitrogen and particulate manganese (Mn^{4+}) concentrations were calculated according to (1) supplemented by the introduction of a particulate matter sinking rate term:

$$\frac{\partial C_i}{\partial t} + W \frac{\partial(C_i)}{\partial z} = \frac{\partial}{\partial z} K_z \frac{\partial C_i}{\partial z} + R_{Ci} \quad (2)$$

where W = sinking rate of the particulate matter (Table 1). In contrast to the previous versions of this model [9,11] on the base of estimates obtained in [1] we accepted for particulate Mn: $W=W+W_{Mn}$, where $W_{Mn}=5 \text{ m/day}$ - accelerated rate of sedimentation of particles covered with particulate Mn

Table 2. Formulations, names of processes, dependence on oxygen content

Process, Formula	Dependence on oxygen	Process, Formula	Dependence on oxygen
ammonification: $Am = K_{Am} [N_{org}] F_{Am}(\text{O}_2)$		1 and 2 stages of sulphate reduction: $Sr1 = m_1 K_{Sr1} [N_{org}] F_{Sr}(\text{O}_2)$ $Sr2 = K_{Sr2} [S_2O_3^{2-}] F_{Sr}(\text{O}_2)$	
1 and 2 stages of nitrification: $Nf1 = K_{Nf1} [NH_4^+] F_{Nf}(\text{O}_2)$ $Nf2 = K_{Nf2} [NO_2^-] F_{Nf}(\text{O}_2)$		thiodenitrification: $Td = K_{Td} [H_2S] F_{Td}(\text{O}_2) F_i(\text{NO}_3^-)$	
nitrate reduction: $Nr1 = K_{Nr1} [NO_3^-] F_{Nr}(\text{O}_2)$ denitrification: $Nr2 = K_{Nr2} [NO_2^-] F_{Nr}(\text{O}_2)$		manganese oxidation: $Mox = K_{Mox} [Mn^{2+}] F_{mox}(\text{O}_2)$	
1, 2 and 3 stages of H2S oxidation: $Th1 = K_{Th1} [H_2S] F_{Th}(\text{O}_2)$ $Th2 = K_{Th2} [S^0] F_{Th}(\text{O}_2)$ $Th3 = K_{Th3} [S_2O_3^{2-}] F_{Th}(\text{O}_2)$		manganese reduction: $Mr = K_{Mr} [Mn^{4+}] F_{mox}(\text{O}_2)$	

Where K_i are constants of the corresponding reactions, m_i are the stoichiometric coefficients and $F_i(\text{O}_2)$, $F_i(\text{NO}_3^-)$ are the dependencies of reaction rates on oxygen and nitrate content respectively.

Boundary conditions. It was assumed that at the upper boundary of the water columns being studied here, the chemical, biological and physical processes are balanced and maintain constant concentrations of most chemical elements throughout the year. Therefore, we specify constant values of all model components at the upper boundary.

The values of all the compounds in the model were set to zero, except for the following: $N_{org}=3.8 \mu\text{M/l}$, $\text{NO}_3^- = 1.0 \mu\text{M/l}$, $\text{O}_2=300 \mu\text{M/l}$, $\text{SO}_4=15 \text{ M/l}$.

The pronounced halocline (pycnocline) in the Black Sea restricts vertical motion and hence the contact of deep waters with the surface. Therefore, at the lower boundary in the Black Sea model, a flux boundary condition (radiation condition) was implemented for all compounds (except the Mn^{2+} and sulfate ion) as described in [11]

The implication of this radiation condition is that the value at the lower boundary is determined by parameter concentration changes within the integrated area. Therefore concentrations at the lower boundary in the Black Sea model are consequently formed only by the processes that occur within the zone of integration.

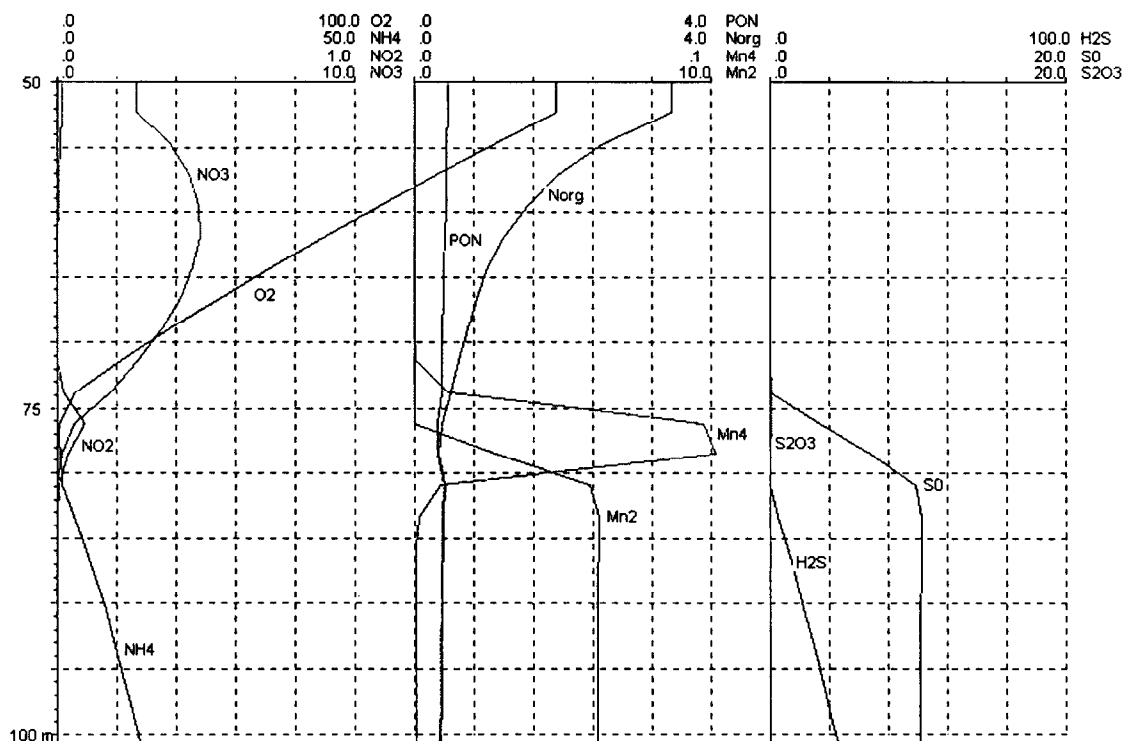


Fig.2. Vertical distribution of the model' comopounds in redox zone.

For sulfate at the lower boundary, a boundary condition of the first order was given, because model processes do not essentially change the content of this compartment. The constant value was accepted also for the Mn^{2+} ($Mn^{2+}=5.3 \mu M$)

For all sulfur compounds, with the exception of sulfates, zero concentrations were given as initial conditions; for nitrogen compounds and oxygen, constant values at all depths corresponding to the upper boundary values were given.

Therefore, the calculations were started with initial conditions characteristic of an "oxic" sea, without any anoxia even at the lower boundary.

The model was calculated for the layer 50-150 m with vertical resolution of 2 m. The model equations (1) were integrated using a first-order Eulelian method with time step of 0.1 day for at least 1 year after the stable solution was reached (Fig. 2).

Results

In Fig. 2 the calculated vertical distribution of the chemical compounds concentrations is presented.

It reflects the main features of the vertical structure of compounds in the aphotic layer. One can see the decrease of oxygen concentrations from about $300 \mu M$ at the upper boundary to zero at a depth about 100 m.

The vertical profiles of nitrogen compounds (N_{org} , NH_4^+ , NO_2^- , NO_3^-) calculated in the model reflect the main features of the distributions of these compounds observed in nature [4,12].

H_2S profile also reflects the observed situation of an increasing concentration of this parameter with depth [6]. Elemental sulphur values increase near the depth at which hydrogen sulphide appears. Then the distribution of this parameter is uniform. This is a consequence of the model assumption that S^0 forms as an intermediate compound in sulphide oxidation processes which take place near the upper boundary of the anoxic zone. In the layers below there are no sources or sinks for this parameter. Thiosulfates are intermediate products of both the sulfate reduction and sulphide oxidation processes.

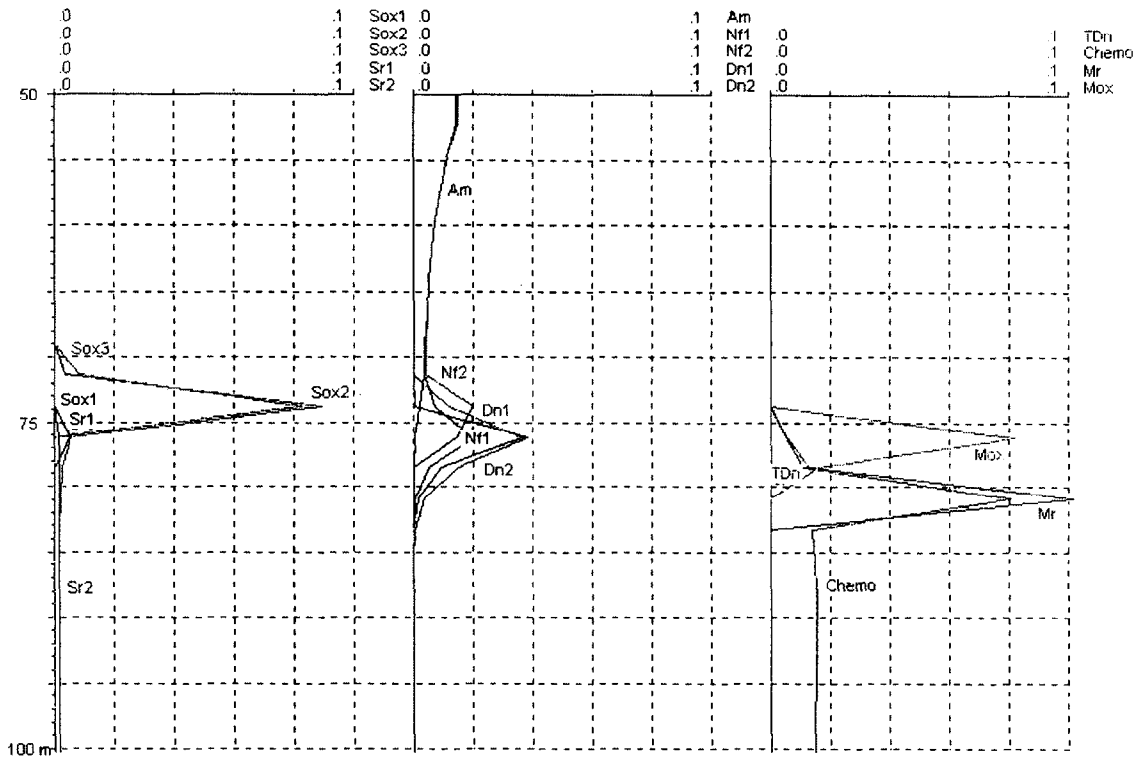


Fig. 3. Vertical distribution of the processes rates in the redox zone. Processes names are described in Table 2.

Manganese compound profiles derived in the model also reflect the main features of this parameter's vertical distribution in nature. Dissolved manganese is oxidised by oxygen and the particulate manganese forms. The particulate manganese reacts with hydrogen sulphide and is transformed into dissolved manganese. A dissolved manganese maximum appeared in the model experiments when the oxygen supply increased and both processes intensified.

Differ from the previous versions of the model, now it was possible to obtain a 15-m distant between the H_2S depletion point and the oxycline depletion point. In the frames of the model, such situation can be reached if particulate Mn will oxidise all the amount of the hydrogen sulphide. Hence, the present model can explain H_2S oxidation in the absence of oxygen.

In Fig.3. the vertical distribution of the rates of processes is presented. One can see that the maximums of rates of nitrogen and sulfur cycles processes are located at approximately the same level (with distance of 2-3 m), while rates of Mn reduction and oxidation occurs at different layers (with distance of 10 m). That

demonstrates the effect of intensification of sedimentation of the particles covered with particulate Mn, and therefore of accelerating of transport of this oxidiser.

In Fig.4 the main processes responsible for oxygen consumption and reduced sulfur forms oxidation are presented. In the frames of the model the first stage of sulfide oxidation can be provided by particulate Mn, while the second and third stages are provided by dissolved oxygen several meters higher. That agrees with observations on dominating of S_0 and S_2O_3 in the redox zone [3,6].

Therefore, model supports the estimates that particulate Mn can be the basic oxidiser of deep H_2S on horizon of its disappearance [1]. The intensive consumption of this oxidiser is compensated by its intensive flux of this oxidiser in particulate form.

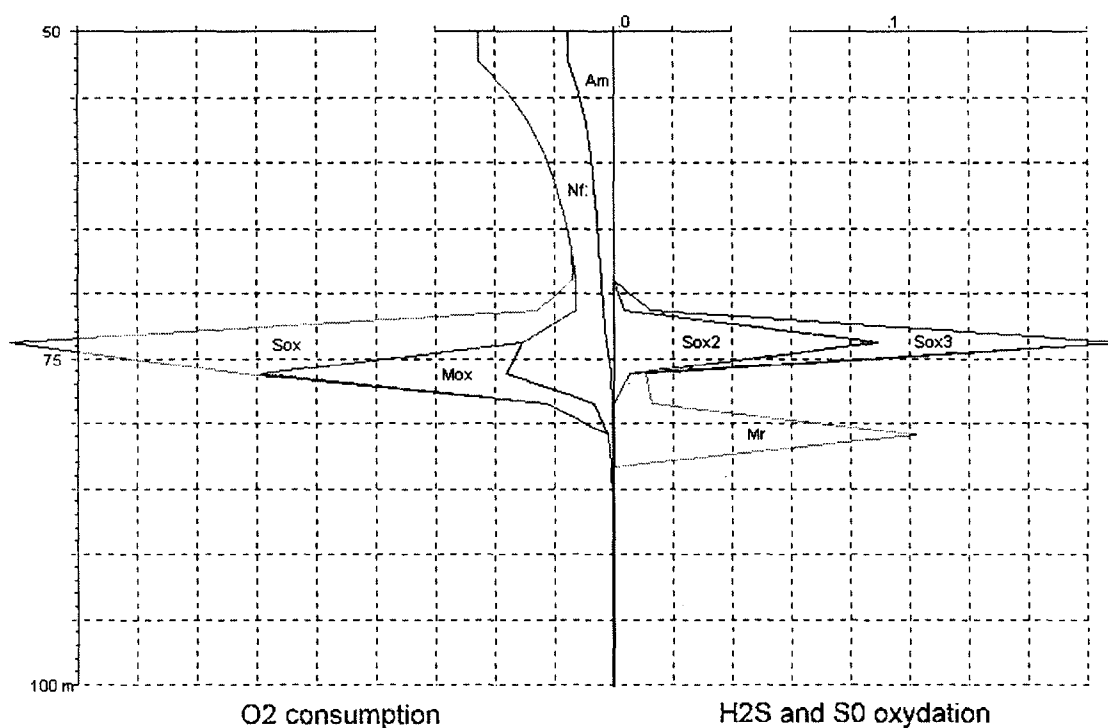


Fig.4. Vertical distribution of processes of oxygen consumption and reduced sulfur compounds oxydation. Processes names are described in Table 2.

Conclusion

- Peculiarities of the fine structure of the zone of contact of oxic and anoxic waters in the Black Sea are connected with the simultaneous cycling of several elements (O, N, S, P, Mn). The key role belongs to a Mn cycle connected with phase transitions and formation of heavy detrital particles, that accelerates the transport of this oxidiser to the deeper layers;
- The most intensive regions of particulate Mn formation and therefore intensive H_2S oxidation can be connected with peculiarities of the redox layer hydrophysical structure. As it is supported by optical observations [3] the leading role should belong to the Black Sea coastal anticyclonic eddies.

Acknowledgement

This work was conducted with the financial support of the Russian Foundation for Basic Research, grants 96-05-66169 and 96-15-98440.

References

1. E.V.Yakushev and E.I.Debolskaya (in press, this volume) Particulate manganese as a main factor of oxidation of hydrogen sulfide in redox zone of the Black Sea.
2. J.W.Murray, L.A. Codispoti and G.E.Friederich, 1995, The suboxic zone in the Black Sea, in C.P.Huang, R.O'Melia and J.J.Morgan (eds.) *Aquatic chemistry: interfacial and interspecies processes*, NY:American Chemical Society, 157-176.
3. I.I.Volkov, E.A.Kontar, Yu.F.Lukashev, L.N.Neretin, F.Nyffeler and A.G.Rozanov, 1997, The top border of hydrogen sulfide and the nature of Nepheloid Redox Layer in waters of a Caucasian slope of the Black sea, *Geochemistry International*, 6, 618-629.
4. B.A.Skopintsev, 1975. *Formirovaniye sovremennogo chimicheskogo sostava Chernogo morya [Formation of the recent chemical composition of the Black Sea]*, 336 Leningrad:Gidrometeoizdat (Russian), 276.
5. A.G.Rozanov, 1995, Redox stratification of waters of the Black Sea, *Oceanology*, 35, 4, 544-549.
6. I.I.Volkov, A.G.Rozanov and T.P.Demidova, 1992, Soedineniya neorganicheskoy vosstanovlennoy sery i rasvorennyy marganets v vode Chernogo morya [Inorganic reduced sulfur compounds and dissolved manganese in the Black Sea water column], in M.E.Vinogradov (ed.) *Zimnee sostoyaniye ekosystemy otkrytoy chasti Chernogo morya*, IO RAS, Moscow, 38-50. (Russian).
7. O.Basturk, I.I.Volkov, S.Gokmen, H.Gungor, A.S.Romanov and E.V. Yakushev E.V, 1998, International expedition on r/v "Bilim" in July 1997 in the Black Sea, *Oceanology*, 38,3, 1-4.
8. B.M. Tebo, 1991, Mn (II) oxidation in the suboxic zone of the Black Sea, *Deep Sea Res.*, 38, S883-S906.
9. E.V.Yakushev, 1998, Mathematical Modelling of Oxygen, Nitrogen, Sulfur and Manganese Cycling in the Black Sea In: 'NATO TU-Black Sea Project Ecosystem Modeling as a management tool for the Black Sea. Symposium on scientific results', L.Ivanov & T.Oguz (eds.) Kluwer Academic Publishers, V.1, 373-384.
10. B.L.Lewis and W.M.Landing, 1991, The biogeochemistry of manganese and iron in the Black Sea, *Deep Sea Res.*, 38 (2A), S773-S803.
11. E.V.Yakushev. and L.N.Neretin, 1997, One-Dimensional Modeling of Nitrogen and Sulfur Cycles in the Aphotic Zones of the Black and Arabian Seas, *Global Biogeochemical Cycles*, 11, 3, 401-414.
12. A.A.Bezborodov and V.N. Eremeev, 1993, *Chernoje more. Zona vzaimodeystviya aerobnykh i anaerobnykh vod [Black Sea. The oxic/anoxic interface]*, Sevastopol: AS of the Ukraine, the Marine Hydrophysical Institute, 299, (Russian).

NOVEL EXACT SOLUTIONS DESCRIBING THE EVOLUTION OF LENSES FRONTAL VORTICITY

A.A. Yurova, V.A. Gritsenko

The State Technical University of Kaliningrad, Sovetskiy pr., 1, Kaliningrad, 236000, Russia

The process of collapse the of the frontal lenses vortex is described by the non-linear Schrödinger equation and with the help of the "virtual solitons". Exact solutions with the exponential (the first phase) and the algebraic (the second phase) collapse are constructed. Using the commutativity of Darboux transformation the non-linear superposition formulae for these solutions is obtained. The novel solution falling off exponentially by the small time and algebraically by the t tries to the infinity.

1. Problem.

In [1] Hasimoto shows that in a special case, when the vorticity is limited by a narrow and long tube (vortex filament), where its value is constant across the tube, the evolution of curvature and torsion of this filament is described by non-linear differential equations in terms of partial derivatives and those in some cases could be suitable for integration. For example, if velocity of vortex filament is directed along its binormal, then such filament is "serviced" by non-linear equation of Schrödinger (NLS). Let us take vector tangential to vertical filament as $\vec{v}, \vec{n}, \vec{b}$ - normal and binormal vectors, respectively. Those values are interrelated through the Frene formulas. Let k - curvature, χ - torsion of space straight line, l - natural parameter. As it was mentioned above, if velocity of vertical filament is directed along the vector \vec{b} , then the value U is as follows:

$$U(t, l) \equiv 2k(t, l) \exp \left\{ i \left(\int_0^l dl' \chi(t, l') + \frac{1}{2} \int_0^l dt' A(t') \right) \right\}, \quad (1)$$

where $A(t)$ - an arbitrary function, t - the time, and it satisfies for NS:

$$i \frac{\partial U}{\partial t} + \frac{\partial^2 U}{\partial l^2} + 2|U|^2 U = 0. \quad (2)$$

Using of the known solutions (2) provides for obtaining of compliant vertical filament. Thus, if we have the solutions of the NLS, then the curvature $k(t, l)$ and torsion $\chi(t, l)$ are easily found if use (1) jointly with the NLS. The next step includes finding of a shape of corresponding vertical filament by means of parameterisation:

$$\vec{r}(t, l) = \int_0^l dl' \vec{v}(t, l'), \quad (3)$$

where $\vec{r}(t, l)$ - radius-vector of points on the curve.

The problem thus is reduced to finding the tangent vector, which is the function of natural parameter and time. In this case it is necessary to solve three equations of Riccati:

$$\frac{\partial \varphi_k}{\partial l} + ik(t,l)\varphi_k - \frac{i\chi(t,l)}{2}(1 - \varphi_k^2) = 0, \quad k = -1, 2, 3. \quad (4)$$

Here

$$\varphi_k \equiv \frac{v_k + in_k}{1 - b_k},$$

v_k , n_k and b_k are the components of appropriate vectors.

Knowledge of φ allows to recover \vec{v} , with one ambiguousness, which results from different ways of taking co-ordinate systems. In this paper we will not determine the shape of vortex filament, and consider only some explicit expressions for curvature and torsion. Let us nevertheless note the occurrence of one interesting circumstance. If linearizing (4) by substituting of

$$\varphi = \frac{2}{i\chi} \frac{\partial \ln \Phi}{\partial l}$$

into it (indices are omitted), we obtain equation of the second order:

$$\frac{\partial^2 \Phi}{\partial l^2} + \left(ik(t,l) - \frac{\partial \ln \chi(t,l)}{\partial l} \right) \frac{\partial \Phi}{\partial l} + \frac{\chi(t,l)^2}{4} \Phi = 0. \quad (5)$$

In general case it can't be integrated, but if for some values $k(t,l)$ and $\chi(t,l)$ finding of full set of precise linearly independent solutions $\{\Phi_{1,2}\}$:

$$\Phi_2 = \frac{\Phi_1}{\sqrt{\chi}} \exp \left\{ \frac{i}{2} \int dl' k \right\} \cdot \int dl' \frac{\chi}{\Phi_1^2} \exp \{ i \int dl'' k \}, \quad (6)$$

then development of systematic procedure of construction of new integrated potentials, by analogy with the known Darboux's transformation is possible. Let Φ_1 and Φ_2 to be solutions for (5). Direct test evidences that the function

$$\Phi_2[l] = \frac{S}{\Phi_1} \left(\frac{\partial \Phi_2}{\partial l} \Phi_1 - \frac{\partial \Phi_1}{\partial l} \Phi_2 \right) \quad (7)$$

satisfies (5) with new potentials:

$$\chi[l] = \pm 2 \sqrt{-\frac{\chi^2}{4} - up - u' - \frac{S'' + S'(u+p)}{S} + (\ln \Phi_1)' \left(2u + p + 2 \left(\ln \frac{S}{\Phi_1} \right)' \right)} \quad (8)$$

$$k[l] = k - ip + i \left(\ln \frac{\chi[l]}{\chi} \right)'$$

For reality of the $k[l]$ and $\chi[l]$ it is necessary to take the function S by the special manner and to solve not one but two integrable linear equations of the second order [2].

2. Some precise solutions.

This paper is confined with demonstration of three precise solutions for the NLS, which lead to closed vortex filaments. We are interested first of all with possible models of frontal vorticity for intra-thermocline lenses. Using the Hirota method it is possible to construct such solution [2]:

$$\chi = -\frac{2p \sin(pl) \sin(2\alpha) E (AE^2 + 1)}{A^2 E^4 + 4A \cos(pl) \cos(2\alpha) E^3 + 2(2 \cos^2(pl) + A \cos(4\alpha)) E^2 + 4 \cos(pl) \cos(2\alpha) E + 1}, \quad (9)$$

$$k = \frac{a \sqrt{A^2 E^4 + 4 \cos(pl) \cos(2\alpha) E (1 + AE^2) + 2E^2 (A \cos(4\alpha) + \cos(2pl) + 2) + 1}}{2(AE^2 + 2 \cos(pl) E + 1)}.$$

It is assumed here that a is real, $E \equiv \exp(\mu t + v)$ and

$$b_1 = b_2 = \exp\{2ia\}, b_3 = A b_1^2, b_4 = 1, b_5 = a, \quad (10)$$

$$\mu = \pm p \sqrt{4a^2 - p^2}, p = 2a \sin \alpha, A = \frac{1}{\cos^2 \alpha}.$$

If $\alpha \neq \pi k$, where $k \in \mathbf{Z}$, then the solution of NLS will be non-singular. It can be easily seen that at $t \rightarrow +\infty$ ($\mu > 0$), $\chi \rightarrow 0$, while $k \rightarrow a/2 = \text{const}$. In other words, the filament degrades with time into a flat curve of constant curvature, i.e. circle. We believe that this result is satisfactory proceeding from the above interpretation. Indeed, ratio of characteristic vertical and horizontal scales for lenses in the ocean was found to be $\sim 10^{-3}$. Intrusive flows, extending along intrinsic horizontal isopycnal surfaces, are assumed to be one of the possible "sources" of lens generation. Speed of the intrusive tongue in the centre and outmost is different due to viscosity, so the area of an arbitrary "liquid contour" will be changed in time. In accordance with the Bjorknes theorem the Coriolis's force results in the change of the vorticity existing at the time being. Numerical experiments show that if the initial vorticity is non-homogeneous, than the evolution of intrusive flow will result in separation of eddy, where the latter may be assumed as lens at the initial stage. Non-coincidence of isobaric-isopycnal surfaces provides for origination of vertical vorticity, which due to smallness of mixing effects will be focused on frontal zone and is being the vortex tube under investigation. Following the lens formation, the horizontal pressure gradient oblates the lens in vertical, leading thus to its horizontal diffuence. In so doing, the frontal vortex filament is transforming into a flat curve. Therefore the solution suggested above can be used as a dynamical model for description of evolution of frontal vorticity in collapsing submesoscale coherent eddy, which occurs in the reference frame moving on average at the speed of \bar{v}_N .

Let us take one more example of the similar solution, which is also suitable for simulation of collapse. We will exclude the explicit form of torsion due to excessive complexity of formulation, but will be confined to curvature, which is expressed by compact expression:

$$k = \sqrt{A^2 - \frac{4m^2 s^2 (1 + \cosh(4\lambda st) \cos(sl))}{(s \cosh(4\lambda st) + m \cos(sl))^2}}, \quad (11)$$

where $s = \sqrt{A^2 - \lambda^2}$, $m = \frac{\lambda s}{A}$ and A и λ - real parameters, satisfying to condition $A^2 - \lambda^2 > 0$.

Expressions (9) and (11) are characterised by l periodicity and demonstrate exponentially quick collapse of lenses. So we can to identify this solution with the first phase of the lenses evolution (see experimental work [3]).

Analysis have shown the possibility of such NLS solutions which have the same asymptotic limit, but expression tends to it as polynomial (second phase of the lenses evolution [4]), and are not periodical. Curvature and torsion are described by relationships:

$$k = \frac{A\sqrt{256A^8t^4 + 128A^6(it)^2 + 16A^4(l^4 + 10t^2) - 24A^2l^2 + 9}}{2(16A^4t^2 + 4A^2l^2 + 1)}, \quad (12)$$

$$\chi = -\frac{128A^4it}{256A^8t^4 + 128A^6(it)^2 + 16A^4(l^4 + 10t^2) - 24A^2l^2 + 9},$$

where $\text{Im } A=0$. At $t \rightarrow +\infty$, $\chi \rightarrow 0$, and $k \rightarrow a/2 = \text{const}$, analogously to (9) and (11). Let us note that all above mentioned solutions permit introduction of new parameters, for which the asymptotic limit of torsion is any infinitesimal value, but not zero. In this case the filament degrades into quasi-flat (not absolutely flat) curve. For example in case of (9) it will be represented as narrow closed spiral with the step $2\pi\rho$.

It can be checked, by analysing asymptotic limit of corresponding solution (1). We present the solution of the non-linear Schrödinger equation in the form:

$$U(t,l) = U_{as}(1 - Q(t,l)), \quad U_{as} = a \exp\{2ia^2 t\}, \quad (13)$$

where $Q(t,l)$ is a small perturbation, which will consider periodic on l with the period L . Substituting it into NLS we get the single-line equation for $Q(t,l)$ in the first drawing which can be solved by the Fourier method. Modes with direct numbers satisfying the inequality:

$$0 < N < \frac{|a|L}{\pi}$$

bring about the exponential growing of amplitude with a time, being indicative of instability [5].

It is possible to construct the superposition of exponential and rational solutions (11) and (12). For this aim it is necessary to obtain the non-linear superposition formulas of NLS via Darboux transformation. LA-pair for NLS has the form:

$$\Psi_t = i\sigma_3 \Psi \Lambda + Q\Psi, \quad \Psi_l = 2i\sigma_3 \Psi \Lambda^2 + 2Q\Psi \Lambda + W\Psi, \quad (14)$$

where

$$Q = i \begin{pmatrix} 0 & U^* \\ U & 0 \end{pmatrix}, \quad \Psi = \begin{pmatrix} \psi_1 & \psi_2 \\ -\psi_2^* & \psi_1^* \end{pmatrix}, \quad \Lambda = \begin{pmatrix} \lambda & 0 \\ 0 & \lambda^* \end{pmatrix}, \quad W = \begin{pmatrix} -i|U|^2 & U_l^* \\ -U_l & i|U|^2 \end{pmatrix},$$

λ - complex spectral parameter, σ_3 - Pauli matrix.

Let $\Psi_{1,2}$ are solution of the system (14) by the some values of the spectral parameters $\lambda_{1,2}$ and fixed Q . We define matrix functions $\tau_k = \Psi_k \Lambda_k \Psi_k^{-1}$, $k=1,2$. Then, the LA-pair equations are invariant under the Darboux transformation:

$$\begin{aligned}
\Psi &\rightarrow \Psi(1) = \Psi\Lambda - \tau\Psi, \\
\mathcal{Q} &\rightarrow \mathcal{Q}(1) = \mathcal{Q} + i[\sigma_3, \tau], \\
\mathcal{W} &\rightarrow \mathcal{W}(1) = \mathcal{W} + 2[\mathcal{Q}, \tau] + 2i[\sigma_3, \tau],
\end{aligned} \tag{15}$$

where square brackets denote the commutator and $\tau = \tau_1$ or τ_2 . The solutions (11) and (12) were obtained by (15) with U from the (13).

Non-linear superposition formulas can be obtained by the fact that two sequential Darboux transformation are commuting operators. In particular:

$$\mathcal{Q}(1,2) = \mathcal{Q}(2,1) = \mathcal{Q}_3.$$

Therefore

$$\mathcal{Q}_3 = \frac{1}{2}(\mathcal{Q}_1 + \mathcal{Q}_2) + \mathcal{Q}_{\text{int}}, \tag{16}$$

where \mathcal{Q}_1 and \mathcal{Q}_2 are calculated by the solutions (11)-(12), and:

$$\begin{aligned}
\mathcal{Q}_{\text{int}} &= \frac{1}{\Delta} ((\mathcal{Q}_2 - \mathcal{Q}_1)(\tau_2 + \tau_1)_D \sigma_1 (\tau_2 - \tau_1)_D \sigma_1 - (\tau_2 - \tau_1)_D (\tau_2 + \tau_1)_D (\mathcal{Q}_2 - \mathcal{Q}_1) + \\
&+ (\tau_2 - \tau_1)_D (\mathcal{Q}_1 + \mathcal{Q}_2 - 2\mathcal{Q}) \sigma_1 (\tau_2 - \tau_1)_D \sigma_1 + \frac{1}{4} (\mathcal{Q}_2 - \mathcal{Q}_1)(2\mathcal{Q} - \mathcal{Q}_1 - \mathcal{Q}_2)(\mathcal{Q}_2 - \mathcal{Q}_1))
\end{aligned}$$

with

$$\Delta = \det(\tau_2 - \tau_1), \quad \sigma_1 = \begin{pmatrix} 0 & 1 \\ 1 & 0 \end{pmatrix},$$

τ_D is the diagonal path of the matrix τ whereas

$$\tau_{k,F} = \frac{1}{2i} \sigma_3 (\mathcal{Q}_k - \mathcal{Q}), \quad k=1,2.$$

Let $\tau_{k,D} \equiv \text{diag}(a_k/2, a_k^*/2)$. Using the third formula from the (15) and the explicit form of the matrix \mathcal{W} we get

$$b_k = -i \frac{U w_{k,l}^* - U_k^* w_{k,l}}{|U_k|^2 - |U|^2}, \quad w_k \equiv U_k - U. \tag{17}$$

After substitution (17) into (16) we get non-linear superposition formula for the solution (11) (U_1) and (12) (U_2):

$$U_3 = \frac{1}{2}(U_1 + U_2) + U_{\text{int}}, \tag{18}$$

where

$$U_{\text{int}} = \frac{(b_1^* - b_1^*)^2 (U_1 + U_2 - 2U) + (U_1 - U_2)^2 (U_1 + U_2 - 2U)^* - 2(b_1^2 - b_2^2)^* (U_1 - U_2)}{|b_1 - b_2|^2 + |U_1 - U_2|^2}.$$

It is possible to choose parameters such the way that the exponential solution U_1 will be dominating by the small times and the rational solution U_2 will be dominating by the $t \rightarrow \infty$. Thus the (11) is the unification model of the collapsing vortex filament which contain the first (exponential) phase and the second (rational) phase.

Literature

1. Hasimoto H.J. // Fluid Mech. 1972. 51, p. 477-485.
2. Gritsenko V.A., Yurova A.A. On the dynamics the vortex filament. In. Intrusion currents. Kaliningrad. 1997, p.102-110.
3. Kitamura Yo., Nagata Yu. // J. of the Ocean. Sosiet. of Japan. 1983. V. 39, p. 89-100.
4. Kostianoy A.G., Shapiro G.I. // Izvestiya. Atmospheric and Oceanic Physics. 1986. V. 22, N. 10, p. 1098-1105.
5. Zatsepin A.G. On the problem of evolution of an intrusive density lens in a rotating fluid. // Intrathermocline eddies in the ocean. M: IO AN USSR, 1986, p. 50-55.

MODELING AND OBSERVATIONS OF CURRENTS OFF SOUTHERN BRAZIL AND URUGUAY: THE RIO GRANDE CURRENT

P. O. Zavialov and O. O. Moller Jr.

University of Rio Grande, Rio Grande, 96201-900, RS, Brazil

Abstract. The pattern of circulation in the area adjacent to Southern Brazil and Uruguay was investigated with the help of an inverse model based on heat and mass budgets closure requirements. The model predicted energetic northward flow over the shelf, between the coast and the Brazil Current flowing southwards along the shelf break. This previously unknown northward current on the shelf was then directly observed during 90 days of current measurements at mooring station (virtually the first *in situ* velocity measurements in the region).

1. Introduction

The area of this study is adjacent to the coast of Southern Brazil and Uruguay, between $30 - 35^{\circ}S$ and $50 - 55^{\circ}W$. Until recently, there were no *in situ* data on circulation in the area, while a large array of data on sea temperature and surface heat fluxes collected through the last 30 years is available. The region is located near the Brazil-Malvinas confluence front. There is strong influence of both the Brazil and the Malvinas currents on circulation in the area. The other important factor contributing to local physics is considerable fresh water input from the Patos-Mirim lagoon, which is among the largest lagoons of the world, and especially from the Rio de la Plata (Plata river) estuary. Little is known about the pattern of coastal circulation in the area. Very few, if any, direct measurements of currents have been previously made, though some information have been obtained by indirect means such as water masses analysis. However, as discussed in [1], conventional TS analysis which depends on isopicnal mixing hypothesis and discriminates between three water masses at the most, may not be applicable in this complex region of intense mixing activity and water mass transformation.

Previously, it has been generally believed that in summer the southward flow should dominate the region, while in winter the northward circulation should prevail. There were good reasons to believe so, because, as it is known, during the austral summer the poleward transport of the Brazil current increases while the equatorward transport of the Malvinas current weakens, and during the austral winter the situation is opposite, e.g. [2]. In addition to this, in winter the prevailing winds are southwest, while in summer the northeastern winds are most frequent.

We shall show below, however, that the equatorward flow bringing fresh waters from the Plata estuary to the north of the region exists even in summer, despite of the prevailing northeastern winds. This conclusion was first drawn based on inverse modeling, as previously reported in [4]. In the present paper, we also discuss experimental evidence of the southward shelf current as revealed from 90 days of direct current measurements at mooring station.

2. The model

The model is based on joint analysis of observed seasonal cycle of SST along with the fields of insolation and surface heat fluxes. From the integrated heat equation, the "residual" flux required to heat budget

closure was computed. This residual flux may account for advection, diffusion and entrainment. Diffusion has been neglected based on scaling estimates of term sizes, while the entrainment was parameterized through the observed changes of the mixed layer depth. The rest of the “residual flux” was assumed to be associated with advection. The fields of advection together with the fields of SST determine the cross-isotherm velocity components, while the along-isotherm components cannot be determined from the heat equation. However, cross-isotherm components given, along-isotherm components can be found from the mass conservation, with the help of boundary conditions.

The heat equation applied to the transition between two subsequent seasons 1 and 2 reads

$$c\rho(T_2h_2 - T_1h_1 - T_0\Delta h) = Q_{(1,2)}\Delta t + A_{(1,2)} \cdot h_{(1,2)} \cdot \Delta t$$

where T is surface temperature, h is mixed layer depth, Q is net surface heat flux, A is advection, t is time, the subscripts 1 and 2 correspond to the seasons 1 and 2, respectively, and the subscript (1, 2) indicates average value between the two seasons. Further, $\Delta h = h_2 - h_1$, and T_0 is the average temperature in the entrained “seasonal thermocline”. If the temperature in the entrained layer is approximately linear in depth, then $T_0 \sim (T_1 + T_2)/2$. With this assumption, the equation above was used to determine the fields of advection. The next step was to reconstruct the velocity fields starting from advection and temperature. By definition,

$$A = -c\rho\nabla \cdot (\vec{U}T).$$

With the assumption of a horizontally non-divergent flow, this expression reduces to

$$A = -c\rho\vec{U} \cdot \nabla T.$$

Thus the component of velocity parallel to the gradient of temperature (hereafter called the *cross-isotherm* component \vec{U}_{cr}) can be determined simply as

$$\vec{U}_{cr} = -\frac{1}{c\rho} \frac{A}{|\nabla T|^2} \nabla T.$$

However, an arbitrarily large *along-isotherm* component \vec{U}_{al} can be added to the velocity determined thereby without changing advection. Additional physical constraints are required to find \vec{U}_{al} . These constraints can be provided by the requirement of continuity, with the addition of boundary conditions. The problem then is to find the vector field $\vec{U}_{al}(x, y)$, which is *orthogonal* to the field $\vec{U}_{cr}(x, y)$ determined as above, and such that

$$\begin{aligned} \nabla \cdot (\vec{U}_{cr} + \vec{U}_{al}) &= 0, \\ (\vec{U}_{cr} + \vec{U}_{al})|_c &= 0, \end{aligned}$$

where $|_c$ means at the coast, and

$$\vec{U}_{cr} \cdot \vec{U}_{al} = 0.$$

Further details about the inverse model can be found in [4].

3. Direct current measurements

The observations were conducted during the period from March 4 to May 27, 1997, corresponding to austral summer and autumn. A conventional current meter was used at a mooring station at 32°41'S and 52°27'W. The instrument was deployed at the depth of 15 meters, while total depth at the station was of 50 meters. Another current meter was installed at 45 meters depth, however, due to instrument malfunction, the data series obtained at 40 meters was much shorter than that of 15 meters. In the present paper, we restrict our discussion to the upper current meter. The speed and direction of current was recorder every 30 minutes. We used also the wind data obtained simultaneously at coastal meteorostation in the city of Rio Grande at approximately 32°S, 52°W, some 40 miles away of the mooring station. More experimental details are given in [3].

4. Results and discussion

The seasonal fields of surface velocity as obtained from the inverse model are shown in Fig. 1. Perhaps the most interesting finding is the energetic *northward* flow on the shelf, between the Brazil Current and the coast of the Brazilian state of Rio Grande do Sul. This equatorward current can be seen in all seasons including summer (in fact, especially in summer), in notable disagreement with previous views. However, the direct measurements generally confirmed the model results. The low passed series of the along-shore and cross-shore velocity components, along with those of wind stress, are depicted in Fig. 2 (day 1 in the figure corresponds to March 4, 1997). The positive (i.e. northward) along-shore velocity predominated throughout the observations, except during exceptionally strong events of northern winds. A contour plot of the along-shore velocity as a function of the along-shore and cross-shore wind stress is shown in Fig. 3 (darker tones correspond to southward flow direction, contours are drawn with the increment of 10 cm/s, zero contour is indicated with an arrow). As it can be seen in the figure, the contour of zero velocity is displaced relative to a zero line of the along-shore wind stress. Thus, only strong northern winds can overcome the “background” northward flow which otherwise predominates over the study region.

As we argued in [4], this circulation pattern is likely to have barotropic nature and be related with massive freshwater discharge from the Plata and Patos estuaries along with the on-shore component of Ekman transport. The flow, which can be often clearly seen in satellite imagery, starts at about 35°S and can be traced to as far north as 27°S or farther, occupying the entire shelf. The characteristic values for the velocity are up to 50 cm/s in seasonal average, however instantaneous values of over 100 cm/s have been registered at the mooring station. The corresponding equatorward volume transport over the shelf, by some estimates, can be as large as up to 1 Sv. Thus, the observed flow represents a major coastal current which largely determines oceanographic conditions off Uruguay and Southern Brazil. Since a large part of the current extension lies along the coast of Rio Grande do Sul, we propose to refer to the flow as the Rio Grande Current.

References

1. Maamaatuaiahutapu, K., V. C. Garçon, C. Provost, M. Boulahdid, and A. P. Osiroff, 1992. Brazil-Malvinas Confluence: Water mass composition. *J. Geophys. Res.*, **97**, 9493–9506.
2. Matano, R. P., M. G. Schlax, and D. B. Chelton, 1993. Seasonal variability in the southwestern Atlantic. *J. Geophys. Res.*, **98**, 18 027 – 18 035.
3. Moller Jr., O. O., D. F. Urbano Neto, and P. O. Zavialov, 1998. Dinâmica da plataforma continental interna do Rio Grande do Sul. Proc. XI Semana Nacional de Oceanografia, Rio Grande, Brazil.
4. Zavialov, P. O., R. D. Ghisolfi, and C. A. E. Garcia, 1998. An inverse model for seasonal circulation over the southern Brazilian shelf: near-surface velocity from the heat budget. *J. Phys. Oceanogr.*, **28**, 545–562.

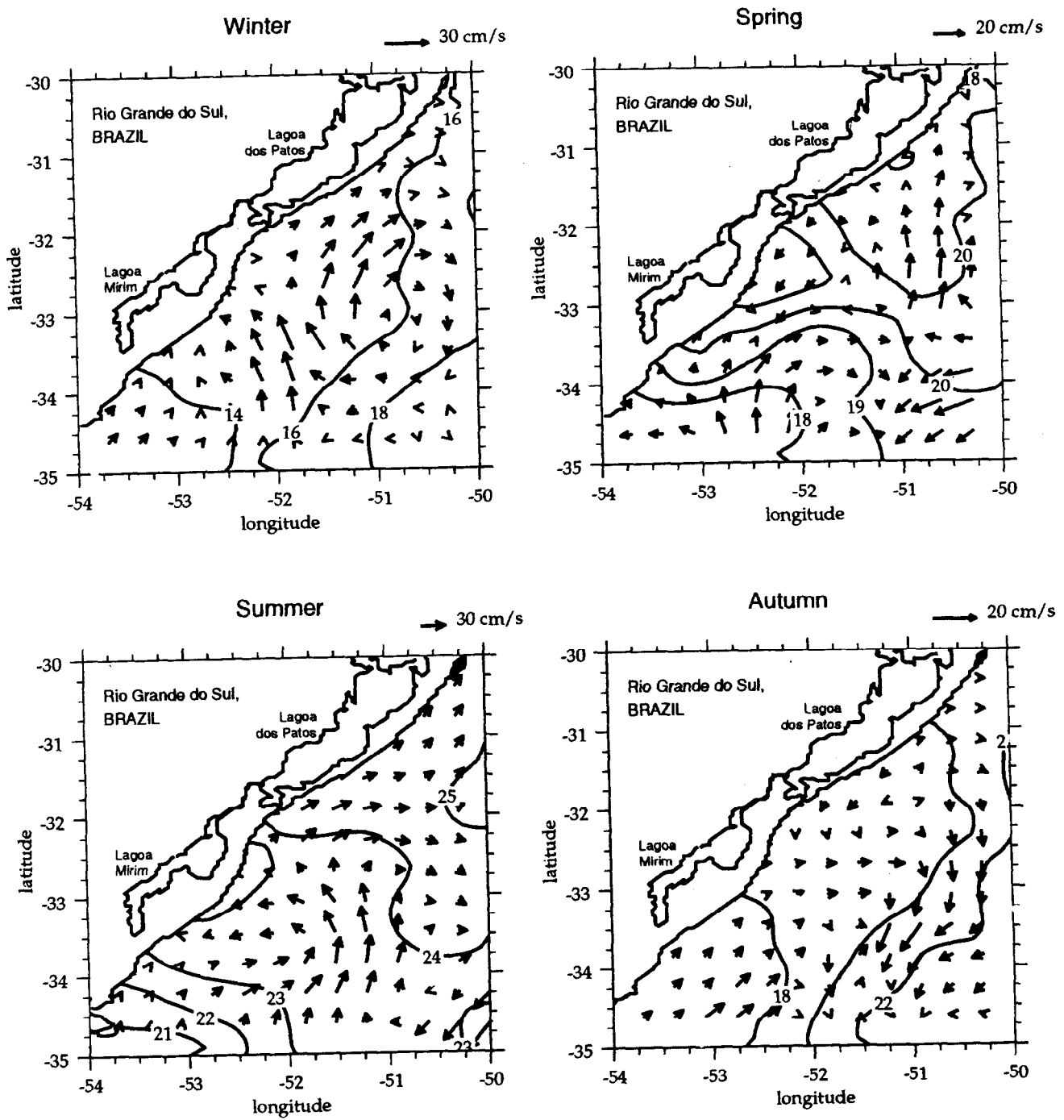


FIG. I. SST contours and model velocity fields.

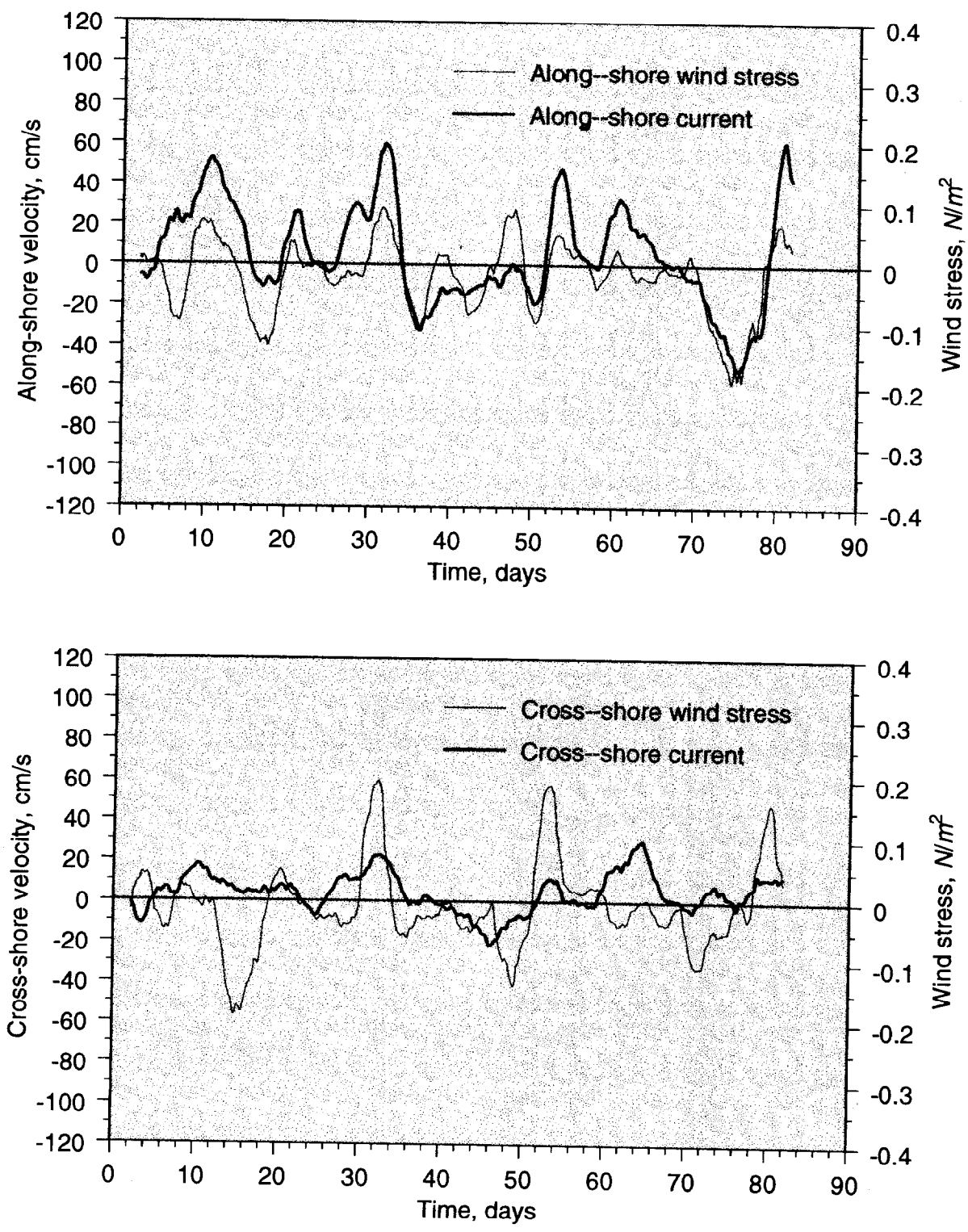


Fig. 2. Low-passed series of current velocity and wind stress.

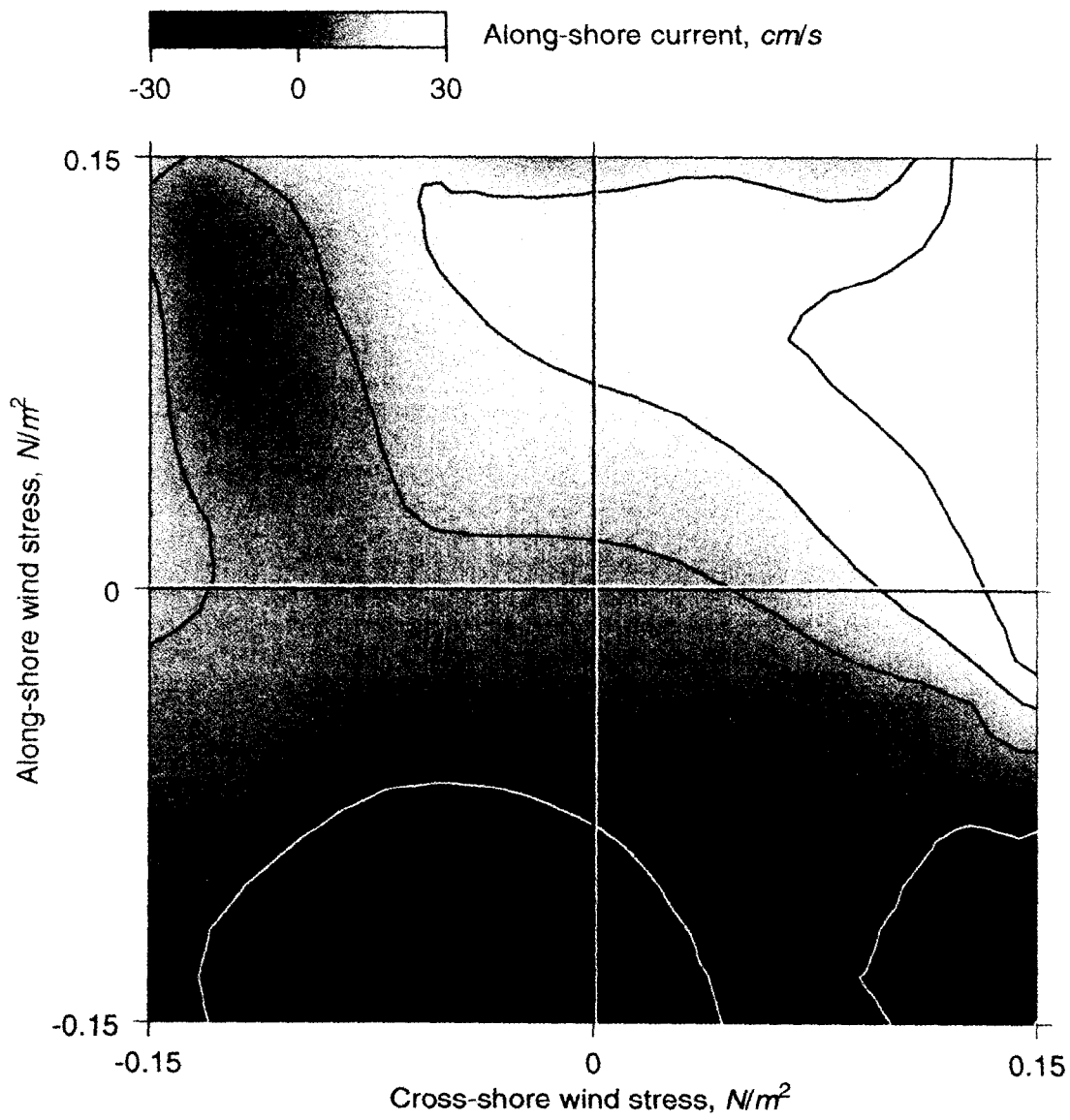


Fig. 3. Along-shore current velocity versus along-shore and cross-shore components of wind stress.

LOW FREQUENCY SST VARIABILITY IN SOUTHWESTERN ATLANTIC

P. O. Zavialov and J. M. Absy

University of Rio Grande, Rio Grande, 96201-900, RS, Brazil

Abstract. Over 300,000 quality controlled local reports from ships of opportunity complemented with the data extracted from global data records is used to investigate the variability off the coast of Southern Brazil and Uruguay in a range of temporal scales from interannual to secular. With respect to behaviour at these scales, three distinct areas can be identified in the study region. The first one, located over the shelf and controlled by winter invasions of subantarctic water along with the Plata river and Patos-Mirim lagoon discharges, is characterized by energetic mean square variability (from 1.4 to 2.2°C², after removal of seasonal signal), and extremely high secular trend towards warming (1.2 to 1.6°C per 100 years), especially in proximity of the estuaries. The second one, area of the Brazil Current influence, exhibits smaller variability (1 to 1.4°C²). The secular trend is from 1 to 1.2°C per 100 years, smaller than observed in the shelf, but still high compared to the global average. The third area, which encompasses eastern deep ocean part of the region away from the influence of either major currents or coastal discharges, exhibits less energetic variability at all examined scales, as compared to the rest of the region. In winter, a thermal front forms in the study region. The position of this frontal zone is a subject to strong year-to-year changes. The interannual variability of the front position is investigated.

1. Introduction

The study region lies between 27° and 35° of southern latitude, and between 41° and 54° of western longitude, near the Brazil-Malvinas confluence. The confluence region, one of the most energetic areas of the world ocean (e.g. [3]), is characterized by strong thermohaline gradients and intense mesoscale activity (e.g. [4,6,7]). The shelf of the area is under large influence of freshwater discharges from the Plata and the Patos-Mirim estuaries (e.g. [5,8]). Coastal waters discharged from the estuaries tend to propagate northwards over the shelf [12]. In austral winter, a thermal front forms in the study region, separating warm tropical water associated with the Brazil Current and cold subantarctic water flowing northward on the shelf with an admixture of coastal freshwater discharges.

The behavior of the confluence region at different temporal scales and interactive relationship of this behavior with climate variability have been a subject of many studies. However, most of previous works have addressed annual or shorter temporal scales. The interannual and lower frequency variability in the region is less well known. In the present work we use a set of local historical data (1854-1994) to investigate SST variability at temporal scales from interannual to secular.

2. Data and procedure

The dataset used in this study was made up of over 300,000 individual surface marine observations collected between 1854 and 1979 mostly by ships of opportunity and accumulated by the US National Climatic Center (Tape Data Family 11), [1,2]. This local historical data, available only until 1979, was then complemented with the monthly "optimum interpolation" (OI) SSTs for 1981-1994 [11]. The OI

fields were produced based on the U.S. National Meteorological Center (NMC) file of in situ surface marine observations, blended with satellite based SSTs which served to improve the analysis in the areas with inadequate in situ sampling. Thus we obtained a regional 1×1 degree set of historical SSTs for the period from 1854 to 1994, at monthly temporal resolution, although with a number of gaps, especially in the beginning of the series.

The mean SST and the seasonal cycle were removed from the series, and secular trend was then found at all grid nodes as a best linear fit to a corresponding series of anomalies. We then subtracted the trend from the anomalies series and computed the mean square variability. An important part of the work was the investigation of interannual migrations of the frontal zone on the shelf. We restrict this part of discussion to the month of July only, which had the best historical data coverage of all winter months. As an indicator of the position of the front, we adopted the 17°C isotherm of SST (see also [10]).

3. Results

3.1. "Global change": secular trends of SST

The spatial distribution of secular trend (converted to units of $^\circ\text{C} / 100$ years) is shown in Fig. 1. Everywhere in the region the trend is positive, indicating warming. Detailed look at the SST series reveals that most of this warming has been occurring during the last 6 decades, while little or no trend was observed before 1940s. It seems also that the increase of winter SSTs was larger than that of summer ones.

In global average, the increase of SST over the past century is believed to be about 0.4°C (e.g. [9]). For most of the area of this study, the secular warming is significantly above this global average. In the deep ocean part of the region, the isopleths of secular trend are oriented predominantly along the shore. From a minimum of about $0.5^\circ\text{C} / 100$ yrs in the southeastern extremity of the region, the trend increases towards the shelf and attains local maximum with the values over $1.2^\circ\text{C} / 100$ yrs in a broad zone adjacent to the continental slope, probably controlled by the Brazil Current.

The secular trend shows small local minimum near the shelf break, and then continues to grow towards the coast. Over the shelf, the warming is remarkably strong (1.2 to $1.6^\circ\text{C} / 100$ yrs) and is distributed again as a tongue-like pattern narrowing northwards. The maximum trend is observed in the areas directly adjacent to the Rio de la Plata estuary and Patos–Mirim complex mouth, suggesting that this anomalously strong secular change may be related to the influence of river runoff.

3.2. Interannual variability

Next, the secular trends were subtracted from the series of anomalies and the mean square variability was computed. The map in Fig. 2 illustrates its spatial distribution. Overall, it ranges from less than 1°C^2 to over 2.2°C^2 . In most of the deep ocean portion of the region, the overall mean square variability is between 1 and 1.6°C^2 . The variability on the shelf is higher than that in the deep part of the study area. Along the coast in the southern part of the region, the already expected tongue-like spatial pattern can be observed, which has been recurrent throughout this study. There, the SST variability attains maximum values (up to 2.3°C^2).

3.3. Variability of frontal position

A set of maps was plotted (not shown) representing the July positions of the 17°C isotherm for all individual years, in order to assess the interannual migrations of the frontal zone. Fig. 3 gives a summary of this variability. In order to prepare the figure, we first determined the overall mean position of the isotherm, shown as a bold contour labelled "3". The individual years were then grouped in two classes: if in a given year the 17° isotherm merged into the coast north of the mean position, the year was classified as "cold", otherwise it was considered "warm". Fig. 3 shows average positions of the isotherm in "cold" (contour labelled as "2") and warm (contour "4") years. The figure shows also the northernmost (year 1911, contour "1") and southernmost (year 1992, contour "5") observed positions.

The data coverage allowed to determine the front position for 104 individual years. In these years, the northernmost latitude varied with a range of more than 7 degrees of latitude, or about 1400 km of along-coast distance, from about 27.0°S (in 1911) to 34.3°S (in 1992). The mean value was 30.1°S , with standard deviation of 1.6° .

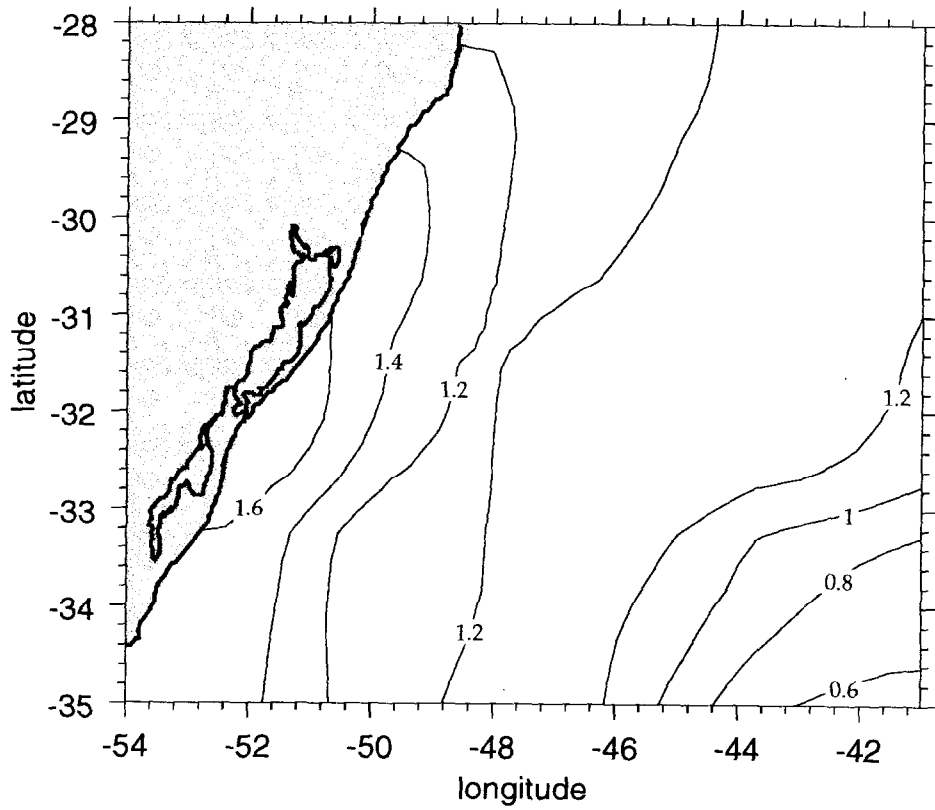


FIG. I. Secular trend of SST, °C per 100 years.

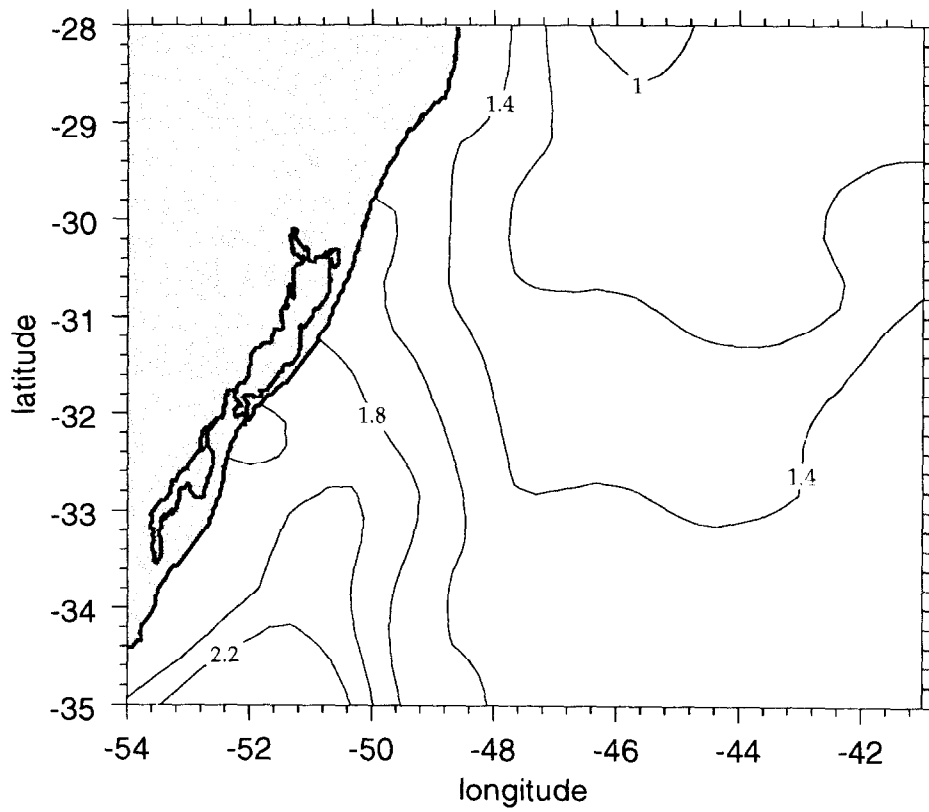


FIG. 2. Mean square variability, $^{\circ}\text{C}^2$.

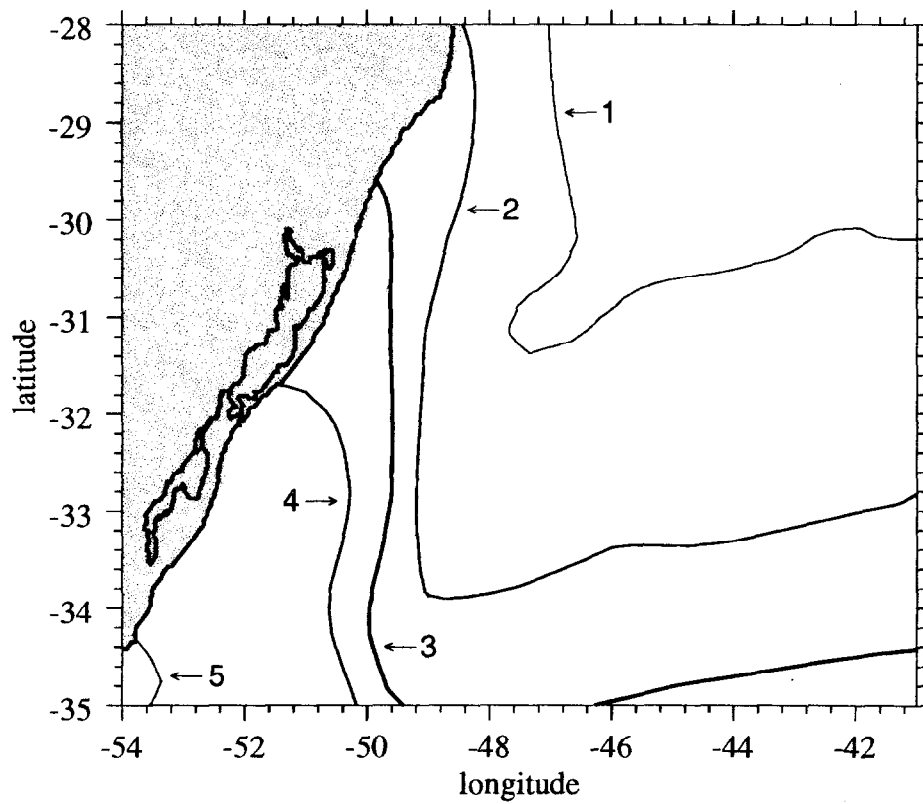


FIG. 3. Summary of interannual migrations of the frontal zone (see text for explanation).

4. Conclusions

One can divide the region into 3 areas, each area exhibiting distinct behaviour with respect to the low frequency variability.

Area 1, adjacent to the coast as a belt narrowing northwards, appears to be controlled by Plata and Patos–Mirim runoff along with invasions of subantarctic water. The interannual variations in this area are very energetic, with mean square variability ranging from 1.4 to 2.3°C². The area shows also very strong secular trend towards warming, with maximum values of up to 1.6°C per 100 years are observed near the estuaries.

Area 2, in central part of the region, may be identified as the area under the influence from the Brazil Current. The mean square variability ranges from 1 to 1.4°C², while secular trend is of 1 to 1.2°C per 100 years, i.e. smaller than observed in the area 1, but still high compared to the global average.

Area 3 in the eastern part of the region is away from the influence of either major currents or coastal discharges and therefore, as compared to the rest of the region, exhibits less energetic behaviour. It shows moderate interannual changes (mean square variability is about 1.2°C² in most part of the area) and relatively small (0.5°C to 1°C per 100 years) secular trend, comparable to global average.

References

1. Bakun, A., and R. H. Parrish, 1990. Comparative studies of coastal pelagic fish reproductive habitats: the Brazilian sardine (*Sardinella aurita*). *J. Cons. Int. Explor. Mer.*, 46, 269–283.
2. Bakun, A., and R. H. Parrish, 1991. Comparative studies of coastal pelagic fish reproductive habitats: the anchovy (*Engraulis anchoita*) of the southwestern Atlantic. *J. Marine Science*, 48, 343–361.
3. Chelton, D. B., M. G. Schlax, D. L. Witter, and J. G. Richman, 1990. Geosat altimeter observations of the surface circulation of the southern ocean. *J. Geophys. Res.*, 95, 17 877–17 903.
4. Cheney, R. E., J. G. Marsh, and B. D. Beckley, 1983. Global mesoscale variability from collinear tracks of Seasat altimetry data. *J. Geophys. Res.*, 88, 4343–4351.
5. Ciotti, A. M., C. Odebrecht, G. Fillmann, and O. O. Moller Jr, 1995. Freshwater outflow and Subtropical Convergence influence on phytoplankton biomass on the southern Brazilian continental shelf. *Continental Shelf Res.*, 15, 14, 1737–1756.
6. Gordon, A. L., 1981. South Atlantic thermocline ventilation. *Deep-Sea Research*, 28, 1239–1264.
7. Gordon, A. L., and C. L. Greengrove, 1986. Geostrophic circulation of the Brazil–Falkland confluence. *Deep-Sea Research*, 33, 5,
8. Hubold, G., 1980. Hydrography and plankton off Southern Brazil and Rio de la Plata (August – November 1977). *Atlântica*, 4, 1–78.
9. Lau, K. M., and H. Weng, 1995. Climate signal detection using wavelet transform: How to make a time series sing. *Bull. Am. Meteorol. Soc.*, 76, 2391–2402.
10. Lima, I. D., and J. P. Castello, 1995. Distribution and abundance of Southwest Atlantic anchovy spawners (*Engraulis anchoita*) in relation to oceanographic processes in the southern Brazilian shelf. *Fish. Oceanogr.*, 4, 1, 1–16.
11. Reynolds, R. W., and T. M. Smith, 1994. Improved global sea surface analyses using optimum interpolation. *J. Climate*, 7, 929–948.
12. Zavialov, P. O., R. D. Ghisolfi, and C. A. E. Garcia, 1998. An inverse model for seasonal circulation over the Southern Brazilian shelf: near-surface velocity from the heat budget. *J. Phys. Oceanogr.*, 28, 545–561.

STOLPE CHANNEL OVERFLOW IN THE BALTIC SEA: OBSERVATIONS AND MODELING

**V. M. Zhurbas¹, V. T. Paka², M.V. Anisimov¹, N. N. Golenko², M. M. Subbotina¹,
and G. A. Koshkosh¹**

¹Shirshov Institute of Oceanology, 36 Nachimovski Prospect, 117851 Moscow, Russia

²Atlantic Branch of Shirshov Institute of Oceanology, 1 Prospect Mira, 236000 Kaliningrad, Russia

E-mail: zhurbas@glasnet.ru; paka@ioran.kern.ru; mva@sio.rssi.ru; golenko@ioran.kern.ru; mms@sio.rssi.ru

Abstract

The Stolpe Channel is the deepest trench in the Baltic Proper which allows salty waters from the North Sea to penetrate eastward into relatively deep basins of the Central and Northern Baltic. We examine closely spaced CTD transects across the Stolpe Channel, measured between April 1993 and November 1996, to investigate the variability of the thermohaline structure of overflow water. When the winds are weak, moderate, or fresh, the transects show a fan-like spread of isopycnals approaching the southern slope of the channel, pinching of isopycnals approaching the northern slope, and a displacement of the densest water towards the northern slope. Under gale winds from the west-south-west, this observed fanned/pinched structure disappeared. We suggest that this feature of density field results from the Ekman transport in the bottom boundary layer provided that the overflow consists of two competitive components: a permanent density current and a variable wind-induced geostrophically-adjusted barotropic flow in the channel. A 3D numerical model of wind-driven circulation in the Stolpe Channel is developed. The model confirms the suggested driving mechanism of the fanning/pinching effect.

1. Introduction

The Stolpe Channel, or the Slupsk Furrow in Polish, is the only channel for salty North Sea water to enter the Eastern Gotland Basin and the Gdansk Basin, this basin is extremely important for deep water ventilation in the Central and Northern Baltic (see Fig. 1). The Stolpe Channel is zonally elongated and is approximately 100 km long and 30 km wide. At the Slupsk Sill, which separates it from the Bornholm Basin, the maximum depth is about 67 m. In the central part of the channel, the depth increases to 90 m, and then decreases eastward to about 75 m at a less prominent sill in the eastern part of the channel. The Stolpe Channel overflow water has a thickness of about 10 m at the western, major sill, and a density jump of about 4-5 kg m⁻³. Estimates of the mean eastward transport of salty water through the Stolpe Channel from different box-type, budget models fall in the range from 1.1×10⁴ m³ s⁻¹ [3] to 3.3×10⁴ m³ s⁻¹ [8] and (2.3-5.4)×10⁴ m³ s⁻¹ [13].

In general, the overflow through the Stolpe Channel is expected to be similar to a well-documented overflow of cold, relatively fresh, dense water from the Norwegian Sea into the North Atlantic through the Faroebank Channel [1, 5, 15]. However, there are substantial difference in scales between these two overflows. In the Faroebank Channel overflow, the depth of channel, the layer thickness, the density jump, and the transport differ by factor 13, 30, 0.1, 50 from respective estimates for the Stolpe Channel. The difference in the depth of channel is of first-order importance for the dynamics of the overflow. Salty water transport through relatively shallow Stolpe Channel depends on the wind [9], and a standard deviation of the transport due to wind forcing is expected to be about the same as the mean. Salinity in a layer of overflowing water can vary by 2 psu within a few days, notably in periods following the major inflows [2]. By contrast, the cold water overflow through the Faroebank Channel is pretty persistent: the standard deviation of along-channel current is much smaller than the mean [15].

The structure of density field in the Faroebank Channel was characterized by pinching of isopycnals observed at the left channel's wall with respect to the downstream direction for the cold water overflow [1, 5]. Johnson and Sanford [5] explained this feature of density field by a cross-channel, secondary, clock-wise circulation created by the Ekman transport in the bottom boundary layer and a cross-channel flow observed at the upper interface of the cold water. In this paper, we focus on similar phenomena observed lately in the Stolpe Channel.

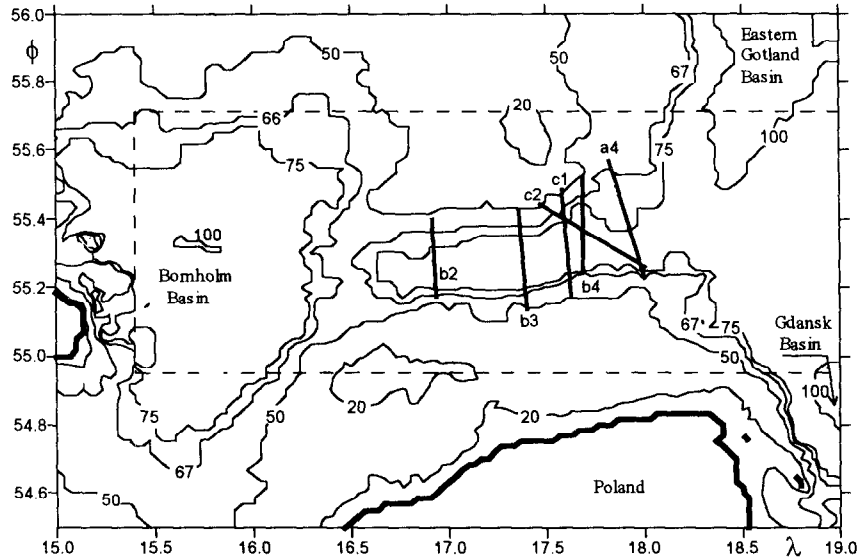


Fig. 1. Map of a part of the Baltic Sea showing the ship tracks with CTD profiling in the Stolpe Channel (bold lines) and a domain of the model (dashed rectangular).

2. Data

We will examine six closely spaced CTD transects across the eastern part of the Stolpe Channel, measured between April 1993 and November 1996. The data were obtained with a Neil Brown Instrument System Mark III CTD profiler. To achieve high horizontal resolution, the CTD profiling was carried out from a winch-driven, towed undulating vehicle. The vehicle was equipped with a freely-suspended, long, heavy chain to prevent the profiler from touching the ground. Using this technique, we were able to obtain a horizontal resolution of a few hundred meters and to obtain measurements as close as 2 m to the sea bed [14].

The ship tracks with CTD profiling are shown in Fig. 1. A transect, labeled *a4*, was made in April, 1993 (the 29th cruise of the R/V *Professor Shtockman*); the next three transects, *b2-b4*, were obtained in September 1994 (the 33rd cruise of the R/V *Professor Shtockman*); and the last two transects, *c1-c2*, were made in October-November, 1996 (the 66th cruise of the R/V *Shelf*).

The wind conditions varied during the field measurements. On April 14, 1993 (transect *a4*), the wind was from the NE at 4 to 9 m s^{-1} . On September 22-23, 1994 (transects *b2-b4*), the prevailing wind over the Stolpe Channel was from the west at 2 to 8 m s^{-1} . On 20 October 1996 (transect *c1*), the wind of 4 to 7 m s^{-1} was from the NW. Finally, on November 1, 1996 (transect *c2*), there was a gale from the WSW with wind speeds of 14-19 m s^{-1} .

3. Thermohaline structure of the overflow water

Figure 2 shows two-dimensional plots of salinity versus distance and depth for all six transects. In the halocline and the overflow (bottom) layer, the contribution of salinity to the density stratification is more than 20 times greater than that of temperature, so we will consider salinity field only.

A striking feature of all the transects but one (*c2*) is that the halocline is very narrow (pinched) in the northern part of the channel and widens to the south producing a picturesque fan-like image. The densest and saltiest water in the channel is not located at the deepest depths of the channel, but is found on the northern slope of the channel. For brevity, this triple effect (pinching and fanning of isopycnals at opposite channel sides, and the displacement of the densest water towards the side with pinched isopycnals) is referred to as the fanning/ pinching effect. The sole exception is the *c2* transect, which was obtained under a gale south-westerly wind.

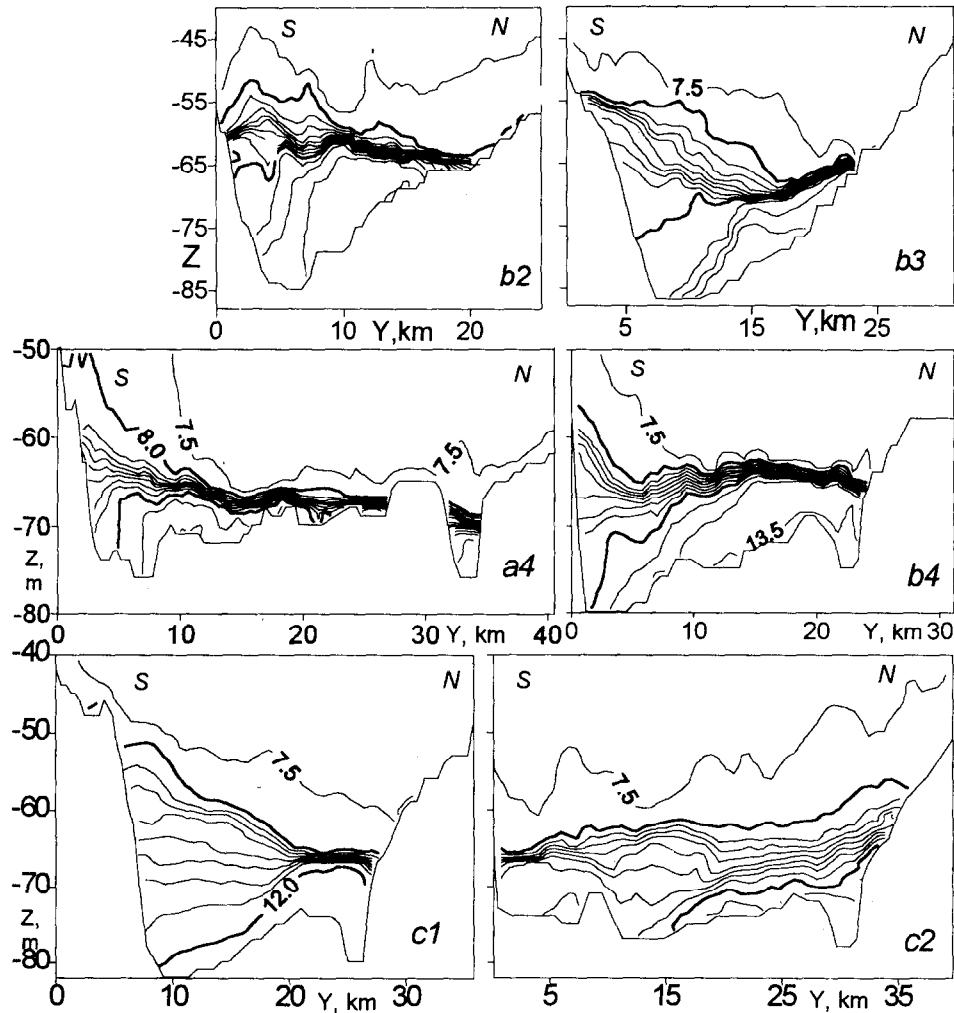


Fig. 2. Salinity vs. distance and depth in the transects across the Stolpe Channel.

From the data shown in Fig. 2, we infer that the fanning/pinching effect exists permanently in the eastern part of the Stolpe Channel in low to fresh winds of any direction, and disappears under gales from the west-south-west. Objectives of this paper is to answer the following questions: 1) what are the likely dynamics of fanning/pinching phenomenon?; and 2) why was the phenomenon observed under weak to fresh winds of any direction but not observed under a west-south-west gale?

Actually an explanation of similar phenomenon observed in the Faroebank Channel been already done by Johnson and Sanford [5]. They observed a very sharp, pinched in density interface between the cold overflow water and the water above near the southwest wall of the Faroebank Channel (i.e., by the left wall with respect to the downstream direction of the outflow). The isopycnals spread to the northwest, i.e., approaching the right wall of the channel. Measurements of vertical profiles of the current showed a well defined Ekman transport in the bottom boundary layer (BBL) to the southeast here. A flow of similar magnitude but to the southwest was found at the interface. The shear at the interface was sufficiently strong to overcome the stratification and generate shear instabilities. Hence, on the basis of these data, Johnson and Sanford [5] suggested that pinching

of isopycnals near the southwest wall was present owing to upwelling of the Ekman flow in the BBL, while the isopycnals spread to the northeast owing to mixing through shear instabilities at the interface.

According to [5], two different mechanisms are responsible for the fanning/pinching effect observed in the Faroebank Channel overflow: the bottom friction in rotating fluid and enhanced mixing at the interface between the overflow water and the water above. Observing a similar fanning/pinching effect in the Stolpe Channel we are not sure that both these mechanisms do work here. Namely, we have some doubt whether the fan-like spread of isopycnals towards the southern wall of the Stolpe Channel is due to shear instabilities at the interface. We suggest that both pinching and fanning of isopycnals as well as the displacement of the densest water towards the "pinched" wall of the channel can be produced by the Ekman transport in the BBL solely.

In order to understand why the fanned/pinched structures were observed in the channel regardless of the wind direction, provided that the wind velocity is not too high, the following consideration could be applied. The overflow can be considered as a superposition of a climate, long-term eastward component, and a synoptic, wind-driven component of variable direction and intensity. At slow to fresh winds, the long-term component dominates, so overflow water is moving towards the east, producing the fanning/pinching pattern of isopycnals. At southerly and westerly gales, as in the *c2* transect, the wind-driven component of circulation dominates, and, being directed to the west, destroys the fanning/pinching structure and even can produce the reverse structure with pinching by the southern wall and fanning by the northern wall.

To examine the effect of wind on the structure of overflow water in the Stolpe Channel we apply to numerical modeling.

4. Numerical modeling

In the last decade, the most popular tool for the Baltic Sea circulation modeling was a free surface version of the GFDL ocean circulation model [6] which is based on the Brian-Cox-Semtner code developed at the Princeton University. In this model, turbulence is considered as viscosity for momentum and diffusion for temperature and salinity, and the coefficients of turbulent viscosity and diffusion are prescribed as a given function of vertical coordinate. This model has been used for different aspects of Baltic Sea studies [3, 10, 16].

The rigid lid version of the model was used by Krauss and Brüggel [9] to learn the wind-produced water exchange between deep basins of the Baltic Sea. The model predicted the eastward transport in the lower layers of the Stolpe Channel for northerly and easterly winds, and the opposite, westward transport for southerly and westerly winds. Note that the model [5] did not consider a long-term climate component of salty water overflow in the Stolpe Channel originated from the North Sea.

Following [5] we focus on numerical modeling of wind-driven circulation in the Stolpe Channel. The present modeling is based on a 3D, primitive equation, numerical ocean model created in the Princeton University by Blumberg and Mellor [11]. It is a σ -coordinate model in that the vertical coordinate is scaled on the water column depth. The vertical component of momentum is treated by the hydrostatic approach which filters out short internal gravity waves. The model has a free surface and a split time step. It contains an embedded second moment turbulence closure based on hypotheses by Rotta and Kolmogorov extended to stratified flow cases [12]. The latter is a great advantage of this model with respect to the GFDL model provided that one is interested in adequate description of turbulent bottom boundary layer. To describe the bottom stress, the logarithmic boundary layer hypothesis is applied which reduces a bottom boundary condition for the momentum equations to prescribing the roughness parameter.

The selected model domain covered an area 15.4°-19.0°E, 54.95°-55.71°N, or 228.0×84.5 km (see Fig. 1 where the model area is marked by a dashed line). This area includes the whole Stolpe Channel, the main body of the Bornholm Basin, and a part of the Gotland/Gdansk Basin of about the same space as that of the Bornholm Basin. The bottom topography is taken from [17]. Horizontal grid steps are chosen at 6.33 km and 2.22 km in x and y directions (eastward and northward respectively). Such steps yield reasonably good resolution of the Stolpe Channel geometry. To achieve a fine vertical resolution in the bottom boundary layer we use a variable step in σ -coordinate from 10% of the water column near the sea surface to 2% of the water column near the bottom. The model grid has altogether 37×39×20 points, so the calculations can be performed using an ordinary PC Pentium. To avoid the problem of open lateral boundary conditions we set an artificial coastline at lateral boundaries of the model domain. Despite the artificial coastline can generate some changes in the structure of

currents in the channel it does not seem critical if one intends to learn which currents are favorable for the development of fanning/pinching effect.

As to the initial conditions, a horizontally uniform initial distribution of temperature and salinity within the whole model domain is applied, and respective vertical profiles are taken from CTD measurements in the Bornholm Basin in April 2, 1993 at 15°59'E, 55°14'N [4]. Zero heat/salt fluxes are applied at the sea surface and the sea bottom. The roughness parameter, z_* , is taken at 1 cm. The model runs are performed at different magnitudes of a steady, horizontally uniform wind forcing described by the surface wind stress vector (τ_x, τ_y) .

Fig. 3 is an example of numerical computation of the wind-driven overflow of salty water in the channel. The easterly wind induces geostrophically-balanced eastward flow of salty water in the channel. Therefore, the bottom Ekman transport is to the north, producing the convergence (divergence) of secondary circulation at the northern (southern) walls of the channel, and as a consequence, the fanning/pinching of the isopycnals. The wind of opposite direction (from the west) produces the reverse pattern of fanning and pinching, just as it was observed under a westerly gale (see Fig. 2, c2).

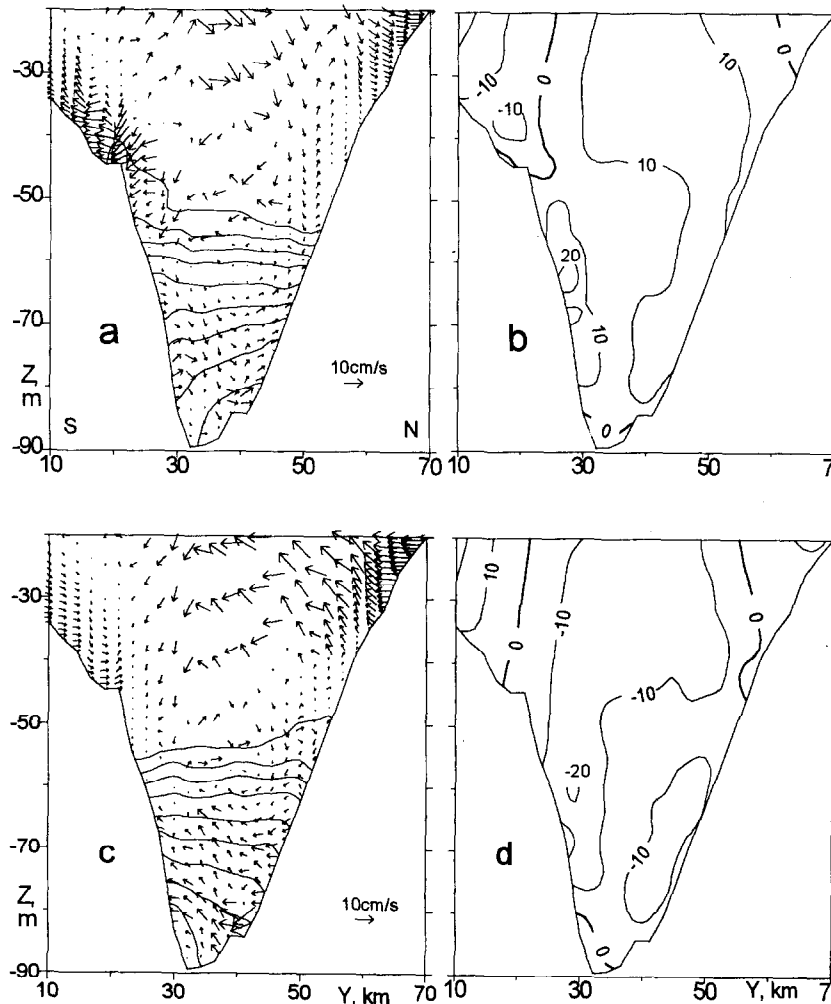


Fig. 3. Contours of along-channel component of the current (b, d), and vectors of cross-channel components of the current imposed on isopycnals (a, c) for 17.4°E transect. Top: $\tau_x = -0.5 \text{ kg m}^{-1} \text{ s}^{-2}$, $t = 1 \text{ day}$ (easterly wing); Bottom: the same as top panels but for the westerly wind ($\tau_x = 0.5 \text{ kg m}^{-1} \text{ s}^{-2}$).

It is worth noting that the model does not show a significant shear at the interface between the overflow water and the water above which could produce widening of isopycnals due to mixing through shear instability as it was suggested in the case of the Faroebank Channel outflow [5].

Because the model is capable to describe the wind-driven circulation only, it is reasonable to compare the modeled volume rates of salty water overflow with respective climate estimates cited above. We define the overflow water as the water with density of 1007 kg m^{-3} (respective value of salinity is about 8.8) or more. Then, using the x -component of current at the 17.4°E transect taken from the model runs we can calculate V , the volume rate of overflow water through the channel. Such calculation was done for $t = 1, 2, 3$ day and $\tau_x = -0.1, -0.2, -0.3, -0.5, -1.0 \text{ kg m}^{-1}\text{s}^{-2}$. Runs of the model under these values of steady wind stress show that V varies within 20% for a period of 1-3 days, and it makes possible to calculate V_m , a time-averaged value of V . The volume rate of wind-driven overflow increases about linearly with the wind stress: the linear log-log regression yields a dependence

$$V_m = 1.13 \times 10^5 |\tau_x|^{0.79}, \quad (1)$$

where V_m is in m^3s^{-1} , and τ_x is in $\text{kg m}^{-1}\text{s}^{-2}$. In accordance with (1), V_m varies from 1.83×10^4 to $1.13 \times 10^5 \text{ m}^3\text{s}^{-1}$ with the increase of wind stress from 0.1 to $1.0 \text{ kg m}^{-1}\text{s}^{-2}$ (respective range of the wind velocity is from 8 to 16 m s^{-1}) [7]. Taking a value of $5 \times 10^4 \text{ m}^3\text{s}^{-1}$ as the upper estimate for the climate (presumably density-driven) eastward transport of salty water in the Stolpe Channel we found from (1) that the overflow of the same volume rate can be driven by applying the easterly wind stress of $0.36 \text{ kg m}^{-1}\text{s}^{-2}$ (equivalent wind velocity is about 13 m s^{-1}). Hence we may assume that the opposite, westerly wind of the same or higher value of stress will be able to destroy the fanned/pinched structure of isopycnals in the channel, as it was observed in transect $c2$ (Fig.2).

Acknowledgments

This research was made possible in part by grants 97-05-65381 from the Russian Foundation for Basic Research and the Joint German - Russian Programme for the Baltic Sea Research.

References

- [1] Borenäs, K. M., and P. A. Lundberg, 1988, On the deep-water flow through the Faroe Bank Channel, J. Geophys. Res., **93**, 1281-1292.
- [2] Dahlin, H., S. Fosnelius, and B. Sjöberg, 1993, The changes in the hydrographic conditions in the Baltic proper due to inflow to the Baltic Sea, paper presented at Statutory Meeting of International Council for Exploration of Sea, Int. Council. for the Explor. of the Sea, Dublin, Ireland, Sept. 23 to Oct. 1.
- [3] Elken, J. (Ed.), 1996, Deep water overflow, circulation and vertical exchange in the Baltic Proper, 91 pp., Estonian Marine Institute Report Series, No. 6, Tallinn.
- [4] Grelowski, A., and T. Wojewódski, 1993, Distribution of highly saline waters observed in April 1993 - After the inflow into the Southern Baltic, paper presented at Statutory Meeting of International Council for Exploration of Sea, Int. Council. for the Explor. of the Sea, Dublin, Ireland, Sept. 23 to Oct. 1.
- [5] Johnson, G. C., and T. B. Sanford, 1992, Secondary Circulation in the Faroe Bank Channel Outflow, J. Phys. Oceanogr., **22**, 927-933.
- [6] Killworth, P., D. D. Stainforth, D. J. Webbs, and S. M. Paterson, 1989, A free surface Bryan-Cox-Semtner model, Rep. 270, 184 pp., Deacon Laboratory, Institute of Oceanographic Sciences, UK.
- [7] Kitaigorodskii, S. A., 1970, Physics of atmosphere-ocean interaction, (in Russian), 284 pp., Gidrometeoizdat, Leningrad.
- [8] Köuts, T., and A. Omstedt, 1993, Deep water exchange in the Baltic Proper, Tellus, **45A**, 311-324.
- [9] Krauss, W., B. Brüggel, 1991, Wind-produced water exchange between the deep basins of the Baltic Sea. J. Phys. Oceanogr. **21**(3), 373-384.
- [10] Lehmann, A., 1994, A model study of major Baltic inflows, Proceedings of the 19th Conference of the Baltic Oceanographers, Sopot 1994, Sopot, Poland, 410-421.
- [11] Mellor, G. L., 1993, Users guide for a three-dimensional, primitive equation, numerical ocean model, Tech. Rep., 35 pp., Atmospheric and Oceanic Sciences Program, Princeton University, Princeton, NJ.

- [12] Mellor, G. L., and T. Yamada, 1982, Development of a turbulence closure model for geophysical fluid problems, Rev. Geophys. Space Phys., 20, 851-875.
- [13] Pedersen, Bo F., 1977, On dense bottom currents in the Baltic deep water, Nordic Hydrology, 297-316.
- [14] Paka, V. T., 1996, Thermohaline structure in the Stolpe Furrow of the Baltic Sea in the spring 1993. Oceanology, Engl. Transl., 36(2), 201-217.
- [15] Saunders, P.M., 1990, Cold outflow from the Faroe Bank Channel, J. Phys. Oceanogr., 20, 29-43.
- [16] Seifert, T., and W. Fennel, 1994, Numerical experiments in the transition area between Baltic Sea and North Sea, Proceedings of the 19th Conference of the Baltic Oceanographers, Sopot 1994, Sopot, Poland, 422-437.
- [17] Seifert, T., and B. Kayser, 1995, A high resolution spherical grid topography of the Baltic Sea, Meereswissenschaftliche Berichte, Marine Science Reports, Institut für Ostseeforschung Warnemünde, Germany.

YEAR-TO-YEAR CHANGES OF DENSE BOTTOM WATER SPREADING IN PETER THE GREAT BAY SHELF (THE JAPAN SEA) AND POSSIBILITY OF CASCADING

Yu.I. Zuenko

Pacific Fisheries Research Center (TINRO-Center), Shevchenko Alley, 4, Vladivostok 690600;
Russia

E-mail: root@tinro.marine.su

Distribution of cold bottom water over the shelf of Peter the Great Bay was investigated by the data of water temperature at the bottom obtained in winter and spring of 1960-1991. Very cold (usually below -1 C) bottom water mass forms here in winter and in some years it approaches the shelf edge. Episodic salinity measurements display the high salinity (> 34.2 psu) of this water, so its density is enough for cascading down the continental slope. Ice freezing is suspected as mechanism of this water formation. Maximal spreading of the cold water is observed in February-March usually. Approximately in a half of winters the cold water approaches the edge of Peter the Great Bay shelf. It happens in two points usually: southward off Gamov Cape (western part of the Bay) and in the central part of the Bay where a canyon had been found. The year-to-year deviation of the cold water spreading from climatic boundaries shows periods of predominance of extremely vast / minimal spreading. The cascading was possible in 1965-1966, 1977-1979, and especially in 1983-1986 when the spreading was vast. During long periods in early 70-ies and in 90-ies the cold water spreading was insignificant so cascading was impossible. This conclusion is confirmed by recent studies of the bottom water in the Japan Sea basins, which have showed cessation of renovation in the last decade.

Coastal Ocean Workshop

What is the reason of active ventilation of the Japan Sea deep and bottom layers? Some authors (as [1, 4], and others) suggest that a dense water forms in winter on Primorye shelf. Indeed, in Peter the Great Bay we have found very cold and salted water (the Bottom Shelf Water = BSW) with the density higher than 27.4 at the bottom (Fig.1) that had be able to sink to the deepest layers of the Sea. As any water mass, the BSW is limited by front that is especially sharp in the field of temperature. This fact allows us to use the data of rather frequent temperature observations from the last 3 decades (since 1960 to 1991) for investigation of year-to-year changes of this dense water spreading and to determine the possibility of cascading as the hypothetical process of its sinking along the continental slope.

Although the BSW could be traced in the field of temperature, it is important that it isn't formed by thermal convection, but by ice-freezing, other words, it is a brine. The intensity of the brine formation depends on complex of hydrometeorological parameters during the freezing and before it [7]. The most important conditions favorable for intensive formation of the densest BSW are: shallow water (with low heat content), high initial salinity of freezing water, low temperature during freezing, and strong off-shore wind (that leads to repeated or permanent freezing).

Climatic positions of the front that limits the BSW for every 10-days period during January-April are presented at Fig.2. The BSW locates in inner part of the bay in January – early February, then (from middle of February to middle of March) it approaches to the shelf edge, but later, in spring, it forms a cold spot in the central area of the Bay with flat bottom where disappears gradually. There are two places where the BSW is closer to the shelf edge: southward off Gamov Cape (western part of the Bay) and in the central part of Peter the Great Bay where a canyon had been found. In both places the BSW doesn't reach the shelf edge usually, but in severe years it does. An example of vast spreading of the BSW is presented at Fig.3: in 1983 it reached the shelf edge in the western part of the Bay, especially at two underwater canyons.

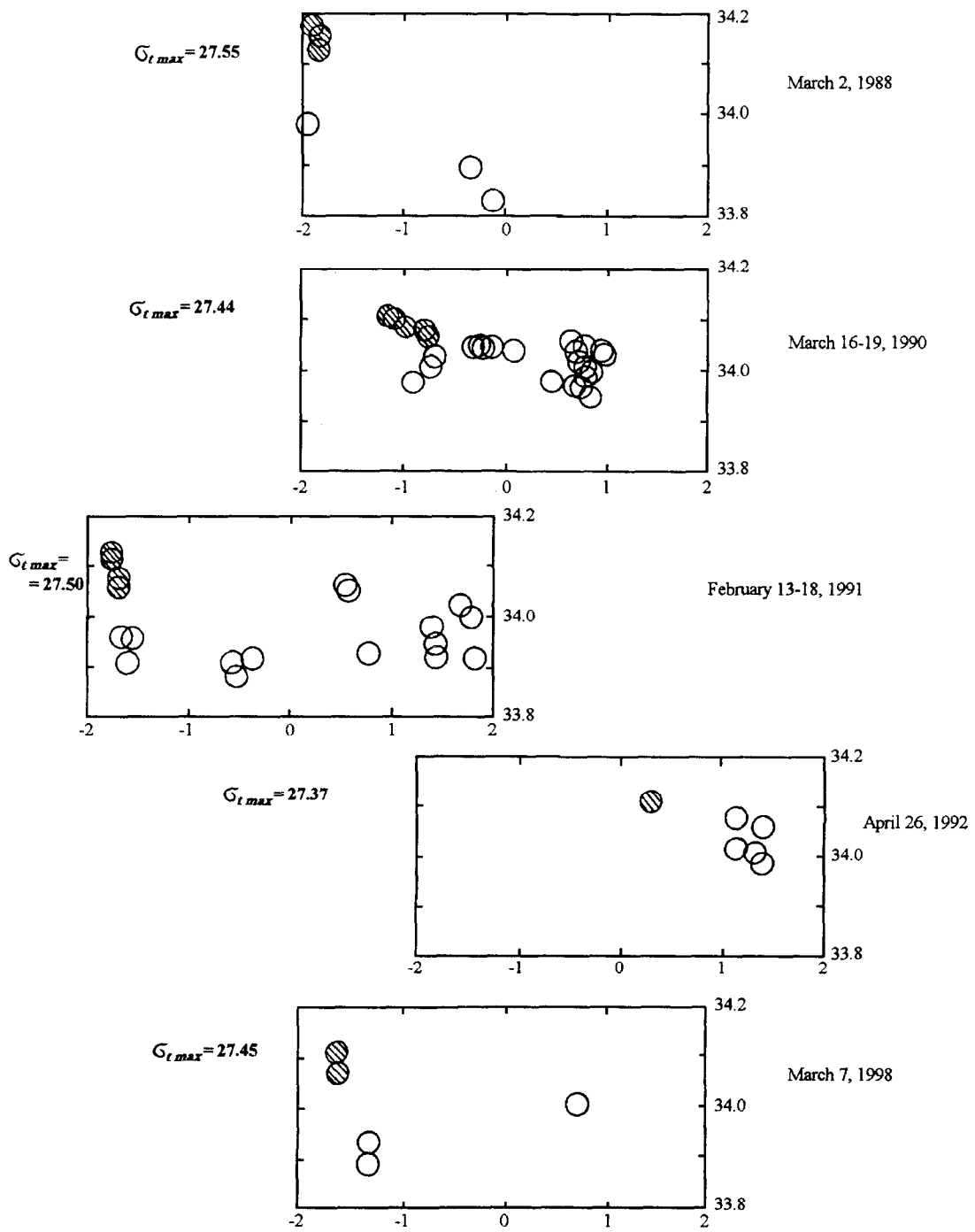


Fig.1. Temperature-salinity scattering diagram of near-bottom layer in Peter the Great Bay for several winter surveys in the last decade. Stations with very cold, salted, and dense Bottom Shelf Water (able to cascading) are shaded.

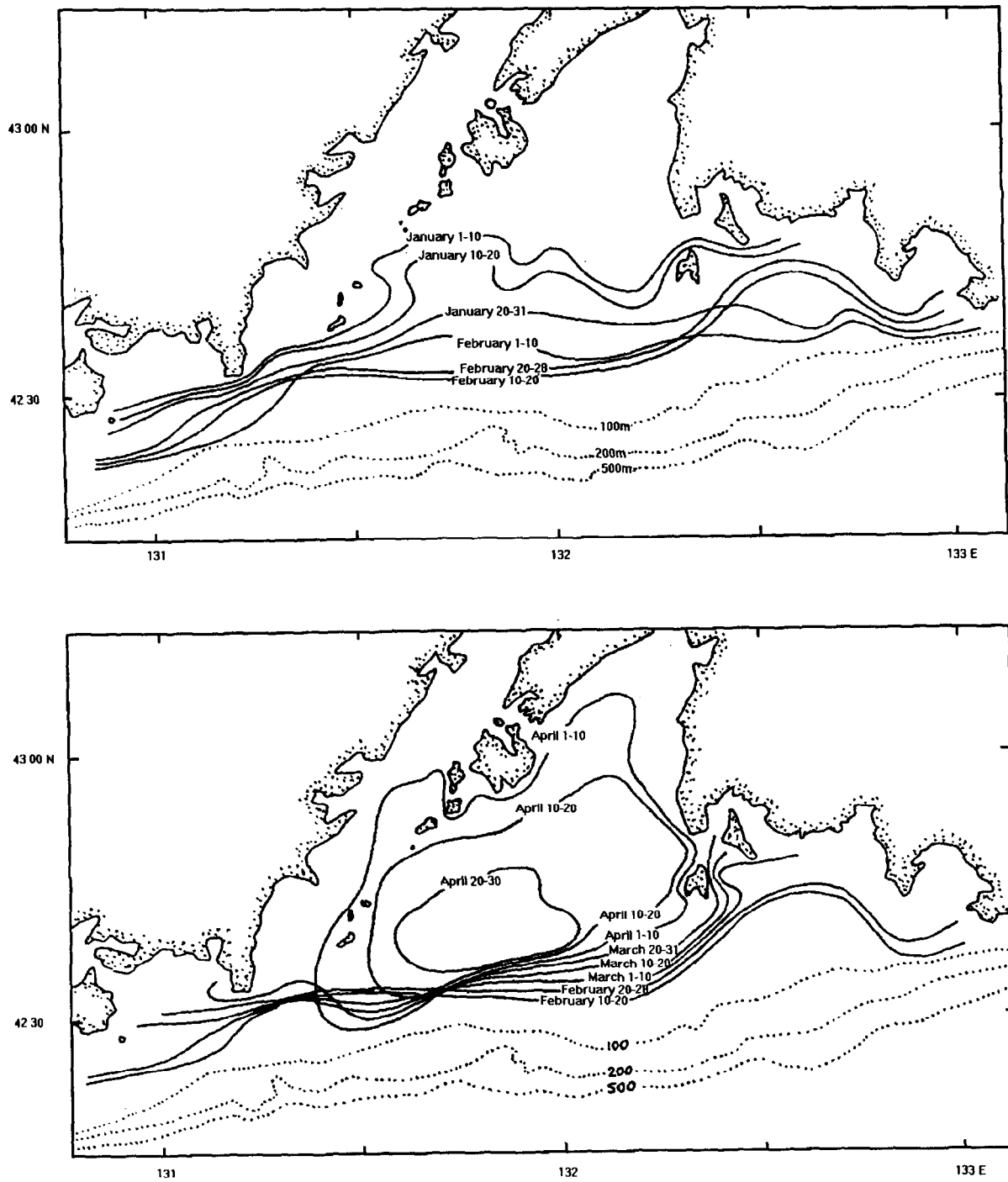


Fig.2. Climate spreading of very cold and dense Bottom Shelf Water at the bottom of Peter the Great Bay in January-February (up) and February-April (down) determined by averaging the data of 1960-1991.

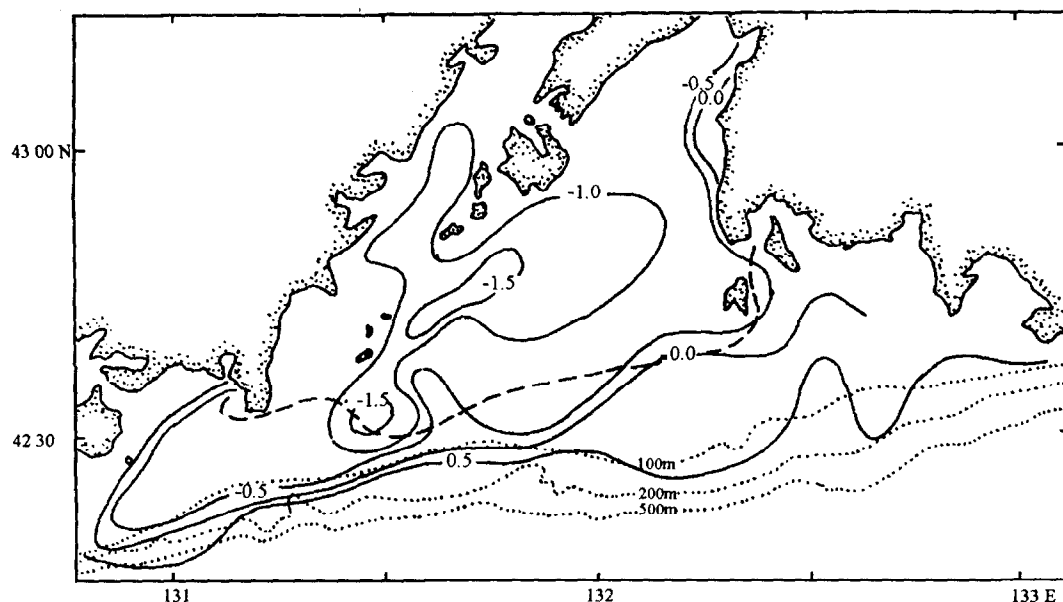


Fig.3. Distribution of temperature at the bottom when vast spreading of the Bottom Shelf Water in March 21-29 of 1983 (R/V "Omar"). Dotted line is the climate boundary of the BSW in late March.

So, cascading and deep ventilation are possible in February-March of certain severe years in the western and central parts of Peter the Great Bay. Unfortunately, we have no any observations of the process of cascading. Usually even in the areas of the BSW approaching to the shelf edge the slope is occupied by less dense (relatively warm and low salted) water, as it was observed in March of 1998 (Fig.4). During 1960-1991 there were 3 periods of wide spreading of the BSW (Fig.5): in the middle of 60-ies, in early 70-ies, and especially in 80-ies, where in 1986 and 1988 the vast spreading had coincide with abnormally low temperature that lead to the highest values of specific density of the BSW up to 27.55. Since that time, during a decade, there weren't any evidences of the BSW approaching to the shelf edge, thus, any chances of cascading and deep ventilation by this mechanism, till 1998, when cascading was possible.

The last decade was the time of detailed study of the process of deep ventilation of the Japan Sea, and a conclusion was formed on cessation of bottom water renovation [3, 5, 6] and even on re-construction of water structure of the Japan Sea [2]. The absence of cascading could be regarded as possible, perhaps the main important reason of the bottom water warming and deoxidization, and the cascading itself – as the important process of the Japan Sea ventilation.

References

1. T.Gamo, Y.Nosaki, H.Sakai, T.Nakai, and H.Tsubota, 1986, Spatial and temporal variations of water characteristics in the Japan Sea bottom layer, *J.Mar.Res.*, 44, N 4, 781-793.
2. K.-R.Kim, K.Kim, and M.-K.Park (in print), What is happening in the East Sea (Japan Sea)?: recent chemical observations during CREAMS 93-96, *J.Korean Soc.Oceanogr.*
3. S.Minobe, 1996, Interdecadal temperature variation of Deep Water in the Japan Sea (East Sea), *Proc.4th CREAMS Workshop, Vladivostok (Russia)*, 81-88.
4. H.Nitani, 1972, On the deep and the bottom waters in the Japan Sea, *Researches in Hydrography and Oceanography*, Tokyo: Hydrogr.Dep.Japan, 151-201.
5. V.I.Ponomarev and A.N.Salyuk, 1997, The climate regime shifts and heat accumulation in the Sea of Japan, *Proc.CREAMS'97 Int.Symp., Fukuoka (Japan)*, P.157-161.
6. V.I.Ponomarev, A.N.Salyuk, and A.S.Bychkov, 1996, The Japan Sea water variability and ventilation processes, *Proc.CREAMS 4th Workshop, Vladivostok (Russia)*, 63-70.
7. V.I.Ponomarev, G.I.Yurasov, and Yu.I.Zuenko, 1991, High salinity bottom water generation on the Japan Sea continental shelf, *Abst.6th JECSS Workshop, Fukuoka (Japan)*, 84.

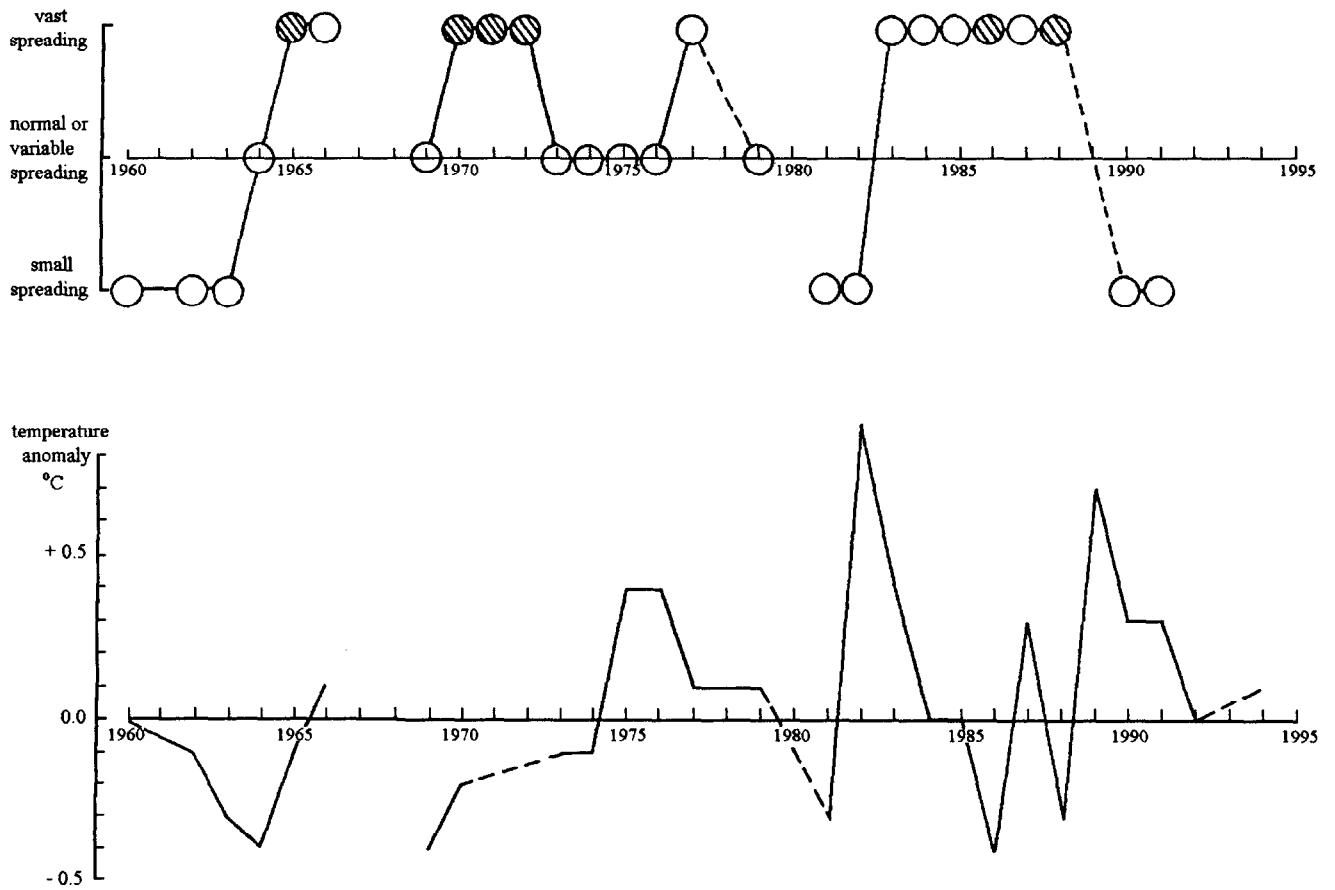


Fig.4. Year-to-year changes of the spreading of very cold and dense Bottom Shelf water at the bottom of Peter the Great Bay (up) and its mean temperature anomalies (down). The years are shaded when cascading has possible (vast spreading + low temperature).

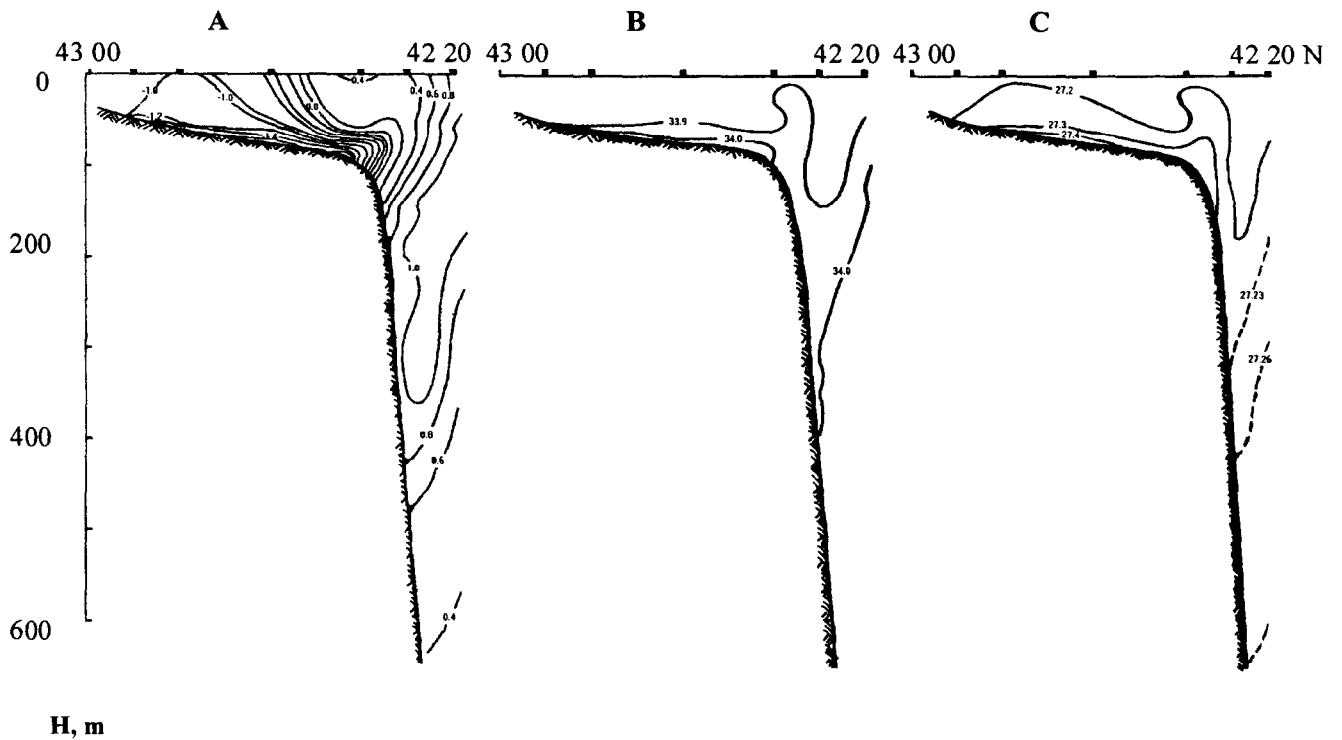


Fig.5. Temperature (A), salinity (B), and specific density (C) on cross-shelf section along 132 N in March 7, 1998 (R/V "Shursha").

IOC Workshop Reports

The Scientific Workshops of the Intergovernmental Oceanographic Commission are sometimes jointly sponsored with other intergovernmental or non-governmental bodies. In most cases, IOC assures responsibility for printing, and copies may be requested from:

Intergovernmental Oceanographic Commission – UNESCO
1, rue Miollis, 75732 Paris Cedex 15, France

No.	Title	Languages	No.	Title	Languages	No.	Title	Languages
1	CCOP-IOC, 1974, Metallogenesis, Hydrocarbons and Tectonic Patterns in Eastern Asia (Report of the IDOE Workshop on); Bangkok, Thailand, 24-29 September 1973 UNDP (CCOP).	E (out of stock)	16	Workshop on the Western Pacific, Tokyo, 19-20 February 1979.	E, F, R	32	Papers submitted to the UNU/IOC/ UNESCO Workshop on International Co-operation in the Development of Marine Science and the Transfer of Technology in the Context of the New Ocean Regime; Paris, France, 27 September-1 October 1982.	E
2	ICAR Ichthyoplankton Workshop, Mexico City, 16-27 July 1974 (UNESCO Technical Paper in Marine Sciences, No. 20).	E (out of stock) S (out of stock)	17	Joint IOC/WMO Workshop on Oceanographic Products and the IGOS Data Processing and Services System (IPSS); Moscow, 9-11 April 1979.	E	33	Workshop on the IREP Component of the IOC Programme on Ocean Science in Relation to Living Resources (OSLR); Halifax, 26-30 September 1983.	E
3	Report of the IOC/GFCM/ICSEM International Workshop on Marine Pollution in the Mediterranean; Monte Carlo, 9-14 September 1974.	E, F E (out of stock)	17	Papers submitted to the Joint IOC/WMO Seminar on Oceanographic Products and the IGOS Data Processing and Services System; Moscow, 2-6 April 1979.	E	34	IOC Workshop on Regional Co-operation in Marine Science in the Central Eastern Atlantic (Western Africa); Tenerife, 12-17 December 1963.	E, F, S
4	Report of the Workshop on the Phenomenon known as 'El Niño'; Guayaquil, Ecuador, 4-12 December 1974.	E (out of stock) S (out of stock)	18	IOC/UNESCO Workshop on Syllabus for Training Marine Technicians; Miami, U.S.A., 22-26 May 1978 (UNESCO reports in marine sciences, No. 4 published by the Division of Marine Sciences, UNESCO).	E (out of stock), R (out of stock), U (out of stock)	35	CCOP/SOPAC-IOC-UNU Workshop on Basic Geoscientific Marine Research Required for Assessment of Minerals and Hydrocarbons in the South Pacific; Suva, Fiji, 3-7 October 1983.	E
5	IDOE International Workshop on Marine Geology and Geophysics of the Caribbean Region and its Resources; Kingston, Jamaica, 17-22 February 1975.	E (out of stock) S	19	IOC Workshop on Marine Science Syllabus for Secondary Schools; Llantwit Major, Wales, U.K., 5-9 June 1978 (UNESCO reports in marine sciences, No. 5, published by the Division of Marine Sciences, UNESCO).	E (out of stock), S, R, Ar	36	IOC/FAO Workshop on the Improved Uses of Research Vessels; Lisbon, Portugal, 28 May-2 June 1984.	E
6	Report of the CCOP/SOPAC-IOC IDOE International Workshop on Geology, Mineral Resources and Geophysics of the South Pacific; Suva, Fiji, 1-6 September 1975.	E	20	Second CCOP-IOC Workshop on IDOE Studies of East Asia Tectonics and Resources; Bandung, Indonesia, 17-21 October 1978.	E	36	Papers submitted to the IOC/FAO Workshop on the Improved Uses of Research Vessels; Lisbon, 28 May-2 June 1984.	E
7	Report of the Scientific Workshop to Initiate Planning for a Co-operative Investigation in the North and Central Western Indian Ocean, organized within the IDOE under the sponsorship of IOC/FAO (IOFC)/UNESCO/ EAC; Nairobi, Kenya, 25 March-2 April 1976.	E, F, S, R	21	Second IDOE Symposium on Turbulence in the Ocean; Liège, Belgium, 7-18 May 1979.	E, F, S, R	37	IOC/UNESCO Workshop on Regional Co-operation in Marine Science in the Central Indian Ocean and Adjacent Seas and Gulfs; Colombo, 8-13 July 1985.	E
8	Joint IOC/FAO (IPFC)/UNEP International Workshop on Marine Pollution in East Asian Waters; Penang, 7-13 April 1976.	E (out of stock)	22	Third IOC/WMO Workshop on Marine Pollution Monitoring; New Delhi, 11-15 February 1980.	E, F, S, R	38	IOC/ROPME/UNEP Symposium on Fate and Fluxes of Oil Pollutants in the Kuwait Action Plan Region; Basrah, Iraq, 8-12 January 1984.	E
9	IOC/CMG/SCOR Second International Workshop on Marine Geoscience; Mauritius 9-13 August 1976.	E, F, S, R	23	WESTPAC Workshop on the Marine Geology and Geophysics of the North-West Pacific; Tokyo, 27-31 March 1980.	E, R	39	CCOP (SOPAC)-IOC-IFREMER-ORSTOM Workshop on the Uses of Submersibles and Remotely Operated Vehicles in the South Pacific; Suva, Fiji, 24-29 September 1985.	E
10	IOC/WMO Second Workshop on Marine Pollution (Petroleum) Monitoring; Monaco, 14-18 June 1976.	E, F E (out of stock) R	24	WESTPAC Workshop on Coastal Transport of Pollutants; Tokyo, Japan, 27-31 March 1980.	E (out of stock)	40	IOC Workshop on the Technical Aspects of Tsunami Analysis, Prediction and Communications; Sidney, B.C., Canada, 29-31 July 1985.	E
11	Report of the IOC/FAO/UNEP International Workshop on Marine Pollution in the Caribbean and Adjacent Regions; Port of Spain, Trinidad, 13-17 December 1976.	E, S (out of stock)	25	Workshop on the Inter-calibration of Sampling Procedures of the IOC/ WMO UNEP Pilot Project on Monitoring Background Levels of Selected Pollutants in Open-Ocean Waters; Bermuda, 11-26 January 1980.	E (Superseded by IOC Technical Series No.22)	40	First International Tsunami Workshop on Tsunami Analysis, Prediction and Communications, Submitted Papers; Sidney, B.C., Canada, 29 July-1 August 1985.	E
11 Suppl.	Collected contributions of invited lecturers and authors to the IOC/FAO/UNEP International Workshop on Marine Pollution in the Caribbean and Adjacent Regions; Port of Spain, Trinidad, 13-17 December 1976.	E (out of stock), S	26	IOC Workshop on Coastal Area Management in the Caribbean Region; Mexico City, 24 September- 5 October 1979.	E, S	41	First Workshop of Participants in the Joint FAO/IOC/WHO/IAEA/UNEP Project on Monitoring of Pollution in the Marine Environment of the West and Central African Region (WACAF/2); Dakar, Senegal, 28 October- 1 November 1985.	E
12	Report of the IOC/ARIBE Interdisciplinary Workshop on Scientific Programmes in Support of Fisheries Projects; Fort-de-France, Martinique, 28 November-2 December 1977.	E, F, S	27	CCOP/SOPAC-IOC Second International Workshop on Geology, Mineral Resources and Geophysics of the South Pacific; Nouméa, New Caledonia, 9-15 October 1980.	E	43	IOC Workshop on the Results of MEDALPEX and Future Oceanographic Programmes in the Western Mediterranean; Venice, Italy, 23-25 October 1985.	E
13	Report of the IOC/ARIBE Workshop on Environmental Geology of the Caribbean Coastal Area; Port of Spain, Trinidad, 16-18 January 1978.	E, S	28	FAO/IOC Workshop on the effects of environmental variation on the survival of larval pelagic fishes. Lima, 20 April-5 May 1980.	E	44	IOC-FAO Workshop on Recruitment in Tropical Coastal Demersal Communities; Ciudad del Carmen, Campeche, Mexico, 21-25 April 1986.	E (out of stock) S
14	IOC/FAO/WHO/UNEP International Workshop on Marine Pollution in the Gulf of Guinea and Adjacent Areas; Abidjan, Côte d'Ivoire, 2-9 May 1978.	E, F	29	WESTPAC Workshop on Marine Biological Methodology; Tokyo, 9-14 February 1981.	E	44	IOC-FAO Workshop on Recruitment in Tropical Coastal Demersal Communities, Submitted Papers; Ciudad del Carmen, Campeche, Mexico, 21-25 April 1986.	E
15	CPPS/FAO/IOC/UNEP International Workshop on Marine Pollution in the South-East Pacific; Santiago de Chile, 6-10 November 1978.	E (out of stock)	30	International Workshop on Marine Pollution in the South-West Atlantic; Montevideo, 10-14 November 1980.	E (out of stock) S	45	IOC/ARIBE Workshop on Physical Oceanography and Climate; Cartagena Colombia, 19-22 August 1986.	E
			31	Third International Workshop on Marine Geoscience; Heidelberg, 19-24 July 1982.	E, F, S			
			32	UNU/IOC/UNESCO Workshop on International Co-operation in the Development of Marine Science and the Transfer of Technology in the context of the New Ocean Regime; Paris, France, 27 September-1 October 1982.	E, F, S			

No.	Title	Languages	No.	Title	Languages	No.	Title	Languages
6	Reunión de Trabajo para Desarrollo del Programa "Ciencia Oceánica en Relación a los Recursos No Vivos en la Región del Atlántico Sud-occidental". Porto Alegre, Brazil, 7-11 de abril de 1986.	S	65	Second IOC Workshop on Sardine/Anchovy Recruitment Project (SARP) in the Southwest Atlantic; Montevideo, Uruguay, 21-23 August 1989.	E	85	IOC Workshop on Coastal Oceanography in Relation to Integrated Coastal Zone Management; Kona, Hawaii, 1-5 June 1992.	E
17	IOC Symposium on Marine Science in the Western Pacific: The Indo-Pacific Convergence; Townsville, 1-6 December 1986	E	66	IOC ad hoc Expert Consultation on Sardine/Anchovy Recruitment Programme; La Jolla, California, U.S.A., 1989	E	86	International Workshop on the Black Sea; Varna, Bulgaria, 30 September - 4 October 1991	E
18	IOCARIBE Mini-Symposium for the Regional Development of the IOC-UN (OETB) Programme on "Ocean Science in Relation to Non-Living Resources (OSNLR)"; Havana, Cuba, 4-7 December 1986	E, S	67	Interdisciplinary Seminar on Research Problems in the IOCARIBE Region; Caracas, Venezuela, 28 November-1 December 1989.	E (out of stock)	87	Taller de trabajo sobre efectos biológicos del fenómeno «El Niño» en ecosistemas costeros del Pacífico Sudeste; Santa Cruz, Galápagos, Ecuador, 5-14 de octubre de 1989.	S only (summary in E, F, S)
9	AGU-IOC-WMO-CPPS Chapman Conference: An International Symposium on 'El Niño'; Guayaquil, Ecuador, 27-31 October 1986.	E	68	International Workshop on Marine Acoustics; Beijing, China, 26-30 March 1990.	E	88	IOC-CEC-ICSU-ICES Regional Workshop for Member States of Eastern and Northern Europe (GODAR Project); Obninsk, Russia, 17-20 May 1993.	E
0	CCALR-IOC Scientific Seminar on Antarctic Ocean Variability and its Influence on Marine Living Resources, particularly Krill (organized in collaboration with SCAR and SCOR); Paris, France, 2-6 June 1987.	E	69	IOC-SCAR Workshop on Sea-Level Measurements in the Antarctica; Leningrad, USSR, 28-31 May 1990.	E	89	IOC-ICSEM Workshop on Ocean Sciences in Non-Living Resources; Perpignan, France, 15-20 October 1990.	E
1	CCOP/SOPAC-IOC Workshop on Coastal Processes in the South Pacific Island Nations; Lae, Papua-New Guinea, 1-8 October 1987.	E	70	IOC-SAREC-UNEP-FAO-IAEA-WHO Workshop on Regional Aspects of Marine Pollution; Mauritius, 29 October - 9 November 1990.	E	90	IOC Seminar on Integrated Coastal Management; New Orleans, U.S.A., 17-18 July 1993.	E
2	SCOR-IOC-UNESCO Symposium on Vertical Motion in the Equatorial Upper Ocean and its Effects upon Living Resources and the Atmosphere; Paris, France, 6-10 May 1985.	E	71	IOC-FAO Workshop on the Identification of Penaeid Prawn Larvae and Postlarvae; Cleveland, Australia, 23-28 September 1990.	E	91	Hydroblack'91 CTD Intercalibration Workshop; Woods Hole, U.S.A., 1-10 December 1991.	E
3	IOC Workshop on the Biological Effects of Pollutants; Oslo, 11-29 August 1986.	E	72	IOC/WESTPAC Scientific Steering Group Meeting on Co-Operative Study of the Continental Shelf Circulation in the Western Pacific; Kuala Lumpur, Malaysia, 9-11 October 1990.	E	92	Réunion de travail IOCEA-OSNLR sur le Projet « Budgets sédimentaires le long de la côte occidentale d'Afrique » Abidjan, côte d'Ivoire, 26-28 juin 1991.	E
4	Workshop on Sea-Level Measurements in Hostile Conditions; Bidston, UK, 28-31 March 1988.	E	73	Expert Consultation for the IOC Programme on Coastal Ocean Advanced Science and Technology Study; Liège, Belgium, 11-13 May 1991.	E	93	IOC-UNEP Workshop on Impacts of Sea-Level Rise due to Global Warming; Dhaka, Bangladesh, 16-19 November 1992.	E
5	IBCCA Workshop on Data Sources and Compilation; Boulder, Colorado, 18-19 July 1988.	E	74	IOC-UNEP Review Meeting on Oceanographic Processes of Transport and Distribution of Pollutants in the Sea; Zagreb, Yugoslavia, 15-18 May 1989.	E	94	BMT-IOC-POLARMAR International Workshop on Training Requirements in the Field of Eutrophication in Semi-enclosed Seas and Harmful Algal Blooms; Bremerhaven, Germany, 29 September-3 October 1992.	E
6	IOC-FAO Workshop on Recruitment of Penaeid Prawns in the Indo-West Pacific Region (PREP); Cleveland, Australia, 24-30 July 1988.	E	75	IOC-SCOR Workshop on Global Ocean Ecosystem Dynamics; Solomons, Maryland, U.S.A., 29 April-2 May 1991.	E	95	SAREC-IOC Workshop on Donor Collaboration in the Development of Marine Scientific Research Capabilities in the Western Indian Ocean Region; Brussels, Belgium, 23-25 November 1993.	E
7	IOC Workshop on International Co-operation in the Study of Red Tides and Ocean Blooms; Takamatsu, Japan, 16-17 November 1987.	E	76	IOC/WESTPAC Scientific Symposium on Marine Science and Management of Marine Areas of the Western Pacific; Penang, Malaysia, 2-6 December 1991.	E	96	IOC-UNEP-WMO-SAREC Planning Workshop on an Integrated Approach to Coastal Erosion, Sea Level Changes and their Impacts; Zanzibar, United Republic of Tanzania, 17-21 January 1994.	E
8	International Workshop on the Technical Aspects of the Tsunami Warning System; Novosibirsk, USSR, 4-5 August 1989.	E	77	IOC-SAREC-KMFRI Regional Workshop on Causes and Consequences of Sea-Level Changes on the Western Indian Ocean Coasts and Islands; Mombasa, Kenya, 24-28 June 1991.	E	96 Suppl.	IOC-UNEP-WMO-SAREC Planning Workshop on an Integrated Approach to Coastal Erosion, Sea Level Changes and their Impacts; Submitted Papers 1. Coastal Erosion; Zanzibar, United Republic of Tanzania 17-21 January 1994.	E
9	Second International Workshop on the Technical Aspects of Tsunami Warning Systems, Tsunami Analysis, Preparedness, Observation and Instrumentation. Submitted Papers; Novosibirsk, USSR, 4-5 August 1989.	E	78	IOC-CEC-ICES-WMO-ICSU Ocean Climate Data Workshop Goddard Space Flight Center, Greenbelt, Maryland, U.S.A., 18-21 February 1992.	E	96 Suppl.	IOC-UNEP-WMO-SAREC Planning Workshop on an Integrated Approach to Coastal Erosion, Sea Level Changes and their Impacts; Submitted Papers 2. Sea Level; Zanzibar, United Republic of Tanzania 17-21 January 1994.	E
0	IOC-UNEP Regional Workshop to Review Priorities for Marine Pollution Monitoring Research, Control and Abatement in the Wider Caribbean; San José, Costa Rica, 24-30 August 1989.	E, F, S	79	IOC/WESTPAC Workshop on River Inputs of Nutrients to the Marine Environment in the WESTPAC Region; Penang, Malaysia, 26-29 November 1991.	E	97	IOC Workshop on Small Island Oceanography in Relation to Sustainable Economic Development and Coastal Area Management of Small Island Development States; Fort-de-France, Martinique, 8-10 November, 1993.	E
1	IOC Workshop to Define IOCARIBE-TRODERP proposals; Caracas, Venezuela, 12-16 September 1989.	E	80	IOC-SCOR Workshop on Programme Development for Harmful Algae Blooms; Newport, U.S.A., 2-3 November 1991.	E	98	CoMSBlack '92A Physical and Chemical Intercalibration Workshop; Erdemli, Turkey, 15-29 January 1993.	E
2	Second IOC Workshop on the Biological Effects of Pollutants; Bermuda, 10 September-2 October 1988.	E	81	Joint IAPSO-IOC Workshop on Sea Level Measurements and Quality Control; Paris, France, 12-13 October 1992.	E	99	IOC-SAREC Field Study Exercise on Nutrients in Tropical Marine Waters; Mombasa, Kenya, 5-15 April 1994.	E
3	Second Workshop of Participants in the Joint FAO-IOC-WHO-IAEA-UNEP Project on Monitoring of Pollution in the Marine Environment of the West and Central African Region; Accra, Ghana, 13-17 June 1988.	E	82	BORDOMER 92: International Convention on Rational Use of Coastal Zones. A Preparatory Meeting for the Organization of an International Conference on Coastal Change; Bordeaux, France, 30 September-2 October 1992.	E	100	IOC-SOA-NOAA Regional Workshop for Member States of the Western Pacific - GODAR-II (Global Oceanographic Data Archeology and Rescue Project); Tianjin, China, 8-11 March 1994.	E
4	IOC/WESTPAC Workshop on Co-operative Study of the Continental Shelf Circulation in the Western Pacific; Bangkok, Thailand, 31 October-3 November 1989.	E	83	IOC Workshop on Donor Collaboration in the Development of Marine Scientific Research Capabilities in the Western Indian Ocean Region; Brussels, Belgium, 12-13 October 1992.	E	101	IOC Regional Science Planning Workshop on Harmful Algal Blooms; Montevideo, Uruguay, 15-17 June 1994.	E
5	Second IOC-FAO Workshop on Recruitment of Penaeid Prawns in the Indo-West Pacific Region (PREP); Phuket, Thailand, 25-31 September 1989.	E	84	Workshop on Atlantic Ocean Climate Variability; Moscow, Russian Federation, 13-17 July 1992	E			

No.	Title	Languages	No.	Title	Languages	No.	Title	Languages
102	First IOC Workshop on Coastal Ocean Advanced Science and Technology Study (COASTS); Liège, Belgium, 5-9 May 1994.	E	121	IOC-EU-BSH-NOAA-(WDC-A) International Workshop on Oceanographic Biological and Chemical Data Management, Hamburg, Germany, 20-23 May 1996.	E	143	Geosphere-biosphere coupling: Carbonate Mud Mounds and Cold Water Reefs; Gent, Belgium, 7-11 February 1998.	E
103	IOC Workshop on GIS Applications in the Coastal Zone Management of Small Island Developing States; Barbados, 20-22 April 1994.	E	122	IOC-EU-BSH-NOAA-(WDC-A) International Workshop on Oceanographic Biological and Chemical Data Management, Hamburg, Germany, 20-23 May 1996.	E	144	IOC-SOPAC Workshop Report on Pacific Regional Global Ocean Observing Systems; Suva, Fiji, 13-17 February 1998.	E
104	Workshop on Integrated Coastal Management; Dartmouth, Canada, 19-20 September 1994.	E	123	Second IOC Regional Science Planning Workshop on Harmful Algal Blooms in South America; Mar del Plata, Argentina, 30 October - 1 November 1995.	E, S	145	IOC-Black Sea Regional Committee Workshop: 'Black Sea Fluxes' Istanbul, Turkey, 10-12 June 1997.	E
105	BORDOMER 95: Conference on Coastal Change; Bordeaux, France, 6-10 February 1995.	E	124	GLOBEC-IOC-SAHFOS-MBA Workshop on the Analysis of Time Series with Particular Reference to the Continuous Plankton Recorder Survey; Plymouth, U.K., 4-7 May 1993.	E	146	Living Marine Resources Panel Meeting, Paris, France, 23-25 March 1998.	E
105 Suppl.	Conference on Coastal Change: Proceedings; Bordeaux, France, 6-10 February 1995.	E	125	Atelier sous-régional de la COI sur les ressources marines vivantes du Golfe de Guinée; Cotonou, Bénin, 1-4 juillet 1996.	E	147	IOC-SOA International Training Workshop on the Integration of Marine Sciences into the Process of Integrated Coastal Management, Dalian, China, 19-24 May 1997.	E
106	IOC/WESTPAC Workshop on the Paleographic Map; Bali, Indonesia, 20-21 October 1994.	E	126	IOC-UNEP-PERSGA-ACOPS-IUCN Workshop on Oceanographic Input to Integrated Coastal Zone Management in the Red Sea and Gulf of Aden, Jeddah, Saudi Arabia, 8 October 1995.	E	148	IOC/WESTPAC International Scientific Symposium - Role of Ocean Sciences for Sustainable Development Okinawa, Japan, 2-7 February 1998.	E
107	IOC-ICSU-NOAA Regional Workshop for Member States of the Indian Ocean - GODAR-III; Dona Paula, Goa, India, 6-9 December 1994.	E	127	IOC Regional Workshop for Member States of the Caribbean and South America GODAR-V (Global Oceanographic Data Archeology and Rescue Project); Cartagena de Indias, Colombia, 8-11 October 1996.	E	149	Workshops on Marine Debris & Waste Management in the Gulf of Guinea, 1995-97.	E
108	UNESCO-IHP-IOC-IAEA Workshop on Sea-Level Rise and the Multidisciplinary Studies of Environmental Processes in the Caspian Sea Region; Paris, France, 9-12 May 1995.	E	128	Atelier IOC-Banque Mondiale-Sida/SAREC-ONE sur la Gestion Intégrée des Zones Côtières; Nosy Bé, Madagascar, 14-18 octobre 1996.	E	150	First IOCARIBE-ANCA Workshop Havana, Cuba, 29 June-1 July 1998.	E
108 Suppl.	UNESCO-IHP-IOC-IAEA Workshop on Sea-Level Rise and the Multidisciplinary Studies of Environmental Processes in the Caspian Sea Region; Submitted Papers; Paris, France, 9-12 May 1995.	E	129	Gas and Fluids in Marine Sediments, Amsterdam, the Netherlands; 27-29 January 1997.	E	151	Taller Pluridisciplinario TEMA sobre Redes del Gran Caribe en Gestión Integrada de Areas Costeras Cartagena de Indias, Colombia, 7-12 de septiembre de 1998.	S
109	First IOC-UNEP CEPOL Symposium; San José, Costa Rica, 14-15 April 1993.	E	130	Atelier régional de la COI sur l'océanographie côtière et la gestion de la zone côtière; Moroni, RFI des Comores, 16-19 décembre 1996.	E	152	Workshop on Data for Sustainable Integrated Coastal Management (SICOM) Maputo, Mozambique, 18-22 July 1998.	E
110	IOC-ICSU-CEC regional Workshop for Member States of the Mediterranean - GODAR-IV (Global Oceanographic Data Archeology and Rescue Project) Foundation for International Studies, University of Malta, Valletta, Malta, 25-28 April 1995.	E	131	GOOS Coastal Module Planning Workshop; Miami, USA, 24-28 February 1997.	E	153	IOC/WESTPAC-Sida (SAREC) Workshop on Atmospheric Inputs of Pollutants to the Marine Environment Qingdao, China, 24-26 June 1998.	E
111	Chapman Conference on the Circulation of the Intra-Americas Sea; La Parguera, Puerto Rico, 22-26 January 1995.	E	132	Third IOC-FANSA Workshop; Punta-Arenas, Chile, 28-30 July 1997.	S/E	154	IOC-Sida-Flanders-SFRI Workshop on Ocean Data Management in the IOCINCWIO Region (ODINEA project) Capetown, South Africa, 30 November-11 December 1998.	E
112	IOC-IAEA-UNEP Group of Experts on Standards and Reference Materials (GESREM) Workshop; Miami, U.S.A., 7-8 December 1993.	E	133	Joint IOC-CIESM Training Workshop on Sea-level Observations and Analysis for the Countries of the Mediterranean and Black Seas; Birkenhead, U.K., 16-27 June 1997.	E	155	Science of the Mediterranean Sea and its applications UNESCO, Paris 29-31 July 1997.	E
113	IOC Regional Workshop on Marine Debris and Waste Management in the Gulf of Guinea; Lagos, Nigeria, 14-16 December 1994.	E	134	IOC/WESTPAC-CCOP Workshop on Paleogeographic Mapping (Holocene Optimum); Shanghai, China, 27-29 May 1997.	E	156	IOC-LUC-KMFRI Workshop on RECOSCIX-WIO in the Year 2000 and Beyond, Mombasa, Kenya, 12-16 April 1999.	E
114	International Workshop on Integrated Coastal Zone Management (ICZM) Karachi, Pakistan, 10-14 October 1994.	E	135	Regional Workshop on Integrated Coastal Zone Management; Chabahar, Iran; February 1996.	E	157	IOC-KMI International Workshop on Integrated Coastal Management (ICM), Seoul, Republic of Korea 18-18 April 1998.	E
115	IOC/GLOSS-IAPSO Workshop on Sea Level Variability and Southern Ocean Dynamics; Bordeaux, France, 31 January 1995.	E	136	IOC Regional Workshop for Member States of Western Africa (GODAR-VI); Accra, Ghana, 22-25 April 1997.	E	158	The IOCARIBE Users and the Global Ocean Observing System (GOOS) Capacity Building Workshop, San José, Costa Rica, 22-24 April 1999.	E
116	IOC/WESTPAC International Scientific Symposium on Sustainability of Marine Environment: Review of the WESTPAC Programme, with Particular Reference to ICAM, Bali, Indonesia, 22-26 November 1994.	E	137	GOOS Planning Workshop for Living Marine Resources, Dartmouth, USA; 1-5 March 1996.	E	159	Oceanic Fronts and Related Phenomena (Konstantin Federov Memorial Symposium) - Proceedings, Pushkin, Russian Federation, 18-22 May 1998.	E
117	Joint IOC-CIDA-Sida (SAREC) Workshop on the Benefits of Improved Relationships between International Development Agencies, the IOC and other Multilateral Inter-governmental Organizations in the Delivery of Ocean, Marine Affairs and Fisheries Programmes; Sidney B.C., Canada, 26-28 September 1995.	E	138	Gestión de Sistemas Oceanográficos del Pacífico Oriental; Concepción, Chile, 9-16 de abril de 1996.	S			
118	IOC-UNEP-NOAA-Sea Grant Fourth Caribbean Marine Debris Workshop; La Romana, Santo Domingo, 21-24 August 1995.	E	139	Sistemas Oceanográficos del Atlántico Sudoccidental, Taller, TEMA:Furg, Rio Grande, Brasil, 3-11 de noviembre de 1997.	S			
119	IOC Workshop on Ocean Colour Data Requirements and Utilization; Sydney B.C., Canada, 21-22 September 1995.	E	140	IOC Workshop on GOOS Capacity Building for the Mediterranean Region; Valletta, Malta, 26-29 November 1997.	E			
120	International Training Workshop on Integrated Coastal Management; Tampa, Florida, U.S.A., 15-17 July 1995.	E	141	IOC/WESTPAC Workshop on Co-operative Study in the Gulf of Thailand: A Science Plan; Bangkok, Thailand, 25-28 February 1997.	E			
			142	Pelagic Biogeography ICoPB II. Proceedings of the 2nd International Conference. Final Report of SCOR/IOC Working Group 93; Noordwijkerhout, The Netherlands, 9-14 July 1995.	E			

Intergovernmental Oceanographic Commission

Workshop Report No. 159

**OCEANIC FRONTS
AND RELATED PHENOMENA**
Konstantin Fedorov International Memorial Symposium

Pushkin, Saint Petersburg
Russian Federation
18-22 May 1998

Proceedings

Publishing office GEOS
7, Pyzhevsky per., Moscow, 109017, Russian Federation
Tel.: (095) 230-80-92/ Fax: (095) 951-04-43. E-mail: geos@ginran.msk.ru

Подписано к печати 16.10.2000 г.
Формат 62x94 1/8. Бумага офсет № 1, 80 г/м²
Усл. печ. л. 82,0. Тираж 400 экз.
Тип. зак. № 562С, Москва